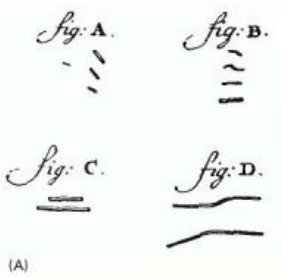

(A)

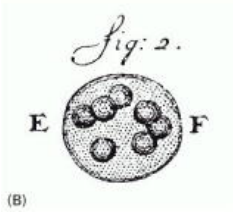

(B)

Figure 8-1. Microscopic life. A sample of "diverse animalcules" seen by van Leeuwenhoek using his simple microscope. (A) Bacteria seen in material he excavated from between his teeth. Those in fig. B he described as "swimming first forward and then backwards" (1692). (B) The eucaryotic green alga *Volvox* (1700). (Courtesy of the John Innes Foundation.)

An egg cell. The DNA of this single cell contains the genetic information needed to specify construction of an entire multicellular animal - in this case, a frog, *Xenopus laevis.* (Courtesy of Tony Mills.)

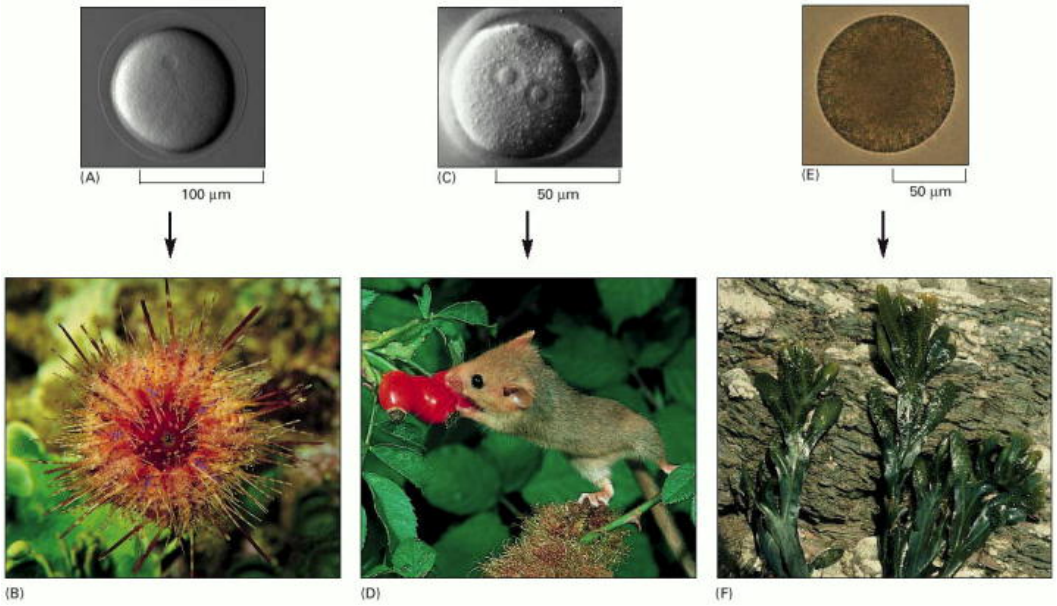

Figure 1-1. The hereditary information in the egg cell determines the nature of the whole multicellular organism. (A and B) A sea urchin egg gives rise to a sea urchin. (C and D) A mouse egg gives rise to a mouse. (E and F) An egg of the seaweed *Fucus* gives rise to a *Fucus* seaweed. (A, courtesy of David McClay; B, courtesy of M. Gibbs, Oxford Scientific Films; C, courtesy of Patricia Calarco, from G. Martin, *Science* 209:768776, 1980. © AAAS; D, courtesy of O. Newman, Oxford Scientific Films; E and F, courtesy of Colin Brownlee.)

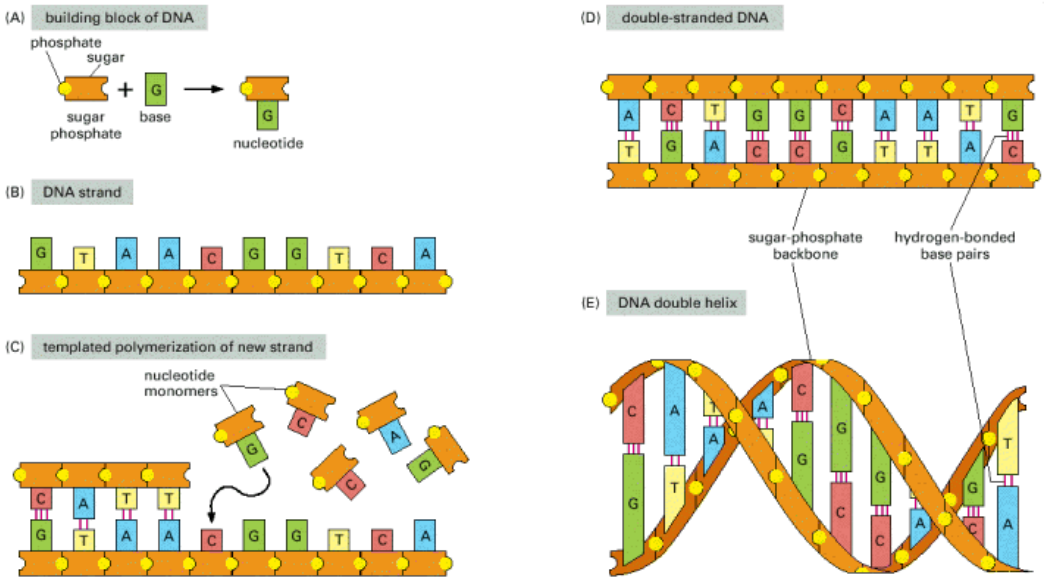

Figure 1-2. DNA and its building blocks. (A) DNA is made from simple subunits, called nucleotides, each consisting of a sugar-phosphate molecule with a nitrogen-containing sidegroup, or base, attached to it. The bases are of four types (adenine, guanine, cytosine, and thymine), corresponding to four distinct nucleotides, labeled A, G, C, and T. (B) A single strand of DNA consists of nucleotides joined together by sugar-phosphate linkages. Note that the individual sugar-phosphate units are asymmetric, giving the backbone of the strand a definite directionality, or polarity. This directionality guides the molecular processes by which the information in DNA is interpreted and copied in cells: the information is always "read" in a consistent order, just as written English text is read from left to right. (C) Through templated polymerization, the sequence of nucleotides in an existing DNA strand controls the sequence in which nucleotides are joined together in a new DNA strand; T in one strand pairs with A in the other, and G in one strand with C in the other. The new strand has a nucleotide sequence complementary to that of the old strand, and a backbone with opposite directionality: corresponding to the GTAA... of the original strand, it has ...TTAC. (D) A normal DNA molecule consists of two such complementary strands. The nucleotides within each strand are linked by strong (covalent) chemical bonds; the complementary nucleotides on opposite strands are held together more weakly, by hydrogen bonds. (E) The two strands twist around each other to form a double helix - a robust structure that can accommodate any sequence of nucleotides without altering its basic structure.

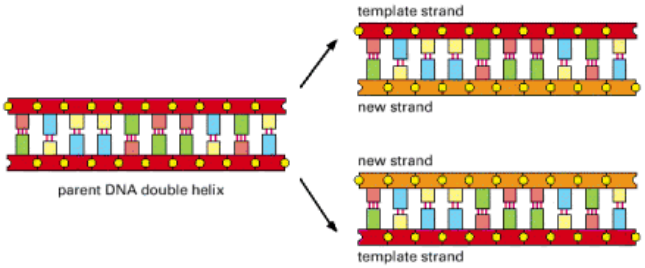

Figure 1-3. The duplication of genetic information by DNA replication. In this process, the two strands of a DNA double helix are pulled apart, and each serves as a template for synthesis of a new complementary strand.

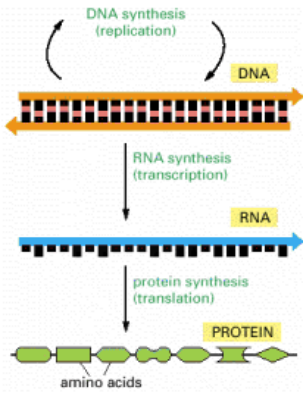

Figure 1-4. From DNA to protein. Genetic information is read out and put to use through a two-step process. First, in *transcription*, segments of the DNA sequence are used to guide the synthesis of molecules of RNA. Then, in *translation*, the RNA molecules are used to guide the synthesis of molecules of protein.

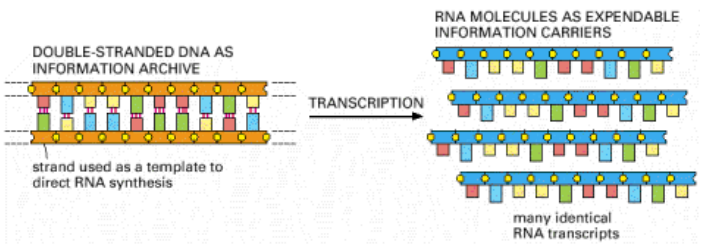

Figure 1-5. How genetic information is broadcast for use inside the cell. Each cell contains a fixed set of DNA molecules - its archive of genetic information. A given segment of this DNA serves to guide the synthesis of many identical RNA transcripts, which serve as working copies of the information stored in the archive. Many different sets of RNA molecules can be made by transcribing selected parts of a long DNA sequence, allowing each cell to use its information store differently.

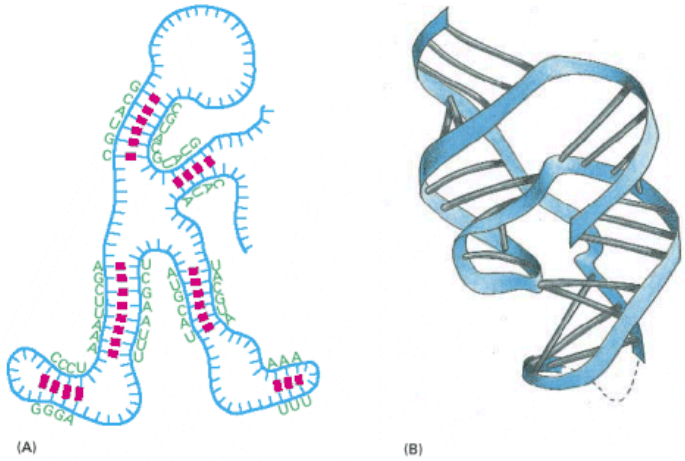

Figure 1-6. The conformation of an RNA molecule. (A) Nucleotide pairing between different regions of the same RNA polymer chain causes the molecule to adopt a distinctive shape. (B) The three-dimensional structure of an actual RNA molecule, from hepatitis delta virus, that catalyzes RNA strand cleavage. (B, based on A.R. Ferré D'Amaré, K. Zhou, and J.A. Doudna, *Nature* 395:567574, 1998. © Macmillan Magazines Ltd.)

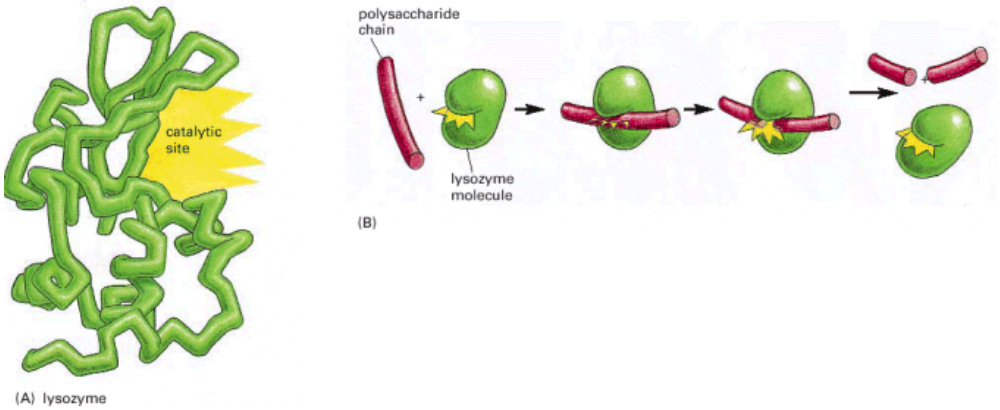

Figure 1-7. How a protein molecule acts as catalyst for a chemical reaction. (A) In a protein molecule the polymer chain folds up to into a specific shape defined by its amino acid sequence. A groove in the surface of this particular folded molecule, the enzyme lysozyme, forms a catalytic site. (B) A polysaccharide molecule *(red)* - a polymer chain of sugar monomers - binds to the catalytic site of lysozyme and is broken apart, as a result of a covalent bond-breaking reaction catalyzed by the amino acids lining the groove.

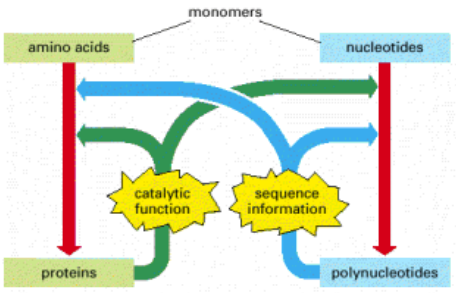

Figure 1-8. Life as an autocatalytic process. Polynucleotides (nucleotide polymers) and proteins (amino acid polymers) provide the sequence information and the catalytic functions that serve - through a complex set of chemical reactions - to bring about the synthesis of more polynucleotides and proteins of the same types.

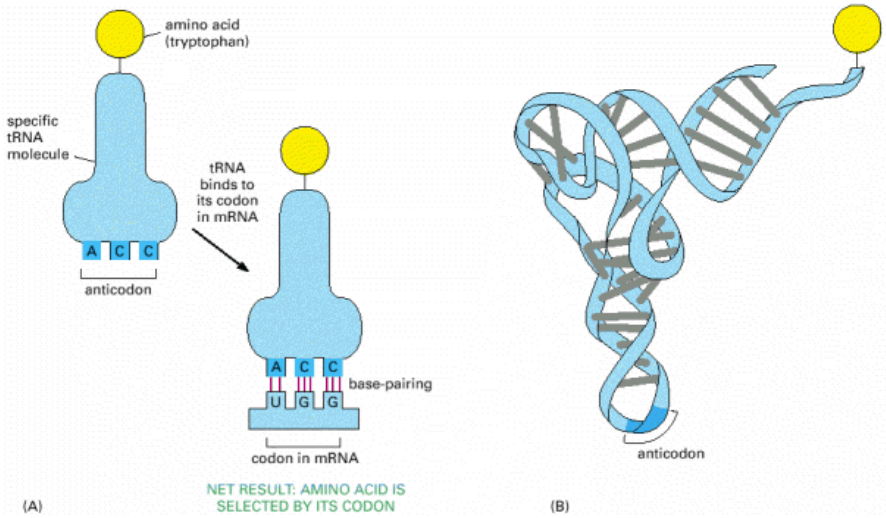

Figure 1-9. Transfer RNA. (A) A tRNA molecule specific for the amino acid tryptophan. One end of the tRNA molecule has tryptophan attached to it, while the other end displays the triplet nucleotide sequence CCA (its anticodon), which recognizes the tryptophan codon in messenger RNA molecules. (B) The three-dimensional structure of the tryptophan tRNA molecule. Note that the codon and the anticodon in (A) are in antiparallel orientations, like the two strands in a DNA double helix (see Figure 1-2), so that the sequence of the anticodon in the tRNA is read from right to left, while that of the codon in the mRNA is read from left to right.

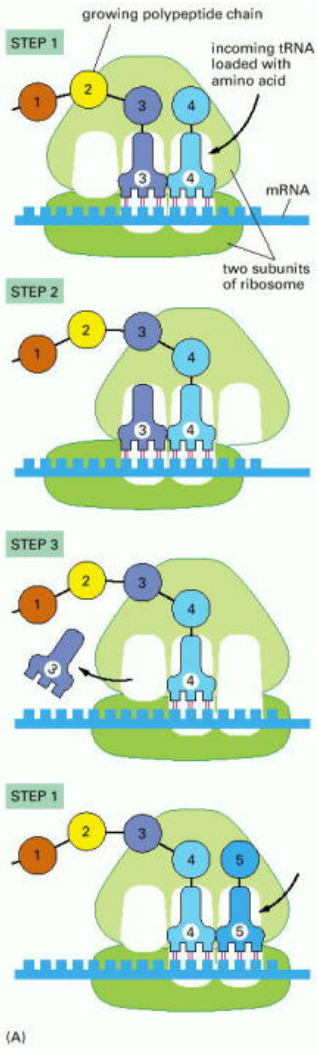

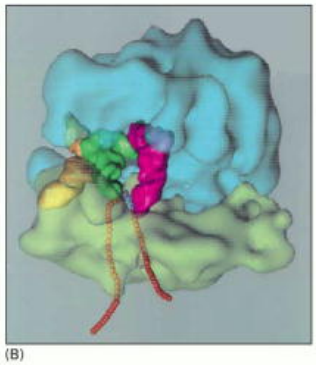

Figure 1-10. A ribosome at work. (A) The diagram shows how a ribosome moves along an mRNA molecule, capturing tRNA molecules that match the codons in the mRNA and using them to join amino acids into a protein chain. The mRNA specifies the sequence of amino acids. (B) The three-dimensional structure of a bacterial ribosome *(pale green* and *blue),* moving along an mRNA molecule *(orange* beads*),* with three tRNA molecules *(yellow*, *green*, and *pink)* at different stages in their process of capture and release. The ribosome is a giant assembly of more than 50 individual protein and RNA molecules. (B, courtesy of Joachim Frank, Yanhong Li, and Rajendra Agarwal.)

Figure 1-11. (A) A diagram of a small portion of the genome of the bacterium Escherichia coli, containing genes (called *lacI, lacZ, lacY,* and *lacA)* coding for four different proteins. The protein-coding DNA segments *(red)* have regulatory and other noncoding DNA segments *(yellow)* between them. (B) An electron micrograph of DNA from this region, with a protein molecule

(encoded by the *lac1* gene) bound to the regulatory segment; this protein controls the rate of transcription of the *lacZ*, *lacY*, and *lacA* genes. (C) A drawing of the structures shown in (B). (B, courtesy of Jack Griffith.)

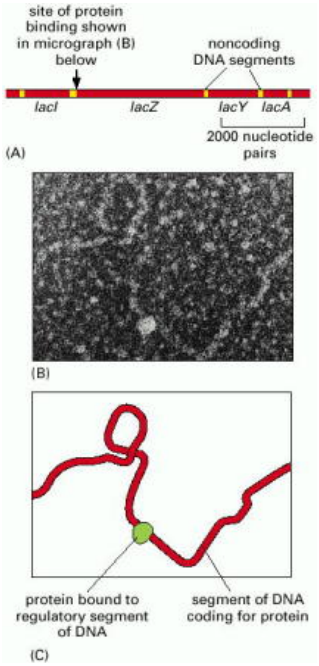

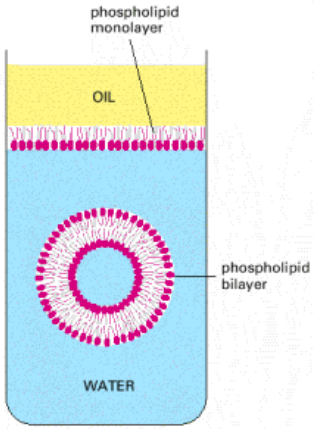

Figure 1-12. Formation of a membrane by amphipathic phospholipid molecules. These have a hydrophilic (water-loving, phosphate) head group and a hydrophobic (water-avoiding, hydrocarbon) tail. At an interface between oil and water, they arrange themselves as a single sheet with their head groups facing the water and their tail groups facing the oil. When immersed in water, they aggregate to form bilayers enclosing aqueous compartments.

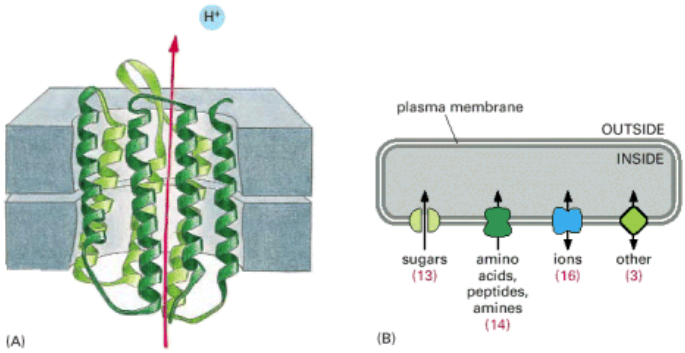

Figure 1-13. Membrane transport proteins. (A) Structure of a molecule of bacteriorhodopsin, from the archaean (archaebacterium) *Halobacterium halobium*. This transport protein uses the energy of absorbed light to pump protons (H^+ ions) out of the cell. The polypeptide chain threads to and fro across the membrane; in several regions it is twisted into a helical conformation, and the helical segments are arranged to form the walls of a channel through which ions are transported. (B) Diagram of the set of transport proteins found in the membrane of the bacterium *Thermotoga maritima*. The numbers in parentheses refer to the number of different membrane transport proteins of each type. Most of the proteins within each class are evolutionarily related to one another and to their counterparts in other species.

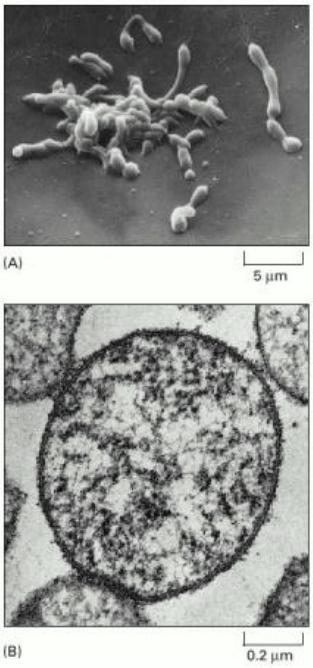

Figure 1-14. *Mycoplasma genitalium.* (A) Scanning electron micrograph showing the irregular shape of this small bacterium, reflecting the lack of any rigid wall. (B) Cross section (transmission electron micrograph) of a *Mycoplasma* cell. Of the 477 genes of *Mycoplasma genitalium*, 37 code for transfer, ribosomal, and other nonmessenger RNAs. Functions are known, or can be guessed, for 297 of the genes coding for protein: of these, 153 are involved in DNA replication, transcription, and translation and related processes involving DNA, RNA, and protein; 29 in the membrane and surface structures of the cell; 33 in the transport of nutrients and other molecules across the membrane; 71 in energy conversion and the synthesis and degradation of small molecules; and 11 in the regulation of cell division and other processes. (A, from S. Razin, M. Banai, H. Gamliel, A. Pollack, W. Bredt, and I. Kahane, *Infect. Immun.* 30:538546, 1980; B, courtesy of Roger Cole, in Medical Microbiology, 4th edn., [S. Baron ed.]. Galveston: University of Texas Medical Branch, 1996.)

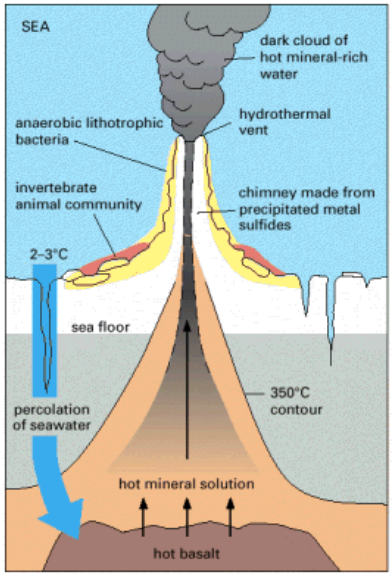

Figure 1-15. The geology of a hot hydrothermal vent in the ocean floor . Water percolates down toward the hot molten rock upwelling from the Earth's interior and is heated and driven back upward, carrying minerals leached from the hot rock. A temperature gradient is set up, from more than 350°C near the core of the vent, down to 23°C in the surrounding ocean. Minerals precipitate from the water as it cools, forming a chimney. Different classes of organisms, thriving at different temperatures, live in different neighborhoods of the chimney. A typical chimney might be a few meters tall, with a flow rate of 12 m/sec.

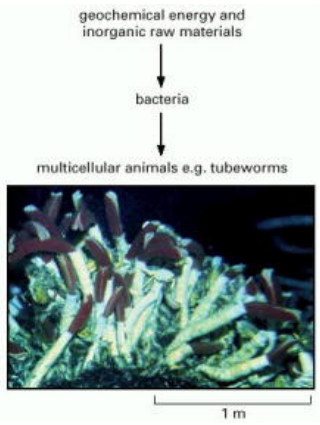

Figure 1-16. Living organisms at a hot hydrothermal vent. Close to the vent, at temperatures up to about 150°C, various lithotrophic species of bacteria and archaea (archaebacteria) live, directly fuelled by geochemical energy. A little further away, where the temperature is lower, various invertebrate animals live by feeding on these microorganisms. Most remarkable are the giant (2-meter) tube worms, which, rather than feed on the lithotrophic cells, live in symbiosis with them: specialized organs in the worms harbor huge numbers of symbiotic sulfur-oxidizing bacteria. These bacteria harness geochemical energy and supply nourishment to their hosts, which have no mouth, gut, or anus. The dependence of the tube worms on the bacteria for the harnessing of geothermal energy is analogous to the dependence of plants on chloroplasts for the harnessing of solar energy, discussed later in this chapter. The tube worms, however, are thought to have evolved from more conventional animals, and to have become secondarily adapted to life at hydrothermal vents. (Courtesy of Dudley Foster, Woods Hole Oceanographic Institution.)

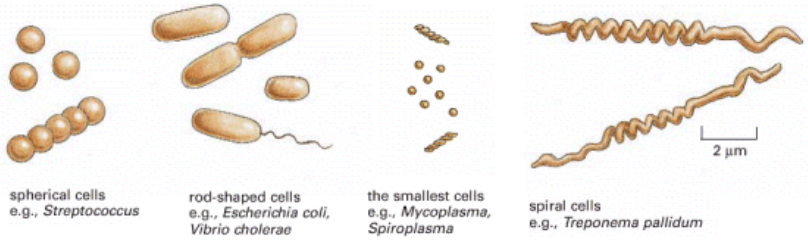

Figure 1-17. Shapes and sizes of some bacteria. Although most are small, as shown, there are also some giant species. An extreme example (not shown) is the cigar-shaped bacterium *Epulopiscium fishelsoni*, which lives in the gut of the surgeon fish and can be up to 600 µm long.

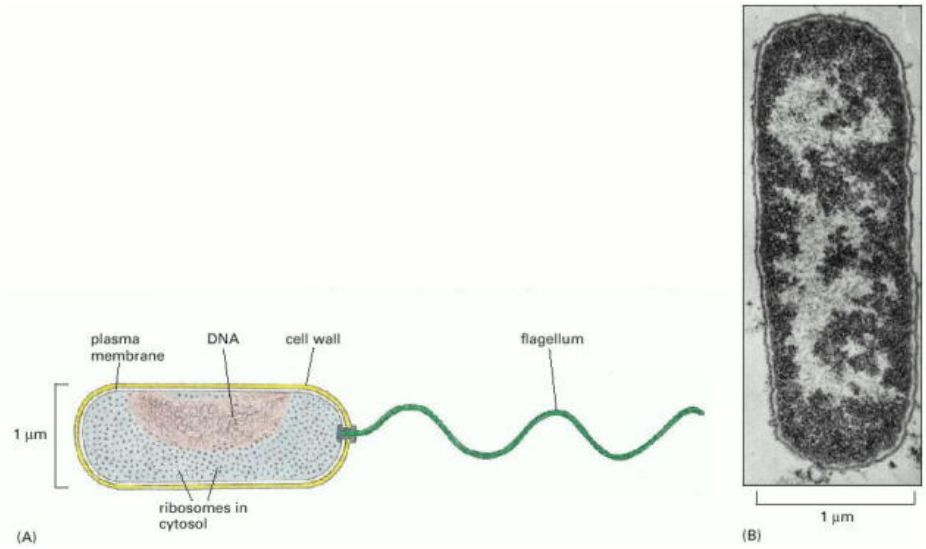

Figure 1-18. The structure of a bacterium. (A) The bacterium *Vibrio cholerae*, showing its simple internal organization. Like many other species, *Vibrio* has a helical appendage at one end - a flagellum - that rotates as a propeller to drive the cell forward. (B) An electron micrograph of a longitudinal section through the widely studied bacterium *Escherichia coli (E. coli).* This is related to *Vibrio* but lacks a flagellum. The cell's DNA is concentrated in the lightly stained region. (B, courtesy of E. Kellenberger.)

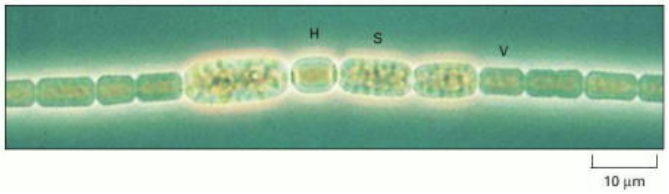

Figure 1-19. The phototrophic bacterium *Anabaena cylindrica* viewed in the light microscope. The cells of this species form long, multicellular filaments. Most of the cells (labeled *V)* perform photosynthesis, while others become specialized for nitrogen fixation (labeled *H),* or develop into resistant spores (labeled *S).* (Courtesy of Dave G. Adams.)

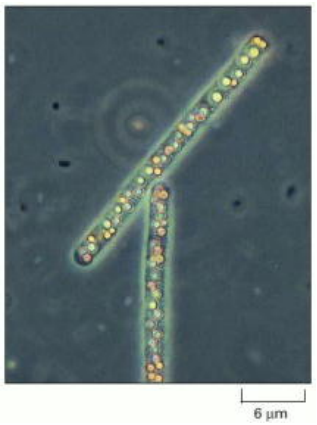

Figure 1-20. A lithotrophic bacterium. *Beggiatoa,* which lives in sulfurous environments, gets its energy by oxidizing H_2S and can fix carbon even in the dark. Note the yellow deposits of sulfur inside the cells. (Courtesy of Ralph W. Wolfe.)

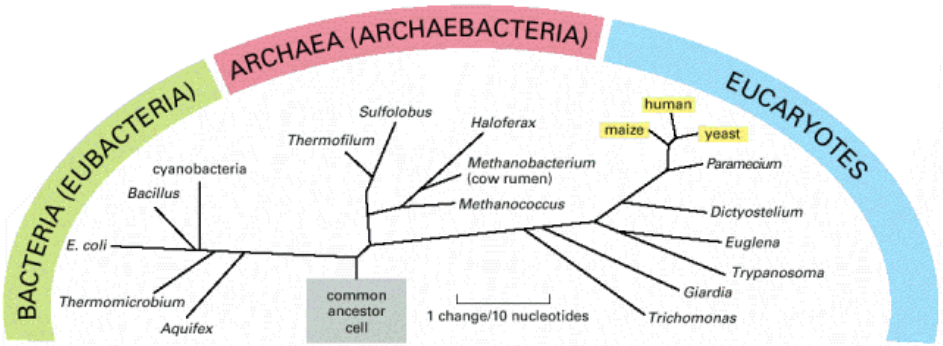

Figure 1-21. The three major divisions (domains) of the living world. Note that traditionally the word *bacteria* has been used to refer to procaryotes in general, but more recently has been redefined to refer to eubacteria specifically. Where there might be ambiguity, we use the term *eubacteria* when the narrow meaning is intended. The tree is based on comparisons of the nucleotide sequence of a ribosomal RNA subunit in the different species. The lengths of the lines represent the numbers of evolutionary changes that have occurred in this molecule in each lineage (see Figure 1-22).

Figure 1-22. Genetic information conserved since the beginnings of life. A part of the gene for the smaller of the two main RNA components of the ribosome is shown. Corresponding segments of nucleotide sequence from an archaean *(Methanococcus jannaschii)*, a eubacterium *(Escherichia coli)* and a eucaryote *(Homo sapiens)* are aligned in parallel. Sites where the nucleotides are identical between species are indicated by a vertical line; the human sequence is repeated at the bottom of the alignment so that all three two-way comparisons can be seen. A dot halfway along the *E. coli* sequence denotes a site where a nucleotide has been either deleted from the eubacterial lineage in the course of evolution, or inserted in the other two lineages. Note that the sequences from these three organisms, representative of the three domains of the living world, all differ from one another to a roughly similar degree, while still retaining unmistakable similarities.

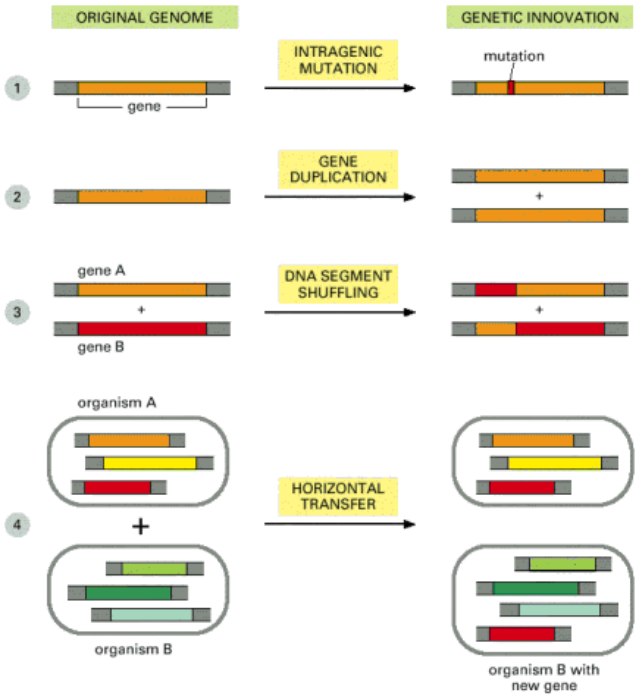

Figure 1-23. Four modes of genetic innovation and their effects on the DNA sequence of an organism.

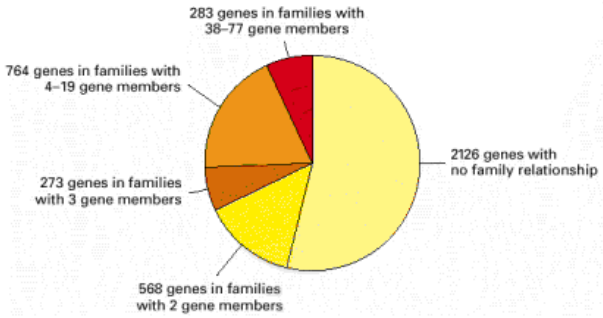

Figure 1-24. Families of evolutionarily related genes in the genome of *Bacillus subtilis.* The biggest family consists of 77 genes coding for varieties of ABC transporters - a class of membrane transport proteins found in all three domains of the living world. (After F. Kunst et al., *Nature* 390:249256, 1997. © Macmillan Magazines Ltd.)

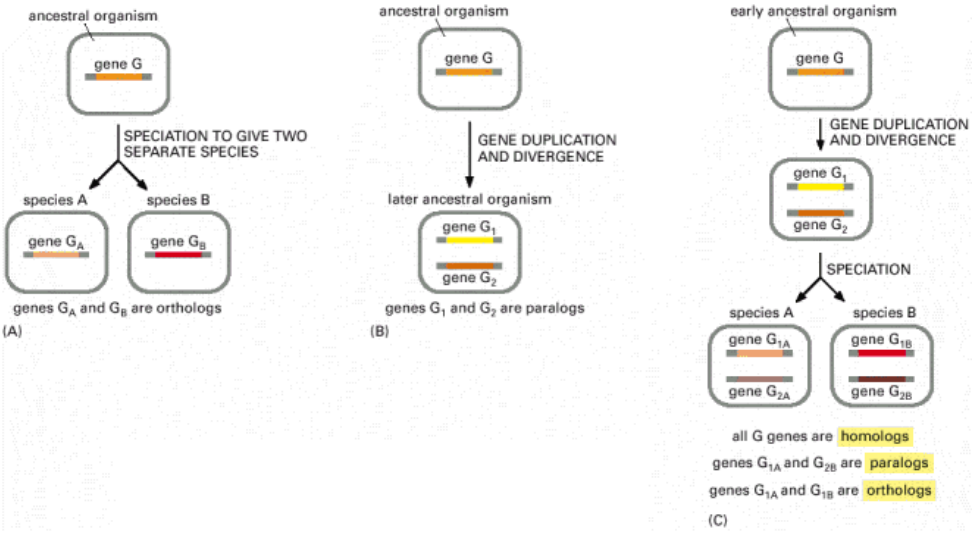

Figure 1-25. Paralogous genes and orthologous genes: two types of gene homology based on different evolutionary pathways. (A) and (B) The most basic possibilities. (C) A more complex pattern of events that can occur.

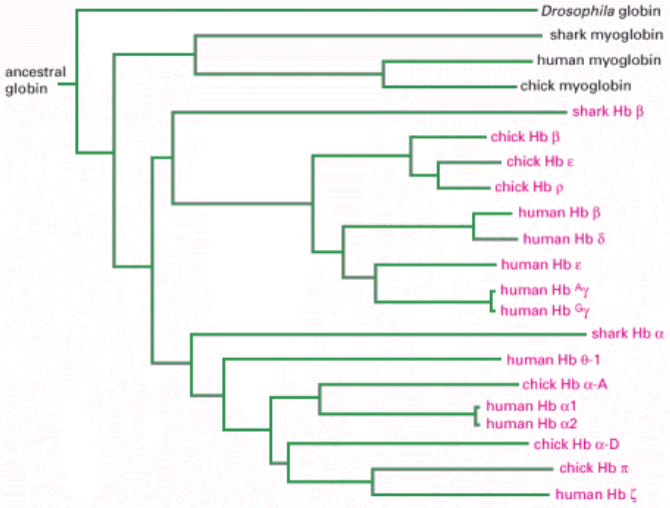

Figure 1-26. A complex family of homologous genes. This diagram shows the pedigree of the hemoglobin (Hb), myoglobin, and globin genes of human, chick, shark, and *Drosophila*. The lengths of the lines represent the amount of divergence in amino acid sequence.

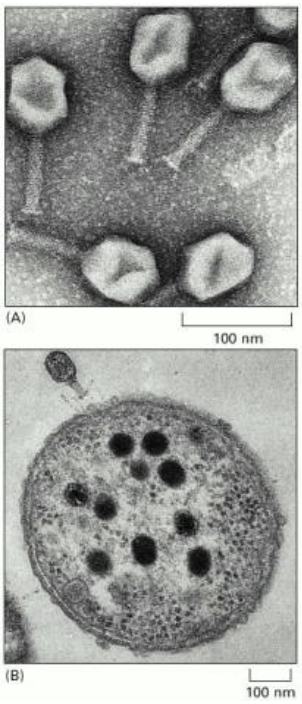

Figure 1-27. The viral transfer of DNA from one cell to another . (A) An electron micrograph of particles of a bacterial virus, the T4 bacteriophage. The head of this virus contains the viral DNA; the tail contains apparatus for injecting the DNA into a host bacterium. (B) A cross section of a bacterium with a T4 bacteriophage latched onto its surface. The large dark objects inside the bacterium are the heads of new T4 particles in course of assembly. When they are mature, the bacterium will burst open to release them. (A, courtesy of James Paulson; B, courtesy of Jonathan King and Erika Hartwig from G. Karp, Cell and Molecular Biology, 2nd edn. New York: John Wiley & Sons, 1999. © John Wiley.)

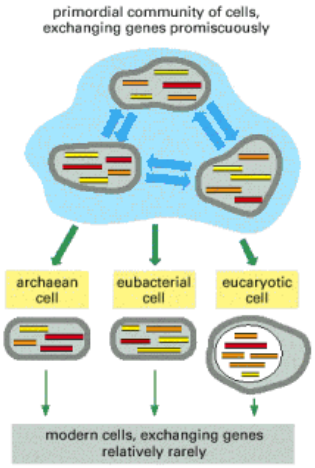

Figure 1-28. Horizontal gene transfers in early evolution. In the early days of life on Earth, cells may have been less capable of maintaining their separate identities and may have exchanged genes much more readily than now. In this way, the archaean, eubacterial, and eucaryotic lineages may have inherited different but overlapping subsets of genes from a primordial community of cells that were exchanging genes promiscuously.

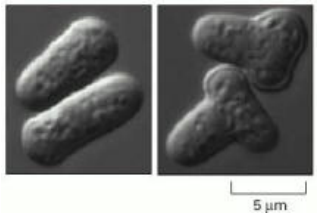

Figure 1-29. A mutant phenotype reflecting the function of a gene. A normal yeast (of the species *Schizosaccharomyces pombe)* is compared with a mutant in which a change in a single gene has converted the cell from a cigar shape *(left)* to a T shape *(right).* The mutant gene therefore has a function in the control of cell shape. But how, in molecular terms, does the gene product perform that function? That is a harder question, and needs biochemical analysis to answer it. (Courtesy of Kenneth Sawin and Paul Nurse.)

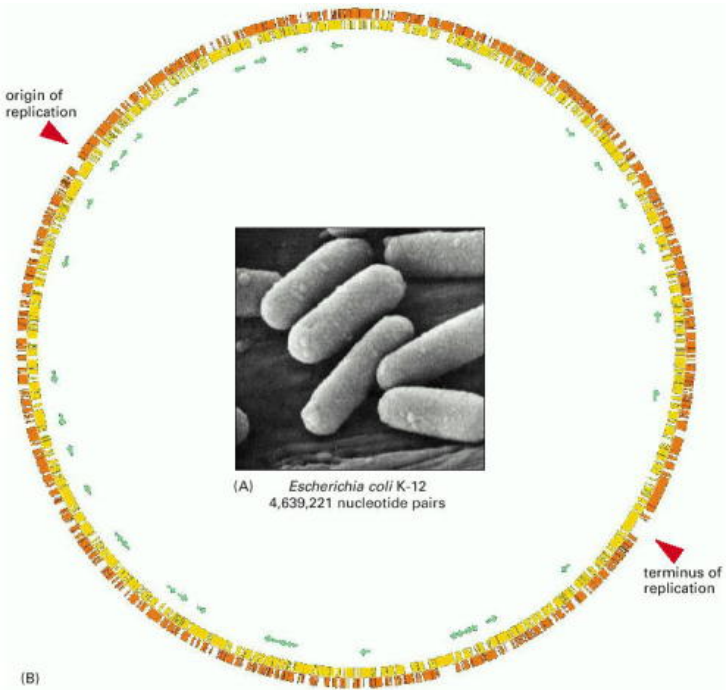

Figure 1-30. The genome of *E. coli.* (A) A cluster of *E. coli* cells. (B) A diagram of the *E. coli* genome of 4,639,221 nucleotide pairs (for *E. coli* strain K-12). The diagram is circular because the DNA of *E. coli*, like that of other procaryotes, forms a single, closed loop. Protein-coding genes are shown as *yellow* or *orange bars*, depending on the DNA strand from which they are transcribed; genes encoding only RNA molecules are indicated by *green arrows*. Some genes are transcribed from one strand of the DNA double helix (in a clockwise direction in this diagram), others from the other strand (counterclockwise). (A, courtesy of Tony Brain and the Science Photo Library; B, after F. R. Blattner et al., *Science* 277:14531462, 1997. © AAAS.)

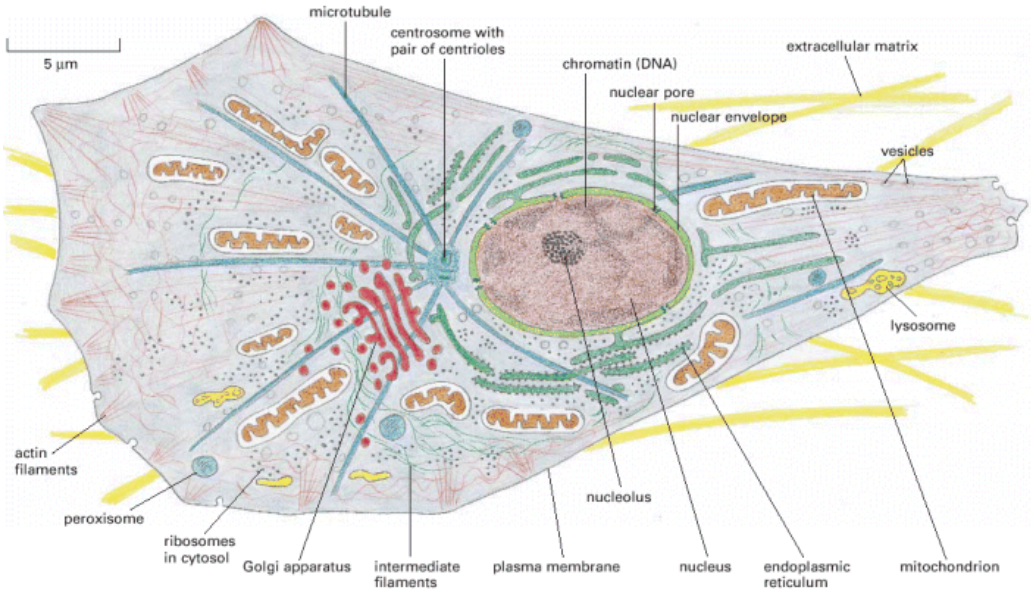

Figure 1-31. The major features of eucaryotic cells. The drawing depicts a typical animal cell, but almost all the same components are found in plants and fungi and in single-celled eucaryotes such as yeasts and protozoa. Plant cells contain chloroplasts in addition to the components shown here, and their plasma membrane is surrounded by a tough external wall formed of cellulose.

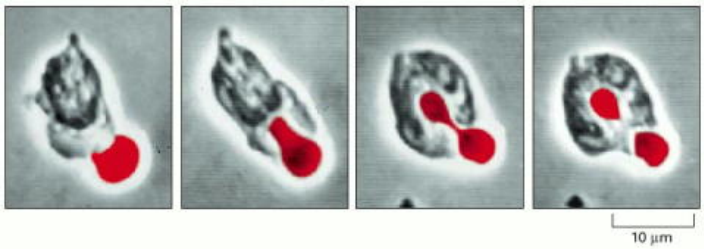

Figure 1-32. Phagocytosis. This series of stills from a movie shows a human white blood cell (a neutrophil) engulfing a red blood cell (artificially colored *red)* that has been treated with antibody. (Courtesy of Stephen E. Malawista and Anne de Boisfleury Chevance.)

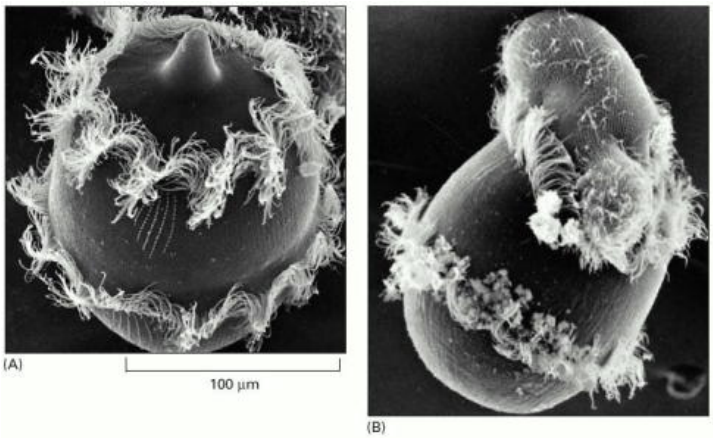

Figure 1-33. A single-celled eucaryote that eats other cells. (A) *Didinium* is a carnivorous protozoan, belonging to the group known as *ciliates*. It has a globular body, about 150 µm in diameter, encircled by two fringes of cilia - sinuous, whiplike appendages that beat continually; its front end is flattened except for a single protrusion, rather like a snout. (B) *Didinium* normally swims around in the water at high speed by means of the synchronous beating of its cilia. When it encounters a suitable prey, usually another type of protozoan, it releases numerous small paralyzing darts from its snout region. Then, the *Didinium* attaches to and devours the other cell by phagocytosis, inverting like a hollow ball to engulf its victim, which is almost as large as itself. (Courtesy of D. Barlow.)

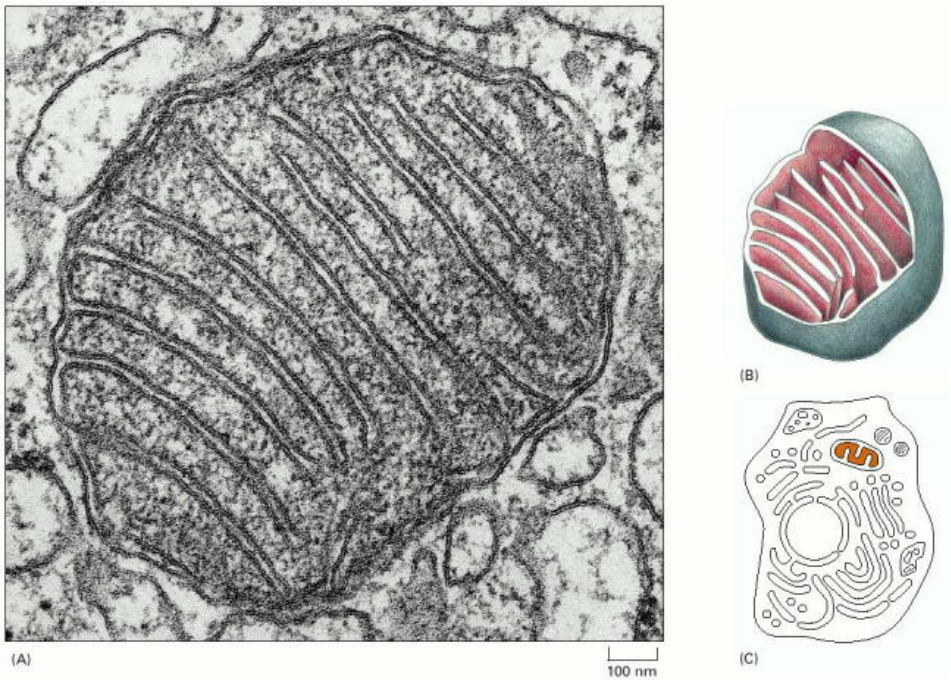

Figure 1-34. A mitochondrion. (A) A cross section, as seen in the electron microscope. (B) A drawing of a mitochondrion with part of it cut away to show the three-dimensional structure. (C) A schematic eucaryotic cell, with the interior space of a mitochondrion, containing the mitochondrial DNA and ribosomes, colored. Note the smooth outer membrane and the convoluted inner membrane, which houses the proteins that generate ATP from the oxidation of food molecules. (A, courtesy of Daniel S. Friend.)

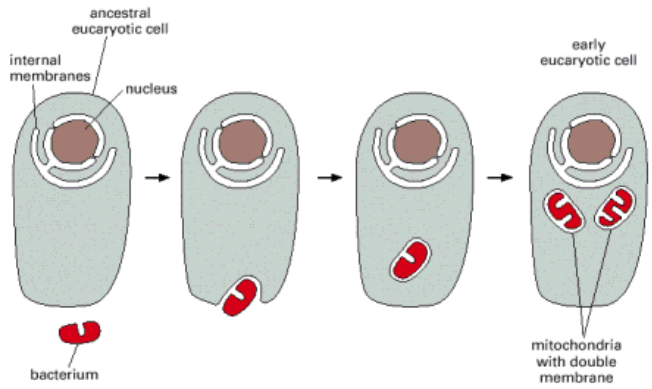

Figure 1-35. The origin of mitochondria. An ancestral eucaryotic cell is thought to have engulfed the bacterial ancestor of mitochondria, initiating a symbiotic relationship.

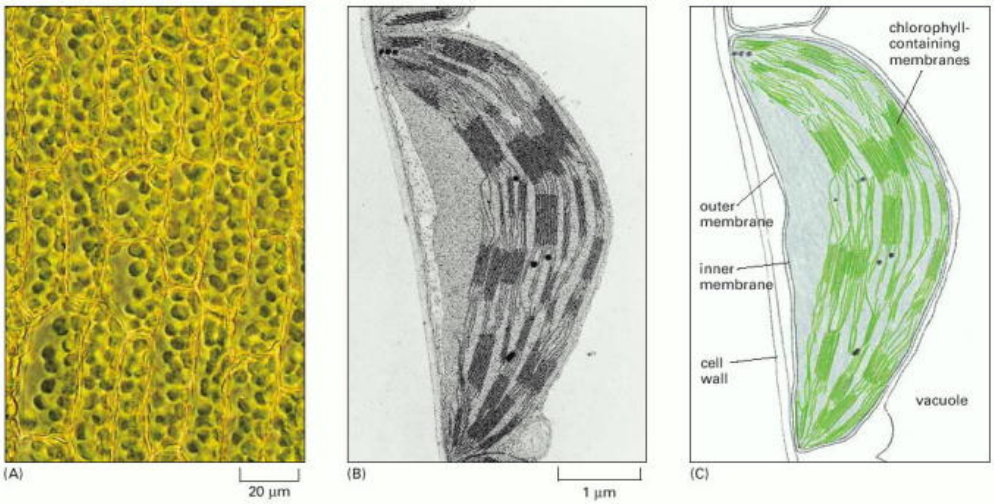

Figure 1-36. Chloroplasts. These organelles capture the energy of sunlight in plant cells and some single-celled eucaryotes. (A) Leaf cells in a moss seen in the light microscope, showing the green chloroplasts. (B) An electron micrograph of a chloroplast in a leaf of grass, showing the highly folded system of internal membranes containing the chlorophyll molecules by which light is absorbed. (C) An interpretative drawing of (B). (B, courtesy of Eldon Newcomb.)

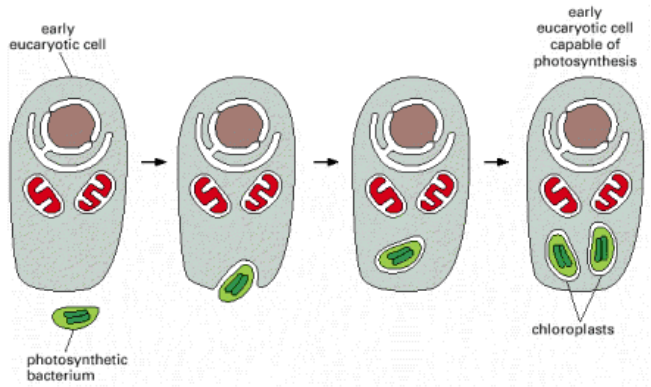

Figure 1-37. The origin of chloroplasts. An early eucaryotic cell, already possessing mitochondria, engulfed a photosynthetic bacterium (a cyanobacterium) and retained it in symbiosis. All present-day chloroplasts are thought to trace their ancestry back to a single species of cyanobacterium that was adopted as an internal symbiont (an endosymbiont) over a billion years ago.

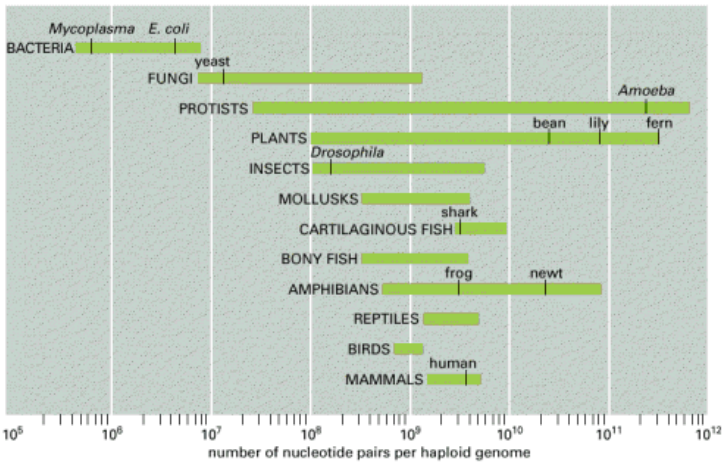

Figure 1-38. Genome sizes compared. Genome size is measured in nucleotide pairs of DNA per haploid genome, that is, per single copy of the genome. (The cells of sexually reproducing organisms such as ourselves are generally diploid: they contain two copies of the genome, one inherited from the mother, the other from the father.) Closely related organisms can vary widely in the quantity of DNA in their genomes, even though they contain similar numbers of functionally distinct genes. (Data from W.-H. Li, Molecular Evolution, pp. 380383. Sunderland, MA: Sinauer, 1997.)

Figure 1-39. The puffer fish *(Fugu rubripes).* This organism has a genome size of 400 million nucleotide pairs - about one-quarter as much as a zebrafish, for example, even though the two species of fish have similar numbers of genes. (From a woodcut by Hiroshige, courtesy of Arts and Designs of Japan.)

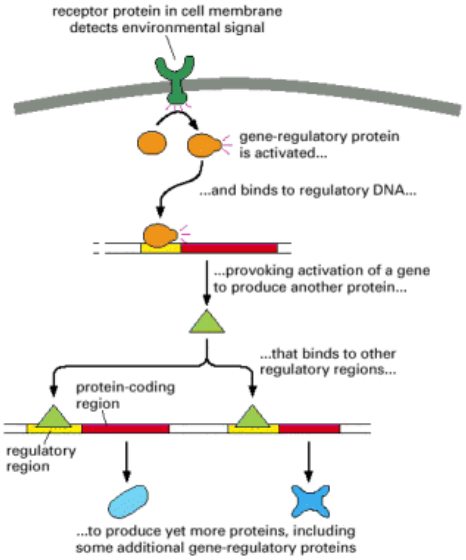

Figure 1-40. Controlling gene readout by environmental signals. Regulatory DNA allows gene expression to be controlled by regulatory proteins, which are in turn the products of other genes. This diagram shows how a cell's gene expression is adjusted according to a signal from the cell's environment. The initial effect of the signal is to activate a regulatory protein already present in the cell; the signal may, for example, trigger the attachment of a phosphate group to the regulatory protein, altering its chemical properties.

Figure 1-41. Genetic control of the program of multicellular development. The role of a regulatory gene is demonstrated in the snapdragon *Antirrhinum*. In this example, a mutation in a single gene coding for a regulatory protein causes leafy shoots to develop in place of flowers: because a regulatory protein has been changed, the cells adopt characters that would be appropriate to a different location in the normal plant. The mutant is on the left, the normal plant on the right. (Courtesy of Enrico Coen and Rosemary Carpenter.)

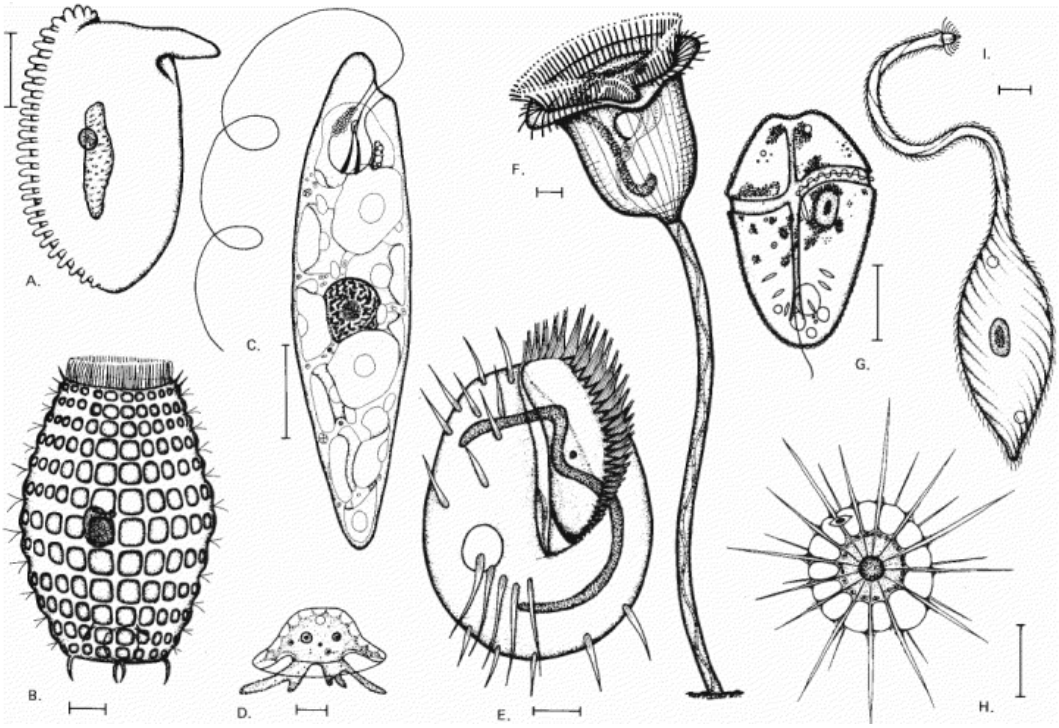

Figure 1-42. An assortment of protists: a small sample of an extremely diverse class of organisms. The drawings are done to different scales, but in each case the scale bar represents 10 µm. The organisms in (A), (B), (E), (F), and (I) are ciliates; (C) is a euglenoid; (D) is an amoeba; (G) is a dinoflagellate; (H) is a heliozoan. (From M.A. Sleigh, Biology of Protozoa. Cambridge, UK: Cambridge University Press, 1973.)

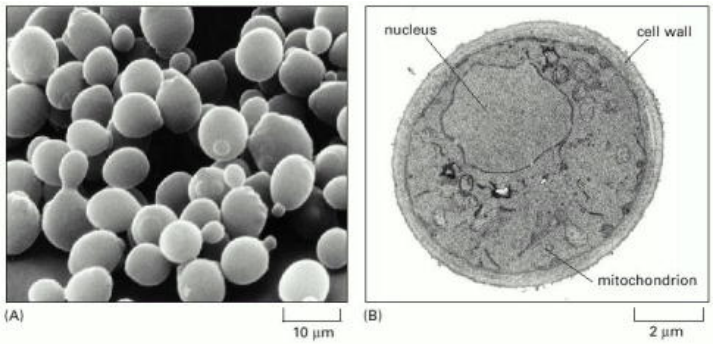

Figure 1-43. The yeast *Saccharomyces cerevisiae.* (A) A scanning electron micrograph of a cluster of the cells. This species is also known as budding yeast; it proliferates by forming a protrusion or bud that enlarges and then separates from the rest of the original cell. Many cells with buds are visible in this micrograph. (B) A transmission electron micrograph of a cross section of a yeast cell, showing its nucleus, mitochondrion, and thick cell wall. (A, courtesy of Ira Herskowitz and Eric Schabatach.)

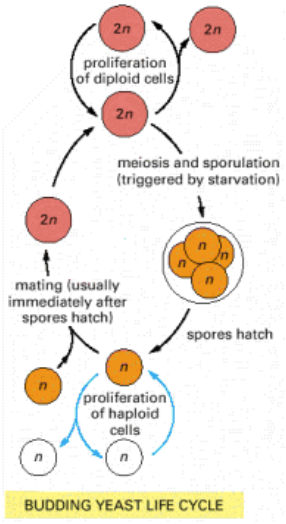

Figure 1-44. The reproductive cycles of the yeast *S. cerevisiae.* Depending on environmental conditions and on details of the genotype, cells of this species can exist in either a diploid state, with a double chromosome set, or a haploid state, with a single chromosome set. The diploid form can either proliferate by ordinary cell-division cycles or undergo meiosis to produce haploid cells. The haploid form can either proliferate by ordinary cell-division cycles or undergo sexual fusion with another haploid cell to become diploid. Meiosis is triggered by starvation and gives rise to spores - haploid cells in a dormant state, resistant to harsh environmental conditions.

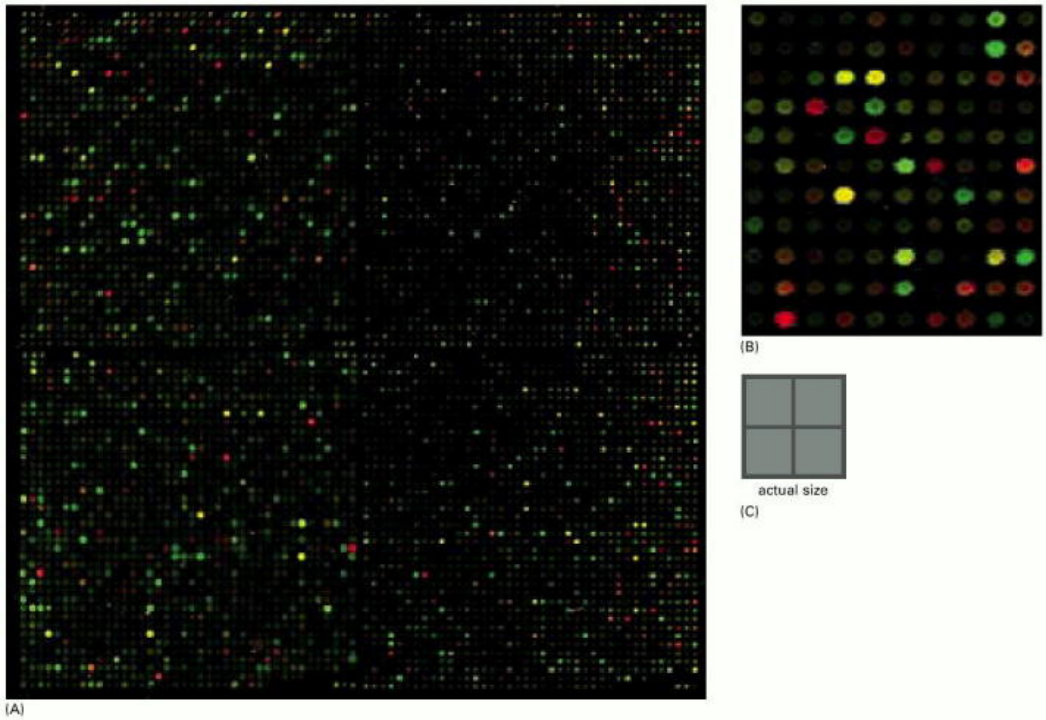

Figure 1-45. Monitoring changes in yeast gene expression using a DNA array. Samples of DNA sequence corresponding to each of the ~6300 protein-coding genes in the yeast genome are deposited in a square array on a glass microscope slide: (A) shows the entire array of 6400 spots; (B) shows a small region at higher magnification; (C) shows the actual size of array (A). The array has been used here to compare the sets of mRNA molecules produced by yeast cells with and without glucose in their culture medium. If the cells supplied with glucose transcribe a particular gene into mRNA, a preparation of mRNA from these cells will contain molecules that can bind selectively to the corresponding DNA spot in the array. In practice, the mRNA extracted from the cells is not applied directly to the array but is used (as we explain in Chapter 8) to generate another mixture of nucleic acid molecules, called cDNA molecules, that correspond in sequence to the mRNA molecules. In this experiment, they are tagged with a chemical label that fluoresces green. When the cDNA mixture is applied to the array, each cDNA in the mixture binds to its corresponding spot in the array: a bright *green* fluorescence at a given spot indicates strong expression of a specific gene. The whole procedure is now repeated with yeast cells deprived of glucose, tagging their cDNAs with a *red* fluorescent label and applying it to the same DNA array. Therefore, a *green* spot indicates a gene expressed more strongly in the presence of glucose than in its absence; a *red* spot indicates the opposite. Spots in the array corresponding to genes that are expressed equally in the two conditions bind both green and red cDNA molecules equally and therefore glow *yellow*. (From J.L. DeRisi et al., *Science* 278:680686, 1997. © AAAS.)

Figure 1-46. ***Arabidopsis thaliana,*** **the plant chosen as the primary model for studying plant molecular genetics.** (Courtesy of Toni Hayden and the John Innes Foundation.)

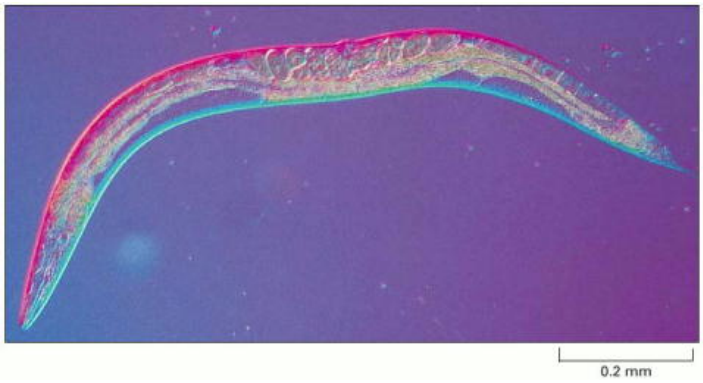

Figure 1-47. ***Caenorhabditis elegans,*** **the first multicellular organism to have its complete genome sequence determined.** This small nematode, about 1 mm long, lives in the soil. Most individuals are hermaphrodites, producing both eggs and sperm. (Courtesy of Ian Hope.)

Figure 1-48. Drosophila melanogaster. Molecular genetic studies on this fly have provided the main key to understanding how all animals develop from a fertilized egg into an adult. (From E.B. Lewis, *Science* 221:cover, 1983. © AAAS.)

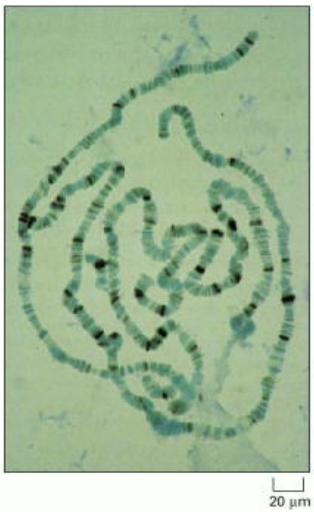

Figure 1-49. Giant chromosomes from salivary gland cells of *Drosophila.* Because many rounds of DNA replication have occurred without an intervening cell division, each of the chromosomes in these unusual cells contains over a 1000 identical DNA molecules, all aligned in register. This makes them easy to see in the light microscope, where they display a characteristic and reproducible banding pattern. Specific bands can be identified as the locations of specific genes: a mutant fly with a region of the banding pattern missing shows a phenotype reflecting loss of the genes in that region. Genes that are being transcribed at a high rate correspond to bands with a "puffed" appearance. The bands stained dark brown in the micrograph are sites where a particular regulatory protein is bound to the DNA. (Courtesy of B. Zink and R. Paro, from R. Paro, *Trends Genet.* 6:416421, 1990. © Elsevier.)

Figure 1-50. Two species of the frog genus *Xenopus.* *X. tropicalis*, above, has an ordinary diploid genome; *X. laevis*, below, has twice as much DNA per cell. From the banding patterns of their chromosomes and the arrangement of genes along them, as well as from comparisons of gene sequences, it is clear that the high-ploidy species have evolved through duplications of the whole genome. These duplications are thought to have occurred in the aftermath of matings between frogs of slightly divergent *Xenopus* species. (Courtesy of E. Amaya, M. Offield, and R. Grainger, *Trends Gen.* 14:253255, 1998. © Elsevier.)

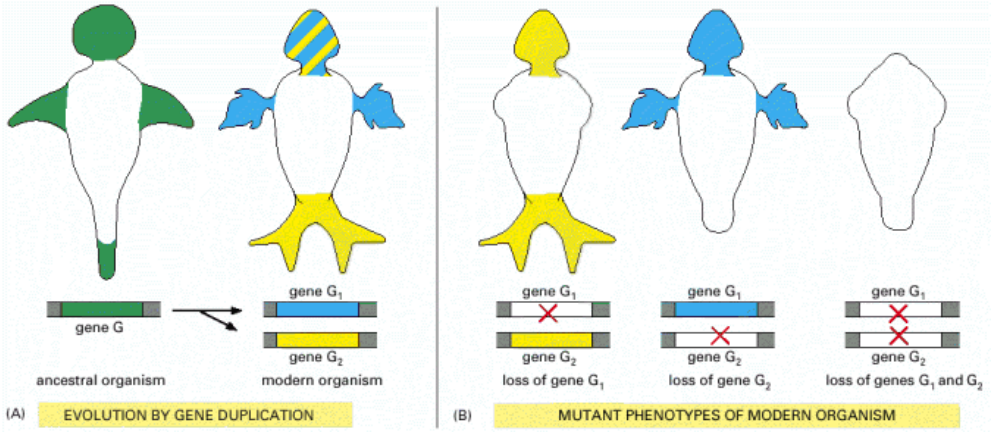

Figure 1-51. The consequences of gene duplication for mutational analyses of gene function. In this hypothetical example, an ancestral multicellular organism has a genome containing a single copy of gene G, which performs its function at several sites in the body, indicated in *green*. (A) Through gene duplication, a modern descendant of the ancestral organism has two copies of gene G, called G_1 and G_2. These have diverged somewhat in their patterns of expression and in their activities at the sites where they are expressed, but they still retain important similarities. At some sites, they are expressed together, and each independently performs the same old function as the ancestral gene G (alternating *green* and *yellow stripes);* at other sites, they are expressed alone and serve new purposes. (B) Because of a functional overlap, the loss of one of the two genes by mutation *(red cross)* reveals only a part of its role; only the loss of both genes in the double mutant reveals the full range of processes for which these genes are responsible. Analogous principles apply to duplicated genes that operate in the same place (for example, in a single-celled organism) but are called into action together or individually in response to varying circumstances. Thus, gene duplications complicate genetic analyses in all organisms.

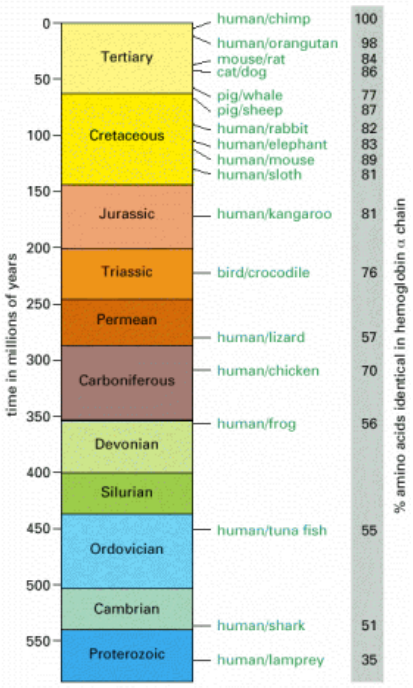

Figure 1-52. Times of divergence of different vertebrates. The scale on the left shows the estimated date and geological era of the last common ancestor of each specified pair of animals. Each time estimate is based on comparisons of the amino acid sequences of orthologous proteins; the longer a pair of animals have had to evolve independently, the smaller the percentage of amino acids that remain identical. Data from many different classes of proteins have been averaged to arrive at the final estimates, and the time scale has been calibrated to match the fossil evidence that the last common ancestor of mammals and birds lived 310 million years ago. The figures on the right give data on sequence divergence for one particular protein (chosen arbitrarily) - the α chain of hemoglobin. Note that although there is a clear general trend of increasing divergence with increasing time for this protein, there are also some irregularities. These reflect the randomness of the evolutionary process and, probably, the action of natural selection driving especially rapid changes of hemoglobin sequence in some organisms that experienced special physiological demands. On average, within any particular evolutionary lineage, hemoglobins accumulate changes at a rate of about 6 altered amino acids per 100 amino acids every 100 million years. Some proteins, subject to stricter functional constraints, evolve much more slowly than this, others as much as 5 times faster. All this gives rise to substantial uncertainties in estimates of divergence times, and some experts believe that the major groups of mammals diverged from one another as much as 60 million years more recently than shown here. (Adapted from S. Kumar and S.B. Hedges, *Nature* 392:917920, 1998.)

Figure 1-53. Human and mouse: similar genes and similar development. The human baby and the mouse shown here have similar white patches on their foreheads because both have mutations in the same gene (called *kit)*, required for the development and maintenance of pigment cells. (From R.A. Fleischman, *Proc. Natl. Acad. Sci. USA* 88:1088510889, 1991. © National Academy of Sciences.)

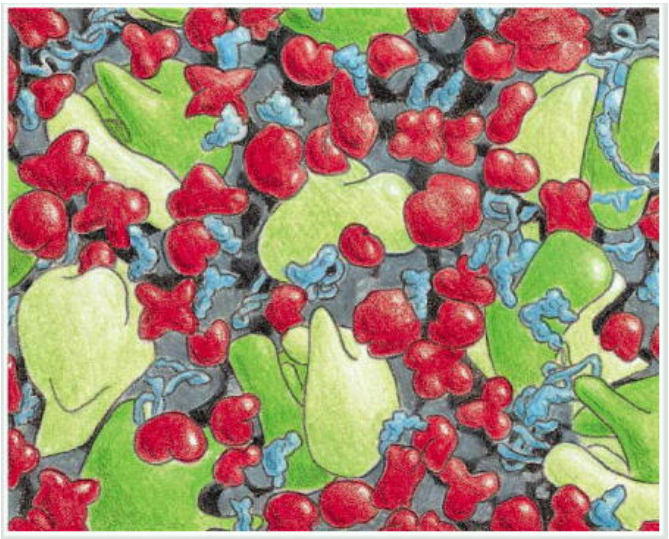

Crowded cytoplasm. This scale drawing, which shows only the macromolecules, gives a good impression of how crowded the cytoplasm is. RNAs are shown in *blue*, ribosomes in *green* and proteins in *red.* (Adapted from D.S. Goodsell, *Trends Biochem. Sci.* 16:203206, 1991.)

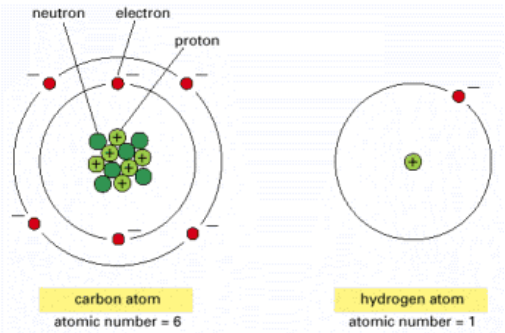

Figure 2-1. Highly schematic representations of an atom of carbon and an atom of hydrogen. Although the electrons are shown here as individual particles, in reality their behavior is governed by the laws of quantum mechanics, and there is no way of predicting exactly where an electron is at any given instant of time. The nucleus of every atom except hydrogen consists of both positively charged protons and electrically neutral neutrons. The number of electrons in an atom is equal to its number of protons (the atomic number), so that the atom has no net charge. The neutrons, protons, and electrons are in reality minute in relation to the atom as a whole; their size is greatly exaggerated here. In addition, the diameter of the nucleus is only about 10^{-4} that of the electron cloud.

A **mole** is X grams of a substance, where X is its relative molecular mass (molecular weight). A mole will contain 6×10^{23} molecules of the substance.

1 mole of carbon weighs 12 g
1 mole of glucose weighs 180 g
1 mole of sodium chloride weighs 58 g

Molar solutions have a concentration of 1 mole of the substance in 1 liter of solution. A molar solution (denoted as 1 M) of glucose, for example, has 180 g/l, while a millimolar solution (1 mM) has 180 mg/l.

The standard abbreviation for gram is g; the abbreviation for liter is l.

Figure 2-2. Moles and molar solutions.

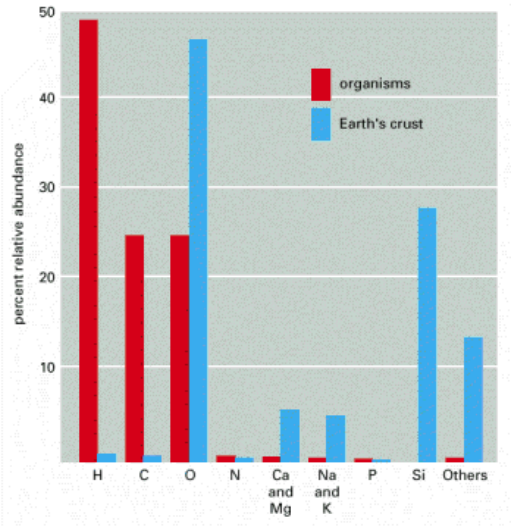

Figure 2-3. The abundances of some chemical elements in the nonliving world (the Earth's crust) compared with their abundances in the tissues of an animal. The abundance of each element is expressed as a percentage of the total number of atoms present in the sample. Thus, for example, nearly 50% of the atoms in a living organism are hydrogen atoms. The survey here excludes mineralized tissues such as bone and teeth, as they contain large amounts of inorganic salts of calcium and phosphorus. The relative abundance of elements is similar in all living organisms.

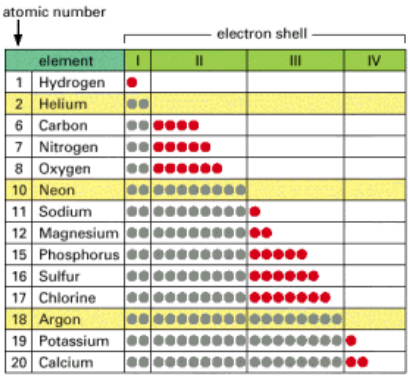

Figure 2-4. Filled and unfilled electron shells in some common elements. All the elements commonly found in living organisms have unfilled outermost shells *(red)* and can thus participate in chemical reactions with other atoms. For comparison, some elements that have only filled shells *(yellow)* are shown; these are chemically unreactive.

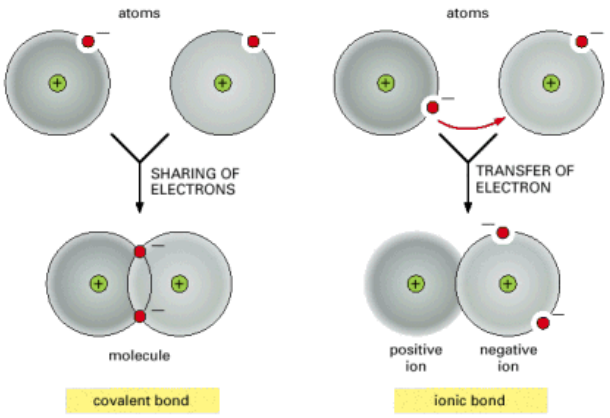

Figure 2-5. Comparison of covalent and ionic bonds. Atoms can attain a more stable arrangement of electrons in their outermost shell by interacting with one another. An ionic bond is formed when electrons are transferred from one atom to the other. A covalent bond is formed when electrons are shared between atoms. The two cases shown represent extremes; often, covalent bonds form with a partial transfer (unequal sharing of electrons), resulting in a polar covalent bond (see Figure 2-43).

Figure 2-6. Sodium chloride: an example of ionic bond formation. (A) An atom of sodium (Na) reacts with an atom of chlorine (Cl). Electrons of each atom are shown schematically in their different energy levels; electrons in the chemically reactive (incompletely filled) shells are *red.* The reaction takes place with transfer of a single electron from sodium to chlorine, forming two electrically charged atoms, or ions, each with complete sets of electrons in their outermost levels. The two ions with opposite charge are held together by electrostatic attraction. (B) The product of the reaction between sodium and chlorine, crystalline sodium chloride, consists of sodium and chloride ions packed closely together in a regular array in which the charges are exactly balanced. (C) Color photograph of crystals of sodium chloride.

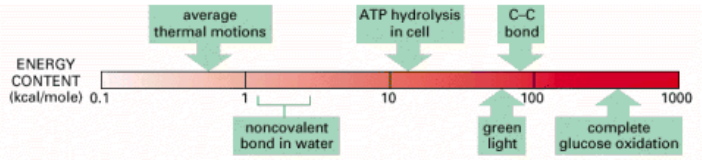

Figure 2-7. Some energies important for cells. Note that these energies are compared on a logarithmic scale.

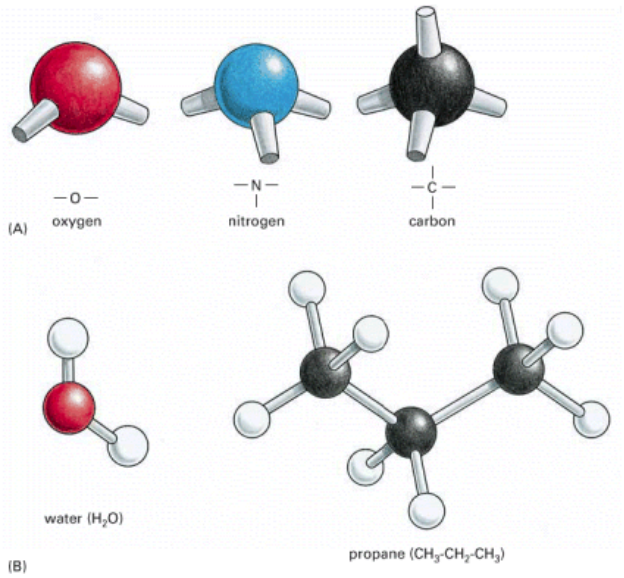

Figure 2-8. The geometry of covalent bonds. (A) The spatial arrangement of the covalent bonds that can be formed by oxygen, nitrogen, and carbon. (B) Molecules formed from these atoms have a precise three-dimensional structure, as shown here by ball and stick models for water and propane. A structure can be specified by the bond angles and bond lengths for each covalent linkage.

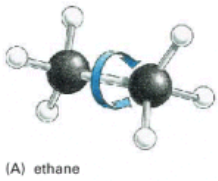

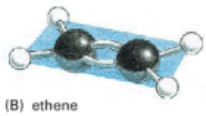

Figure 2-9. Carbon-carbon double bonds and single bonds compared. (A) The ethane molecule, with a single covalent bond between the two carbon atoms, illustrates the tetrahedral arrangement of single covalent bonds formed by carbon. One of the CH_3 groups joined by the covalent bond can rotate relative to the other around the bond axis. (B) The double bond between the two carbon atoms in a molecule of ethene (ethylene) alters the bond geometry of the carbon atoms and brings all the atoms into the same plane *(blue)*; the double bond prevents the rotation of one CH_2 group relative to the other.

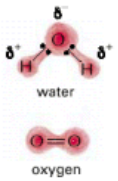

Figure 2-10. Polar and nonpolar covalent bonds. The electron distributions in the polar water molecule (H_2O) and the nonpolar oxygen molecule (O_2) are compared (δ^+, partial positive charge; δ^-, partial negative charge).

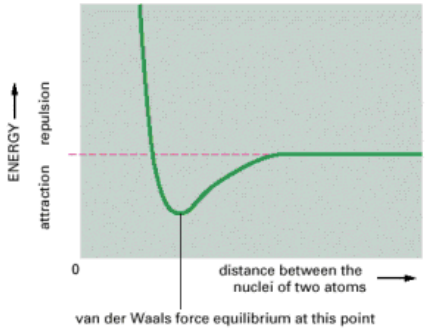

Figure 2-11. The balance of van der Waals forces between two atoms. As the nuclei of two atoms approach each other, they initially show a weak bonding interaction due to their fluctuating electric charges. However, the same atoms will strongly repel each other if they are brought too close together. The balance of these van der Waals attractive and repulsive forces occurs at the indicated energy minimum.

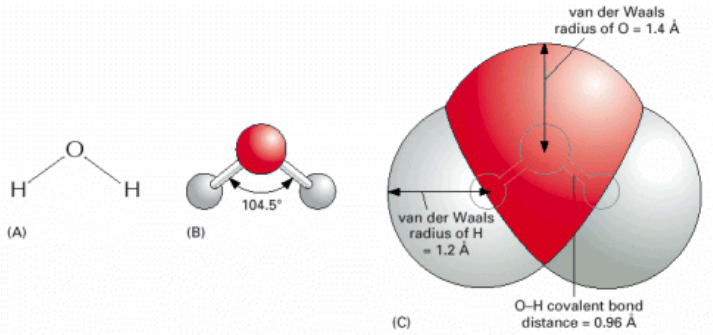

Figure 2-12. Three representations of a water molecule. (A) The usual line drawing of the structural formula, in which each atom is indicated by its standard symbol, and each line represents a covalent bond joining two atoms. (B) A ball and stick model, in which atoms are represented by spheres of arbitrary diameter, connected by sticks representing covalent bonds. Unlike (A), bond angles are accurately represented in this type of model (see also Figure 2-8). (C) A space-filling model, in which both bond geometry and van der Waals radii are accurately represented.

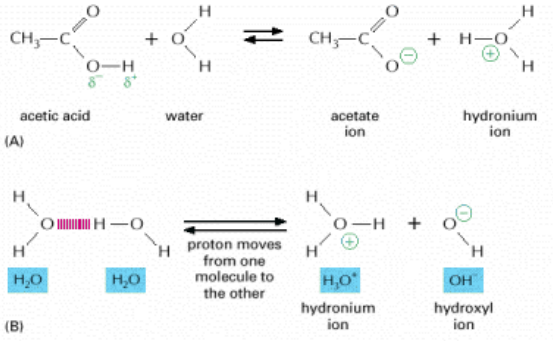

Figure 2-13. Acids in water. (A) The reaction that takes place when a molecule of acetic acid dissolves in water. (B) Water molecules are continuously exchanging protons with each other to form hydronium and hydroxyl ions. These ions in turn rapidly recombine to form water molecules.

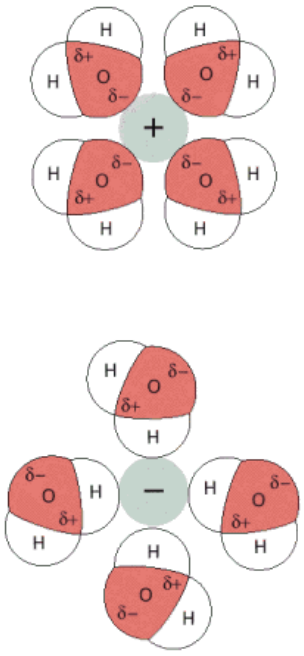

Figure 2-14. How the dipoles on water molecules orient to reduce the affinity of oppositely charged ions or polar groups for each other.

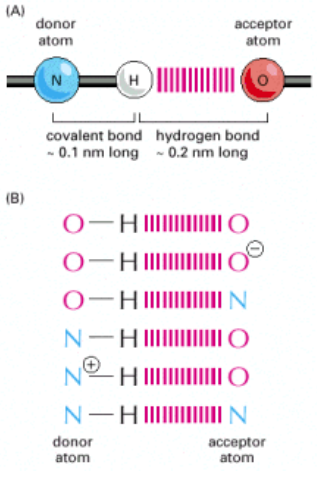

Figure 2-15. Hydrogen bonds. (A) Ball- and-stick model of a typical hydrogen bond. The distance between the hydrogen and the oxygen atom here is less than the sum of their van der Waals radii, indicating a partial sharing of electrons. (B) The most common hydrogen bonds in cells.

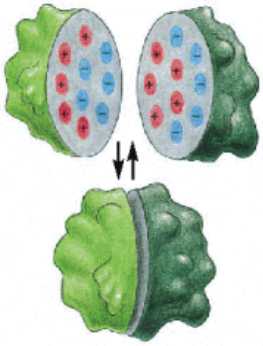

Figure 2-16. How two macro-molecules with complementary surfaces can bind tightly to one another through noncovalent interactions. In this schematic illustration, plus and minus are used to mark chemical groups that can form attractive interactions when paired.

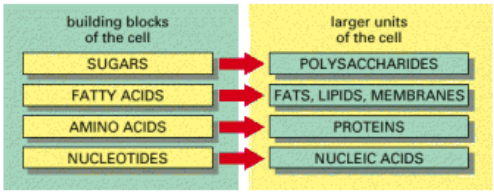

Figure 2-17. The four main families of small organic molecules in cells. These small molecules form the monomeric building blocks, or subunits, for most of the macromolecules and other assemblies of the cell. Some, like the sugars and the fatty acids, are also energy sources.

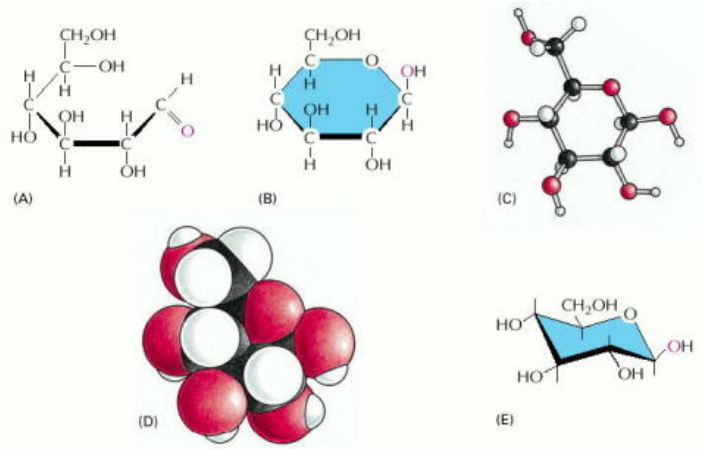

Figure 2-18. The structure of glucose, a simple sugar. As illustrated previously for water (see Figure 2-12), any molecule can be represented in several ways. In the structural formulas shown in (A), (B) and (E), the atoms are shown as chemical symbols linked together by lines representing the covalent bonds. The *thickened lines* here are used to indicate the plane of the sugar ring, in an attempt to emphasize that the -H and -OH groups are not in the same plane as the ring. (A) The open-chain form of this sugar, which is in equilibrium with the more stable cyclic or ring form in (B). (C) A ball-and-stick model in which the three-dimensional arrangement of the atoms in space is shown. (D) A space-filling model, which, as well as depicting the three-dimensional arrangement of the atoms, also uses the van der Waals radii to represent the surface contours of the molecule. (E) The chair form is an alternative way to draw the cyclic molecule that reflects the geometry more accurately than the structural formula in (B). The atoms in (C) and (D) are drawn according to the conventional color coding for atoms. For example, these colors are H, *white*; C, *black*; O, *red*; N, *blue* (see also Figure 2-8).

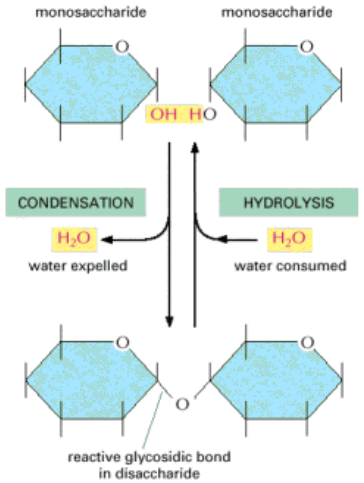

Figure 2-19. The reaction of two monosaccharides to form a disaccharide. This reaction belongs to a general category of reactions termed *condensation reactions*, in which two molecules join together as a result of the loss of a water molecule. The reverse reaction (in which water is added) is termed *hydrolysis*. Note that one of the two partners (the one on the *left* here) is the carbon joined to two oxygens through which the sugar ring forms (see Figure 2-18). As indicated, this common type of covalent bond between two sugar molecules is known as a *glycosidic bond* (see also Figure 2-20).

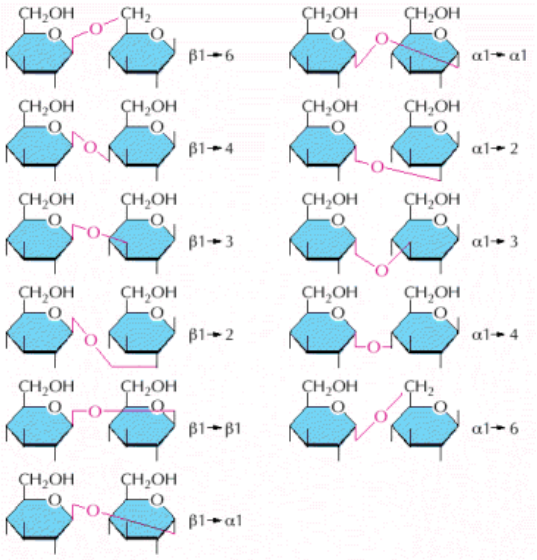

Figure 2-20. Eleven disaccharides consisting of two D-glucose units. Although these differ only in the type of linkage between the two glucose units, they are chemically distinct. Since the oligosaccharides associated with proteins and lipids may have six or more different kinds of sugar joined in both linear and branched arrangements through glycosidic bonds such as those illustrated here, the number of distinct types of oligosaccharides that can be used in cells is extremely large. For an explanation of α and β linkages, see Panel 2-4 (pp. 116117).

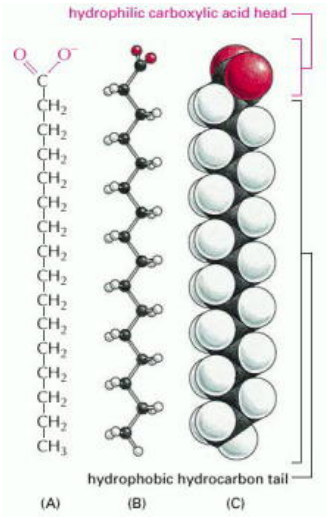

Figure 2-21. A fatty acid. A fatty acid is composed of a hydrophobic hydrocarbon chain to which is attached a hydrophilic carboxylic acid group. Palmitic acid is shown here. Different fatty acids have different hydrocarbon tails. (A) Structural formula. The carboxylic acid group is shown in its ionized form. (B) Ball-and-stick model. (C) Space-filling model.

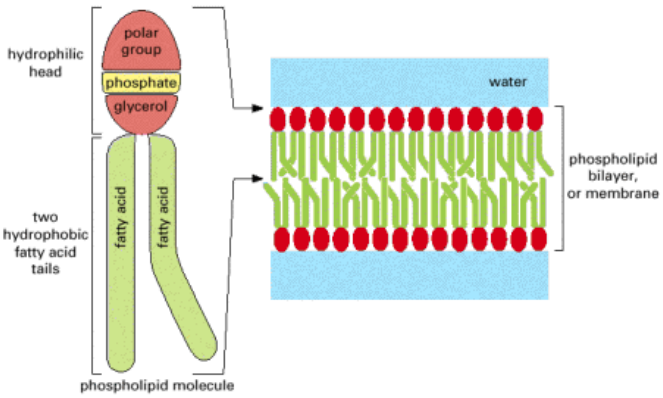

Figure 2-22. Phospholipid structure and the orientation of phospholipids in membranes. In an aqueous environment, the hydrophobic tails of phospholipids pack together to exclude water. Here they have formed a bilayer with the hydrophilic head of each phospholipid facing the water. Lipid bilayers are the basis for cell membranes, as discussed in detail in Chapter 10.

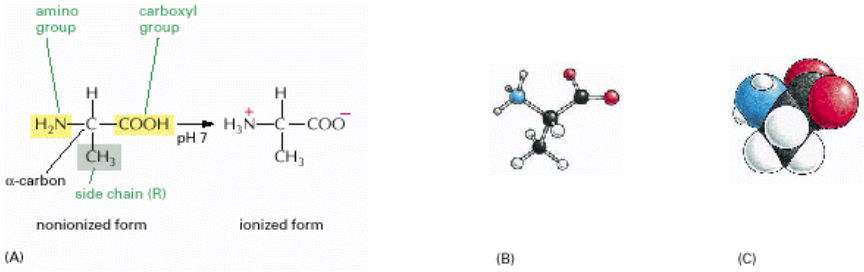

Figure 2-23. The amino acid alanine. (A) In the cell, where the pH is close to 7, the free amino acid exists in its ionized form; but when it is incorporated into a polypeptide chain, the charges on the amino and carboxyl groups disappear. (B) A ball-and-stick model and (C) a space-filling model of alanine (H, *white;* C, *black;* O, *red;* N, *blue*).

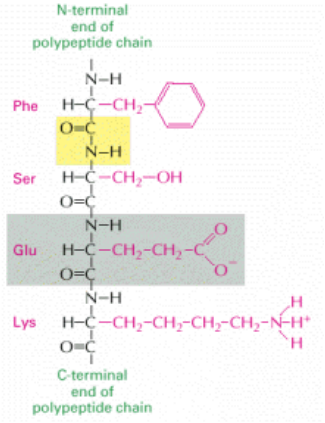

Figure 2-24. A small part of a protein molecule. The four amino acids shown are linked together by three peptide bonds, one of which is highlighted in *yellow.* One of the amino acids is shaded in *gray.* The amino acid side chains are shown in *red.* The two ends of a polypeptide chain are chemically distinct. One end, the N-terminus, terminates in an amino group, and the other, the C-terminus, in a carboxyl group. The sequence is always read from the N-terminal end; hence this sequence is Phe-Ser-Glu-Lys.

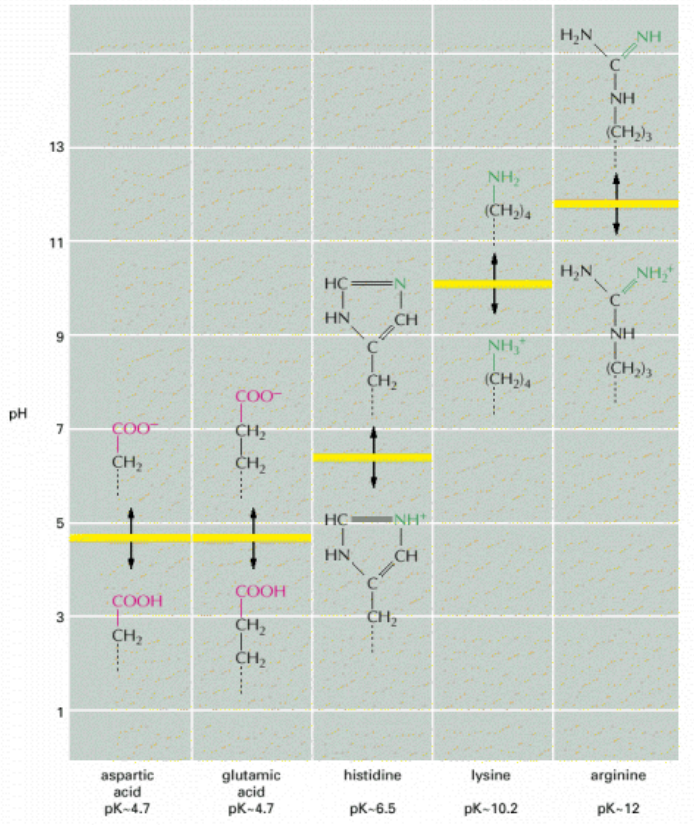

Figure 2-25. The charge on amino acid side chains depends on the pH. The five different side chains that can carry a charge are shown. Carboxylic acids can readily lose H^+ in aqueous solution to form a negatively charged ion, which is denoted by the suffix "-ate," as in aspart*ate* or glutam*ate*. A comparable situation exists for amines, which in aqueous solution can take up H^+ to form a positively charged ion (which does not have a special name). These reactions are rapidly reversible, and the amounts of the two forms, charged and uncharged, depend on the pH of the solution. At a high pH, carboxylic acids tend to be charged and amines uncharged. At a low pH, the opposite is true - the carboxylic acids are uncharged and amines are charged. The pH at which exactly *half* of the carboxylic acid or amine residues are charged is known as the pK of that amino acid side chain. In the cell the pH is close to 7, and almost all carboxylic acids and amines are in their fully charged form.

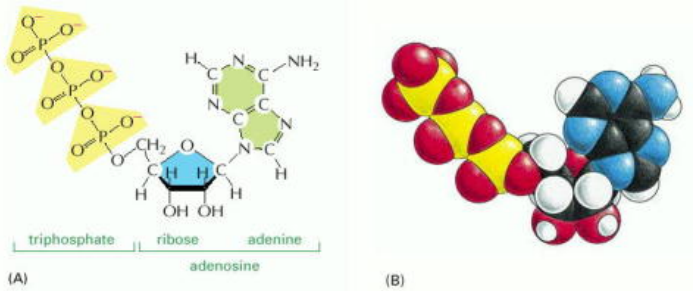

Figure 2-26. Chemical structure of adenosine triphosphate (ATP). (A) Structural formula. (B) Space-filling model. In (B) the colors of the atoms are C, *black;* N, *blue;* H, *white;* O, *red;* and P, *yellow.*

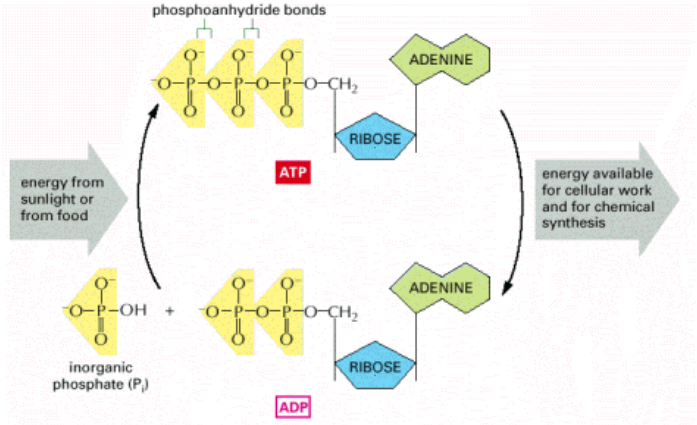

Figure 2-27. The ATP molecule serves as an energy carrier in cells. The energy-requiring formation of ATP from ADP and inorganic phosphate is coupled to the energy-yielding oxidation of foodstuffs (in animal cells, fungi, and some bacteria) or to the capture of light energy (in plant cells and some bacteria). The hydrolysis of this ATP back to ADP and inorganic phosphate in turn provides the energy to drive many cellular reactions.

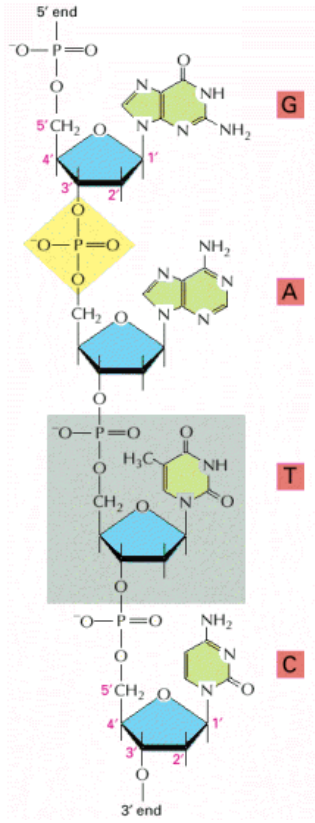

Figure 2-28. A small part of one chain of a deoxyribonucleic acid (DNA) molecule. Four nucleotides are shown. One of the phosphodiester bonds that links adjacent nucleotide residues is highlighted in *yellow*, and one of the nucleotides is shaded in *gray*. Nucleotides are linked together by a phosphodiester linkage between specific carbon atoms of the ribose, known as the 5 and 3 atoms. For this reason, one end of a polynucleotide chain, the 5 end, will have a free phosphate group and the other, the 3 end, a free hydroxyl group. The linear sequence of nucleotides in a polynucleotide chain is commonly abbreviated by a one-letter code, and the sequence is always read from the 5 end. In the example illustrated the sequence is G-A-T-C.

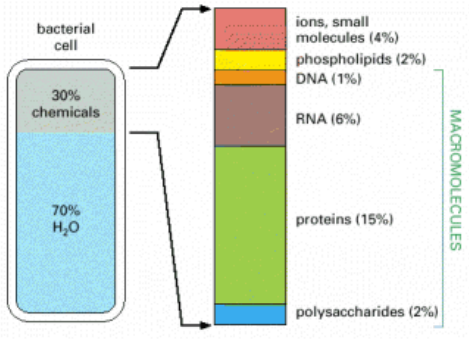

Figure 2-29. Macromolecules are abundant in cells. The approximate composition of a bacterial cell is shown by weight. The composition of an animal cell is similar (see Table 2-4).

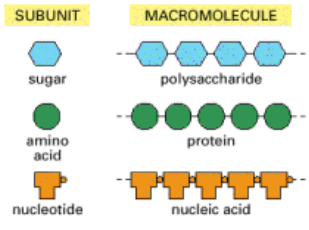

Figure 2-30. Three families of macromolecules. Each is a polymer formed from small molecules (called monomers, or subunits) linked together by covalent bonds.

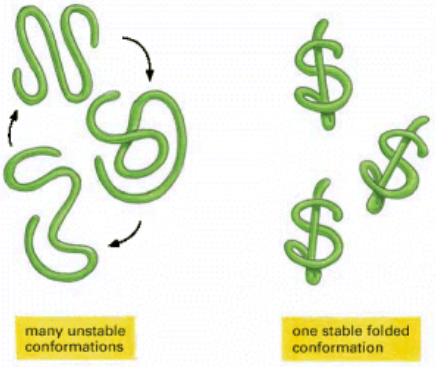

Figure 2-31. Most proteins and many RNA molecules fold into only one stable conformation. If the noncovalent bonds maintaining this stable conformation are disrupted, the molecule becomes a flexible chain that usually has no biological value.

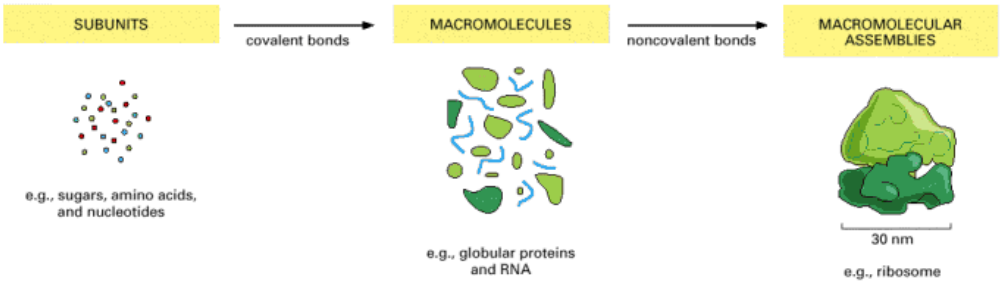

Figure 2-32. Small molecules, proteins, and a ribosome drawn approximately to scale. Ribosomes are a central part of the machinery that the cell uses to make proteins: each ribosome is formed as a complex of about 90 macromolecules (protein and RNA molecules).

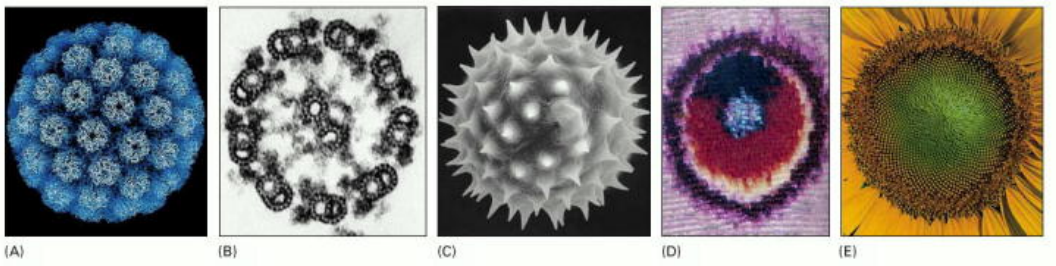

Figure 2-33. Order in biological structures. Well-defined, ornate, and beautiful spatial patterns can be found at every level of organization in living organisms. In order of increasing size: (A) protein molecules in the coat of a virus; (B) the regular array of microtubules seen in a cross section of a sperm tail; (C) surface contours of a pollen grain (a single cell); (D) close-up of the wing of a butterfly showing the pattern created by scales, each scale being the product of a single cell; (E) spiral array of seeds, made of millions of cells, in the head of a sunflower. (A, courtesy of R.A. Grant and J.M. Hogle; B, courtesy of Lewis Tilney; C, courtesy of Colin MacFarlane and Chris Jeffree; D and E, courtesy of Kjell B. Sandved.)

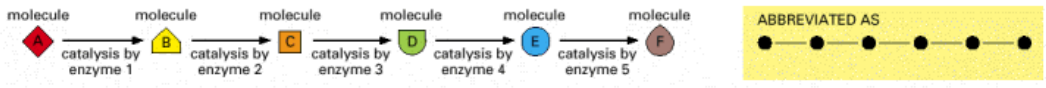

Figure 2-34. How a set of enzyme-catalyzed reactions generates a metabolic pathway. Each enzyme catalyzes a particular chemical reaction, leaving the enzyme unchanged. In this example, a set of enzymes acting in series converts molecule A to molecule F, forming a metabolic pathway.

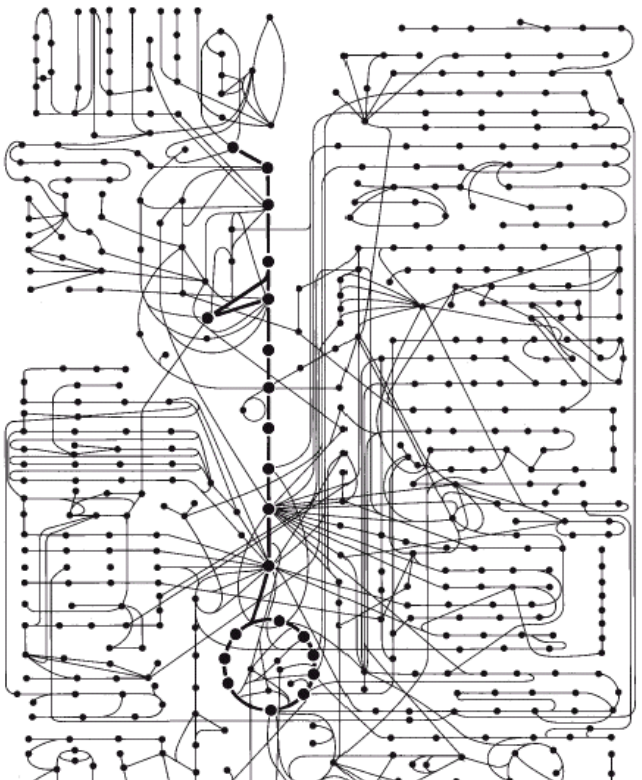

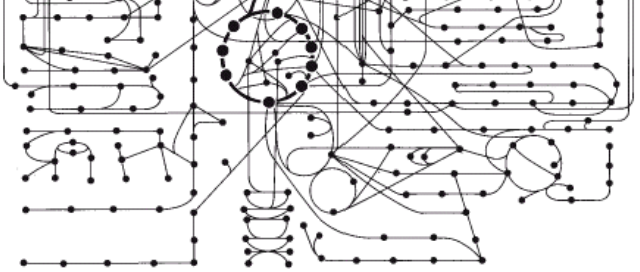

Figure 2-35. Some of the metabolic pathways and their interconnections in a typical cell. About 500 common metabolic reactions are shown diagrammatically, with each molecule in a metabolic pathway represented by a filled circle, as in the *yellow* box in Figure 2-34.

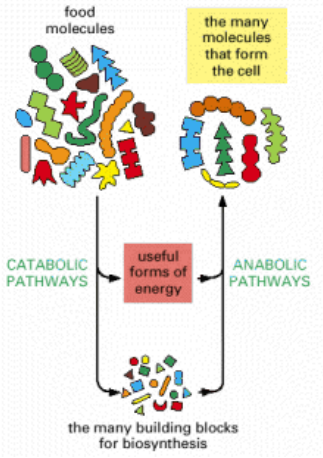

Figure 2-36. Schematic representation of the relationship between catabolic and anabolic pathways in metabolism. As suggested here, since a major portion of the energy stored in the chemical bonds of food molecules is dissipated as heat, the mass of food required by any organism that derives all of its energy from catabolism is much greater than the mass of the molecules that can be produced by anabolism.

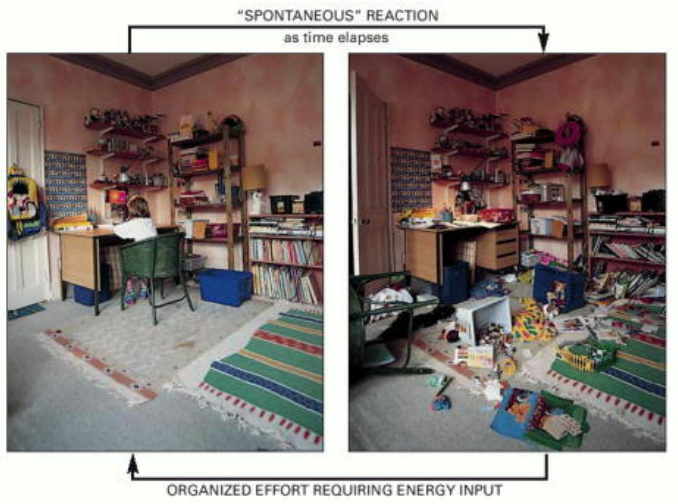

Figure 2-37. An everyday illustration of the spontaneous drive toward disorder. Reversing this tendency toward disorder requires an intentional effort and an input of energy: it is not spontaneous. In fact, from the second law of thermodynamics, we can be certain that the human intervention required will release enough heat to the environment to more than compensate for the reordering of the items in this room.

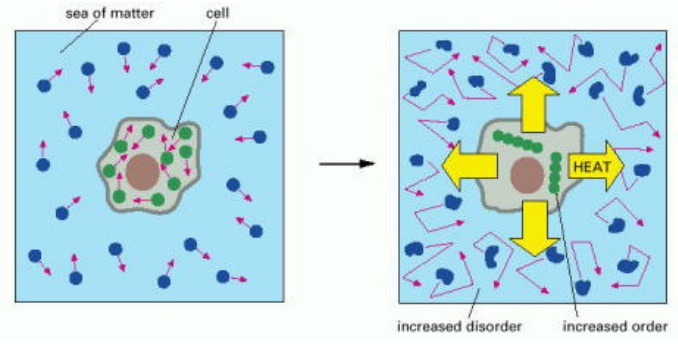

Figure 2-38. A simple thermodynamic analysis of a living cell. In the diagram on the left the molecules of both the cell and the rest of the universe (the sea of matter) are depicted in a relatively disordered state. In the diagram on the right the cell has taken in energy from food molecules and released heat by a reaction that orders the molecules the cell contains. Because the heat increases the disorder in the environment around the cell (depicted by the *jagged arrows* and distorted molecules, indicating the increased molecular motions caused by heat), the second law of thermodynamics - which states that the amount of disorder in the universe must always increase - is satisfied as the cell grows and divides. For a detailed discussion, see Panel 2-7 (pp. 122123).

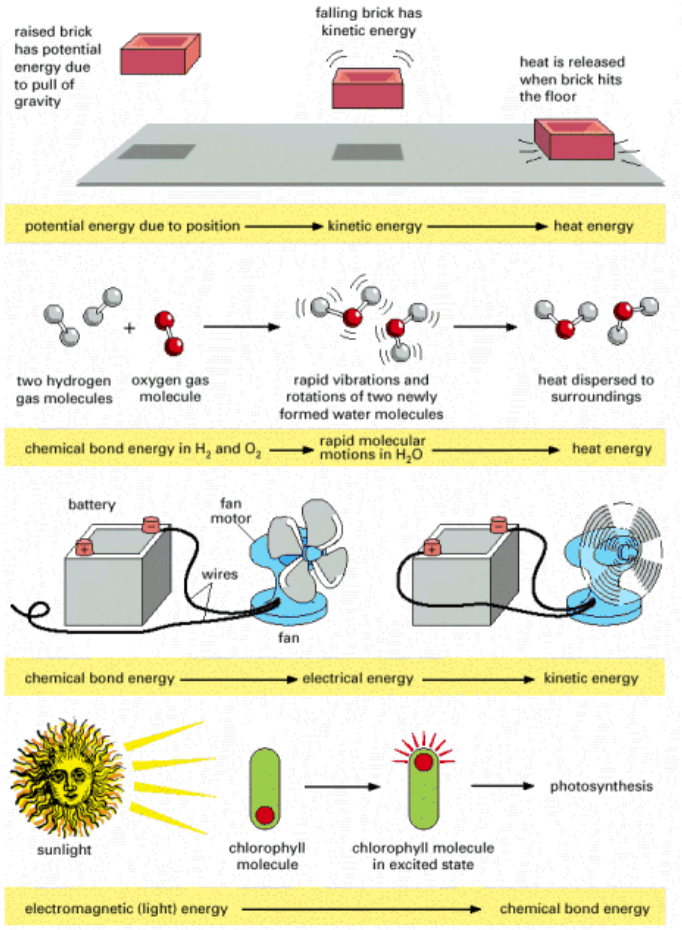

Figure 2-39. Some interconversions between different forms of energy. All energy forms are, in principle, interconvertible. In all these processes the total amount of energy is conserved; thus, for example, from the height and weight of the brick in the first example, we can predict exactly how much heat will be released when it hits the floor. In the second example, note that the large amount of chemical bond energy released when water is formed is initially converted to very rapid thermal motions in the two new water molecules; but collisions with other molecules almost instantaneously spread this kinetic energy evenly throughout the surroundings (heat transfer), making the new molecules indistinguishable from all the rest.

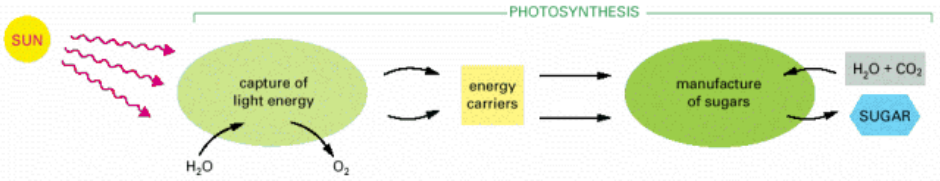

Figure 2-40. Photosynthesis. The two stages of photosynthesis. The energy carriers created in the first stage are two molecules that we discuss shortly - ATP and NADPH.

Figure 2-41. Photosynthesis and respiration as complementary processes in the living world. Photosynthesis uses the energy of sunlight to produce sugars and other organic molecules. These molecules in turn serve as food for other organisms. Many of these organisms carry out respiration, a process that uses O_2 to form CO_2 from the same carbon atoms that had been taken up as CO_2 and converted into sugars by photosynthesis. In the process, the organisms that respire obtain the chemical bond energy that they need to survive. The first cells on the Earth are thought to have been capable of neither photosynthesis nor respiration (discussed in Chapter 14). However, photosynthesis must have preceded respiration on the Earth, since there is strong evidence that billions of years of photosynthesis were required before O_2 had been released in sufficient quantity to create an atmosphere rich in this gas. (The Earth's atmosphere presently contains 20% O_2.)

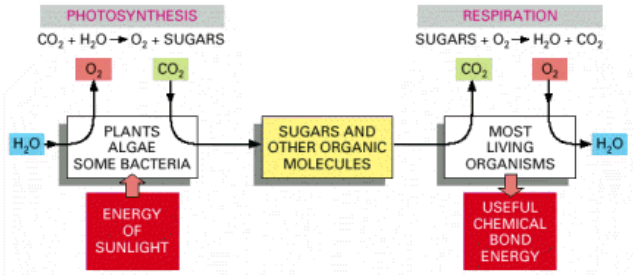

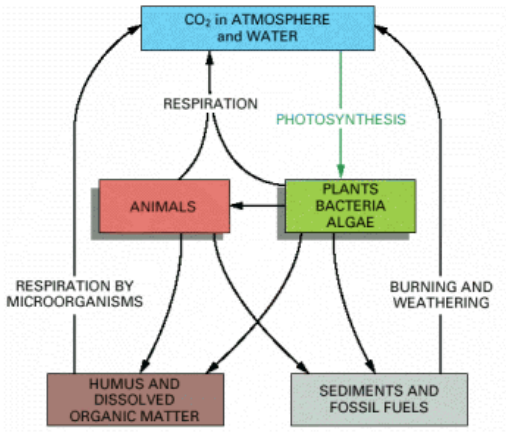

Figure 2-42. The carbon cycle. Individual carbon atoms are incorporated into organic molecules of the living world by the photosynthetic activity of plants, bacteria, and marine algae. They pass to animals, microorganisms, and organic material in soil and oceans in cyclic paths. CO_2 is restored to the atmosphere when organic molecules are oxidized by cells or burned by humans as fossil fuels.

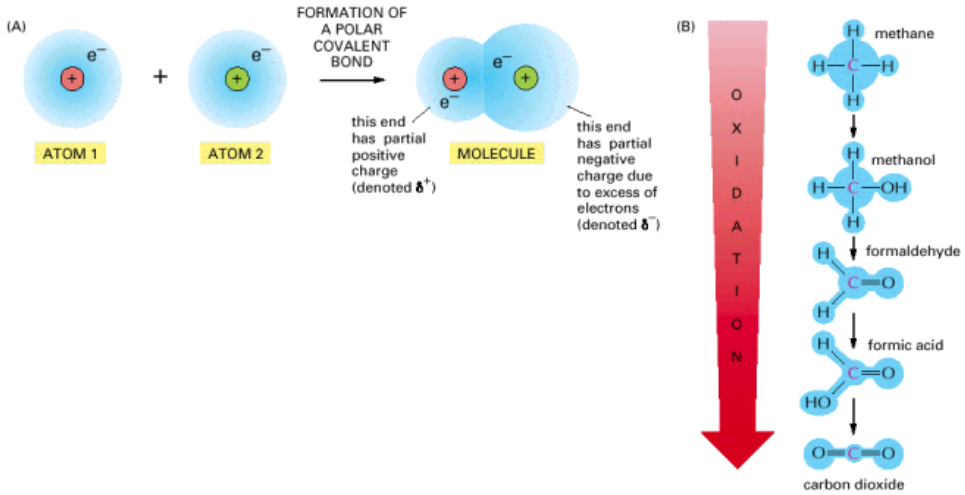

Figure 2-43. Oxidation and reduction. (A) When two atoms form a *polar* covalent bond (see p. 54), the atom ending up with a greater share of electrons is said to be reduced, while the other atom acquires a lesser share of electrons and is said to be oxidized. The reduced atom has acquired a partial negative charge (δ^-) as the positive charge on the atomic nucleus is now more than equaled by the total charge of the electrons surrounding it, and conversely, the oxidized atom has acquired a partial positive charge (δ^+). (B) The single carbon atom of methane can be converted to that of carbon dioxide by the successive replacement of its covalently bonded hydrogen atoms with oxygen atoms. With each step, electrons are shifted away from the carbon (as indicated by the *blue* shading), and the carbon atom becomes progressively more oxidized. Each of these steps is energetically favorable under the conditions present inside a cell.

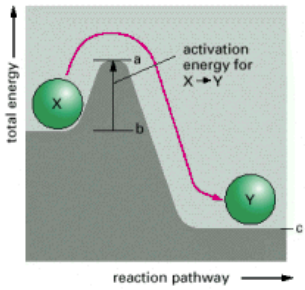

Figure 2-44. The important principle of activation energy. Compound X is in a stable state, and energy is required to convert it to compound Y, even though Y is at a lower overall energy level than X. This conversion will not take place, therefore, unless compound X can acquire enough activation energy (*energy a minus energy b*) from its surroundings to undergo the reaction that converts it into compound Y. This energy may be provided by means of an unusually energetic collision with other molecules. For the reverse reaction, Y X, the activation energy will be much larger (*energy a minus energy c*); this reaction will therefore occur much more rarely. Activation energies are always positive; note, however, that the total energy change for the energetically favorable reaction X Y is *energy c minus energy b*, a negative number.

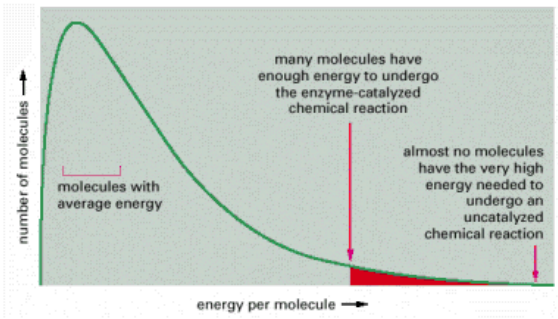

Figure 2-45. Lowering the activation energy greatly increases the probability of reaction. A population of identical substrate molecules will have a range of energies that is distributed as shown on the graph at any one instant. The varying energies come from collisions with surrounding molecules, which make the substrate molecules jiggle, vibrate, and spin. For a molecule to undergo a chemical reaction, the energy of the molecule must exceed the activation energy for that reaction; for most biological reactions, this almost never happens without enzyme catalysis. Even with enzyme catalysis, the substrate molecules must experience a particularly energetic collision to react, as indicated here.

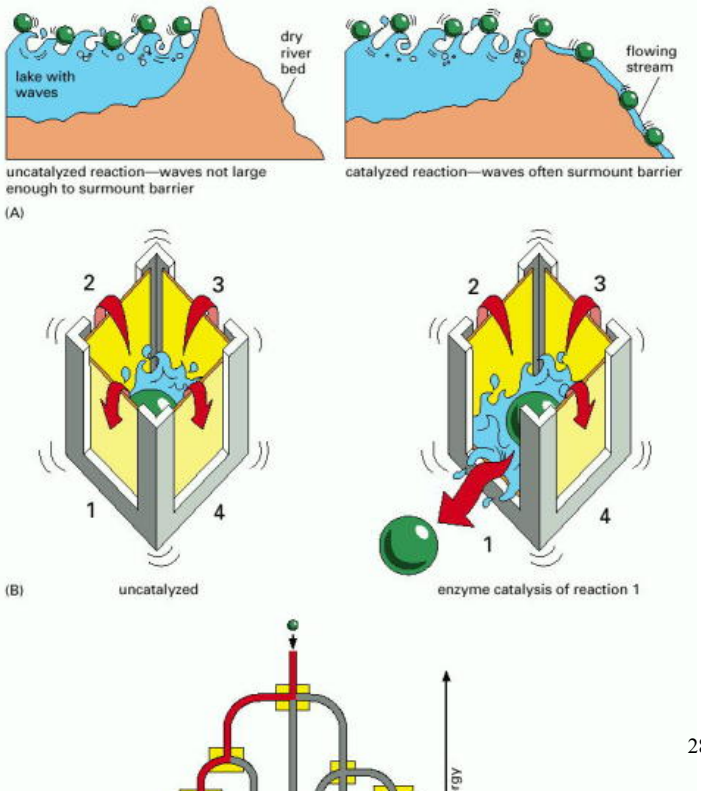

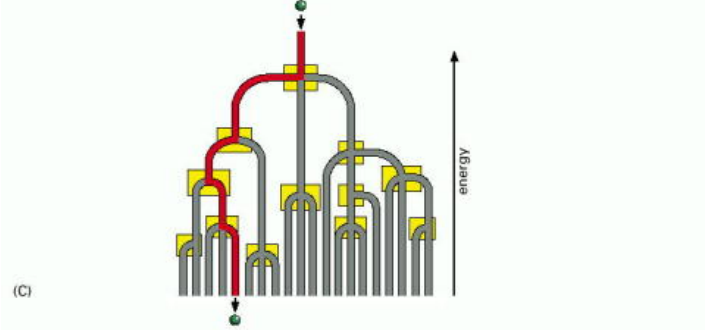

Figure 2-46. Floating ball analogies for enzyme catalysis. (A) A barrier dam is lowered to represent enzyme catalysis. The *green ball* represents a potential enzyme substrate (compound X) that is bouncing up and down in energy level due to constant encounters with waves (an analogy for the thermal bombardment of the substrate with the surrounding water molecules). When the barrier (activation energy) is lowered significantly, it allows the energetically favorable movement of the ball (the substrate) downhill. (B) The four walls of the box represent the activation energy barriers for four different chemical reactions that are all energetically favorable, in the sense that the products are at lower energy levels than the substrates. In the *left-hand* box, none of these reactions occurs because even the largest waves are not large enough to surmount any of the energy barriers. In the *right-hand* box, enzyme catalysis lowers the activation energy for reaction number 1 only; now the jostling of the waves allows passage of the molecule over this energy barrier only, inducing reaction 1. (C) A branching river with a set of barrier dams *(yellow boxes)* serves to illustrate how a series of enzyme-catalyzed reactions determines the exact reaction pathway followed by each molecule inside the cell.

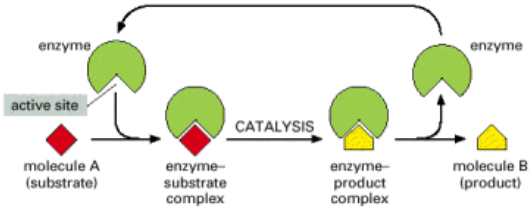

Figure 2-47. How enzymes work. Each enzyme has an active site to which one or two *substrate* molecules bind, forming an enzyme-substrate complex. A reaction occurs at the active site, producing an enzyme-product complex. The *product* is then released, allowing the enzyme to bind additional substrate molecules.

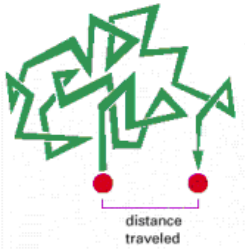

Figure 2-48. A random walk. Molecules in solution move in a random fashion due to the continual buffeting they receive in collisions with other molecules. This movement allows small molecules to diffuse rapidly from one part of the cell to another, as described in the text.

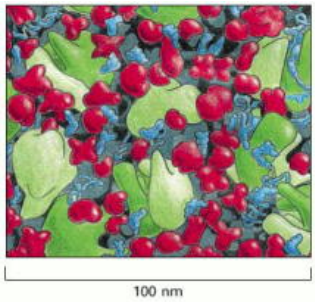

Figure 2-49. The structure of the cytoplasm. The drawing is approximately to scale and emphasizes the crowding in the cytoplasm. Only the macromolecules are shown: RNAs are shown in *blue*, ribosomes in *green*, and proteins in *red*. Enzymes and other macromolecules diffuse relatively slowly in the cytoplasm, in part because they interact with many other macromolecules; small molecules, by contrast, diffuse nearly as rapidly as they do in water. (Adapted from D.S. Goodsell, *Trends Biochem. Sci.* 16:203206, 1991.)

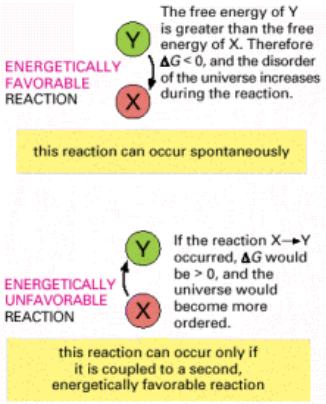

Figure 2-50. The distinction between energetically favorable and energetically unfavorable reactions.

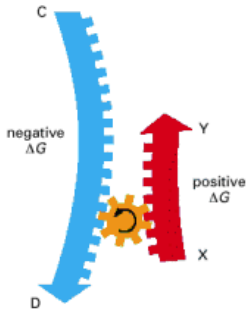

Figure 2-51. How reaction coupling is used to drive energetically unfavorable reactions.

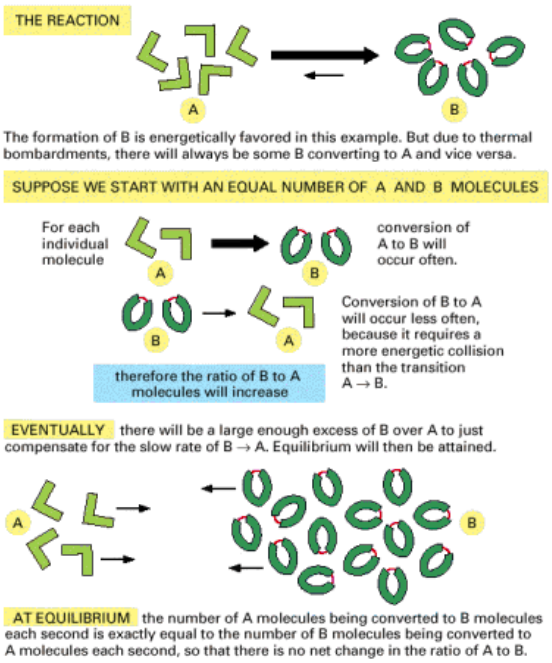

Figure 2-52. Chemical equilibrium. When a reaction reaches equilibrium, the forward and backward flux of reacting molecules are equal and opposite.

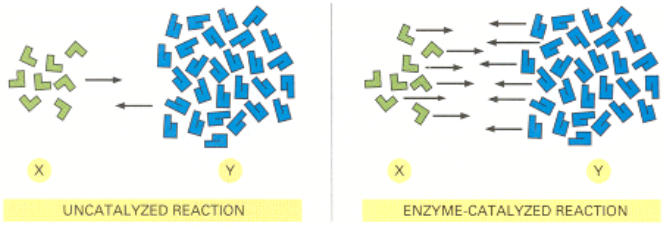

Figure 2-53. Enzymes cannot change the equilibrium point for reactions. Enzymes, like all catalysts, speed up the forward and backward rates of a reaction by the same factor. Therefore, for both the catalyzed and the uncatalyzed reactions shown here, the number of molecules undergoing the transition X Y is equal to the number of molecules undergoing the transition Y X when the ratio of Y molecules to X molecules is 3.5 to 1. In other words, the two reactions reach equilibrium at exactly the same point.

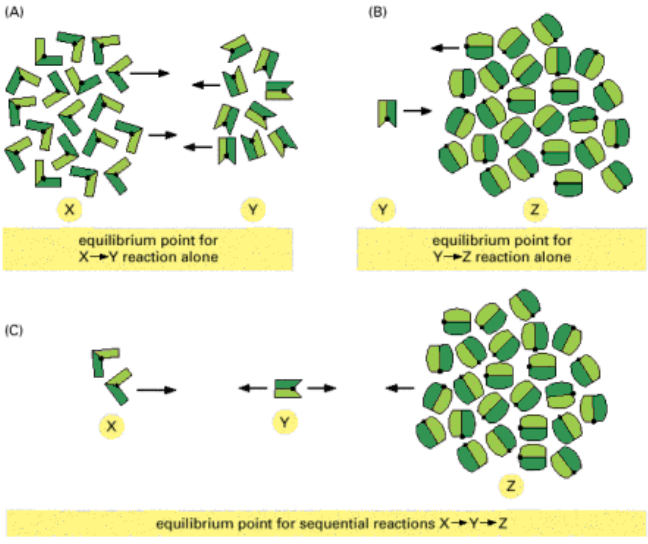

Figure 2-54. How an energetically unfavorable reaction can be driven by a second, following reaction. (A) At equilibrium, there are twice as many X molecules as Y molecules, because X is of lower energy than Y. (B) At equilibrium, there are 25 times more Z molecules than Y molecules, because Z is of much lower energy than Y. (C) If the reactions in (A) and (B) are coupled, nearly all of the X molecules will be converted to Z molecules, as shown.

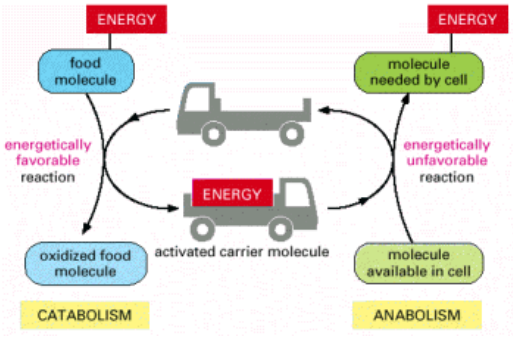

Figure 2-55. Energy transfer and the role of activated carriers in metabolism. By serving as energy shuttles, activated carrier molecules perform their function as go-betweens that link the breakdown of food molecules and the release of energy *(catabolism)* to the energy-requiring biosynthesis of small and large organic molecules *(anabolism)*.

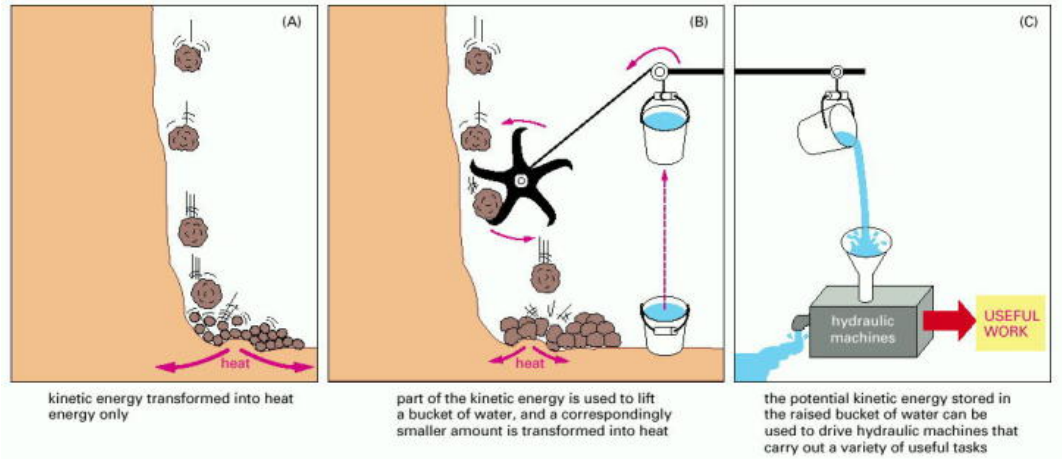

Figure 2-56. A mechanical model illustrating the principle of coupled chemical reactions. The spontaneous reaction shown in (A) could serve as an analogy for the direct oxidation of glucose to CO_2 and H_2O, which produces heat only. In (B) the same reaction is coupled to a second reaction; this second reaction could serve as an analogy for the synthesis of activated carrier molecules. The energy produced in (B) is in a more useful form than in (A) and can be used to drive a variety of otherwise energetically unfavorable reactions (C).

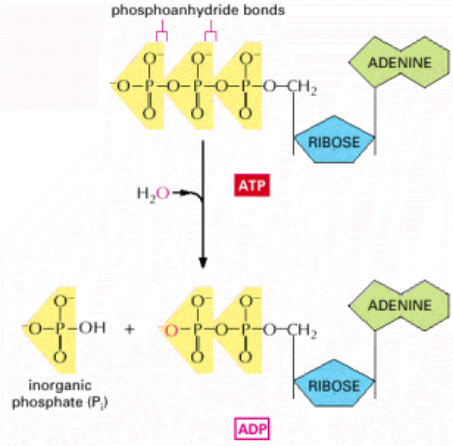

Figure 2-57. The hydrolysis of ATP to ADP and inorganic phosphate. The two outermost phosphates in ATP are held to the rest of the molecule by high-energy phosphoanhydride bonds and are readily transferred. As indicated, water can be added to ATP to form ADP and inorganic phosphate (P_i). This hydrolysis of the terminal phosphate of ATP yields between 11 and 13 kcal/mole of usable energy, depending on the intracellular conditions. The large negative ΔG of this reaction arises from a number of factors. Release of the terminal phosphate group removes an unfavorable repulsion between adjacent negative charges; in addition, the inorganic phosphate ion (P_i) released is stabilized by resonance and by favorable hydrogen-bond formation with water.

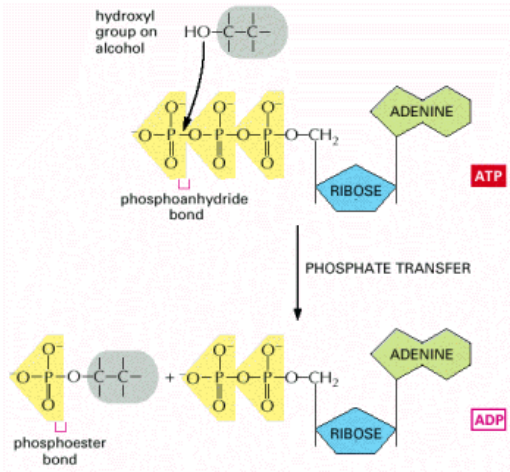

Figure 2-58. An example of a phosphate transfer reaction. Because an energy-rich phosphoanhydride bond in ATP is converted to a phosphoester bond, this reaction is energetically favorable, having a large negative ΔG. Reactions of this type are involved in the synthesis of phospholipids and in the initial steps of reactions that catabolize sugars.

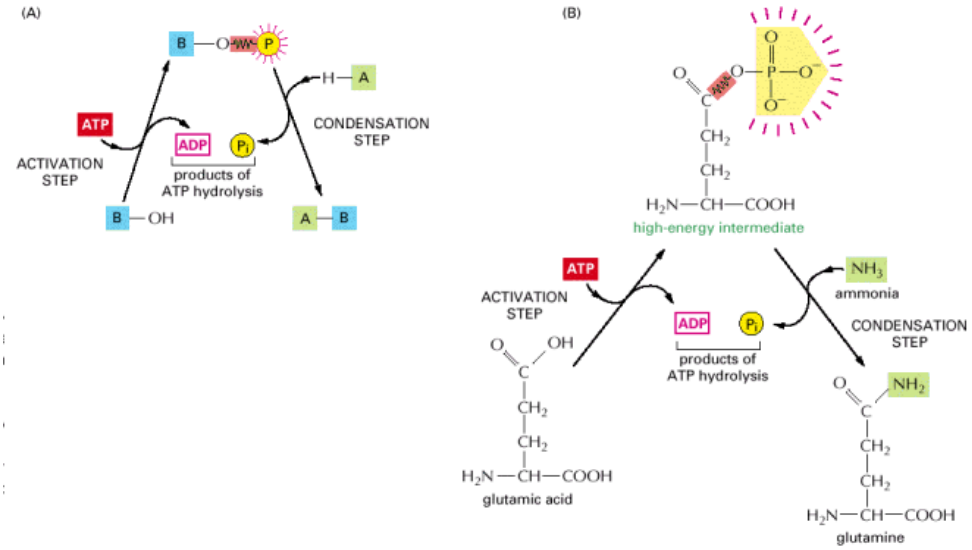

Figure 2-59. An example of an energetically unfavorable biosynthetic reaction driven by ATP hydrolysis. (A) Schematic illustration of the formation of A-B in the condensation reaction described in the text. (B) The biosynthesis of the common amino acid glutamine. Glutamic acid is first converted to a high-energy phosphorylated intermediate (corresponding to the compound B-O-PO_3 described in the text), which then reacts with ammonia (corresponding to A-H) to form glutamine. In this example both steps occur on the surface of the same enzyme, *glutamine synthase*. Note that, for clarity, the amino acids are shown in their uncharged form.

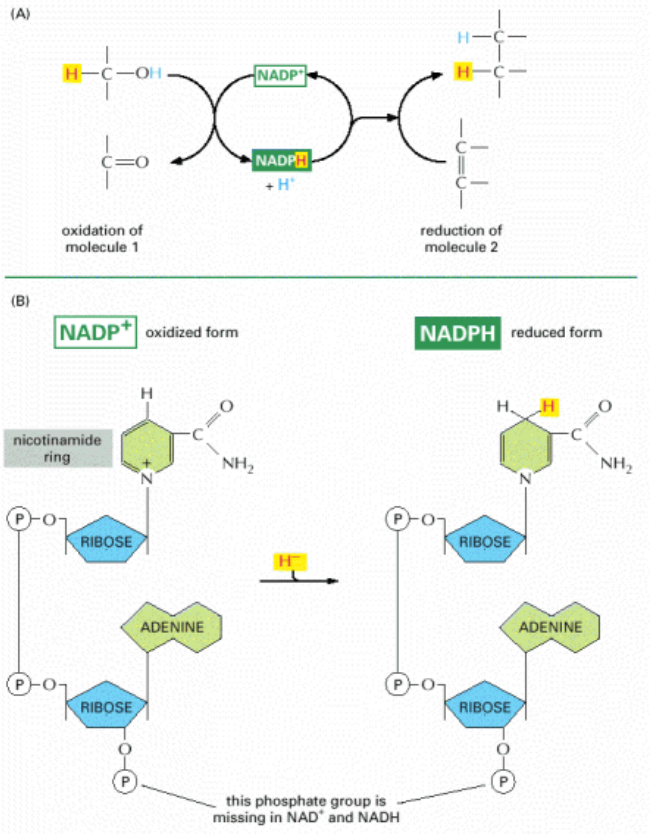

Figure 2-60. NADPH, an important carrier of electrons. (A) NADPH is produced in reactions of the general type shown on the left, in which two hydrogen atoms are removed from a substrate. The oxidized form of the carrier molecule, $NADP^+$, receives one hydrogen atom plus an electron (a hydride ion), and the proton (H^+) from the other H atom is released into solution. Because NADPH holds its hydride ion in a high-energy linkage, the added hydride ion can easily be transferred to other molecules, as shown on the right. (B) The structure of $NADP^+$ and NADPH. The part of the $NADP^+$ molecule known as the nicotinamide ring accepts two electrons together with a proton (the equivalent of a hydride ion, H^-), forming NADPH. The molecules NAD^+ and NADH are identical in structure to $NADP^+$ and NADPH, respectively, except that the indicated phosphate group is absent from both.

Figure 2-61. The final stage in one of the biosynthetic routes leading to cholesterol. As in many other biosynthetic

reactions, the reduction of the C=C bond is achieved by the transfer of a hydride ion from the carrier molecule NADPH, plus a proton (H^+) from the solution.

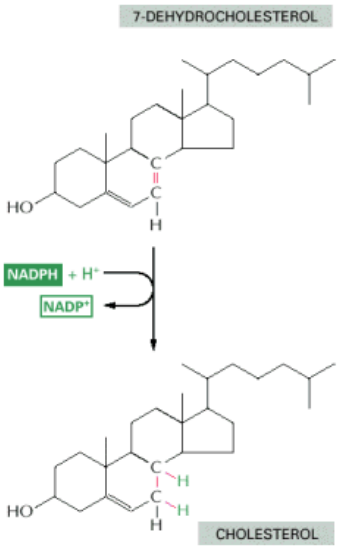

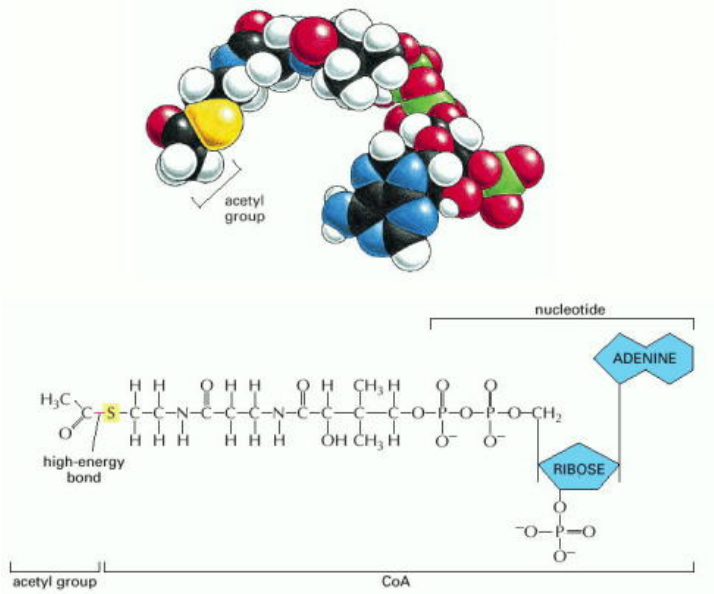

Figure 2-62. The structure of the important activated carrier molecule acetyl CoA. A space-filling model is shown above the structure. The sulfur atom *(yellow)* forms a thioester bond to acetate. Because this is a high-energy linkage, releasing a large amount of free energy when it is hydrolyzed, the acetate molecule can be readily transferred to other molecules.

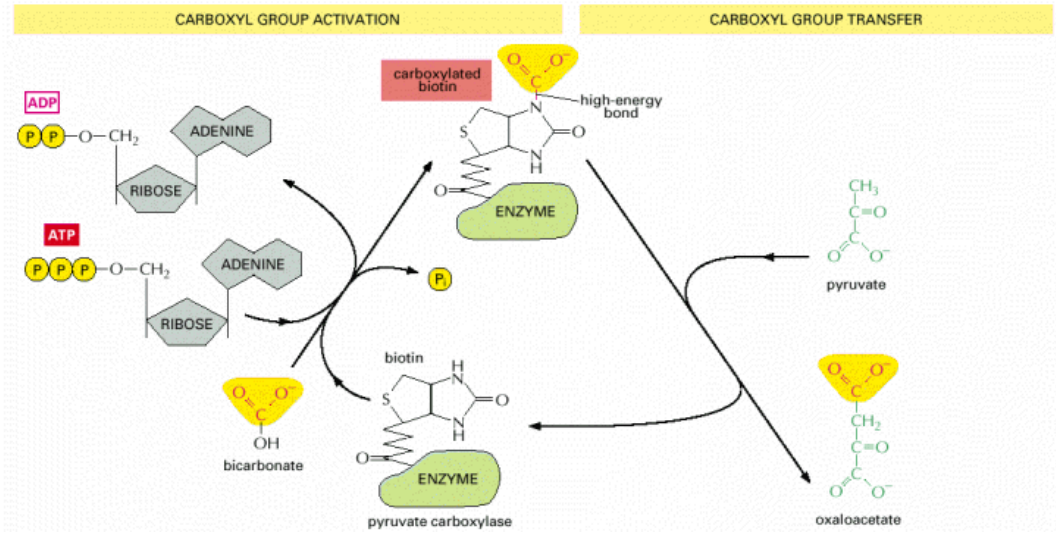

Figure 2-63. A carboxyl group transfer reaction using an activated carrier molecule. Carboxylated biotin is used by the enzyme *pyruvate carboxylase* to transfer a carboxyl group in the production of oxaloacetate, a molecule needed for the citric acid cycle. The acceptor molecule for this group transfer reaction is pyruvate. Other enzymes use biotin to transfer carboxyl groups to other acceptor molecules. Note that synthesis of carboxylated biotin requires energy that is derived from ATP - a general feature of many activated carriers.

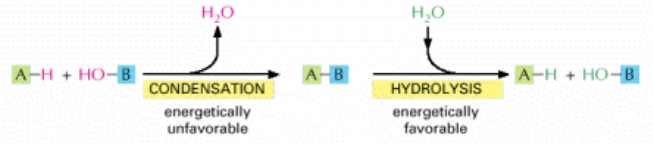

Figure 2-64. Condensation and hydrolysis as opposite reactions. The macromolecules of the cell are polymers that are formed from subunits (or monomers) by a condensation reaction and are broken down by hydrolysis. The condensation reactions are all energetically unfavorable.

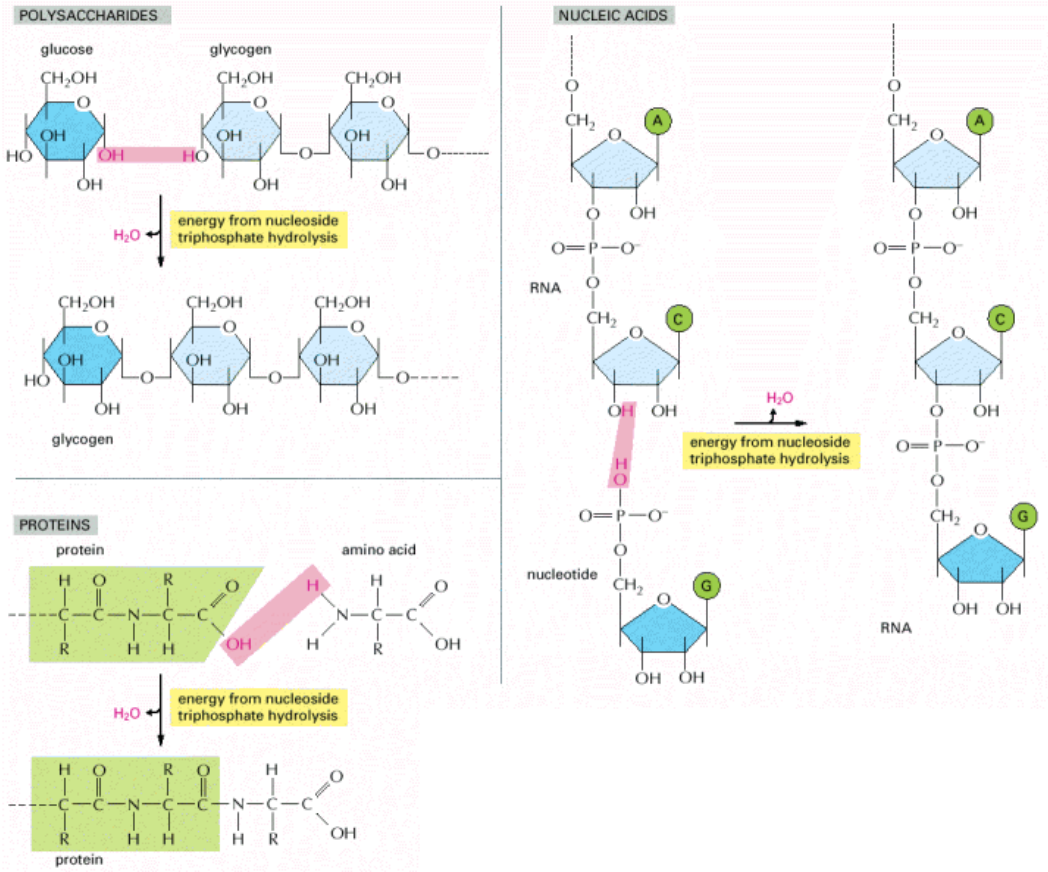

Figure 2-65. The synthesis of polysaccharides, proteins, and nucleic acids. Synthesis of each kind of biological polymer involves the loss of water in a condensation reaction. Not shown is the consumption of high-energy nucleoside triphosphates that is required to activate each monomer prior to its addition. In contrast, the reverse reaction - the breakdown of all three types of polymers - occurs by the simple addition of water (hydrolysis).

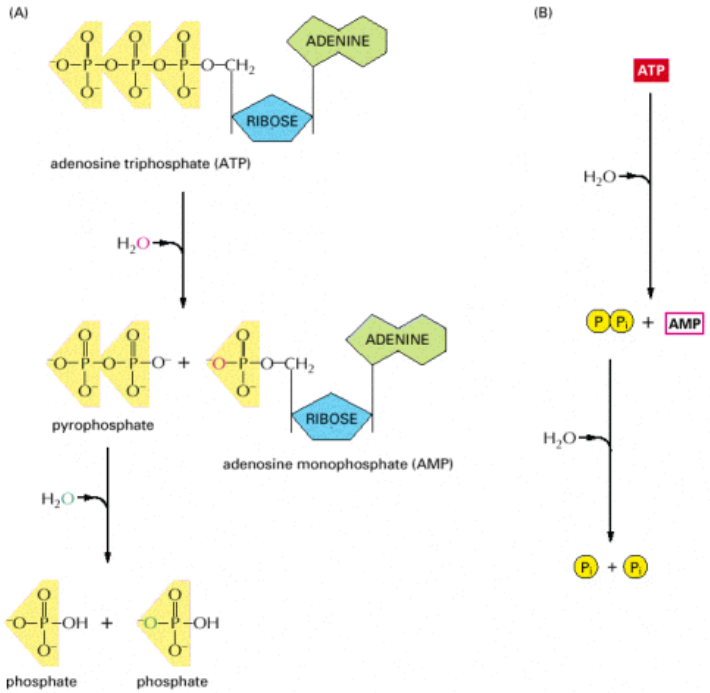

Figure 2-66. An alternative route for the hydrolysis of ATP, in which pyrophosphate is first formed and then hydrolyzed. This route releases about twice as much free energy as the reaction shown earlier in Figure 2-57. (A) In the two successive hydrolysis reactions, oxygen atoms from the participating water molecules are retained in the products, as indicated, whereas the hydrogen atoms dissociate to form free hydrogen ions, (H^+, not shown). (B) Diagram of overall reaction in summary form.

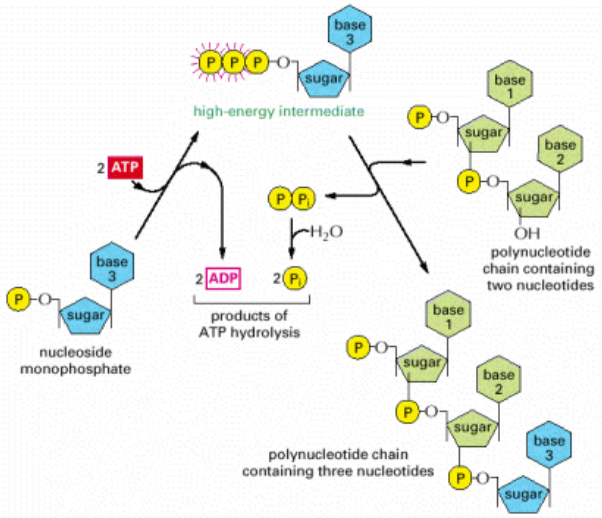

Figure 2-67. Synthesis of a polynucleotide, RNA or DNA, is a multistep process driven by ATP hydrolysis. In the first step, a nucleoside monophosphate is activated by the sequential transfer of the terminal phosphate groups from two ATP molecules. The high-energy intermediate formed - a nucleoside triphosphate - exists free in solution until it reacts with the growing end of an RNA or a DNA chain with release of pyrophosphate. Hydrolysis of the latter to inorganic phosphate is highly favorable and helps to drive the overall reaction in the direction of polynucleotide synthesis. For details, see Chapter 5.

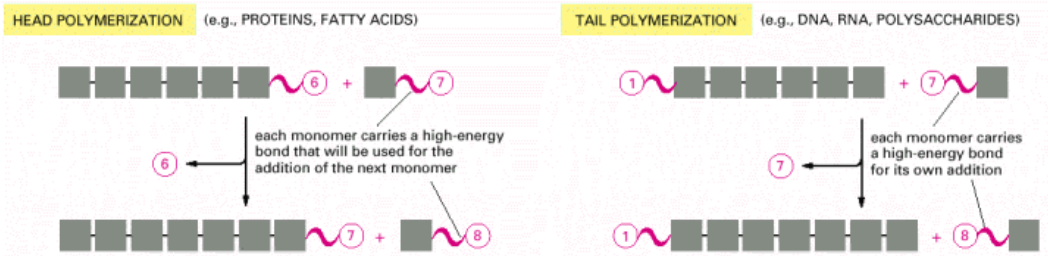

Figure 2-68. The orientation of the active intermediates in biological polymerization reactions. The head growth of polymers is compared with its alternative tail growth. As indicated, these two mechanisms are used to produce different biological macromolecules.

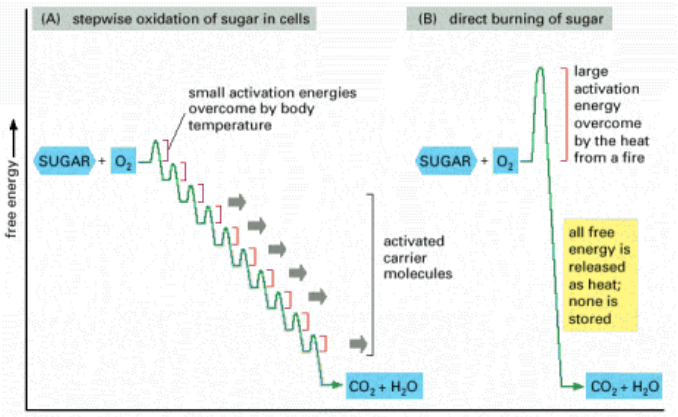

Figure 2-69. Schematic representation of the controlled stepwise oxidation of sugar in a cell, compared with ordinary burning. (A) In the cell, enzymes catalyze oxidation via a series of small steps in which free energy is transferred in conveniently sized packets to carrier molecules - most often ATP and NADH. At each step, an enzyme controls the reaction by reducing the activation energy barrier that has to be surmounted before the specific reaction can occur. The total free energy released is exactly the same in (A) and (B). But if the sugar was instead oxidized to CO_2 and H_2O in a single step, as in (B), it would release an amount of energy much larger than could be captured for useful purposes.

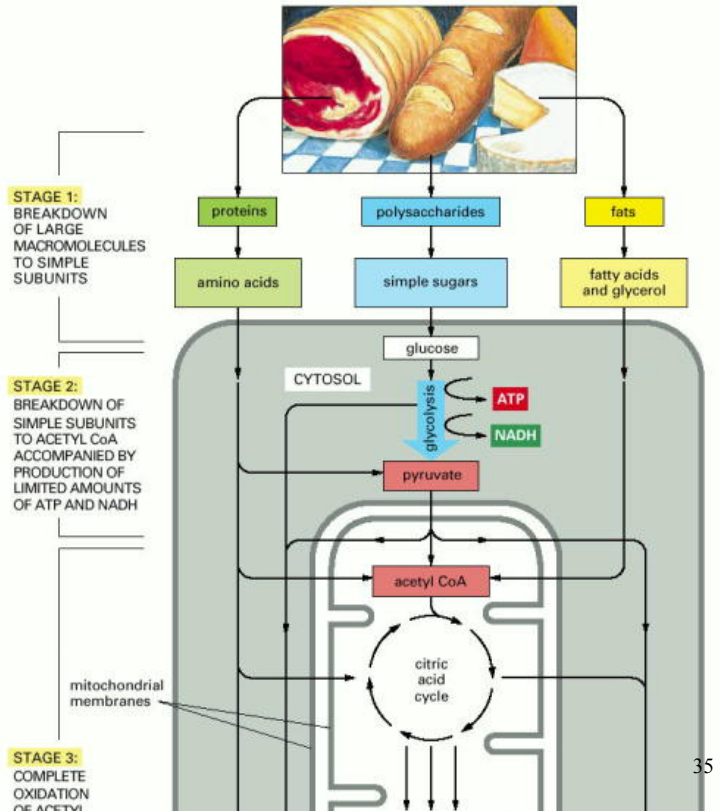

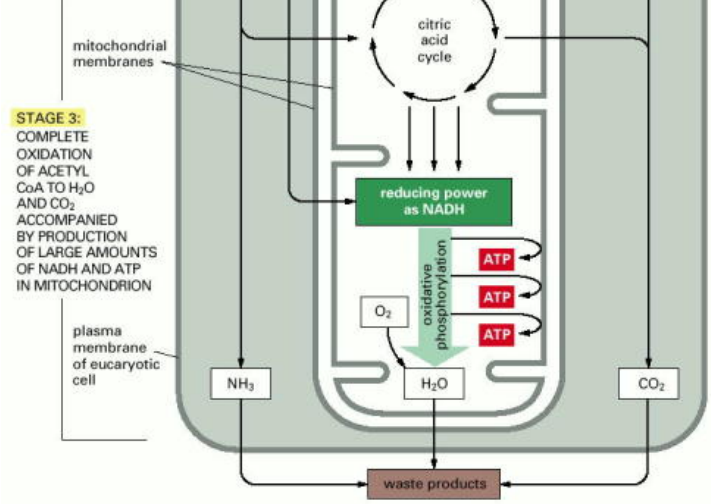

Figure 2-70. Simplified diagram of the three stages of cellular metabolism that lead from food to waste products in animal cells. This series of reactions produces ATP, which is then used to drive biosynthetic reactions and other energy-requiring processes in the cell. Stage 1 occurs outside cells. Stage 2 occurs mainly in the cytosol, except for the final step of conversion of pyruvate to acetyl groups on acetyl CoA, which occurs in mitochondria. Stage 3 occurs in mitochondria.

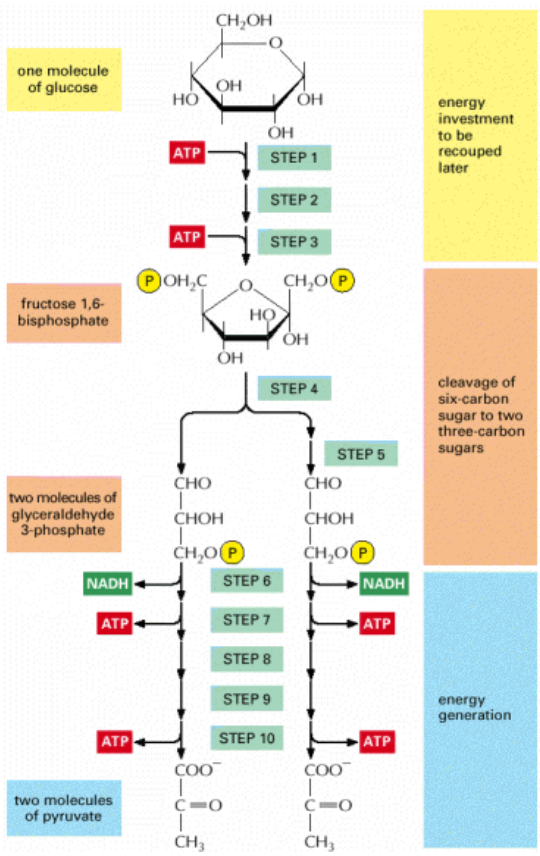

Figure 2-71. An outline of glycolysis. Each of the 10 steps shown is catalyzed by a different enzyme. Note that step 4 cleaves a six-carbon sugar into two three-carbon sugars, so that the number of molecules at every stage after this doubles. As indicated, step 6 begins the energy generation phase of glycolysis, which causes the net synthesis of ATP and NADH molecules (see also Panel 2-8).

Figure 2-72. Two pathways for the anaerobic breakdown of pyruvate. (A) When inadequate oxygen is present, for example, in a muscle cell undergoing vigorous contraction, the pyruvate produced by glycolysis is converted to lactate as shown. This reaction regenerates the NAD^+ consumed in step 6 of glycolysis, but the whole pathway yields much less energy overall than complete oxidation. (B) In some organisms that can grow anaerobically, such as yeasts, pyruvate is converted via acetaldehyde into carbon dioxide and ethanol. Again, this pathway regenerates NAD^+ from NADH, as required to enable glycolysis to continue. Both (A) and (B) are examples of *fermentations.*

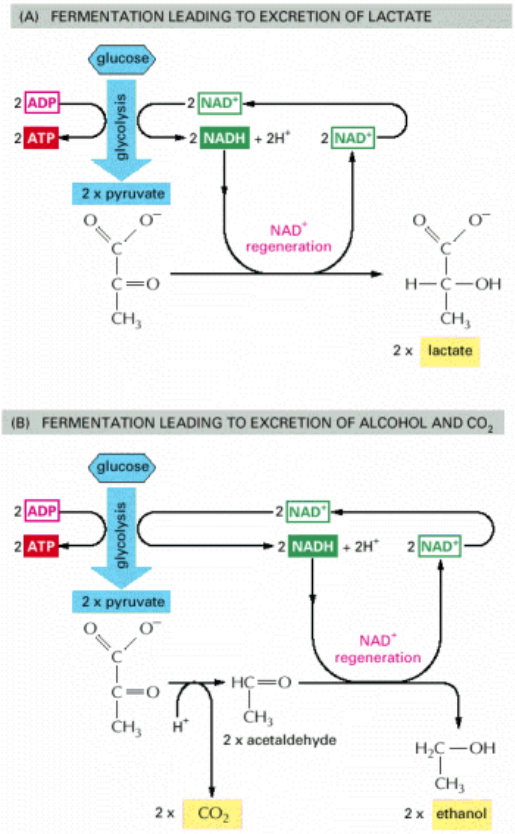

Figure 2-73. Energy storage in steps 6 and 7 of glycolysis. In these steps the oxidation of an aldehyde to a carboxylic acid is coupled to the formation of ATP and NADH. (A) Step 6 begins with the formation of a covalent bond between the substrate (glyceraldehyde 3-phosphate) and an -SH group exposed on the surface of the enzyme (glyceraldehyde 3-phosphate dehydrogenase). The enzyme then catalyzes transfer of hydrogen (as a hydride ion - a proton plus two electrons) from the bound glyceraldehyde 3-phosphate to a molecule of NAD^+. Part of the energy released in this oxidation is used to form a molecule of NADH and part is used to convert the original linkage between the enzyme and its substrate to a high-energy thioester bond (shown in *red).* A molecule of inorganic phosphate then displaces this high-energy bond on the enzyme, creating a high-energy sugar-phosphate bond instead *(red).* At this point the enzyme has not only stored energy in NADH, but also coupled the energetically favorable oxidation of an aldehyde to the energetically unfavorable formation of a high-energy phosphate bond. The second reaction has been driven by

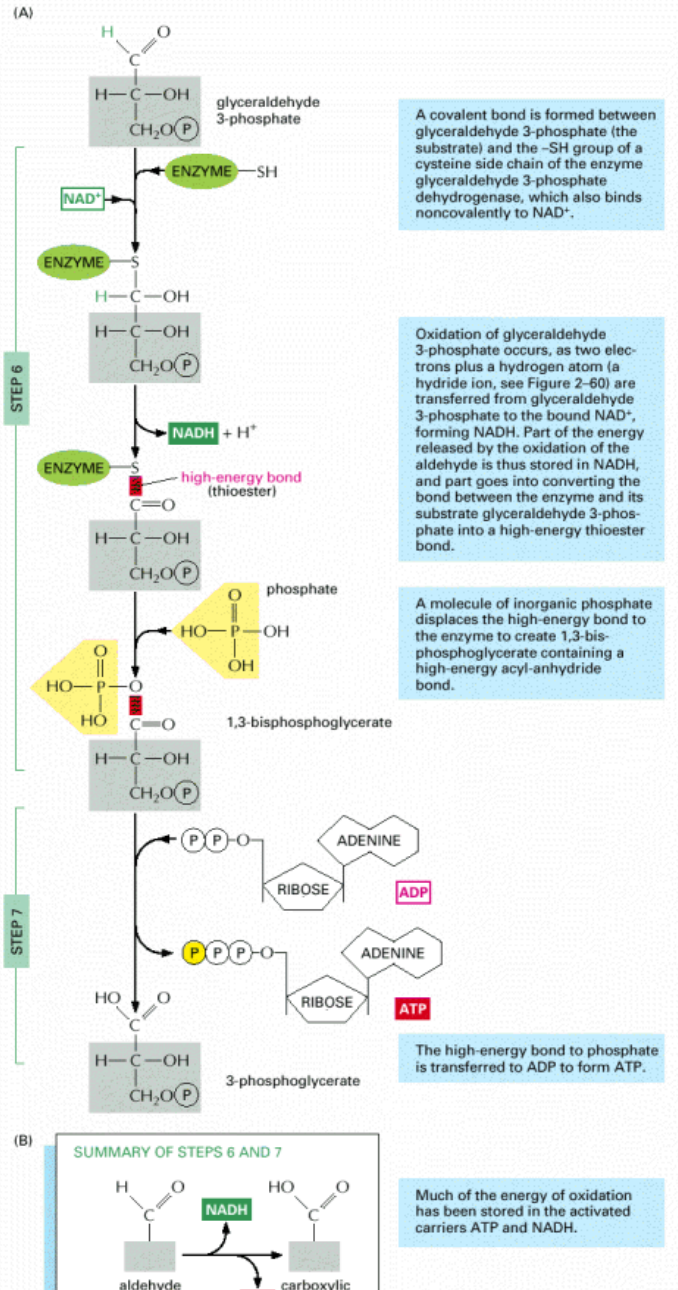

the first, thereby acting like the "paddle wheel" coupler in Figure 2-56. In reaction step 7, the high-energy sugar-phosphate intermediate just made, 1,3-bisphosphoglycerate, binds to a second enzyme, phosphoglycerate kinase. The reactive phosphate is transferred to ADP, forming a molecule of ATP and leaving a free carboxylic acid group on the oxidized sugar. (B) Summary of the overall chemical change produced by reactions 6 and 7.

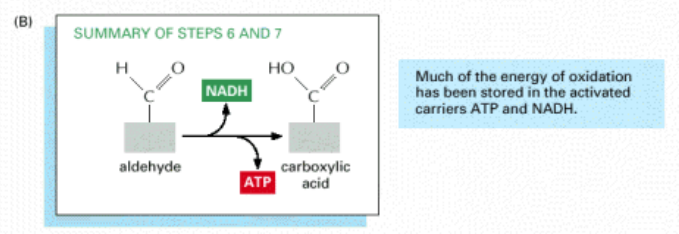

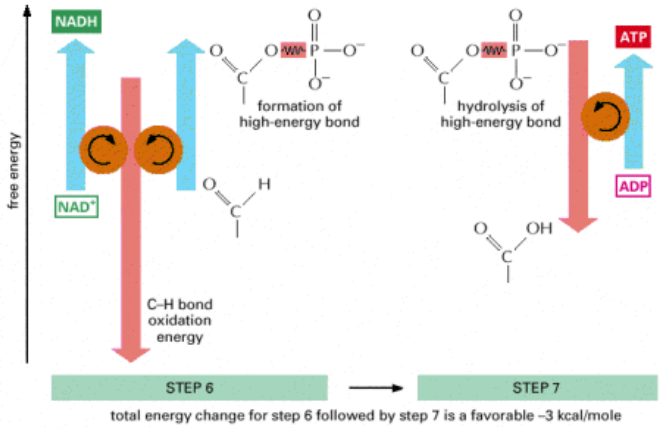

Figure 2-74. Schematic view of the coupled reactions that form NADH and ATP in steps 6 and 7 of glycolysis. The C-H bond oxidation energy drives the formation of both NADH and a high-energy phosphate bond. The breakage of the high-energy bond then drives ATP formation.

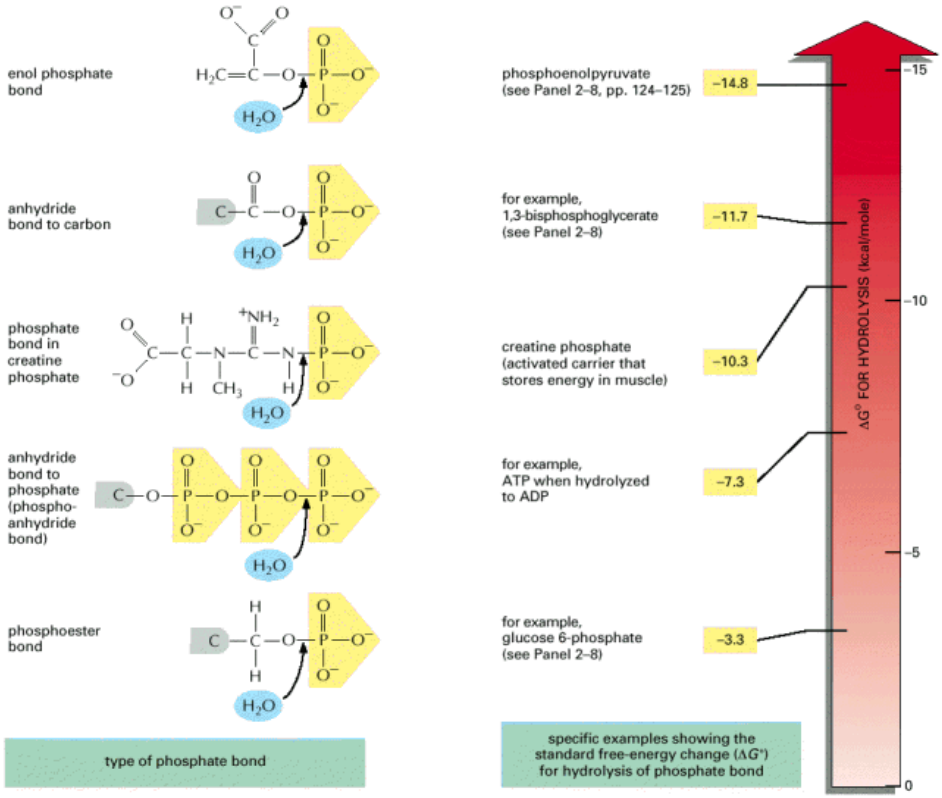

Figure 2-75. Some phosphate bond energies. The transfer of a phosphate group from any molecule 1 to any molecule 2 is energetically favorable if the standard free-energy change ($\Delta G°$) for the hydrolysis of the phosphate bond in molecule 1 is more negative than that for hydrolysis of the phosphate bond in molecule 2. Thus, for example, a phosphate group is readily transferred from 1,3-bisphosphoglycerate to ADP, forming ATP. Note that the hydrolysis reaction can be viewed as the transfer of the phosphate group to water.

Figure 2-76. The oxidation of pyruvate to acetyl CoA and CO_2. (A) The structure of the pyruvate dehydrogenase complex, which contains 60 polypeptide chains. This is an example of a large multienzyme complex in which reaction intermediates are passed directly from one enzyme to another. In eucaryotic cells it is located in the mitochondrion. (B) The reactions carried out by

the pyruvate dehydrogenase complex. The complex converts pyruvate to acetyl CoA in the mitochondrial matrix; NADH is also produced in this reaction. A, B, and C are the three enzymes *pyruvate decarboxylase*, *lipoamide reductase-transacetylase*, and *dihydrolipoyl dehydrogenase*, respectively. These enzymes are illustrated in (A); their activities are linked as shown.

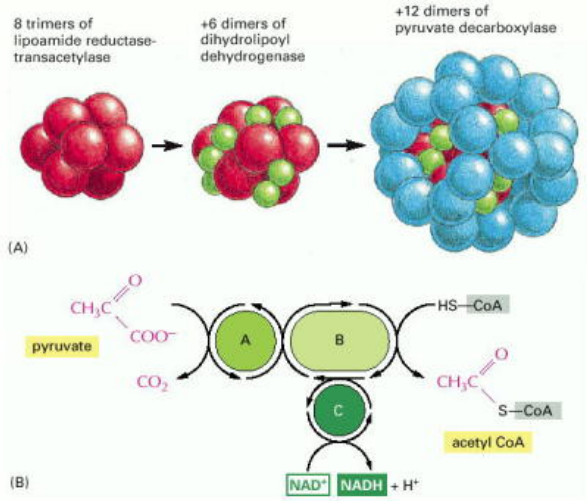

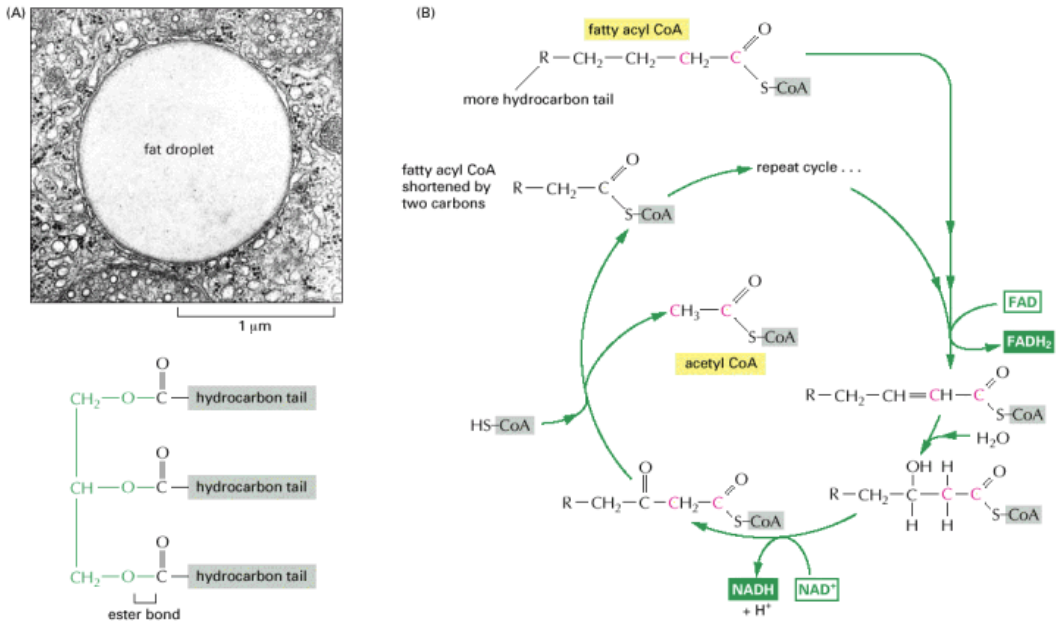

Figure 2-77. The oxidation of fatty acids to acetyl CoA. (A) Electron micrograph of a lipid droplet in the cytoplasm *(top)*, and the structure of fats *(bottom)*. Fats are triacylglycerols. The glycerol portion, to which three fatty acids are linked through ester bonds, is shown here in *green*. Fats are insoluble in water and form large lipid droplets in the specialized fat cells (called adipocytes) in which they are stored. (B) The fatty acid oxidation cycle. The cycle is catalyzed by a series of four enzymes in the mitochondrion. Each turn of the cycle shortens the fatty acid chain by two carbons (shown in *red)* and generates one molecule of acetyl CoA and one molecule each of NADH and $FADH_2$. The structure of $FADH_2$ will be presented in Figure 2-80B. (A, courtesy of Daniel S. Friend.)

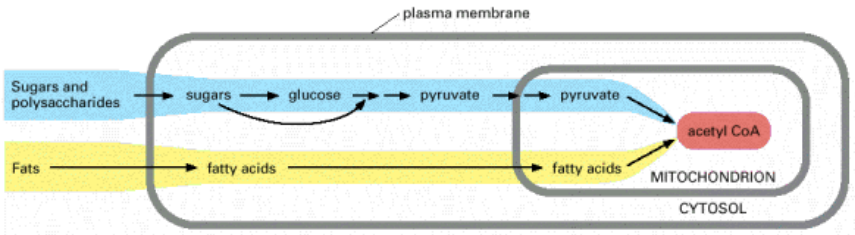

Figure 2-78. Pathways for the production of acetyl CoA from sugars and fats. The mitochondrion in eucaryotic cells is the place where acetyl CoA is produced from both types of major food molecules. It is therefore the place where most of the cell's oxidation reactions occur and where most of its ATP is made.

Figure 2-79. Simple overview of the citric acid cycle. The reaction of acetyl CoA with oxaloacetate starts the cycle by producing citrate (citric acid). In each turn of the cycle, two molecules of CO_2 are produced as waste products, plus three molecules of NADH, one molecule of GTP, and one molecule of $FADH_2$. The number of carbon atoms in each intermediate is shown in a *yellow box.* For details, see Panel 2-9 (pp. 126127).

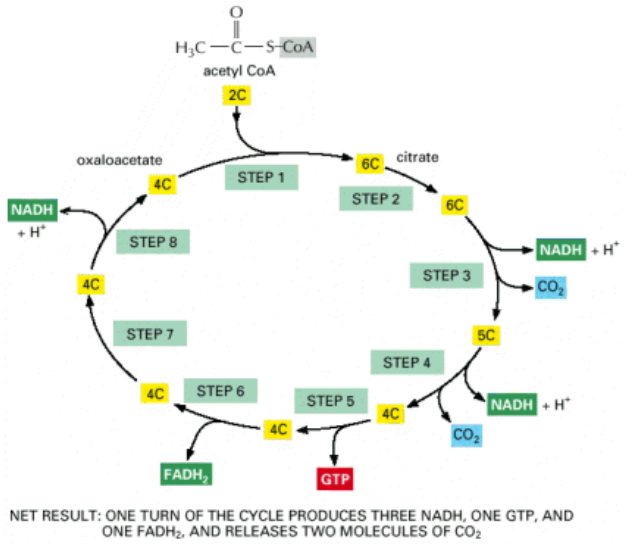

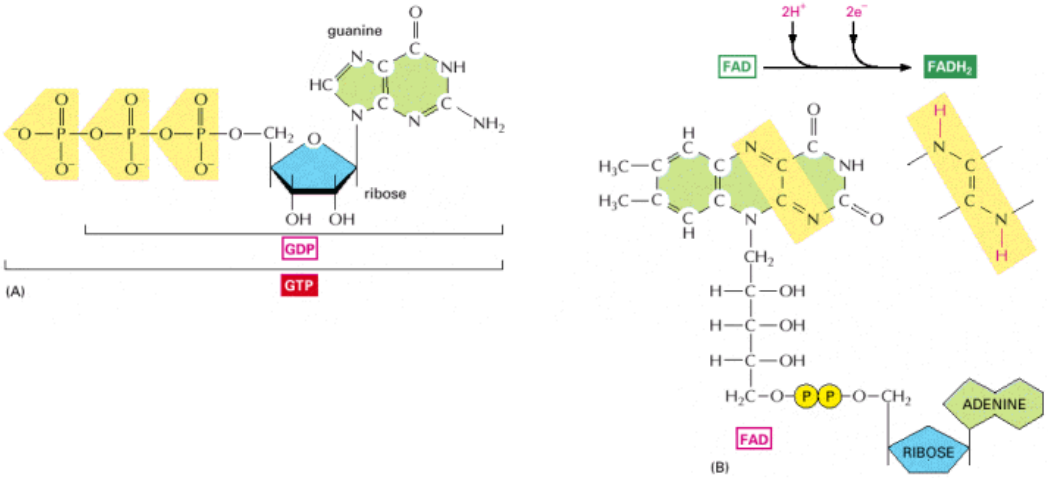

Figure 2-80. The structures of GTP and $FADH_2$. (A) GTP and GDP are close relatives of ATP and ADP, respectively. (B) $FADH_2$ is a carrier of hydrogens and high-energy electrons, like NADH and NADPH. It is shown here in its oxidized form (FAD) with the hydrogen-carrying atoms highlighted in *yellow.*

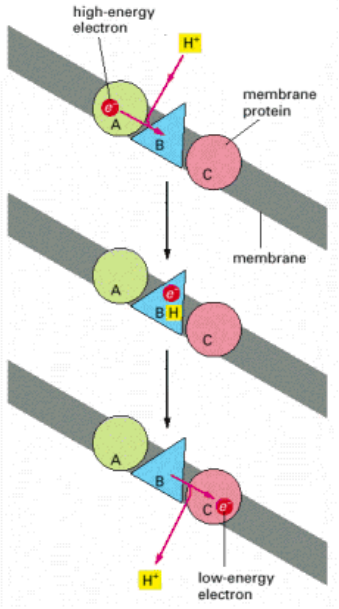

Figure 2-81. The generation of an H^+ gradient across a membrane by electron-transport reactions. A high-energy electron (derived, for example, from the oxidation of a metabolite) is passed sequentially by carriers A, B, and C to a lower energy state. In this diagram carrier B is arranged in the membrane in such a way that it takes up H^+ from one side and releases it to the other as the electron passes. The result is an H^+ gradient. This gradient represents a form of stored energy that is harnessed by other membrane proteins to drive the formation of ATP.

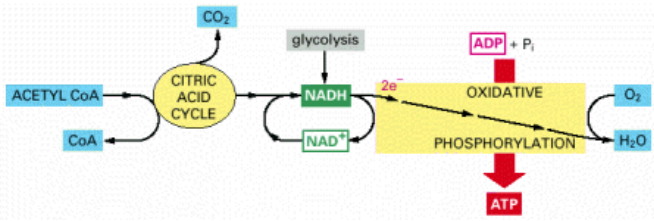

Figure 2-82. The final stages of oxidation of food molecules. Molecules of NADH and $FADH_2$ ($FADH_2$ is not shown) are produced by the citric acid cycle. These activated carriers donate high-energy electrons that are eventually used to reduce oxygen gas to water. A major portion of the energy released during the transfer of these electrons along an electron-transfer chain in the mitochondrial inner membrane (or in the plasma membrane of bacteria) is harnessed to drive the synthesis of ATP: hence the name oxidative phosphorylation.

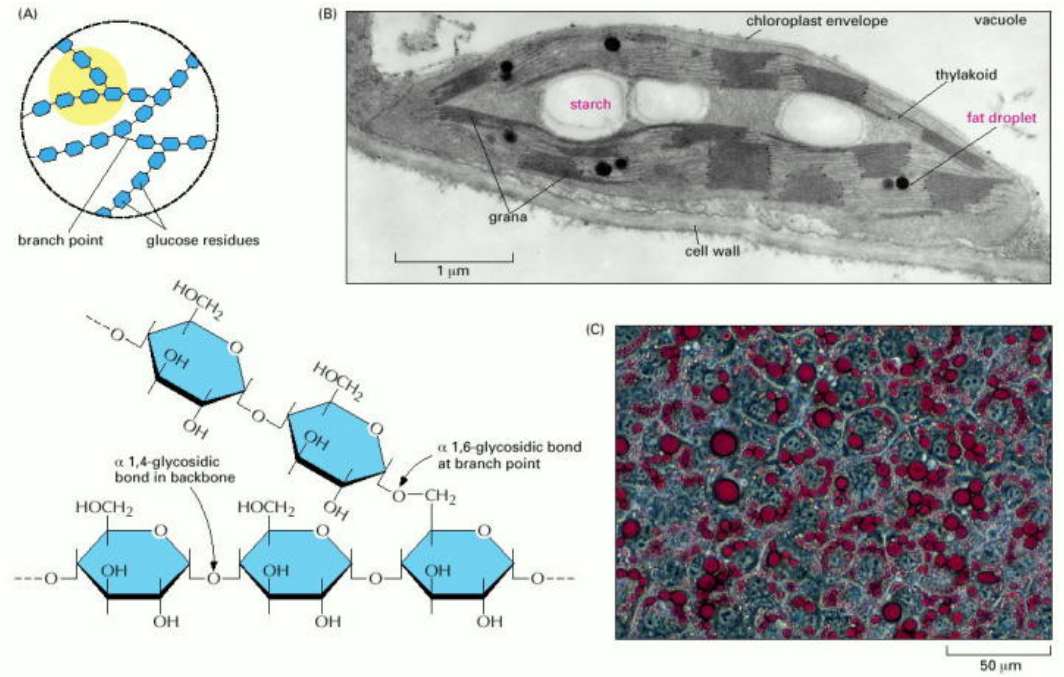

Figure 2-83. The storage of sugars and fats in animal and plant cells. (A) The structures of starch and glycogen, the storage form of sugars in plants and animals, respectively. Both are storage polymers of the sugar glucose and differ only in the frequency of branch points (the region in *yellow* is shown enlarged below). There are many more branches in glycogen than in starch. (B) A thin section of a single chloroplast from a plant cell, showing the starch granules and lipid droplets that have accumulated as a result of the biosyntheses occurring there. (C) Fat droplets (stained *red)* beginning to accumulate in developing fat cells of an animal. (B, courtesy of K. Plaskitt; C, courtesy of Ronald M. Evans and Peter Totonoz.)

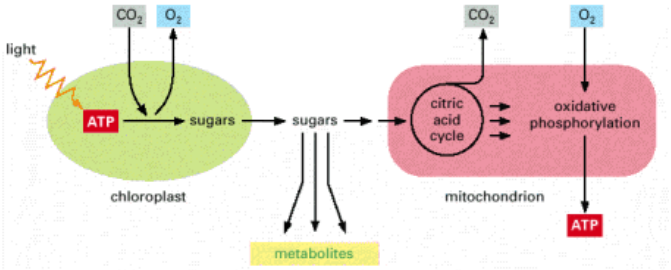

Figure 2-84. How the ATP needed for most plant cell metabolism is made. In plants, the chloroplasts and mitochondria collaborate to supply cells with metabolites and ATP.

Figure 2-85. Some plant seeds that serve as important foods for humans. Corn, nuts, and peas all contain rich stores of starch and fat that provide the young plant embryo in the seed with energy and building blocks for biosynthesis. (Courtesy of the John Innes Foundation.)

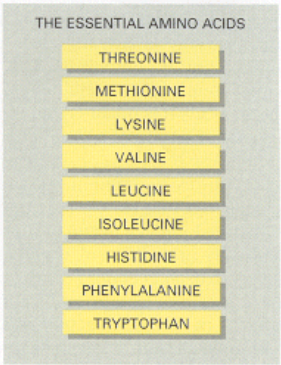

Figure 2-86. The nine essential amino acids. These cannot be synthesized by human cells and so must be supplied in the diet.

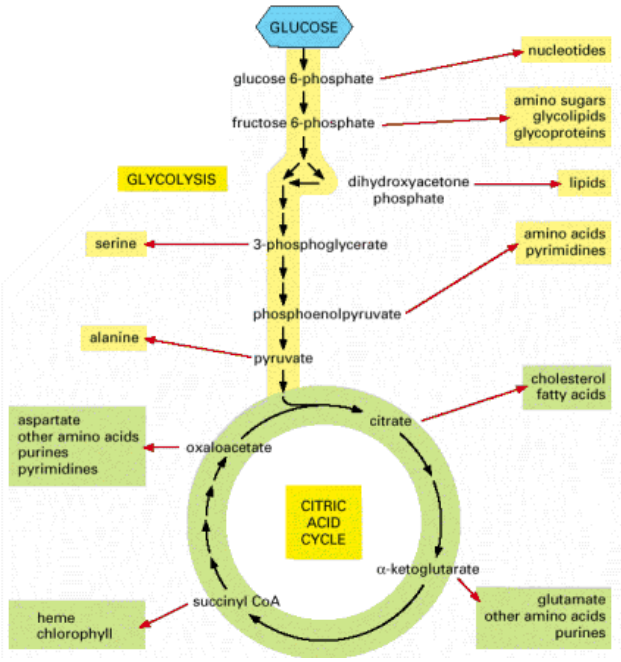

Figure 2-87. Glycolysis and the citric acid cycle provide the precursors needed to synthesize many important biological molecules. The amino acids, nucleotides, lipids, sugars, and other molecules - shown here as products - in turn serve as the precursors for the many macromolecules of the cell. Each *black arrow* in this diagram denotes a single enzyme-catalyzed reaction; the *red arrows* generally represent pathways with many steps that are required to produce the indicated products.

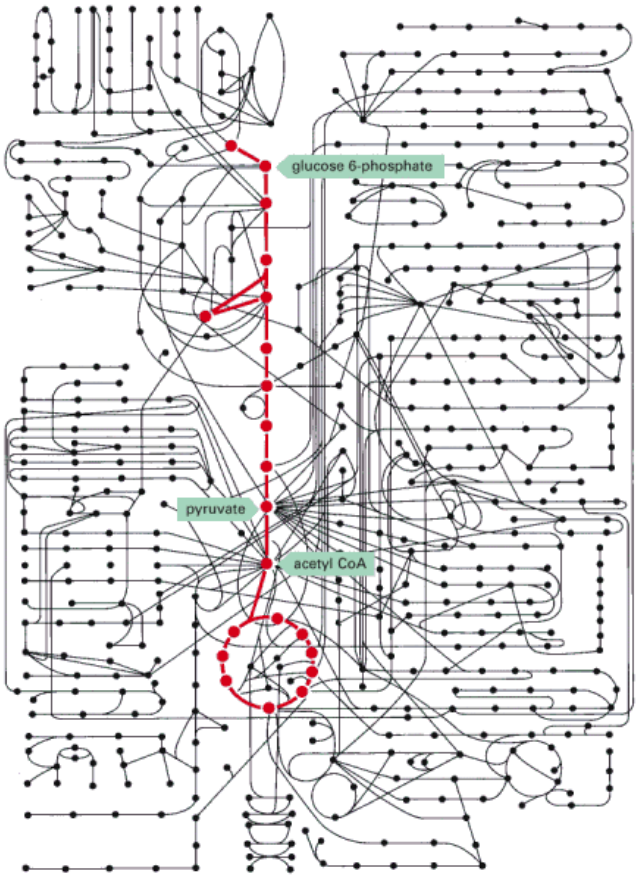

Figure 2-88. Glycolysis and the citric acid cycle are at the center of metabolism. Some 500 metabolic reactions of a typical cell are shown schematically with the reactions of glycolysis and the citric acid cycle in *red*. Other reactions either lead into these two central pathways - delivering small molecules to be catabolized with production of energy - or they lead outward and thereby supply carbon compounds for the purpose of biosynthesis.

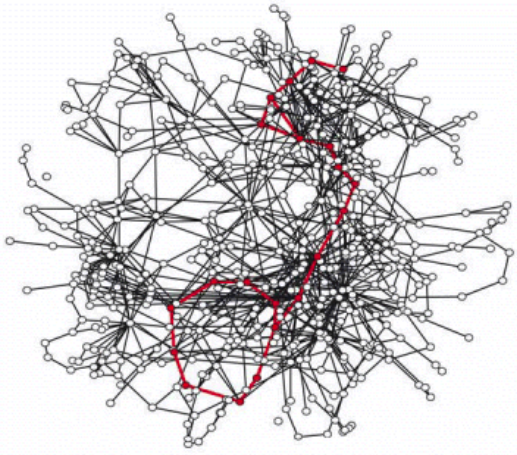

Figure 2-89. A representation of all of the known metabolic reactions involving small molecules in a yeast cell. As in Figure 2-88, the reactions of glycolysis and the citric acid cycle are highlighted in *red*. This metabolic map is unusual in making use of three-dimensions, so as to allow the many interactions between pathways to be emphasized. It is meant to be viewed on a computer screen, where it can be rotated and inspected from every angle. (From H. Jeong, S.P. Mason, A-L. Barabási and N. Oltava, *Nature* 411:4142, 2001. © Macmillan Magazines Ltd.)

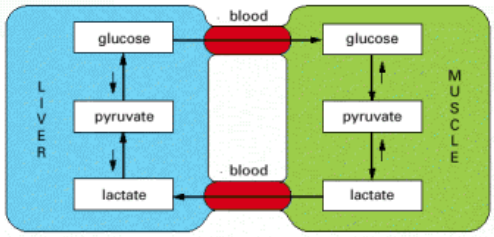

Figure 2-90. Schematic view of the metabolic cooperation between liver and muscle cells. The principal fuel of actively contracting muscle cells is glucose, much of which is supplied by liver cells. Lactic acid, the end product of anaerobic glucose breakdown by glycolysis in muscle, is converted back to glucose in the liver by the process of gluconeogenesis.

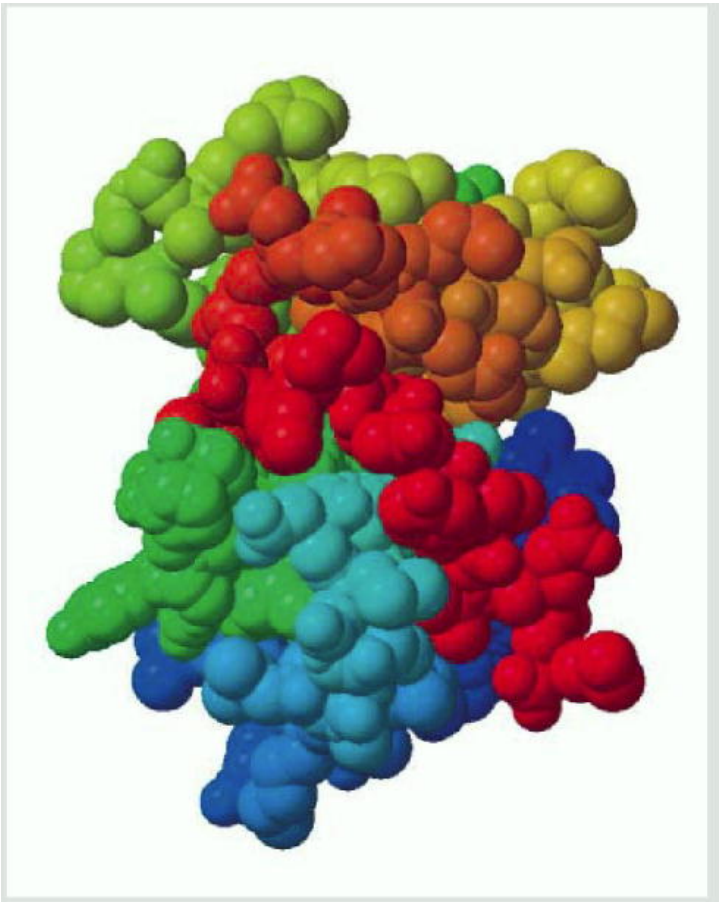

Protein structure A small protein domain, the SH2 domain, is shown here in a space-filling representation. For further views, see Panel 3-2.(Courtesy of David Lawson.)

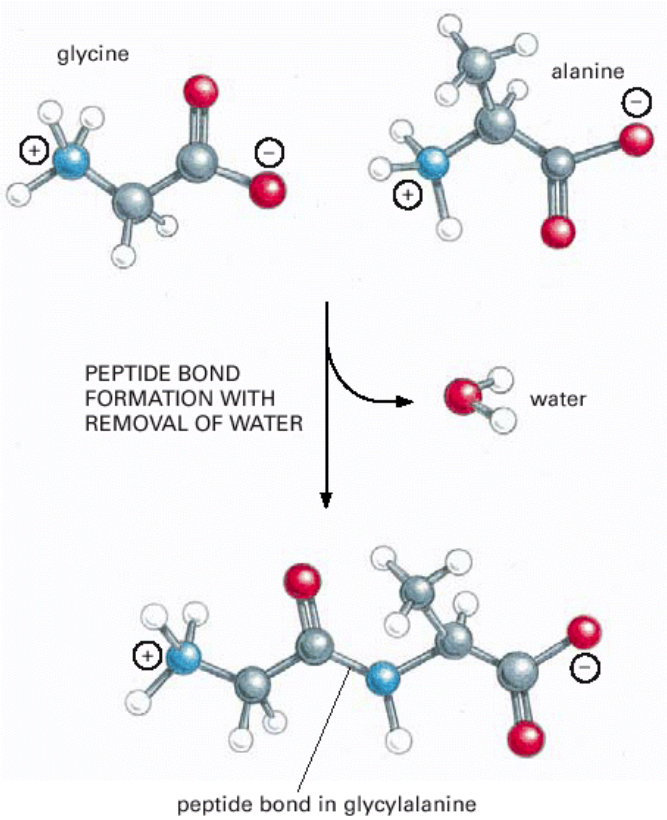

Figure 3-1. A peptide bond. This covalent bond forms when the carbon atom from the carboxyl group of one amino acid shares electrons with the nitrogen atom *(blue)* from the amino group of a second amino acid. As indicated, a molecule of water is lost in this

peptide bond in glycylalanine

condensation reaction.

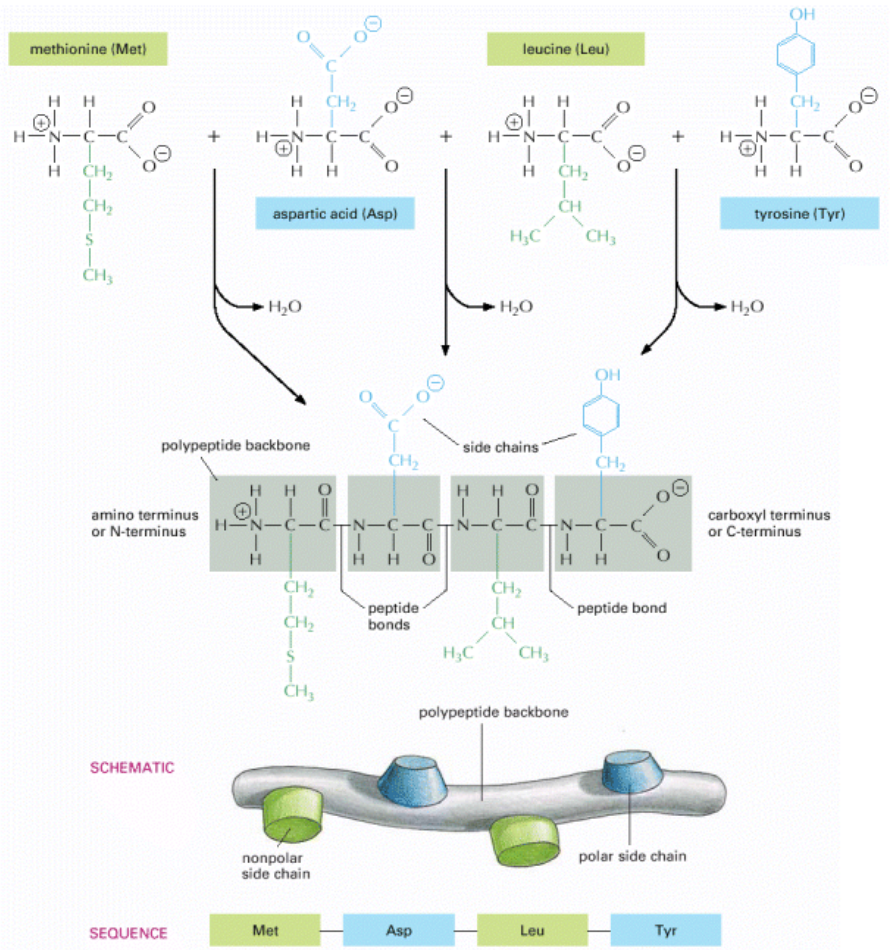

Figure 3-2. The structural components of a protein. A protein consists of a polypeptide backbone with attached side chains. Each type of protein differs in its sequence and number of amino acids; therefore, it is the sequence of the chemically different side chains that makes each protein distinct. The two ends of a polypeptide chain are chemically different: the end carrying the free amino group (NH_3^+, also written NH_2) is the amino terminus, or N-terminus, and that carrying the free carboxyl group (COO, also written COOH) is the carboxyl terminus or C-terminus. The amino acid sequence of a protein is always presented in the N-to-C direction, reading from left to right.

AMINO ACID			SIDE CHAIN
Aspartic acid	Asp	D	negative
Glutamic acid	Glu	E	negative
Arginine	Arg	R	positive
Lysine	Lys	K	positive
Histidine	His	H	positive
Asparagine	Asn	N	uncharged polar
Glutamine	Gln	Q	uncharged polar
Serine	Ser	S	uncharged polar
Threonine	Thr	T	uncharged polar
Tyrosine	Tyr	Y	uncharged polar

POLAR AMINO ACIDS

AMINO ACID			SIDE CHAIN
Alanine	Ala	A	nonpolar
Glycine	Gly	G	nonpolar
Valine	Val	V	nonpolar
Leucine	Leu	L	nonpolar
Isoleucine	Ile	I	nonpolar
Proline	Pro	P	nonpolar
Phenylalanine	Phe	F	nonpolar
Methionine	Met	M	nonpolar
Tryptophan	Trp	W	nonpolar
Cysteine	Cys	C	nonpolar

NONPOLAR AMINO ACIDS

Figure 3-3. The 20 amino acids found in proteins. Both three-letter and one-letter abbreviations are listed. As shown, there are equal numbers of polar and nonpolar side chains. For their atomic structures, see Panel 3-1 (pp. 132133).

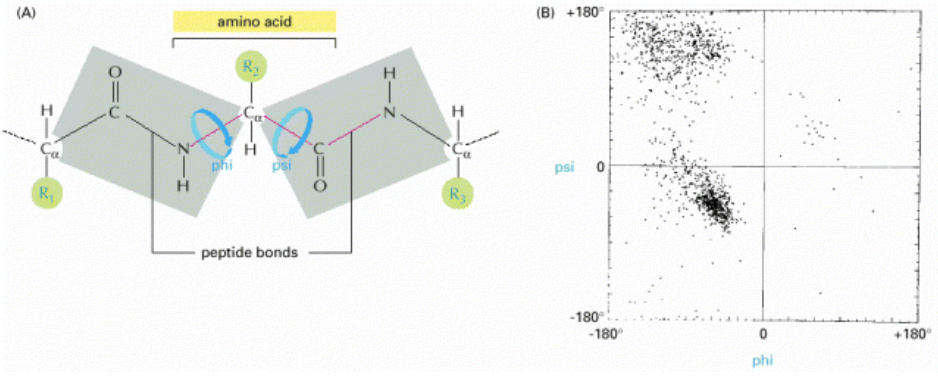

Figure 3-4. Steric limitations on the bond angles in a polypeptide chain. (A) Each amino acid contributes three bonds *(red)* to the backbone of the chain. The peptide bond is planar *(gray shading)* and does not permit rotation. By contrast, rotation can occur about the $C_\alpha C$ bond, whose angle of rotation is called psi (ψ), and about the NC_α bond, whose angle of rotation is called phi (ϕ). By convention, an R group is often used to denote an amino acid side chain *(green circles)*. (B) The conformation of the main-chain atoms in a protein is determined by one pair of ϕ and ψ angles for each amino acid; because of steric collisions between atoms within each amino acid, most pairs of ϕ and ψ angles do not occur. In this so-called Ramachandran plot, each dot represents an observed pair of angles in a protein. (B, from J. Richardson, *Adv. Prot. Chem.* 34:174175, 1981. © Academic Press.)

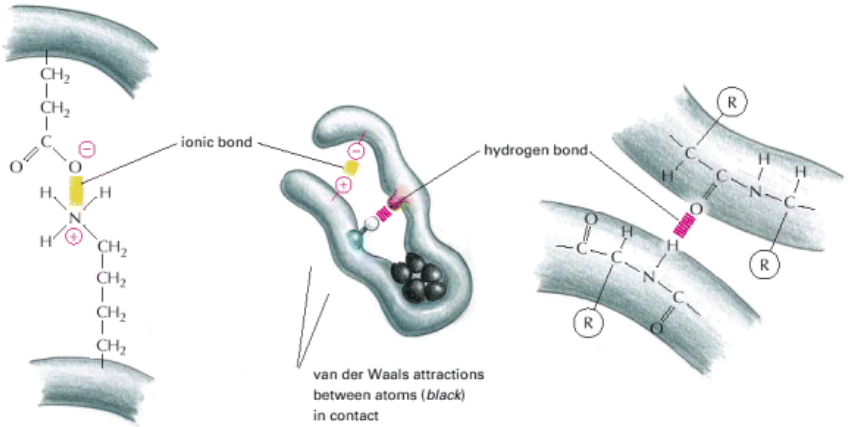

Figure 3-5. Three types of noncovalent bonds that help proteins fold. Although a single one of these bonds is quite weak, many of them often form together to create a strong bonding arrangement, as in the example shown. As in the previous figure, R is used as a general designation for an amino acid side chain.

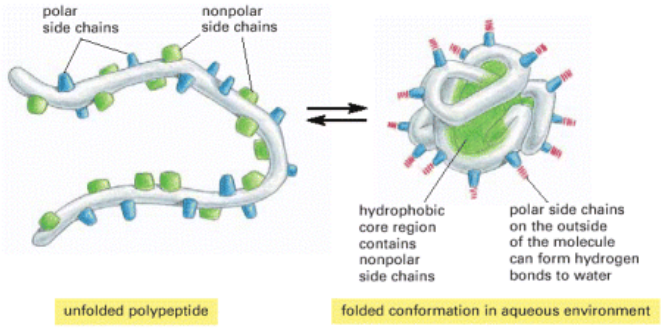

Figure 3-6. How a protein folds into a compact conformation. The polar amino acid side chains tend to gather on the outside of the protein, where they can interact with water; the nonpolar amino acid side chains are buried on the inside to form a tightly packed hydrophobic core of atoms that are hidden from water. In this schematic drawing, the protein contains only about 30 amino acids.

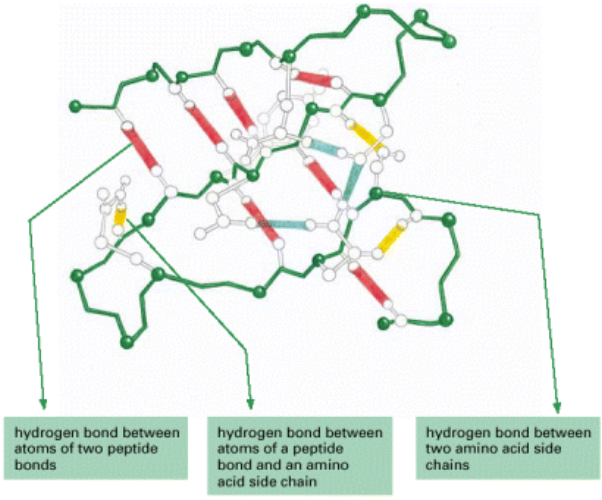

Figure 3-7. Hydrogen bonds in a protein molecule. Large numbers of hydrogen bonds form between adjacent regions of the folded polypeptide chain and help stabilize its three-dimensional shape. The protein depicted is a portion of the enzyme lysozyme, and the hydrogen bonds between the three possible pairs of partners have been differently colored, as indicated. (After C.K. Mathews and K.E. van Holde, Biochemistry. Redwood City, CA: Benjamin/Cummings, 1996.)

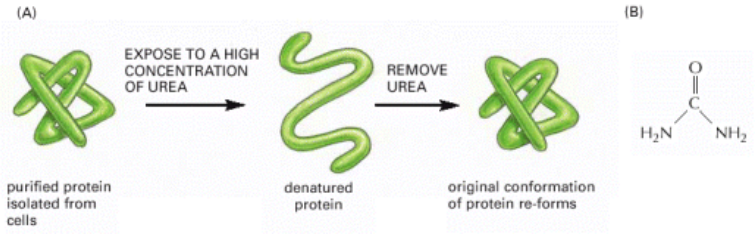

Figure 3-8. The refolding of a denatured protein. (A) This experiment demonstrates that the conformation of a protein is determined solely by its amino acid sequence. (B) The structure of urea. Urea is very soluble in water and unfolds proteins at high concentrations, where there is about one urea molecule for every six water molecules.

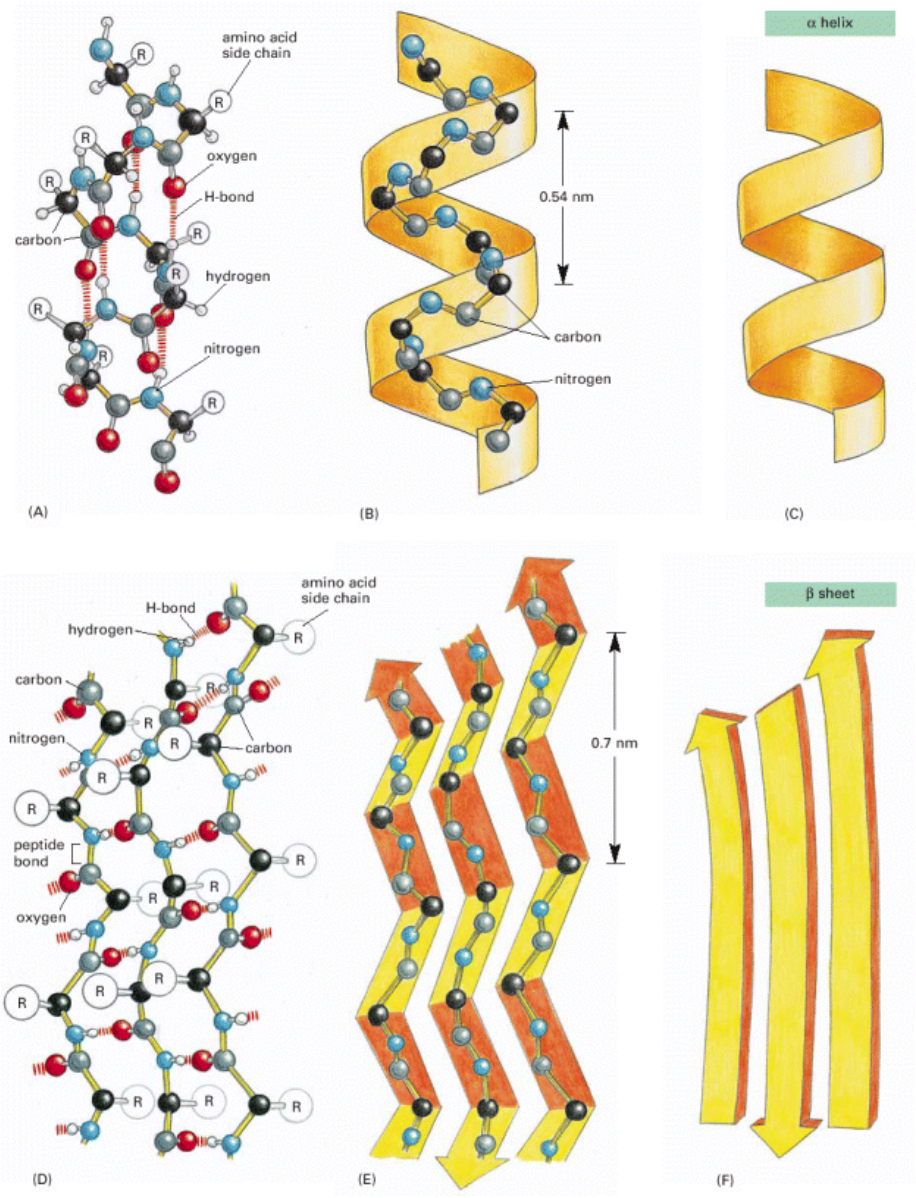

Figure 3-9. The regular conformation of the polypeptide backbone observed in the α helix and the β sheet. (A, B, and C) The α helix. The NH of every peptide bond is hydrogen-bonded to the C=O of a neighboring peptide bond located four peptide bonds away in the same chain. (D, E, and F) The β sheet. In this example, adjacent peptide chains run in opposite (antiparallel) directions. The individual polypeptide chains (strands) in a β sheet are held together by hydrogen-bonding between peptide bonds in different strands, and the amino acid side chains in each strand alternately project above and below the plane of the sheet. (A) and (D) show all the atoms in the polypeptide backbone, but the amino acid side chains are truncated and denoted by R. In contrast, (B) and (E) show the backbone atoms only, while (C) and (F) display the shorthand symbols that are used to represent the α helix and the β sheet in ribbon drawings of proteins (see Panel 3-2B).

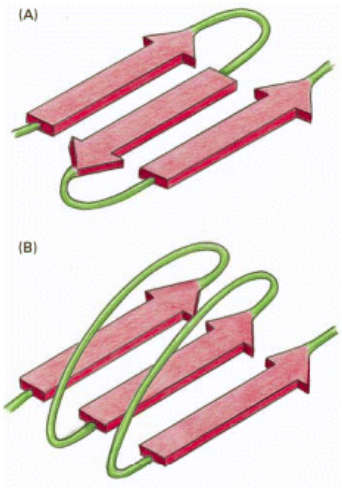

Figure 3-10. Two types of β sheet structures. (A) An antiparallel β sheet (see Figure 3-9D). (B) A parallel β sheet. Both of these structures are common in proteins.

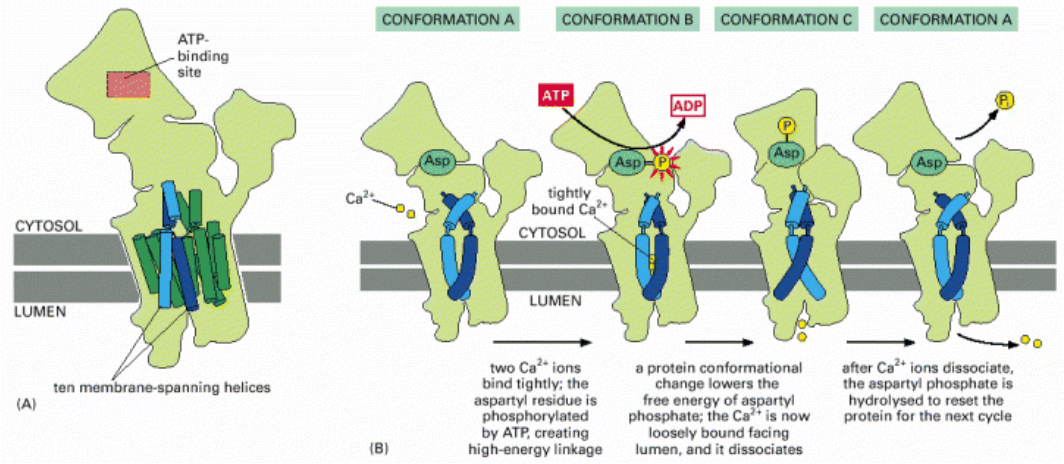

Figure 3-77. The transport of calcium ions by the Ca^{2+} pump. (A) The structure of the pump protein, formed from a single subunit of 994 amino acids (see Figure 11-15 for details). (B) A model for ion pumping. For simplicity, only two of the four transmembrane α helices that bind Ca^{2+} are shown.

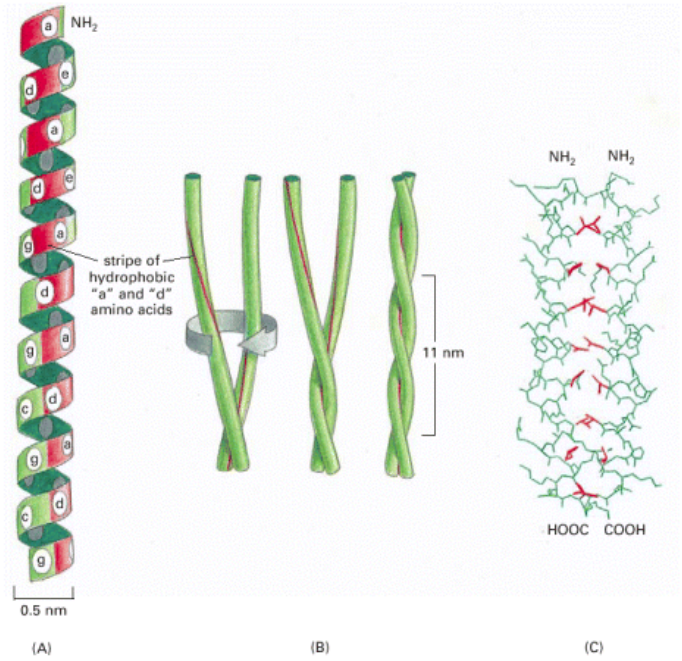

Figure 3-11. The structure of a coiled-coil. (A) A single α helix, with successive amino acid side chains labeled in a sevenfold sequence, "abcdefg" (from bottom to top). Amino acids "a" and "d" in such a sequence lie close together on the cylinder surface, forming a "stripe" (*red*) that winds slowly around the α helix. Proteins that form coiled-coils typically have nonpolar amino acids at positions "a" and "d." Consequently, as shown in (B), the two α helices can wrap around each other with the nonpolar side chains of one α helix interacting with the nonpolar side chains of the other, while the more hydrophilic amino acid side chains are left exposed to the aqueous environment. (C) The atomic structure of a coiled-coil determined by x-ray crystallography. The *red* side chains are nonpolar.

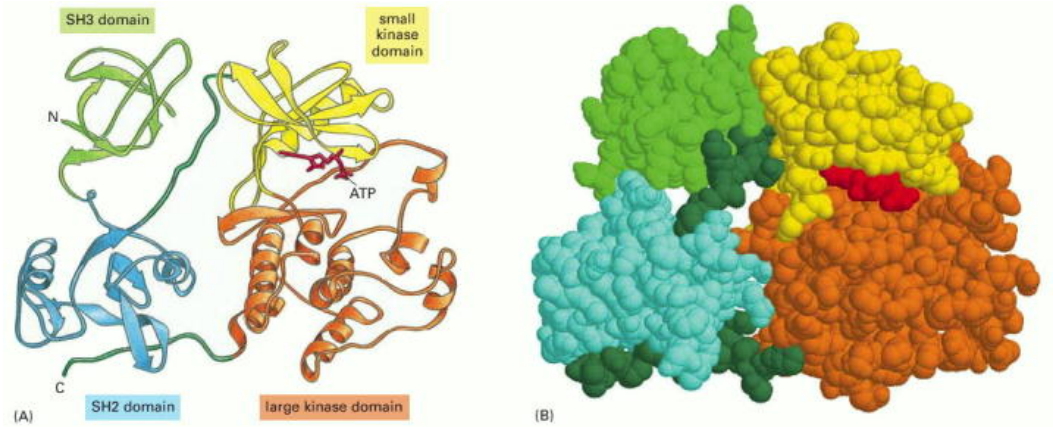

Figure 3-12. A protein formed from four domains. In the Src protein shown, two of the domains form a protein kinase enzyme, while the SH2 and SH3 domains perform regulatory functions. (A) A ribbon model, with ATP substrate in *red*. (B) A spacing-filling model, with ATP substrate in *red*. Note that the site that binds ATP is positioned at the interface of the two domains that form the kinase. The detailed structure of the SH2 domain is illustrated in Panel 3-2 (pp. 138139).

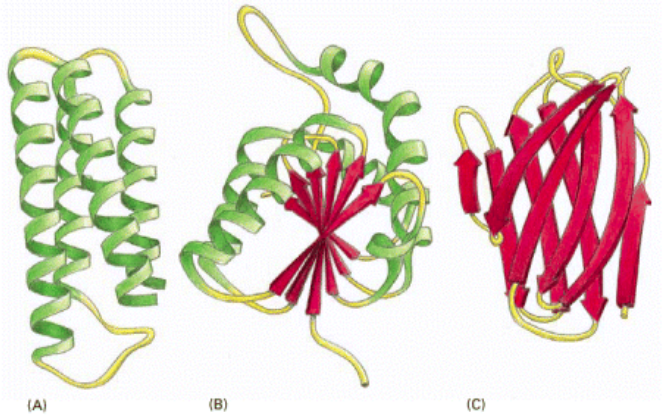

Figure 3-13. Ribbon models of three different protein domains. (A) Cytochrome b_{562}, a single-domain protein involved in electron transport in mitochondria. This protein is composed almost entirely of α helices. (B) The NAD-binding domain of the enzyme lactic dehydrogenase, which is composed of a mixture of α helices and β sheets. (C) The variable domain of an immunoglobulin (antibody) light chain, composed of a sandwich of two β sheets. In these examples, the α helices are shown in *green*, while strands organized as β sheets are denoted by *red arrows*. Note that the polypeptide chain generally traverses back and forth across the entire domain, making sharp turns only at the protein surface. It is the protruding loop regions *(yellow)* that often form the binding sites for other molecules. (Adapted from drawings courtesy of Jane Richardson.)

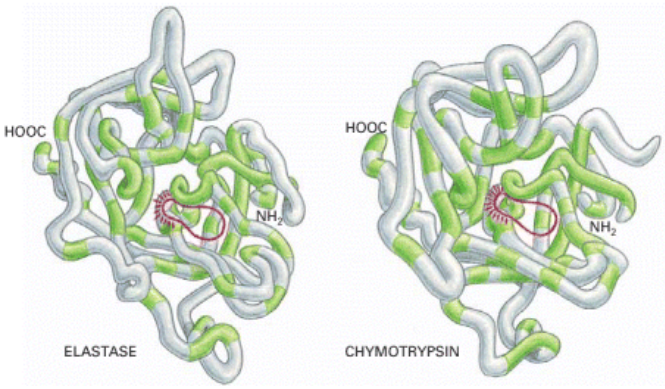

Figure 3-14. The conformations of two serine proteases compared. The backbone conformations of elastase and chymotrypsin. Although only those amino acids in the polypeptide chain shaded in *green* are the same in the two proteins, the two conformations are very similar nearly everywhere. The active site of each enzyme is circled in *red;* this is where the peptide bonds of the proteins that serve as substrates are bound and cleaved by hydrolysis. The serine proteases derive their name from the amino acid serine, whose side chain is part of the active site of each enzyme and directly participates in the cleavage reaction.

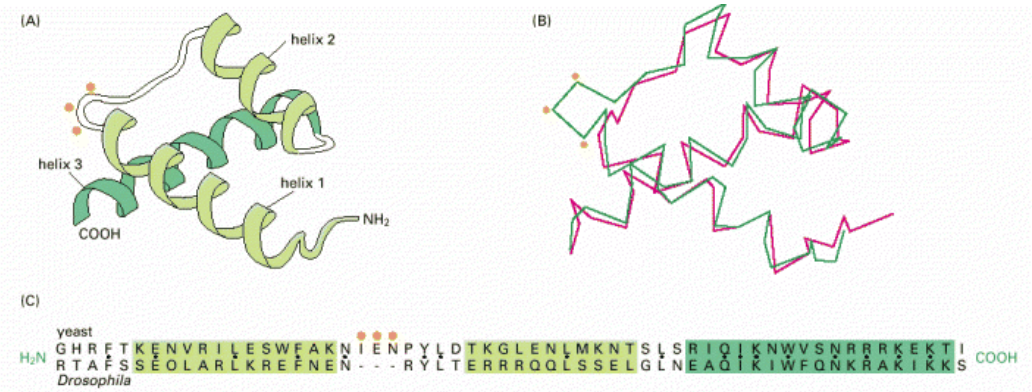

Figure 3-15. A comparison of a class of DNA-binding domains, called homeodomains, in a pair of proteins from two organisms separated by more than a billion years of evolution. (A) A ribbon model of the structure common to both proteins. (B) A trace of the α-carbon positions. The three-dimensional structures shown were determined by x-ray crystallography for the yeast α2 protein *(green)* and the *Drosophila* engrailed protein *(red).* (C) A comparison of amino acid sequences for the region of the proteins shown in (A) and (B). *Black dots* mark sites with identical amino acids. *Orange dots* indicate the position of a three amino acid insert in the α2 protein. (Adapted from C. Wolberger et al., *Cell* 67:517528, 1991.)

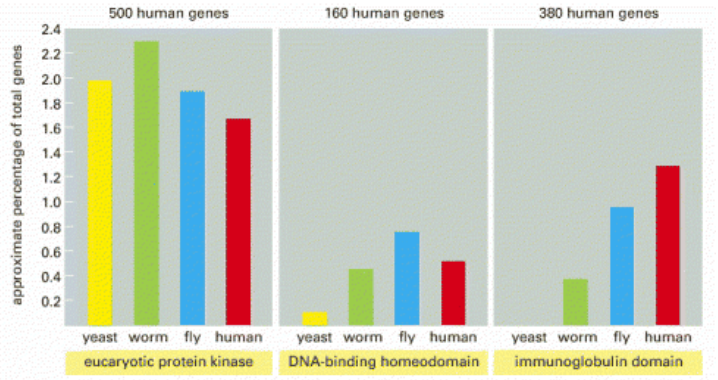

Figure 3-16. Percentage of total genes containing one or more copies of the indicated protein domain, as derived from complete genome sequences. Note that one of the three domains selected, the immunoglobulin domain, has been a relatively late addition, and its relative abundance has increased in the vertebrate lineage. The estimates of human gene numbers are approximate.

Figure 3-17. The use of short signature sequences to find homologous protein domains. The two short sequences of 15 and 9 amino acids shown *(green)* can be used to search large databases for a protein domain that is found in many proteins, the SH2 domain. Here, the first 50 amino acids of the SH2 domain of 100 amino acids is compared for the human and *Drosophila* Src protein (see Figure 3-12). In the computer-generated sequence comparison *(yellow row)*, exact matches between the human and *Drosophila* proteins are noted by the one-letter abbreviation for the amino acid; the positions with a similar but nonidentical amino acid are denoted by +, and nonmatches are blank. In this diagram, wherever one or both proteins contain an exact match to a position in the *green* sequences, both aligned sequences are colored *red*.

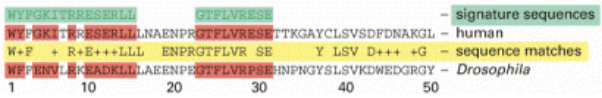

Figure 3-18. Domain shuffling. An extensive shuffling of blocks of protein sequence (protein domains) has occurred during protein evolution. Those portions of a protein denoted by the same shape and color in this diagram are evolutionarily related. Serine proteases like chymotrypsin are formed from two domains *(brown)*. In the three other proteases shown, which are highly regulated and more specialized, these two protease domains are connected to one or more domains homologous to domains found in epidermal growth factor (EGF; *green)*, to a calcium-binding protein *(yellow)*, or to a "kringle" domain *(blue)* that contains three internal disulfide bridges. Chymotrypsin is illustrated in Figure 3-14.

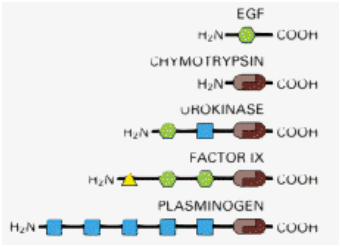

Figure 3-19. The three-dimensional structures of some protein modules. In these ribbon diagrams, β-sheet strands are shown as *arrows*, and the N- and C-termini are indicated by *red spheres.* (Adapted from M. Baron, D.G. Norman, and I.D. Campbell, *Trends Biochem. Sci.* 16:1317, 1991, and D.J. Leahy et al., *Science* 258:987991, 1992.)

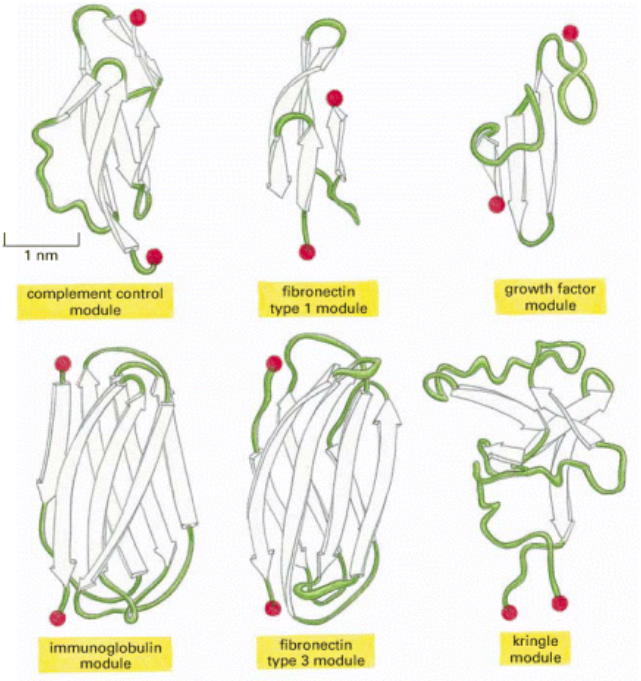

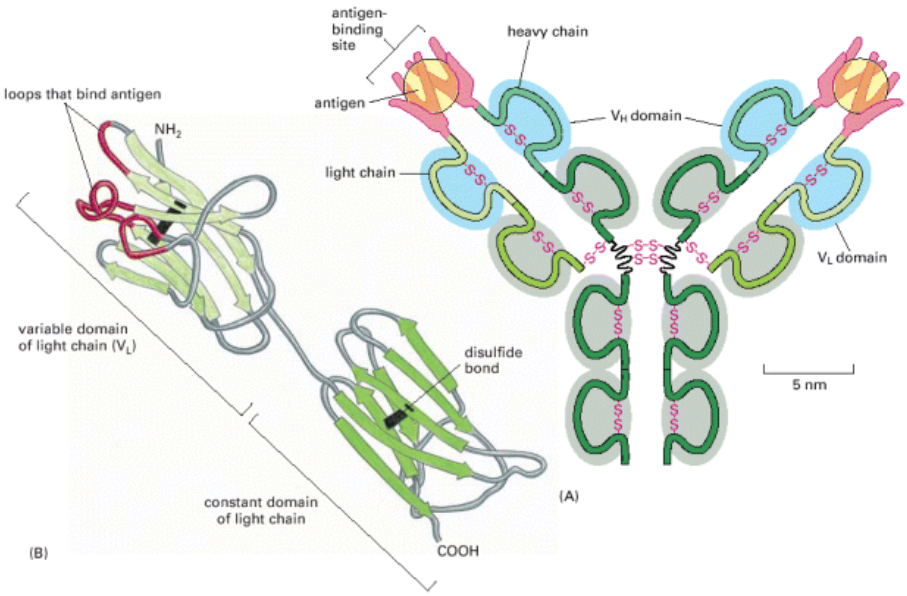

Figure 3-42. An antibody molecule. (A) A typical antibody molecule is Y-shaped and has two identical binding sites for its antigen, one on each arm of the Y. The protein is composed of four polypeptide chains (two identical heavy chains and two identical and smaller light chains) held together by disulfide bonds. Each chain is made up of several different immunoglobulin domains, here shaded either *blue* or *gray*. The antigen-binding site is formed where a heavy-chain variable domain (V_H) and a light-chain variable domain (V_L) come close together. These are the domains that differ most in their sequence and structure in different antibodies. (B) This ribbon model of a light chain shows the parts of the V_L domain most closely involved in binding to the antigen in *red.* They contribute half of the fingerlike loops that fold around each of the antigen molecules in (A).

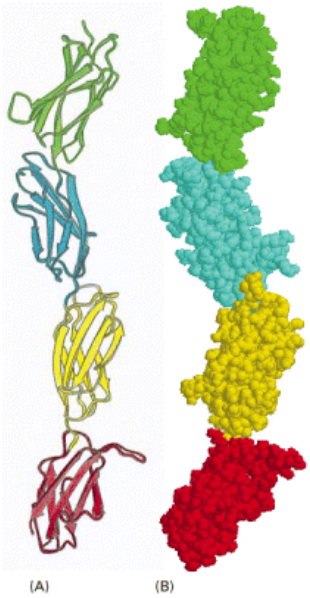

Figure 3-20. An extended structure formed from a series of in-line protein modules. Four fibronectin type 3 modules (see Figure 3-19) from the extracellular matrix molecule fibronectin are illustrated in (A) ribbon and (B) space-filling models. (Adapted from D.J. Leahy, I. Aukhil, and H.P. Erickson, *Cell* 84:155164, 1996.)

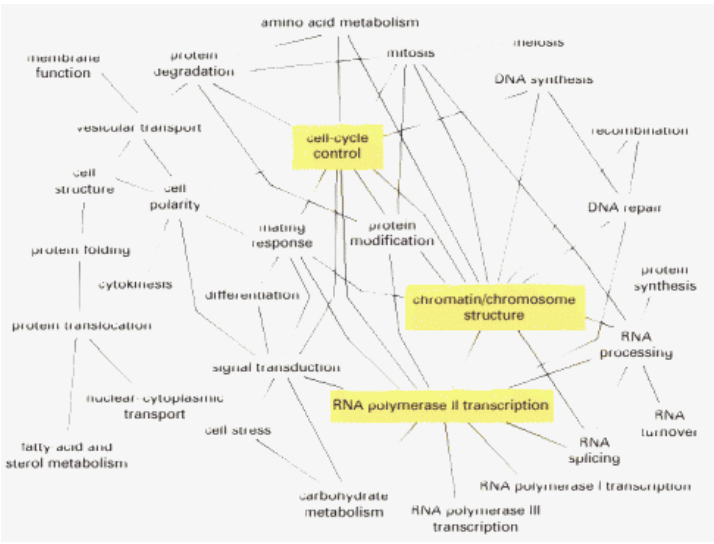

Figure 3-78. A map of the proteinprotein interactions observed between different functional groups of proteins in the yeast *S. cerevisiae.* To produce this map, more than 1500 proteins were assigned to the indicated 31 functional groups. About 70 percent of the known proteinprotein interactions were observed to occur between proteins assigned to the same functional group. However, as indicated, a surprisingly large number of interactions crossed between these groups. Each line in this diagram designates that more than 15 proteinprotein interactions were observed between proteins in the two functional groups that are connected by that line. The three functional groups highlighted in *yellow* display at least 15 interactions with 10 or more of the 31 functional groups defined in the study. (From C.L. Tucker, J.F. Gera, and P. Uetz, *Trends Cell Biol.* 11:102106, 2001.)

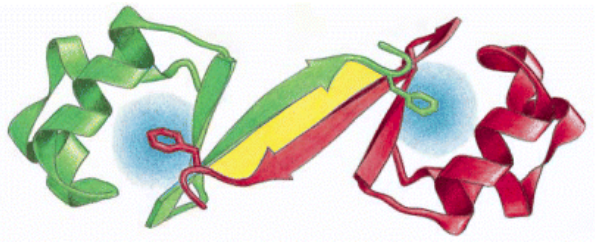

Figure 3-21. Two identical protein subunits binding together to form a symmetric protein dimer. The Cro repressor protein from bacteriophage lambda binds to DNA to turn off viral genes. Its two identical subunits bind head-to-head, held together by a combination of hydrophobic forces *(blue)* and a set of hydrogen bonds *(yellow* region). (Adapted from D.H. Ohlendorf, D.E. Tronrud, and B.W. Matthews, *J. Mol. Biol*. 280:129136, 1998.)

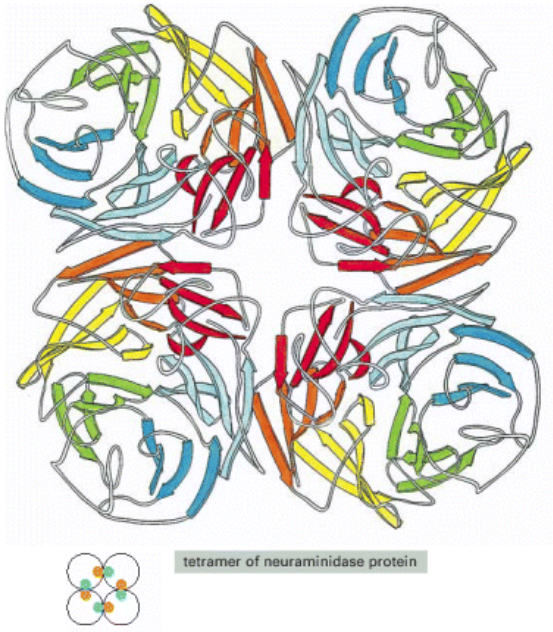

Figure 3-22. A protein molecule containing multiple copies of a single protein subunit. The enzyme neuraminidase exists as a ring of four identical polypeptide chains. The small diagram shows how the repeated use of the same binding interaction forms the structure.

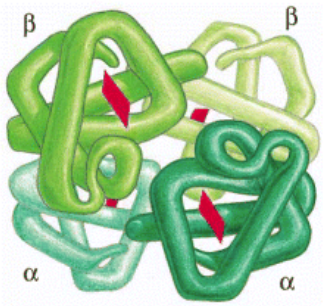

Figure 3-23. A protein formed as a symmetric assembly of two different subunits. Hemoglobin is an abundant protein in red blood cells that contains two copies of α globin and two copies of β globin. Each of these four polypeptide chains contains a heme molecule *(red)*, which is the site where oxygen (O_2) is bound. Thus, each molecule of hemoglobin in the blood carries four molecules of oxygen.

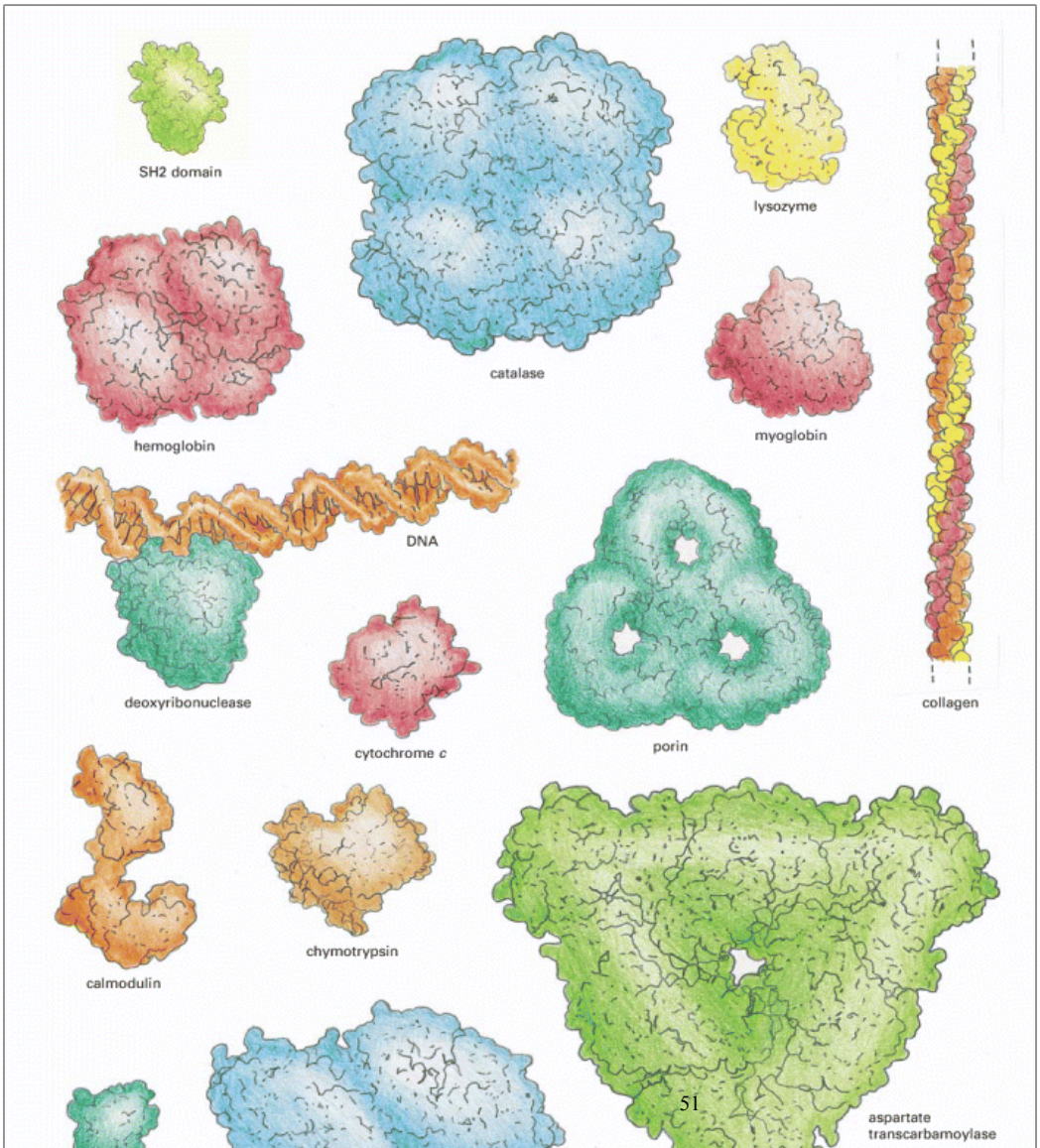

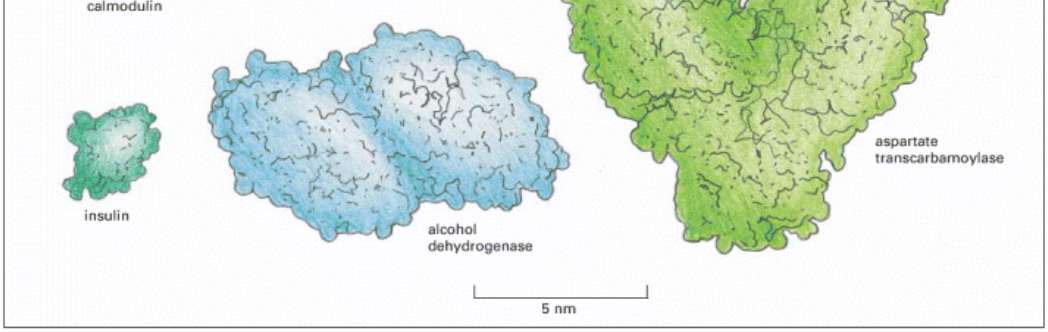

Figure 3-24. A collection of protein molecules, shown at the same scale. For comparison, a DNA molecule bound to a protein is also illustrated. These space-filling models represent a range of sizes and shapes. Hemoglobin, catalase, porin, alcohol dehydrogenase, and aspartate transcarbamoylase are formed from multiple copies of subunits. The SH2 domain *(top left)* is presented in detail in Panel 3-2 (pp. 138139). (After David S. Goodsell, Our Molecular Nature. New York: Springer-Verlag, 1996.)

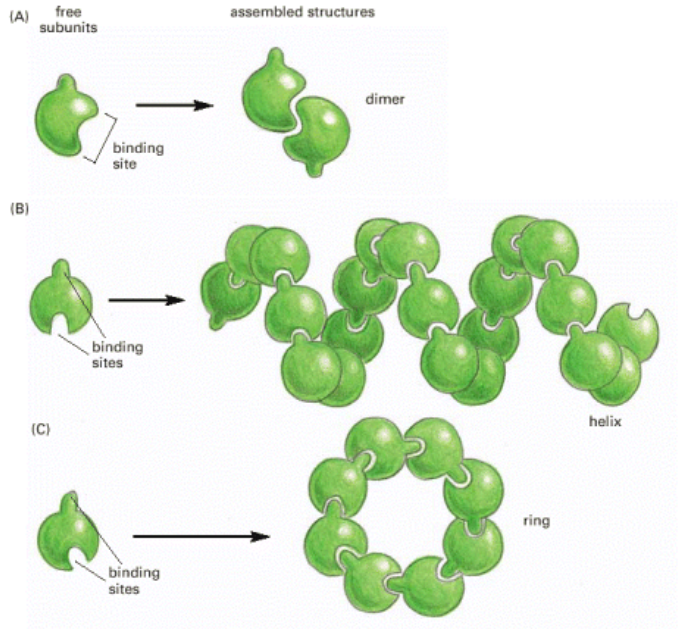

Figure 3-25. Protein assemblies. (A) A protein with just one binding site can form a dimer with another identical protein. (B) Identical proteins with two different binding sites often form a long helical filament. (C) If the two binding sites are disposed appropriately in relation to each other, the protein subunits may form a closed ring instead of a helix. (For an example of A, see Figure 3-21; for an example of C, see Figure 3-22.)

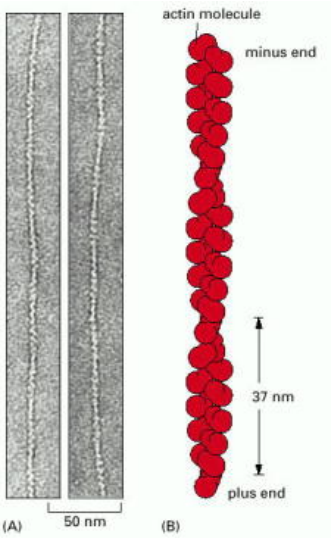

Figure 3-26. Actin filaments. (A) Transmission electron micrographs of negatively stained actin filaments. (B) The helical arrangement of actin molecules in an actin filament. (A, courtesy of Roger Craig.)

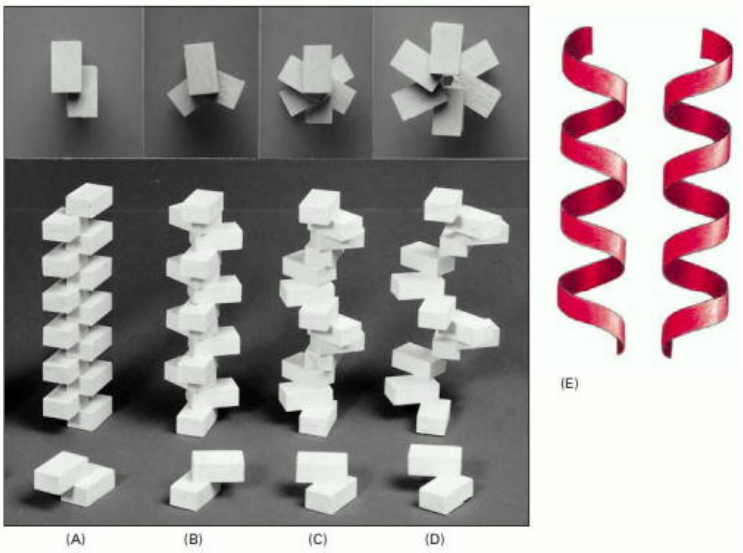

Figure 3-27. Some properties of a helix. (AD) A helix forms when a series of subunits bind to each other in a regular way. At the bottom, the interaction between two subunits is shown; behind them are the helices that result. These helices have two (A), three (B), and six (C and D) subunits per helical turn. At the top, the arrangement of subunits has been photographed from directly above the helix. Note that the helix in (D) has a wider path than that in (C), but the same number of subunits per turn. (E) A helix can be either right-handed or left-handed. As a reference, it is useful to remember that standard metal screws, which insert when turned clockwise, are right-handed. Note that a helix retains the same handedness when it is turned upside down.

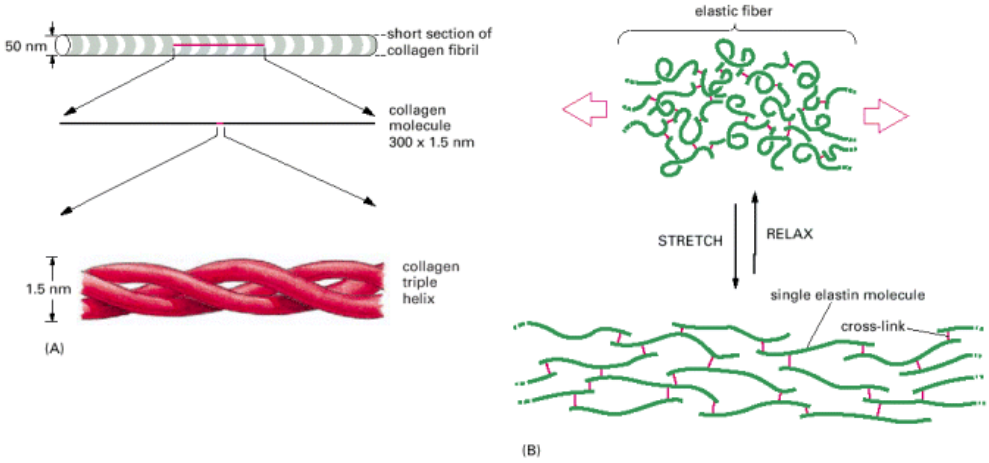

Figure 3-28. Collagen and elastin. (A) Collagen is a triple helix formed by three extended protein chains that wrap around one another *(bottom).* Many rodlike collagen molecules are cross-linked together in the extracellular space to form unextendable collagen fibrils *(top)* that have the tensile strength of steel. The striping on the collagen fibril is caused by the regular repeating arrangement of the collagen molecules within the fibril. (B) Elastin polypeptide chains are cross-linked together to form rubberlike, elastic fibers. Each elastin molecule uncoils into a more extended conformation when the fiber is stretched and recoils spontaneously as soon as the stretching force is relaxed.

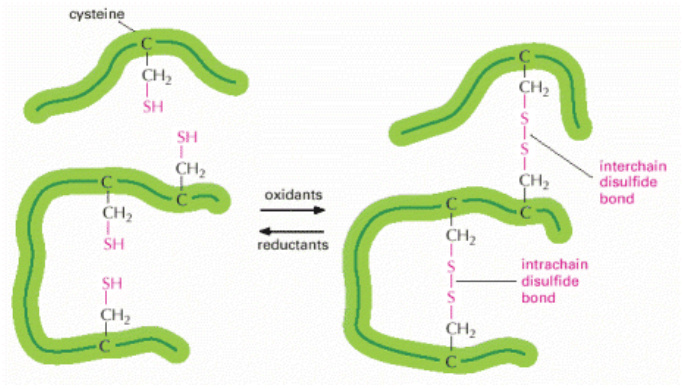

Figure 3-29. Disulfide bonds. This diagram illustrates how covalent disulfide bonds form between adjacent cysteine side chains. As indicated, these cross-linkages can join either two parts of the same polypeptide chain or two different polypeptide chains. Since the energy required to break one covalent bond is much larger than the energy required to break even a whole set of noncovalent bonds (see Table 2-2, p. 57), a disulfide bond can have a major stabilizing effect on a protein.

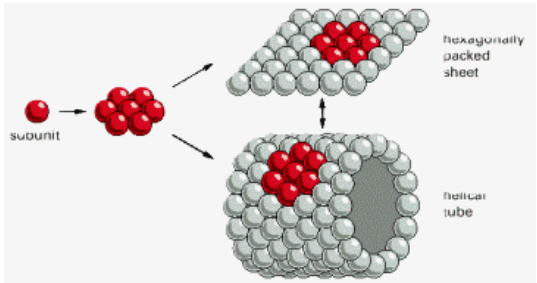

Figure 3-30. An example of single protein subunit assembly requiring multiple proteinprotein contacts. Hexagonally packed globular protein subunits can form either a flat sheet or a tube.

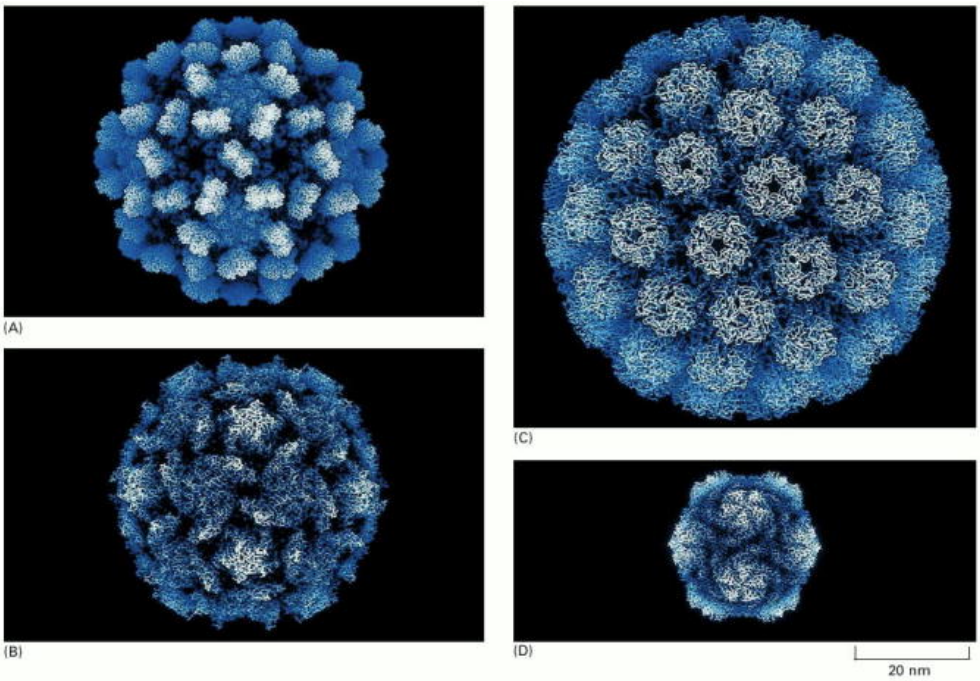

Figure 3-31. The capsids of some viruses, all shown at the same scale. (A) Tomato bushy stunt virus; (B) poliovirus; (C) simian virus 40 (SV40); (D) satellite tobacco necrosis virus. The structures of all of these capsids have been determined by x-ray crystallography and are known in atomic detail. (Courtesy of Robert Grant, Stephan Crainic, and James M. Hogle.)

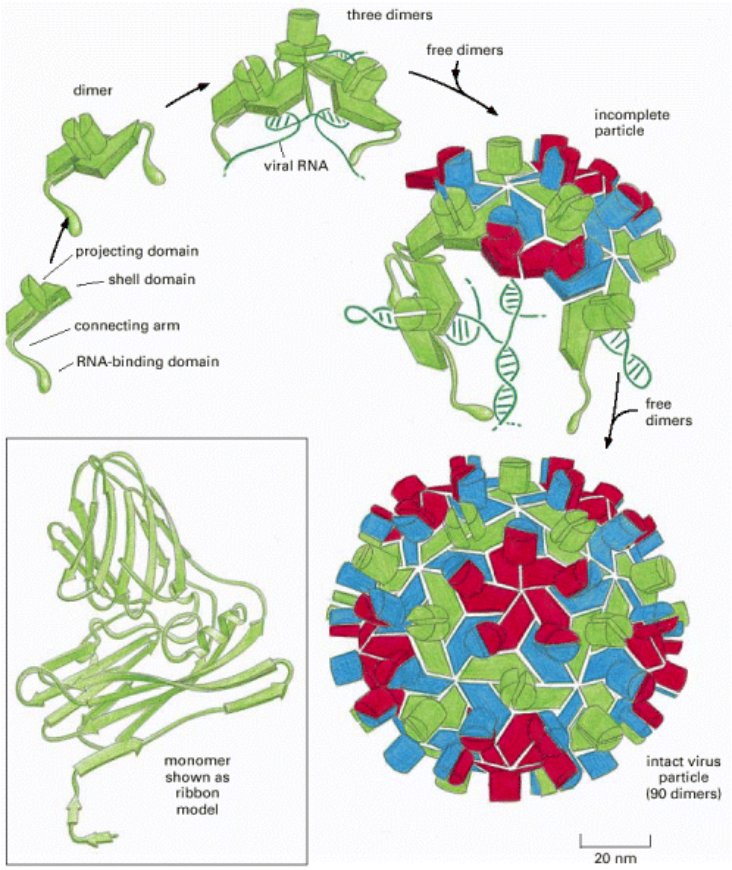

Figure 3-32. The structure of a spherical virus. In many viruses, identical protein subunits pack together to create a spherical shell (a capsid) that encloses the viral genome, composed of either RNA or DNA (see also Figure 3-31). For geometric reasons, no more than 60 identical subunits can pack together in a precisely symmetric way. If slight irregularities are allowed, however, more subunits can be used to produce a larger capsid. The tomato bushy stunt virus (TBSV) shown here, for example, is a spherical virus about 33 nm in diameter formed from 180 identical copies of a 386 amino acid capsid protein plus an RNA genome of 4500 nucleotides. To construct such a large capsid, the protein must be able to fit into three somewhat different environments, each of which is differently colored in the virus particle shown here. The postulated pathway of assembly is shown; the precise three-dimensional structure has been determined by x-ray diffraction. (Courtesy of Steve Harrison.)

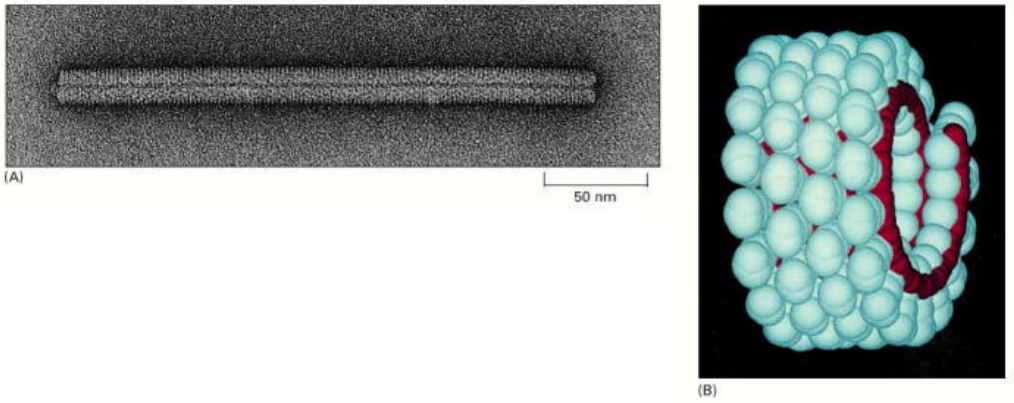

Figure 3-33. The structure of tobacco mosaic virus (TMV). (A) An electron micrograph of the viral particle, which consists of a single long RNA molecule enclosed in a cylindrical protein coat composed of identical protein subunits. (B) A model showing part of the structure of TMV. A single-stranded RNA molecule of 6000 nucleotides is packaged in a helical coat constructed from 2130 copies of a coat protein 158 amino acids long. Fully infective viral particles can self-assemble in a test tube from purified RNA and protein molecules. (A, courtesy of Robley Williams; B, courtesy of Richard J. Feldmann.)

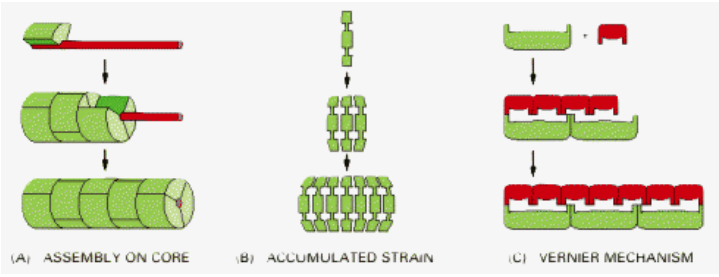

Figure 3-34. Three mechanisms of length determination for large protein assemblies. (A) Coassembly along an elongated core protein or other macromolecule that acts as a measuring device. (B) Termination of assembly because of strain that accumulates in the polymeric structure as additional subunits are added, so that beyond a certain length the energy required to fit another subunit onto the chain becomes excessively large. (C) A vernier type of assembly, in which two sets of rodlike molecules differing in length form a staggered complex that grows until their ends exactly match. The name derives from a measuring device based on the same principle, used in mechanical instruments.

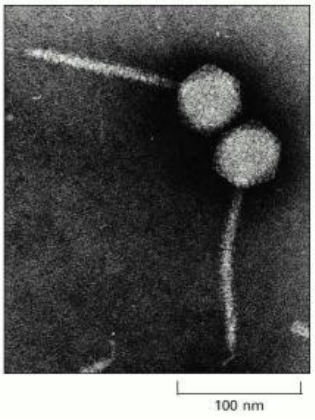

Figure 3-35. An electron micrograph of bacteriophage lambda. The tip of the virus tail attaches to a specific protein on the surface of a bacterial cell, after which the tightly packaged DNA in the head is injected through the tail into the cell. The tail has a precise length, determined by the mechanism shown in Figure 3-34A.

Figure 3-36. Proteolytic cleavage in insulin assembly. The polypeptide hormone insulin cannot spontaneously re-form efficiently if its disulfide bonds are disrupted. It is synthesized as a larger protein *(proinsulin)* that is cleaved by a proteolytic enzyme after the protein chain has folded into a specific shape. Excision of part of the proinsulin polypeptide chain removes some of the information needed for the protein to fold spontaneously into its normal conformation once it has been denatured

and its two polypeptide chains separated.

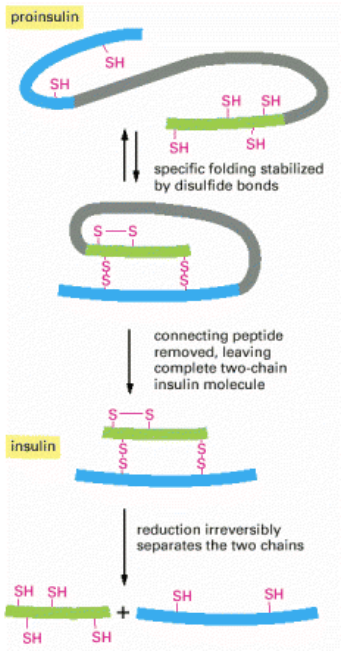

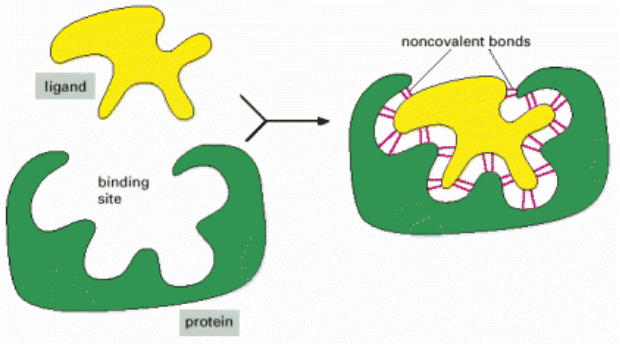

Figure 3-37. The selective binding of a protein to another molecule. Many weak bonds are needed to enable a protein to bind tightly to a second molecule, which is called a *ligand* for the protein. A ligand must therefore fit precisely into a protein's binding site, like a hand into a glove, so that a large number of noncovalent bonds can be formed between the protein and the ligand.

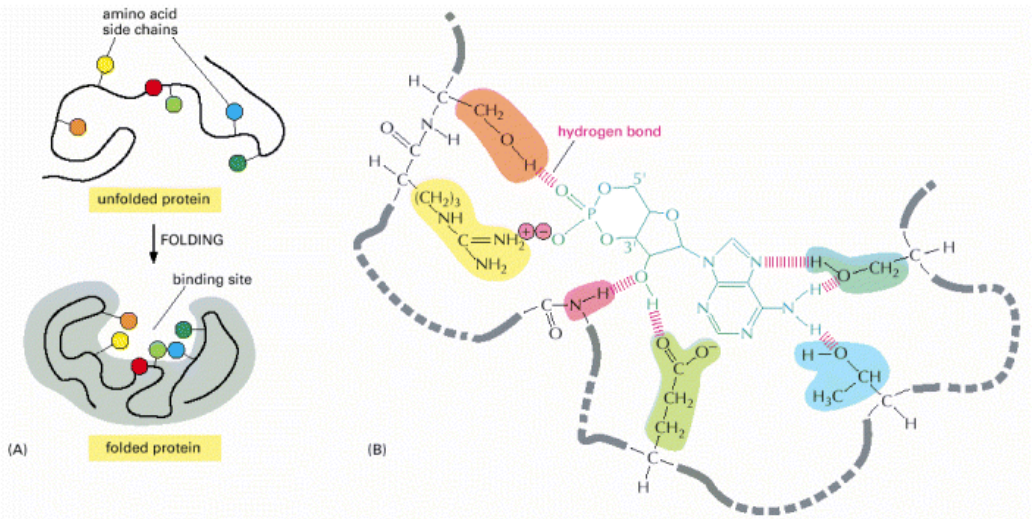

Figure 3-38. The binding site of a protein. (A) The folding of the polypeptide chain typically creates a crevice or cavity on the protein surface. This crevice contains a set of amino acid side chains disposed in such a way that they can make noncovalent bonds only with certain ligands. (B) A close-up of an actual binding site showing the hydrogen bonds and ionic interactions formed between a protein and its ligand (in this example, cyclic AMP is the bound ligand).

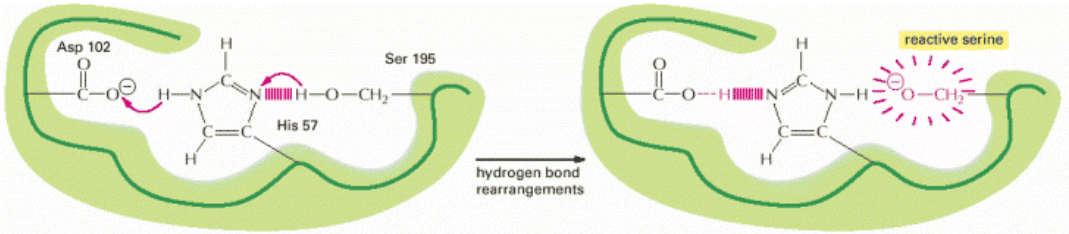

Figure 3-39. An unusually reactive amino acid at the active site of an enzyme. This example is the "catalytic triad" found in chymotrypsin, elastase, and other serine proteases (see Figure 3-14). The aspartic acid side chain (Asp 102) induces the histidine (His 57) to remove the proton from serine 195. This activates the serine to form a covalent bond with the enzyme substrate, hydrolyzing a peptide bond.

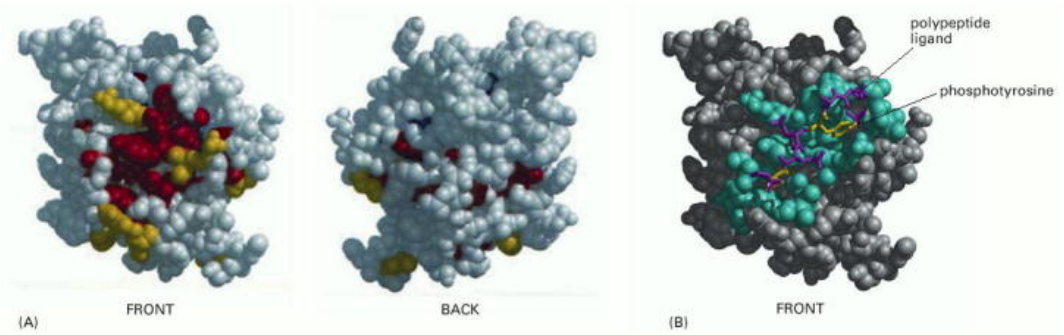

Figure 3-40. The evolutionary trace method applied to the SH2 domain. (A) Front and back views of a space-filling model of the SH2 domain, with evolutionarily conserved amino acids on the protein surface colored *yellow*, and those more toward the protein interior colored *red.* (B) The structure of the SH2 domain with its bound polypeptide. Here, those amino acids located within 0.4 nm of the bound ligand are colored *blue*. The two key amino acids of the ligand are *yellow*, and the others are *purple*. (Adapted from O. Lichtarge, H.R. Bourne, and F.E. Cohen, *J. Mol. Biol.* 257:342358, 1996.)

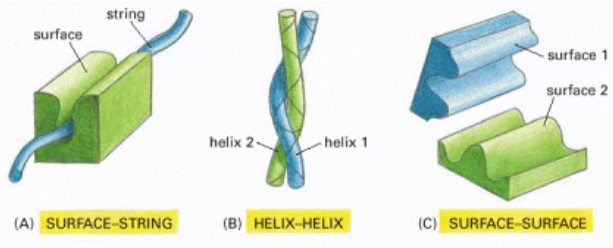

Figure 3-41. Three ways in which two proteins can bind to each other. Only the interacting parts of the two proteins are shown. (A) A rigid surface on one protein can bind to an extended loop of polypeptide chain (a "string") on a second protein. (B) Two α helices can bind together to form a coiled-coil. (C) Two complementary rigid surfaces often link two proteins together.

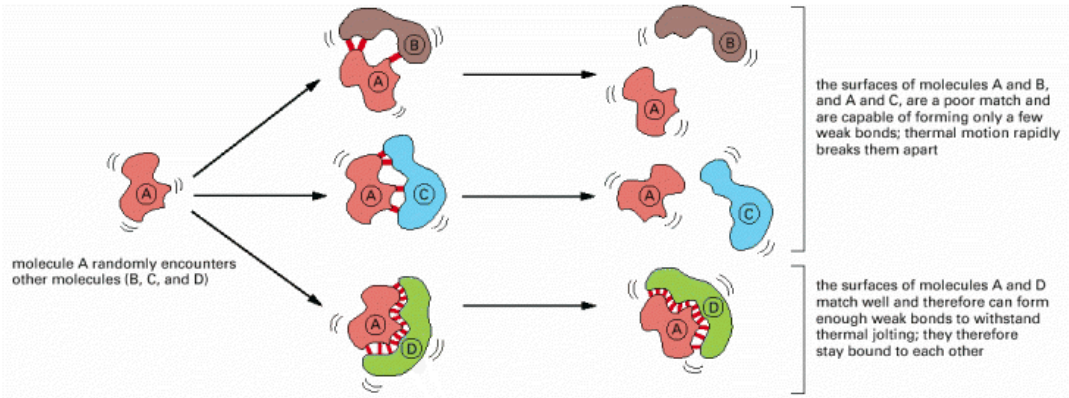

Figure 3-43. How noncovalent bonds mediate interactions between macromolecules.

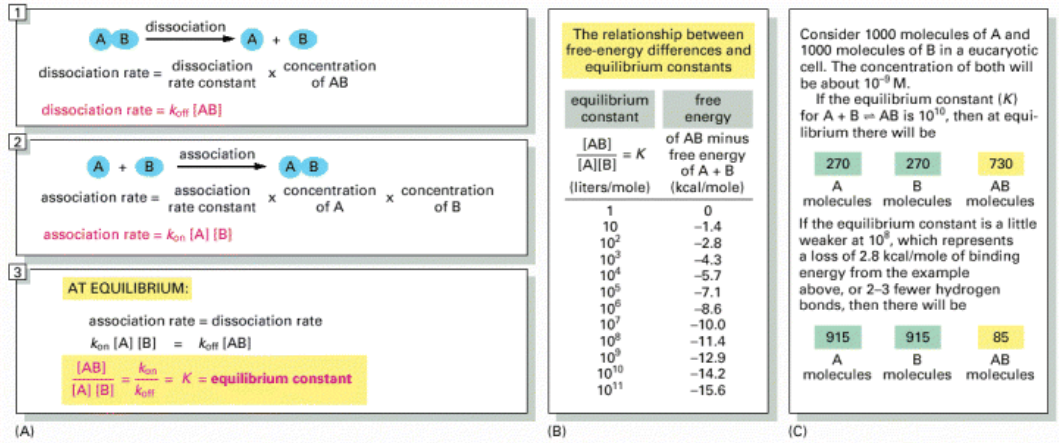

Figure 3-44. Relating binding energies to the equilibrium constant. (A) The equilibrium between molecules A and B and the complex AB is maintained by a balance between the two opposing reactions shown in panels 1 and 2. Molecules A and B must collide if they are to react, and the association rate is therefore proportional to the product of their individual concentrations [A] × [B]. (Square brackets indicate concentration.) As shown in panel 3, the ratio of the rate constants for the association and the dissociation reactions is equal to the equilibrium constant (*K*) for the reaction. (B) The equilibrium constant in panel 3 is that for the association reaction A + B AB, and the larger its value, the stronger the binding between A and B. Note that, for every 1.4 kcal/mole of free-energy drop, the equilibrium constant increases by a factor of 10. (C) An example of the dramatic effect that the presence or absence of a few weak bonds can have in a biological context. The equilibrium constant here has units of liters/mole: for simple binding interactions it is also called the *affinity constant* or *association constant*, denoted K_a. The reciprocal of K_a is called the *dissociation constant*, K_d (in units of moles/liter).

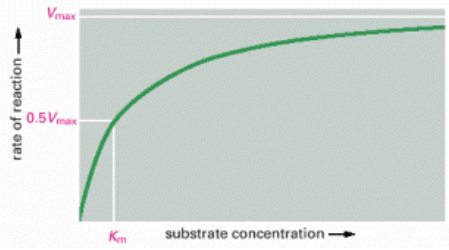

Figure 3-45. Enzyme kinetics. The rate of an enzyme reaction *(V)* increases as the substrate concentration increases until a maximum value (V_{max}) is reached. At this point all substrate-binding sites on the enzyme molecules are fully occupied, and the rate of reaction is limited by the rate of the catalytic process on the enzyme surface. For most enzymes, the concentration of substrate at which the reaction rate is half-maximal (K_m) is a measure of how tightly the substrate is bound, with a large value of K_m corresponding to weak binding.

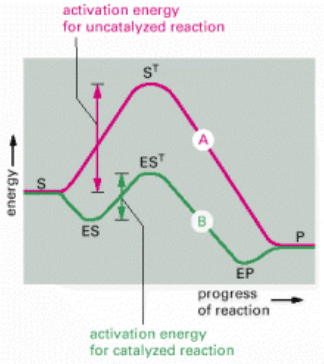

Figure 3-46. Enzymatic acceleration of chemical reactions by decreasing the activation energy. Often both the uncatalyzed reaction (A) and the enzyme-catalyzed reaction (B) can go through several transition states. It is the transition state with the highest energy (S^T and ES^T) that determines the activation energy and limits the rate of the reaction. (S = substrate; P = product of the reaction.)

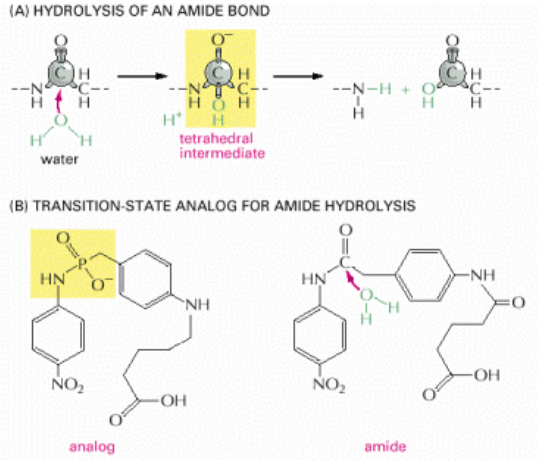

Figure 3-47. Catalytic antibodies. The stabilization of a transition state by an antibody creates an enzyme. (A) The reaction path for the hydrolysis of an amide bond goes through a tetrahedral intermediate, the high-energy transition state for the reaction. (B) The molecule on the left was covalently linked to a protein and used as an antigen to generate an antibody that binds tightly to the region of the molecule shown in *yellow*. Because this antibody also bound tightly to the transition state in (A), it was found to function as an enzyme that efficiently catalyzed the hydrolysis of the amide bond in the molecule on the right.

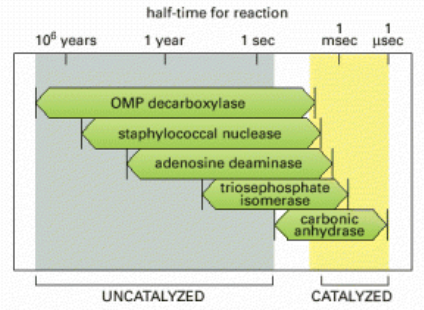

Figure 3-48. The rate accelerations caused by five different enzymes. (Modified from A. Radzicka and R. Wolfenden, *Science* 267:9093, 1995.)

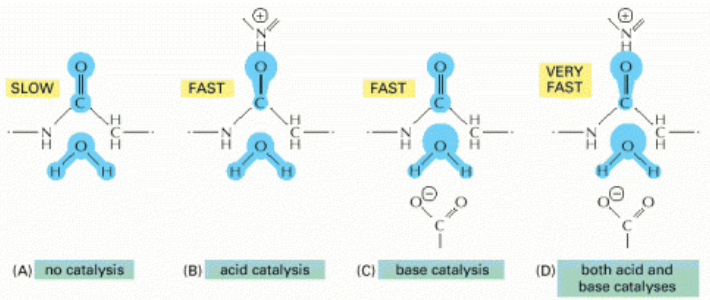

Figure 3-49. Acid catalysis and base catalysis. (A) The start of the uncatalyzed reaction shown in Figure 3-47A is diagrammed, with *blue* indicating electron distribution in the water and carbonyl bonds. (B) An acid likes to donate a proton (H^+) to other atoms. By pairing with the carbonyl oxygen, an acid causes electrons to move away from the carbonyl carbon, making this atom much more attractive to the electronegative oxygen of an attacking water molecule. (C) A base likes to take up H^+. By pairing with a hydrogen of the attacking water molecule, a base causes electrons to move toward the water oxygen, making it a better attacking group for the carbonyl carbon. (D) By having appropriately positioned atoms on its surface, an enzyme can perform both acid catalysis and base catalysis at the same time.

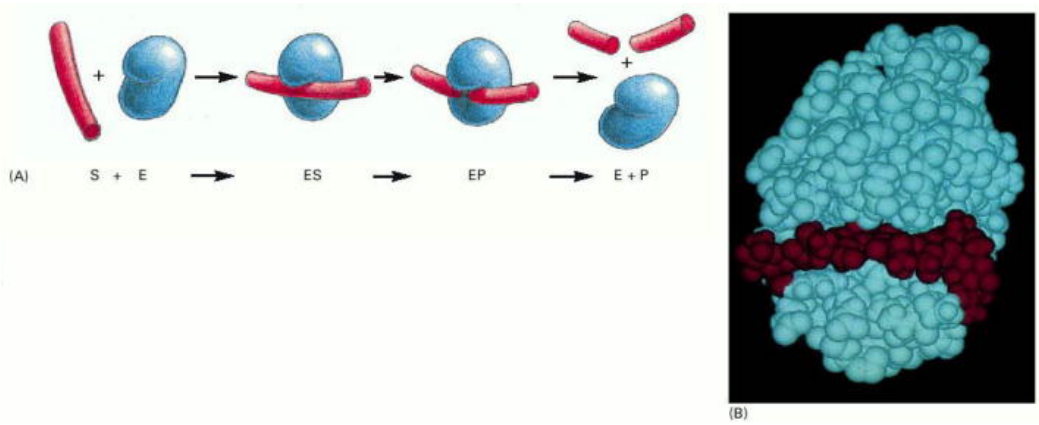

Figure 3-50. The reaction catalyzed by lysozyme. (A) The enzyme lysozyme (denoted as E) catalyzes the cutting of a polysaccharide chain, which is its substrate (S). The enzyme first binds to the chain to form an enzymesubstrate complex (ES) and then catalyzes the cleavage of a specific covalent bond in the backbone of the polysaccharide, forming an enzymeproduct complex (EP) that rapidly dissociates. Release of the severed chain (the products P) leaves the enzyme free to act on another substrate molecule. (B) A space-filling model of the lysozyme molecule bound to a short length of polysaccharide chain before cleavage. (B, courtesy of Richard J. Feldmann.)

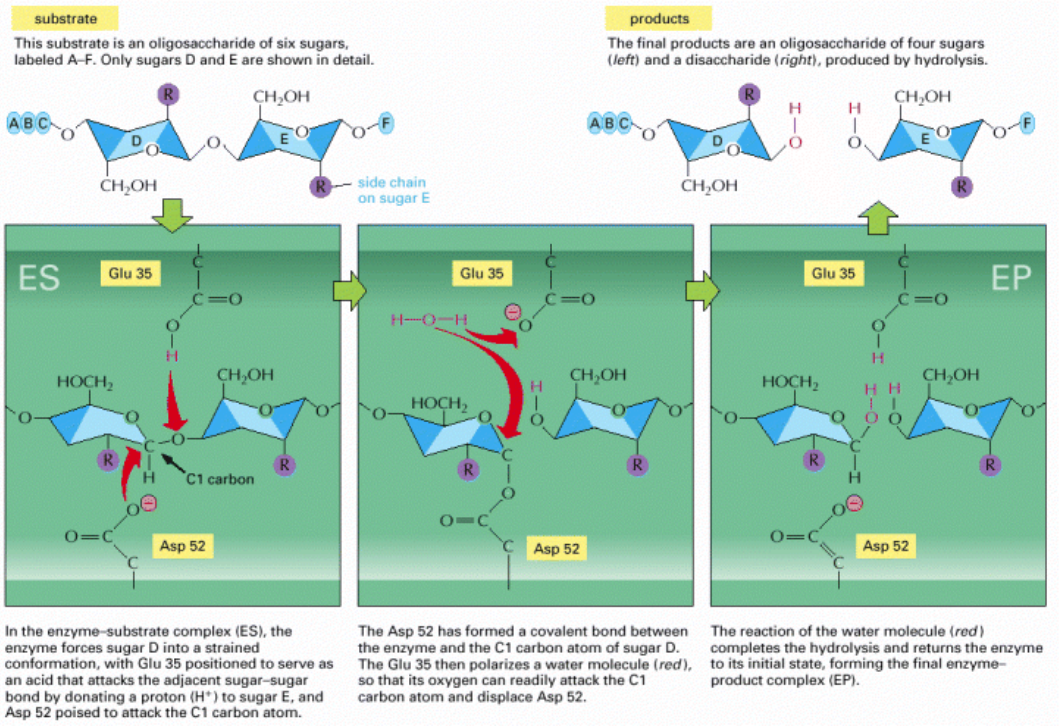

Figure 3-51. Events at the active site of lysozyme. The top left and top right drawings depict the free substrate and the free products, respectively, whereas the other three drawings depict the sequential events at the enzyme active site. Note the change in the conformation of sugar D in the enzymesubstrate complex; this shape change stabilizes the oxocarbenium ion-like transition states required for formation and hydrolysis of the covalent intermediate shown in the middle panel. (Based on D.J. Vocadlo et al., *Nature* 412:835838, 2001.)

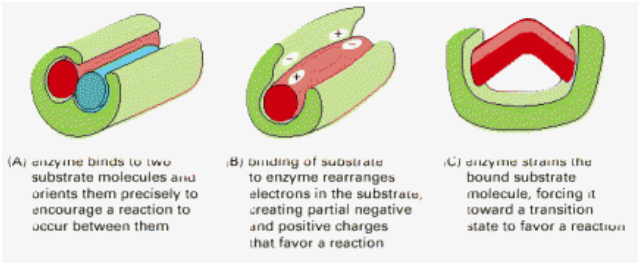

Figure 3-52. Some general strategies of enzyme catalysis. (A) Holding substrates together in a precise alignment. (B) Charge stabilization of reaction intermediates. (C) Altering bond angles in the substrate to increase the rate of a particular reaction.

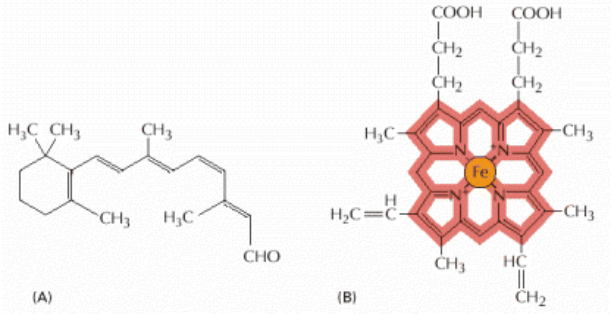

Figure 3-53. Retinal and heme. (A) The structure of retinal, the light-sensitive molecule attached to rhodopsin in the eye. (B) The structure of a heme group. The carbon-containing heme ring is *red* and the iron atom at its center is *orange*. A heme group is tightly bound to each of the four polypeptide chains in hemoglobin, the oxygen-carrying protein whose structure is shown in Figure 3-23.

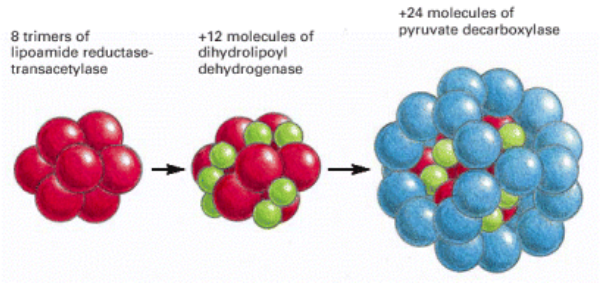

Figure 3-54. The structure of pyruvate dehydrogenase. This enzyme complex catalyzes the conversion of pyruvate to acetyl CoA, as part of the pathway that oxidizes sugars to CO_2 and H_2O. It is an example of a large multienzyme complex in which reaction intermediates are passed directly from one enzyme to another.

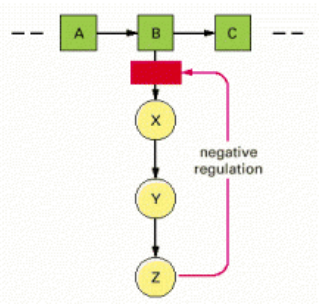

Figure 3-55. Feedback inhibition of a single biosynthetic pathway. The end-product Z inhibits the first enzyme that is unique to its synthesis and thereby controls its own level in the cell. This is an example of negative regulation.

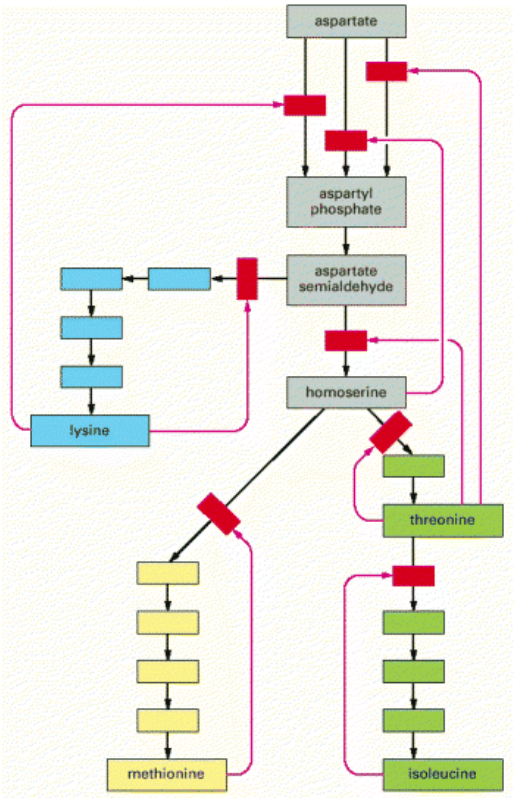

Figure 3-56. Multiple feedback inhibition. In this example, which shows the biosynthetic pathways for four different amino acids in bacteria, the *red arrows* indicate positions at which products feed back to inhibit enzymes. Each amino acid controls the first enzyme specific to its own synthesis, thereby controlling its own levels and avoiding a wasteful buildup of intermediates. The products can also separately inhibit the initial set of reactions common to all the syntheses; in this case, three different enzymes catalyze the initial reaction, each inhibited by a different product.

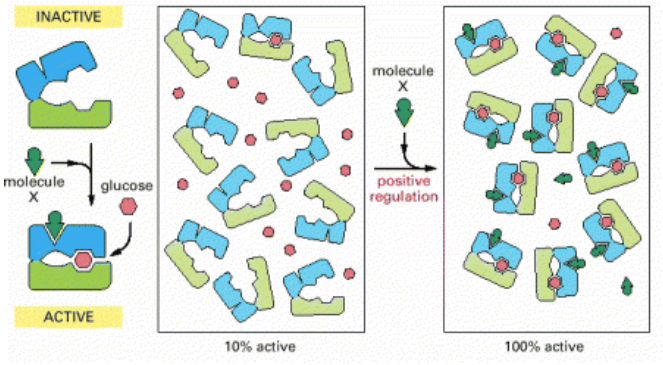

Figure 3-57. Positive regulation caused by conformational coupling between two distant binding sites. In this example, both glucose and molecule X bind best to the *closed* conformation of a protein with two domains. Because both glucose and molecule X drive the protein toward its closed conformation, each ligand helps the other to bind. Glucose and molecule X are therefore said to bind *cooperatively* to the protein.

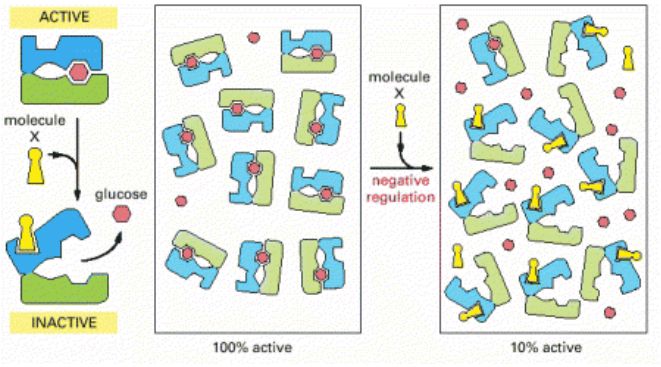

Figure 3-58. Negative regulation caused by conformational coupling between two distant binding sites. The scheme here resembles that in the previous figure, but here molecule X prefers the *open* conformation, while glucose prefers the *closed* conformation. Because glucose and molecule X drive the protein toward opposite conformations (closed and open, respectively), the presence of either ligand interferes with the binding of the other.

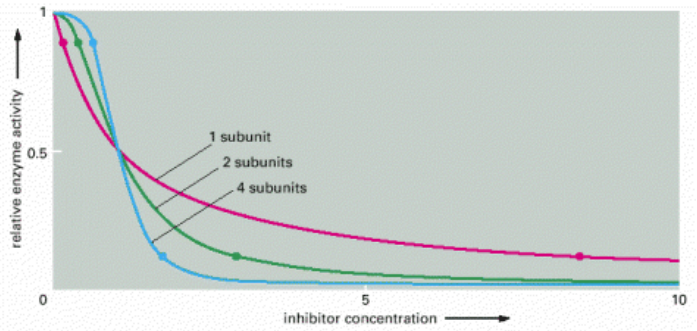

Figure 3-59. Enzyme activity versus the concentration of inhibitory ligand for single-subunit and multi-subunit allosteric enzymes. For an enzyme with a single subunit *(red line)*, a drop from 90% enzyme activity to 10% activity (indicated by the two dots on the curve) requires a 100-fold increase in the concentration of inhibitor. The enzyme activity is calculated from the simple equilibrium relationship $K = [I][P]/[IP]$, where P is active protein, I is inhibitor, and IP is the inactive protein bound to inhibitor. An identical curve applies to any simple binding interaction between two molecules, A and B. In contrast, a multisubunit allosteric enzyme can respond in a switchlike manner to a change in ligand concentration: the steep response is caused by a cooperative binding of the ligand molecules, as explained in Figure 3-60. Here, the *green line* represents the idealized result expected for the cooperative binding of two inhibitory ligand molecules to an allosteric enzyme with two subunits, and the *blue line* shows the idealized response of an enzyme with four subunits. As indicated by the two dots on each of these curves, the more complex enzymes drop from 90% to 10% activity over a much narrower range of inhibitor concentration than does the enzyme composed of a single subunit.

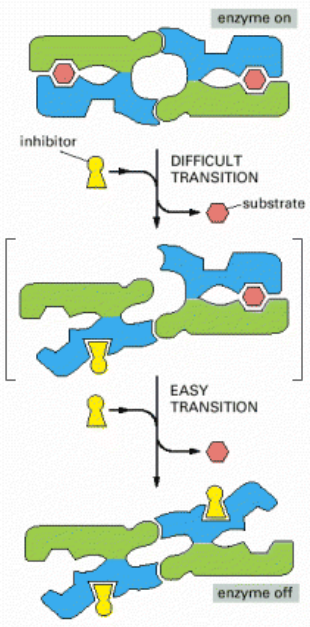

Figure 3-60. A cooperative allosteric transition in an enzyme composed of two identical subunits. This diagram illustrates how the conformation of one subunit can influence that of its neighbor. The binding of a single molecule of an inhibitory ligand *(yellow)* to one subunit of the enzyme occurs with difficulty because it changes the conformation of this subunit and thereby destroys the symmetry of the enzyme. Once this conformational change has occurred, however, the energy gained by restoring the symmetric pairing interaction between the two subunits makes it especially easy for the second subunit to bind the inhibitory ligand and undergo the same conformational change. Because the binding of the first molecule of ligand increases the affinity with which the other subunit binds the same ligand, the response of the enzyme to changes in the concentration of the ligand is much steeper than the response of an enzyme with only one subunit (see Figure 3-59).

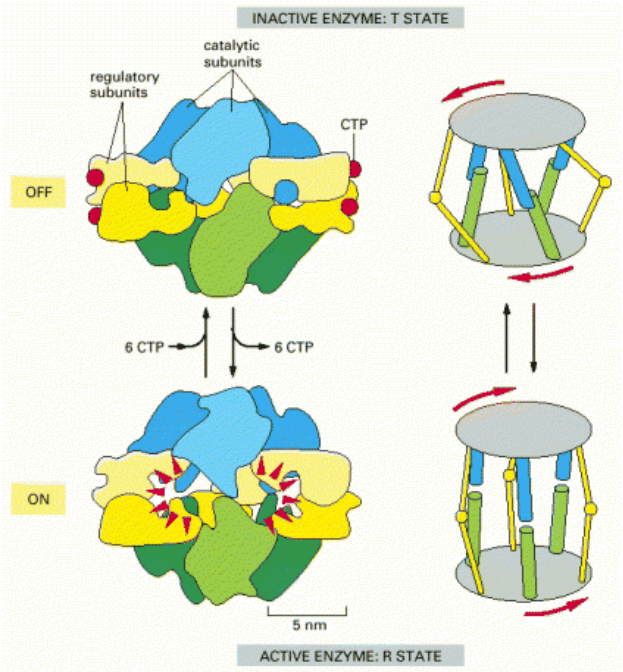

Figure 3-61. The transition between R and T states in the enzyme aspartate transcarbamoylase. The enzyme consists of a complex of six catalytic subunits and six regulatory subunits, and the structures of its inactive (T state) and active (R state) forms have been determined by x-ray crystallography. The enzyme is turned off by feedback inhibition when CTP concentrations rise. Each regulatory subunit can bind one molecule of CTP, which is one of the final products in the pathway. By means of this negative feedback regulation, the pathway is prevented from producing more CTP than the cell needs. (Based on K.L. Krause, K.W. Volz, and W.N. Lipscomb, *Proc. Natl. Acad. Sci. USA* 82:16431647, 1985.)

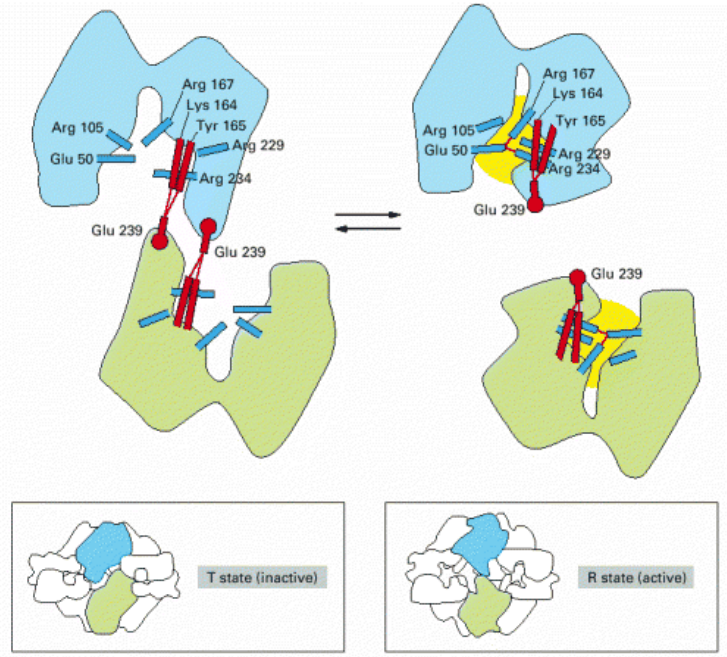

Figure 3-62. Part of the onoff switch in the catalytic subunits of aspartate transcarbamoylase. Changes in the indicated hydrogen-bonding interactions are partly responsible for switching this enzyme's active site between active *(yellow)* and inactive conformations. Hydrogen bonds are indicated by *thin red lines.* The amino acids involved in the subunitsubunit interaction are shown in *red,* while those that form the active site of the enzyme are shown in *blue.* The large drawings show the catalytic site in the interior of the enzyme; the boxed sketches show the same subunits viewed from the enzyme's external surface. (Adapted from E.R. Kantrowitz and W.N. Lipscomb, *Trends Biochem. Sci.* 15:5359, 1990.)

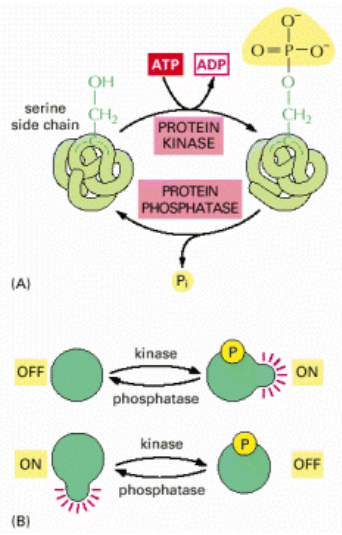

Figure 3-63. Protein phosphorylation. Many thousands of proteins in a typical eucaryotic cell are modified by the covalent addition of a phosphate group. (A) The general reaction, shown here, entails the transfer of a phosphate group from ATP to an amino acid side chain of the target protein by a protein kinase. Removal of the phosphate group is catalyzed by a second enzyme, a protein phosphatase. In this example, the phosphate is added to a serine side chain; in other cases, the phosphate is instead linked to the OH group of a threonine or a tyrosine in the protein. (B) The phosphorylation of a protein by a protein kinase can either increase or decrease the protein's activity, depending on the site of phosphorylation and the structure of the protein.

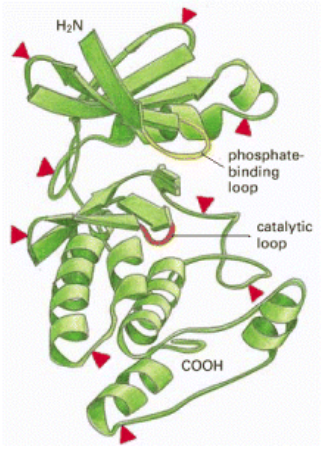

Figure 3-64. The three-dimensional structure of a protein kinase. Superimposed on this structure are *red arrowheads* to indicate sites where insertions of 5100 amino acids are found in some members of the protein kinase family. These insertions are located in loops on the surface of the enzyme where other ligands interact with the protein. Thus, they distinguish different kinases and confer on them distinctive interactions with other proteins. The ATP (which donates a phosphate group) and the peptide to be phosphorylated are held in the active site, which extends between the phosphate-binding loop *(yellow)* and the catalytic loop *(orange).* See also Figure 3-12. (Adapted from D.R. Knighton et al., *Science* 253:407414, 1991.)

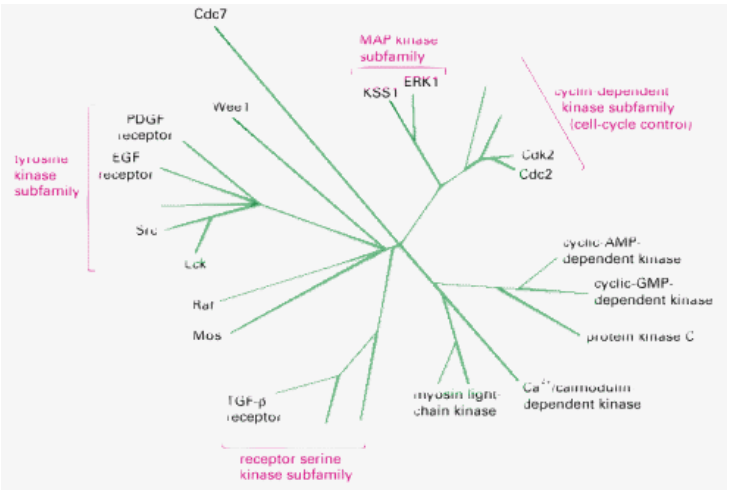

Figure 3-65. An evolutionary tree of selected protein kinases. Although a higher eucaryotic cell contains hundreds of such enzymes, and the human genome codes for more than 500, only some of those discussed in this book are shown.

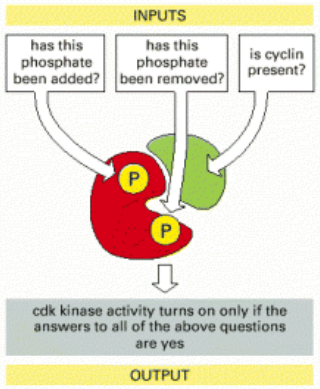

Figure 3-66. How a Cdk protein acts as an integrating device. The function of these central regulators of the cell cycle is discussed in Chapter 17.

Figure 3-67. The domain structure of the Src family of protein kinases, mapped along the amino acid sequence.

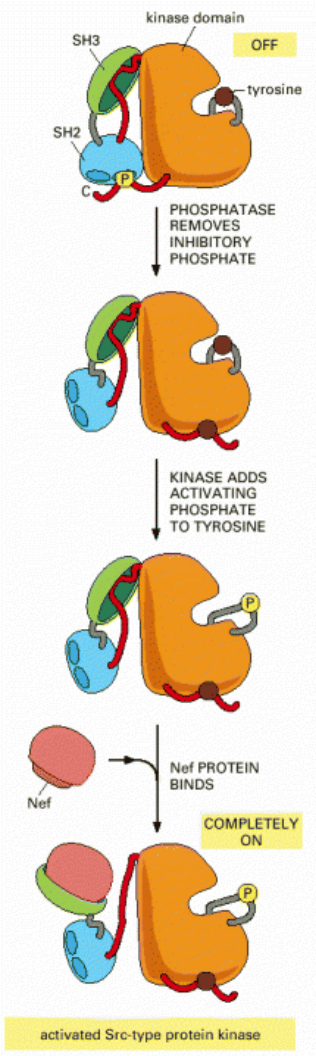

Figure 3-68. The activation of a Src-type protein kinase by two sequential events. (Adapted from I. Moareti, et al., *Nature* 385:650653, 1997.)

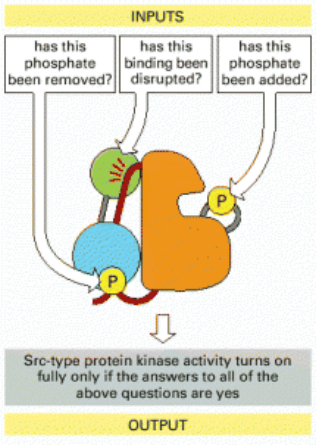

Figure 3-69. How a Src-type protein kinase acts as an integrating device. The disruption of the SH3 domain interaction *(green)* can involve replacing its binding to the indicated *red* linker region with a tighter interaction with the Nef protein, as illustrated in Figure 3-68.

Figure 3-70. GTP-binding proteins as molecular switches. The activity of a GTP-binding protein (also called a GTPase) generally requires the presence of a tightly bound GTP molecule (switch "on"). Hydrolysis of this GTP molecule produces GDP and inorganic phosphate (P_i), and it causes the protein to convert to a different, usually inactive, conformation (switch "off"). As shown here, resetting the switch requires the tightly bound GDP to dissociate, a slow step that is greatly accelerated by specific signals; once the GDP has dissociated, a molecule of GTP is quickly rebound.

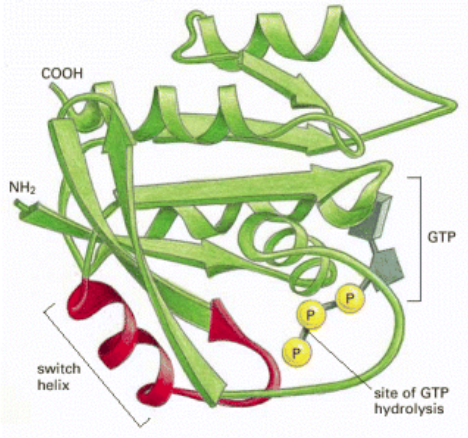

Figure 3-71. The structure of the Ras protein in its GTP-bound form. This monomeric GTPase illustrates the structure of a GTP-binding domain, which is present in a large family of GTP-binding proteins. The *red* regions change their conformation when the GTP molecule is hydrolyzed to GDP and inorganic phosphate by the protein; the GDP remains bound to the protein, while the inorganic phosphate is released. The special role of the "switch helix" in proteins related to Ras is explained next (see Figure 3-74).

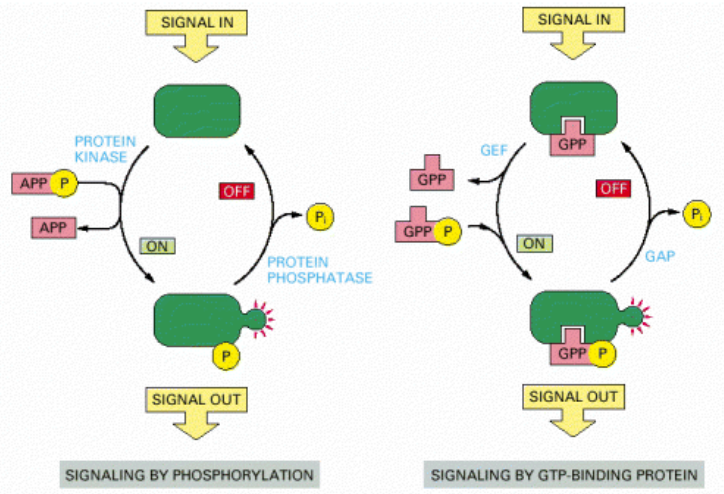

Figure 3-72. A comparison of the two major intracellular signaling mechanisms in eucaryotic cells. In both cases, a signaling protein is activated by the addition of a phosphate group and inactivated by the removal of this phosphate. To emphasize the similarities in the two pathways, ATP and GTP are drawn as APPP and GPPP, and ADP and GDP as APP and GPP, respectively. As shown in Figure 3-63, the addition of a phosphate to a protein can also be inhibitory.

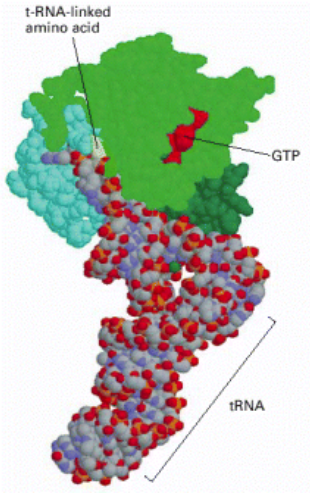

Figure 3-73. An aminoacyl tRNA molecule bound to EF-Tu. The three domains of the EF-Tu protein are colored differently, to match Figure 3-74. This is a bacterial protein; however, a very similar protein exists in eukaryotes, where it is called EF-1. (Coordinates determined by P. Nissen et al., *Science* 270:14641472, 1995.)

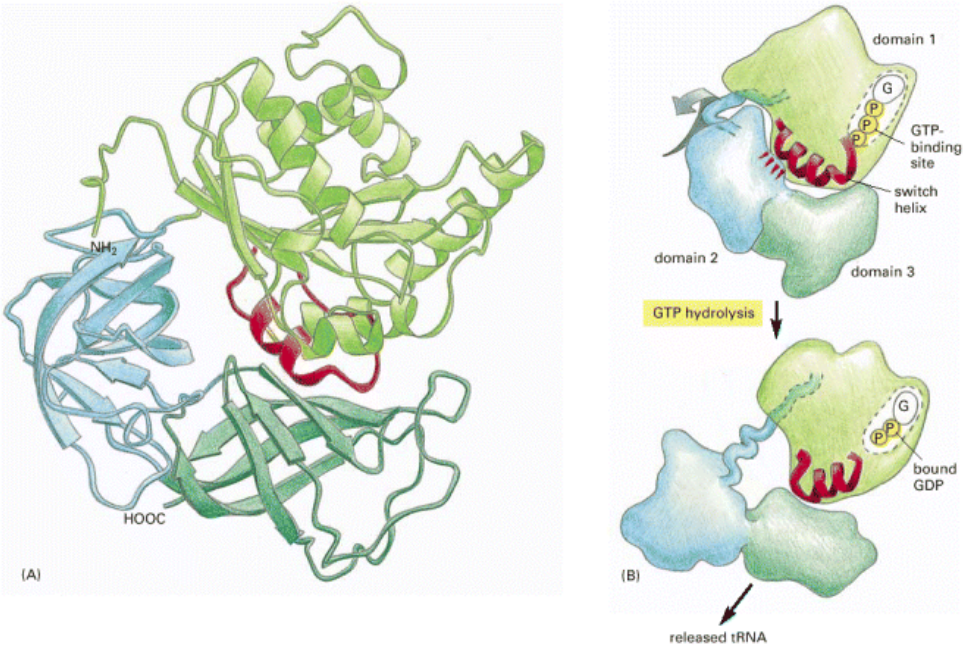

Figure 3-74. The large conformational change in EF-Tu caused by GTP hydrolysis. (A) The three-dimensional structure of EF-Tu with GTP bound. The domain at the top is homologous to the Ras protein, and its *red*α helix is the switch helix, which moves after GTP hydrolysis, as shown in Figure 3-71. (B) The change in the conformation of the switch helix in domain 1 causes domains 2 and 3 to rotate as a single unit by about 90° toward the viewer, which releases the tRNA that was shown bound to this structure in Figure 3-73. (A, adapted from H. Berchtold et al., *Nature* 365:126132, 1993; B, courtesy of Mathias Sprinzl and Rolf Hilgenfeld.)

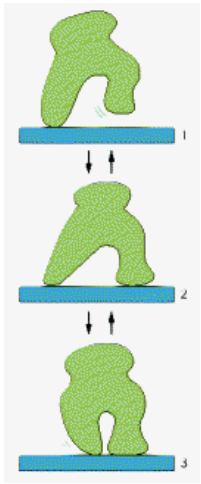

Figure 3-75. An allosteric "walking" protein. Although its three different conformations allow it to wander randomly back and forth while bound to a thread or a filament, the protein cannot move uniformly in a single direction.

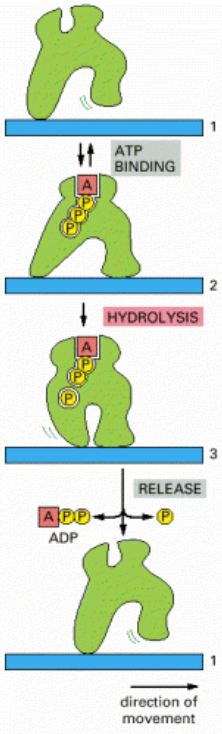

Figure 3-76. An allosteric motor protein. The transition between three different conformations includes a step driven by the hydrolysis of a bound ATP molecule, and this makes the entire cycle essentially irreversible. By repeated cycles, the protein therefore moves continuously to the right along the thread.

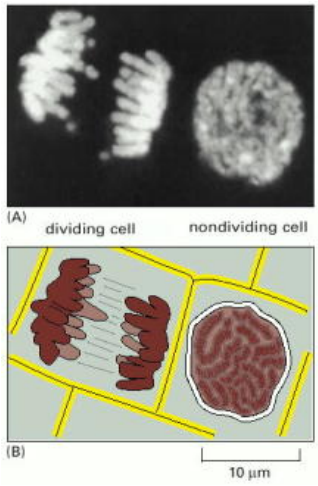

Figure 4-1. Chromosomes in cells. (A) Two adjacent plant cells photographed through a light microscope. The DNA has been stained with a fluorescent dye (DAPI) that binds to it. The DNA is present in chromosomes, which become visible as distinct structures in the light microscope only when they become compact structures in preparation for cell division, as shown on the left. The cell on the right, which is not dividing, contains identical chromosomes, but they cannot be clearly distinguished in the light microscope at this phase in the cell's life cycle, because they are in a more extended conformation. (B) Schematic diagram of the outlines of the two cells along with their chromosomes. (A, courtesy of Peter Shaw.)

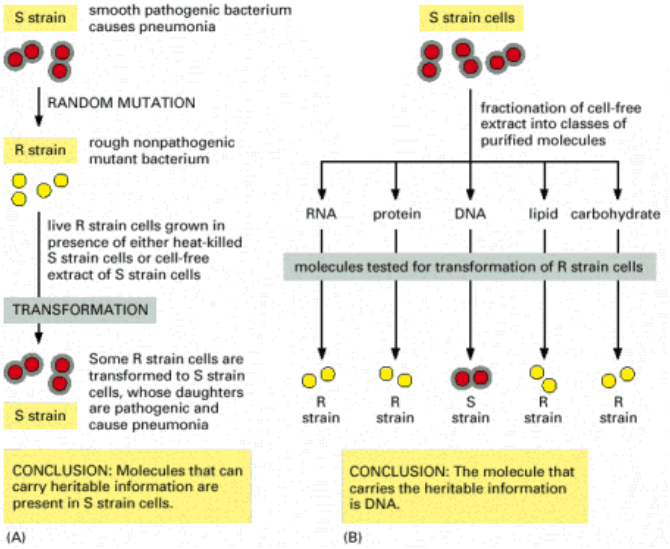

Figure 4-2. Experimental demonstration that DNA is the genetic material. These experiments, carried out in the 1940s, showed that adding purified DNA to a bacterium changed its properties and that this change was faithfully passed on to subsequent generations. Two closely related strains of the bacterium *Streptococcus pneumoniae* differ from each other in both their appearance under the microscope and their pathogenicity. One strain appears smooth (S) and causes death when injected into mice, and the other appears rough (R) and is nonlethal. (A) This experiment shows that a substance present in the S strain can change (or transform) the R strain into the S strain and that this change is inherited by subsequent generations of bacteria. (B) This experiment, in which the R strain has been incubated with various classes of biological molecules obtained from the S strain, identifies the substance as DNA.

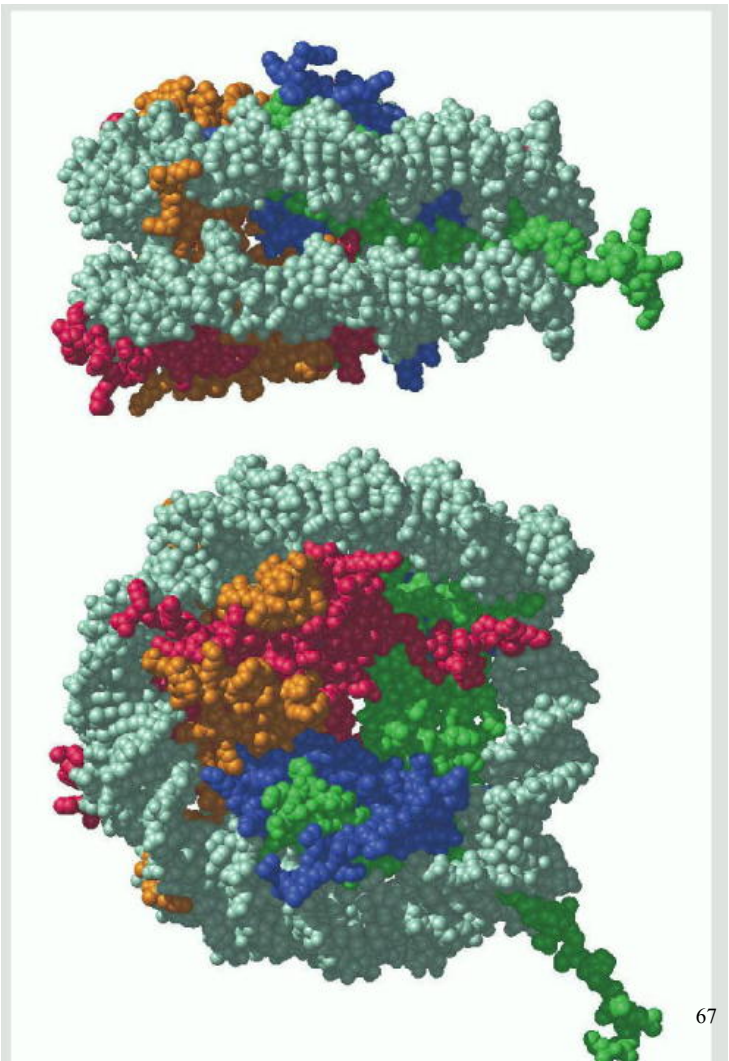

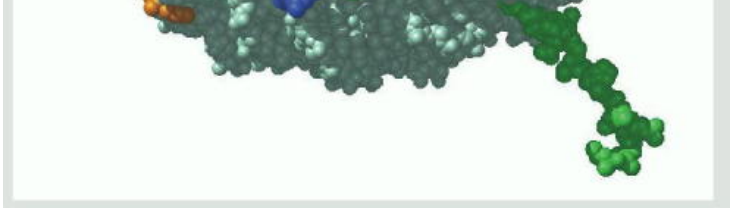

The nucleosome. The DNA double helix *(gray)* is wrapped around a core particle of histone proteins (colored) to create the nucleosome. Nucleosomes are spaced roughly 200 nucleotide pairs apart along the chromosomal DNA. (Reprinted by permission from K. Luger et al., *Nature* 389:251260, 1997. © Macmillan Magazines Ltd.)

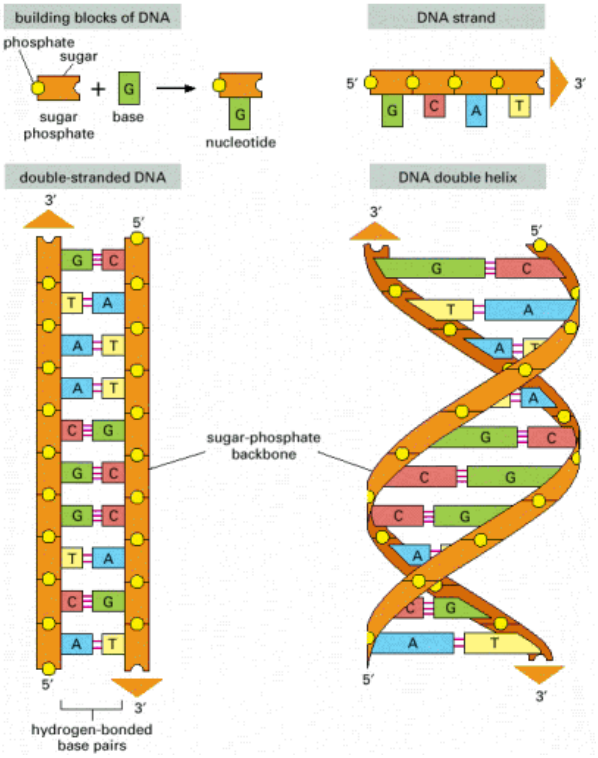

Figure 4-3. DNA and its building blocks. DNA is made of four types of nucleotides, which are linked covalently into a polynucleotide chain (a DNA strand) with a sugar-phosphate backbone from which the bases (A, C, G, and T) extend. A DNA molecule is composed of two DNA strands held together by hydrogen bonds between the paired bases. The *arrowheads* at the ends of the DNA strands indicate the polarities of the two strands, which run antiparallel to each other in the DNA molecule. In the diagram at the bottom left of the figure, the DNA molecule is shown straightened out; in reality, it is twisted into a double helix, as shown on the right. For details, see Figure 4-5.

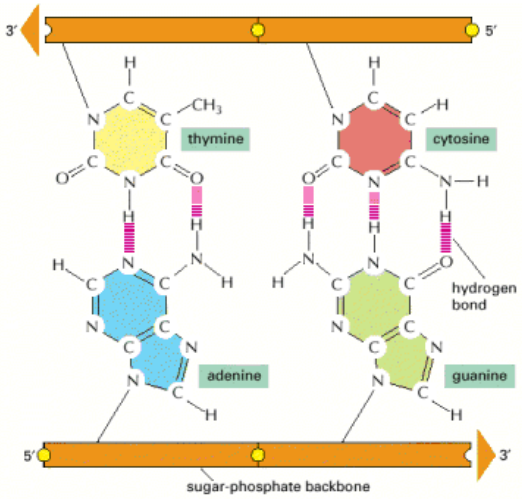

Figure 4-4. Complementary base pairs in the DNA double helix. The shapes and chemical structure of the bases allow hydrogen bonds to form efficiently only between A and T and between G and C, where atoms that are able to form hydrogen bonds (see Panel 2-3, pp. 114115) can be brought close together without distorting the double helix. As indicated, two hydrogen bonds form between A and T, while three form between G and C. The bases can pair in this way only if the two polynucleotide chains that contain them are antiparallel to each other.

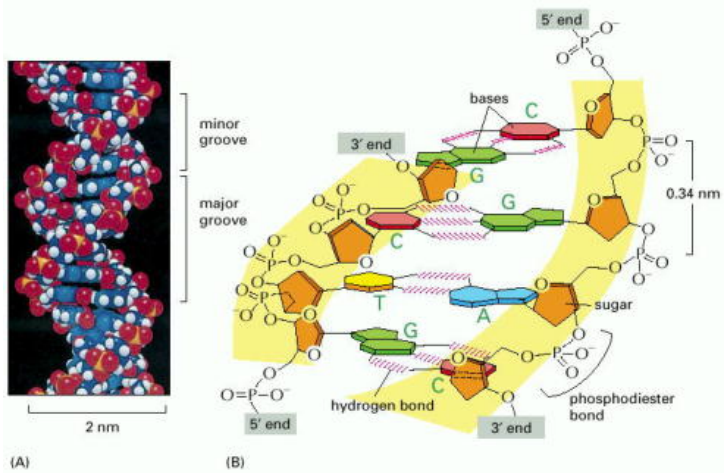

Figure 4-5. The DNA double helix. (A) A space-filling model of 1.5 turns of the DNA double helix. Each turn of DNA is made up of 10.4 nucleotide pairs and the center-to-center distance between adjacent nucleotide pairs is 3.4 nm. The coiling of the two strands around each other creates two grooves in the double helix. As indicated in the figure, the wider groove is called the major groove, and the smaller the minor groove. (B) A short section of the double helix viewed from its side, showing four base pairs. The nucleotides are linked together covalently by phosphodiester bonds through the 3-hydroxyl (-OH) group of one sugar and the 5-phosphate (P) of the next. Thus, each polynucleotide strand has a chemical polarity; that is, its two ends are chemically different. The 3 end carries an unlinked -OH group attached to the 3 position on the sugar ring; the 5 end carries a free phosphate group attached to the 5 position on the sugar ring.

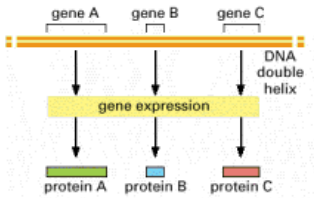

Figure 4-6. The relationship between genetic information carried in DNA and proteins.

CCCTGTGGAGCCACACCCTAGGGTTGGCCA
ATCTACTCCCAGGAGCAGGGAGGGCAGGAG
CCAGGGCTGGGCATAAAAGTCAGGGCAGAG
CCATCTATTGCTTACATTTGCTTCTGACAC
AACTGTGTTCACTAGCAACTCAAACAGACA
CCATGGTGCACCTGACTCCTGAGGAGAAGT
CTGCCGTTACTGCCCTGTGGGGCAAGGTGA
ACGTGGATGAAGTTGGTGGTGAGGCCCTGG
GCAGGTTGGTATCAAGGTTACAAGACAGGT
TTAAGGAGACCAATAGAAACTGGGCATGTG
GAGACAGAGAAGACTCTTGGGTTTCTGATA
GGCACTGACTCTCTCTGCCTATTGGTCTAT
TTTCCCACCCTTAGGCTGCTGGTGGTCTAC
CCTTGGACCCAGAGGTTCTTTGAGTCCTTT
GGGGATCTGTCCACTCCTGATGCTGTTATG
GGCAACCCTAAGGTGAAGGCTCATGGCAAG
AAAGTGCTCGGTGCCTTTAGTGATGGCCTG
GCTCACCTGGACAACCTCAAGGGCACCTTT
GCCACACTGAGTGAGCTGCACTGTGACAAG
CTGCACGTGGATCCTGAGAACTTCAGGGTG
AGTCTATGGGACCCTTGATGTTTTCTTTCC
CCTTCTTTTCTATGGTTAAGTTCATGTCAT
AGGAAGGGGAGAAGTAACAGGGTACAGTTT
AGAATGGGAAACAGACGAATGATTGCATCA
GTGTGGAAGTCTCAGGATCGTTTTAGTTTC
TTTTATTTGCTGTTCATAACAATTGTTTTC
TTTTGTTTAATTCTTGCTTTCTTTTTTTTT
CTTCTCCGCAATTTTTACTATTATACTTAA
TGCCTTAACATTGTGTATAACAAAAGGAAA
TATCTCTGAGATACATTAAGTAACTTAAAA
AAAAACTTTACACAGTCTGCCTAGTACATT
ACTATTTGGAATATATGTGTGCTTATTTGC
ATATTCATAATCTCCCTACTTTATTTTCTT
TTATTTTTAATTGATACATAATCATTATAC
ATATTTATGGGTTAAAGTGTAATGTTTTAA
TATGTGTACACATATTGACCAAATCAGGGT
AATTTTGCATTTGTAATTTTAAAAAATGCT
TTCTTCTTTTAATATACTTTTTTGTTTATC
TTATTTCTAATACTTTCCCTAATCTCTTTC
TTTCAGGGCAATAATGATACAATGTATCAT
GCCTCTTTGCACCATTCTAAAGAATAACAG
TGATAATTTCTGGGTTAAGGCAATAGCAAT
ATTTCTGCATATAAATATTTCTGCATATAA
ATTGTAACTGATGTAAGAGGTTTCATATTG
CTAATAGCAGCTACAATCCAGCTACCATTC
TGCTTTTATTTTATGGTTGGGATAAGGCTG
GATTATTCTGAGTCCAAGCTAGGCCCTTTT
GCTAATCATGTTCATACCTCTTATCTTCCT
CCCACAGCTCCTGGGCAACGTGCTGGTCTG
TGTGCTGGCCCATCACTTTGGCAAAGAATT
CACCCCACCAGTGCAGGCTGCCTATCAGAA
AGTGGTGGCTGGTGTGGCTAATGCCCTGGC
CCACAAGTATCACTAAGCTCGCTTTCTTGC
TGTCCAATTTCTATTAAAGGTTCCTTTGTT
CCCTAAGTCCAACTACTAAACTGGGGGATA
TTATGAAGGCCTTGAGCATCTGGATTCTG
CCTAATAAAAAACATTTATTTTCATTGCAA
TGATGTATTTAAATTATTTCTGAATATTTT
ACTAAAAAGGGAATGTGGGAGGTCAGTGCA
TTTAAAACATAAAGAAATGATGAGCTGTTC
AAACCTTGGGAAAATACACTATATCTTAAA
CTCCATGAAAGAAGGTGAGGCTGCAACCAG
CTAATGCACATTGGCAACAGCCCCTGATGC
CTATGCCTTATTCATCCCTCAGAAAAGGAT
TCTTGTAGAGGCTTGATTTGCAGGTTAAAG
TTTTGCTATGCTGTATTTTACATTACTTAT
TGTTTTAGCTGTCCTCATGAATGTCTTTTC

Figure 4-7. The nucleotide sequence of the human β-globin gene. This gene carries the information for the amino acid sequence of one of the two types of subunits of the hemoglobin molecule, which carries oxygen in the blood. A different gene, the α-globin gene, carries the information for the other type of hemoglobin subunit (a hemoglobin molecule has four subunits, two of each type). Only one of the two strands of the DNA double helix containing the β-globin gene is shown; the other strand has the exact complementary sequence. By convention, a nucleotide sequence is written from its 5 end to its 3 end, and it should be read from left to right in successive lines down the page as though it were normal English text. The DNA sequences highlighted in *yellow* show the three regions of the gene that specify the amino sequence for the β-globin protein. We see in Chapter 6 how the cell connects these three sequences together to synthesize a full-length β-globin protein.

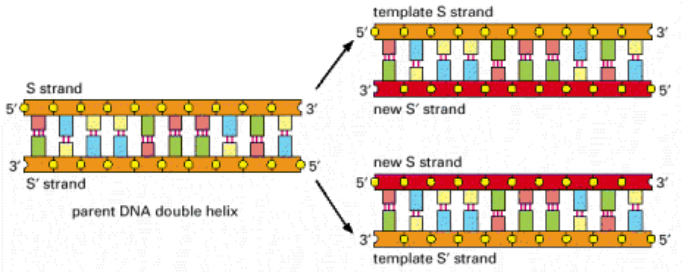

Figure 4-8. DNA as a template for its own duplication. As the nucleotide A successfully pairs only with T, and G with C, each strand of DNA can specify the sequence of nucleotides in its complementary strand. In this way, double-helical DNA can be copied precisely.

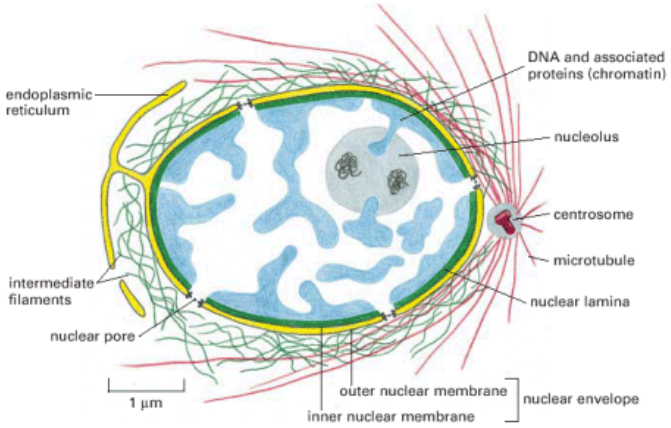

Figure 4-9. A cross-sectional view of a typical cell nucleus. The nuclear envelope consists of two membranes, the outer one being continuous with the endoplasmic reticulum membrane (see also Figure 12-9). The space inside the endoplasmic reticulum (the ER lumen) is colored *yellow;* it is continuous with the space between the two nuclear membranes. The lipid bilayers of the inner and outer nuclear membranes are connected at each nuclear pore. Two networks of intermediate filaments *(green)* provide mechanical support for the nuclear envelope; the intermediate filaments inside the nucleus form a special supporting structure called the nuclear lamina.

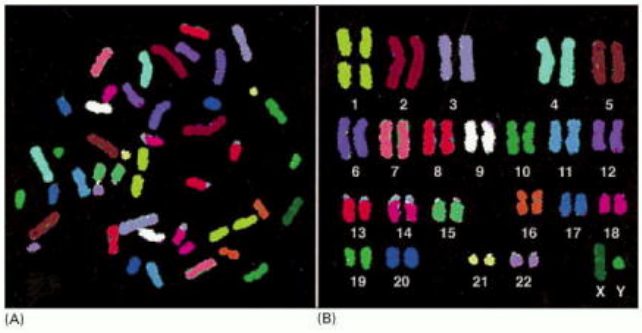

Figure 4-10. Human chromosomes. These chromosomes, from a male, were isolated from a cell undergoing nuclear division (mitosis) and are therefore highly compacted. Each chromosome has been "painted" a different color to permit its unambiguous identification under the light microscope. Chromosome painting is performed by exposing the chromosomes to a collection of human DNA molecules that have been coupled to a combination of fluorescent dyes. For example, DNA molecules derived from chromosome 1 are labeled with one specific dye combination, those from chromosome 2 with another, and so on. Because the labeled DNA can form base pairs, or hybridize, only to the chromosome from which it was derived (discussed in Chapter 8), each chromosome is differently labeled. For such experiments, the chromosomes are subjected to treatments that separate the double-helical DNA into individual strands, designed to permit base-pairing with the single-stranded labeled DNA while keeping the chromosome structure relatively intact. (A) The chromosomes visualized as they originally spilled from the lysed cell. (B) The same chromosomes artificially lined up in their numerical order. This arrangement of the full chromosome set is called a karyotype. (From E. Schröck et al., *Science* 273:494497, 1996. © AAAS.)

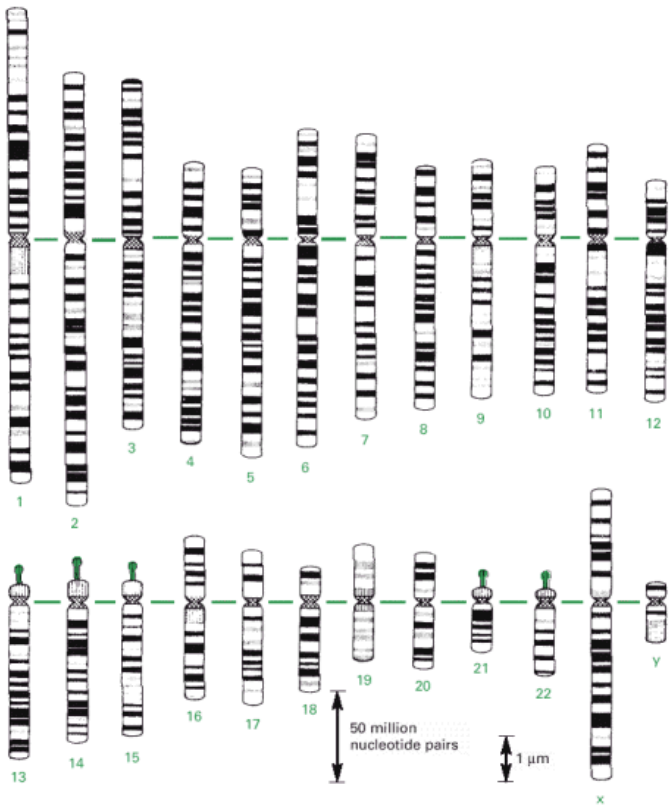

Figure 4-11. The banding patterns of human chromosomes. Chromosomes 122 are numbered in approximate order of size. A typical human somatic (non-germ line) cell contains two of each of these chromosomes, plus two sex chromosomes - two X chromosomes in a female, one X and one Y chromosome in a male. The chromosomes used to make these maps were stained at an early stage in mitosis, when the chromosomes are incompletely compacted. The *horizontal green line* represents the position of the centromere (see Figure 4-22), which appears as a constriction on mitotic chromosomes; the knobs on chromosomes 13, 14, 15, 21, and 22 indicate the positions of genes that code for the large ribosomal RNAs (discussed in Chapter 6). These patterns are obtained by staining chromosomes with Giemsa stain, and they can be observed under the light microscope. (Adapted from U. Franke, *Cytogenet. Cell Genet.* 31:2432, 1981.)

Figure 4-12. An aberrant human chromosome. (A) Two pairs of chromosomes, stained with Giemsa (see Figure 4-11), from a patient with ataxia, a disease characterized by progressive deterioration of motor skills. The patient has a normal pair of chromosome 4s *(left-hand pair)*, but one normal chromosome 12 and one aberrant chromosome 12, as seen by its greater length *(right-hand pair)*. The additional material contained on the aberrant chromosome 12 was deduced, from its pattern of bands, as a piece of chromosome 4 that had become attached to chromosome 12 through an abnormal recombination event, called a chromosomal translocation. (B) The same two chromosome pairs, "painted" *blue* for chromosome 4 DNA and *purple* for chromosome 12 DNA. The two techniques give rise to the same conclusion regarding the nature of the aberrant chromosome 12, but chromosome painting provides better resolution, and the clear identification of even short pieces of chromosomes that have become translocated. However, Giemsa staining is easier to perform. (From E. Schröck et al., *Science* 273:494497, 1996. © AAAS.)

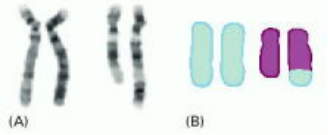

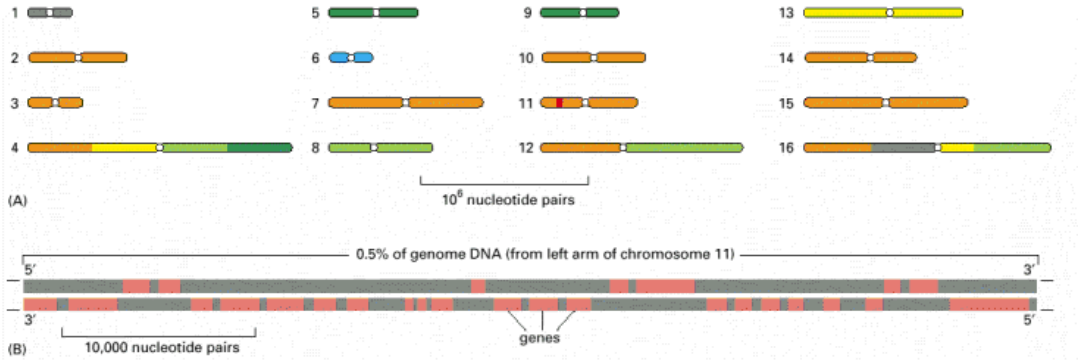

Figure 4-13. The genome of S. cerevisiae (budding yeast). (A) The genome is distributed over 16 chromosomes, and its complete nucleotide sequence was determined by a cooperative effort involving scientists working in many different locations, as indicated *(gray,* Canada; *orange,* European Union; *yellow,* United Kingdom; *blue,* Japan; *light green,* St Louis, Missouri; *dark green,* Stanford, California). The constriction present on each chromosome represents the position of its centromere (see Figure 4-22). (B) A small region of chromosome 11, highlighted in *red* in part A, is magnified to show the high density of genes characteristic of this species. As indicated by *orange,* some genes are transcribed from the lower strand (see Figure 1-5), while others are transcribed from the upper strand. There are about 6000 genes in the complete genome, which is 12,147,813 nucleotide pairs long.

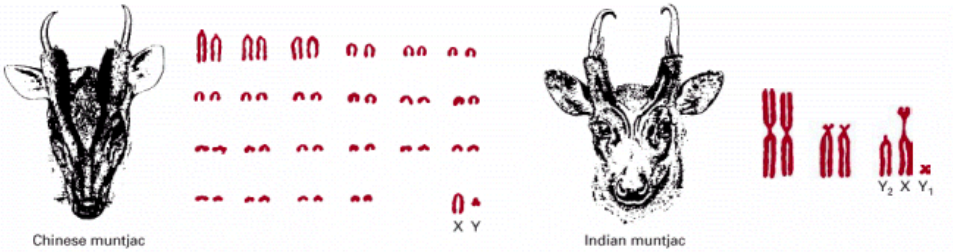

Figure 4-14. Two closely related species of deer with very different chromosome numbers. In the evolution of the Indian muntjac, initially separate chromosomes fused, without having a major effect on the animal. These two species have roughly the same number of genes. (Adapted from M.W. Strickberger, Evolution, 3rd edition, 2000, Sudbury, MA: Jones & Bartlett Publishers.)

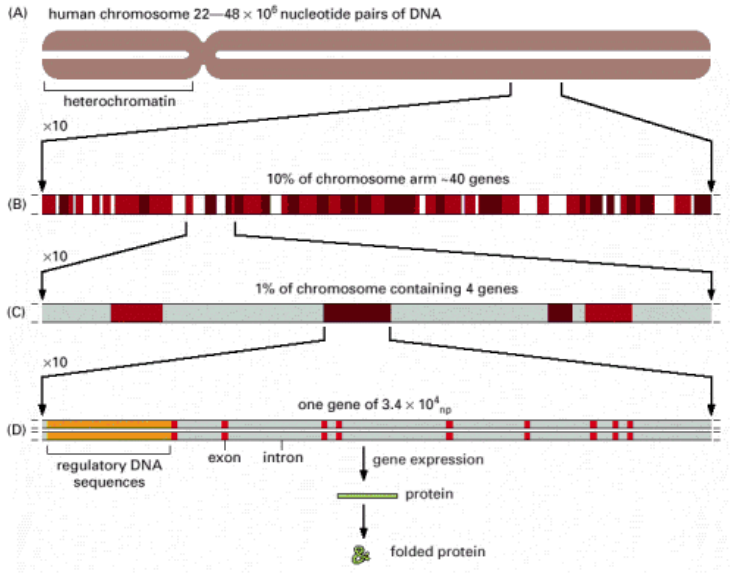

Figure 4-15. The organization of genes on a human chromosome. (A) Chromosome 22, one of the smallest human chromosomes, contains 48×10^6 nucleotide pairs and makes up approximately 1.5% of the entire human genome. Most of the left arm of chromosome 22 consists of short repeated sequences of DNA that are packaged in a particularly compact form of chromatin (heterochromatin), which is discussed later in this chapter. (B) A tenfold expansion of a portion of chromosome 22, with about 40 genes indicated. Those in *dark brown* are known genes and those in *light brown* are predicted genes. (C) An expanded portion of (B) shows the entire length of several genes. (D) The intron-exon arrangement of a typical gene is shown after a further tenfold expansion. Each exon *(red)* codes for a portion of the protein, while the DNA sequence of the introns *(gray)* is relatively unimportant. The entire human genome (3.2×10^9 nucleotide pairs) is distributed over 22 autosomes and 2 sex chromosomes (see Figures 4-10 and 4-11). The term *human genome sequence* refers to the complete nucleotide sequence of DNA in these 24 chromosomes. Being diploid, a human somatic cell therefore contains roughly twice this amount of DNA. Humans differ from one another by an average of one nucleotide in every thousand, and a wide variety of humans contributed DNA for the genome sequencing project. The published human genome sequence is therefore a composite of many individual sequences. (Adapted from International Human Genome Sequencing Consortium, *Nature* 409:860921, 2001.)

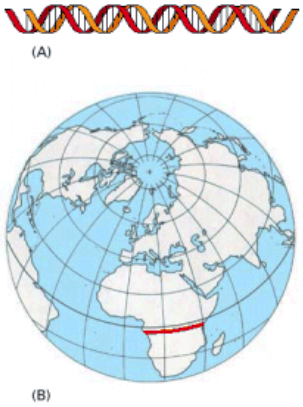

Figure 4-16. Scale of the human genome. If each nucleotide pair is drawn as 1 mm as in (A), then the human genome would extend 3200 km (approximately 2000 miles), far enough to stretch across the center of Africa, the site of our human origins *(red line* in B). At this scale, there would be, on average, a protein-coding gene every 300 m. An average gene would extend for 30 m, but the coding sequences in this gene would add up to only just over a meter.

Figure 4-17. Representation of the nucleotide sequence content of the human genome. LINES, SINES, retroviral-like elements, and DNA-only transposons are all mobile genetic elements that have multiplied in our genome by replicating themselves and inserting the new copies in different positions. Mobile genetic elements are discussed in Chapter 5. Simple sequence repeats are short nucleotide sequences (less than 14 nucleotide pairs) that are repeated again and again for long stretches. Segmental duplications are large blocks of the genome (1000200,000 nucleotide pairs) that are present at two or more locations in the genome. Over half of the unique sequence consists of genes and the remainder is probably regulatory DNA. Most of the DNA present in heterochromatin, a specialized type of chromatin (discussed later in this chapter) that contains relatively few genes, has not yet been sequenced. (Adapted from Unveiling the Human Genome, Supplement to the Wellcome Trust Newsletter. London: Wellcome Trust, February 2001.)

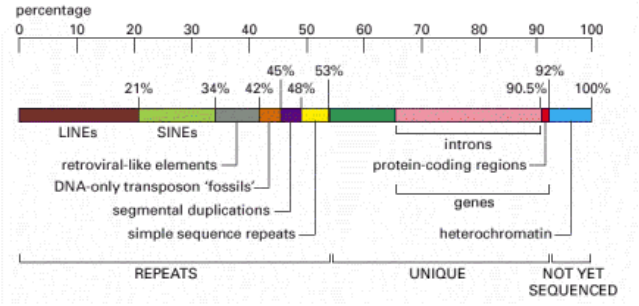

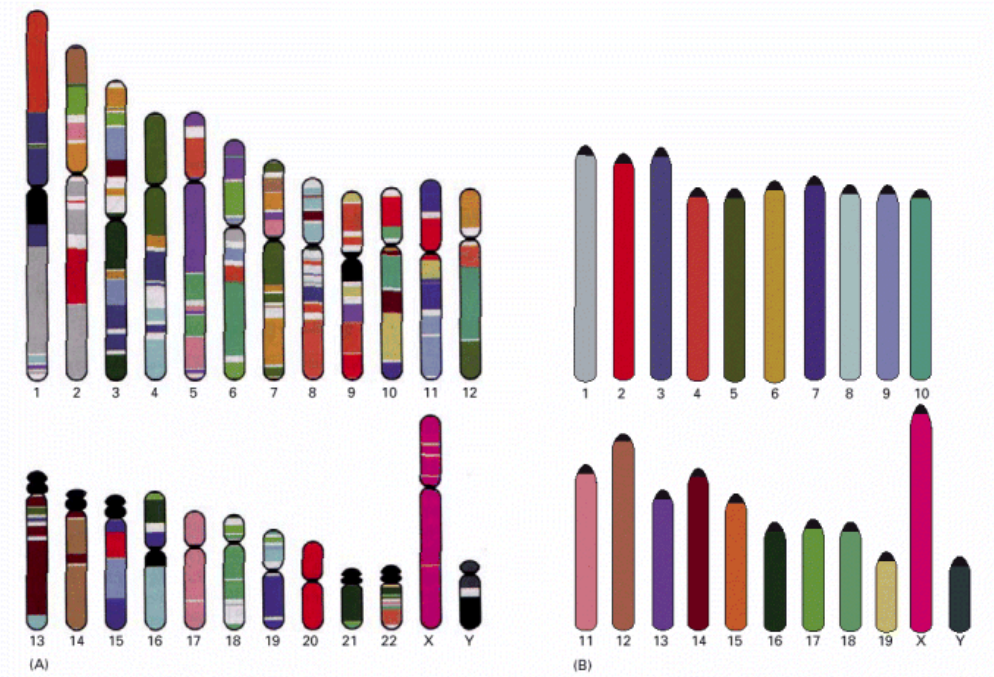

Figure 4-18. Conserved synteny between the human and mouse genomes. Regions from different mouse chromosomes (indicated by the colors of each mouse in B) show conserved synteny (gene order) with the indicated regions of the human genome (A). For example the genes present in the upper portion of human chromosome 1 *(orange)* are present in the same order in a portion of mouse chromosome 4. Regions of human chromosomes that are composed primarily of short, repeated sequences are shown in *black.* Mouse centromeres (indicated in *black* in B) are located at the ends of chromosomes; no known genes lie beyond the centromere on any mouse chromosome. For the most part, human centromeres, indicated by constrictions, occupy more internal positions on chromosomes (see Figure 4-11). (Adapted from International Human Genome Sequencing Consortium, *Nature* 409:860921, 2001.)

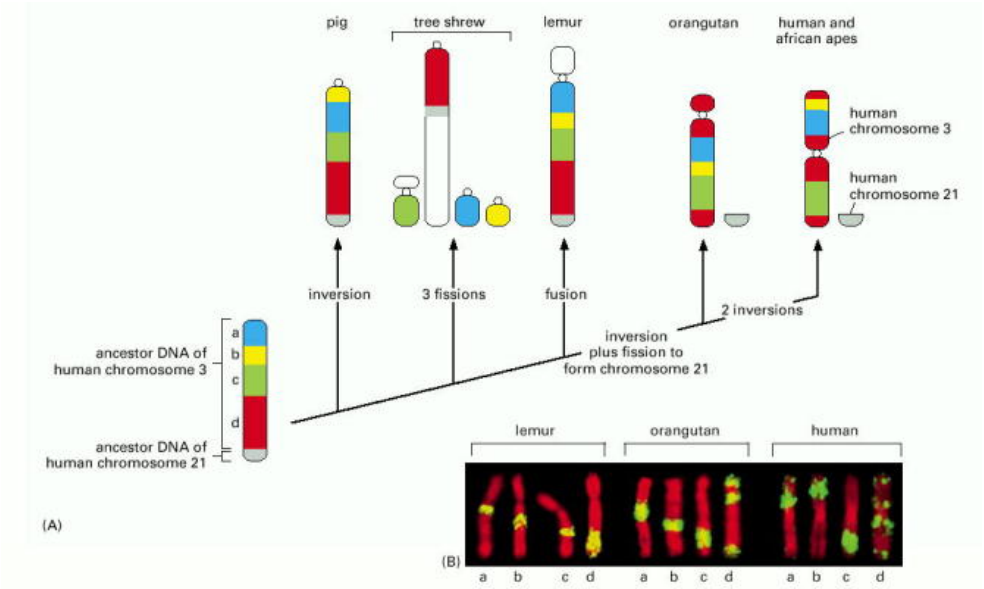

Figure 4-19. A proposed evolutionary history of human chromosome 3 and its relatives in other mammals. (A) At the *lower left* is the order of chromosome 3 segments hypothesized to be present on a chromosome of a mammalian ancestor. Along the *top* are the patterns of chromosome sequences found in the chromosomes of modern mammals. The minimum changes necessary to account for the appearance of the modern chromosomes from the hypothetical ancestor are marked along each branch. In mammals, these types of changes in chromosome organization are thought to occur once every 510×10^6 years. The *small circles* depicted in the modern chromosomes represent the positions of centromeres. (B) Some of the chromosome painting experiments that led to the diagram in (A). Each image shows the chromosome most closely related to human chromosome 3, painted *green* by hybridization with different segments of DNA, lettered a, b, c, and d along the *bottom* of the figure. These letters correspond to the colored segments of the diagram in (A). (From S. Müller et al., *Proc. Natl. Acad. Sci. USA* 97:206211, 2000. © National Academy of Sciences.)

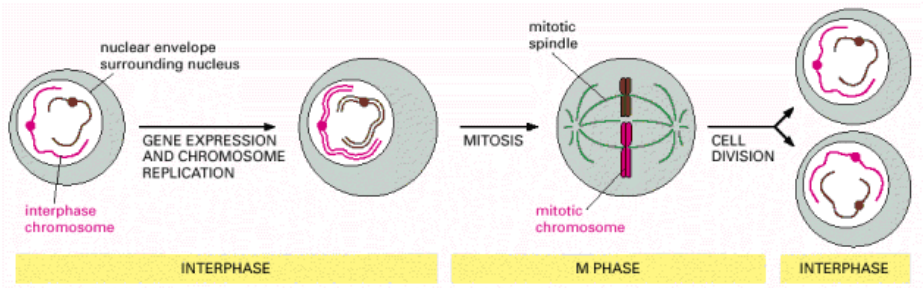

Figure 4-20. A simplified view of the eucaryotic cell cycle. During interphase, the cell is actively expressing its genes and is therefore synthesizing proteins. Also, during interphase and before cell division, the DNA is replicated and the chromosomes are duplicated. Once DNA replication is complete, the cell can enter *M phase*, when mitosis occurs and the nucleus is divided into two daughter nuclei. During this stage, the chromosomes condense, the nuclear envelope breaks down, and the mitotic spindle forms from microtubules and other proteins. The condensed mitotic chromosomes are captured by the mitotic spindle, and one complete set of chromosomes is then pulled to each end of the cell. A nuclear envelope re-forms around each chromosome set, and in the final step of M phase, the cell divides to produce two daughter cells. Most of the time in the cell cycle is spent in interphase; M phase is brief in comparison, occupying only about an hour in many mammalian cells.

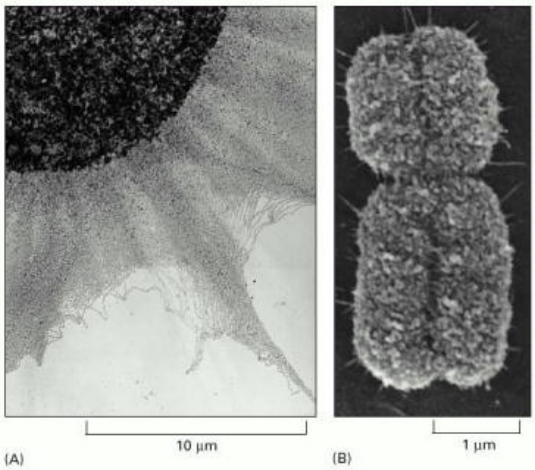

Figure 4-21. A comparison of extended interphase chromatin with the chromatin in a mitotic chromosome. (A) An electron micrograph showing an enormous tangle of chromatin spilling out of a lysed interphase nucleus. (B) A scanning electron micrograph of a mitotic chromosome: a condensed duplicated chromosome in which the two new chromosomes are still linked together (see Figure 4-22). The constricted region indicates the position of the centromere. Note the difference in scales. (A, courtesy of Victoria Foe; B, courtesy of Terry D. Allen.)

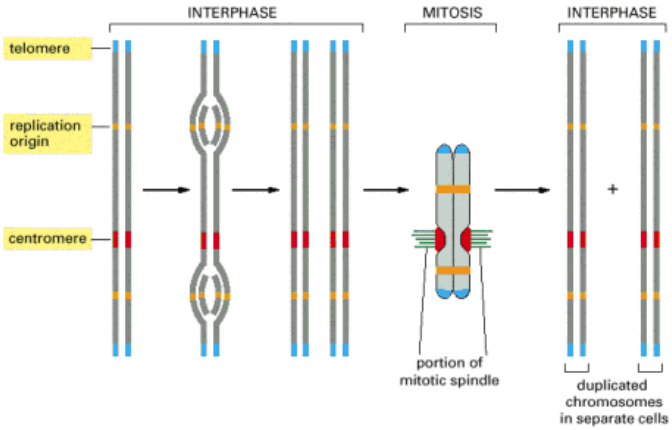

Figure 4-22. The three DNA sequences required to produce a eucaryotic chromosome that can be replicated and then segregated at mitosis. Each chromosome has multiple origins of replication, one centromere, and two telomeres. Shown here is the sequence of events a typical chromosome follows during the cell cycle. The DNA replicates in interphase beginning at the origins of replication and proceeding bidirectionally from the origins across the chromosome. In M phase, the centromere attaches the duplicated chromosomes to the mitotic spindle so that one copy is distributed to each daughter cell during mitosis. The centromere also helps to hold the duplicated chromosomes together until they are ready to be moved apart. The telomeres form special caps at each chromosome end.

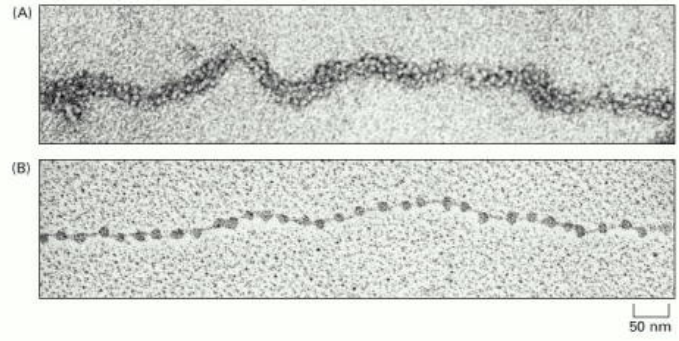

Figure 4-23. Nucleosomes as seen in the electron microscope. (A) Chromatin isolated directly from an interphase nucleus appears in the electron microscope as a thread 30 nm thick. (B) This electron micrograph shows a length of chromatin that has been experimentally unpacked, or decondensed, after isolation to show the nucleosomes. (A, courtesy of Barbara Hamkalo; B, courtesy of Victoria Foe.)

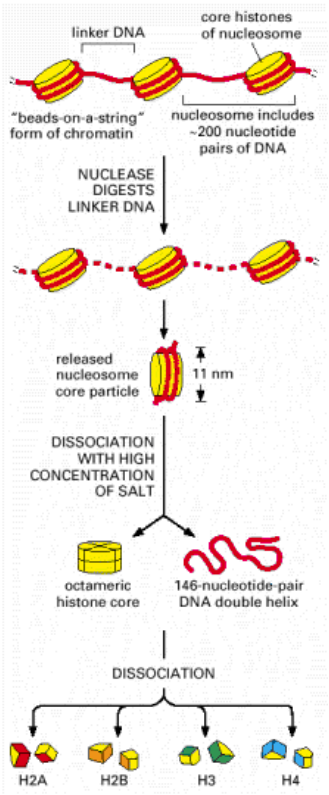

Figure 4-24. Structural organization of the nucleosome. A nucleosome contains a protein core made of eight histone molecules. As indicated, the nucleosome core particle is released from chromatin by digestion of the linker DNA with a nuclease, an enzyme that breaks down DNA. (The nuclease can degrade the exposed linker DNA but cannot attack the DNA wound tightly around the nucleosome core.) After dissociation of the isolated nucleosome into its protein core and DNA, the length of the DNA that was wound around the core can be determined. This length of 146 nucleotide pairs is sufficient to wrap 1.65 times around the histone core.

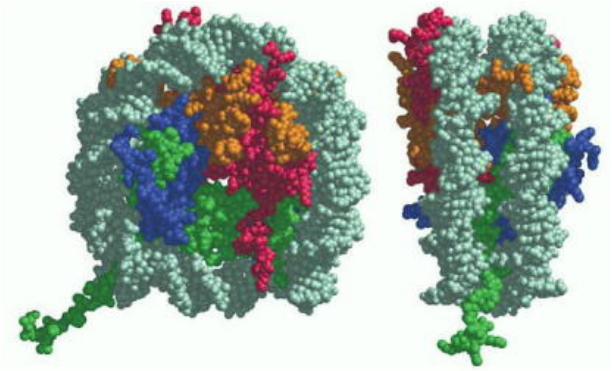

Figure 4-25. The structure of a nucleosome core particle, as determined by x-ray diffraction analyses of crystals. Each histone is colored according to the scheme of Figure 4-24, with the DNA double helix in *light gray*. (Reprinted by permission from K. Luger et al., *Nature* 389:251260, 1997. © Macmillan Magazines Ltd.)

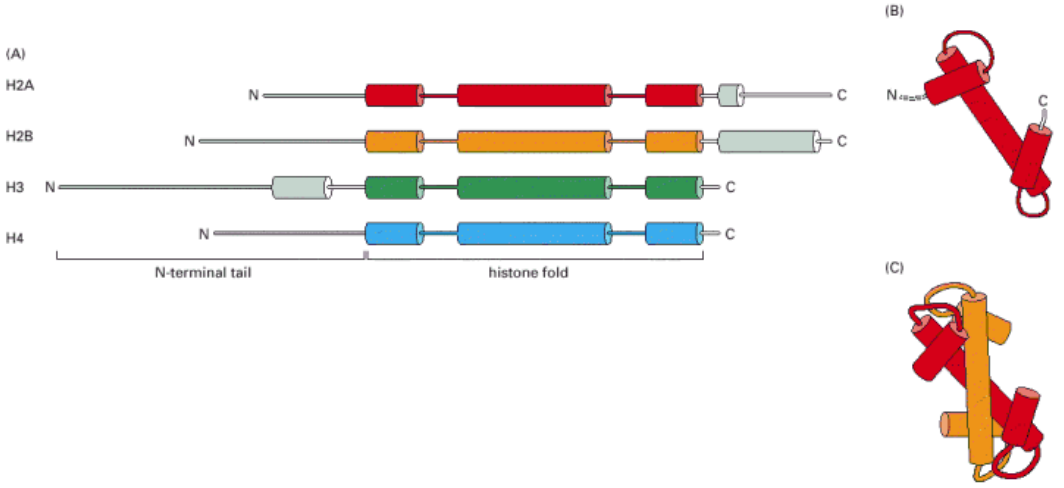

Figure 4-26. The overall structural organization of the core histones. (A) Each of the core histones contains an N-terminal tail, which is subject to several forms of covalent modification, and a histone fold region, as indicated. (B) The structure of the histone fold, which is formed by all four of the core histones. (C) Histones 2A and 2B form a dimer through an interaction known as the "handshake." Histones H3 and H4 form a dimer through the same type of interaction, as illustrated in Figure 4-27.

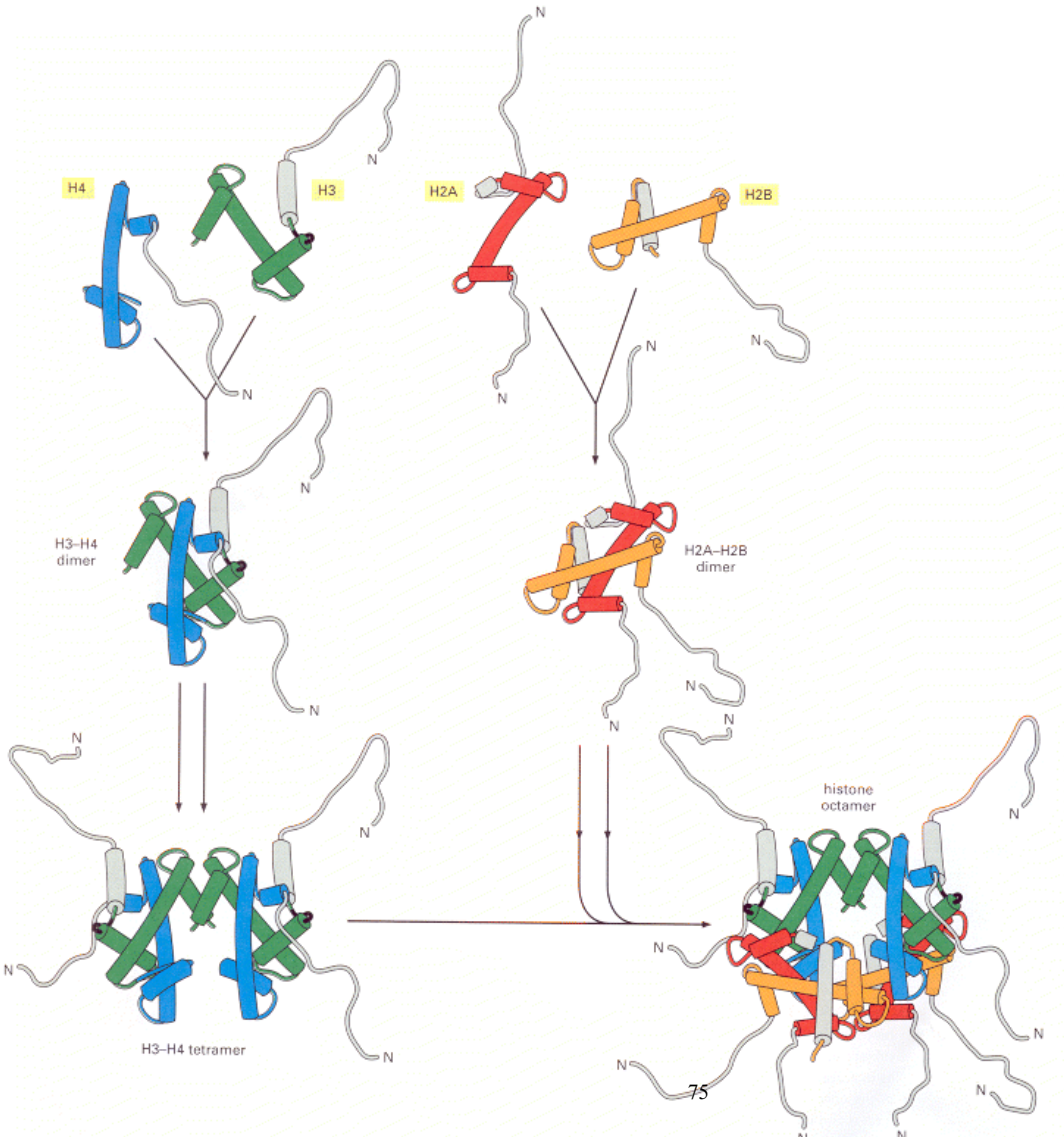

Figure 4-27. The assembly of a histone octamer. The histone H3H4 dimer and the H2A-H2B dimer are formed from the handshake interaction. An H3-H4 tetramer forms the scaffold of the octamer onto which two H2A-H2B dimers are added, to complete the assembly. The histones are colored as in Figure 4-26. Note that all eight N-terminal tails of the histones protrude from the disc-shaped core structure. In the x-ray crystal (Figure 4-25), most of the histone tails were unstructured (and therefore not visible in the structure), suggesting that their conformations are highly flexible. (Adapted from figures by J. Waterborg.)

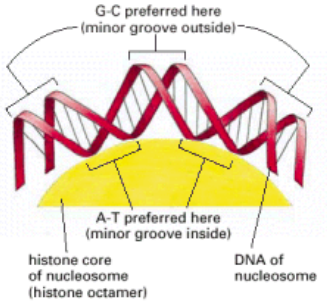

Figure 4-28. The bending of DNA in a nucleosome. The DNA helix makes 1.65 tight turns around the histone octamer. This diagram is drawn approximately to scale, illustrating how the minor groove is compressed on the inside of the turn. Owing to certain structural features of the DNA molecule, A-T base pairs are preferentially accommodated in such a narrow minor groove.

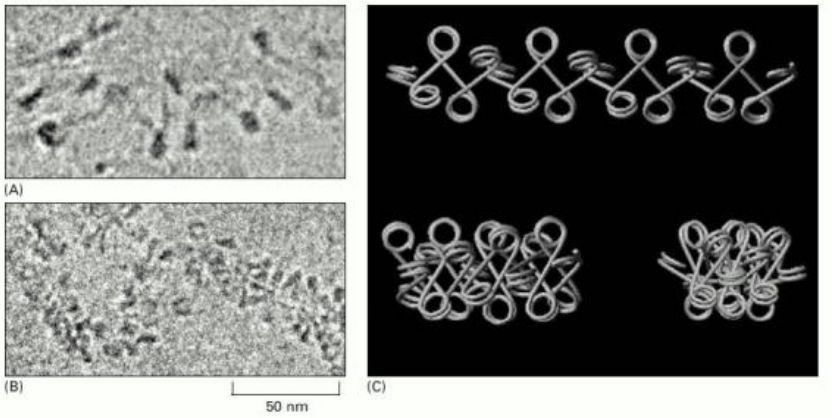

Figure 4-29. Variations on the Zigzag model for the 30-nm chromatin fiber. (A and B) Electron microscopic evidence for the *top* and *bottom-left* model structures depicted in (C). (C) Zigzag variations. An interconversion between these three variations is proposed to occur by an accordion-like expansion and contraction of the fiber length. Differences in the length of the linker between adjacent nucleosome beads can be accommodated by snaking or coiling of the linker DNA, or by small local changes in the width of the fiber. Formation of the 30-nm fiber requires both histone H1 and the core histone tails; for simplicity, neither is shown here, but see Figures 4-30 and 4-32. (From J. Bednar et al., *Proc. Natl. Acad. Sci. USA* 95:1417314178, 1998. © National Academy of Sciences.)

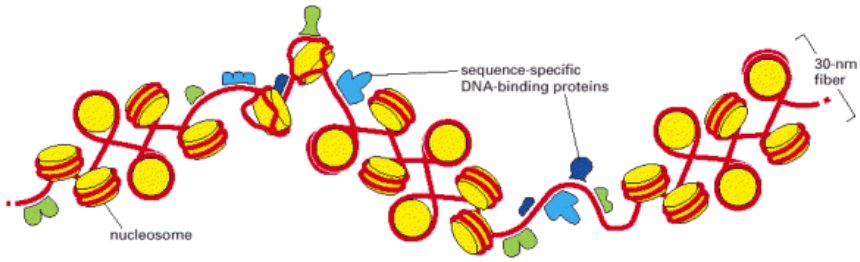

Figure 4-30. Irregularities in the 30-nm fiber. This schematic view of the 30-nm fiber illustrates its interruption by sequence-specific DNA-binding proteins. How these proteins bind tightly to DNA is explained in Chapter 7. The interruptions in the 30-nm fiber may be due to regions of DNA that lack nucleosomes altogether or, more probably, to regions that contain altered or remodeled nucleosomes. Regions of chromatin that are nucleosome free or contain remodeled nucleosome can often be detected experimentally by the unusually high susceptibility of their DNA to digestion by nucleases - as compared with the DNA in nucleosomes.

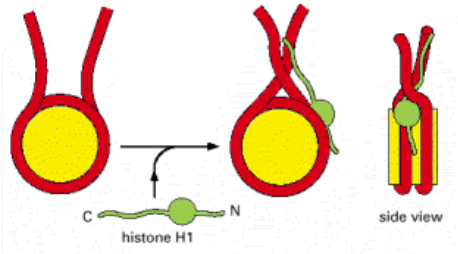

Figure 4-31. A speculative model for how histone H1 could change the path of DNA as it exits from the nucleosome. Histone H1 *(green)* consists of a globular core and two extended tails. Part of the effect of H1 on the compaction of nucleosome organization may result from charge neutralization: like the core histones, H1 is positively charged (especially its C-terminal tail), and this helps to compact the negatively charged DNA. Unlike the core histones, H1 does not seem to be essential for cell viability; in one ciliated protozoan the nucleus expands nearly twofold in the absence of H1, but the cells otherwise appear normal.

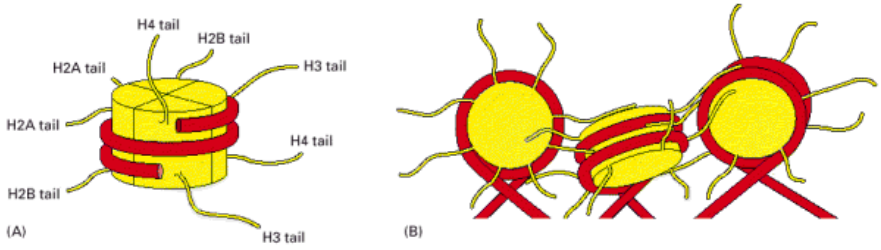

Figure 4-32. A speculative model for histone tails in the formation of the 30-nm fiber. (A) The approximate exit points of the eight histone tails, four from each histone subunit, that extend from each nucleosome. In the high-resolution structure of the nucleosome (see Figure 4-25), the tails are largely unstructured, suggesting that they are highly flexible. (B) A speculative model showing how the histone tails may help to pack nucleosomes together into the 30-nm fiber. This model is based on (1) experimental evidence that histone tails aid in the formation of the 30-nm fiber, (2) the x-ray crystal structure of the nucleosome, which showed that the tails of one nucleosome contact the histone core of an adjacent nucleosome in the crystal lattice, and (3) evidence that the histone tails interact with DNA.

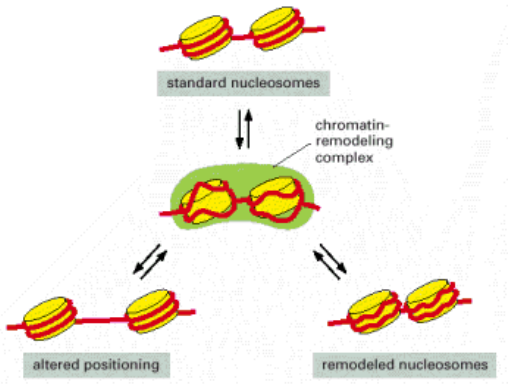

Figure 4-33. Model for the mechanism of some chromatin remodeling complexes. In the absence of remodeling complexes, the interconversion between the three nucleosomal states shown is very slow because of a high activation energy barrier. Using ATP hydrolysis, chromatin-remodeling complexes *(green)* create an activated intermediate (shown in the center of the figure) in which the histone-DNA contacts have been partly disrupted. This activated state can then decay to any one of the three nucleosomal configurations shown. In this way, the remodeling complexes greatly increase the rate of interconversion between different nucleosomal states. The remodeled state, in which the histone-DNA contacts have been loosened, has a higher free energy level than that of standard nucleosomes and will slowly revert to the standard nucleosome conformation, even in the absence of a remodeling complex. Cells have many different chromatin remodeling complexes, and they differ in their detailed biochemical properties; for example, not all can change the position of a nucleosome, but all use the energy of ATP hydrolysis to alter nucleosome structure. (Adapted from R.E. Kingston and G.J. Narlikar, *Genes Dev.* 13:23392352, 1999.)

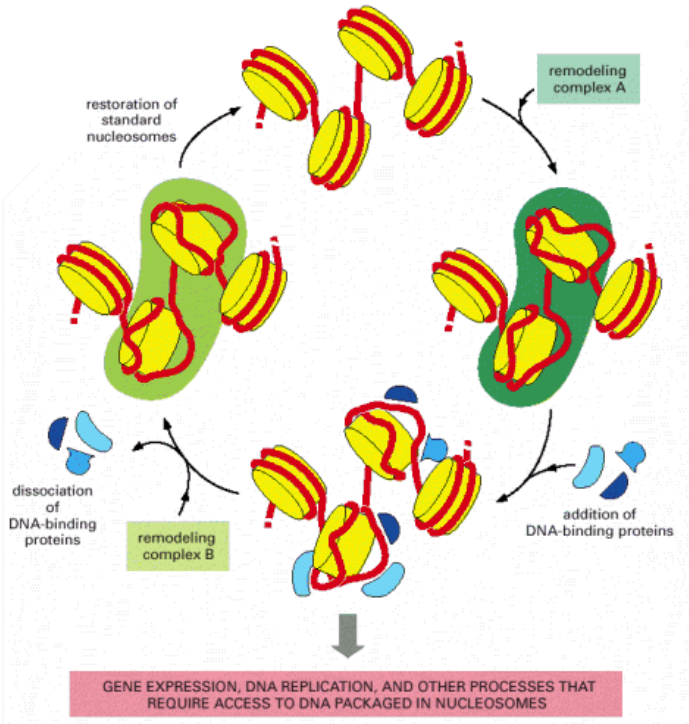

Figure 4-34. A cyclic mechanism for nucleosome disruption and re-formation. According to this model, different chromatin remodeling complexes disrupt and re-form nucleosomes, although, in principle, the same complex might catalyze both reactions. The DNA-binding proteins could function in gene expression, DNA replication, or DNA repair, and in some cases their binding could lead to the dissociation of the histone core to form nucleosome-free regions of DNA like those illustrated in Figure 4-30. (Adapted from A. Travers, *Cell* 96:311314, 1999.)

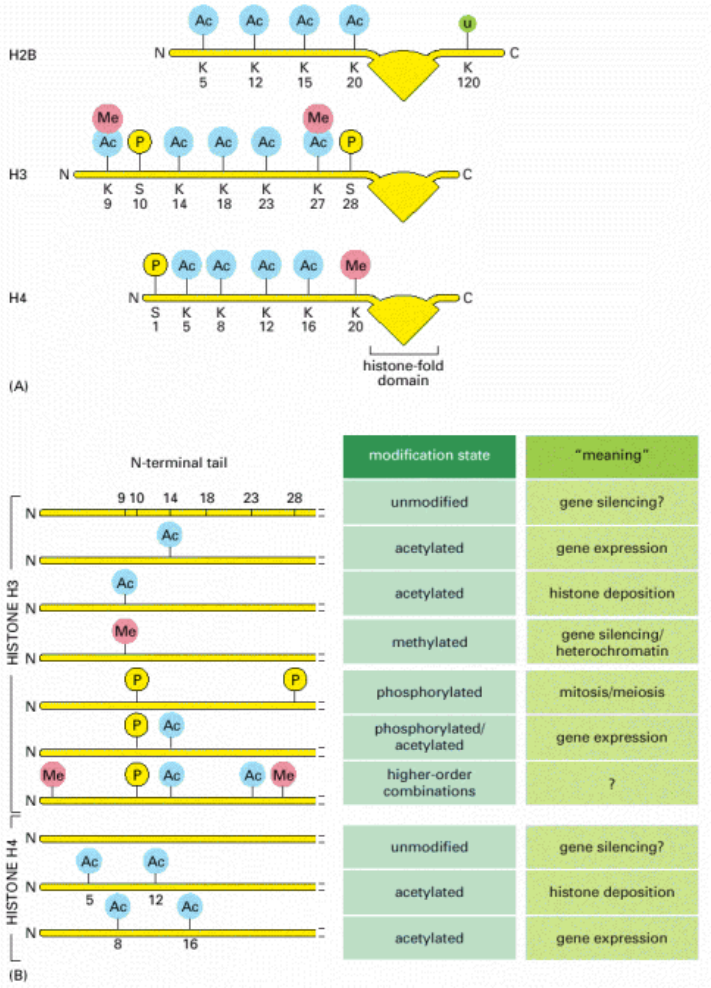

Figure 4-35. Covalent modification of core histone tails. (A) Known modifications of the four histone core proteins are indicated: Me = methyl group, Ac = acetyl group, P = phosphate, u = ubiquitin. Note that some positions (e.g., lysine 9 of H3) can be modified in more than one way. Most of these modifications add a relatively small molecule onto the histone tails; the exception is ubiquitin, a 76 amino acid protein also used in other cellular processes (see Figure 6-87). The function of ubiquitin in chromatin is not well understood: histone H2B can be modified by a single ubiquitin molecule; H2A can be modified by the addition of several ubiquitins. (B) A histone code hypothesis. Histone tails can be marked by different combinations of modifications. According to this hypothesis, each marking conveys a specific meaning to the stretch of chromatin on which it occurs. Only a few of the meanings of the modifications are known. In Chapter 7, we discuss the way a doubly-acetylated H4 tail is "read" by a protein required for gene expression. In another well-studied case, an H3 tail methylated at lysine 9 is recognized by a set of proteins that create an especially compact form of chromatin, which silences gene expression. The acetylation of lysine 14 of histone H3 and lysines 8 and 16 of histone H4 - usually associated with gene expression - is performed by the type A histone acetylases (HATs) in the nucleus. In contrast, the acetylation of lysines 5 and 12 of histone H4 and a lysine of histone H3 takes place in the cytosol, after the histones have been synthesized but before they have been incorporated into nucleosomes; these modifications are catalyzed by type B HATs. These modified histones are deposited onto DNA after DNA replication (see Figure 5-41), and their acetyl groups are taken off shortly afterwards by histone deacetylases (HDACs). Thus, the acetylation at these positions signals newly replicated chromatin. Modification of a particular position in a histone tail can take on different meanings depending on other features of the local chromatin structure. For example, the phosphorylation of position 10 of histone H3 is associated not only with the condensation of chromosomes that takes place in mitosis and meiosis but also with the expression of certain genes. Some histone tail modifications are interdependent. For example methylation of H3 position 9 blocks the phosphorylation of H3 position 10, and vice versa.

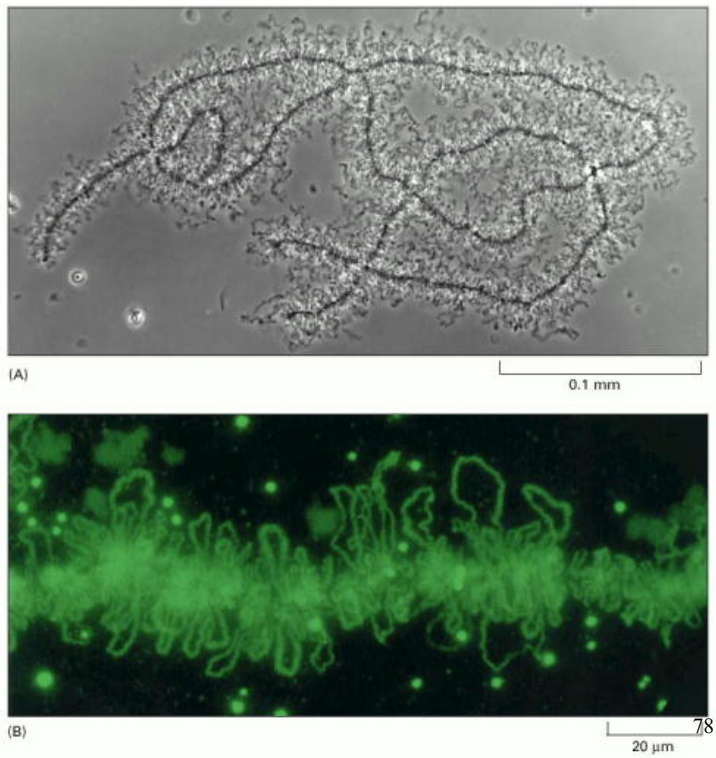

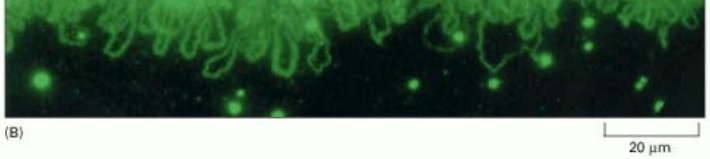

Figure 4-36. Lampbrush chromosomes. (A) A light micrograph of lampbrush chromosomes in an amphibian oocyte. Early in oocyte differentiation, each chromosome replicates to begin meiosis, and the homologous replicated chromosomes pair to form this highly extended structure containing a total of four replicated DNA molecules, or chromatids. The lampbrush chromosome stage persists for months or years, while the oocyte builds up a supply of materials required for its ultimate development into a new individual. (B) Fluorescence light micrograph showing a portion of an amphibian lampbrush chromosome. The regions of the chromosome that are being actively expressed are stained *green* by using antibodies against proteins that process RNA during one of the steps of gene expression (discussed in Chapter 6). The round granules are thought to correspond to large complexes of the RNA-splicing machinery that will also be discussed in Chapter 6. (A, courtesy of Joseph G. Gall; B, courtesy of Joseph G. Gall and Christine Murphy.)

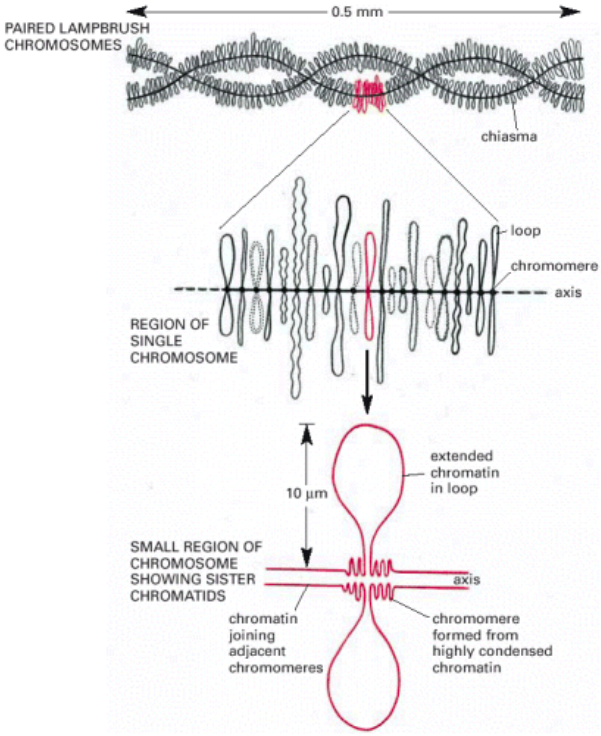

Figure 4-37. A model for the structure of a lampbrush chromosome. The set of lampbrush chromosomes in many amphibians contains a total of about 10,000 chromatin loops, although most of the DNA in each chromosome remains highly condensed in the chromomeres. Each loop corresponds to a particular DNA sequence. Four copies of each loop are present in each cell, since each of the two chromosomes shown at the top consists of two closely apposed, newly replicated chromosomes. This four-stranded structure is characteristic of this stage of development of the oocyte, the diplotene stage of meiosis; see Figure 20-12.

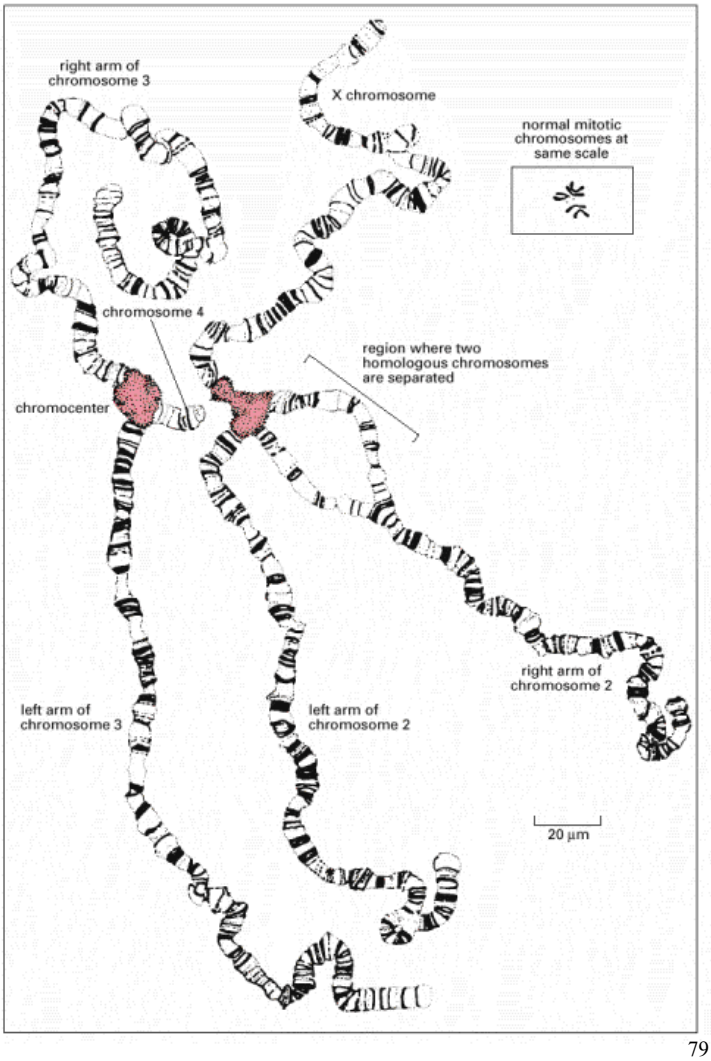

Figure 4-38. The entire set of polytene chromosomes in one *Drosophila* salivary cell. These chromosomes have been spread out for viewing by squashing them against a microscope slide. *Drosophila* has four chromosomes, and there are four different chromosome pairs present. But each chromosome is tightly paired with its homolog (so that each pair appears as a single structure), which is not true in most nuclei (except in meiosis). The four polytene chromosomes are normally linked together by regions near their centromeres that aggregate to create a single large chromocenter *(pink region).* In this preparation, however, the chromocenter has been split into two halves by the squashing procedure used. (Modified from T.S. Painter, *J. Hered.* 25:465476, 1934.)

Figure 4-39. A light micrograph of a portion of a polytene chromosome from *Drosophila* salivary glands. The distinct pattern produced by bands and interbands is readily seen. The bands are regions of increased chromatin concentration that occur in interphase chromosomes. Although they are detectable only in polytene chromosomes, it is thought that they reflect a structure common to the chromosomes of most eucaryotes. (Courtesy of Joseph G. Gall.)

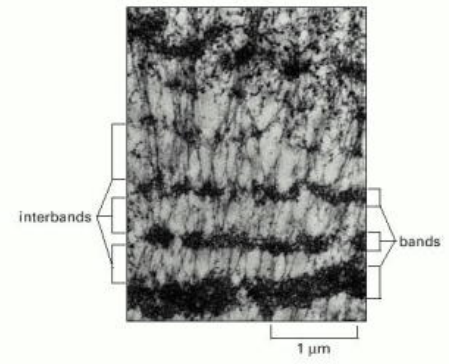

Figure 4-40. An electron micrograph of a small section of a *Drosophila* polytene chromosome seen in thin section. Bands of very different thickness can be readily distinguished, separated by interbands, which contain less condensed chromatin. (Courtesy of Veikko Sorsa.)

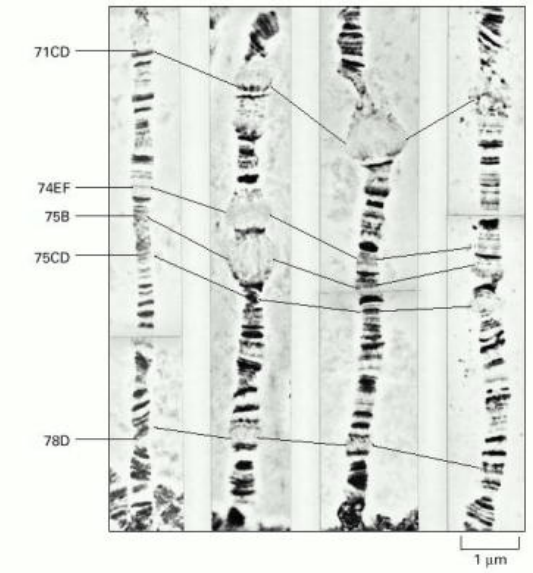

Figure 4-41. Chromosome puffs. This series of time-lapse photographs shows how puffs arise and recede in the polytene chromosomes of *Drosophila* during larval development. A region of the *left* arm of chromosome 3 is shown. It exhibits five very large puffs in salivary gland cells, each active for only a short developmental period. The series of changes shown occur over a period of 22 hours, appearing in a reproducible pattern as the organism develops. The designations of the indicated bands are given at the left of the photographs. (Courtesy of Michael Ashburner.)

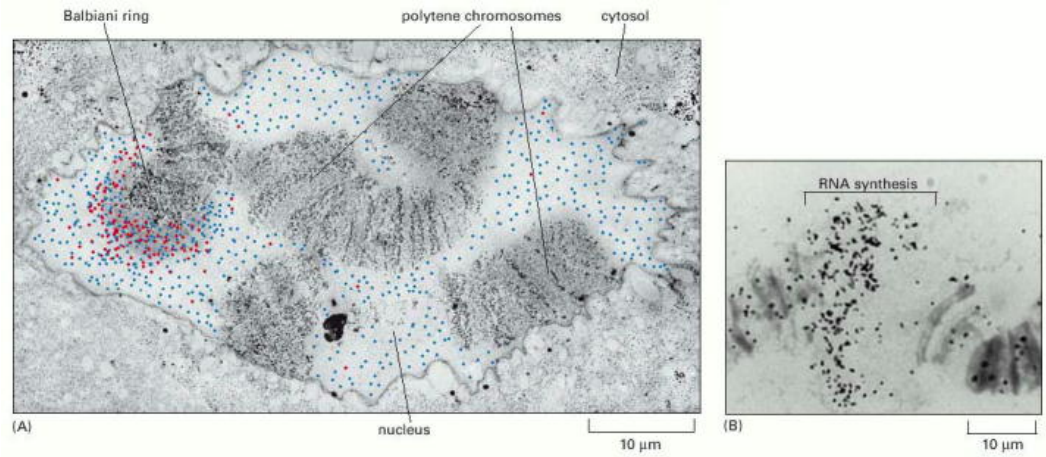

Figure 4-42. RNA synthesis in chromosome puffs. (A) Polytene chromosomes from the salivary glands of the insect *C. tentans.* As outlined in Chapter 1 and described in detail in Chapter 6, the first step in gene expression is the synthesis of an RNA molecule using the DNA as a template. In this electron micrograph, newly synthesized RNA from a Balbiani ring gene is indicated in *red.* Cells were exposed to a brief pulse of BrUTP (an analog of UTP), which was incorporated into RNA. Cells were then fixed and the newly synthesized RNAs were identified by using antibodies against BrU. Balbiani ring RNAs could be distinguished from other RNAs by their characteristic shape (see Figure 4-43). The *blue dots* in the figure represent positions of Balbiani ring RNAs that were synthesized before the addition of BrUTP. The experiment shows that Balbiani ring RNAs are synthesized in puffs and then diffuse through the nucleoplasm. (B) An autoradiogram of a single puff in a polytene chromosome. The portion of the chromosome indicated is undergoing RNA synthesis and has therefore become labeled with ^{3}H-uridine. (A, courtesy of B. Daneholt, from O.P Singh et al., *Exp. Cell Res.* 251:135146, 1999. © Academic Press; B, courtesy of José Bonner.)

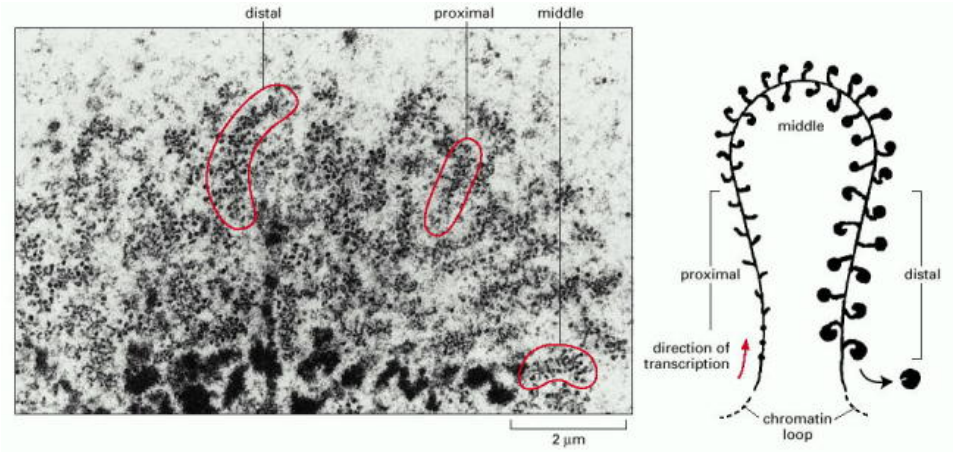

Figure 4-43. Polytene chromosomes from *C. tentans*. The electron micrograph shows a thin section of the chromatin in a Balbiani ring, a chromosome puff very active in gene expression. The Balbiani ring gene codes for secretory proteins the larvae uses to spin a protective tube. The chromatin is arranged in loops, but because the sample has been sectioned, only portions of the loops are visible. As they are synthesized on the chromatin, the RNA molecules are bound up by protein molecules, making them visible as knobs on stalks in the electron microscope. From the size of the RNA-protein complex, the extent of RNA synthesis (transcription) can be inferred; a whole chromatin loop (shown on the right) can then be reconstructed from a set of electron micrograph sections such as that shown here. (Courtesy of B. Daneholt, from U. Skoglund et al., *Cell* 34:847855, 1983. © Elsevier.)

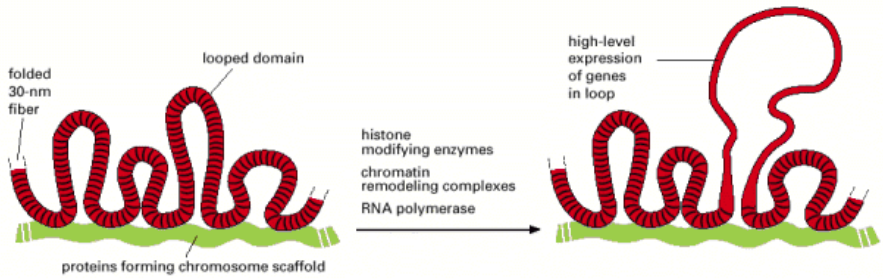

Figure 4-44. A model for the structure of an interphase chromosome. A section of an interphase chromosome is shown folded into a series of looped domains, each containing 20,000100,000 nucleotide pairs of double-helical DNA condensed into a 30-nm fiber. Individual loops can decondense, perhaps in part through an accordionlike expansion of the 30-nm fiber (see Figure 4-29), when the cell requires direct access to the DNA packaged in these loops. This decondensation is brought about by enzymes that directly modify chromatin structure - as well as by proteins, such as RNA polymerase (discussed in Chapter 6), that act directly on the underlying DNA. It is not understood how the folded 30-nm fiber is anchored to the chromosome axis, but evidence suggests that the base of chromosomal loops is rich in DNA topoisomerases, which are enzymes that allow DNA to swivel when anchored (see pp. 251253).

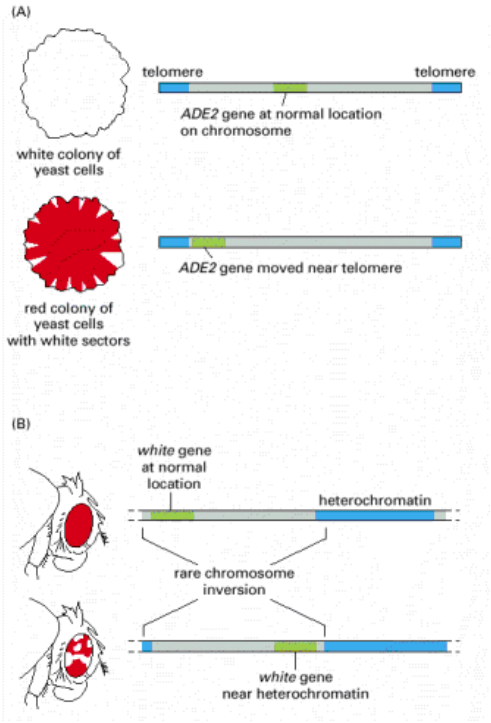

Figure 4-45. Position effects on gene expression in two different eucaryotic organisms. (A) The yeast *ADE2* gene at its normal chromosomal location is expressed in all cells. When moved near the end of a yeast chromosome, which is inferred to be folded into a form of heterochromatin, the gene is no longer expressed in most cells of the population. The *ADE2* gene codes for one of the enzymes of adenine biosynthesis, and the absence of the *ADE2* gene product leads to the accumulation of a red pigment. Therefore, a colony of cells that expresses *ADE2* is *white*, and one composed of cells where the *ADE2* gene is not expressed is *red.* The *white* sectors that fan out from the middle of the *red* colony grown on an agar surface represent the descendants of cells in which the *ADE2* gene has spontaneously become active. These white sectors are thought to result from a heritable change to a less tightly packed state of chromatin near the *ADE2* gene in these cells. Although yeast chromosomes are too small to be seen under the light microscope, the chromatin structure at the ends of yeast chromosomes is thought to have many of the same structural features as the heterochromatin in the chromosomes of larger organisms. (B) Position effects can also be observed for the *white* gene in the fruit fly *Drosophila.* The *white* gene controls eye pigment production and is named after the mutation that first identified it. Wild-type flies with a normal *white* gene *(white)* have normal pigment production, which gives them red eyes, but if the *white* gene is mutated and inactivated, the mutant flies *(white)* make no pigment and have *white* eyes. In flies in which a normal *white*$^+$ gene has been moved near a region of heterochromatin, the eyes are mottled, with both *red* and *white* patches. The *white* patches represent cells in which the *white*$^+$ gene has been silenced by the effects of the heterochromatin. In contrast, the red patches represent cells that express the *white*$^+$ gene because the heterochromatin did not spread across this gene at the time, early in development, when the heterochromatin first formed. As in the yeast, the presence of large patches of *red* and *white* cells indicates that the state of transcriptional activity of the gene is inherited, once determined by its chromatin packaging in the early embryo.

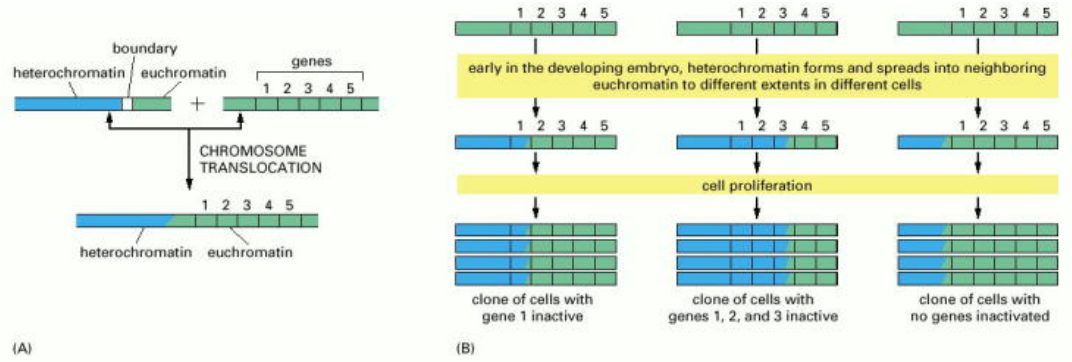

Figure 4-46. The cause of position effect variegation in *Drosophila.* (A) Heterochromatin *(blue)* is normally prevented from spreading into adjacent regions of euchromatin *(green)* by special boundary DNA sequences, which we discuss in Chapter 7. In flies that inherit certain chromosomal rearrangements, however, this barrier is no longer present. (B) During the early development of such flies, heterochromatin can spread into neighboring chromosomal DNA, proceeding for different distances in different cells. This spreading soon stops, but the established pattern of heterochromatin is inherited, so that large clones of progeny cells are produced that have the same neighboring genes condensed into heterochromatin and thereby inactivated (hence the "variegated" appearance of some of these flies; see Figure 4-45B). Although "spreading" is used to describe the formation of new heterochromatin near previously existing heterochromatin, the term may not be wholly accurate. There is evidence that during expansion, heterochromatin can "skip over" some regions of chromatin, sparing the genes that lie within them from repressive effects. One possibility is that heterochromatin can expand across the base of some DNA loops, thus bypassing the chromatin contained in the loop.

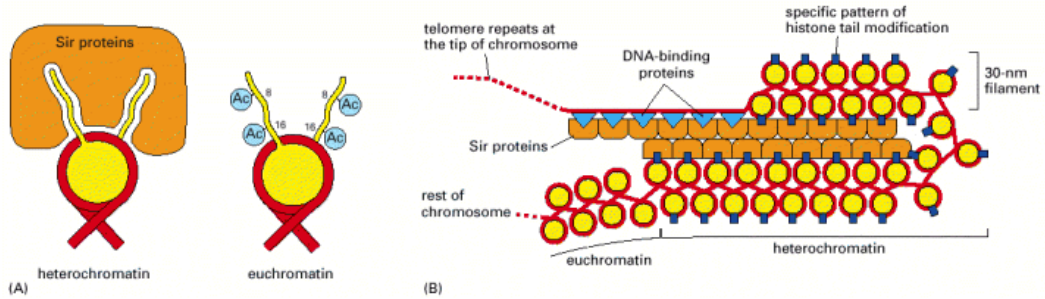

Figure 4-47. Speculative model for the heterochromatin at the ends of yeast chromosomes. (A) Heterochromatin is generally underacetylated, and underacetylated tails of histone H4 are proposed to interact with a complex of Sir proteins, thus stabilizing the association of these proteins with nucleosomes. Although shown as fully unacetylated, the exact pattern of histone H4 tail modification required to bind to the Sir complex is not known with certainty. In some organisms, the methylation of lysine 9 of histone H3 is also a critical signal for heterochromatin formation. In euchromatin, histone tails are typically highly acetylated. Those of H4 are shown as partially acetylated but, in reality, the acetylation state varies across euchromatin. (B) Specialized DNA-binding proteins *(blue triangles)* recognize DNA sequences near the ends of chromosomes and attract the Sir proteins, one of which (Sir2) is an NAD^+-dependent histone deacetylase. This then leads to the cooperative spreading of the Sir protein complex down the chromosome. As this complex spreads, the deacetylation catalyzed by Sir2 helps create new binding sites on nucleosomes for more Sir protein complexes. A "fold back" structure of the type shown may also form.

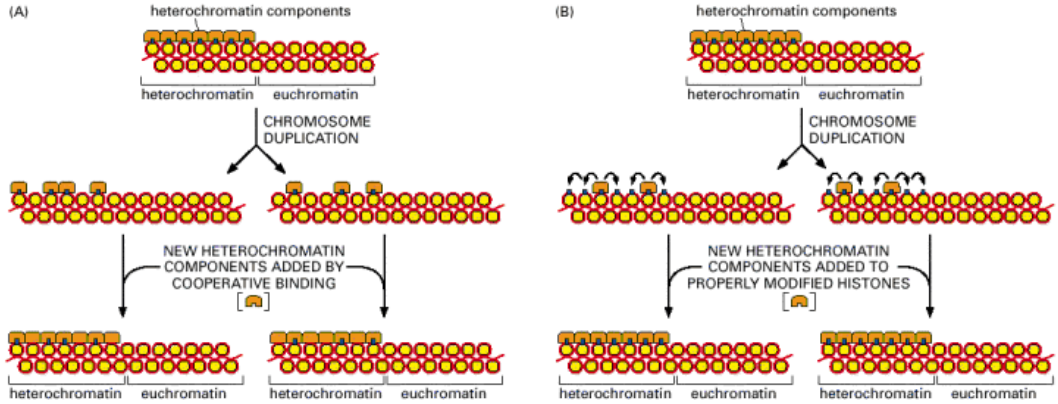

Figure 4-48. Two speculative models for how the tight packaging of DNA in heterochromatin can be inherited during chromosome replication. In both cases, half of the specialized heterochromatin components have been distributed to each daughter chromosome after DNA duplication. (A) In this model, new heterochromatin components bind cooperatively to the inherited components, thereby beginning the process of new heterochromatin formation. The process is completed with the assembly of additional proteins and the eventual covalent modification of the histones (not shown). (B) In this model, the inherited heterochromatin components change the pattern of histone modification on the newly formed daughter nucleosomes nearby, creating new binding sites for free heterochromatin components, which assemble and complete the structure. Both models can account for the spreading effects of heterochromatin, and indeed, both processes may occur simultaneously in cells.

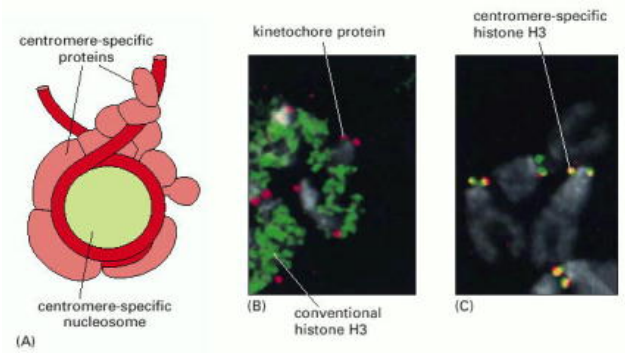

Figure 4-49. The specialized nucleosome formed on centromeres. (A) A model for the proteins that assemble on a yeast centromere. The specialized nucleosome contains an H3 variant (called CENP-A in most organisms), along with core histones H2A, H2B, and H4. The folding of DNA into this nucleosome facilitates the assembly of the other centromere-binding proteins, which form the kinetochore that attaches the centromere to the mitotic spindle (B) The localization of conventional histone H3 on *Drosophila* mitotic chromosomes. The conventional H3 has been fused to a fluorescent protein and appears *green.* A component of the kinetochore has been stained *red* with antibodies against a specific kinetochore protein. (C) The same experiment, but with the centromere-specific histone H3 (instead of the conventional H3) labeled *green.* When the *red* and *green* stains are coincident, the staining appears *yellow.* (A, adapted from P.B. Meluh et al., *Cell* 94:607613, 1998; B and C, from S. Henikoff et al., *Proc. Natl. Acad. Sci. USA* 97:716721, 2000. © National Academy of Sciences.)

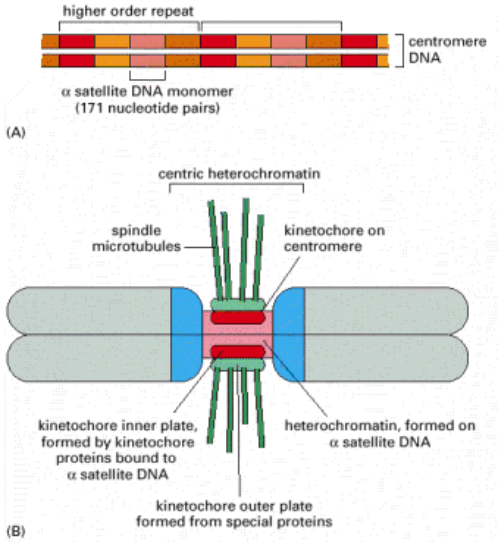

Figure 4-50. The structure of a human centromere. (A) The organization of the alpha satellite DNA sequences, which are repeated many thousands of times at a centromere. (B) An entire chromosome. The alpha satellite DNA sequences *(red)* are AT-rich and consist of a large number of repeats that vary slightly from one another in their DNA sequence. *Blue* represents the position of flanking centric heterochromatin, which contains DNA sequences composed of different types of repeats. As indicated, the kinetochore consists of an inner and an outer plate, formed by a set of kinetochore proteins. The spindle microtubules attach to the kinetochore in M phase of the cell cycle (see Figure 4-22). (B, adapted from T.D. Murphy and G. H. Karpen, *Cell* 93:317320, 1998.)

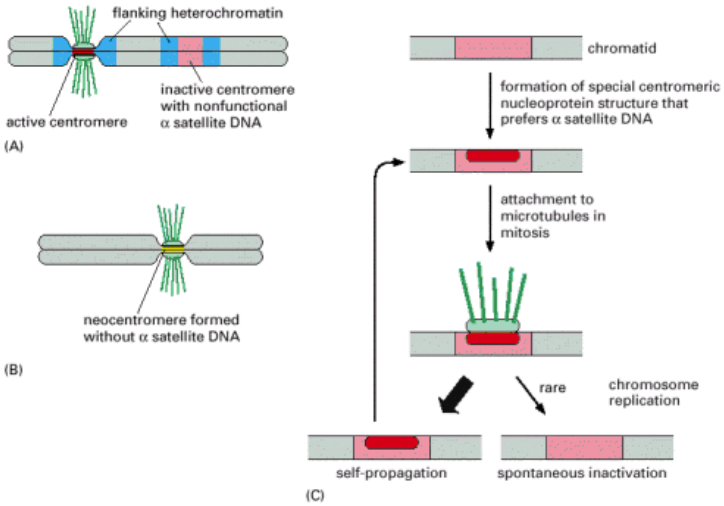

Figure 4-51. The plasticity of human centromere formation. (A) Owing to an ancient chromosome breakage and rejoining event, some human chromosomes contain two blocks of alpha satellite DNA *(red)*, each of which presumably functioned as a centromere in its original chromosome. Usually, these dicentric chromosomes are not stably propagated because they are attached improperly to the spindle and are broken apart during mitosis. In those chromosomes that survive, one of the centromeres has spontaneously inactivated, even though it contains all the necessary DNA sequences. This allows the chromosome to be stably propagated. (B) In a small fraction (1/2000) of human births, extra chromosomes are observed in cells of the offspring. Some of these extra chromosomes, which have formed from a breakage event, lack alpha satellite DNA altogether, yet new centromeres have arisen from what was originally euchromatic DNA. (C) A model to explain the plasticity and inheritance of centromeres.

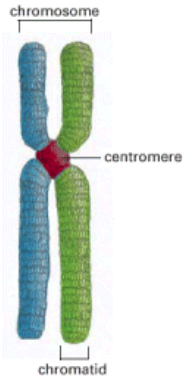

Figure 4-52. A typical mitotic chromosome at metaphase. Each sister chromatid contains one of two identical daughter DNA molecules generated earlier in the cell cycle by DNA replication.

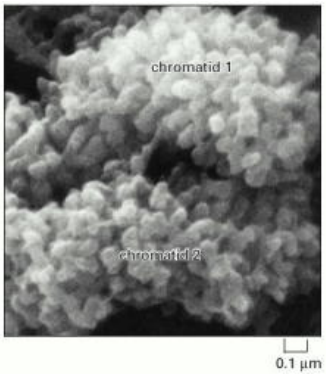

Figure 4-53. A scanning electron micrograph of a region near one end of a typical mitotic chromosome. Each knoblike projection is believed to represent the tip of a separate looped domain. Note that the two identical paired chromatids drawn in Figure 4-52 can be clearly distinguished. (From M.P. Marsden and U.K. Laemmli, *Cell* 17:849858, 1979. © Elsevier.)

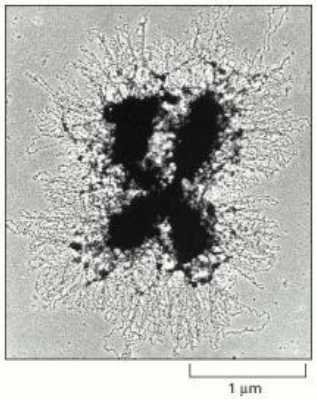

Figure 4-54. An electron micrograph of a mitotic chromosome. This chromosome (from an insect) was treated to reveal loops of chromatin fibers that emanate from a central scaffold of the chromatid. Such micrographs support the idea that the chromatin in all chromosomes is folded into a series of looped domains (see Figure 4-55). (Courtesy of Uli Laemmli.)

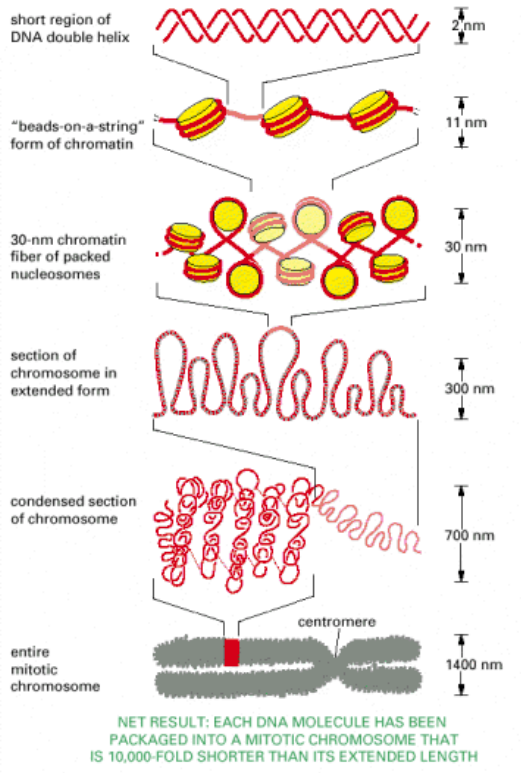

Figure 4-55. Chromatin packing. This model shows some of the many levels of chromatin packing postulated to give rise to the highly condensed mitotic chromosome.

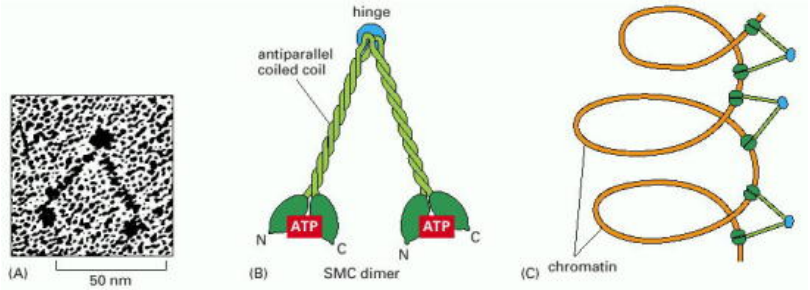

Figure 4-56. The SMC proteins in condensins. (A) Electron micrographs of a purified SMC dimer. (B) The structure of an SMC dimer. The long central region of this protein is an antiparallel coiled coil (see Figure 3-11) with a flexible hinge in its middle, as demonstrated by the electron micrograph in (A). (C) A model for the way in which the SMC proteins in condensins might compact chromatin. In reality, SMC proteins are components of a much larger condensin complex. It has been proposed that, in the cell, condensins coil long strings of looped chromatin domains (see Figure 4-55). In this way the condensins would form a structural framework that maintains the DNA in a highly organized state during M phase of the cell cycle. (A, courtesy of H.P. Erickson; B and C, adapted from T. Hirano, *Genes Dev.* 13:1119, 1999.)

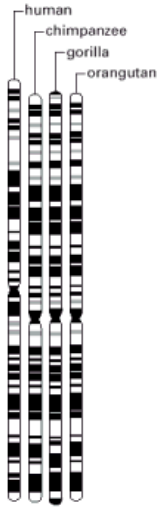

Figure 4-57. Comparison of the Giemsa pattern of the largest human chromosome (chromosome 1) with that of chimpanzee, gorilla, and orangutan. Comparisons among the staining patterns of all the chromosomes indicate that human chromosomes are more closely related to those of chimpanzee than to those of gorilla and that they are more distantly related to those of orangutan. (Adapted from M.W. Strickberger, Evolution, 3rd edn. Sudbury, MA: Jones & Bartlett Publishers, 2000.)

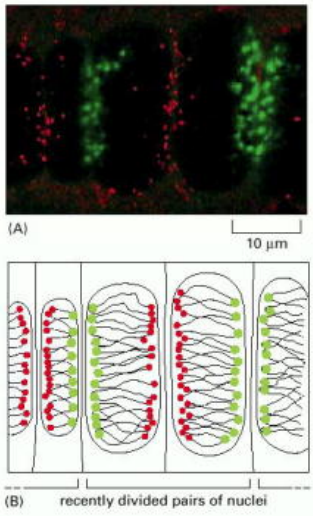

Figure 4-58. The polarized orientation of chromosomes found in certain interphase nuclei. (A) Fluorescent light micrograph of interphase nuclei from the rapidly growing root tip of a plant. Centromeres are stained *green* and teleomeres *red* by *in situ* hybridization of centromere- and telomere-specific DNA sequences coupled to the different fluorescent dyes. (B) Interpretation of (A) showing chromosomes in the Rab1 orientation with all the centromeres facing one side of a nucleus and all the telomeres pointing toward the opposite side. (A, from R. Abranches et al., *J. Cell Biol.* 143:512, 1998. © The Rockefeller University Press.)

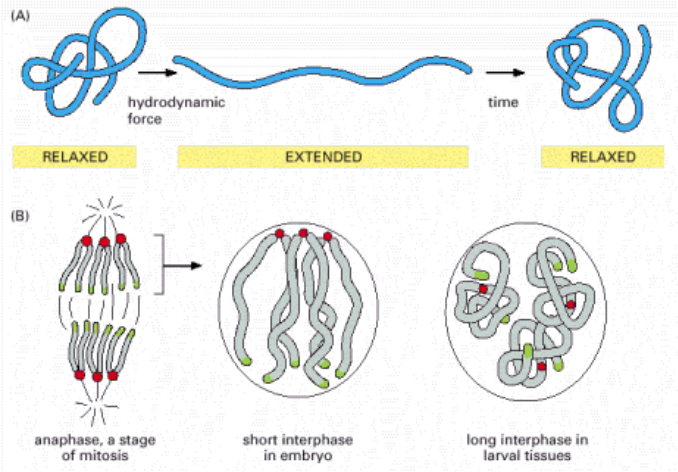

Figure 4-59. A polymer analogy for interphase chromosome organization. (A) The behavior of a polymer in solution. Entropy drives a long polymer into a compact conformation in the absence of an externally applied force. If the polymer is subjected to shear or hydrodynamic force, it becomes extended. But once the force is removed, the polymer chain returns to a more favorable, compact conformation. (B) The behavior of interphase chromosomes may reflect the same simple principles. In *Drosophila* embryos, for example, mitotic divisions occur at intervals of about 10 minutes; during the short intervening interphases, the chromosomes have little time to relax from the Rabl orientation induced by their movement during mitosis. However, in later stages of development, when interphase is much longer, the chromosomes have time to fold up. This folding may be strongly affected by specific associations between different regions of the same chromosome. (Adapted from A.F. Dernburg et al., *Cell* 85:745759, 1996.)

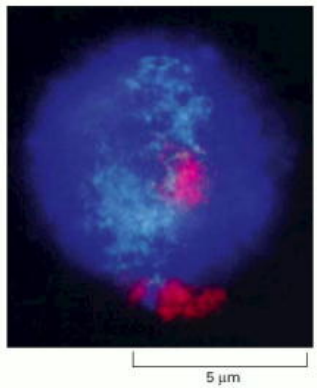

Figure 4-60. Selective "painting" of two interphase chromosomes in a human peripheral lymphocyte. The fluorescent light micrograph shows that the two copies of human chromosome 18 *(red)* and chromosome 19 *(turquoise)* occupy discrete territories of the nucleus. (From J.A. Croft et al., *J. Cell Biol.* 145:11191131, 1999. © The Rockefeller University Press.)

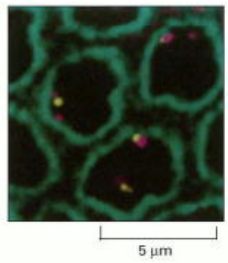

Figure 4-61. Specific regions of interphase chromosomes in close proximity to the nuclear envelope. This high-resolution microscopic view of nuclei from a *Drosophila* embryo shows the localization of two different regions of chromosome 2 *(yellow* and *magenta)* close to the nuclear envelope (stained green with antilamina antibodies). Other regions of the same chromosome are more distant from the envelope. (From W.F. Marshall et al., *Mol. Biol. Cell* 7:825842, 1996.)

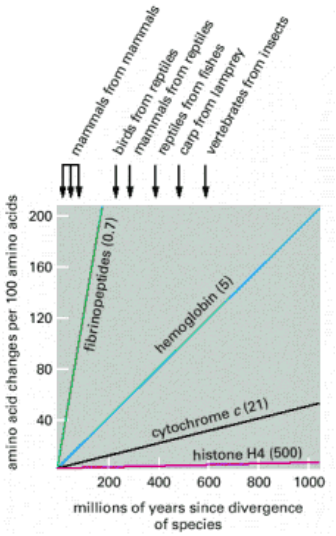

Figure 5-1. Different proteins evolve at very different rates. A comparison of the rates of amino acid change found in hemoglobin, histone H4, cytochrome *c*, and the fibrinopeptides. The first three proteins have changed much more slowly during evolution than the fibrinopeptides, the number in parentheses indicating how many million years it has taken, on average, for one *acceptable* amino acid change to appear for every 100 amino acids that the protein contains. In determining rates of change per year, it is important to realize that two species that diverged from a common ancestor 100 million years ago are separated from each other by 200 million years of evolutionary time.

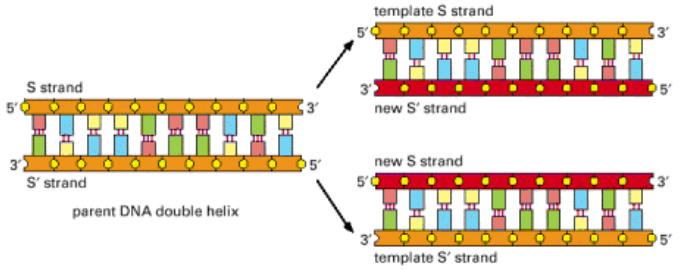

Figure 5-2. The DNA double helix acts as a template for its own duplication. Because the nucleotide A will successfully pair only with T, and G only with C, each strand of DNA can serve as a template to specify the sequence of nucleotides in its complementary strand by DNA base-pairing. In this way, a double-helical DNA molecule can be copied precisely.

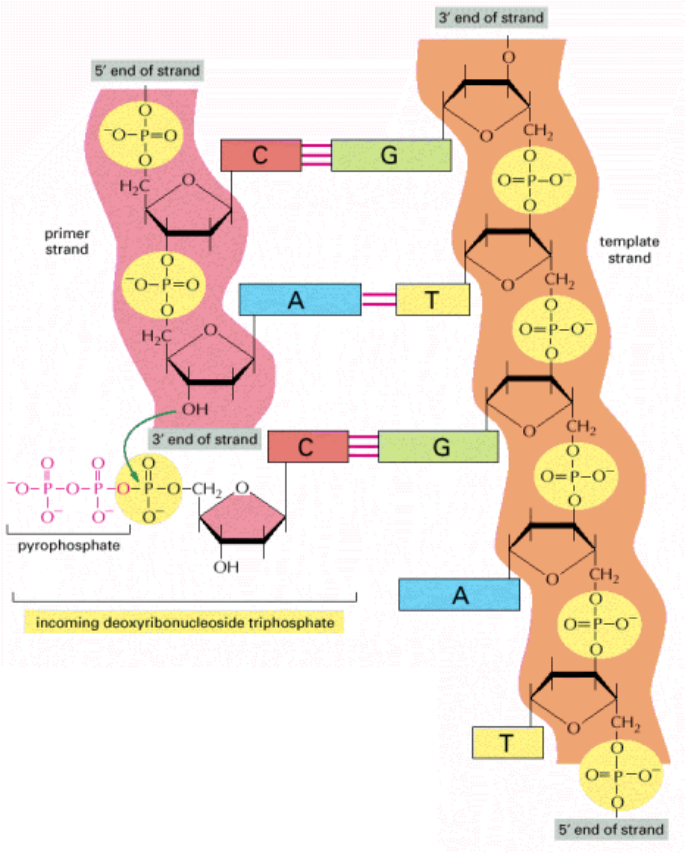

Figure 5-3. The chemistry of DNA synthesis. The addition of a deoxyribonucleotide to the 3 end of a polynucleotide chain (the *primer strand)* is the fundamental reaction by which DNA is synthesized. As shown, base-pairing between an incoming deoxyribonucleoside triphosphate and an existing strand of DNA (the *template strand)* guides the formation of the new strand of DNA and causes it to have a complementary nucleotide sequence.

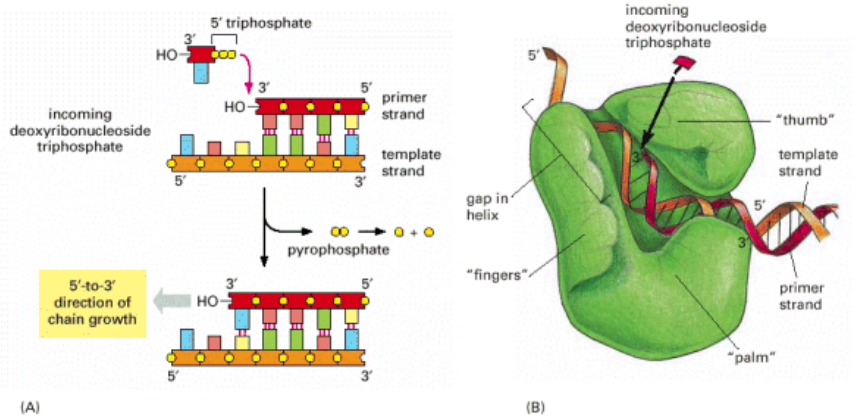

Figure 5-4. DNA synthesis catalyzed by DNA polymerase. (A) As indicated, DNA polymerase catalyzes the stepwise addition of a deoxyribonucleotide to the 3-OH end of a polynucleotide chain, the *primer strand*, that is paired to a second *template strand*. The newly synthesized DNA strand therefore polymerizes in the 5-to-3 direction as shown in the previous figure. Because each incoming deoxyribonucleoside triphosphate must pair with the template strand to be recognized by the DNA polymerase, this strand determines which of the four possible deoxyribonucleotides (A, C, G, or T) will be added. The reaction is driven by a large, favorable free-energy change, caused by the release of pyrophosphate and its subsequent hydrolysis to two molecules of inorganic phosphate. (B) The structure of an *E. coli* DNA polymerase molecule, as determined by x-ray crystallography. Roughly speaking, it resembles a right hand in which the palm, fingers, and thumb grasp the DNA. This drawing illustrates a DNA polymerase that functions during DNA repair, but the enzymes that replicate DNA have similar features. (B, adapted from L.S. Beese, V. Derbyshire, and T.A. Steitz, *Science* 260:352355, 1993.)

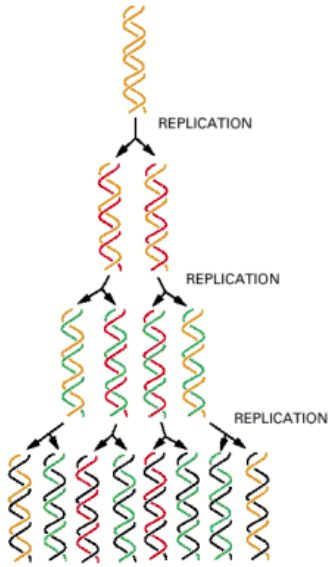

Figure 5-5. The semiconservative nature of DNA replication. In a round of replication, each of the two strands of DNA is used as a template for the formation of a complementary DNA strand. The original strands therefore remain intact through many cell generations.

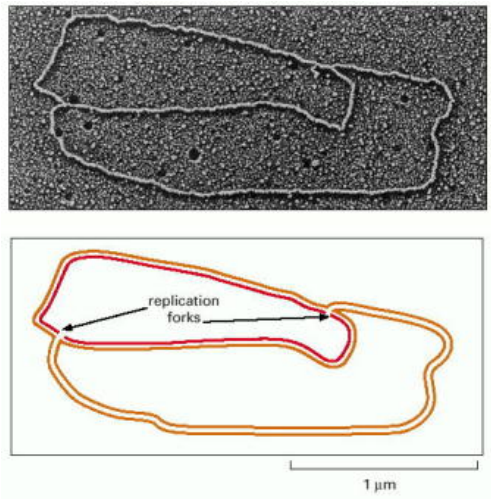

Figure 5-6. Two replication forks moving in opposite directions on a circular chromosome. An active zone of DNA replication moves progressively along a replicating DNA molecule, creating a Y-shaped DNA structure known as a replication fork: the two arms of each Y are the two daughter DNA molecules, and the stem of the Y is the parental DNA helix. In this diagram, parental strands are *orange;* newly synthesized strands are *red*. (Micrograph courtesy of Jerome Vinograd.)

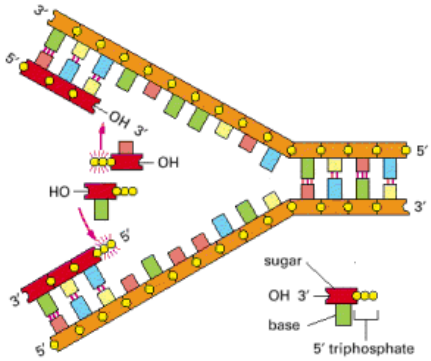

Figure 5-7. An incorrect model for DNA replication. Although it might seem to be the simplest possible model for DNA replication, the mechanism illustrated here is not the one that cells use. In this scheme, both daughter DNA strands would grow continuously, using the energy of hydrolysis of the two terminal phosphates *(yellow circles* highlighted by *red rays)* to add the next nucleotide on each strand. This would require chain growth in both the 5-to-3 direction *(top)* and the 3-to-5 direction *(bottom).* No enzyme that catalyzes 3-to-5 nucleotide polymerization has ever been found.

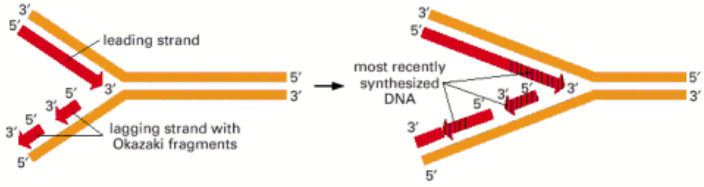

Figure 5-8. The structure of a DNA replication fork. Because both daughter DNA strands are polymerized in the 5-to-3 direction, the DNA synthesized on the lagging strand must be made initially as a series of short DNA molecules, called *Okazaki fragments.*

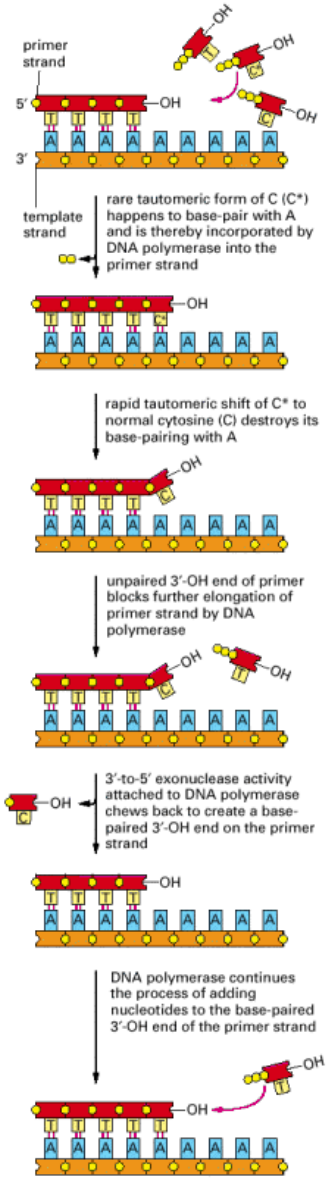

Figure 5-9. Exonucleolytic proofreading by DNA polymerase during DNA replication. In this example, the mismatch is due to the incorporation of a rare, transient tautomeric form of C, indicated by an asterisk. But the same proofreading mechanism applies to any misincorporation at the growing 3-OH end.

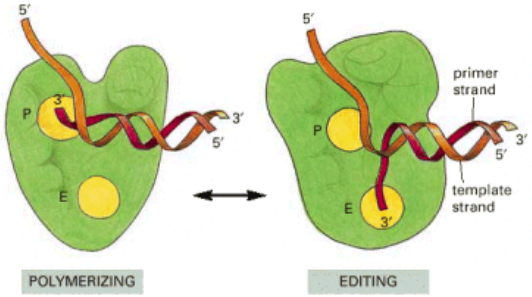

Figure 5-10. Editing by DNA polymerase. Outline of the structures of DNA polymerase complexed with the DNA template in the polymerizing mode *(left)* and the editing mode *(right)*. The catalytic site for the exonucleolytic (E) and the polymerization (P) reactions are indicated. To determine these structures by x-ray crystallography, researchers "froze" the polymerases in these two states, by using either a mutant polymerase defective in the exonucleolytic domain *(right)*, or by withholding the Mg^{2+} required for polymerization *(left)*.

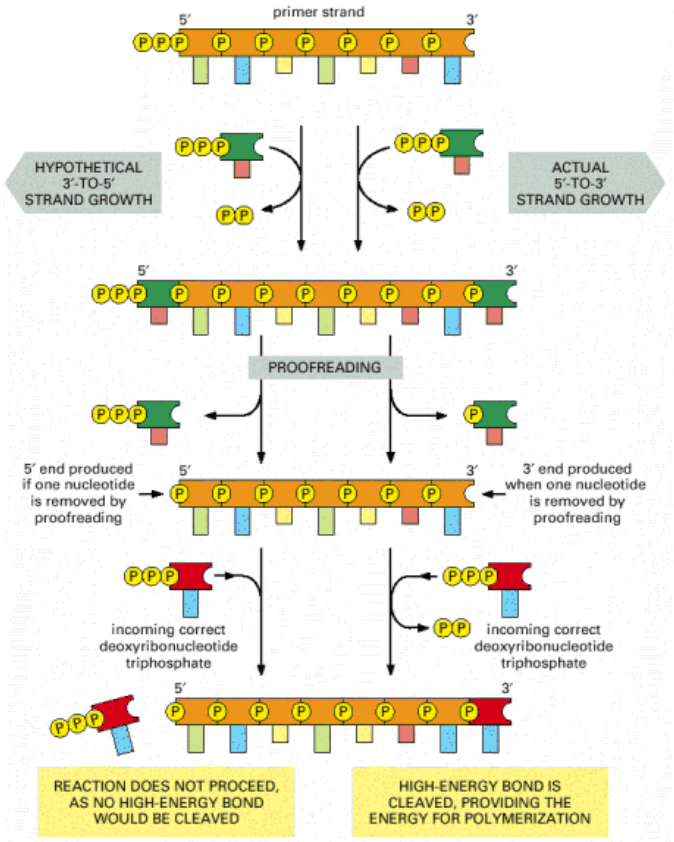

Figure 5-11. An explanation for the 5-to-3 direction of DNA chain growth. Growth in the 5-to-3 direction, shown on the right, allows the chain to continue to be elongated when a mistake in polymerization has been removed by exonucleolytic proofreading (see Figure 5-9). In contrast, exonucleolytic proofreading in the hypothetical 3-to-5 polymerization scheme, shown on the left, would block further chain elongation. For convenience, only the primer strand of the DNA double helix is shown.

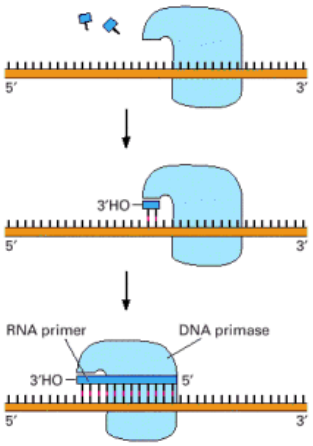

Figure 5-12. RNA primer synthesis. A schematic view of the reaction catalyzed by *DNA primase*, the enzyme that synthesizes the short RNA primers made on the lagging strand using DNA as a template. Unlike DNA polymerase, this enzyme can start a new polynucleotide chain by joining two nucleoside triphosphates together. The primase synthesizes a short polynucleotide in the 5-to-3 direction and then stops, making the 3 end of this primer available for the DNA polymerase.

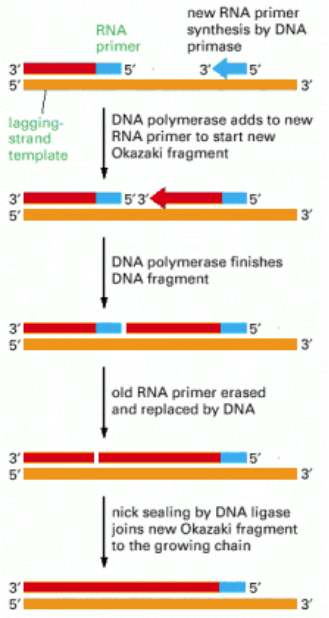

Figure 5-13. The synthesis of one of the many DNA fragments on the lagging strand. In eucaryotes, RNA primers are made at intervals spaced by about 200 nucleotides on the lagging strand, and each RNA primer is approximately 10 nucleotides long. This primer is erased by a special DNA repair enzyme (an RNAse H) that recognizes an RNA strand in an RNA/DNA helix and fragments it; this leaves gaps that are filled in by DNA polymerase and DNA ligase.

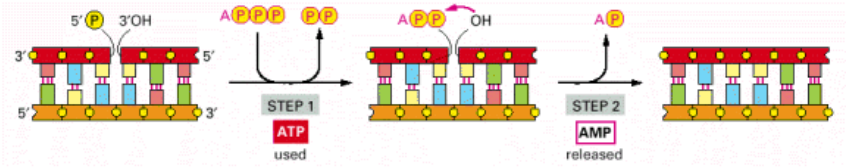

Figure 5-14. The reaction catalyzed by DNA ligase. This enzyme seals a broken phosphodiester bond. As shown, DNA ligase uses a molecule of ATP to activate the 5 end at the nick (step 1) before forming the new bond (step 2). In this way, the energetically unfavorable nick-sealing reaction is driven by being coupled to the energetically favorable process of ATP hydrolysis.

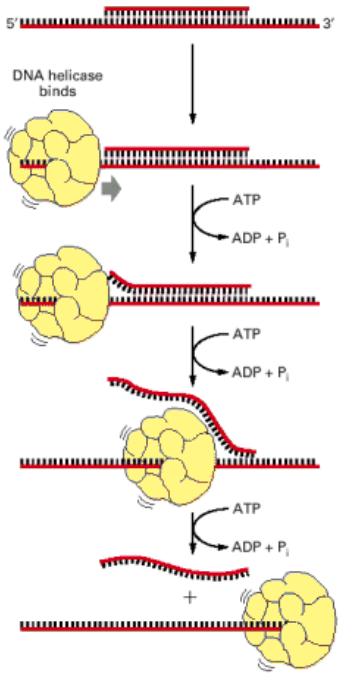

Figure 5-15. An assay used to test for DNA helicase enzymes. A short DNA fragment is annealed to a long DNA single strand to form a region of DNA double helix. The double helix is melted as the helicase runs along the DNA single strand, releasing the short DNA fragment in a reaction that requires the presence of both the helicase protein and ATP. The rapid step-wise movement of the helicase is powered by its ATP hydrolysis (see Figure 3-76).

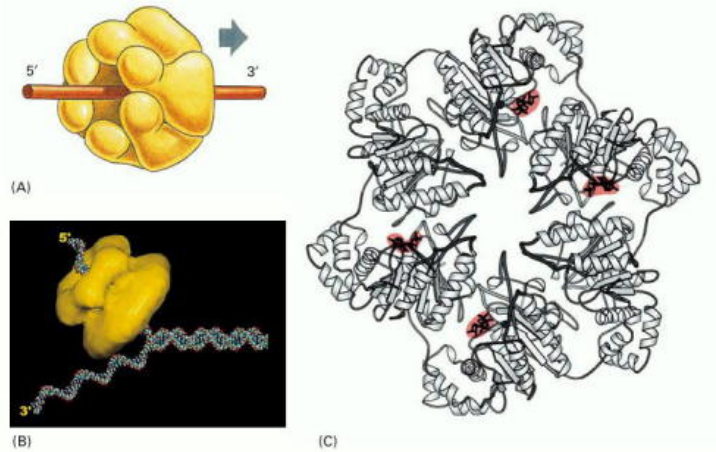

Figure 5-16. The structure of a DNA helicase. (A) A schematic diagram of the protein as a hexameric ring. (B) Schematic diagram showing a DNA replication fork and helicase to scale. (C) Detailed structure of the bacteriophage T7 replicative helicase, as determined by x-ray diffraction. Six identical subunits bind and hydrolyze ATP in an ordered fashion to propel this molecule along a DNA single strand that passes through the central hole. *Red* indicates bound ATP molecules in the structure. (B, courtesy of Edward H. Egelman; C, from M.R. Singleton et al., *Cell* 101:589600, 2000. © Elsevier.)

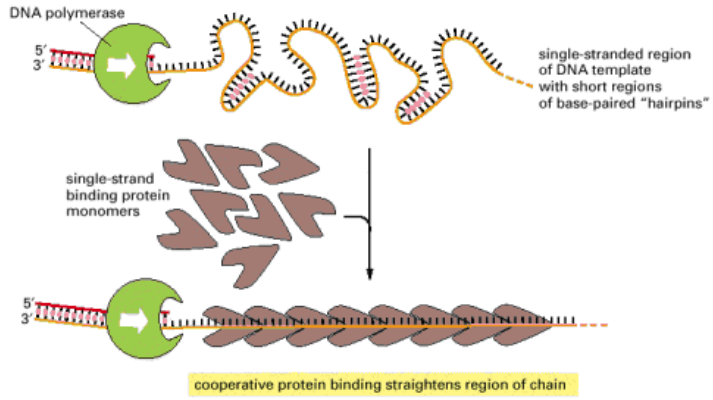

Figure 5-17. The effect of single-strand DNA-binding proteins (SSB proteins) on the structure of single-stranded DNA. Because each protein molecule prefers to bind next to a previously bound molecule, long rows of this protein form on a DNA single strand. This *cooperative binding* straightens out the DNA template and facilitates the DNA polymerization process. The "hairpin helices" shown in the bare, single-stranded DNA result from a chance matching of short regions of complementary nucleotide sequence; they are similar to the short helices that typically form in RNA molecules (see Figure 1-6).

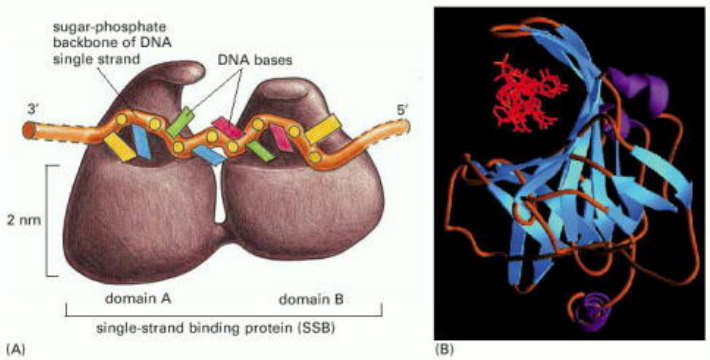

Figure 5-18. The structure of the single-strand binding protein from humans bound to DNA. (A) A front view of the two DNA binding domains of RPA protein, which cover a total of eight nucleotides. Note that the DNA bases remain exposed in this proteinDNA complex. (B) A diagram showing the three-dimensional structure, with the DNA strand *(red)* viewed end-on. (B, from A. Bochkarev et al., *Nature* 385:176181, 1997. © Macmillan Magazines Ltd.)

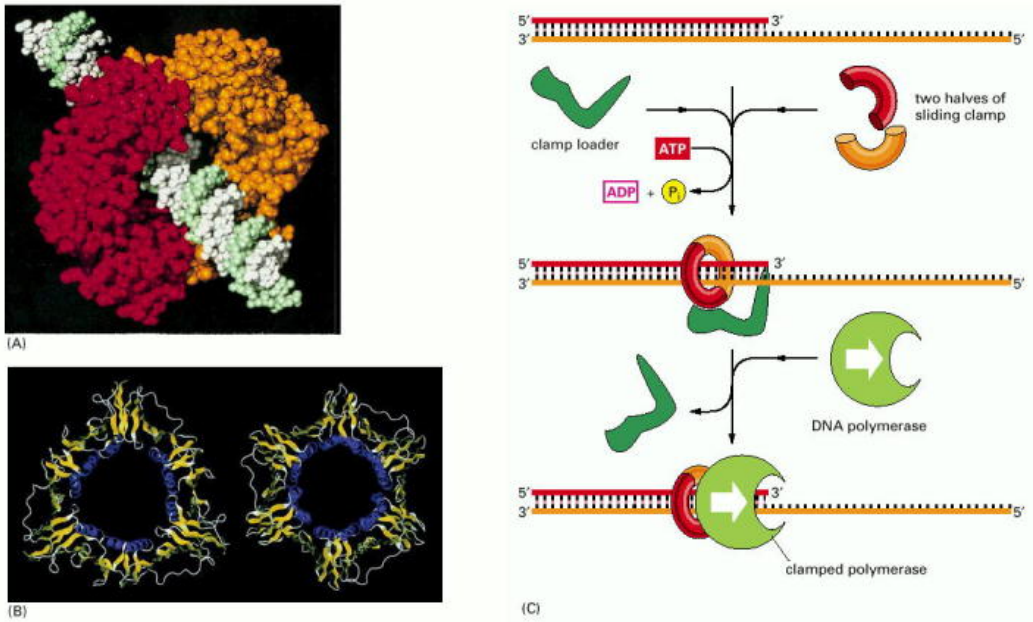

Figure 5-19. The regulated sliding clamp that holds DNA polymerase on the DNA. (A) The structure of the clamp protein from *E. coli*, as determined by x-ray crystallography, with a DNA helix added to indicate how the protein fits around DNA. (B) A similar protein is present in eucaryotes, as illustrated by this comparison of the *E. coli* sliding clamp *(left)* with the PCNA protein from humans *(right)*. (C) Schematic illustration showing how the clamp is assembled to hold a moving DNA polymerase molecule on the DNA. In the simplified reaction shown here, the clamp loader dissociates into solution once the clamp has been assembled. At a true replication fork, the clamp loader remains close to the lagging-strand polymerase, ready to assemble a new clamp at the start of each new Okazaki fragment (see Figure 5-22). (A and B, from X.-P. Kong et al., *Cell* 69:425437, 1992. © Elsevier.)

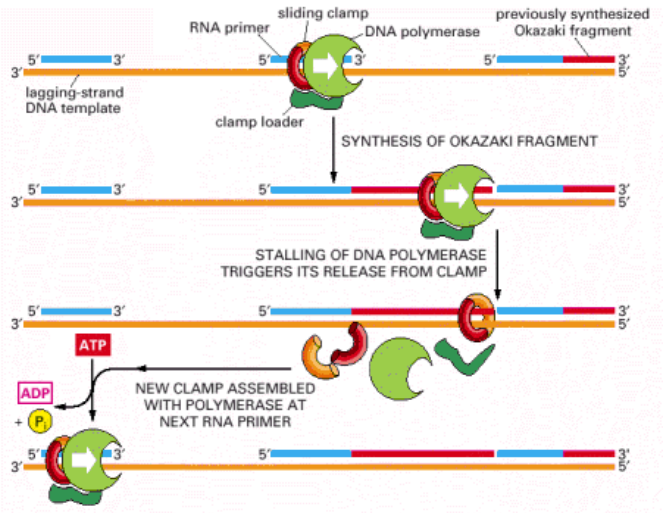

Figure 5-20. A cycle of loading and unloading of DNA polymerase and the clamp protein on the lagging strand. The association of the clamp loader with the lagging-strand polymerase shown here is for illustrative purposes only; in reality, the clamp loader is carried along with the replication fork in a complex that includes both the leading-strand and lagging-strand DNA polymerases (see Figure 5-22).

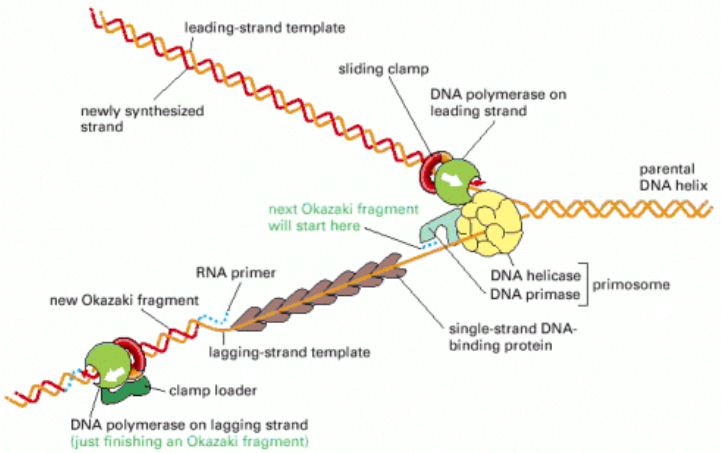

Figure 5-21. The proteins at a bacterial DNA replication fork. The major types of proteins that act at a DNA replication fork are illustrated, showing their approximate positions on the DNA.

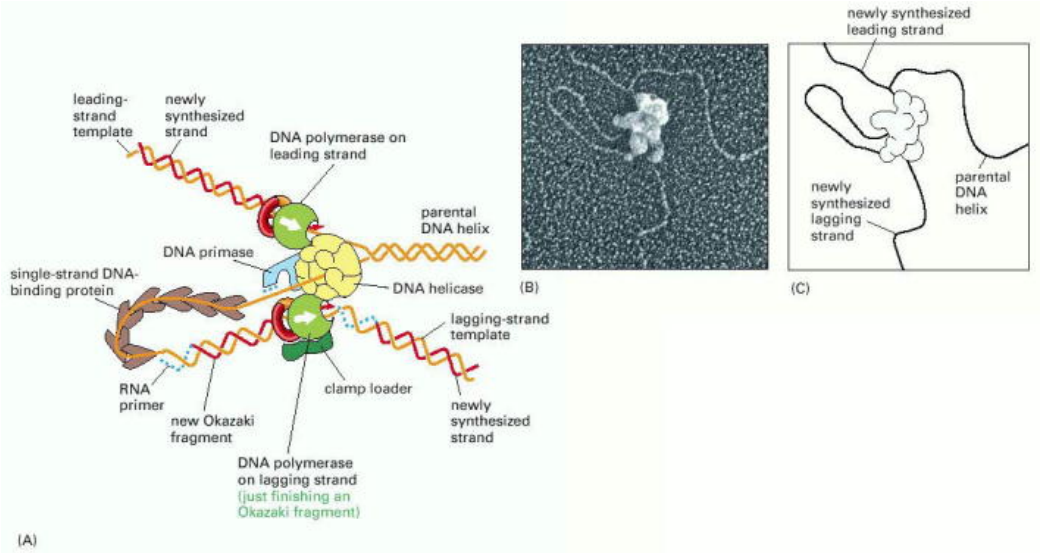

Figure 5-22. A moving replication fork. (A) This schematic diagram shows a current view of the arrangement of replication proteins at a replication fork when the fork is moving. The diagram in Figure 5-21 has been altered by folding the DNA on the lagging strand to bring the lagging-strand DNA polymerase molecule into a complex with the leading-strand DNA polymerase molecule. This folding process also brings the 3 end of each completed Okazaki fragment close to the start site for the next Okazaki fragment (compare with Figure 5-21). Because the lagging-strand DNA polymerase molecule remains bound to the rest of the replication proteins, it can be reused to synthesize successive Okazaki fragments. In this diagram, it is about to let go of its completed DNA fragment and move to the RNA primer that will be synthesized nearby, as required to start the next DNA fragment. Note that one daughter DNA helix extends toward the bottom right and the other toward the top left in this diagram. Additional proteins help to hold the different protein components of the fork together, enabling them to function as a well-coordinated protein machine. The actual protein complex is more compact than indicated, and the clamp loader is held in place by interactions not shown here. (B) An electron micrograph showing the replication machine from the bacteriophage T4 as it moves along a template synthesizing DNA behind it. (C) An interpretation of the micrograph is given in the sketch: note especially the DNA loop on the lagging strand. Apparently, the replication proteins became partly detached from the very front of the replication fork during the preparation of this sample for electron microscopy. (B, courtesy of Jack Griffith.)

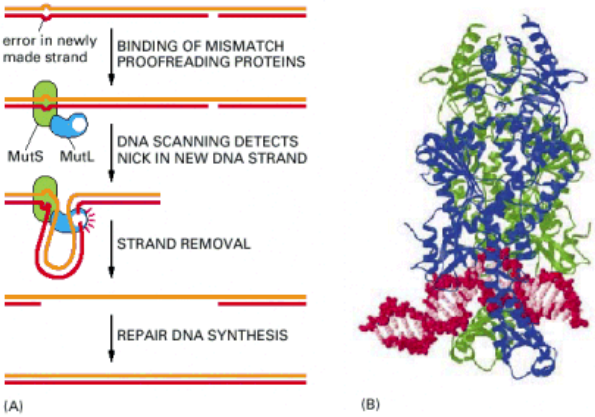

Figure 5-23. A model for strand-directed mismatch repair in eucaryotes. (A) The two proteins shown are present in both bacteria and eucaryotic cells: MutS binds specifically to a mismatched base pair, while MutL scans the nearby DNA for a nick. Once a nick is found, MutL triggers the degradation of the nicked strand all the way back through the mismatch. Because nicks are largely confined to newly replicated strands in eucaryotes, replication errors are selectively removed. In bacteria, the mechanism is the same, except that an additional protein in the complex (MutH) nicks unmethylated (and therefore newly replicated) GATC sequences, thereby beginning the process illustrated here. (B) The structure of the MutS protein bound to a DNA mismatch. This protein is a dimer, which grips the DNA double helix as shown, kinking the DNA at the mismatched base pair. It seems that the MutS protein scans the DNA for mismatches by testing for sites that can be readily kinked, which are those without a normal complementary base pair. (B, from G. Obmolova et al., *Nature* 407:703710, 2000. © Macmillan Magazines Ltd.)

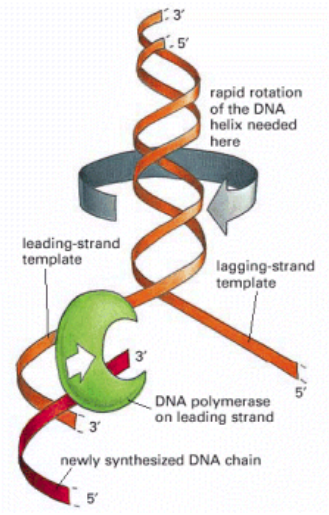

Figure 5-24. The "winding problem" that arises during DNA replication. For a bacterial replication fork moving at 500 nucleotides per second, the parental DNA helix ahead of the fork must rotate at 50 revolutions per second.

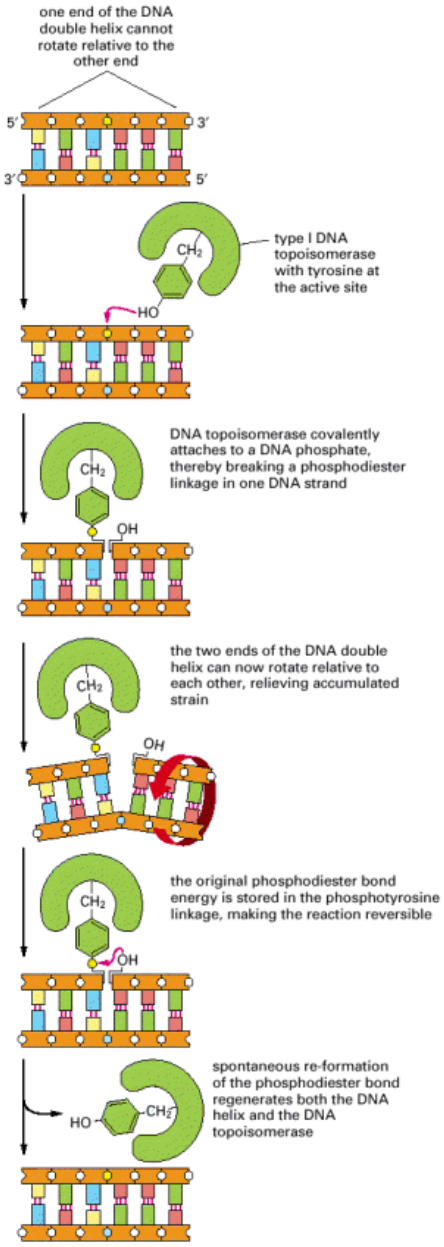

Figure 5-25. The reversible nicking reaction catalyzed by a eucaryotic DNA topoisomerase I enzyme. As indicated, these enzymes transiently form a single covalent bond with DNA; this allows free rotation of the DNA around the covalent backbone bonds linked to the *blue* phosphate.

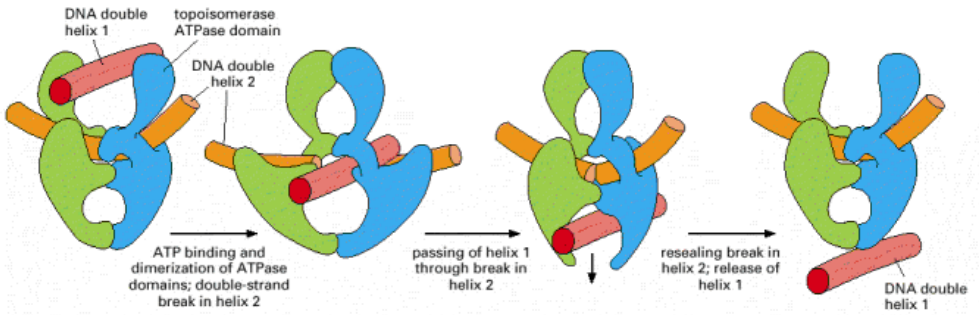

Figure 5-26. A model for topoisomerase II action. As indicated, ATP binding to the two ATPase domains causes them to dimerize and drives the reactions shown. Because a single cycle of this reaction can occur in the presence of a non-hydrolyzable ATP analog, ATP hydrolysis is thought to be needed only to reset the enzyme for each new reaction cycle. This model is based on structural and mechanistic studies of the enzyme. (Modified from J.M. Berger, *Curr. Opin. Struct. Biol.* 8:2632, 1998.)

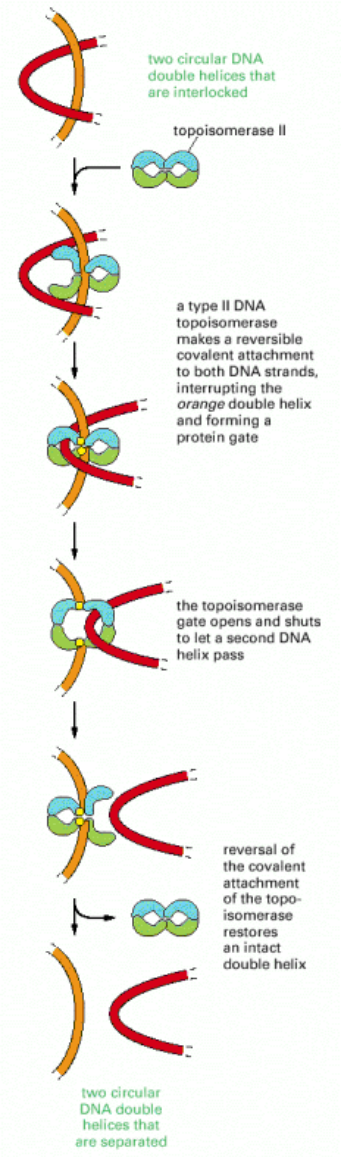

Figure 5-27. The DNA-helix-passing reaction catalyzed by DNA topoisomerase II. Identical reactions are used to untangle DNA inside the cell. Unlike type I topoisomerases, type II enzymes use ATP hydrolysis and some of the bacterial versions can introduce superhelical tension into DNA. Type II topoisomerases are largely confined to proliferating cells in eucaryotes; partly for that reason, they have been popular targets for anticancer drugs.

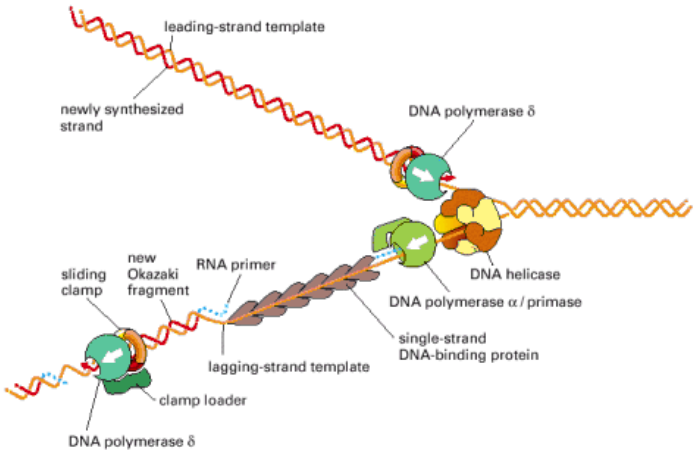

Figure 5-28. A mammalian replication fork. The fork is drawn to emphasize its similarity to the bacterial replication fork depicted in Figure 5-21. Although both forks use the same basic components, the mammalian fork differs in at least two important respects. First, it uses two different DNA polymerases on the lagging strand. Second, the mammalian DNA primase is a subunit of one of the lagging-strand DNA polymerases, DNA polymerase α, while that of bacteria is associated with a DNA helicase in the primosome. The polymerase α (with its associated primase) begins chains with RNA, extends them with DNA, and then hands the chains over to the second polymerase (δ), which elongates them. It is not known why eucaryotic DNA replication requires two different polymerases on the lagging strand. The major mammalian DNA helicase seems to be based on a ring formed from six different Mcm proteins; this ring may move along the leading strand, rather than along the lagging-strand template shown here.

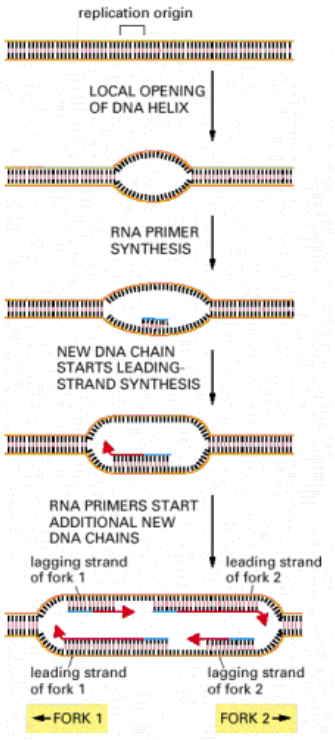

Figure 5-29. A replication bubble formed by replication fork initiation. This diagram outlines the major steps involved in the initiation of replication forks at replication origins. The structure formed at the last step, in which both strands of the parental DNA helix have been separated from each other and serve as templates for DNA synthesis, is called a *replication bubble*.

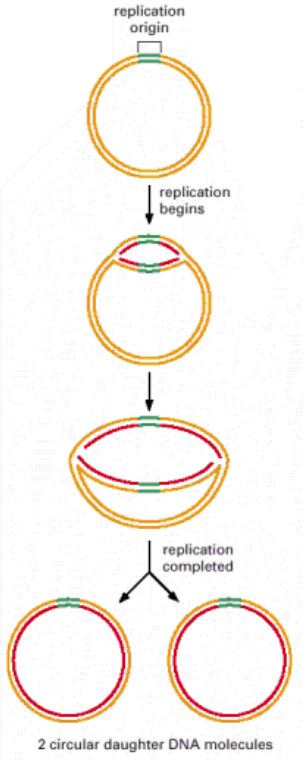

Figure 5-30. DNA replication of a bacterial genome. It takes *E. coli* about 40 minutes to duplicate its genome of 4.6×10^6 nucleotide pairs. For simplicity, no Okazaki fragments are shown on the lagging strand. What happens as the two replication forks approach each other and collide at the end of the replication cycle is not well understood, although the primosome is disassembled as part of the process.

Figure 5-31. The proteins that initiate DNA replication in bacteria. The mechanism shown was established by studies *in vitro* with a mixture of highly purified proteins. For *E. coli* DNA replication, the major initiator protein is the dnaA protein; the primosome is composed of the dnaB (DNA helicase) and dnaG (DNA primase) proteins. In solution, the helicase is bound by an inhibitor protein (the dnaC protein), which is activated by the initiator proteins to load the helicase onto DNA at the replication origin and then released. This inhibitor prevents the helicase from inappropriately entering other single-stranded stretches of DNA in the bacterial genome. Subsequent steps result in the initiation of three more DNA chains (see Figure 5-29) by a pathway whose details are incompletely specified.

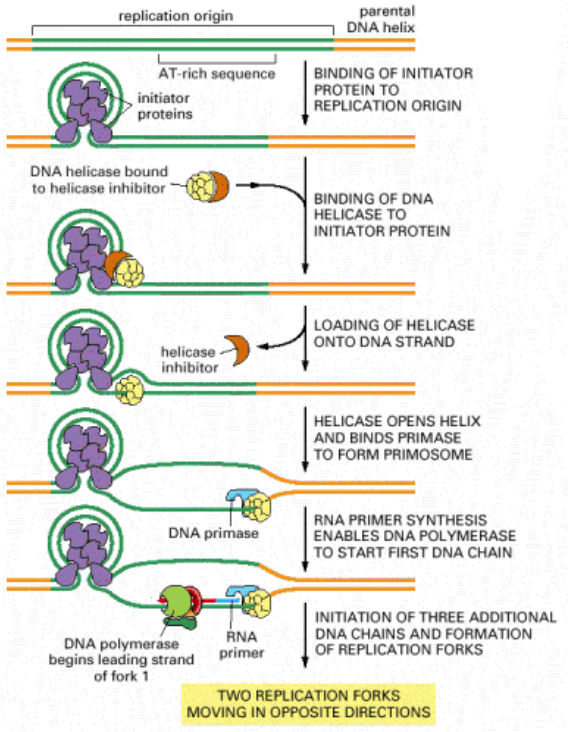

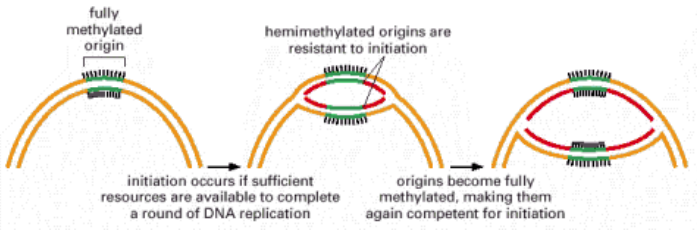

Figure 5-32. Methylation of the *E. coli* replication origin creates a refractory period for DNA initiation. DNA methylation occurs at GATC sequences, 11 of which are found in the origin of replication (spanning about 250 nucleotide pairs). About 10 minutes after replication is initiated, the hemimethylated origins become fully methylated by a DNA methylase enzyme. As discussed earlier, the lag in methylation after the replication of GATC sequences is also used by the *E. coli* mismatch proofreading system to distinguish the newly synthesized DNA strand from the parental DNA strand; in that case, the relevant GATC sequences are scattered throughout the chromosome. A single enzyme, the *dam* methylase, is responsible for methylating *E. coli* GATC sequences.

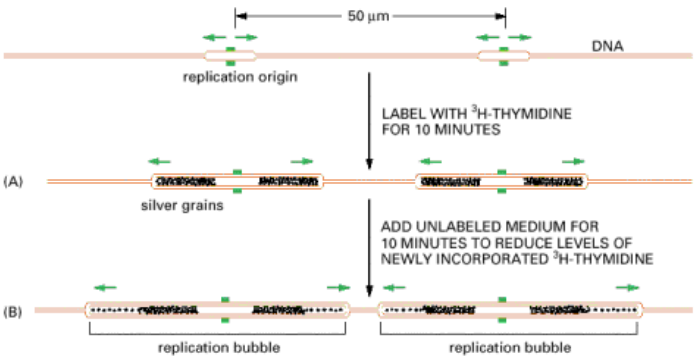

Figure 5-33. The experiments that demonstrated the pattern in which replication forks are formed and move on eucaryotic chromosomes. The new DNA made in human cells in culture was labeled briefly with a pulse of highly radioactive thymidine (^{3}H-thymidine). (A) In this experiment, the cells were lysed, and the DNA was stretched out on a glass slide that was subsequently covered with a photographic emulsion. After several months the emulsion was developed, revealing a line of silver grains over the radioactive DNA. The *brown* DNA in this figure is shown only to help with the interpretation of the autoradiograph; the unlabeled DNA is invisible in such experiments. (B) This experiment was the same except that a further incubation in unlabeled medium allowed additional DNA, with a lower level of radioactivity, to be replicated. The pairs of dark tracks in (B) were found to have silver grains tapering off in opposite directions, demonstrating bidirectional fork movement from a central replication origin where a replication bubble forms (see Figure 5-29). A replication fork is thought to stop only when it encounters a replication fork moving in the opposite direction or when it reaches the end of the chromosome; in this way, all the DNA is eventually replicated.

Figure 5-34. The four successive phases of a standard eucaryotic cell cycle. During the G_1, S, and G_2 phases, the cell grows continuously. During M phase growth stops, the nucleus divides, and the cell divides in two. DNA replication is confined to the part of interphase known as S phase. G_1 is the gap between M phase and S phase; G_2 is the gap between S phase and M phase.

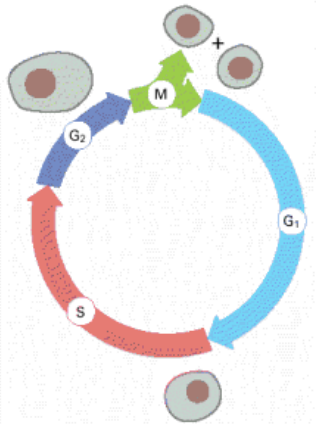

Figure 5-35. Different regions of a chromosome are replicated at different times in S phase. These light micrographs show stained mitotic chromosomes in which the replicating DNA has been differentially labeled during different defined intervals of the preceding S phase. In these experiments, cells were first grown in the presence of BrdU (a thymidine analog) and in the absence of thymidine to label the DNA uniformly. The cells were then briefly pulsed with thymidine in the absence of BrdU during early, middle, or late S phase. Because the DNA made during the thymidine pulse is a double helix with thymidine on one strand and BrdU on the other, it stains more darkly than the remaining DNA (which has BrdU on both strands) and shows up as a bright band *(arrows)* on these negatives. Broken lines connect corresponding positions on the three identical copies of the chromosome shown. (Courtesy of Elton Stubblefield.)

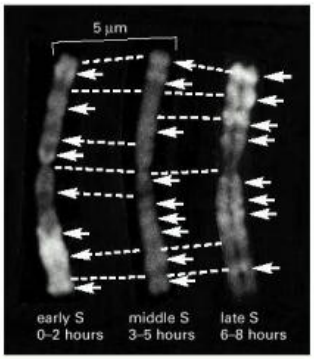

Figure 5-36. The strategy used to identify replication origins in yeast cells. Each of the yeast DNA sequences identified in this way was called an autonomously replicating sequence (ARS), since it enables a plasmid that contains it to replicate in the host cell without having to be incorporated into a host cell chromosome.

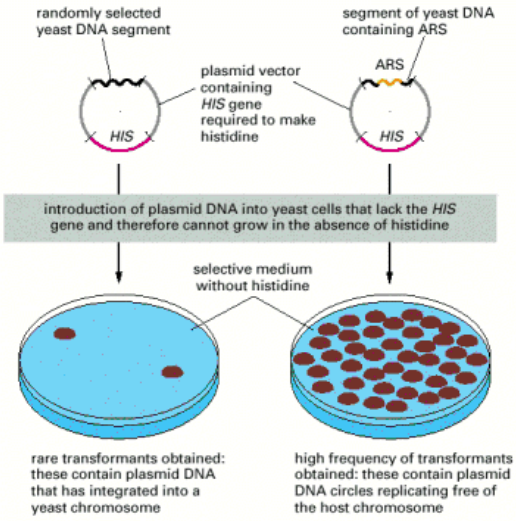

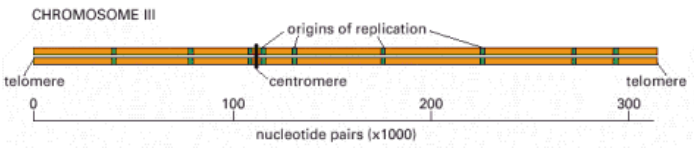

Figure 5-37. The origins of DNA replication on chromosome III of the yeast *S. cerevisiae*. This chromosome, one of the smallest eucaryotic chromosomes known, carries a total of 180 genes. As indicated, it contains nine replication origins.

Figure 5-38. An origin of replication in yeast. Comprising about 150 nucleotide pairs, this yeast origin (identified by the procedure shown in Figure 5-36) has a binding site for ORC, a complex of proteins that binds to every origin of replication. The origin depicted also has binding sites (B1, B2, and B3) for other required proteins, which can differ between various origins. Although best characterized in yeast, a similar ORC is used to initiate DNA replication in more complex eucaryotes, including humans.

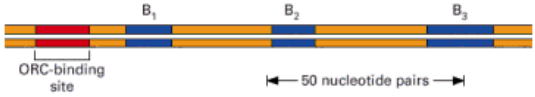

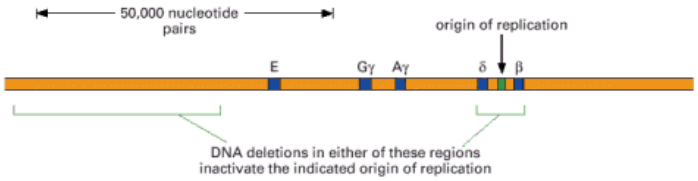

Figure 5-39. Deletions that inactivate an origin of replication in humans. These two deletions are found separately in two individuals who suffer from *thalassemia*, a disorder caused by the failure to express one or more of the genes in the β-globin gene cluster shown. In both of these deletion mutants, the DNA in this region is replicated by forks that begin at replication origins outside the β-globin gene cluster. As explained in the text, the deletion on the *left* removes DNA sequences that control the chromatin structure of the replication origin on the *right*.

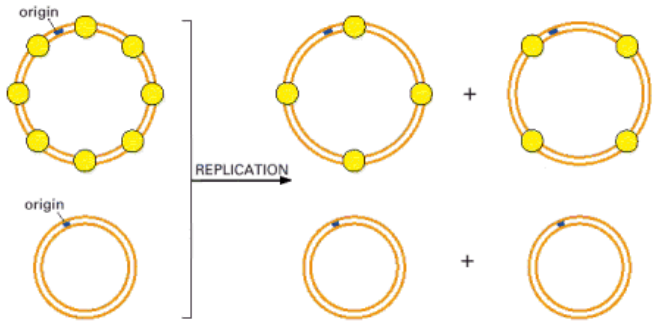

Figure 5-40. A demonstration that histones remain associated with DNA after the replication fork passes. In this experiment, performed *in vitro*, a mixture of two different-sized circular molecules of DNA (only one of which is assembled into nucleosomes) are replicated with purified proteins. After a round of DNA replication, only the daughter DNA molecules that derived from the nucleosomal parent have inherited nucleosomes. This experiment also demonstrates that both newly synthesized DNA helices inherit old histones.

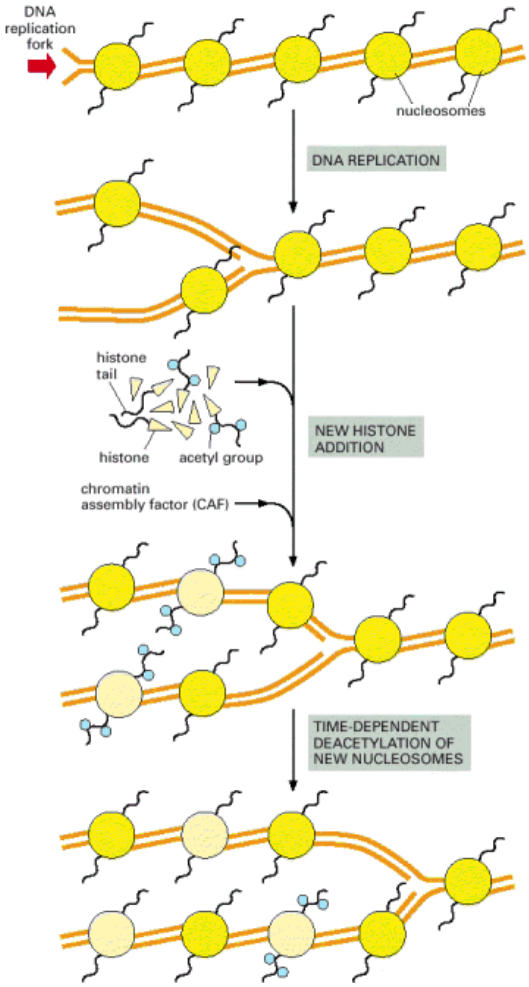

Figure 5-41. The addition of new histones to DNA behind a replication fork. The new nucleosomes are those colored *light yellow* in this diagram; as indicated, some of the histones that form them initially have specifically acetylated lysine side chains (see Figure 4-35), which are later removed.

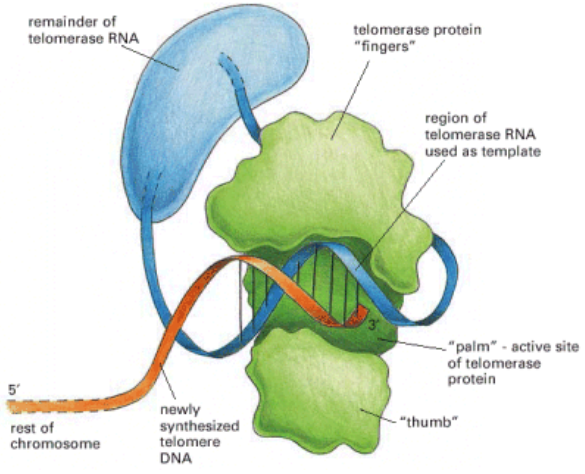

Figure 5-42. The structure of telomerase. The telomerase is a proteinRNA complex that carries an RNA template for synthesizing a repeating, G-rich telomere DNA sequence. Only the part of the telomerase protein homologous to reverse transcriptase is shown here *(green).* A reverse transcriptase is a special form of polymerase enzyme that uses an RNA template to make a DNA strand; telomerase is unique in carrying its own RNA template with it at all times. (Modified from J. Lingner and T.R. Cech, *Curr. Opin. Genet. Dev.* 8:226232, 1998.)

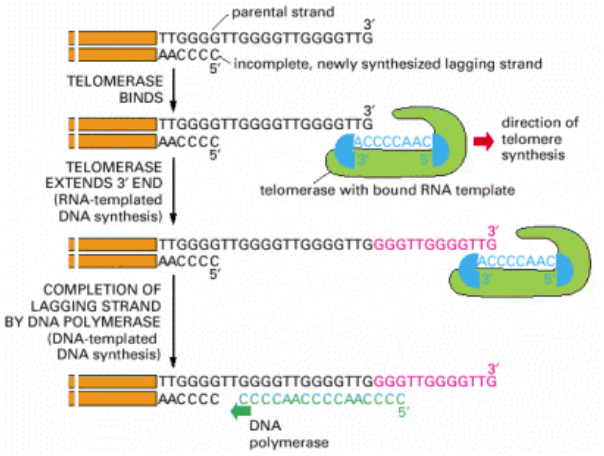

Figure 5-43. Telomere replication. Shown here are the reactions involved in synthesizing the repeating G-rich sequences that form the ends of the chromosomes (telomeres) of diverse eucaryotic organisms. The 3 end of the parental DNA strand is extended by RNA-templated DNA synthesis; this allows the incomplete daughter DNA strand that is paired with it to be extended in its 5 direction. This incomplete, lagging strand is presumed to be completed by DNA polymerase α, which carries a DNA primase as one of its subunits (see Figure 5-28). The telomere sequence illustrated is that of the ciliate *Tetrahymena*, in which these reactions were first discovered. The telomere repeats are GGGTTG in the ciliate *Tetrahymena*, GGGTTA in humans, and $G_{13}A$ in the yeast *S. cerevisiae*.

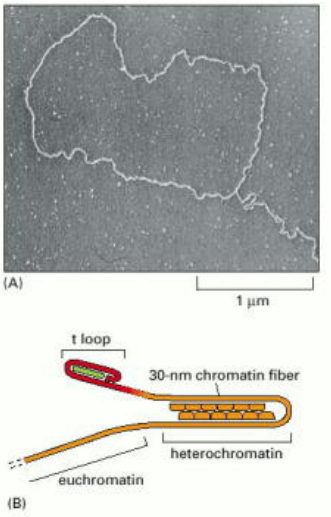

Figure 5-44. The t-loops at the end of mammalian chromosomes. (A) Electron micrograph of the DNA at the end of an interphase human chromosome. The chromosome was fixed, deproteinated, and artificially thickened before viewing. The loop seen here is approximately 15,000 nucleotide pairs in length. (B) Model for telomere structure. The insertion of the single-stranded end into the duplex repeats to form a t-loop is carried out and maintained by specialized proteins, schematized in *green*. In addition it is possible, as shown, that the chromosome end is looped once again on itself through the formation of heterochromatin adjacent to the t-loop (see Figure 4-47). (A, from J.D. Griffith et al., *Cell* 97:503514, 1999. © Elsevier.)

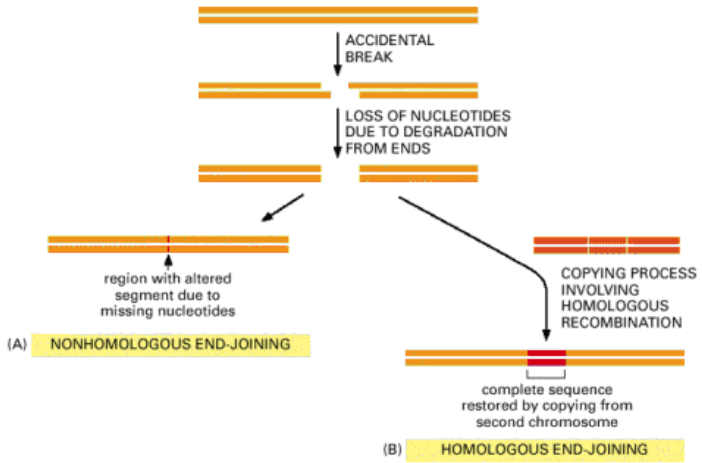

Figure 5-53. Two different types of end-joining for repairing double-strand breaks. (A) Nonhomologous end-joining alters the original DNA sequence when repairing broken chromosomes. These alterations can be either deletions (as shown) or short insertions. (B) Homologous end-joining is more difficult to accomplish, but is much more precise.

Figure 5-45. A demonstration that yeast cells control the length of their telomeres. In this experiment, the telomere at one end of a particular chromosome is artificially made either longer *(left)* or shorter *(right)* than average. After many cell divisions, the chromosome recovers, showing an average telomere length and a length distribution that is typical of the other chromosomes in the yeast cell. A similar feedback mechanism for controlling telomere length has been proposed to exist for the cells in the germ-line cells

of animals.

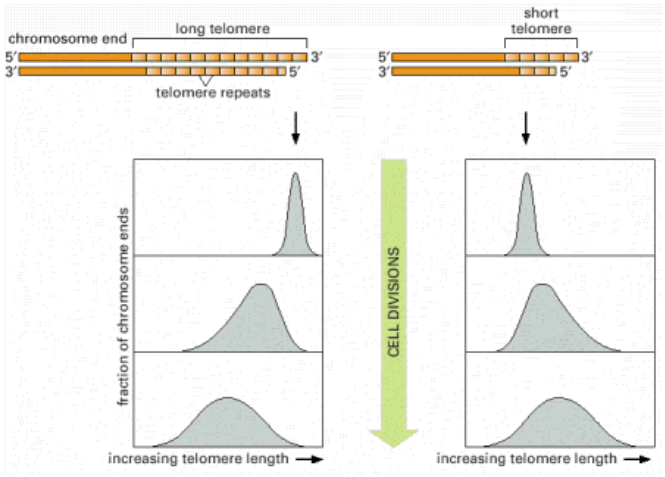

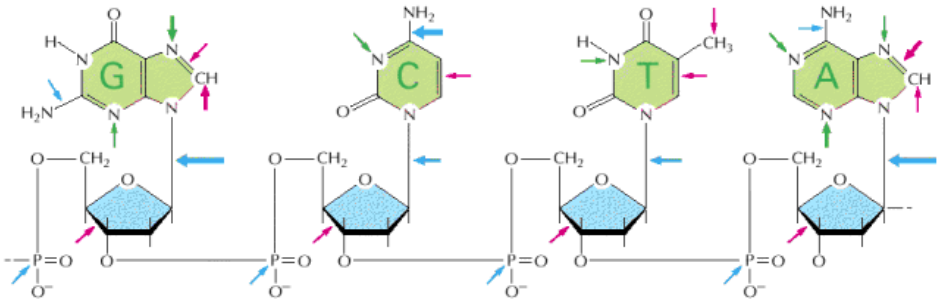

Figure 5-46. A summary of spontaneous alterations likely to require DNA repair. The sites on each nucleotide that are known to be modified by spontaneous oxidative damage *(red arrows)*, hydrolytic attack *(blue arrows)*, and uncontrolled methylation by the methyl group donor S-adenosylmethionine *(green arrows)* are shown, with the width of each arrow indicating the relative frequency of each event. (After T. Lindahl, *Nature* 362:709715, 1993. © Macmillan Magazines Ltd.)

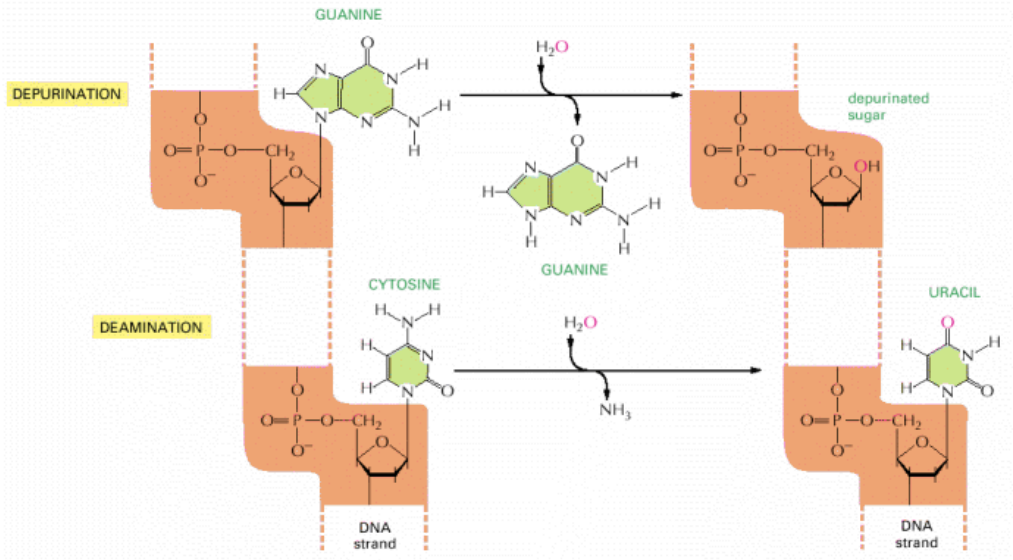

Figure 5-47. Depurination and deamination. These two reactions are the most frequent spontaneous chemical reactions known to create serious DNA damage in cells. Depurination can release guanine (shown here), as well as adenine, from DNA. The major type of deamination reaction (shown here) converts cytosine to an altered DNA base, uracil, but deamination occurs on other bases as well. These reactions take place on double-helical DNA; for convenience, only one strand is shown.

Figure 5-48. The thymine dimer. This type of damage is introduced into DNA in cells that are exposed to ultraviolet irradiation

(as in sunlight). A similar dimer will form between any two neighboring pyrimidine bases (C or T residues) in DNA.

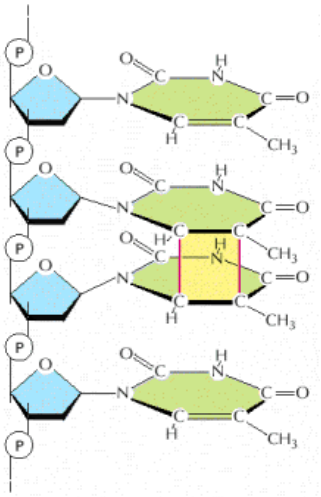

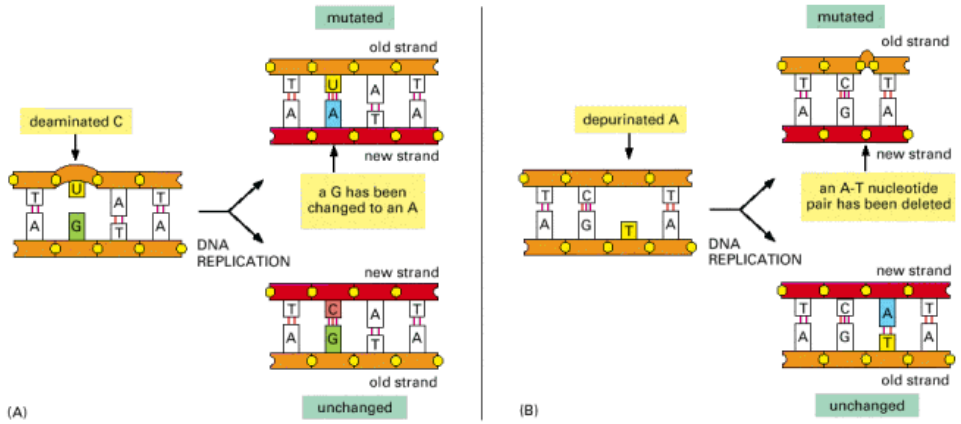

Figure 5-49. How chemical modifications of nucleotides produce mutations. (A) Deamination of cytosine, if uncorrected, results in the substitution of one base for another when the DNA is replicated. As shown in Figure 5-47, deamination of cytosine produces uracil. Uracil differs from cytosine in its base-pairing properties and preferentially base-pairs with adenine. The DNA replication machinery therefore adds an adenine when it encounters a uracil on the template strand. (B) Depurination, if uncorrected, can lead to either the substitution or the loss of a nucleotide pair. When the replication machinery encounters a missing purine on the template strand, it may skip to the next complete nucleotide as illustrated here, thus producing a nucleotide deletion in the newly synthesized strand. Many other types of DNA damage (see Figure 5-46) also produce mutations when the DNA is replicated if left uncorrected.

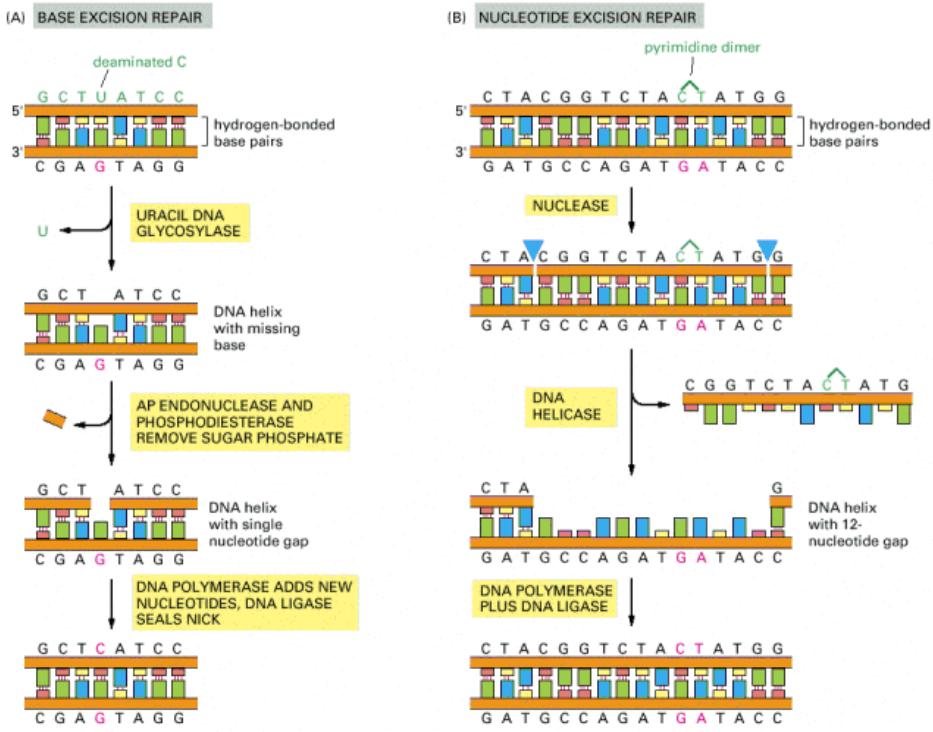

Figure 5-50. A comparison of two major DNA repair pathways. (A) *Base excision repair*. This pathway starts with a DNA glycosylase. Here the enzyme uracil DNA glycosylase removes an accidentally deaminated cytosine in DNA. After the action of this glycosylase (or another DNA glycosylase that recognizes a different kind of damage), the sugar phosphate with the missing base is cut out by the sequential action of AP endonuclease and a phosphodiesterase. (These same enzymes begin the repair of depurinated sites directly.) The gap of a single nucleotide is then filled by DNA polymerase and DNA ligase. The net result is that the U that was created by accidental deamination is restored to a C. The AP endonuclease derives its name from the fact that it recognizes any site in the DNA helix that contains a deoxyribose sugar with a missing base; such sites can arise either by the loss of a purine *(ap*urinic sites) or by the loss of a pyrimidine *(ap*yrimidinic sites). (B) *Nucleotide excision repair*. After a multienzyme complex has recognized a bulky lesion such as a pyrimidine dimer (see Figure 5-48), one cut is made on each side of the lesion, and an associated DNA helicase then removes the entire portion of the damaged strand. The multienzyme complex in bacteria leaves the gap of 12 nucleotides shown; the gap produced in human DNA is more than twice this size. The nucleotide excision repair machinery can recognize and repair many different types of DNA damage.

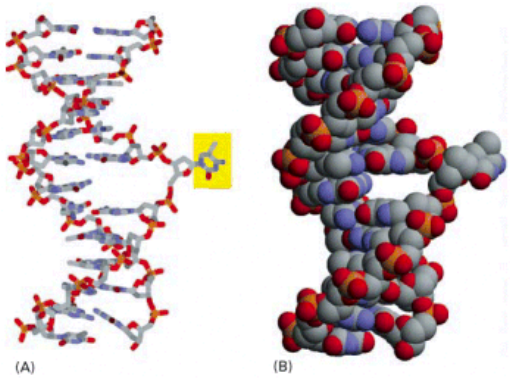

Figure 5-51. The recognition of an unusual nucleotide in DNA by base-flipping. The DNA glycosylase family of enzymes recognizes specific bases in the conformation shown. Each of these enzymes cleaves the glycosyl bond that connects a particular recognized base *(yellow)* to the backbone sugar, removing it from the DNA. (A) Stick model; (B) space-filling model.

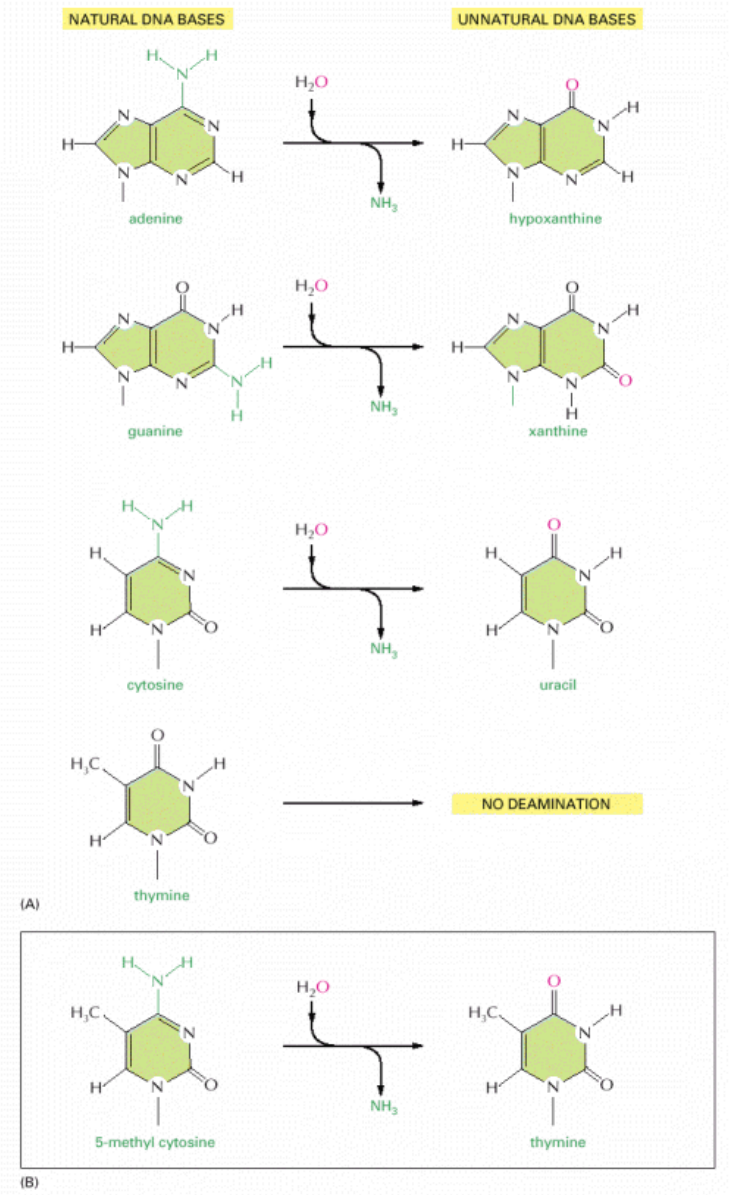

Figure 5-52. The deamination of DNA nucleotides. In each case the oxygen atom that is added in this reaction with water is colored *red*. (A) The spontaneous deamination products of A and G are recognizable as unnatural when they occur in DNA and thus are readily recognized and repaired. The deamination of C to U was previously illustrated in Figure 5-47; T has no amino group to deaminate. (B) About 3% of the C nucleotides in vertebrate DNAs are methylated to help in controlling gene expression (discussed in Chapter 7). When these 5-methyl C nucleotides are accidentally deaminated, they form the natural nucleotide T. This T would be paired with a G on the opposite strand, forming a mismatched base pair.

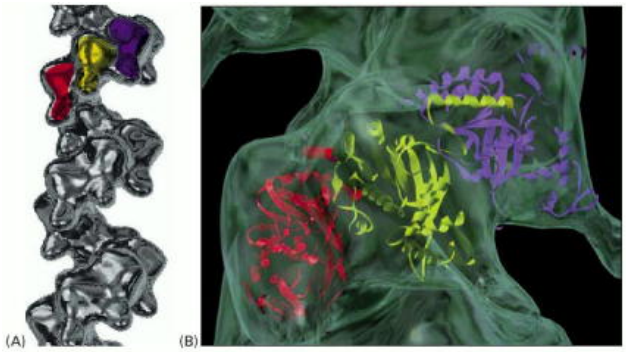

Figure 5-58. The structure of the RecA and Rad51 proteinDNA filaments. (A) The Rad51 protein bound to a DNA single strand. Rad51 is a human homolog of the bacterial RecA protein; three successive monomers in this helical filament are colored. (B) A short section of the RecA filament, with the three-dimensional structure of the protein fitted to the image of the filament determined by electron microscopy. The two DNAprotein filaments appear to be quite similar. There are about six RecA monomers per turn of the helix, holding 18 nucleotides of single-stranded DNA that is stretched out by the protein. The exact path of the DNA in this structure is not known. (A, courtesy of Edward Egelman; B, from X. Yu et al., *J. Mol. Biol.* 283:985992, 1998.)

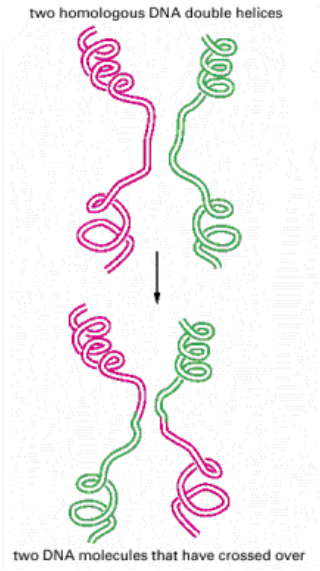

Figure 5-54. General recombination. The breaking and rejoining of two homologous DNA double helices creates two DNA molecules that have "crossed over." In meiosis, this process causes each chromosome in a germ cell to contain a mixture of maternally and paternally inherited genes.

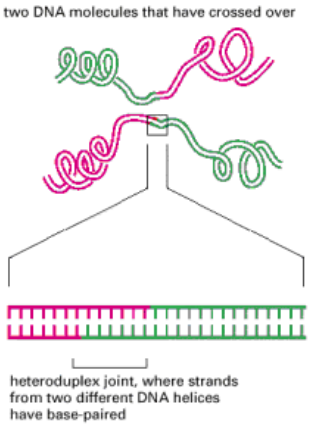

Figure 5-55. A heteroduplex joint. This structure unites two DNA molecules where they have crossed over. Such a joint is often thousands of nucleotides long.

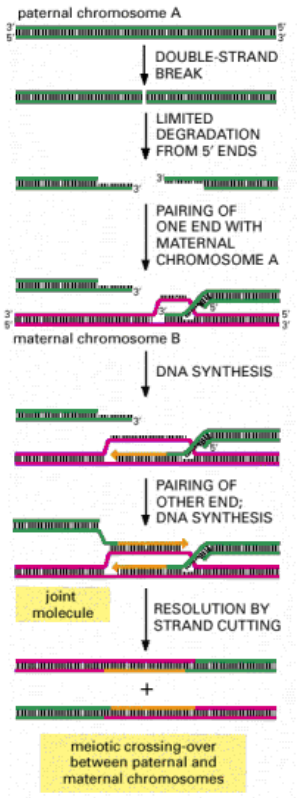

Figure 5-56. General recombination in meiosis. As indicated, the process begins when an endonuclease makes a double-strand break in a chromosome. An exonuclease then creates two protruding 3 single-stranded ends, which find the homologous region of a second chromosome to begin DNA synapsis. The joint molecule formed can eventually be resolved by selective strand cuts to produce two chromosomes that have crossed over, as shown.

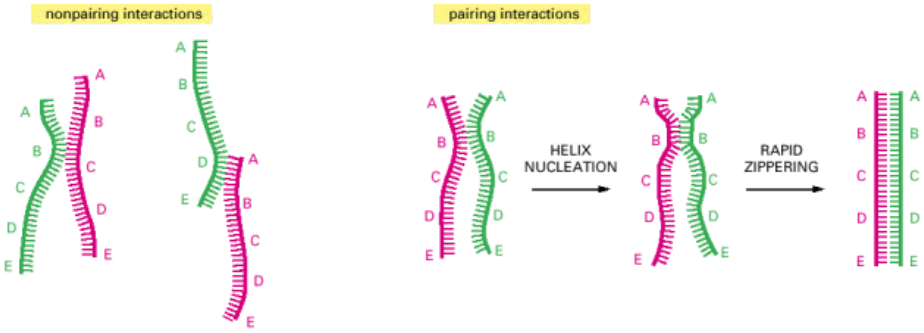

Figure 5-57. DNA hybridization. DNA double helices re-form from their separated strands in a reaction that depends on the random collision of two complementary DNA strands. The vast majority of such collisions are not productive, as shown on the left, but a few result in a short region where complementary base pairs have formed (helix nucleation). A rapid zipper then leads to the formation of a complete double helix. Through this trial-and-error process, a DNA strand will find its complementary partner even in the midst of millions of nonmatching DNA strands. A related, highly efficient trial-and-error recognition of a complementary partner DNA sequence seems to initiate all general recombination events.

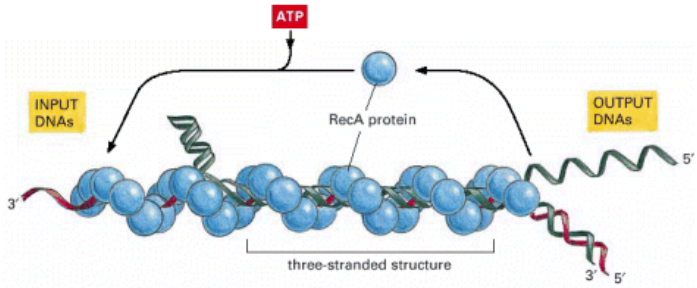

Figure 5-59. DNA synapsis catalyzed by the RecA protein. *In vitro* experiments show that several types of complex are formed between a DNA single strand covered with RecA protein *(red)* and a DNA double helix *(green).* First a non-base-paired complex is formed, which is converted through transient base-flipping (see Figure 5-51) to a three-stranded structure as soon as a region of homologous sequence is found. This complex is unstable because it involves an unusual form of DNA, and it spins out a DNA heteroduplex (one strand *green* and the other strand *red)* plus a displaced single strand from the original helix *(green).* Thus the structure shown in this diagram migrates to the left, reeling in the "input DNAs" while producing the "output DNAs." The net result is a DNA strand exchange identical to that diagrammed earlier in Figure 5-56. (Adapted from S.C. West, *Annu. Rev. Biochem.* 61:603640, 1992.)

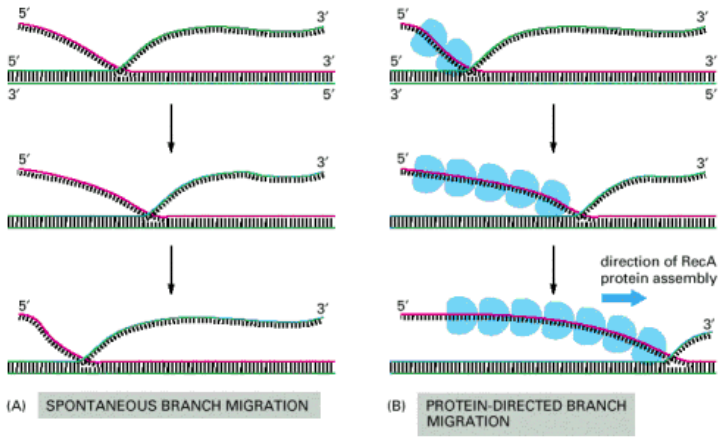

Figure 5-60. Two types of DNA branch migration observed in experiments in vitro. (A) Spontaneous branch migration is a back-and-forth, random-walk process, and it therefore makes little progress over long distances. (B) RecA-protein-directed branch migration proceeds at a uniform rate in one direction and may be driven by the polarized assembly of the RecA protein filament on a DNA single strand, which occurs in the direction indicated. Special DNA helicases that catalyze branch migration even more efficiently are also involved in recombination (for example see Figure 5-63).

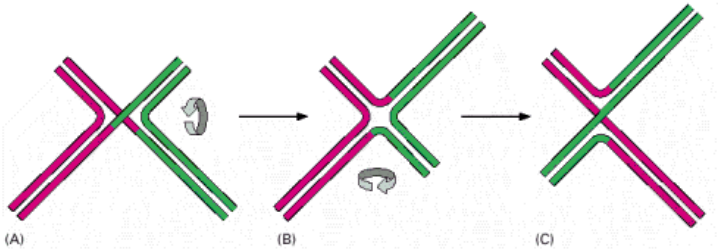

Figure 5-61. A Holliday junction and its isomerization. As described in the text, the synapsis step in general recombination is catalyzed by a RecA type of protein bound to a DNA single strand. This step is often followed by a reciprocal exchange of strands between two DNA double helices that have thereby paired with each other. This exchange produces a unique DNA structure known as a Holliday junction, named after the scientist who first proposed its formation. (A) The initially formed structure contains two crossing (inside) strands and two noncrossing (outside) strands. (B) An isomerization of the Holliday junction produces an open, symmetrical structure. (C) Further isomerization can interconvert the crossing and noncrossing strands, producing a structure that is otherwise the same as that in (A).

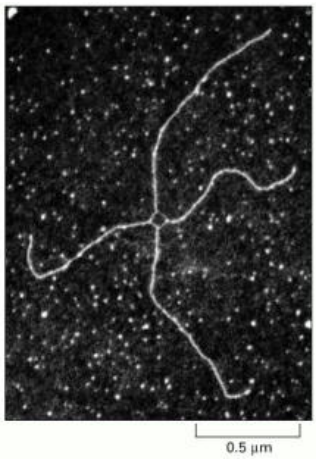

Figure 5-62. Electron micrograph of a Holliday junction. This view of the junction corresponds to the open structure illustrated in Figure 5-61B. (Courtesy of Huntington Potter and David Dressler.)

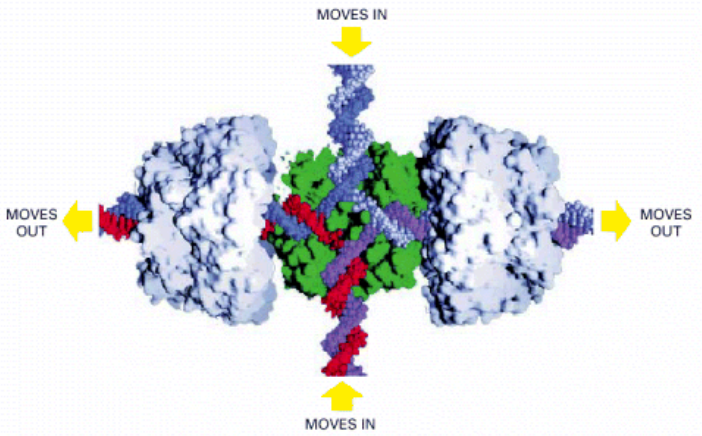

Figure 5-63. Enzyme-catalyzed double branch migration at a Holliday junction. In *E. coli*, a tetramer of the RuvA protein *(green)* and two hexamers of the RuvB protein *(pale gray)* bind to the open form of the junction. The RuvB protein uses the energy of ATP hydrolysis to move the crossover point rapidly along the paired DNA helices, extending the heteroduplex region as shown. There is evidence that similar proteins perform this function in vertebrate cells. (Image courtesy of P. Artymiuk; modified from S.C. West, *Cell* 94:699701, 1998.)

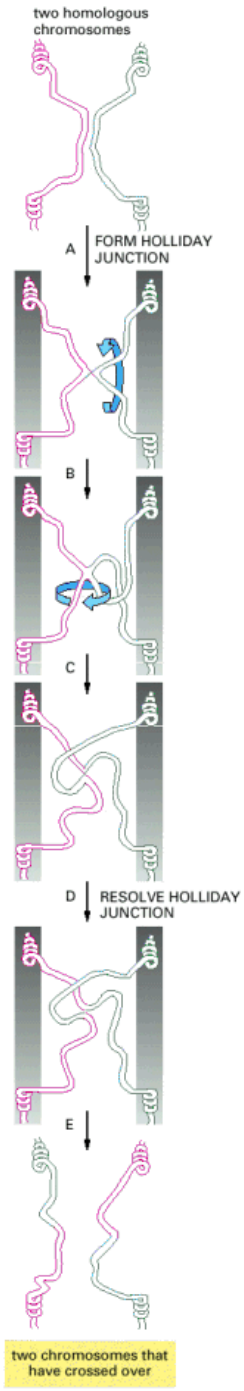

Figure 5-64. The resolution of a Holliday junction to produce crossed-over chromosomes. In this example, homologous regions of a *red* and a *green* chromosome have formed a Holliday junction by exchanging two strands. Cutting these two strands would terminate the exchange without crossing-over. With isomerization of the Holliday junction (steps B and C), the original noncrossing strands become the two crossing strands; cutting them now creates two DNA molecules that have crossed over *(bottom).* This type of isomerization may be involved in the breaking and rejoining of two homologous DNA double helices in meiotic general recombination. The grey bars in the central panels have been drawn to make it clear that the isomerization events shown can occur without disturbing the rest of the two chromosomes.

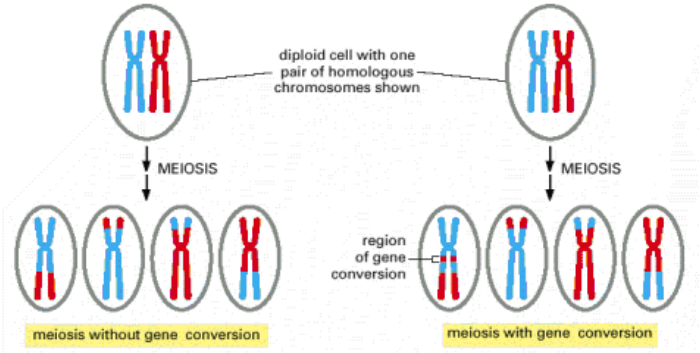

Figure 5-65. Gene conversion in meiosis. As described in Chapter 20, meiosis is the process through which a diploid cell gives rise to four haploid cells. Germ cells (eggs and sperm, for example) are produced by meiosis.

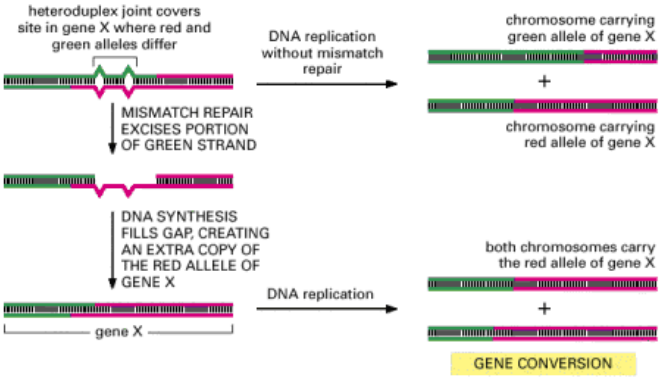

Figure 5-66. Gene conversion by mismatch correction. In this process, heteroduplex joints are formed at the sites of the crossing-over between homologous maternal and paternal chromosomes. If the maternal and paternal DNA sequences are slightly different, the heteroduplex joint will include some mismatched base pairs. The resulting mismatch in the double helix may then be corrected by the DNA mismatch repair machinery (see Figure 5-23), which can erase nucleotides on either the paternal or the maternal strand. The consequence of this mismatch repair is gene conversion, dectected as a deviation from the segregation of equal copies of maternal and paternal alleles that normally occurs in meiosis.

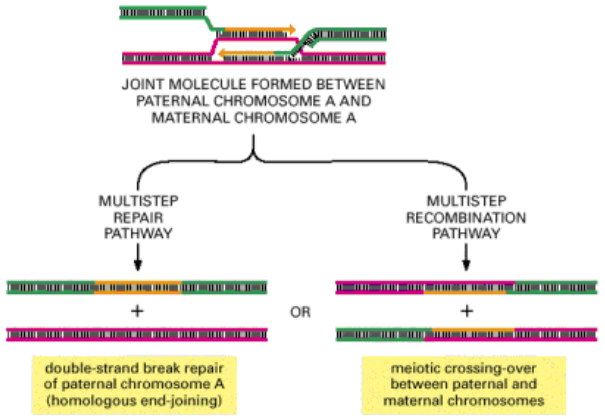

Figure 5-67. The different resolutions of a general recombination intermediate in mitotic and meiotic cells. As shown previously in Figure 5-56, general recombination begins when a double-strand break is generated in one double helix *(green)*, followed by DNA degradation and strand invasion into a homologous DNA duplex *(red)*. New DNA synthesis *(orange)* follows to generate the joint molecule shown. Depending on subsequent events, resolution of the joint molecule can lead either to a precise repair of the initial double-strand break *(left)* or to chromosome crossing-over *(right)*. The experimental induction of double-strand breaks at specific DNA sites has allowed the outcome of general recombination to be quantified in both mitotic and meiotic cells. More than 99% of these events fail to produce a crossover in mitotic cells, whereas crossovers are often the outcome in meiotic cells. In either case, if the maternal and paternal chromosomes differ in DNA sequence in the region of new DNA synthesis shown here, the sequence of the *green* DNA duplex in the region of new DNA synthesis is converted to that of the *red* duplex (a gene conversion).

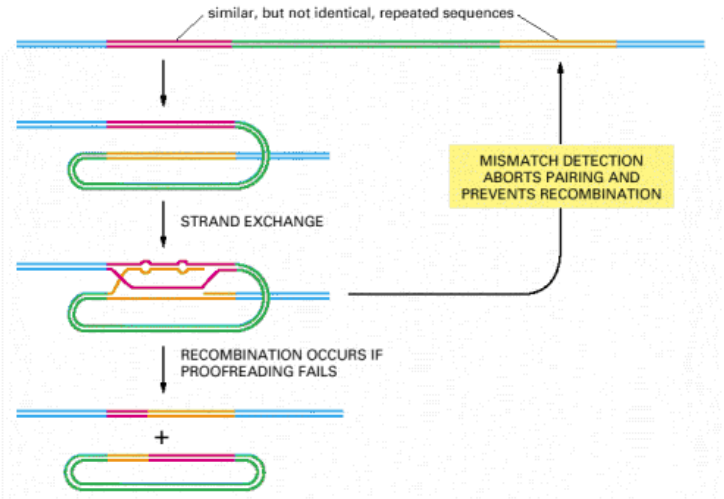

Figure 5-68. The mechanism that prevents general recombination from destabilizing a genome that contains repeated sequences. Studies with bacterial and yeast cells suggest that components of the mismatch proofreading system, diagrammed previously in Figure 5-23, have the additional function shown here.

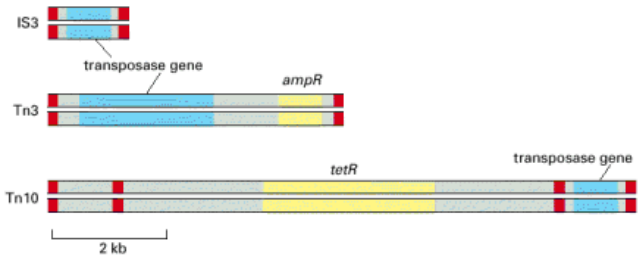

Figure 5-69. Three of the many types of mobile genetic elements found in bacteria. Each of these DNA elements contains a gene that encodes a *transposase*, an enzyme that conducts at least some of the DNA breakage and joining reactions needed for the element to move. Each mobile element also carries short DNA sequences (indicated in *red)* that are recognized only by the transposase encoded by that element and are necessary for movement of the element. In addition, two of the three mobile elements shown carry genes that encode enzymes that inactivate the antibiotics ampicillin *(ampR)* and tetracycline *(tetR)*. The transposable element Tn10, shown in the bottom diagram, is thought to have evolved from the chance landing of two short mobile elements on either side of a tetracyclin-resistance gene; the wide use of tetracycline as an antibiotic has aided the spread of this gene through bacterial populations. The three mobile elements shown are all examples of *DNA-only transposons* (see text).

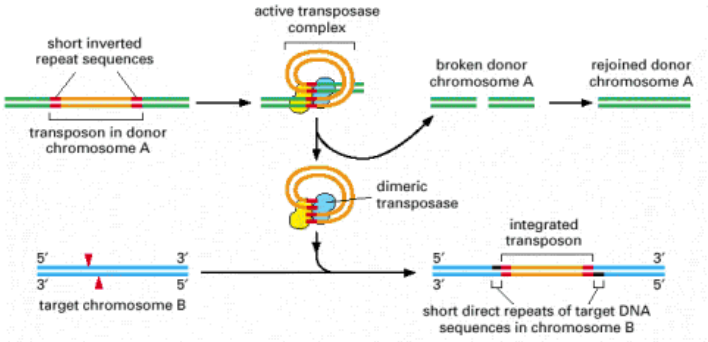

Figure 5-70. Cut-and-paste transposition. DNA-only transposons can be recognized in chromosomes by the "inverted repeat DNA sequences" *(red)* at their ends. Experiments show that these sequences, which can be as short as 20 nucleotides, are all that is necessary for the DNA between them to be transposed by the particular transposase enzyme associated with the element. The cut-and-paste movement of a DNA-only transposable element from one chromosomal site to another begins when the transposase brings the two inverted DNA sequences together, forming a DNA loop. Insertion into the target chromosome, catalyzed by the transposase, occurs at a random site through the creation of staggered breaks in the target chromosome *(red arrowheads)*. As a result, the insertion site is marked by a short direct repeat of the target DNA sequence, as shown. Although the break in the donor chromosome *(green)* is resealed, the breakage-and-repair process often alters the DNA sequence, causing a mutation at the original site of the excised transposable element (not shown).

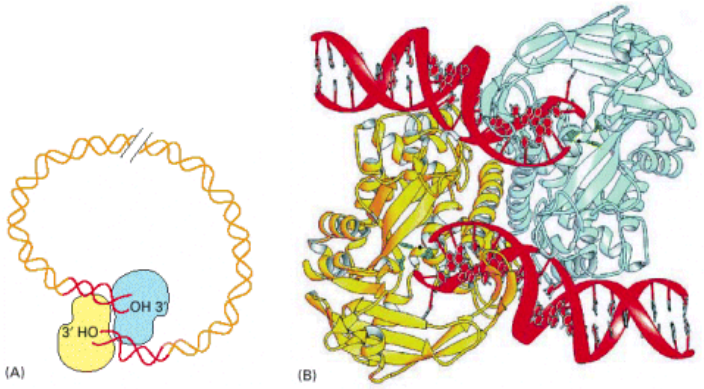

Figure 5-71. The structure of the central intermediate formed by a cut-and-paste transposase. (A) Schematic view of the overall structure. (B) The detailed structure of a transposase holding the two DNA ends, whose 3-OH groups are poised to attack a target chromosome. (B, from D.R. Davies et al., *Science* 289:7785, 2000. © AAAS.)

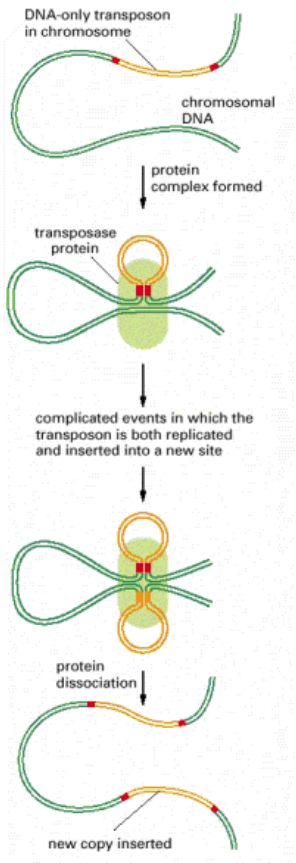

Figure 5-72. Replicative transposition. In the course of replicative transposition, the DNA sequence of the transposon is copied by DNA replication. The end products are a DNA molecule that is identical to the original donor and a target DNA molecule that has a transposon inserted into it. In general, a particular DNA-only transposon moves either by the cut-and-paste pathway shown in Figure 5-70 or by the replicative pathway outlined here. However, the two mechanisms have many enzymatic similarities, and a few transposons can move by either pathway.

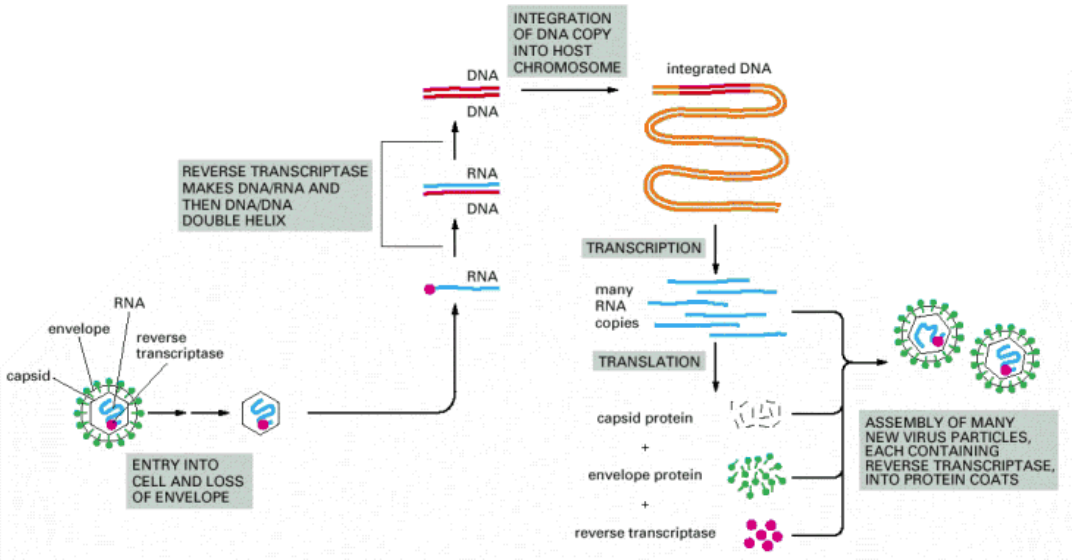

Figure 5-73. The life cycle of a retrovirus. The retrovirus genome consists of an RNA molecule of about 8500 nucleotides; two such molecules are packaged into each viral particle. The enzyme *reverse transcriptase* first makes a DNA copy of the viral RNA molecule and then a second DNA strand, generating a double-stranded DNA copy of the RNA genome. The integration of this DNA double helix into the host chromosome is then catalyzed by a virus-encoded *integrase* enzyme (see Figure 5-75). This integration is required for the synthesis of new viral RNA molecules by the host cell RNA polymerase, the enzyme that transcribes DNA into RNA (discussed in Chapter 6).

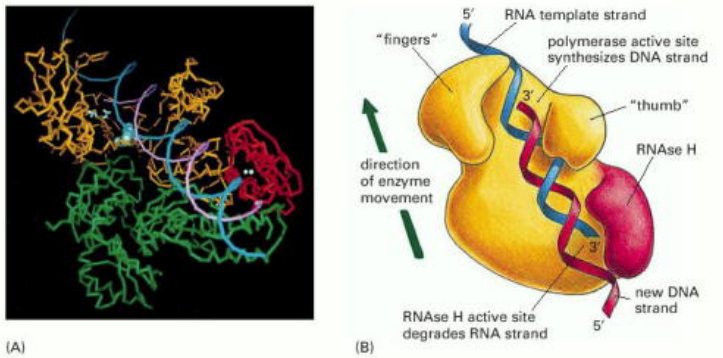

Figure 5-74. Reverse transcriptase. (A) The three-dimensional structure of the enzyme from HIV (the human AIDS virus) determined by x-ray crystallography. (B) A model showing the enzyme's activity on an RNA template. Note that the polymerase domain *(yellow* in B) has a covalently attached RNAse H (H for "Hybrid") domain *(red)* that degrades an RNA strand in an RNA/DNA helix. This activity helps the polymerase to convert the initial hybrid helix into a DNA double helix (A, courtesy of Tom Steitz; B, adapted from L.A. Kohlstaedt et al., *Science* 256:17831790, 1990.)

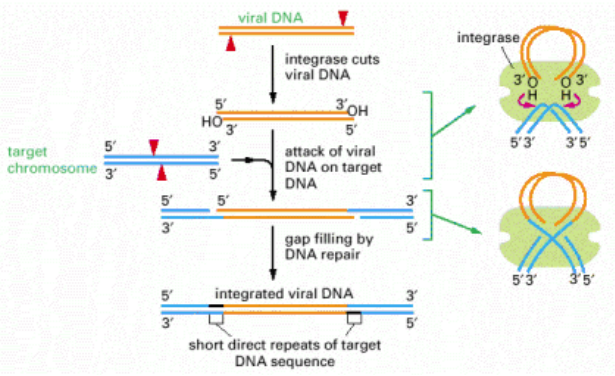

Figure 5-75. Transpositional site-specific recombination by a retrovirus or a retroviral-like retrotransposon. Outline of the strand-breaking and strand-rejoining events that lead to integration of the linear double-stranded DNA *(orange)* of a retrovirus (such as HIV) or a retroviral-like retrotransposon (such as *Ty1*) into the host cell chromosome *(blue).* In an initial step, the integrase enzyme forms a DNA loop and cuts one strand at each end of the viral DNA sequence, exposing a protruding 3-OH group. Each of these 3-OH ends then directly attacks a phosphodiester bond on opposite strands of a randomly selected site on a target chromosome *(red arrowheads).* This inserts the viral DNA sequence into the target chromosome, leaving short gaps on each side that are filled in by DNA repair processes. Because of the gap filling, this type of mechanism (like that of cut-and-paste transposons) leaves short repeats of target DNA sequence *(black)* on each side of the integrated DNA segment; these are 312 nucleotides long, depending on the integrase enzyme.

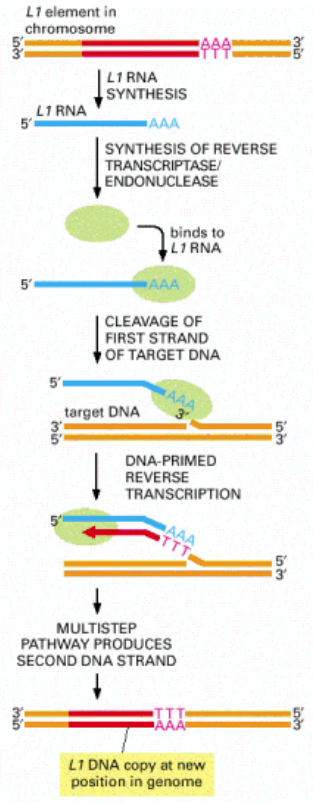

Figure 5-76. Transpositional site-specific recombination by a nonretroviral retrotransposon. Transposition by the *L1* element *(red)* begins when an endonuclease attached to the *L1* reverse transcriptase and the *L1* RNA *(blue)* makes a nick in the target DNA at the point at which insertion will occur. This cleavage releases a 3-OH DNA end in the target DNA, which is then used as a primer for the reverse transcription step shown. This generates a single-stranded DNA copy of the element that is directly linked to the target DNA. In subsequent reactions, not yet understood in detail, further processing of the single-stranded DNA copy results in the generation of a new double-stranded DNA copy of the *L1* element that is inserted at the site where the initial nick was made.

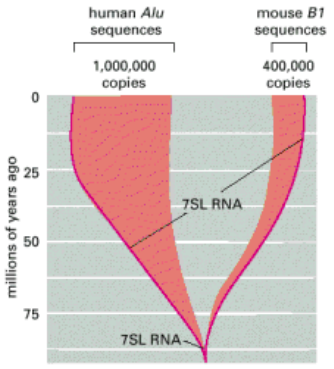

Figure 5-77. The proposed pattern of expansion of the abundant *Alu* and *B1* sequences found in the human and mouse genomes, respectively. Both of these transposable DNA sequences are thought to have evolved from the essential 7SL RNA gene which encodes the SRP RNA (see Figure 12-41). On the basis of the species distribution and sequence similarity of these highly repeated elements, the major expansion in copy numbers seems to have occurred independently in mice and humans (see Figure 5-78). (Adapted from P.L. Deininger and G.R. Daniels, *Trends Genet.* 2:7680, 1986 and International Human Genome Sequencing Consortium, *Nature* 409:860921, 2001.)

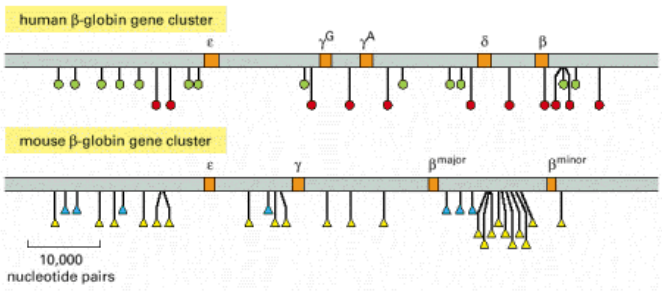

Figure 5-78. A comparison of the β-globin gene cluster in the human and mouse genomes, showing the location of transposable elements. This stretch of human genome contains five functional β-globin-like genes *(orange);* the comparable region from the mouse genome has only four. The positions of the human *Alu* sequence are indicated by *green circles*, and the human *L1* sequences by *red circles*. The mouse genome contains different but related transposable elements: the positions of *B1* elements (which are related to the human Alu sequences) are indicated by *blue triangles*, and the positions of the mouse *L1* elements (which are related to the human *L1* sequences) are indicated by *yellow triangles*. Because the DNA sequences and positions of the transposable elements found in the mouse and human β-globin gene clusters are so different, it is believed that they accumulated in each of these genomes independently, relatively recently in evolutionary time. (Courtesy of Ross Hardison and Webb Miller.)

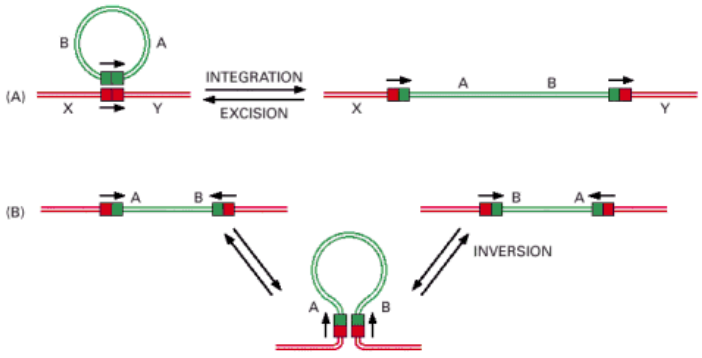

Figure 5-79. Two types of DNA rearrangement produced by conservative site-specific recombination. The only difference between the reactions in (A) and B) is the relative orientation of the two DNA sites (indicated by *arrows)* at which a site-specific recombination event occurs. (A) Through an integration reaction, a circular DNA molecule can become incorporated into a second DNA molecule; by the reverse reaction (excision), it can exit to reform the original DNA circle. Bacteriophage lambda and other bacterial viruses move in and out of their host chromosomes in precisely this way. (B) Conservative site-specific recombination can also invert a specific segment of DNA in a chromosome. A well-studied example of DNA inversion through site-specific recombination occurs in the bacterium *Salmonella typhimurium*, an organism that is a major cause of food poisoning in humans; the inversion of a DNA segment changes the type of flagellum that is produced by the bacterium (see Figure 7-64).

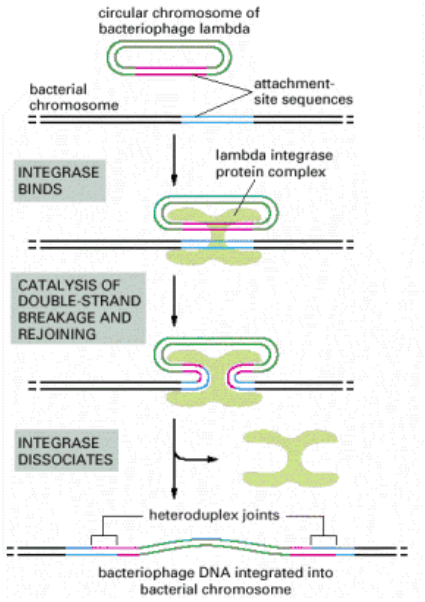

Figure 5-80. The insertion of a circular bacteriophage lambda DNA chromosome into the bacterial chromosome. In this example of site-specific recombination, the lambda integrase enzyme binds to a specific "attachment site" DNA sequence on each chromosome, where it makes cuts that bracket a short homologous DNA sequence. The integrase then switches the partner strands and reseals them to form a heteroduplex joint that is seven nucleotide pairs long. A total of four strand-breaking and strand-joining reactions is required; for each of them, the energy of the cleaved phosphodiester bond is stored in a transient covalent linkage between the DNA and the enzyme, so that DNA strand resealing occurs without a requirement for ATP or DNA ligase.

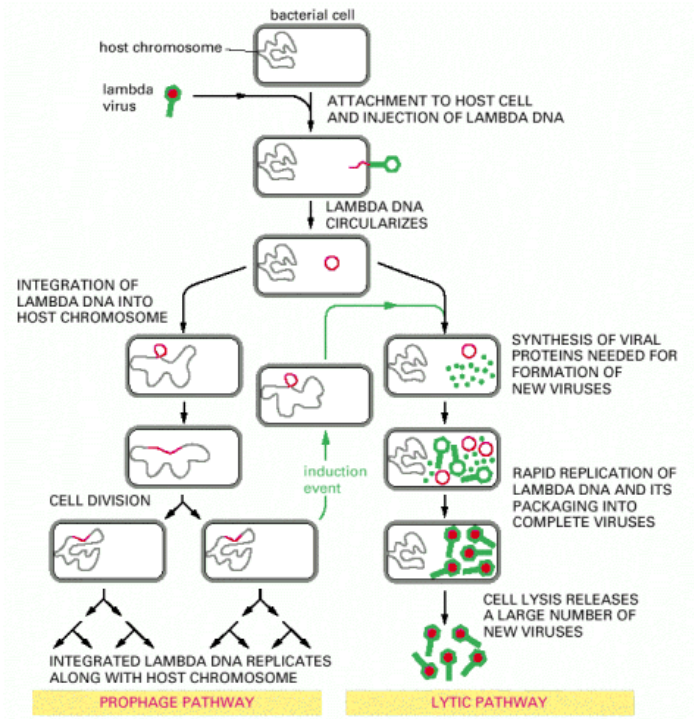

Figure 5-81. The life cycle of bacteriophage lambda. The double-stranded DNA lambda genome contains 50,000 nucleotide pairs and encodes 5060 different proteins. When the lambda DNA enters the cell, the ends join to form a circular DNA molecule. This bacteriophage can multiply in *E. coli* by a lytic pathway, which destroys the cell, or it can enter a latent prophage state. Damage to a cell carrying a lambda prophage induces the prophage to exit from the host chromosome and shift to lytic growth *(green arrows).* Both the entrance of the lambda DNA to, and its exit from, the bacterial chromosome are accomplished by a conservative site-specific recombination event, catalyzed by the lambda integrase enzyme (see Figure 5-80).

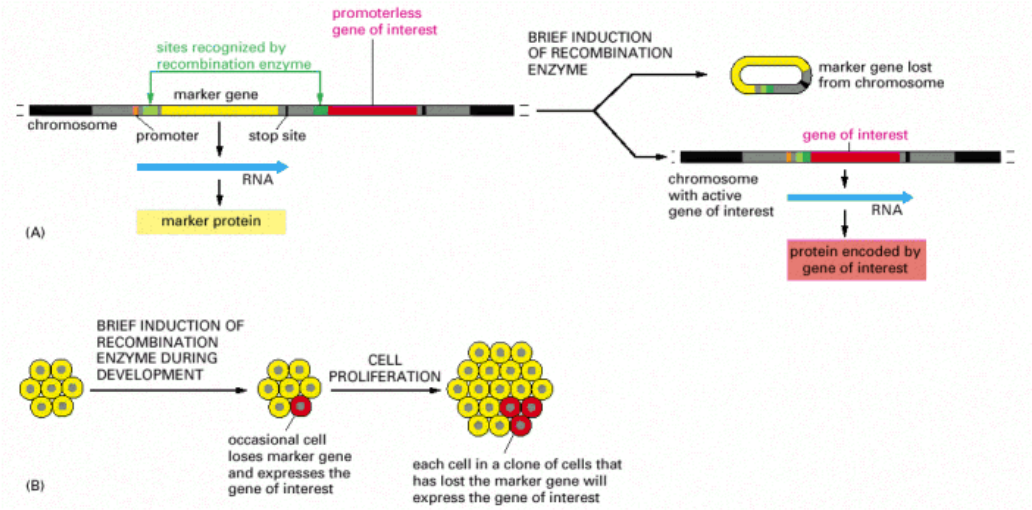

Figure 5-82. How a conservative site-specific recombination enzyme is used to turn on a specific gene in a group of cells in a transgenic animal. This technique requires the insertion of two specially engineered DNA molecules into the animal's germ line. (A) The DNA molecule shown has been engineered with specific recognition sites *(green)* so that the gene of interest *(red)* is transcribed only after a site-specific recombination enzyme that uses these sites is induced. As shown on the right, this induction removes a marker gene *(yellow)* and brings the promoter DNA *(orange)* adjacent to the gene of interest. The recombination enzyme is inducible, because it is encoded by a second DNA molecule (not shown) that has been engineered to ensure that the enzyme is made only when the animal is treated with a special small molecule or its temperature is raised. (B) Transient induction of the recombination enzyme causes a brief burst of synthesis of that enzyme, which in turn causes a DNA rearrangement in an occasional cell. For this cell and all its progeny, the marker gene is inactivated and the gene of interest is simultaneously activated (as shown in A). Those clones of cells in the developing animal that express the gene of interest can be identified by their loss of the marker protein. This technique is widely used in mice and *Drosophila*, because it allows one to study the effect of expressing any gene of interest in a group of cells in an intact animal. In one version of the technique, the Cre recombination enzyme of bacteriophage P1 is employed along with its loxP recognition sites (see pp. 542543).

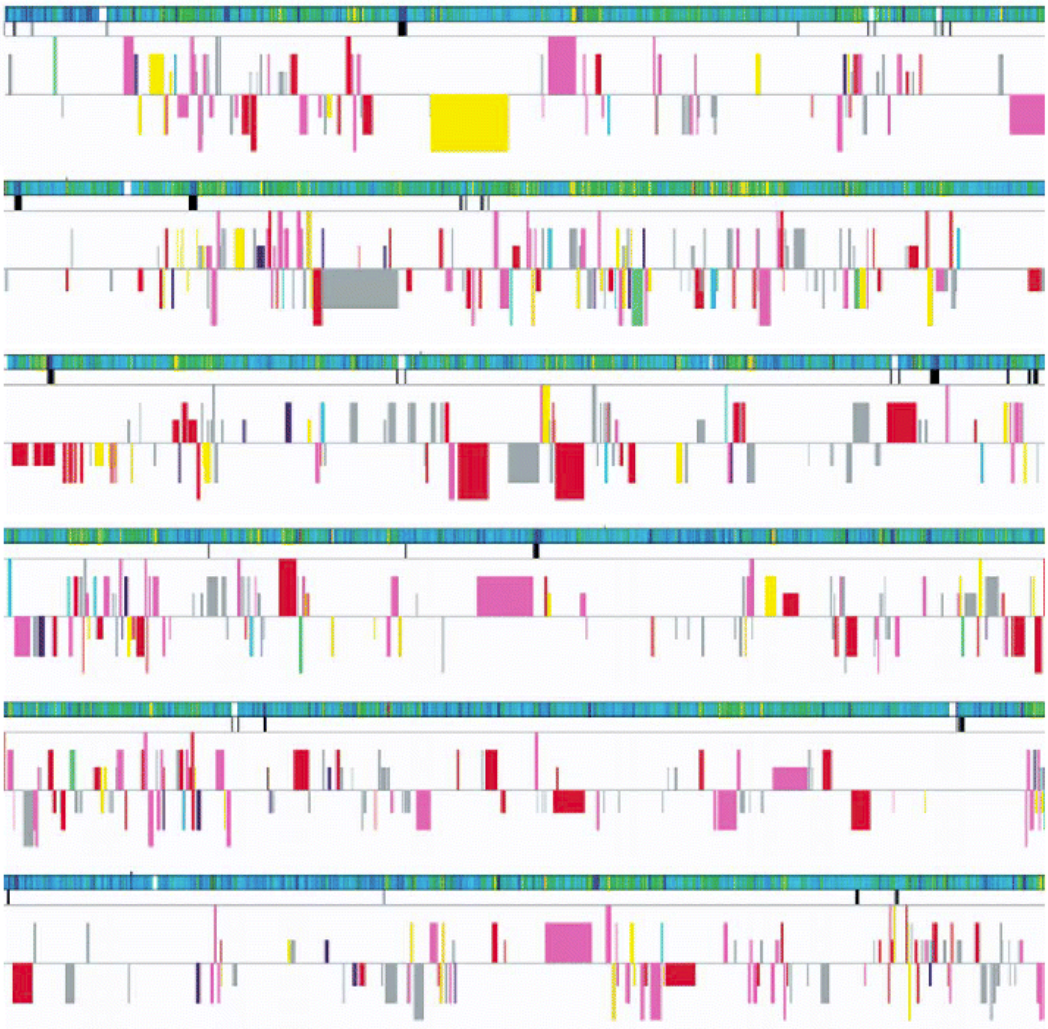

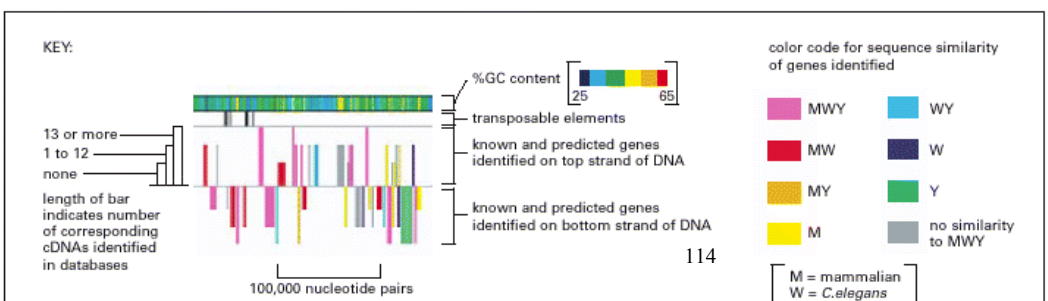

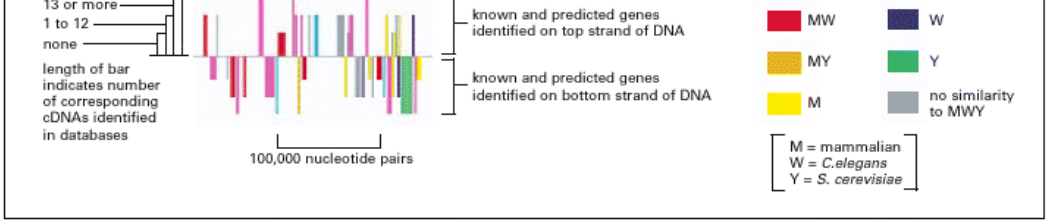

Figure 6-1. Schematic depiction of a portion of chromosome 2 from the genome of the fruit fly Drosophila melanogaster . This figure represents approximately 3% of the total *Drosophila* genome, arranged as six contiguous segments. As summarized in the key, the symbolic representations are: *rainbow-colored bar*: G-C base-pair content; *black vertical lines* of various thicknesses: locations of transposable elements, with thicker bars indicating clusters of elements; *colored boxes*: genes (both known and predicted) coded on one strand of DNA (boxes *above* the midline) and genes coded on the other strand (boxes *below* the midline). The length of each predicted gene includes both its exons (protein-coding DNA) and its introns (non-coding DNA) (see Figure 4-25). As indicated in the key, the height of each gene box is proportional to the number of cDNAs in various databases that match the gene. As described in Chapter 8, cDNAs are DNA copies of mRNA molecules, and large collections of the nucleotide sequences of cDNAs have been deposited in a variety of databases. The higher the number of matches between the nucleotide sequences of cDNAs and that of a particular predicted gene, the higher the confidence that the predicted gene is transcribed into RNA and is thus a genuine gene. The color of each gene box (see *color code* in the key) indicates whether a closely related gene is known to occur in other organisms. For example, MWY means the gene has close relatives in mammals, in the nematode worm *Caenorhabditis elegans*, and in the yeast *Saccharomyces cerevisiae*. MW indicates the gene has close relatives in mammals and the worm but not in yeast. (From Mark D. Adams et al., *Science* 287:21852195, 2000. © AAAS.)

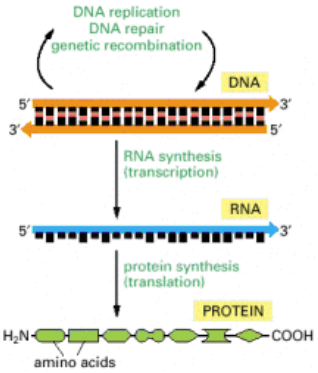

Figure 6-2. The pathway from DNA to protein. The flow of genetic information from DNA to RNA (transcription) and from RNA to protein (translation) occurs in all living cells.

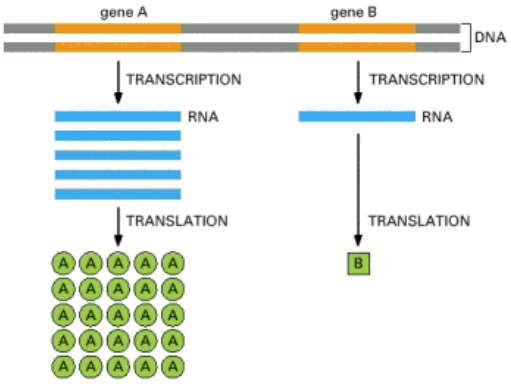

Figure 6-3. Genes can be expressed with different efficiencies. Gene A is transcribed and translated much more efficiently than gene B. This allows the amount of protein A in the cell to be much greater than that of protein B.

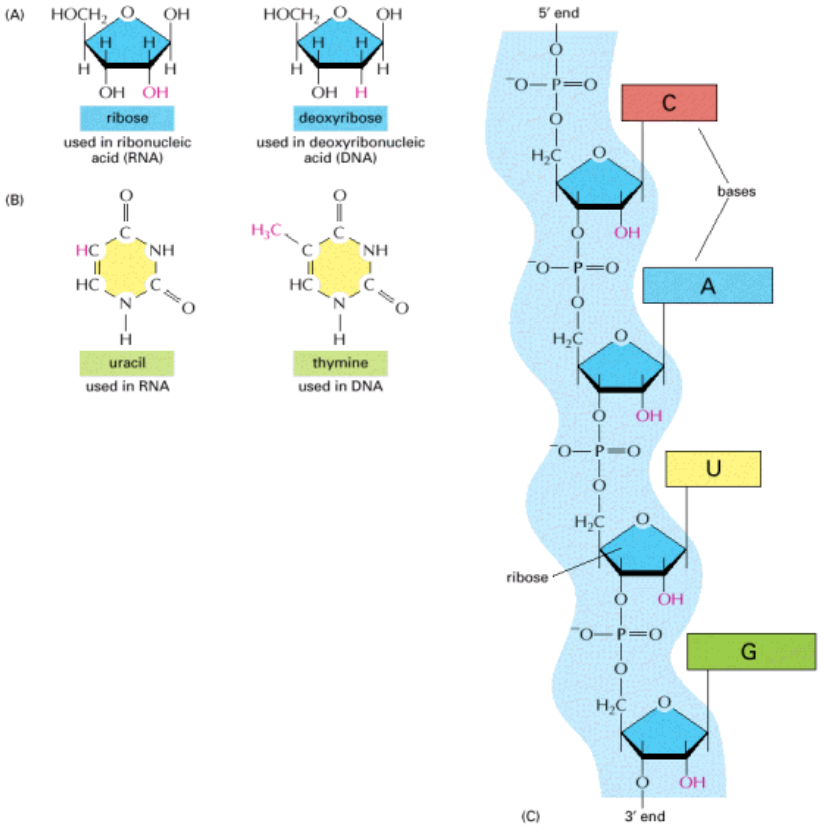

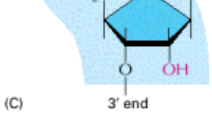

Figure 6-4. The chemical structure of RNA. (A) RNA contains the sugar ribose, which differs from deoxyribose, the sugar used in DNA, by the presence of an additional -OH group. (B) RNA contains the base uracil, which differs from thymine, the equivalent base in DNA, by the absence of a $-CH_3$ group. (C) A short length of RNA. The phosphodiester chemical linkage between nucleotides in RNA is the same as that in DNA.

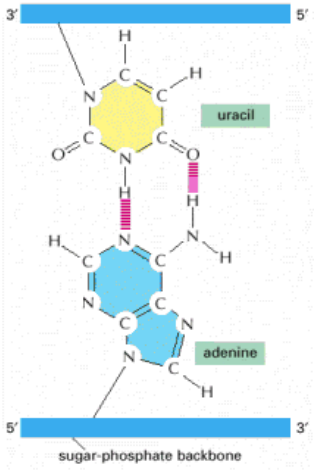

Figure 6-5. Uracil forms base pairs with adenine. The absence of a methyl group in U has no effect on base-pairing; thus, U-A base pairs closely resemble T-A base pairs (see Figure 4-4).

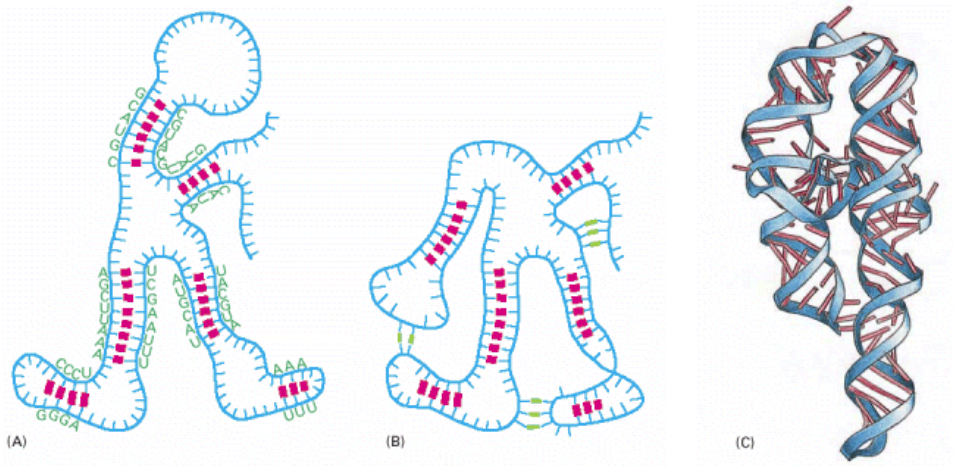

Figure 6-6. RNA can fold into specific structures. RNA is largely single-stranded, but it often contains short stretches of nucleotides that can form conventional base-pairs with complementary sequences found elsewhere on the same molecule. These interactions, along with additional "nonconventional" base-pair interactions, allow an RNA molecule to fold into a three-dimensional structure that is determined by its sequence of nucleotides. (A) Diagram of a folded RNA structure showing only conventional base-pair interactions; (B) structure with both conventional *(red)* and nonconventional *(green)* base-pair interactions; (C) structure of an actual RNA, a portion of a group 1 intron (see Figure 6-36). Each conventional base-pair interaction is indicated by a "rung" in the double helix. Bases in other configurations are indicated by broken rungs.

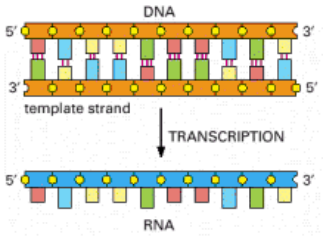

Figure 6-7. DNA transcription produces a single-stranded RNA molecule that is complementary to one strand of DNA.

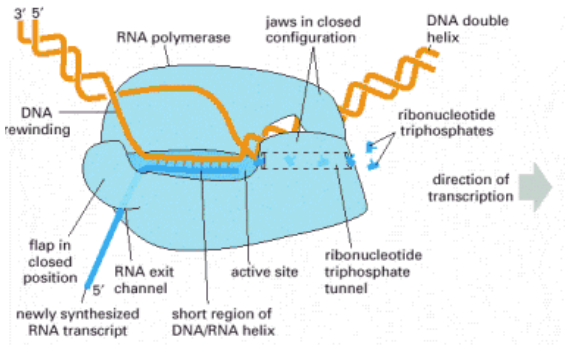

Figure 6-8. DNA is transcribed by the enzyme RNA polymerase. The RNA polymerase *(pale blue)* moves stepwise along the DNA, unwinding the DNA helix at its active site. As it progresses, the polymerase adds nucleotides (here, *small "T" shapes)* one by one to the RNA chain at the polymerization site using an exposed DNA strand as a template. The RNA transcript is thus a single-stranded complementary copy of one of the two DNA strands. The polymerase has a rudder (see Figure 6-11) that displaces the newly formed RNA, allowing the two strands of DNA behind the polymerase to rewind. A short region of DNA/RNA helix (approximately nine nucleotides in length) is therefore formed only transiently, and a "window" of DNA/RNA helix therefore moves along the DNA with the polymerase. The incoming nucleotides are in the form of ribonucleoside triphosphates (ATP, UTP, CTP, and GTP), and the energy stored in their phosphate-phosphate bonds provides the driving force for the polymerization reaction (see Figure 5-4). (Adapted from a figure kindly supplied by Robert Landick.)

Figure 6-9. Transcription of two genes as observed under the electron microscope. The micrograph shows many molecules of RNA polymerase simultaneously transcribing each of two adjacent genes. Molecules of RNA polymerase are visible as a series of dots along the DNA with the newly synthesized transcripts (fine threads) attached to them. The RNA molecules (ribosomal RNAs) shown in this example are not translated into protein but are instead used directly as components of ribosomes, the machines on which translation takes place. The particles at the 5 end (the free end) of each rRNA transcript are believed to reflect the beginnings of ribosome assembly. From the lengths of the newly synthesized transcripts, it can be deduced that the RNA polymerase molecules are transcribing from left to right. (Courtesy of Ulrich Scheer.)

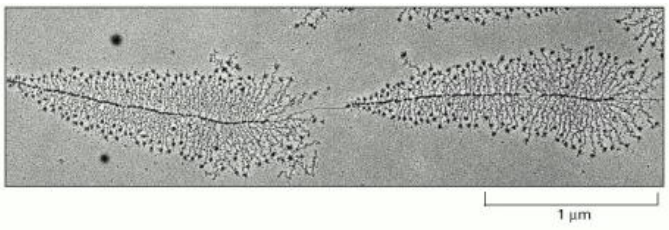

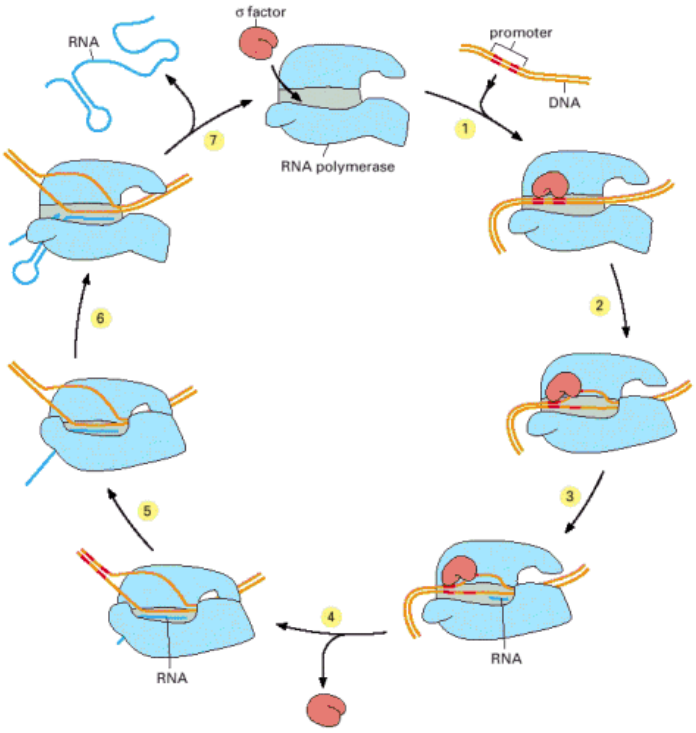

Figure 6-10. The transcription cycle of bacterial RNA polymerase. In step 1, the RNA polymerase holoenzyme (core polymerase plus σ factor) forms and then locates a promoter (see Figure 6-12). The polymerase unwinds the DNA at the position at which transcription is to begin (step 2) and begins transcribing (step 3). This initial RNA synthesis (sometimes called "abortive initiation") is relatively inefficient. However, once RNA polymerase has managed to synthesize about 10 nucleotides of RNA, σ relaxes its grip, and the polymerase undergoes a series of conformational changes (which probably includes a tightening of its jaws and the placement of RNA in the exit channel [see Figure 6-11]). The polymerase now shifts to the elongation mode of RNA synthesis (step 4), moving rightwards along the DNA in this diagram. During the elongation mode (step 5) transcription is highly processive, with the polymerase leaving the DNA template and releasing the newly transcribed RNA only when it encounters a termination signal (step 6). Termination signals are encoded in DNA and many function by forming an RNA structure that destabilizes the polymerase's hold on the RNA, as shown here. In bacteria, all RNA molecules are synthesized by a single type of RNA polymerase and the cycle depicted in the figure therefore applies to the production of mRNAs as well as structural and catalytic RNAs. (Adapted from a figure kindly supplied by Robert Landick.)

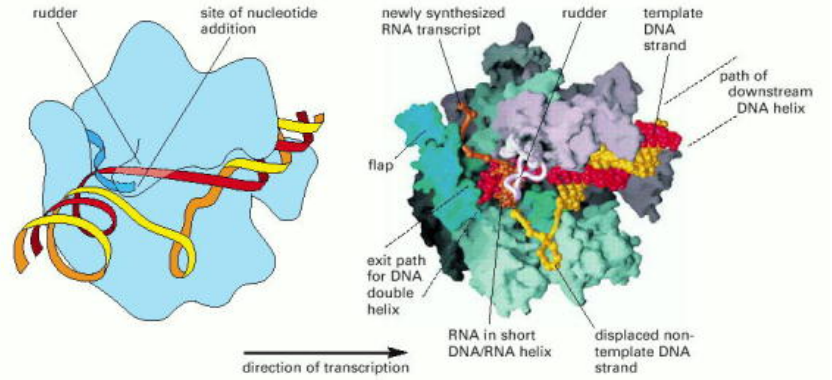

Figure 6-11. The structure of a bacterial RNA polymerase. Two depictions of the three-dimensional structure of a bacterial RNA polymerase, with the DNA and RNA modeled in. This RNA polymerase is formed from four different subunits, indicated by different colors *(right)*. The DNA strand used as a template is *red*, and the non-template strand is *yellow*. The rudder wedges apart the DNA-RNA hybrid as the polymerase moves. For simplicity only the polypeptide backbone of the rudder is shown in the right-hand figure, and the DNA exiting from the polymerase has been omitted. Because the RNA polymerase is depicted in the elongation mode, the σ factor is absent. (Courtesy of Seth Darst.)

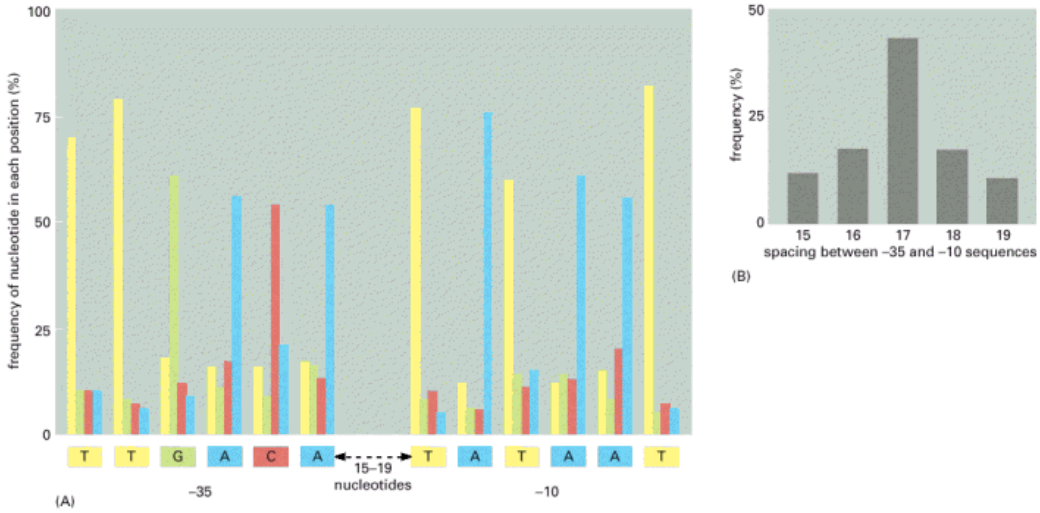

Figure 6-12. Consensus sequence for the major class of *E. coli* promoters. (A) The promoters are characterized by two hexameric DNA sequences, the -35 sequence and the -10 sequence named for their approximate location relative to the start point of transcription (designated +1). For convenience, the nucleotide sequence of a single strand of DNA is shown; in reality the RNA polymerase recognizes the promoter as double-stranded DNA. On the basis of a comparison of 300 promoters, the frequencies of the four nucleotides at each position in the -35 and -10 hexamers are given. The consensus sequence, shown *below* the graph, reflects the most common nucleotide found at each position in the collection of promoters. The sequence of nucleotides between the -35 and -10 hexamers shows no significant similarities among promoters. (B) The distribution of spacing between the -35 and -10 hexamers found in *E. coli* promoters. The information displayed in these two graphs applies to *E. coli* promoters that are recognized by RNA polymerase and the major σ factor (designated σ^{70}). As we shall see in the next chapter, bacteria also contain minor σ factors, each of which recognizes a different promoter sequence. Some particularly strong promoters recognized by RNA polymerase and σ^{70} have an additional sequence, located upstream (to the *left*, in the figure) of the -35 hexamer, which is recognized by another subunit of RNA polymerase.

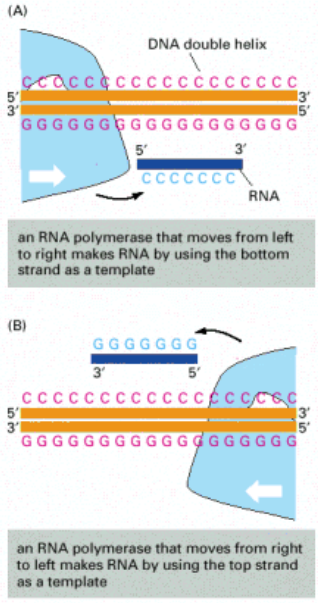

Figure 6-13. The importance of RNA polymerase orientation. The DNA strand serving as template must be traversed in a 3 to 5 direction, as illustrated in Figure 6-9. Thus, the direction of RNA polymerase movement determines which of the two DNA strands is to serve as a template for the synthesis of RNA, as shown in (A) and (B). Polymerase direction is, in turn, determined by the orientation of the promoter sequence, the site at which the RNA polymerase begins transcription.

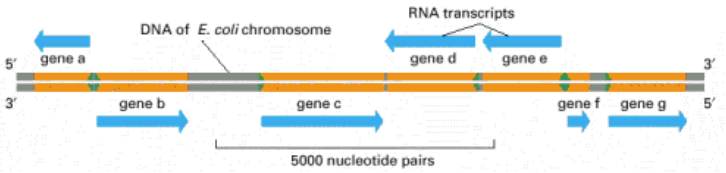

Figure 6-14. Directions of transcription along a short portion of a bacterial chromosome. Some genes are transcribed using one DNA strand as a template, while others are transcribed using the other DNA strand. The direction of transcription is determined by the promoter at the beginning of each gene *(green arrowheads)*. Approximately 0.2% (9000 base pairs) of the *E. coli* chromosome is depicted here. The genes transcribed from *left* to *right* use the bottom DNA strand as the template; those transcribed from *right* to *left* use the top strand as the template.

Figure 6-15. Structural similarity between a bacterial RNA polymerase and a eucaryotic RNA polymerase II. Regions of the two RNA polymerases that have similar structures are indicated in *green*. The eucaryotic polymerase is larger than the bacterial enzyme (12 subunits instead of 5), and some of the additional regions are shown in *gray*. The *blue* spheres represent Zn atoms that serve as structural components of the polymerases, and the *red* sphere represents the Mg atom present at the active site, where polymerization takes place. The RNA polymerases in all modern-day cells (bacteria, archaea, and eucaryotes) are closely related,

indicating that the basic features of the enzyme were in place before the divergence of the three major branches of life. (Courtesy of P. Cramer and R. Kornberg.)

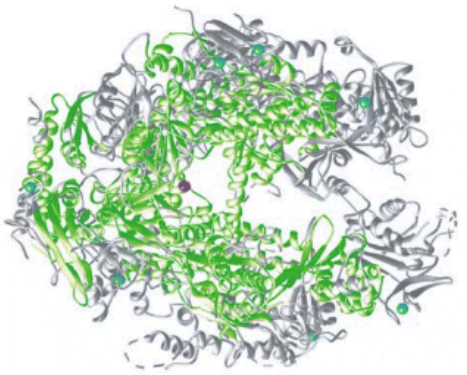

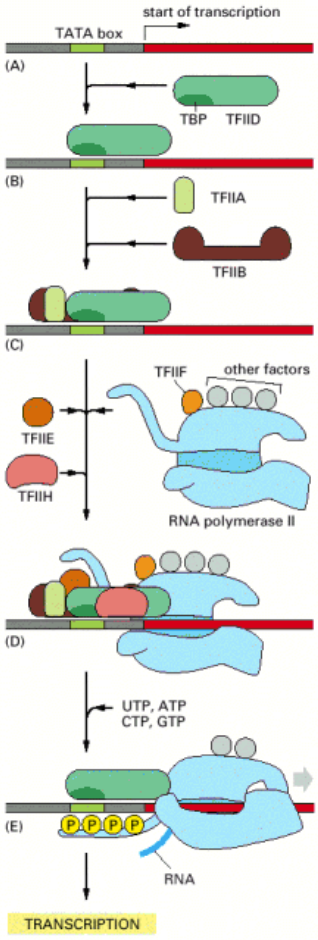

Figure 6-16. Initiation of transcription of a eucaryotic gene by RNA polymerase II. To begin transcription, RNA polymerase requires a number of general transcription factors (called TFIIA, TFIIB, and so on). (A) The promoter contains a DNA sequence called the TATA box, which is located 25 nucleotides away from the site at which transcription is initiated. (B) The TATA box is recognized and bound by transcription factor TFIID, which then enables the adjacent binding of TFIIB (C). For simplicity the DNA distortion produced by the binding of TFIID (see Figure 6-18) is not shown. (D) The rest of the general transcription factors, as well as the RNA polymerase itself, assemble at the promoter. (E) TFIIH then uses ATP to pry apart the DNA double helix at the transcription start point, allowing transcription to begin. TFIIH also phosphorylates RNA polymerase II, changing its conformation so that the polymerase is released from the general factors and can begin the elongation phase of transcription. As shown, the site of phosphorylation is a long C-terminal polypeptide tail that extends from the polymerase molecule. The assembly scheme shown in the figure was deduced from experiments performed *in vitro*, and the exact order in which the general transcription factors assemble on promoters in cells is not known with certainty. In some cases, the general factors are thought to first assemble with the polymerase, with the whole assembly subsequently binding to the DNA in a single step. The general transcription factors have been highly conserved in evolution; some of those from human cells can be replaced in biochemical experiments by the corresponding factors from simple yeasts.

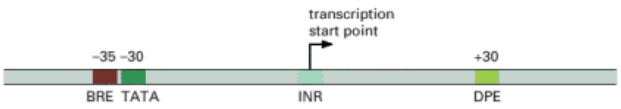

element	consensus sequence	general transcription factor
BRE	G/C G/C G/A C G C C	TFIIB
TATA	T A T A A/T A A/T	TBP
INR	C/T C/T A N T/A C/T C/T	TFIID
DPE	A/G G A/T C G T G	TFIID

Figure 6-17. Consensus sequences found in the vicinity of eucaryotic RNA polymerase II start points. The name given to each consensus sequence *(first column)* and the general transcription factor that recognizes it *(last column)* are indicated. N indicates any nucleotide, and two nucleotides separated by a slash indicate an equal probability of either nucleotide at the indicated position. In reality, each consensus sequence is a shorthand representation of a histogram similar to that of Figure 6-12. For most RNA polymerase II transcription start points, only two or three of the four sequences are present. For example, most polymerase II promoters have a TATA box sequence, and those that do not typically have a "strong" INR sequence. Although most of the DNA sequences that influence transcription initiation are located "upstream" of the transcription start point, a few, such as the DPE shown in the figure, are located in the transcribed region.

Figure 6-18. Three-dimensional structure of TBP (TATA-binding protein) bound to DNA. The TBP is the subunit of the general transcription factor TFIID that is responsible for recognizing and binding to the TATA box sequence in the DNA *(red).* The unique DNA bending caused by TBP - two kinks in the double helix separated by partly unwound DNA - may serve as a landmark that helps to attract the other general transcription factors. TBP is a single polypeptide chain that is folded into two very similar domains *(blue* and *green).* (Adapted from J.L. Kim et al., *Nature* 365:520527, 1993.)

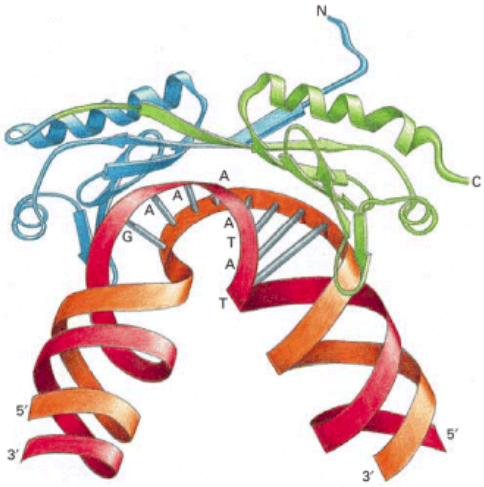

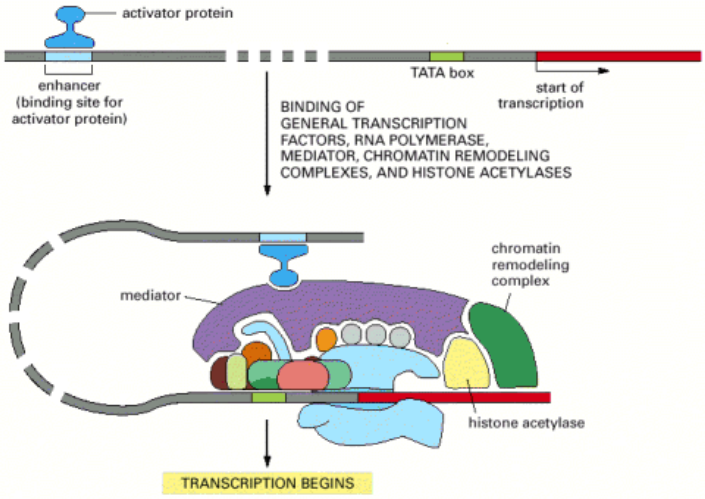

Figure 6-19. Transcription initiation by RNA polymerase II in a eucaryotic cell. Transcription initiation *in vivo* requires the presence of transcriptional activator proteins. As described in Chapter 7, these proteins bind to specific short sequences in DNA. Although only one is shown here, a typical eucaryotic gene has many activator proteins, which together determine its rate and pattern of transcription. Sometimes acting from a distance of several thousand nucleotide pairs (indicated by the dashed DNA molecule), these gene regulatory proteins help RNA polymerase, the general factors, and the mediator all to assemble at the promoter. In addition, activators attract ATP-dependent chromatin-remodeling complexes and histone acetylases.

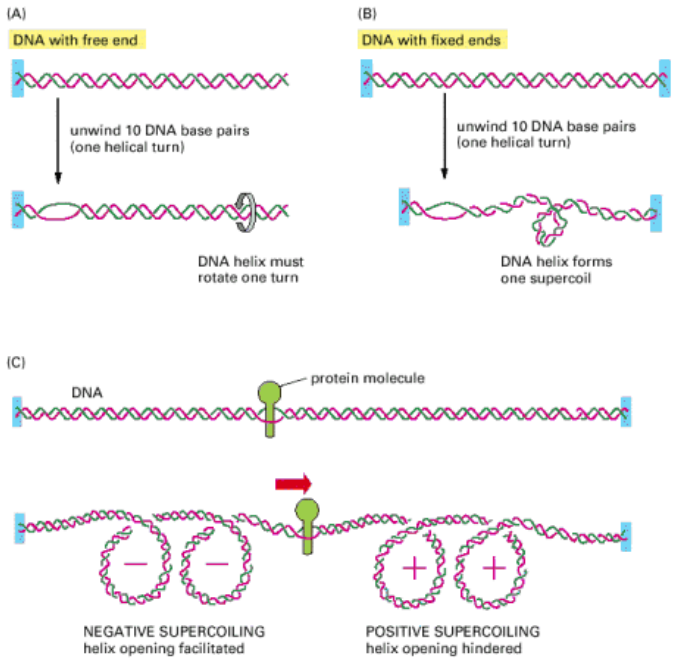

Figure 6-20. Superhelical tension in DNA causes DNA supercoiling. (A) For a DNA molecule with one free end (or a nick in one strand that serves as a swivel), the DNA double helix rotates by one turn for every 10 nucleotide pairs opened. (B) If rotation is prevented, superhelical tension is introduced into the DNA by helix opening. One way of accommodating this tension would be to increase the helical twist from 10 to 11 nucleotide pairs per turn in the double helix that remains in this example; the DNA helix, however, resists such a deformation in a springlike fashion, preferring to relieve the superhelical tension by bending into supercoiled loops. As a result, one DNA supercoil forms in the DNA double helix for every 10 nucleotide pairs opened. The supercoil formed in this case is a positive supercoil. (C) Supercoiling of DNA is induced by a protein tracking through the DNA double helix. The two ends of the DNA shown here are unable to rotate freely relative to each other, and the protein molecule is assumed also to be prevented from rotating freely as it moves. Under these conditions, the movement of the protein causes an excess of helical turns to accumulate in the DNA helix ahead of the protein and a deficit of helical turns to arise in the DNA behind the protein, as shown.

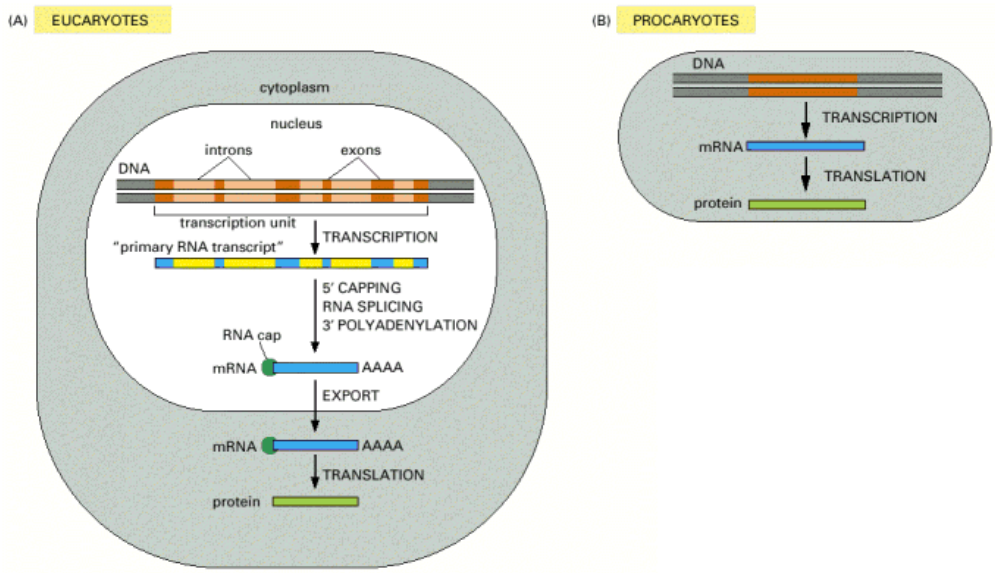

Figure 6-21. Summary of the steps leading from gene to protein in eucaryotes and bacteria. The final level of a protein in the cell depends on the efficiency of each step and on the rates of degradation of the RNA and protein molecules. (A) In eucaryotic cells the RNA molecule produced by transcription alone (sometimes referred to as the primary transcript) would contain both coding (exon) and noncoding (intron) sequences. Before it can be translated into protein, the two ends of the RNA are modified, the introns are removed by an enzymatically catalyzed RNA splicing reaction, and the resulting mRNA is transported from the nucleus to the cytoplasm. Although these steps are depicted as occurring one at a time, in a sequence, in reality they are coupled and different steps can occur simultaneously. For example, the RNA cap is added and splicing typically begins before transcription has been completed. Because of this coupling, complete primary RNA transcripts do not typically exist in the cell. (B) In procaryotes the production of mRNA molecules is much simpler. The 5 end of an mRNA molecule is produced by the initiation of transcription by RNA polymerase, and the 3 end is produced by the termination of transcription. Since procaryotic cells lack a nucleus, transcription and translation take place in a common compartment. In fact, translation of a bacterial mRNA often begins before its synthesis has been completed.

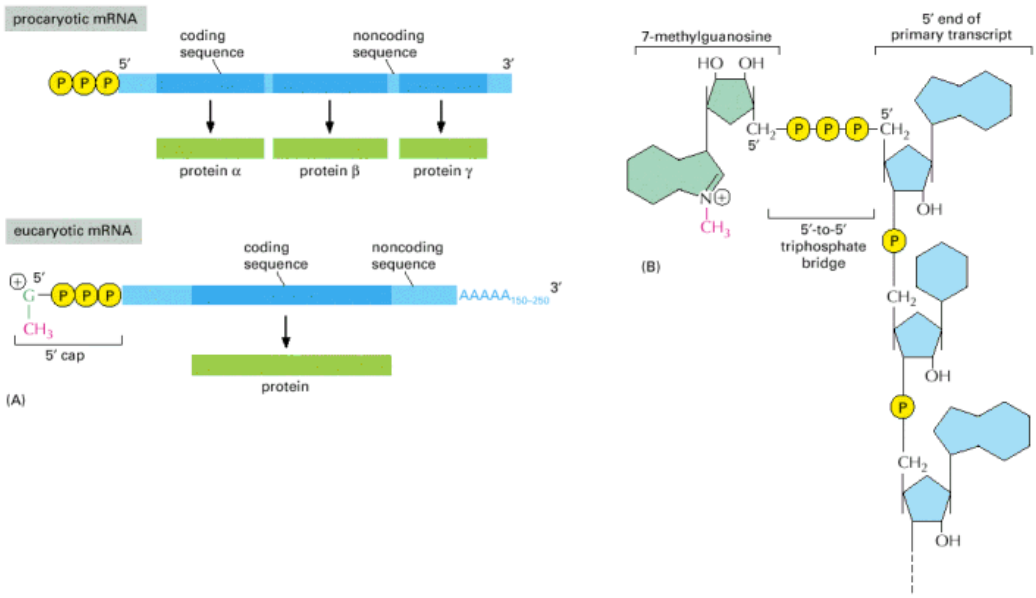

Figure 6-22. A comparison of the structures of procaryotic and eucaryotic mRNA molecules. (A) The 5 and 3 ends of a bacterial mRNA are the unmodified ends of the chain synthesized by the RNA polymerase, which initiates and terminates transcription at those points, respectively. The corresponding ends of a eucaryotic mRNA are formed by adding a 5 cap and by cleavage of the pre-mRNA transcript and the addition of a poly-A tail, respectively. The figure also illustrates another difference between the procaryotic and eucaryotic mRNAs: bacterial mRNAs can contain the instructions for several different proteins, whereas eucaryotic mRNAs nearly always contain the information for only a single protein. (B) The structure of the cap at the 5 end of eucaryotic mRNA molecules. Note the unusual 5-to-5 linkage of the 7-methyl G to the remainder of the RNA. Many eucaryotic mRNAs carry an additional modification: the 2-hydroxyl group on the second ribose sugar in the mRNA is methylated (not shown).

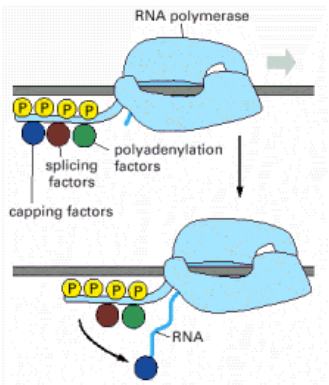

Figure 6-23. The "RNA factory" concept for eucaryotic RNA polymerase II. Not only does the polymerase transcribe DNA into RNA, but it also carries pre-mRNA-processing proteins on its tail, which are then transferred to the nascent RNA at the appropriate time. There are many RNA-processing enzymes, and not all travel with the polymerase. For RNA splicing, for example, only a few critical components are carried on the tail; once transferred to an RNA molecule, they serve as a nucleation site for the remaining components. The RNA-processing proteins first bind to the RNA polymerase tail when it is phosphorylated late in the process of transcription initiation (see Figure 6-16). Once RNA polymerase II finishes transcribing, it is released from DNA, the phosphates on its tail are removed by soluble phosphatases, and it can reinitiate transcription. Only this dephosphorylated form of RNA polymerase II is competent to start RNA synthesis at a promoter.

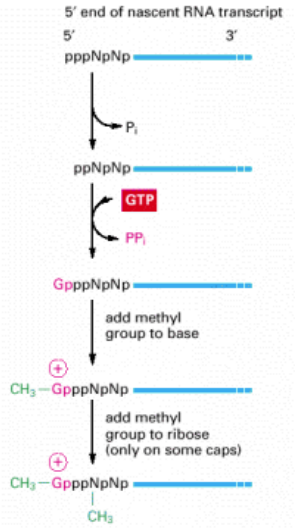

Figure 6-24. The reactions that cap the 5 end of each RNA molecule synthesized by RNA polymerase II. The final cap contains a novel 5-to-5 linkage between the positively charged 7-methyl G residue and the 5 end of the RNA transcript (see Figure 6-22B). The letter N represents any one of the four ribonucleotides, although the nucleotide that starts an RNA chain is usually a purine (an A or a G). (After A.J. Shatkin, *BioEssays* 7:275277, 1987. © ICSU Press.)

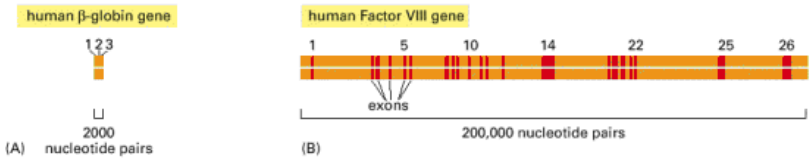

Figure 6-25. Structure of two human genes showing the arrangement of exons and introns. (A) The relatively small β-globin gene, which encodes one of the subunits of the oxygen-carrying protein hemoglobin, contains 3 exons (see also Figure 4-7). (B) The much larger Factor VIII gene contains 26 exons; it codes for a protein (Factor VIII) that functions in the blood-clotting pathway. Mutations in this gene are responsible for the most prevalent form of hemophilia.

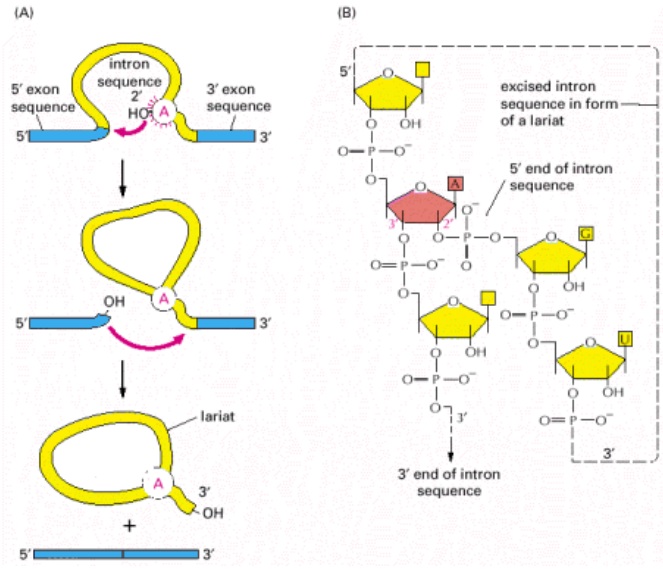

Figure 6-26. The RNA splicing reaction. (A) In the first step, a specific adenine nucleotide in the intron sequence (indicated in *red)* attacks the 5 splice site and cuts the sugar-phosphate backbone of the RNA at this point. The cut 5 end of the intron becomes covalently linked to the adenine nucleotide, as shown in detail in (B), thereby creating a loop in the RNA molecule. The released free 3-OH end of the exon sequence then reacts with the start of the next exon sequence, joining the two exons together and releasing the intron sequence in the shape of a *lariat.* The two exon sequences thereby become joined into a continuous coding sequence; the released intron sequence is degraded in due course.

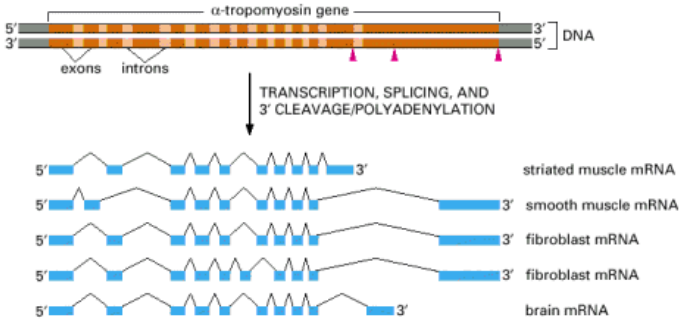

Figure 6-27. Alternative splicing of the α-tropomyosin gene from rat. α-tropomyosin is a coiled-coil protein (see Figure 3-11) that regulates contraction in muscle cells. The primary transcript can be spliced in different ways, as indicated in the figure, to produce distinct mRNAs, which then give rise to variant proteins. Some of the splicing patterns are specific for certain types of cells. For example, the α-tropomyosin made in striated muscle is different from that made from the same gene in smooth muscle. The arrowheads in the top part of the figure demark the sites where cleavage and poly-A addition can occur.

Figure 6-28. The consensus nucleotide sequences in an RNA molecule that signal the beginning and the end of most introns in humans. Only the three blocks of nucleotide sequences shown are required to remove an intron sequence; the rest of the intron can be occupied by any nucleotide. Here A, G, U, and C are the standard RNA nucleotides; R stands for either A or G; Y stands for either C or U. The A highlighted in *red* forms the branch point of the lariat produced by splicing. Only the GU at the start of the intron and the AG at its end are invariant nucleotides in the splicing consensus sequences. The remaining positions (even the branch point A) can be occupied by a variety of nucleotides, although the indicated nucleotides are preferred. The distances along the RNA between the three splicing consensus sequences are highly variable; however, the distance between the branch point and 3 splice junction is typically much shorter than that between the 5 splice junction and the branch point.

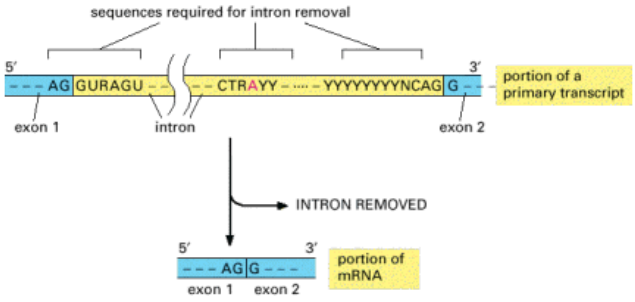

Figure 6-29. The RNA splicing mechanism. RNA splicing is catalyzed by an assembly of snRNPs (shown as *colored circles)* plus other proteins (most of which are not shown), which together constitute the spliceosome. The spliceosome recognizes the splicing signals on a pre-mRNA molecule, brings the two ends of the intron together, and provides the enzymatic activity for the two reaction steps (see Figure 6-26). The branch-point site is first recognized by the BBP (branch-point binding protein) and U2AF, a helper protein. In the next steps, the U2 snRNP displaces BBP and U2AF and forms base pairs with the branch-point site consensus sequence, and the U1 snRNP forms base-pairs with the 5 splice junction (see Figure 6-30). At this point, the U4/U6U5 "triple" snRNP enters the spliceosome. In this triple snRNP, the U4 and U6 snRNAs are held firmly together by base-pair interactions and the U5 snRNP is more loosely associated. Several RNA-RNA rearrangements then occur that break apart the U4/U6 base pairs (as shown, the U4 snRNP is ejected from the splicesome before splicing is complete) and allow the U6 snRNP to displace U1 at the 5 splice junction (see Figure 6-30). Subsequent rearrangements create the active site of the spliceosome and position the appropriate portions of the pre-mRNA substrate for the splicing reaction to occur. Although not shown in the figure, each splicing event requires additional proteins, some of which hydrolyze ATP and promote the RNA-RNA rearrangements.

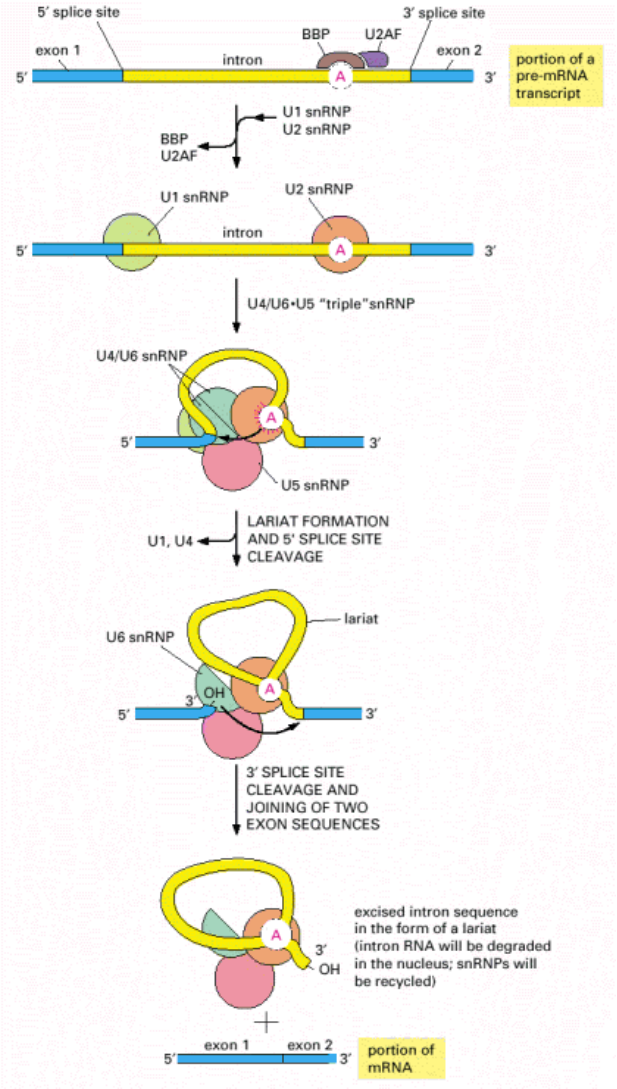

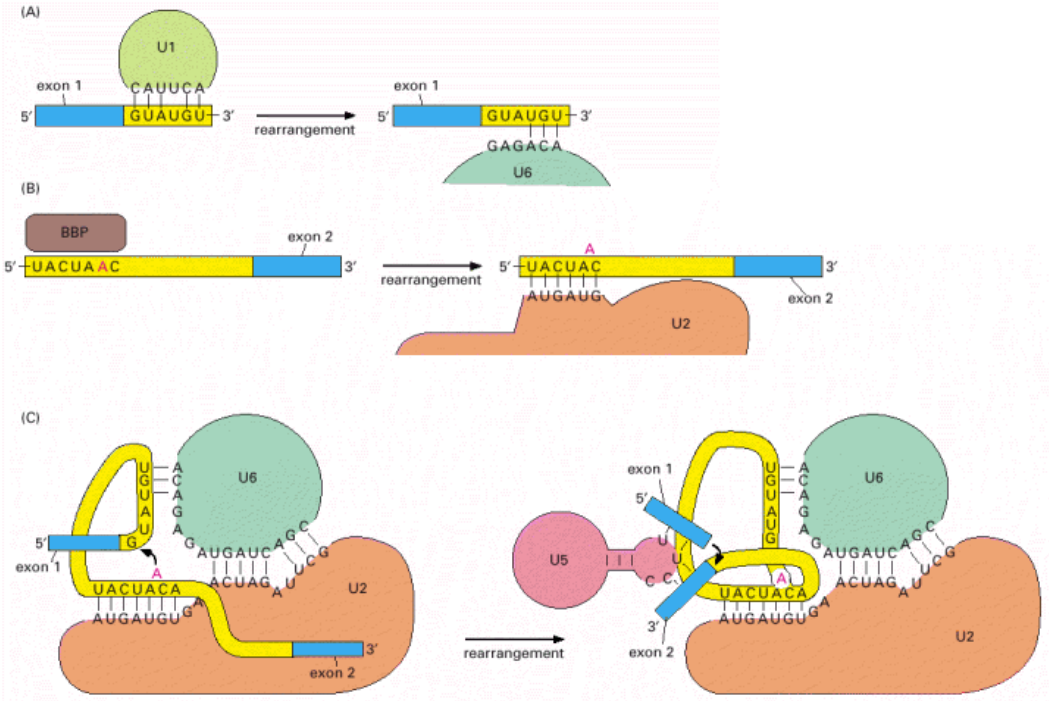

Figure 6-30. Several of the rearrangements that take place in the spliceosome during pre-mRNA splicing. Shown here are the details for the yeast *Saccharomyces cerevisiae*, in which the nucleotide sequences involved are slightly different from those in human cells. (A) The exchange of U1 snRNP for U6 snRNP occurs before the first phosphoryl-transfer reaction (see Figure 6-29). This exchange allows the 5 splice site to be read by two different snRNPs, thereby increasing the accuracy of 5 splice site selection by the spliceosome. (B) The branch-point site is first recognized by BBP and subsequently by U2 snRNP; as in (A), this "check and recheck" strategy provides increased accuracy of site selection. The binding of U2 to the branch-point forces the appropriate adenine (in *red)* to be unpaired and thereby activates it for the attack on the 5 splice site (see Figure 6-29). This, in combination with recognition by BBP, is the way in which the spliceosome accurately chooses the adenine that is ultimately to form the branch point. (C) After the first phosphoryl-transfer reaction *(left)* has occurred, U5 snRNP undergoes a rearrangement that brings the two exons into close proximity for the second phosphoryl-transfer reaction *(right).* The snRNAs both position the reactants and provide (either all or in part) the catalytic site for the two reactions. The U5 snRNP is present in the spliceosome before this rearrangement occurs; for clarity it has been omitted from the left panel. As discussed in the text, all of the RNA-RNA rearrangements shown in this figure (as well as others that occur in the spliceosome but are not shown) require the participation of additional proteins and ATP hydrolysis.

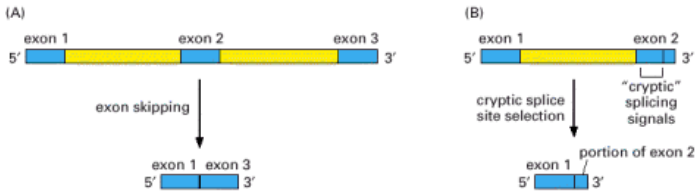

Figure 6-31. Two types of splicing errors. Both types might be expected to occur frequently if splice-site selection were performed by the spliceosome on a preformed, protein-free RNA molecule. "Cryptic" splicing signals are nucleotide sequences of RNA that closely resemble true splicing signals.

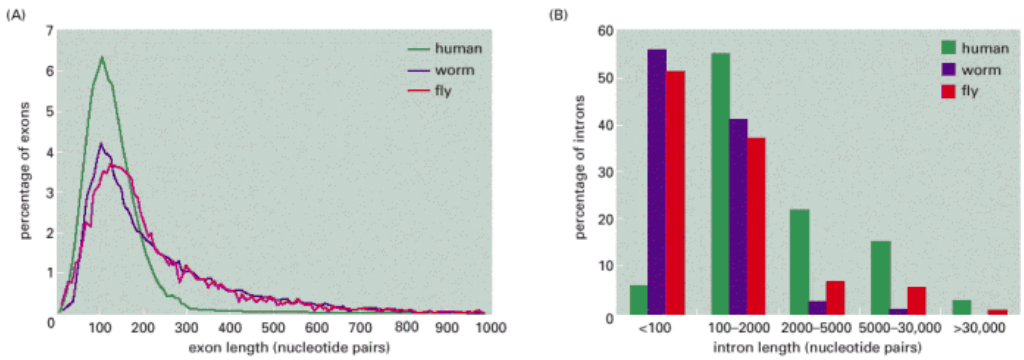

Figure 6-32. Variation in intron and exon lengths in the human, worm, and fly genomes. (A) Size distribution of exons. (B) Size distribution of introns. Note that exon length is much more uniform than intron length. (Adapted from International Human Genome Sequencing Consortium, *Nature* 409:860921, 2001.)

Figure 6-33. The exon definition hypothesis. According to one proposal, SR proteins bind to each exon sequence in the pre-mRNA and thereby help to guide the snRNPs to the proper intron/exon boundaries. This demarcation of exons by the SR proteins occurs co-transcriptionally, beginning at the CBC (cap-binding complex) at the 5 end. As indicated, the intron sequences in the pre-mRNA, which can be extremely long, are packaged into hnRNP (heterogeneous nuclear ribonucleoprotein) complexes that compact them into more manageable structures and perhaps mask cryptic splice sites. Each hnRNP complex forms a particle approximately twice the diameter of a nucleosome, and the core is composed of a set of at least eight different proteins. It has been proposed that hnRNP proteins preferentially associate with intron sequences and that this preference also helps the spliceosome distinguish introns from exons. However, as shown, at least some hnRNP proteins may bind to exon sequences but their role, if any, in exon definition has yet to be established. (Adapted from R. Reed, *Curr.*

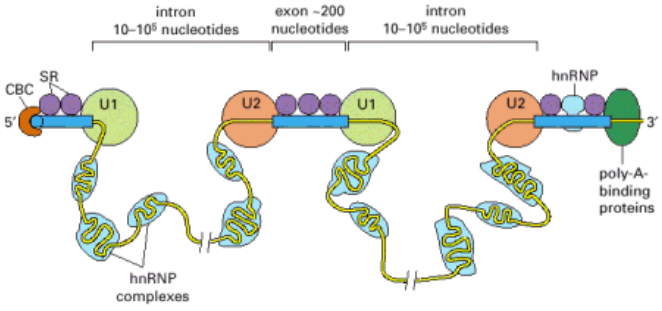

Opin. Cell Biol. 12:340345, 2000.)

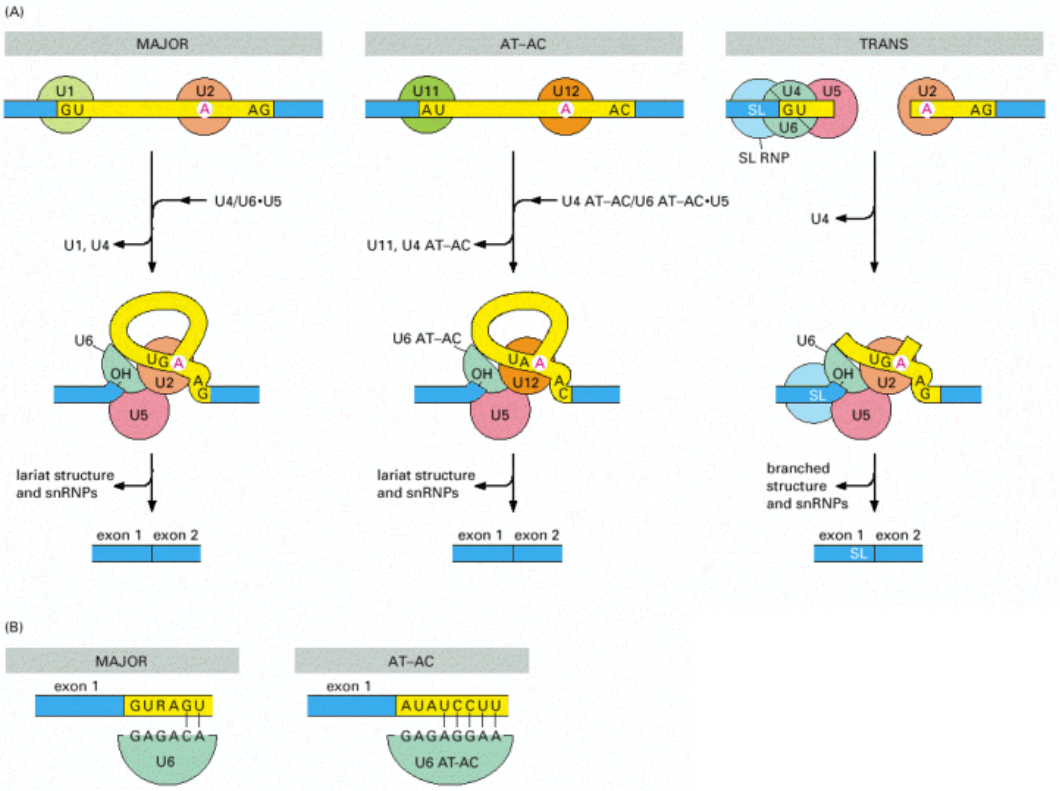

Figure 6-34. Outline of the mechanisms used for three types of RNA splicing. (A) Three types of spliceosomes. The major spliceosome *(left)*, the AT-AC spliceosome (middle), and the trans-spliceosome *(right)* are each shown at two stages of assembly. The U5 snRNP is the only component that is common to all three spliceosomes. Introns removed by the AT-AC spliceosome have a different set of consensus nucleotide sequences from those removed by the major spliceosome. In humans, it is estimated that 0.1% of introns are removed by the AT-AC spliceosome. In trans-splicing, the SL snRNP is consumed in the reaction because a portion of the SL snRNA becomes the first exon of the mature mRNA. (B) The major U6 snRNP and the U6 AT-AC snRNP both recognize the 5 splice junction, but they do so through a different set of base-pair interactions. The sequences shown are from humans. (Adapted from Y.-T. Yu et al., The RNA World, pp. 487524. Cold Spring Harbor, New York: Cold Spring Harbor Laboratory Press, 1999.)

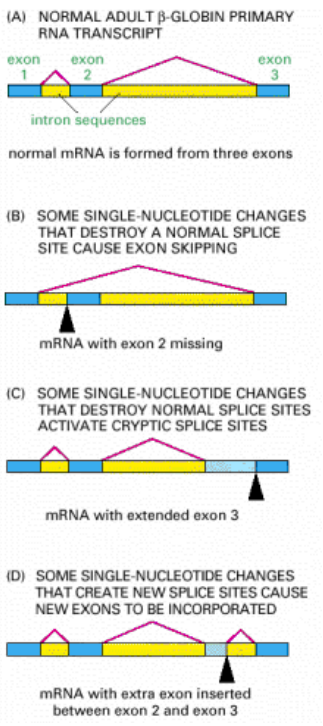

Figure 6-35. Abnormal processing of the β-globin primary RNA transcript in humans with the disease β thalassemia. In the examples shown, the disease is caused by splice-site mutations, denoted by *black arrowheads*. The *dark blue boxes* represent the three normal exon sequences; the *red lines* are used to indicate the 5 and 3 splice sites that are used in splicing the RNA transcript. The *light blue boxes* depict new nucleotide sequences included in the final mRNA molecule as a result of the mutation. Note that when a mutation leaves a normal splice site without a partner, an exon is skipped or one or more abnormal "cryptic" splice sites nearby is used as the partner site, as in (C) and (D). (Adapted in part from S.H. Orkin, in The Molecular Basis of Blood Diseases [G. Stamatoyannopoulos et al., eds.], pp. 106126. Philadelphia: Saunders, 1987.)

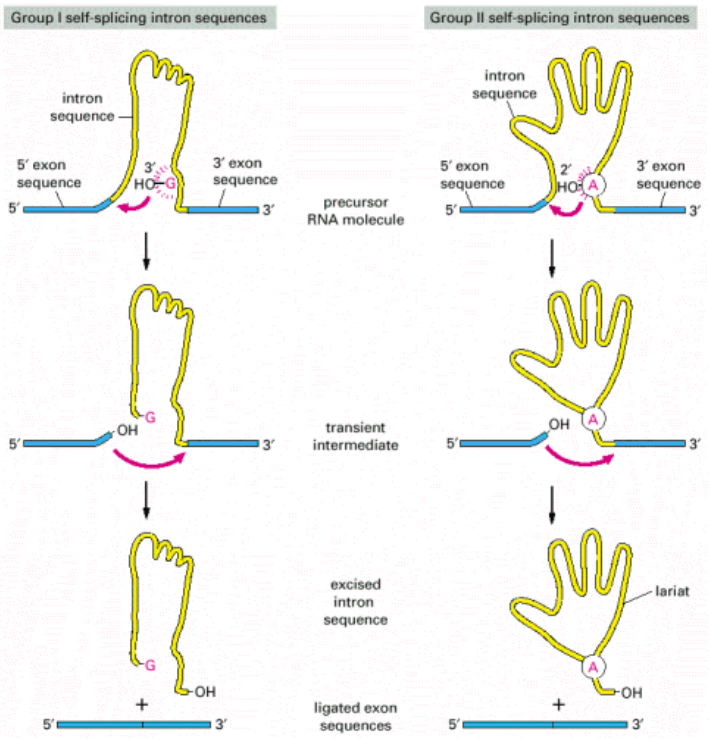

Figure 6-36. The two known classes of self-splicing intron sequences. The group I intron sequences bind a free G nucleotide to a specific site on the RNA to initiate splicing, while the group II intron sequences use an especially reactive A nucleotide in the intron sequence itself for the same purpose. The two mechanisms have been drawn to emphasize their similarities. Both are normally aided in the cell by proteins that speed up the reaction, but the catalysis is nevertheless mediated by the RNA in the intron sequence. Both types of self-splicing reactions require the intron to be folded into a highly specific three-dimensional structure that provides the catalytic activity for the reaction (see Figure 6-6). The mechanism used by group II intron sequences releases the intron as a lariat structure and closely resembles the pathway of pre-mRNA splicing catalyzed by the spliceosome (compare with Figure 6-29). The great majority of RNA splicing in eucaryotic cells is performed by the spliceosome, and self-splicing RNAs represent unusual cases. (Adapted from T.R. Cech, *Cell* 44:207210, 1986.)

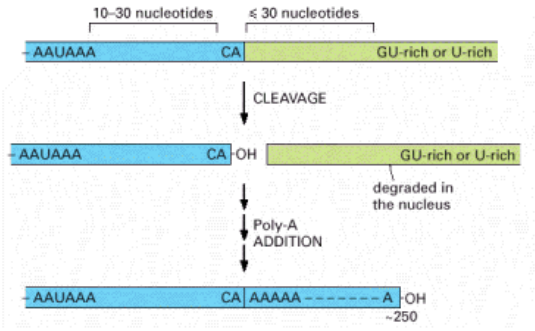

Figure 6-37. Consensus nucleotide sequences that direct cleavage and polyadenylation to form the 3 end of a eucaryotic mRNA. These sequences are encoded in the genome and are recognized by specific proteins after they are transcribed into RNA. The hexamer AAUAAA is bound by CPSF, the GU-rich element beyond the cleavage site by CstF (see Figure 6-38), and the CA sequence by a third factor required for the cleavage step. Like other consensus nucleotide sequences discussed in this chapter (see Figure 6-12), the sequences shown in the figure represent a variety of individual cleavage and polyadenylation signals.

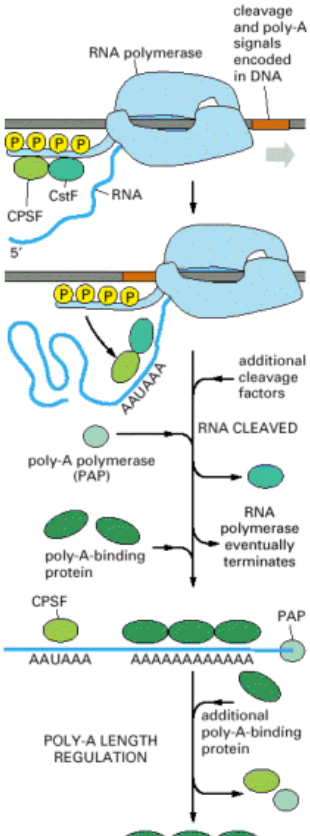

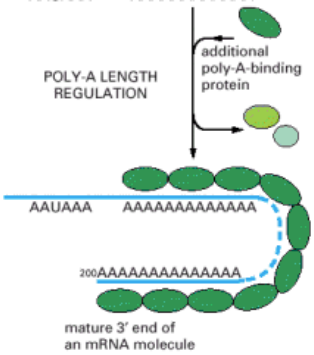

Figure 6-38. Some of the major steps in generating the 3 end of a eucaryotic mRNA. This process is much more complicated than the analogous process in bacteria, where the RNA polymerase simply stops at a termination signal and releases both the 3 end of its transcript and the DNA template (see Figure 6-10).

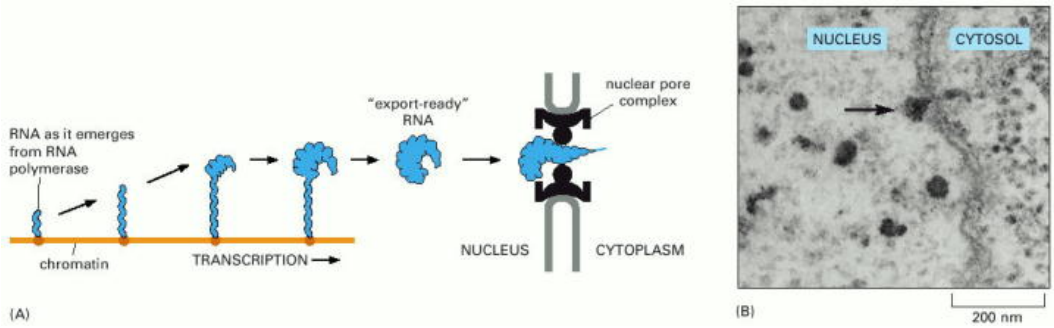

Figure 6-39. Transport of a large mRNA molecule through the nuclear pore complex. (A) The maturation of a Balbiani Ring mRNA molecule as it is synthesized by RNA polymerase and packaged by a variety of nuclear proteins. This drawing of unusually abundant RNA produced by an insect cell is based on EM micrographs such as that shown in (B). Balbiani Rings are described in Chapter 4. (A, adapted from B. Daneholt, *Cell* 88:585588, 1997; B, from B.J. Stevens and H. Swift, *J. Cell Biol.* 31:5577, 1966. © The Rockefeller University Press.)

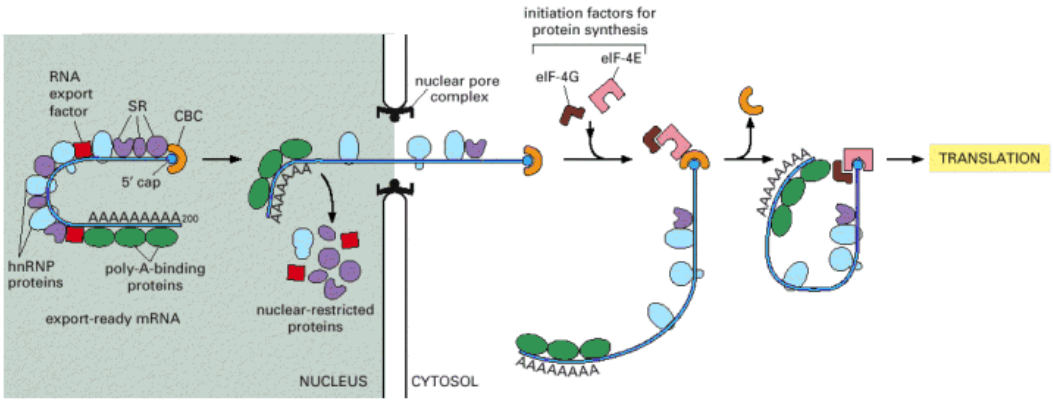

Figure 6-40. Schematic illustration of an "export-ready" mRNA molecule and its transport through the nuclear pore. As indicated, some proteins travel with the mRNA as it moves through the pore, whereas others remain in the nucleus. Once in the cytoplasm, the mRNA continues to shed previously bound proteins and acquire new ones; these substitutions affect the subsequent translation of the message. Because some are transported with the RNA, the proteins that become bound to an mRNA in the nucleus can influence its subsequent stability and translation in the cytosol. RNA export factors, shown in the nucleus, play an active role in transporting the mRNA to the cytosol (see Figure 12-16). Some are deposited at exon-exon boundaries as splicing is completed, thus signifying those regions of the RNA that have been properly spliced.

Figure 6-41. Transcription from tandemly arranged rRNA genes, as seen in the electron microscope. The pattern of alternating transcribed gene and nontranscribed spacer is readily seen. A higher-magnification view was shown in Figure 6-9. (From V.E. Foe, *Cold Spring Harbor Symp. Quant. Biol.* 42:723740, 1978.)

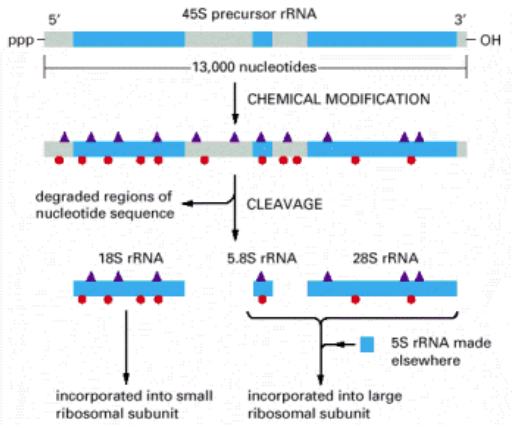

Figure 6-42. The chemical modification and nucleolytic processing of a eucaryotic 45S precursor rRNA molecule into three separate ribosomal RNAs. As indicated, two types of chemical modifications (shown in Figure 6-43) are made to the precursor rRNA before it is cleaved. Nearly half of the nucleotide sequences in this precursor rRNA are discarded and degraded in the nucleus. The rRNAs are named according to their "S" values, which refer to their rate of sedimentation in an ultra-centrifuge. The larger the S value, the larger the rRNA.

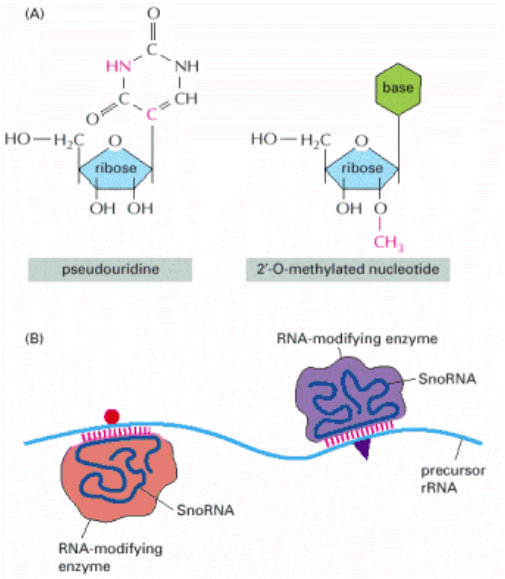

Figure 6-43. Modifications of the precursor rRNA by guide RNAs. (A) Two prominent covalent modifications occur after rRNA synthesis; the differences from the initially incorporated nucleotide are indicated by *red* atoms. (B) As indicated, snoRNAs locate the sites of modification by base-pairing to complementary sequences on the precursor rRNA. The snoRNAs are bound to proteins, and the complexes are called snoRNPs. snoRNPs contain the RNA modification activities, presumably contributed by the proteins but possibly by the snoRNAs themselves.

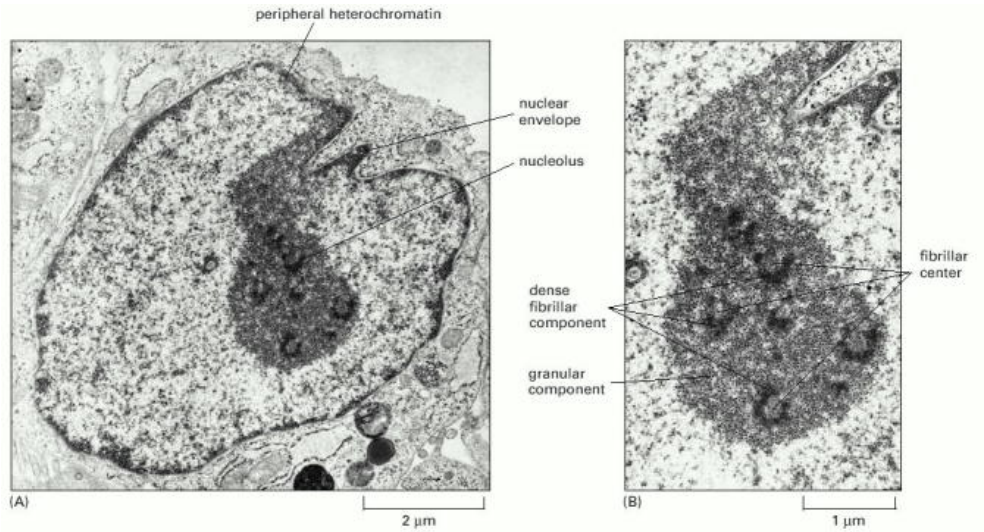

Figure 6-44. Electron micrograph of a thin section of a nucleolus in a human fibroblast, showing its three distinct zones. (A) View of entire nucleus. (B) High-power view of the nucleolus. It is believed that transcription of the rRNA genes takes place between the fibrillar center and the dense fibrillar component and that processing of the rRNAs and their assembly into ribosomes proceeds outward from the dense fibrillar component to the surrounding granular components. (Courtesy of E. G. Jordan and J. McGovern.)

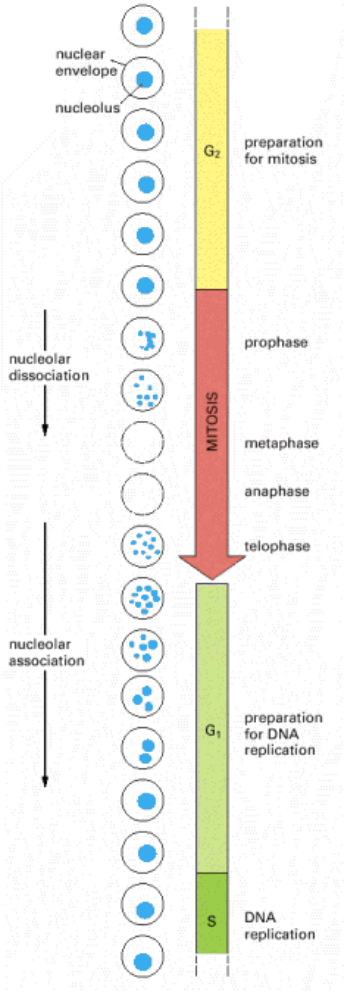

Figure 6-45. Changes in the appearance of the nucleolus in a human cell during the cell cycle. Only the cell nucleus is represented in this diagram. In most eucaryotic cells the nuclear membrane breaks down during mitosis, as indicated by the dashed circles.

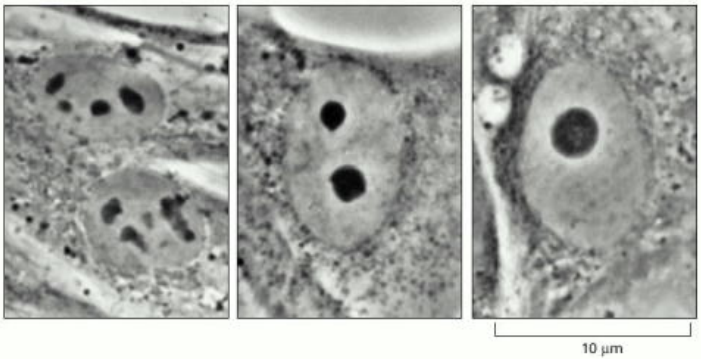

Figure 6-46. Nucleolar fusion. These light micrographs of human fibroblasts grown in culture show various stages of nucleolar fusion. After mitosis, each of the ten human chromosomes that carry a cluster of rRNA genes begins to form a tiny nucleolus, but these rapidly coalesce as they grow to form the single large nucleolus typical of many interphase cells. (Courtesy of E.G. Jordan and J. McGovern.)

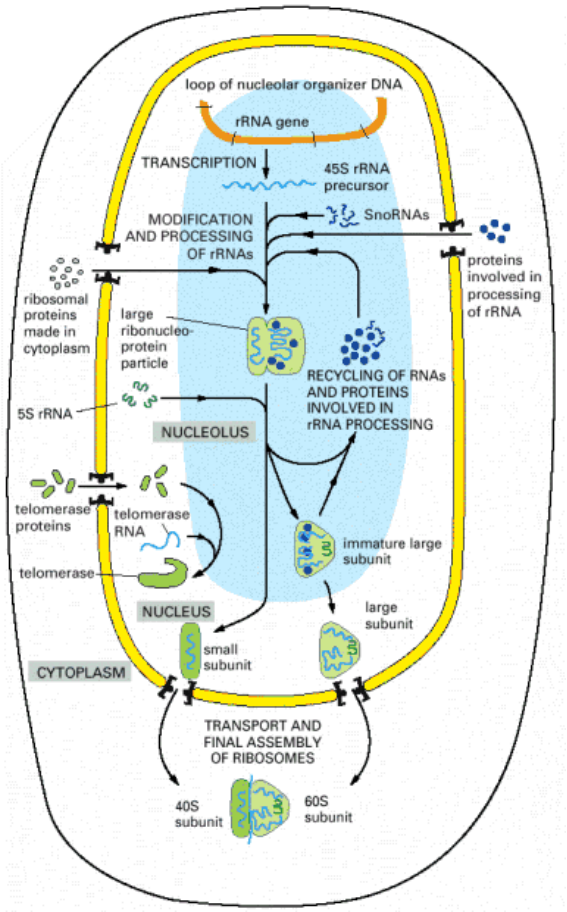

Figure 6-47. The function of the nucleolus in ribosome and other ribonucleoprotein synthesis. The 45S precursor rRNA is packaged in a large ribonucleoprotein particle containing many ribosomal proteins imported from the cytoplasm. While this particle remains in the nucleolus, selected pieces are added and others discarded as it is processed into immature large and small ribosomal subunits. The two ribosomal subunits are thought to attain their final functional form only as each is individually transported through the nuclear pores into the cytoplasm. Other ribonucleoprotein complexes, including telomerase shown here, are also assembled in the nucleolus.

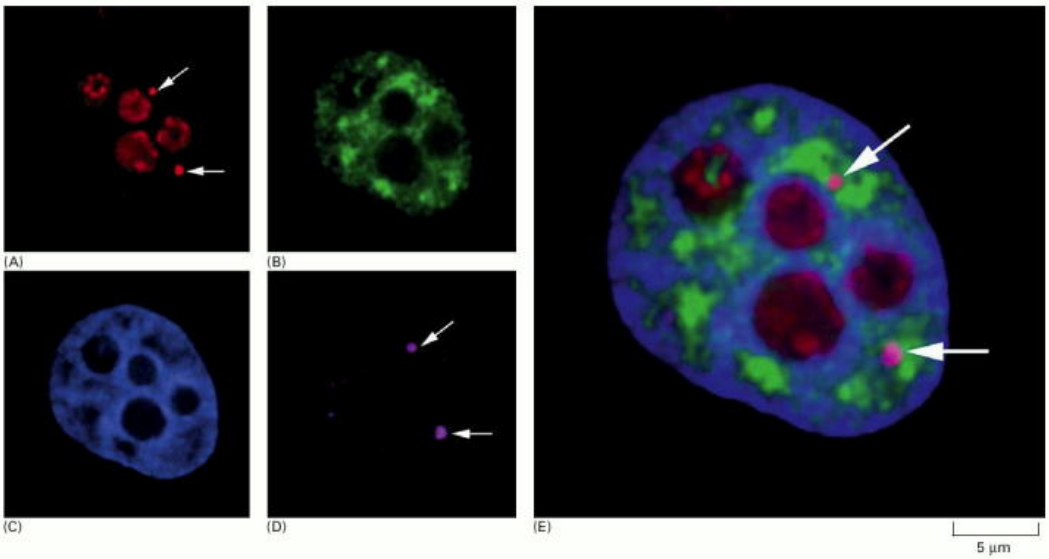

Figure 6-48. Visualization of chromatin and nuclear bodies. (A)-(D) show micrographs of the same human cell nucleus, each processed differently to show a particular set of nuclear structures. (E) shows an enlarged superposition of all four individual images. (A) shows the location of the protein fibrillarin (a component of several snoRNPs), which is present at both nucleoli and Cajal bodies, the latter indicated by arrows. (B) shows interchromatin granule clusters or "speckles" detected by using antibodies against a protein involved in pre-mRNA splicing. (C) is stained to show bulk chromatin. (D) shows the location of the protein coilin, which is present at Cajal bodies (indicated by arrows). (From J.R. Swedlow and A.I. Lamond, *Gen. Biol.* 2:17, 2001; micrographs courtesy of Judith Sleeman.)

Figure 6-49. Schematic view of subnuclear structures. A typical vertebrate nucleus has several Cajal bodies, which are proposed to be the sites where snRNPs and snoRNPs undergo their final modifications. Interchromatin granule clusters are proposed to be storage sites for fully mature snRNPs. A typical vertebrate nucleus has 2050 interchromatin granule clusters. After their initial synthesis, snRNAs are exported from the nucleus, after which they undergo 5 and 3 end-processing and assemble with the seven common snRNP proteins (called Sm

proteins). These complexes are reimported into the nucleus and the snRNPs undergo their final modification in Cajal bodies. In addition, the U6 snRNP requires chemical modification by snoRNAs in the nucleolus. The sites of active transcription and splicing (approximately 20003000 sites per vertebrate nucleus) correspond to the "perichromatin fibers" seen under the electron microscope. (Adapted from J.D. Lewis and D. Tollervey, *Science*288:13851389, 2000.)

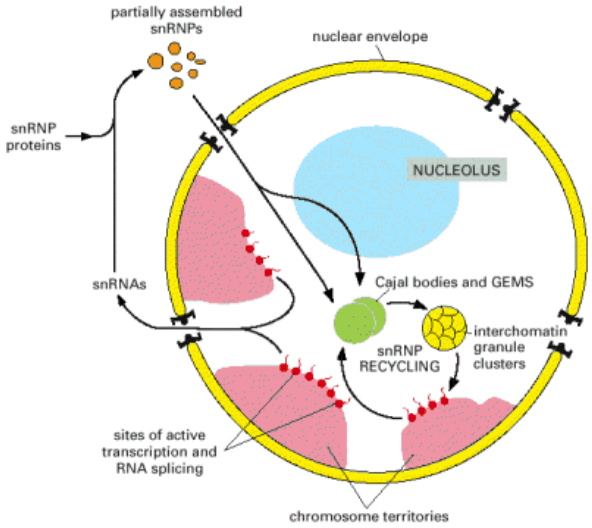

GCA GCC GCG GCU	AGA AGG CGA CGC CGG CGU	GAC GAU	AAC AAU	UGC UGU	GAA GAG	CAA CAG	GGA GGC GGG GGU	CAC CAU	AUA AUC AUU	UUA UUG CUA CUC CUG CUU	AAA AAG	AUG	UUC UUU	CCA CCC CCG CCU	AGC AGU UCA UCC UCG UCU	ACA ACC ACG ACU	UGG	UAC UAU	GUA GUC GUG GUU	UAA UAG UGA
Ala	Arg	Asp	Asn	Cys	Glu	Gln	Gly	His	Ile	Leu	Lys	Met	Phe	Pro	Ser	Thr	Trp	Tyr	Val	stop
A	R	D	N	C	E	Q	G	H	I	L	K	M	F	P	S	T	W	Y	V	

Figure 6-50. The genetic code. The standard one-letter abbreviation for each amino acid is presented below its three-letter abbreviation (see Panel 3-1, pp. 132133, for the full name of each amino acid and its structure). By convention, codons are always written with the 5-terminal nucleotide to the left. Note that most amino acids are represented by more than one codon, and that there are some regularities in the set of codons that specifies each amino acid. Codons for the same amino acid tend to contain the same nucleotides at the first and second positions, and vary at the third position. Three codons do not specify any amino acid but act as termination sites (stop codons), signaling the end of the protein-coding sequence. One codon - AUG - acts both as an initiation codon, signaling the start of a protein-coding message, and also as the codon that specifies methionine.

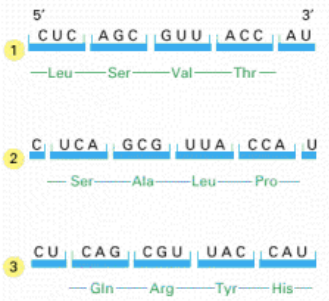

Figure 6-51. The three possible reading frames in protein synthesis. In the process of translating a nucleotide sequence *(blue)* into an amino acid sequence *(green)*, the sequence of nucleotides in an mRNA molecule is read from the 5 to the 3 end in sequential sets of three nucleotides. In principle, therefore, the same RNA sequence can specify three completely different amino acid sequences, depending on the reading frame. In reality, however, only one of these reading frames contains the actual message.

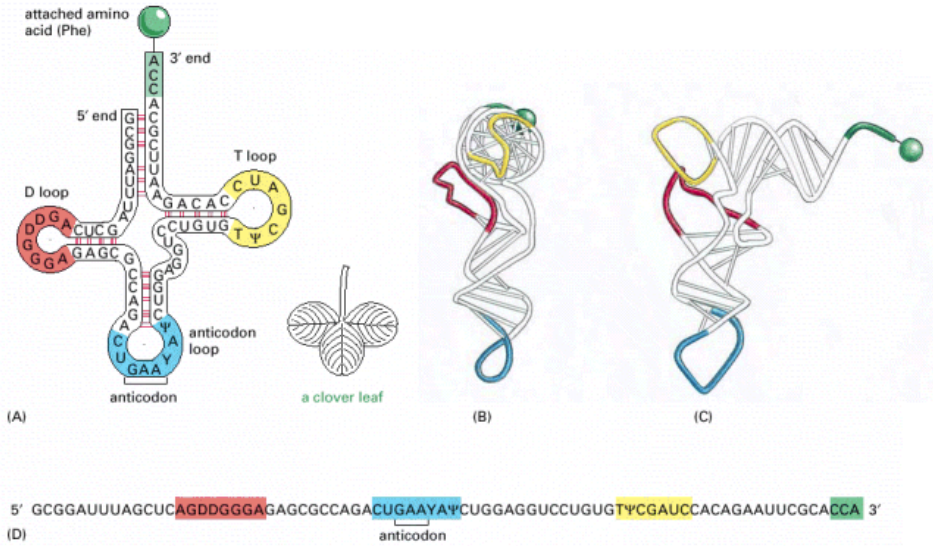

Figure 6-52. A tRNA molecule. In this series of diagrams, the same tRNA molecule - in this case a tRNA specific for the amino acid phenylalanine (Phe) - is depicted in various ways. (A) The cloverleaf structure, a convention used to show the complementary base-pairing *(red lines)* that creates the double-helical regions of the molecule. The anticodon is the sequence of three nucleotides that base-pairs with a codon in mRNA. The amino acid matching the codon/anticodon pair is attached at the 3 end of the tRNA. tRNAs contain some unusual bases, which are produced by chemical modification after the tRNA has been synthesized. For example, the bases denoted Ψ (for pseudouridine - see Figure 6-43) and D (for dihydrouridine - see Figure 6-55) are derived from uracil. (B and C) Views of the actual L-shaped molecule, based on x-ray diffraction analysis. Although a particular tRNA, that for the amino acid phenylalanine, is depicted, all other tRNAs have very similar structures. (D) The linear nucleotide sequence of the molecule, color-coded to match A, B, and C.

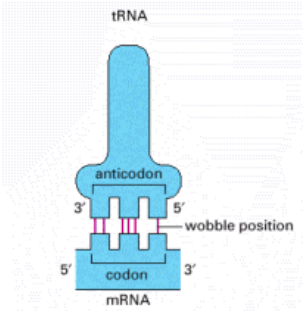

bacteria

wobble codon base	possible anticodon bases
U	A, G, or I
C	G or I
A	U or I
G	C or U

eucaryotes

wobble codon base	possible anticodon bases
U	G or I
C	G or I
A	U
G	C

Figure 6-53. Wobble base-pairing between codons and anticodons. If the nucleotide listed in the first column is present at the third, or wobble, position of the codon, it can base-pair with any of the nucleotides listed in the second column. Thus, for example, when inosine (I) is present in the wobble position of the tRNA anticodon, the tRNA can recognize any one of three different codons in bacteria and either of two codons in eucaryotes. The inosine in tRNAs is formed from the deamination of guanine (see Figure 6-55), a chemical modification which takes place after the tRNA has been synthesized. The nonstandard base pairs, including those made with inosine, are generally weaker than conventional base pairs. Note that codon-anticodon base pairing is more stringent at positions 1 and 2 of the codon: here only conventional base pairs are permitted. The differences in wobble base-pairing interactions between bacteria and eucaryotes presumably result from subtle structural differences between bacterial and eucaryotic ribosomes, the molecular machines that perform protein synthesis. (Adapted from C. Guthrie and J. Abelson, in The Molecular Biology of the Yeast *Saccharomyces*: Metabolism and Gene Expression, pp. 487528. Cold Spring Harbor, New York: Cold Spring Harbor Laboratory Press, 1982.)

Figure 6-54. Structure of a tRNA-splicing endonuclease docked to a precursor tRNA. The endonuclease (a four-subunit enzyme) removes the tRNA intron *(blue).* A second enzyme, a multifunctional tRNA ligase (not shown), then joins the two tRNA halves together. (Courtesy of Hong Li, Christopher Trotta, and John Abelson.)

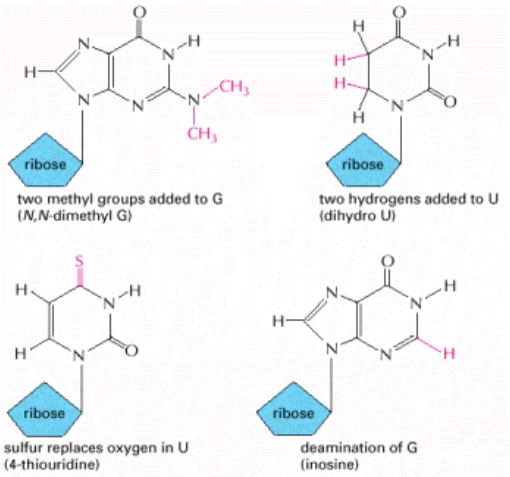

Figure 6-55. A few of the unusual nucleotides found in tRNA molecules. These nucleotides are produced by covalent modification of a normal nucleotide after it has been incorporated into an RNA chain. In most tRNA molecules about 10% of the nucleotides are modified (see Figure 6-52).

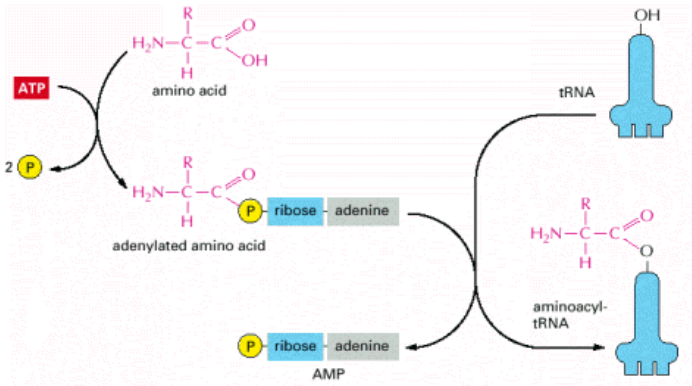

Figure 6-56. Amino acid activation. The two-step process in which an amino acid (with its side chain denoted by R) is activated for protein synthesis by an aminoacyl-tRNA synthetase enzyme is shown. As indicated, the energy of ATP hydrolysis is used to attach each amino acid to its tRNA molecule in a high-energy linkage. The amino acid is first activated through the linkage of its carboxyl group directly to an AMP moiety, forming an *adenylated amino acid*; the linkage of the AMP, normally an unfavorable reaction, is driven by the hydrolysis of the ATP molecule that donates the AMP. Without leaving the synthetase enzyme, the AMP-linked carboxyl group on the amino acid is then transferred to a hydroxyl group on the sugar at the 3 end of the tRNA molecule. This transfer joins the amino acid by an activated ester linkage to the tRNA and forms the final aminoacyl-tRNA molecule. The synthetase enzyme is not shown in this diagram.

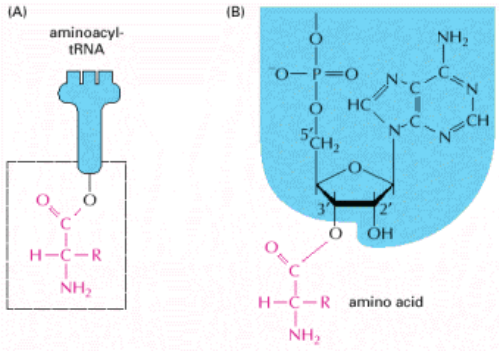

Figure 6-57. The structure of the aminoacyl-tRNA linkage. The carboxyl end of the amino acid forms an ester bond to ribose. Because the hydrolysis of this ester bond is associated with a large favorable change in free energy, an amino acid held in this way is said to be activated. (A) Schematic drawing of the structure. The amino acid is linked to the nucleotide at the 3 end of the tRNA (see Figure 6-52). (B) Actual structure corresponding to boxed region in (A). These are two major classes of synthetase enzymes: one links the amino acid directly to the 3-OH group of the ribose, and the other links it initially to the 2-OH group. In the latter case, a subsequent transesterification reaction shifts the amino acid to the 3 position. As in Figure 6-56, the "R-group" indicates the side chain of the amino acid.

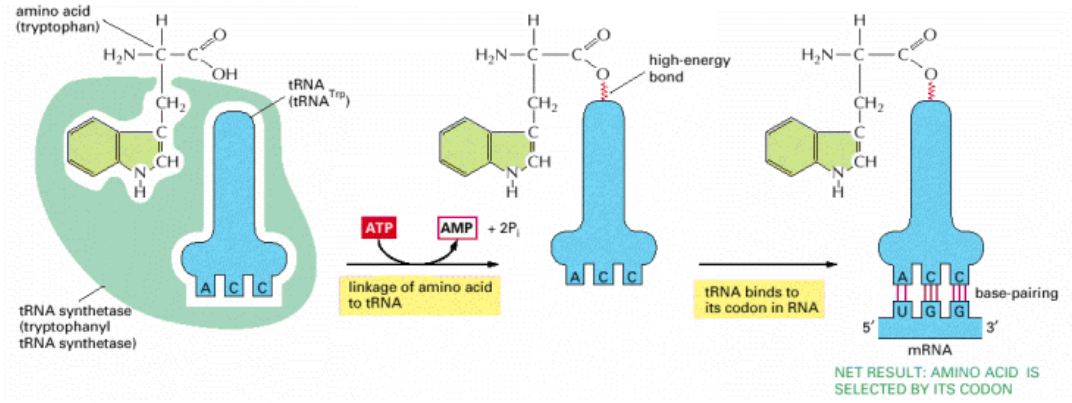

Figure 6-58. The genetic code is translated by means of two adaptors that act one after another. The first adaptor is the aminoacyl-tRNA synthetase, which couples a particular amino acid to its corresponding tRNA; the second adaptor is the tRNA molecule itself, whose *anticodon* forms base pairs with the appropriate *codon* on the mRNA. An error in either step would cause the wrong amino acid to be incorporated into a protein chain. In the sequence of events shown, the amino acid tryptophan (Trp) is selected by the codon UGG on the mRNA.

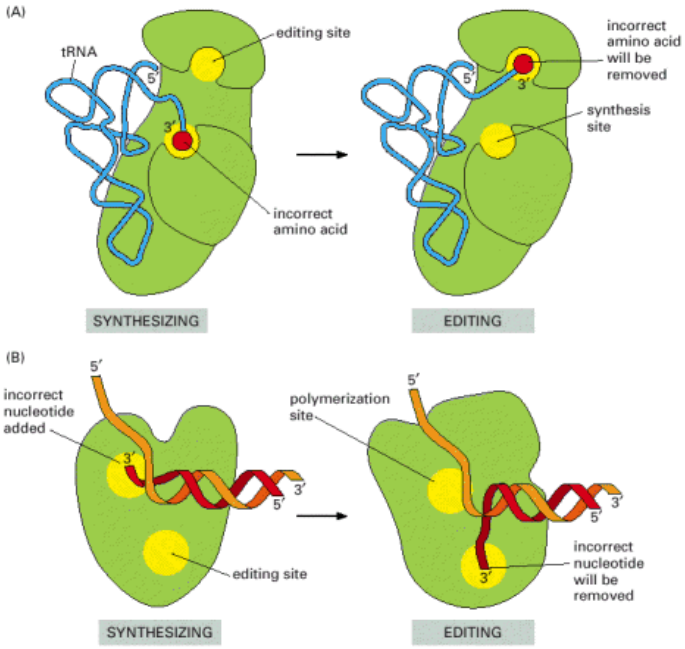

Figure 6-59. Hydrolytic editing. (A) tRNA synthetases remove their own coupling errors through hydrolytic editing of incorrectly attached amino acids. As described in the text, the correct amino acid is rejected by the editing site. (B) The error-correction process performed by DNA polymerase shows some similarities; however, it differs so far as the removal process depends strongly on a mispairing with the template (see Figure 5-9).

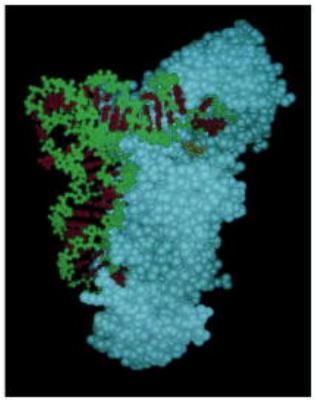

Figure 6-60. The recognition of a tRNA molecule by its aminoacyl-tRNA synthetase. For this tRNA ($tRNA^{Gln}$), specific nucleotides in both the anticodon *(bottom)* and the amino acid-accepting arm allow the correct tRNA to be recognized by the synthetase enzyme *(blue).* (Courtesy of Tom Steitz.)

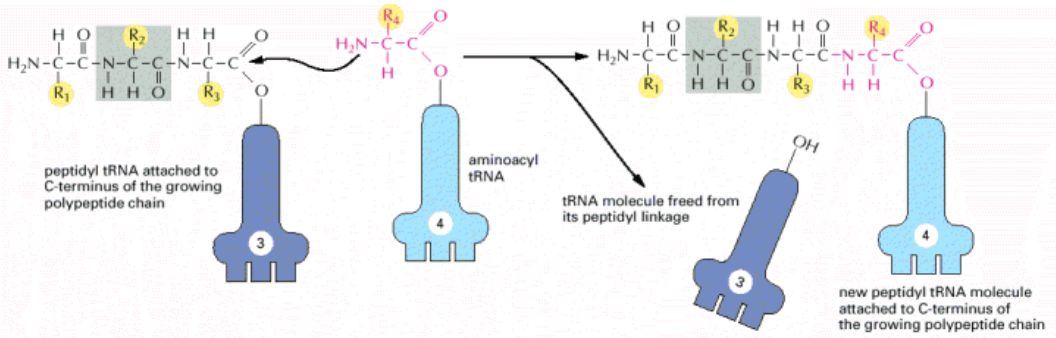

Figure 6-61. The incorporation of an amino acid into a protein. A polypeptide chain grows by the stepwise addition of amino acids to its C-terminal end. The formation of each peptide bond is energetically favorable because the growing C-terminus has been activated by the covalent attachment of a tRNA molecule. The peptidyl-tRNA linkage that activates the growing end is regenerated during each addition. The amino acid side chains have been abbreviated as R_1, R_2, R_3, and R_4; as a reference point, all of the atoms in the second amino acid in the polypeptide chain are shaded *gray*. The figure shows the addition of the fourth amino acid to the growing chain.

Figure 6-62. Ribosomes in the cytoplasm of a eucaryotic cell. This electron micrograph shows a thin section of a small region of cytoplasm. The ribosomes appear as black dots *(red arrows).* Some are free in the cytosol; others are attached to membranes of the endoplasmic

reticulum. (Courtesy of Daniel S. Friend.)

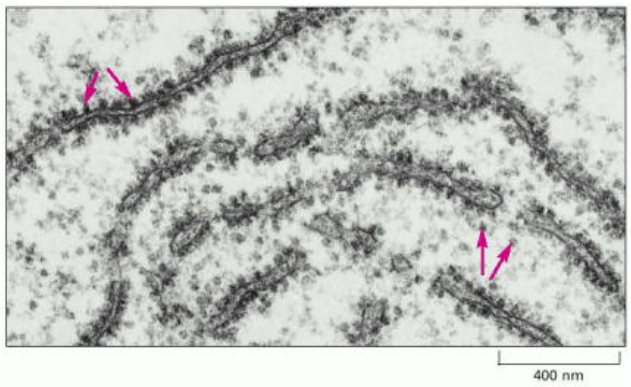

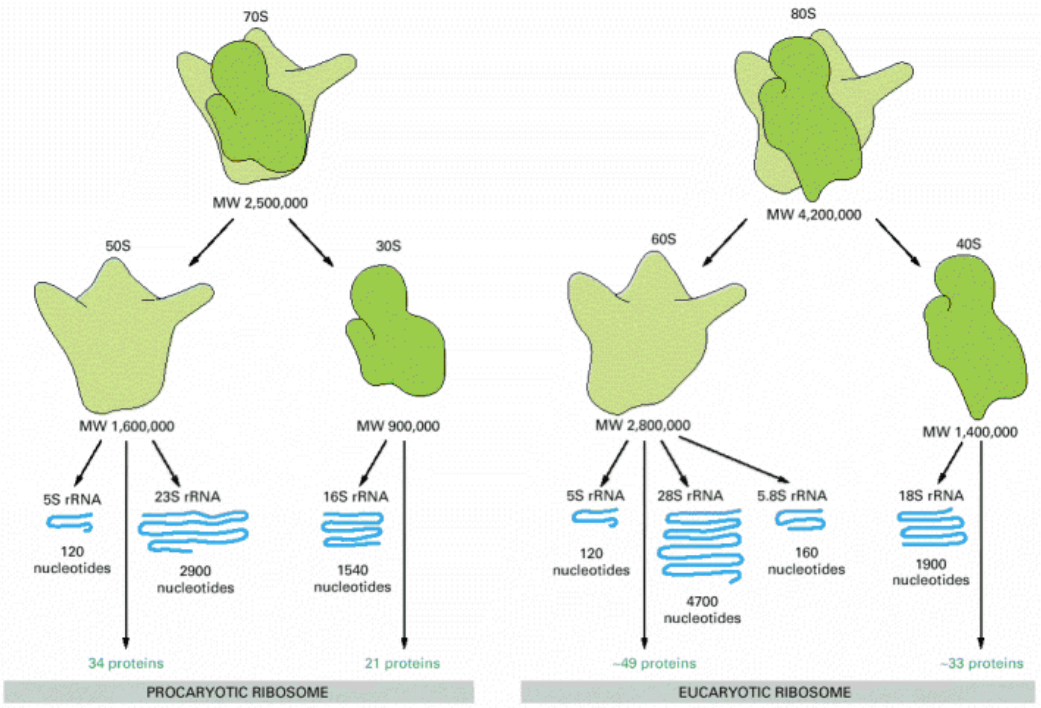

Figure 6-63. A comparison of the structures of procaryotic and eucaryotic ribosomes. Ribosomal components are commonly designated by their "S values," which refer to their rate of sedimentation in an ultracentrifuge. Despite the differences in the number and size of their rRNA and protein components, both procaryotic and eucaryotic ribosomes have nearly the same structure and they function similarly. Although the 18S and 28S rRNAs of the eucaryotic ribosome contain many extra nucleotides not present in their bacterial counterparts, these nucleotides are present as multiple insertions that form extra domains and leave the basic structure of each rRNA largely unchanged.

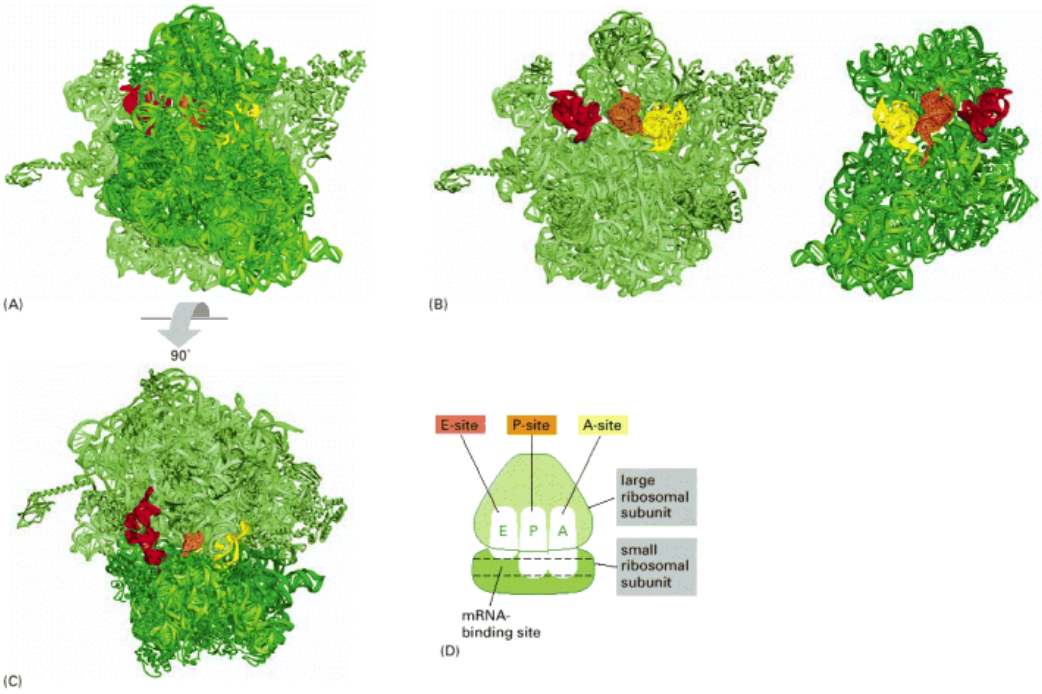

Figure 6-64. The RNA-binding sites in the ribosome. Each ribosome has three binding sites for tRNA: the A-, P-, and E-sites (short for aminoacyl-tRNA, peptidyl-tRNA, and exit, respectively) and one binding site for mRNA. (A) Structure of a bacterial ribosome with the small subunit in the front *(dark green)* and the large subunit in the back *(light green)*. Both the rRNAs and the ribosomal proteins are shown. tRNAs are shown bound in the E-site *(red)*, the P-site *(orange)* and the A-site *(yellow)*. Although all three tRNA sites are shown occupied here, during the process of protein synthesis not more than two of these sites are thought to contain tRNA molecules at any one time (see Figure 6-65). (B) Structure of the large *(left)* and small *(right)* ribosomal subunits arranged as though the ribosome in (A) were opened like a book. (C) Structure of the ribosome in (A) viewed from the top. (D) Highly schematic representation of a ribosome (in the same orientation as C), which will be used in subsequent figures. (A, B, and C, adapted from M.M. Yusupov et al., *Science* 292:883896, 2001, courtesy of Albion Bausom and Harry Noller.)

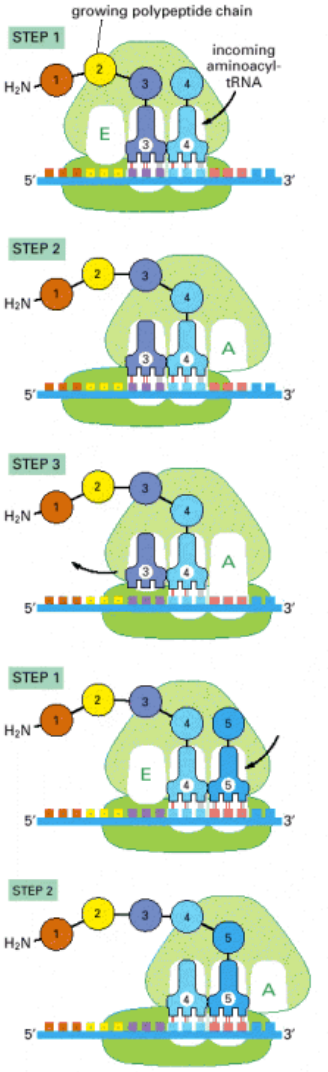

Figure 6-65. Translating an mRNA molecule. Each amino acid added to the growing end of a polypeptide chain is selected by complementary base-pairing between the anticodon on its attached tRNA molecule and the next codon on the mRNA chain. Because only one of the many types of tRNA molecules in a cell can base-pair with each codon, the codon determines the specific amino acid to be added to the growing polypeptide chain. The three-step cycle shown is repeated over and over during the synthesis of a protein. An aminoacyl-tRNA molecule binds to a vacant A-site on the ribosome in step 1, a new peptide bond is formed in step 2, and the mRNA moves a distance of three nucleotides through the small-subunit chain in step 3, ejecting the spent tRNA molecule and "resetting" the ribosome so that the next aminoacyl-tRNA molecule can bind. Although the figure shows a large movement of the small ribosome subunit relative to the large subunit, the conformational changes that actually take place in the ribosome during translation are more subtle. It is likely that they involve a series of small rearrangements within each subunit as well as several small shifts between the two subunits. As indicated, the mRNA is translated in the 5-to-3 direction, and the N-terminal end of a protein is made first, with each cycle adding one amino acid to the C-terminus of the polypeptide chain. The position at which the growing peptide chain is attached to a tRNA does not change during the elongation cycle: it is always linked to the tRNA present in the P site of the large subunit.

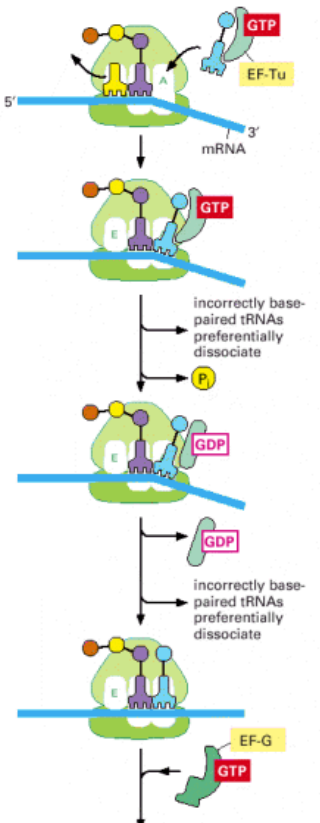

Figure 6-66. Detailed view of the translation cycle. The outline of translation presented in Figure 6-65 has been supplemented with additional features, including the participation of elongation factors and a mechanism by which translational accuracy is improved. In the initial binding event *(top panel)* an aminoacyl-tRNA molecule that is tightly bound to EF-Tu pairs transiently

with the codon at the A-site in the small subunit. During this step *(second panel)*, the tRNA occupies a hybrid-binding site on the ribosome. The codon-anticodon pairing triggers GTP hydrolysis by EF-Tu causing it to dissociate from the aminoacyl-tRNA, which now enters the A-site *(fourth panel)* and can participate in chain elongation. A delay between aminoacyl-tRNA binding and its availability for protein synthesis is thereby inserted into the protein synthesis mechanism. As described in the text, this delay increases the accuracy of translation. In subsequent steps, elongation factor EF-G in the GTP-bound form enters the ribosome and binds in or near the A-site on the large ribosomal subunit, accelerating the movement of the two bound tRNAs into the A/P and P/E hybrid states. Contact with the ribosome stimulates the GTPase activity of EF-G, causing a dramatic conformational change in EF-G as it switches from the GTP to the GDP-bound form. This change moves the tRNA bound to the A/P hybrid state to the P-site and advances the cycle of translation forward by one codon. During each cycle of translation elongation, the tRNAs molecules move through the ribosome in an elaborate series of gyrations during which they transiently occupy several "hybrid" binding states. In one, the tRNA is simultaneously bound to the A site of the small subunit and the P site of the large subunit; in another, the tRNA is bound to the P site of the small subunit and the E site of the large subunit. In a single cycle, a tRNA molecule is considered to occupy six different sites, the initial binding site (called the A/T hybrid state), the A/A site, the A/P hybrid state, the P/P site, the P/E hybrid state, and the E-site. Each tRNA is thought to ratchet through these positions, undergoing rotations along its long axis at each change in location. EF-Tu and EF-G are the designations used for the bacterial elongation factors; in eucaryotes, they are called EF-1 and EF-2, respectively. The dramatic change in the three-dimensional structure of EF-Tu that is caused by GTP hydrolysis was illustrated in Figure 3-74. For each peptide bond formed, a molecule of EF-Tu and EF-G are each released in their inactive, GDP-bound forms. To be used again, these proteins must have their GDP exchanged for GTP. In the case of EF-Tu, this exchange is performed by a specific member of a large class of proteins known as *GTP exchange factors.*

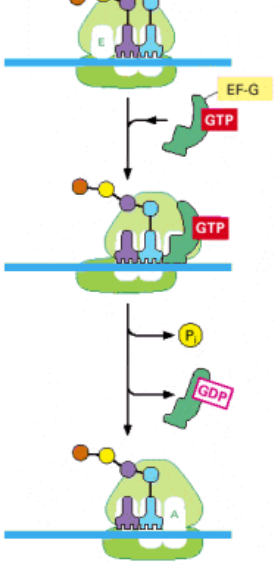

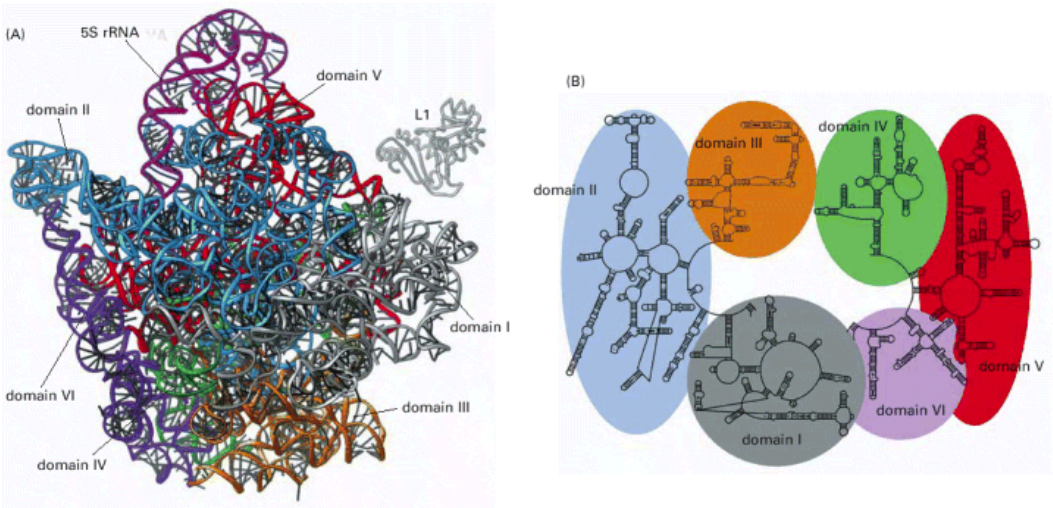

Figure 6-67. Structure of the rRNAs in the large subunit of a bacterial ribosome, as determined by x-ray crystallography. (A) Three-dimensional structures of the large-subunit rRNAs (5S and 23S) as they appear in the ribosome. One of the protein subunits of the ribosome (L1) is also shown as a reference point, since it forms a characteristic protrusion on the ribosome. (B) Schematic diagram of the secondary structure of the 23S rRNA showing the extensive network of base-pairing. The structure has been divided into six structural 'domains' whose colors correspond to those of the three-dimensional structure in (A). The secondary-structure diagram is highly schematized to represent as much of the structure as possible in two dimensions. To do this, several discontinuities in the RNA chain have been introduced, although in reality the 23S RNA is a single RNA molecule. For example, the base of Domain III is continuous with the base of Domain IV even though a gap appears in the diagram. (Adapted from N. Ban et al., *Science* 289:905920, 2000.)

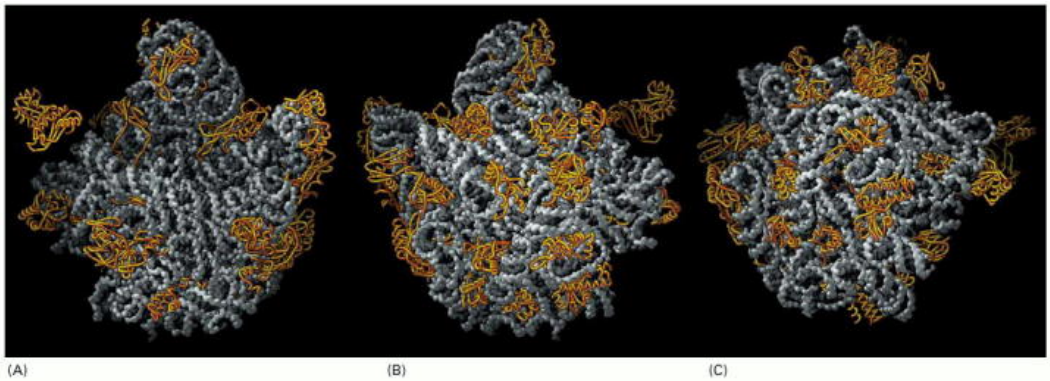

Figure 6-68. Location of the protein components of the bacterial large ribosomal subunit. The rRNAs (5S and 23S) are depicted in *gray* and the large-subunit proteins (27 of the 31 total) in *gold*. For convenience, the protein structures depict only the polypeptide backbones. (A) View of the interface with the small subunit, the same view shown in Figure 6-64B. (B) View of the back of the large subunit, obtained by rotating (A) by 180° around a vertical axis. (C) View of the bottom of the large subunit showing the peptide exit channel in the center of the structure. (From N. Ban et al., *Science* 289:905920, 2000. © AAAS.)

Figure 6-69. Structure of the L15 protein in the large subunit of the bacterial ribosome. The globular domain of the protein lies on the surface of the ribosome and an extended region penetrates deeply into the RNA core of the ribosome. The L15 protein is shown in *yellow* and a portion of the ribosomal RNA core is shown in *red*. (Courtesy of D. Klein, P.B. Moore and T.A. Steitz.)

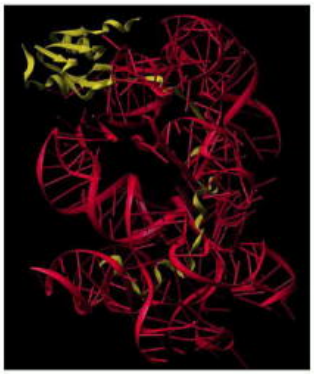

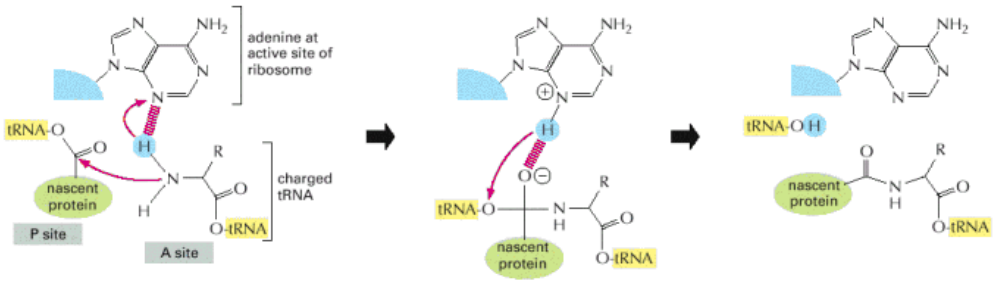

Figure 6-70. A possible reaction mechanism for the peptidyl transferase activity present in the large ribosomal subunit. The overall reaction is catalyzed by an active site in the 23S rRNA. In the first step of the proposed mechanism, the N3 of the active-site adenine abstracts a proton from the amino acid attached to the tRNA at the ribosome's A-site, allowing its amino nitrogen to attack the carboxyl group at the end of the growing peptide chain. In the next step this protonated adenine donates its hydrogen to the oxygen linked to the peptidyl-tRNA, causing this tRNA's release from the peptide chain. This leaves a polypeptide chain that is one amino acid longer than the starting reactants. The entire reaction cycle would then repeat with the next aminoacyl tRNA that enters the A-site. (Adapted from P. Nissen et al., *Science* 289:920930, 2000.)

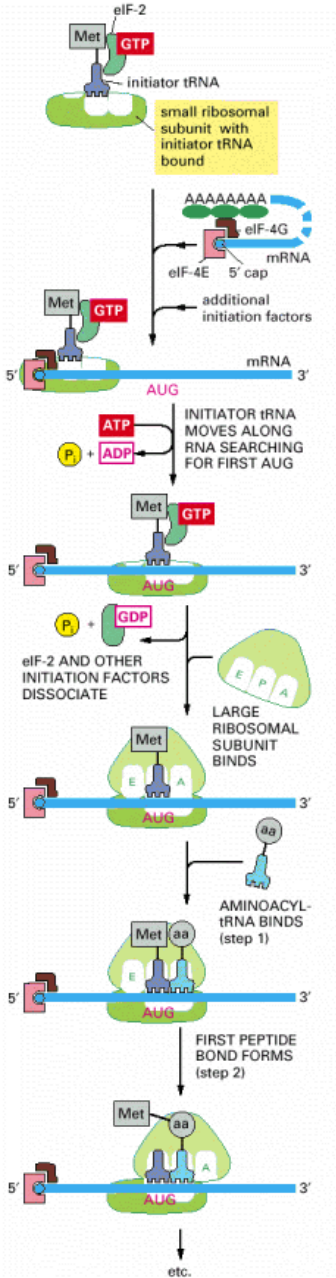

Figure 6-71. The initiation phase of protein synthesis in eucaryotes. Only three of the many translation initiation factors

required for this process are shown. Efficient translation initiation also requires the poly-A tail of the mRNA bound by poly-A-binding proteins which, in turn, interact with eIF4G. In this way, the translation apparatus ascertains that both ends of the mRNA are intact before initiating (see Figure 6-40). Although only one GTP hydrolysis event is shown in the figure, a second is known to occur just before the large and small ribosomal subunits join.

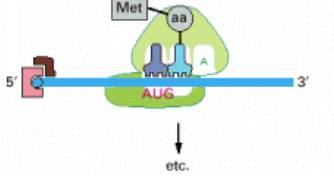

Figure 6-72. Structure of a typical bacterial mRNA molecule. Unlike eucaryotic ribosomes, which typically require a capped 5 end, procaryotic ribosomes initiate transcription at ribosome-binding sites (Shine-Dalgarno sequences), which can be located anywhere along an mRNA molecule. This property of ribosomes permits bacteria to synthesize more than one type of protein from a single mRNA molecule.

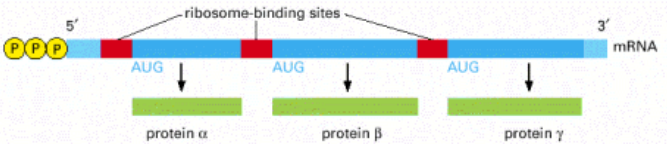

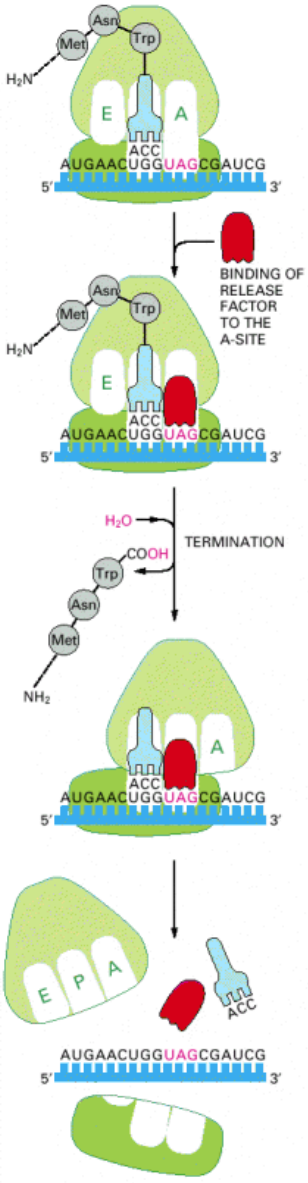

Figure 6-73. The final phase of protein synthesis. The binding of a release factor to an A-site bearing a stop codon terminates translation. The completed polypeptide is released and, after the action of a *ribosome recycling factor* (not shown), the ribosome dissociates into its two separate subunits.

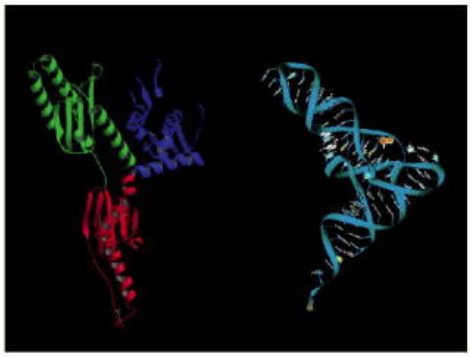

Figure 6-74. The structure of a human translation release factor (eRF1) and its resemblance to a tRNA molecule. The protein is on the *left* and the tRNA on the *right.* (From H. Song et al., *Cell* 100:311321, 2000. © Elsevier.)

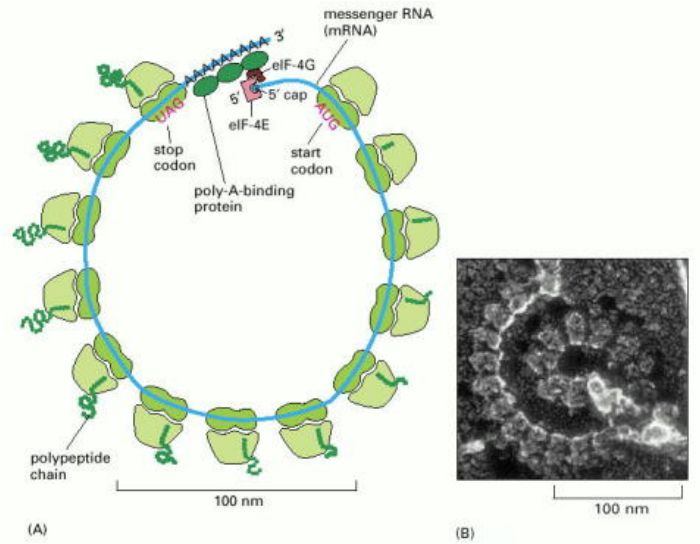

Figure 6-75. A polyribosome. (A) Schematic drawing showing how a series of ribosomes can simultaneously translate the same eucaryotic mRNA molecule. (B) Electron micrograph of a polyribosome from a eucaryotic cell. (B, courtesy of John Heuser.)

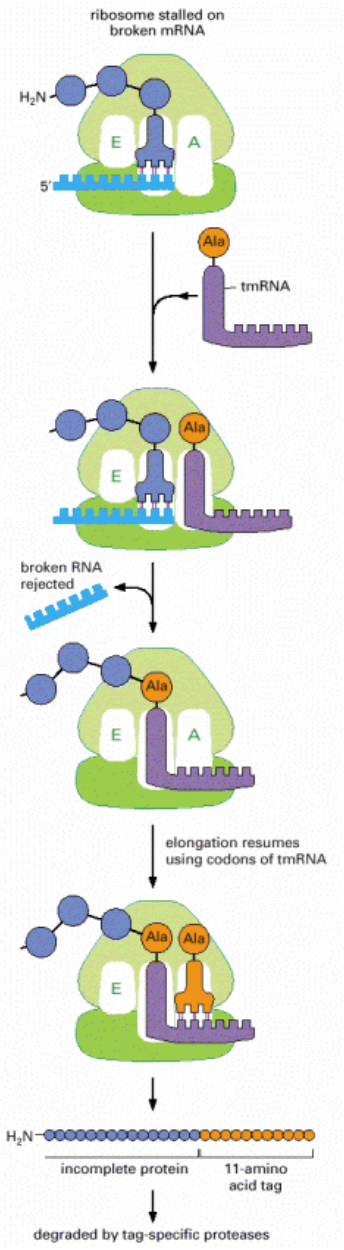

Figure 6-76. The rescue of a bacterial ribosome stalled on an incomplete mRNA molecule. The tmRNA shown is a 363-nucleotide RNA with both tRNA and mRNA functions, hence its name. It carries an alanine and can enter the vacant A-site of a stalled ribosome to add this alanine to a polypeptide chain, mimicking a tRNA except that no codon is present to guide it. The ribosome then translates ten codons from the tmRNA, completing an 11-amino acid tag on the protein. This tag is recognized by proteases that then degrade the entire protein.

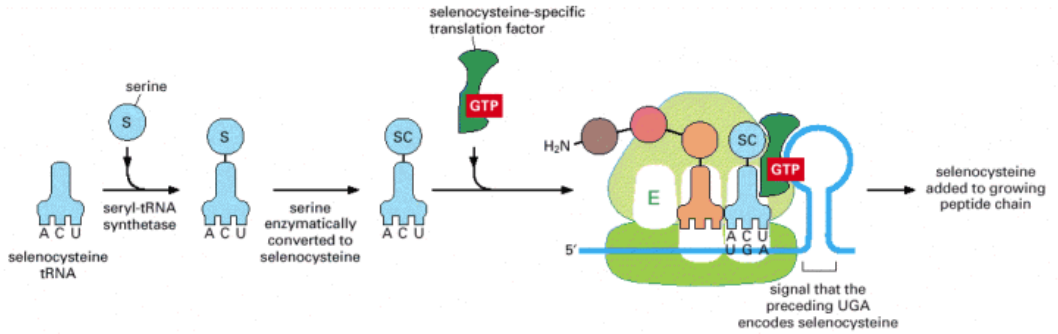

Figure 6-77. Incorporation of selenocysteine into a growing polypeptide chain. A specialized tRNA is charged with serine by the normal seryl-tRNA synthetase, and the serine is subsequently converted enzymatically to selenocysteine. A specific RNA structure in the mRNA (a stem and loop structure with a particular nucleotide sequence) signals that selenocysteine is to be inserted at the neighboring UGA codon. As indicated, this event requires the participation of a selenocysteine-specific translation factor.

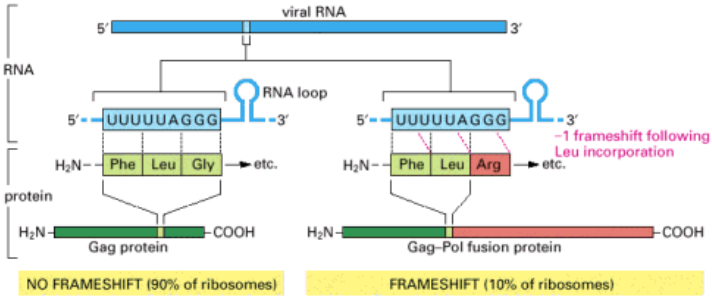

Figure 6-78. The translational frameshifting that produces the reverse transcriptase and integrase of a retrovirus. The viral reverse transcriptase and integrase are produced by proteolytic processing of a large protein (the Gag-Pol fusion protein) consisting of both the Gag and Pol amino acid sequences. The viral capsid proteins are produced by proteolytic processing of the more abundant Gag protein. Both the Gag and the Gag-Pol fusion proteins start identically, but the Gag protein terminates at an in-frame stop codon (not shown); the indicated frameshift bypasses this stop codon, allowing the synthesis of the longer Gag-Pol fusion protein. The frameshift occurs because features in the local RNA structure (including the RNA loop shown) cause the $tRNA^{Leu}$ attached to the C-terminus of the growing polypeptide chain occasionally to slip backward by one nucleotide on the ribosome, so that it pairs with a UUU codon instead of the UUA codon that had initially specified its incorporation; the next codon (AGG) in the new reading frame specifies an arginine rather than a glycine. This controlled slippage is due in part to a stem and loop structure that forms in the viral mRNA, as indicated in the figure. The sequence shown is from the human AIDS virus, HIV. (Adapted from T. Jacks et al., *Nature* 331:280283, 1988.)

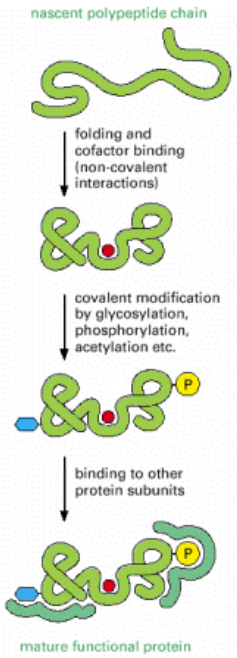

Figure 6-79. Steps in the creation of a functional protein. As indicated, translation of an mRNA sequence into an amino acid sequence on the ribosome is not the end of the process of forming a protein. To be useful to the cell, the completed polypeptide chain must fold correctly into its three-dimensional conformation, bind any cofactors required, and assemble with its partner protein chains (if any). These changes are driven by noncovalent bond formation. As indicated, many proteins also have covalent modifications made to selected amino acids. Although the most frequent of these are protein glycosylation and protein phosphorylation, more than 100 different types of covalent modifications are known (see, for example, Figure 4-35).

Figure 6-80. The structure of a molten globule. (A) A molten globule form of cytochrome b_{562} is more open and less highly ordered than the final folded form of the protein, shown in (B). Note that the molten

globule contains most of the secondary structure of the final form, although the ends of the α helices are frayed and one of the helices is only partly formed. (Courtesy of Joshua Wand, from Y. Feng et al., *Nat. Struct. Biol.* 1:3035, 1994.)

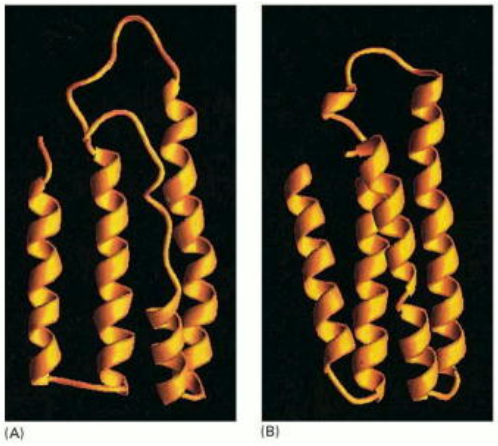

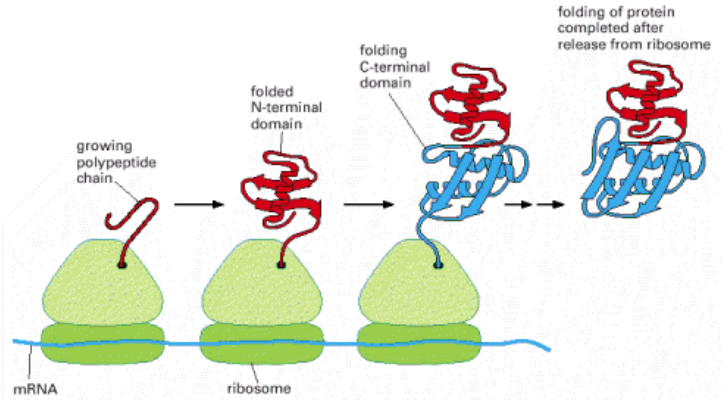

Figure 6-81. The co-translational folding of a protein. A growing polypeptide chain is shown acquiring its secondary and tertiary structure as it emerges from a ribosome. The N-terminal domain folds first, while the C-terminal domain is still being synthesized. In this case, the protein has not yet achieved its final conformation by the time it is released from the ribosome. (Modified from A.N. Federov and T.O. Baldwin, *J. Biol. Chem.* 272:3271532718, 1997.)

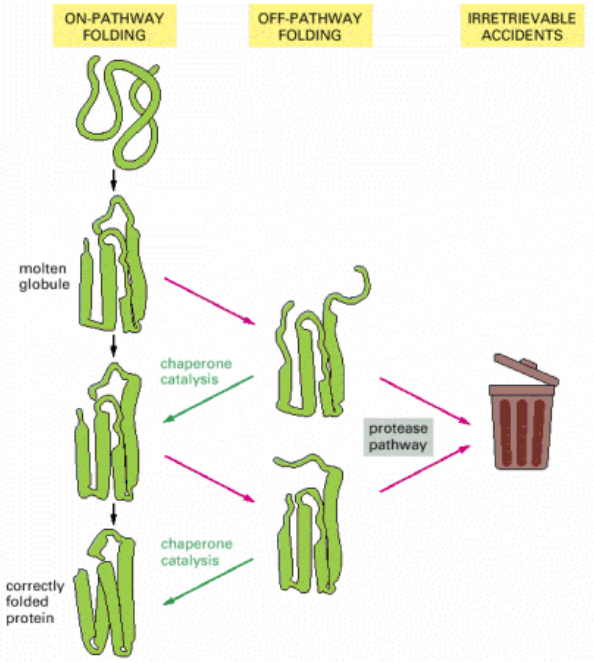

Figure 6-82. A current view of protein folding. Each domain of a newly synthesized protein rapidly attains a "molten globule" state. Subsequent folding occurs more slowly and by multiple pathways, often involving the help of a molecular chaperone. Some molecules may still fail to fold correctly; as explained shortly, these are recognized and degraded by specific proteases.

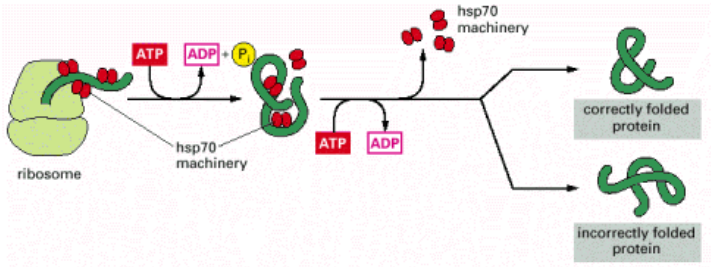

Figure 6-83. The hsp70 family of molecular chaperones. These proteins act early, recognizing a small stretch of hydrophobic amino acids on a protein's surface. Aided by a set of smaller hsp40 proteins, an hsp70 monomer binds to its target protein and then hydrolyzes a molecule of ATP to ADP, undergoing a conformational change that causes the hsp70 to clamp down very tightly on the target. After the hsp40 dissociates, the dissociation of the hsp70 protein is induced by the rapid re-binding of ATP after ADP release. Repeated cycles of hsp protein binding and release help the target protein to refold, as schematically illustrated in Figure 6-82.

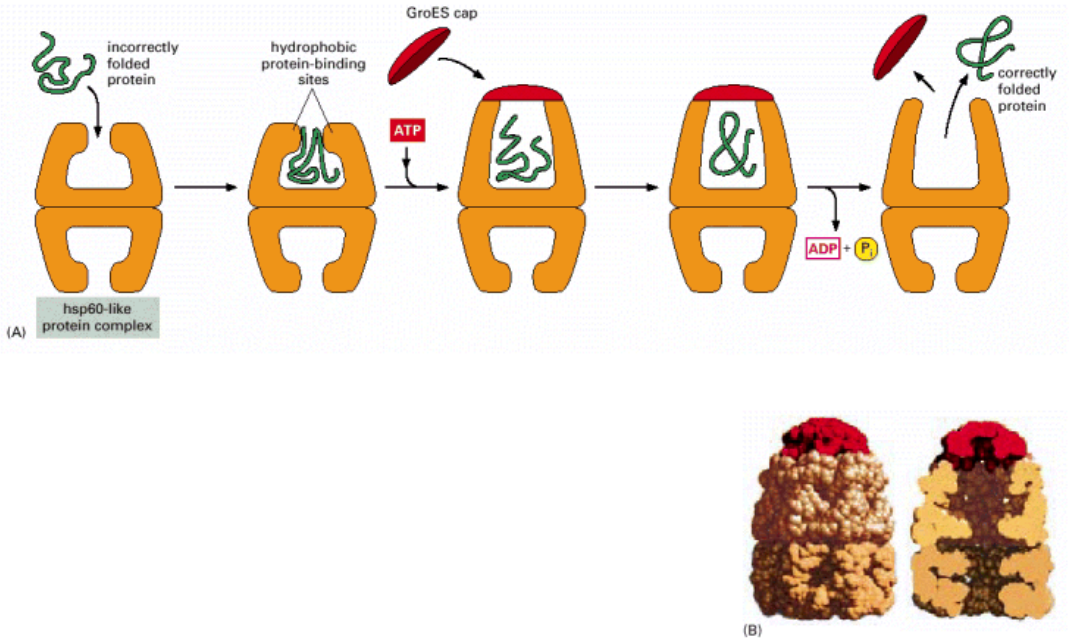

Figure 6-84. The structure and function of the hsp60 family of molecular chaperones. (A) The catalysis of protein refolding. As indicated, a misfolded protein is initially captured by hydrophobic interactions along one rim of the barrel. The subsequent binding of ATP plus a protein cap increases the diameter of the barrel rim, which may transiently stretch (partly unfold) the client protein. This also confines the protein in an enclosed space, where it has a new opportunity to fold. After about 15 seconds, ATP hydrolysis ejects the protein, whether folded or not, and the cycle repeats. This type of molecular chaperone is also known as a chaperonin; it is designated as hsp60 in mitochondria, TCP-1 in the cytosol of vertebrate cells, and GroEL in bacteria. As indicated, only half of the symmetrical barrel operates on a client protein at any one time. (B) The structure of GroEL bound to its GroES cap, as determined by x-ray crystallography. On the *left* is shown the outside of the barrel-like structure and on the *right* a cross section through its center. (B, adapted from B. Bukace and A.L. Horwich, *Cell* 92:351366, 1998.)

Figure 6-85. The cellular mechanisms that monitor protein quality after protein synthesis. As indicated, a newly synthesized protein sometimes folds correctly and assembles with its partners on its own, in which case it is left alone. Incompletely folded proteins are helped to refold by molecular chaparones: first by a family of hsp70 proteins, and if this fails, then by hsp60-like proteins. In both cases the client proteins are recognized by an abnormally exposed patch of hydrophobic amino acids on their surface. These processes compete with a different system that recognizes an abnormally exposed patch and transfers the protein that contains it to a proteasome for complete destruction. The combination of all of these processes is needed to prevent massive protein aggregation in a cell, which can occur when many hydrophobic regions on proteins clump together and precipitate the entire mass out of solution.

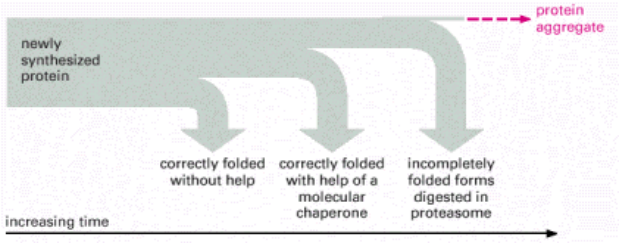

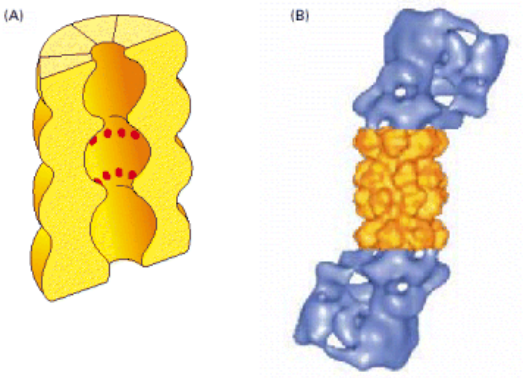

Figure 6-86. The proteasome. (A) A cut-away view of the structure of the central 20S cylinder, as determined by x-ray crystallography, with the active sites of the proteases indicated by *red dots.* (B) The structure of the entire proteasome, in which the central cylinder *(yellow)* is supplemented by a 19S cap *(blue)* at each end, whose structure has been determined by computer processing of electron microscope images. The complex cap structure selectively binds those proteins that have been marked for destruction; it then uses ATP hydrolysis to unfold their polypeptide chains and feed them into the inner chamber of the 20S cylinder for digestion to short peptides. (B, from W. Baumeister et al., *Cell* 92:367380, 1998. © Elsevier.)

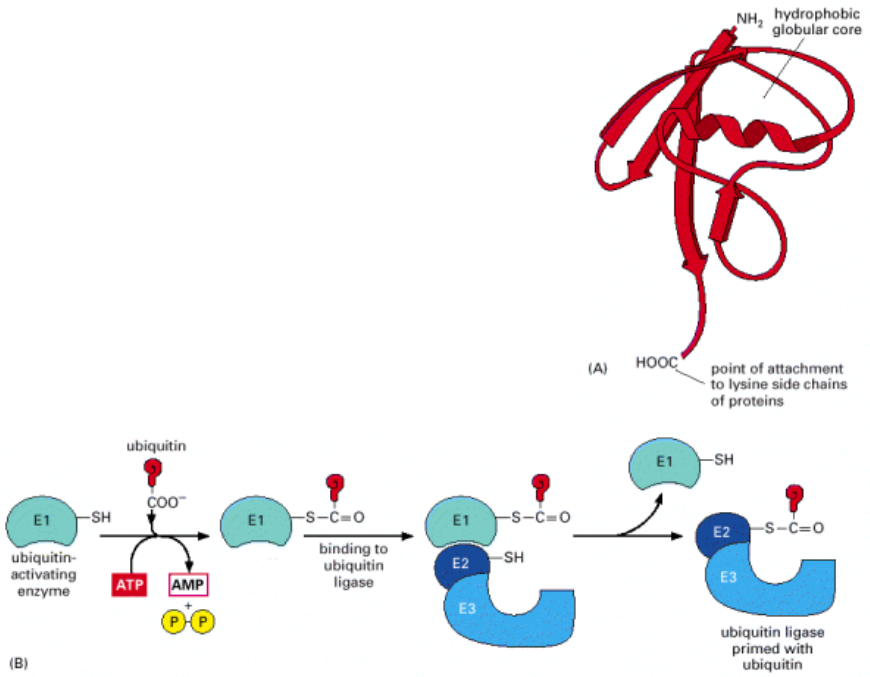

Figure 6-87. Ubiquitin and the marking of proteins with multiubiquitin chains. (A) The three-dimensional structure of ubiquitin; this relatively small protein contains 76 amino acids. (B) The C-terminus of ubiquitin is initially activated through its high-energy thioester linkage to a cysteine side chain on the E1 protein. This reaction requires ATP, and it proceeds via a covalent AMP-ubiquitin intermediate. The activated ubiquitin on E1, also known as the ubiquitin-activating enzyme, is then transferred to the cysteines on a set of E2 molecules. These E2s exist as complexes with an even larger family of E3 molecules. (C) The addition of a multiubiquitin chain to a target protein. In a mammalian cell there are roughly 300 distinct E2-E3 complexes, each of which recognizes a different degradation signal on a target protein by means of its E3 component. The E2s are called ubiquitin-conjugating enzymes. The E3s have been referred to traditionally as ubiquitin ligases, but it is more accurate to reserve this name for the functional E2-E3 complex.

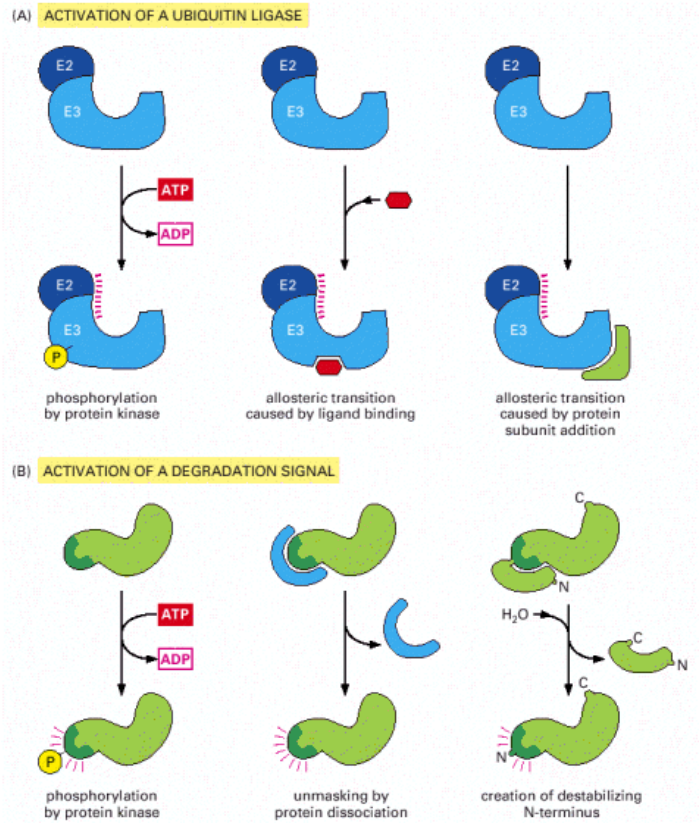

Figure 6-88. Two general ways of inducing the degradation of a specific protein. (A) Activation of a specific E3 molecule creates a new ubiquitin ligase. (B) Creation of an exposed degradation signal in the protein to be degraded. This signal binds a ubiquitin ligase, causing the addition of a multiubiquitin chain to a nearby lysine on the target protein. All six pathways shown are known to be used by cells to induce the movement of selected proteins into the proteasome.

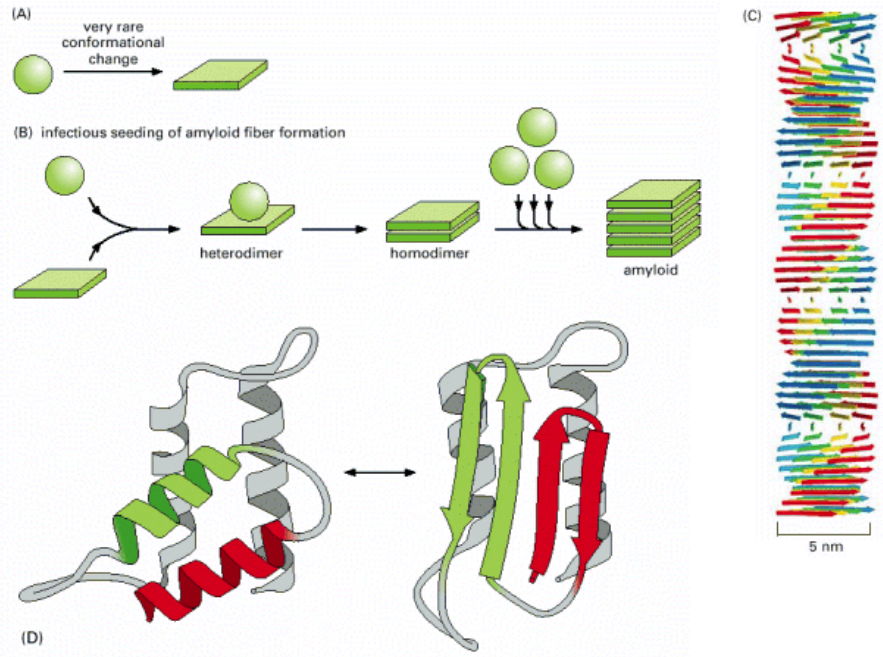

Figure 6-89. Protein aggregates that cause human disease. (A) Schematic illustration of the type of conformational change in a protein that produces material for a cross-beta filament. (B) Diagram illustrating the self-infectious nature of the protein aggregation that is central to prion diseases. PrP is highly unusual because the misfolded version of the protein, called PrP*, induces the normal PrP protein it contacts to change its conformation, as shown. Most of the human diseases caused by protein aggregation are caused by the overproduction of a variant protein that is especially prone to aggregation, but because this structure is not infectious in this way, it cannot spread from one animal to another. (C) Drawing of a cross-beta filament, a common type of protease-resistant protein aggregate found in a variety of human neurological diseases. Because the hydrogen-bond interactions in a β sheet form between polypeptide backbone atoms (see Figure 3-9), a number of different abnormally folded proteins can produce this structure. (D) One of several possible models for the conversion of PrP to PrP*, showing the likely change of two α-helices into four β-strands. Although the structure of the normal protein has been determined accurately, the structure of the infectious form is not yet known with certainty because the aggregation has prevented the use of standard structural techniques. (C, courtesy of Louise Serpell, adapted from M. Sunde et al., *J. Mol. Biol.* 273:729739, 1997; D, adapted from S.B. Prusiner, *Trends Biochem. Sci.* 21:482487, 1996.)

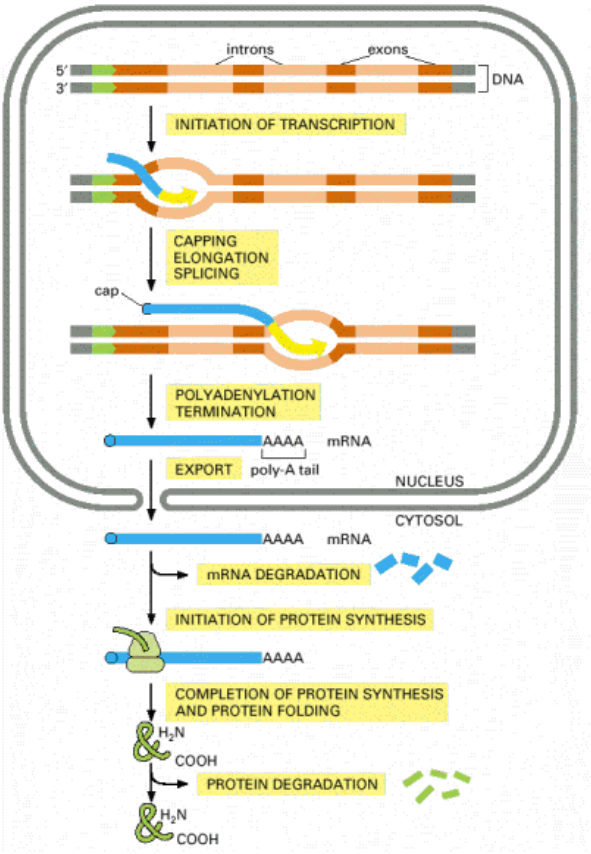

Figure 6-90. The production of a protein by a eucaryotic cell. The final level of each protein in a eucaryotic cell depends upon the efficiency of each step depicted.

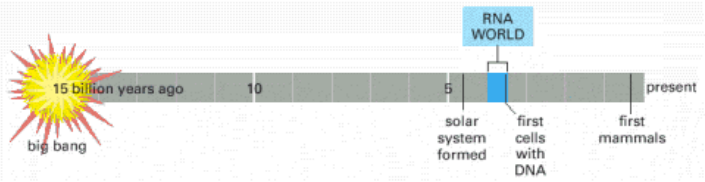

Figure 6-91. Time line for the universe, suggesting the early existence of an RNA world of living systems.

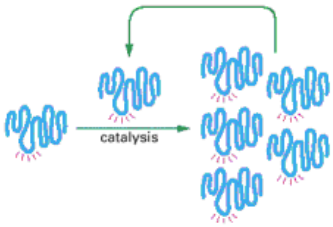

Figure 6-92. An RNA molecule that can catalyze its own synthesis. This hypothetical process would require catalysis of the production of both a second RNA strand of complementary nucleotide sequence and the use of this second RNA molecule as a template to form many molecules of RNA with the original sequence. The *red* rays represent the active site of this hypothetical RNA enzyme.

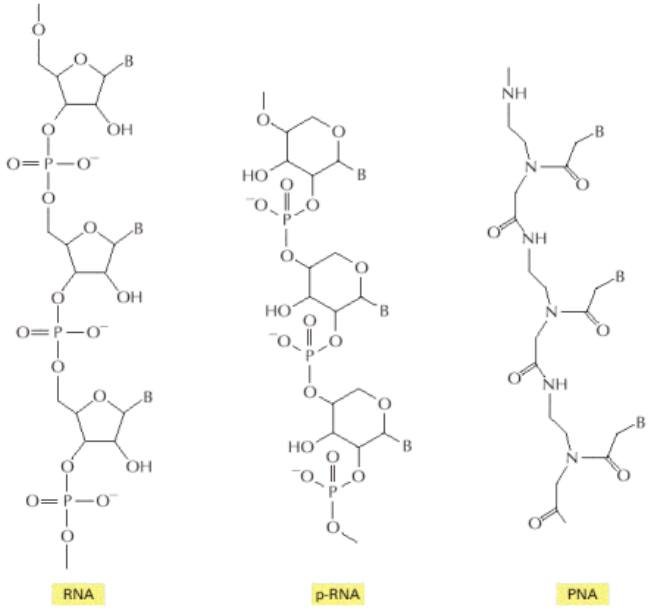

Figure 6-93. Structures of RNA and two related information-carrying polymers. In each case, B indicates the positions of purine and pyrimidine bases. The polymer p-RNA (pyranosyl-RNA) is RNA in which the furanose (five-membered ring) form of ribose has been replaced by the pyranose (six-membered ring) form. In PNA (peptide nucleic acid), the ribose phosphate backbone of RNA has been replaced by the peptide backbone found in proteins. Like RNA, both p-RNA and PNA can form double helices through complementary base-pairing, and each could therefore in principle serve as a template for its own synthesis (see Figure 6-92).

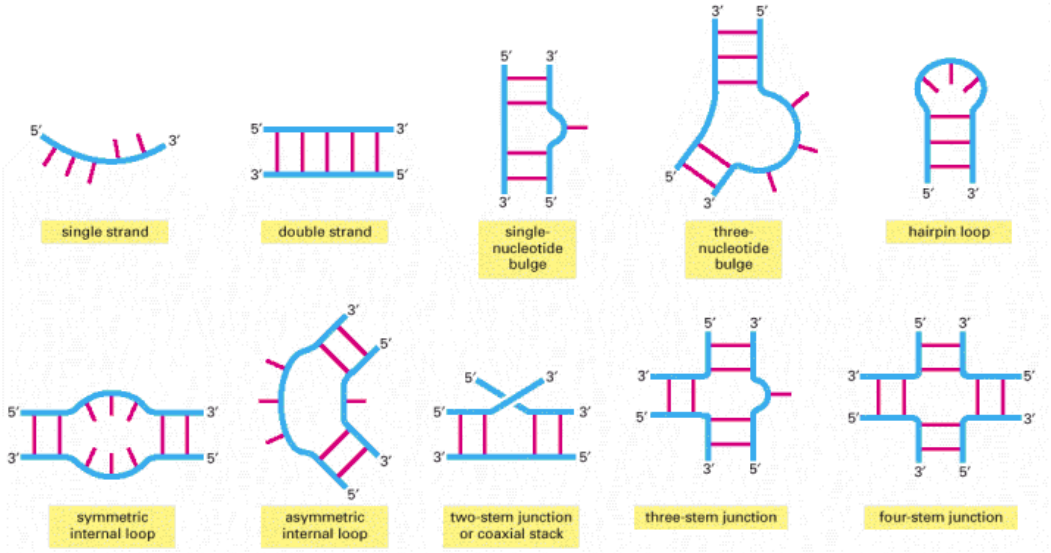

Figure 6-94. Common elements of RNA secondary structure. Conventional, complementary base-pairing interactions are indicated by *red* "rungs" in double-helical portions of the RNA.

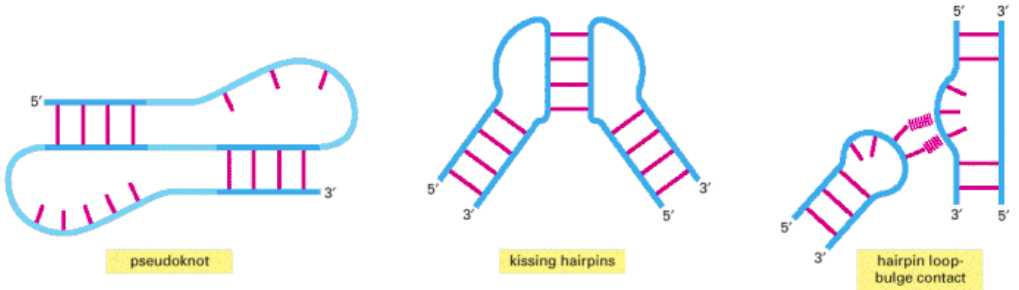

Figure 6-95. Examples of RNA tertiary interactions. Some of these interactions can join distant parts of the same RNA molecule or bring two separate RNA molecules together.

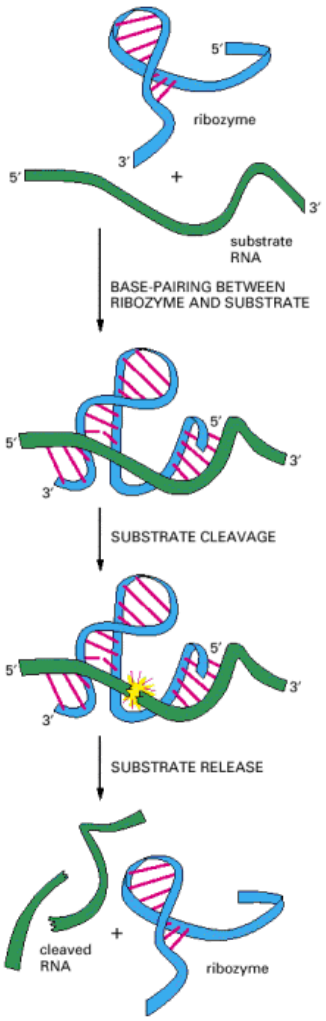

Figure 6-96. ***(above)*****A ribozyme.** This simple RNA molecule catalyzes the cleavage of a second RNA at a specific site. This ribozyme is found embedded in larger RNA genomes - called viroids - which infect plants. The cleavage, which occurs in nature at a distant location on the same RNA molecule that contains the ribozyme, is a step in the replication of the viroid genome. Although not shown in the figure, the reaction requires a molecule of Mg positioned at the active site. (Adapted from T. R. Cech and O.C. Uhlenbeck, *Nature* 372:3940, 1994.)

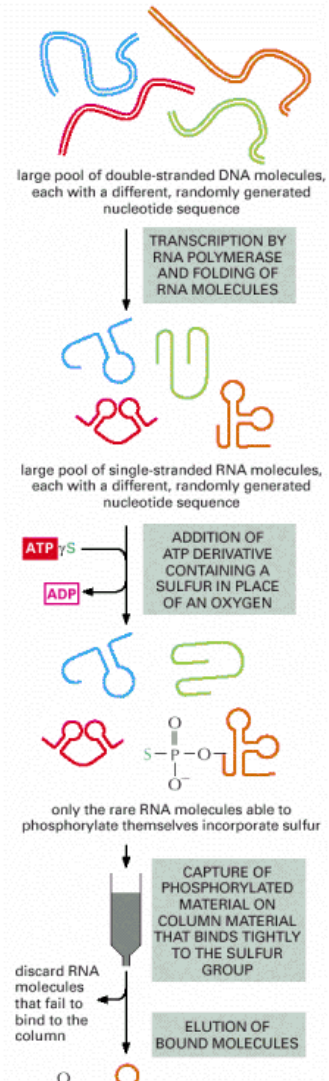

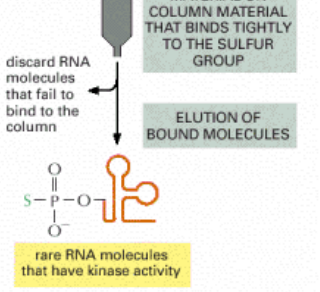

Figure 6-97. ***(left) In vitro*** **selection of a synthetic ribozyme.** Beginning with a large pool of nucleic acid molecules synthesized in the laboratory, those rare RNA molecules that possess a specified catalytic activity can be isolated and studied. Although a specific example (that of an autophosphorylating ribozyme) is shown, variations of this procedure have been used to generate many of the ribozymes listed in Table 6-4. During the autophosphorylation step, the RNA molecules are sufficiently dilute to prevent the "cross"-phosphorylation of additional RNA molecules. In reality, several repetitions of this procedure are necessary to select the very rare RNA molecules with catalytic activity. Thus the material initially eluted from the column is converted back into DNA, amplified many fold (using reverse transcriptase and PCR as explained in Chapter 8), transcribed back into RNA, and subjected to repeated rounds of selection. (Adapted from J.R. Lorsch and J.W. Szostak, *Nature* 371:3136, 1994.)

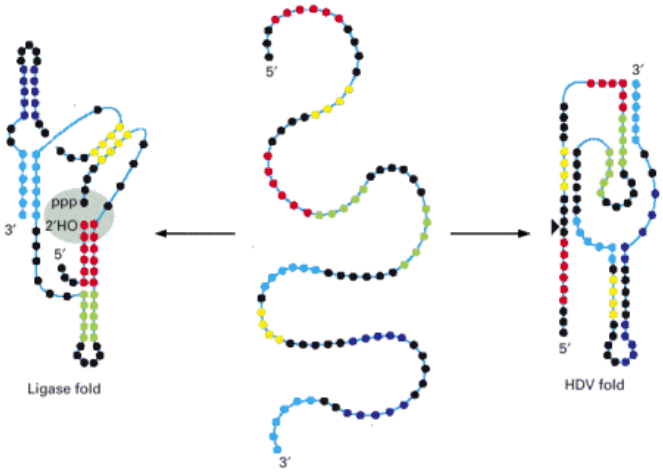

Figure 6-98. An RNA molecule that folds into two different ribozymes. This 88-nucleotide RNA, created in the laboratory, can fold into a ribozyme that carries out a self-ligation reaction *(left)* or a self-cleavage reaction *(right)*. The ligation reaction forms a 2,5 phosphodiester linkage with the release of pyrophosphate. This reaction seals the gap *(gray* shading), which was experimentally introduced into the RNA molecule. In the reaction carried out by the HDV fold, the RNA is cleaved at this same position, indicated by the *arrowhead*. This cleavage resembles that used in the life cycle of HDV, a hepatitis B satellite virus, hence the name of the fold. Each nucleotide is represented by a *colored dot*, with the colors used simply to clarify the two different folding patterns. The folded structures illustrate the secondary structures of the two ribozymes with regions of base-pairing indicated by close oppositions of the *colored dots*. Note that the two ribozyme folds have no secondary structure in common. (Adapted from E.A. Schultes and D.P. Bartel, *Science* 289:448452, 2000.)

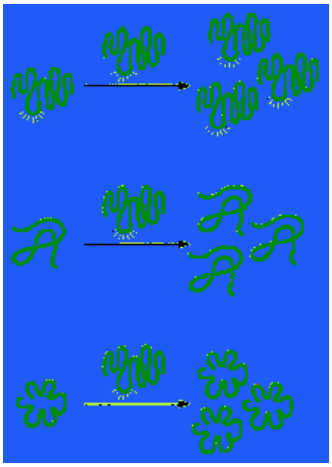

Figure 6-99. A family of mutually supportive RNA molecules, one catalyzing the reproduction of the others.

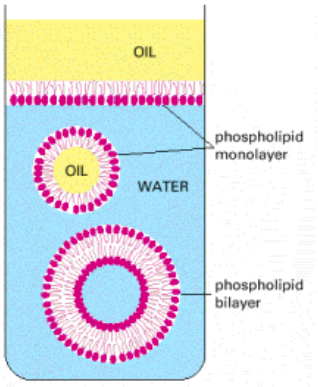

Figure 6-100. Formation of membrane by phospholipids. Because these molecules have hydrophilic heads and lipophilic tails, they align themselves at an oil/water interface with their heads in the water and their tails in the oil. In the water they associate to form closed bilayer vesicles in which the lipophilic tails are in contact with one another and the hydrophilic heads are exposed to the water.

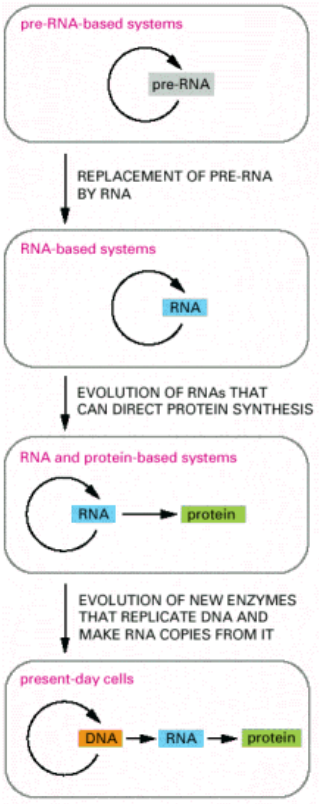

Figure 6-101. The hypothesis that RNA preceded DNA and proteins in evolution. In the earliest cells, pre-RNA molecules would have had combined genetic, structural, and catalytic functions and these functions would have gradually been replaced by RNA. In present-day cells, DNA is the repository of genetic information, and proteins perform the vast majority of catalytic functions in cells. RNA primarily functions today as a go-between in protein synthesis, although it remains a catalyst for a number of crucial reactions.

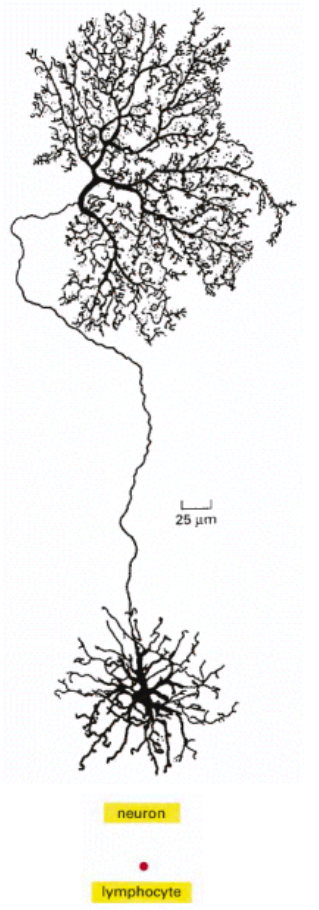

Figure 7-1. A mammalian neuron and a lymphocyte. The long branches of this neuron from the retina enable it to receive electrical signals from many cells and carry those signals to many neighboring cells. The lymphocyte is a white blood cell involved in the immune response to infection and moves freely through the body. Both of these cells contain the same genome, but they express different RNAs and proteins. (From B.B. Boycott, Essays on the Nervous System [R. Bellairs and E.G. Gray, eds.]. Oxford, UK: Clarendon Press, 1974.)

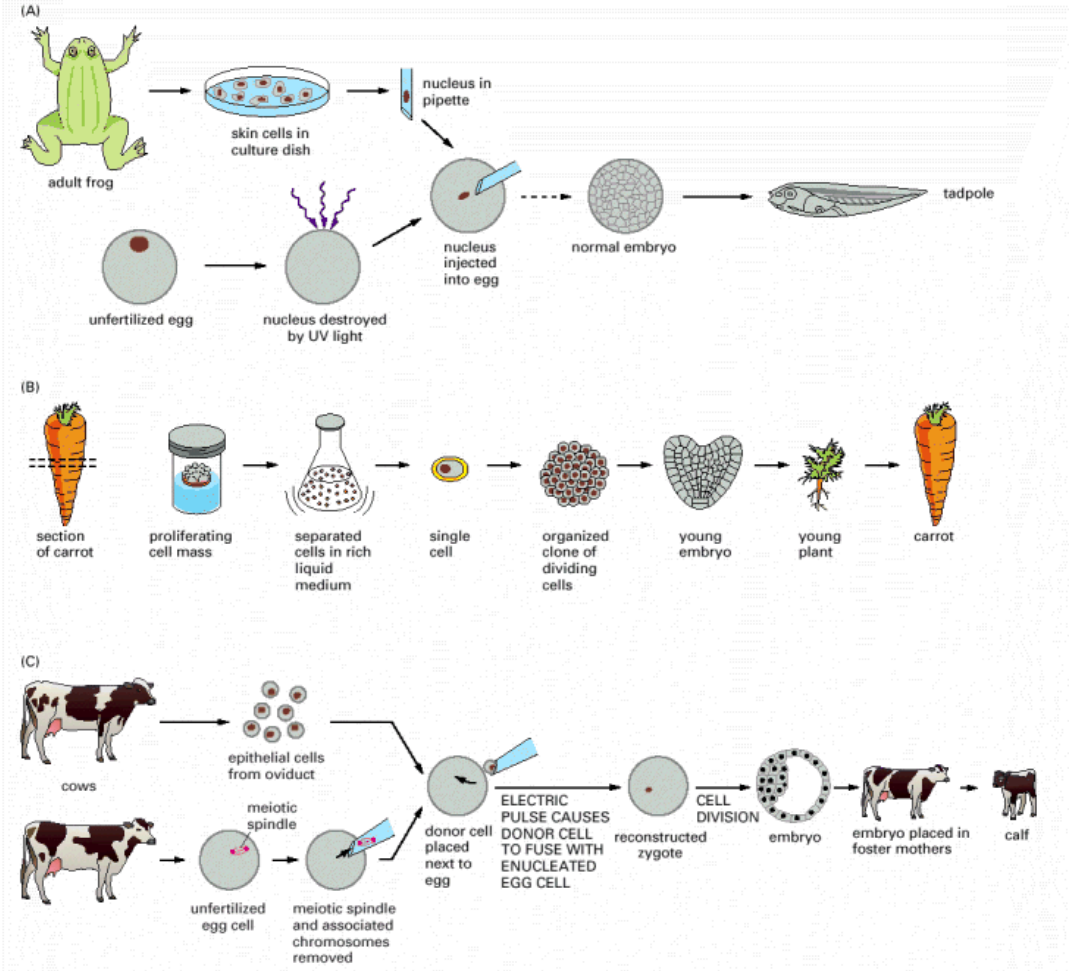

Figure 7-2. Evidence that a differentiated cell contains all the genetic instructions necessary to direct the formation of a complete organism. (A) The nucleus of a skin cell from an adult frog transplanted into an enucleated egg can give rise to an entire tadpole. The *broken arrow* indicates that, to give the transplanted genome time to adjust to an embryonic environment, a further transfer step is required in which one of the nuclei is taken from the early embryo that begins to develop and is put back into a second enucleated egg. (B) In many types of plants, differentiated cells retain the ability to "dedifferentiate," so that a single cell can form a clone of progeny cells that later give rise to an entire plant. (C) A differentiated cell from an adult cow introduced into an enucleated egg from a different cow can give rise to a calf. Different calves produced from the same differentiated cell donor are genetically identical and are therefore clones of one another. (A, modified from J.B. Gurdon, *Sci. Am*. 219(6):2435, 1968.)

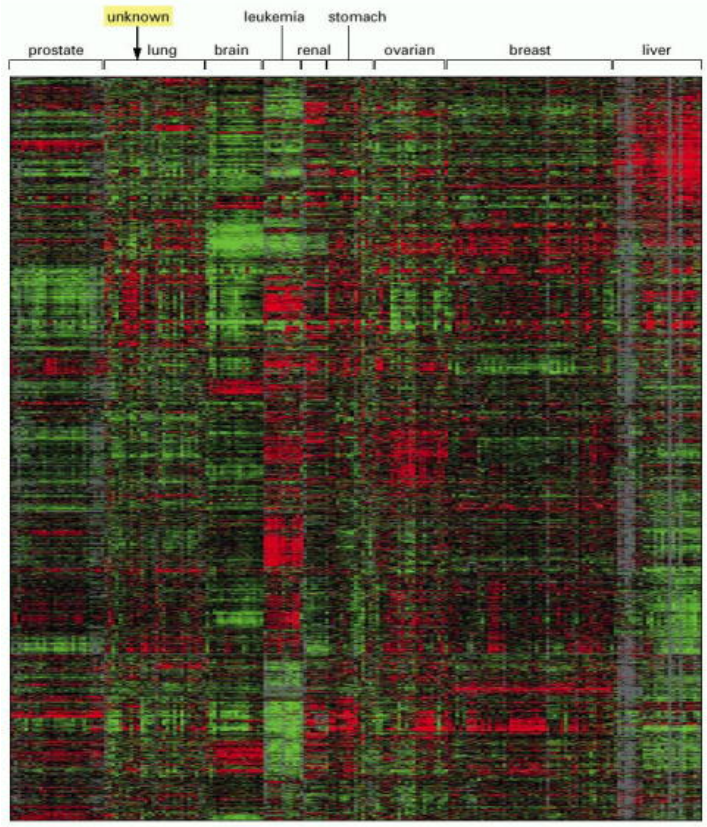

Figure 7-3. Differences in mRNA expression patterns among different types of human cancer cells. This figure summarizes a very large set of measurements in which the mRNA levels of 1800 selected genes (arranged *top* to *bottom)* were determined for 142 different human tumors (arranged *left* to *right),* each from a different patient. Each small *red* bar indicates that the given gene in the given tumor is transcribed at a level significantly higher than the average across all the cell lines. Each small *green* bar indicates a less-than-average expression level, and each *black* bar denotes an expression level that is close to average across the different tumors. The procedure used to generate these data - mRNA isolation followed by hybridization to DNA microarrays - is described in Chapter 8 (see pp. 533535). The figure shows that the relative expression levels of each of the 1800 genes analyzed vary among the different tumors (seen by following a given gene *left* to *right* across the figure). This analysis also shows that each type of tumor has a characteristic gene expression pattern. This information can be used to "type" cancer cells of unknown tissue origin by matching the gene expression profiles to those of known tumors. For example, the unknown sample in the figure has been identified as a lung cancer. (Courtesy of Patrick O. Brown, David Botstein, and the Stanford Expression Collaboration.)

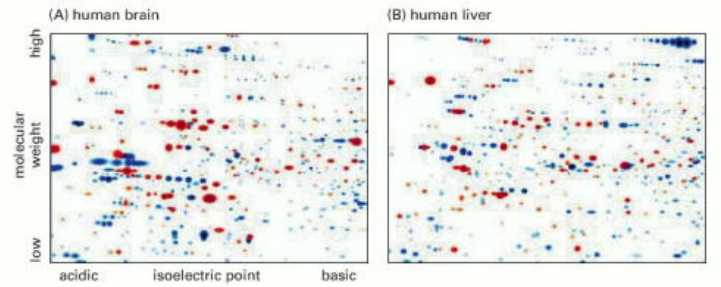

Figure 7-4. Differences in the proteins expressed by two human tissues. In each panel, the proteins have been displayed using two-dimensional polyacrylamide gel electrophoresis (see pp. 485487). The proteins have been separated by molecular weight *(top* to *bottom)* and isoelectric point, the pH at which the protein has no net charge *(right* to *left).* The protein spots artificially colored *red* are common to both samples; those in *blue* are specific to one of the two tissues. The differences between the two tissue samples vastly outweigh their similarities: even for proteins that are shared between the two tissues, their relative abundance is usually different. Note that this technique separates proteins both by size and charge; therefore a protein that has, for example, several different phosphorylation states will appear as a series of *horizontal spots* (see *upper right-hand* portion of *right* panel). Only a small portion of the complete protein spectrum is shown for each sample. (Courtesy of Tim Myers and Leigh Anderson, Large Scale Biology Corporation.)

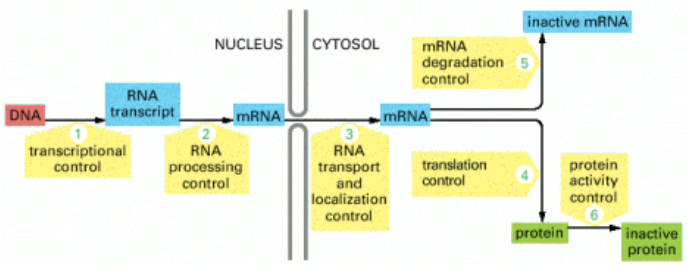

Figure 7-5. Six steps at which eucaryotic gene expression can be controlled. Controls that operate at steps 1 through 5 are discussed in this chapter. Step 6, the regulation of protein activity, includes reversible activation or inactivation by protein phosphorylation (discussed in Chapter 3) as well as irreversible inactivation by proteolytic degradation (discussed in Chapter 6).

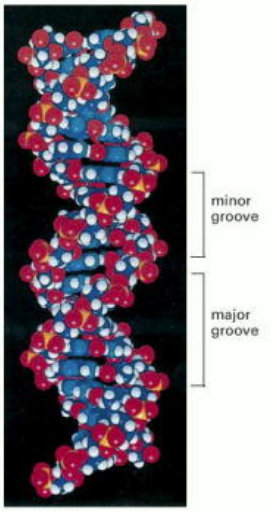

Figure 7-6. Double-helical structure of DNA. The major and minor grooves on the outside of the double helix are indicated. The atoms are colored as follows: carbon, *dark blue;* nitrogen, *light blue;* hydrogen, *white;* oxygen, *red;* phosphorus, *yellow.*

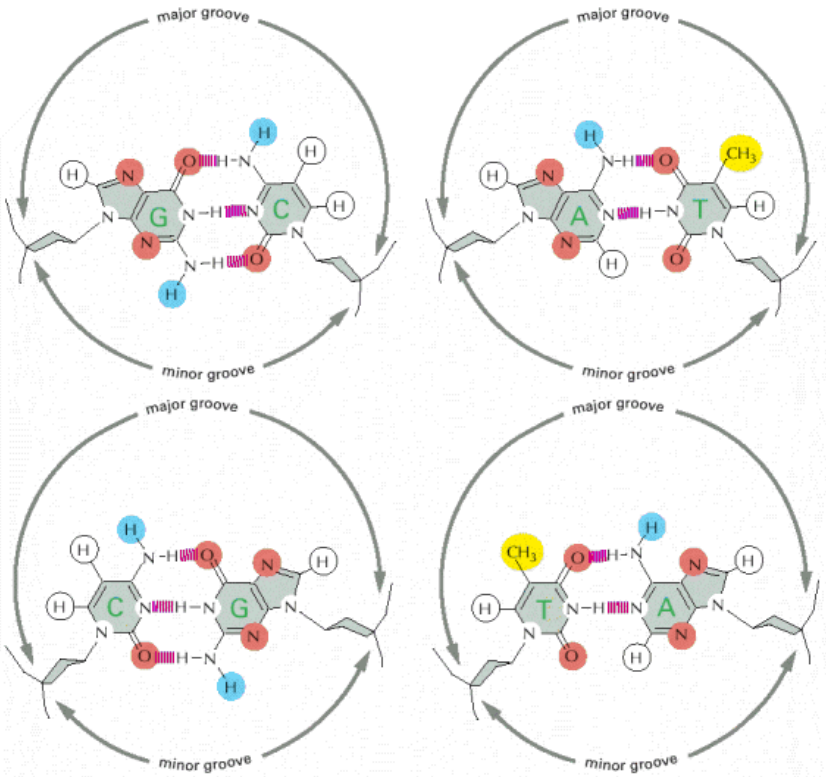

Figure 7-7. How the different base pairs in DNA can be recognized from their edges without the need to open the double helix. The four possible configurations of base pairs are shown, with potential hydrogen bond donors indicated in *blue*, potential hydrogen bond acceptors in *red*, and hydrogen bonds of the base pairs themselves as a series of short parallel *red* lines. Methyl groups, which form hydrophobic protuberances, are shown in *yellow*, and hydrogen atoms that are attached to carbons, and are therefore unavailable for hydrogen bonding, are *white*. (From C. Branden and J. Tooze, Introduction to Protein Structure, 2nd edn. New York: Garland Publishing, 1999.)

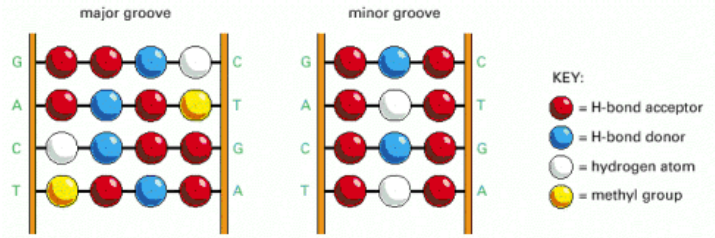

Figure 7-8. A DNA recognition code. The edge of each base pair, seen here looking directly at the major or minor groove, contains a distinctive pattern of hydrogen bond donors, hydrogen bond acceptors, and methyl groups. From the major groove, each of the four base-pair configurations projects a unique pattern of features. From the minor groove, however, the patterns are similar for G-C and C-G as well as for A-T and T-A. The color code is the same as that in Figure 7-7. (From C. Branden and J. Tooze, Introduction to Protein Structure, 2nd edn. New York: Garland Publishing, 1999.)

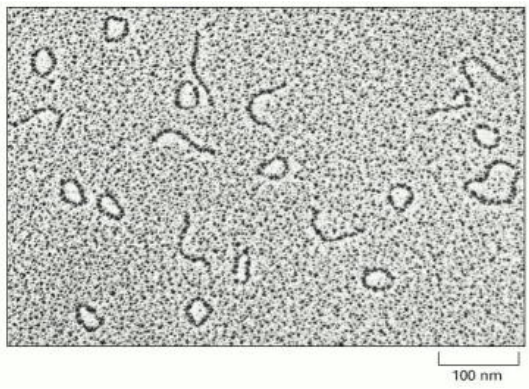

Figure 7-9. Electron micrograph of fragments of a highly bent segment of DNA double helix. The DNA fragments are derived from the small, circular mitochondrial DNA molecules of a trypanosome. Although the fragments are only about 200 nucleotide pairs long, many of them have bent to form a complete circle. On average, a normal DNA helix of this length would bend only enough to produce one-fourth of a circle (one smooth right-angle turn). (From J. Griffith, M. Bleyman, C.A. Raugh, P.A. Kitchin, and P.T. Englund, *Cell* 46:717724, 1986. © Elsevier.)

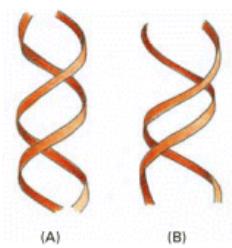

Figure 7-10. DNA deformation induced by protein binding. The figure shows the changes of DNA structure, from the conventional double-helix (A) to a distorted form (B) observed when a well-studied gene regulatory protein (the bacteriophage 434 repressor, a close relative of the lambda repressor) binds to specific sequences of DNA. The ease with which a DNA sequence can be deformed often affects the affinity of protein binding.

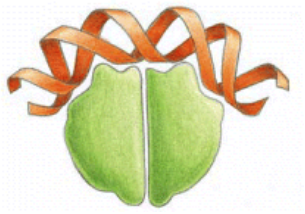

Figure 7-11. The bending of DNA induced by the binding of the catabolite activator protein (CAP). CAP is a gene regulatory protein from *E. coli*. In the absence of the bound protein, this DNA helix is straight.

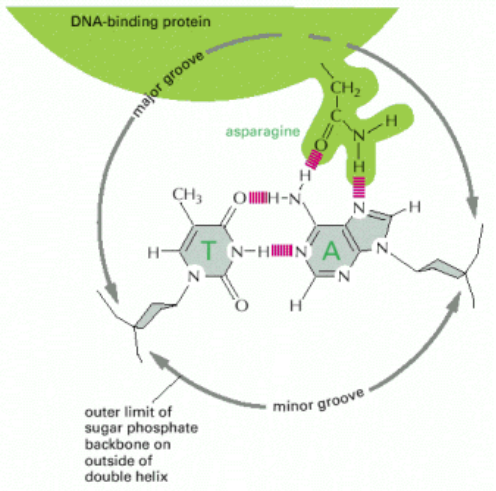

Figure 7-12. The binding of a gene regulatory protein to the major groove of DNA. Only a single contact is shown. Typically, the protein-DNA interface would consist of 10 to 20 such contacts, involving different amino acids, each contributing to the strength of the protein-DNA interaction.

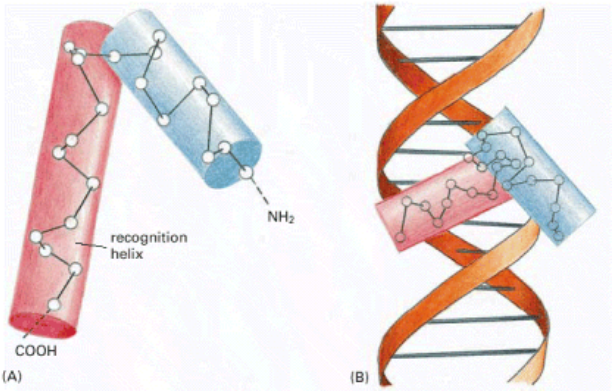

Figure 7-13. The DNA-binding helix-turn-helix motif. The motif is shown in (A), where each *white* circle denotes the central carbon of an amino acid. The C-terminal α helix *(red)* is called the recognition helix because it participates in sequence-specific recognition of DNA. As shown in (B), this helix fits into the major groove of DNA, where it contacts the edges of the base pairs (see also Figure 7-7). The N-terminal α-helix *(blue)* functions primarily as a structural component that helps to position the recognition helix.

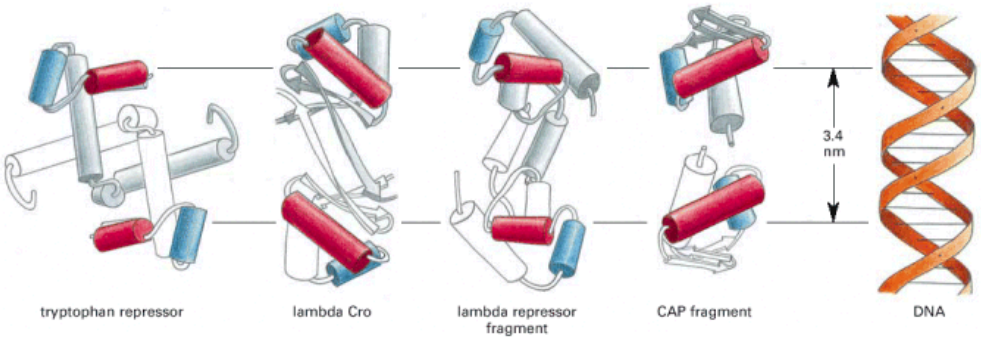

Figure 7-14. Some helix-turn-helix DNA-binding proteins. All of the proteins bind DNA as dimers in which the two copies of the recognition helix *(red cylinder)* are separated by exactly one turn of the DNA helix (3.4 nm). The other helix of the helix-turn-helix motif is colored *blue*, as in Figure 7-13. The lambda repressor and Cro proteins control bacteriophage lambda gene expression, and the tryptophan repressor and the catabolite activator protein (CAP) control the expression of sets of *E. coli* genes.

Figure 7-15. A specific DNA sequence recognized by the bacteriophage lambda Cro protein. The nucleotides labeled in *green* in this sequence are arranged symmetrically, allowing each half of the DNA site to be recognized in the same way by each protein monomer, also shown in *green.* See Figure 7-14 for the actual structure of the protein.

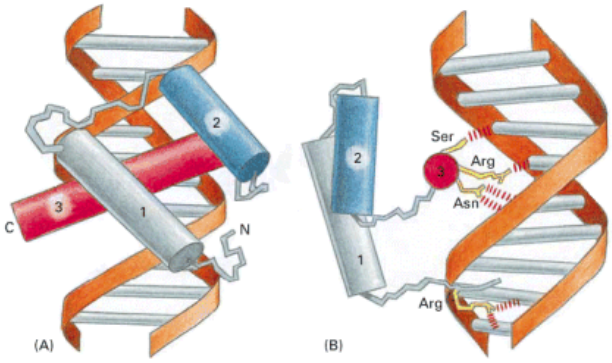

Figure 7-16. A homeodomain bound to its specific DNA sequence. Two different views of the same structure are shown. (A) The homeodomain is folded into three α helices, which are packed tightly together by hydrophobic interactions. The part containing helix 2 and 3 closely resembles the helix-turn-helix motif. (B) The recognition helix (helix 3, *red)* makes important contacts with the major groove of DNA. The asparagine (Asn) of helix 3, for example, contacts an adenine, as shown in Figure 7-12. Nucleotide pairs are also contacted in the minor groove by a flexible arm attached to helix 1. The homeodomain shown here is from a yeast gene regulatory protein, but it closely resembles homeodomains from many eucaryotic organisms. (Adapted from C. Wolberger et al., *Cell* 67:517528, 1991.)

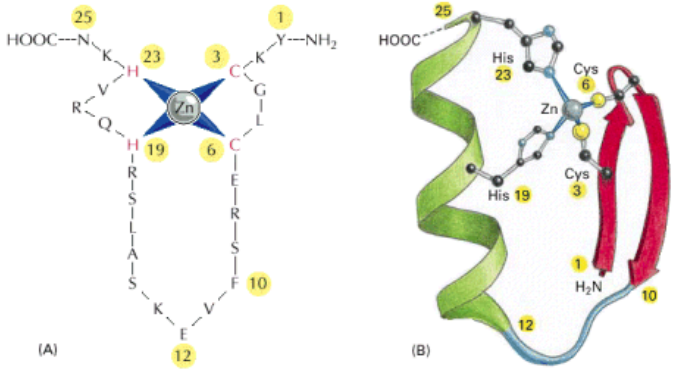

Figure 7-17. One type of zinc finger protein. This protein belongs to the Cys-Cys-His-His family of zinc finger proteins, named after the amino acids that grasp the zinc. (A) Schematic drawing of the amino acid sequence of a zinc finger from a frog protein of this class. (B) The three-dimensional structure of this type of zinc finger is constructed from an antiparallel β sheet (amino acids 1 to 10) followed by an α helix (amino acids 12 to 24). The four amino acids that bind the zinc (Cys 3, Cys 6, His 19, and His 23) hold one end of the α helix firmly to one end of the β sheet. (Adapted from M.S. Lee et al., *Science* 245:635637, 1989.)

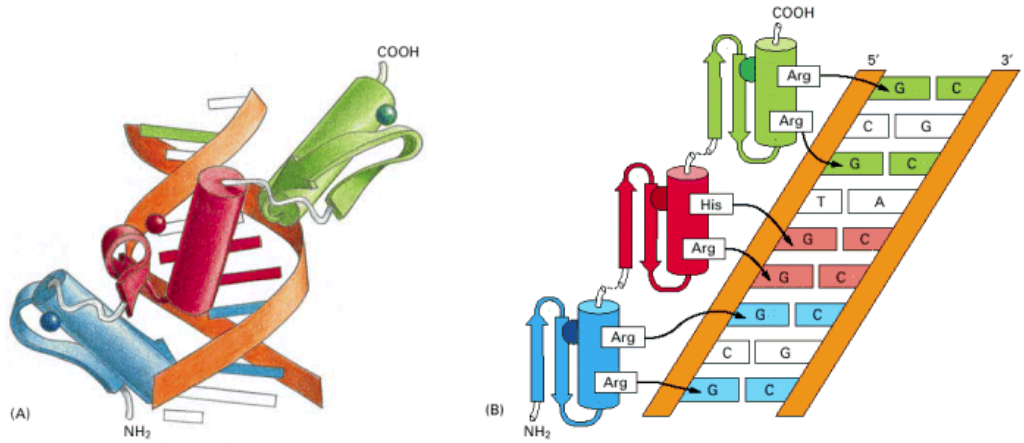

Figure 7-18. DNA binding by a zinc finger protein. (A) The structure of a fragment of a mouse gene regulatory protein bound to a specific DNA site. This protein recognizes DNA using three zinc fingers of the Cys-Cys-His-His type (see Figure 7-17) arranged as direct repeats. (B) The three fingers have similar amino acid sequences and contact the DNA in similar ways. In both (A) and (B) the zinc atom in each finger is represented by a small sphere. (Adapted from N. Pavletich and C. Pabo, *Science* 252:810817, 1991.)

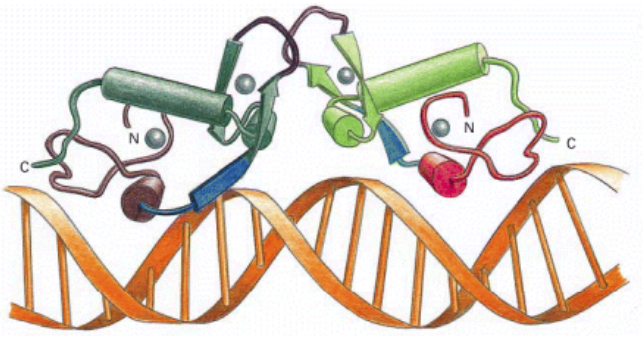

Figure 7-19. A dimer of the zinc finger domain of the intracellular receptor family bound to its specific DNA sequence. Each zinc finger domain contains two atoms of Zn (indicated by the small *gray spheres);* one stabilizes the DNA recognition helix (shown in *brown* in one subunit and *red* in the other), and one stabilizes a loop (shown in *purple)* involved in dimer formation. Each Zn atom is coordinated by four appropriately spaced cysteine residues. Like the helix-turn-helix proteins shown in Figure 7-14, the two recognition helices of the dimer are held apart by a distance corresponding to one turn of the DNA double helix. The specific example shown is a fragment of the glucocorticoid receptor. This is the protein through which cells detect and respond transcriptionally to the glucocorticoid hormones produced in the adrenal gland in response to stress. (Adapted from B.F. Luisi et al., *Nature* 352:497505, 1991.)

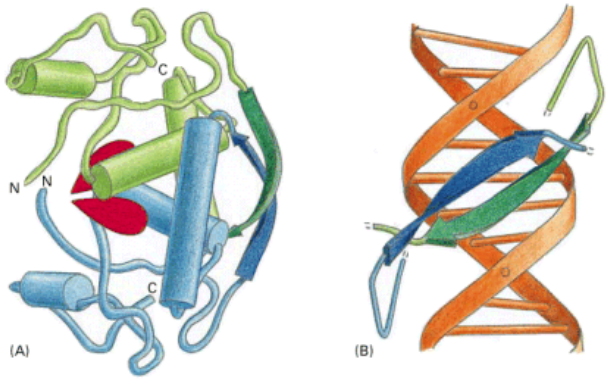

Figure 7-20. The bacterial *met* repressor protein. The bacterial *met* repressor regulates the genes encoding the enzymes that catalyze methionine synthesis. When this amino acid is abundant, it binds to the repressor, causing a change in the structure of the protein that enables it to bind to DNA tightly, shutting off the synthesis of the enzymes. (A) In order to bind to DNA tightly, the *met* repressor must be complexed with S-adenosyl methionine, shown in *red*. One subunit of the dimeric protein is shown in *green*, while the other is shown in *blue*. The two-stranded β sheet that binds to DNA is formed by one strand from each subunit and is shown in *dark green* and *dark blue*. (B) Simplified diagram of the *met* repressor bound to DNA, showing how the two-stranded β sheet of the repressor binds to the major groove of DNA. For clarity, the other regions of the repressor have been omitted. (A, adapted from S. Phillips, *Curr. Opin. Struct. Biol.* 1:8998, 1991; B, adapted from W. Somers and S. Phillips, *Nature* 359:387393, 1992.)

Figure 7-21. A leucine zipper dimer bound to DNA. Two α-helical DNA-binding domains (*bottom*) dimerize through their α-helical leucine zipper region (*top*) to form an inverted Y-shaped structure. Each arm of the Y is formed by a single α helix, one from each monomer, that mediates binding to a specific DNA sequence in the major groove of DNA. Each α helix binds to one-half of a symmetric DNA structure. The structure shown is of the yeast Gcn4 protein, which regulates transcription in response to the availability of amino acids in the environment. (Adapted from T.E. Ellenberger et al., *Cell* 71:12231237, 1992.)

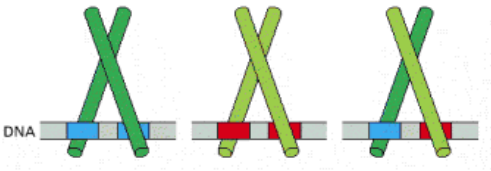

Figure 7-22. Heterodimerization of leucine zipper proteins can alter their DNA-binding specificity. Leucine zipper homodimers bind to symmetric DNA sequences, as shown in the left-hand and center drawings. These two proteins recognize different DNA sequences, as indicated by the *red* and *blue* regions in the DNA. The two different monomers can combine to form a heterodimer, which now recognizes a hybrid DNA sequence, composed from one *red* and one *blue* region.

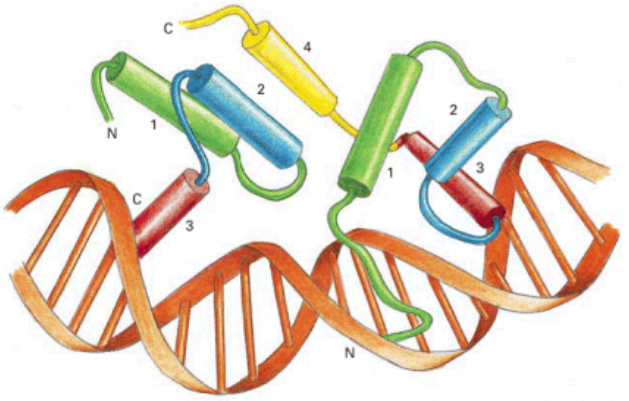

Figure 7-23. A heterodimer composed of two homeodomain proteins bound to its DNA recognition site. The *yellow* helix 4 of the protein on the right (Matα2) is unstructured in the absence of the protein on the left (Mata1), forming a helix only upon heterodimerization. The DNA sequence is thereby recognized jointly by both proteins; some of the protein-DNA contacts made by Matα2 were shown in Figure 7-16. These two proteins are from budding yeast, where the heterodimer specifies a particular cell type (see Figure 7-65). The helices are numbered in accordance with Figure 7-16. (Adapted from T. Li et al., *Science* 270:262269, 1995.)

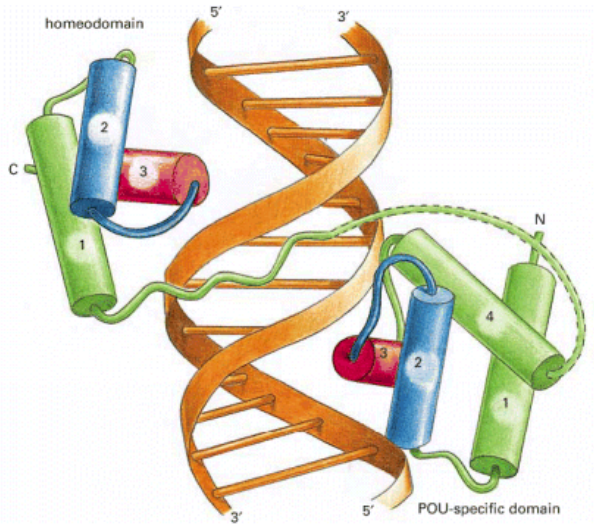

Figure 7-24. Two DNA-binding domains covalently joined by a flexible polypeptide. The structure shown (called a POU-domain) consists of both a homeodomain and a helix-turn-helix structure (closely related to the bacteriophage λ repressor - see Figure 7-14) joined by a flexible polypeptide "leash," indicated by the broken lines. The entire protein is encoded in a single gene and is synthesized as a continuous polypeptide chain. The covalent joining of two structures in this way results in a large increase in the affinity of the protein for its specific DNA sequence compared with the DNA affinity of either separate structure. The group of mammalian gene regulatory proteins exemplified by this structure regulate the production of growth factors, immunoglobulins, and other molecules involved in development. The particular example shown is from the Oct-1 protein. (Adapted from J.D. Klemm et al., *Cell* 77:2132, 1994.)

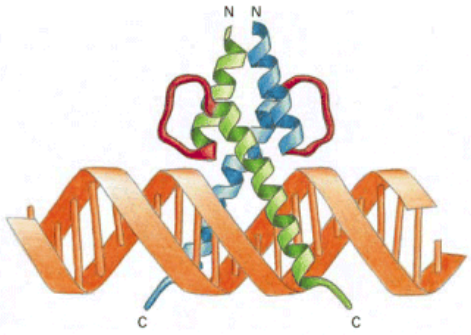

Figure 7-25. A helix-loop-helix dimer bound to DNA. The two monomers are held together in a four-helix bundle: each monomer contributes two α helices connected by a flexible loop of protein (*red*). A specific DNA sequence is bound by the two α helices that project from the four-helix bundle. (Adapted from A.R. Ferre-D'Amare et al., *Nature* 363:3845, 1993.)

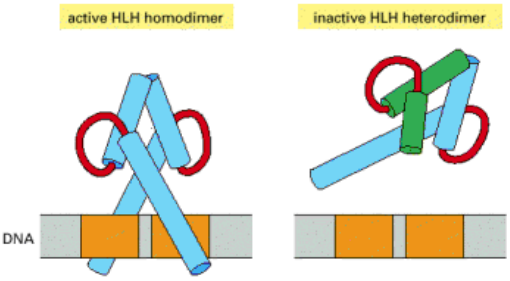

Figure 7-26. Inhibitory regulation by truncated HLH proteins. The HLH motif is responsible for both dimerization and DNA binding. On the *left*, an HLH homodimer recognizes a symmetric DNA sequence. On the *right*, the binding of a full-length HLH protein *(blue)* to a truncated HLH protein *(green)* that lacks the DNA-binding α helix generates a heterodimer that is unable to bind DNA tightly. If present in excess, the truncated protein molecule blocks the homodimerization of the full-length HLH protein and thereby prevents it from binding to DNA.

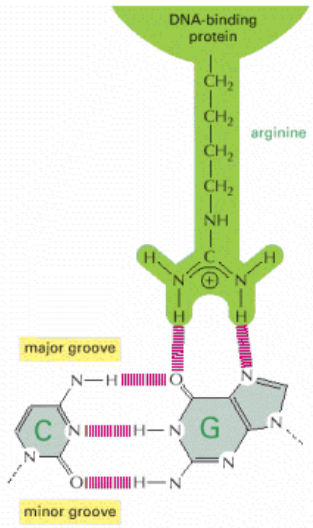

Figure 7-27. One of the most common protein-DNA interactions. Because of its specific geometry of hydrogen-bond acceptors (see Figure 7-7), guanine can be unambiguously recognized by the side chain of arginine. Another common protein-DNA interaction was shown in Figure 7-12.

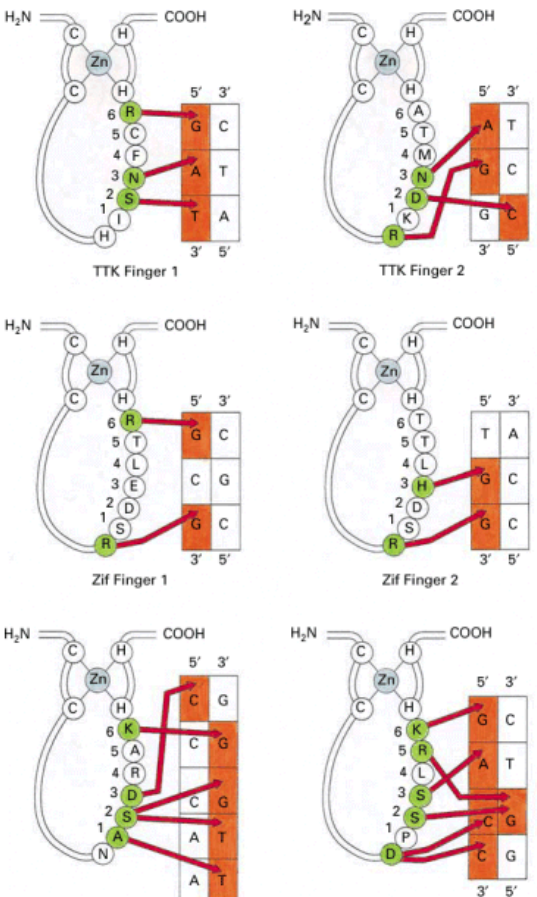

Figure 7-28. Summary of sequence-specific interactions between different six zinc fingers and their DNA recognition sequences. Even though all six Zn fingers have the same overall structure (see Figure 7-17), each binds to a different DNA sequence. The numbered amino acids form the α helix that recognizes DNA (Figures 7-17 and 7-18), and those that make sequence-specific DNA contacts are colored *green*. Bases contacted by protein are *orange.* Although arginine-guanine contacts are common (see Figure 7-27), guanine can also be recognized by serine, histidine, and lysine, as

shown. Moreover, the same amino acid (serine, in this example) can recognize more than one base. Two of the Zn fingers depicted are from the TTK protein (a *Drosophila* protein that functions in development); two are from the mouse protein (Zif268) that was shown in Figure 7-18; and two are from a human protein (GL1), whose aberrant forms can cause certain types of cancers. (Adapted from C. Branden and J. Tooze, Introduction to Protein Structure, 2nd edn. New York: Garland Publishing, 1999.)

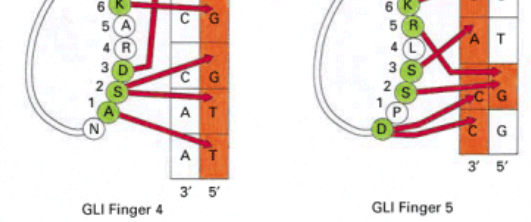

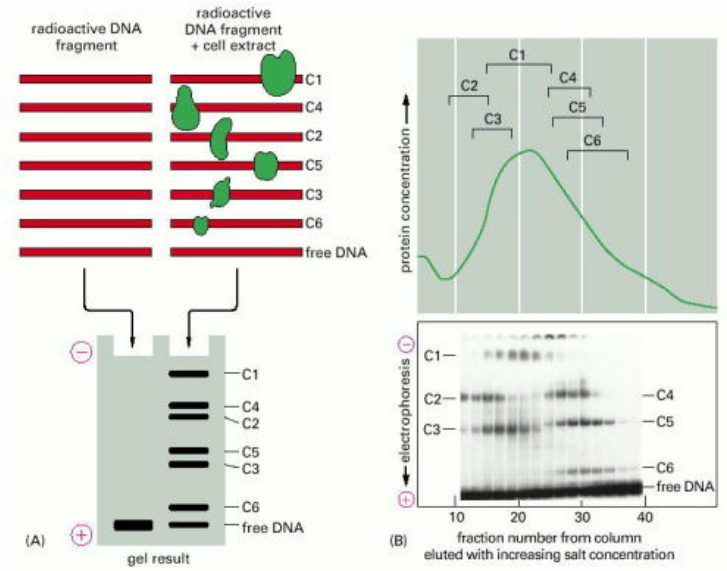

Figure 7-29. A gel-mobility shift assay. The principle of the assay is shown schematically in (A). In this example an extract of an antibody-producing cell line is mixed with a radioactive DNA fragment containing about 160 nucleotides of a regulatory DNA sequence from a gene encoding the light chain of the antibody made by the cell line. The effect of the proteins in the extract on the mobility of the DNA fragment is analyzed by polyacrylamide-gel electrophoresis followed by autoradiography. The free DNA fragments migrate rapidly to the bottom of the gel, while those fragments bound to proteins are retarded; the finding of six retarded bands suggests that the extract contains six different sequence-specific DNA-binding proteins (indicated as C1C6) that bind to this DNA sequence. (For simplicity, any DNA fragments with more than one protein bound have been omitted from the figure.) In (B) the extract was fractionated by a standard chromatographic technique *(top)*, and each fraction was mixed with the radioactive DNA fragment, applied to one lane of a polyacrylamide gel, and analyzed as in (A). (B, modified from C. Scheidereit, A. Heguy, and R.G. Roeder, *Cell* 51:783793, 1987.)

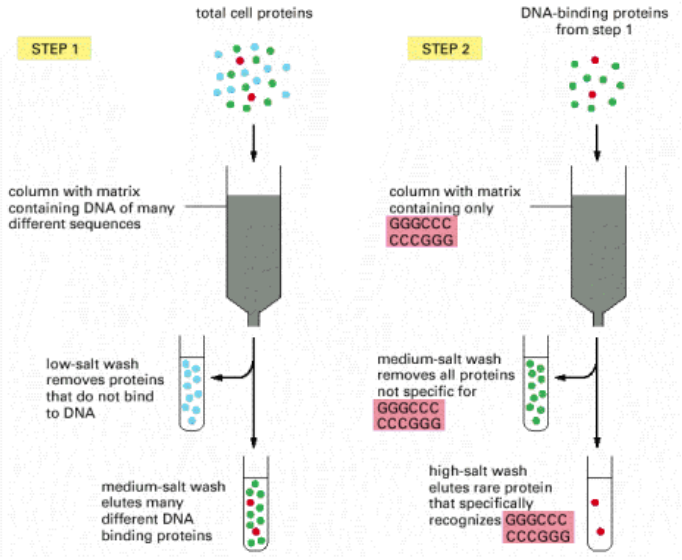

Figure 7-30. DNA affinity chromatography. In the first step, all the proteins that can bind DNA are separated from the remainder of the cellular proteins on a column containing a huge number of different DNA sequences. Most sequence-specific DNA-binding proteins have a weak (nonspecific) affinity for bulk DNA and are therefore retained on the column. This affinity is due largely to ionic attractions, and the proteins can be washed off the DNA by a solution that contains a moderate concentration of salt. In the second step, the mixture of DNA-binding proteins is passed through a column that contains only DNA of a particular sequence. Typically, all the DNA-binding proteins will stick to the column, the great majority by nonspecific interactions. These are again eluted by solutions of moderate salt concentration, leaving on the column only those proteins (typically one or only a few) that bind specifically and therefore very tightly to the particular DNA sequence. These remaining proteins can be eluted from the column by solutions containing a very high concentration of salt.

Figure 7-31. A method for determining the DNA sequence recognized by a gene regulatory protein. A purified gene regulatory protein is mixed with millions of different short DNA fragments, each with a different sequence of nucleotides. A collection of such DNA fragments can be produced by programming a DNA synthesizer, a machine that chemically synthesizes DNA of any desired sequence (discussed in Chapter 8). For example, there are 4^{11}, or approximately 4.2 million possible

sequences for a DNA fragment of 11 nucleotides. The double-stranded DNA fragments that bind tightly to the gene regulatory protein are then separated from the DNA fragments that fail to bind. One method for accomplishing this separation is through gel-mobility shifts, as described in Figure 7-29. After separation of the DNA-protein complexes from the free DNA, the DNA fragments are removed from the protein, and several additional rounds of the same selection process are carried out. The nucleotide sequences of those DNA fragments that remain through multiple rounds of selection can be determined, and a consensus DNA recognition sequence can be generated.

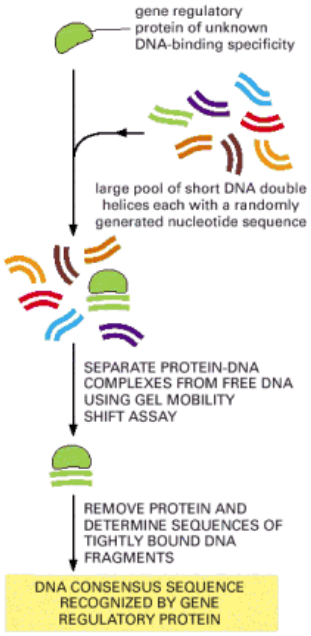

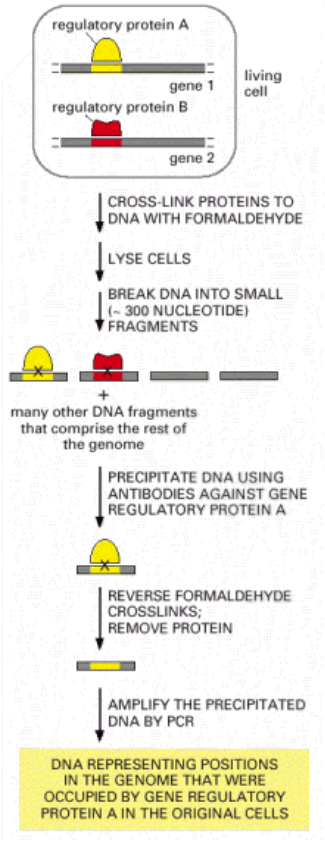

Figure 7-32. Chromatin immunoprecipitation. This methodology allows the identification of the sites in a genome that are occupied *in vivo* by a gene regulatory protein. The amplification of DNA by the polymerase chain reaction (PCR) is described in Chapter 8. The identities of the precipitated, amplified DNA fragments can be determined by hybridizing the mixture of fragments to DNA microarrays, described in Chapter 8.

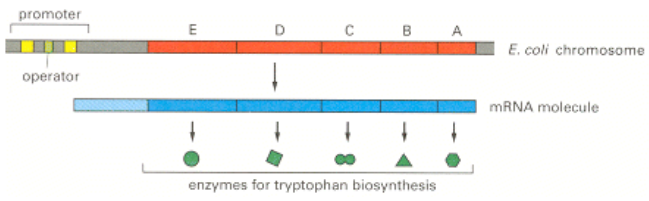

Figure 7-33. The clustered genes in *E. coli* that code for enzymes that manufacture the amino acid tryptophan. These five genes are transcribed as a single mRNA molecule, a feature that allows their expression to be controlled coordinately. Clusters of genes transcribed as a single mRNA molecule are common in bacteria. Each such cluster is called an operon.

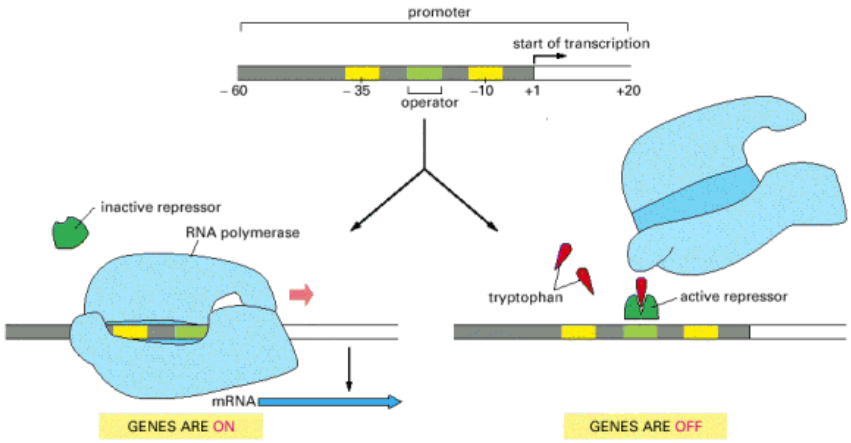

Figure 7-34. Switching the tryptophan genes on and off. If the level of tryptophan inside the cell is low, RNA polymerase binds to the promoter and transcribes the five genes of the tryptophan *(trp)* operon. If the level of tryptophan is high, however, the tryptophan repressor is activated to bind to the operator, where it blocks the binding of RNA polymerase to the promoter. Whenever the level of intracellular tryptophan drops, the repressor releases its tryptophan and becomes inactive, allowing the polymerase to begin transcribing these genes. The promoter includes two key blocks of DNA sequence information, the -35 and -10 regions highlighted in *yellow* (see Figure 6-12).

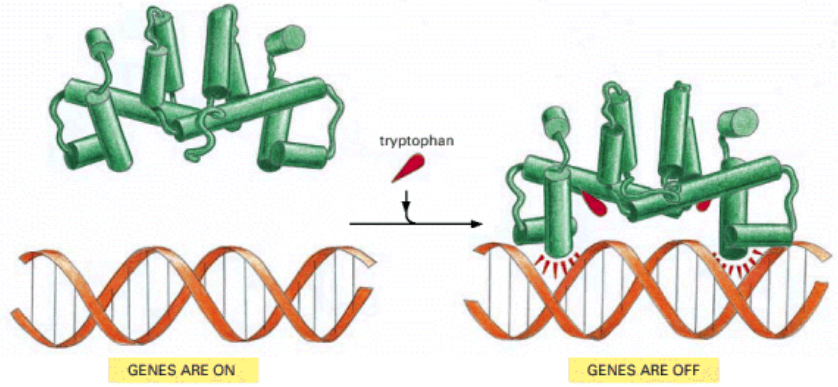

Figure 7-35. The binding of tryptophan to the tryptophan repressor protein changes the conformation of the repressor. The conformational change enables this gene regulatory protein to bind tightly to a specific DNA sequence (the operator), thereby blocking transcription of the genes encoding the enzymes required to produce tryptophan (the *trp* operon). The three-dimensional structure of this bacterial helix-turn-helix protein, as determined by x-ray diffraction with and without tryptophan bound, is illustrated. Tryptophan binding increases the distance between the two recognition helices in the homodimer, allowing the repressor to fit snugly on the operator. (Adapted from R. Zhang et al., *Nature* 327:591597, 1987.)

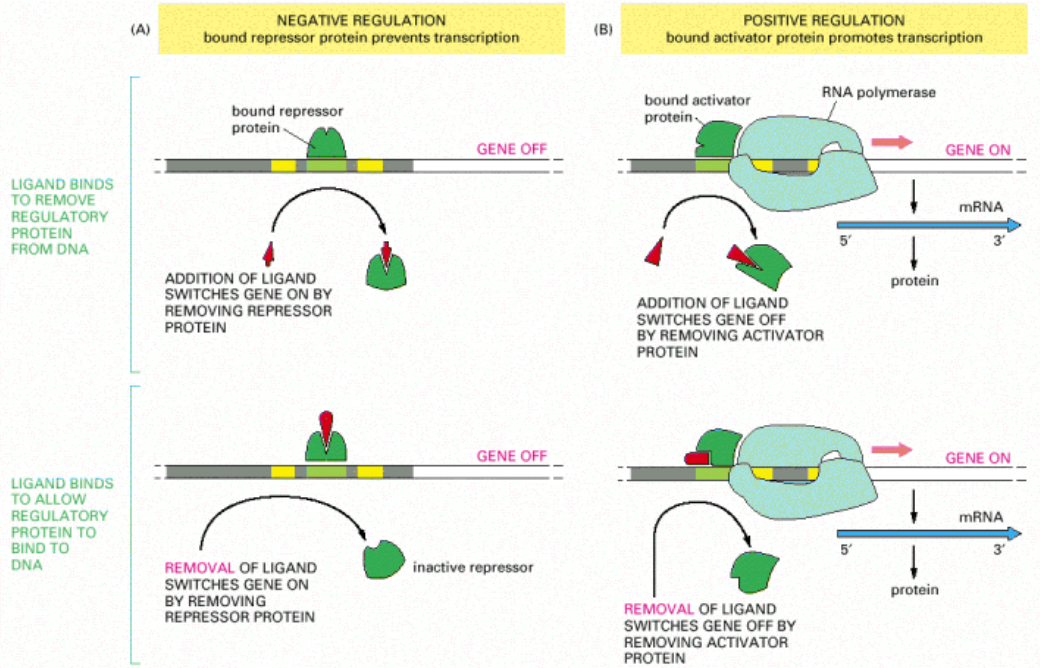

Figure 7-36. Summary of the mechanisms by which specific gene regulatory proteins control gene transcription in procaryotes. (A) Negative regulation; (B) positive regulation. Note that the addition of an "inducing" ligand can turn on a gene either by removing a gene repressor protein from the DNA *(upper left panel)* or by causing a gene activator protein to bind *(lower right panel).* Likewise, the addition of an "inhibitory" ligand can turn off a gene either by removing a gene activator protein from the DNA *(upper right panel)* or by causing a gene repressor protein to bind *(lower left panel).*

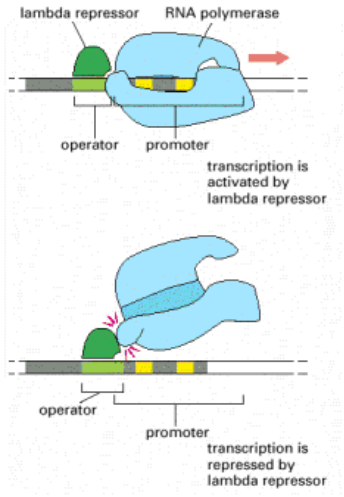

Figure 7-37. Some bacterial gene regulatory proteins can act as both a transcriptional activator and a repressor, depending on the precise placement of its binding sites in DNA. An example is the bacteriophage lambda repressor. For some genes, the protein acts as a transcriptional activator by providing a favorable contact for RNA polymerase *(top).* At other genes *(bottom)*, the operator is located one base pair closer to the promoter, and, instead of helping polymerase, the repressor now competes with it for binding to the DNA. The lambda repressor recognizes its operator by a helix-turn-helix motif, as shown in Figure 7-14.

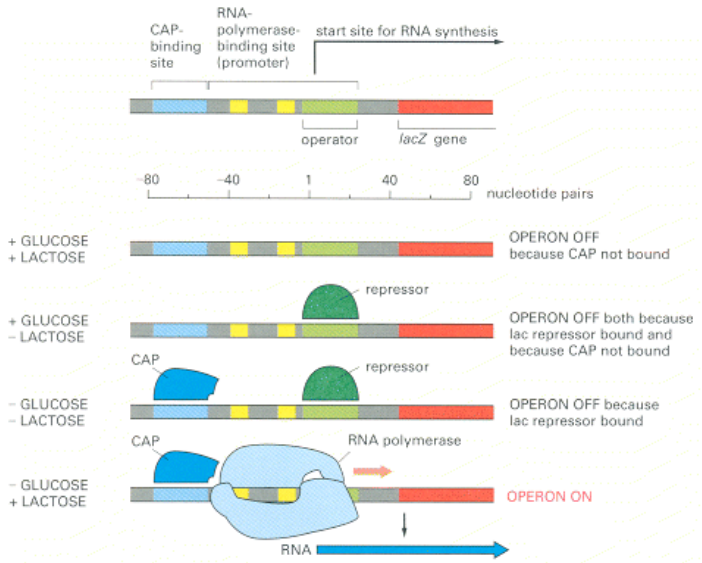

Figure 7-38. Dual control of the *lac* operon. Glucose and lactose levels control the initiation of transcription of the *lac* operon through their effects on the lac repressor protein and CAP. Lactose addition increases the concentration of allolactose, which binds to the repressor protein and removes it from the DNA. Glucose addition decreases the concentration of cyclic AMP; because cyclic AMP no longer binds to CAP, this gene activator protein dissociates from the DNA, turning off the operon. As shown in Figure 7-11, CAP is known to induce a bend in the DNA when it binds; for simplicity, the bend is not shown here. *LacZ*, the first gene of the *lac* operon, encodes the enzyme β-galactosidase, which breaks down the disaccharide lactose to galactose and glucose. The essential features of the *lac* operon are summarized in the figure, but in reality the situation is more complex. For one thing, there are several *lac* repressor binding sites located at different positions along the DNA. Although the one illustrated exerts the greatest effect, the others are required for full repression. In addition, expression of the *lac* operon is never completely shut down. A small amount of the enzyme β-galactosidase is required to convert lactose to allolactose thereby permitting the *lac* repressor to be inactivated when lactose is added to the growth medium.

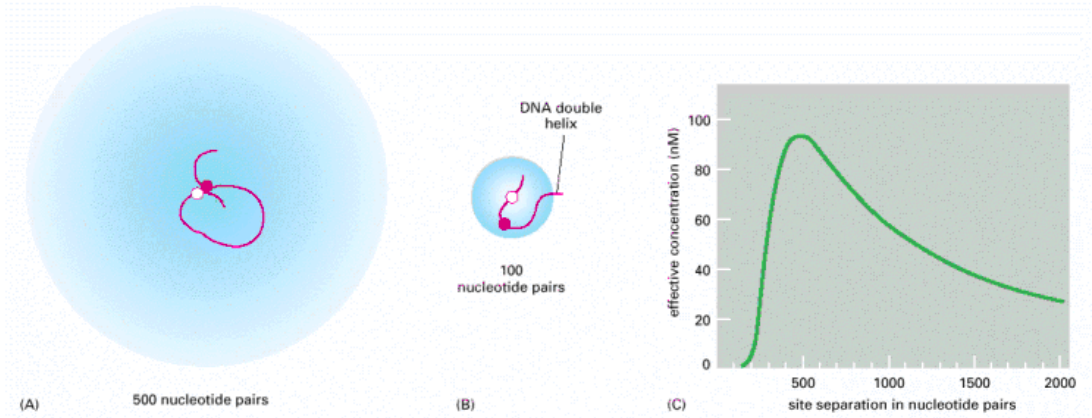

Figure 7-39. Binding of two proteins to separate sites on the DNA double helix can greatly increase their probability of interacting. (A) The tethering of one protein to the other via an intervening DNA loop of 500 nucleotide pairs increases their frequency of collision. The intensity of *blue* coloring reflects the probability that the *red* protein will be located at each position in space relative to the *white* protein. (B) The flexibility of DNA is such that an average sequence makes a smoothly graded 90° bend (a curved turn) about once every 200 nucleotide pairs. Thus, when two proteins are tethered by only 100 nucleotide pairs, their contact is relatively restricted. In such cases the protein interaction is facilitated when the two protein-binding sites are separated by a multiple of about 10 nucleotide pairs, which places both proteins on the same side of the DNA helix (which has about 10 nucleotides per turn) and thus on the inside of the DNA loop, where they can best reach each other. (C) The theoretical effective concentration of the *red* protein at the site where the *white* protein is bound, as a function of their separation. (C, courtesy of Gregory Bellomy, modified from M.C. Mossing and M.T. Record, *Science* 233:889892, 1986. © AAAS.)

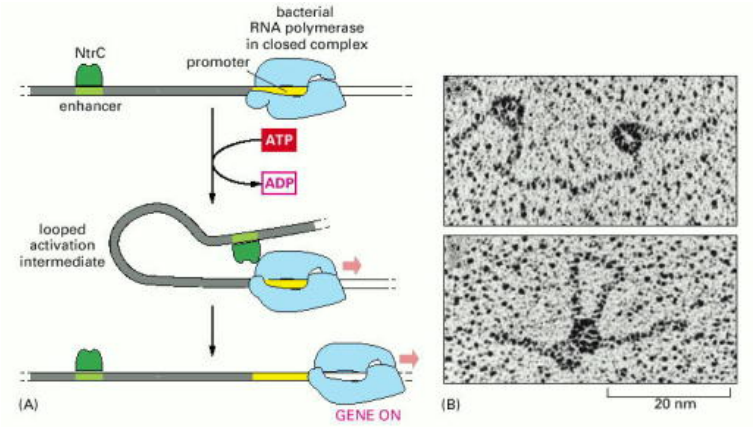

Figure 7-40. Gene activation at a distance. (A) NtrC is a bacterial gene regulatory protein that activates transcription by facilitating the transition between the initial binding of RNA polymerase to the promoter and the formation of an initiating complex (discussed in Chapter 6). As indicated, the transition stimulated by NtrC requires the energy produced by ATP hydrolysis, although this requirement is unusual for bacterial transcription initiation. (B) The interaction of NtrC and RNA polymerase, with the intervening DNA looped out, can be seen in the electron microscope. Although transcriptional activation by DNA looping is unusual in bacteria, it is typical of eucaryotic gene regulatory proteins. (B, courtesy of Harrison Echols and Sydney Kustu.)

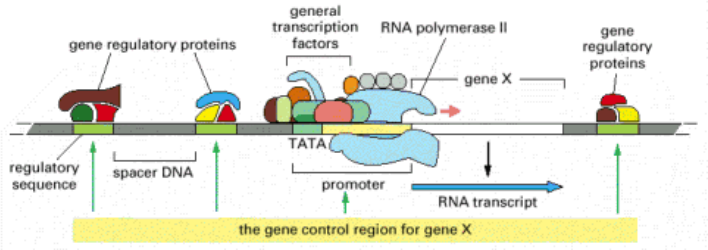

Figure 7-41. The gene control region of a typical eucaryotic gene. The *promoter* is the DNA sequence where the general transcription factors and the polymerase assemble (see Figure 6-16). The *regulatory sequences* serve as binding sites for gene regulatory proteins, whose presence on the DNA affects the rate of transcription initiation. These sequences can be located adjacent to the promoter, far upstream of it, or even within introns or downstream of the gene. DNA looping is thought to allow gene regulatory proteins bound at any of these positions to interact with the proteins that assemble at the promoter. Whereas the general transcription factors that assemble at the promoter are similar for all polymerase II transcribed genes, the gene regulatory proteins and the locations of their binding sites relative to the promoter are different for each gene.

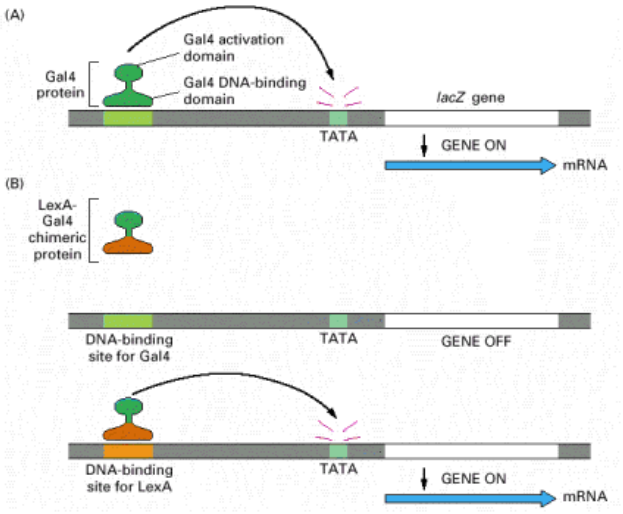

Figure 7-42. The modular structure of a gene activator protein. Outline of an experiment that reveals the presence of independent DNA-binding and transcription-activating domains in the yeast gene activator protein Gal4. A functional activator can be reconstituted from the C-terminal portion of the yeast Gal4 protein if it is attached to the DNA-binding domain of a bacterial gene regulatory protein (the LexA protein) by gene fusion techniques. When the resulting bacterial-yeast hybrid protein is produced in yeast cells, it will activate transcription from yeast genes provided that the specific DNA-binding site for the bacterial protein has been inserted next to them. (A) The normal activation of gene transcription produced by the Gal4 protein. (B) The chimeric gene regulatory protein requires the LexA protein DNA-binding site for its activity. Gal4 is normally responsible for activating the transcription of yeast genes that code for the enzymes that convert galactose to glucose. In the experiments shown here, the control region for one of these genes was fused to the *E. coli lacZ* gene, which codes for the enzyme β-galactosidase (see Figure 7-38). β-galactosidase is very simple to detect biochemically and thus provides a convenient way to monitor the expression level specified by a gene control region; *lacZ* thus serves as a *reporter gene* since it "reports" the activity of a gene control region.

Figure 7-43. Activation of transcription initiation in eucaryotes by recruitment of the eucaryotic RNA polymerase II holoenzyme complex. (A) An activator protein bound in proximity to a promoter attracts the holoenzyme complex to the promoter. According to this model, the holoenzyme (which contains over 100 protein subunits) is brought to the promoter

separately from the general transcription factors TFIID and TFIIA. The "broken" DNA in this and subsequent figures indicates that this portion of the DNA molecule can be very long and of variable length. (B) Diagram of an *in vivo* experiment whose outcome supports the holoenzyme recruitment model for gene activator proteins. The DNA-binding domain of a protein has been fused directly to a protein component of the mediator, a 20-subunit protein complex which is part of the holoenzyme complex, but which is easily dissociable from the remainder of the holoenzyme. When the binding site for the hybrid protein is experimentally inserted near a promoter, transcription initiation is strongly increased. In this experiment, the "activation domain" of the activator (see Figure 7-42) has been omitted, suggesting that an important function of the activation domain is simply to interact with the RNA polymerase holoenzyme complex and thereby aid in its assembly at the promoter. The ability of gene activator proteins to recruit the transcription machinery to promoters has also been demonstrated directly, using chromatin immunoprecipitation (see Figure 7-32). DNA-bound activator proteins typically increase the rate of transcription by up to 1000-fold, which is consistent with a relatively weak and nonspecific interaction between the activator and the holoenzyme (a 1000-fold change in affinity corresponds to a change in ΔG of ~4 kcal/mole, which could be accounted for by just a few weak, noncovalent bonds).

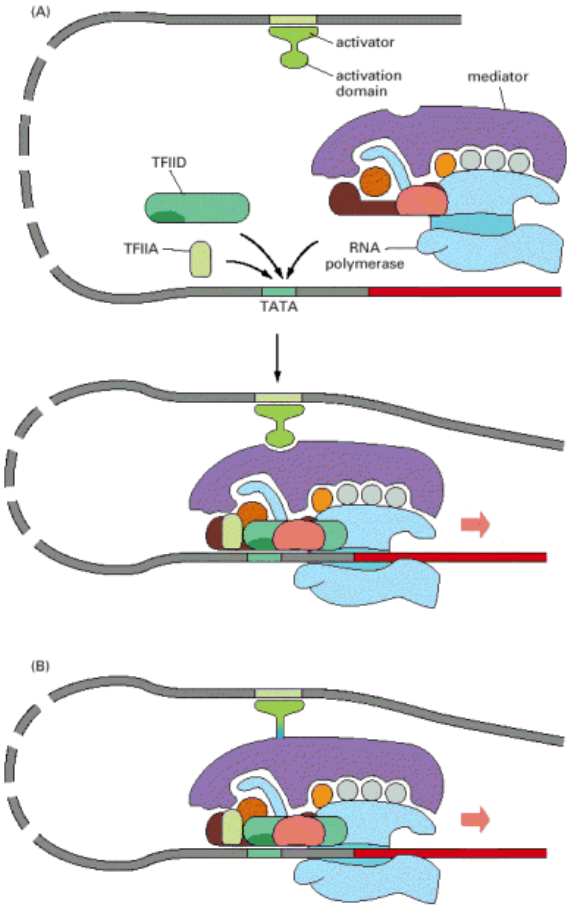

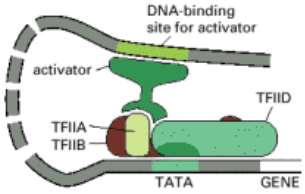

Figure 7-44. A model for the action of some eucaryotic transcriptional activators. The gene activator protein, bound to DNA in the rough vicinity of the promoter, facilitates the assembly of some of the general transcription factors. Although some activator proteins may be dedicated to particular steps in the pathway for transcription initiation, many seem to be capable of acting at several steps.

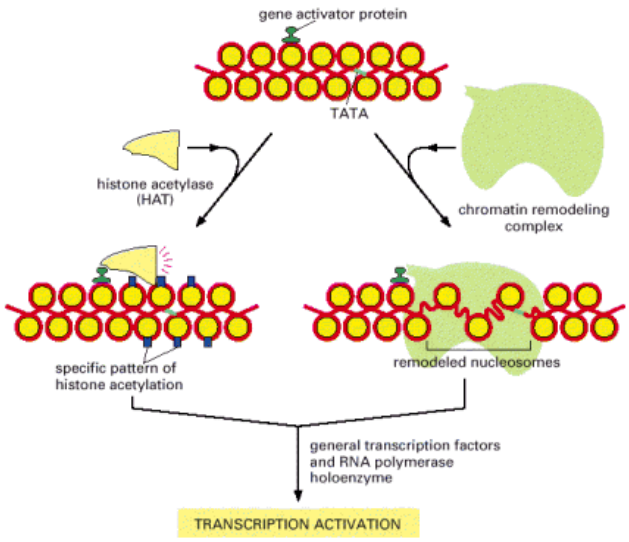

Figure 7-45. Local alterations in chromatin structure directed by eucaryotic gene activator proteins. Histone acetylation and nucleosome remodeling generally render the DNA packaged in chromatin more accessible to other proteins in the cell, including those required for transcription initiation. In addition, specific patterns of histone modification directly aid in the assembly of the general transcription factors at the promoter (see Figure 7-46). Transcription initiation and the formation of a compact chromatin structure can be regarded as competing biochemical assembly reactions. Enzymes that increase, even transiently, the accessibility of DNA in chromatin will tend to favor transcription initiation (see Figure 4-34).

Figure 7-46. Two specific ways that local histone acetylation can stimulate transcription initiation. (A) Some gene activator proteins can bind directly to DNA that is packaged in unmodified chromatin. By attracting histone acetylases (and nucleosome remodeling complexes), these "pioneer" activators can facilitate the binding to DNA of additional activator proteins that cannot bind to unmodified chromatin. These additional proteins can in turn carry out additional modifications of chromatin or act directly on the transcription machinery as shown in Figures 7-43 and 7-44. (B) A subunit of the general transcription factor TFIID contains two 120-amino acid protein domains called *bromodomains*. Each bromodomain forms a binding pocket for an acetylated lysine side chain (designated Ac in the figure); in TFIID the two pockets are separated by 25 Å, which is the optimal spacing for

recognizing a pair of acetylated lysines separated by six or seven amino acids on the N-terminal tail of histone H4. In addition to the pattern of acetylation shown, this subunit of TFIID also recognizes the histone H4 tail acetylated at positions 5 and 12 and the fully acetylated tail. It has no appreciable affinity for an unacetylated H4 tail and only low affinity for an H4 tail acetylated at a single lysine. As shown in Figure 4-35, certain patterns of histone H4 acetylation, including those recognized by TFIID, are associated with transcriptionally active regions of chromatin.

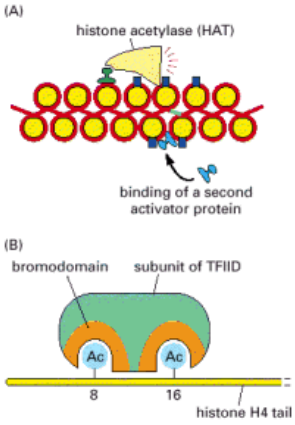

Figure 7-47. Transcriptional synergy. In this experiment, the rate of transcription produced by three experimentally constructed regulatory regions is compared in a eucaryotic cell. Transcriptional synergy, the greater than additive effect of the activators, is observed when several molecules of gene activator protein are bound upstream of the promoter. Synergy is also typically observed between different gene activator proteins from the same organism and even between activator proteins from widely different eucaryotic species when they are experimentally introduced into the same cell. This last observation reflects the high degree of conservation of the transcription machinery.

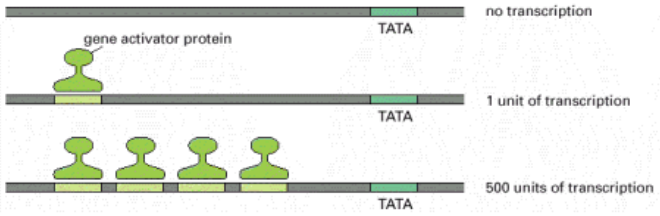

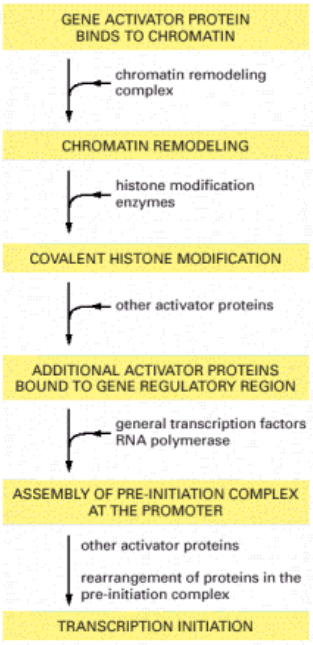

Figure 7-48. An order of events leading to transcription initiation at a specific promoter. The well-studied example shown is from a promoter in the budding yeast *S. cerevisiae*. The chromatin remodeling complex and histone acetylase apparently dissociate from the DNA after they sequentially act. The order of steps on the pathway to transcription initiation appears to be different for different promoters. For example, in a well-studied example from humans, histone acetylases function first, followed by RNA polymerase recruitment, followed by chromatin remodeling complex recruitment.

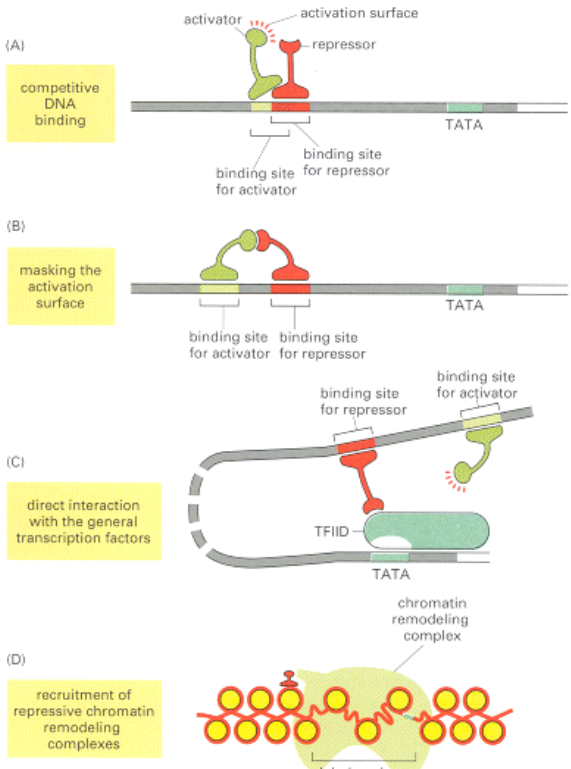

Figure 7-49. Five ways in which eucaryotic gene repressor proteins can operate. (A) Gene activator proteins and gene repressor proteins compete for binding to the same regulatory DNA sequence. (B) Both proteins can bind DNA, but the repressor binds to the activation domain of the activator protein thereby preventing it from carrying out its activation functions. In a variation of this strategy, the repressor binds tightly to the activator

without having to be bound to DNA directly. (C) The repressor interacts with an early stage of the assembling complex of general transcription factors, blocking further assembly. Some repressors also act at late stages in transcription initiation, for example, by preventing the release of the RNA polymerase from the general transcription factors. (D) The repressor recruits a chromatin remodeling complex which returns the nucleosomal state of the promoter region to its pre-transcriptional form. Certain types of remodeling complexes appear dedicated to restoring the repressed nucleosomal state of a promoter, whereas others (for example, those recruited by activator proteins) render DNA packaged in nucleosomes more accessible (see Figure 4-34). However the same remodeling complex could in principle be used either to activate or repress transcription: depending on the concentration of other proteins in the nucleus, either the remodeled state or the repressed state could be stabilized. According to this view, the remodeling complex simply allows chromatin structure to change. (E) The repressor attracts a histone deacetylase to the promoter. Local histone deacetylation reduces the affinity of TFIID for the promoter (see Figure 7-46) and decreases the accessibility of DNA in the affected chromatin. A sixth mechanism of negative control - inactivation of a transcriptional activator by heterodimerization - was illustrated in Figure 7-26. For simplicity, nucleosomes have been omitted from (A)-(C), and the scale of (D) and (E) has been reduced relative to (A)-(C).

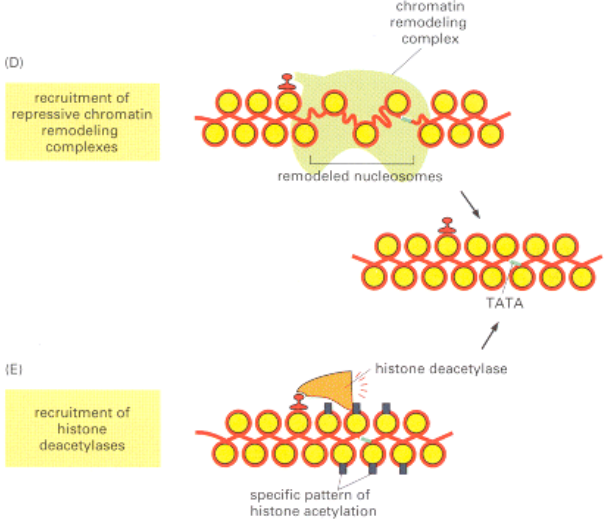

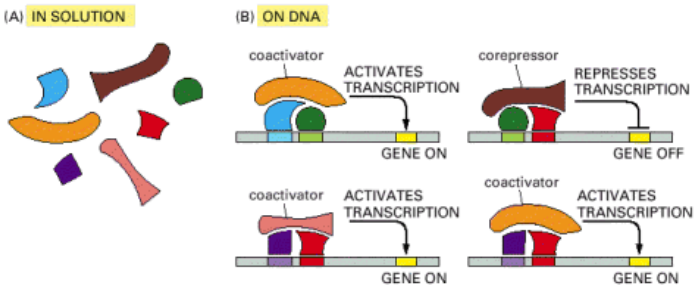

Figure 7-50. Eucaryotic gene regulatory proteins often assemble into complexes on DNA. Seven gene regulatory proteins are shown in (A). The nature and function of the complex they form depends on the specific DNA sequence that seeds their assembly. In (B), some assembled complexes activate gene transcription, while another represses transcription. Note that the *red* protein is shared by both activating and repressing complexes.

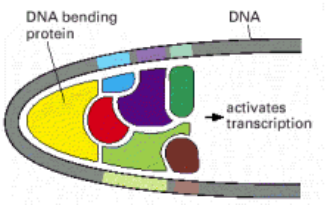

Figure 7-51. Schematic depiction of an enhancesome. The protein depicted in *yellow* is termed an architectural protein since its main role is to bend the DNA to allow the cooperative assembly of the other components. The protein surface of this enhancesome interacts with a coactivator which activates transcription at a nearby promoter. The enhancesome depicted here is based on that found in the control region of the gene that codes for a subunit of the T cell receptor (discussed in Chapter 24). The complete set of protein components for the enhancesome are present only in certain cells of the developing immune system, which eventually give rise to mature T cells.

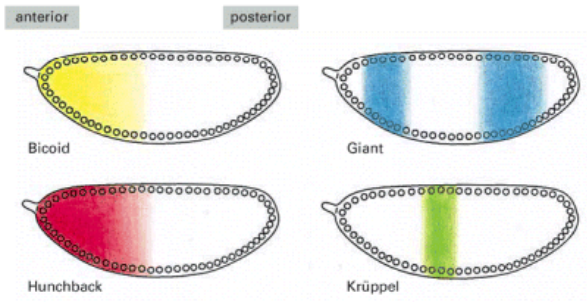

Figure 7-52. The nonuniform distribution of four gene regulatory proteins in an early *Drosophila* embryo. At this stage the embryo is a syncytium, with multiple nuclei in a common cytoplasm. Although not illustrated in these drawings, all of these proteins are concentrated in the nuclei.

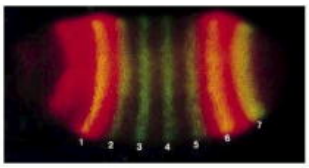

Figure 7-53. The seven stripes of the protein encoded by the *even-skipped (eve)* gene in a developing *Drosophila* embryo. Two and one-half hours after fertilization, the egg was fixed and stained with antibodies that recognize the Eve protein *(green)* and antibodies that recognize the Giant protein *(red).* Where Eve and Giant proteins are both present, the staining appears *yellow.* At this stage in development, the egg contains approximately 4000 nuclei. The Eve and Giant proteins are both located in the nuclei, and the Eve stripes are about four nuclei wide. The staining pattern of the Giant protein is also shown in Figure 7-52. (Courtesy of Michael Levine.)

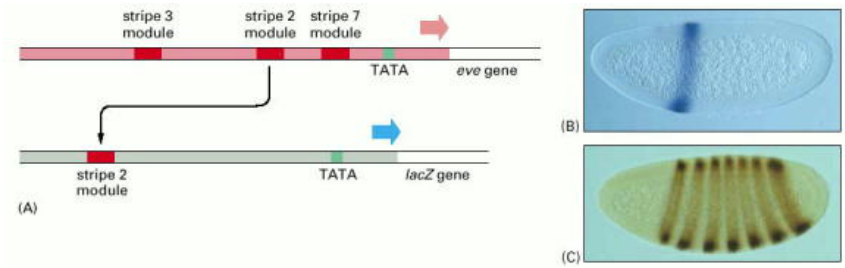

Figure 7-54. Experiment demonstrating the modular construction of the *eve* gene regulatory region. (A) A 480-nucleotide-pair piece of the *eve* regulatory region was removed and inserted upstream of a test promoter that directs the synthesis of the enzyme β-galactosidase (the product of the *E. coli lacZ* gene). (B) When this artificial construct was reintroduced into the genome of *Drosophila* embryos, the embryos expressed β-galactosidase (detectable by histochemical staining) precisely in the position of the second of the seven Eve stripes (C). (B and C, courtesy of Stephen Small and Michael Levine.)

Figure 7-55. Close-up view of the *eve* stripe 2 unit. The segment of the *eve* gene control region identified in the previous figure contains regulatory sequences, each of which binds one or another of four gene regulatory proteins. It is known from genetic experiments that these four regulatory proteins are responsible for the proper expression of *eve* in stripe 2. Flies that are deficient in the two gene activators Bicoid and Hunchback, for example, fail to efficiently express *eve in* stripe 2. In flies deficient in either of the two gene repressors, Giant and Krüppel, stripe 2 expands and covers an abnormally broad region of the embryo. The DNA-binding sites for these gene regulatory proteins were determined by cloning the genes encoding the proteins, overexpressing the proteins in *E. coli*, purifying them, and performing DNA-footprinting experiments as described in Chapter 8. The *top* diagram indicates that, in some cases, the binding sites for the gene regulatory proteins overlap and the proteins can compete for binding to the DNA. For example, binding of Krüppel and binding of Bicoid to the site at the far right are thought to be mutually exclusive.

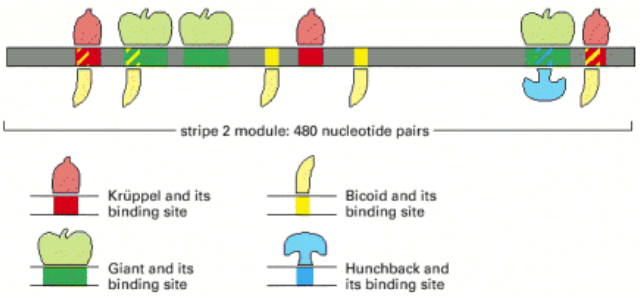

Figure 7-56. Distribution of the gene regulatory proteins responsible for ensuring that *eve* is expressed in stripe 2. The distributions of these proteins were visualized by staining a developing *Drosophila* embryo with antibodies directed against each of the four proteins (see Figures 7-52 and 7-53). The expression of *eve* in stripe 2 occurs only at the position where the two activators (Bicoid and Hunchback) are present and the two repressors (Giant and Krüppel) are absent. In fly embryos that lack Krüppel, for example, stripe 2 expands posteriorly. Likewise, stripe 2 expands posteriorly if the DNA-binding sites for Krüppel in the stripe 2 module (see Figure 7-55) are inactivated by mutation and this regulatory region is reintroduced into the genome. The *eve* gene itself encodes a gene regulatory protein, which, after its pattern of expression is set up in seven stripes, regulates the expression of other *Drosophila* genes. As development proceeds, the embryo is thus subdivided into finer and finer regions that eventually give rise to the different body parts of the adult fly, as discussed in Chapter 21. This example from *Drosophila* embryos is unusual in that the nuclei are exposed directly to positional cues in the form of concentrations of gene regulatory proteins. In embryos of most other organisms, individual nuclei are in separate cells, and extracellular positional information must either pass across the plasma membrane or, more usually, generate signals in the cytosol in order to influence the genome.

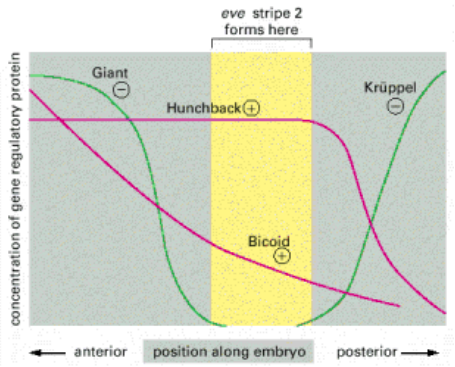

Figure 7-57. Integration at a promoter. Multiple sets of gene regulatory proteins can work together to influence transcription initiation at a promoter, as they do in the *eve* stripe 2 module illustrated previously in Figure 7-55. It is not yet understood in detail how the integration of multiple inputs is achieved, but it is likely that the final transcriptional activity of the gene results from a competition between activators and repressors that act by the mechanisms summarized in Figures 7-43, 7-44, 7-45, 7-46, and 7-49.

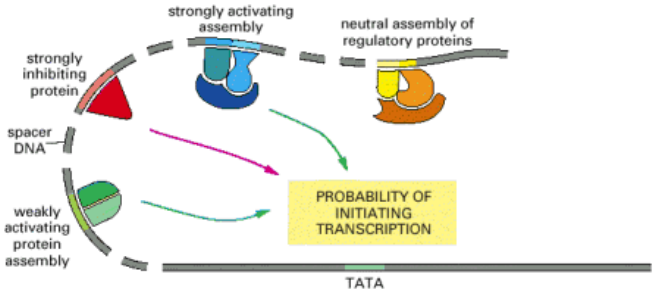

Figure 7-58. Some ways in which the activity of gene regulatory proteins is regulated in eucaryotic cells. (A) The protein is synthesized only when needed and is rapidly degraded by proteolysis so that it does not accumulate. (B) Activation by ligand binding. (C) Activation by phosphorylation. (D) Formation of a complex between a DNA-binding protein and a separate protein with a transcription-activating domain. (E) Unmasking of an activation domain by the phosphorylation of an inhibitor protein. (F) Stimulation of nuclear entry by removal of an inhibitory protein that otherwise keeps the regulatory protein from entering the nucleus. (G) Release of a gene regulatory protein from a membrane bilayer by regulated proteolysis. Each of these mechanisms is typically controlled by extracellular signals which are communicated across the plasma membrane to the gene regulatory proteins in the cell. The ways in which this signaling occurs is discussed in Chapter 15. Mechanisms (A)-(F) are readily reversible and therefore also provide the means to selectively inactivate gene regulatory proteins.

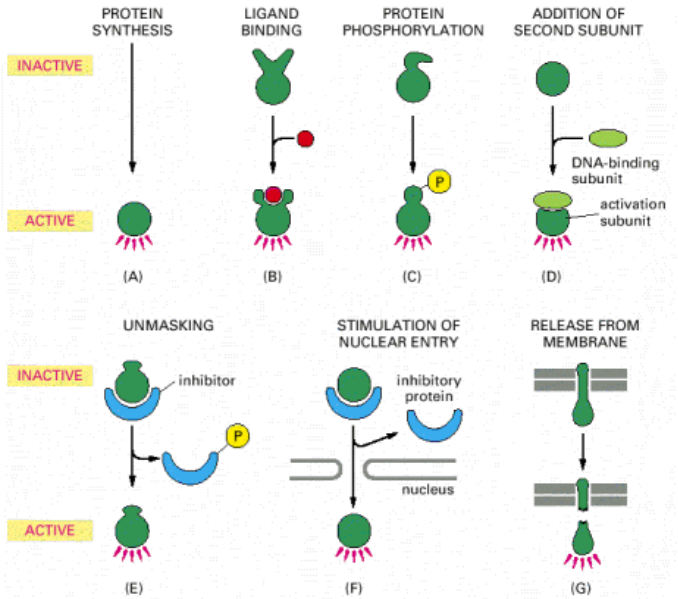

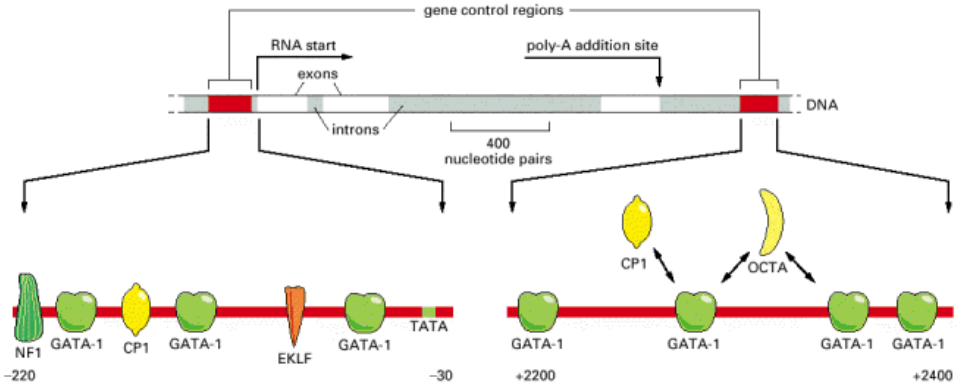

Figure 7-59. Model for the control of the human β-globin gene. The diagram shows some of the gene regulatory proteins thought to control expression of the gene during red blood cell development (see Figure 7-60). Some of the gene regulatory proteins shown, such as CP1, are found in many types of cells, while others, such as GATA-1, are present in only a few types of cells - including red blood cells - and therefore are thought to contribute to the cell-type specificity of β-globin gene expression. As indicated by the *double-headed arrows*, several of the binding sites for GATA-1 overlap those of other gene regulatory proteins; it is thought that occupancy of these sites by GATA-1 excludes binding of other proteins. Once bound to DNA, the gene regulatory proteins recruit chromatin remodeling complexes, histone modifying enzymes, the general transcription factors and RNA polymerase to the promoter. (Adapted from B. Emerson, in Gene Expression: General and Cell-Type Specific [M. Karin, ed.], pp. 116161. Boston: Birkhauser, 1993.)

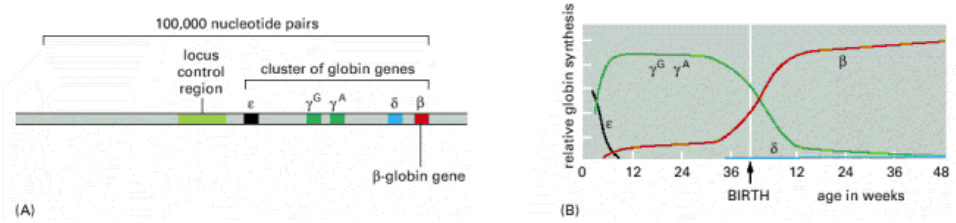

Figure 7-60. The cluster of β-like globin genes in humans. (A) The large chromosomal region shown spans 100,000 nucleotide pairs and contains the five globin genes and a locus control region (LCR). (B) Changes in the expression of the β-like globin genes at various stages of human development. Each of the globin chains encoded by these genes combines with an α-globin chain to form the hemoglobin in red blood cells (see Figure 7-115). (A, after F. Grosveld, G.B. van Assendelft, D.R. Greaves, and G. Kollias, *Cell* 51:975985, 1987. © Elsevier.)

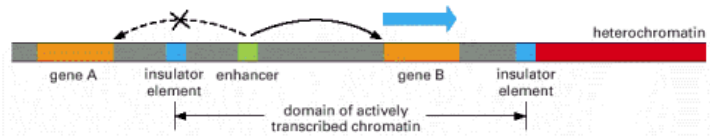

Figure 7-61. Schematic diagram summarizing the properties of insulators. Insulators both prevent the spread of heterochromatin *(right-hand side* of diagram) and directionally block the action of enhancers *(left-hand side)*. Thus gene B is properly regulated and gene B's enhancer is prevented from influencing the transcription of gene A.

Figure 7-62. Localization of a *Drosophila* insulator-binding protein on polytene chromosomes. A polytene chromosome (see pp. 218220) was stained with propidium iodide *(red)* to show its banding patterns - with bands appearing *bright red* and interbands as dark gaps in the pattern *(top)*. The positions on this polytene chromosome that are bound by a particular insulator protein (called BEAF) are stained *bright green* using antibodies directed against the protein *(bottom)*. BEAF is seen to be preferentially localized to interband regions suggesting a role for it in organizing domains of chromatin. For convenience, these two micrographs of the same polytene chromosome are arranged as mirror images. (Courtesy of Uli Laemmli, from K. Zhao et al., *Cell* 81:879889, 1995. © Elsevier.)

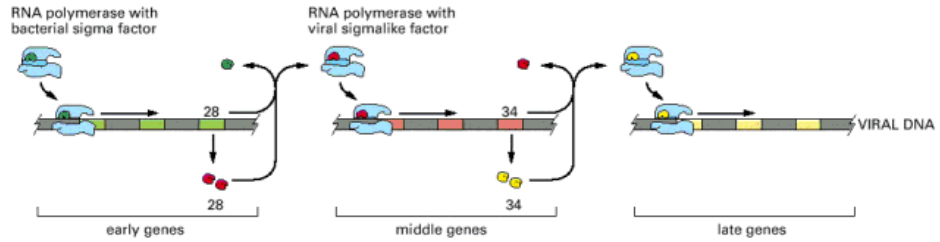

Figure 7-63. Interchangeable RNA polymerase subunits as a strategy to control gene expression in a bacterial virus. The bacterial virus SPO1, which infects the bacterium *B. subtilis*, uses the bacterial polymerase to transcribe its early genes immediately after the viral DNA enters the cell. One of the early genes, called 28, encodes a sigmalike factor that binds to RNA polymerase and displaces the bacterial sigma factor. This new form of polymerase specifically initiates transcription of the SPO1 "middle" genes. One of the middle genes encodes a second sigmalike factor, 34, that displaces the 28 product and directs RNA polymerase to transcribe the "late" genes. This last set of genes produces the proteins that package the virus chromosome into a virus coat and lyse the cell. By this strategy, sets of virus genes are expressed in the order in which they are needed; this ensures a rapid and efficient viral replication.

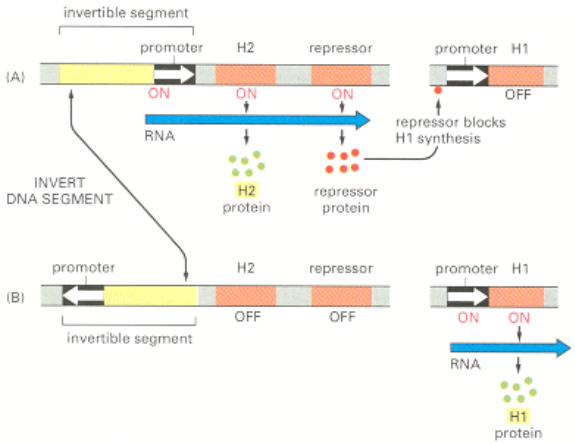

Figure 7-64. Switching gene expression by DNA inversion in bacteria. Alternating transcription of two flagellin genes in a *Salmonella* bacterium is caused by a simple site-specific recombination event that inverts a small DNA segment containing a promoter. (A) In one orientation, the promoter activates transcription of the H2 flagellin gene as well as that of a repressor protein that blocks the expression of the H1 flagellin gene. (B) When the promoter is inverted, it no longer turns on H2 or the repressor, and the H1 gene, which is thereby released from repression, is expressed instead. The recombination mechanism is activated only rarely (about once every 10^5 cell divisions). Therefore, the production of one or other flagellin tends to be faithfully inherited in each clone of cells.

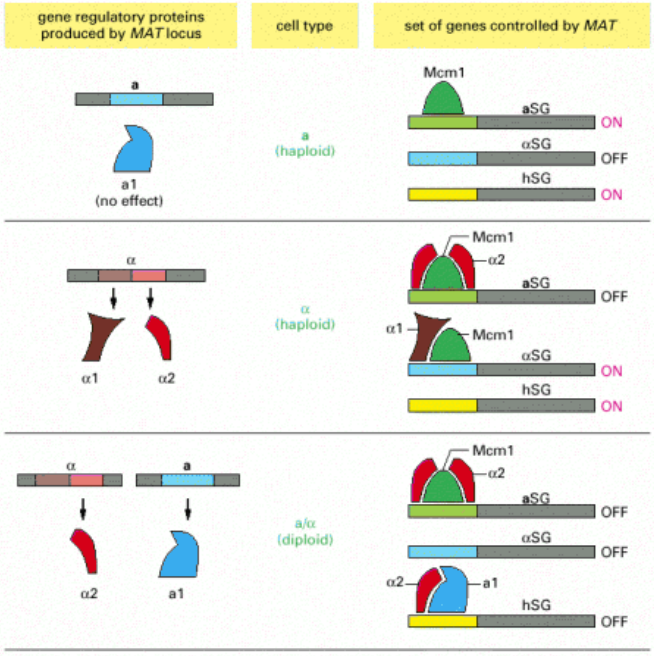

Figure 7-65. Control of cell type in yeasts. Yeast cell type is determined by three gene regulatory proteins (α1, α2, and a1) produced by the *MAT* locus. Different sets of genes are transcribed in haploid cells of type **a**, in haploid cells of type α, and in diploid cells (type a/α). The haploid cells express a set of haploid-specific genes (hSG) and either a set of α-specific genes (αSG) or a set of a-specific genes (aSG). The diploid cells express none of these genes. The α1, α2, and a1 proteins control many target genes in each type of cell by binding, in various combinations, to specific regulatory sequences upstream of these genes. Note that the α1 protein is a gene activator protein, whereas the α2 protein is a gene repressor protein. Both work in combination with a gene regulatory protein called Mcm1 that is present in all three cell types. In the diploid cell type, α2 and a1 form a heterodimer (shown in detail in Figure 7-23) that turns off a set of genes (including the gene encoding the α1 activator protein) different from that turned off by the α2 and Mcm1 proteins. This relatively simple system of gene regulatory proteins is an example of combinatorial control of gene expression (see Figure 7-50). The a1 and α2 proteins each recognize their DNA-binding sites using a homeodomain motif (see Figure 7-16).

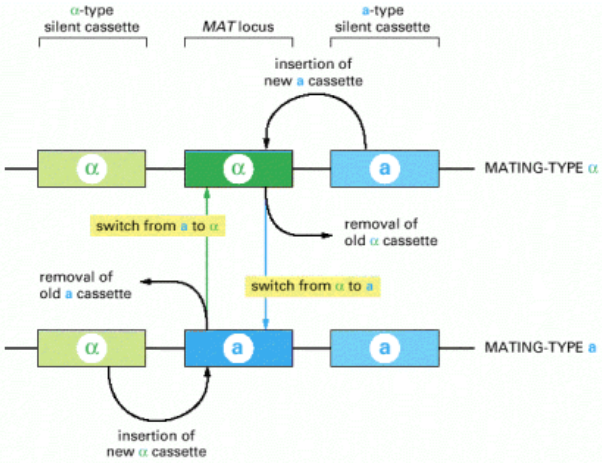

Figure 7-66. Cassette model of yeast mating-type switching. Cassette switching occurs by a gene-conversion process that involves a specialized enzyme (the HO endonuclease) that makes a double-stranded cut at a specific DNA sequence in the *MAT* locus. The DNA near the cut is then excised and replaced by a copy of the silent cassette of opposite mating type. The mechanism of this specialized form of gene conversion is similar to the general mechanism of homologous end joining discussed in Chapter 5 (see pp. 283284).

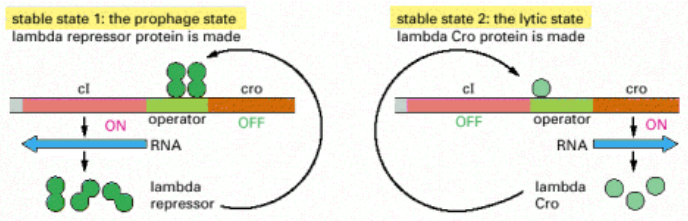

Figure 7-67. A simplified version of the regulatory system that determines the mode of growth of bacteriophage lambda in the *E. coli* host cell. In stable state 1 (the prophage state) the bacteriophage synthesizes a repressor protein, which activates its own synthesis and turns off the synthesis of several other bacteriophage proteins, including the Cro protein. In state 2 (the lytic state) the bacteriophage synthesizes the Cro protein, which turns off the synthesis of the repressor protein, so that many bacteriophage proteins are made and the viral DNA replicates freely in the *E. coli* cell, eventually producing many new bacteriophage particles and killing the cell. This example shows how two gene regulatory proteins can be combined in a circuit to produce two heritable states. Both the lambda repressor and the Cro protein recognize the operator through a helix-turn-helix motif (see Figure 7-14).

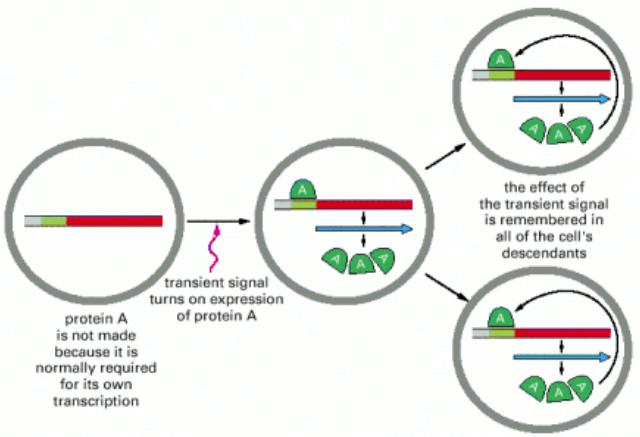

Figure 7-68. Schematic diagram showing how a positive feedback loop can create cell memory. Protein A is a gene regulatory protein that activates its own transcription. All of the descendants of the original cell will therefore "remember" that the progenitor cell had experienced a transient signal that initiated the production of the protein.

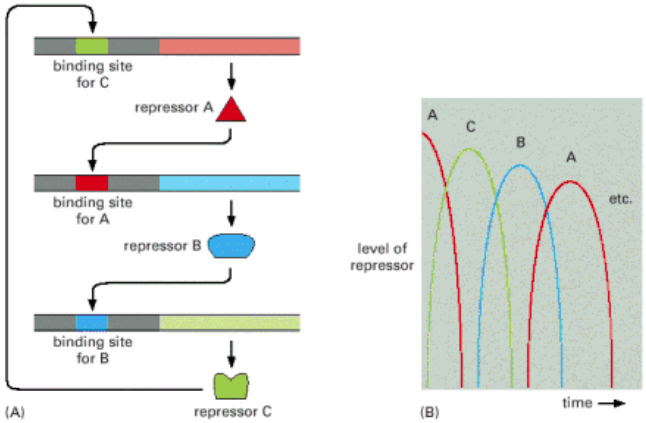

Figure 7-69. A simple gene clock designed in the laboratory. (A) Recombinant DNA techniques were used to place the genes for each of three different bacterial repressor proteins under the control of a different repressor. These repressors (denoted A, B, and C in the figure) are the *lac* repressor (see Figure 7-38), the lambda repressor (see Figure 7-67), and the *tet* repressor, which regulates genes in response to tetracycline. (B) A population of cells will cycle between the three different states shown in (A). For example, if the cells start in a state where only repressor A has accumulated to high levels, the gene for repressor B will be fully repressed. As repressor C is gradually synthesized, it begins to shut off production of repressor A, and repressor B begins to accumulate and eventually shuts off production of repressor C. As this cycling continues a synchronized population of cells oscillates among three states in a specified order. (Adapted from M.B. Elowitz and S. Leibler, *Nature* 403:335338, 2000.)

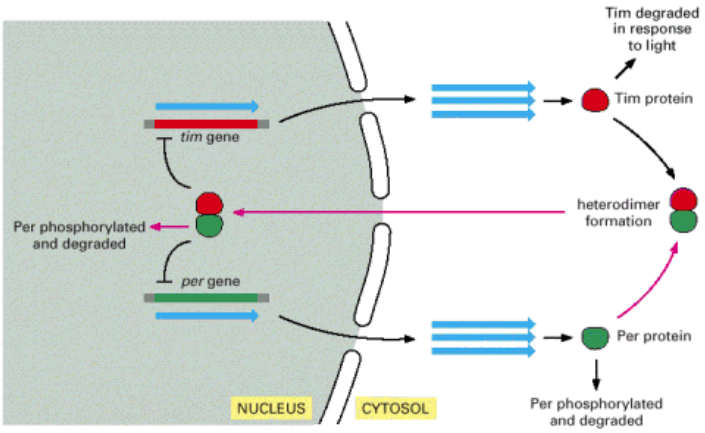

Figure 7-70. Outline of the mechanism of the circadian clock in *Drosophila* cells. The central feature of the clock is the periodic accumulation and decay of two gene regulatory proteins, Tim (short for timeless, based on the phenotype of a gene mutation) and Per (short for period). These proteins are translated in the cytosol, and, when they have accumulated to critical levels, they form a heterodimer. This heterodimer is transported into the nucleus where it regulates a number of genes in concert with the clock. The Tim-Per heterodimer also represses the *tim* and *per* genes, creating a feedback system that causes the levels of Tim and Per to rise and fall periodically. In addition to this transcriptional feedback, the clock depends on the phosphorylation and subsequent degradation of the Per protein, which occurs in both the nucleus and the cytoplasm and is regulated by an additional clock protein, Dbt (short for double-time). This degradation imposes delays in the periodic accumulation of Tim and Per, which are crucial to the functioning of the clock. For example, the accumulation of Per in the cytoplasm is delayed by the phosphorylation and degradation of free Per monomers. Steps at which specific delays are imposed are shown in *red*. Entrainment (or resetting) of the clock occurs in response to new light-dark cycles. Although most *Drosophila* cells do not have true photoreceptors, light is sensed by intracellular flavoproteins, and it rapidly causes the destruction of the Tim protein, thus resetting the clock.

Figure 7-71. A single gene regulatory protein can coordinate the expression of several different genes. The action of the glucocorticoid receptor is illustrated schematically. On the *left* is a series of genes, each of which has various gene activator proteins bound to its regulatory region. However, these bound proteins are not sufficient on their own to fully activate transcription. On the *right* is shown the effect of adding an additional gene regulatory protein - the glucocorticoid receptor in a complex with glucocorticoid hormone - that can bind to the regulatory region of each gene. The glucocorticoid receptor completes the combination of gene regulatory proteins required for maximal initiation of transcription, and the genes are now switched on as a set. In the absence of the hormone, the glucocorticoid receptor is retained in the cytosol and is therefore unavailable to bind to DNA. In addition to

activating gene expression, the hormone-bound form of the glucocorticoid receptor represses transcription of certain genes, depending on the gene regulatory proteins already present on their control regions. The effect of the glucocorticoid receptor on any given gene therefore depends upon the type of cell, the gene regulatory proteins contained within it, and the regulatory region of the gene. The structure of the DNA-binding portion of the glucocorticoid receptor is shown in Figure 7-19.

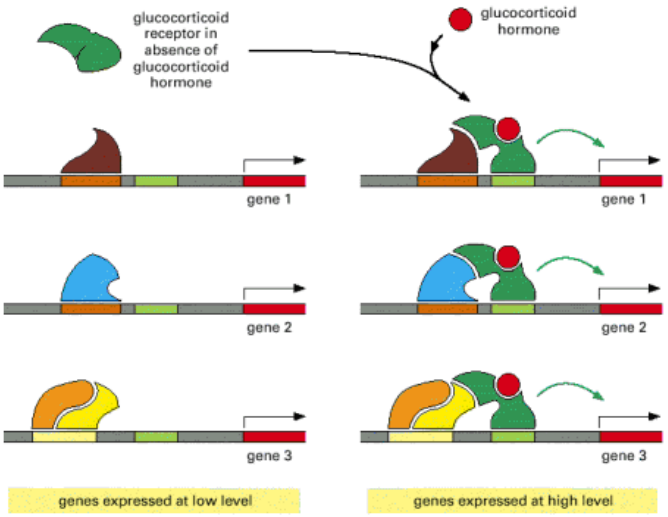

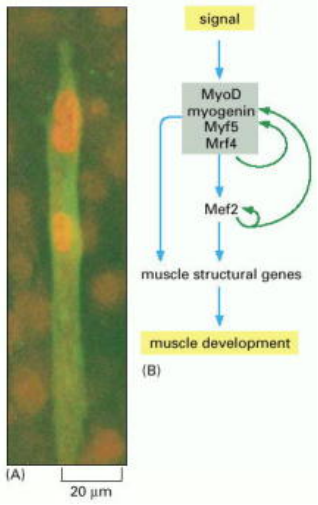

Figure 7-72. Role of the myogenic regulatory proteins in muscle development. (A) The effect of expressing the MyoD protein in fibroblasts. As shown in this immunofluorescence micrograph, fibroblasts from the skin of a chick embryo have been converted to muscle cells by the experimentally induced expression of the *myoD* gene. The fibroblasts that have been induced to express the *myoD* gene have fused to form elongated multinucleate muscle-like cells, which are stained *green* with an antibody that detects a muscle-specific protein. Fibroblasts that do not express the *myoD* gene are barely visible in the background. (B) Simplified scheme for some of the gene regulatory proteins involved in skeletal muscle development. The commitment of mesodermal progenitor cells to the muscle-specific pathway involves the synthesis of the four myogenic gene regulatory proteins, MyoD, Myf5, myogenin and Mrf4. These proteins directly activate transcription of muscle structural genes as well as the *MEF2* gene, which encodes an additional gene regulatory protein. Mef2 acts in combination with the myogenic proteins to further activate transcription of muscle structural genes and to create a positive feedback loop that acts to maintain transcription of the myogenic genes. (A, courtesy of Stephen Tapscott and Harold Weintraub; B, adapted from J.D. Molkentin and E.N. Olson, *Proc. Natl. Acad. Sci. USA* 93:93669373, 1996.)

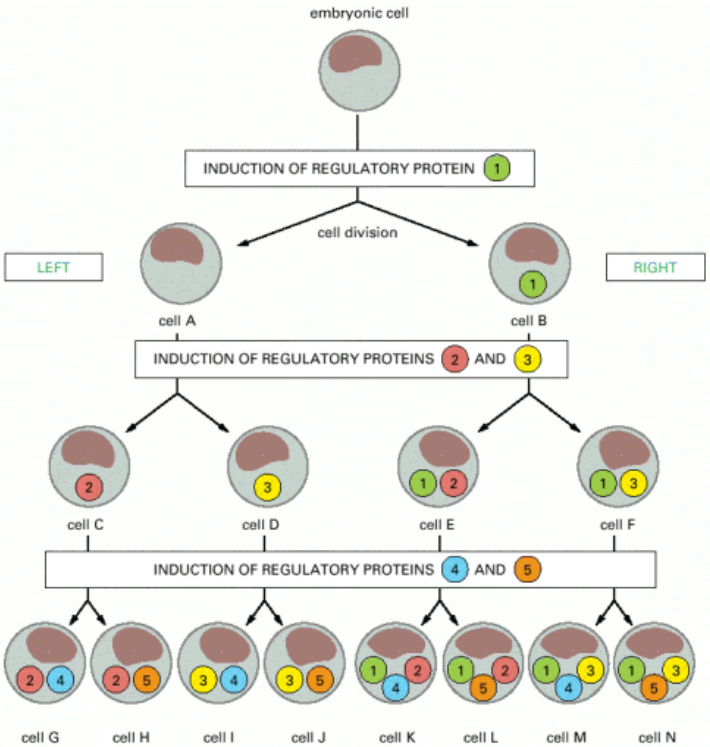

Figure 7-73. The importance of combinatorial gene control for development. Combinations of a few gene regulatory proteins can generate many cell types during development. In this simple, idealized scheme a "decision" to make one of a pair of different gene regulatory proteins (shown as numbered *circles)* is made after each cell division. Sensing its relative position in the embryo, the daughter cell toward the *left side* of the embryo is always induced to synthesize the even-numbered protein of each pair, while the daughter cell toward the *right side* of the embryo is induced to synthesize the odd-numbered protein. The production of each gene regulatory protein is assumed to be self-perpetuating once it has become initiated (see Figure 7-68). In this way, through cell memory, the final combinatorial specification is built up step by step. In this purely hypothetical example, eight final cell types (G-N) have been created using five different gene regulatory proteins.

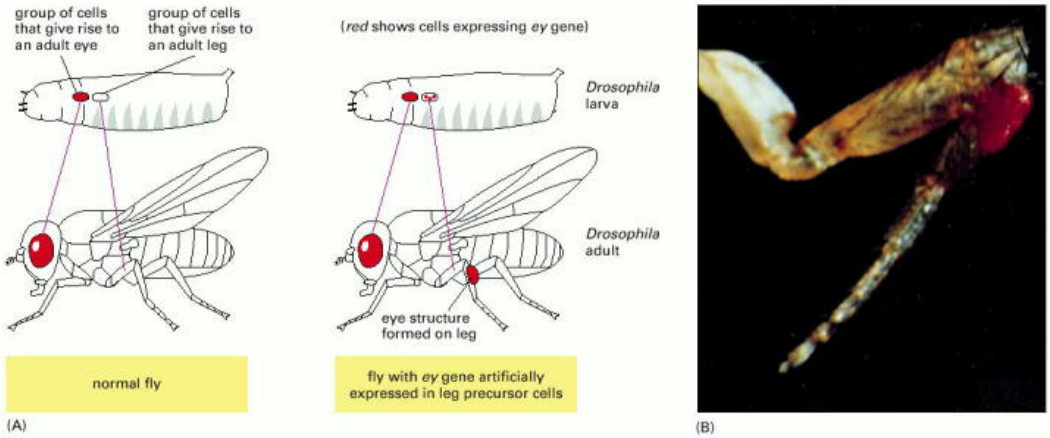

Figure 7-74. Expression of the *Drosophila ey* gene in precursor cells of the leg triggers the development of an eye on the leg. (A) Simplified diagrams showing the result when a fruit fly larva contains either the normally expressed *ey* gene (*left*) or an *ey* gene that is additionally expressed artificially in cells that normally give rise to leg tissue (*right*). (B) Photograph of an abnormal leg that contains a misplaced eye. (B, courtesy of Walter Gehring.)

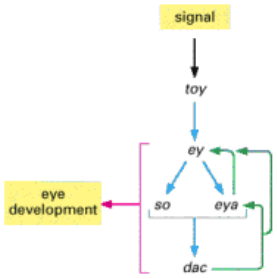

Figure 7-75. Gene regulatory proteins that specify eye development in *Drosophila.* *toy (twin of eyeless)* and *ey (eyeless)* encode similar gene regulatory proteins, Toy and Ey, either of which, when ectopically expressed, can trigger eye development. In normal eye development, expression of *ey* requires the *toy* gene. Once its transcription is activated by Toy, Ey activates transcription of *so (sine oculis)* and *eya (eyes absent)* which act together to express the *dac (dachshund)* gene. As indicated by the *green* arrows, some of the gene regulatory proteins form positive feedback loops which reinforce the initial commitment to eye development. The Ey protein is known to bind directly to numerous target genes for eye development, including those encoding lens crystallins (see Figure 7-119), rhodopsins, and other photoreceptor proteins. (Adapted from T. Czerny et al., *Mol. Cell* 3:297307, 1999.)

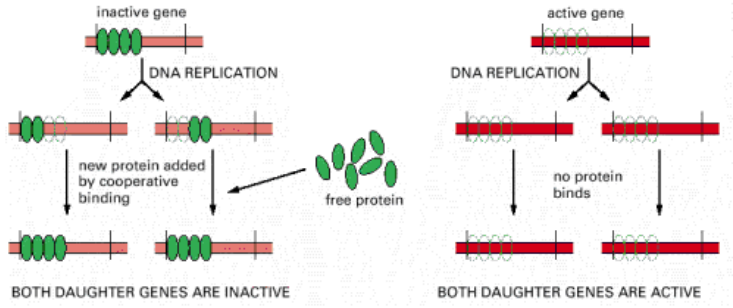

Figure 7-76. A general scheme that permits the direct inheritance of states of gene expression during DNA replication. In this hypothetical model, portions of a cooperatively bound cluster of chromosomal proteins are transferred directly from the parental DNA helix *(top left)* to both daughter helices. The inherited cluster then causes each of the daughter DNA helices to bind additional copies of the same proteins. Because the binding is cooperative, DNA synthesized from an identical parental DNA helix that lacks the bound proteins *(top right)* will remain free of them. If the bound proteins turn off gene transcription, then the inactive gene state will be directly inherited, as illustrated. If the bound proteins activate transcription, then the active gene state will be directly inherited (not shown). When the cooperative protein binding requires specific DNA sequences, these events will be limited to specific gene control regions; if the binding can be propagated all along the chromosome, however, it could account for the spreading effect associated with the heritable chromatin states discussed in Chapter 4. Although the proteins are depicted as being identical, the same principle can explain how cooperatively assembling combinations of different proteins can be propagated stably.

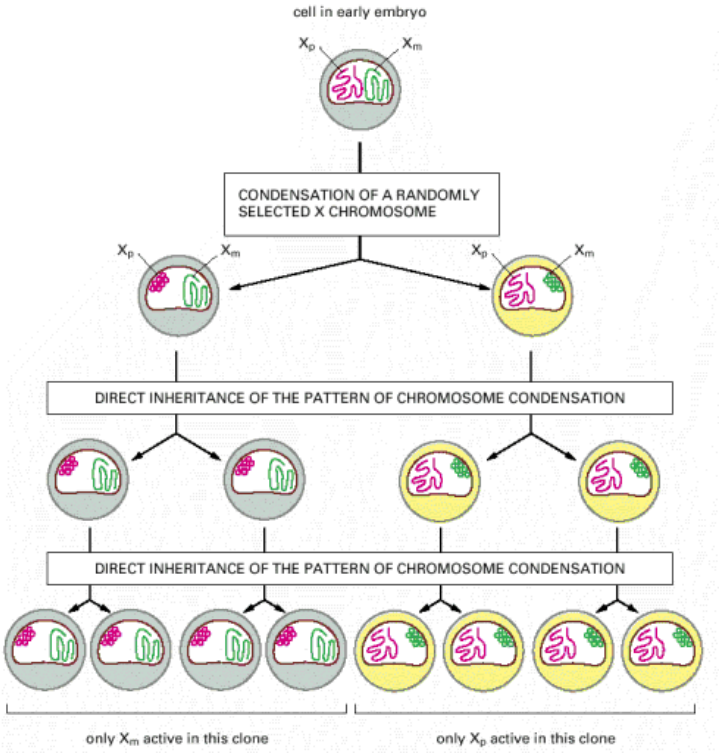

Figure 7-77. X-inactivation. The clonal inheritance of a condensed inactive X chromosome that occurs in female mammals.

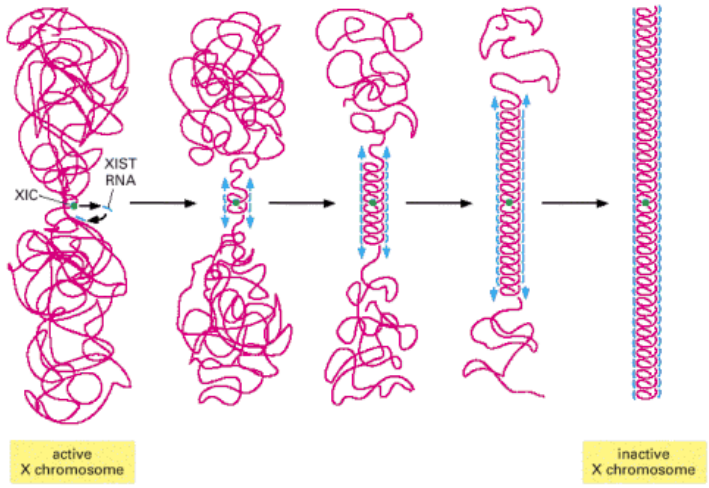

Figure 7-78. Mammalian X-chromosome inactivation. X-chromosome inactivation begins with the synthesis of XIST (X-inactivation specific transcript) RNA from the XIC (X-inactivation center) locus. The association of XIST RNA with the X chromosome is correlated with the condensation of the chromosome. Both XIST association and chromosome condensation gradually move from the XIC locus outward to the chromosome ends. The details of how this occurs remain to be deciphered.

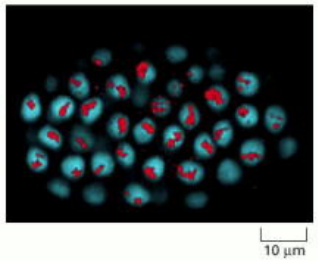

Figure 7-79. Localization of dosage compensation proteins to the X chromosomes of *C. elegans* hermaphrodite (XX) nuclei. Many nuclei from a developing embryo are visible in this image. Total DNA is stained *blue* with the DNA-intercalating dye DAPI, and the Sdc-2 protein is stained *red* using anti-Sdc-2 antibodies coupled to a fluorescent dye. This experiment shows that the Sdc-2 protein associates with only a limited set of chromosomes, identified by other experiments to be the two X chromosomes. Sdc-2 is bound along the entire length of the X chromosome and attracts other proteins, including a condensin-like complex, that complete the specialized structure of these chromosomes. (From H.E. Dawes et al., *Science* 284:18001804, 1999. © AAAS.)

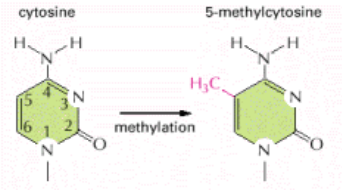

Figure 7-80. Formation of 5-methylcytosine occurs by methylation of a cytosine base in the DNA double helix. In vertebrates this event is confined to selected cytosine (C) nucleotides located in the sequence CG.

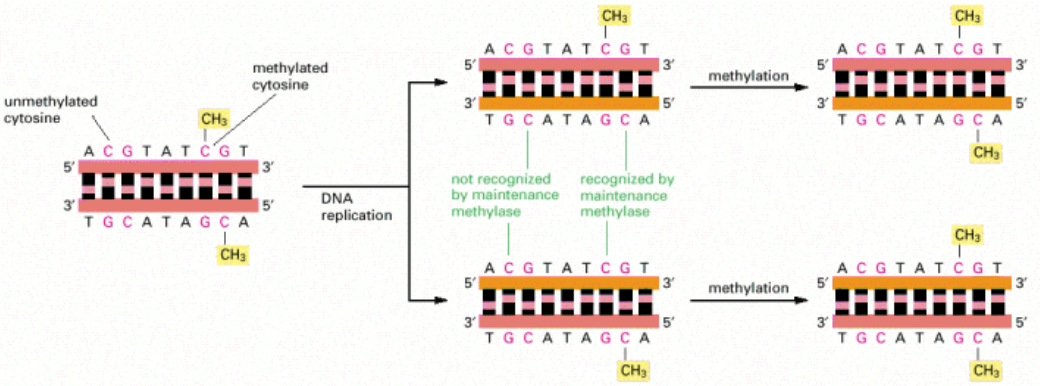

Figure 7-81. How DNA methylation patterns are faithfully inherited. In vertebrate DNAs a large fraction of the cytosine nucleotides in the sequence CG are methylated (see Figure 7-80). Because of the existence of a methyl-directed methylating enzyme (the maintenance methyltransferase), once a pattern of DNA methylation is established, each site of methylation is inherited in the progeny DNA, as shown.

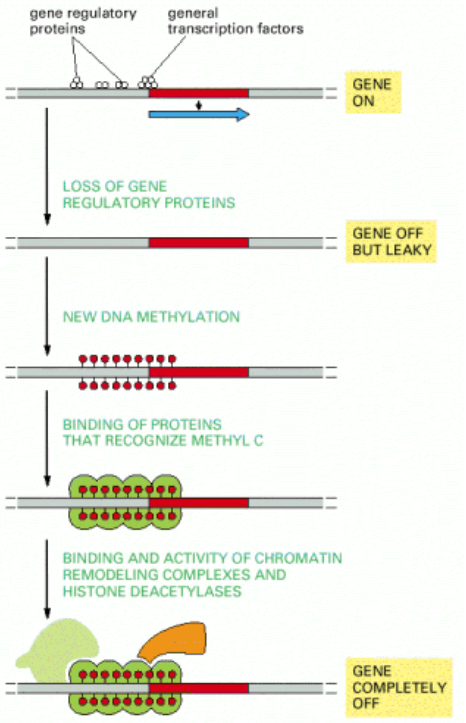

Figure 7-82. How DNA methylation may help turn off genes. The binding of gene regulatory proteins and the general transcription machinery near an active promoter may prevent DNA methylation by excluding *de novo* methylases. If most of these proteins dissociate from the DNA, however, as generally occurs when a cell no longer produces the required activator proteins, the DNA becomes methylated, which enables other proteins to bind, and these shut down the gene completely by further altering chromatin structure (see Figure 7-49).

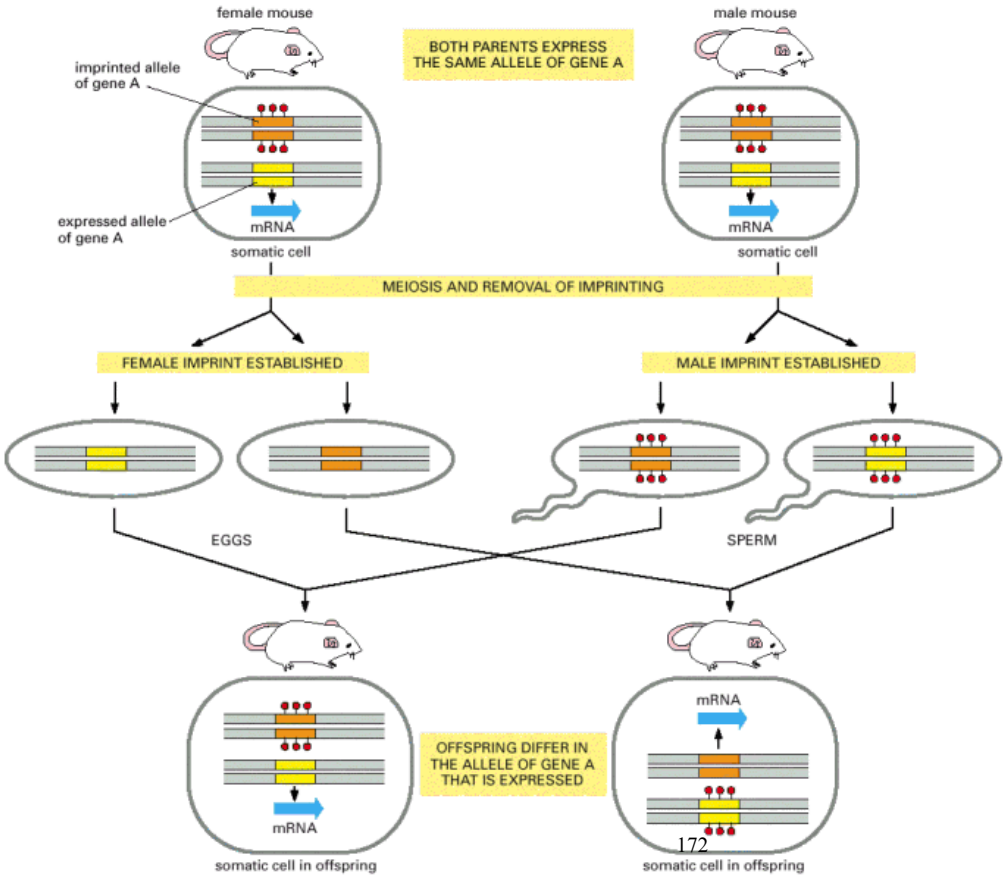

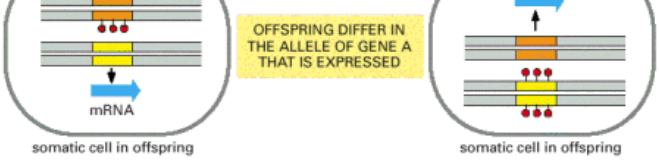

Figure 7-83. Imprinting in the mouse. The *top* portion of the figure shows a pair of homologous chromosomes in the somatic cells of two adult mice, one male and one female. In this example, both mice have inherited the top homolog from their father and the bottom homolog from their mother, and the paternal copy of a gene subject to imprinting (indicated in *orange)* is methylated, which prevents its expression. The maternally-derived copy of the same gene *(yellow)* is expressed. The remainder of the figure shows the outcome of a cross between these two mice. During meiosis and germ cell formation, the imprints are first erased and then reimposed *(middle* portion of figure). In eggs produced from the female, neither allele of the A gene is methylated. In sperm from the male, both alleles of gene A are methylated. Shown at the *bottom* of the figure are two of the possible imprinting patterns inherited by the progeny mice; the mouse on the *left* has the same imprinting pattern as each of the parents, whereas the mouse on the *right* has the opposite pattern. If the two alleles of A gene are distinct, these different imprinting patterns can cause phenotypic differences in the progeny mice, even though they carry exactly the same DNA sequences of the two A gene alleles. Imprinting provides an important exception to classical genetic behavior, and more than 100 mouse genes are thought to be affected in this way. However, the great majority of mouse genes are not imprinted, and therefore the rules of Mendelian inheritance apply to most of the mouse genome.

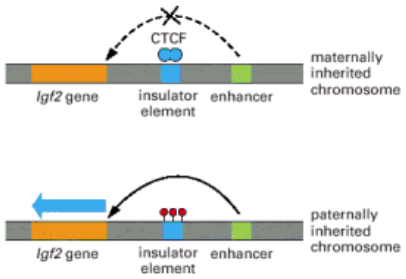

Figure 7-84. Mechanism of imprinting of the mouse *Igf2* gene. On chromosomes inherited from the female, a protein called CTCF binds to an insulator, (see Figure 7-61) blocking communication between the enhancer *(green)* and the *Igf2* gene *(orange). Igf2* is therefore not expressed from the maternally inherited chromosome. Because of imprinting, the insulator on the male-derived chromosome is methylated; this inactivates the insulator, by blocking the binding of the CTCF protein, and allows the enhancer to activate transcription of the *Igf2* gene. In other examples of imprinting, methylation blocks gene expression by interfering with the binding of proteins required for the gene's transcription. The methylation patterns (imprints) on the chromosome, inherited by the zygote after fertilization, are maintained in subsequent generations by maintenance methyl transferases (see Figure 7-81).

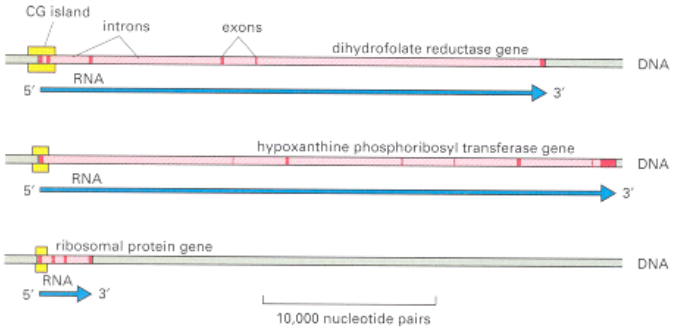

Figure 7-85. The CG islands surrounding the promoter in three mammalian housekeeping genes. The *yellow* boxes show the extent of each island. As for most genes in mammals (see Figure 6-25), the exons *(dark red)* are very short relative to the introns *(light red).* (Adapted from A.P. Bird, *Trends Genet.* 3:342347, 1987.)

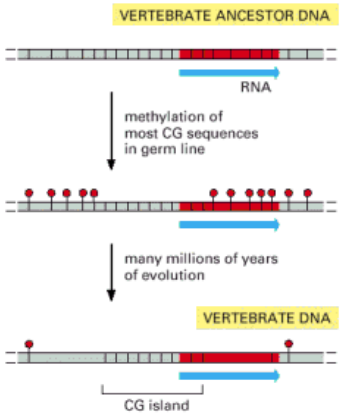

Figure 7-86. A mechanism to explain both the marked overall deficiency of CG sequences and their clustering into CG islands in vertebrate genomes. A *black line* marks the location of a CG dinucleotide in the DNA sequence, while a *red* "lollipop" indicates the presence of a methyl group on the CG dinucleotide. CG sequences that lie in regulatory sequences of genes that are transcribed in germ cells are unmethylated and therefore tend to be retained in evolution. Methylated CG sequences, on the other hand, tend to be lost through deamination of 5-methyl C to T, unless the CG sequence is critical for survival.

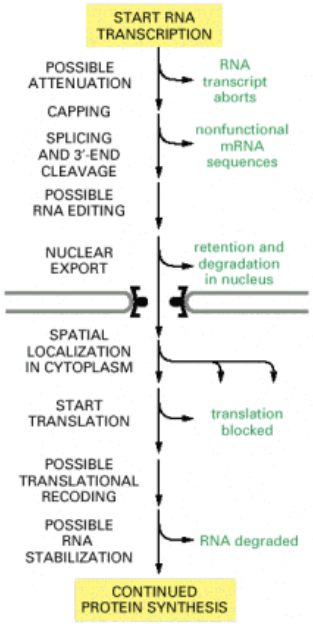

Figure 7-87. Possible post-transcriptional controls on gene expression. Only a few of these controls are likely to be important for any one gene.

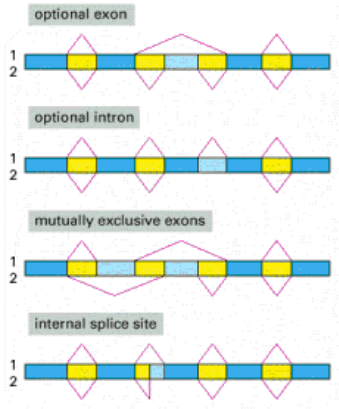

Figure 7-88. Four patterns of alternative RNA splicing. In each case a single type of RNA transcript is spliced in two alternative ways to produce two distinct mRNAs (1 and 2). The *dark blue boxes* mark exon sequences that are retained in both mRNAs. The *light blue boxes* mark possible exon sequences that are included in only one of the mRNAs. The boxes are joined by *red lines* to indicate where intron sequences *(yellow)* are removed. (Adapted with permission from A. Andreadis, M.E. Gallego, and B. Nadal-Ginard, *Annu. Rev. Cell Biol.* 3:207242, 1987.)

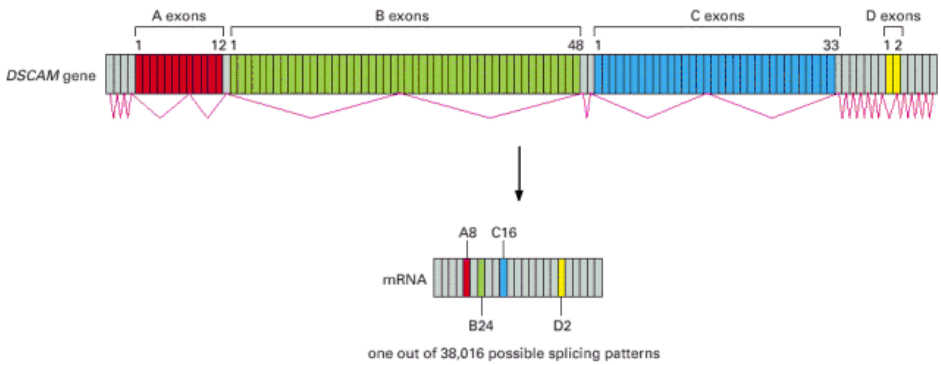

Figure 7-89. Alternative splicing of RNA transcripts of the *Drosophila DSCAM* gene. DSCAM proteins are axon guidance receptors that help to direct growth cones to their appropriate targets in the developing nervous system. The final mRNA contains 24 exons, four of which (denoted A, B, C, and D) are present in the *DSCAM* gene as arrays of alternative exons. Each RNA contains 1 of 12 alternatives for exon A *(red)*, 1 of 48 alternatives for exon B *(green)*, 1 of 33 alternatives for exon C *(blue)*, and 1 of 2 alternatives for exon D *(yellow)*. If all possible splicing combinations are used, 38,016 different proteins could in principle be produced from the *DSCAM* gene. Only one of the many possible splicing patterns (indicated by the *red line* and by the mature mRNA below it) is shown. Each variant DSCAM protein would fold into roughly the same structure [predominantly a series of extracellular immunoglobulin-like domains linked to a membrane-spanning region (see Figure 24-71)], but the amino acid sequence of the domains would vary according to the splicing pattern. It is possible that this receptor diversity contributes to the formation of complex neural circuits, but the precise properties and functions of the many DSCAM variants are not yet understood. (Adapted from D.L. Black, *Cell* 103:367370, 2000.)

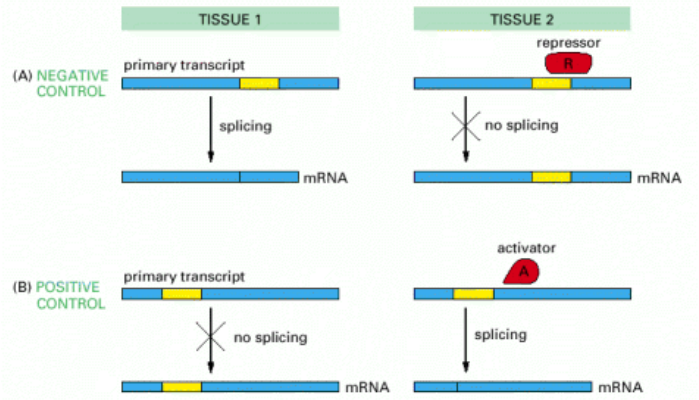

Figure 7-90. Negative and positive control of alternative RNA splicing. (A) Negative control, in which a repressor protein binds to the primary RNA transcript in tissue 2, thereby preventing the splicing machinery from removing an intron sequence. (B) Positive control, in which the splicing machinery is unable to efficiently remove a particular intron sequence without assistance from an activator protein.

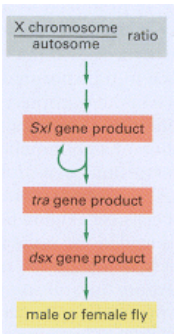

Figure 7-91. Sex determination in *Drosophila.* The gene products shown act in a sequential cascade to determine the sex of the fly according to the X chromosome/autosome ratio. The genes are called *sex-lethal (Sxl), transformer (tra),* and *doublesex (dsx)* because of the phenotypes that result when the gene is inactivated by mutation. The function of these gene products is to transmit the information about the X chromosome/autosome ratio to the many other genes that create the sex-related phenotypes. These other genes function as two alternative sets: those that specify female features and those that specify male features (see Figure 7-92).

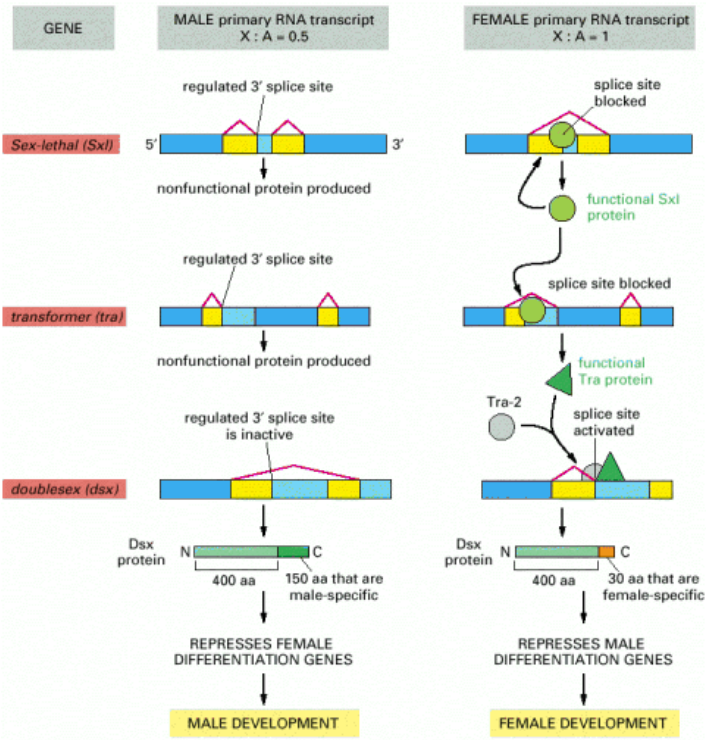

Figure 7-92. The cascade of changes in gene expression that determines the sex of a fly through alternative RNA splicing. An X chromosome/ autosome ratio of 0.5 results in male development. Male is the "default" pathway in which the *Sxl* and *tra* genes are both transcribed, but the RNAs are spliced constitutively to produce only nonfunctional RNA molecules, and the *dsx* transcript is spliced to produce a protein that turns off the genes that specify female characteristics. An X chromosome/ autosome ratio of 1 triggers the female differentiation pathway in the embryo by transiently activating a promoter within the *Sxl* gene that causes synthesis of a special class of *Sxl* transcripts that are constitutively spliced to give functional Sx1 protein. Sxl is a splicing regulatory protein with two sites of action: (1) it binds to the constitutively produced *Sxl* RNA transcript, causing a female-specific splice that continues the production of a functional Sxl protein, and (2) it binds to the constitutively produced *tra* RNA and causes an alternative splice of this transcript, which now produces an active Tra regulatory protein. The Tra protein acts with the constitutively produced Tra-2 protein to produce the female-specific spliced form of the *dsx* transcript; this encodes the female form of the Dsx protein, which turns off the genes that specify male features. The components in this pathway were all initially identified through the study of *Drosophila* mutants that are altered in their sexual development. The *dsx* gene, for example, derives its name *(doublesex)* from the observation that a fly lacking this gene product expresses both male- and female-specific features. Note that, although both the Sxl and the Tra proteins bind to specific RNA sites, Sxl is a repressor that acts negatively to block a splice site, whereas the Tra proteins are activators that act positively to induce a splice (see Figure 7-90). Sx1 binds to the pyrimidine-rich stretch of nucleotides that is part of the standard splicing consensus sequence (see Figure 6-28) and blocks access by the normal splicing factor, U2AF (see Figure 6-29). Tra binds to specific RNA sequences in an exon and activates a normally suboptimal splicing signal.

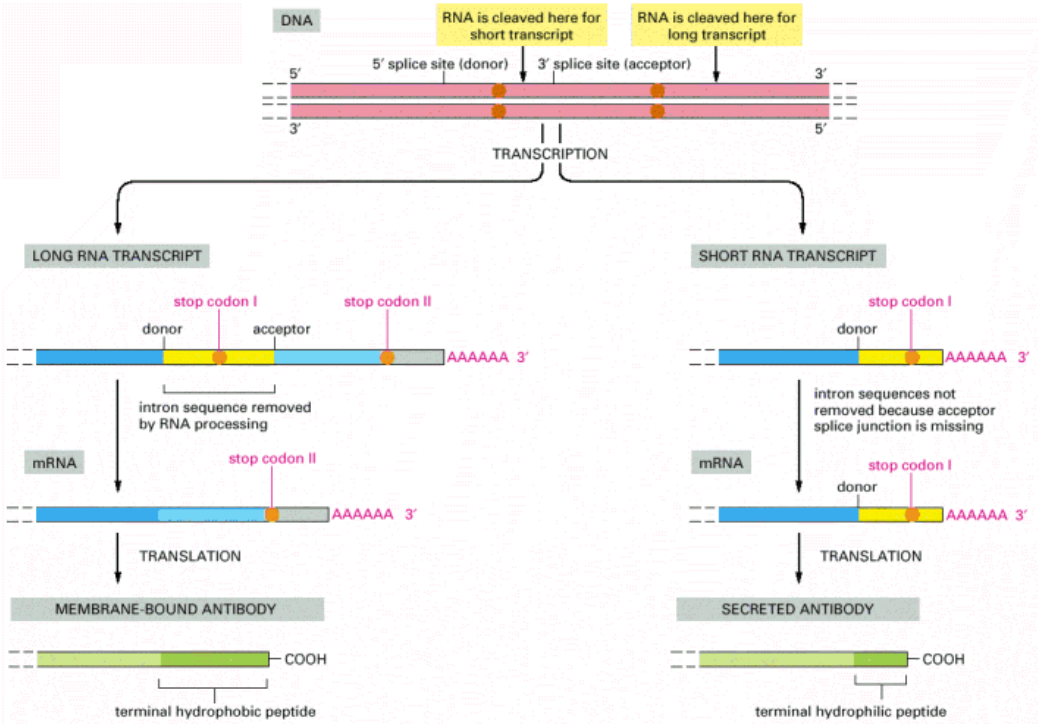

Figure 7-93. Regulation of the site of RNA cleavage and poly-A addition determines whether an antibody molecule is secreted or remains membrane-bound. In unstimulated B lymphocytes *(left)*, a long RNA transcript is produced, and the intron sequence near its 3 end is removed by RNA splicing to give rise to an mRNA molecule that codes for a membrane-bound antibody molecule. In contrast, after antigen stimulation *(right)* the primary RNA transcript is cleaved upstream from the splice site in front of the last exon sequence. As a result, some of the intron sequence that is removed from the long transcript remains as coding sequence in the short transcript. These are the nucleotide sequences that encode the hydrophilic C-terminal portion of the secreted antibody molecule.

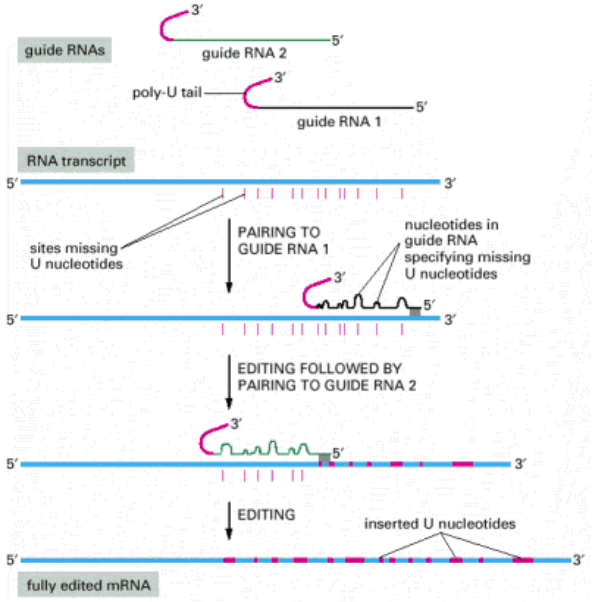

Figure 7-94. RNA editing in the mitochondria of trypanosomes. Guide RNAs contain at their 3 end a stretch of poly U, which donates U nucleotides to sites on the RNA transcript that mispair with the guide RNA; thus the poly-U tail gets shorter as editing proceeds (not shown). Editing generally starts near the 3 end and progresses toward the 5 end of the RNA transcript, as shown, because the "anchor sequence" at the 5 end of most guide RNAs can pair only with edited sequences.

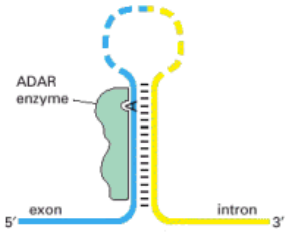

Figure 7-95. Mechanism of A-to-I RNA editing in mammals. The position of an edit is signaled by RNA sequences carried on the same RNA molecule. Typically, a sequence complementary to the position of the edit is present in an intron, and the resulting double-stranded RNA attracts the A-to-I editing enzyme ADAR. Mice and humans have three ADAR enzymes: ADR1 is required in the liver for proper red blood cell development, ADR2 is required for proper brain development (as described in the text), and the role of ADR3 is not yet known.

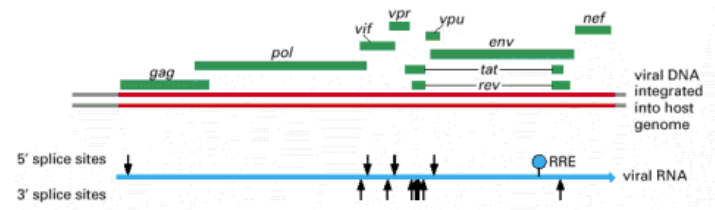

Figure 7-96. The compact genome of HIV, the human AIDS virus. The positions of the nine HIV genes are shown in *green*. The *red double line* indicates a DNA copy of the viral genome which has become integrated into the host DNA *(gray)*. Note that the coding regions of many genes overlap, and those of *tat* and *rev* are split by introns. The *blue line* at the *bottom* of the figure represents the pre-mRNA transcript of the viral DNA showing the locations of all the possible splice sites *(arrows)*. There are many alternative ways of splicing the viral transcript; for example the *env* mRNAs retain the intron that has been spliced out of the *tat* and *rev* mRNAs. The Rev response element (RRE) is indicated by a blue ball and stick. It is a 234-nucleotide long stretch of RNA that folds into a defined structure; Rev recognizes a particular hairpin (see Figure 6-94) within this larger structure. The *gag* gene codes for a protein that is cleaved into several smaller proteins that form the viral capsid. The *pol* gene codes for a protein that is cleaved to produce reverse transcriptase (which transcribes RNA into DNA) as well as the integrase involved in integrating the viral genome (as double-stranded DNA) into the host genome. Pol is produced by ribosomal frameshifting of translation that begins at *gag* (see Figure 6-78). The *env* gene codes for the envelope proteins (see Figure 5-73). Tat, Rev, Vif, Vpr, Vpu, and Nef are small proteins with a variety of functions. For example, Rev regulates nuclear export (see Figure 7-97) and Tat regulates the elongation of transcription across the integrated viral genome (see p. 436).

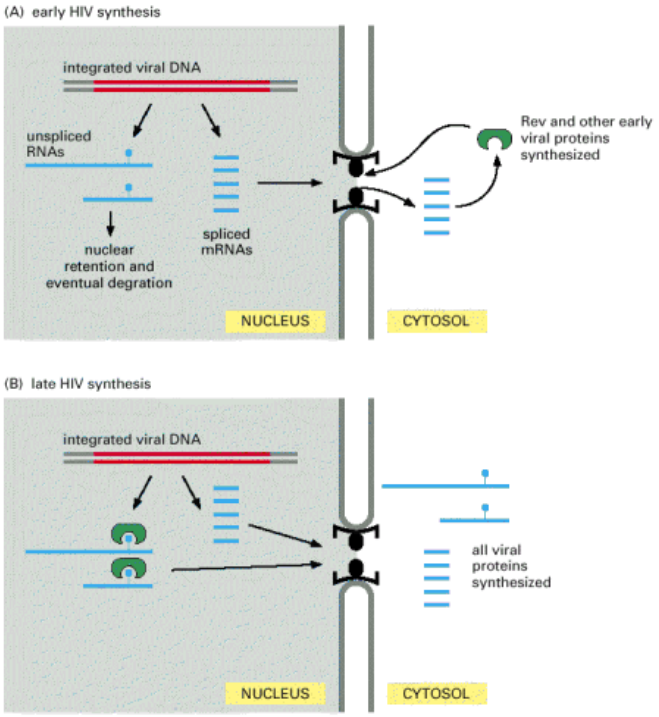

Figure 7-97. Regulation of nuclear export by the HIV Rev protein. Early in HIV infection (A), only the fully spliced RNAs (which contain the coding sequences for Rev, Tat, and Nef) are exported from the nucleus and translated. Once sufficient Rev protein has accumulated and been transported into the nucleus (B), unspliced viral RNAs can be exported from the nucleus. Many of these RNAs are translated into protein, and the full length transcripts are packaged into new viral particles.

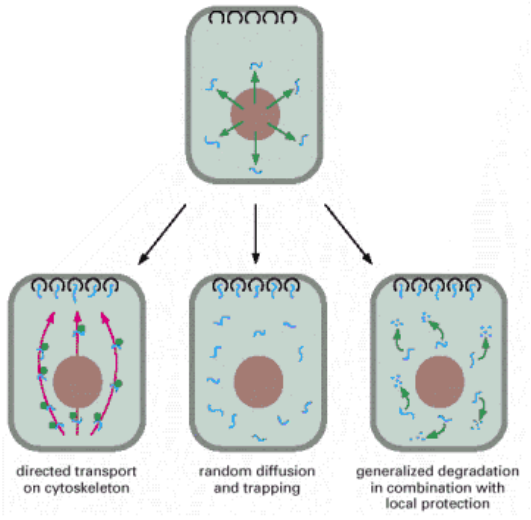

Figure 7-98. Three mechanisms for the localization of mRNAs. The mRNA to be localized leaves the nucleus through nuclear pores *(top)*. Some localized mRNAs *(left diagram)* travel to their destination by associating with cytoskeleton motors *(green)*. As described in Chapter 16, these motors use the energy of ATP hydrolysis to move unidirectionally along components of the cytoskeleton. At their destination, the mRNAs are held in place by anchor proteins *(black)*. Other mRNAs randomly diffuse through the cytosol and are simply trapped and therefore concentrated at their sites of localization *(center diagram)*. Still other mRNAs *(right diagram)* are degraded in the cytosol unless they have bound, through random diffusion, a localized protein complex that anchors and protects the mRNA from degradation *(black)*. Each of these mechanisms requires specific signals on the mRNA, which are typically located in the 3 UTR (see Figure 7-99). In many cases of mRNA localization, additional mechanisms block the translation of the mRNA until it is properly localized. (Adapted from H.D. Lipshitz and C.A. Smibert, *Curr. Opin. Gen. Dev.* 10:476488, 2000.)

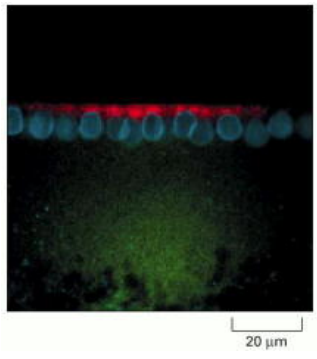

Figure 7-99. The importance of the 3 UTR in localizing mRNAs to specific regions of the cytoplasm. For this experiment, two different fluorescently-labeled RNAs were prepared by transcribing DNA *in vitro* in the presence of fluorescently-labeled derivatives of UTP. One RNA (labeled with a *red* fluorochrome) contains the coding region for the *Drosophila* hairy protein and includes the adjacent 3 UTR. The other RNA (labeled *green)* contains the hairy coding region but the 3 UTR has been deleted. The two RNAs were mixed and injected into a *Drosophila* embryo at a stage of development when multiple nuclei reside in a common cytoplasm (see Figure 7-52). When the fluorescent RNAs were visualized 10 minutes later, the full-length hairy RNA *(red)* was localized to the apical side of nuclei *(blue)* but the transcript missing the 3 UTR *(green)* failed to localize. Hairy is one of many gene regulatory proteins that specifies positional information in the developing *Drosophila* embryo discussed in Chapter 21). The localization of its mRNA (shown in this experiment to depend on its 3 UTR) is thought to be critical for proper fly development. (Courtesy of Simon Bullock and David Ish-Horowicz.)

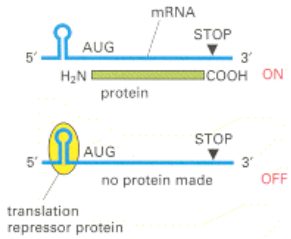

Figure 7-100. Negative translational control. This form of control is mediated by a sequence-specific RNA-binding protein that acts as a translation repressor. Binding of the protein to an mRNA molecule decreases the translation of the mRNA. Several cases of this type of translational control are known. The illustration is modeled on the mechanism that causes more ferritin (an iron storage protein) to be synthesized when the free iron concentration in the cytosol rises; the iron-sensitive translation repressor protein is called aconitase (see also Figure 7-105). In other examples, a complementary RNA molecule, rather than a protein, regulates translation initiation by blocking a critical region of the mRNA through the formation of a short region of double-helical RNA.

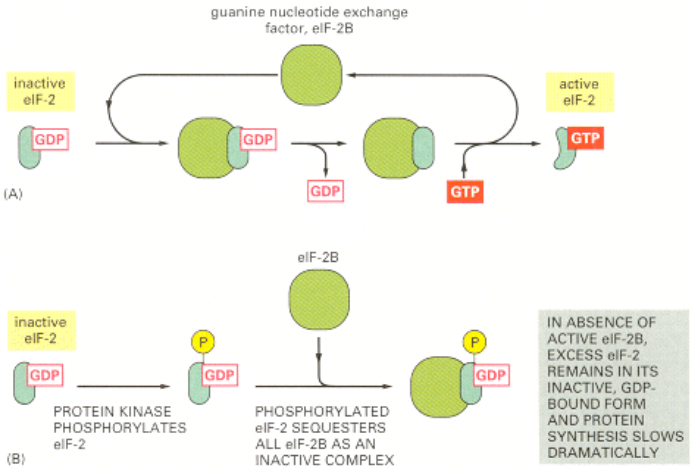

Figure 7-101. The eIF-2 cycle. (A) The recycling of used eIF-2 by a guanine nucleotide exchange factor (eIF-2B). (B) eIF-2 phosphorylation controls protein synthesis rates by tying up eIF-2B.

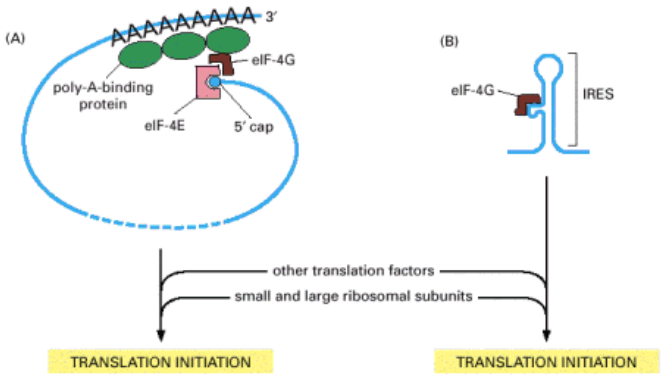

Figure 7-102. Two mechanisms of translation initiation. (A) The cap-dependent mechanism requires a set of initiation factors whose assembly on the mRNA is stimulated by the presence of a 5 cap and a poly-A tail (see also Figure 6-71). (B) The IRES-dependent mechanism requires only a subset of the normal translation initiating factors, and these assemble directly on the folded IRES. (Adapted from A. Sachs, *Cell* 101:243245, 2000.)

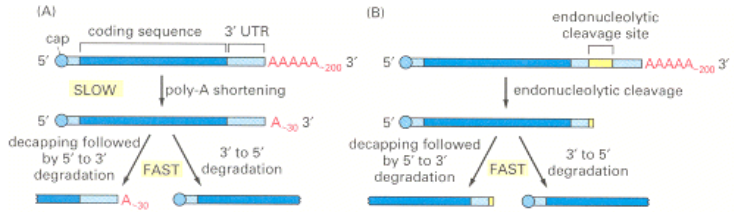

Figure 7-103. Two mechanisms of eucaryotic mRNA decay. (A) Deadenylation-dependent decay. Most eucaryotic mRNAs are degraded by this pathway. The critical threshold of poly-A tail length that induces decay may correspond to the loss of the poly-A binding proteins (see Figure 6-40). As shown in Figure 7-104, the deadenylation enzyme associates with both the 3 poly-A tail and the 5 cap, and this arrangement may coordinate decapping with poly-A shortening. Although 5 to 3 and 3 to 5 degradation are shown on separate RNA molecules, these two processes can occur together on the same molecule. (B) Deadenylation-independent decay. It is not yet known with certainty whether decapping follows endonucleolytic cleavage of the mRNA. (Adapted from C.A. Beelman and R. Parker, *Cell* 81:179183, 1995.)

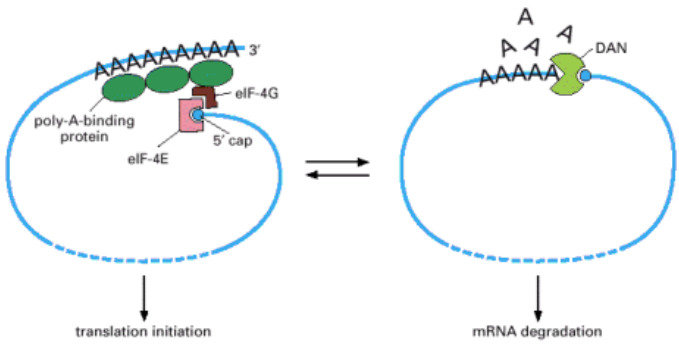

Figure 7-104. The competition between mRNA translation and mRNA decay. The same two features of mRNA - the 5 cap and the 3 poly-A site - are used in both translation initiation and deadenylation-dependent mRNA decay (see Figure 7-103). The enzyme (called DAN) that shortens the poly-A tail in the 3 to 5 direction associates with the 5 cap. As described in Chapter 6 (see Figure 6-71), the translation initiation machinery also associates with both the 5 cap and the poly-A tail. (Adapted from M. Gao et al., *Mol. Cell* 5:479488, 2000.)

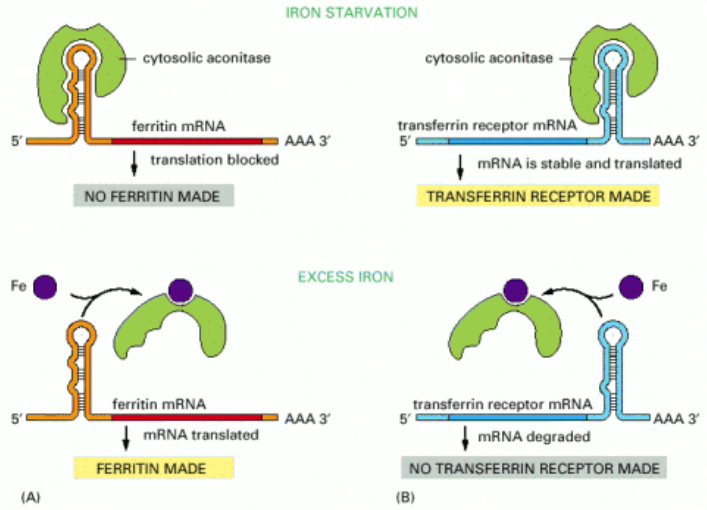

Figure 7-105. Two posttranslational controls mediated by iron. In response to an increase in iron concentration in the cytosol, a cell increases its synthesis of ferritin in order to bind the extra iron (A) and decreases its synthesis of transferrin receptors in order to import less iron across the plasma membrane (B). Both responses are mediated by the same iron-responsive regulatory protein, aconitase, which recognizes common features in a stem-and-loop structure in the mRNAs encoding ferritin and transferrin receptor. Aconitase dissociates from the mRNA when it binds iron. But because the transferrin receptor and ferritin are regulated by different types of mechanisms, their levels respond oppositely to iron concentrations even though they are regulated by the same iron-responsive regulatory protein. The binding of aconitase to the 5 UTR of the ferritin receptor mRNA blocks translation initiation; its binding to the 3 UTR of the ferritin receptor mRNA blocks an endonuclease cleavage site and thereby stabilizes the mRNA (see Figure 7-103). (Adapted from M.W. Hentze et al., *Science* 238:15701573, 1987 and J.L. Casey et al., *Science* 240:924928, 1988.)

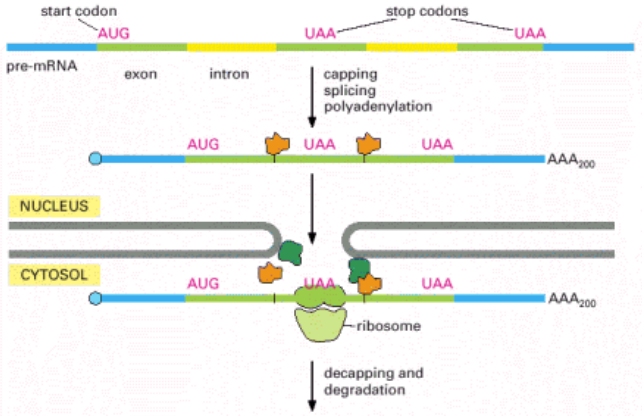

Figure 7-106. A model for nonsense-mediated mRNA decay. According to this model, nuclear proteins *(orange)* mark the exon-exon boundaries on a spliced mRNA molecule. These proteins are thought to assemble in concert with the splicing reaction and may also be involved in the transport of mature mRNAs from the nucleus (see Figure 6-40). A mature mRNA molecule is exported from the nucleus but remains in the vicinity of the nuclear envelope where a "test" round of translation is performed by the ribosome *(green)* aided by additional surveillance proteins *(dark green).* If an in-frame stop codon is encountered before the final exon-exon boundary is reached, the mRNA is subject to nonsense-mediated decay. If not, the mRNA is released from the nuclear envelope (perhaps because of a displacement of the exon-exon marking proteins by the ribosome) and is free to undergo multiple rounds of translation in the cytosol. According to the model shown, the test round of translation occurs just outside the nucleus; however, it is also possible that it takes place within the nucleus, just before the mRNA is exported. (Adapted from J. Lykke-Anderson et al., *Cell* 103:11211131, 2000.)

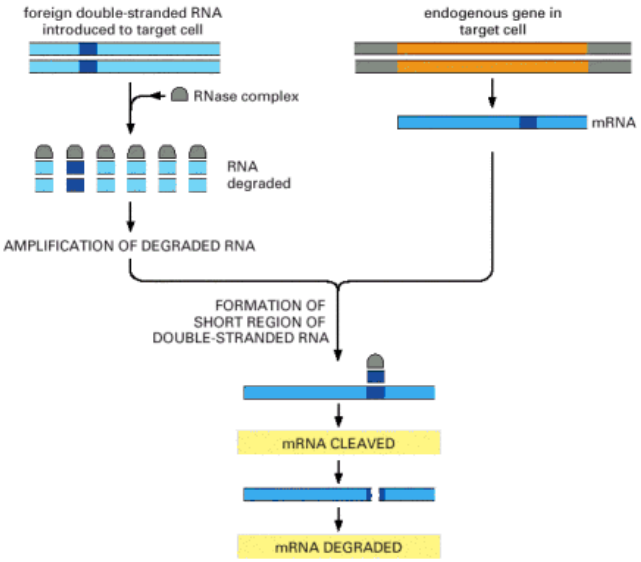

Figure 7-107. The mechanism of RNA interference. On the left is shown the fate of foreign double-stranded RNA molecules. They are recognized by an RNase, present in a large protein complex, and degraded into short fragments that are approximately 23 nucleotide pairs in length. These fragments are sometimes amplified by an RNA-dependent RNA polymerase and, in this case, can be efficiently transmitted to progeny cells. If the foreign RNA has a nucleotide sequence similar to that of a cellular gene *(right* side of figure), mRNA produced by this gene will also be degraded, by the pathway shown. In this way, the expression of a cellular gene can be experimentally shut off by introducing double-stranded RNA into the cell that matches the nucleotide sequence of the gene. RNA interference also requires ATP hydrolysis and RNA helicases, probably to produce single-stranded RNA molecules that can form base pairs with additional RNA molecules.

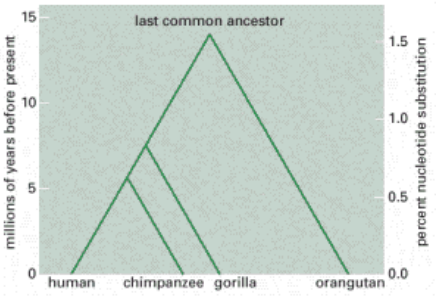

Figure 7-108. A phylogenetic tree showing the relationship between the human and the great apes based on nucleotide sequence data. As indicated, the sequences of the genomes of all four species are estimated to differ from the sequence of the genome of their last common ancestor by a little over 1.5%. Because changes occur independently on both diverging lineages, pairwise comparisons reveal twice the sequence divergence from the last common ancestor. For example, human-orangutan comparisons typically show sequence divergences of a little over 3%, while human-chimpanzee comparisons show divergences of approximately 1.2%. (Modified from F.-C. Chen and W.-H. Li, *Am. J. Hum. Genet.* 68:444456, 2001.)

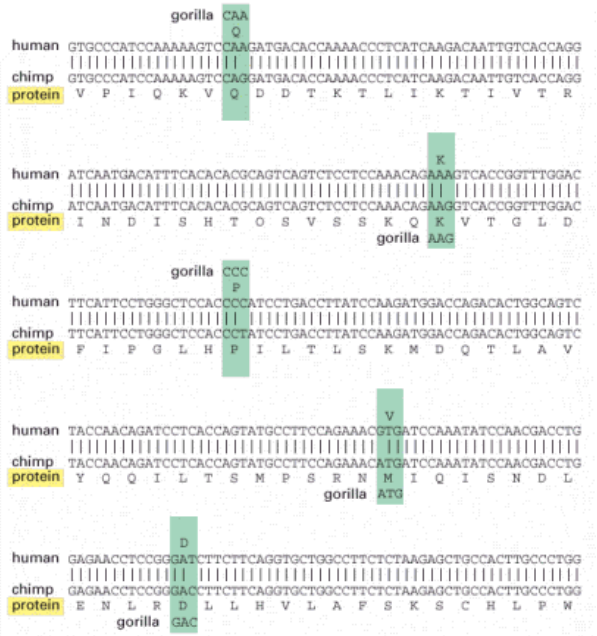

Figure 7-109. Tracing the ancestor sequence from a sequence comparison of the coding regions of human and chimpanzee leptin genes. Leptin is a hormone that regulates food intake and energy utilization in response to the adequacy of fat reserves. As indicated by the codons boxed in *green*, only 5 (of 441 nucleotides total) differ between these two sequences. Moreover, when the amino acids encoded by both the human and chimpanzee sequences are examined, in only one of the 5 positions does the encoded amino acid differ. For each of the 5 variant nucleotide positions the corresponding sequence in the gorilla is also indicated. In two cases, the gorilla sequence agrees with the human sequence, while in three cases it agrees with the chimpanzee sequence. What was the sequence of the leptin gene in the last common ancestor? An evolutionary model that seeks to minimize the number of mutations postulated to have occurred during the evolution of the human and chimpanzee genes would assume that the leptin sequence of the last common ancestor was the same as the human and chimpanzee sequences when they agree; when they disagree, it would use the gorilla sequence as a tie-breaker. For convenience, only the first 300 nucleotides of the leptin coding sequences are given. The remaining 141 are identical between humans and chimpanzees.

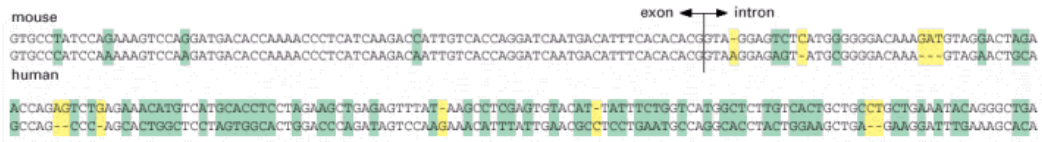

Figure 7-110. Comparison of a portion of the mouse and human leptin genes. Positions where the sequences differ by a single nucleotide substitution are boxed in *green*, and positions that differ by the addition or deletion of nucleotides are boxed in *yellow*. Note that the coding sequence of the exon is much more conserved than the adjacent intron sequence.

Figure 7-111. A comparison of the β-globin gene cluster in the human and mouse genomes, showing the location of transposable elements. This stretch of human genome contains five functional β-globin-like genes *(orange);* the comparable region from the mouse genome has only four. The positions of the human *Alu* sequence are indicated by *green circles*, and the human *L1* sequences by *red circles*. The mouse genome contains different but related transposable elements: the positions of *B1* elements (which are related to the human Alu sequences) are indicated by *blue triangles*, and the positions of the mouse *L1* elements (which are related to the human *L1* sequences) are indicated by *yellow triangles*. The absence of transposable elements from the globin structural genes can be attributed to purifying selection, which would have eliminated any insertion that compromised gene function. (Courtesy of Ross Hardison and Webb Miller.)

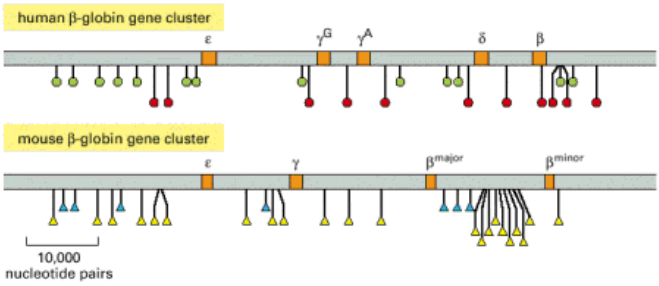

Figure 7-112. The puffer fish, *Fugu rubripes.* (Courtesy of Byrappa Venkatesh.)

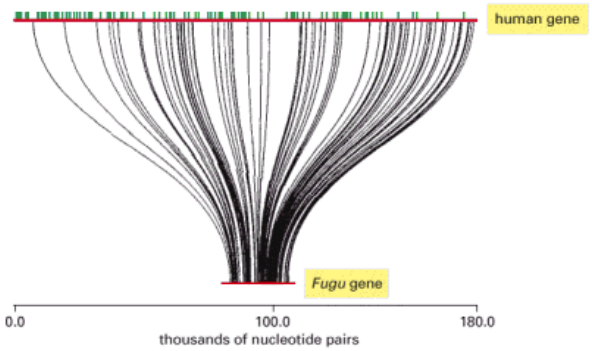

Figure 7-113. Comparison of the genomic sequences of the human and *Fugu* genes encoding the protein huntingtin. Both genes (indicated in *red)* contain 67 short exons that align in 1:1 correspondence to one another; these exons are connected by curved lines. The human gene is 7.5 times larger than the *Fugu* gene (180,000 versus 24,000 nucleotide pairs). The size difference is entirely due to larger introns in the human gene. The larger size of the human introns is due in part to the presence of retrotransposons, whose positons are represented by *green vertical lines;* the *Fugu* introns lack retrotransposons. In humans, mutation of the huntingtin gene causes Huntington's disease, an inherited neurodegenerative disorder (see p. 362). (Adapted from S. Baxendale et al., *Nat. Genet.* 10:6776, 1995.)

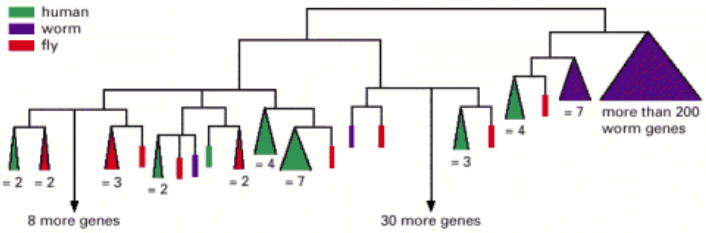

Figure 7-114. A phylogenetic tree based on the inferred protein sequences for all nuclear hormone receptors encoded in the genomes of human *(H. sapiens)*, a nematode worm *(C. elegans)*, and a fruit fly *(D. melanogaster).* *Triangles* represent protein subfamilies that have expanded within individual evolutionary lineages; the width of these triangles indicates the number of genes encoding members of these subfamilies. *Colored vertical bars* represent a single gene. There is no simple pattern to the historical duplications and divergences that have created the gene families encoding nuclear receptors in the three contemporary organisms. The structure of a portion of a particular nuclear hormone receptor is shown in Figure 7-14, and a general description of their functions is discussed in Chapter 15. (Adapted from International Human Genome Sequencing Consortium, *Nature* 409:860921, 2001.)

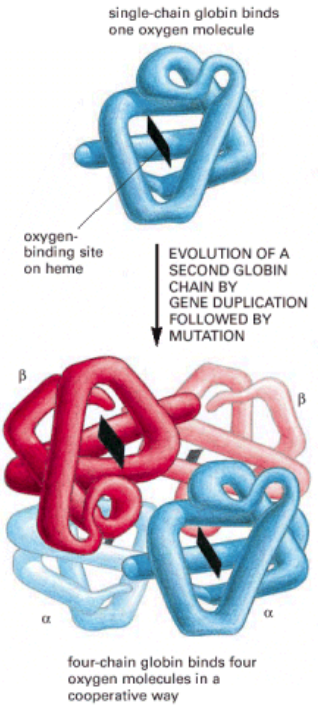

Figure 7-115. A comparison of the structure of one-chain and four-chain globins. The four-chain globin shown is hemoglobin, which is a complex of two α- and β-globin chains. The one-chain globin in some primitive vertebrates forms a dimer that dissociates when it binds oxygen, representing an intermediate in the evolution of the four-chain globin.

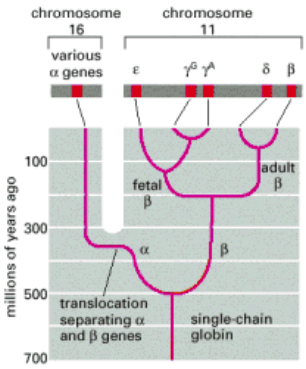

Figure 7-116. An evolutionary scheme for the globin chains that carry oxygen in the blood of animals. The scheme emphasizes the β-like globin gene family. A relatively recent gene duplication of the γ-chain gene produced γ^G and γ^A, which are fetal β-like chains of identical function. The location of the globin genes in the human genome is shown at the top of the figure (see also Figure 7-60).

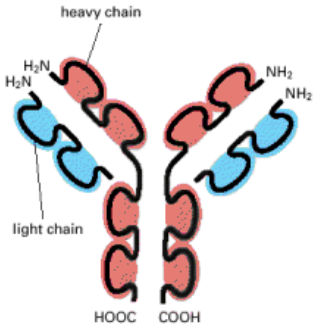

Figure 7-117. Schematic view of an antibody (immunoglobulin) molecule. This molecule is a complex of two identical heavy chains and two identical light chains. Each heavy chain contains four similar, covalently linked domains, while each light chain contains two such domains. Each domain is encoded by a separate exon, and all of the exons are thought to have evolved by the serial duplication of a single ancestral exon.

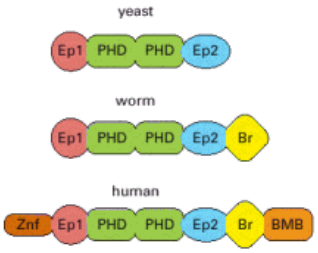

Figure 7-118. Domain structure of a group of evolutionary related proteins that are thought to have a similar function. In general, there is a tendency for the proteins in more complex organisms, such as ourselves, to contain additional domains - as is the case for the DNA-binding protein compared here.

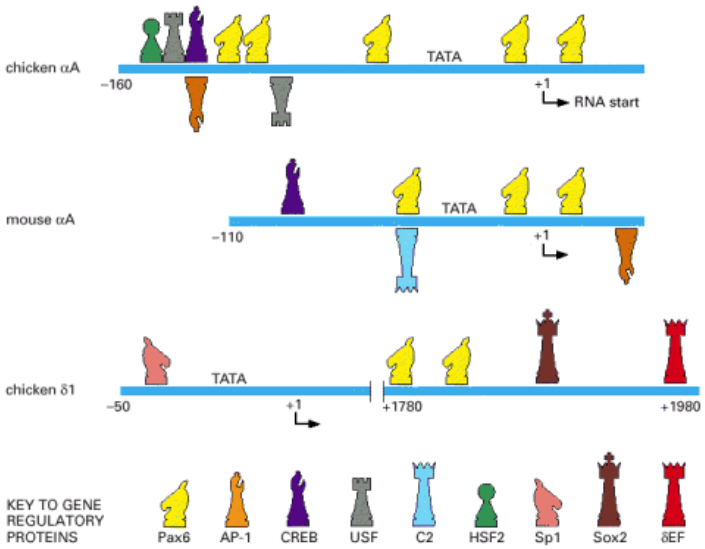

Figure 7-119. Gene control regions for mouse and chicken eye lens crystallins. Crystallins make up the bulk of the lens and are responsible for refracting and focusing light onto the retina. Many proteins in the cell have properties (high solubility, proper refractive index, etc.) suitable for lens function, and a wide variety of such proteins have been co-opted during evolution for use in the lens. For example, the α crystallins *(top two lines)* are closely related to heat shock proteins and are found in all vertebrate lenses. In contrast, δ crystallin *(third line)* is closely related to an enzyme involved in amino acid metabolism and is found only in birds and reptiles. The three crystallin gene control regions shown are a patchwork of different regulatory sequences that reflect the evolutionary history of each gene. The common feature of all three control regions is the presence of binding sites for the gene regulatory protein Pax6. Pax6 is the vertebrate homolog of the fly Toy and Eyeless proteins (see Figure 7-75) and is one of the key regulators that specifies eye development. Proteins above each gene control region are transcriptional activators and those below the line are repressors. (Adapted from E.H. Davidson, Genomic Regulatory Systems: Development and Evolution, pp. 191201. San Diego: Academic Press, 2001 and A. Cvekl and J. Piatigarsky, *BioEssays* 18:621630, 1996.)

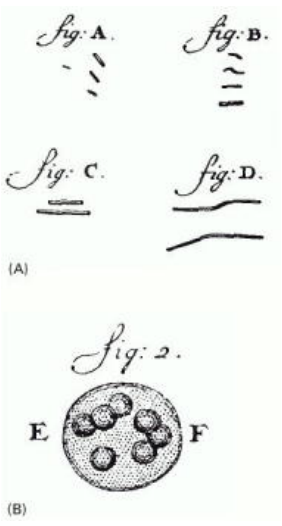

Figure 8-1. Microscopic life. A sample of "diverse animalcules" seen by van Leeuwenhoek using his simple microscope. (A) Bacteria seen in material he excavated from between his teeth. Those in fig. B he described as "swimming first forward and then backwards" (1692). (B) The eucaryotic green alga *Volvox* (1700). (Courtesy of the John Innes Foundation.)

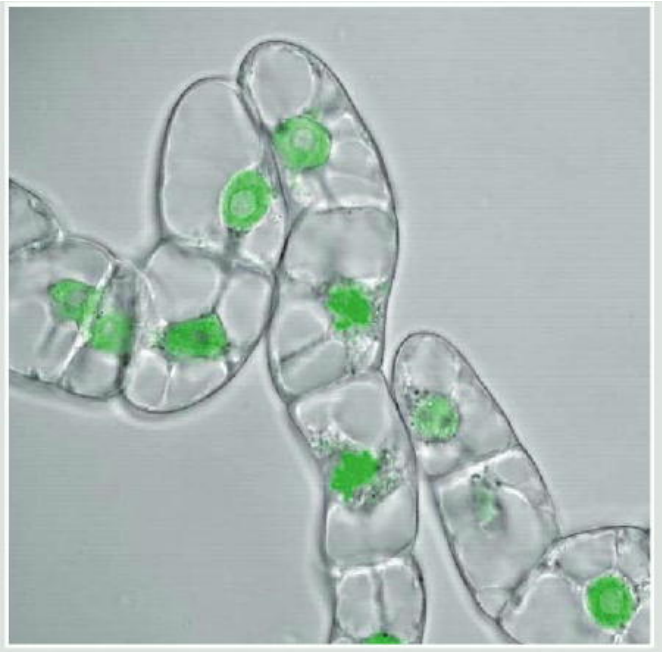

Plant cells in culture. These tobacco cells are growing in liquid culture. A histone protein that has been tagged with the green fluorescent protein (GFP) has been incorporated into chromatin. Some of the cells are dividing and are seen to have condensed chromosomes. Cultures of both animal and plant cells have been valuable research tools in all areas of cell biology. (Courtesy of Gethin Roberts.)

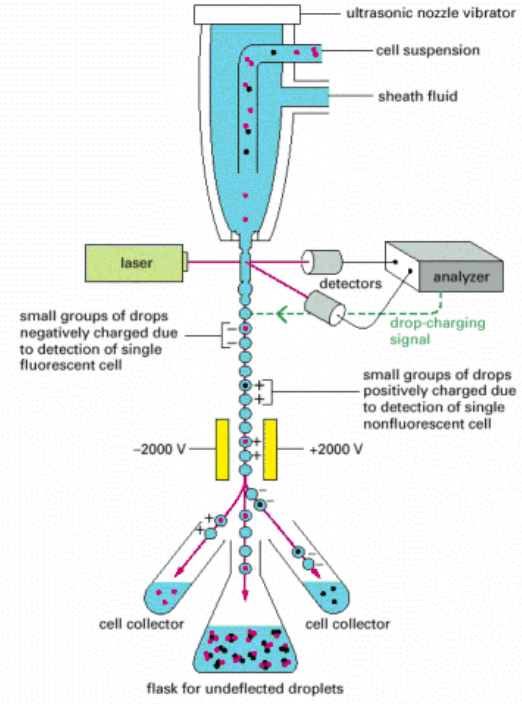

Figure 8-2. A fluorescence-activated cell sorter. . A cell passing through the laser beam is monitored for fluorescence. Droplets containing single cells are given a negative or positive charge, depending on whether the cell is fluorescent or not. The droplets are then deflected by an electric field into collection tubes according to their charge. Note that the cell concentration must be adjusted so that most droplets contain no cells and flow to a waste container together with any cell clumps.

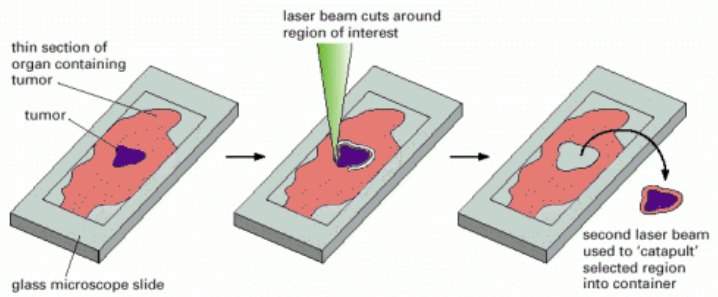

Figure 8-3. Microdissection techniques allow selected cells to be isolated from tissue slices. This method uses a laser beam to excise a region of interest and eject it into a container, and it permits the isolation of even a single cell from a tissue sample.

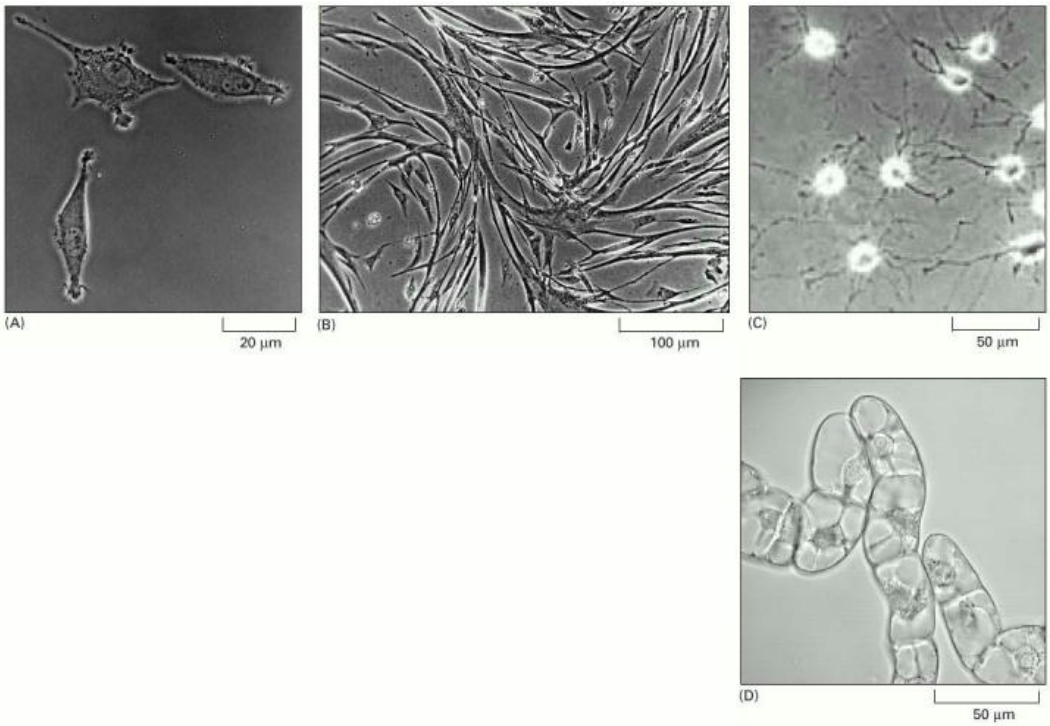

Figure 8-4. Cells in culture. (A) Phase-contrast micrograph of fibroblasts in culture. (B) Micrograph of myoblasts in culture shows cells fusing to form multinucleate muscle cells. (C) Oligodendrocyte precursor cells in culture. (D) Tobacco cells, from a fast-growing immortal cell line called BY2, in liquid culture. Nuclei and vacuoles can be seen in these cells. (A, courtesy of Daniel Zicha; B, courtesy of Rosalind Zalin; C, from D.G. Tang et al., *J. Cell Biol*. 148:971984, 2000. © The Rockefeller University Press; D, courtesy of Gethin Roberts.)

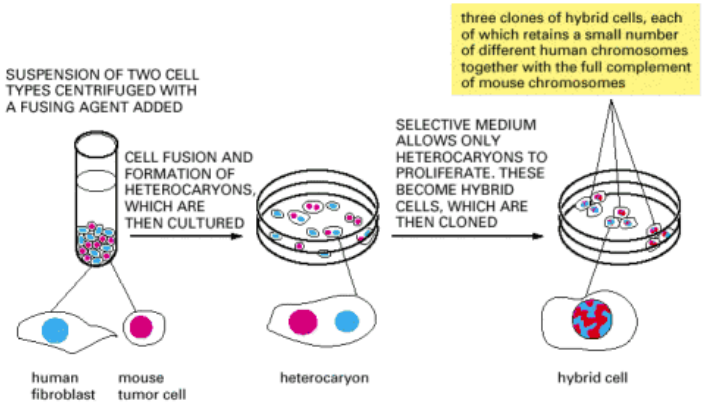

Figure 8-5. The production of hybrid cells. Human cells and mouse cells are fused to produce heterocaryons (each with two or more nuclei), which eventually form hybrid cells (each with one fused nucleus). These particular hybrid cells are useful for mapping human genes on specific human chromosomes because most of the human chromosomes are quickly lost in a random manner, leaving clones that retain only one or a few. The hybrid cells produced by fusing other types of cells often retain most of their chromosomes.

Figure 8-6. Preparation of hybridomas that secrete monoclonal antibodies against a particular antigen. Here the antigen of interest is designated as "antigen X." The selective growth medium used after the cell fusion step contains an inhibitor (aminopterin) that blocks the normal biosynthetic pathways by which nucleotides are made. The cells must therefore use a bypass pathway to synthesize their nucleic acids. This pathway is defective in the mutant cell line derived from the tumor, but it is intact in the cells obtained from the immunized mouse. Because neither cell type used for the initial fusion can grow on its own, only the hybrid cells survive.

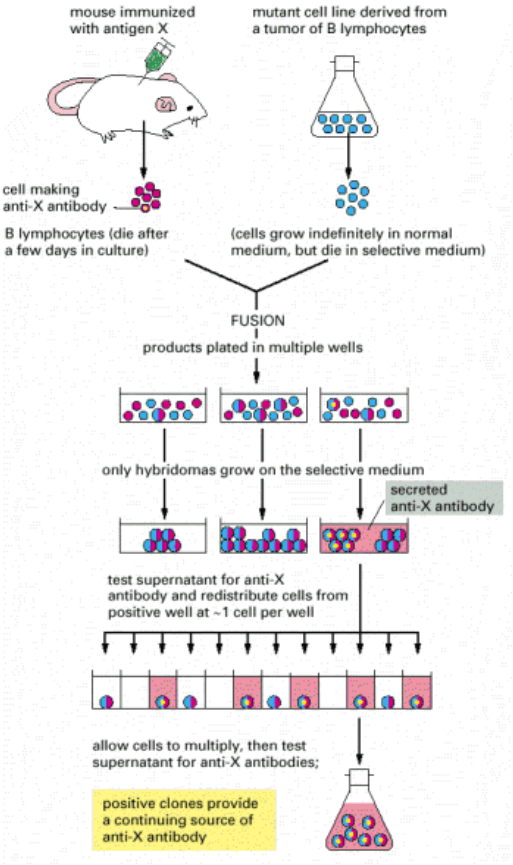

Figure 8-7. The preparative ultracentrifuge. The sample is contained in tubes that are inserted into a ring of cylindrical holes in a metal *rotor*. Rapid rotation of the rotor generates enormous centrifugal forces, which cause particles in the sample to sediment. The vacuum reduces friction, preventing heating of the rotor and allowing the refrigeration system to maintain the sample at 4°C.

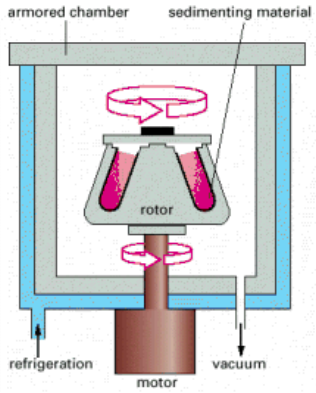

Figure 8-8. Cell fractionation by centrifugation. Repeated centrifugation at progressively higher speeds will fractionate homogenates of cells into their components. In general, the smaller the subcellular component, the greater is the centrifugal force

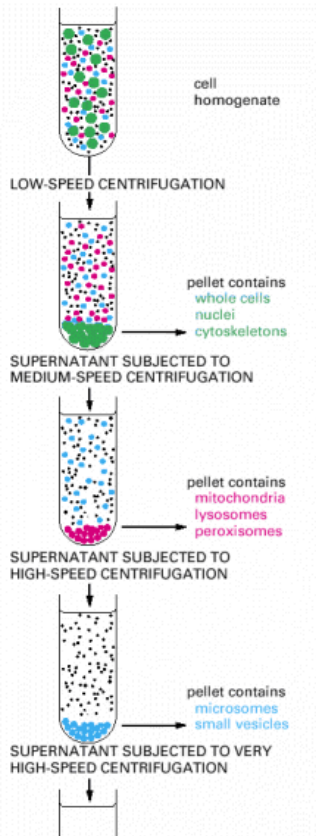

required to sediment it. Typical values for the various centrifugation steps referred to in the figure are:

low speed	1000 times gravity for 10 minutes
medium speed	20,000 times gravity for 20 minutes
high speed	80,000 times gravity for 1 hour
very high speed	150,000 times gravity for 3 hour

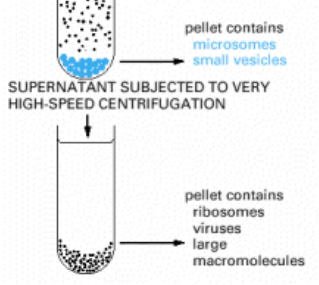

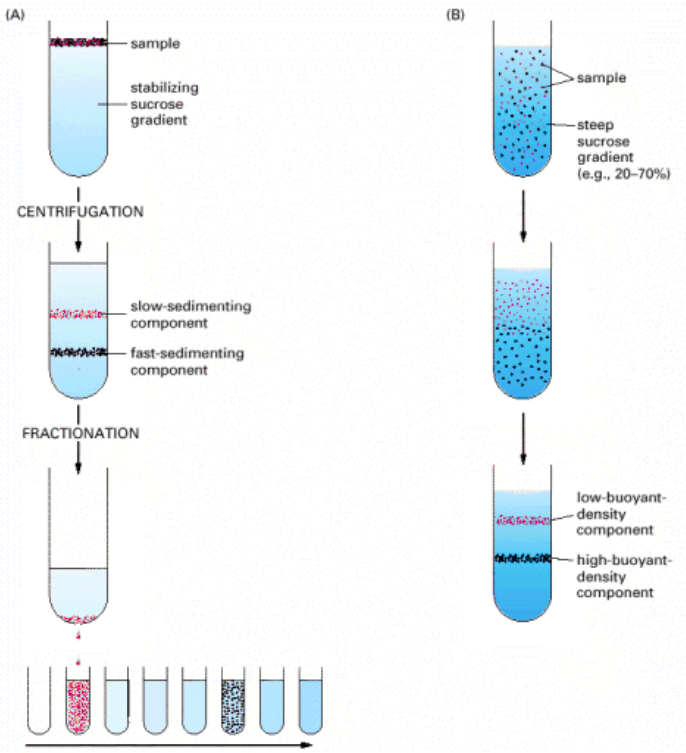

Figure 8-9. Comparison of velocity sedimentation and equilibrium sedimentation. In velocity sedimentation (A) subcellular components sediment at different speeds according to their size and shape when layered over a dilute solution containing sucrose. To stabilize the sedimenting bands against convective mixing caused by small differences in temperature or solute concentration, the tube contains a continuous shallow gradient of sucrose that increases in concentration toward the bottom of the tube (typically from 5% to 20% sucrose). Following centrifugation, the different components can be collected individually, most simply by puncturing the plastic centrifuge tube and collecting drops from the bottom, as illustrated here. In equilibrium sedimentation (B) subcellular components move up or down when centrifuged in a gradient until they reach a position where their density matches their surroundings. Although a sucrose gradient is shown here, denser gradients, which are especially useful for protein and nucleic acid separation, can be formed from cesium chloride. The final bands, at equilibrium, can be collected as in (A).

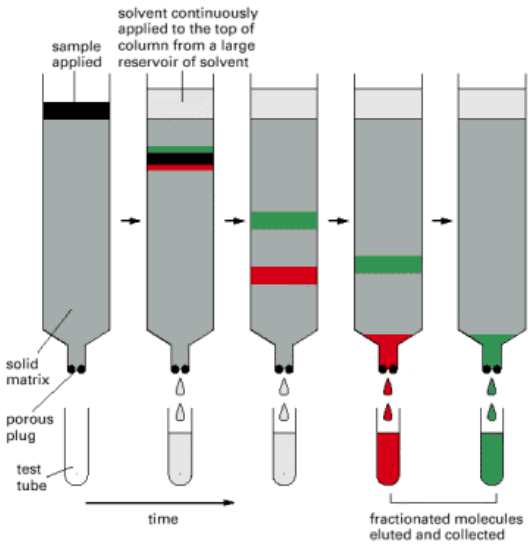

Figure 8-10. The separation of molecules by column chromatography. The sample, a mixture of different molecules, is applied to the top of a cylindrical glass or plastic column filled with a permeable solid matrix, such as cellulose, immersed in solvent. A large amount of solvent is then pumped slowly through the column and collected in separate tubes as it emerges from the bottom. Because various components of the sample travel at different rates through the column, they are fractionated into different tubes.

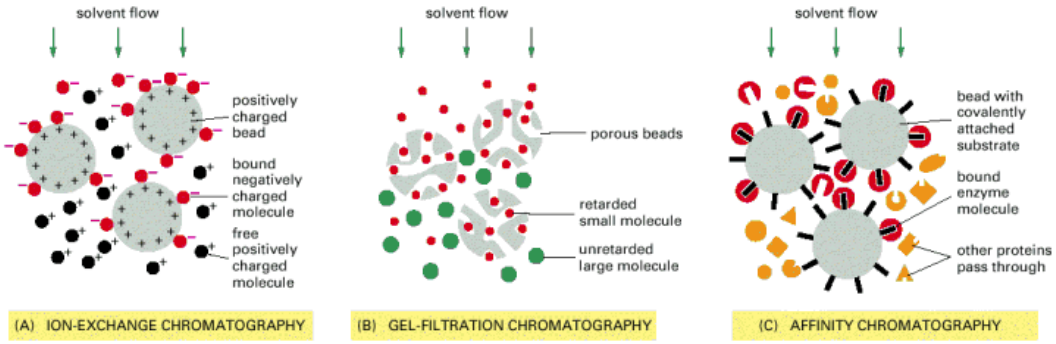

Figure 8-11. Three types of matrices used for chromatography. In ion-exchange chromatography (A) the insoluble matrix carries ionic charges that retard the movement of molecules of opposite charge. Matrices used for separating proteins include diethylaminoethylcellulose (DEAE-cellulose), which is positively charged, and carboxymethylcellulose (CM-cellulose) and phosphocellulose, which are negatively charged. Analogous matrices based on agarose or other polymers are also frequently used. The strength of the association between the dissolved molecules and the ion-exchange matrix depends on both the ionic strength and the pH of the solution that is passing down the column, which may therefore be varied systematically (as in Figure 8-12) to achieve an effective separation. In gel-filtration chromatography (B) the matrix is inert but porous. Molecules that are small enough to penetrate into the matrix are thereby delayed and travel more slowly through the column. Beads of cross-linked polysaccharide (dextran, agarose, or acrylamide) are available commercially in a wide range of pore sizes, making them suitable for the fractionation of molecules of various molecular weights, from less than 500 to more than 5×10^6. Affinity chromatography (C) uses an insoluble matrix that is covalently linked to a specific ligand, such as an antibody molecule or an enzyme substrate, that will bind a specific protein. Enzyme molecules that bind to immobilized substrates on such columns can be eluted with a concentrated solution of the free form of the substrate molecule, while molecules that bind to immobilized antibodies can be eluted by dissociating the antibody-antigen complex with concentrated salt solutions or solutions of high or low pH. High degrees of purification are often achieved in a single pass through an affinity column.

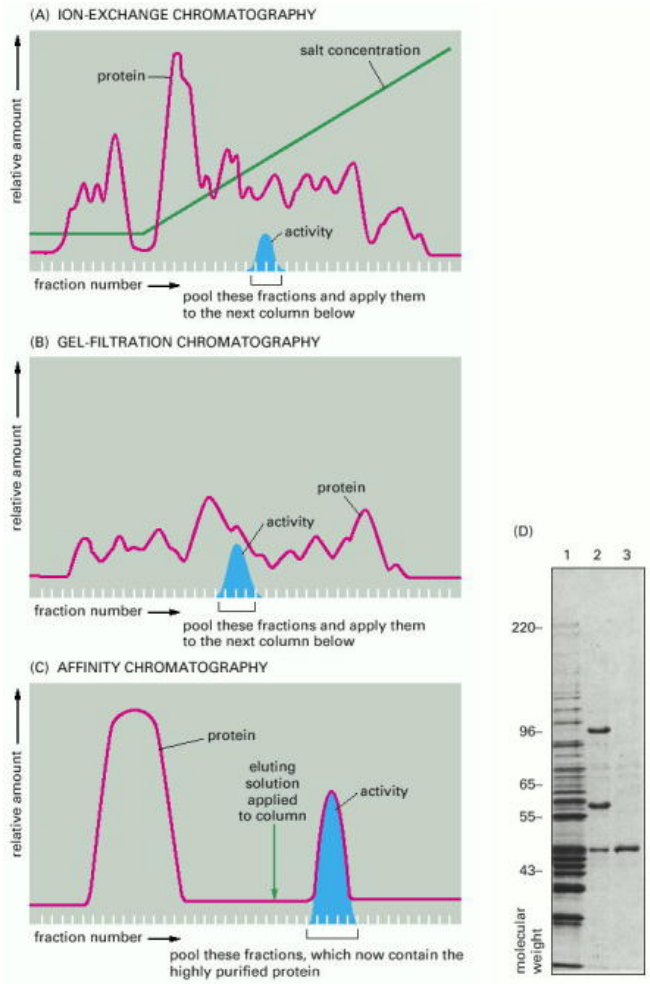

Figure 8-12. Protein purification by chromatography. Typical results obtained when three different chromatographic steps are used in succession to purify a protein. In this example a homogenate of cells was first fractionated by allowing it to percolate through an ion-exchange resin packed into a column (A). The column was washed, and the bound proteins were then eluted by passing a solution containing a gradually increasing concentration of salt onto the top of the column. Proteins with the lowest affinity for the ion-exchange resin passed directly through the column and were collected in the earliest fractions eluted from the bottom of the column. The remaining proteins were eluted in sequence according to their affinity for the resin - those proteins binding most tightly to the resin requiring the highest concentration of salt to remove them. The protein of interest was eluted in several fractions and was detected by its enzymatic activity. The fractions with activity were pooled and then applied to a second, gel-filtration column (B). The elution position of the still-impure protein was again determined by its enzymatic activity and the active fractions were pooled and purified to homogeneity on an affinity column (C) that contained an immobilized substrate of the enzyme. (D) Affinity purification of cyclin-binding proteins from *S. cerevisiae*, as analyzed by SDS polyacrylamide-gel electrophoresis (see Figure 8-14). Lane 1 is a total cell extract; lane 2 shows the proteins eluted from an affinity column containing cyclin B2; lane 3 shows one major protein eluted from a cyclin B3 affinity column. Proteins in lanes 2 and 3 were eluted with salt and the gels was stained with Coomassie blue. (D, from D. Kellogg et al., *J. Cell Biol.* 130:675685, 1995. © The Rockefeller University Press.)

Figure 8-48. Epitope tagging allows the localization or purification of proteins. Using standard genetic engineering

techniques, a short epitope tag can be added to a protein of interest. The resulting protein contains the protein being analyzed plus a short peptide that can be recognized by commercially available antibodies. The labeled antibody can be used to follow the cellular localization of the protein or to purify it by immunoprecipitation or affinity chromatography.

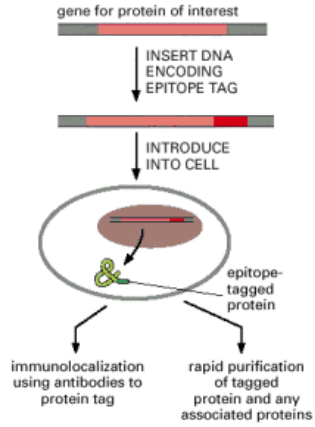

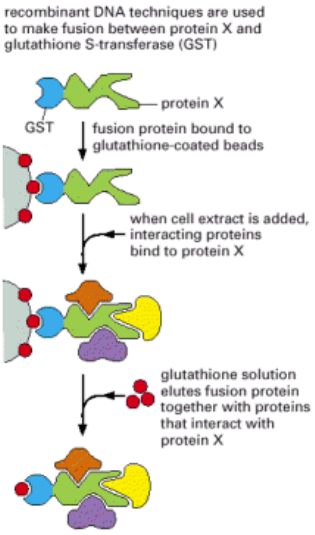

Figure 8-50. Purification of protein complexes using a GST-tagged fusion protein. GST fusion proteins, generated by standard recombinant DNA techniques, can be captured on an affinity column containing beads coated with glutathione. To look for proteins that bind to protein X, cell extracts can be passed through this column. The hybrid protein and its binding partners can then be eluted with glutathione. The identities of these interacting proteins can be determined by mass spectrometry (see Figure 8-20). In an alternative approach, a cell extract can be made from a cell producing the GST fusion protein and passed directly through the glutathione affinity column. The GST fusion protein, along with proteins that have associated with it in the cell, are thereby retained. Affinity columns can also be made to contain antibodies against GST or another convenient small protein or epitope tag (see Figure 8-48).

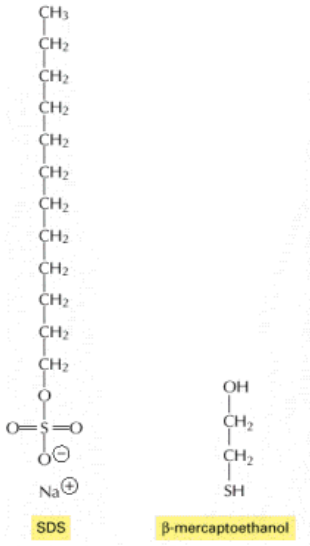

Figure 8-13. The detergent sodium dodecyl sulfate (SDS) and the reducing agent β-mercaptoethanol. These two chemicals are used to solubilize proteins for SDS polyacrylamide-gel electrophoresis. The SDS is shown here in its ionized form.

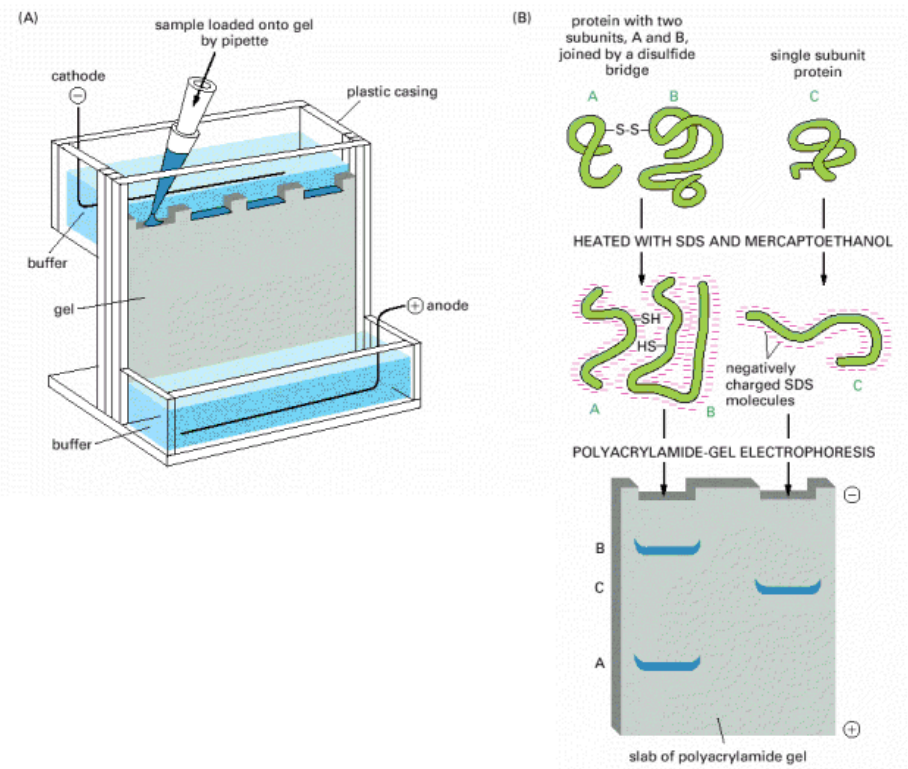

Figure 8-14. SDS polyacrylamide-gel electrophoresis (SDS-PAGE). (A) An electrophoresis apparatus. (B) Individual polypeptide chains form a complex with negatively charged molecules of sodium dodecyl sulfate (SDS) and therefore migrate as a negatively charged SDS-protein complex through a porous gel of polyacrylamide. Because the speed of migration under these conditions is greater the smaller the polypeptide, this technique can be used to determine the approximate molecular weight of a polypeptide chain as well as the subunit composition of a protein. If the protein contains a large amount of carbohydrate, however, it will move anomalously on the gel and its apparent molecular weight estimated by SDS-PAGE will be misleading.

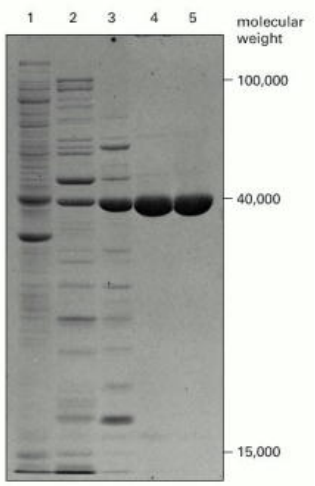

Figure 8-15. Analysis of protein samples by SDS polyacrylamide-gel electrophoresis. The photograph shows a Coomassie-stained gel that has been used to detect the proteins present at successive stages in the purification of an enzyme. The leftmost lane (lane 1) contains the complex mixture of proteins in the starting cell extract, and each succeeding lane analyzes the proteins obtained after a chromatographic fractionation of the protein sample analyzed in the previous lane (see Figure 8-12). The same total amount of protein (10 μg) was loaded onto the gel at the top of each lane. Individual proteins normally appear as sharp, dye-stained bands; a band broadens, however, when it contains too much protein. (From T. Formosa and B.M. Alberts, *J. Biol. Chem.* 261:61076118, 1986.)

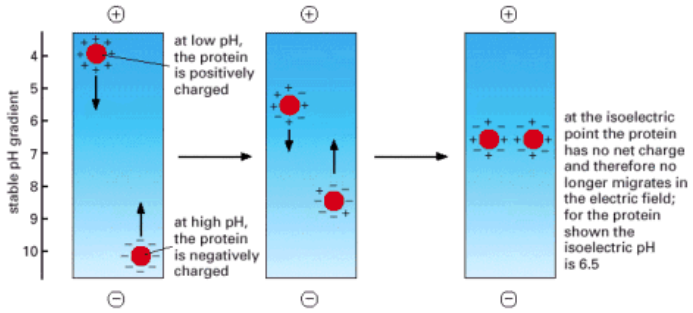

Figure 8-16. Separation of protein molecules by isoelectric focusing. At low pH (high H^+ concentration) the carboxylic acid groups of proteins tend to be uncharged (-COOH) and their nitrogen-containing basic groups fully charged (for example, $-NH_3^+$), giving most proteins a net positive charge. At high pH the carboxylic acid groups are negatively charged ($-COO^-$) and the basic groups tend to be uncharged (for example, $-NH_2$), giving most proteins a net negative charge. At its *isoelectric pH* a protein has no net charge since the positive and negative charges balance. Thus, when a tube containing a fixed pH gradient is subjected to a strong electric field in the appropriate direction, each protein species present migrates until it forms a sharp band at its isoelectric pH, as shown.

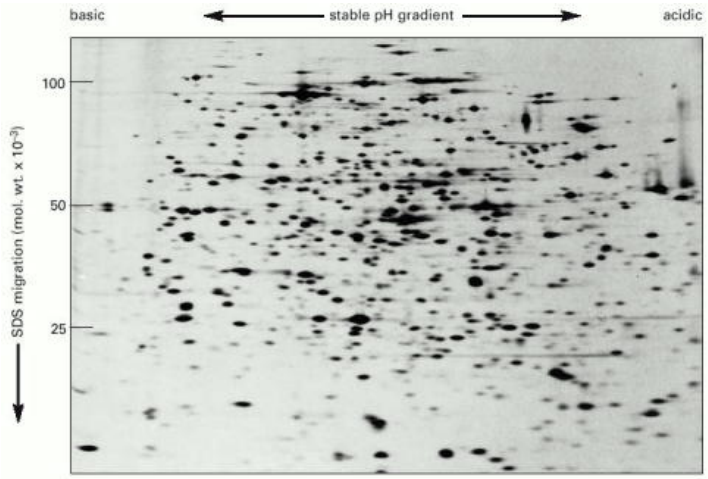

Figure 8-17. Two-dimensional polyacrylamide-gel electrophoresis. All the proteins in an *E. coli* bacterial cell are separated in this gel, in which each spot corresponds to a different polypeptide chain. The proteins were first separated on the basis of their isoelectric points by isoelectric focusing from left to right. They were then further fractionated according to their molecular weights by electrophoresis from top to bottom in the presence of SDS. Note that different proteins are present in very different amounts. The bacteria were fed with a mixture of radioisotope-labeled amino acids so that all of their proteins were radioactive and could be detected by autoradiography (see pp. 578579). (Courtesy of Patrick O'Farrell.)

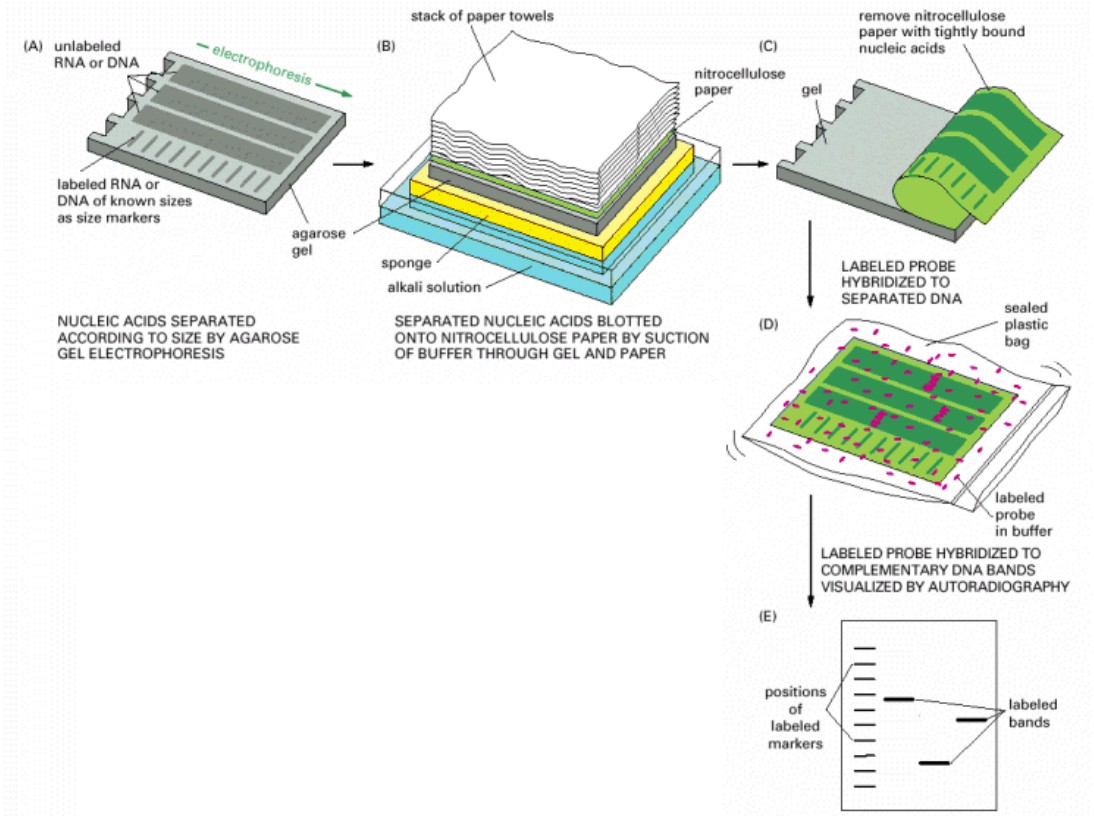

Figure 8-27. Detection of specific RNA or DNA molecules by gel-transfer hybridization. In this example, the DNA probe is detected by its radioactivity. DNA probes detected by chemical or fluorescence methods are also widely used (see Figure 8-24). (A) A mixture of either single-stranded RNA molecules *(Northern blotting)* or the double-stranded DNA molecules created by restriction nuclease treatment *(Southern blotting)* is separated according to length by electrophoresis. (B) A sheet of either nitrocellulose paper or nylon paper is laid over the gel, and the separated RNA or DNA fragments are transferred to the sheet by blotting. (C) The nitrocellulose sheet is carefully peeled off the gel. (D) The sheet containing the bound nucleic acids is placed in a sealed plastic bag together with a buffered salt solution containing a radioactively labeled DNA probe. The paper sheet is exposed to a labeled DNA probe for a prolonged period under conditions favoring hybridization. (E) The sheet is removed from the bag and washed thoroughly, so that only probe molecules that have hybridized to the RNA or DNA immobilized on the paper remain attached. After autoradiography, the DNA that has hybridized to the labeled probe shows up as bands on the autoradiograph. For Southern blotting, the strands of the double-stranded DNA molecules on the paper must be separated before the hybridization process; this is done by exposing the DNA to alkaline denaturing conditions after the gel has been run (not shown).

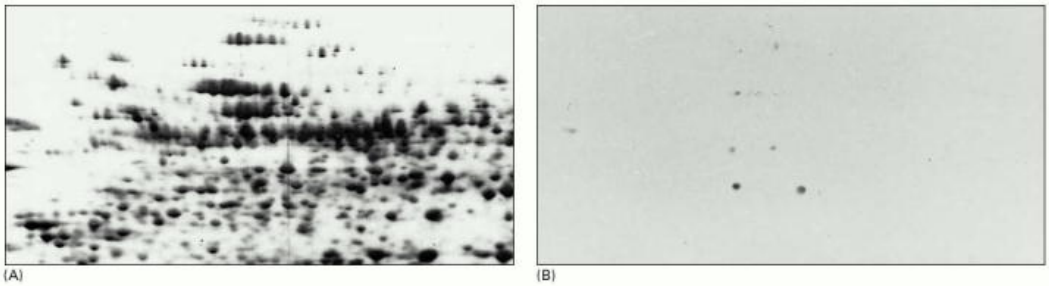

Figure 8-18. Western blotting. The total proteins from dividing tobacco cells in culture are first separated by two-dimensional polyacrylamide-gel electrophoresis and in (A) their positions are revealed by a sensitive protein stain. In (B) the separated proteins on an identical gel were then transferred to a sheet of nitrocellulose and exposed to an antibody that recognizes only those proteins that are phosphorylated on threonine residues during mitosis. The positions of the dozen or so proteins that are recognized by this antibody are revealed by an enzyme-linked second antibody. This technique is also known as immunoblotting. (From J.A. Traas, A.F. Bevan, J.H. Doonan, J. Cordewener, and P.J. Shaw, *Plant J.* 2:723732, 1992. © Blackwell Scientific Publications.)

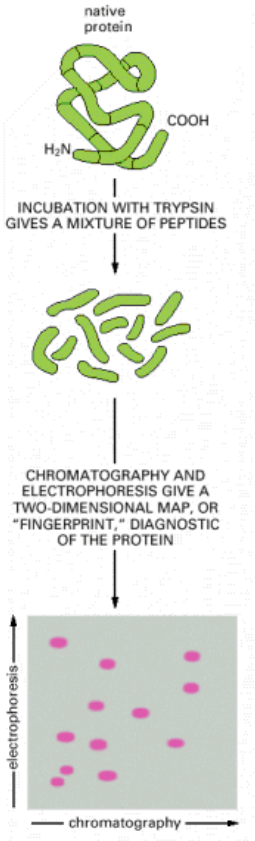

Figure 8-19. Production of a peptide map, or fingerprint, of a protein. Here, the protein was digested with trypsin to generate a mixture of polypeptide fragments, which was then fractionated in two dimensions by electrophoresis and partition chromatography. The latter technique separates peptides on the basis of their differential solubilities in water, which is preferentially bound to the solid matrix, as compared to the solvent in which they are applied. The resulting pattern of spots obtained from such a digest is diagnostic of the protein analyzed. It is also used to detect posttranslational modifications of proteins.

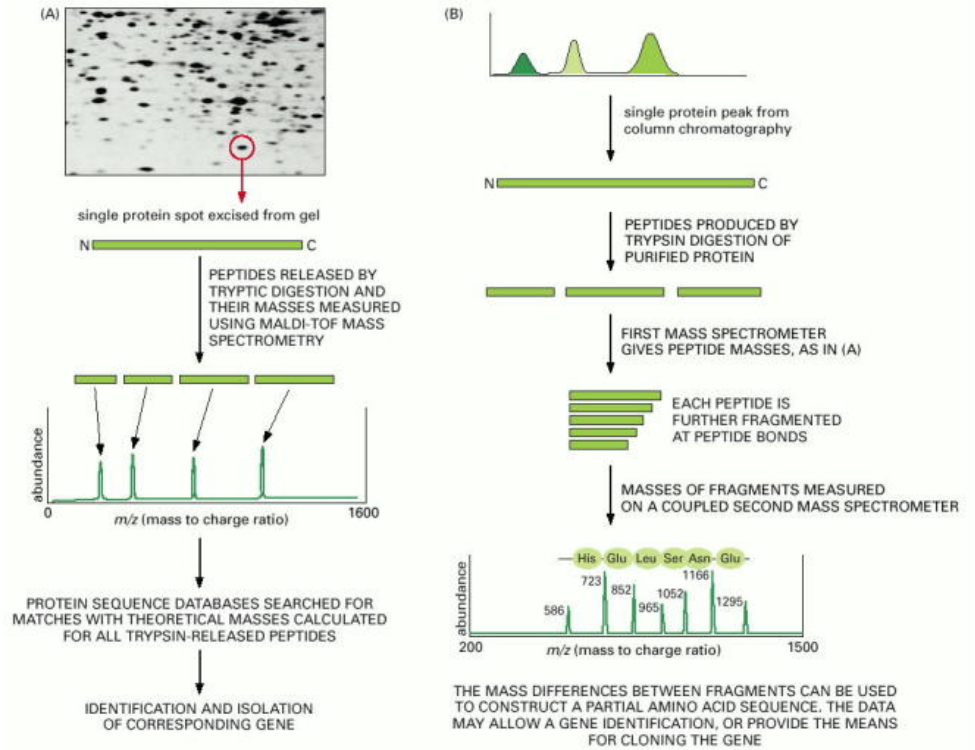

Figure 8-20. Mass-spectrometric approaches to identify proteins and sequence peptides. (A) Mass spectrometry can be used to identify proteins by determining their precise masses, and the masses of peptides derived from them, and using that information to search a genomic database for the corresponding gene. In this example, the protein of interest is excised from a two-dimensional polyacrylamide gel and then digested with trypsin. The peptide fragments are loaded into the mass spectrometer and their masses are measured. Sequence databases are then searched to find the gene that encodes a protein whose calculated tryptic digest profile matches these values. (B) Mass spectrometry can also be used to determine directly the amino acid sequence of peptide fragments. In this example, proteins that form a macromolecular complex have been separated by chromatography, and a single protein selected for digestion with trypsin. The masses of these tryptic fragments are then determined by mass spectrometry as in (A). To determine their exact amino acid sequence, each peptide is further fragmented, primarily by cleaving its peptide bonds. This treatment generates a nested set of peptides, each differing in size by one amino acid. These fragments are fed into a second coupled mass spectrometer and their masses are determined. The difference in masses between two closely related peptides can be used to deduce the "missing" amino acid. By repeated applications of this procedure, a partial amino acid sequence of the original protein can be determined. (Micrograph courtesy of Patrick O'Farrell.)

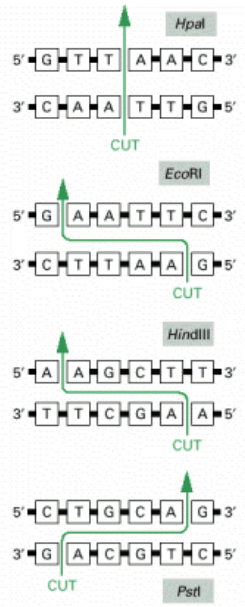

Figure 8-21. The DNA nucleotide sequences recognized by four widely used restriction nucleases. As in the examples shown, such sequences are often six base pairs long and "palindromic" (that is, the nucleotide sequence is the same if the helix is turned by 180 degrees around the center of the short region of helix that is recognized). The enzymes cut the two strands of DNA at or near the recognition sequence. For some enzymes, such as *Hpa*I, the cleavage leaves blunt ends; for others, such as *Eco*RI, *Hin*dIII, and *Pst*I, the cleavage is staggered and creates cohesive ends. Restriction nucleases are obtained from various species of bacteria: *Hpa*I is from *Hemophilus parainfluenzae*, *Eco*RI is from *Escherichia coli*, *Hin*dIII is from *Hemophilus influenzae*, and *Pst*I is from *Providencia stuartii*.

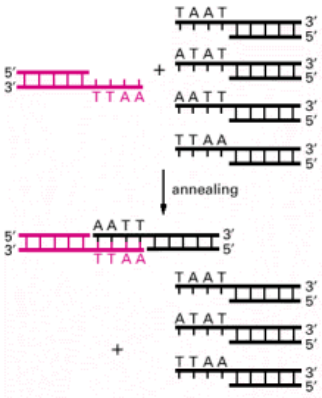

Figure 8-22. Restriction nucleases produce DNA fragments that can be easily joined together. Fragments with the same cohesive ends can readily join by complementary base-pairing between their cohesive ends, as illustrated. The two DNA fragments that join in this example were both produced by the *Eco*RI restriction nuclease, whereas the three other fragments were produced by different restriction nucleases that generated different cohesive ends (see Figure 8-21). Blunt-ended fragments, like those generated by *Hpa*I (see Figure 8-21), can be spliced together with more difficulty.

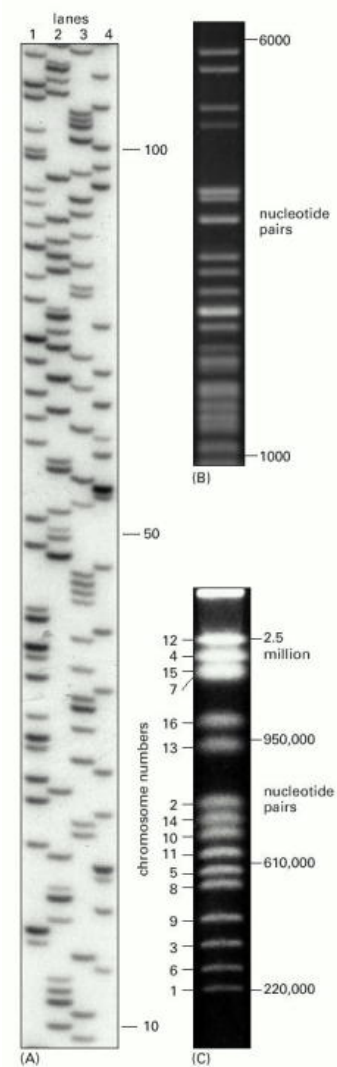

Figure 8-23. Gel electrophoresis techniques for separating DNA molecules by size. In the three examples shown, electrophoresis is from top to bottom, so that the largest - and thus slowest-moving - DNA molecules are near the top of the gel. In (A) a polyacrylamide gel with small pores is used to fractionate single-stranded DNA. In the size range 10 to 500 nucleotides, DNA molecules that differ in size by only a single nucleotide can be separated from each other. In the example, the four lanes represent sets of DNA molecules synthesized in the course of a DNA-sequencing procedure. The DNA to be sequenced has been artificially replicated from a fixed start site up to a variable stopping point, producing a set of partial replicas of differing lengths. (Figure 8-36 explains how such sets of partial replicas are synthesized.) Lane 1 shows all the partial replicas that terminate in a G, lane 2 all those that terminate in an A, lane 3 all those that terminate in a T, and lane 4 all those that terminate in a C. Since the DNA molecules used in these reactions are radiolabeled, their positions can be determined by autoradiography, as shown. In (B) an agarose gel with medium-sized pores is used to separate double-stranded DNA molecules. This method is most useful in the size range 300 to 10,000 nucleotide pairs. These DNA molecules are fragments produced by cleaving the genome of a bacterial virus with a restriction nuclease, and they have been detected by their fluorescence when stained with the dye ethidium bromide. In (C) the technique of pulsed-field agarose gel electrophoresis has been used to separate 16 different

yeast *(Saccharomyces cerevisiae)* chromosomes, which range in size from 220,000 to 2.5 million nucleotide pairs (see Figure 4-13). The DNA was stained as in (B). DNA molecules as large as 10^7 nucleotide pairs can be separated in this way. (A, courtesy of Leander Lauffer and Peter Walter; B, courtesy of Ken Kreuzer; C, from D. Vollrath and R.W. Davis, *Nucleic Acids Res.* 15:78657876, 1987. © Oxford University Press.)

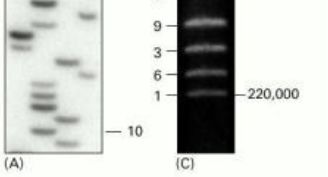

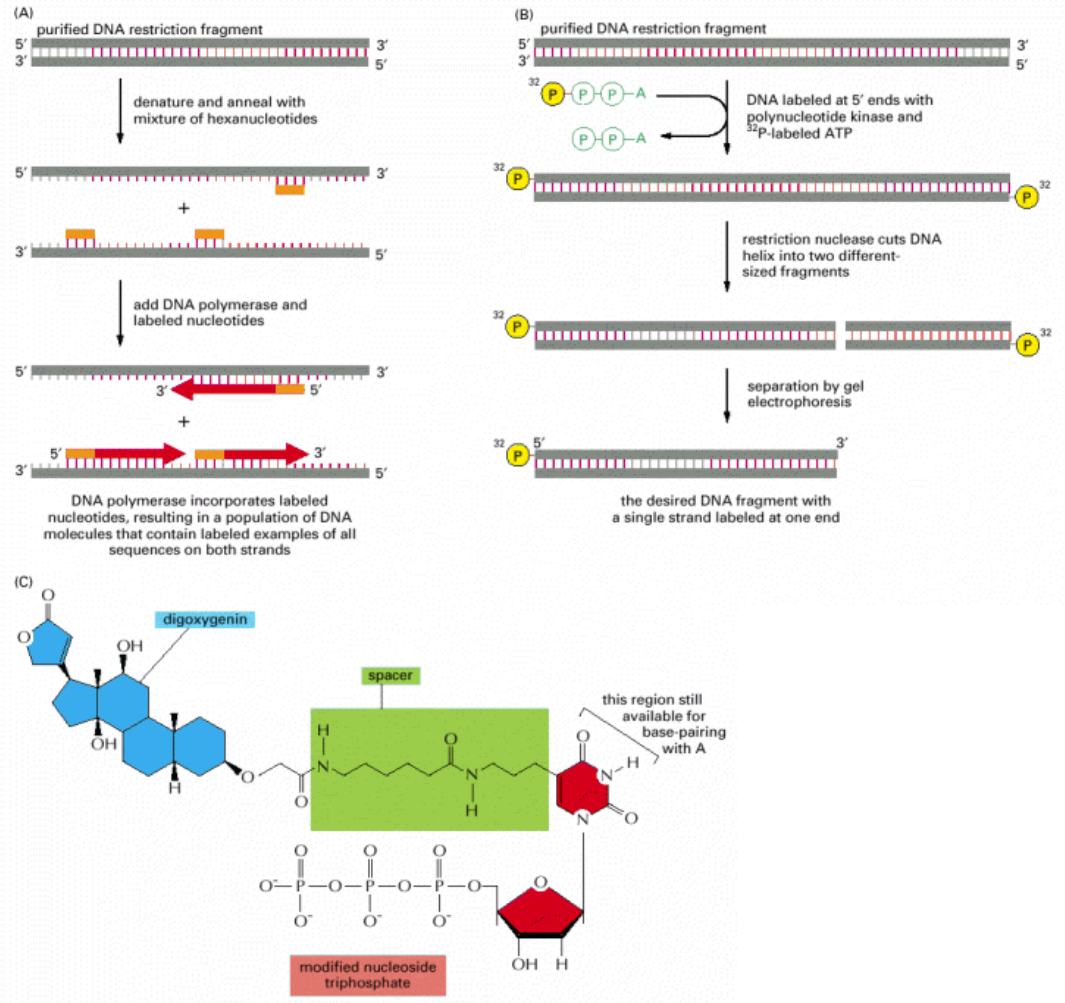

Figure 8-24. Methods for labeling DNA molecules *in vitro*. (A) A purified DNA polymerase enzyme labels all the nucleotides in a DNA molecule and can thereby produce highly radioactive DNA probes. (B) Polynucleotide kinase labels only the 5 ends of DNA strands; therefore, when labeling is followed by restriction nuclease cleavage, as shown, DNA molecules containing a single 5-end-labeled strand can be readily obtained. (C) The method in (A) is also used to produce nonradioactive DNA molecules that carry a specific chemical marker that can be detected with an appropriate antibody. The modified nucleotide shown can be incorporated into DNA by DNA polymerase so as to allow the DNA molecule to serve as a probe that can be readily detected. The base on the nucleoside triphosphate shown is an analog of thymine in which the methyl group on T has been replaced by a spacer arm linked to the plant steroid digoxigenin. To visualize the probe, the digoxigenin is detected by a specific antibody coupled to a visible marker such as a fluorescent dye. Other chemical labels such as biotin can be attached to nucleotides and used in essentially the same way.

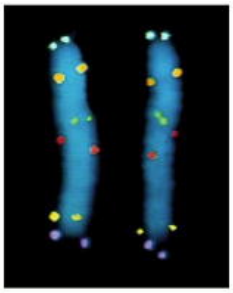

Figure 8-28. *In situ* hybridization to locate specific genes on chromosomes. Here, six different DNA probes have been used to mark the location of their respective nucleotide sequences on human chromosome 5 at metaphase. The probes have been chemically labeled and detected with fluorescent antibodies. Both copies of chromosome 5 are shown, aligned side by side. Each probe produces two dots on each chromosome, since a metaphase chromosome has replicated its DNA and therefore contains two identical DNA helices. (Courtesy of David C. Ward.)

Figure 8-25. Different hybridization conditions allow less than perfect DNA matching. When only an identical match with a DNA probe is desired, the hybridization reaction is kept just a few degrees below the temperature at which a perfect DNA helix denatures in the solvent used (its *melting temperature)*, so that all imperfect helices formed are unstable. When a DNA probe is being used to find DNAs that are related, but not identical, in sequence, hybridization is performed at a lower temperature. This allows even imperfectly paired double helices to form. Only the lower-temperature hybridization conditions can be used to search for genes (C and E in this example) that are nonidentical but related to gene A (see Figure 10-18).

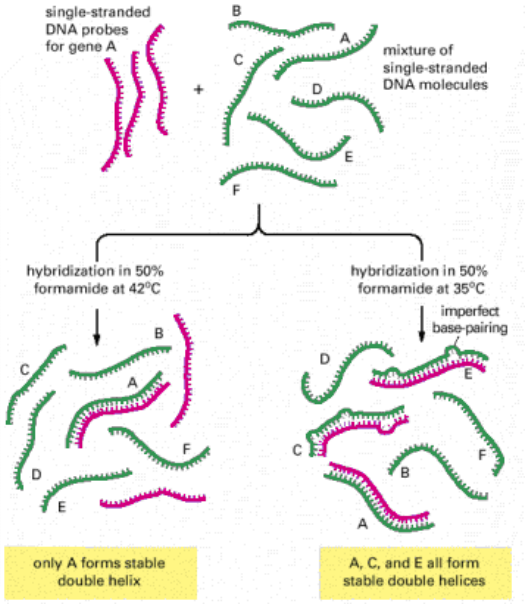

Figure 8-26. The use of nucleic acid hybridization to determine the region of a cloned DNA fragment that is present in an mRNA molecule. The method shown requires a nuclease that cuts the DNA chain only where it is not base-paired to a complementary RNA chain. The positions of the introns in eucaryotic genes are mapped by the method shown; the beginning and the end of an RNA molecule can be determined in the same way. For this type of analysis the DNA is electrophoresed through a denaturing agarose gel, which causes it to migrate as single-stranded molecules.

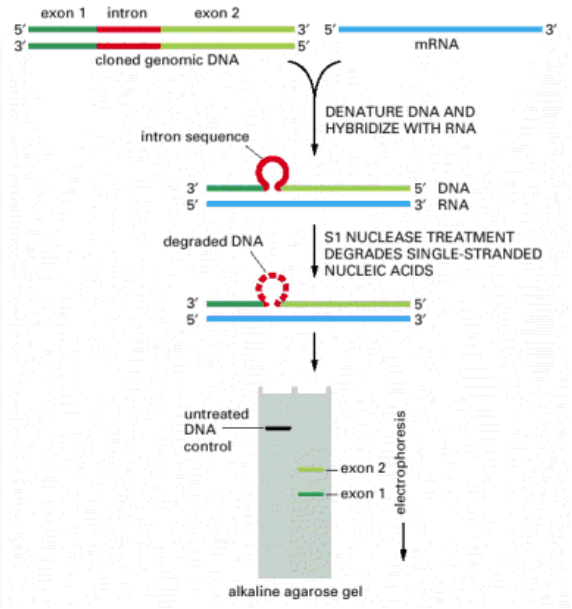

Figure 8-29. *In situ* hybridization for RNA localization. (A) Expression pattern of *deltaC* in the early zebrafish embryo. This gene codes for a ligand in the Notch signaling pathway (discussed in Chapter 15), and the pattern shown here reflects its role in the development of somites - the future segments of the vertebrate trunk and tail. (B) High-resolution RNA *in situ* localization reveals the sites within the nucleolus of a pea cell where ribosomal RNA is synthesized. The sausage-like structures, 0.51 μm in diameter, correspond to the loops of chromosomal DNA that contain the genes encoding rRNA. Each small, white spot represents transcription of a single rRNA gene. (A, courtesy of Yun-Jin Jiang; B, courtesy of Peter Shaw.)

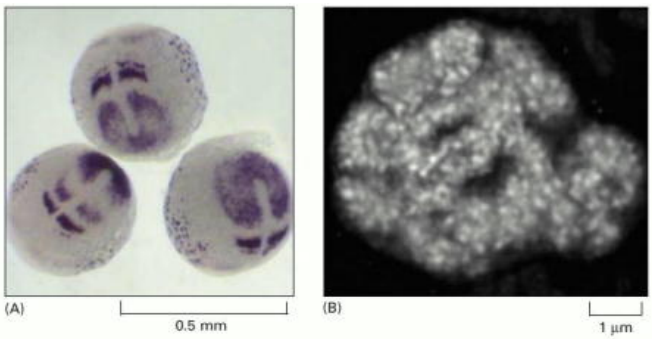

Figure 8-30. The insertion of a DNA fragment into a bacterial plasmid with the enzyme DNA ligase. The plasmid is cut open with a restriction nuclease (in this case one that produces cohesive ends) and is mixed with the DNA fragment to be cloned (which has been prepared with the same restriction nuclease), DNA ligase, and ATP. The cohesive ends base-pair, and DNA ligase seals the nicks in the DNA backbone, producing a complete recombinant DNA molecule. (Micrographs courtesy of Huntington Potter and David Dressler.)

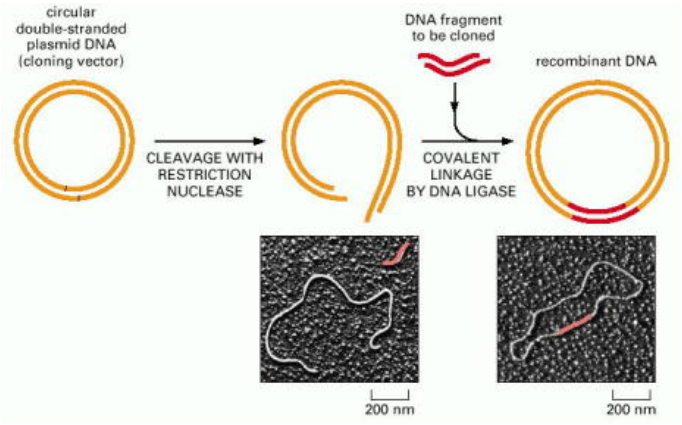

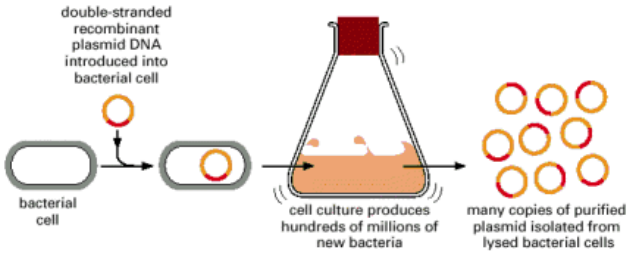

Figure 8-31. Purification and amplification of a specific DNA sequence by DNA cloning in a bacterium. To produce many copies of a particular DNA sequence, the fragment is first inserted into a plasmid vector, as shown in Figure 8-30. The resulting recombinant plasmid DNA is then introduced into a bacterium, where it can be replicated many millions of times as the bacterium multiplies.

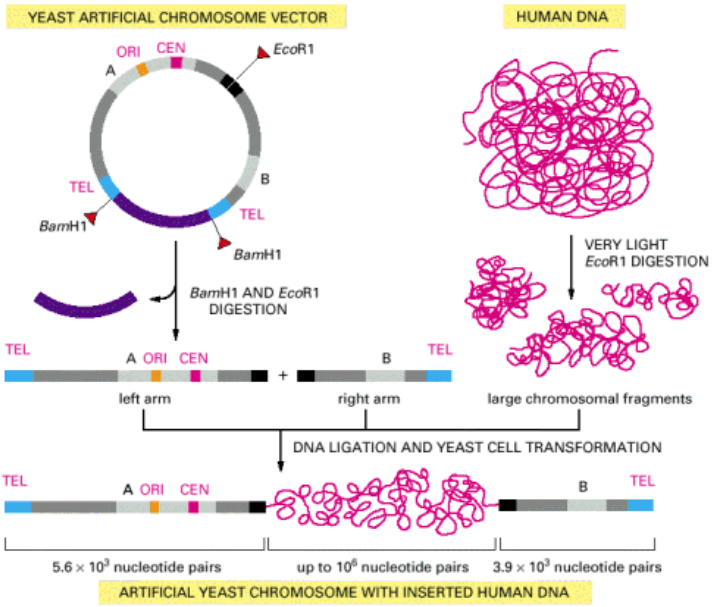

Figure 8-32. The making of a yeast artificial chromosome (YAC). A YAC vector allows the cloning of very large DNA molecules. TEL, CEN, and ORI are the telomere, centromere, and origin of replication sequences, respectively, for the yeast *Saccharomyces cerevisiae*. *Bam*H1 and *Eco*R1 are sites where the corresponding restriction nucleases cut the DNA double helix. The sequences denoted A and B encode enzymes that serve as selectable markers to allow the easy isolation of yeast cells that have taken up the artificial chromosome. (Adapted from D.T. Burke, G.F. Carle, and M.V. Olson, *Science* 236:806812, 1987.)

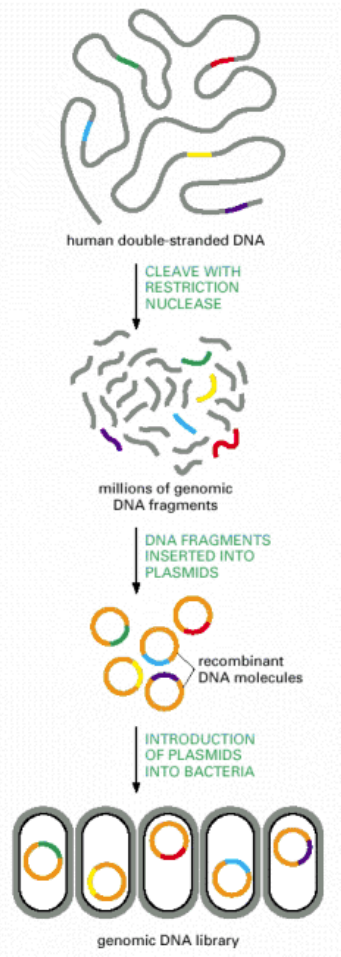

Figure 8-33. Construction of a human genomic DNA library. A genomic library is usually stored as a set of bacteria, each carrying a different fragment of human DNA. For simplicity, cloning of just a few representative fragments *(colored)* is shown. In reality, all of the *gray* DNA fragments would also be cloned.

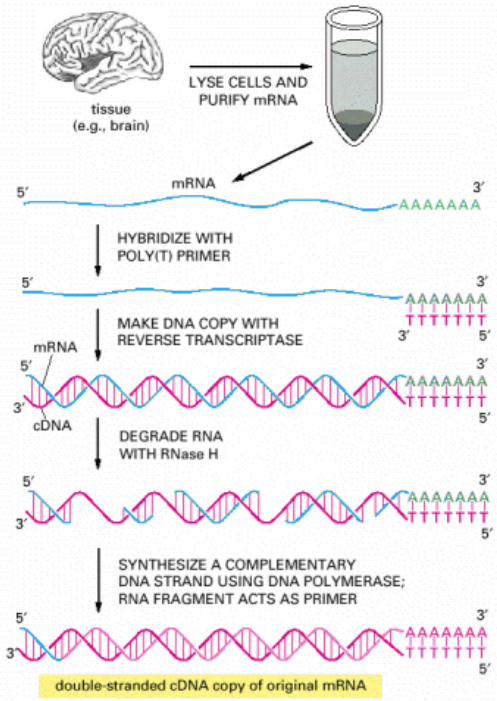

Figure 8-34. The synthesis of cDNA. Total mRNA is extracted from a particular tissue, and DNA copies (cDNA) of the mRNA molecules are produced by the enzyme reverse transcriptase (see p. 289). For simplicity, the copying of just one of these mRNAs into cDNA is illustrated. A short oligonucleotide complementary to the poly-A tail at the 3 end of the mRNA (discussed in Chapter 6) is first hybridized to the RNA to act as a primer for the reverse transcriptase, which then copies the RNA into a complementary DNA chain, thereby forming a DNA/RNA hybrid helix. Treating the DNA/RNA hybrid with RNase H (see Figure 5-13) creates nicks and gaps in the RNA strand. The remaining single-stranded cDNA is then copied into double-stranded cDNA by the enzyme DNA polymerase. The primer for this synthesis reaction is provided by a fragment of the original mRNA, as shown. Because the DNA polymerase used to synthesize the second DNA strand can synthesize through the bound RNA molecules, the RNA fragment that is base-paired to the 3 end of the first DNA strand usually acts as the primer for the final product of the second strand synthesis. This RNA is eventually degraded during subsequent cloning steps. As a result, the nucleotide sequences at the extreme 5 ends of the original mRNA molecules are often absent from cDNA libraries.

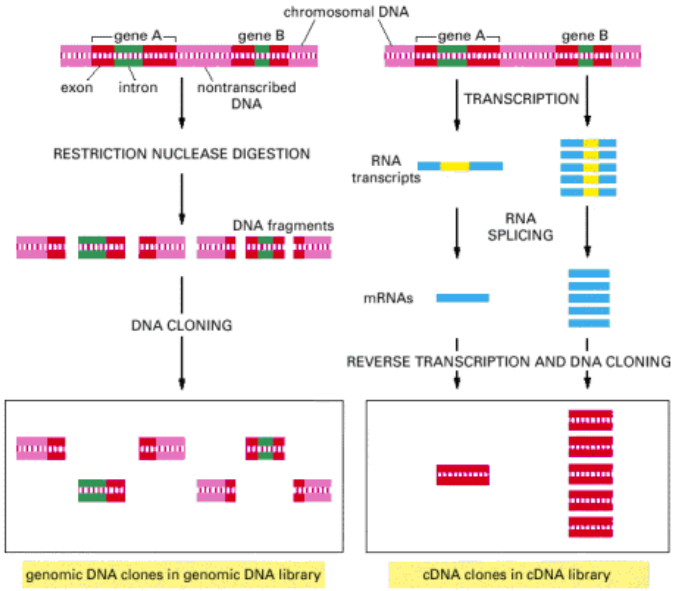

Figure 8-35. The differences between cDNA clones and genomic DNA clones derived from the same region of DNA. In this example gene A is infrequently transcribed, whereas gene B is frequently transcribed, and both genes contain introns *(green).* In the genomic DNA library, both the introns and the nontranscribed DNA *(pink)* are included in the clones, and most clones contain, at most, only part of the coding sequence of a gene *(red).* In the cDNA clones the intron sequences *(yellow)* have been removed by RNA splicing during the formation of the mRNA *(blue),* and a continuous coding sequence is therefore present in each clone. Because gene B is transcribed more abundantly than in gene A in the cells from which the cDNA library was made, it is represented much more frequently than A in the cDNA library. In contrast, A and B are in principle represented equally in the genomic DNA library.

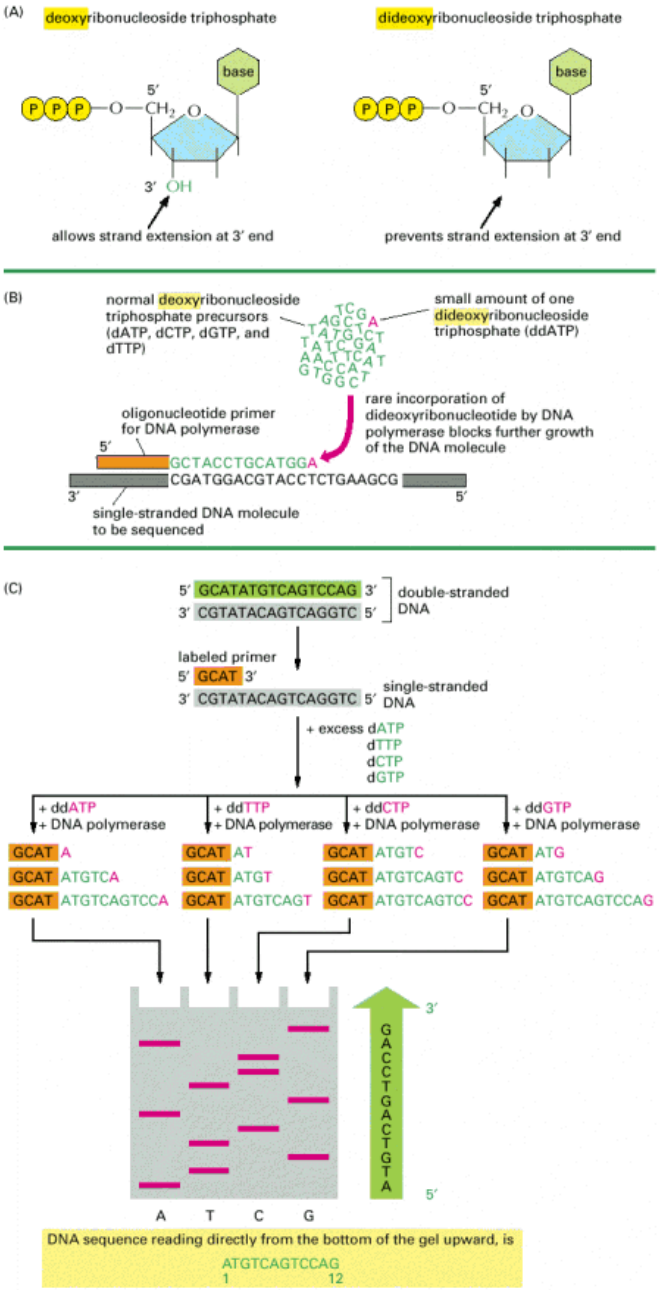

Figure 8-36. The enzymatic - or dideoxy - method of sequencing DNA. (A) This method relies on the use of dideoxyribonucleoside triphosphates, derivatives of the normal deoxyribonucleoside triphosphates that lack the 3 hydroxyl group. (B) Purified DNA is synthesized *in vitro* in a mixture that contains single-stranded molecules of the DNA to be sequenced *(gray),* the enzyme DNA polymerase, a short primer DNA *(orange)* to enable the polymerase to start DNA synthesis, and the four deoxyribonucleoside triphosphates (dATP, dCTP, dGTP, dTTP: *green* A, C, G, and T). If a dideoxyribonucleotide analog *(red)* of one of these nucleotides is also present in the nucleotide mixture, it can become incorporated into a growing DNA chain. Because this chain now lacks a 3 OH group, the addition of the next nucleotide is blocked, and the DNA chain terminates at that point. In the example illustrated, a small amount of dideoxyATP (ddATP, symbolized here as a *red* A) has been included in the nucleotide mixture. It competes with an excess of the normal deoxyATP (dATP, *green* A), so that ddATP is occasionally incorporated, at random, into a growing DNA strand. This reaction mixture will eventually produce a set of DNAs of different lengths complementary to the template DNA that is being sequenced and terminating at each of the different A's. The exact lengths of the DNA synthesis products can then be used to determine the position of each A in the growing chain. (C) To determine the complete sequence of a DNA fragment, the double-stranded DNA is first separated into its single strands and one of the strands is used as the template for sequencing. Four different chain-terminating dideoxyribonucleoside triphosphates (ddATP, ddCTP, ddGTP, ddTTP, again shown in *red)* are used in four separate DNA synthesis reactions on copies of the same single-stranded DNA template *(gray).* Each reaction produces a set of DNA copies that terminate at different points in the sequence. The products of these four reactions are separated by electrophoresis in four parallel lanes of a polyacrylamide gel (labeled here A, T, C, and G). The newly synthesized fragments are detected by a label (either radioactive or fluorescent) that has been incorporated either into the primer or into one of the deoxyribonucleoside triphosphates used to extend the DNA chain. In each lane, the bands represent fragments that have terminated at a given nucleotide (e.g., A in the leftmost lane) but at different positions in the DNA. By reading off the bands in order, starting at the bottom of the gel and working across all lanes, the DNA sequence of the newly synthesized strand can be determined. The sequence is given in the *green arrow* to the right of the gel. This sequence is identical to that of the 5 3 strand *(green)* of the original double-stranded

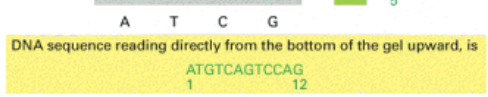

DNA molecule.

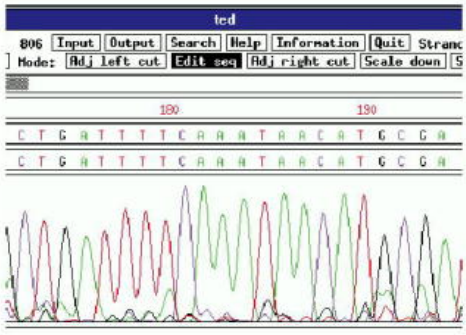

Figure 8-37. Automated DNA sequencing. Shown here is a tiny part of the data from an automated DNA-sequencing run as it appears on the computer screen. Each colored peak represents a nucleotide in the DNA sequence - a clear stretch of nucleotide sequence can be read here between positions 173 and 194 from the start of the sequence. This particular example is taken from the international project that determined the complete nucleotide sequence of the genome of the plant *Arabidopsis*. (Courtesy of George Murphy.)

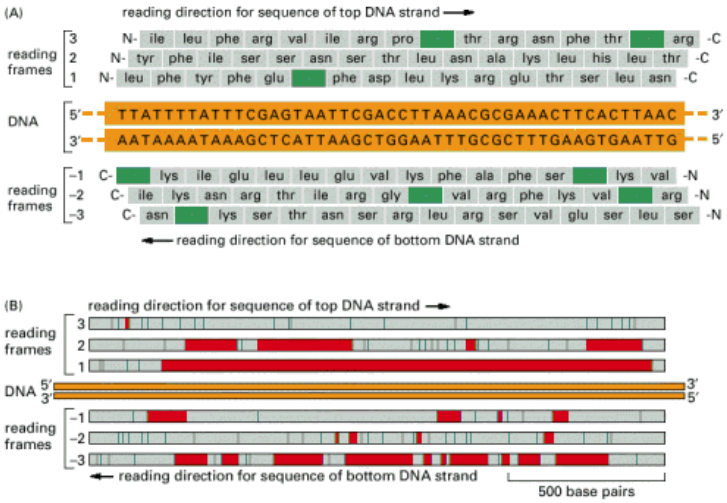

Figure 8-38. Finding the regions in a DNA sequence that encode a protein. (A) Any region of the DNA sequence can, in principle, code for six different amino acid sequences, because any one of three different reading frames can be used to interpret the nucleotide sequence on each strand. Note that a nucleotide sequence is always read in the 5-to-3 chain direction and encodes a polypeptide from the amino (N) to the carboxyl (C) terminus. For a random nucleotide sequence read in a particular frame, a stop signal for protein synthesis is encountered, on average, about once every 21 amino acids (once every 63 nucleotides). In this sample sequence of 48 base pairs, each such signal *(stop codon)* is colored *green*, and only reading frame 2 lacks a stop signal. (B) Search of a 1700 base-pair DNA sequence for a possible protein-encoding sequence. The information is displayed as in (A), with each stop signal for protein synthesis denoted by a *green line*. In addition, all of the regions between possible start and stop signals for protein synthesis (see pp. 348350) are displayed as *red bars*. Only reading frame 1 actually encodes a protein, which is 475 amino acid residues long.

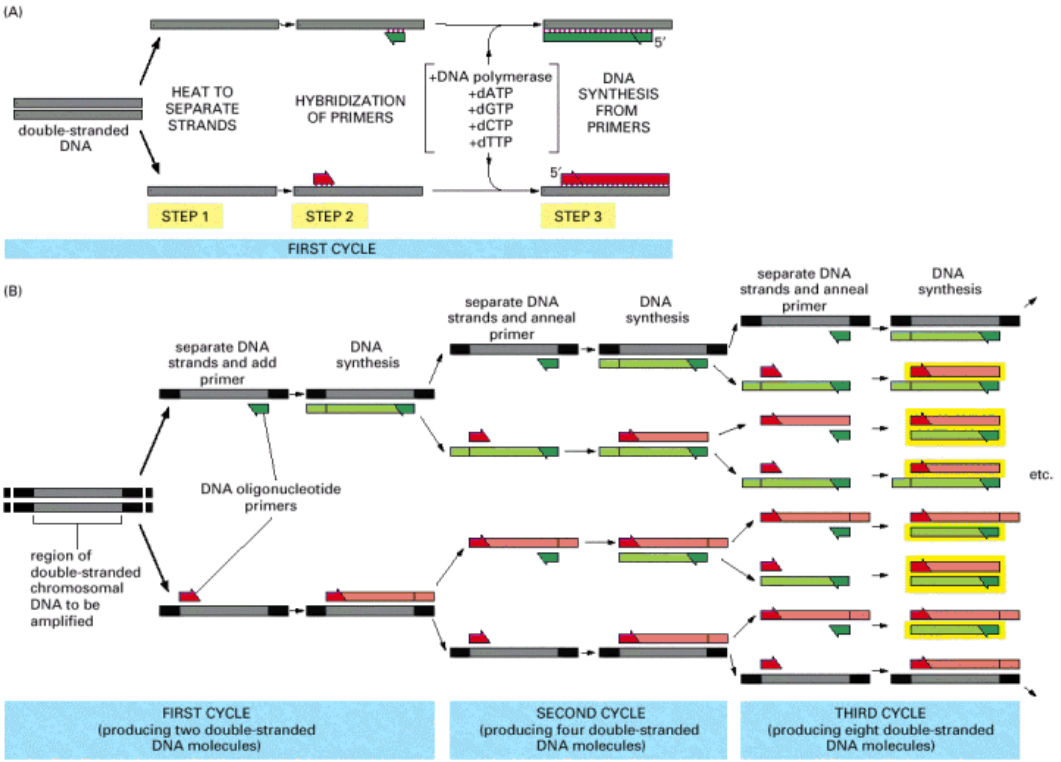

Figure 8-39. Amplification of DNA using the PCR technique. Knowledge of the DNA sequence to be amplified is used to design two synthetic DNA oligonucleotides, each complementary to the sequence on one strand of the DNA double helix at opposite ends of the region to be amplified. These oligonucleotides serve as primers for *in vitro* DNA synthesis, which is performed by a DNA polymerase, and they determine the segment of the DNA that is amplified. (A) PCR starts with a double-stranded DNA, and each cycle of the reaction begins with a brief heat treatment to separate the two strands (step 1). After strand separation, cooling of the DNA in the presence of a large excess of the two primer DNA oligonucleotides allows these primers to hybridize to complementary sequences in the two DNA strands (step 2). This mixture is then incubated with DNA polymerase and the four deoxyribonucleoside triphosphates so that DNA is synthesized, starting from the two primers (step 3). The entire cycle is then begun again by a heat treatment to separate the newly synthesized DNA strands. (B) As the procedure is performed over and over again, the newly synthesized fragments serve as templates in their turn, and within a few cycles the predominant DNA is identical to the sequence bracketed by and including the two primers in the original template. Of the DNA put into the original reaction, only the sequence bracketed by the two primers is amplified because there are no primers attached anywhere else. In the example illustrated in (B), three cycles of reaction produce 16 DNA chains, 8 of which *(boxed in yellow)* are the same length as and correspond exactly to one or the other strand of the original bracketed sequence shown at the far left; the other strands contain extra DNA downstream of the original sequence, which is replicated in the first few cycles. After three more cycles, 240 of the 256 DNA chains correspond exactly to the original bracketed sequence, and after several more cycles, essentially all of the DNA strands have this unique length.

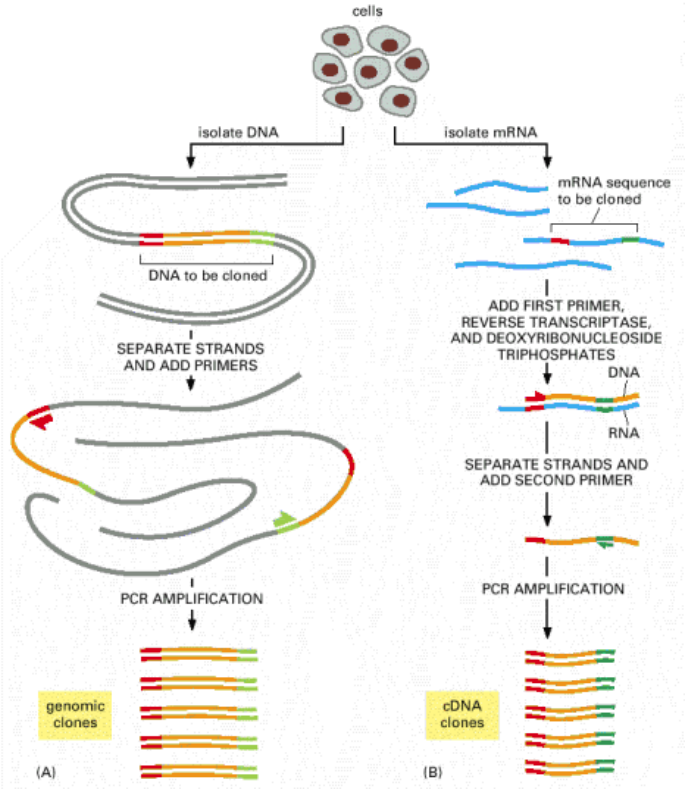

Figure 8-40. Use of PCR to obtain a genomic or cDNA clone. (A) To obtain a genomic clone by using PCR, chromosomal DNA is first purified from cells. PCR primers that flank the stretch of DNA to be cloned are added, and many cycles of the reaction are completed (see Figure 8-39). Since only the DNA between (and including) the primers is amplified, PCR provides a way to obtain a short stretch of chromosomal DNA selectively in a pure form. (B) To use PCR to obtain a cDNA clone of a gene, mRNA is first purified from cells. The first primer is then added to the population of mRNAs, and reverse transcriptase is used to make a complementary DNA strand. The second primer is then added, and the single-stranded DNA molecule is amplified through many cycles of PCR, as shown in Figure 8-39. For both types of cloning, the nucleotide sequence of at least part of the region to be cloned must be known beforehand.

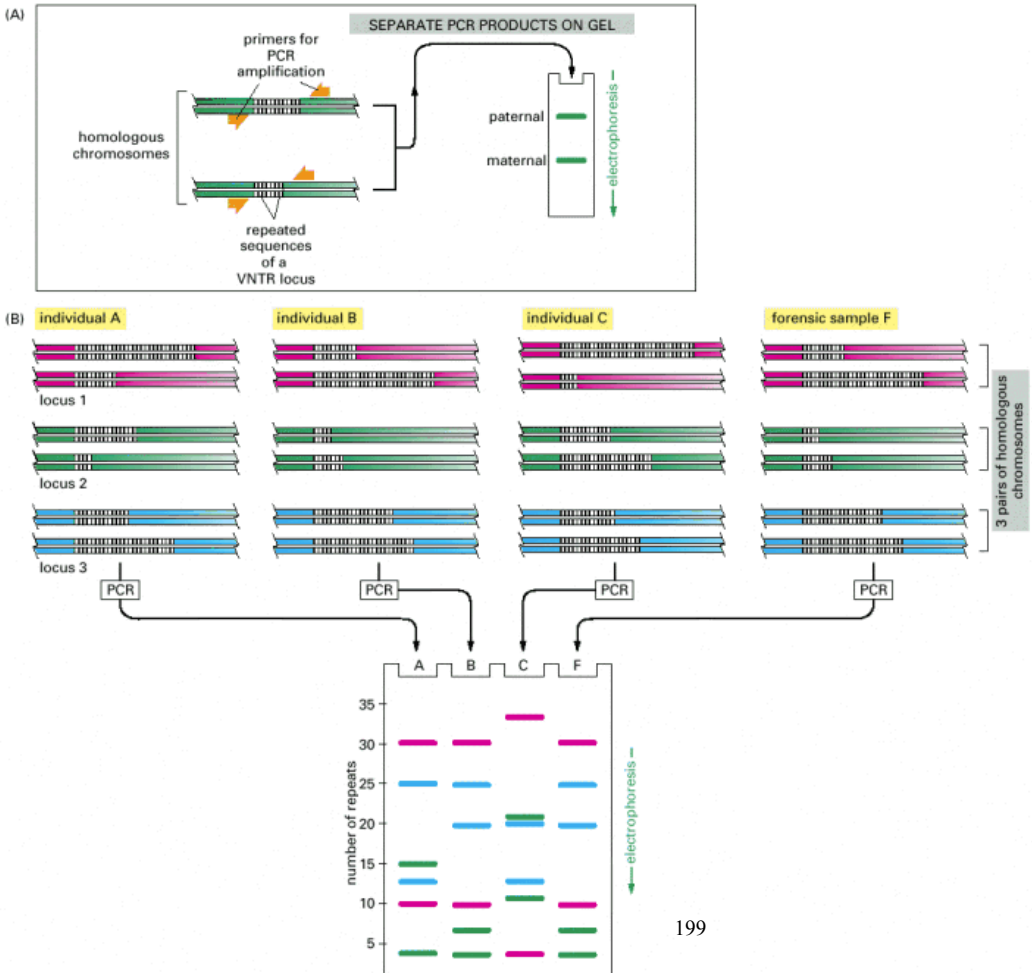

Figure 8-41. How PCR is used in forensic science. (A) The DNA sequences that create the variability used in this analysis contain runs of short, repeated sequences, such as CACACA . . . , which are found in various positions (loci) in the human genome. The number of repeats in each run can be highly variable in the population, ranging from 4 to 40 in different individuals. A run of repeated nucleotides of this type is commonly referred to as a *hypervariable microsatellite* sequence - also known as a VNTR *(variable number of tandem repeat)* sequence. Because of the variability in these sequences at each locus, individuals usually inherit a different variant from their mother and from their father; two unrelated individuals therefore do not usually contain the same pair of sequences. A PCR analysis using primers that bracket the locus produces a pair of bands of amplified DNA from each individual, one band representing the maternal variant and the other representing the paternal variant. The length of the amplified DNA, and thus the position of the band it produces after electrophoresis, depends on the exact number of repeats at the locus. (B) In the schematic example shown here, the same three VNTR loci are analyzed (requiring three different pairs of specially selected oligonucleotide primers) from three suspects (individuals A, B, and C), producing six DNA bands for each person after polyacrylamide gel electrophoresis. Although some individuals have several bands in common, the overall pattern is quite distinctive for each. The band pattern can therefore serve as a "fingerprint" to identify an individual nearly uniquely. The fourth lane (F) contains the products of the same reactions carried out on a forensic sample. The starting material for such a PCR can be a single hair or a tiny sample of blood that was left at the crime scene. When examining the variability at 5 to 10 different VNTR loci, the odds that two random individuals would share the same genetic pattern by chance can be approximately one in 10 billion. In the case shown here, individuals A and C can be eliminated from further enquiries, whereas individual B remains a clear suspect for committing the crime. A similar approach is now routinely used for paternity testing.

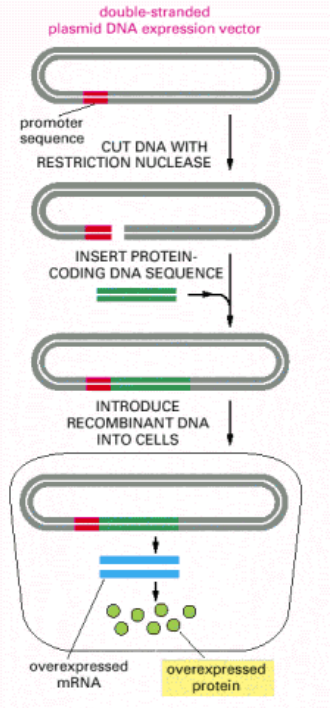

Figure 8-42. Production of large amounts of a protein from a protein-coding DNA sequence cloned into an expression vector and introduced into cells. A plasmid vector has been engineered to contain a highly active promoter, which causes unusually large amounts of mRNA to be produced from an adjacent protein-coding gene inserted into the plasmid vector. Depending on the characteristics of the cloning vector, the plasmid is introduced into bacterial, yeast, insect, or mammalian cells, where the inserted gene is efficiently transcribed and translated into protein.

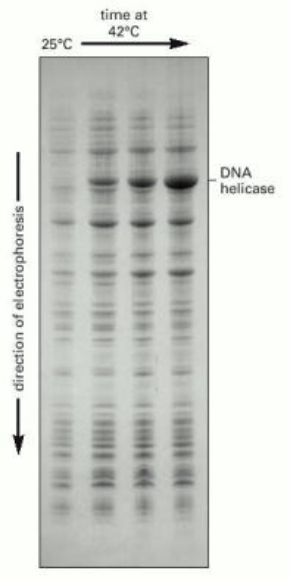

Figure 8-43. Production of large amounts of a protein by using a plasmid expression vector. In this example, bacterial cells have been transfected with the coding sequence for an enzyme, DNA helicase; transcription from this coding sequence is under the control of a viral promoter that becomes active only at temperatures of 37°C or higher. The total cell protein has been analyzed by SDS-polyacrylamide gel electrophoresis, either from bacteria grown at 25°C (no helicase protein made), or after a shift of the same bacteria to 42°C for up to 2 hours (helicase protein has become the most abundant protein species in the lysate). (Courtesy of Jack Barry.)

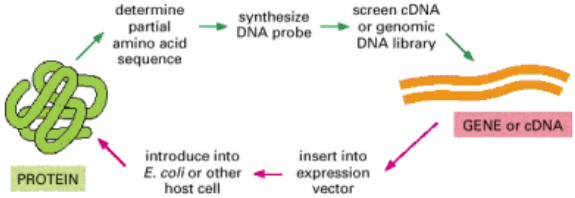

Figure 8-44. Knowledge of the molecular biology of cells makes it possible to experimentally move from gene to protein and from protein to gene. A small quantity of a purified protein is used to obtain a partial amino acid sequence. This provides sequence information that enables the corresponding gene to be cloned from a DNA library. Once the gene has been cloned, its protein-coding sequence can be inserted into an expression vector and used to produce large quantities of the protein from genetically engineered cells.

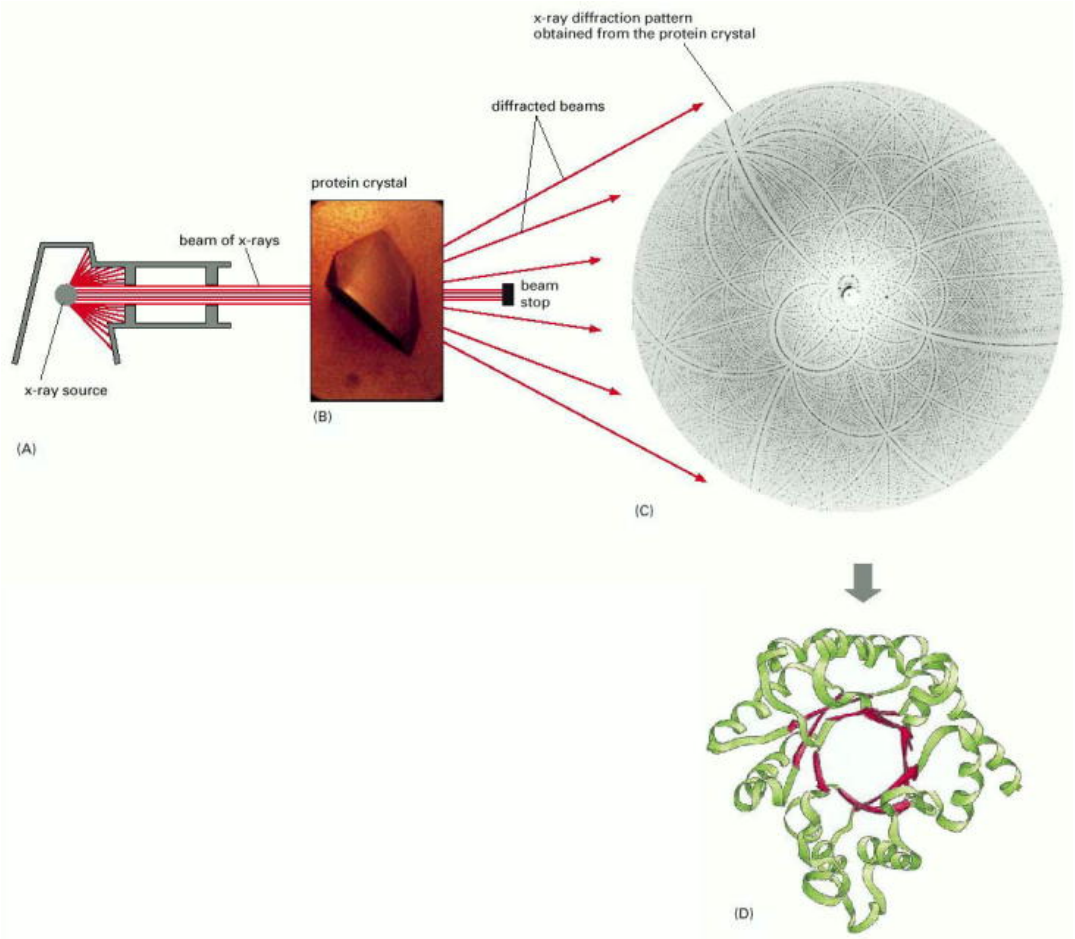

Figure 8-45. X-ray crystallography. (A) A narrow parallel beam of x-rays is directed at a well-ordered crystal (B). Shown here is a protein crystal of ribulose bisphosphate carboxylase, an enzyme with a central role in CO_2 fixation during photosynthesis. Some of the beam is scattered by the atoms in the crystal. The scattered waves reinforce one another at certain points and appear as a pattern of diffraction spots (C). This diffraction pattern, together with the amino acid sequence of the protein, can be used to produce an atomic model (D). The complete atomic model is hard to interpret, but this simplified version, derived from the x-ray diffraction data, shows the protein's structural features clearly (α helices, *green*; β strands, *red*). Note that the components pictured in A to D are not shown to scale. (B, courtesy of C. Branden; C, courtesy of J. Hajdu and I. Andersson; D, adapted from original provided by B. Furugren.)

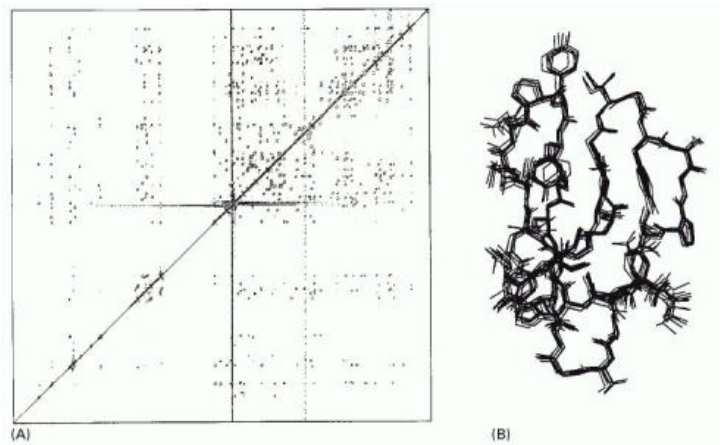

Figure 8-46. NMR spectroscopy. (A) An example of the data from an NMR machine. This two-dimensional NMR spectrum is derived from the C-terminal domain of the enzyme cellulase. The spots represent interactions between hydrogen atoms that are near neighbors in the protein and hence reflects the distance that separates them. Complex computing methods, in conjunction with the known amino acid sequence, enable possible compatible structures to be derived. In (B) 10 structures, which all satisfy the distance constraints equally well, are shown superimposed on one another, giving a good indication of the probable three-dimensional structure. (Courtesy of P. Kraulis.)

```
 Score =  399 bits (1025), Expect = e-111
 Identities = 198/290 (68%), Positives = 241/290 (82%), Gaps = 1/290

Query: 57  MENFQKVEKIGEGTYGVVYKARNKLTGEVVALKKIRLDTETEGVPSTAIREISLLKELNH 116
           ME ++KVEKIGEGTYGVVYKA +K T E +ALKKIRL+ E EGVPSTAIREISLLKE+NH
Sbjct: 1   MEQYEKVEKIGEGTYGVVYKALDKATNETIALKKIRLEQEDEGVPSTAIREISLLKEMNH 60

Query: 117 PNIVKLLDVIHTENKLYLVFEFLHQDLKKFMDASALTGIPLPLIKSYLFQLLQGLAFCHS 176
            NIV+L  DV+H+E ++YLVFE+L  DLKKFMD+          LIKSYL+Q+L  G+A+CHS
Sbjct: 61  GNIVRLHDVVHSEKRIYLVFEYLDLDLKKFMDSCPEFAKNPTLIKSYLYQILHGVAYCHS 120

Query: 177 HRVLHRDLKPQNLLINTE-GAIKLADFGLARAFGVPVRTYTHEVVTLWYRAPEILLGCKY 235
           HRVLHRDLKPQNLLI+    A+KLADFGLARAFG+PVRT+THEVVTLWYRAPEILLG  +
Sbjct: 121 HRVLHRDLKPQNLLIDRRTNALKLADFGLARAFGIPVRTFTHEVVTLWYRAPEILLGARQ 180

Query: 236 YSTAVDIWSLGCIFAEMVTRRALFPGDSEIDQLFRIFRTLGTPDEVVWPGVTSMPDYKPS 295
           YST VD+WS+GCIFAEMV ++ LFPGDSEID+LF+IFR LGTP+E  WPGV+ +PD+K +
Sbjct: 181 YSTPVDVWSVGCIFAEMVNQKPLFPGDSEIDELFKIFRILGTPNEQSWPGVSCLPDFKTA 240

Query: 296 FPKWARQDFSKVVPPLDEDGRSLLSQMLHYDPNKRISAKAALAHPFFQDV 345
           FP+W  QD + VVP LD  G  LLS+ML Y+P+KRI+A+ AL H +F+D+
Sbjct: 241 FPRWQAQDLATVVPNLDPAGLDLLSKMLRYEPSKRITARQALEHEYFKDL 290
```

Figure 8-47. Results of a BLAST search. Sequence databases can be searched to find similar amino acid or nucleic acid sequences. Here a search for proteins similar to the human cell-cycle regulatory protein cdc2 *(Query)* locates maize cdc2 *(Subject)*, which is 68% identical (and 82% similar) to human cdc2 in its amino acid sequence. The alignment begins at residue 57 of the Query protein, suggesting that the human protein has an N-terminal region that is absent from the maize protein. The *green* blocks indicate differences in sequence, and the *yellow* bar summarizes the similarities: when the two amino acid sequences are identical, the residue is shown; conservative amino acid substitutions are indicated by a plus sign (+). Only one small gap has been introduced - indicated by the *red arrow* at position 194 in the Query sequence - to align the two sequences maximally. The alignment score *(Score)* takes into account penalties for substitution and gaps; the higher the alignment score, the better the match. The significance of the alignment is reflected in the *Expectation* (E) value, which represents the number of alignments with scores equal to or better than the given score that are expected to occur by chance. The lower the E value, the more significant the match; the extremely low value here indicates certain significance. E values much higher than 0.1 are unlikely to reflect true relatedness.

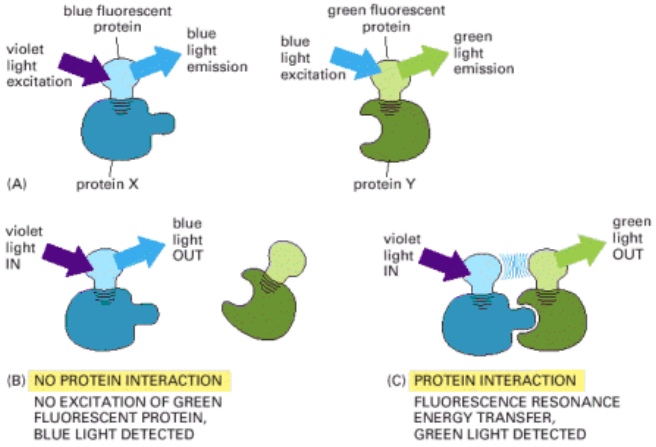

Figure 8-49. Fluorescence resonance energy transfer (FRET). To determine whether (and when) two proteins interact inside the cell, the proteins are first produced as fusion proteins attached to different variants of GFP. (A) In this example, protein X is coupled to a blue fluorescent protein, which is excited by violet light (370440 nm) and emits blue light (440480 nm); protein Y is coupled to a green fluorescent protein, which is excited by blue light and emits green light (510 nm). (B) If protein X and Y do not interact, illuminating the sample with violet light yields fluorescence from the blue fluorescent protein only. (C) When protein X and protein Y interact, FRET can now occur. Illuminating the sample with violet light excites the blue fluorescent protein, whose emission in turn excites the green fluorescent protein, resulting in an emission of green light. The fluorochromes must be quite close together - within about 110 nm of one another - for FRET to occur. Because not every molecule of protein X and protein Y is bound at all times, some blue light may still be detected. But as the two proteins begin to interact, emission from the donor GFP falls as the emission from the acceptor GFP rises.

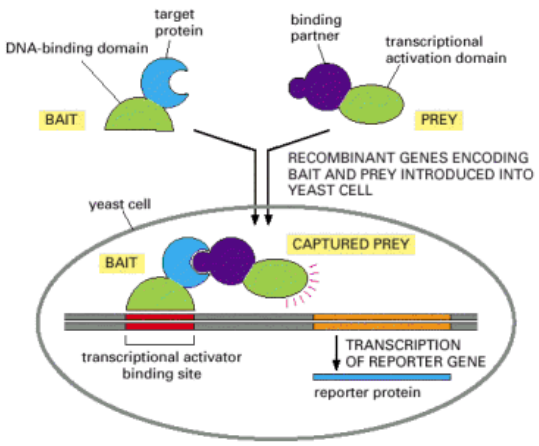

Figure 8-51. The yeast two-hybrid system for detecting protein-protein interactions. The target protein is fused to a DNA-binding domain that localizes it to the regulatory region of a reporter gene as "bait." When this target protein binds to another specially designed protein in the cell nucleus ("prey"), their interaction brings together two halves of a transcriptional activator, which then switches on the expression of the reporter gene. The reporter gene is often one that will permit growth on a selective medium. Bait and prey fusion proteins are generated by standard recombinant DNA techniques. In most cases, a single bait protein is used to fish for interacting partners among a large collection of prey proteins produced by ligating DNA encoding the activation domain of a transcriptional activator to a large mixture of DNA fragments from a cDNA library.

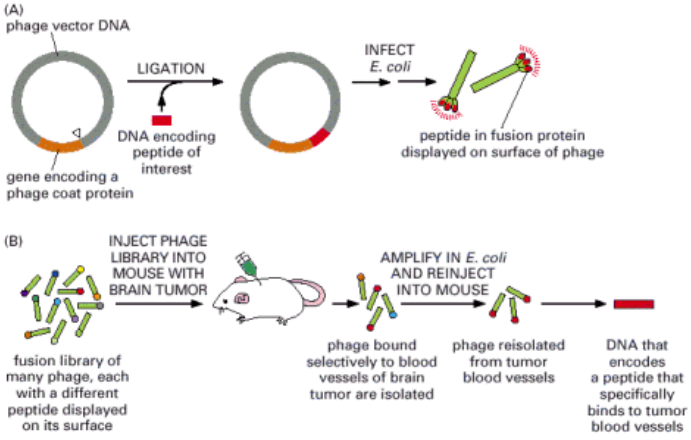

Figure 8-52. The phage display method for investigating protein interactions. (A) Preparation of the bacteriophage. DNA encoding the desired peptide is ligated into the phage vector, fused with the gene encoding the viral protein coat. The engineered phage are then introduced into *E. coli*, which produce phage displaying a hybrid coat protein that contains the peptide. (B) Phage libraries containing billions of different peptides can also be generated. In this example, the library is injected into a mouse with a brain tumor and phage that bind selectively to the blood vessels that supply the tumor are isolated and amplified. A peptide that binds specifically to tumor blood vessels can then be isolated from the purified phage. Such a peptide could be used to target drugs or toxins to the tumor.

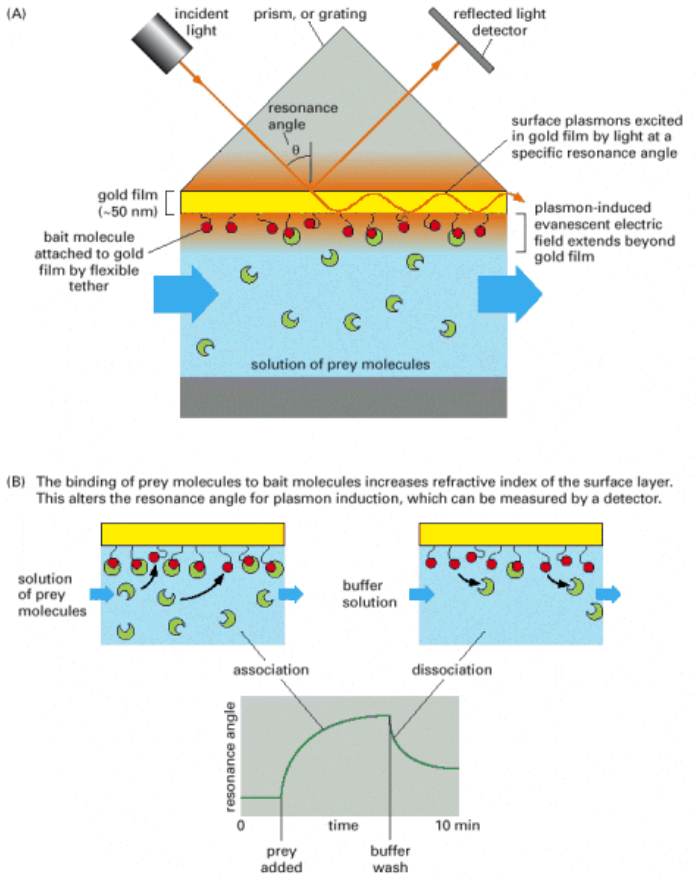

Figure 8-53. Surface plasmon resonance. (A) SPR can detect binding interactions by monitoring the reflection of a beam of light off the interface between an aqueous solution of potential binding molecules *(green)* and a biosensor surface coated with an immobilized bait protein *(red)*. (B) A solution of prey proteins is allowed to flow past the immobilized bait protein. Binding of prey molecules to bait proteins produces a measurable change in the resonance angle. These changes, monitored in real time, reflect the association and dissociation of the molecular complexes.

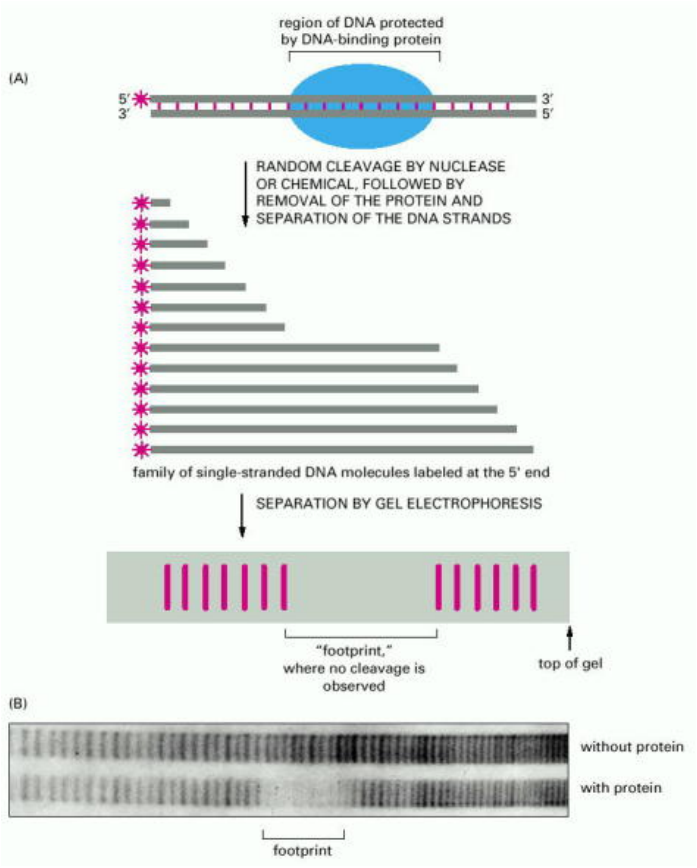

Figure 8-54. The DNA footprinting technique. (A) This technique requires a DNA molecule that has been labeled at one end (see Figure 8-24B). The protein shown binds tightly to a specific DNA sequence that is seven nucleotides long, thereby protecting these seven nucleotides from the cleaving agent. If the same reaction were performed without the DNA-binding protein, a complete ladder of bands would be seen on the gel (not shown). (B) An actual footprint used to determine the binding site for a human protein that stimulates the transcription of specific eucaryotic genes. These results locate the binding site about 60 nucleotides upstream from the start site for RNA synthesis. The cleaving agent was a small, iron-containing organic molecule that normally cuts at every phosphodiester bond with nearly equal frequency. (B, courtesy of Michele Sawadogo and Robert Roeder.)

Figure 8-55. Insertional mutant of the snapdragon, *Antirrhinum.* A mutation in a single gene coding for a regulatory protein causes leafy shoots to develop in place of flowers. The mutation allows cells to adopt a character that would be appropriate to a different part of the normal plant. The mutant plant is on the left, the normal plant on the right. (Courtesy of Enrico Coen and Rosemary Carpenter.)

Figure 8-56. Screens can detect mutations that affect an animal's behavior. (A) Wild-type *C. elegans* engage in social feeding. The worms swim around until they encounter their neighbors and commence feeding. (B) Mutant animals feed by themselves. (Courtesy of Cornelia Bargmann, *Cell* 94:cover, 1998. © Elsevier.)

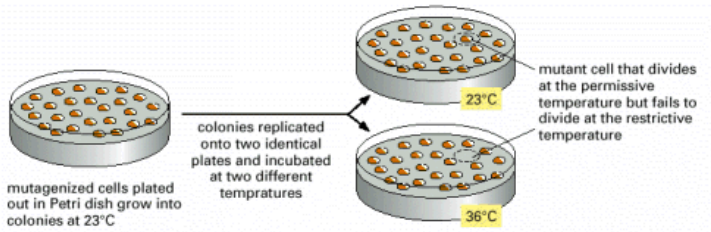

Figure 8-57. Screening for temperature-sensitive bacterial or yeast mutants. Mutagenized cells are plated out at the permissive temperature. The resulting colonies are transferred to two identical Petri dishes by replica plating; one of these plates is incubated at the permissive temperature, the other at the non-permissive temperature. Cells containing a temperature-sensitive mutation in a gene essential for proliferation can divide at the normal, permissive temperature but fail to divide at the elevated, non-permissive temperature.

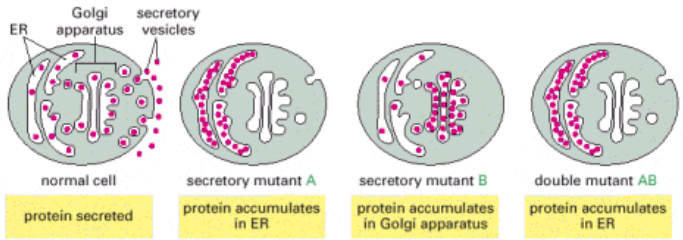

Figure 8-58. Using genetics to determine the order of function of genes. In normal cells, proteins are loaded into vesicles, which fuse with the plasma membrane and secrete their contents into the extracellular medium. In secretory mutant A, proteins accumulate in the ER. In a different secretory mutant B, proteins accumulate in the Golgi. In the double mutant AB, proteins accumulate in the ER; this indicates that the gene defective in mutant A acts before the gene defective in mutant B in the secretory pathway.

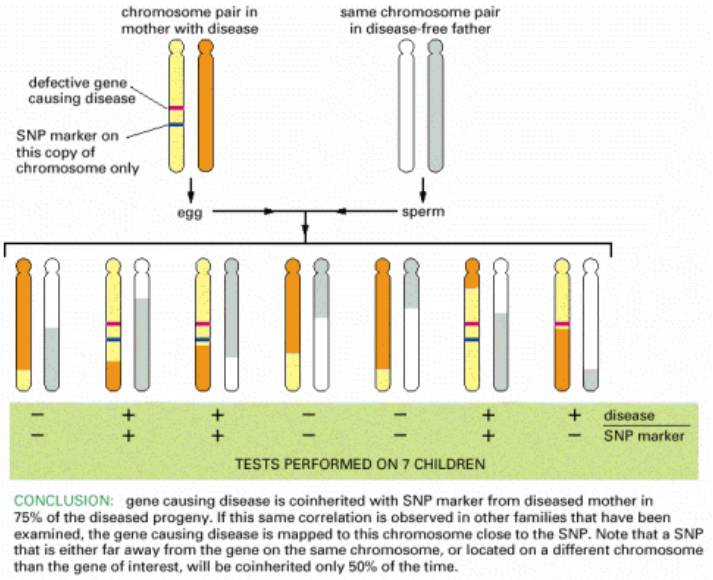

Figure 8-59. Genetic linkage analysis using physical markers on the DNA to find a human gene. In this example, one studies the coinheritance of a specific human phenotype (here a genetic disease) with a SNP marker. If individuals who inherit the disease nearly always inherit a particular SNP marker, then the gene causing the disease and the SNP are likely to be close together on the chromosome, as shown here. To prove that an observed linkage is statistically significant, hundreds of individuals may need to be examined. Note that the linkage will not be absolute unless the SNP marker is located in the gene itself. Thus, occasionally the SNP will be separated from the disease gene by meiotic crossing-over during the formation of the egg or sperm: this has happened in the case of the chromosome pair on the far right. When working with a sequenced genome, this procedure would be repeated with SNPs located on either side of the initial SNP, until a 100% coinheritance is found.

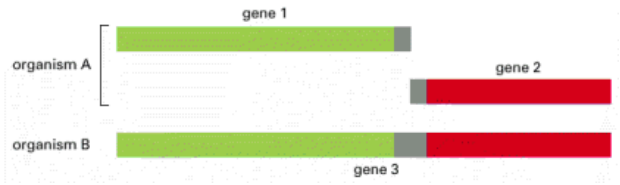

Figure 8-60. Domain fusions reveal relationships between functionally linked genes. In this example, the functional interaction of genes 1 and 2 in organism A is inferred by the fusion of homologous domains into a single gene (gene 3) in organism B.

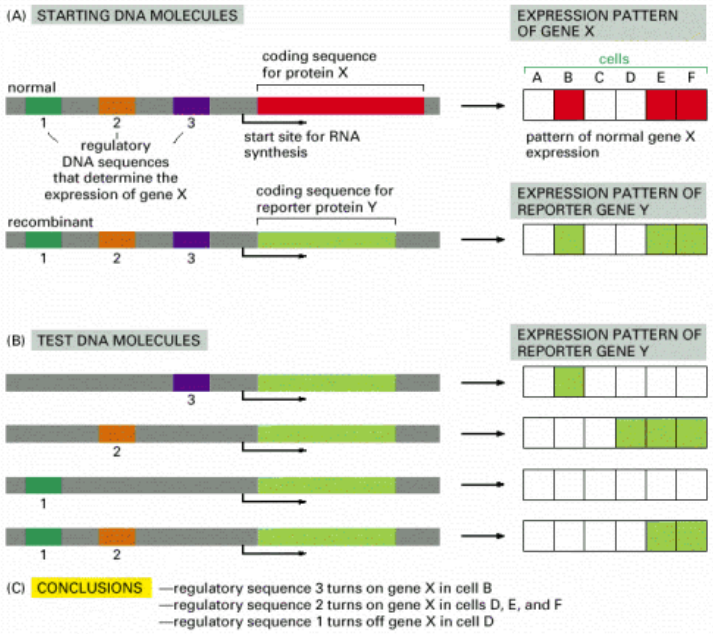

Figure 8-61. Using a reporter protein to determine the pattern of a gene's expression. (A) In this example the coding sequence for protein X is replaced by the coding sequence for protein Y. (B) Various fragments of DNA containing candidate regulatory sequences are added in combinations. The recombinant DNA molecules are then tested for expression after their transfection into a variety of different types of mammalian cells, and the results are summarized in (C). For experiments in eucaryotic cells, two commonly used reporter proteins are the enzymes β-galactosidase *(β-gal)* and green fluorescent protein or GFP (see Figure 9-44). Figure 7-39 shows an example in which the β-*gal* gene is used to monitor the activity of the *eve* gene regulatory sequence in a *Drosophila* embryo.

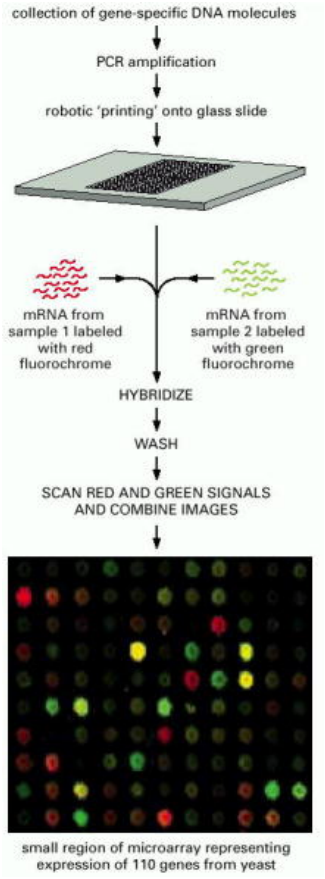

Figure 8-62. Using DNA microarrays to monitor the expression of thousands of genes simultaneously. To prepare the microarray, DNA fragments - each corresponding to a gene - are spotted onto a slide by a robot. Prepared arrays are also available commercially. In this example, mRNA is collected from two different cell samples for a direct comparison of their relative levels of gene expression. These samples are converted to cDNA and labeled, one with a red fluorochrome, the other with a green fluorochrome. The labeled samples are mixed and then allowed to hybridize to the microarray. After incubation, the array is washed and the fluorescence scanned. In the portion of a microarray shown, which represents the expression of 110 yeast genes, *red* spots indicate that the gene in sample 1 is expressed at a higher level than the corresponding gene in sample 2; *green* spots indicate that expression of the gene is higher in sample 2 than in sample 1. *Yellow* spots reveal genes that are expressed at equal levels in both cell samples. Dark spots indicate little or no expression in either sample of the gene whose fragment is located at that position in the array. For details see Figure 1-45. (Microarray courtesy of J.L. DeRisi et al., *Science* 278:680686, 1997. © AAAS.)

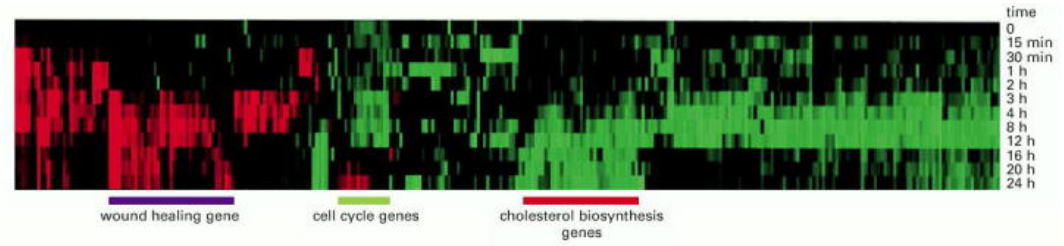

Figure 8-63. Using cluster analysis to identify sets of genes that are coordinately regulated. Genes that belong to the same cluster may be involved in common cellular pathways or processes. To perform a cluster analysis, microarray data are obtained from cell samples exposed to a variety of different conditions, and genes that show coordinate changes in their expression pattern are grouped together. In this experiment, human fibroblasts were deprived of serum for 48 hours; serum was then added back to the cultures at time 0 and the cells were harvested for microarray analysis at different time points. Of the 8600 genes analyzed on the DNA microarray, just over 300 showed threefold or greater variation in their expression patterns in response to serum reintroduction. Here, *red* indicates an increase in expression; *green* is a decrease in expression. On the basis of the results of many microarray experiments, the 8600 genes have been grouped in clusters based on similar patterns of expression. The results of this analysis show that genes involved in wound healing are turned on in response to serum, while genes involved in regulating cell cycle progression and cholesterol biosynthesis are shut down. (From M.B. Eisen et al., *Proc. Natl. Acad. Sci. USA* 95:1486314868, 1998. © National Academy of Sciences.)

Figure 8-64. Gene replacement, gene knockout, and gene addition. A normal gene can be altered in several ways in a genetically engineered organism. (A) The normal gene *(green)* can be completely replaced by a mutant copy of the gene *(red)*, a process called gene replacement. This provides information on the activity of the mutant gene without interference from the normal gene, and thus the effects of small and subtle mutations can be determined. (B) The normal gene can be inactivated completely, for example, by making a large deletion in it; the gene is said to have suffered a knockout. (C) A mutant gene can simply be added to the genome. In some organisms this is the easiest type of genetic engineering to perform. This approach can provide useful information when the introduced mutant gene overrides the function of the normal gene.

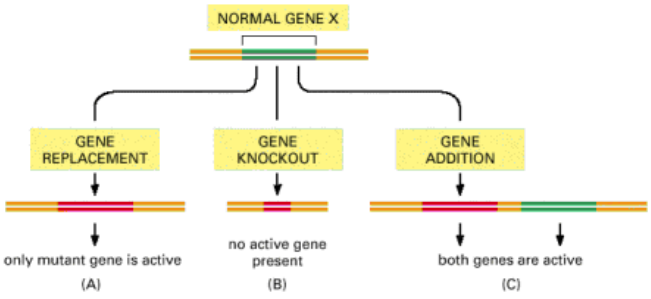

Figure 8-65. The antisense RNA strategy for generating dominant negative mutations. Mutant genes that have been engineered to produce antisense RNA, which is complementary in sequence to the RNA

made by the normal gene X, can cause double-stranded RNA to form inside cells. If a large excess of the antisense RNA is produced, it can hybridize with - and thereby inactivate - most of the normal RNA produced by gene X. Although in the future it may become possible to inactivate any gene in this way, at present the technique seems to work for some genes but not others.

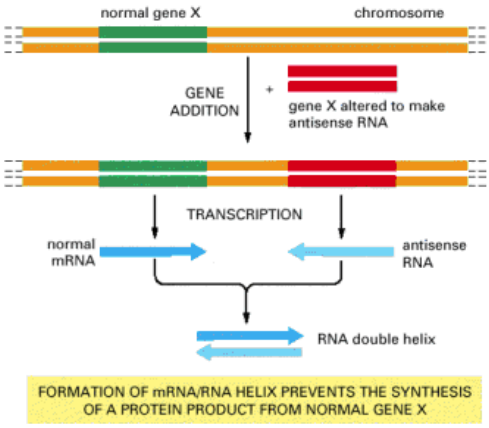

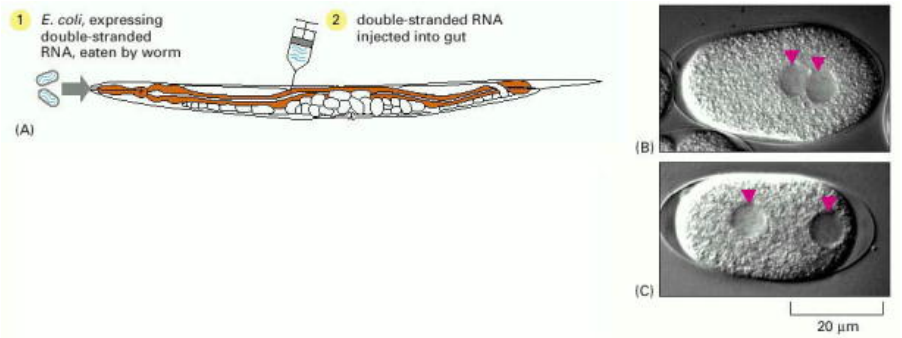

Figure 8-66. Dominant negative mutations created by RNA interference. (A) Double-stranded RNA (dsRNA) can be introduced into *C. elegans* (1) by feeding the worms with *E. coli* expressing the dsRNA or (2) by injecting dsRNA directly into the gut. (B) Wild-type worm embryo. (C) Worm embryo in which a gene involved in cell division has been inactivated by RNAi. The embryo shows abnormal migration of the two unfused nuclei of the egg and sperm. (B, C, from P. Gönczy et al., *Nature* 408:331336, 2000. © Macmillan Magazines Ltd.)

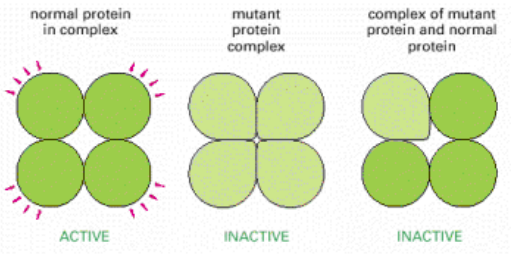

Figure 8-67. A dominant negative effect of a protein. Here a gene is engineered to produce a mutant protein that prevents the normal copies of the same protein from performing their function. In this simple example, the normal protein must form a multisubunit complex to be active, and the mutant protein blocks function by forming a mixed complex that is inactive. In this way a single copy of a mutant gene located anywhere in the genome can inactivate the normal products produced by other gene copies.

Figure 8-68. Ectopic misexpression of Wnt, a signaling protein that affects development of the body axis in the early *Xenopus* embryo. In this experiment, mRNA coding for Wnt was injected into the ventral vegetal blastomere, inducing a second body axis (discussed in Chapter 21). (From S. Sokol et al., *Cell* 67:741752, 1992. © Elsevier.)

Figure 8-69. The use of a synthetic oligonucleotide to modify the protein-coding region of a gene by site-directed mutagenesis. (A) A recombinant plasmid containing a gene insert is separated into its two DNA strands. A synthetic oligonucleotide primer corresponding to part of the gene sequence but containing a single altered nucleotide at a predetermined point is added to the single-stranded DNA under conditions that permit less than perfect DNA hybridization. (B) The primer hybridizes to the DNA, forming a single mismatched nucleotide pair. (C) The recombinant plasmid is made double-stranded by *in vitro* DNA synthesis starting from the primer and sealed by DNA ligase. (D) The double-stranded DNA is introduced into a cell, where it is replicated.

Replication using one strand of the template produces a normal DNA molecule, but replication using the other (the strand that contains the primer) produces a DNA molecule carrying the desired mutation. Only half of the progeny cells will end up with a plasmid that contains the desired mutant gene. However, a progeny cell that contains the mutated gene can be identified, separated from other cells, and cultured to produce a pure population of cells, all of which carry the mutated gene. Only one of the many changes that can be engineered in this way is shown here. With an oligonucleotide of the appropriate sequence, more than one amino acid substitution can be made at a time, or one or more amino acids can be inserted or deleted. Although not shown in this figure, it is also possible to create a site-directed mutation by using the appropriate oligonucleotides and PCR (instead of plasmid replication) to amplify the mutated gene.

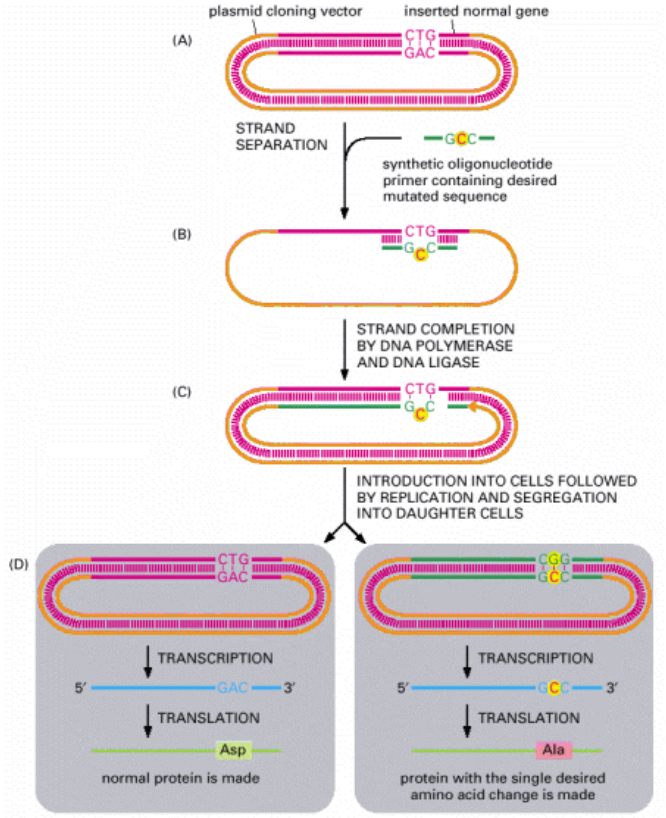

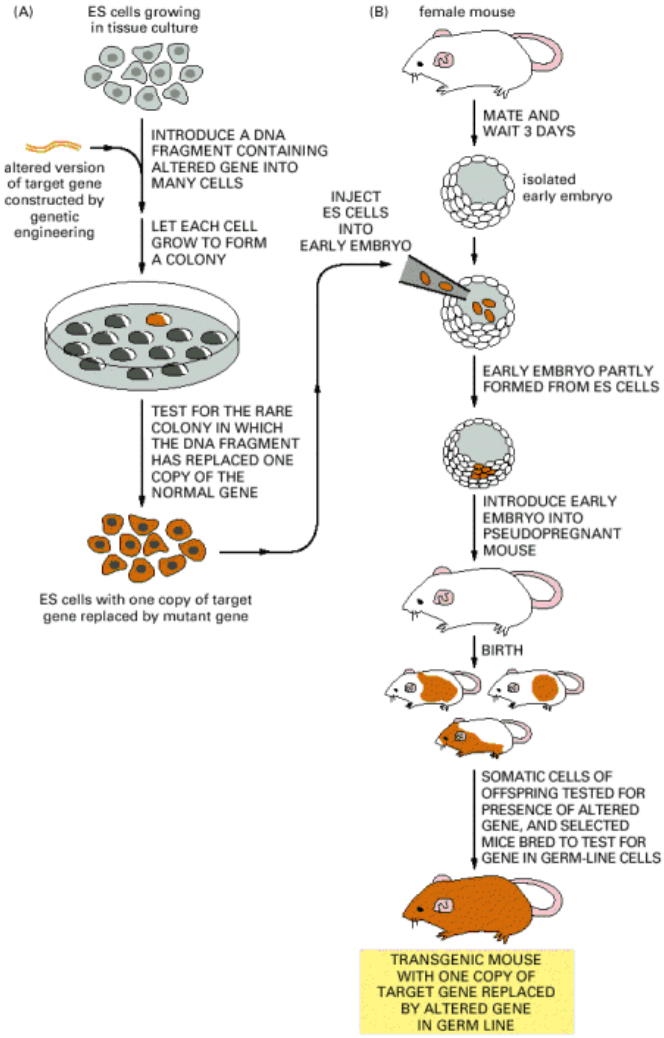

Figure 8-70. Summary of the procedures used for making gene replacements in mice. In the first step (A), an altered version of the gene is introduced into cultured ES (embryonic stem) cells. Only a few rare ES cells will have their corresponding normal genes replaced by the altered gene through a homologous recombination event. Although the procedure is often laborious, these rare cells can be identified and cultured to produce many descendants, each of which carries an altered gene in place of one of its two normal corresponding genes. In the next step of the procedure (B), these altered ES cells are injected into a very early mouse embryo; the cells are incorporated into the growing embryo, and a mouse produced by such an embryo will contain some somatic cells (indicated by *orange)* that carry the altered gene. Some of these mice will also contain germ-line cells that contain the altered gene. When bred with a normal mouse, some of the progeny of these mice will contain the altered gene in all of their cells. If two such mice are in turn bred (not shown), some of the progeny will contain two altered genes (one on each chromosome) in all of their cells. If the original gene alteration completely inactivates the function of the gene, these mice are known as knockout mice. When such mice are missing genes that function during development, they often die with specific defects long before they reach adulthood. These defects are carefully analyzed to help decipher the normal function of the missing gene.

Figure 8-71. Mouse with an engineered defect in fibroblast growth factor 5 (FGF5). FGF5 is a negative regulator of hair formation. In a mouse lacking FGF5 *(right)*, the hair is long compared with its heterozygous littermate *(left)*. Transgenic mice with phenotypes that mimic aspects of a variety of human disorders, including Alzheimer's disease, atherosclerosis, diabetes, cystic fibrosis, and some type of cancers, have been generated. Their study may lead to the development of more effective treatments. (Courtesy of Gail Martin, from J.M. Hebert et al., *Cell* 78:10171025, 1994. © Elsevier.)

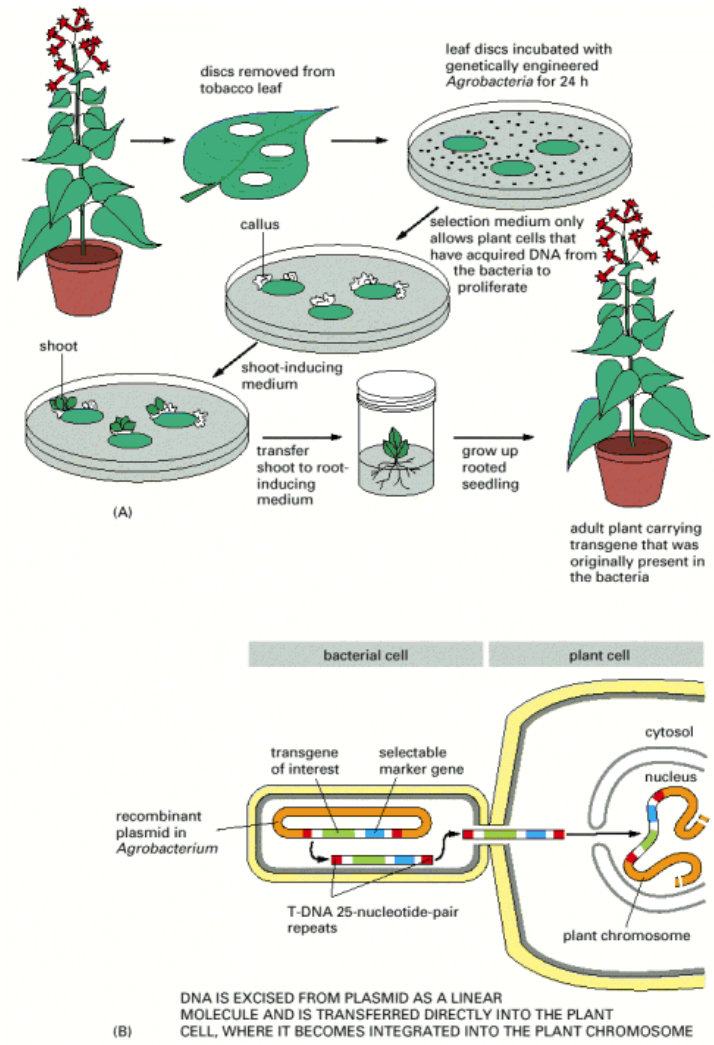

Figure 8-72. A procedure used to make a transgenic plant. (A) Outline of the process. A disc is cut out of a leaf and incubated in culture with *Agrobacteria* that carry a recombinant plasmid with both a selectable marker and a desired transgene. The wounded cells at the edge of the disc release substances that attract the *Agrobacteria* and cause them to inject DNA into these cells. Only those plant cells that take up the appropriate DNA and express the selectable marker gene survive to proliferate and form a callus. The manipulation of growth factors supplied to the callus induces it to form shoots that subsequently root and grow into adult plants carrying the transgene. (B) The preparation of the recombinant plasmid and its transfer to plant cells. An *Agrobacterium* plasmid that normally carries the T-DNA sequence is modified by substituting a selectable marker (such as the kanamycin-resistance gene) and a desired transgene between the 25-nucleotide-pair T-DNA repeats. When the *Agrobacterium* recognizes a plant cell, it efficiently passes a DNA strand that carries these sequences into the plant cell, using the special machinery that normally transfers the plasmid's T-DNA sequence.

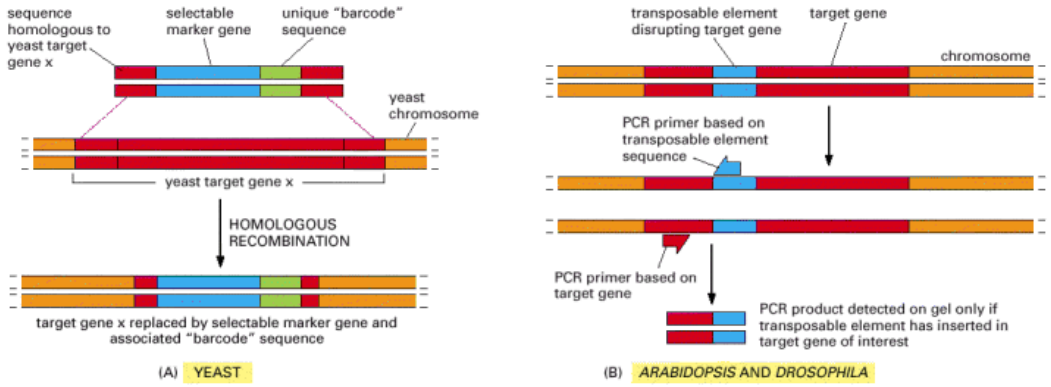

Figure 8-73. Making collections of mutant organisms. (A) A deletion cassette for use in yeast contains sequences homologous to each end of a target gene x *(red)*, a selectable marker *(blue)*, and a unique "barcode" sequence, approximately 20 nucleotide pairs in length *(green)*. This DNA is introduced into yeast, where it readily replaces the target gene by homologous recombination. (B) A similar approach can be taken to prepare tagged knockout mutants in *Arabidopsis* and *Drosophila*. In this case, mutants are generated by the accidental insertion of a transposable element into a target gene. The total DNA from the resulting organism can be collected and quickly screened for disruption of a gene of interest by using PCR primers that bind to the transposable element and to the target gene. A PCR product is detected on the gel only if the transposable element has inserted into the target gene.

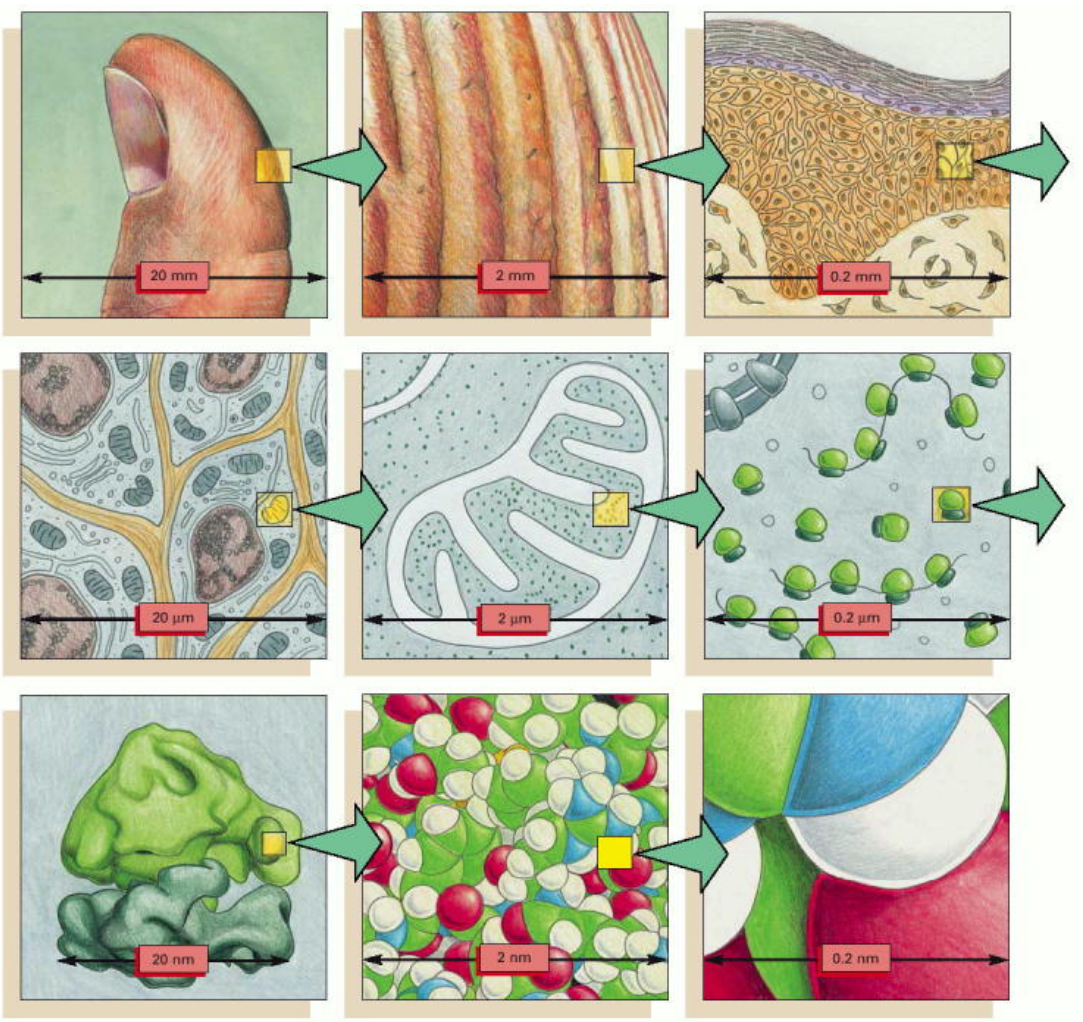

Figure 9-1. A sense of scale between living cells and atoms. Each diagram shows an image magnified by a factor of ten in an imaginary progression from a thumb, through skin cells, to a ribosome, to a cluster of atoms forming part of one of the many protein molecules in our body. Details of molecular structure, as shown in the last two panels, are beyond the power of the electron microscope.

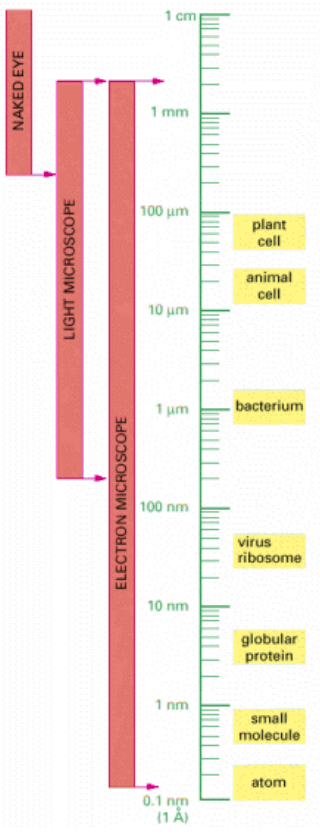

Figure 9-2. Resolving power. Sizes of cells and their components are drawn on a logarithmic scale, indicating the range of objects that can be readily resolved by the naked eye and in the light and electron microscopes. The following units of length are commonly employed in microscopy:

µm (micrometer) = 10^{-6} m

nm (nanometer) = 10^{-9} m
Å (Ångström unit) = 10^{-10} m

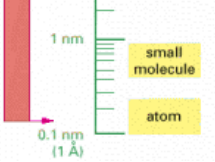

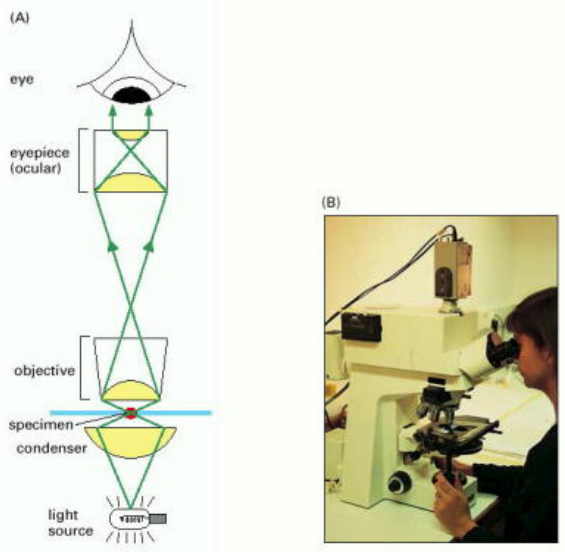

Figure 9-3. A light microscope. (A) Diagram showing the light path in a compound microscope. Light is focused on the specimen by lenses in the condensor. A combination of objective lenses and eyepiece lenses are arranged to focus an image of the illuminated specimen in the eye. (B) A modern research light microscope.

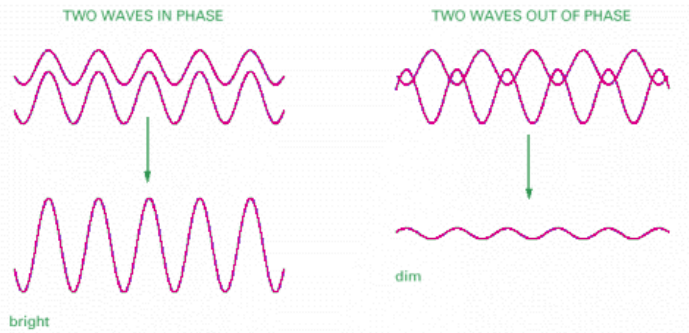

Figure 9-4. Interference between light waves. When two light waves combine in phase, the amplitude of the resultant wave is larger and the brightness is increased. Two light waves that are out of phase cancel each other partly and produce a wave whose amplitude, and therefore brightness, is decreased.

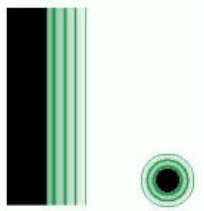

Figure 9-5. Edge effects. The interference effects observed at high magnification when light passes the edges of a solid object placed between the light source and the observer are shown here.

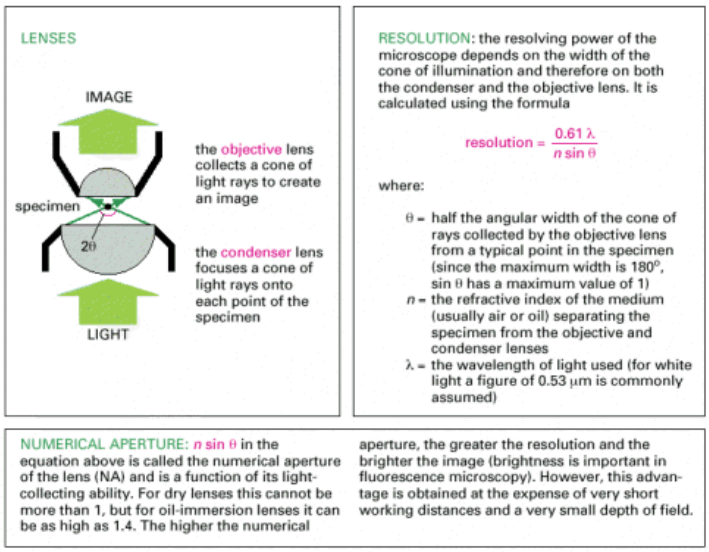

Figure 9-6. Numerical aperture. The path of light rays passing through a transparent specimen in a microscope illustrate the concept of numerical aperture and its relation to the limit of resolution.

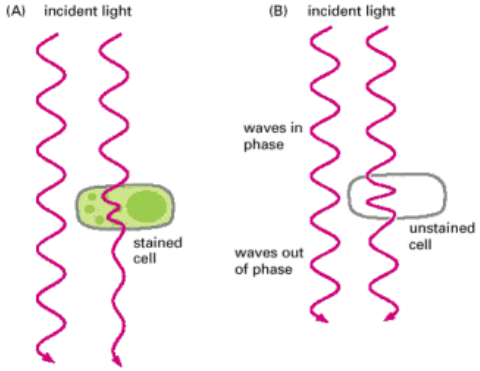

Figure 9-7. Two ways to obtain contrast in light microscopy. (A) The stained portions of the cell reduce the amplitude of light waves of particular wavelengths passing through them. A colored image of the cell is thereby obtained that is visible in the ordinary way. (B) Light passing through the unstained, living cell undergoes very little change in amplitude, and the structural details cannot be seen even if the image is highly magnified. The phase of the light, however, is altered by its passage through the cell, and small phase differences can be made visible by exploiting interference effects using a phase-contrast or a differential-interference-contrast microscope.

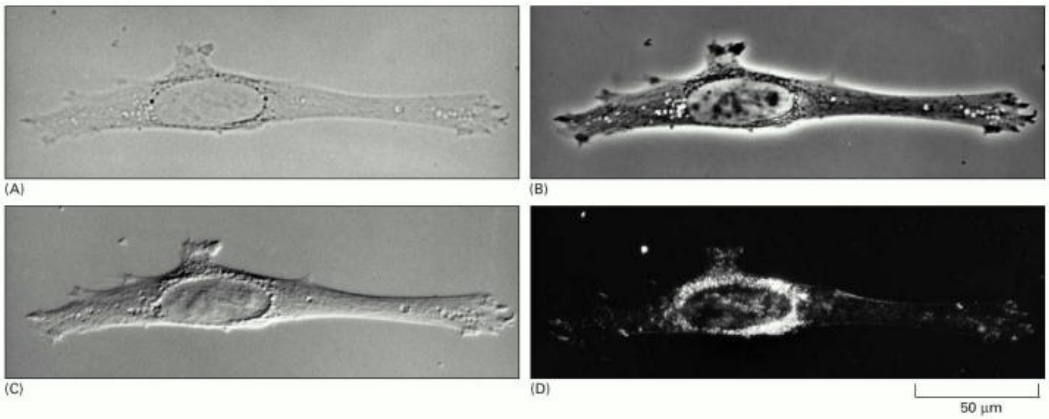

Figure 9-8. Four types of light microscopy. Four images are shown of the same fibroblast cell in culture. All four types of images can be obtained with most modern microscopes by interchanging optical components. (A) Bright-field microscopy. (B) Phase-contrast microscopy. (C) Nomarski differential-interference-contrast microscopy. (D) Dark-field microscopy.

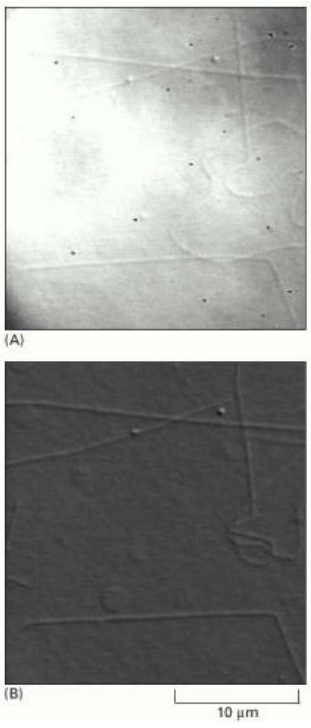

Figure 9-9. Image processing. (A) Unstained microtubules are shown here in an unprocessed digital image, captured using differential-interference-contrast microscopy. (B) The image has now been processed, first by digitally subtracting the unevenly illuminated background, and second by digitally enhancing the contrast. The result of this image processing is a far more interpretable picture. Note that the microtubules are dynamic and some have changed length or position between the before-and-after images. (Courtesy of Viki Allan.)

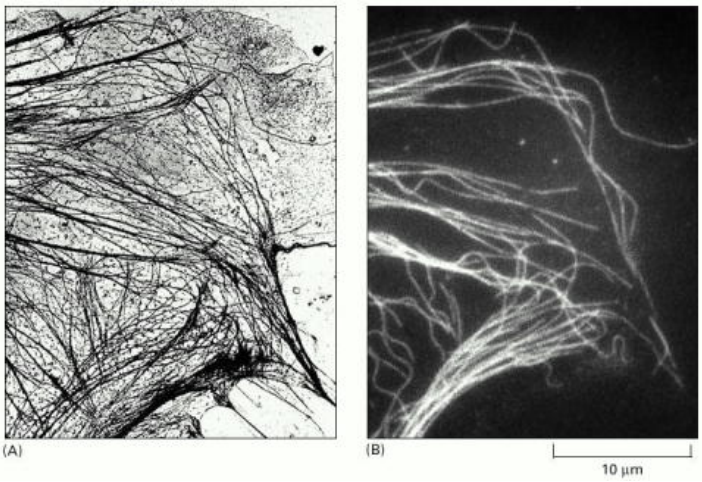

Figure 9-15. Immunofluorescence. (A) A transmission electron micrograph of the periphery of a cultured epithelial cell showing the distribution of microtubules and other filaments. (B) The same area stained with fluorescent antibodies against tubulin, the protein subunit of microtubules, using the technique of indirect immunocytochemistry (see Figure 9-16). *Arrows* indicate individual microtubules that are readily recognizable in both images. Note that, because of diffraction effects, the microtubules in the light microscope appear 0.2 µm wide rather than their true width of 0.025 µm. (From M. Osborn, R. Webster, and K. Weber, *J. Cell Biol.* 77: R27R34, 1978. © The Rockefeller University Press.)

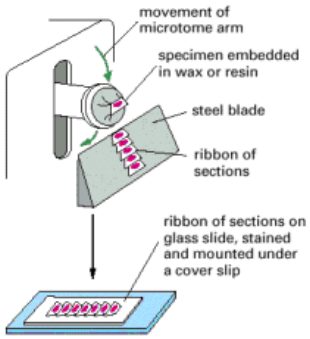

Figure 9-10. Making tissue sections. This illustration shows how an embedded tissue is sectioned with a microtome in preparation for examination in the light microscope.

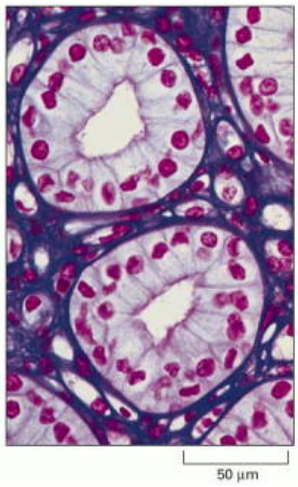

Figure 9-11. A stained tissue section . This section of cells in the urine-collecting ducts of the kidney was stained with a combination of dyes, hematoxylin and eosin, commonly used in histology. Each duct is made of closely packed cells (with nuclei stained *red)* that form a ring. The ring is surrounded by extracellular matrix, stained *purple.* (From P.R. Wheater et al., Functional Histology, 2nd edn. London: Churchill Livingstone, 1987.)

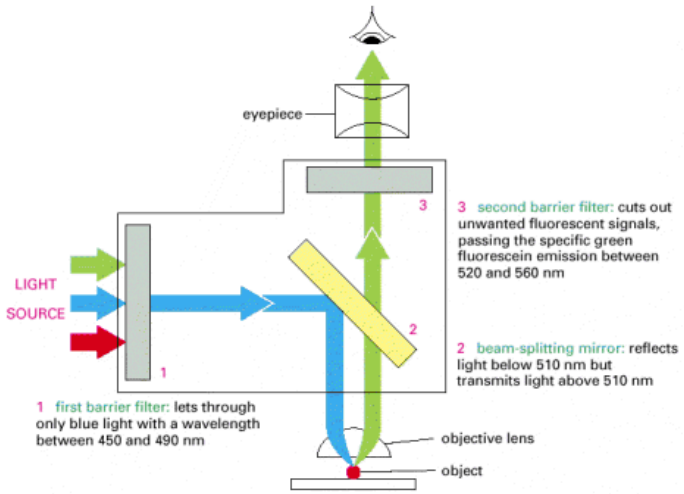

Figure 9-12. The optical system of a fluorescence microscope. A filter set consists of two barrier filters (1 and 3) and a dichroic (beam-splitting) mirror (2). In this example, the filter set for detection of the fluorescent molecule fluorescein is shown. High-numerical-aperture objective lenses are especially important in this type of microscopy because, for a given magnification, the brightness of the fluorescent image is proportional to the fourth power of the numerical aperture (see also Figure 9-6).

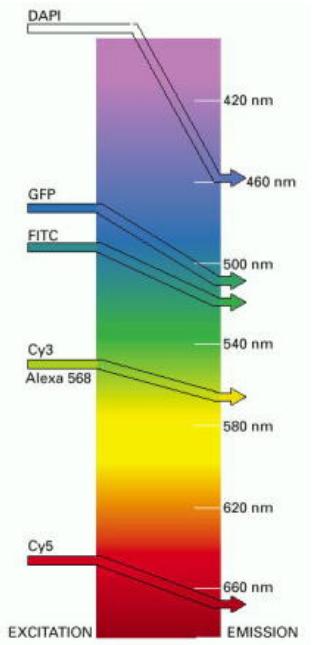

Figure 9-13. Fluorescent dyes. The maximum excitation and emission wavelengths of several commonly used fluorescent dyes are shown in relation to the corresponding colours of the spectrum. The photon emitted by a dye molecule is necessarily of lower energy (longer wavelength) than the photon absorbed and this accounts for the difference between the excitation and emission peaks. GFP is a green fluorescent protein, not a dye, and is discussed in detail later in the chapter. DAPI is widely used as a general fluorescent DNA dye, that absorbs UV light and fluoresces bright blue. The other dyes are all commonly used to fluorescently label antibodies and other proteins.

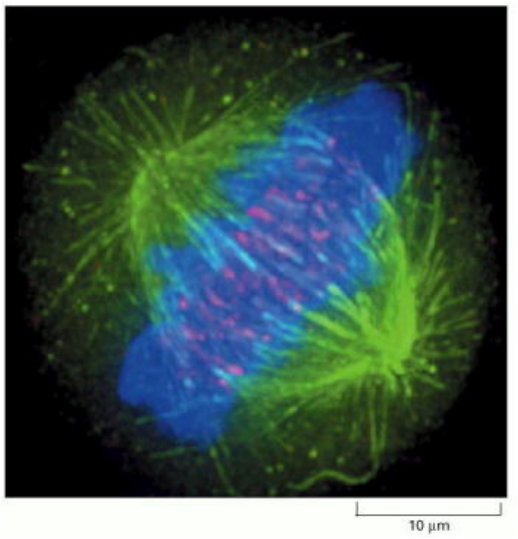

Figure 9-14. Multiple-fluorescent-probe microscopy. In this composite micrograph of a cell in mitosis, three different fluorescent probes have been used to stain three different cellular components. The spindle microtubules are revealed with a *green* fluorescent antibody, centromeres with a *red* fluorescent antibody and the DNA of the condensed chromosomes with the *blue* fluorescent dye DAPI. (Courtesy of Kevin F. Sullivan.)

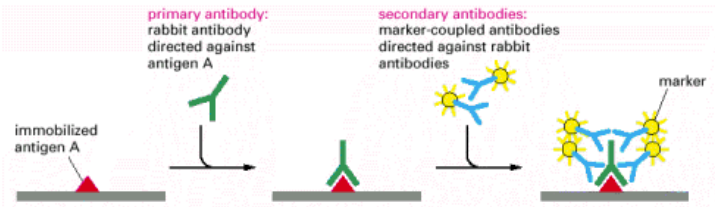

Figure 9-16. Indirect immuno-cytochemistry. This detection method is very sensitive because the primary antibody is itself recognized by many molecules of the secondary antibody. The secondary antibody is covalently coupled to a marker molecule that makes it readily detectable. Commonly used marker molecules include fluorescent dyes (for fluorescence microscopy), the enzyme horseradish peroxidase (for either conventional light microscopy or electron microscopy), colloidal gold spheres (for electron microscopy), and the enzymes alkaline phosphatase or peroxidase (for biochemical detection).

Figure 9-17. Image deconvolution. (A) A light micrograph of the large polytene chromosomes from *Drosophila*, stained with a fluorescent DNA-binding dye. (B) The same field of view after image deconvolution clearly reveals the banding pattern on the chromosomes. Each band is about 0.25 µm

thick, approaching the resolution limit of the light microscope. (Courtesy of the John Sedat Laboratory.)

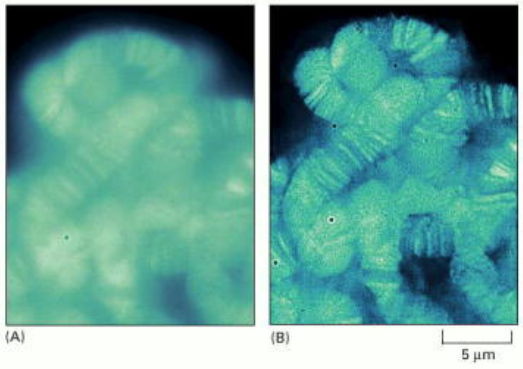

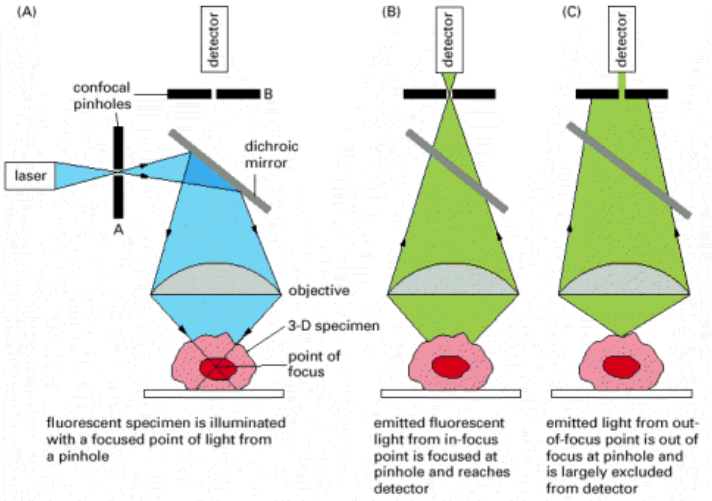

Figure 9-18. The confocal fluorescence microscope. This simplified diagram shows that the basic arrangement of optical components is similar to that of the standard fluorescence microscope shown in Figure 9-12, except that a laser is used to illuminate a small pinhole whose image is focused at a single point in the specimen (A). Emitted fluorescence from this focal point in the specimen is focused at a second (confocal) pinhole (B). Emitted light from elsewhere in the specimen is not focused here and therefore does not contribute to the final image (C). By scanning the beam of light across the specimen, a very sharp two-dimensional image of the exact plane of focus is built up that is not significantly degraded by light from other regions of the specimen.

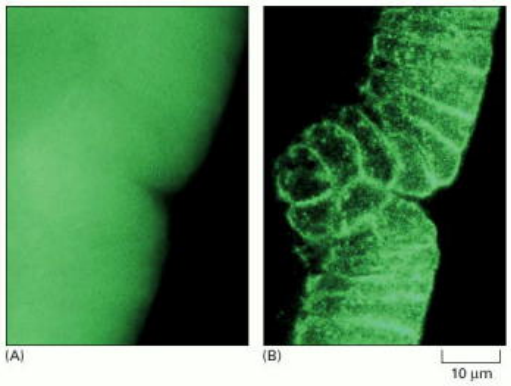

Figure 9-19. Conventional and confocal fluorescence microscopy compared. These two micrographs are of the same intact gastrula-stage *Drosophila* embryo that has been stained with a fluorescent probe for actin filaments. (A) The conventional, unprocessed image is blurred by the presence of fluorescent structures above and below the plane of focus. (B) In the confocal image, this out-of-focus information is removed, resulting in a crisp optical section of the cells in the embryo. (Courtesy of Richard Warn and Peter Shaw.)

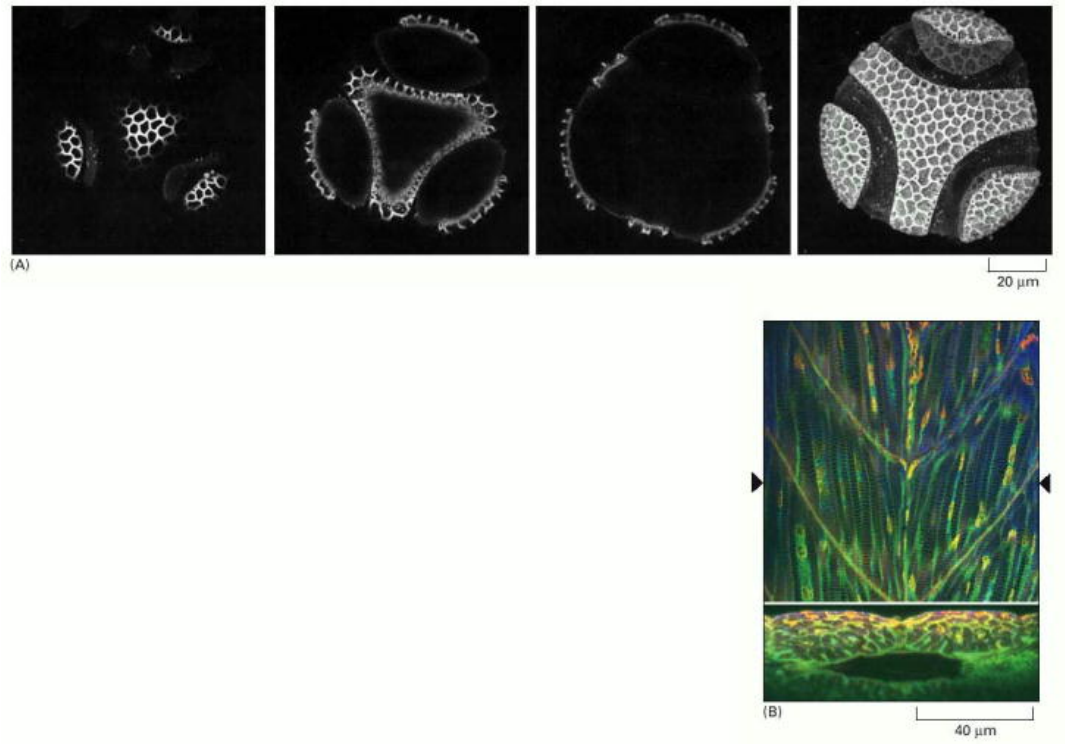

Figure 9-20. Three-dimensional reconstruction from confocal microscope images. (A) Pollen grains, in this case from a passion flower, have a complex sculptured cell wall that contains fluorescent compounds. Images obtained at different depths through the grain, using a confocal microscope, can be recombined to give a three-dimensional view of the whole grain, shown on the right. Three selected individual optical sections from the full set of 30, each of which shows little contribution from its neighbors, are shown on the left. (B) The tail region of this zebrafish embryo has been stained with two fluorescent dyes and imaged in a confocal microscope. The image below is a transverse optical section of the tail, digitally constructed by scanning the laser in a single line (indicated by arrowheads) while progressively varying the focus level. The dark cavity in the centre is the developing notochord. (A, courtesy of Brad Amos; B, courtesy of S. Reichelt and W.B. Amos.)

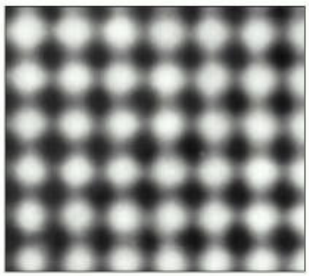

Figure 9-21. The limit of resolution of the electron microscope. This transmission electron micrograph of a thin layer of gold shows the individual files of atoms in the crystal as bright spots. The distance between adjacent files of gold atoms is about 0.2 nm (2 Å). (Courtesy of Graham Hills.)

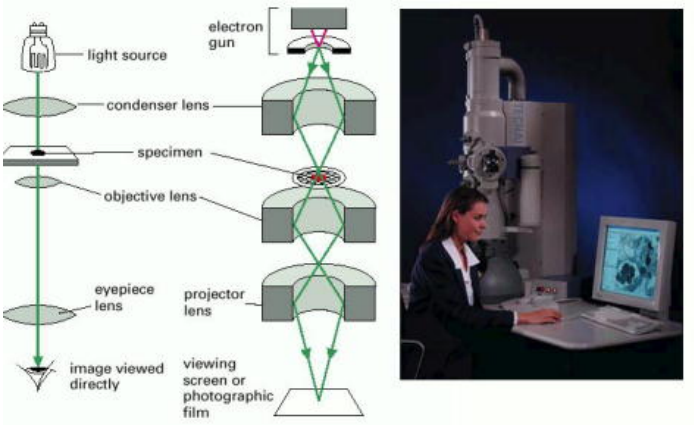

Figure 9-22. The principal features of a light microscope and a transmission electron microscope. These drawings emphasize the similarities of overall design. Whereas the lenses in the light microscope are made of glass, those in the electron microscope are magnetic coils. The electron microscope requires that the specimen be placed in a vacuum. The inset shows a transmission electron microscope in use. (Photograph courtesy of FEI Company Ltd.)

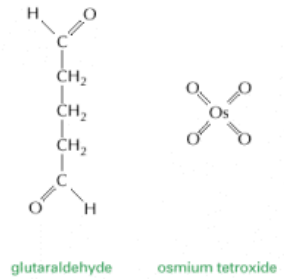

Figure 9-23. Two common chemical fixatives used for electron microscopy. The two reactive aldehyde groups of glutaraldehyde enable it to cross-link various types of molecules, forming covalent bonds between them. Osmium tetroxide is reduced by many organic compounds with which it forms cross-linked complexes. It is especially useful for fixing cell membranes, since it reacts with the C=C double bonds present in many fatty acids.

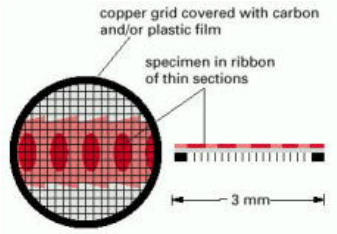

Figure 9-24. The copper grid that supports the thin sections of a specimen in a TEM.

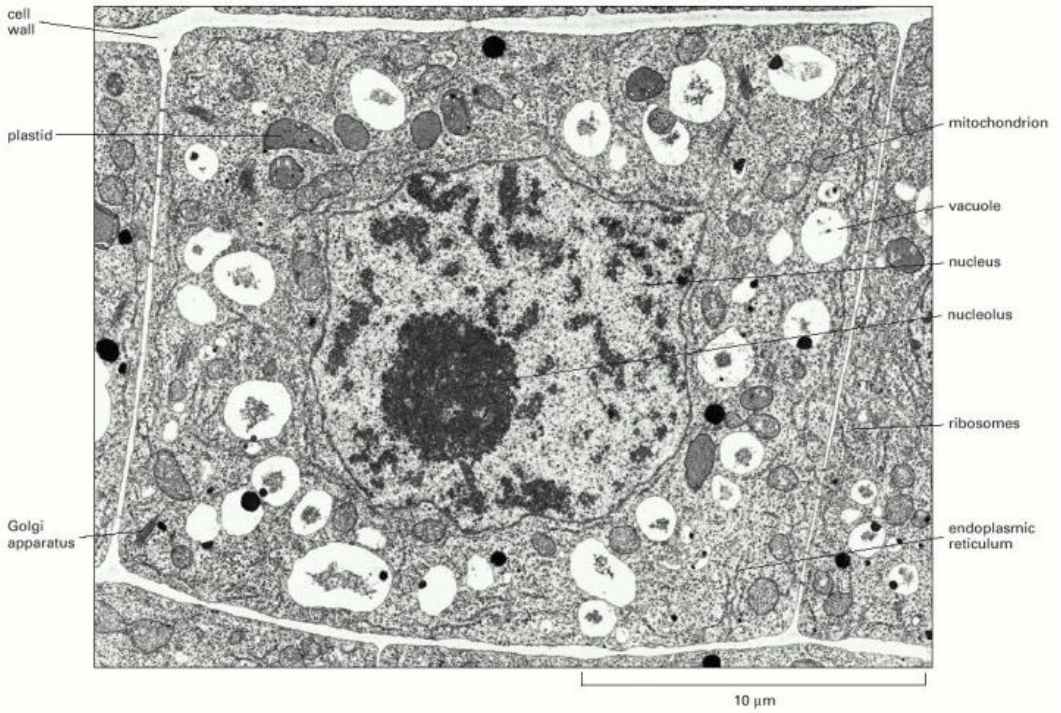

Figure 9-25. A root-tip cell stained with osmium and other heavy metal ions. The cell wall, nucleus, vacuoles, mitochondria, endoplasmic reticulum, Golgi apparatus, and ribosomes are easily visible in this transmission electron micrograph. (Courtesy of Brian Gunning.)

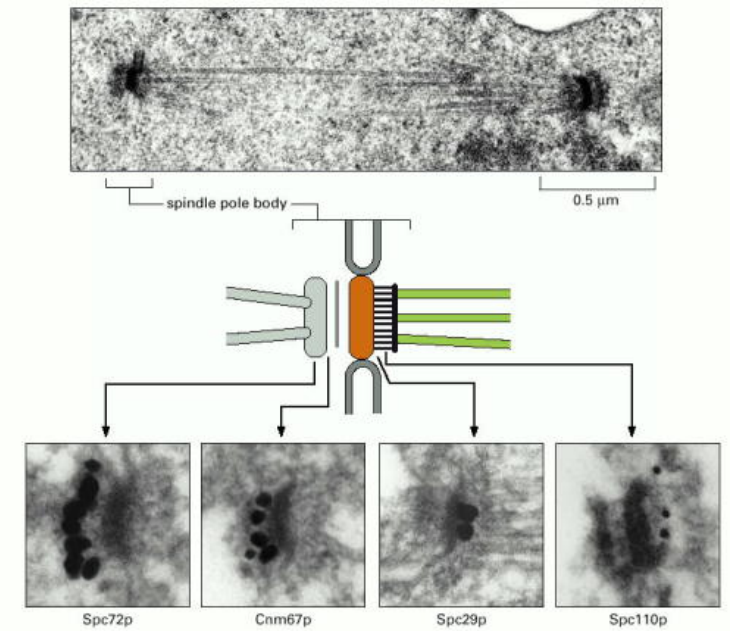

Figure 9-26. Localizing proteins in the electron microscope. Immunogold electron microscopy is used here to localize four different protein components to particular locations within the spindle pole body of yeast. At the top is a thin section of a yeast mitotic spindle showing the spindle microtubules that cross the nucleus, and connect at each end to spindle pole bodies embedded in the nuclear envelope. A diagram of the components of a single spindle pole body is shown below. Antibodies against four different proteins of the spindle pole body are used, together with colloidal gold particles (black dots), to reveal where within the complex structure each protein is located. (Courtesy of John Kilmartin.)

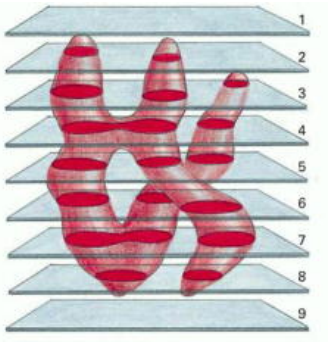

Figure 9-27. A three-dimensional reconstruction from serial sections. Single thin sections sometimes give misleading impressions. In this example, most sections through a cell containing a branched mitochondrion seem to contain two or three separate mitochondria. Sections 4 and 7, moreover, might be interpreted as showing a mitochondrion in the process of dividing. The true three-dimensional shape, however, can be reconstructed from serial sections.

Figure 9-28. A developing wheat flower, or spike. This delicate flower spike was rapidly frozen, coated with a thin metal film, and examined in the frozen state in a SEM. This micrograph, which is at a low magnification, demonstrates the large depth of focus of the SEM. (Courtesy of Kim Findlay.)

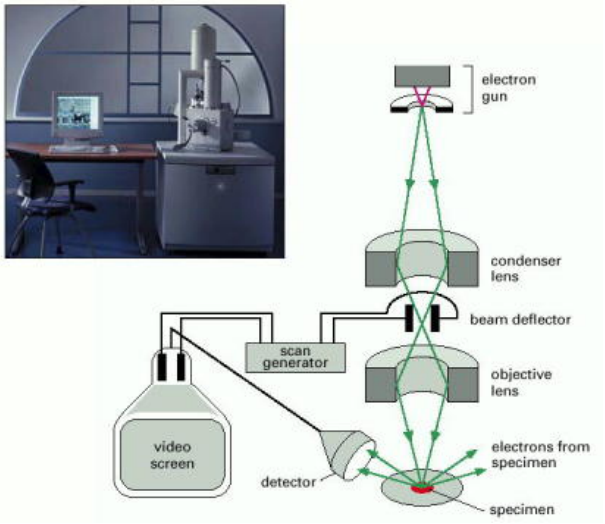

Figure 9-29. The scanning electron microscope. In a SEM, the specimen is scanned by a beam of electrons brought to a focus on the specimen by the electromagnetic coils that act as lenses. The quantity of electrons scattered or emitted as the beam bombards each successive point on the surface of the specimen is measured by the detector and is used to control the intensity of successive points in an image built up on a video screen. The SEM creates striking images of three-dimensional objects with great depth of focus and a resolution between 3 nm and 20 nm depending on the instrument. (Photograph courtesy of FEI Company Ltd.)

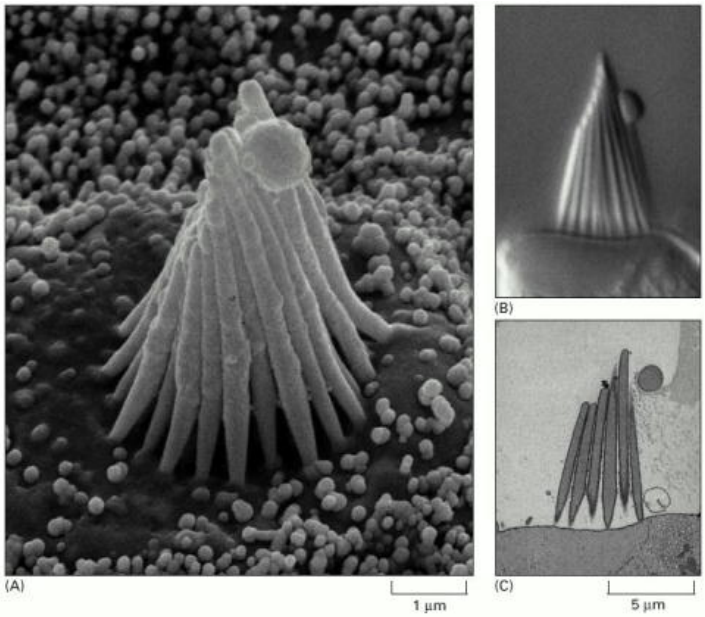

Figure 9-30. Scanning electron microscopy. (A) A scanning electron micrograph of the stereocilia projecting from a hair cell in the inner ear of a bullfrog. For comparison, the same structure is shown by (B) differential-interference-contrast light microscopy and (C) thin-section transmission electron microscopy. (Courtesy of Richard Jacobs and James Hudspeth.)

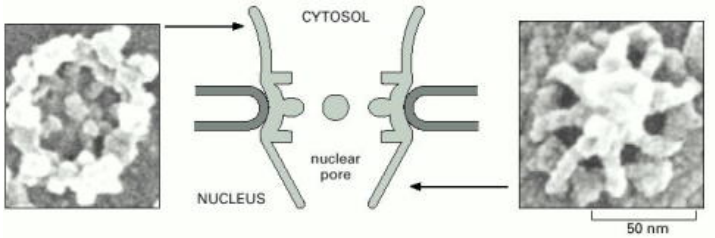

Figure 9-31. The nuclear pore. Rapidly frozen nuclear envelopes were imaged in a high-resolution SEM, equipped with a field emission gun as the source of electrons. These views of each side of a nuclear pore represent the limit of resolution of the SEM, and should be compared with Figure 12-10. (Courtesy of Martin Goldberg and Terry Allen.)

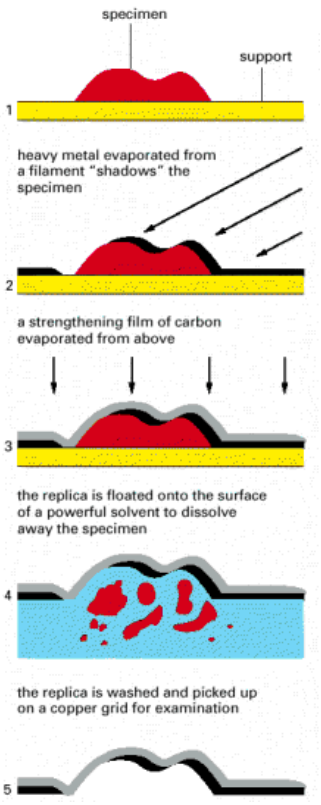

Figure 9-32. The preparation of a metal-shadowed replica of the surface of a specimen. Note that the thickness of the metal reflects the surface contours of the original specimen.

Figure 9-33. The thylakoid membranes from the chloroplast of a plant cell. In this freeze-fracture electron micrograph, the thylakoid membranes, which perform photosynthesis, are stacked up in multiple layers (see Figure 14-34). The plane of the fracture has moved from layer to layer, passing through the middle of each lipid bilayer and exposing transmembrane proteins that have sufficient bulk in the interior of the bilayer to cast a shadow and show up as intramembrane particles in this platinum replica. The largest particles seen in the membrane are the complete photosystem II - a complex of multiple proteins. (Courtesy of L.A. Staehelin.)

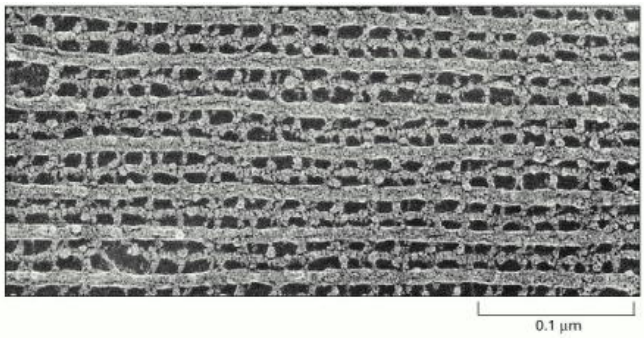

Figure 9-34. A regular array of protein filaments in an insect muscle. To obtain this image, the muscle cells were rapidly frozen to liquid helium temperature, fractured through the cytoplasm, and subjected to deep etching. A metal-shadowed replica was then prepared and examined at high magnification. (Courtesy of Roger Cooke and John Heuser.)

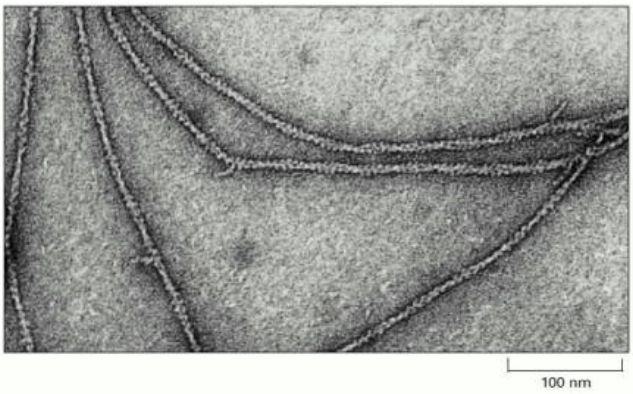

Figure 9-35. Negatively stained actin filaments. In this transmission electron micrograph, each filament is about 8 nm in diameter and is seen, on close inspection, to be composed of a helical chain of globular actin molecules. (Courtesy of Roger Craig.)

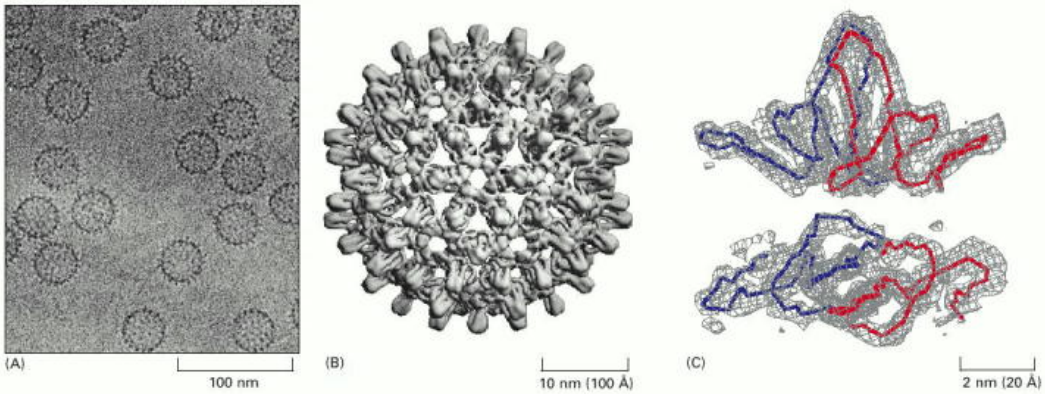

Figure 9-36. EM tomography. Spherical protein shells of the hepatitis B virus are preserved in a thin film of ice (A) and imaged in the transmission electron microscope. Thousands of individual particles were combined by EM tomography to produce the three-dimensional map of the icosahedral particle shown in (B). The two views of a single protein dimer (C), that forms the spikes on the surface of the shell, show that the resolution of the reconstruction (7.4 Å) is sufficient to resolve the complete fold of the polypeptide chain. (A, courtesy of B. Böttcher, S.A. Wynne and R.A. Crowther; B and C, from B. Böttcher, S.A. Wynne and R.A. Crowther, *Nature* 386:8891, 1997. © Macmillan Magazines Ltd.)

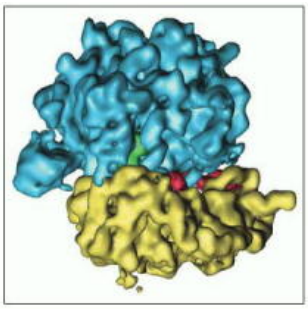

Figure 9-37. The three-dimensional structure of the 70S ribosome from *E. coli* determined by EM tomography. The small subunit is colored *yellow*, the large subunit *blue*. The overall resolution is 11.2 Å. (From I.S. Gabashvili et al., *Cell* 100: 537549, 2000. © Elsevier.)

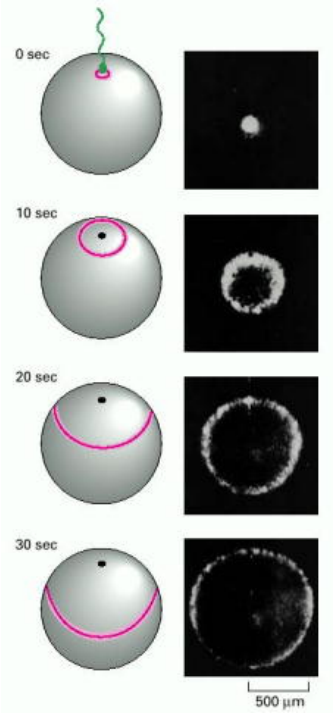

Figure 9-38. Aequorin, a luminescent protein. The luminescent protein aequorin emits light in the presence of free Ca^{2+}. Here, an egg of the medaka fish has been injected with aequorin, which has diffused throughout the cytosol, and the egg has then been fertilized with a sperm and examined with the help of an image intensifier. The four photographs were taken looking down on the site of sperm entry at intervals of 10 seconds and reveal a wave of release of free Ca^{2+} into the cytosol from internal stores just beneath the plasma membrane. This wave sweeps across the egg starting from the site of sperm entry, as indicated in the diagrams on the *left.* (Photographs reproduced from J.C. Gilkey, L.F. Jaffe, E.B. Ridgway, and G.T. Reynolds, *J. Cell Biol.* 76:448466, 1978. © The Rockefeller University Press.)

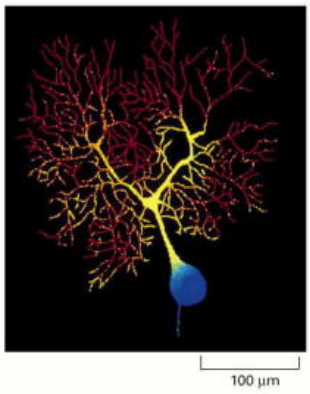

Figure 9-39. Visualizing intracellular Ca^{2+} concentrations by using a fluorescent indicator. The branching tree of dendrites of a Purkinje cell in the cerebellum receives more than 100,000 synapses from other neurons. The output from the cell is conveyed along the single axon seen leaving the cell body at the bottom of the picture. This image of the intracellular Ca^{2+} concentration in a single Purkinje cell (from the brain of a guinea pig) was taken with a low-light camera and the Ca^{2+}-sensitive fluorescent indictor fura-2. The concentration of free Ca^{2+} is represented by different colors, *red* being the highest and *blue* the lowest. The highest Ca^{2+} levels are present in the thousands of dendritic branches. (Courtesy of D.W. Tank, J.A. Connor, M. Sugimori, and R. R. Llinas.)

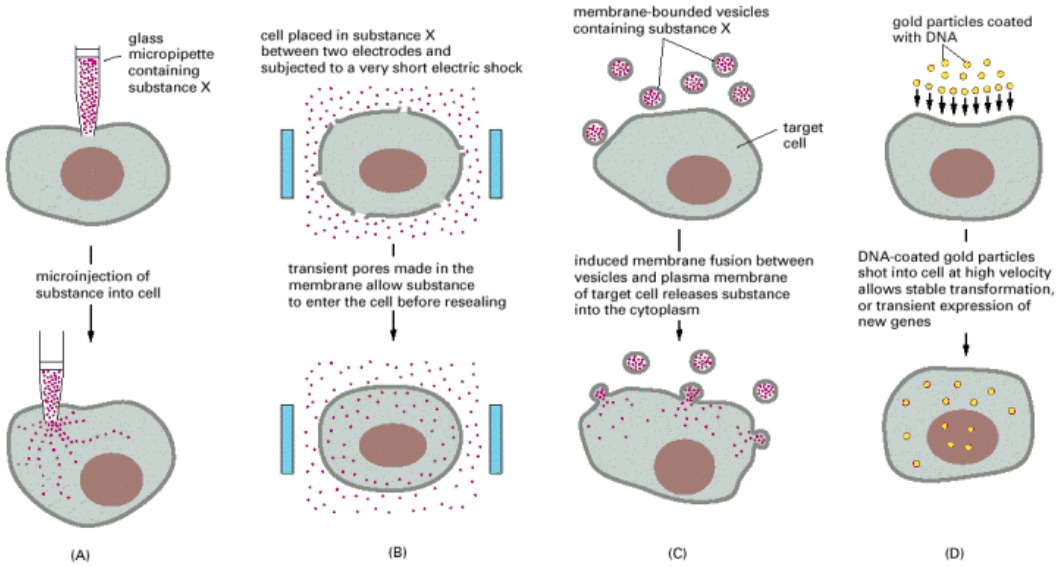

Figure 9-40. Methods of introducing a membrane-impermeant substance into a cell. (A) The substance is injected through a micropipette, either by applying pressure or, if the substance is electrically charged, by applying a voltage that drives the substance into the cell as an ionic current (a technique called *iontophoresis*). (B) The cell membrane is made transiently permeable to the substance by disrupting the membrane structure with a brief but intense electric shock (2000 V/cm for 200 µsec, for example). (C) Membrane-enclosed vesicles are loaded with the desired substance and then induced to fuse with the target cells. (D) Gold particles coated with DNA are used to introduce a novel gene into the nucleus.

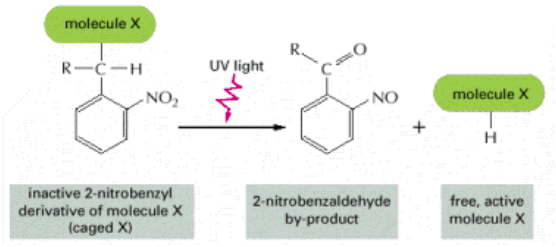

Figure 9-41. Caged molecules. This diagram shows how a light-sensitive caged derivative of a molecule (designated X) can be converted by a flash of UV light to its free, active form. Small molecules such as ATP can be caged in this way. Even ions like Ca^{2+} can be indirectly caged; in this case a Ca^{2+}-binding chelator is used, which is inactivated by photolysis, thus releasing its Ca^{2+}.

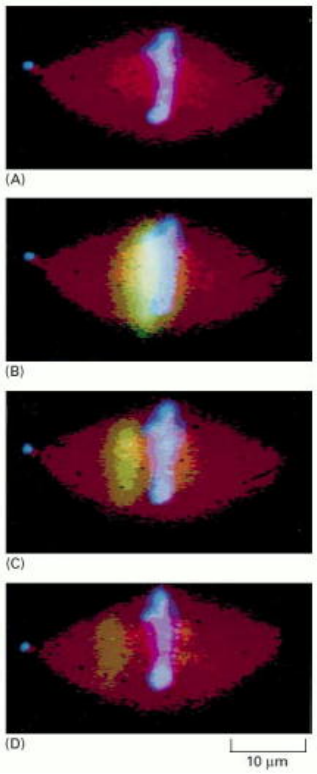

Figure 9-42. Determining microtubule flux in the mitotic spindle with caged fluorescein linked to tubulin. (A) A metaphase spindle formed *in vitro* from an extract of *Xenopus* eggs has incorporated three fluorescent markers: rhodamine-labeled tubulin (*red*) to mark all the microtubules, a *blue* DNA-binding dye that labels the chromosomes, and caged-fluorescein-labeled tubulin, which is also incorporated into all the microtubules but is invisible because it is nonfluorescent until activated by ultraviolet light. (B) A beam of UV light is used to uncage the caged-fluorescein-labeled tubulin locally, mainly just to the left side of the metaphase plate. Over the next few minutes (after 1.5 minutes in C, after 2.5 minutes in D), the uncaged fluorescein-tubulin signal is seen to move toward the left spindle pole, indicating that tubulin is continuously moving poleward even though the spindle (visualized by the *red* rhodamine-labeled tubulin fluorescence) remains largely unchanged. (From K.E. Sawin and T.J. Mitchison, *J. Cell Biol.* 112:941954, 1991. © The Rockefeller University Press.)

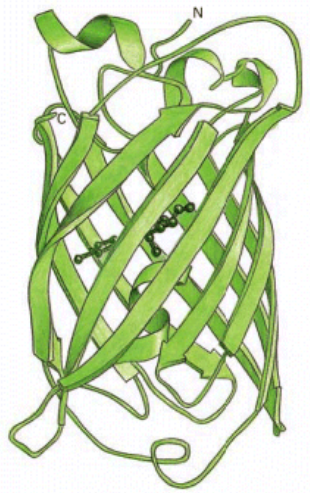

Figure 9-43. Green fluorescent protein (GFP). The structure of GFP, shown here schematically, highlights the eleven β strands that form the staves of a barrel. Buried within the barrel is the active chromaphore *(dark green)* that is formed post-translationally from the protruding side chains of three amino acid residues. (Adapted from M. Ormö et al., *Science* 273:13921395, 1995.)

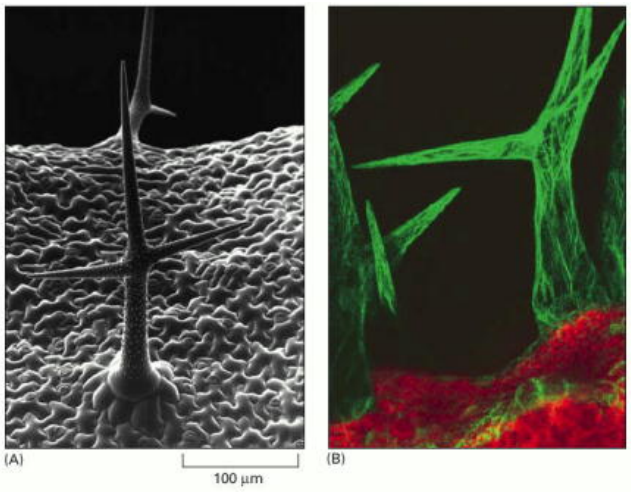

Figure 9-44. GFP tagging. (A) The upper surface of the leaves of *Arabidopsis* plants are covered with huge branched single-cell hairs that rise up from the surface of the epidermis. These hairs, or trichomes, can be imaged in the SEM. (B) If an *Arabidopsis* plant is transformed with a DNA sequence coding for talin (an actin-binding protein), fused to a DNA sequence coding for GFP, the fluorescent talin protein produced binds to actin filaments in all the living cells of the transgenic plant. Confocal microscopy can reveal the dynamics of the entire actin cytoskeleton of the trichome *(green).* The red fluorescence arises from chlorophyl in cells within the leaf below the epidermis. (A, courtesy of Paul Linstead; B, courtesy of Jaideep Mathur.)

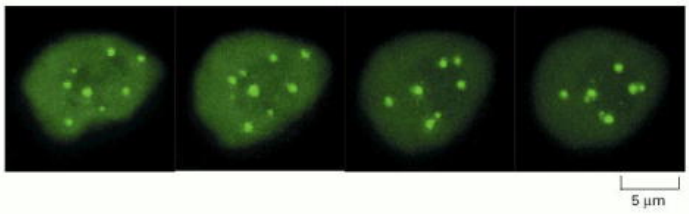

Figure 9-45. Dynamics of GFP tagging. This sequence of micrographs shows a set of three-dimensional images of a living nucleus taken over the course of an hour. Tobacco cells have been stably transformed with GFP fused to a spliceosomal protein that is concentrated in small nuclear bodies called Cajal Bodies (see Figure 6-48). The fluorescent Cajal bodies, easily visible in a living cell with confocal microscopy, are dynamic structures that move around within the nucleus. (Courtesy of Kurt Boudonck, Liam Dolan and Peter Shaw.)

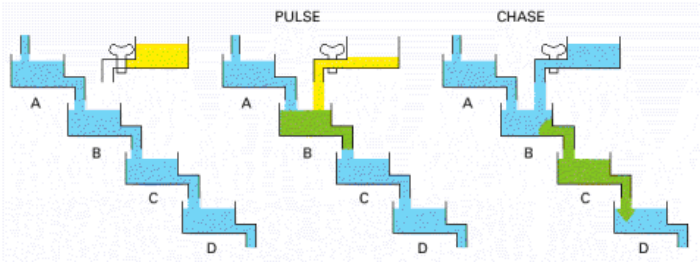

Figure 9-46. The logic of a typical pulse-chase experiment using radioisotopes. The chambers labeled A, B, C, and D represent either different compartments in the cell (detected by autoradiography or by cell-fractionation experiments) or different chemical compounds (detected by chromatography or other chemical methods). The results of a real pulse-chase experiment can be seen in Figure 9-47.

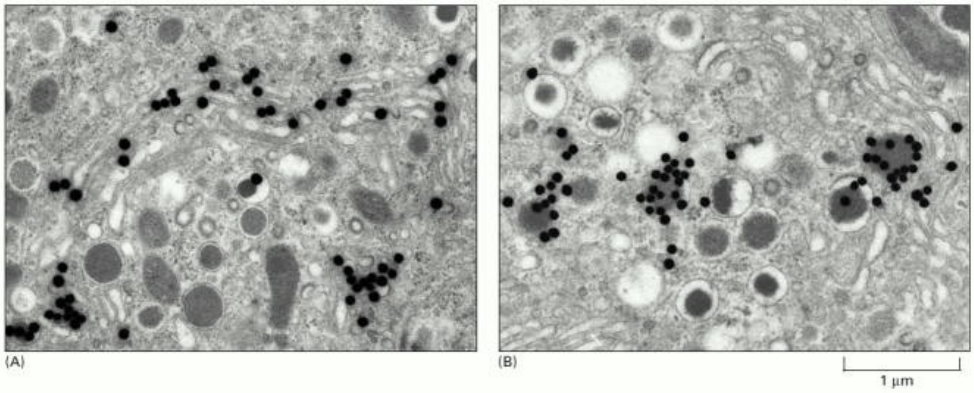

Figure 9-47. Electron-microscopic autoradiography. The results of a pulse-chase experiment in which pancreatic B cells were fed with ^{3}H-leucine for 5 minutes (the pulse) followed by excess unlabeled leucine (the chase). The amino acid is largely incorporated into insulin, which is destined for secretion. After a 10-minute chase the labeled protein has moved from the rough ER to the Golgi stacks (A), where its position is revealed by the black silver grains in the photographic emulsion. After a further 45-minute chase the labeled protein is found in electron-dense secretory granules (B). The small round silver grains seen here are produced by using a special photographic developer and should not be confused with the similar-looking black dots seen with immunogold labeling methods (e.g., Figure 9-26). Experiments similar to this were important in establishing the intracellular pathway taken by newly synthesized secretory proteins. (Courtesy of L. Orci, from *Diabetes* 31:538565, 1982. © American Diabetes Association, Inc.)

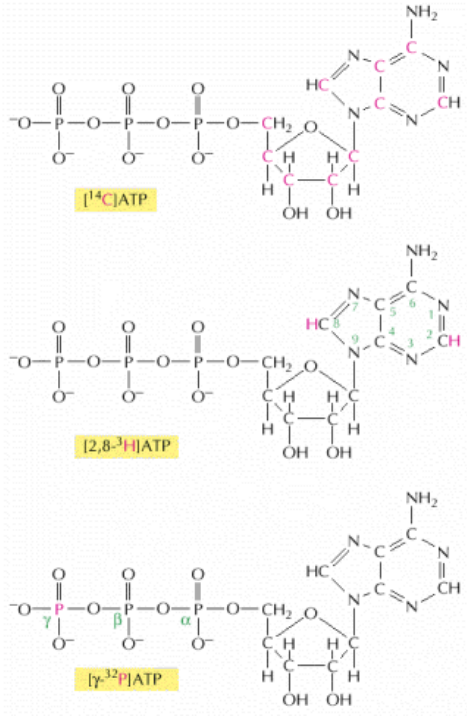

Figure 9-48. Radioisotopically labeled molecules. Three commercially available radioactive forms of ATP, with the radioactive atoms shown in *red*. The nomenclature used to identify the position and type of the radioactive atoms is also shown.

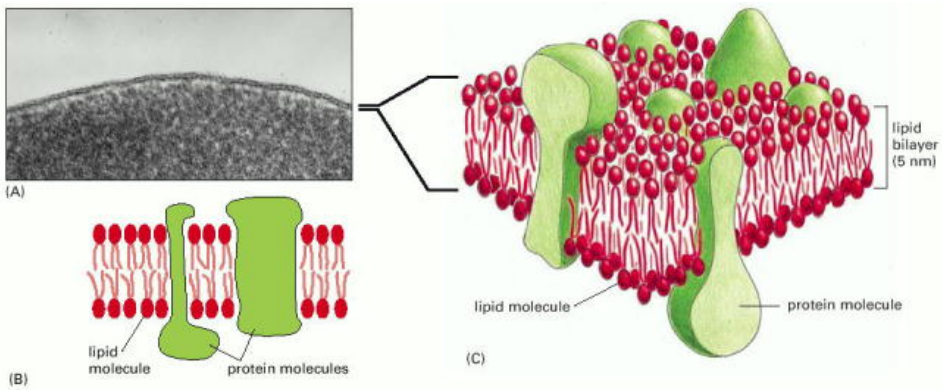

Figure 10-1. Three views of a cell membrane. (A) An electron micrograph of a plasma membrane (of a human red blood cell) seen in cross section. (B and C) These drawings show two-dimensional and three-dimensional views of a cell membrane. (A, courtesy of Daniel S. Friend.)

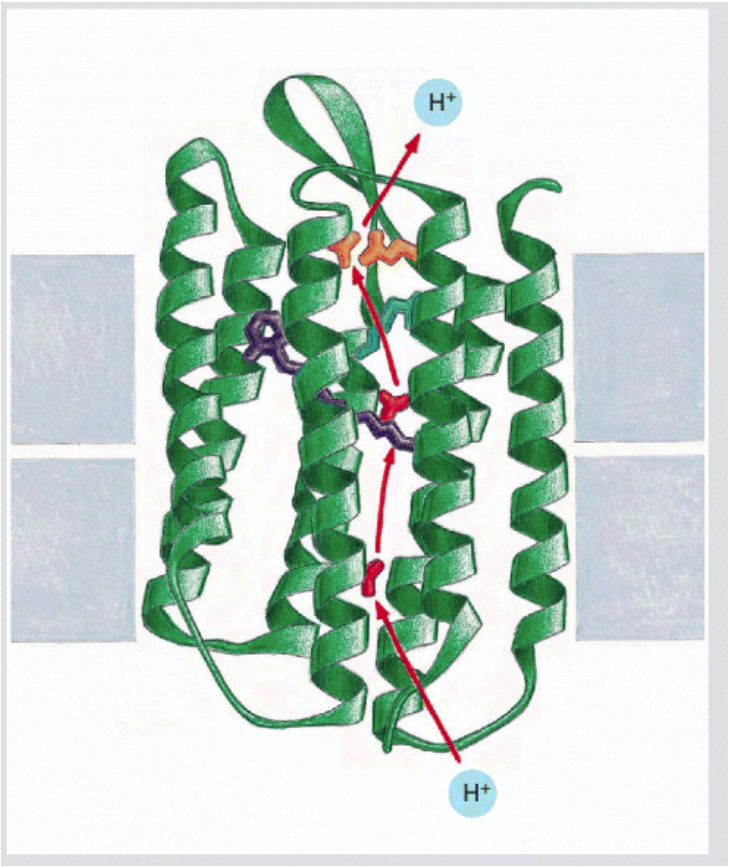

Membrane protein. Special proteins inserted in cellular membranes create pores that permit the passage of molecules across them. The bacterial protein shown here uses the energy from light (photons) to activate the pumping of protons across the plasma membrane. (Adapted from H. Luecke et al., *Science* 286:255260, 1999.)

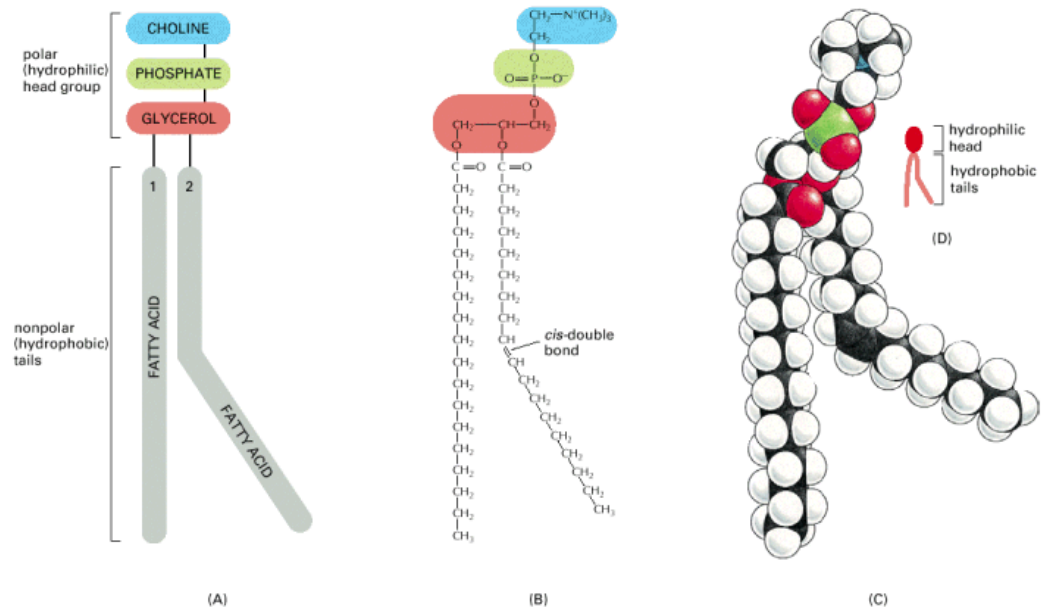

Figure 10-2. The parts of a phospholipid molecule. This example is phosphatidylcholine, represented (A) schematically, (B) by a formula, (C) as a space-filling model, and (D) as a symbol. The kink resulting from the *cis*-double bond is exaggerated for emphasis.

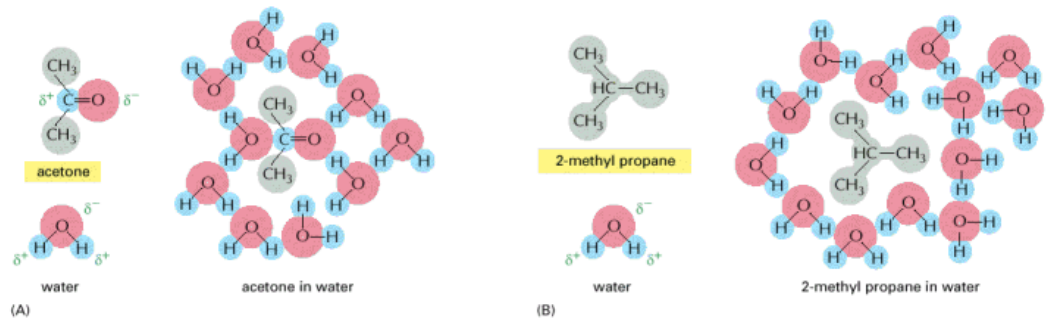

Figure 10-3. How hydrophilic and hydrophobic molecules interact differently with water. (A) Because acetone is polar, it can form favorable electrostatic interactions with water molecules, which are also polar. Thus, acetone readily dissolves in water. (B) By contrast, 2-methyl propane is entirely hydrophobic. It cannot form favorable interactions with water and it would force adjacent water molecules to reorganize into icelike cage structures, which increases the free energy. This compound therefore is virtually insoluble in water. The symbol δ^- indicates a partial negative charge, and δ^+ indicates a partial positive charge. Polar atoms are shown in color and nonpolar groups are shown in *gray*.

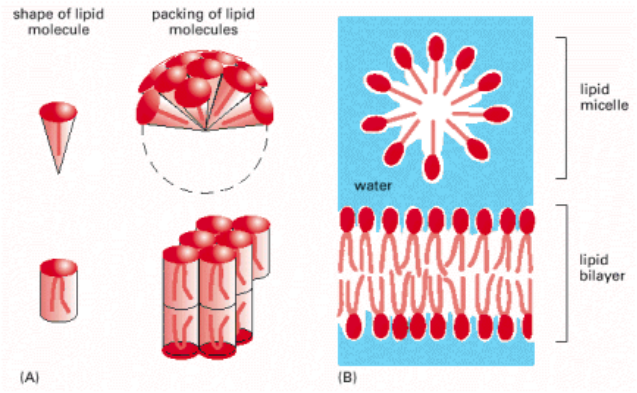

Figure 10-4. Packing arrangements of lipid molecules in an aqueous environment. (A) Wedge-shaped lipid molecules *(above)* form micelles, whereas cylinder-shaped phospholipid molecules *(below)* form bilayers. (B) A lipid micelle and a lipid bilayer seen in cross section. Lipid molecules spontaneously form one or other of these structures in water, depending on their shape.

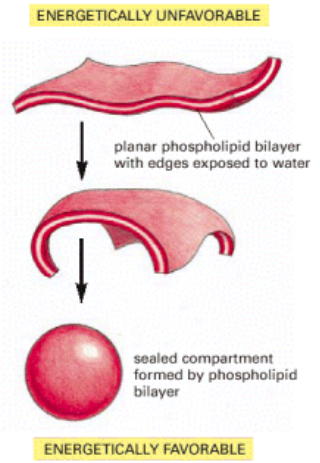

Figure 10-5. The spontaneous closure of a phospholipid bilayer to form a sealed compartment. The closed structure is stable because it avoids the exposure of the hydrophobic hydrocarbon tails to water, which would be energetically unfavorable.

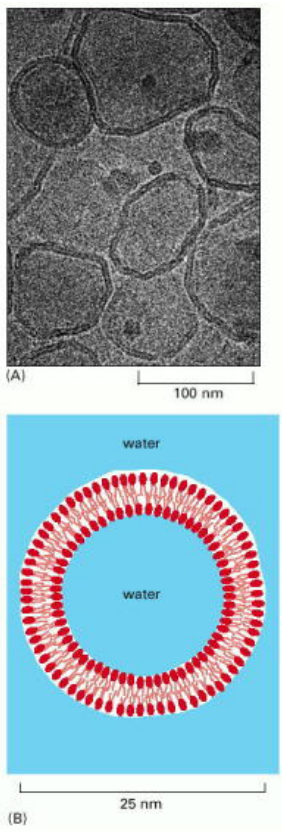

Figure 10-6. Liposomes. (A) An electron micrograph of unfixed, unstained phospholipid vesicles - liposomes - in water rapidly frozen to liquid nitrogen temperature. The bilayer structure of the liposomes is readily apparent. (B) A drawing of a small spherical liposome seen in cross section. Liposomes are commonly used as model membranes in experimental studies. (A, courtesy of Jean Lepault.)

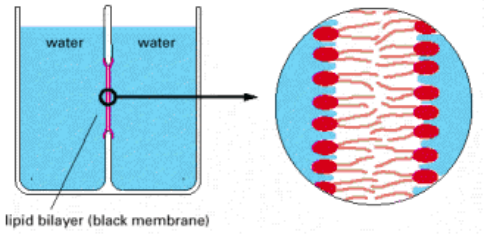

Figure 10-7. A cross-sectional view of a black membrane, a synthetic lipid bilayer. This planar bilayer appears black when it forms across a small hole in a partition separating two aqueous compartments. Black membranes are used to measure the permeability properties of synthetic membranes.

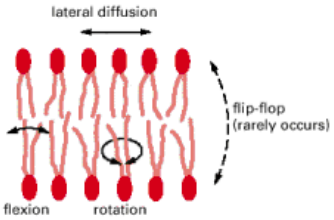

Figure 10-8. Phospholipid mobility. The types of movement possible for phospholipid molecules in a lipid bilayer.

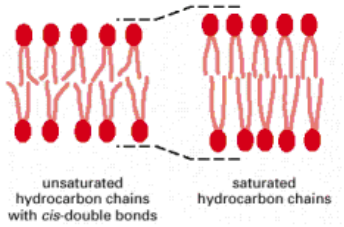

Figure 10-9. The influence of *cis*-double bonds in hydrocarbon chains. The double bonds make it more difficult to pack the chains together, thereby making the lipid bilayer more difficult to freeze. In addition, because the fatty acid chains of unsaturated lipids are more spread apart, lipid bilayers containing them are thinner than bilayers formed exclusively from saturated lipids.

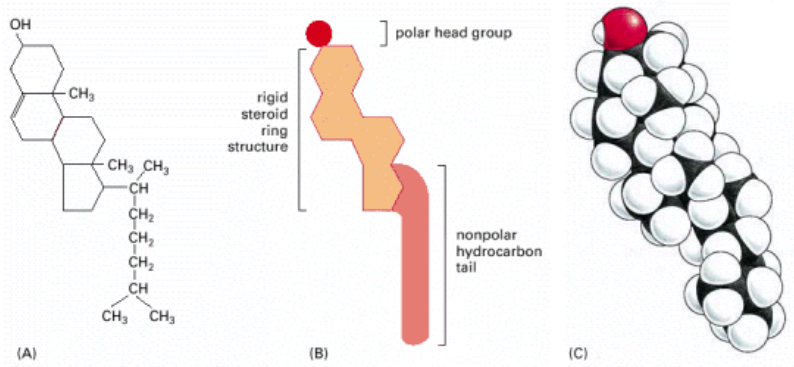

Figure 10-10. The structure of cholesterol. Cholesterol is represented (A) by a formula, (B) by a schematic drawing, and (C) as a space-filling model.

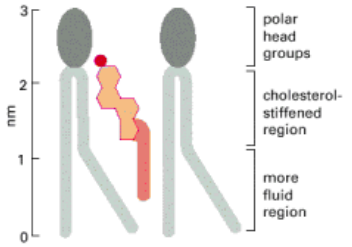

Figure 10-11. Cholesterol in a lipid bilayer. Schematic drawing of a cholesterol molecule interacting with two phospholipid molecules in one monolayer of a lipid bilayer.

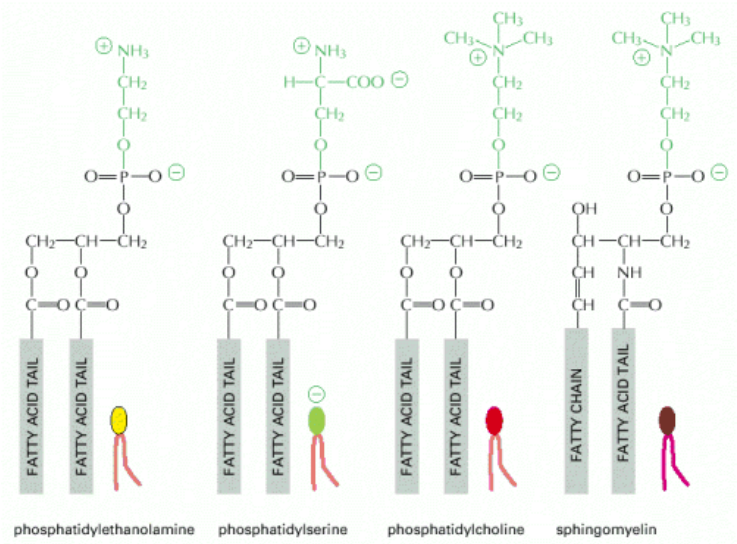

Figure 10-12. Four major phospholipids in mammalian plasma membranes. Note that different head groups are represented by different colors. All the lipid molecules shown are derived from glycerol except for sphingomyelin, which is derived from serine.

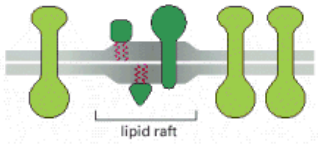

Figure 10-13. A lipid raft. Lipid rafts are small, specialized areas in membranes where some lipids (primarily sphingolipids and cholesterol) and proteins *(green)* are concentrated. Because the lipid bilayer is somewhat thicker in the rafts, certain membrane proteins accumulate. A more detailed view of a lipid raft is shown in Figure 13-63.

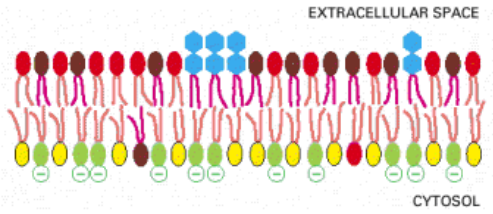

Figure 10-14. The asymmetrical distribution of phospholipids and glycolipids in the lipid bilayer of human red blood cells. The colors used for the phospholipid head groups are those introduced in Figure 10-12. In addition, glycolipids are drawn with hexagonal polar head groups *(blue)*. Cholesterol (not shown) is thought to be distributed about equally in both monolayers.

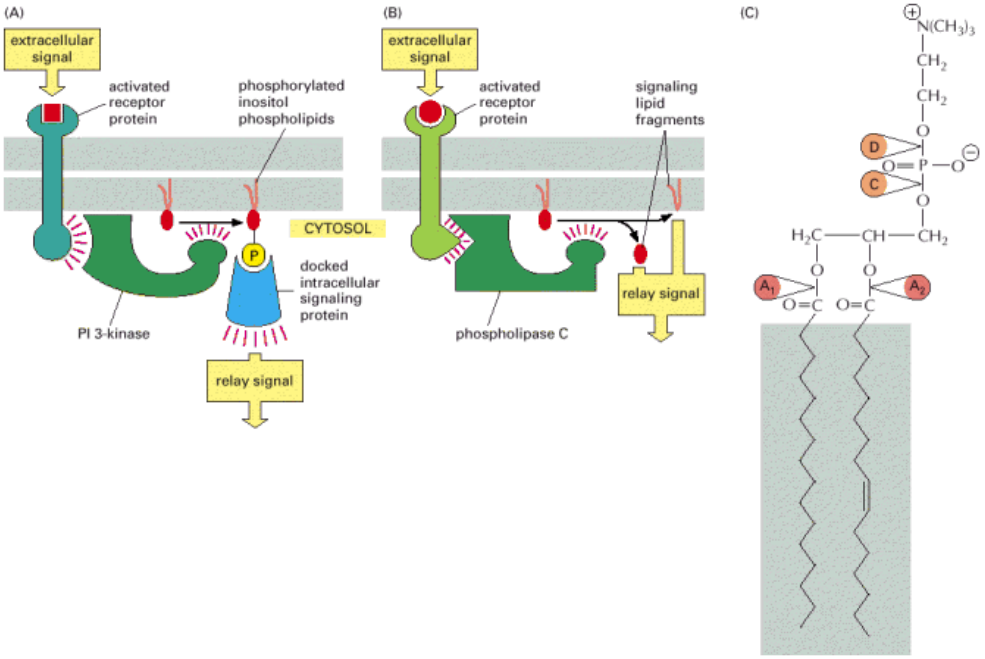

Figure 10-15. Some functions of membrane phospholipids in cell signaling. (A) Extracellular signals can activate PI 3-kinase, which phosphorylates inositol phospholipids in the plasma membrane. Various intracellular signaling molecules then bind to these phosphorylated lipids and are thus recruited to the membrane, where they can interact and help relay the signal into the cell. (B) Other extracellular signals activate phospholipases that cleave phospholipids. The lipid fragments then act as signaling molecules to relay the signal into the cell. (C) Illustration of the sites where different classes of phospholipases cleave phospholipids. As indicated, phospholipases A_1 and A_2 cleave ester bonds, whereas phospholipases C and D cleave at phosphoester bonds.

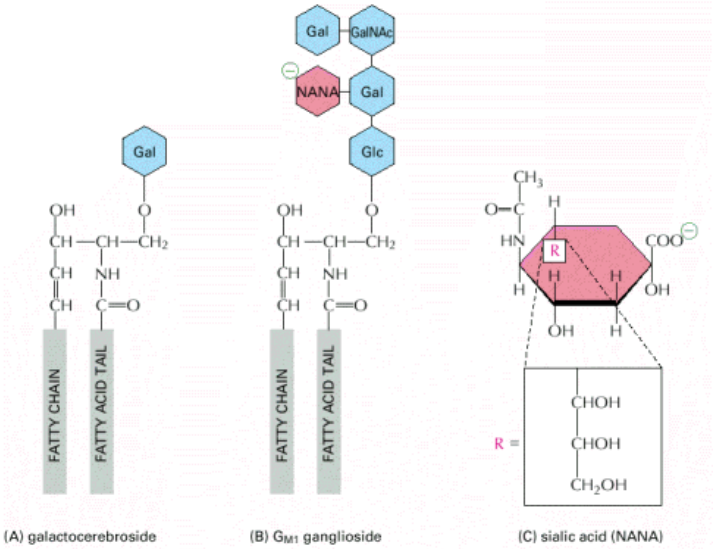

Figure 10-16. Glycolipid molecules. (A) Galactocerebroside is called a *neutral glycolipid* because the sugar that forms its head group is uncharged. (B) A ganglioside always contains one or more negatively charged sialic acid residues (also called *N*-acetylneuraminic acid, or NANA), whose structure is shown in (C). Whereas in bacteria and plants almost all glycolipids are derived from glycerol, as are most phospholipids, in animal cells they are almost always produced from serine, as is the case for the phospholipid sphingomyelin (see Figure 10-12). Gal = galactose; Glc = glucose, GalNAc = *N*-acetylgalactosamine; these three sugars are uncharged.

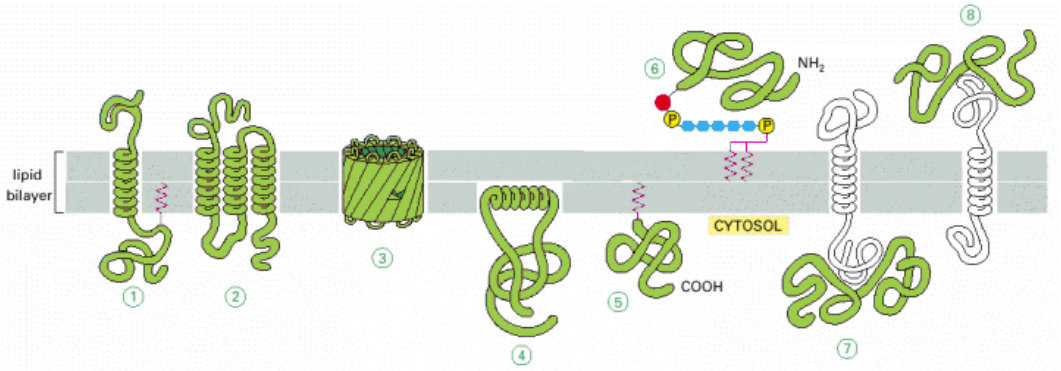

Figure 10-17. Various ways in which membrane proteins associate with the lipid bilayer. Most trans-membrane proteins are thought to extend across the bilayer as (1) a single α helix, (2) as multiple α helices, or (3) as a rolled-up β sheet (a β barrel). Some of these "single-pass" and "multipass" proteins have a covalently attached fatty acid chain inserted in the cytosolic lipid monolayer (1). Other membrane proteins are exposed at only one side of the membrane. (4) Some of these are anchored to the cytosolic surface by an amphipathic α helix that partitions into the cytosolic monolayer of the lipid bilayer through the hydrophobic face of the helix. (5) Others are attached to the bilayer solely by a covalently attached lipid chain - either a fatty acid chain or a prenyl group - in the cytosolic monolayer or, (6) via an oligosaccharide linker, to phosphatidylinositol in the noncytosolic monolayer. (7, 8) Finally, many proteins are attached to the membrane only by noncovalent interactions with other membrane proteins. The way in which the structure in (5) is formed is illustrated in Figure 10-18. The details of how membrane proteins become associated with the lipid bilayer are discussed in Chapter 12.

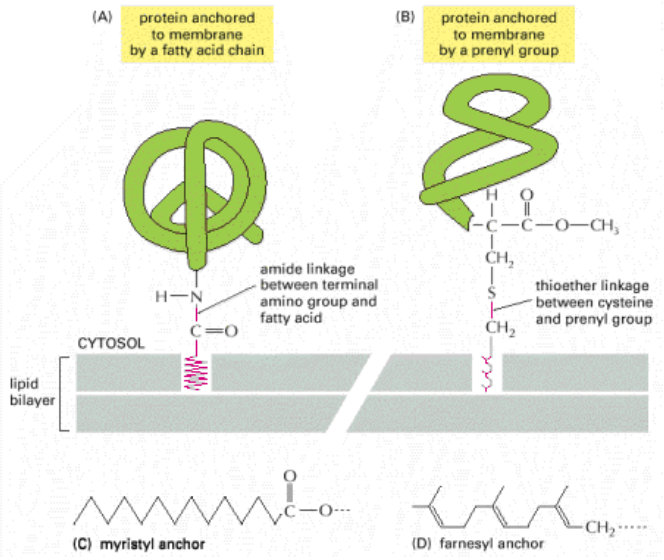

Figure 10-18. Membrane protein attachment by a fatty acid chain or a prenyl group. The covalent attachment of either type of lipid can help localize a water-soluble protein to a membrane after its synthesis in the cytosol. (A) A fatty acid chain (myristic acid) is attached via an amide linkage to an N-terminal glycine. (B) A prenyl group (either farnesyl or a longer geranylgeranyl group) is attached via a thioether linkage to a cysteine residue that is initially located four residues from the protein's C-terminus. After this prenylation, the terminal three amino acids are cleaved off, and the new C-terminus is methylated before insertion into the membrane. Palmitic acid, an 18 carbon saturated fatty acid, can also be attached to some proteins via thioester bonds formed with internal cysteine side chains. This modification is often reversible, allowing proteins to become recruited to membranes only when needed. The structures of two lipid anchors are shown below: (C) a myristyl anchor (a 14-carbon saturated fatty acid chain), and (D) a farnesyl anchor (a 15-carbon unsaturated hydrocarbon chain).

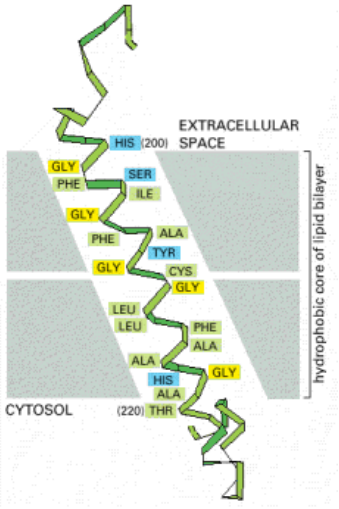

Figure 10-19. A segment of a transmembrane polypeptide chain crossing the lipid bilayer as an α helix. Only the α-carbon backbone of the polypeptide chain is shown, with the hydrophobic amino acids in *green* and *yellow*. The polypeptide segment shown is part of the bacterial photosynthetic reaction center illustrated in Figure 10-38, the structure of which was determined by x-ray diffraction. (Based on data from J. Deisenhofer et al., *Nature* 318:618624, 1985, and H. Michel et al., *EMBO J.* 5:11491158, 1986.)

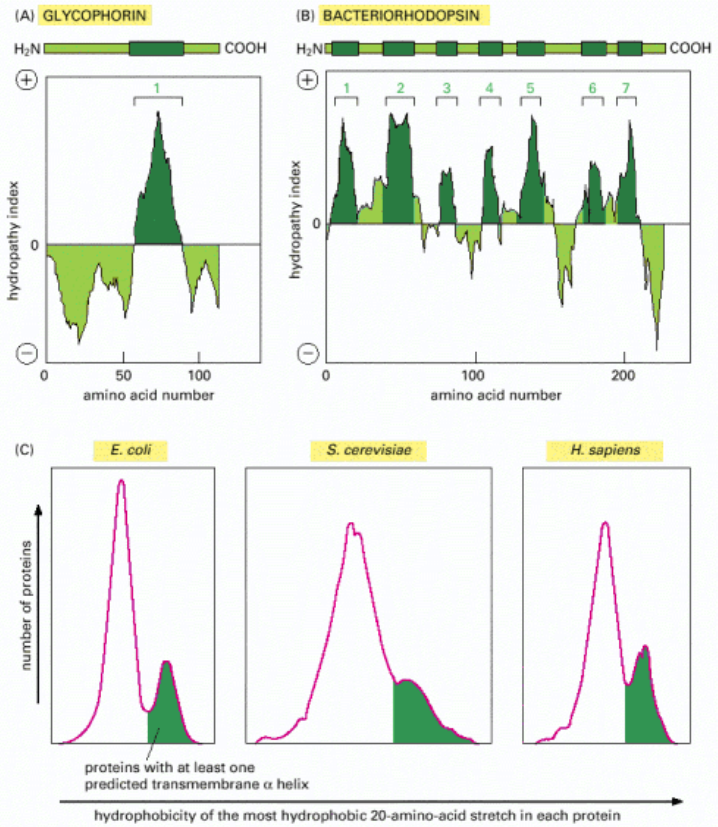

Figure 10-20. Using hydropathy plots to localize potential α-helical membrane-spanning segments in a polypeptide chain. The free energy needed to transfer successive segments of a polypeptide chain from a nonpolar solvent to water is calculated from the amino acid composition of each segment using data obtained with model compounds. This calculation is made for segments of a fixed size (usually around 1020 amino acids), beginning with each successive amino acid in the chain. The "hydropathy index" of the segment is plotted on the y axis as a function of its location in the chain. A positive value indicates that free energy is required for transfer to water (i.e., the segment is hydrophobic), and the value assigned is an index of the amount of energy needed. Peaks in the hydropathy index appear at the positions of hydrophobic segments in the amino acid sequence. (A and B) Two examples of membrane proteins discussed later in this chapter are shown. Glycophorin (A) has a single membrane-spanning α helix and one corresponding peak in the hydropathy plot. Bacteriorhodopsin (B) has seven membrane-spanning α helices and seven corresponding peaks in the hydropathy plot. (C) The proportion of predicted membrane proteins in the genomes of *E. coli*, *S. cerevisiae*, and human. The area shaded in *green* indicates the fraction of proteins that contain at least one predicted transmembrane helix. The curves for *E. coli* and *S. cerevisiae* represent the whole genome; the curve for human proteins represents an incomplete set; in each case, the area under the curve is proportional to the number of genes analysed. (A, adapted from D. Eisenberg, *Annu. Rev. Biochem.* 53:595624, 1984; C, adapted from D. Boyd et al., *Protein Sci.* 7:201205, 1998.)

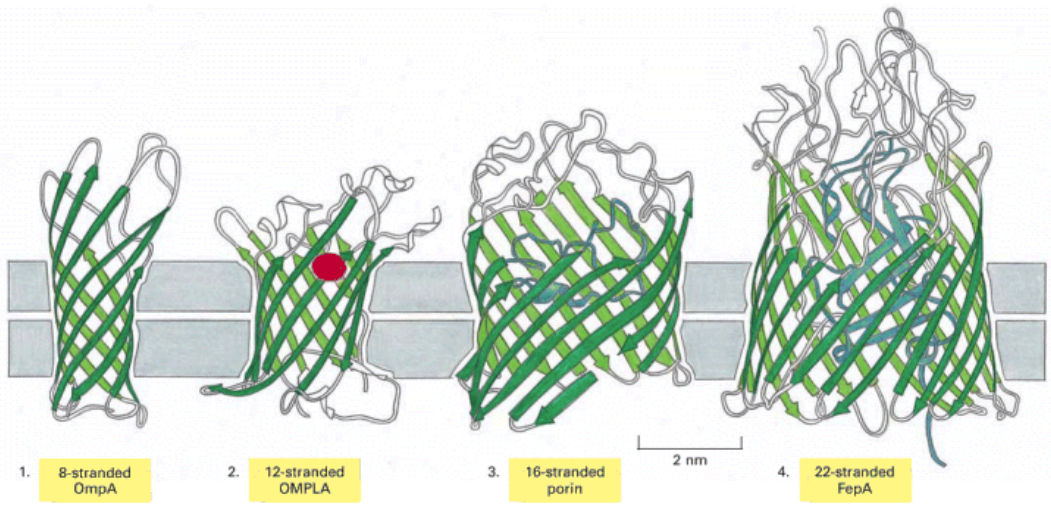

Figure 10-21. β barrels formed from different numbers of β strands. (1) The *E. coli* OmpA protein (8 β strands), which serves as a receptor for a bacterial virus. (2) The *E. coli* OMPLA protein (12 β strands), is a lipase that hydrolyses lipid molecules. The amino acids that catalyze the enzymatic reaction (shown in *red)* protrude from the outside surface of the barrel. (3) A porin from the bacterium *Rhodobacter capsulatus*, which forms water-filled pores across the outer membrane (16 β strands). The diameter of the channel is restricted by loops (shown in *blue)* that protrude into the channel. (4) The *E. coli* FepA protein (22 β strands), which transports iron ions. The inside of the barrel is completely filled by a globular protein domain (shown in *blue)* that contains an iron-binding site. This domain is thought to change its conformation to transport the bound iron, but the molecular details of the changes are not known.

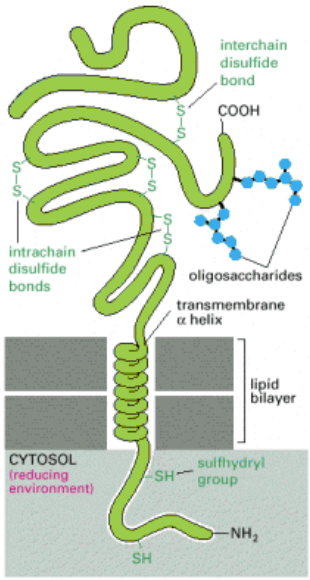

Figure 10-22. A single-pass transmembrane protein. Note that the polypeptide chain traverses the lipid bilayer as a right-handed α helix and that the oligosaccharide chains and disulfide bonds are all on the noncytosolic surface of the membrane. The sulfhydryl groups in the cytosolic domain of the protein do not normally form disulfide bonds because the reducing environment in the cytosol maintains these groups in their reduced (-SH) form.

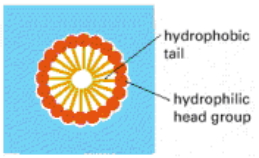

Figure 10-23. A detergent micelle in water, shown in cross section. Because they have both polar and nonpolar ends, detergent molecules are amphipathic. Because they are wedge-shaped, they form micelles rather than bilayers (see Figure 10-4).

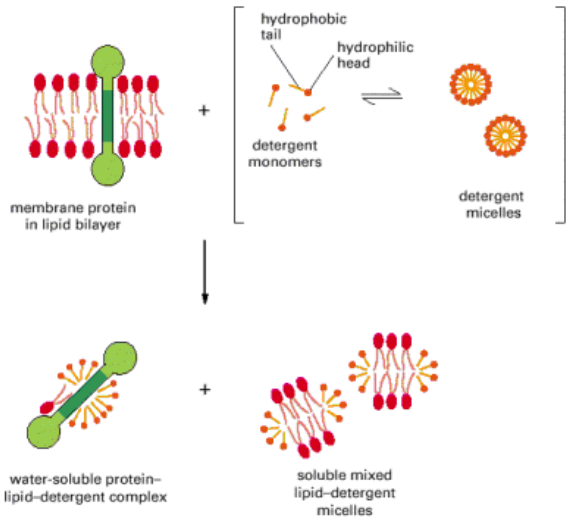

Figure 10-24. Solubilizing membrane proteins with a mild detergent. The detergent disrupts the lipid bilayer and brings the proteins into solution as protein-lipid-detergent complexes. The phospholipids in the membrane are also solubilized by the detergent.

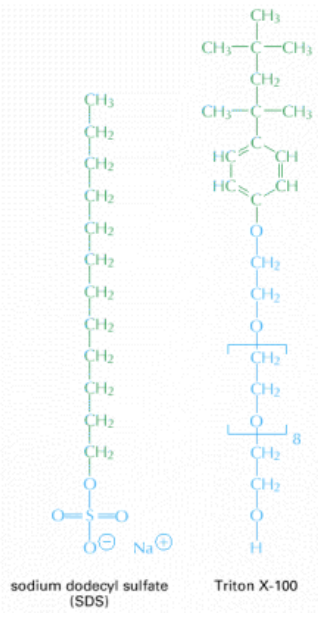

Figure 10-25. The structures of two commonly used detergents. Sodium dodecyl sulfate (SDS) is an anionic detergent, and Triton X-100 is a nonionic detergent. The hydrophobic portion of each detergent is shown in *green*, and the hydrophilic portion is shown in *blue*. The bracketed portion of Triton X-100 is repeated about eight times.

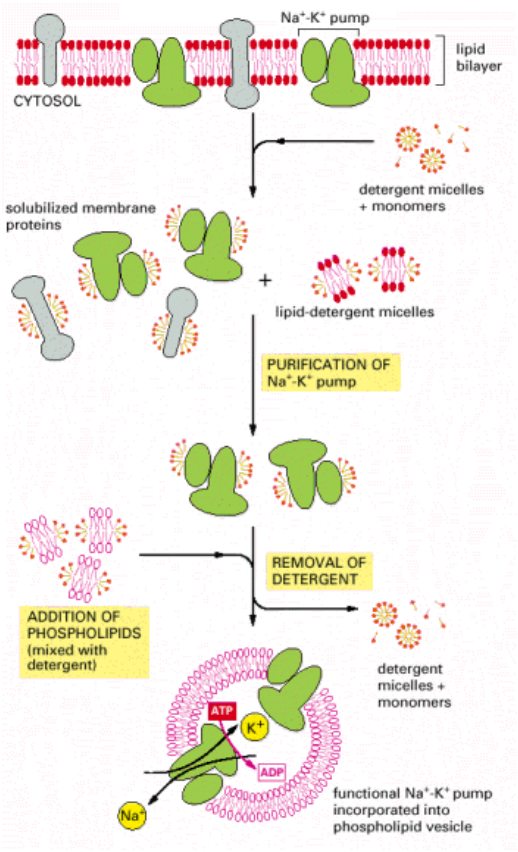

Figure 10-26. The use of mild detergents for solubilizing, purifying, and reconstituting functional membrane protein systems. In this example, functional Na^+-K^+ pump molecules are purified and incorporated into phospholipid vesicles. The Na^+-K^+ pump is an ion pump that is present in the plasma membrane of most animal cells; it uses the energy of ATP hydrolysis to pump Na^+ out of the cell and K^+ in, as discussed in Chapter 11.

Figure 10-27. A scanning electron micrograph of human red blood cells. The cells have a biconcave shape and lack a nucleus and other organelles. (Courtesy of Bernadette Chailley.)

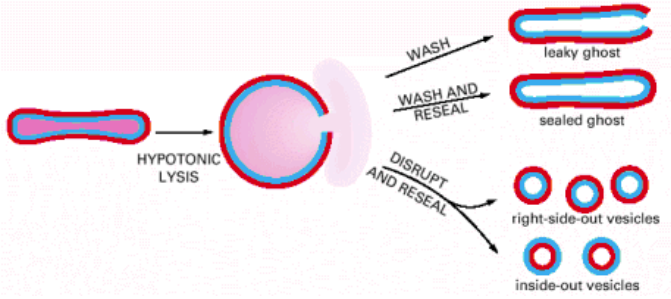

Figure 10-28. The preparation of sealed and unsealed red blood cell ghosts and of right-side-out and inside-out vesicles. As indicated, the red cells tend to rupture in only one place, giving rise to ghosts with a single hole in them. The smaller vesicles are produced by mechanically disrupting the ghosts; the orientation of the membrane in these vesicles can be either right-side-out or inside-out, depending on the ionic conditions used during the disruption and resealing procedures.

Figure 10-29. SDS polyacrylamide-gel electrophoresis pattern of the proteins in the human red blood cell membrane. (A) The gel is stained with Coomassie blue. (B) The positions of some of the major proteins in the gel are indicated in the drawing. Glycophorin is shown in *red* to distinguish it from band 3. Other bands in the gel are omitted from the drawing. The large amount of negatively charged carbohydrate in glycophorin molecules slows their migration so that they run almost as slowly as the much larger band 3 molecules. (A, courtesy of Ted Steck.)

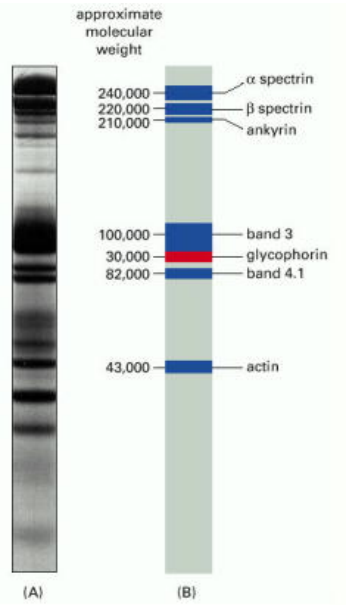

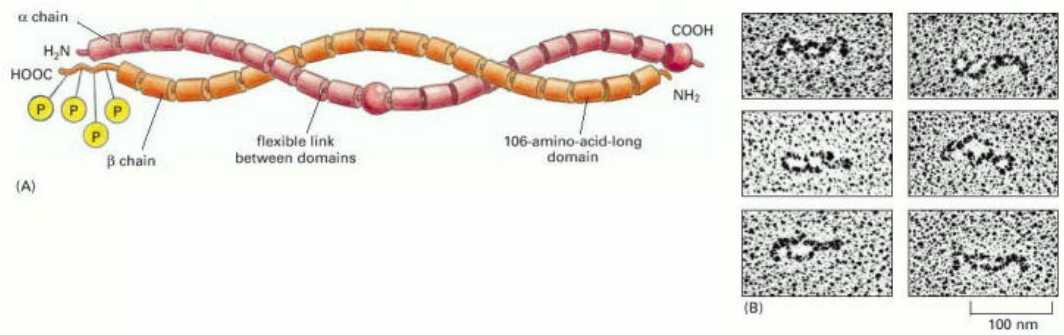

Figure 10-30. Spectrin molecules from human red blood cells. The protein is shown (A) schematically and (B) in electron micrographs. Each spectrin heterodimer consists of two antiparallel, loosely intertwined, flexible polypeptide chains called α and β. These are attached noncovalently to each other at multiple points, including both ends. The phosphorylated "head" end, where two dimers associate to form a tetramer, is on the left. Both the α and the β chains are composed largely of repeating domains 106 amino acids long. In the micrographs, the spectrin molecules have been shadowed with platinum. (A, adapted from D.W. Speicher and V.T. Marchesi, *Nature* 311:177180, 1984; B, courtesy of D.M. Shotton, with permission from D.M. Shotton, B.E. Burke, and D. Branton, *J. Mol. Biol.* 131:303329, 1979. © Academic Press Inc. [London] Ltd.)

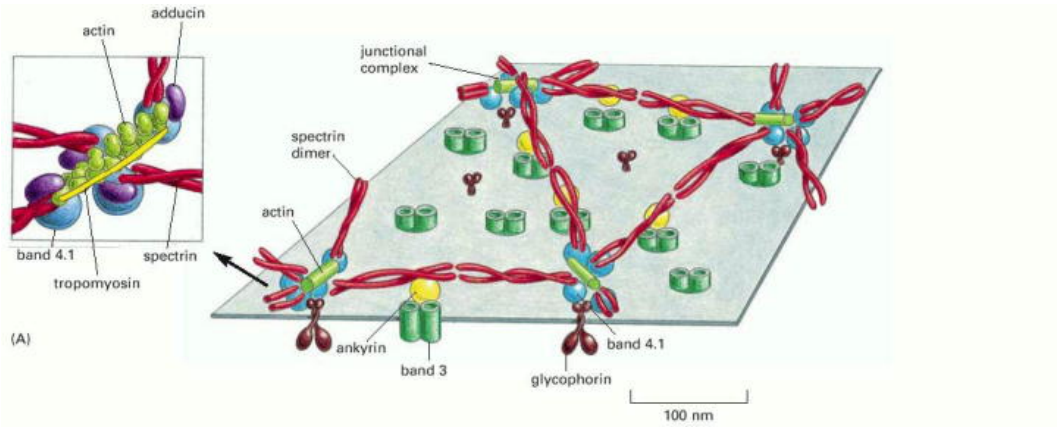

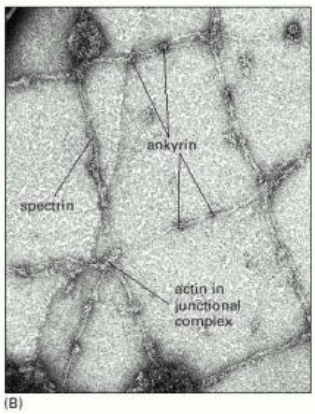

Figure 10-31. The spectrin-based cytoskeleton on the cytosolic side of the human red blood cell membrane. The structure is shown (A) schematically and (B) in an electron micrograph. The arrangement shown in the drawing has been deduced mainly from studies on the interactions of purified proteins *in vitro.* Spectrin dimers are linked together into a netlike meshwork by junctional complexes (enlarged in the box on the *left)* composed of short actin filaments (containing 13 actin monomers), band 4.1, adducin, and a tropomyosin molecule that probably determines the length of the actin filaments. The cytoskeleton is linked to the membrane by the indirect binding of spectrin tetramers to some band 3 proteins via ankyrin molecules, as well as by the binding of band 4.1 proteins to both band 3 and glycophorin (not shown). The electron micrograph shows the cytoskeleton on the cytosolic side of a red blood cell membrane after fixation and negative staining. The spectrin meshwork has been purposely stretched out to allow the details of its structure to be seen. In a normal cell, the meshwork shown would be much more crowded and occupy only about one-tenth of this area. (B, courtesy of T. Byers and D. Branton, *Proc. Natl. Acad. Sci. USA* 82:61536157, 1985. © National Academy of Sciences.)

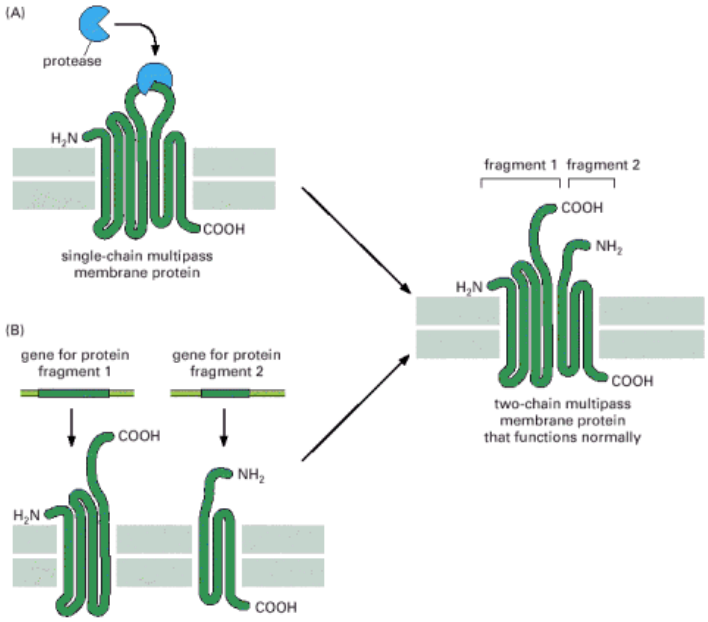

Figure 10-32. Converting a single-chain multipass protein into a two-chain multipass protein. (A) Proteolytic cleavage of one loop to create two fragments that stay together and function normally. (B) Expression of the same two fragments from separate genes gives rise to a similar protein that functions normally.

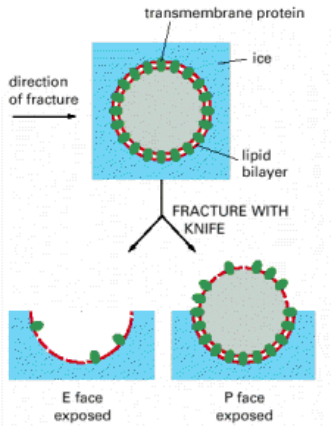

Figure 10-33. Freeze-fracture electron microscopy. This drawing shows how the technique provides images of both the hydrophobic interior of the cytosolic half of the bilayer (the P face) and the hydrophobic interior of the external half of the bilayer (the E face). After the fracturing process, the exposed fracture faces are shadowed with platinum and carbon, the organic material is digested away, and the resulting platinum replica is examined in an electron microscope (see also Figure 9-32).

Figure 10-34. Freeze-fracture electron micrograph of human red blood cells. Note that the density of intramembrane particles on the cytosolic (P) face is higher than on the external (E) face. (Courtesy of L. Engstrom and D. Branton.)

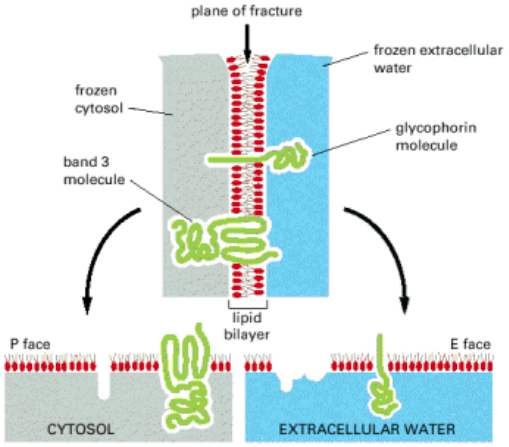

Figure 10-35. Probable fates of band 3 and glycophorin molecules in the human red blood cell membrane during freeze-fracture. When the lipid bilayer is split, either the inside or the outside half of each transmembrane protein is pulled out of the frozen monolayer with which it is associated; the protein tends to remain with the monolayer that contains the main bulk of the protein. For this reason, band 3 molecules usually remain with the inner (P) face; since they have sufficient mass above the fracture plane, they are readily seen as intramembrane particles. Glycophorin molecules usually remain with the outer (E) face, but it is thought that their cytosolic tails have insufficient mass to be seen.

Figure 10-36. Drawing of the archaean *Halobacterium salinarum* showing the patches of purple membrane that contain bacteriorhodopsin molecules. These archaeans, which live in saltwater pools where they are exposed to sunlight, have evolved a variety of light-activated proteins, including bacteriorhodopsin, which is a light-activated proton pump in the plasma membrane.

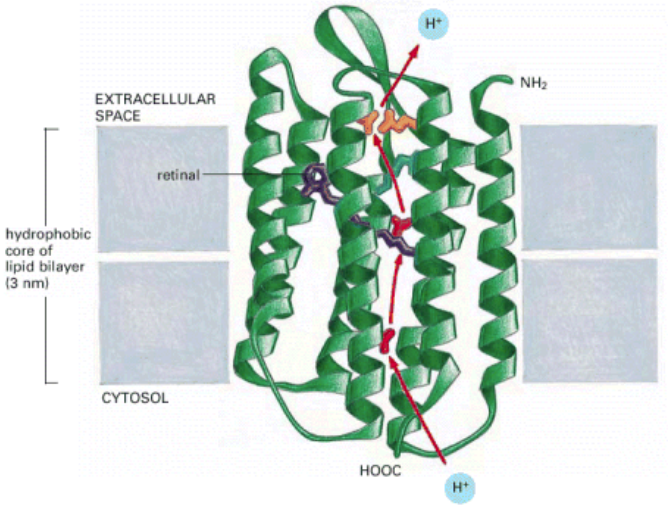

Figure 10-37. The three-dimensional structure of a bacteriorhodopsin molecule. The polypeptide chain crosses the lipid bilayer seven times as α helices. The location of the retinal chromophore *(purple)* and the probable pathway taken by protons during the light-activated pumping cycle are shown. The first and key step is the passing of a H^+ from the chromophore to the side chain of aspartic acid 85 *(red,* located next to the chromophore) that occurs upon absorption of a photon by the chromophore. Subsequently, other H^+ transfers - utilizing the hydrophilic amino acid side chains that line a path through the membrane - complete the pumping cycle and return the enzyme to its starting state. Color code: glutamic acid *(orange),* aspartic acid *(red),* arginine *(blue).* (Adapted from H. Luecke et al., *Science* 286:255260, 1999.)

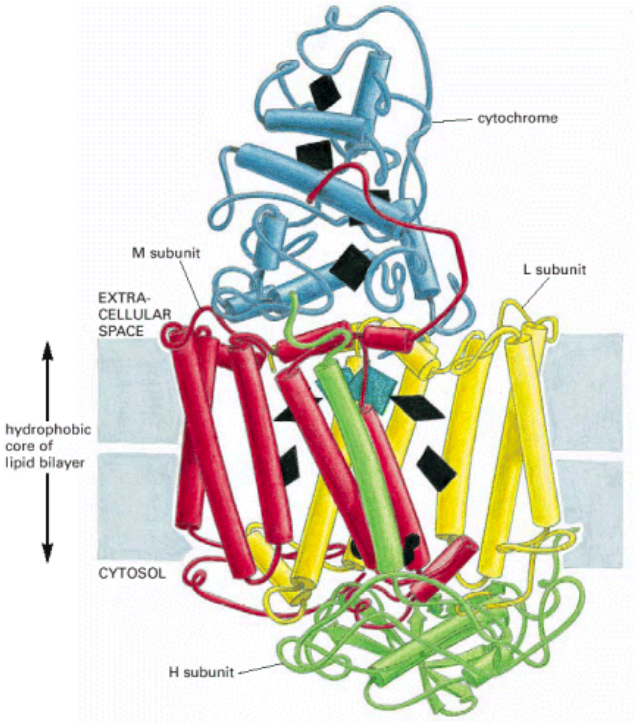

Figure 10-38. The three-dimensional structure of the photosynthetic reaction center of the bacterium *Rhodopseudomonas viridis.* The structure was determined by x-ray diffraction analysis of crystals of this transmembrane protein complex. The complex consists of four subunits L, M, H, and a cytochrome. The L and M subunits form the core of the reaction center, and each contains five α helices that span the lipid bilayer. The locations of the various electron carrier coenzymes are shown in *black.* Note that the coenzymes are arranged in the spaces between the helices. (Adapted from a drawing by J. Richardson based on data from J. Deisenhofer, O. Epp, K. Miki, R. Huber, and H. Michel, *Nature* 318:618624, 1985.)

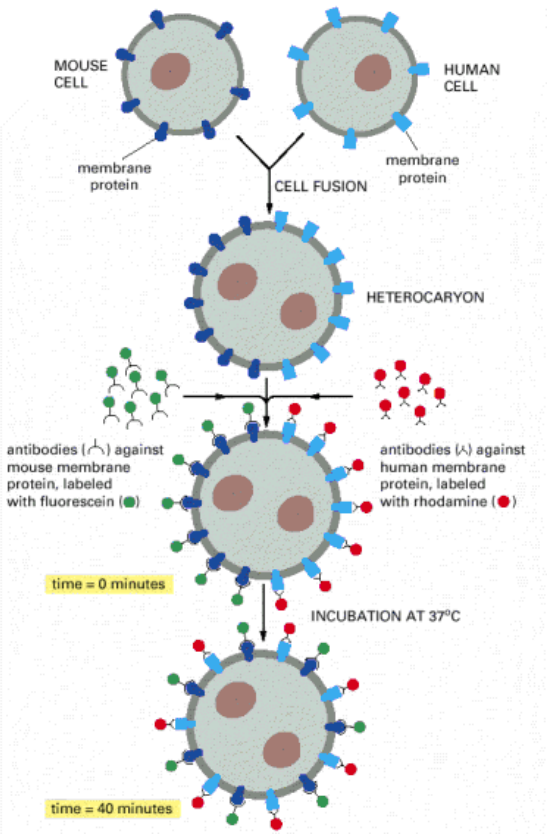

Figure 10-39. An experiment demonstrating the mixing of plasma membrane proteins on mouse-human hybrid cells. The mouse and human proteins are initially confined to their own halves of the newly formed heterocaryon plasma membrane, but they intermix with time. The two antibodies used to visualize the proteins can be distinguished in a fluorescence microscope because fluorescein is green whereas rhodamine is red. (Based on observations of L.D. Frye and M. Edidin, *J. Cell Sci.* 7:319335, 1970. © The Company of Biologists.)

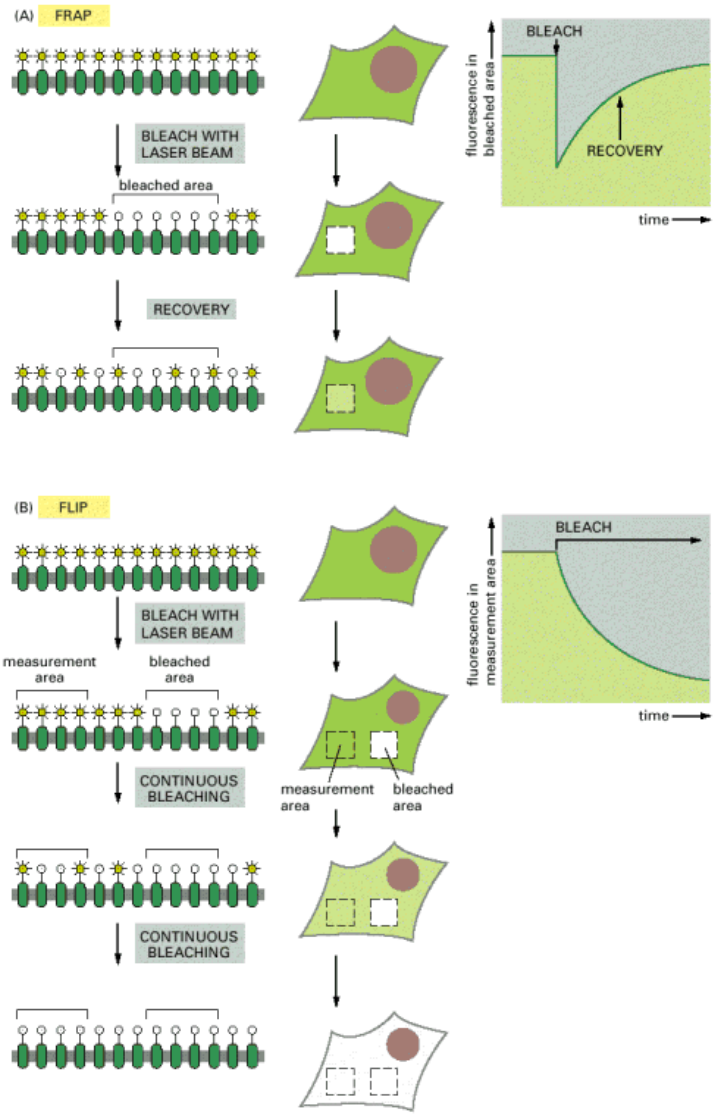

Figure 10-40. Measuring the rate of lateral diffusion of a membrane protein by photobleaching techniques. A specific protein of interest can be labeled with a fluorescent antibody (as shown here), or it can be expressed as a fusion protein with green fluorescent protein (GFP), which is intrinsically fluorescent. (A) In the FRAP technique, fluorescent molecules are bleached in a small area using a laser beam. The fluorescence intensity recovers as the bleached molecules diffuse away and unbleached molecules diffuse into the irradiated area (shown here in side and top views). The diffusion coefficient is calculated from a graph of the rate of recovery: the greater the diffusion coefficient of the membrane protein, the faster the recovery. (B) In the FLIP technique, an area in the membrane is irradiated continuously, and fluorescence is measured in a separate area. Fluorescence in the second area progressively decreases as fluorescent proteins diffuse out and bleached molecules diffuse in; eventually, all of the fluorescent protein molecules will be bleached, as long as they are mobile and not permanently anchored to the cytoskeleton or extracellular matrix.

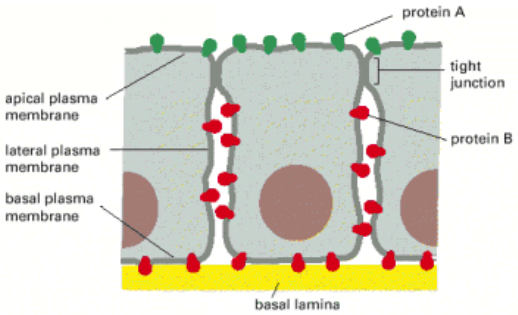

Figure 10-41. How a plasma membrane protein is restricted to a particular membrane domain. In this drawing of an epithelial cell, protein A (in the apical membrane) and protein B (in the basal and lateral membranes) can diffuse laterally in their own domains but are prevented from entering the other domain, at least partly by the specialized cell junction called a tight junction. Lipid molecules in the outer (noncytosolic) monolayer of the plasma membrane are likewise unable to diffuse between the two domains; lipids in the inner (cytosolic) monolayer, however, are able to do so (not shown).

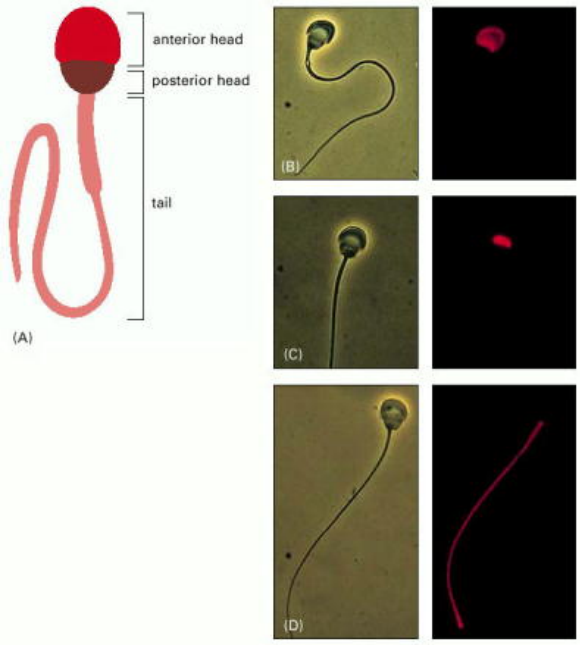

Figure 10-42. Three domains in the plasma membrane of a guinea pig sperm cell. (A) A basic drawing of a guinea pig sperm. In the three pairs of micrographs, phase-contrast micrographs are on the *left*, and the same cell is shown with cell-surface immunofluorescence staining on the *right.* Different monoclonal antibodies label selectively cell-surface molecules on (B) the anterior head, (C) the posterior head, and (D) the tail. (Micrographs courtesy of Selena Carroll and Diana Myles.)

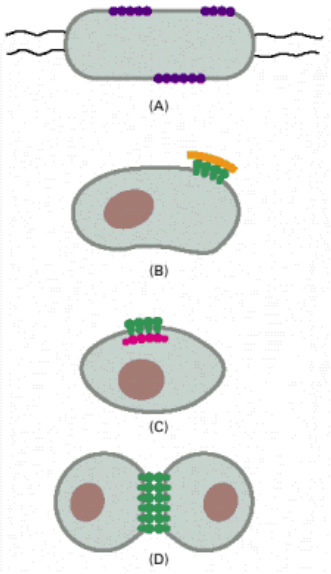

Figure 10-43. Four ways of restricting the lateral mobility of specific plasma membrane proteins. (A) The proteins can self-assemble into large aggregates (as seen for bacteriorhodopsin in the purple membrane of *Halobacterium);* they can be tethered by interactions with assemblies of macromolecules (B) outside or (C) inside the cell; or they can interact with proteins on the surface of another cell (D).

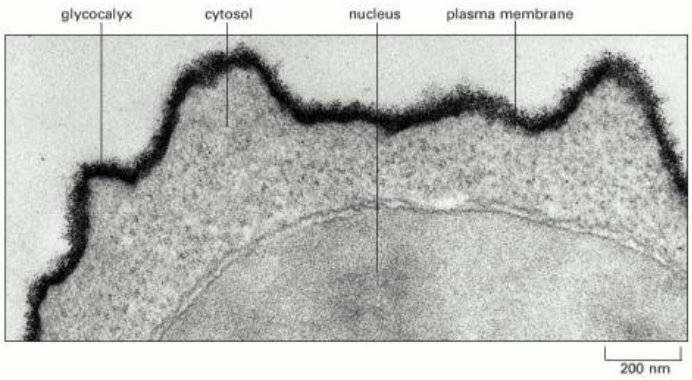

Figure 10-44. The cell coat, or glycocalyx. This electron micrograph of the surface of a lymphocyte stained with ruthenium red emphasizes the thick carbohydrate layer surrounding the cell. (Courtesy of Audrey M. Glauert and G.M.W. Cook.)

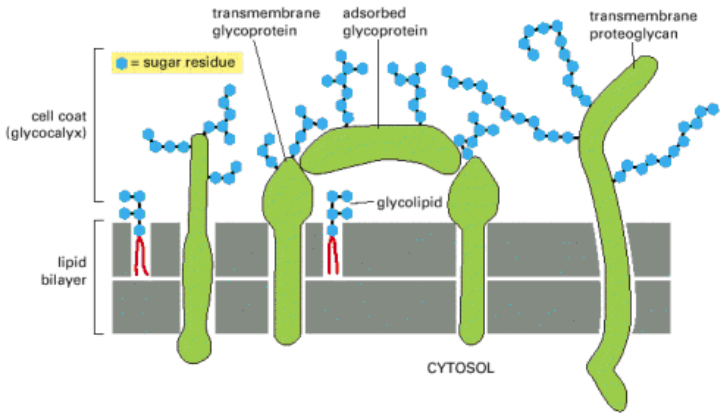

Figure 10-45. Simplified diagram of the cell coat (glycocalyx). The cell coat is made up of the oligosaccharide side chains of glycolipids and integral membrane glycoproteins and the polysaccharide chains on integral membrane proteoglycans. In addition, adsorbed glycoproteins and adsorbed proteoglycans (not shown) contribute to the glycocalyx in many cells. Note that all of the carbohydrate is on the noncytosolic surface of the membrane.

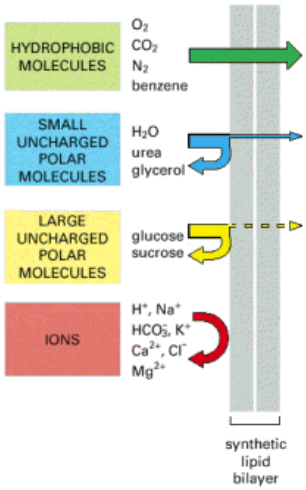

Figure 11-1. The relative permeability of a synthetic lipid bilayer to different classes of molecules. The smaller the molecule and, more importantly, the less strongly it associates with water, the more rapidly the molecule diffuses across the bilayer.

Figure 11-2. Permeability coefficients for the passage of various molecules through synthetic lipid bilayers. The rate of flow of a solute across the bilayer is directly proportional to the difference in its concentration on the two sides of the membrane. Multiplying this concentration

difference (in mol/cm^3) by the permeability coefficient (in cm/sec) gives the flow of solute in moles per second per square centimeter of membrane. A concentration difference of tryptophan of 10^{-4} mol/cm^3 ($10^{-4}/10^{-3}$ L = 0.1 M), for example, would cause a flow of 10^{-4} mol/cm^3 × 10^{-7} cm/sec = 10^{-11} mol/sec through 1 cm^2 of membrane, or 6×10^4 molecules/sec through 1 μm^2 of membrane.

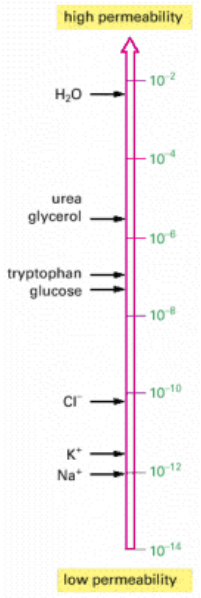

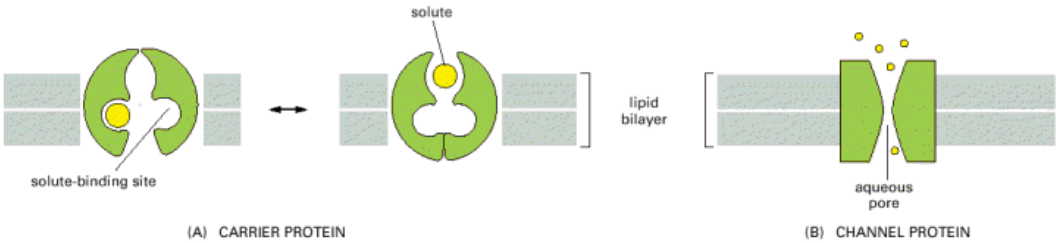

Figure 11-3. Carrier proteins and channel proteins. (A) A carrier protein alternates between two conformations, so that the solute-binding site is sequentially accessible on one side of the bilayer and then on the other. (B) In contrast, a channel protein forms a water-filled pore across the bilayer through which specific solutes can diffuse.

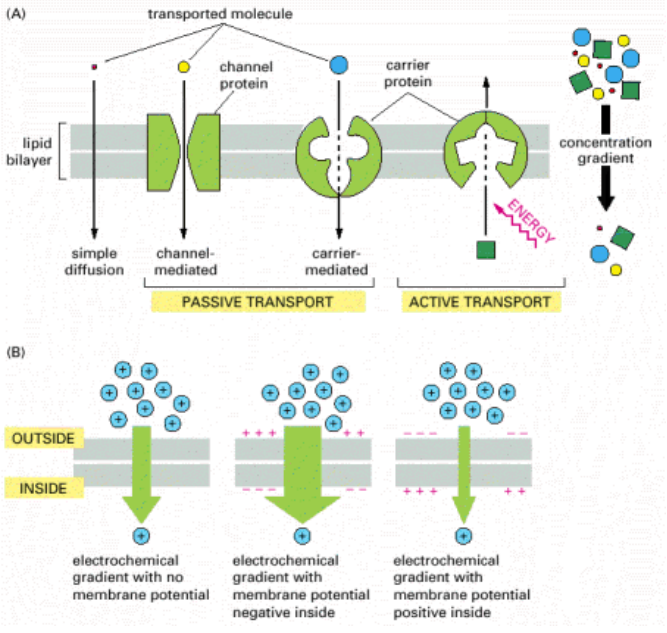

Figure 11-4. Passive and active transport compared. (A) Passive transport down an electrochemical gradient occurs spontaneously, either by simple diffusion through the lipid bilayer or by facilitated diffusion through channels and passive carriers. By contrast, active transport requires an input of metabolic energy and is always mediated by carriers that harvest metabolic energy to pump the solute against its electrochemical gradient. (B) An electrochemical gradient combines the membrane potential and the concentration gradient, which can work additively to increase the driving force on an ion across the membrane *(middle)* or can work against each other *(right)*.

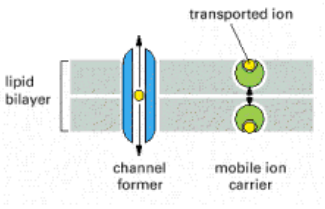

Figure 11-5. Ionophores: a channel-former and a mobile ion carrier. In both cases, net ion flow occurs only down an electrochemical gradient.

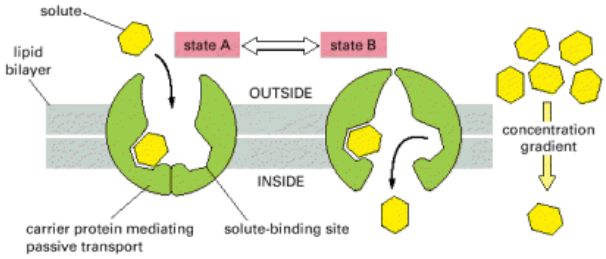

Figure 11-6. A model of how a conformational change in a carrier protein could mediate the passive transport of a solute. The carrier protein shown can exist in two conformational states: in state A, the binding sites for solute are exposed on the outside of the lipid bilayer; in state B, the same sites are exposed on the other side of the bilayer. The transition between the two states can occur randomly. It is completely reversible and does not depend on whether the solute binding site is occupied. Therefore, if the solute concentration is higher on the outside of the bilayer, more solute binds to the carrier protein in the A conformation than in the B conformation, and there is a net transport of solute down its concentration gradient (or, if the solute is an ion, down its electrochemical gradient).

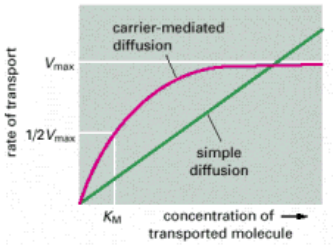

Figure 11-7. The kinetics of simple diffusion and carrier-mediated diffusion. Whereas the rate of the former is always proportional to the solute concentration, the rate of the latter reaches a maximum (V_{max}) when the carrier protein is saturated. The solute concentration when transport is at half its maximal value approximates the binding constant (K_m) of the carrier for the solute and is analogous to the K_m of an enzyme for its substrate. The graph applies to a carrier transporting a single solute; the kinetics of coupled transport of two or more solutes (see text) is more complex but shows basically similar phenomena.

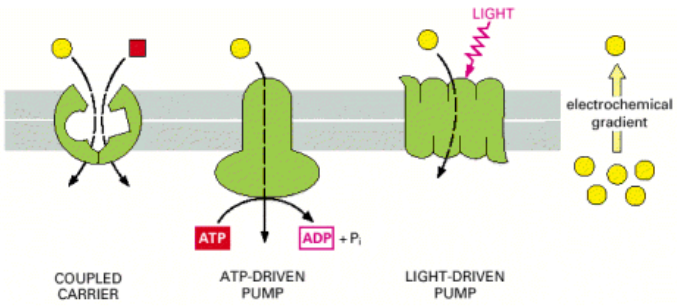

Figure 11-8. Three ways of driving active transport. The actively transported molecule is shown in *yellow*, and the energy source is shown in *red*.

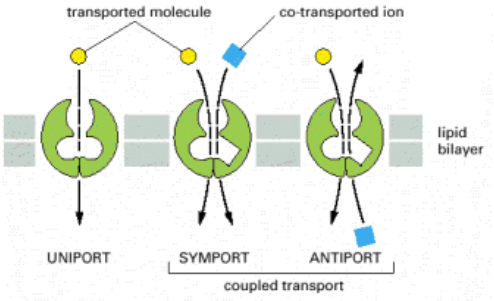

Figure 11-9. Three types of carrier-mediated transport. This schematic diagram shows carrier proteins functioning as uniporters, symporters, and antiporters.

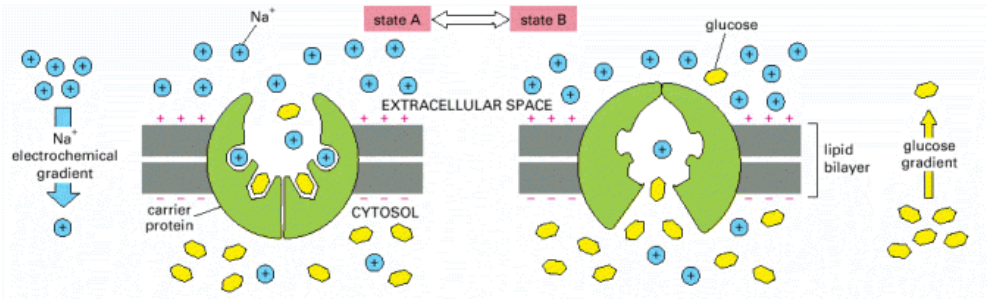

Figure 11-10. One way in which a glucose carrier can be driven by a Na^+ gradient. As in the model shown in Figure 11-6, the carrier oscillates between two alternate states, A and B. In the A state, the protein is open to the extracellular space; in the B state, it is open to the cytosol. Binding of Na^+ and glucose is cooperative - that is, the binding of either ligand induces a conformational change that greatly increases the protein's affinity for the other ligand. Since the Na^+ concentration is much higher in the extracellular space than in the cytosol, glucose is more likely to bind to the carrier in the A state. Therefore, both Na^+ and glucose enter the cell (via an A B transition) much more often than they leave it (via a B A transition). The overall result is the net transport of both Na^+ and glucose into the cell. Note that because the binding is cooperative, if one of the two solutes is missing, the other fails to bind to the carrier. Thus, the carrier undergoes a conformational switch between the two states only if both solutes or neither are bound.

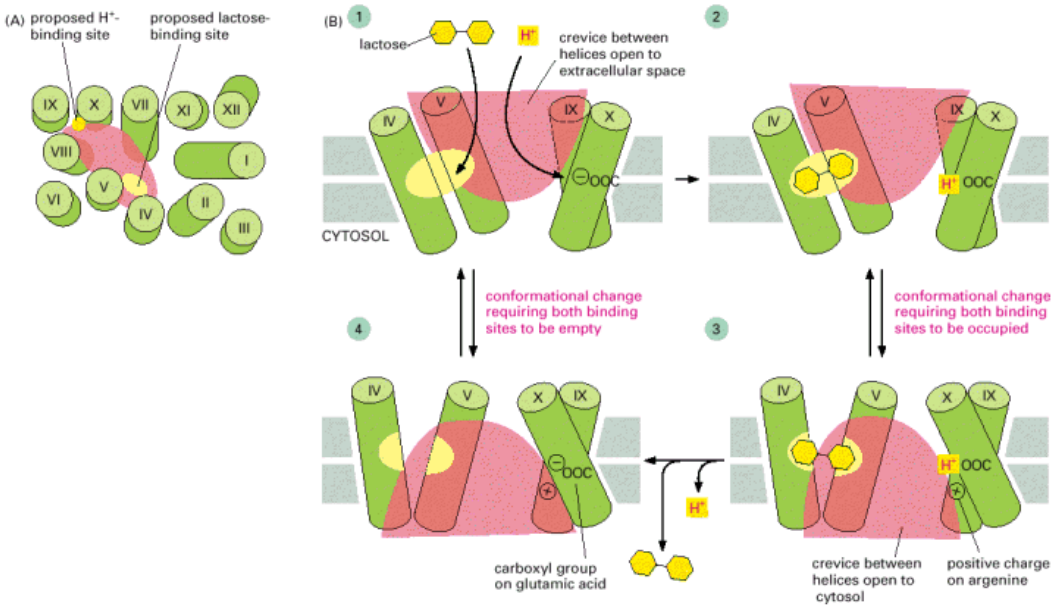

Figure 11-11. A model for the molecular mechanism of action of the bacterial lactose permease. (A) A view from the cytosol of the proposed arrangement of the 12 predicted transmembrane helices in the membrane. The loops that connect the helices on either side of the membrane are omitted for clarity. A glutamic acid on helix X binds H^+, and amino acids contributed by helices IV and V bind lactose. (B) During a transport cycle, the carrier flips between two conformational states: in one, the H^+ - and lactose-binding sites are accessible to the extracellular space (1 and 2); in the other, they are exposed to the cytosol (3 and 4). Unloading of the solutes on the cytosolic face (3 4) is favored because the lactose-binding site is partly disrupted and a positive charge contributed by an arginine on helix IX displaces the H^+ from the glutamic acid on helix X. (A, adapted from H.R. Kaback and J. Wu, *Accts. Chem. Res.* 32:805-813, 1999.)

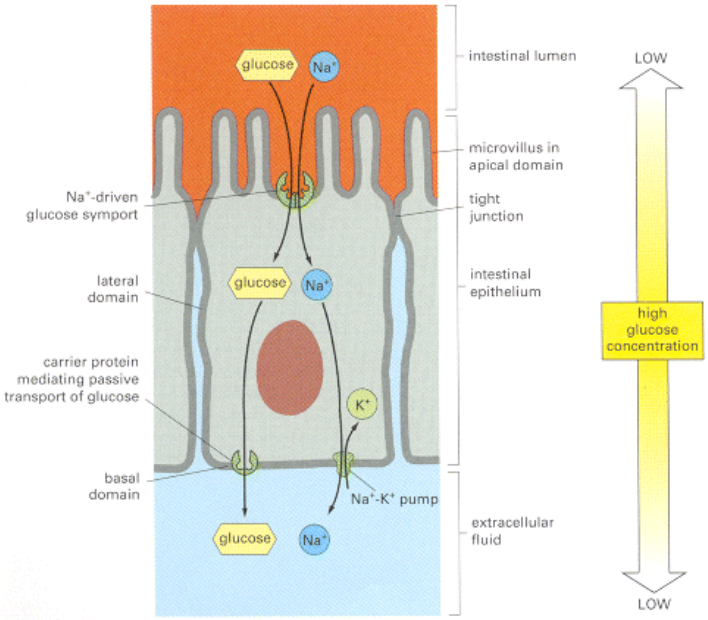

Figure 11-12. Transcellular transport. The transcellular transport of glucose across an intestinal epithelial cell depends on the nonuniform distribution of transport proteins in the cell's plasma membrane. The process shown here results in the transport of glucose from the intestinal lumen to the extracellular fluid (from where it passes into the blood). Glucose is pumped into the cell through the apical domain of the membrane by a Na^+ -powered glucose symport. Glucose passes out of the cell (down its concentration gradient) by passive transport mediated by a different glucose carrier protein in the basal and lateral membrane domains. The Na^+ gradient driving the glucose symport is maintained by a Na^+ pump in the basal and lateral plasma membrane domains, which keeps the internal concentration of Na^+ low. Adjacent cells are connected by impermeable tight junctions, which have a dual function in the transport process illustrated: they prevent solutes from crossing the epithelium between cells, allowing a concentration gradient of glucose to be maintained across the cell sheet, and they also serve as diffusion barriers within the plasma membrane, which help confine the various carrier proteins to their respective membrane domains (see Figure 10-41).

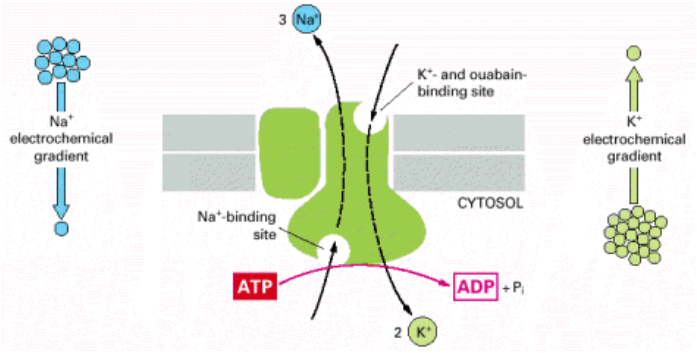

Figure 11-13. The Na^+-K^+pump. This carrier protein actively pumps Na^+ out of and K^+ into a cell against their electrochemical gradients. For every molecule of ATP hydrolyzed inside the cell, three Na^+ are pumped out and two K^+ are pumped in. The specific inhibitor ouabain and K^+ compete for the same site on the extracellular side of the pump.

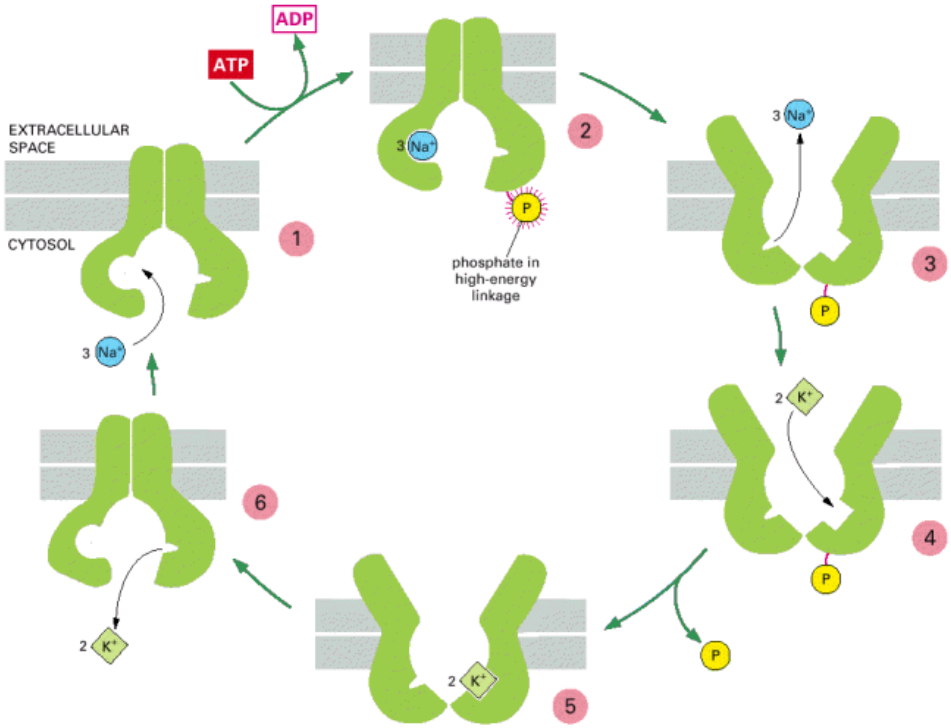

Figure 11-14. A model of the pumping cycle of the Na^+ -K^+ pump. (1) The binding of Na^+ and (2) the subsequent phosphorylation by ATP of the cytoplasmic face of the pump induce the protein to undergo a conformational change that (3) transfers the Na^+ across the membrane and releases it on the outside. (4) Then, the binding of K^+ on the extracellular surface and (5) the subsequent dephosphorylation return the protein to its original conformation, which (6) transfers the K^+ across the membrane and releases it into the cytosol. These changes in conformation are analogous to the A B transitions shown in Figure 11-6, except that here the Na^+ -dependent phosphorylation and the K^+ -dependent dephosphorylation of the protein cause the conformational transitions to occur in an orderly manner, enabling the protein to do useful work. Although for simplicity only one Na^+ - and one K^+ -binding site are shown, in the real pump there are thought to be three Na^+ - and two K^+ -binding sites. Moreover, although the pump is shown as alternating between two conformational states only, there is evidence that it goes through a more complex series of conformational changes during the pumping cycle.

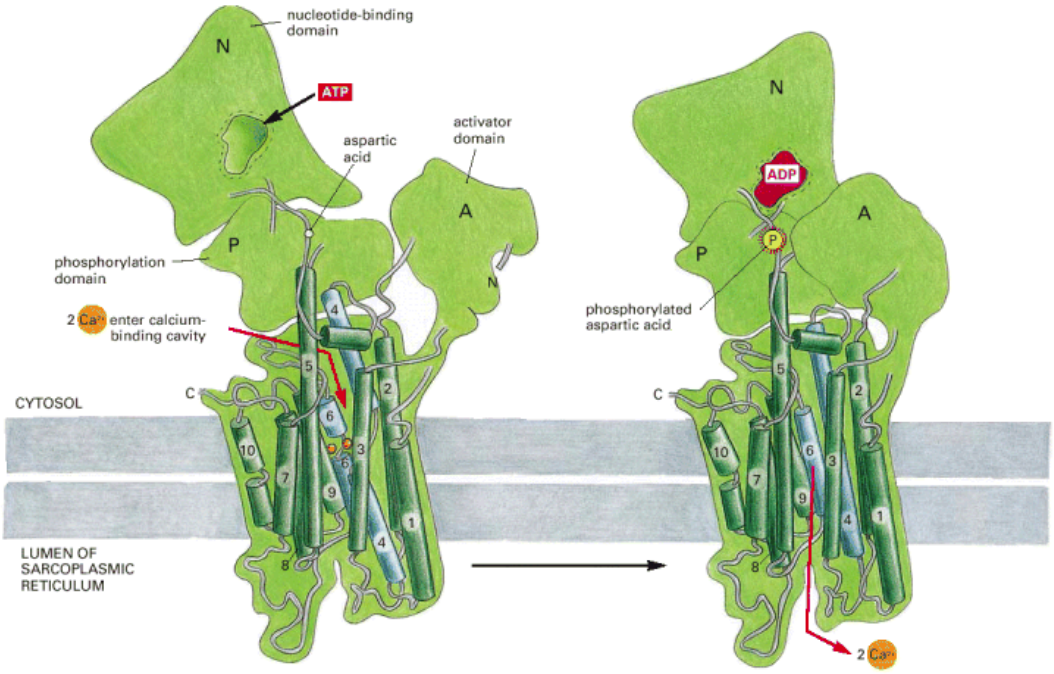

Figure 11-15. A model of how the sarcoplasmic reticulum Ca^{2+} pump moves Ca^{2+}. The structure of the unphosphorylated Ca^{2+} -bound state *(left)* is based on the X-ray crystallographic structure of the pump. The structure of the phosphorylated, Ca^{2+} -free state *(right)* is based on lower-resolution structures determined by electron microscopy, and so the arrangement of the transmembrane helices is speculative. Helices 4 and 6 are disrupted in the unphosphorylated state and form the Ca^{2+} -binding site on the cytosolic side of the membrane. ATP binding and hydrolysis cause drastic conformational changes, bringing the nucleotide-binding (N) and phosphorylation (P) domains into close proximity. This change is thought to cause a 90° rotation of the actuator domain (A), which leads to a rearrangement of the transmembrane helices. The rearrangement eliminates the breaks in helices 4 and 6 abolishing the Ca^{2+} -binding sites and releasing the Ca^{2+} ions on the other side of the membrane into the lumen of the sarcoplasmic reticulum. (Adapted from C. Toyoshima et al., *Nature* 405:647655, 2000.)

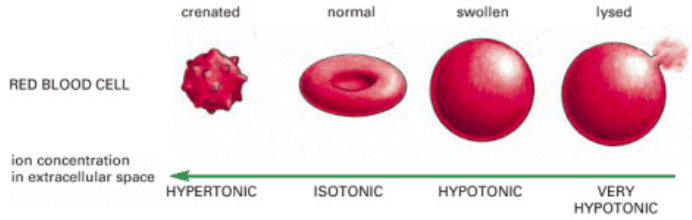

Figure 11-16. Response of a human red blood cell to changes in osmolarity of the extracellular fluid. The cell swells or shrinks as water moves into or out of the cell down its concentration gradient.

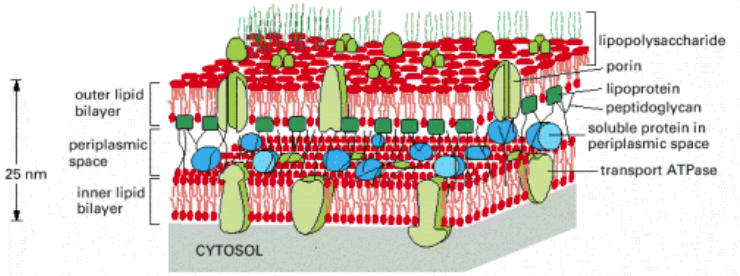

Figure 11-17. A small section of the double membrane of an *E. coli* bacterium. The inner membrane is the cell's plasma membrane. Between the inner and outer lipid bilayer membranes is a highly porous, rigid peptidoglycan, composed of protein and polysaccharide, that constitutes the bacterial cell wall. It is attached to lipoprotein molecules in the outer membrane and fills the *periplasmic space* (only a little of the peptidoglycan is shown). This space also contains a variety of soluble protein molecules. The dashed threads (shown in *green)* at the top represent the polysaccharide chains of the special lipopolysaccharide molecules that form the external monolayer of the outer membrane; for clarity, only a few of these chains are shown. Bacteria with double membranes are called *Gram-negative* because they do not retain the dark blue dye used in Gram staining. Bacteria with single membranes (but thicker cell walls), such as staphylococci and streptococci, retain the blue dye and therefore are called *Gram-positive;* their single membrane is analogous to the inner (plasma) membrane of Gram-negative bacteria.

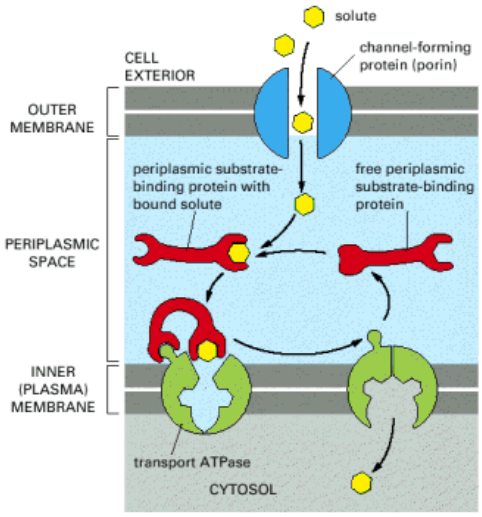

Figure 11-18. The auxiliary transport system associated with transport ATPases in bacteria with double membranes. The solute diffuses through channel-forming proteins (porins) in the outer membrane and binds to a *periplasmic substrate-binding protein.* As a result, the substrate-binding protein undergoes a conformational change that enables it to bind to an ABC transporter in the plasma membrane, which then picks up the solute and actively transfers it across the bilayer in a reaction driven by ATP hydrolysis. The peptidoglycan is omitted for simplicity; its porous structure allows the substrate-binding proteins and water-soluble solutes to move through it by simple diffusion.

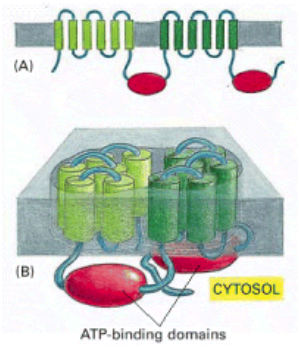

Figure 11-19. A typical ABC transporter. (A) A topology diagram. (B) A hypothetical arrangement of the polypeptide chain in the membrane. The transporter consists of four domains: two highly hydrophobic domains, each with six putative membrane-spanning segments that somehow form the translocation pathway, and two ATP-binding catalytic domains (or cassettes). In some cases the two halves of the transporter are formed by a single polypeptide (as shown), whereas in other cases they are formed by two or more separate polypeptides that assemble into a similar structure (see Figure 10-32).

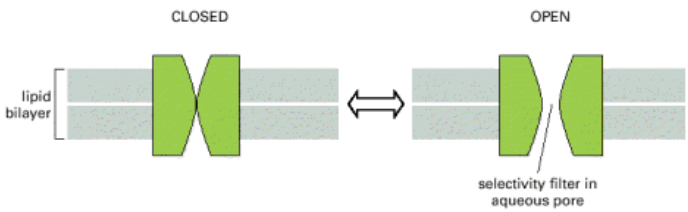

Figure 11-20. A typical ion channel, which fluctuates between closed and open conformations. The channel protein shown here in cross section forms a hydrophilic pore across the lipid bilayer only in the "open" conformational state. Polar groups are thought to line the wall of the pore, while hydrophobic amino acid side chains interact with the lipid bilayer (not shown). The pore narrows to atomic dimensions in one region (the selectivity filter), where the ion selectivity of the channel is largely determined.

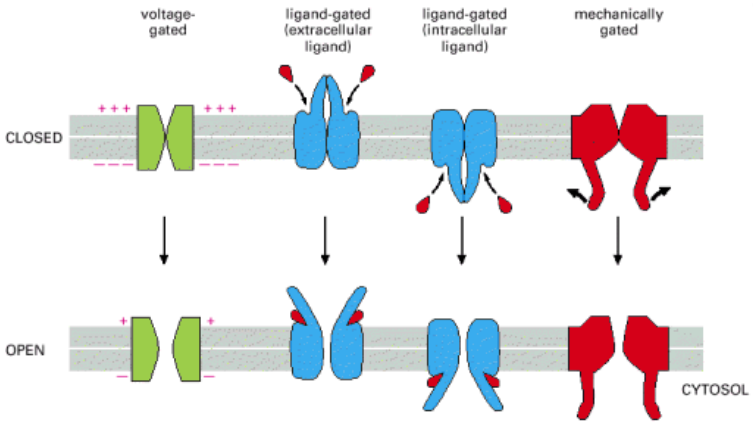

Figure 11-21. The gating of ion channels. This drawing shows different kinds of stimuli that open ion channels. Mechanically gated channels often have cytoplasmic extensions that link the channel to the cytoskeleton (not shown).

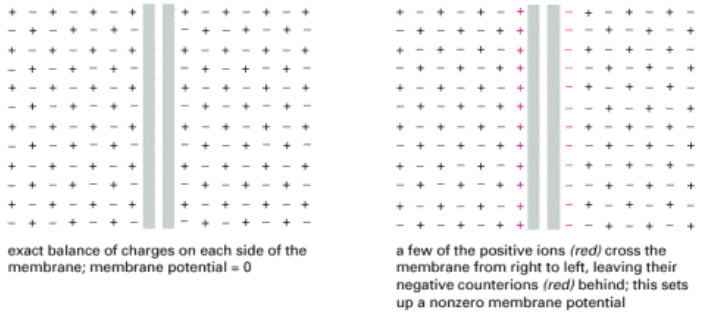

Figure 11-22. The ionic basis of a membrane potential. A small flow of ions carries sufficient charge to cause a large change in the membrane potential. The ions that give rise to the membrane potential lie in a thin (< 1 nm) surface layer close to the membrane, held there by their electrical attraction to their oppositely charged counterparts (counterions) on the other side of the membrane. For a typical cell, 1 microcoulomb of charge (6×10^{12}monovalent ions) per square centimeter of membrane, transferred from one side of the membrane to the other, changes the membrane potential by roughly 1 V. This means, for example, that in a spherical cell of diameter 10 μm, the number of K^+ ions that have to flow out to alter the membrane potential by 100 mV is only about 1/100,000 of the total number of K^+ ions in the cytosol.

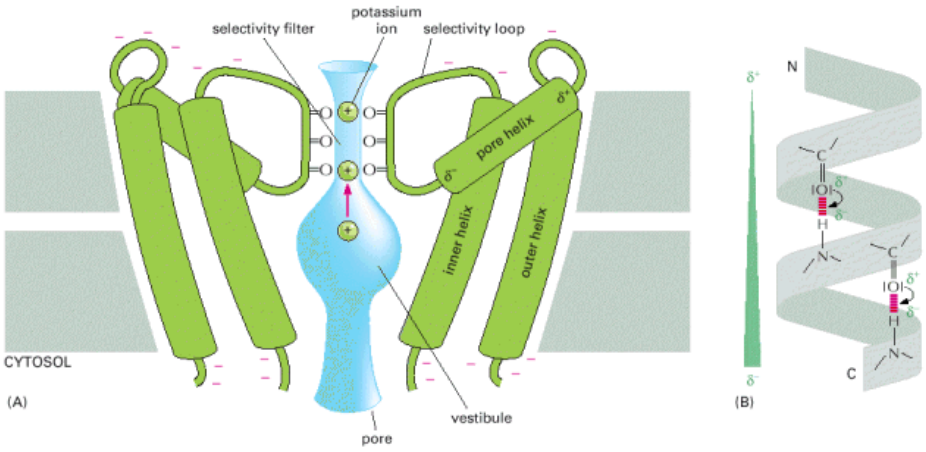

Figure 11-23. The structure of a bacterial K^+ channel. (A) Only two of the four identical subunits are shown. From the cytosolic side, the pore opens up into a vestibule in the middle of the membrane. The vestibule facilitates transport by allowing the K^+ ions to remain hydrated even though they are halfway across the membrane. The narrow selectivity filter links the vestibule to the outside of the cell. Carbonyl oxygens line the walls of the selectivity filter and form transient binding sites for dehydrated K^+ ions. The positions of the K^+ ions in the pore were determined by soaking crystals of the channel protein in a solution containing rubidium ions, which are more electron-dense but only slightly larger than K^+ ions; from the differences in the diffraction patterns with K^+ ions and with rubidium ions in the channel, the positions of the ions could be calculated. Two K^+ ions occupy sites in the selectivity filter, while a third K^+ ion is located in the center of the vestibule, where it is stabilized by electrical interactions with the more negatively charged ends of the pore helices. The ends of the four pore helices point precisely toward the center of the vestibule, thereby guiding K^+ ions into the selectivity filter. (B) Because of the polarity of the hydrogen bonds (in *red)* that link adjacent turns of an α helix, every α helix has an electric dipole along its axis, with a more negatively charged C-terminal end (δ^-) and a more positively charged N-terminal end (δ^+). (A, Adapted from D.A. Doyle et al., *Science* 280:6977, 1998.)

Figure 11-24. K^+ specificity of the selectivity filter in a K^+ channel. The drawing shows K^+ and Na^+ ions (A) in the vestibule and (B) in the selectivity filter of the pore, viewed in cross section. In the vestibule, the ions are hydrated. In the selectivity filter, the carbonyl oxygens are placed

precisely to accommodate a dehydrated K^+ ion. The dehydration of the K^+ ion requires energy, which is precisely balanced by the energy regained by the interaction of the ion with the carbonyl oxygens that serve as surrogate water molecules. Because the Na^+ ion is too small to interact with the oxygens, it could enter the selectivity filter only at a great energetic expense. The filter therefore selects K^+ ions with high specificity. (Adapted from D.A. Doyle et al., *Science* 280:6977, 1998.)

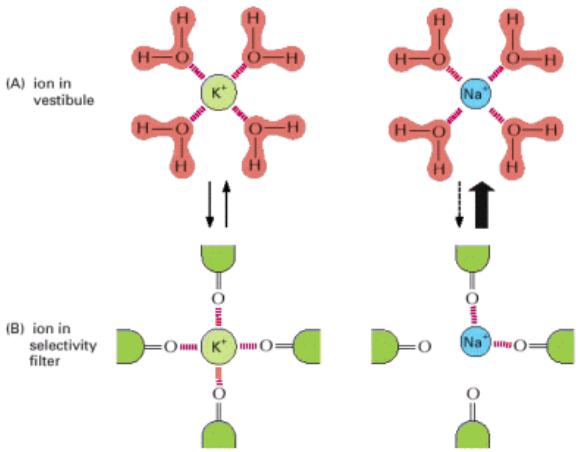

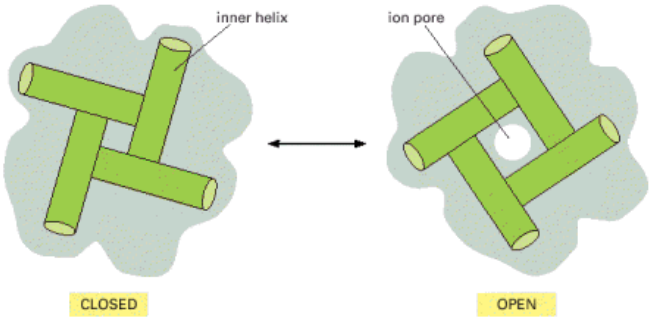

Figure 11-25. A model for the gating of a bacterial K^+ channel. The channel is viewed in cross section. To adopt the closed conformation, the four inner transmembrane helices that line the pore on the cytosolic side of the selectivity filter (see Figure 11-22) rearrange to close the cytosolic entrance to the channel. (Adapted from E. Perozo et al., *Science* 285:7378, 1999.)

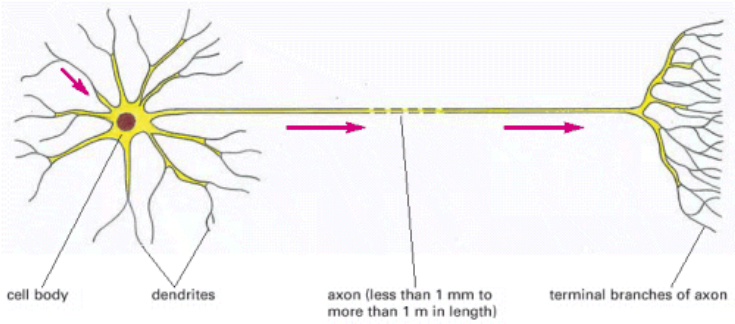

Figure 11-26. A typical vertebrate neuron. The arrows indicate the direction in which signals are conveyed. The single axon conducts signals away from the cell body, while the multiple dendrites receive signals from the axons of other neurons. The nerve terminals end on the dendrites or cell body of other neurons or on other cell types, such as muscle or gland cells.

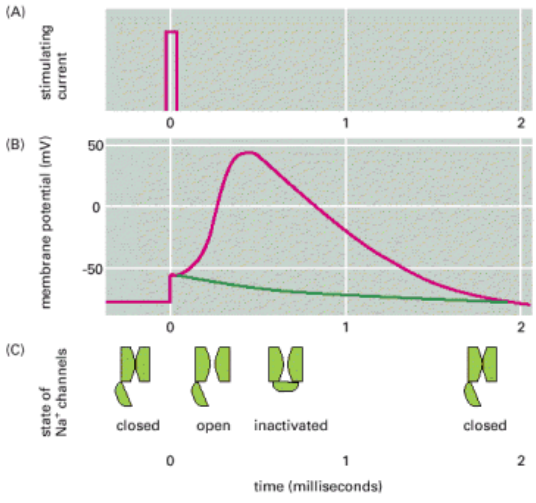

Figure 11-27. An action potential. (A) An action potential is triggered by a brief pulse of current, which (B) partially depolarizes the membrane, as shown in the plot of membrane potential versus time. The *green curve* shows how the membrane potential would have simply relaxed back to the resting value after the initial depolarizing stimulus if there had been no voltage-gated ion channels in the membrane; this relatively slow return of the membrane potential to its initial value of -70 mV in the absence of open Na^+ channels occurs because of the efflux of K^+ through K^+ channels, which open in response to membrane depolarization and drive the membrane back toward the K^+ equilibrium potential. The *red curve* shows the course of the action potential that is caused by the opening and subsequent inactivation of voltage-gated Na^+ channels, whose state is shown in (C). The membrane cannot fire a second action potential until the Na^+ channels have returned to the closed conformation; until then, the membrane is refractory to stimulation.

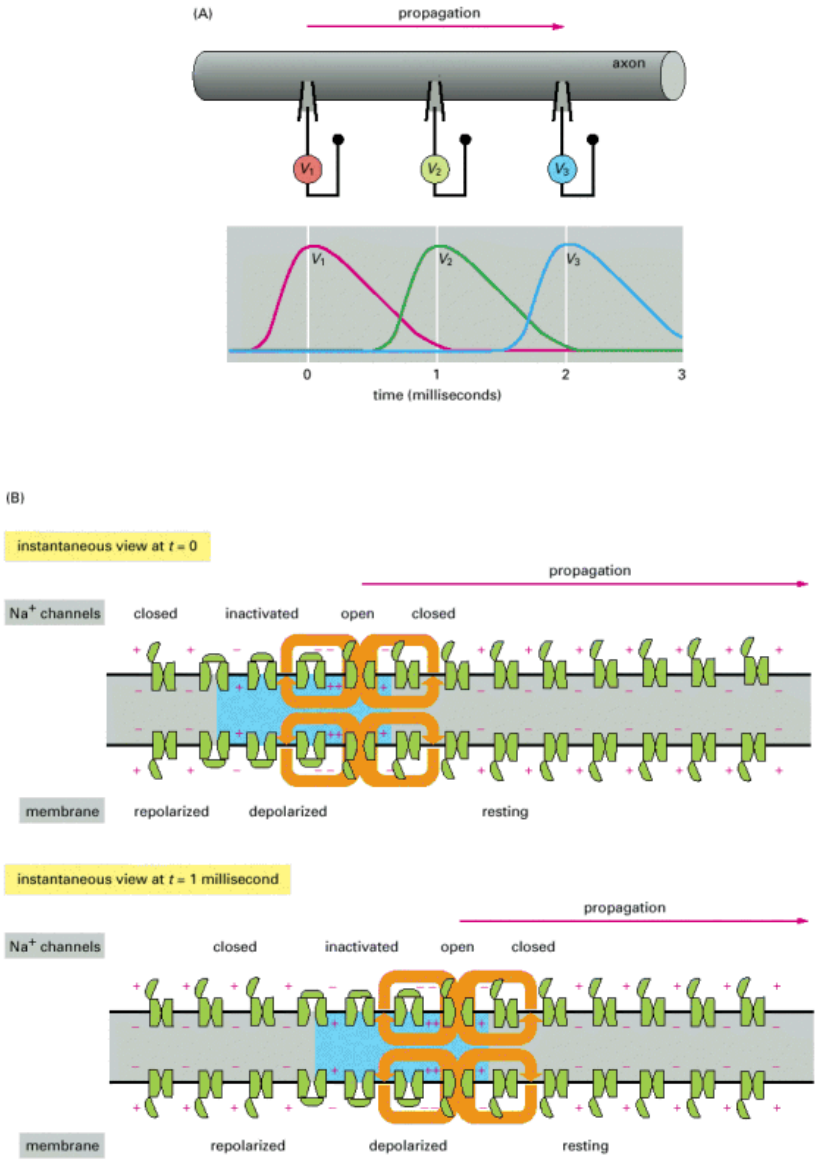

Figure 11-28. The propagation of an action potential along an axon. (A) The voltages that would be recorded from a set of intracellular electrodes placed at intervals along the axon. (B) The changes in the Na^+ channels and the current flows *(orange arrows)* that give rise to the traveling disturbance of the membrane potential. The region of the axon with a depolarized membrane is shaded in *blue*. Note that an action potential can only travel away from the site of depolarization, because Na^+ -channel inactivation prevents the depolarization from spreading backward (see also Figure 11-30). On myelinated axons, clusters of Na^+ channels can be millimeters apart from each other.

Figure 11-29. The "ball-and-chain" model of rapid inactivation for a voltage-gated K^+ channel. When the membrane potential is depolarized, the channel opens and begins to conduct ions. If the depolarization is maintained, the open channel adopts an inactive conformation, where the pore is occluded by the N-terminal 20 amino acid "ball," which is linked to the channel proper by a segment of unfolded polypeptide chain that serves as the "chain." For simplicity, only two balls are shown; in fact, there are four, one from each subunit. A similar mechanism, using a different segment of the polypeptide chain, is thought to operate in Na^+ channel inactivation. Internal forces stabilize each state against small disturbances, but a sufficiently violent collision with other molecules can cause the channel to flip from one of these states to another. The state of lowest energy depends on the membrane potential because the different conformations have different charge distributions. When the membrane is at rest (highly polarized), the closed conformation has the lowest free energy and is therefore most stable; when the membrane is depolarized, the energy of the *open* conformation is lower, so the channel has a high probability of opening. But the free energy of the *inactivated* conformation is lower still; therefore, after a randomly variable period spent in the open state, the channel becomes inactivated. Thus, the open conformation corresponds to a metastable state that can exist only transiently. The *red arrows* indicate the sequence that follows a sudden depolarization; the *black arrow* indicates the return to the original conformation as the lowest energy state after the membrane is repolarized.

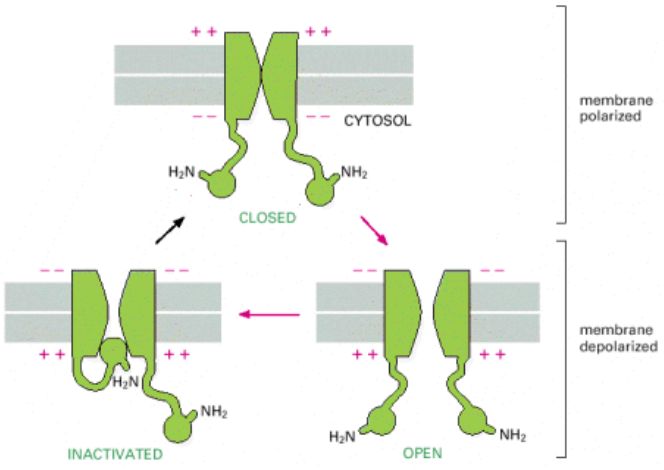

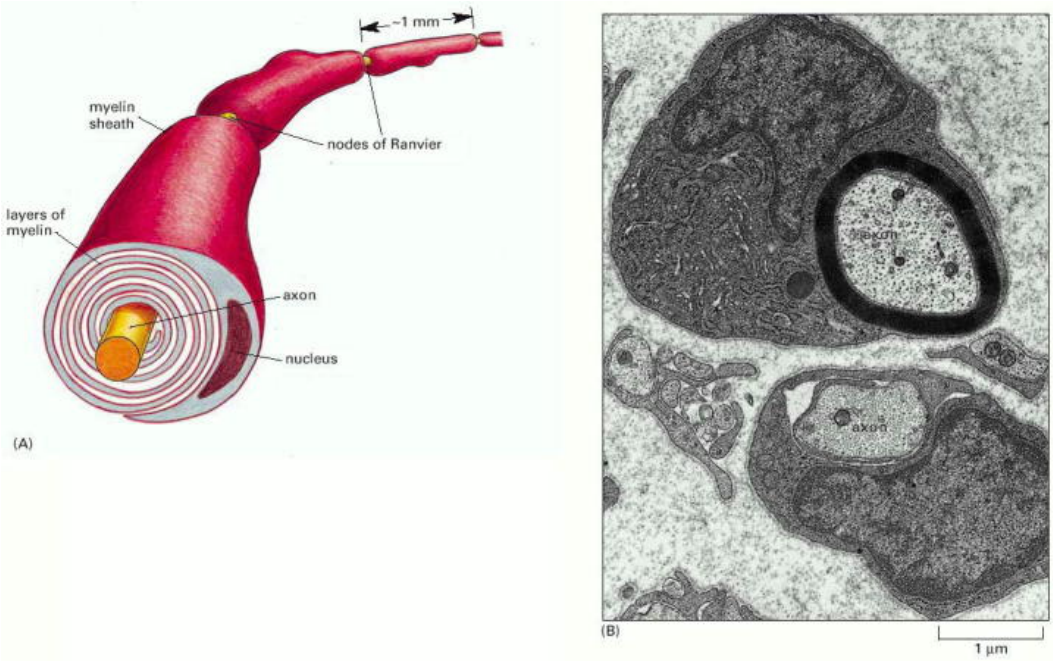

Figure 11-30. Myelination. (A) A myelinated axon from a peripheral nerve. Each Schwann cell wraps its plasma membrane concentrically around the axon to form a segment of myelin sheath about 1 mm long. For clarity, the layers of myelin in this drawing are not shown compacted together as tightly as they are in reality (see part B). (B) An electron micrograph of a section from a nerve in the leg of a young rat. Two Schwann cells can be seen: one near the bottom is just beginning to myelinate its axon; the one above it has formed an almost mature myelin sheath. (B, from Cedric S. Raine, in Myelin [P. Morell, ed.]. New York: Plenum, 1976.)

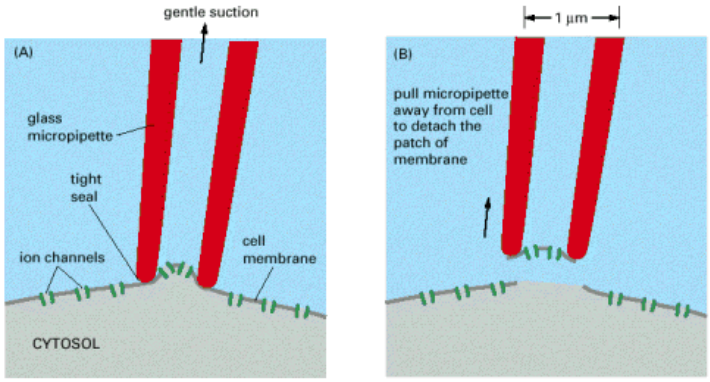

Figure 11-31. The technique of patch-clamp recording. Because of the extremely tight seal between the micropipette and the membrane, current can enter or leave the micropipette only by passing through the channels in the *patch* of membrane covering its tip. The term *clamp* is used because an electronic device is employed to maintain, or "clamp," the membrane potential at a set value while recording the ionic current through individual channels. Recordings of the current through these channels can be made with the patch still attached to the rest of the cell, as in (A), or detached, as in (B). The advantage of the detached patch is that it is easy to alter the composition of the solution on either side of the membrane to test the effect of various solutes on channel behavior. A detached patch can also be produced with the opposite orientation, so that the cytoplasmic surface of the membrane faces the inside of the pipette.

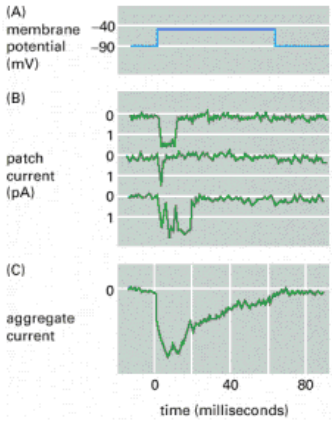

Figure 11-32. Patch-clamp measurements for a single voltage-gated Na^+ channel. A tiny patch of plasma membrane was detached from an embryonic rat muscle cell, as in Figure 11-31. (A) The membrane was depolarized by an abrupt shift of potential. (B) Three current records from three experiments performed on the same patch of membrane. Each major current step in (B) represents the opening and closing of a single channel. A comparison of the three records shows that, whereas the durations of channel opening and closing vary greatly, the rate at which current flows through an open channel is practically constant. The minor fluctuations in the current records arise largely from electrical noise in the recording apparatus. Current is measured in picoamperes (pA). (C) The sum of the currents measured in 144 repetitions of the same experiment. This aggregate current is equivalent to the usual Na^+ current that would be observed flowing through a relatively large region of membrane containing 144 channels. A comparison of (B) and (C) reveals that the time course of the aggregate current reflects the probability that any individual channel will be in the open state; this probability decreases with time as the channels in the depolarized membrane adopt their inactivated conformation. (Data from J. Patlak and R. Horn, *J. Gen. Physiol.* 79:333351, 1982. © The Rockefeller University Press.)

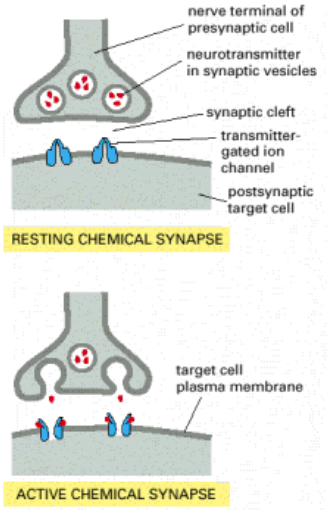

Figure 11-33. A chemical synapse. When an action potential reaches the nerve terminal in a presynaptic cell, it stimulates the terminal to release its neurotransmitter. The neurotransmitter molecules are contained in synaptic vesicles and are released to the cell exterior when the vesicles fuse with the plasma membrane of the nerve terminal. The released neurotransmitter binds to and opens the transmitter-gated ion channels concentrated in the plasma membrane of the postsynaptic target cell at the synapse. The resulting ion flows alter the membrane potential of the target cell, thereby transmitting a signal from the excited nerve.

Figure 11-34. A low-magnification scanning electron micrograph of a neuromuscular junction in a frog. The termination of a single axon on a skeletal muscle cell is shown. (From J. Desaki and Y. Uehara, *J. Neurocytol.* 10:101110, 1981. © Kluwer Academic Publishers.)

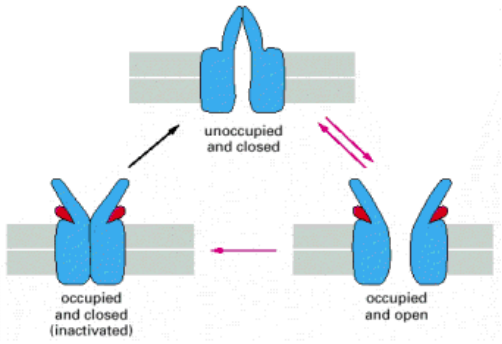

Figure 11-35. Three conformations of the acetylcholine receptor. The binding of two acetylcholine molecules opens this transmitter-gated ion channel. It then maintains a high probability of being open until the acetylcholine has been hydrolyzed. In the persistent presence of acetylcholine, however, the channel inactivates (desensitizes). Normally, the acetylcholine is rapidly hydrolyzed and the channel closes within about 1 millisecond, well before significant desensitization occurs. Desensitization would occur after about 20 milliseconds in the continued presence of acetylcholine.

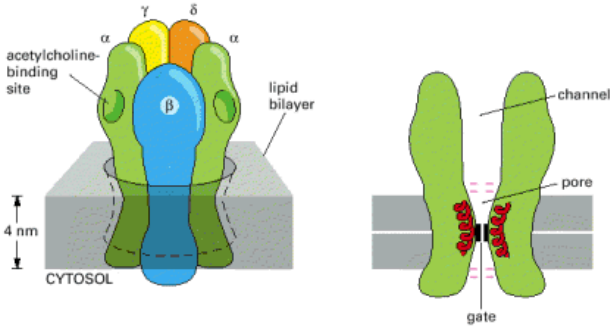

Figure 11-36. A model for the structure of the acetylcholine receptor. Five homologous subunits (α, α, β, γ, δ) combine to form a transmembrane aqueous pore. The pore is lined by a ring of five transmembrane α helices, one contributed by each subunit. In its closed conformation, the pore is thought to be occluded by the hydrophobic side chains of five leucines, one from each α helix, which form a gate near the middle of the lipid bilayer. The negatively charged side chains at either end of the pore ensure that only positively charged ions pass through the channel. Both of the α subunits contain an acetylcholine-binding site; when acetylcholine binds to both sites, the channel undergoes a conformational change that opens the gate, possibly by causing the leucines to move outward. (Adapted from N. Unwin, *Cell/Neuron* 72/10 'Suppl.]:31-41, 1993.)

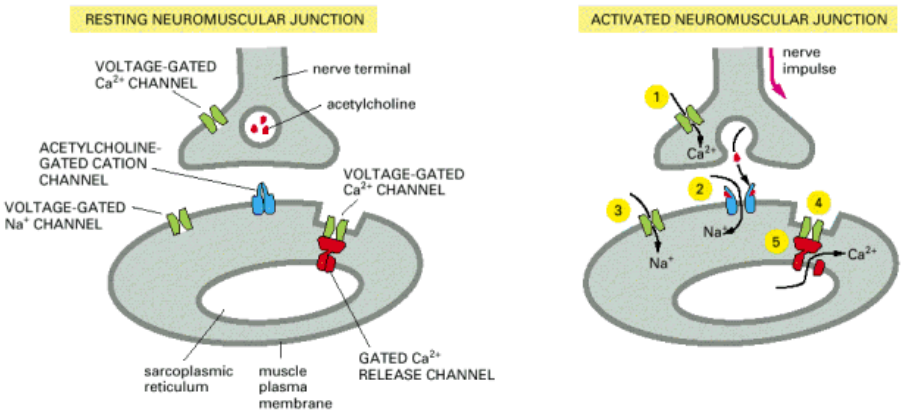

Figure 11-37. The system of ion channels at a neuromuscular junction. These gated ion channels are essential for the stimulation of muscle contraction by a nerve impulse. The various channels are numbered in the sequence in which they are activated, as described in the text.

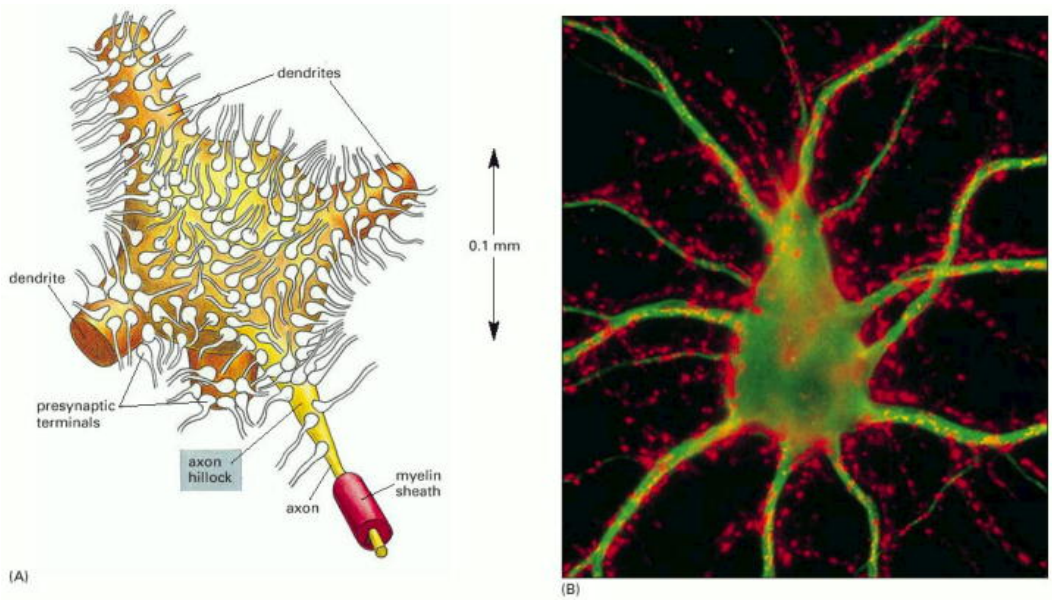

Figure 11-38. A motor neuron cell body in the spinal cord. (A) Many thousands of nerve terminals synapse on the cell body and dendrites. These deliver signals from other parts of the organism to control the firing of action potentials along the single axon of this large cell. (B) Micrograph showing a nerve cell body and its dendrites stained with a fluorescent antibody that recognizes a cytoskeletal protein *(green)*. Thousands of axon terminals *(red)* from other nerve cells (not visible) make synapses on the cell body and dendrites; they are stained with a fluorescent antibody that recognizes a protein in synaptic vesicles. (B, courtesy of Olaf Mundigl and Pietro de Camilli).

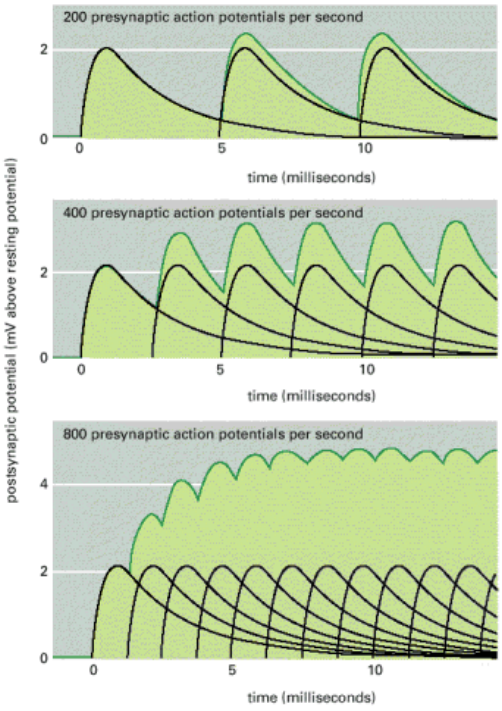

Figure 11-39. The principle of temporal summation. Each presynaptic action potential arriving at a synapse produces a small postsynaptic potential, or PSP *(black lines)*. When successive action potentials arrive at the same synapse, each PSP produced adds to the tail of the preceding one to produce a larger combined PSP *(green lines)*. The greater the frequency of incoming action potentials, the greater the size of the combined PSP.

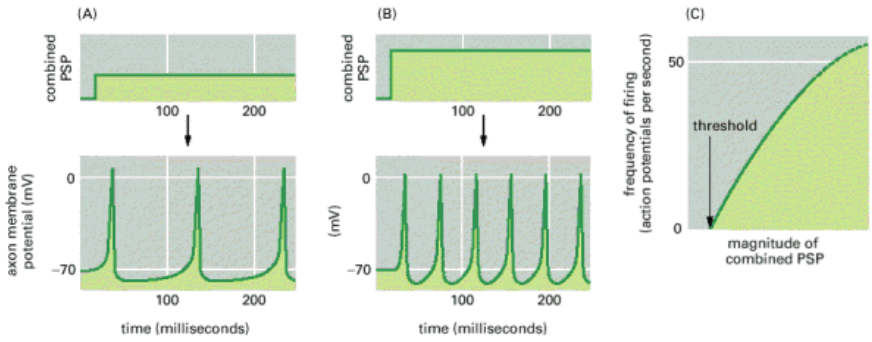

Figure 11-40. The encoding of the combined PSP in the form of the frequency of firing of action potentials by an axon. A comparison of (A) and (B) shows how the firing frequency of an axon increases with an increase in the combined PSP, while (C) summarizes the general relationship.

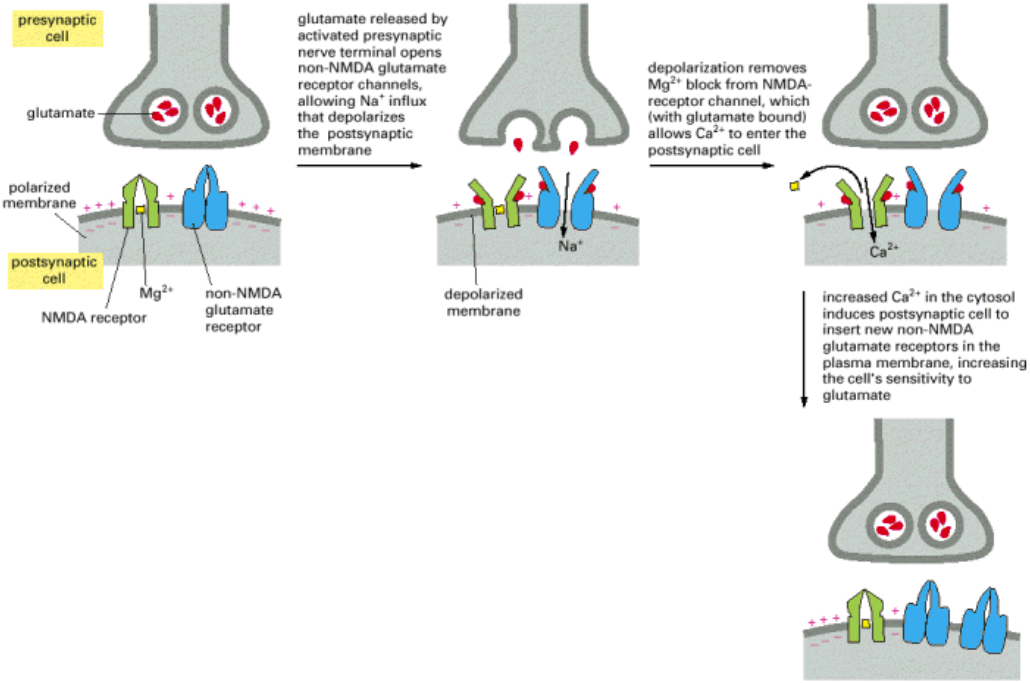

Figure 11-41. The signaling events in long-term potentiation. Although not shown, evidence suggests that changes can also occur in the presynaptic nerve terminals in LTP, which may be stimulated by retrograde signals from the postsynaptic cell.

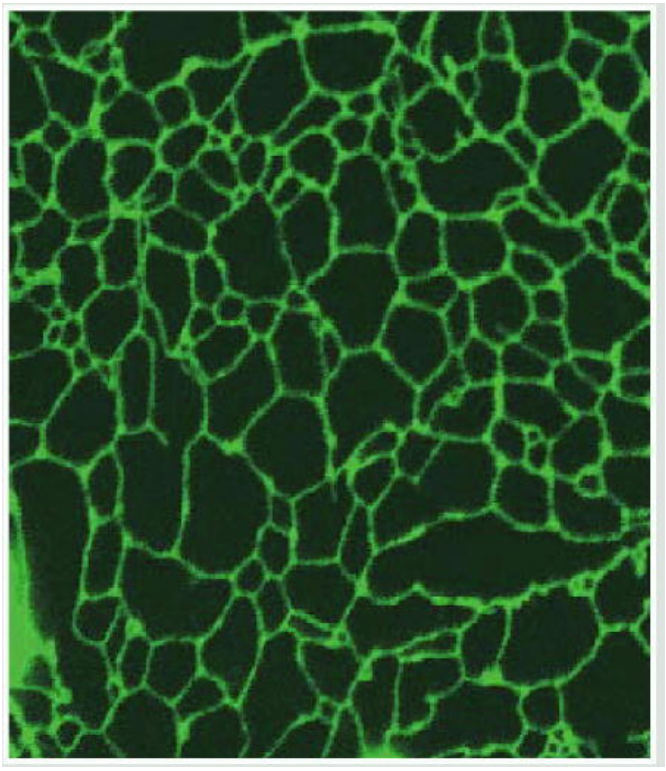

The endoplasmic reticulum (ER). In this tobacco cell, an ER resident protein, which has been coupled to a green fluorescent protein tag, reveals the complex cortical network of ER sheets and tubules within the cell. (Courtesy of Petra Boevink and Chris Hawes.)

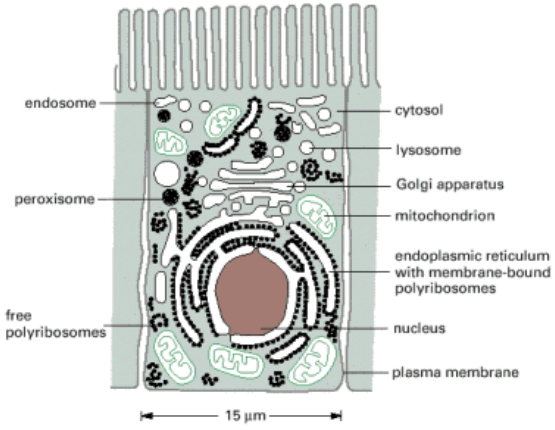

Figure 12-1. The major intracellular compartments of an animal cell. The cytosol *(gray)*, endoplasmic reticulum, Golgi apparatus, nucleus, mitochondrion, endosome, lysosome, and peroxisome are distinct compartments isolated from the rest of the cell by at least one selectively permeable membrane.

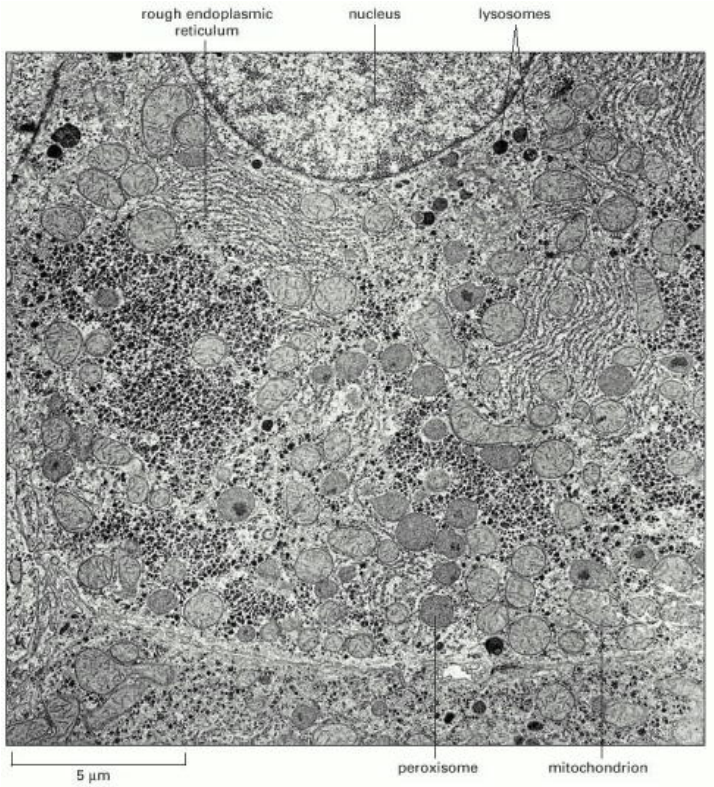

Figure 12-2. An electron micrograph of part of a liver cell seen in cross section. Examples of most of the major intracellular compartments are indicated. (Courtesy of Daniel S. Friend.)

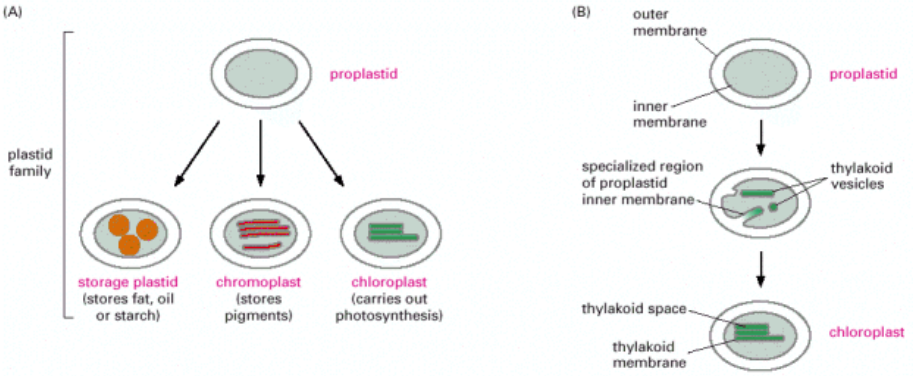

Figure 12-3. Development of plastids. (A) Proplastids are inherited with the cytoplasm of plant egg cells. As immature plant cells differentiate, the proplastids develop according to the needs of the specialized cell: they can become chloroplasts (in green leaf cells), storage plastids that accumulate starch (e.g., in potato tubers) or oil and lipid droplets (e.g., in fatty seeds), or chromoplasts that harbor pigments (e.g., in flower petals). (B) Development of the thylakoid. As chloroplasts develop, invaginated patches of specialized membrane from the proplastid inner membrane pinch off to form thylakoid vesicles, which then develop into the mature thylakoid. The thylakoid membrane forms a separate compartment, the thylakoid space, which is structurally and functionally distinct from the rest of the chloroplast. Thylakoids can grow and divide autonomously as chloroplasts proliferate.

Figure 12-4. Hypothetical schemes for the evolutionary origins of some membrane-enclosed organelles. The origins of mitochondria, chloroplasts, ER, and the cell nucleus can explain the topological relationships of these intra-cellular compartments in eucaryotic cells. (A) A possible pathway for the evolution of the cell nucleus and the ER. In some bacteria the single DNA molecule is attached to an invagination of the plasma membrane. Such an invagination in a very ancient procaryotic cell could have rearranged to form an envelope around the DNA, while still allowing the DNA access to the cell cytosol (as is required for DNA to direct protein synthesis). This envelope is presumed to have eventually pinched off completely from the plasma membrane, producing a nuclear compartment surrounded by a double membrane. As illustrated, the nuclear envelope is penetrated by communicating channels called nuclear pore complexes. Because it is surrounded by two membranes that are in continuity where they are penetrated by these pores, the nuclear compartment is topologically equivalent to the cytosol; in fact, during mitosis the nuclear contents mix with the cytosol. The lumen of the ER is continuous with the

space between the inner and outer nuclear membranes and topologically equivalent to the extracellular space. (B) Mitochondria (and plastids) are thought to have originated when a bacterium was engulfed by a larger pre-eucaryotic cell. They retain their autonomy. This may explain why the lumens of these organelles remain isolated from the membrane traffic that interconnects the lumens of many other intracellular compartments.

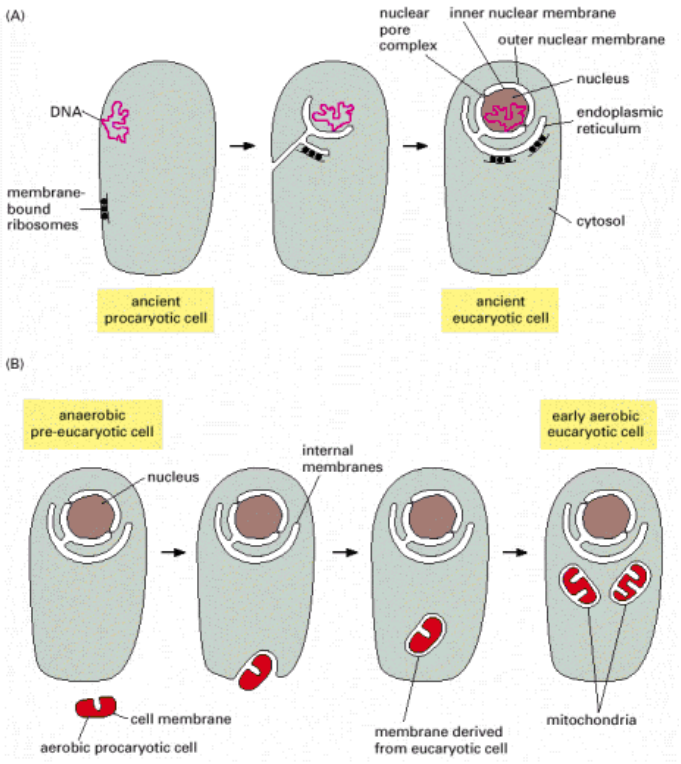

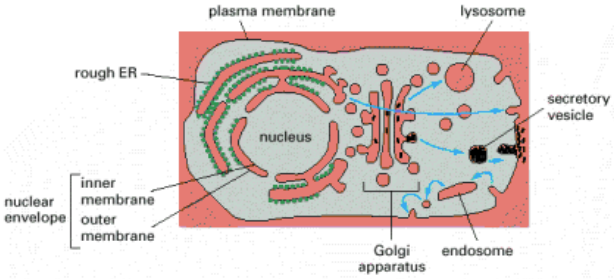

Figure 12-5. Topological relationships between compartments of the secretory and endocytic pathways in a eucaryotic cell. Topologically equivalent spaces are shown in *red*. In principle, cycles of membrane budding and fusion permit the lumen of any of these organelles to communicate with any other and with the cell exterior by means of transport vesicles. *Blue arrows* indicate the extensive network of outbound and inbound traffic routes, which we discuss in Chapter 13. Some organelles, most notably mitochondria and (in plant cells) plastids do not take part in this communication and are isolated from the traffic between organelles shown here.

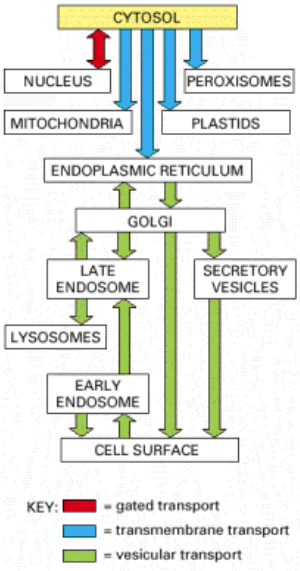

Figure 12-6. A simplified "roadmap" of protein traffic. Proteins can move from one compartment to another by gated transport *(red)*, transmembrane transport *(blue)*, or vesicular transport *(green)*. The signals that direct a given protein's movement through the system, and thereby determine its eventual location in the cell, are contained in each protein's amino acid sequence. The journey begins with the synthesis of a protein on a ribosome in the cytosol and terminates when the final destination is reached. At each intermediate station *(boxes)*, a decision is made as to whether the protein is to be retained in that compartment or transported further. In principle, a signal could be required for either retention in or exit from a compartment. We shall use this figure repeatedly as a guide throughout this chapter and the next, highlighting in color the particular pathway being discussed.

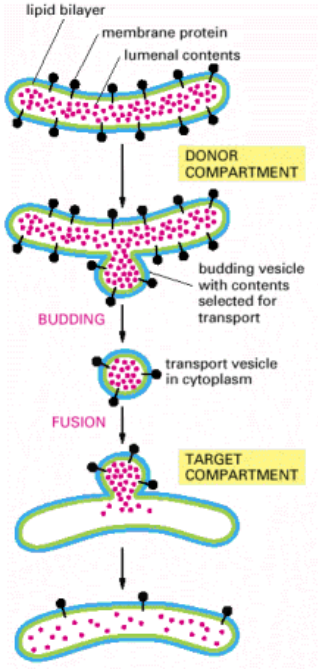

Figure 12-7. Vesicle budding and fusion during vesicular transport. Transport vesicles bud from one compartment (donor) and fuse with another (target) compartment. In the process, soluble components *(red dots)* are transferred from lumen to lumen. Note that membrane is also transferred, and that the original orientation of both proteins and lipids in the donor-compartment membrane is preserved in the target-compartment membrane. Thus, membrane proteins retain their asymmetric orientation, with the same domains always facing the cytosol.

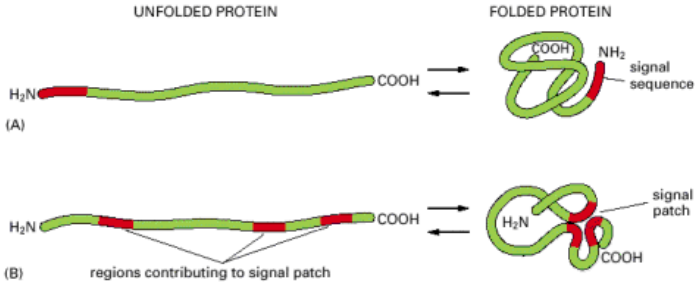

Figure 12-8. Two ways in which a sorting signal can be built into a protein. (A) The signal resides in a single discrete stretch of amino acid sequence, called a signal sequence, that is exposed in the folded protein. Signal sequences often occur at the end of the polypeptide chain (as shown), but they can also be located internally. (B) A signal patch can be formed by the juxtaposition of amino acids from regions that are physically separated before the protein folds (as shown). Alternatively, separate patches on the surface of the folded protein that are spaced a fixed distance apart can form the signal.

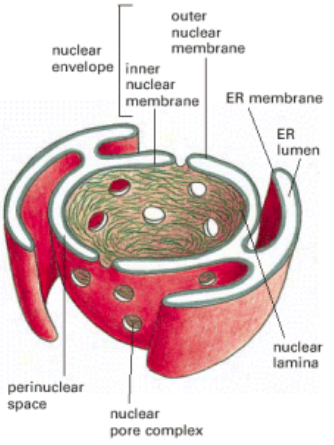

Figure 12-9. The nuclear envelope. The double-membrane envelope is penetrated by nuclear pore complexes and is continuous with the endoplasmic reticulum. The ribosomes that are normally bound to the cytosolic surface of the ER membrane and outer nuclear membrane are not shown. The nuclear lamina is a fibrous meshwork underlying the inner membrane.

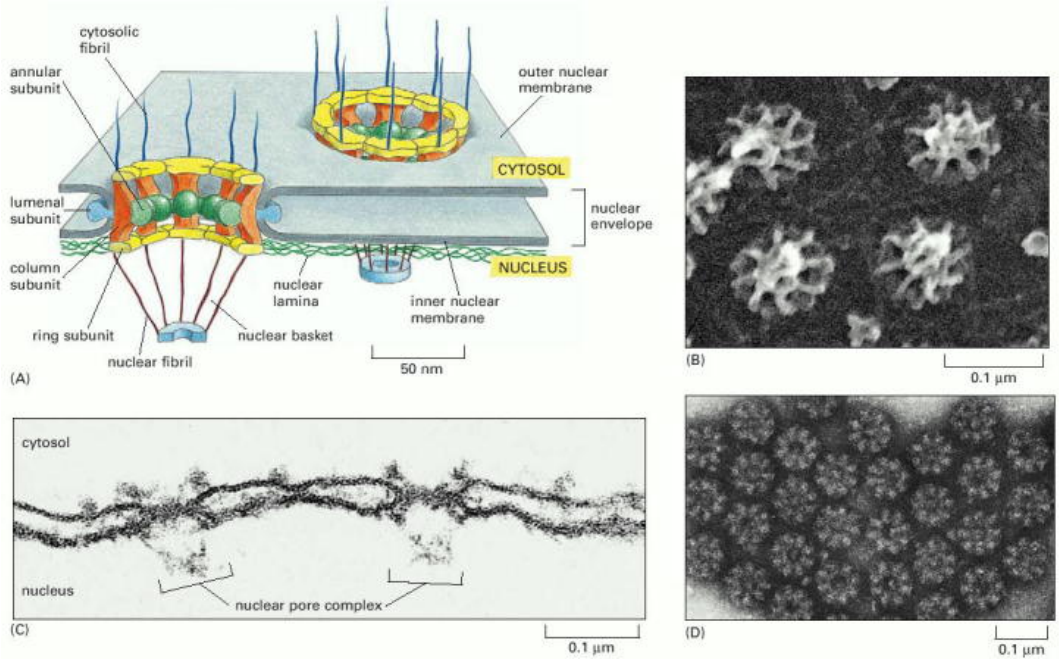

Figure 12-10. The arrangement of nuclear pore complexes in the nuclear envelope. (A) A small region of the nuclear envelope. In cross section, a nuclear pore complex seems to have four structural building blocks: column subunits, which form the bulk of the pore wall; annular subunits, which extend "spokes" (not shown) toward the center of the pore; lumenal subunits, which contain transmembrane proteins that anchor the complex to the nuclear membrane; and ring subunits, which form the cytosolic and nuclear faces of the complex. In addition, fibrils protrude from both the cytosolic and the nuclear sides of the complex. On the nuclear side, the fibrils converge to form basketlike structures. Localization studies using immunoelectron microscopy techniques showed that the proteins that make up the core of the nuclear pore complex are symmetrically distributed across the nuclear envelope so that the nuclear and cytosolic sides look identical. This is in contrast to proteins that make up the fibrils, which are different on each side of the cytosolic or the nuclear side. (B) A scanning electron micrograph of the nuclear side of the nuclear envelope of an oocyte. (C) The continuity of the inner and outer nuclear membrane at the pore is apparent in this thin section electron micrograph, showing a side view of two nuclear pore complexes *(brackets).* (D) This electron micrograph shows face-on views of negatively stained nuclear pore complexes from which the membrane has been removed by detergent extraction. (B, from M.W. Goldberg and T.D. Allen, *J. Cell Biol.* 119:14291440, 1992. © The Rockefeller University Press; C, courtesy of Werner Franke and Ulrich Scheer; D, courtesy of Ron Milligan.)

Figure 12-11. Possible paths for free diffusion through the nuclear pore complex. This drawing shows a hypothetical diaphragm *(gray)* inserted into the pore to restrict the size of the open channel to 9 nm, the pore size estimated from diffusion measurements. Nine nanometers is a much smaller diameter than that of the central opening apparent on the images of the nuclear pore complex derived from electron micrographs. It is also smaller than the opening estimated during active transport, when the pore dilates to allow the transport of particles of up to 26 nm in diameter *(arrow)*. Thus, it is likely that some pore components are lost during the preparation of specimens for electron microscopy, and that these normally restrict free diffusion through the central opening. Such components may form a diaphragm (or plug) that opens and closes to allow the passage of large objects during active transport, which depends on sorting signals (discussed below). Although plugs can be seen in some preparations, it is not clear whether they are components of the pore complex or material that is being transported through it. Three-dimensional computer reconstructions suggest that the channels permitting free diffusion might be located near the rim of the pore complex, between the column subunits, rather than at its center (see Figure 12-10A); this would mean that passive diffusion and active transport take place through different parts of the complex.

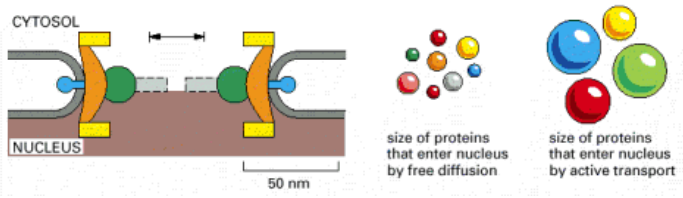

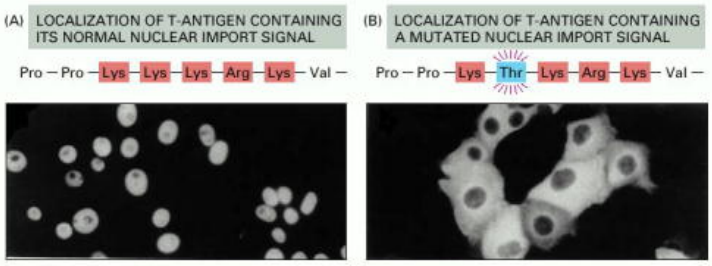

Figure 12-12. The function of a nuclear localization signal. Immunofluorescence micrographs showing the cellular location of SV40 virus T-antigen containing or lacking a short peptide that serves as a nuclear localization signal. (A) The normal T-antigen protein contains the lysine-rich sequence indicated and is imported to its site of action in the nucleus, as indicated by immunofluorescence staining with antibody against the T-antigen. (B) T-antigen with an altered nuclear localization signal (a threonine replacing a lysine) remains in the cytosol. (From D. Kalderon, B. Roberts, W. Richardson, and A. Smith, *Cell* 39:499509, 1984. © Elsevier.)

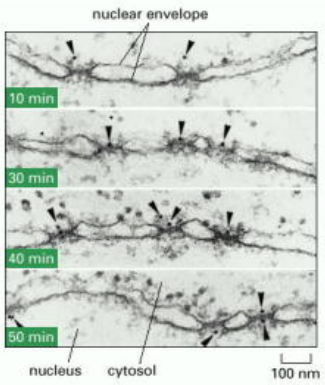

Figure 12-13. Visualizing active import through nuclear pores. This series of electron micrographs shows colloidal gold spheres *(arrowheads)* coated with peptides containing nuclear localization signals entering the nucleus by means of nuclear pore complexes. Gold particles were injected into living cells, which then were fixed and prepared for electron microscopy at various times after injection. At early time points (10 min), gold particles are seen in proximity to the cytosolic fibrils of the nuclear pore complexes. They then migrate to the center of the nuclear pore complexes, where they are first seen exclusively on the cytosolic face (30 and 40 min) and then appear on the nuclear face (50 min). These gold particles are much larger in diameter than the diffusion channel in the pore complex, which implies that the pores have been induced to widen to permit their passage. (From N. Panté and U. Aebi, *Science* 273:17291732, 1996. © AAAS.)

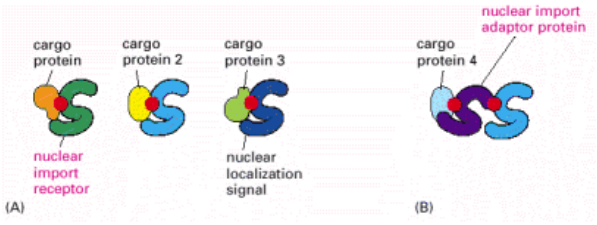

Figure 12-14. Nuclear import receptors. (A) Many nuclear import receptors bind both to nucleoporins and to a nuclear localization signal on the cargo proteins they transport. Cargo proteins 1, 2, and 3 in this example contain different nuclear localization signals, which causes each to bind to a different nuclear import receptor. (B) Cargo protein 4 shown here requires an adaptor protein to bind to its nuclear import receptor. The adaptors are structurally related to nuclear import receptors and recognize nuclear localization signals on cargo proteins. They also contain a nuclear localization signal that binds them to an import receptor.

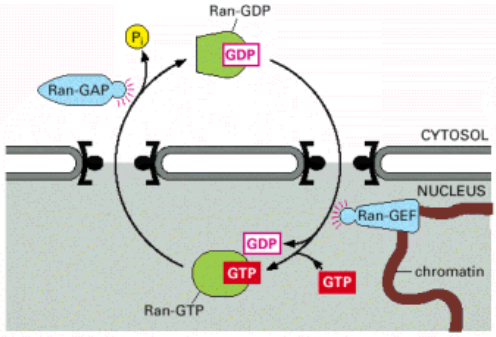

Figure 12-15. The compartmentalization of Ran-GDP and Ran-GTP. Localization of Ran-GDP to the cytosol and Ran-GTP to the nucleus results from the localization of two Ran regulatory proteins: Ran GTPase-activating protein (Ran-GAP) is located in the cytosol and Ran guanine nucleotide exchange factor (Ran-GEF) is bound to chromatin and is hence exclusively found in the nucleus. Another protein, called Ran Binding Protein (omitted here for clarity), collaborates with Ran-GAP in activating GTP hydrolysis.

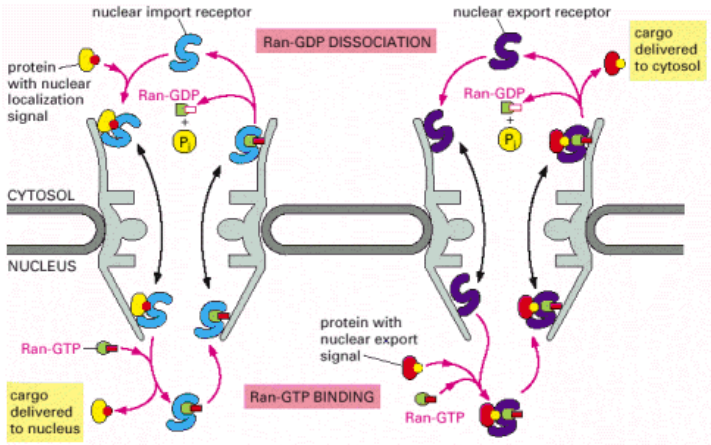

Figure 12-16. A model for how GTP hydrolysis by Ran provides directionality for nuclear transport. Movement through the pore complex of loaded nuclear transport receptors may occur by guided diffusion along the FG-repeats displayed by nucleoporins. The differential localization of Ran-GTP in the nucleus and Ran-GDP in the cytosol provides directionality *(red arrows)* to both nuclear import *(left)* and nuclear export *(right)*. The hydrolysis of GTP to produce Ran-GDP is mediated by Ran-GAP and Ran Binding Protein on the cytosolic side of the nuclear pore complex.

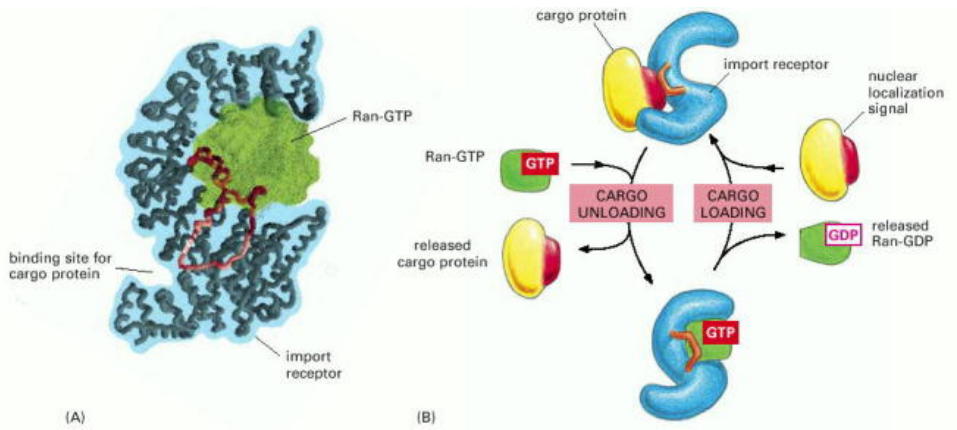

Figure 12-17. A model for how the binding of Ran-GTP might cause nuclear import receptors to release their cargo. (A) Nuclear transport receptors are composed of repeated α-helical motifs that stack into either large arches or snail-shaped coils, depending on the particular receptor or adaptor. Cargo proteins and Ran-GTP bind to different regions at the inside faces of the arches. In a co-crystal of a nuclear import receptor bound to Ran-GTP, a conserved loop *(red)* of the receptor becomes covered by bound Ran-GTP, which, in the Ran-free state of the receptor, is thought to be important for signal sequence binding. (B) The cycle of loading in the cytosol and unloading in the nucleus of a nuclear import receptor. (A, adapted from Y. M. Chook and G. Blobel, *Nature* 399:230237, 1999.)

Figure 12-18. The control of fly embryo development by nuclear transport. The gene regulatory protein *dorsal* is expressed uniformly throughout this early *Drosophila* embryo, which is shown in cross section. It is active only in cells at the ventral side *(bottom)* of the embryo, where it is found in nuclei. The dorsal protein is visualized by staining with an enzyme-coupled antibody that yields a colored product. (Courtesy of Siegfried Roth.)

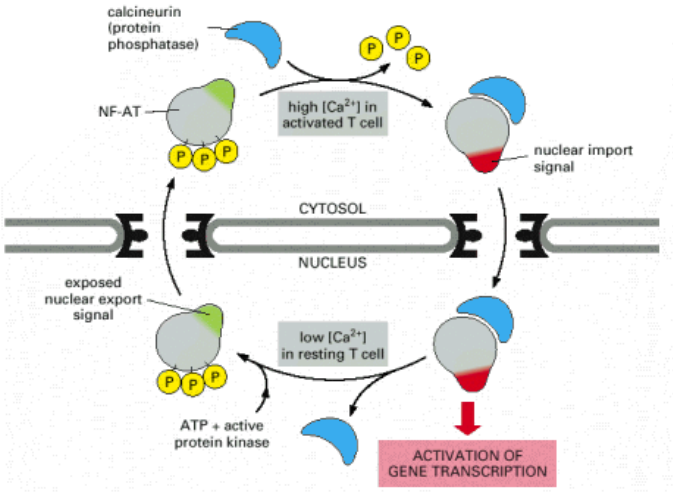

Figure 12-19. The control of nuclear import during T-cell activation. The nuclear factor of activated T cells (NF-AT) is a gene regulatory protein that, in the resting T cell, is found in the cytosol in a phosphorylated state. When T cells are activated, the intracellular Ca^{2+} concentration increases. In high Ca^{2+}, the protein phosphatase, calcineurin, binds to NF-AT. Binding of calcineurin dephosphorylates NF-AT, exposing one or more nuclear import signals, and it may also block a nuclear export signal. The complex of NF-AT bound to calcineurin is then imported into the nucleus, where NF-AT activates the transcription of numerous cytokine and cell-surface protein genes that are required for a proper immune response. During the shut-off of the response, decreased Ca^{2+} levels lead to the release of calcineurin. Rephosphorylation of NF-AT inactivates the nuclear import signal, and it re-exposes the nuclear export signal of NF-AT causing NF-AT to relocate to the cytosol. Some of the most potent immunosuppressive drugs, such as cyclosporin A and FK506, inhibit the ability of calcineurin to dephosphorylate NF-AT; these drugs thereby block the nuclear accumulation of NF-AT.

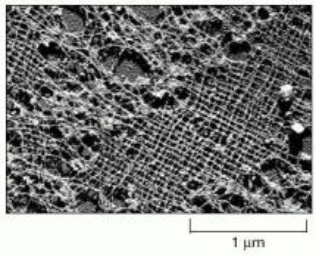

Figure 12-20. The nuclear lamina. An electron micrograph of a portion of the nuclear lamina in a *Xenopus* oocyte prepared by freeze-drying and metal shadowing. The lamina is formed by a regular lattice of specialized intermediate filaments. (Courtesy of Ueli Aebi.)

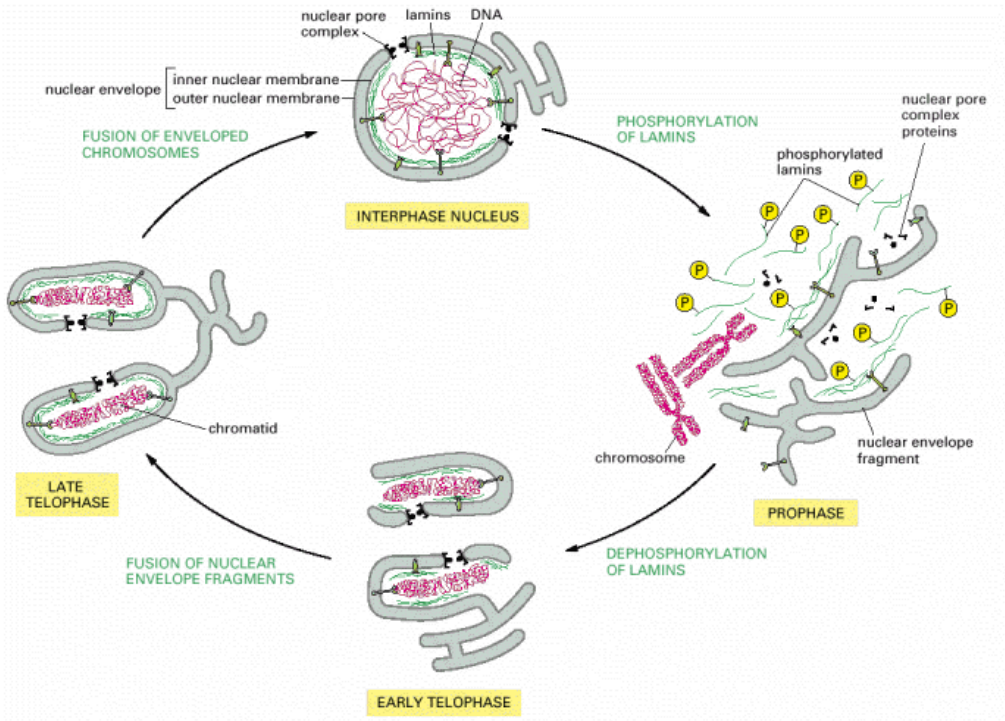

Figure 12-21. The breakdown and re-formation of the nuclear envelope during mitosis. The phosphorylation of the lamins is thought to trigger the disassembly of the nuclear lamina, which in turn causes the nuclear envelope to break up. Dephosphorylation of the lamins is thought to help to reverse the process.

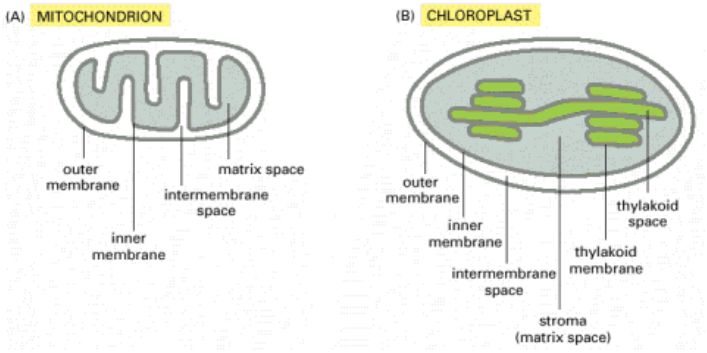

Figure 12-22. The subcompartments of mitochondria and chloroplasts. In contrast to the cristae of mitochondria (A), the thylakoids of chloroplasts (B) are not connected to the inner membrane and therefore form a compartment with a separate internal space (see Figure 12-3).

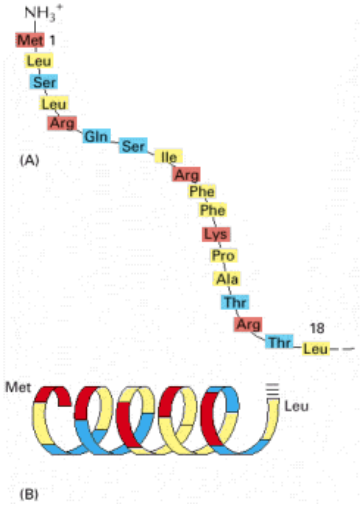

Figure 12-23. A signal sequence for mitochondrial protein import. Cytochrome oxidase is a large multiprotein complex located in the inner mitochondrial membrane, where it functions as the terminal enzyme in the electron-transport chain (discussed in Chapter 14). (A) The first 18 amino acids of the precursor to subunit IV of this enzyme serve as a signal sequence for import of the subunit into the mitochondrion. (B) When the signal sequence is folded as an α helix, the positively charged residues *(red)* are seen to be clustered on one face of the helix, while the nonpolar residues *(yellow)* are clustered primarily on the opposite face. Mitochondrial matrix-targeting sequences always have the potential to form such an amphipathic α helix, which is recognized by specific receptor proteins on the mitochondrial surface.

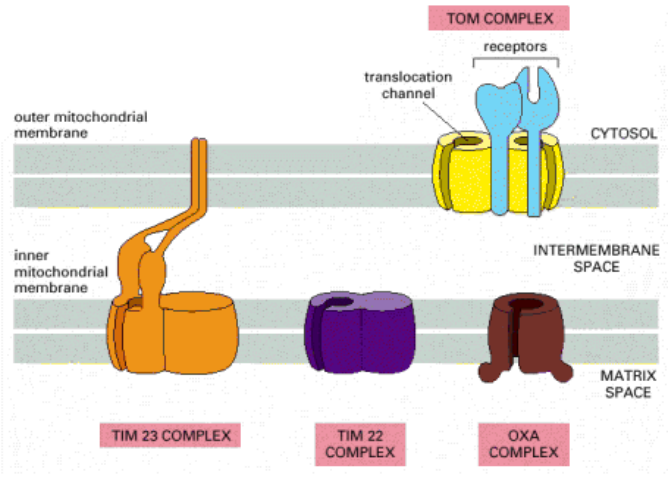

Figure 12-24. Three protein translocators in the mitochondrial membranes. The TOM and TIM complexes and the OXA complex are multimeric membrane protein assemblies that catalyze protein transport across mitochondrial membranes. The protein components of the TIM22 and TIM23 complexes that line the import channel are structurally related, suggesting a common evolutionary origin of both TIM complexes. As indicated, one of the core components of the TIM23 complex contains a hydrophobic α-helical extension that is inserted into the outer mitochondrial membrane; the complex is therefore unusual in that it simultaneously spans two membranes.

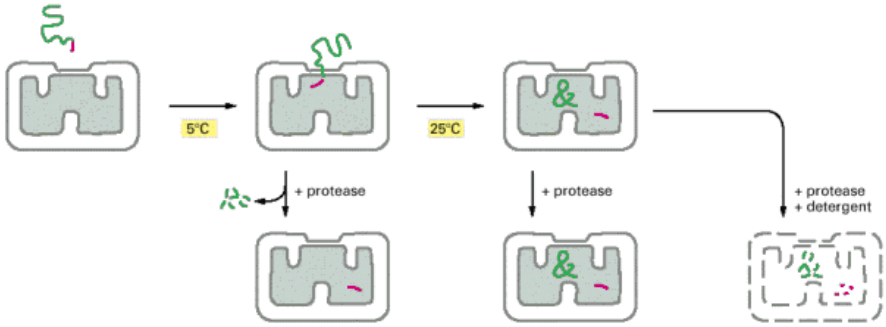

Figure 12-25. Proteins transiently spanning the inner and outer mitochondrial membranes during their translocation into the matrix. When isolated mitochondria are incubated with a precursor protein at 5°C, the precursor is only partly translocated. The N-terminal signal sequence *(red)* is cleaved off in the matrix; but most of the polypeptide chain remains outside the mitochondrion, where it is accessible to proteolytic enzymes. Upon warming to 25°C, the translocation is completed. Once inside the mitochondrion, the polypeptide chain is protected from externally added proteolytic enzymes. As a control, when detergents are added to disrupt the mitochondrial membranes, the imported proteins can be readily digested by the same protease treatment.

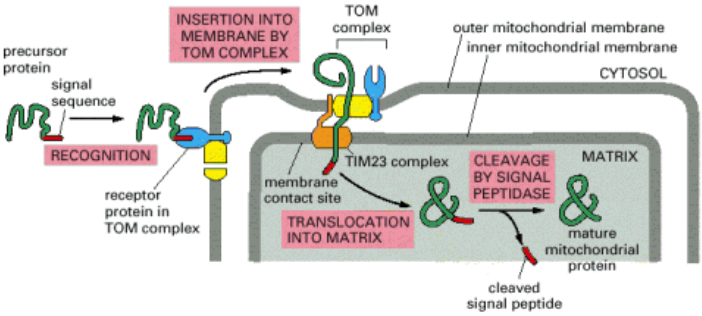

Figure 12-26. Protein import by mitochondria. The N-terminal signal sequence of the precursor protein is recognized by receptors of the TOM complex. The protein is thought to be translocated across both mitochondrial membranes at or near special contact sites. The signal sequence is cleaved off by a signal peptidase in the matrix to form the mature protein. The free signal sequence is then rapidly degraded (not shown).

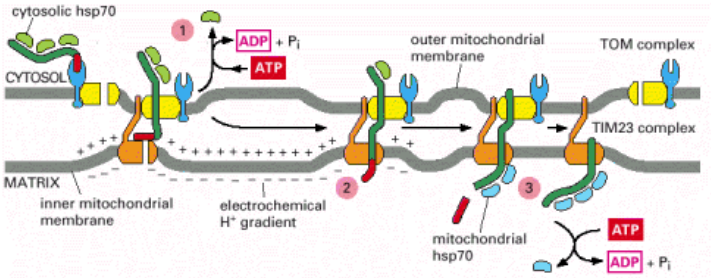

Figure 12-27. The role of energy in protein import into the mitochondrial matrix. (1) Bound *cytosolic hsp70* is released from the protein in a step that depends on ATP hydrolysis. After initial insertion of the signal sequence and of adjacent portions of the polypeptide chain into the TOM complex, the signal sequence interacts with a TIM complex. (2) The signal sequence is then translocated into the matrix in a process that requires an electrochemical H^+ gradient across the inner membrane, positioning the unfolded polypeptide chain so that it transiently spans both membranes. (3) *Mitochondrial hsp70* binds to regions of the polypeptide chain as they become exposed in the matrix, thereby "pulling" the protein into the matrix. ATP hydrolysis then removes the mitochondrial hsp70, allowing the imported protein to fold.

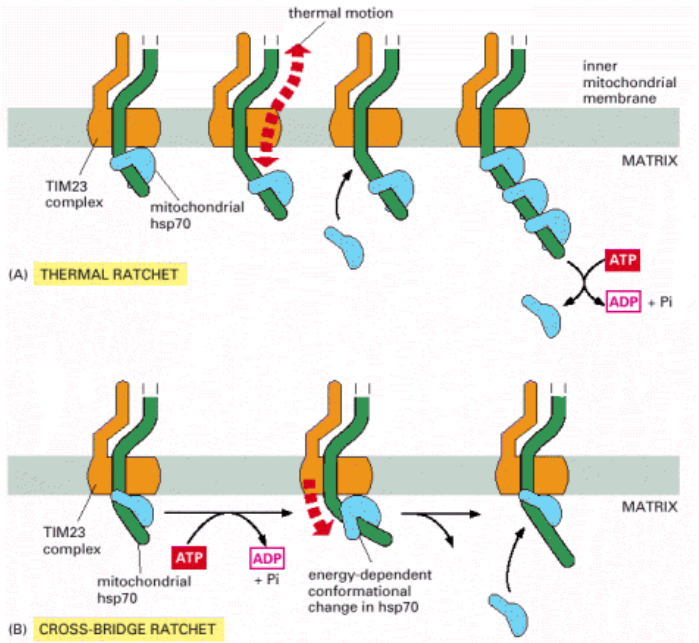

Figure 12-28. Two plausible models of how mitochondrial hsp70 could drive protein import. (A) In the thermal ratchet model, the translocating polypeptide chain slides back and forth, driven by thermal motion, and it is successively trapped in the matrix by hsp70 binding. (B) In the cross-bridge ratchet model, a conformational change in hsp70 actively pulls the chain into the matrix. In both models, hsp70 binds to the TIM23 complex, which loads the hsp70 onto the translocating polypeptide chain as it emerges from the complex into the matrix.

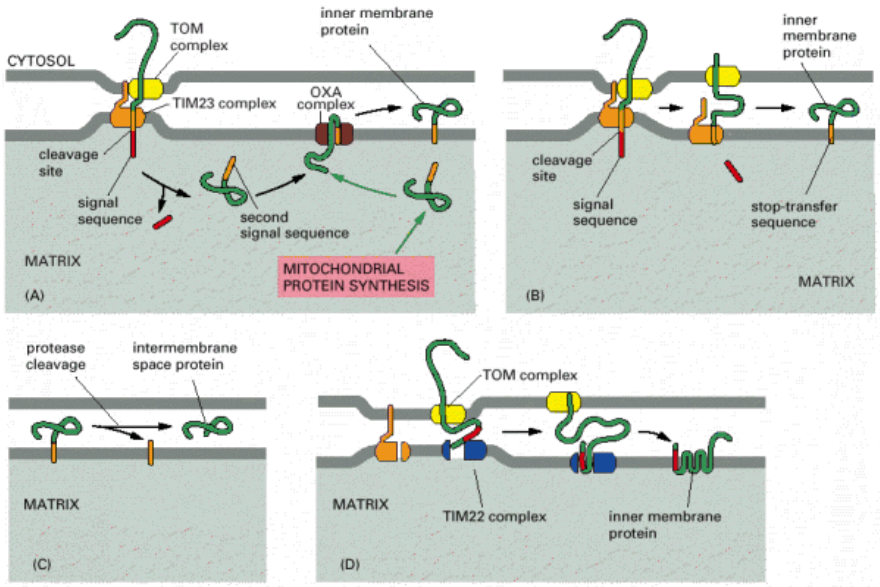

Figure 12-29. Protein import from the cytosol into the inner mitochondrial membrane or intermembrane space. (A) A pathway that requires two signal sequences and two translocation events is thought to be used to move some proteins from the cytosol to the inner membrane. The precursor protein is first imported into the matrix space (see Figure 12-26). Cleavage of the signal sequence *(red)* used for the initial translocation, however, unmasks an adjacent hydrophobic signal sequence *(orange)* at the new N terminus. This signal then directs the protein into the inner membrane, presumably by the same OXA-dependent pathway that is used to insert proteins encoded by the mitochondrial genome. (B) In some cases, the hydrophobic sequence that follows the matrix-targeting signal binds to the TIM23 translocator in the inner membrane and stops translocation. The remainder of the protein is then pulled into the intermembrane space through the TOM translocator in the outer membrane, and the hydrophobic sequence is released into the inner membrane. (C) Some soluble proteins of the intermembrane space may also use the pathways shown in (A) and (B) before they are released into the intermembrane space by a second signal peptidase, which has its active site in the intermembrane space and removes the hydrophobic signal sequence. (D) The import pathway used to insert metabolite carrier proteins into the inner mitochondrial membrane utilizes the TIM22 complex, which is specialized for the translocation of multipass membrane proteins.

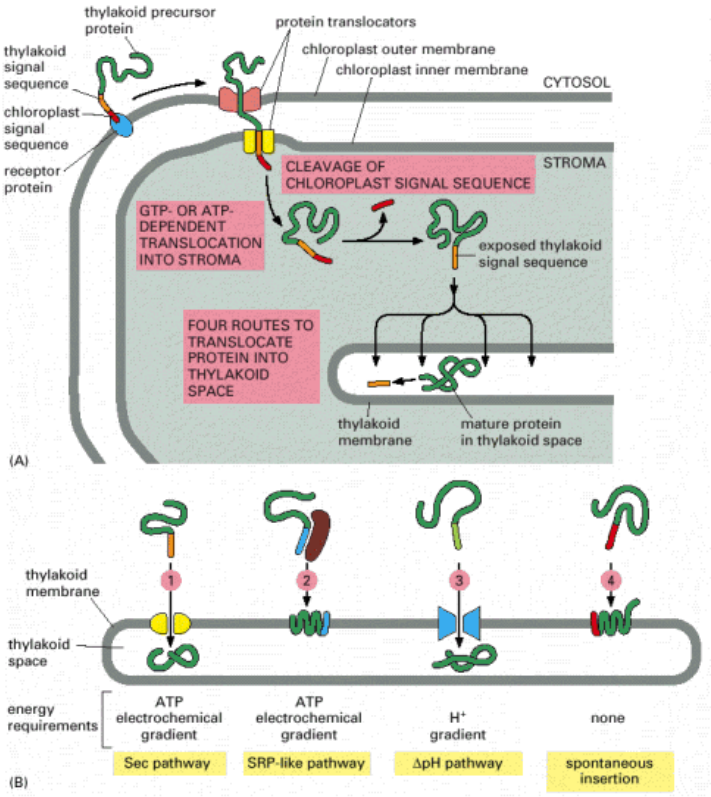

Figure 12-30. Translocation of a precursor protein into the thylakoid space of chloroplasts. (A) The precursor protein contains an N-terminal chloroplast signal sequence *(red)*, followed immediately by a thylakoid signal sequence *(orange)*. The chloroplast signal sequence initiates translocation into the stroma through a membrane contact site by a mechanism similar to that used for translocation into the mitochondrial matrix. The signal sequence is then cleaved off, unmasking the thylakoid signal sequence, which initiates translocation across the thylakoid membrane. (B) Translocation into the thylakoid space or thylakoid membrane can occur by any one of at least four routes: (1) a Sec pathway, so called because it uses components that are homologs of Sec proteins, which mediate protein translocation across the bacterial plasma membrane (discussed later), (2) an SRP-like pathway, so called because it uses a chloroplast homolog of the signal recognition particle, or SRP (discussed later), (3) a ΔpH pathway, so called because it is driven by the H^+ gradient across the thylakoid membrane, and (4) a spontaneous insertion pathway that seems to require no protein translocator for membrane integration.

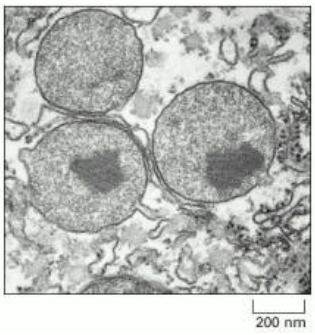

Figure 12-31. An electron micrograph of three peroxisomes in a rat liver cell. The paracrystalline electron-dense inclusions are composed of the enzyme urate oxidase. (Courtesy of Daniel S. Friend.)

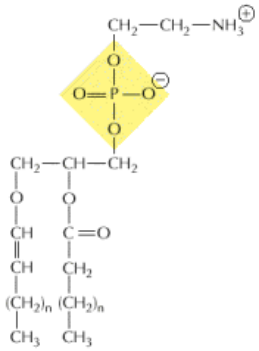

Figure 12-32. The structure of a plasmalogen. Plasmalogens are very abundant in the myelin sheaths that insulate the axons of nerve cells. They make up some 8090% of the myelin membrane phospholipids. In addition to an ethanolamine head group and a long-chain fatty acid attached to the same glycerol phosphate backbone used for phospholipids, plasmalogens contain an unusual fatty alcohol that is attached through an ether linkage *(bottom left).*

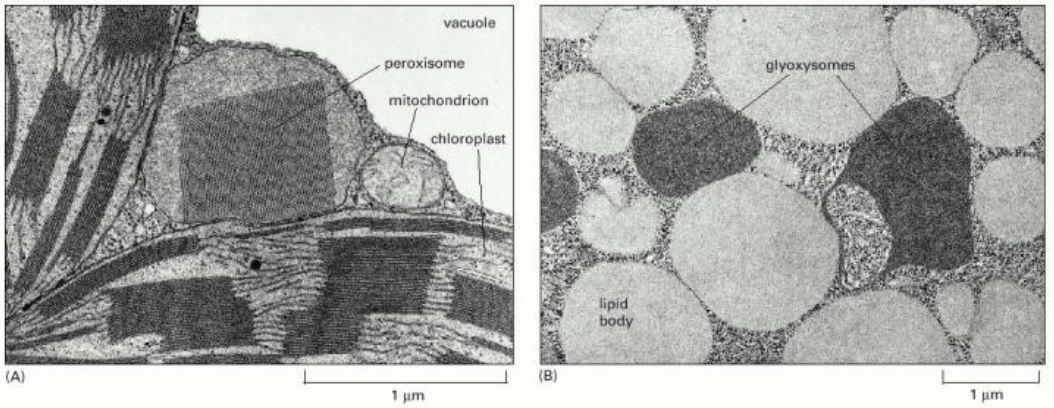

Figure 12-33. Electron micrographs of two types of peroxisomes found in plant cells. (A) A peroxisome with a paracrystalline core in a tobacco leaf mesophyll cell. Its close association with chloroplasts is thought to facilitate the exchange of materials between these organelles during photorespiration. (B) Peroxisomes in a fat-storing cotyledon cell of a tomato seed 4 days after germination. Here, the peroxisomes (glyoxysomes) are associated with the lipid bodies where fat is stored, reflecting their central role in fat mobilization and gluconeogenesis during seed germination. (A, from S.E. Frederick and E.H. Newcomb, *J. Cell Biol.* 43:343353, 1969. © The Rockefeller Press; B, from W.P. Wergin, P.J. Gruber, and E.H. Newcomb, *J. Ultrastruct. Res.* 30:533557, 1970. © Academic Press.)

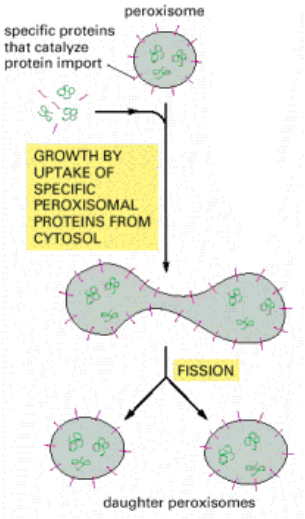

Figure 12-34. A model for how new peroxisomes are produced. The peroxisome membrane contains import receptor proteins. Peroxisomal proteins, including new copies of the import receptor, are synthesized by cytosolic ribosomes and then imported into the organelle. Presumably, the lipids required to make new peroxisome membrane are also imported. (We discuss later how lipids made in the ER can be transported through the cytosol to other organelles.) In this model, peroxisomes are thought to form only from preexisting peroxisomes by a process of growth and fission.

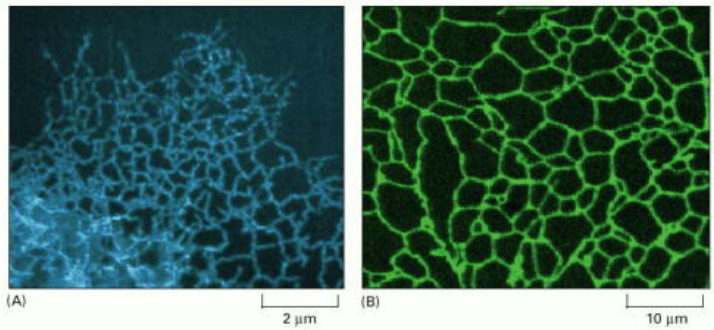

Figure 12-35. Fluorescent micrographs of the endoplasmic reticulum. (A) Part of the ER network in a cultured mammalian cell, stained with an antibody that binds to a protein retained in the ER. The ER extends as a network throughout the entire cytosol, so that all regions of the cytosol are close to some portion of the ER membrane. (B) Part of an ER network in a living plant cell that was genetically engineered to express a fluorescent protein in the ER. (A, courtesy of Hugh Pelham; B, courtesy of Petra Boevink and Chris Hawes.)

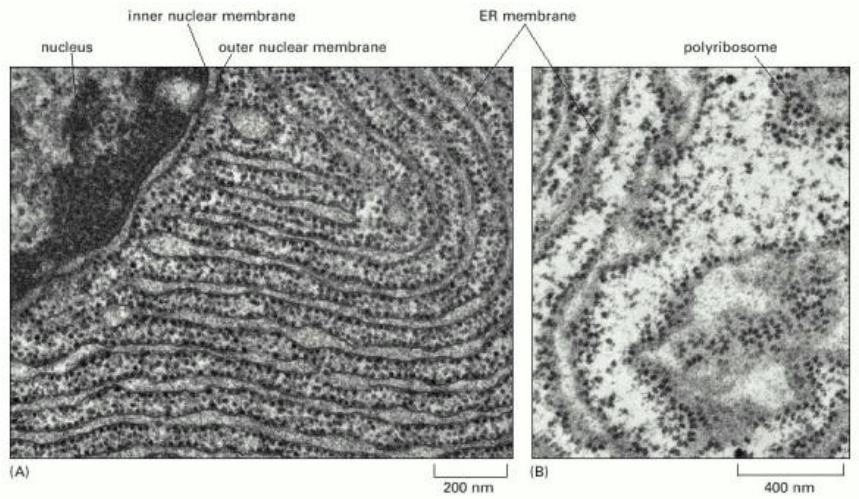

Figure 12-36. The rough ER. (A) An electron micrograph of the rough ER in a pancreatic exocrine cell that makes and secretes large amounts of digestive enzymes every day. The cytosol is filled with closely packed sheets of ER membrane studded with ribosomes. At the top left is a portion of the nucleus and its nuclear envelope; note that the outer nuclear membrane, which is continuous with the ER, is also studded with ribosomes. (B) A thin section electron micrograph of polyribosomes attached to the ER membrane. The plane of section in some places cuts through the ER roughly parallel to the membrane, giving a face-on view of the rosettelike pattern of the polyribosomes. (A, courtesy of Lelio Orci; B, courtesy of George Palade.)

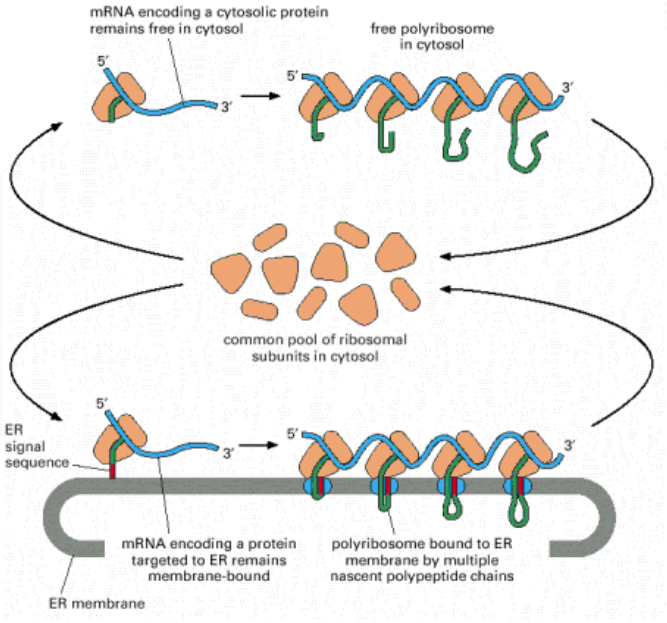

Figure 12-37. Free and membrane-bound ribosomes. A common pool of ribosomes is used to synthesize the proteins that stay in the cytosol and those that are transported into the ER. The ER signal sequence on a newly formed polypeptide chain directs the engaged ribosome to the ER membrane. The mRNA molecule remains permanently bound to the ER as part of a polyribosome, while the ribosomes that move along it are recycled; at the end of each round of protein synthesis, the ribosomal subunits are released and rejoin the common pool in the cytosol.

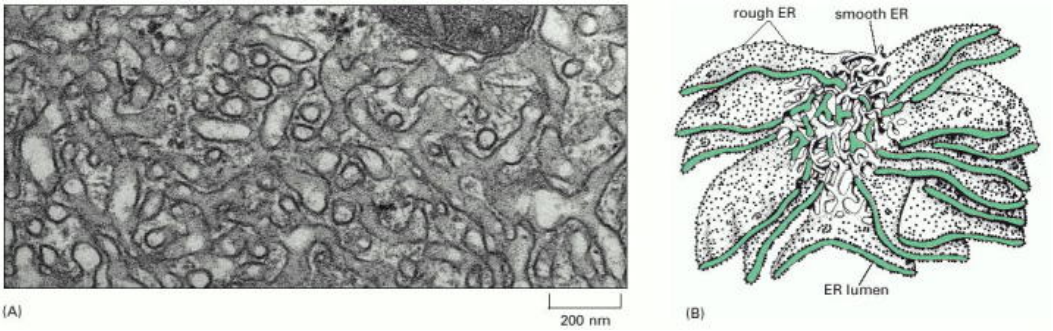

Figure 12-38. The smooth ER. (A) Abundant smooth ER in a steroid-hormone-secreting cell. This electron micrograph is of a testosterone-secreting Leydig cell in the human testis. (B) A three-dimensional reconstruction of a region of smooth ER and rough ER in a liver cell. The rough ER forms oriented stacks of flattened cisternae, each having a lumenal space 2030 nm wide. The smooth ER membrane is connected to these cisternae and forms a fine network of tubules 3060 nm in diameter. (A, courtesy of Daniel S. Friend; B, after R.V. Krstic´, Ultrastructure of the Mammalian Cell. New York: Springer-Verlag, 1979.)

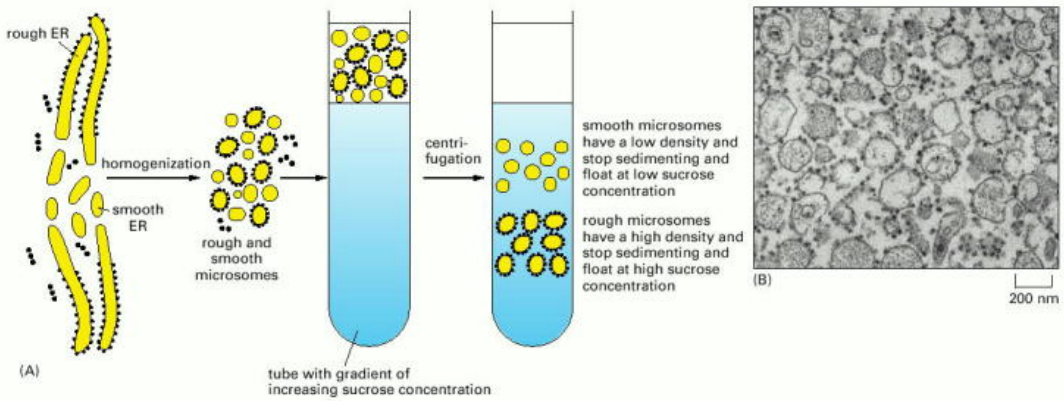

Figure 12-39. The isolation of purified rough and smooth microsomes from the ER. (A) When sedimented to equilibrium through a gradient of sucrose, the two types of microsomes separate from each other on the basis of their different densities. (B) A thin section electron micrograph of the purified rough ER fraction shows an abundance of ribosome-studded vesicles. (B, courtesy of George Palade.)

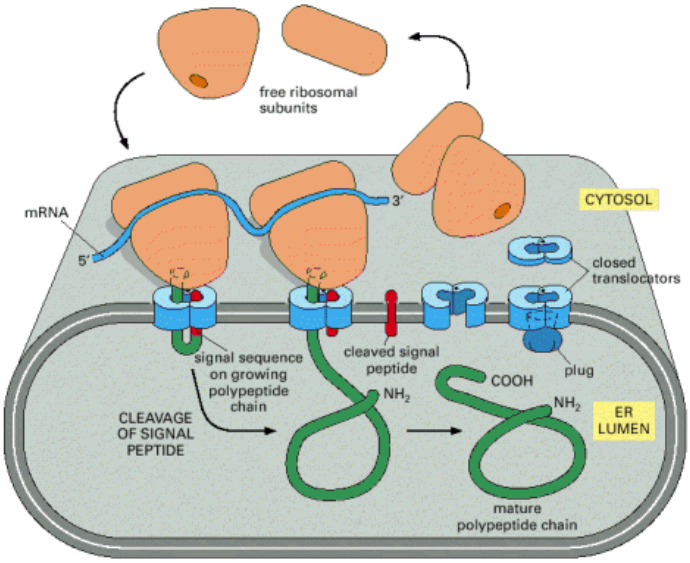

Figure 12-40. The signal hypothesis. A simplified view of protein translocation across the ER membrane, as originally proposed. When the ER signal sequence emerges from the ribosome, it directs the ribosome to a translocator on the ER membrane that forms a pore in the membrane through which the polypeptide is translocated. The signal sequence is clipped off during translation by a signal peptidase, and the mature protein is released into the lumen of the ER immediately after being synthesized. We now know that the hypothesis is correct in outline but that additional components besides those shown in this figure are required.

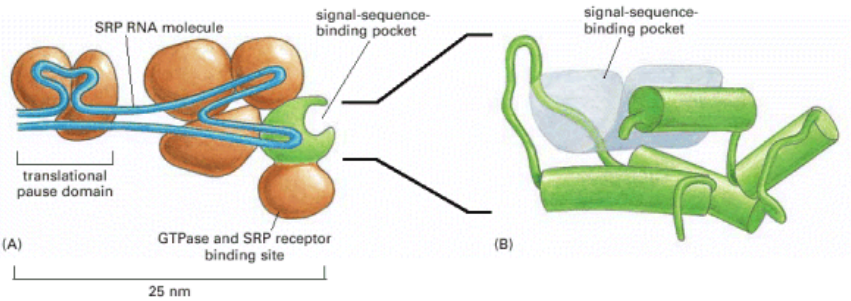

Figure 12-41. The signal-recognition particle (SRP). (A) A mammalian SRP is an elongated complex containing six protein subunits and one RNA molecule (SRP RNA). One end of the SRP binds to an ER signal sequence on a growing polypeptide chain, while the other end binds to the ribosome itself and pauses translation. The RNA in the particle may mediate an interaction with ribosomal RNA. (B) The crystal structure of the signal-sequence-binding domain of a bacterial SRP subunit. The domain contains a large, exposed binding pocket that is lined by hydrophobic amino acids, a large number of which are methionines. The outline of the pocket is shaded in *gray* to emphasize its location. The flexible side chains of methionine are ideal for building adaptable hydrophobic binding sites for other proteins. Calmodulin, for example (discussed in Chapter 15), binds to many different target proteins, and, like SRP, contains patches of methionines to clamp down on differently shaped targets (see Figure 15-40). (A, adapted from V. Siegel and P. Walter, *Nature* 320:8284, 1986; B, adapted from Keenan et al., *Cell* 94:181191,1998.)

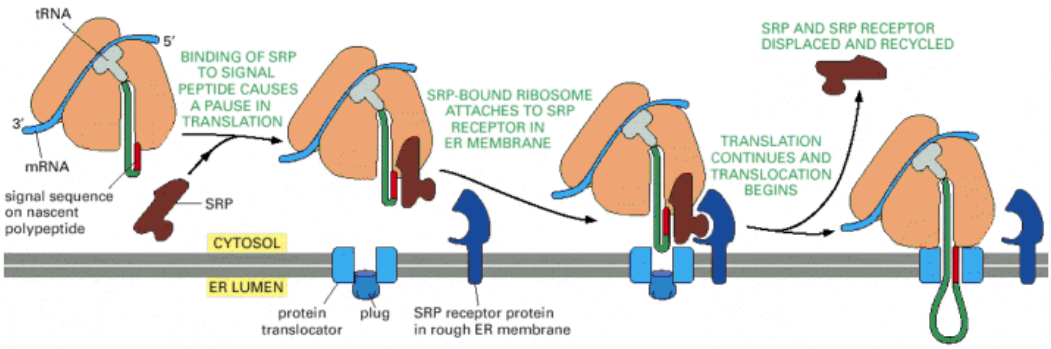

Figure 12-42. How ER signal sequences and SRP direct ribosomes to the ER membrane. The SRP and its receptor are thought to act in concert. The SRP binds to both the exposed ER signal sequence and the ribosome, thereby inducing a pause in translation. The SRP receptor in the ER membrane, which is composed of two different polypeptide chains, binds the SRP-ribosome complex and directs it to the translocator. In a poorly understood reaction, the SRP and SRP receptor are then released, leaving the ribosome bound to the translocator in the ER membrane. The translocator then inserts the polypeptide chain into the membrane and transfers it across the lipid bilayer. Because one of the SRP proteins and both chains of the SRP receptor contain GTP-binding domains, it is thought that conformational changes that occur during cycles of GTP binding and hydrolysis (discussed in Chapter 15) ensure that SRP release occurs only after the ribosome has become properly engaged with the translocator in the ER membrane. The translocator is closed (indicated schematically by the ER-lumenal plug) until the ribosome has bound, so that the permeability barrier of the ER membrane is maintained at all times.

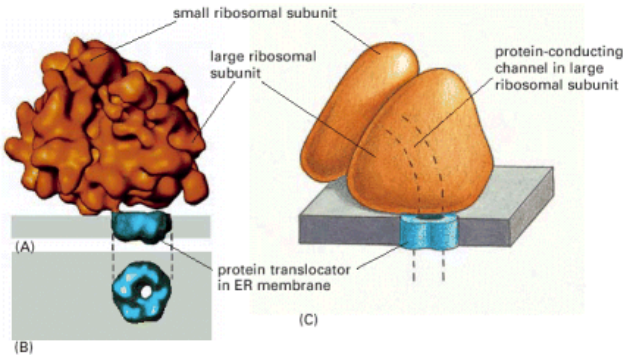

Figure 12-43. A ribosome bound to the Sec61 protein translocator. (A) A reconstruction of the complex from electron microscopic images viewed from the side. (B) A view of the translocator seen from the top (looking down on the membrane). (C) A schematic drawing of a membrane-bound ribosome attached to the translocator. The central pore in the translocator lines up with the tunnel in the large ribosomal subunit, through which the growing polypeptide chain exits from the ribosome (see Figure 6-68C). (A and B, from R. Beckmann et al., *Science* 278:21232126, 1997. © AAAS.)

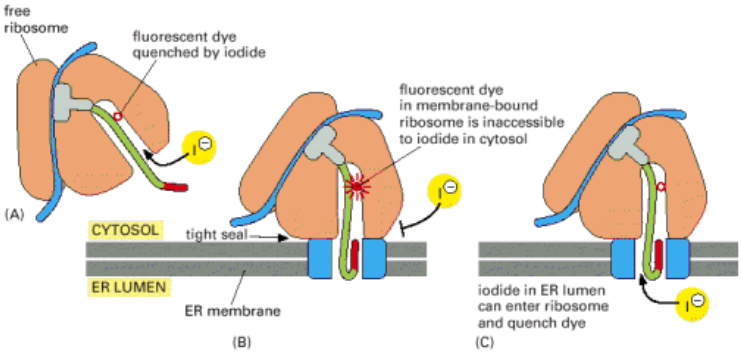

Figure 12-44. Evidence for a continuous aqueous pore joining the ER lumen and the interior of the ribosome. In this experiment, a fluorescent dye is attached to a portion of the growing polypeptide chain that is still contained within the ribosome. (A) In free ribosomes, the dye is accessible to iodide ions in solution in the cytosol. These ions quench the fluorescence when they come in contact with the dye. (B) In contrast, when a ribosome is membrane-bound, a tight seal is formed between the ribosome and the ER membrane that prevents access of the above iodide ions to the dye. (C) When iodide ions are added to the ER lumen, they can diffuse through the translocator all the way into the ribosome tunnel to quench the dye inside the membrane-bound ribosome.

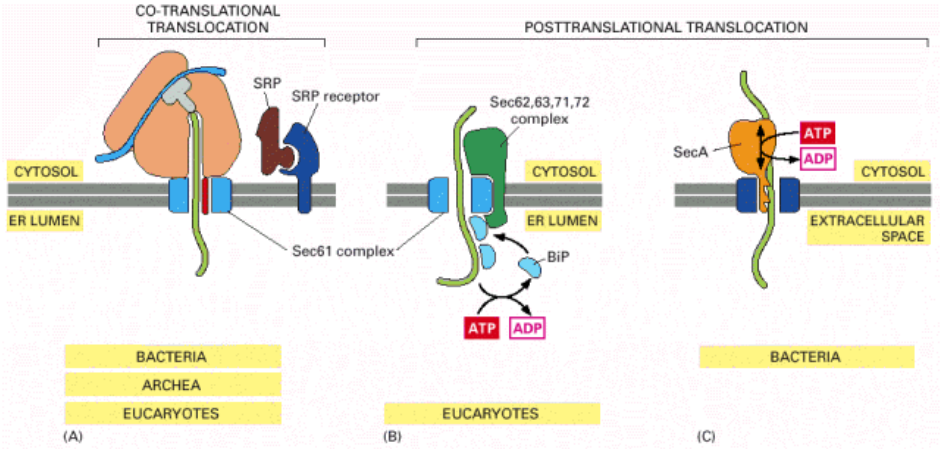

Figure 12-45. Three ways in which protein translocation can be driven through structurally similar translocators. (A) Co-translational translocation. The ribosome is brought to the membrane by the SRP and SRP receptor and forms a tight seal with the Sec61 protein translocator. The growing polypeptide chain is threaded across the membrane as it is made. No additional energy is needed, as the only path available to the growing chain is to cross the membrane. (B) Posttranslational translocation in eucaryotic cells. An additional complex composed of the Sec62, Sec63, Sec71, and Sec72 proteins is attached to the Sec61 translocator and deposits BiP molecules onto the translocating chain as it emerges into the ER lumen. ATP-driven cycles of BiP binding and release pull the protein into the lumen, a mechanism that closely resembles the thermal ratchet model for mitochondrial import in Figure 12-28. (C) Posttranslational translocation in bacteria. The completed polypeptide chain is fed from the cytosolic side into a translocator in the plasma membrane by the SecA ATPase. ATP-hydrolysis-driven conformational changes drive a pistonlike motion in SecA, each cycle pushing about 20 amino acids of the protein chain through the pore of the translocator. The Sec pathway used for protein translocation across the thylakoid membrane in chloroplasts uses a similar mechanism (see Figure 12-30B). Whereas the Sec61 translocator, SRP, and SRP receptor are found in all organisms, SecA is found exclusively in bacteria, and the Sec62, Sec63, Sec71, and Sec72 proteins are found exclusively in eucaryotic cells. (Adapted from P. Walter and A.E. Johnson, *Annu. Rev. Cell Biol.* 10:87119, 1994.)

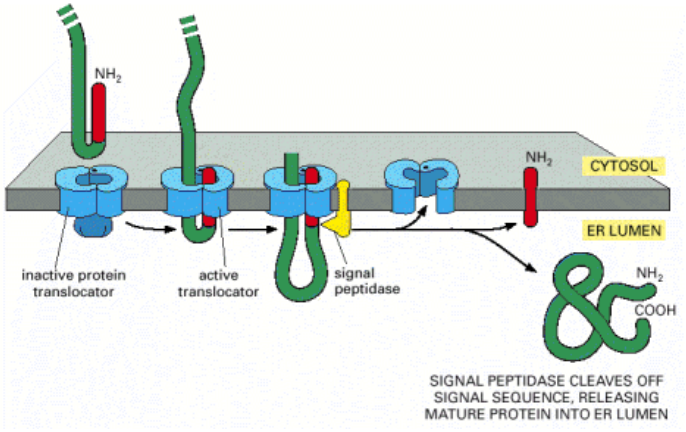

Figure 12-46. A model for how a soluble protein is translocated across the ER membrane. On binding an ER signal sequence (which acts as a start-transfer signal), the translocator opens its pore, allowing the transfer of the polypeptide chain across the lipid bilayer as a loop. After the protein has been completely translocated, the pore closes, but the translocator now opens laterally within the lipid bilayer, allowing the hydrophobic signal sequence to diffuse into the bilayer, where it is rapidly degraded. (In this figure and the three figures that follow, the ribosomes have been omitted for clarity.)

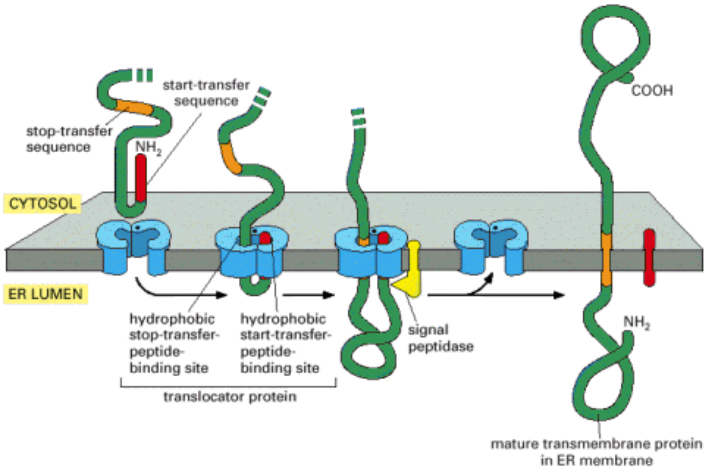

Figure 12-47. How a single-pass transmembrane protein with a cleaved ER signal sequence is integrated into the ER membrane. In this hypothetical protein the co-translational translocation process is initiated by an N-terminal ER signal sequence *(red)* that functions as a start-transfer signal, as in Figure 12-46. In addition to this start-transfer sequence, however, the protein also contains a stop-transfer sequence *(orange)*. When the stop-transfer sequence enters the translocator and interacts with a binding site, the translocator changes its conformation and discharges the protein laterally into the lipid bilayer.

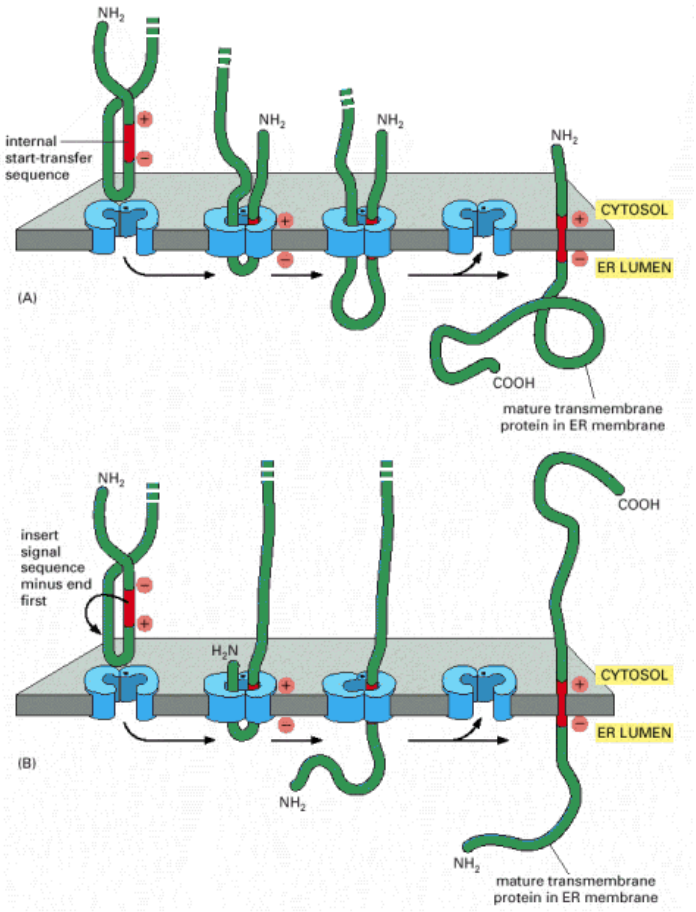

Figure 12-48. Integration of a single-pass membrane protein with an internal signal sequence into the ER membrane. In these hypothetical proteins, an internal ER signal sequence that functions as a start-transfer signal binds to the translocator in such a way that its more positively charged end remains in the cytosol. (A) If there are more positively charged amino acids immediately preceding the hydrophobic core of the start-transfer sequence than there are following it, the start-transfer sequence is inserted into the translocator in the orientation shown here. The part of the protein C-terminal to the start-transfer sequence will therefore be passed across the membrane. (B) If there are more positively charged amino acids immediately following the hydrophobic core of the start-transfer sequence than there are preceding it, the start-transfer sequence is inserted into the translocator in the orientation shown here. The part of the protein N-terminal to the start-transfer sequence will therefore be passed across the membrane. Because translocation cannot start before a start-transfer sequence appears outside the ribosome, translocation of the N-terminal portion of the protein shown in (B) can occur only after this portion has been fully synthesized. Note that there are two ways to insert a single-pass membrane-spanning protein whose N-terminus is located in the ER lumen: that shown in Figure 12-47 and that shown in (B) here.

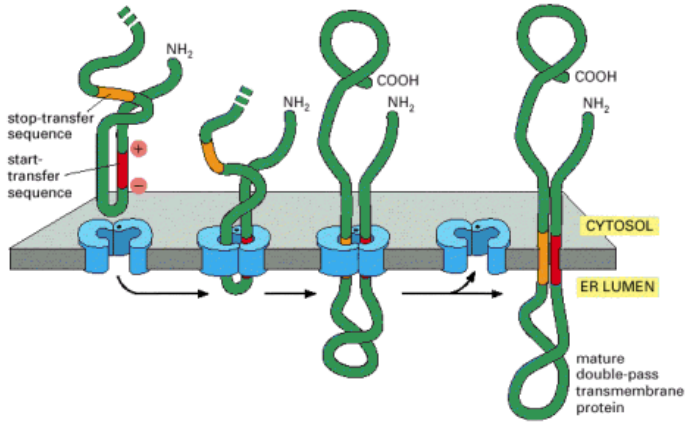

Figure 12-49. Integration of a double-pass membrane protein with an internal signal sequence into the ER membrane. In this hypothetical protein, an internal ER signal sequence acts as a start-transfer signal (as in Figure 12-48) and initiates the transfer of the C-terminal part of the protein. At some point after a stop-transfer sequence has entered the translocator, the translocator discharges the sequence laterally into the membrane.

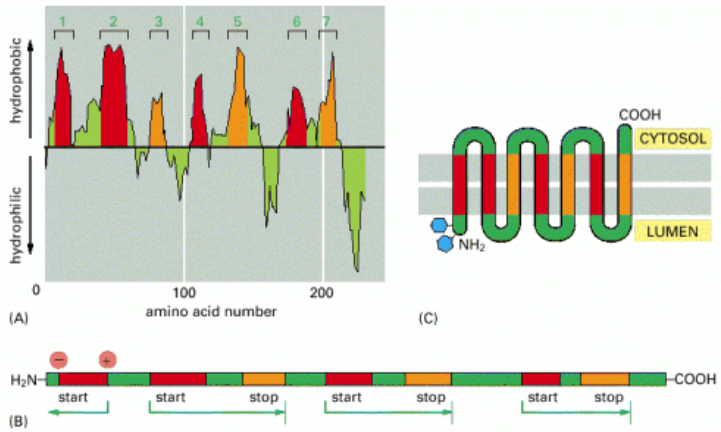

Figure 12-50. The insertion of the multipass membrane protein rhodopsin into the ER membrane. Rhodopsin is the light-sensitive protein in rod photoreceptor cells in the mammalian retina (discussed in Chapter 15). (A) A hydrophobicity plot identifies seven short hydrophobic regions in rhodopsin. (B) The most N-terminal region serves as a start-transfer sequence that causes the preceding N-terminal portion of the protein to be passed across the ER membrane. Subsequent hydrophobic sequences function in alternation as start-transfer and stop-transfer sequences. (C) The final integrated rhodopsin has its N-terminus located in the ER lumen and its C-terminus located in the cytosol. The *blue hexagons* represent covalently attached oligosaccharides. Arrows indicate the parts of the protein that are inserted into the translocator.

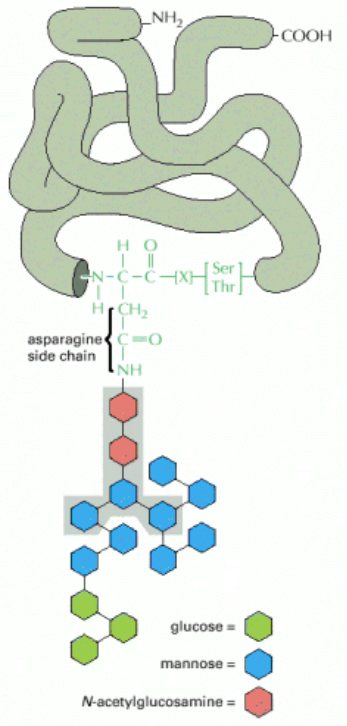

Figure 12-51. The asparagine-linked (*N*-linked) precursor oligosaccharide that is added to most proteins in the rough ER membrane. The five sugars in the *gray box* form the "core region" of this oligosaccharide. For many glycoproteins, only the core sugars survive the extensive oligosaccharide trimming process that takes place in the Golgi apparatus. Only asparagines in the sequences Asn-X-Ser and Asn-X-Thr (where X is any amino acid except proline) become glycosylated. These two sequences occur much less frequently in glycoproteins than in nonglycosylated cytosolic proteins; evidently there has been selective pressure against these sequences during protein evolution, presumably because glycosylation at too many sites would interfere with protein folding.

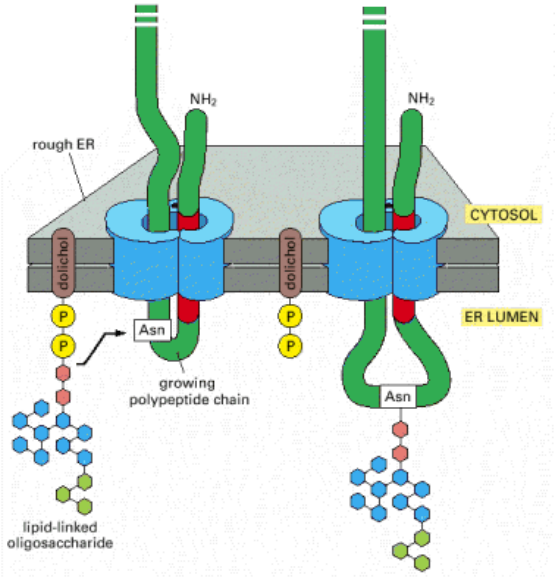

Figure 12-52. Protein glycosylation in the rough ER. Almost as soon as a polypeptide chain enters the ER lumen, it is glycosylated on target asparagine amino acids. The precursor oligosaccharide shown in Figure 12-51 is transferred to the asparagine as an intact unit in a reaction catalyzed by a membrane-bound *oligosaccharyl transferase* enzyme. As with signal peptidase, one copy of this enzyme is associated with each protein translocator in the ER membrane. (The ribosome is not shown for clarity.)

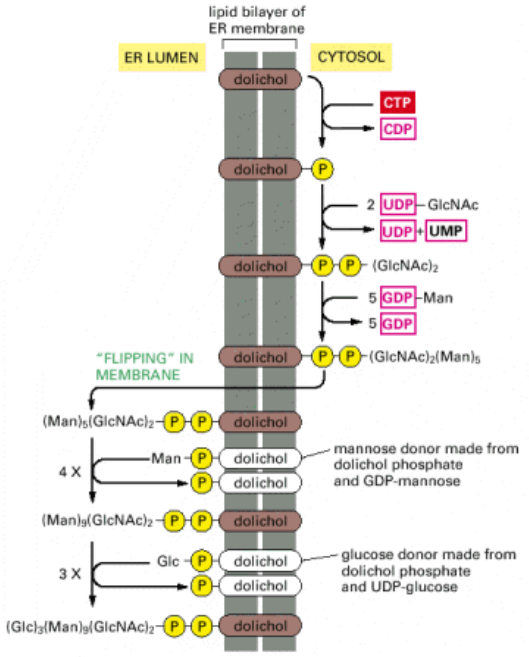

Figure 12-53. Synthesis of the lipid-linked precursor oligosaccharide in the rough ER membrane. The oligosaccharide is assembled sugar by sugar onto the carrier lipid dolichol (a polyisoprenoid; see Panel 2-5, pp. 118119). Dolichol is long and very hydrophobic: its 22 five-carbon units can span the thickness of a lipid bilayer more than three times, so that the attached oligosaccharide is firmly anchored in the membrane. The first sugar is linked to dolichol by a pyrophosphate bridge. This high-energy bond activates the oligosaccharide for its eventual transfer from the lipid to an asparagine side chain of a nascent polypeptide on the lumenal side of the rough ER. As indicated, the synthesis of the oligosaccharide starts on the cytosolic side of the ER membrane and continues on the lumenal face after the $(Man)_5(GlcNAc)_2$ lipid intermediate is flipped across the bilayer by a transporter protein. All the subsequent glycosyl transfer reactions on the lumenal side of the ER involve transfers from dolichol-P-glucose and dolichol-P-mannose; these activated, lipid-linked monosaccharides are synthesized from dolichol phosphate and UDP-glucose or GDP-mannose (as appropriate) on the cytosolic side of the ER and are then thought to be flipped across the ER membrane. GlcNAc = *N*-acetylglucosamine; Man = mannose; Glc = glucose.

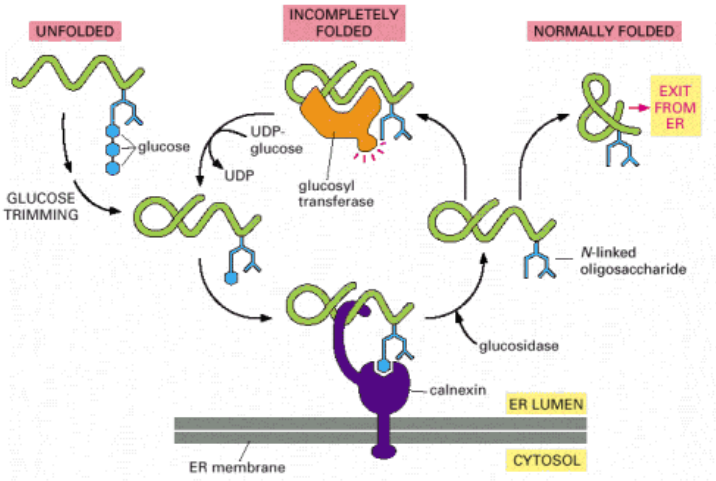

Figure 12-54. The role of *N*-linked glycosylation in ER protein folding. The ER-membrane-bound chaperone protein calnexin binds to incompletely folded proteins containing one terminal glucose on *N*-linked oligosaccharides, trapping the protein in the ER. Removal of the terminal glucose by a glucosidase releases the protein from calnexin. A glucosyl transferase is the crucial enzyme that determines whether the protein is folded properly or not: if the protein is still incompletely folded, the enzyme transfers a new glucose from UDP-glucose to the *N*-linked oligosaccharide, renewing the protein's affinity for calnexin and retaining it in the ER. The cycle repeats until the protein has folded completely. Calreticulin functions similarly, except that it is a soluble ER resident protein. Another ER chaperone, ERp57 (not shown), collaborates with calnexin and calreticulin in retaining an incompletely folded protein in the ER.

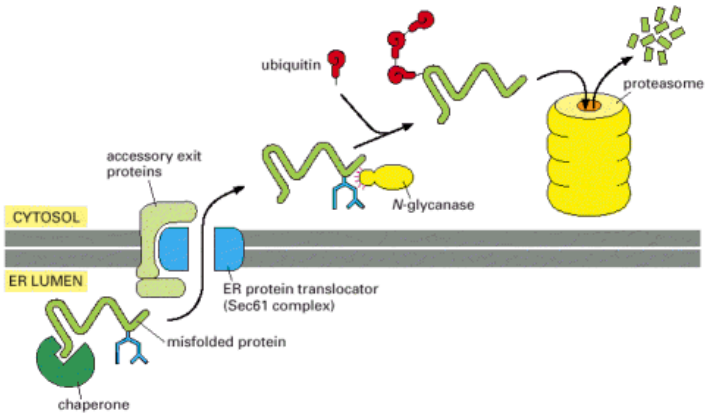

Figure 12-55. The export and degradation of misfolded ER proteins. Misfolded soluble proteins in the ER lumen are translocated back into the cytosol, where they are deglycosylated, ubiquitylated, and degraded in proteasomes. Misfolded membrane proteins follow a similar pathway. Misfolded proteins are exported through the same type of translocator that mediated their import; accessory proteins that are associated with the translocator allow it to operate in the export direction.

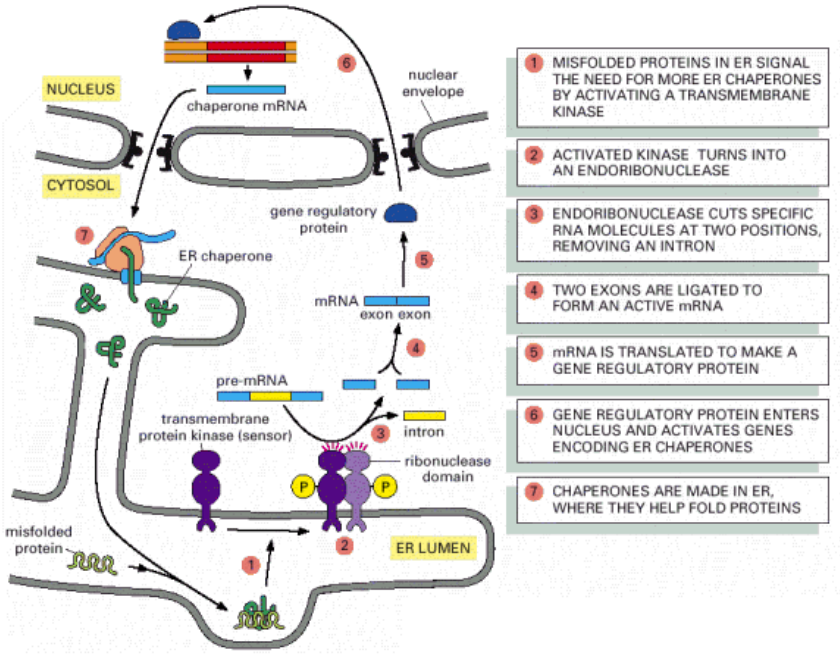

Figure 12-56. The unfolded protein response in yeast. By this novel intracellular signaling pathway, the accumulation of misfolded proteins in the ER lumen signals to the nucleus to activate the transcription of genes that encode proteins that help the cell to cope with the abundance of misfolded proteins in the ER.

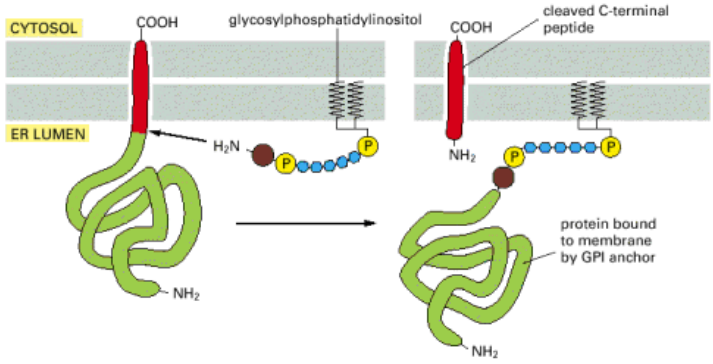

Figure 12-57. The attachment of a GPI anchor to a protein in the ER. Immediately after the completion of protein synthesis, the precursor protein remains anchored in the ER membrane by a hydrophobic C-terminal sequence of 1520 amino acids; the rest of the protein is in the ER lumen. Within less than a minute, an enzyme in the ER cuts the protein free from its membrane-bound C terminus and simultaneously attaches the new C terminus to an amino group on a preassembled GPI intermediate. The signal that specifies this modification is contained within the hydrophobic C-terminal sequence and a few amino acids adjacent to it on the lumenal side of the ER membrane; if this signal is added to other proteins, they too become modified in this way. Because of the covalently linked lipid anchor, the protein remains membrane-bound, with all of its amino acids exposed initially on the lumenal side of the ER and eventually on the cell exterior.

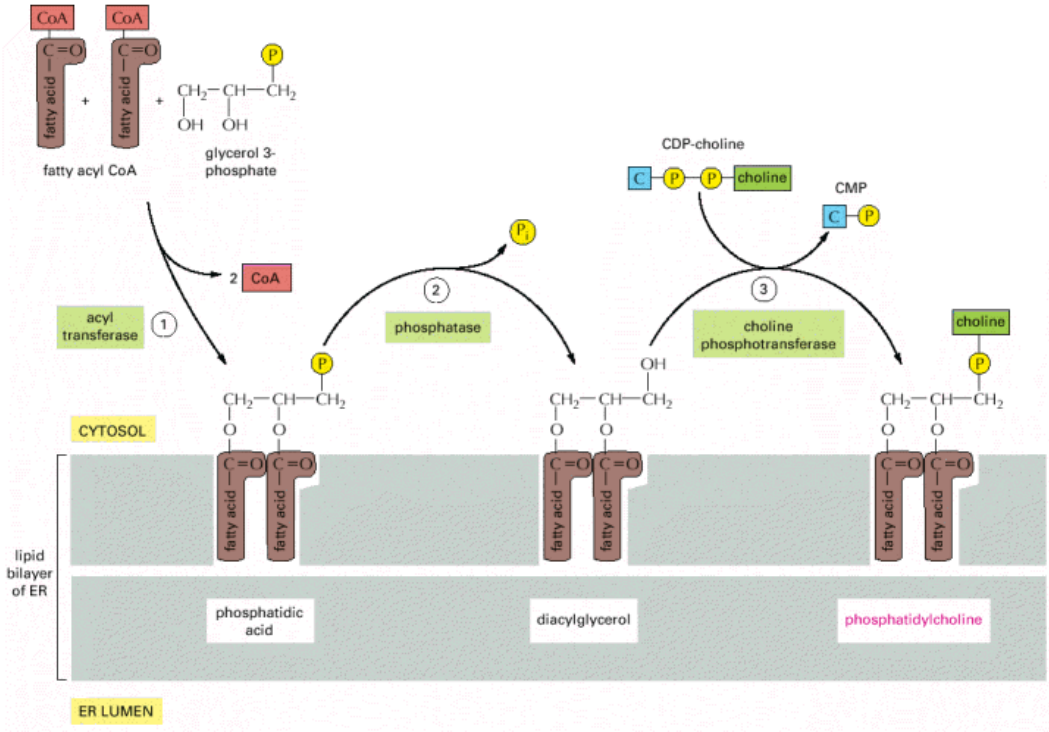

Figure 12-58. The synthesis of phosphatidylcholine. This phospholipid is synthesized from fatty acyl-coenzyme A (fatty acyl CoA), glycerol 3-phosphate, and cytidine-bisphosphocholine (CDP-choline).

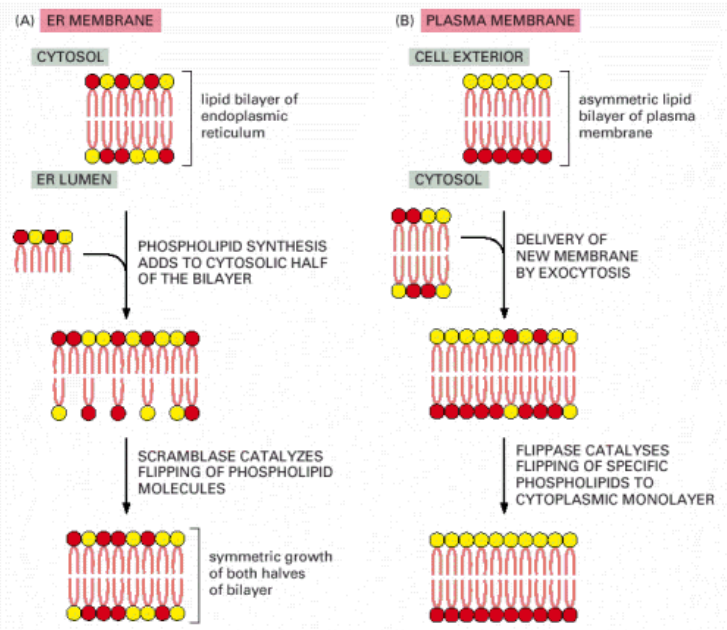

Figure 12-59. The role of phospholipid translocators in lipid bilayer synthesis. (A) Because new lipid molecules are added only to the cytosolic half of the bilayer and lipid molecules do not flip spontaneously from one monolayer to the other, a membrane-bound phospholipid translocator (called a scramblase) is required to transfer lipid molecules from the cytosolic half to the lumenal half so that the membrane grows as a bilayer. The scramblase is not specific for particular phospholipid head groups and therefore equilibrates the different phospholipids between the two monolayers. (B) Fueled by ATP hydrolysis, a head-group-specific flippase in the plasma membrane actively flips phosphatidylserine and phosphatidylethanolamine directionally from the extracellular to the cytosolic leaflet, creating the characteristically asymmetric lipid bilayer of the plasma membrane of animal cells (see Figure 10-14). A scramblase is also present in plasma membranes to ensure that both monolayers remain equally populated with lipids; the continuous action of the flippase is therefore necessary to maintain the phospholipid asymmetry.

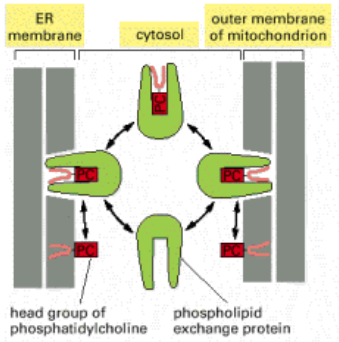

Figure 12-60. Phospholipid exchange proteins. Because phospholipids are insoluble in water, their passage between membranes requires carrier proteins. Phospholipid exchange proteins are water-soluble proteins that carry a single molecule of phospholipid at a time; they can pick up a lipid molecule from one membrane and release it at another, thereby redistributing phospholipids between membrane-enclosed compartments. The net transfer of phosphatidylcholine (PC) from the ER to mitochondria can occur without the input of additional energy, because the concentration of PC is high in the ER membrane (where it is made) and low in the outer mitochondrial membrane. One predicts a lipid translocator in the outer mitochondrial membrane to equilibrate the lipids between the two leaflets of its bilayer, and there must also be a mechanism to transfer lipids between the outer and inner mitochondrial membranes. These postulated pathways, however, remain to be discovered.

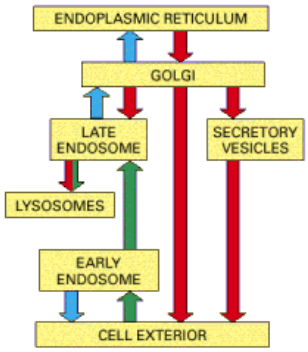

Figure 13-1. The endocytic and biosynthetic-secretory pathways. In this "road map" of biosynthetic protein traffic, which was introduced in Chapter 12, the endocytic and biosynthetic- secretory pathways are illustrated with *green* and *red* arrows, respectively. In addition, *blue* arrows are used to denote retrieval pathways by which the backflow of selected components is maintained (see also Figure 13-3).

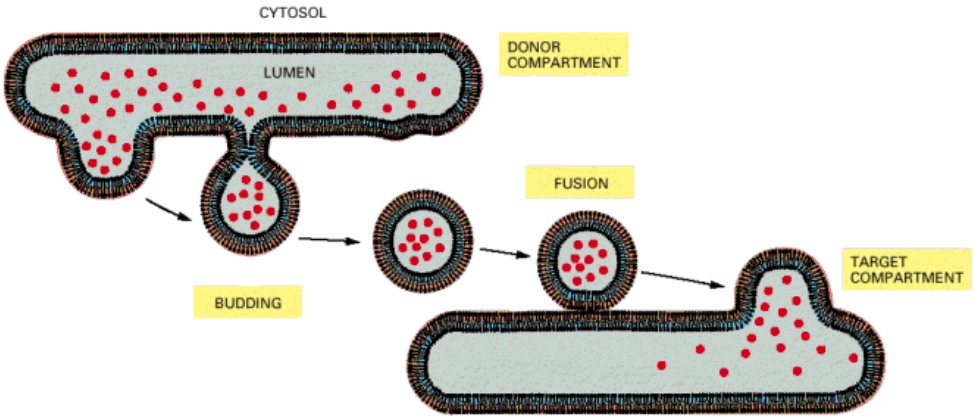

Figure 13-2. Vesicular transport. Transport vesicles bud off from one compartment and fuse with another. As they do so, they carry material as cargo from the lumen and membrane of the donor compartment to the lumen and membrane of the target compartment, as shown.

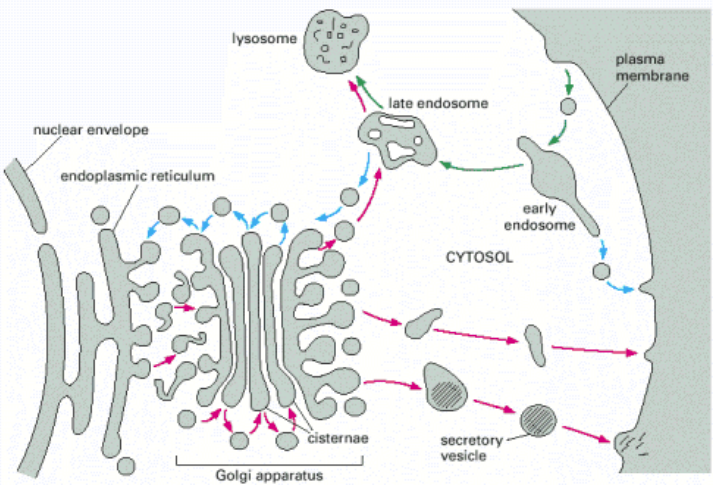

Figure 13-3. The intracellular compartments of the eucaryotic cell involved in the biosynthetic- secretory and endocytic pathways. Each compartment encloses a space, called a *lumen*, that is topologically equivalent to the outside of the cell, and all compartments shown communicate with one another and the outside of the cell by means of transport vesicles. In the biosynthetic-secretory pathway *(red arrows)* protein molecules are transported from the ER to the plasma membrane or (via late endosomes) to lysosomes. In the endocytic pathway *(green arrows)* molecules are ingested in vesicles derived from the plasma membrane and delivered to early endosomes and then (via late endosomes) to lysosomes. Many endocytosed molecules are retrieved from early endosomes and returned to the cell surface for reuse; similarly, some molecules are retrieved from the late endosome and returned to the Golgi apparatus, and some are retrieved from the Golgi apparatus and returned to the ER. All of these retrieval pathways are shown with *blue arrows* (see also Figure 13-1).

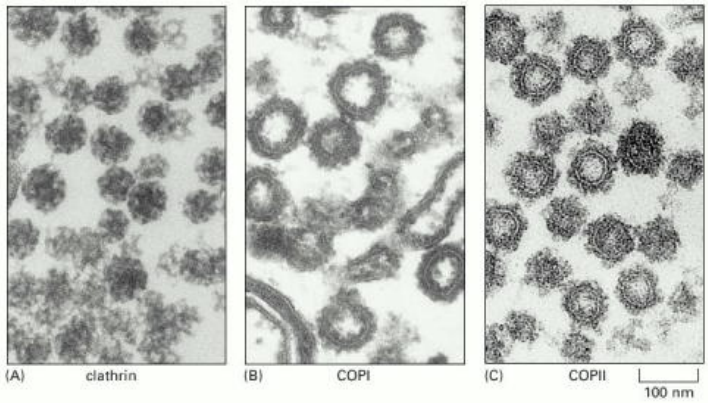

Figure 13-4. Electron micrograph of clathrin-coated, COPI-coated, and COPII-coated vesicles. All are shown in electron micrographs at the same scale. (A) Clathrin-coated vesicles. (B) Golgi cisternae from a cell-free system in which COPI-coated vesicles bud in the test tube. (C) COPII-coated vesicles. Note that the vesicles with clathrin coats have a more regular structure. (A and B, courtesy of Lelio Orci, from L. Orci, B. Glick, and J. Rothman, *Cell* 46:171184, 1986. © Elsevier; C, courtesy of Charles Barlowe and Lelio Orci.)

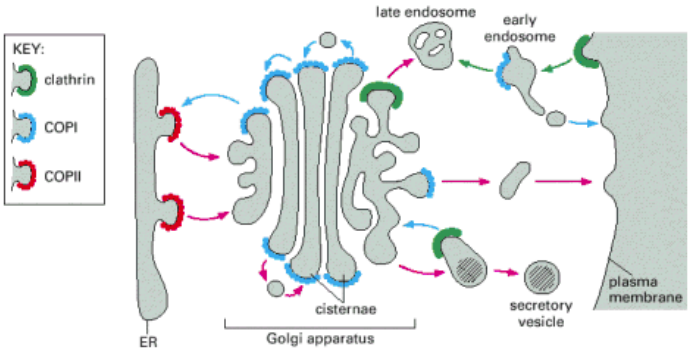

Figure 13-5. Utilization of different coats in vesicular traffic. Different coat proteins select different cargo and shape the transport vesicles that mediate the various steps in the biosynthetic- secretory and endocytic pathways. When the same coats function in different places in the cell, they can incorporate different coat protein subunits that modify their properties (not shown). Many differentiated cells have additional pathways beside those shown in this figure, including a sorting pathway from the *trans* Golgi network to the apical surface in polarized cells and a specialized recycling pathway for proteins of synaptic vesicles in the synapses of neurons.

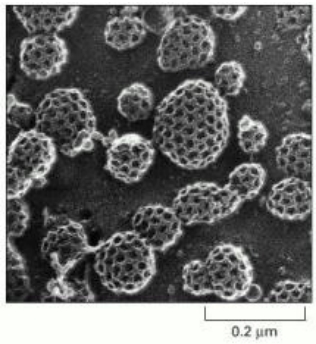

Figure 13-6. Clathrin-coated pits and vesicles. This rapid-freeze, deep-etch electron micrograph shows numerous clathrin-coated pits and vesicles on the inner surface of the plasma membrane of cultured fibroblasts. The cells were rapidly frozen in liquid helium, fractured, and deep-etched to expose the cytoplasmic surface of the plasma membrane. (From J. Heuser, *J. Cell Biol.* 84:560583, 1980. © The Rockefeller University Press.)

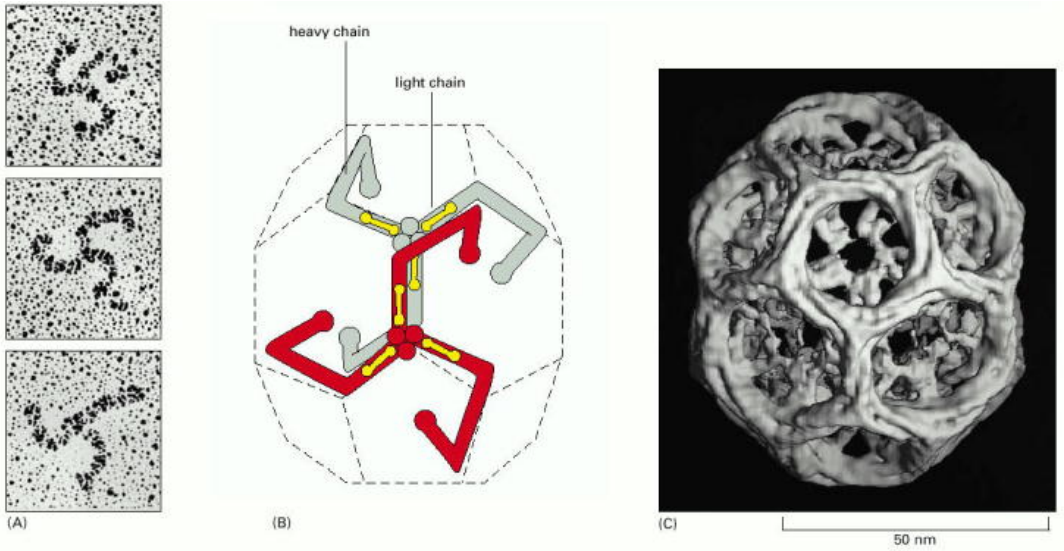

Figure 13-7. The structure of a clathrin coat. (A) Electron micrographs of clathrin triskelions shadowed with platinum. Although this feature cannot be seen in these micrographs, each triskelion is composed of 3 clathrin heavy chains and 3 clathrin light chains. (B) A schematic drawing of the probable arrangement of triskelions on the cytosolic surface of a clathrin-coated vesicle. Two triskelions are shown, with the heavy chains of one in *red* and those of the other in *gray;* the light chains are shown in *yellow*. The overlapping arrangement of the flexible triskelion arms provides both mechanical strength and flexibility. Note that the end of each leg of the triskelion turns inward, so that its N-terminal domain forms an intermediate shell. (C) A cryo electron micrograph taken of a clathrin coat composed of 36 triskelions organized in a network of 12 pentagons and 6 hexagons. The interwoven legs of the clathrin triskelions form an outer shell into which the N-terminal domains of the triskelions protrude to form an inner layer visible through the openings. It is this inner layer that contacts the adaptor proteins (adaptins) shown in the next figure. Although the coat shown is too small to enclose a membrane vesicle, the clathrin coats on vesicles are constructed in a similar way from 12 pentagons plus a larger number of hexagons, resembling the architecture of a soccer ball. (A, from E. Ungewickell and D. Branton, *Nature* 289:420422, 1981. © Macmillan Magazines Ltd.; B, from I.S. Nathke et al., *Cell* 68:899910, 1992. © Elsevier; C, courtesy of B.M.F. Pearse, from C.J. Smith et al., *EMBO J.* 17:49434953, 1998.)

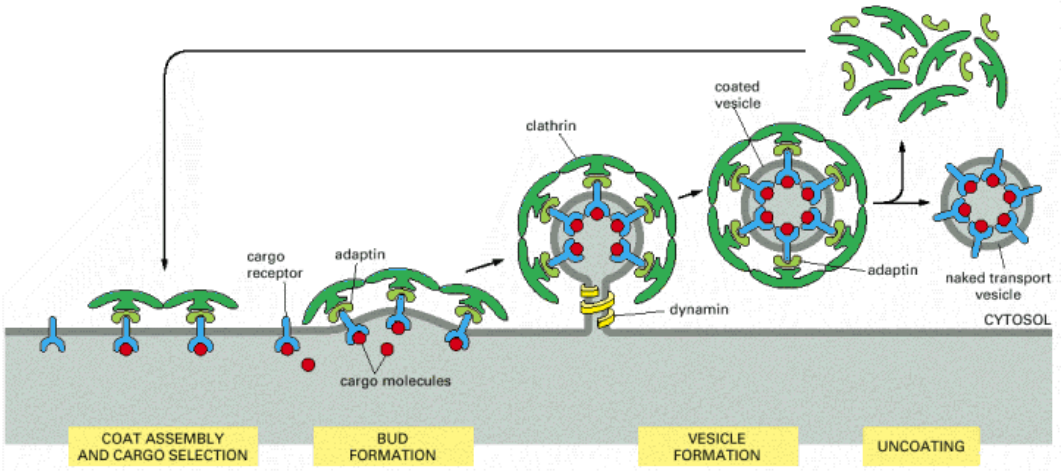

Figure 13-8. The assembly and disassembly of a clathrin coat. The assembly of the coat is thought to introduce curvature into the membrane, which leads in turn to the formation of uniformly sized coated buds. The adaptins bind both clathrin triskelions and membrane-bound cargo receptors, thereby mediating the selective recruitment of both membrane and cargo molecules into the vesicle. The pinching-off of the bud to form a vesicle involves membrane fusion; this is helped by the GTP-binding protein dynamin, which assembles around the neck of the bud. The coat of clathrin-coated vesicles is rapidly removed shortly after the vesicle forms.

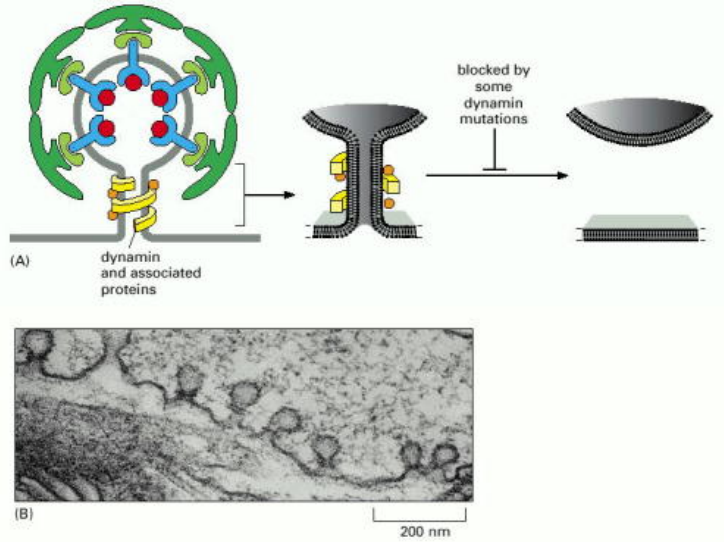

Figure 13-9. The role of dynamin in pinching off clathrin-coated vesicles from the membrane. (A) The dynamin binds to a forming bud on the membrane and assembles into a ring around the neck of the bud. The dynamin ring is thought to be a template that recruits other proteins to the vesicle neck, which together with dynamin destabilize the membrane so that the noncytoplasmic leaflets of the lipid bilayers flow together. The newly formed vesicle then pinches off the membrane. Specific mutations in dynamin can either enhance or block the pinching-off process. (B) Dynamin was discovered as the protein defective in the *shibire* mutant of *Drosophila*. These mutant flies become paralyzed because clathrin-mediated endocytosis stops, and the synaptic vesicle membrane fails to recycle, blocking synaptic signaling. Deeply invaginated clathrin-coated pits form in the fly's nerve cells, with a ring assembled around the neck, as shown in this thin-section electron micrograph, that is assumed to be mutant dynamin. The process then stops because membrane fusion does not take place. (B, from J.H. Koenig and K. Ikeda, *J. Neurosci.* 9:38443860, 1989. © Society of Neuroscience.)

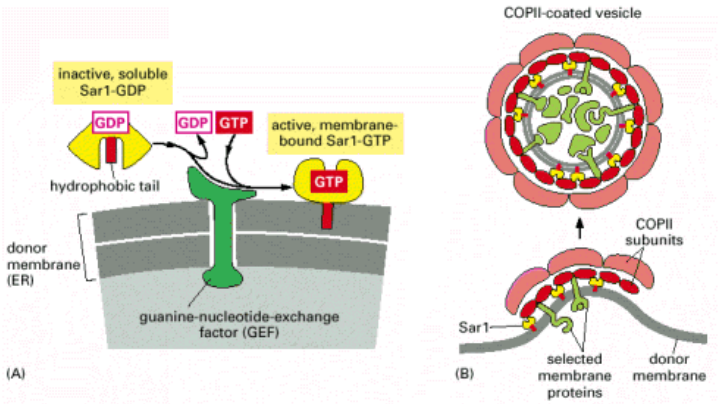

Figure 13-10. A current model of COPII-coated vesicle formation. (A) The Sar1 protein is a coat recruitment GTPase. Inactive, soluble Sar1-GDP binds to a GEF (called Sec12) in the ER membrane, causing the Sar1 to release its GDP and bind GTP. A GTP-triggered conformational change in Sar1 exposes its hydrophobic tail, which inserts into the ER membrane. (B) Membrane-bound, active Sar1-GTP recruits COPII subunits to the membrane. This causes the membrane to form a bud, which includes selected membrane proteins. A subsequent membrane-fusion event pinches off and releases the coated vesicle. Other coated vesicles are thought to form in a similar way. In contrast to Sar1, the coat recruitment GTPase ARF contains a covalently attached fatty acid chain that functions similarly to the hydrophobic tail of Sar1 as a regulated membrane anchor; it is retracted in the GDP-bound state and exposed in the GTP-bound state. As we discuss later in this chapter, Rab proteins regulate their membrane attachment in a similar manner (see Figure 13-14).

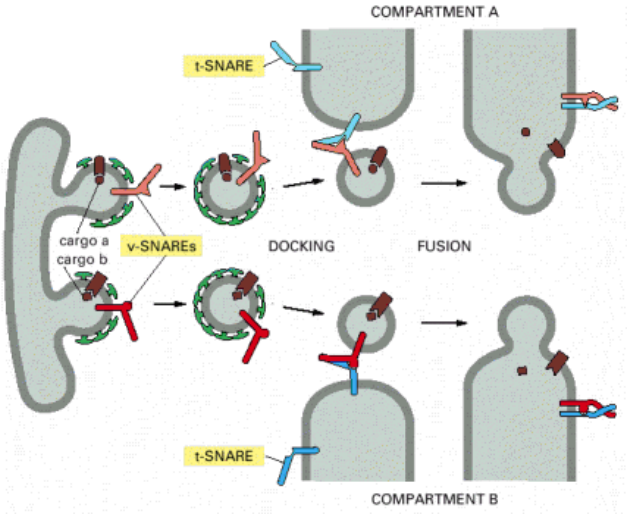

Figure 13-11. The postulated role of SNAREs in guiding vesicular transport. Complementary sets of vesicle SNAREs (v-SNAREs) and target membrane SNAREs (t-SNAREs) contribute to the selectivity of transport-vesicle docking and fusion. The v-SNAREs are packaged together with the coat proteins during the budding of transport vesicles from the donor membrane and bind to complementary t-SNAREs in the target membrane. After fusion, the v- and t-SNAREs remain associated in a tight complex. The complexes have to be dissociated before the t-SNAREs can accept a new vesicle or the v-SNAREs can be recycled to the donor compartment for participation in a new round of vesicular transport. As shown here, different v-SNAREs can be packaged with different cargo molecules (through association with other proteins; not shown) when leaving the donor compartment. In this case, the two sets of cargo will be delivered to different t-SNAREs and therefore to different target membranes.

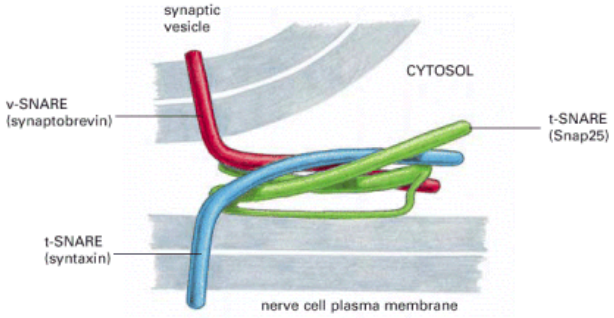

Figure 13-12. The structure of paired SNAREs. The SNAREs responsible for docking synaptic vesicles at the plasma membrane of nerve terminals consist of three proteins. The v-SNARE *synaptobrevin*, and the t-SNARE *syntaxin* are both transmembrane proteins and each contributes one α-helix to the complex. The t-SNARE *Snap25* is a peripheral membrane protein that contributes two α-helices to the four-helix bundle. Trans-SNARE complexes always consists of four tightly intertwined α-helices, three contributed by a t-SNARE and one by a v-SNARE. The t-SNAREs are composed of multiple chains, one of which is always a transmembrane protein and contributes one helix, and one or two additional light chains that may or may not be transmembrane proteins and that contribute the remaining two helices to the four-helix bundle of the trans-SNARE complex. The crystal structure of a stable complex of the four intertwining α helices contributed by these proteins is modeled here in the context of the whole proteins. The α helices are shown as rods for simplicity. (Adapted from R.B. Sutton et al., *Nature* 395:347353, 1998.)

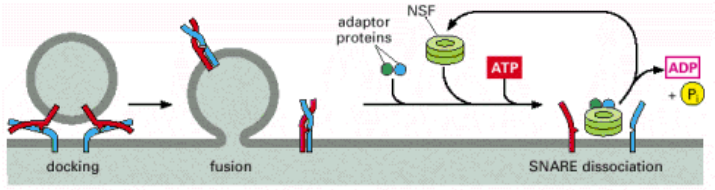

Figure 13-13. Dissociation of SNARE pairs by NSF after a membrane fusion cycle is completed. After the v-SNAREs and t-SNAREs have mediated the fusion of a vesicle on a target membrane, the NSF binds to the SNARE complex via adaptor proteins and hydrolyzes ATP to pry the SNAREs apart.

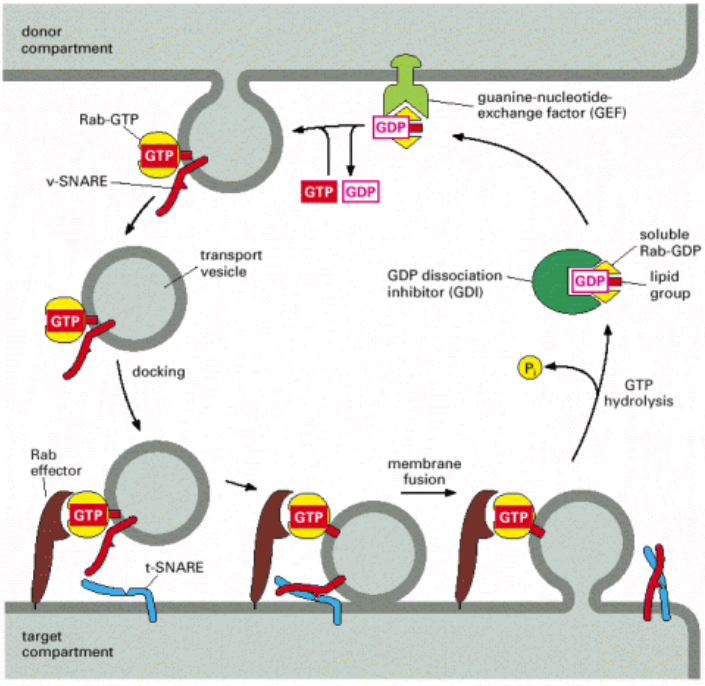

Figure 13-14. A postulated role of Rab proteins in facilitating the docking of transport vesicles. A GEF in the donor membrane recognizes a specific Rab protein and induces it to exchange GDP for GTP. GTP binding alters the conformation of the Rab protein, exposing a covalently attached lipid group, which helps anchor the protein in the membrane. Recall that an analogous mechanism helps to bind the coat-recruitment GTPases to these membranes, although a different GEF is involved (see Figure 13-10). The Rab-GTP remains bound to the surface of the transport vesicle after it pinches off from the donor membrane, and it then binds to varying Rab effector proteins on the target membrane. The Rab protein and its effectors help the vesicle dock and thereby facilitate the pairing of the appropriate v-SNAREs and t-SNAREs. After the vesicle has fused with the target membrane, the Rab protein hydrolyzes its bound GTP, releasing Rab-GDP into the cytosol, from where it can be reused in a new round of transport. As shown, Rab-GDP in the cytosol is bound to a GDP dissociation inhibitor (GDI), which prevents the Rab from releasing its bound GDP until it has interacted with appropriate proteins in the donor membrane. For clarity, we have omitted all of the proteins in the vesicle coats from this figure (see Figure 13-10).

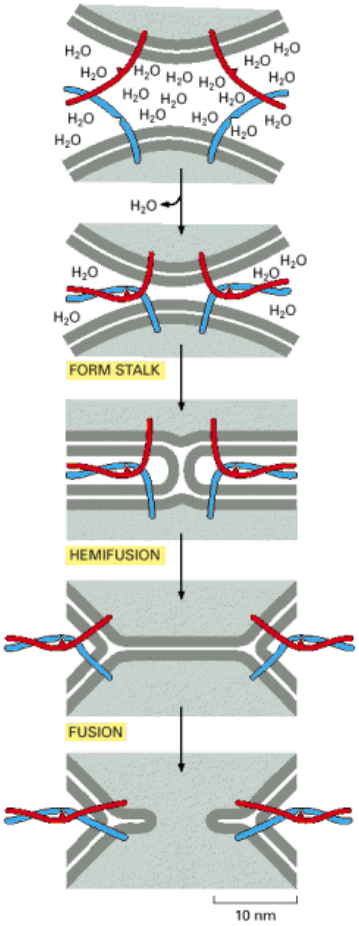

Figure 13-15. A model for how SNARE proteins may concentrate in membrane fusion. Bilayer fusion is proposed to occur in multiple steps. A tight SNARE pairing forces lipid bilayers into close apposition so that water molecules are expelled from the interface. Lipids of the two interacting leaflets of the bilayers then flow between the membranes to form a connecting stalk. Lipids of the other two leaflets then contact each other, forming a new bilayer, which widens the fusion zone *(hemifusion,* or half-fusion). Rupture of the new bilayer completes the fusion reaction.

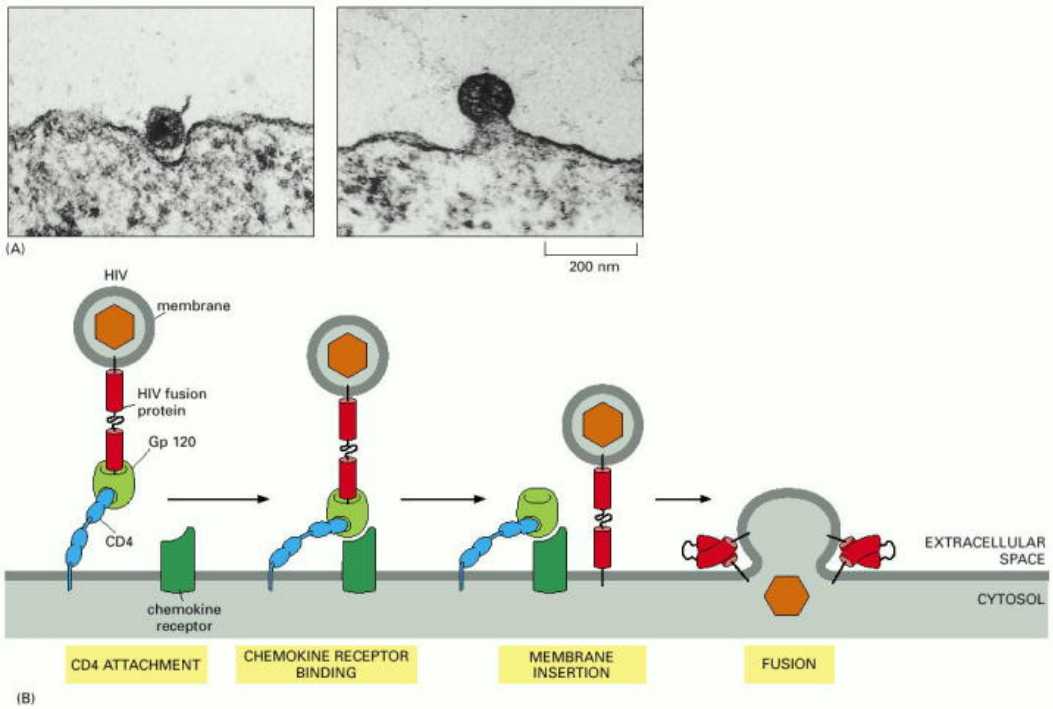

Figure 13-16. The entry of enveloped viruses into cells. (A) Electron micrographs showing how HIV enters a cell by fusing its membrane with the plasma membrane of the cell. (B) A model for the HIV membrane-fusion process. HIV binds first to the CD4 protein on the surface of the lymphocytes. This interaction is mediated by the viral gp120 protein bound to the HIV fusion protein. A second cell-surface protein on the host cell, which normally serves as a receptor for chemokines (discussed in Chapter 24), now interacts with gp120. This interaction releases the HIV fusion protein from gp120 allowing the previously buried hydrophobic fusion peptide, to insert into the plasma membrane. The fusion protein, which is a trimer (not shown), thus becomes transiently anchored as an integral membrane protein in two opposing membranes. The fusion protein then spontaneously rearranges, collapsing into a tightly packed six-helix bundle. The energy released by this rearrangement in multiple copies of the fusion protein is used to pull the two membranes together, overcoming the high activation energy barrier that normally prevents membrane fusion. Thus, like a mouse trap, the HIV fusion protein contains a reservoir of potential energy, which is released and harnessed to do mechanical work. (A, from B.S. Stein et al., *Cell* 49:659668, 1987. © Elsevier; B, adapted from a drawing by Wayne Hendrickson.)

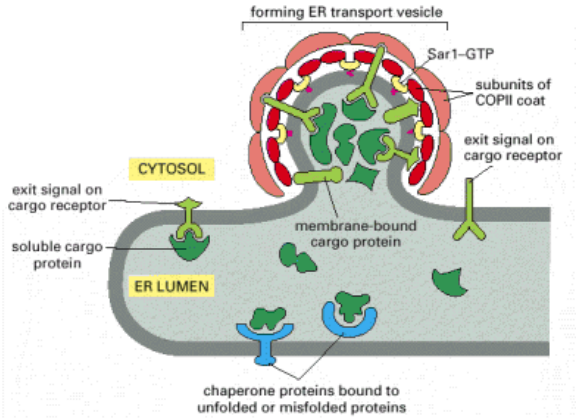

Figure 13-17. The recruitment of cargo molecules into ER transport vesicles. By binding to the COPII coat, membrane and cargo proteins become concentrated in the transport vesicles as they leave the ER. Membrane proteins are packaged into budding transport vesicles through the interactions of exit signals on their cytosolic tails with the COPII coat. Some of the membrane proteins trapped by the coat in turn function as cargo receptors, binding soluble proteins in the lumen and helping to package them into vesicles. A typical 50-nm transport vesicle contains about 200 membrane proteins, which can be of many different types. As indicated, unfolded or incompletely assembled proteins are bound to chaperones and are thereby retained in the ER compartment.

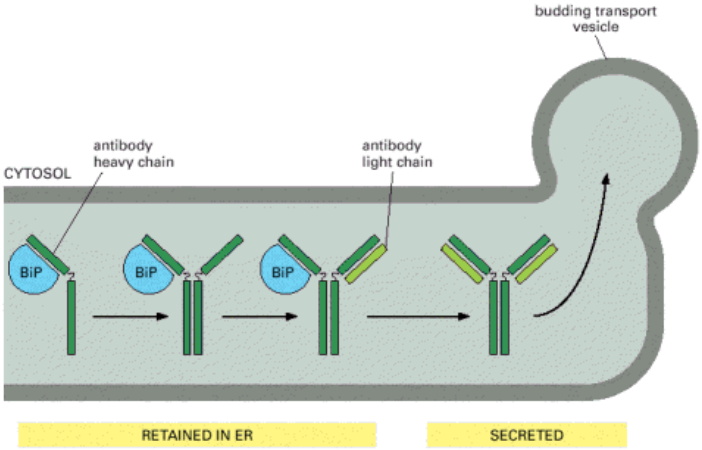

Figure 13-18. Retention of incompletely assembled antibody molecules in the ER. Antibodies are made up of two heavy and two light chains (discussed in Chapter 24), which assemble in the ER. The chaperone BiP is thought to bind to all incompletely assembled antibody molecules and to cover up an exit signal. Thus, only completely assembled antibodies leave the ER and are secreted.

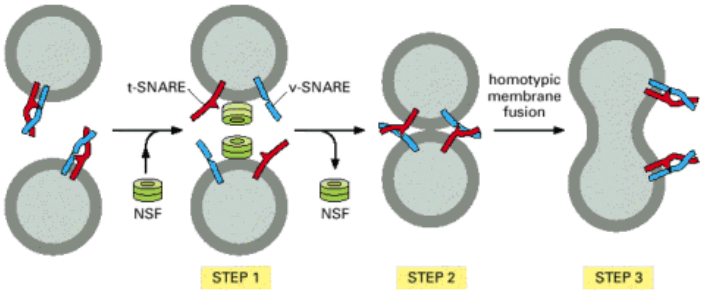

Figure 13-19. Homotypic membrane fusion. In step 1, identical pairs of v-SNAREs and t-SNAREs in both membranes are pried apart by NSF (see Figure 13-13). In steps 2 and 3, the separated matching SNAREs on adjacent identical membranes interact, which leads to membrane fusion and the formation of one continuous compartment. Subsequently, the compartment grows further by homotypic fusion with vesicles from the same kind of membrane, displaying matching SNAREs. Homotypic fusion is not restricted to the formation of vesicular tubular clusters; in a similar process, endosomes fuse to generate larger endosomes. Rab proteins help regulate the extent of homotypic fusion and hence the size of the compartments in a cell (not shown).

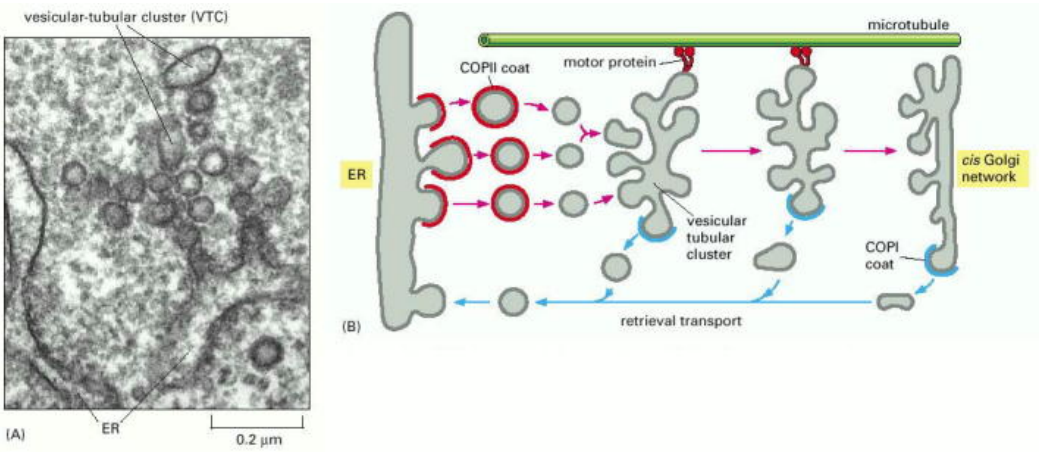

Figure 13-20. Vesicular tubular clusters. (A) An electron micrograph section of vesicular tubular clusters forming from the ER membrane. Many of the vesicle-like structures seen in the micrograph are cross sections of tubules that extend above and below the plane of this thin section and are interconnected. (B) Vesicular tubular clusters move along microtubules to carry proteins from the ER to the Golgi apparatus. COPI coats mediate the budding of vesicles that return to the ER from these clusters. As indicated, the coats quickly disassemble after the vesicles have formed. (A, courtesy of William Balch.)

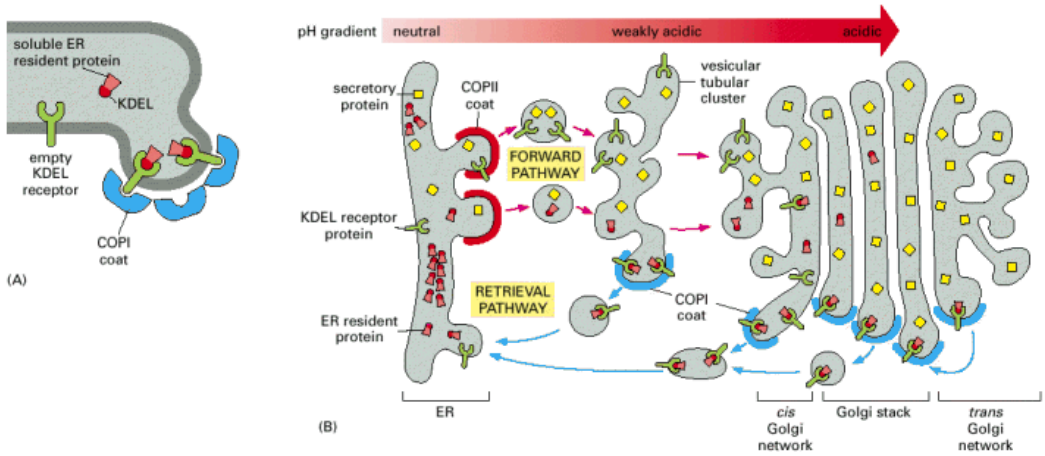

Figure 13-21. A model for the retrieval of ER resident proteins. Those ER resident proteins that escape from the ER are returned to the ER by vesicular transport. (A) The KDEL receptor present in vesicular tubular clusters and the Golgi apparatus, captures the soluble ER resident proteins and carries them in COPI-coated transport vesicles back to the ER. Upon binding its ligands in this low-pH environment, the KDEL receptor may change conformation, so as to facilitate its recruitment into budding COPI-coated vesicles. (B) The retrieval of ER proteins begins in vesicular tubular clusters and continues from all parts of the Golgi apparatus. In the neutral-pH environment of the ER, the ER proteins dissociate from the KDEL receptor, which is then returned to the Golgi for reuse.

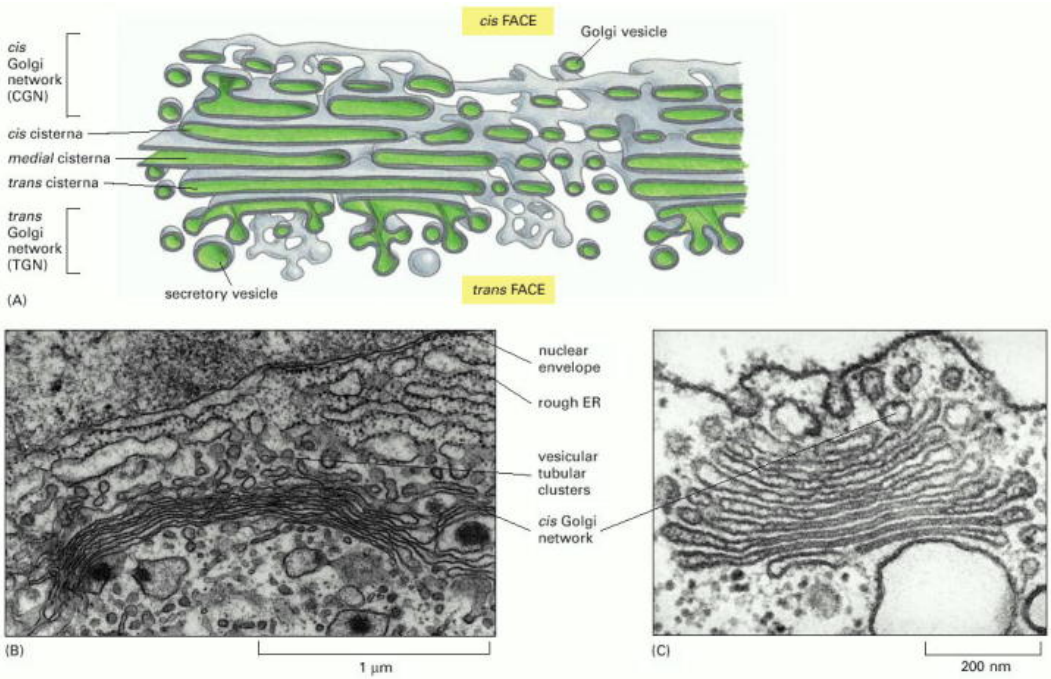

Figure 13-22. The Golgi apparatus. (A) Three-dimensional reconstruction from electron micrographs of the Golgi apparatus in a secretory animal cell. The *cis*-face of the Golgi stack is that closest to the ER. (B) A thin-section electron micrograph emphasizing the transitional zone between the ER and the Golgi apparatus in an animal cell. (C) An electron micrograph of a Golgi apparatus in a plant cell (the green alga *Chlamydomonas*) seen in cross section. In plant cells, the Golgi apparatus is generally more distinct and more clearly separated from other intracellular membranes than in animal cells. (A, redrawn from A. Rambourg and Y. Clermont, *Eur. J. Cell Biol.* 51:189200, 1990; B, courtesy of Brij J. Gupta; C, courtesy of George Palade.)

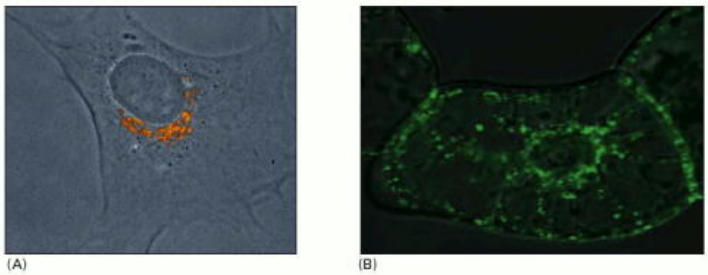

Figure 13-23. Light micrographs of the Golgi apparatus. (A) The Golgi apparatus in a cultured fibroblast stained with a fluorescent antibody that recognizes a Golgi resident protein. The Golgi apparatus is polarized, facing the direction in which the cell was crawling before fixation. (B) The Golgi apparatus in a plant cell that is expressing a fusion protein consisting of a resident Golgi enzyme fused to green fluorescent protein. The bright green spots are Golgi stacks. The faint green network is the ER, which contains some Golgi enzymes that are constantly returned to the ER from the Golgi via the retrieval pathway. (A, courtesy of John Henley and Mark McNiven; B, courtesy of Chris Hawes.)

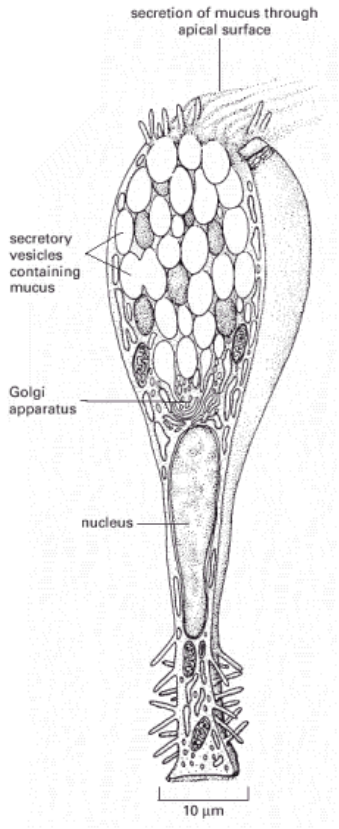

Figure 13-24. A goblet cell of the small intestine. This cell is specialized for secreting mucus, a mixture of glycoproteins and proteoglycans synthesized in the ER and Golgi apparatus. Like all epithelial cells, goblet cells are highly polarized, with the apical domain of their plasma membrane facing the lumen of the gut and the basolateral domain facing the basal lamina. The Golgi apparatus is also highly polarized, which facilitates the discharge of mucus by exocytosis at the apical domain of the plasma membrane. (After R.V. Krstic´, Illustrated Encyclopedia of Human Histology. New York: Springer-Verlag, 1984.)

Figure 13-25. The two main classes of asparagine-linked (*N*-linked) oligosaccharides found in mature glycoproteins. (A) Both complex oligosaccharides and high-mannose oligosaccharides share a common *core region* derived from the original *N*-linked oligosaccharide added in the ER and typically containing two *N*-acetylglucosamines (GlcNAc) and three mannoses (Man). (B) Each complex oligosaccharide consists of a *core region*, together with a *terminal region* that contains a variable number of copies of a special trisaccharide unit *(N-acetylglucosamine-galactose-sialic acid)* linked to the core mannoses. Frequently, the terminal region is truncated and contains only GlcNAc and galactose (Gal) or just GlcNAc. In addition, a fucose residue may be added, usually to the core GlcNAc attached to the asparagine (Asn). Thus, although the steps of processing and subsequent sugar addition are rigidly ordered, complex oligosaccharides can be heterogeneous. Moreover, although the complex oligosaccharide shown has three terminal branches, two and four branches are also common, depending on the glycoprotein and the cell in which it is made. (C) High-mannose oligosaccharides are not trimmed back all the way to the core region and contain additional mannose residues. Hybrid oligosaccharides (not shown) with one Man branch and one GlcNAc and Gal branch are also found. The three amino acids indicated in (A) constitute the sequence recognized by the oligosaccharyl transferase enzyme that adds the initial oligosaccharide to the protein. Ser = serine; Thr = threonine; X = any amino acid.

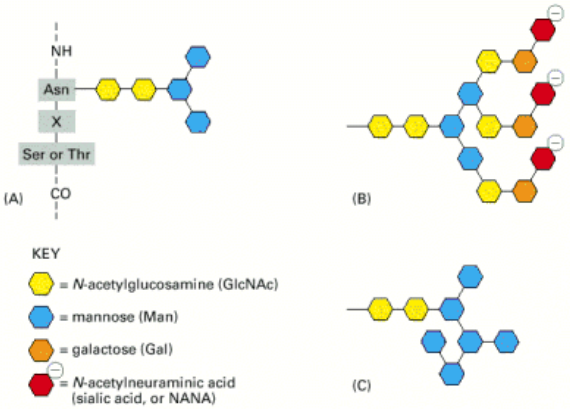

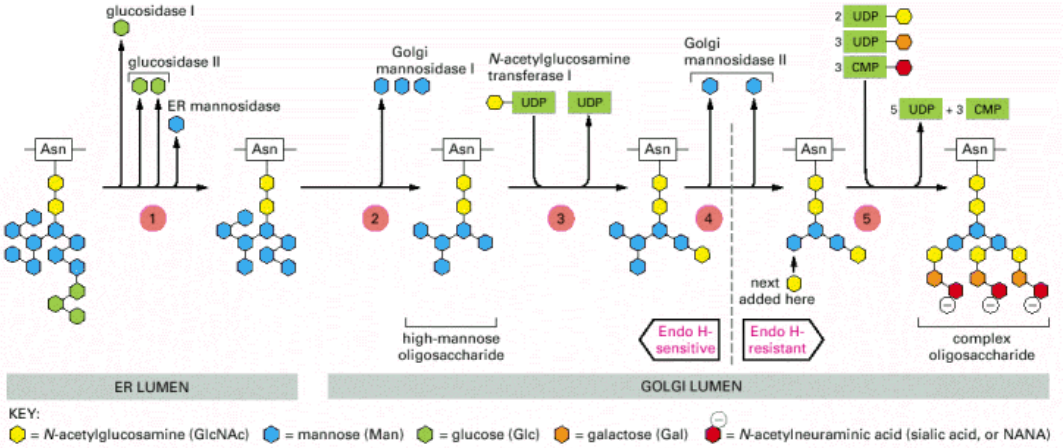

Figure 13-26. Oligosaccharide processing in the ER and the Golgi apparatus. The processing pathway is highly ordered, so that each step shown is dependent on the previous one. Processing begins in the ER with the removal of the glucoses from the oligosaccharide initially transferred to the protein. Then a mannosidase in the ER membrane removes a specific mannose. The remaining steps occur in the Golgi stack, where Golgi mannosidase I first removes three more mannoses and *N*-acetylglucosamine transferase I then adds an *N*-acetylglucosamine, which enables mannosidase II to remove two additional mannoses. This yields the final core of three mannoses that is present in a complex oligosaccharide. At this stage, the bond between the two *N*-acetylglucosamines in the core becomes resistant to attack by a highly specific endoglycosidase *(Endo H).* Since all later structures in the pathway are also Endo H-resistant, treatment with this enzyme is widely used to distinguish complex from high-mannose oligosaccharides. Finally, as shown in Figure 13-24, additional *N*-acetylglucosamines, galactoses, and sialic acids are added. These final steps in the synthesis of a complex oligosaccharide occur in the cisternal compartments of the Golgi apparatus. Three types of glycosyl transferase enzymes act sequentially, using sugar substrates that have been activated by linkage to the indicated nucleotide. The membranes of the Golgi cisternae contain specific carrier proteins that allow each sugar nucleotide to enter in exchange for the nucleoside phosphates that are released after the sugar is attached to the protein on the lumenal face.

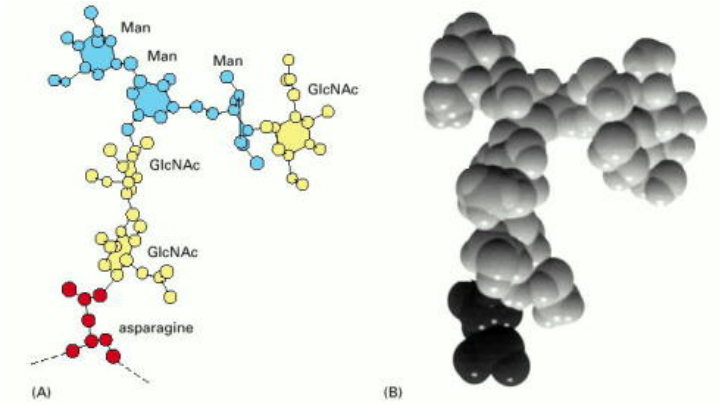

Figure 13-27. The three-dimensional structure of a small *N*-linked oligosaccharide. The structure was determined by x-ray crystallographic analysis of a glycoprotein. This oligosaccharide contains only 6 sugar residues, whereas there are 14 sugar residues in the *N*-linked oligosaccharide that is initially transferred to proteins in the ER (see Figure 12-51). (A) A backbone model showing all atoms except hydrogens. (B) A space-filling model, with the asparagine indicated by dark atoms. (B, courtesy of Richard Feldmann.)

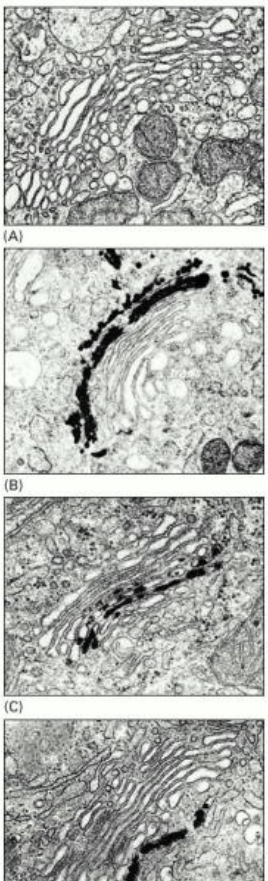

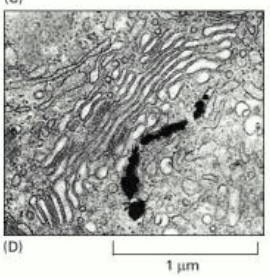

Figure 13-28. Histochemical stains demonstrating the biochemical compartmentalization of the Golgi apparatus. A series of electron micrographs shows the Golgi apparatus (A) unstained, (B) stained with osmium, which is preferentially reduced by the cisternae of the *cis* compartment, and (C and D) stained to reveal the location of a specific enzyme. The enzyme, nucleoside diphosphatase, is found in the *trans* Golgi cisternae (C), while acid phosphatase is found in the *trans* Golgi network (D). Note that usually more than one cisterna is stained. The enzymes are therefore thought to be highly enriched rather than precisely localized to a specific cisterna. (Courtesy of Daniel S. Friend.)

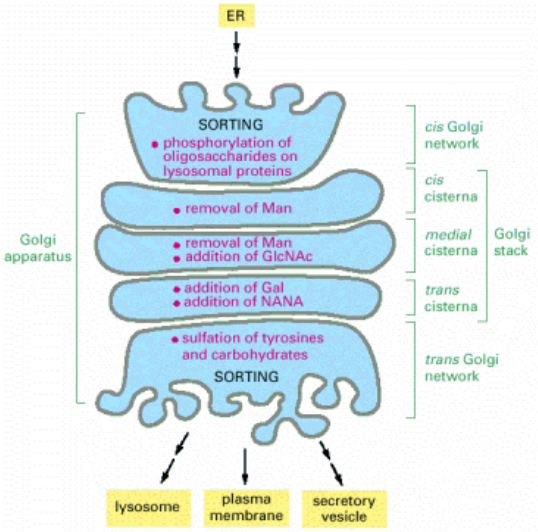

Figure 13-29. The functional compartmentalization of the Golgi apparatus. The localization of each processing step shown was determined by a combination of techniques, including biochemical subfractionation of the Golgi apparatus membranes and electron microscopy after staining with antibodies specific for some of the processing enzymes. The locations of many other processing reactions have not been determined. Although only three distinguishable cisternal compartments have so far been demonstrated, each of these sometimes consists of a group of two or more cisternae in sequence. It is likely that each processing enzyme is not completely restricted to a particular cisterna but that its distribution is graded across the stack - such that early acting enzymes are present mostly in the *cis* Golgi cisternae and later acting enzymes are mostly in the *trans* Golgi cisternae.

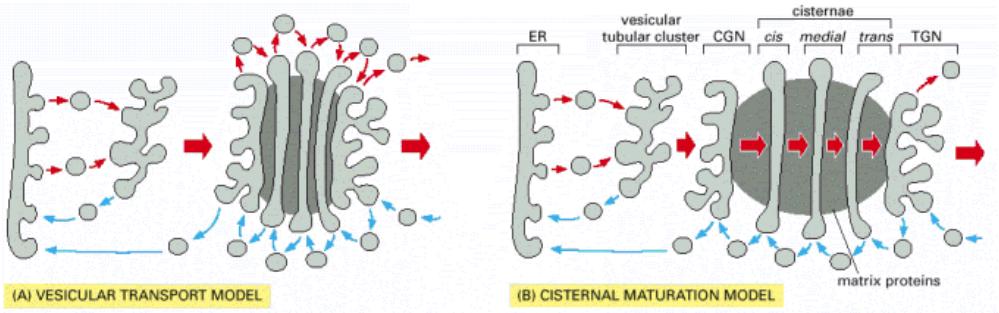

Figure 13-30. Two possible models explaining the organization of the Golgi apparatus and the transport of proteins from one cisterna to the next. It is likely that the transport through the Golgi apparatus in the forward direction *(red arrows)* involves elements of both of the views represented here. (A) In the vesicular transport model, Golgi cisternae are static organelles, which contain a characteristic complement of resident enzymes. The passing of molecules through the Golgi is accomplished by forward-moving transport vesicles, which bud from one cisterna and fuse with the next in a *cis*-to-*trans* direction. (B) According to the alternative cisternal maturation model, each Golgi cisterna matures as it migrates outwards through a stack. At each stage, the Golgi resident proteins that are carried forward in a cisterna are moved backward to an earlier compartment in COPI-coated vesicles. When a newly formed cisterna moves around to a *medial* position, for example, "left-over" *cis* Golgi enzymes would be extracted and transported backward to a new cis cisterna behind. Likewise, the *medial* enzymes would be received by retrograde transport from the cisternae just ahead. In this way, a *cis* cisterna would mature to a *medial* cisterna as it moves.

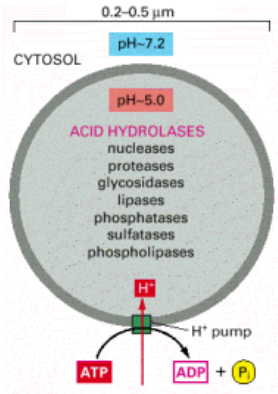

Figure 13-31. Lysosomes. The acid hydrolases are hydrolytic enzymes that are active under acidic conditions. The lumen is maintained at an acidic pH by an H^+ ATPase in the membrane that pumps H^+ into the lysosome.

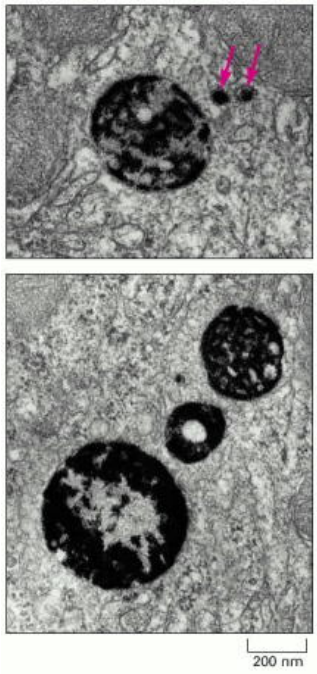

Figure 13-32. Histochemical visualization of lysosomes. These electron micrographs show two sections of a cell stained to reveal the location of acid phosphatase, a marker enzyme for lysosomes. The larger membrane-enclosed organelles, containing dense precipitates of lead phosphate, are lysosomes. Their diverse morphology reflects variations in the amount and nature of the material they are digesting. The precipitates are produced when tissue fixed with glutaraldehyde (to fix the enzyme in place) is incubated with a phosphatase substrate in the presence of lead ions. Two small vesicles thought to be carrying acid hydrolases from the Golgi apparatus are indicated by *red arrows* in the top panel. (Courtesy of Daniel S. Friend.)

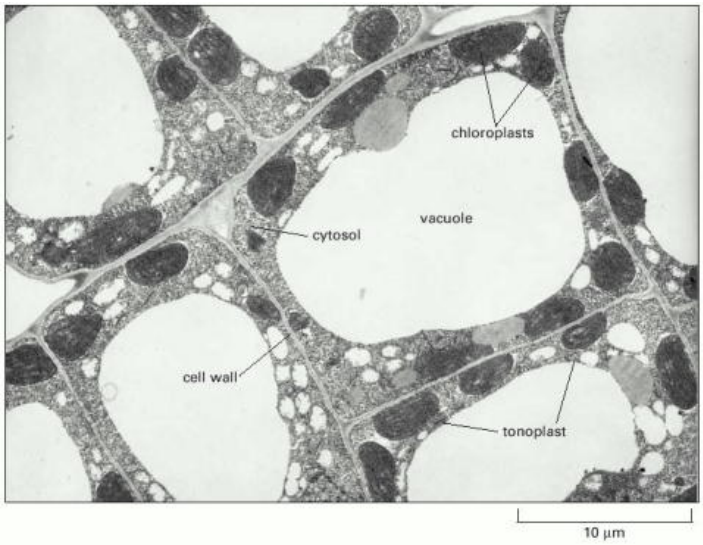

Figure 13-33. The plant cell vacuole. This electron micrograph of cells in a young tobacco leaf shows the cytosol as a thin layer, containing chloroplasts, pressed against the cell wall by the enormous vacuole. The membrane of the vacuole is called the tonoplast. (Courtesy of J. Burgess.)

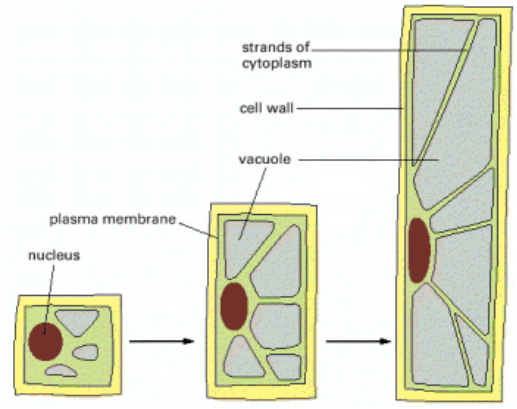

Figure 13-34. The role of the vacuole in controlling the size of plant cells. A large increase in cell volume can be achieved without increasing the volume of the cytosol. Localized weakening of the cell wall orients a turgor-driven cell enlargement that accompanies the uptake of water into an expanding vacuole. The cytosol is eventually confined to a thin peripheral layer, which is connected to the nuclear region by strands of cytosol, which are stabilized by bundles of actin filaments (not shown).

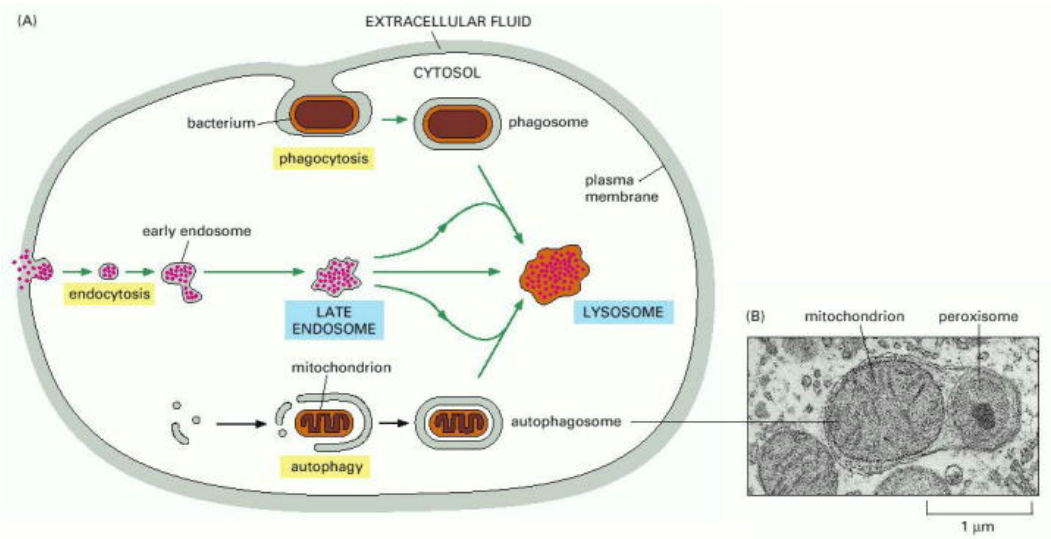

Figure 13-35. Three pathways to degradation in lysosomes. (A) Each pathway leads to the intracellular digestion of materials derived from a different source. (B) An electron micrograph of an autophagosome containing a mitochondrion and a peroxisome. (B, courtesy of Daniel S. Friend, from D.W. Fawcett, A Textbook of Histology, 12th edn. New York: Chapman and Hall, 1994.)

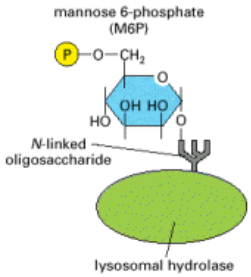

Figure 13-36. The structure of mannose 6-phosphate on a lysosomal enzyme.

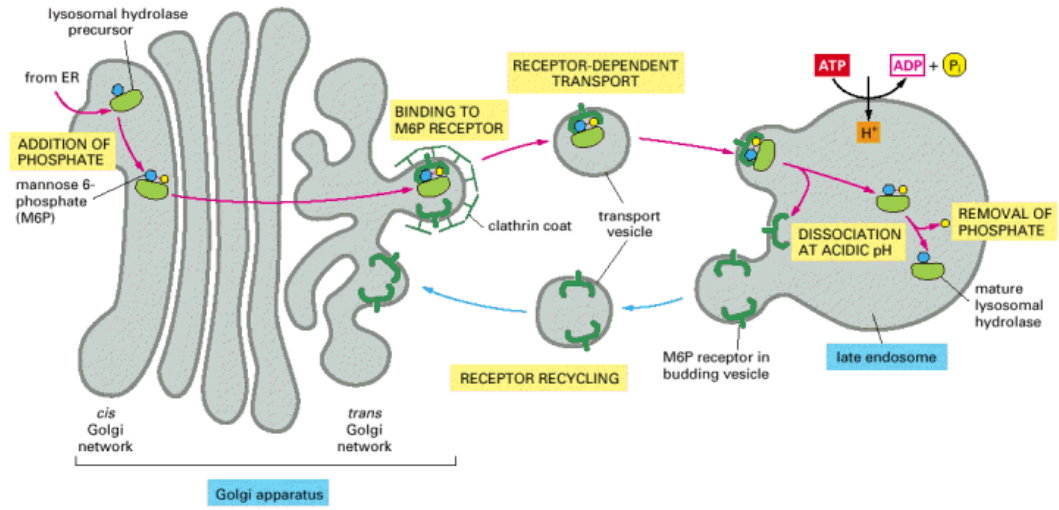

Figure 13-37. The transport of newly synthesized lysosomal hydrolases to lysosomes. The precursors of lysosomal hydrolases are covalently modified by the addition of mannose 6-phosphate (M6P) groups in the *cis* Golgi network. They then become segregated from all other types of proteins in the *trans* Golgi network because adaptins in the clathrin coat bind the M6P receptors, which, in turn, bind the modified lysosomal hydrolases. The clathrin-coated vesicles produced bud off from the *trans* Golgi network and fuse with late endosomes. At the low pH of the late endosome, the hydrolases dissociate from the M6P receptors, and the empty receptors are recycled to the Golgi apparatus for further rounds of transport. It is not known which type of coat mediates vesicle budding in the M6P receptor recycling pathway. In the late endosomes, the phosphate is removed from the mannose sugars attached to the hydrolases, further ensuring that the hydrolases do not return to the Golgi apparatus with the receptor.

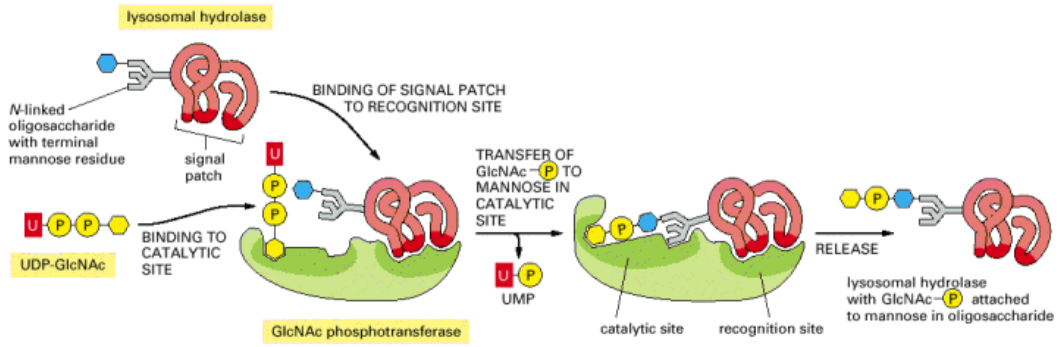

Figure 13-38. The recognition of a lysosomal hydrolase. The GlcNAc phosphotransferase enzyme that recognizes lysosomal hydrolases in the Golgi apparatus has separate catalytic and recognition sites. The catalytic site binds both high-mannose *N*-linked oligosaccharides and UDP-GlcNAc. The recognition site binds to a signal patch that is present only on the surface of lysosomal hydrolases. The GlcNAc is cleaved off by a second enzyme, leaving the M6P exposed (not shown).

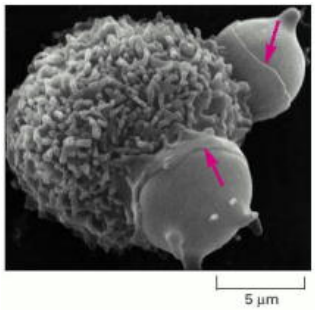

Figure 13-39. Phagocytosis by a macrophage. A scanning electron micrograph of a mouse macrophage phagocytosing two chemically altered red blood cells. The *red arrows* point to edges of thin processes (pseudopods) of the macrophage that are extending as collars to engulf the red cells. (Courtesy of Jean Paul Revel.)

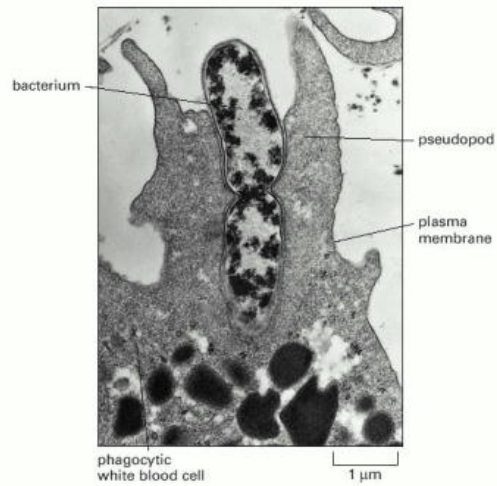

Figure 13-40. Phagocytosis by a neutrophil. An electron micrograph of a neutrophil phagocytosing a bacterium, which is in the process of dividing. (Courtesy of Dorothy F. Bainton, Phagocytic Mechanisms in Health and Disease. New York: Intercontinental Book Corporation, 1971.)

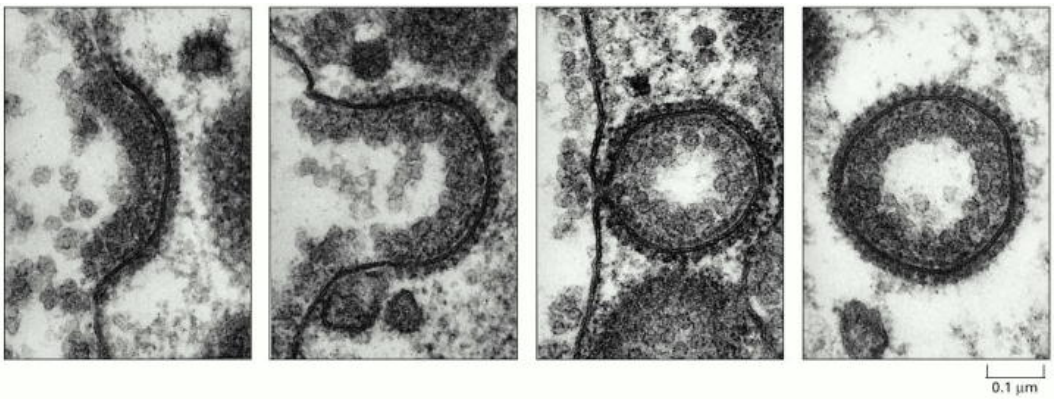

Figure 13-41. The formation of clathrin-coated vesicles from the plasma membrane. These electron micrographs illustrate the probable sequence of events in the formation of a clathrin-coated vesicle from a clathrin-coated pit. The clathrin-coated pits and vesicles shown are larger than those seen in normal-sized cells. They are involved in taking up lipoprotein particles into a very large hen oocyte to form yolk. The lipoprotein particles bound to their membrane-bound receptors can be seen as a dense, fuzzy layer on the extracellular surface of the plasma membrane - which is the inside surface of the vesicle. (Courtesy of M.M. Perry and A.B. Gilbert, *J. Cell Sci.* 39:257272, 1979. © The Company of Biologists.)

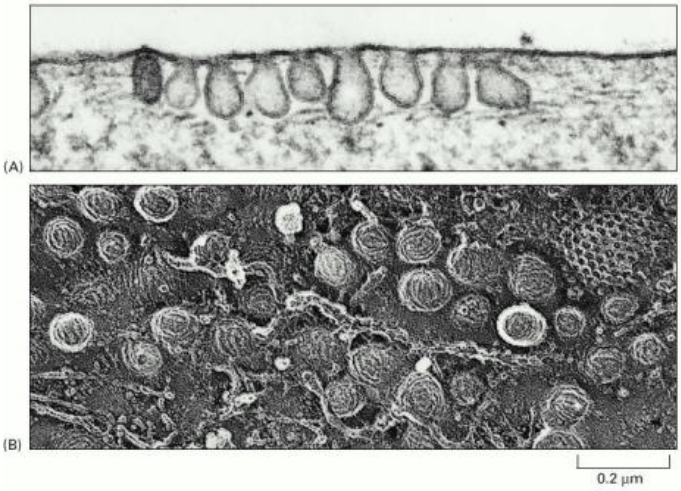

Figure 13-42. Caveolae in the plasma membrane of a fibroblast. (A) This electron micrograph shows a plasma membrane with a very high density of caveolae. Note that no cytosolic coat is visible. (B) This rapid-freeze deep-etch image demonstrates the characteristic "cauliflower" texture of the cytosolic face of the caveolae membrane. The regular texture is thought to result from aggregates of caveolin in the membrane. A clathrin-coated pit is also seen at the upper right. (Courtesy of R.G.W. Anderson, from K.G. Rothberg et al., *Cell* 68:673682, 1992. © Elsevier)

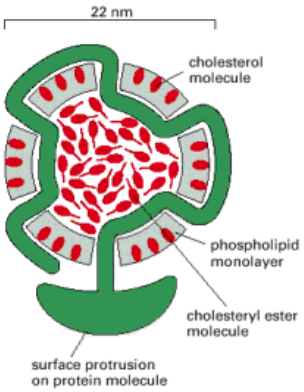

Figure 13-43. A low-density lipoprotein (LDL) particle. Each spherical particle has a mass of 3×10^6 daltons. It contains a core of about 1500 cholesterol molecules esterified to long-chain fatty acids that is surrounded by a lipid monolayer composed of about 800 phospholipid and 500 unesterified cholesterol molecules. A single molecule of a 500,000-dalton protein organizes the particle and mediates the specific binding of LDL to cell-surface receptor proteins.

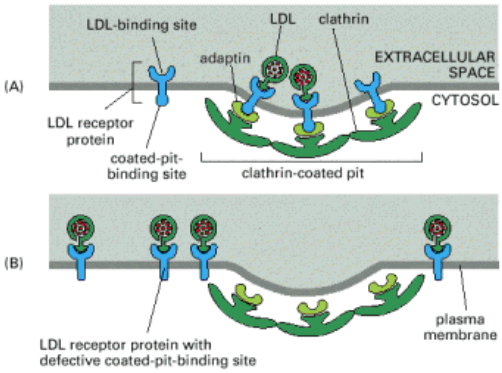

Figure 13-44. Normal and mutant LDL receptors. (A) LDL receptor proteins binding to a coated pit in the plasma membrane of a normal cell. The human LDL receptor is a single-pass transmembrane glycoprotein composed of about 840 amino acids, only 50 of which are on the cytoplasmic side of the membrane. (B) A mutant cell in which the LDL receptor proteins are abnormal and lack the site in the cytoplasmic domain that enables them to bind to adaptins in the clathrin-coated pits. Such cells bind LDL but cannot ingest it. In most human populations, 1 in 500 individuals inherits one defective LDL receptor gene and, as a result, has an increased risk of a heart attack caused by atherosclerosis.

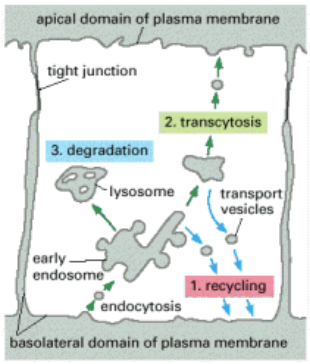

Figure 13-45. Possible fates for transmembrane receptor proteins that have been endocytosed. Three pathways from the endosomal compartment in an epithelial cell are shown. Retrieved receptors are returned (1) to the same plasma membrane domain from which they came *(recycling)* or (2) to a different domain of the plasma membrane *(transcytosis)*. (3) Receptors that are not specifically retrieved from endosomes follow the pathway from the endosomal compartment to lysosomes, where they are degraded *(degradation)*. The formation of oligomeric aggregates in the endosomal membrane may be one of the signals that guides receptors into the degradative pathway. If the ligand that is endocytosed with its receptor stays bound to the receptor in the acidic environment of the endosome, it follows the same pathway as the receptor; otherwise it is delivered to lysosomes.

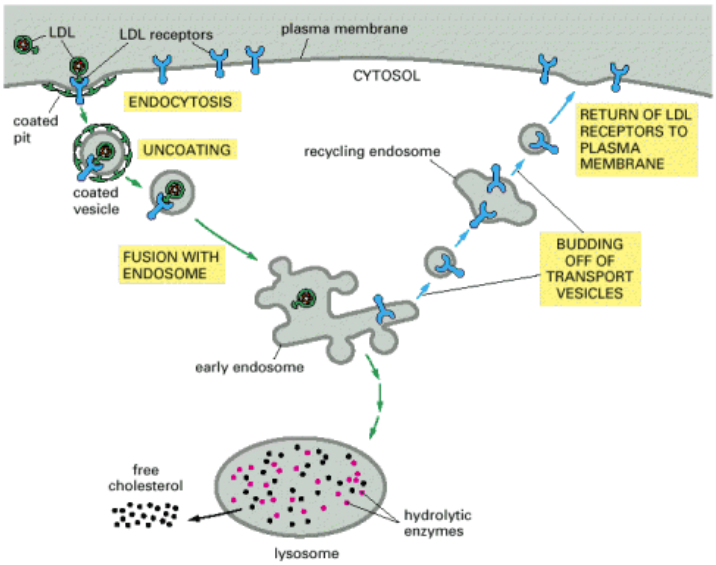

Figure 13-46. The receptor-mediated endocytosis of LDL. Note that the LDL dissociates from its receptors in the acidic environment of the endosome. After a number of steps (see Figure 13-48), the LDL ends up in lysosomes, where it is degraded to release free cholesterol. In contrast, the LDL receptor proteins are returned to the plasma membrane via clathrin-coated transport vesicles that bud off from the tubular region of the early endosome, as shown. For simplicity, only one LDL receptor is shown entering the cell and returning to the plasma membrane. Whether it is occupied or not, an LDL receptor typically makes one round trip into the cell and back to the plasma membrane every 10 minutes, making a total of several hundred trips in its 20-hour life-span.

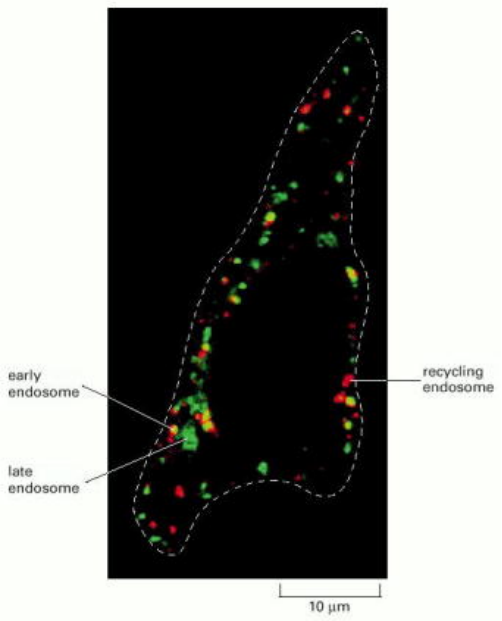

Figure 13-47. Sorting of membrane proteins in the endocytic pathway. Transferrin receptors mediate nutrient uptake and constitutively cycle between endosomes and the plasma membrane. By contrast, opioid receptors are signaling receptors that - after ligand binding - are down-regulated by endocytosis followed by degradation in lysosomes. Endocytosis of both receptors initiates in the same clathrin-coated pits. They are then delivered to the same early endosomes where their journeys part: transferrin receptors are sorted to the recycling endosomes, whereas opioid receptors are sorted to late endosomes. The micrograph shows both receptors - labeled with different fluorescent dyes - 30 min after endocytosis (transferrin receptors labeled in *red* and opioid receptors labeled in *green).* At this time, some early endosomes still contain both receptors and are seen as *yellow* structures (yellow resulting from an overlap of red and green light emitted from the fluorescent dyes). By contrast, recycling and late endosomes are selectively enriched in either transferrin or opioid receptors, respectively - thus appearing as distinct red and green structures. (Courtesy of Mark von Zastrow.)

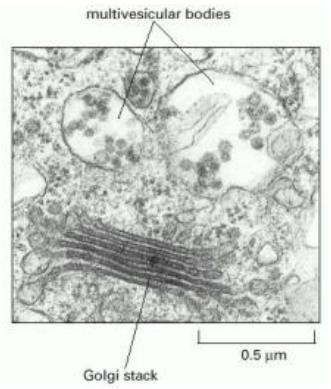

Figure 13-48. Electron micrograph of a multivesicular body in a plant cell. The large amount of internal membrane will be delivered to the vacuole, the plant equivalent of the lysosome, for digestion.

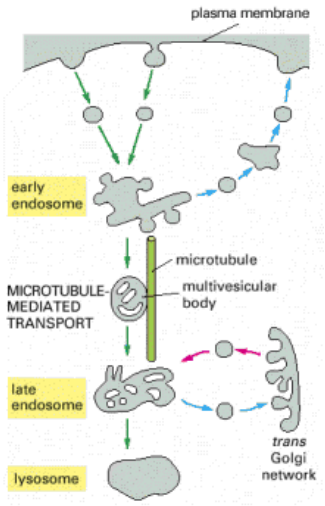

Figure 13-49. The endocytic pathway from the plasma membrane to lysosomes. Maturation from early to late endosomes occurs through the formation of multivesicular bodies, which contain large amounts of invaginated membrane and internal vesicles (hence their name). These bodies move inward along microtubules, and recycling of components to the plasma membrane continues as the bodies move. The multivesicular bodies gradually turn into late endosomes, either by fusing with each other or by fusing with preexisting late endosomes. The late endosomes no longer send vesicles to the plasma membrane but communicate with the *trans* Golgi network via transport vesicles, which deliver the proteins that will convert the late endosome into a lysosome.

Figure 13-50. The sequestration of endocytosed proteins into internal membranes of multivesicular

bodies. Eventually, all of the internal membranes produced by the invaginations shown are digested by proteases and lipases in lysosomes. The invagination is essential to achieve complete digestion of endocytosed membrane proteins. Because the outer membrane of the multivesicular body becomes continuous with the lysosomal membrane, lysosomal hydrolases could not digest the cytosolic domains of transmembrane proteins such as the EGF receptor shown here, if it were not for the invagination.

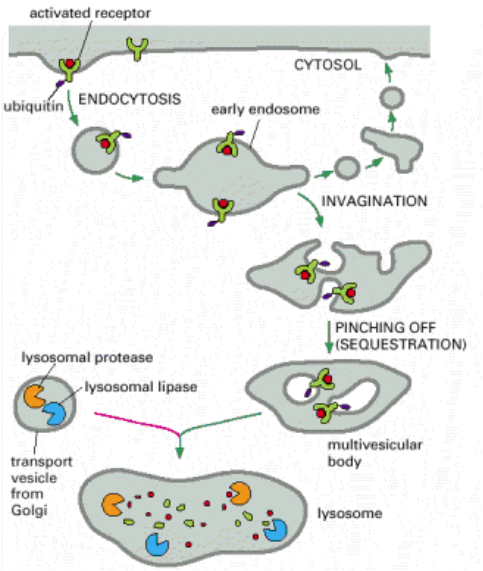

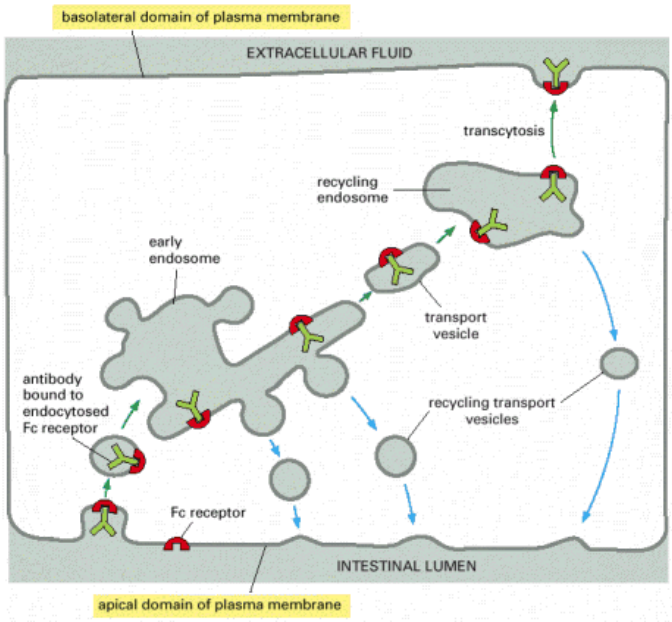

Figure 13-51. Transcytosis. Recycling endosomes form a way-station on the transcytotic pathway. In the example shown here, an antibody receptor on a gut epithelial cell binds antibody and is endocytosed, eventually carrying the antibody to the basolateral plasma membrane in contact with extracellular matrix that is permeated by blood vessels. The receptor is called an Fc receptor because it binds the Fc part of the antibody (discussed in Chapter 24).

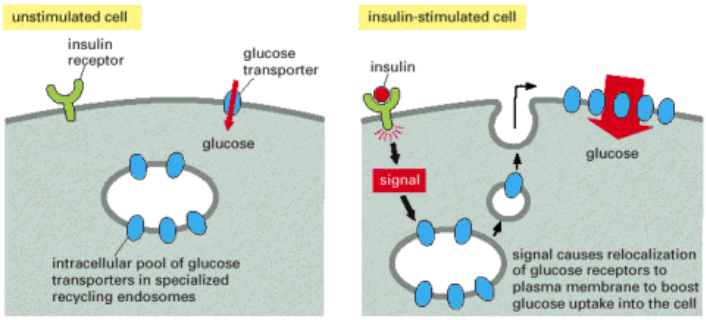

Figure 13-52. Storage of plasma membrane proteins in recycling endosomes. Recycling endosomes can serve as an intracellular pool for specialized plasma membrane proteins, enabling them to be mobilized when needed. In the example shown here, insulin binding to the insulin receptor triggers a signaling pathway that causes the rapid insertion of glucose transporters into the plasma membrane of a fat or muscle cell, greatly increasing glucose intake.

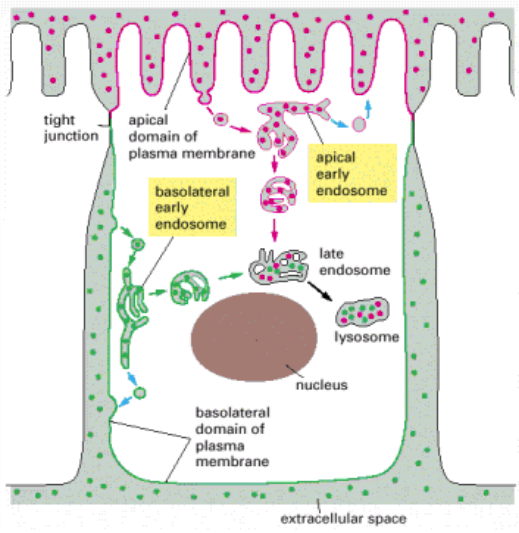

Figure 13-53. The two distinct early endosomal compartments in an epithelial cell. The basolateral and the apical domains of the plasma membrane communicate with separate early endosomal compartments. But endocytosed molecules from both domains that do not contain signals for recycling or transcytosis meet in a common late endosomal compartment before being digested in lysosomes.

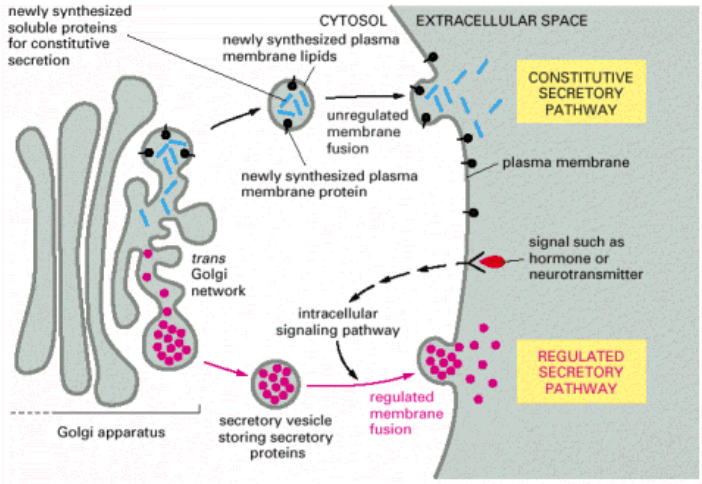

Figure 13-54. The constitutive and regulated secretory pathways. The two pathways diverge in the *trans* Golgi network. The constitutive secretory pathway operates in all cells. Many soluble proteins are continually secreted from the cell by this pathway, which also supplies the plasma membrane with newly synthesized lipids and proteins. Specialized secretory cells also have a regulated secretory pathway, by which selected proteins in the *trans* Golgi network are diverted into secretory vesicles, where the proteins are concentrated and stored until an extracellular signal stimulates their secretion. The regulated secretion of small molecules, such as histamine, occurs by a similar pathway; these molecules are actively transported from the cytosol into preformed secretory vesicles. There they are often complexed to specific macromolecules (proteoglycans, for histamine), so that they can be stored at high concentration without generating an excessively high osmotic pressure.

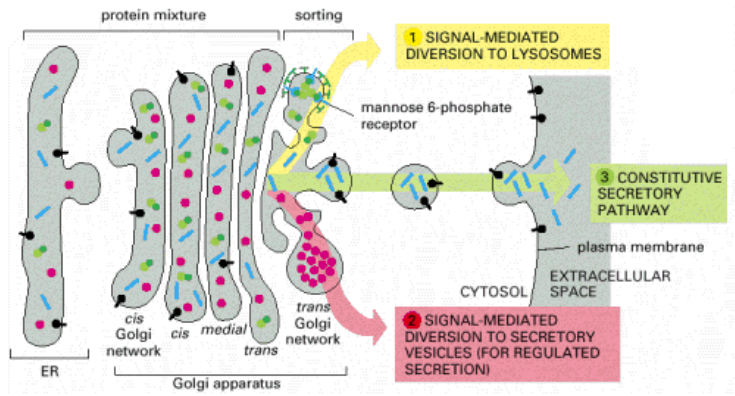

Figure 13-55. The three best-understood pathways of protein sorting in the *trans* Golgi network. (1) Proteins with the mannose 6-phosphate (M6P) marker are diverted to lysosomes (via late endosomes) in clathrin-coated transport vesicles (see Figure 13-37). (2) Proteins with signals directing them to secretory vesicles are concentrated in such vesicles as part of a regulated secretory pathway that is present only in specialized secretory cells. (3) In unpolarized cells, proteins with no special features are delivered to the cell surface by a constitutive secretory pathway. In polarized cells, however, secreted and plasma membrane proteins are selectively directed to either the apical or the basolateral plasma membrane domain, so that at least one of these two pathways must be mediated by a specific signal, as we discuss later.

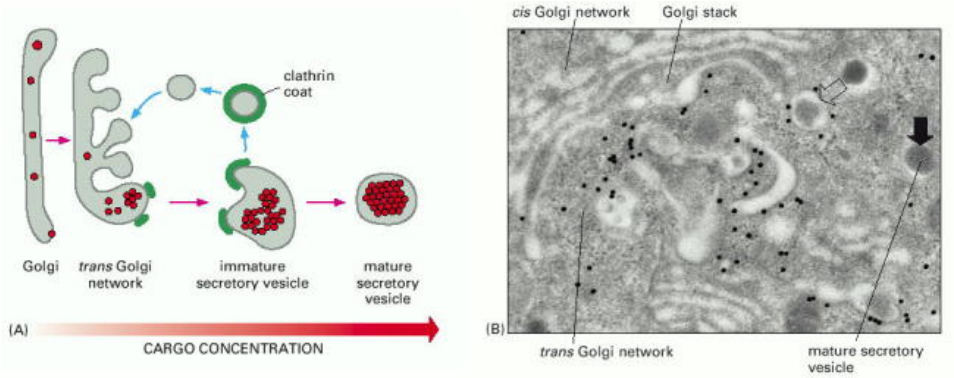

Figure 13-56. The formation of secretory vesicles. (A) Secretory proteins become segregated and highly concentrated in secretory vesicles by two mechanisms. First, they aggregate in the ionic environment of the *trans* Golgi network; often the aggregates become more condensed as secretory vesicles mature and their lumen becomes more acidic. Second, excess membrane and lumenal content present in immature secretory vesicles are retrieved in clathrin-coated vesicles as the secretory vesicles mature. (B) This electron micrograph shows secretory vesicles forming from the *trans* Golgi network in an insulin-secreting β-cell of the pancreas. An antibody conjugated to gold spheres *(black dots)* has been used to locate clathrin molecules. The immature secretory vesicles *(open arrow)*, which contain insulin precursor protein (proinsulin), contain clathrin patches. Clathrin coats are no longer seen on the mature secretory vesicle, which has a highly condensed core *(solid arrow).* (Courtesy of Lelio Orci.)

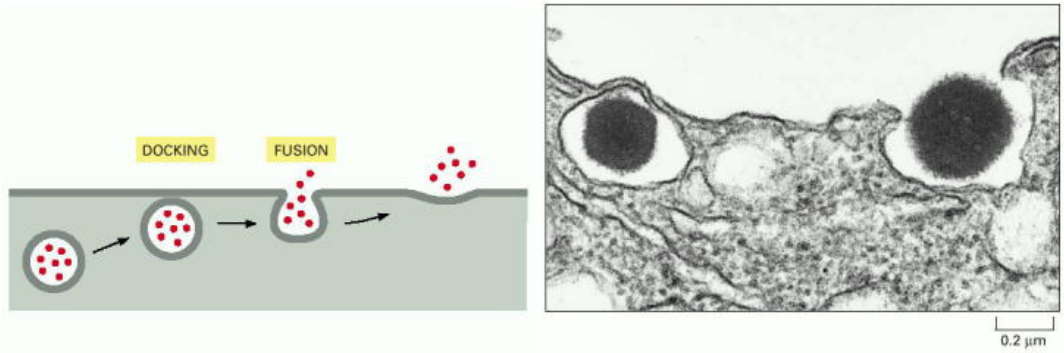

Figure 13-57. Exocytosis of secretory vesicles. The electron micrograph shows the release of insulin from a secretory vesicle of a pancreatic β-cell. (Courtesy of Lelio Orci, from L. Orci, J.-D. Vassali, and A. Perrelet, *Sci. Am.* 256:8594, 1988.)

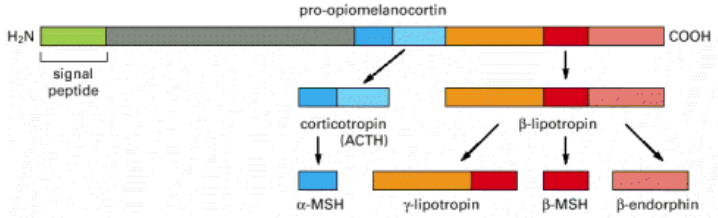

Figure 13-58. Alternative processing pathways for the prohormone proopiomelanocortin. The initial cleavages are made by proteases that cut next to pairs of positively charged amino acids (Lys-Arg, Lys-Lys, Arg-Lys, or Arg-Arg pairs). Trimming reactions then produce the final secreted products. Different cell types produce different concentrations of individual processing enzymes, so that the same prohormone precursor is cleaved to produce different peptide hormones. In the anterior lobe of the pituitary gland, for example, only corticotropin (ACTH) and β-lipotropin are produced from proopiomelanocortin, whereas in the intermediate lobe of the pituitary mainly α-melanocyte stimulating hormone (α-MSH), γ-lipotropin, β-MSH, and β-endorphin are produced.

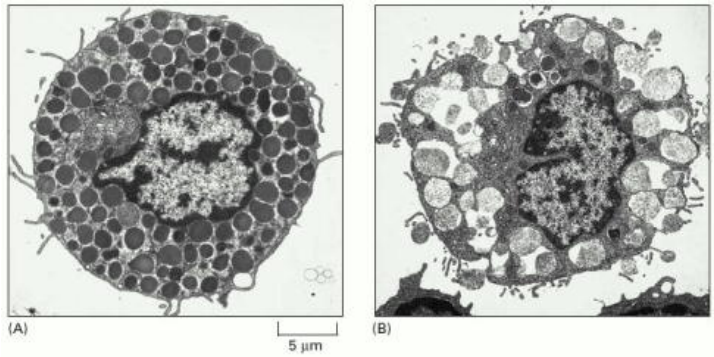

Figure 13-59. Electron micrographs of exocytosis in rat mast cells. (A) An unstimulated mast cell. (B) This cell has been activated to secrete its stored histamine by a soluble extracellular stimulant. Histamine-containing secretory vesicles are dark, while those that have released their histamine are light. The material remaining in the spent vesicles consists of a network of proteoglycans to which the stored histamine was bound. Once a secretory vesicle has fused with the plasma membrane, the secretory vesicle membrane often serves as a target to which other secretory vesicles fuse. Thus, the cell in (B) contains several large cavities lined by the fused membranes of many spent secretory vesicles, which are now in continuity with the plasma membrane. This continuity is not always apparent in one plane of section through the cell. (From D. Lawson, C. Fewtrell, B. Gomperts, and M. Raff, *J. Exp. Med.* 142:391402, 1975. © The Rockefeller University Press.)

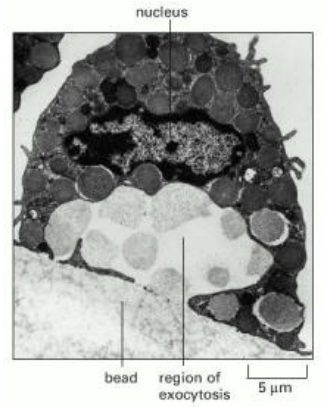

Figure 13-60. Exocytosis as a localized response. This electron micrograph shows a mast cell that has been activated to secrete histamine by a stimulant coupled to a large solid bead. Exocytosis has occurred only in the region of the cell that is in contact with the bead. (From D. Lawson, C. Fewtrell, and M. Raff, *J. Cell Biol.* 79:394400, 1978. © The Rockefeller University Press.)

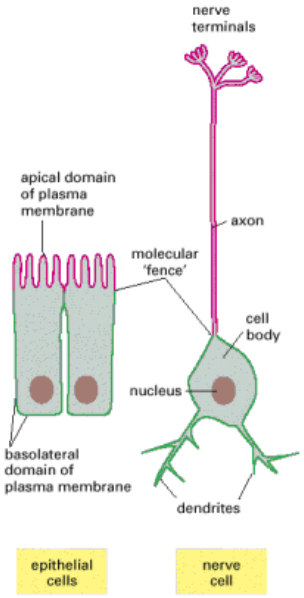

Figure 13-61. A comparison of two types of polarized cells. In terms of the mechanisms used to direct proteins to them, the plasma membrane of the nerve cell body and dendrites resembles the basolateral plasma membrane domain of a polarized epithelial cell, whereas the plasma membrane of the axon and its nerve terminals resembles the apical domain of an epithelial cell. The different membrane domains of both the epithelial cell and the nerve cell are separated by a molecular fence, consisting of a meshwork of membrane proteins tightly associated with the underlying actin cytoskeleton; this barrier - called a tight junction in the epithelial cell and an axonal hillock in neurons - keeps membrane proteins from diffusing between the two distinct domains.

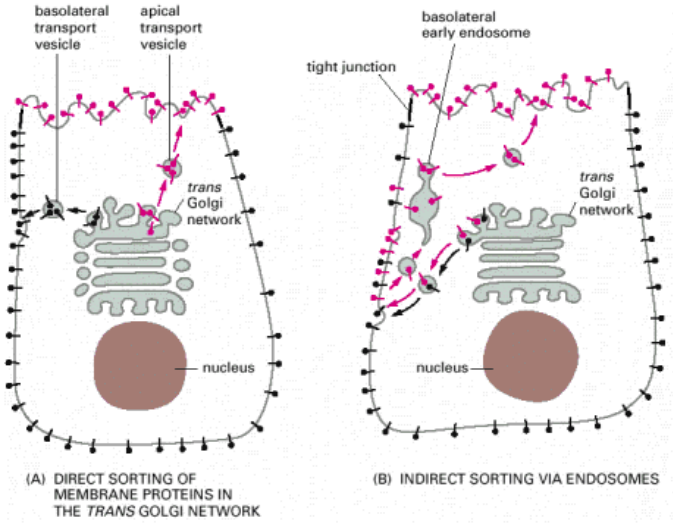

Figure 13-62. Two ways of sorting plasma membrane proteins in a polarized epithelial cell. Newly synthesized proteins can reach their proper plasma membrane domain by either (A) a direct pathway or (B) an indirect pathway. In the indirect pathway, a protein is retrieved from the inappropriate plasma membrane domain by endocytosis and then transported to the correct domain via early endosomes - that is, by transcytosis. The indirect pathway is known to be used in liver hepatocytes to deliver proteins to the apical domain that lines bile ducts. However, in other cases, the direct pathway is used, as described in the text for epithelial cells in the gut.

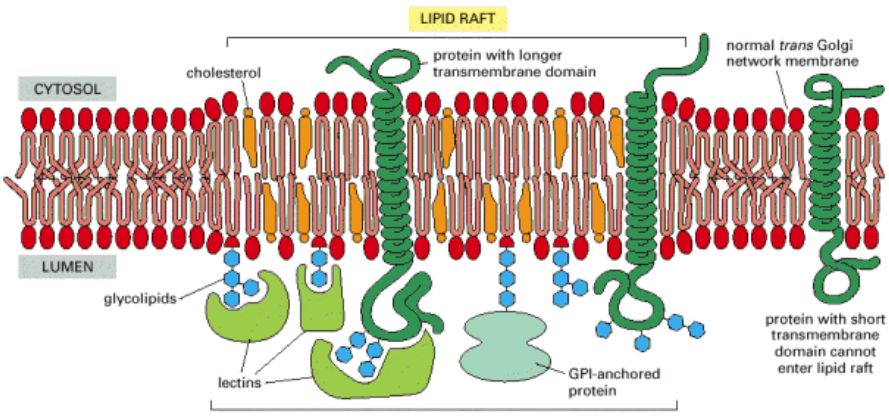

Figure 13-63. Model of lipid rafts in the *trans* Golgi network. Glycosphingolipids and cholesterol are thought to form rafts in the lipid bilayer. Membrane proteins with long enough membrane-spanning segments preferentially partition into the lipid rafts and thus become sorted into transport vesicles. These rafts are subsequently packaged into transport vesicles that carry them to the apical domain of the plasma membrane. Carbohydrate-binding proteins (lectins) in the lumen of the *trans* Golgi network may help stabilize the rafts, as shown.

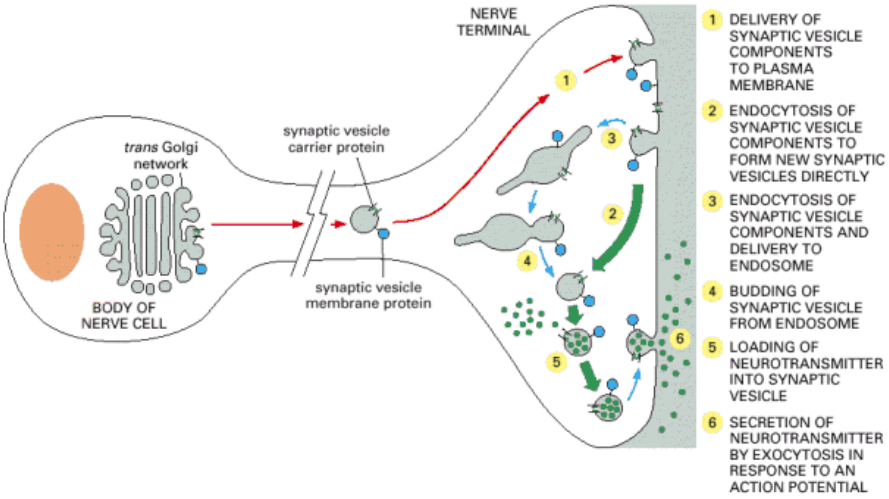

Figure 13-64. The formation of synaptic vesicles. These tiny uniform vesicles are found only in nerve cells and in some endocrine cells, where they store and secrete small-molecule neurotransmitters. The import of neurotransmitter directly into the small endocytic vesicles that form from the plasma membrane is mediated by membrane carrier proteins that function as antiports, being driven by a H^+ gradient maintained by proton pumps in the vesicle membrane.

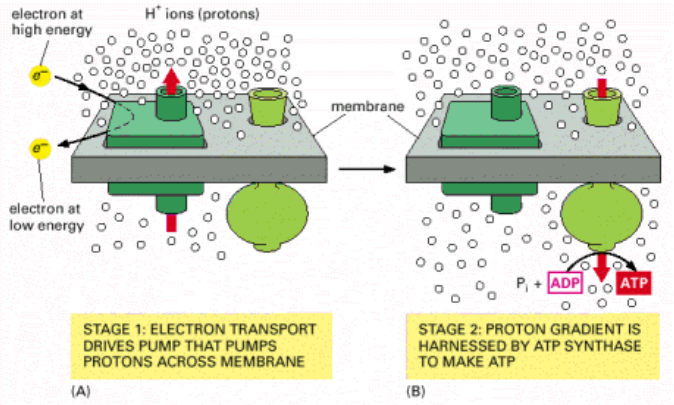

Figure 14-1. Harnessing energy for life. (A) The essential requirements for chemiosmosis are a membrane - in which are embedded a pump protein and an ATP synthase, plus a source of high-energy electrons (e^-). The protons (H^+) shown are freely available from water molecules. The pump harnesses the energy of electron transfer (details not shown here) to pump protons, creating a proton gradient across the membrane. (B) This proton gradient serves as an energy store that can be used to drive ATP synthesis by the ATP synthase enzyme. The *red arrow* shows the direction of proton movement at each stage.

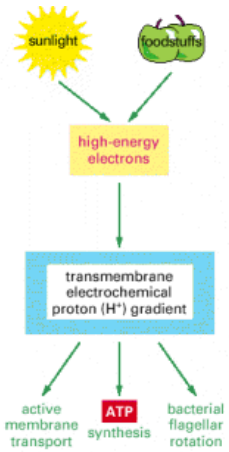

Figure 14-2. Chemiosmotic coupling. Energy from sunlight or the oxidation of foodstuffs is first used to create an electrochemical proton gradient across a membrane. This gradient serves as a versatile energy store and is used to drive a variety of energy-requiring reactions in mitochondria, chloroplasts, and bacteria.

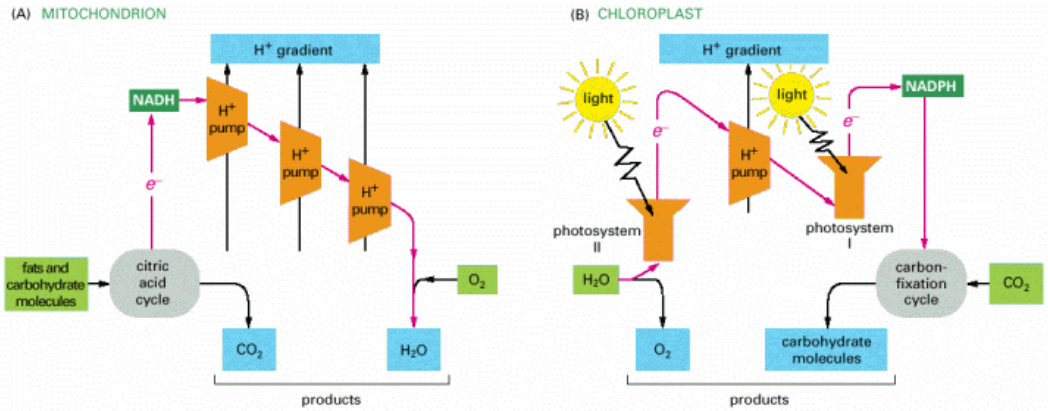

Figure 14-3. Electron transport processes. (A) The mitochondrion converts energy from chemical fuels. (B) The chloroplast converts energy from sunlight. Inputs are *light green*, products are *blue*, and the path of electron flow is indicated by *red arrows.* Each of the protein complexes *(orange)* is embedded in a membrane. Note that the electron-motive force generated by the two chloroplast photosystems enables the chloroplast to drive electron transfer from H_2O to carbohydrate, and that this is *opposite* to the energetically favorable direction of electron transfer in a mitochondrion. Thus, whereas carbohydrate molecules and O_2 are inputs for the mitochondrion, they are products of the chloroplast.

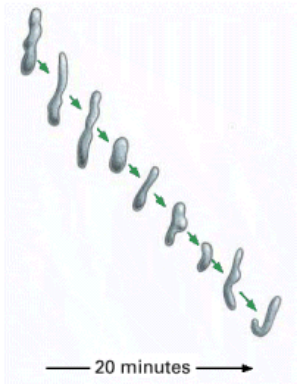

Figure 14-4. Mitochondrial plasticity. Rapid changes of shape are observed when an individual mitochondrion is followed in a living cell.

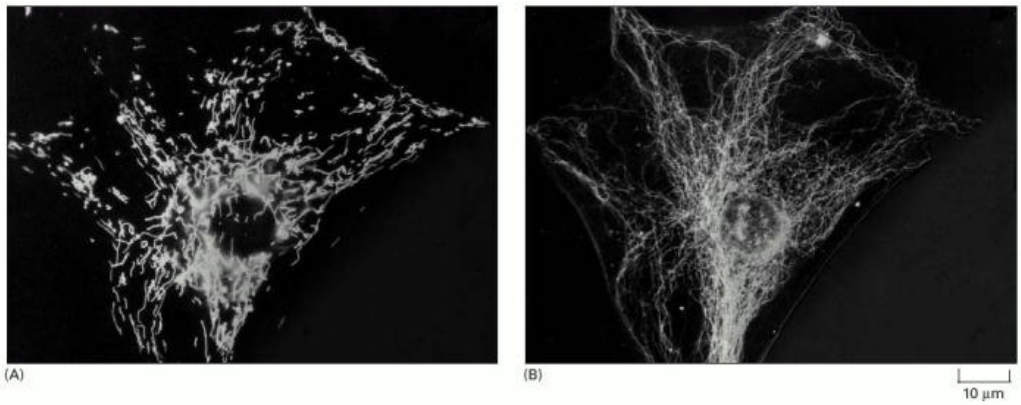

Figure 14-5. The relationship between mitochondria and microtubules. (A) A light micrograph of chains of elongated mitochondria in a living mammalian cell in culture. The cell was stained with a fluorescent dye (rhodamine 123) that specifically labels mitochondria in living cells. (B) An immunofluorescence micrograph of the same cell stained (after fixation) with fluorescent antibodies that bind to microtubules. Note that the mitochondria tend to be aligned along microtubules. (Courtesy of Lan Bo Chen.)

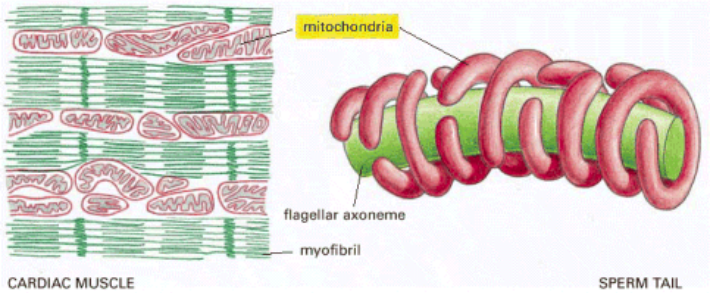

Figure 14-6. Localization of mitochondria near sites of high ATP utilization in cardiac muscle and a sperm tail. During the development of the flagellum of the sperm tail, microtubules wind helically around the axoneme, where they are thought to help localize the mitochondria in the tail; these microtubules then disappear, and the mitochondria fuse with one another to create the structure shown.

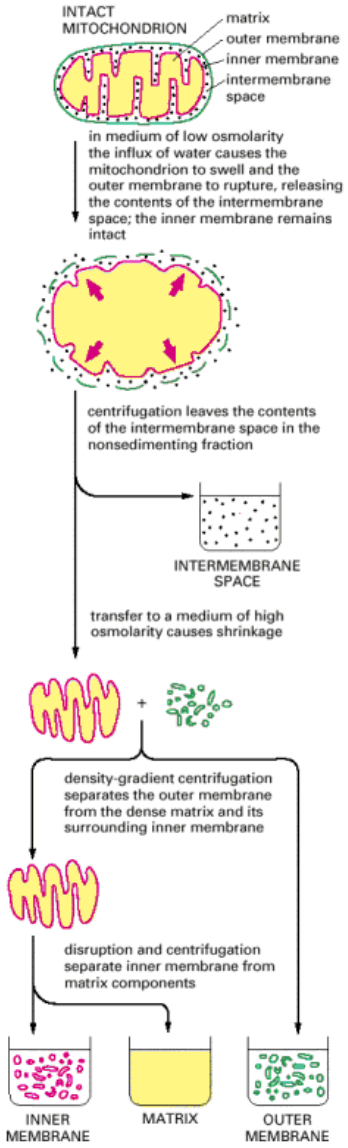

Figure 14-7. Biochemical fractionation of purified mitochondria into separate components. These techniques have made it possible to study the different proteins in each mitochondrial compartment. The method shown allows the processing of large numbers of mitochondria at the same time. It takes advantage of the fact that, in a solution of low osmotic strength, water flows into mitochondria and greatly expands the matrix space *(yellow).* While the cristae of the inner membrane unfold to accommodate the expansion, the outer membrane - which has no folds - breaks, releasing a structure composed of only the inner membrane and the matrix.

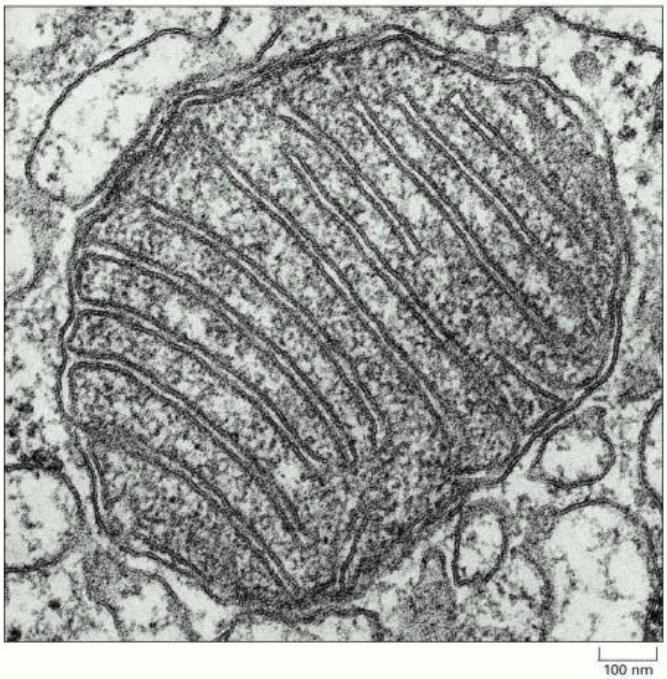

Matrix. This large internal space contains a highly concentrated mixture of hundreds of enzymes, including those required for the oxidation of pyruvate and fatty acids and for the citric acid cycle. The matrix also contains several identical copies of the mitochondrial DNA genome, special mitochondrial ribosomes, tRNAs, and various enzymes required for expression of the mitochondrial genes.

Inner membrane. The inner membrane *(red)* is folded into numerous cristae, greatly increasing its total surface area. It contains proteins with three types of functions: (1) those that carry out the oxidation reactions of the electron-transport chain, (2) the ATP synthase that makes ATP in the matrix, and (3) transport proteins that allow the passage of metabolites into and out of the matrix. An electrochemical gradient of H^+, which drives the ATP synthase, is established across this membrane, so the membrane must be impermeable to ions and most small charged molecules.

Outer membrane. Because it contains a large channel-forming protein (called porin), the outer membrane is permeable to all molecules of 5000 daltons or less. Other proteins in this membrane include enzymes involved in mitochondrial lipid synthe-

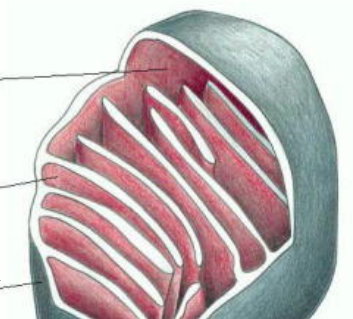

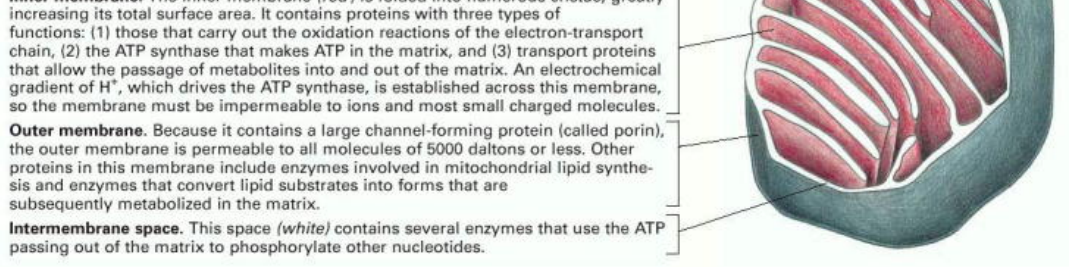

Figure 14-8. The general organization of a mitochondrion. In the liver, an estimated 67% of the total mitochondrial protein is located in the matrix, 21% is located in the inner membrane, 6% in the outer membrane, and 6% in the intermembrane space. As indicated below, each of these four regions contains a special set of proteins that mediate distinct functions. (Courtesy of Daniel S. Friend.)

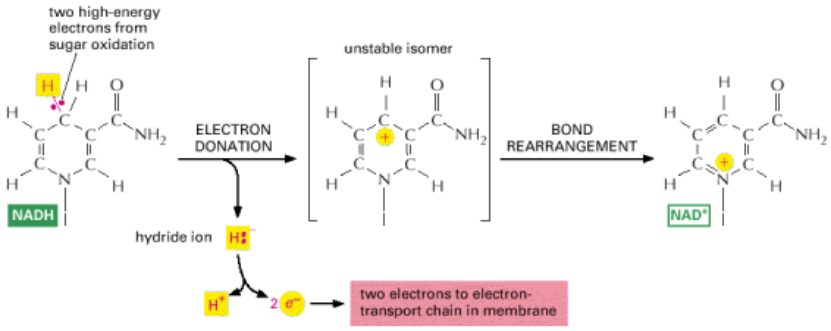

Figure 14-9. How electrons are donated by NADH. In this diagram, the high-energy electrons are shown as two *red dots* on a *yellow* hydrogen atom. A hydride ion (H^- a hydrogen atom and an extra electron) is removed from NADH and is converted into a proton and two high-energy electrons: $H^- \rightarrow H^+ + 2e^-$. Only the ring that carries the electrons in a high-energy linkage is shown; for the complete structure and the conversion of NAD^+ back to NADH, see the structure of the closely related NADPH in Figure 2-60. Electrons are also carried in a similar way by $FADH_2$, whose structure is shown in Figure 2-80.

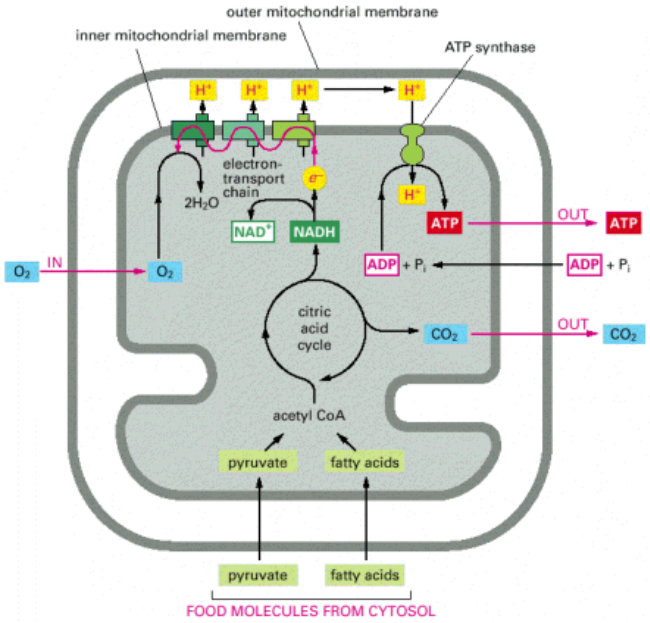

Figure 14-10. A summary of energy-generating metabolism in mitochondria. Pyruvate and fatty acids enter the mitochondrion *(bottom)* and are broken down to acetyl CoA. The acetyl CoA is then metabolized by the citric acid cycle, which reduces NAD^+ to NADH (and FAD to $FADH_2$, not shown). In the process of oxidative phosphorylation, high-energy electrons from NADH (and $FADH_2$) are then passed along the electron-transport chain in the inner membrane to oxygen (O_2). This electron transport generates a proton gradient across the inner membrane, which is used to drive the production of ATP by ATP synthase (see Figure 14-1). The NADH generated by glycolysis in the cytosol also passes electrons to the respiratory chain (not shown). Since NADH cannot pass across the inner mitochondrial membrane, the electron transfer from cytosolic NADH must be accomplished indirectly by means of one of several "shuttle" systems that transport another reduced compound into the mitochondrion; after being oxidized, this compound is returned to the cytosol, where it is reduced by NADH again.

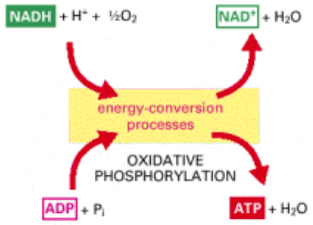

Figure 14-11. The major net energy conversion catalyzed by the mitochondrion. In this process of oxidative phosphorylation, the inner mitochondrial membrane serves as a device that changes one form of chemical bond energy to another, converting a major part of the energy of NADH (and $FADH_2$) oxidation into phosphate-bond energy in ATP.

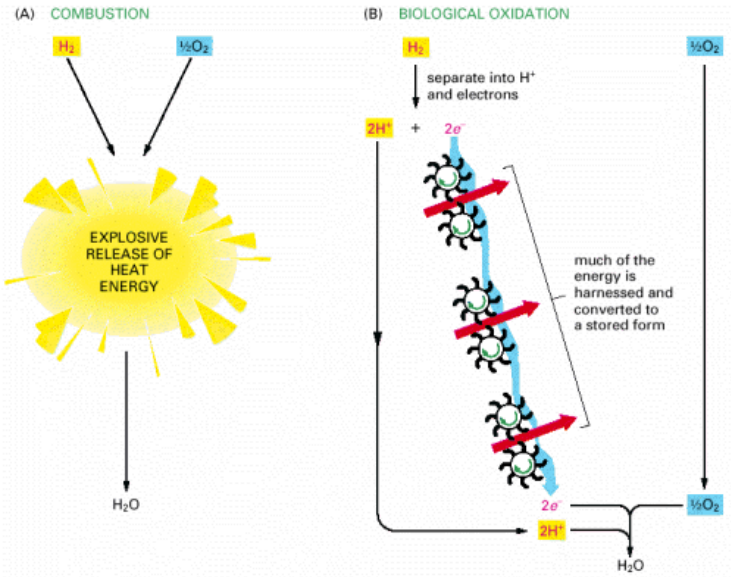

Figure 14-12. A comparison of biological oxidations with combustion. (A) Most of the energy would be released as heat if hydrogen were simply burned. (B) In biological oxidation by contrast, most of the released energy is stored in a form useful to the cell by means of the electron-transport chain in the inner mitochondrial membrane (the respiratory chain). The rest of the oxidation energy is released as heat by the mitochondrion. In reality, the protons and electrons shown are removed from hydrogen atoms that are covalently linked to NADH or $FADH_2$ molecules.

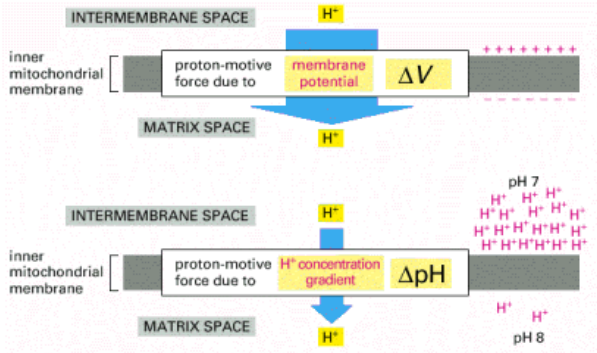

Figure 14-13. The two components of the electrochemical proton gradient. The total proton-motive force across the inner mitochondrial membrane consists of a large force due to the membrane potential (traditionally designated $\Delta\Psi$ by experts, but designated ΔV in this text) and a smaller force due to the H^+ concentration gradient (ΔpH). Both forces act to drive H^+ into the matrix.

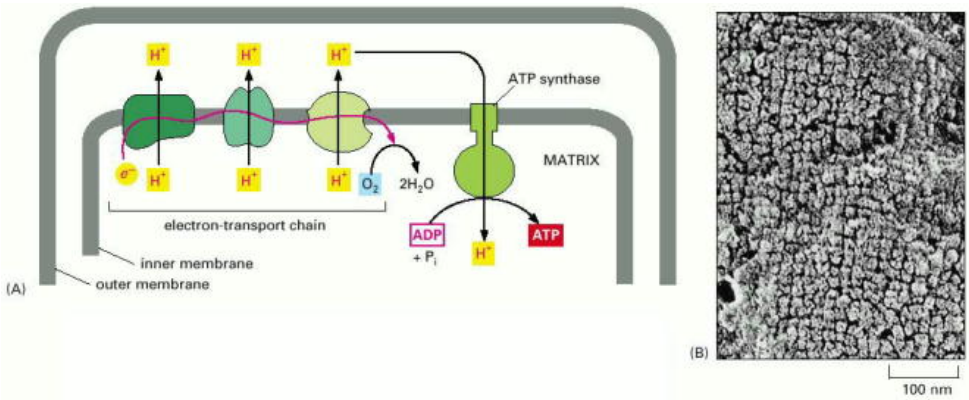

Figure 14-14. The general mechanism of oxidative phosphorylation. (A) As a high-energy electron is passed along the electron-transport chain, some of the energy released is used to drive the three respiratory enzyme complexes that pump H^+ out of the matrix. The resulting electrochemical proton gradient across the inner membrane drives H^+ back through the ATP synthase, a transmembrane protein complex that uses the energy of the H^+ flow to synthesize ATP from ADP and P_i in the matrix. (B) An electron micrograph of the inside surface of the inner mitochondrial membrane in a plant cell. Densely packed particles are visible, due to protruding portions of the ATP synthases and the respiratory enzyme complexes. (Micrograph courtesy of Brian Wells.)

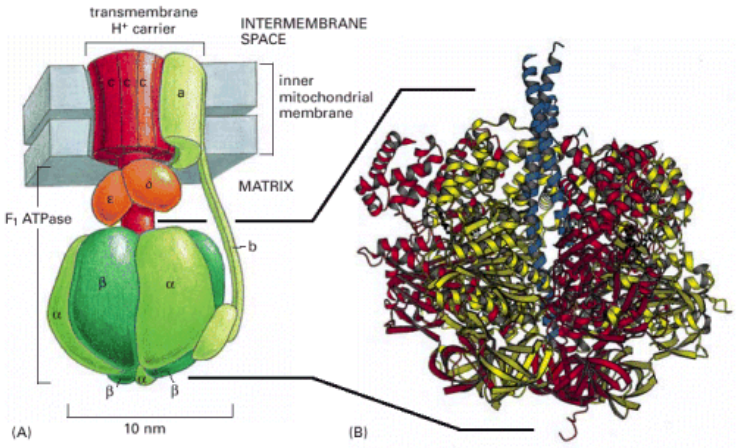

Figure 14-15. ATP synthase. (A) The enzyme is composed of a head portion, called the F_1 ATPase, and a transmembrane H^+ carrier, called F_0. Both F_1 and F_0 are formed from multiple subunits, as indicated. A rotating stalk turns with a rotor formed by a ring of 10 to 14 c subunits in the membrane *(red)*. The stator *(green)* is formed from transmembrane a subunits, tied to other subunits that create an elongated arm. This arm fixes the stator to a ring of 3α and 3β subunits that forms the head. (B) The three-dimensional structure of the F_1 ATPase, determined by x-ray crystallography. This part of the ATP synthase derives its name from its ability to carry out the reverse of the ATP synthesis reaction - namely, the hydrolysis of ATP to ADP and P_i, when detached from the transmembrane portion. (B, courtesy of John Walker, from J.P. Abrahams et al., *Nature* 370:621628, 1994. © Macmillan Magazines Ltd.)

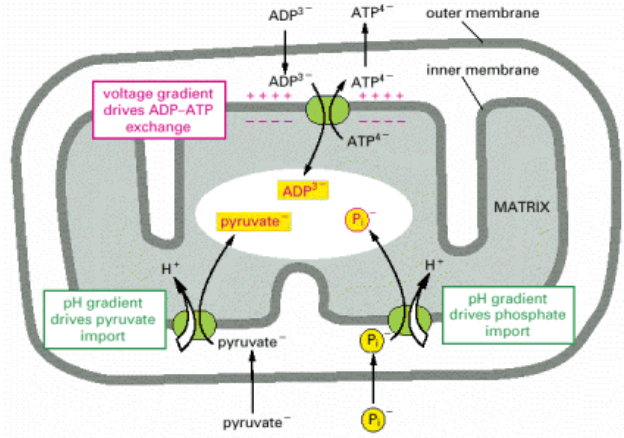

Figure 14-16. Some of the active transport processes driven by the electrochemical proton gradient across the inner mitochondrial membrane. Pyruvate, inorganic phosphate (P_i), and ADP are moved into the matrix, while ATP is pumped out. The charge on each of the transported molecules is indicated for comparison with the membrane potential, which is negative inside, as shown. The outer membrane is freely permeable to all of these compounds. The active transport of molecules across membranes by carrier proteins is discussed in Chapter 11.

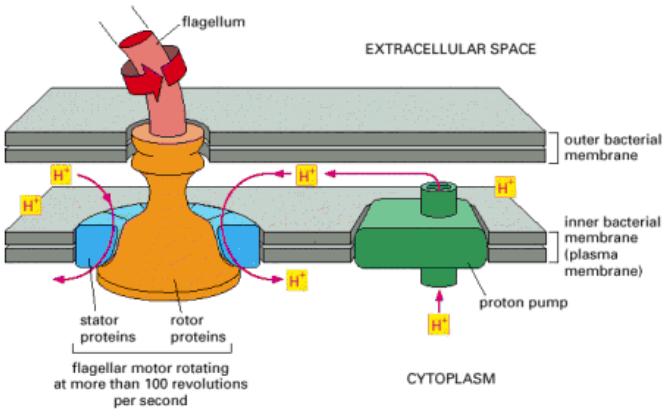

Figure 14-17. The rotation of the bacterial flagellum driven by H^+ flow. The flagellum is attached to a series of protein rings *(orange)*, which are embedded in the outer and inner membranes and rotate with the flagellum. The rotation is driven by a flow of protons through an outer ring of proteins (the stator) by mechanisms that may resemble those used by the ATP synthase, although they are not yet understood.

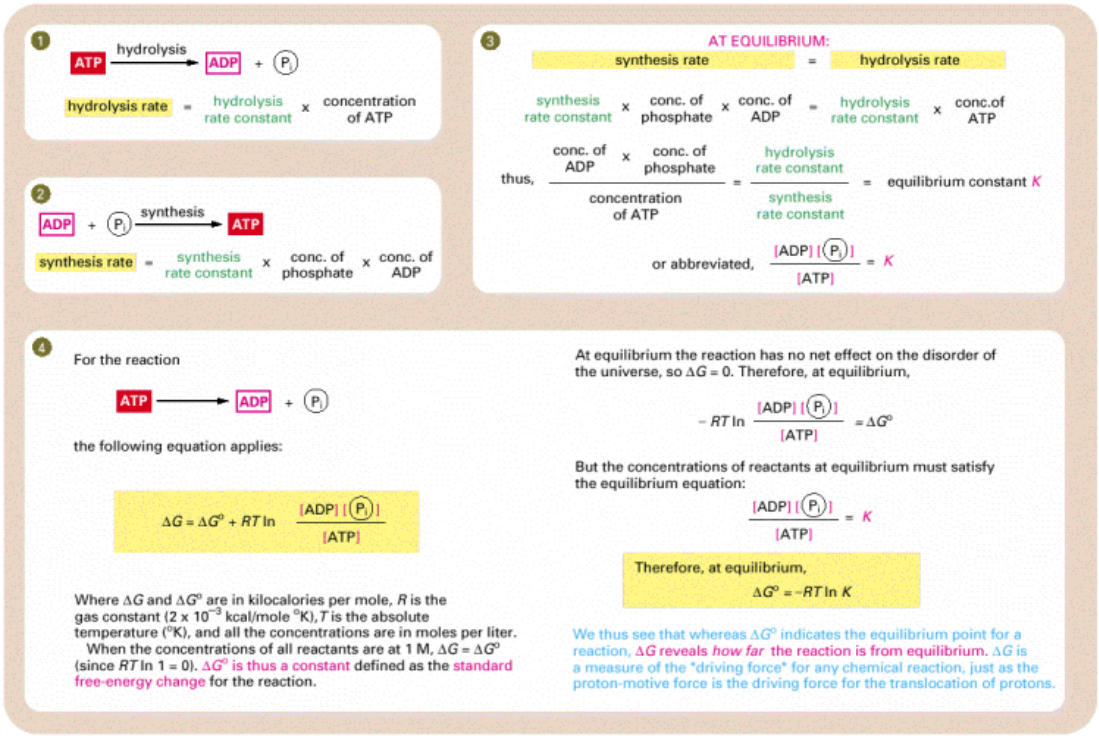

Figure 14-18. The basic relationship between free-energy changes and equilibrium in the ATP hydrolysis reaction. The rate constants in boxes 1 and 2 are determined from experiments in which product accumulation is measured as a function of time. The equilibrium constant shown here, *K*, is in units of moles per liter. (See Panel 2-7, pp. 122123, for a discussion of free energy and p. 160 for a discussion of the equilibrium constant.)

Figure 14-19. The ATP synthase is a reversible coupling device that can convert the energy of the electrochemical proton gradient into chemical-bond energy, or vice versa. The ATP synthase can either (A) synthesize ATP by harnessing the proton-motive force or (B) pump protons against their electrochemical gradient by hydrolyzing ATP. As explained in the text, the direction of operation at any given instant depends on the net free-energy change (ΔG) for the coupled processes of H^+ translocation across the membrane and the synthesis of ATP from ADP and P_i. Measurement of the torque that the ATP synthase can produce when hydrolyzing ATP reveals that the synthase can pump 60 times more strongly than a diesel-engine of equal weight. We have previously shown how the free-energy change (ΔG) for ATP hydrolysis depends on the concentrations of the three reactants ATP, ADP, and P_i (see Figure 14-18); the ΔG for ATP synthesis is the negative of this value. The ΔG for proton translocation across the membrane is proportional to the proton-motive force. The conversion factor between them is the faraday. Thus, $\Delta G_{H^+} = -0.023$ (proton-motive force), where ΔG_{H^+} is in kcal/mole and the proton-motive force is in mV. For an electrochemical proton gradient (proton-motive force) of 200 mV, $\Delta G_{H^+} = -4.6$ kcal/mole.

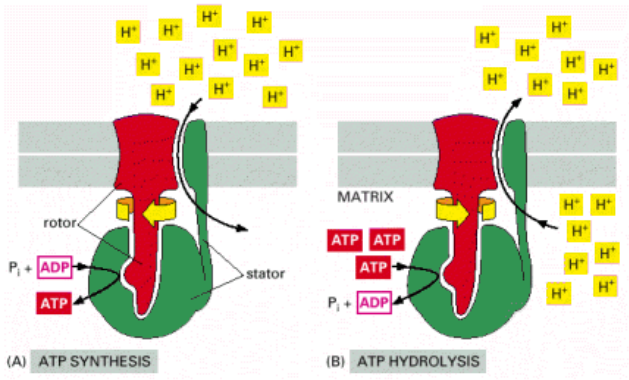

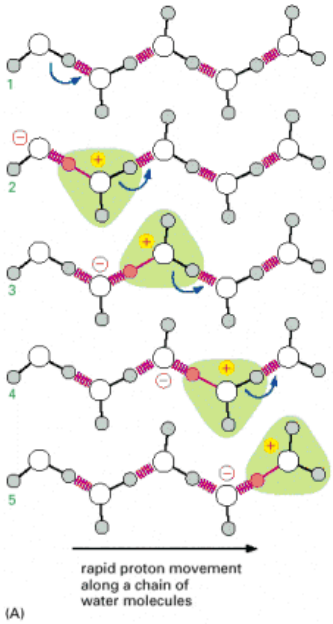

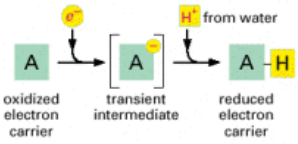

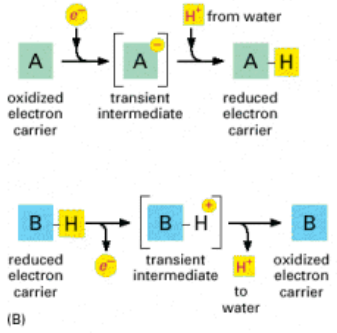

Figure 14-20. How protons behave in water. (A) Protons move very rapidly along a chain of hydrogen-bonded water molecules. In this diagram, proton jumps are indicated by *blue arrows*, and hydronium ions are indicated by *green shading*. As discussed in Chapter 2, naked protons rarely exist as such; they are instead associated with a water molecule in the form of a hydronium ion, H_3O^+. At a neutral pH (pH 7.0), the hydronium ions are present at a concentration of 10^{-7} M. However, for simplicity, one usually refers to this as an H^+ concentration of 10^{-7} M (see Panel 2-2, pp. 112113). (B) Electron transfer can result in the transfer of entire hydrogen atoms, because protons are readily accepted from or donated to water inside cells. In this example, A picks up an electron plus a proton when it is reduced, and B loses an electron plus a proton when it is oxidized.

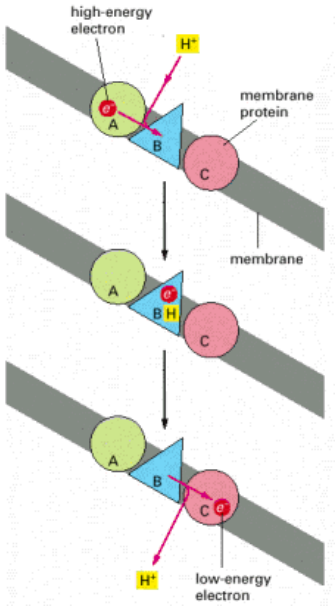

Figure 14-21. How protons can be pumped across membranes. As an electron passes along an electron-transport chain embedded in a lipid-bilayer membrane, it can bind and release a proton at each step. In this diagram, electron carrier B picks up a proton (H^+) from one side of the membrane when it accepts an electron (e^-) from carrier A; it releases the proton to the other side of the membrane when it donates its electron to carrier C.

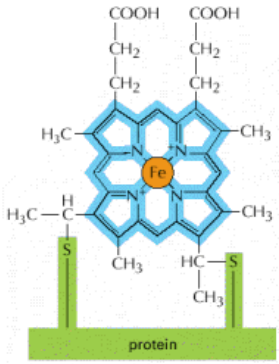

Figure 14-22. The structure of the heme group attached covalently to cytochrome *c*. The porphyrin ring is shown in *blue*. There are five different cytochromes in the respiratory chain. Because the hemes in different cytochromes have slightly different structures and are held by their respective proteins in different ways, each of the cytochromes has a different affinity for an electron.

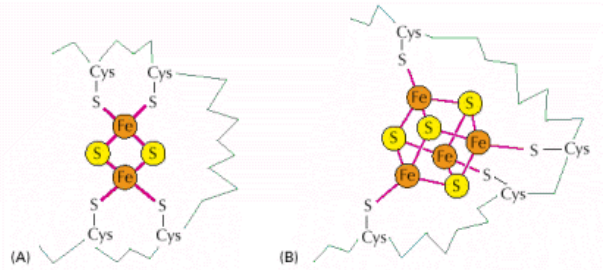

Figure 14-23. The structures of two types of iron-sulfur centers. (A) A center of the 2Fe2S type. (B) A center of the 4Fe4S type. Although they contain multiple iron atoms, each iron-sulfur center can carry only one electron at a time. There are more than seven different iron-sulfur centers in the respiratory chain.

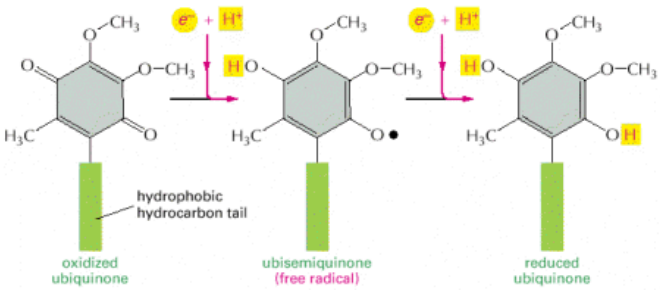

Figure 14-24. Quinone electron carriers. Ubiquinone in the respiratory chain picks up one H^+ from the aqueous environment for every electron it accepts, and it can carry either one or two electrons as part of a hydrogen atom *(yellow)*. When reduced ubiquinone donates its electrons to the next carrier in the chain, these protons are released. A long hydrophobic tail confines ubiquinone to the membrane and consists of 610 five-carbon isoprene units, the number depending on the organism. The corresponding electron carrier in the photosynthetic membranes of chloroplasts is plastoquinone, which is almost identical in structure. For simplicity, both ubiquinone and plastoquinone are referred to in this chapter as quinone (abbreviated as Q).

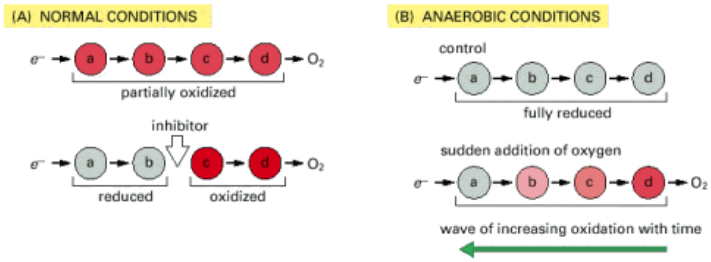

Figure 14-25. The general methods used to determine the path of electrons along an electron-transport chain. The extent of oxidation of electron carriers a, b, c, and d is continuously monitored by following their distinct spectra, which differ in their oxidized and reduced states. In this diagram an increased degree of oxidation is indicated by a *darker red.* (A) Under normal conditions, where oxygen is abundant, all carriers are in a partly oxidized state. The addition of a specific inhibitor causes the downstream carriers to become more oxidized *(red)* and the upstream carriers to become more reduced. (B) In the absence of oxygen, all carriers are in their fully reduced state *(gray).* The sudden addition of oxygen converts each carrier to its partly oxidized form with a delay that is greatest for the most upstream carriers.

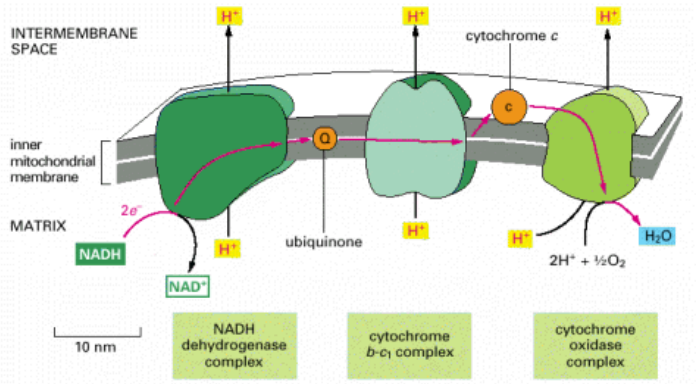

Figure 14-26. The path of electrons through the three respiratory enzyme complexes. The relative size and shape of each complex are shown. During the transfer of electrons from NADH to oxygen *(red lines),* ubiquinone and cytochrome *c* serve as mobile carriers that ferry electrons from one complex to the next. As indicated, protons are pumped across the membrane by each of the respiratory enzyme complexes.

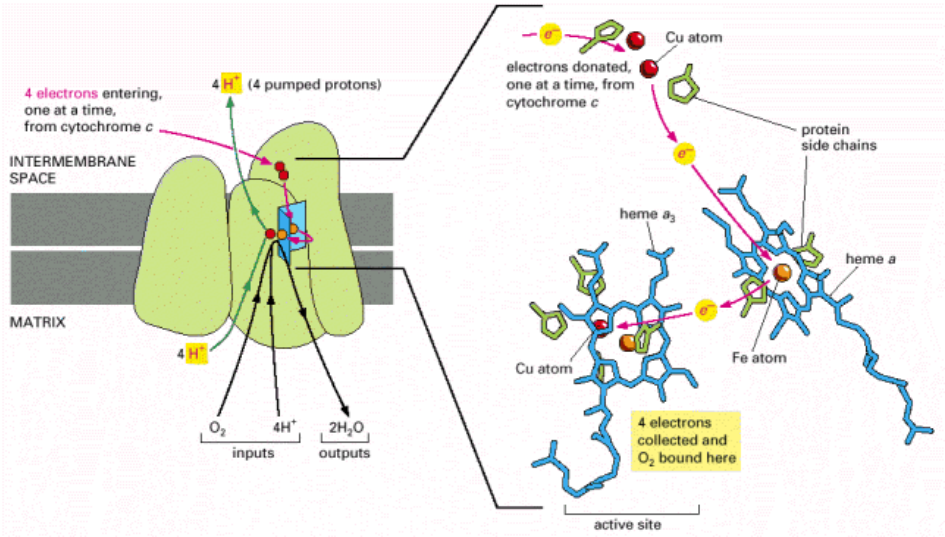

Figure 14-27. The reaction of O_2 with electrons in cytochrome oxidase. As indicated, the iron atom in heme *a* serves as an electron queuing point; this heme feeds four electrons into an O_2 molecule held at the bimetallic center active site, which is formed by the other heme-linked iron and a closely opposed copper atom. Note that four protons are pumped out of the matrix for each O_2 molecule that undergoes the reaction $4e^- + 4H^+ + O_2$ $2H_2O$.

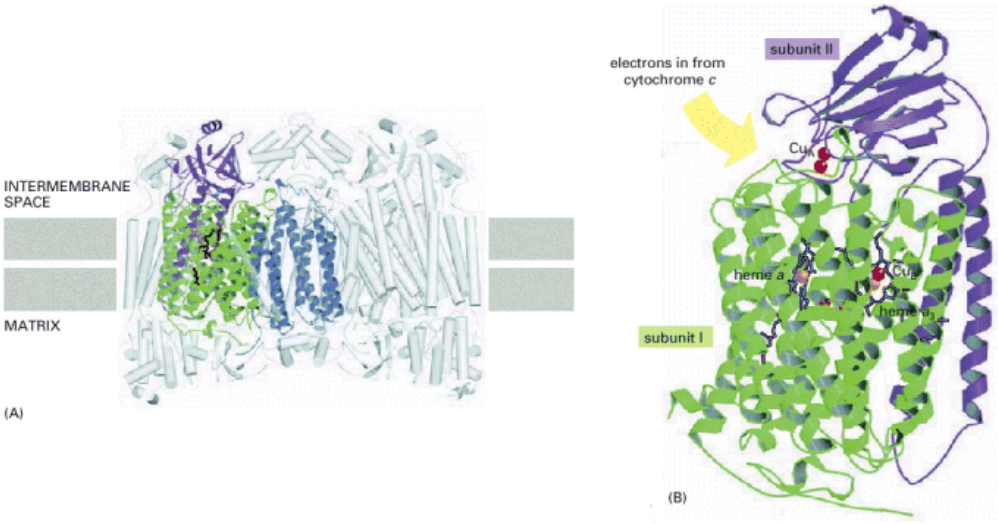

Figure 14-28. The molecular structure of cytochrome oxidase. This protein is a dimer formed from a monomer with 13 different protein subunits (monomer mass of 204,000 daltons). The three colored subunits are encoded by the mitochondrial genome, and they form the functional core of the enzyme. As electrons pass through this protein on the way to its bound O_2 molecule, they cause the protein to pump protons across the membrane (see Figure 14-27). (A) The entire protein is shown, positioned in the inner mitochondrial membrane. (B) The electron carriers are located in subunits I and II, as indicated.

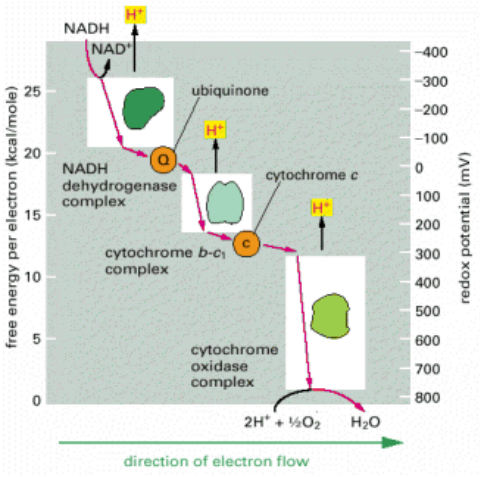

Figure 14-29. Redox potential changes along the mitochondrial electron-transport chain. The redox potential (designated E_0) increases as electrons flow down the respiratory chain to oxygen. The standard free-energy change, $\Delta G°$, for the transfer of each of the two electrons donated by an NADH molecule can be obtained from the left-hand ordinate ($\Delta G = -n(0.023)\,\Delta E_0$, where n is the number of electrons transferred across a redox potential change of ΔE_0 mV). Electrons flow through a respiratory enzyme complex by passing in sequence through the multiple electron carriers in each complex. As indicated, part of the favorable free-energy change is harnessed by each enzyme complex to pump H^+ across the inner mitochondrial membrane. It is thought that the NADH dehydrogenase and cytochrome b-c_1 complexes each pump two H^+ per electron, whereas the cytochrome oxidase complex pumps one. It should be noted that NADH is not the only source of electrons for the respiratory chain. The flavin $FADH_2$ is also generated by fatty acid oxidation (see Figure 2-77) and by the citric acid cycle (see Figure 2-79). Its two electrons are passed directly to ubiquinone, bypassing NADH dehydrogenase; they therefore cause less H^+ pumping than the two electrons transported from NADH.

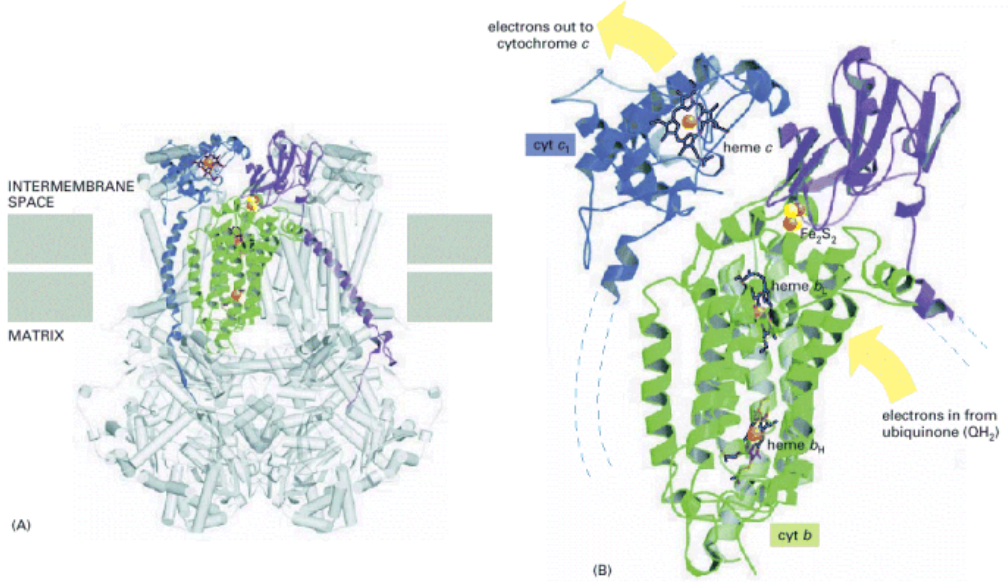

Figure 14-30. The atomic structure of cytochrome b-c_1. This protein is a dimer. The 240,000-dalton monomer is composed of 11 different protein molecules in mammals. The three colored proteins form the functional core of the enzyme: cytochrome *b (green)*, cytochrome c_1*(blue)*, and the Rieske protein containing an iron-sulfur center *(purple)*. (A) The interaction of these three proteins across the two monomers. (B) Their electron carriers, along with the entrance and exit sites for electrons.

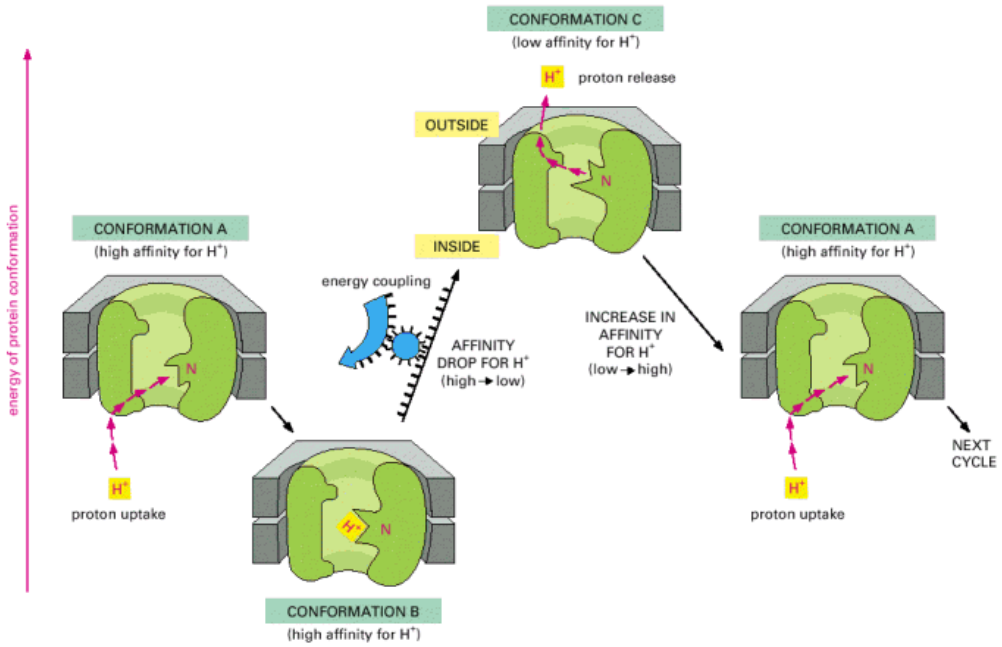

Figure 14-31. A general model for H^+ pumping. This model for H^+ pumping by a transmembrane protein is based on mechanisms that are thought to be used by both cytochrome oxidase and the light-driven procaryotic proton pump, bacteriorhodopsin. The protein is driven through a cycle of three conformations: A, B, and C. As indicated by their vertical spacing, these protein conformations have different energies. In conformation A, the protein has a high affinity for H^+, causing it to pick up a H^+ on the inside of the membrane. In conformation C, the protein has a low affinity for H^+, causing it to release a H^+ on the outside of the membrane. The transition from conformation B to conformation C that releases the H^+ is energetically unfavorable, and it occurs only because it is driven by being allosterically coupled to an energetically favorable reaction occurring elsewhere on the protein *(blue arrow)*. The other two conformational changes, A B and C A, lead to states of lower energy, and they proceed spontaneously. Because the overall cycle A B C A B C releases free energy, H^+ is pumped from the inside (the matrix in mitochondria) to the outside (the intermembrane space in mitochondria). For cytochrome oxidase, the energy required for the transition B C is provided by electron transport, whereas for bacteriorhodopsin, this energy is provided by light (see Figure 10-37). For yet other proton pumps, the energy is derived from ATP hydrolysis.

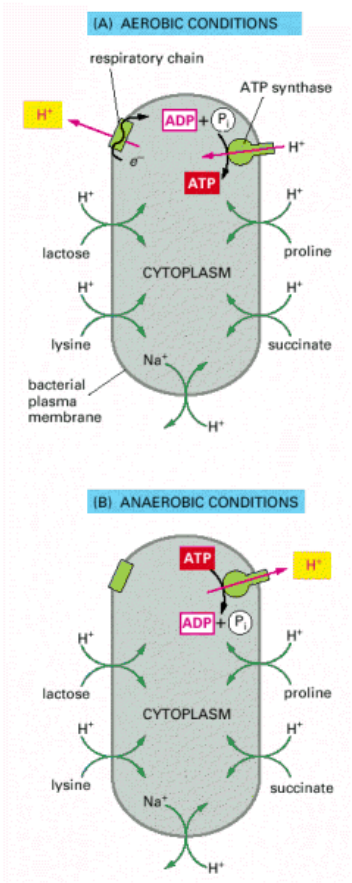

Figure 14-32. The importance of H^+-driven transport in bacteria. A proton-motive force generated across the plasma membrane pumps nutrients into the cell and expels Na^+. (A) In an aerobic bacterium, an electrochemical proton gradient across the plasma membrane is produced by a respiratory chain and is then used both to transport some nutrients into the cell and to make ATP. (B) The same bacterium growing under anaerobic conditions can derive its ATP from glycolysis. Part of this ATP is hydrolyzed by the ATP synthase to establish an electrochemical proton gradient that drives the same transport processes that depend on the respiratory chain in (A).

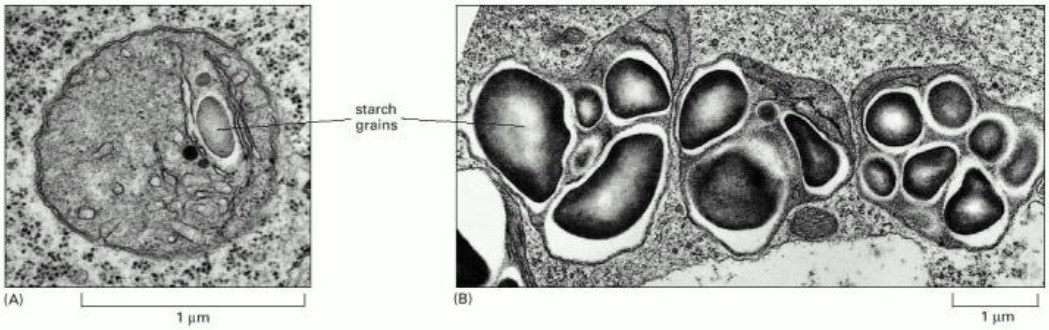

Figure 14-33. Plastid diversity. (A) A proplastid from a root tip cell of a bean plant. Note the double membrane; the inner membrane has also generated the relatively sparse internal membranes present. (B) Three amyloplasts (a form of leucoplast), or starch-storing plastids, in a root tip cell of soybean. (From B. Gunning and M. Steer, Plant Cell Biology: Structure and Function. Sudbury, MA: Jones & Bartlett, 1996. © Jones & Bartlett Publishers.)

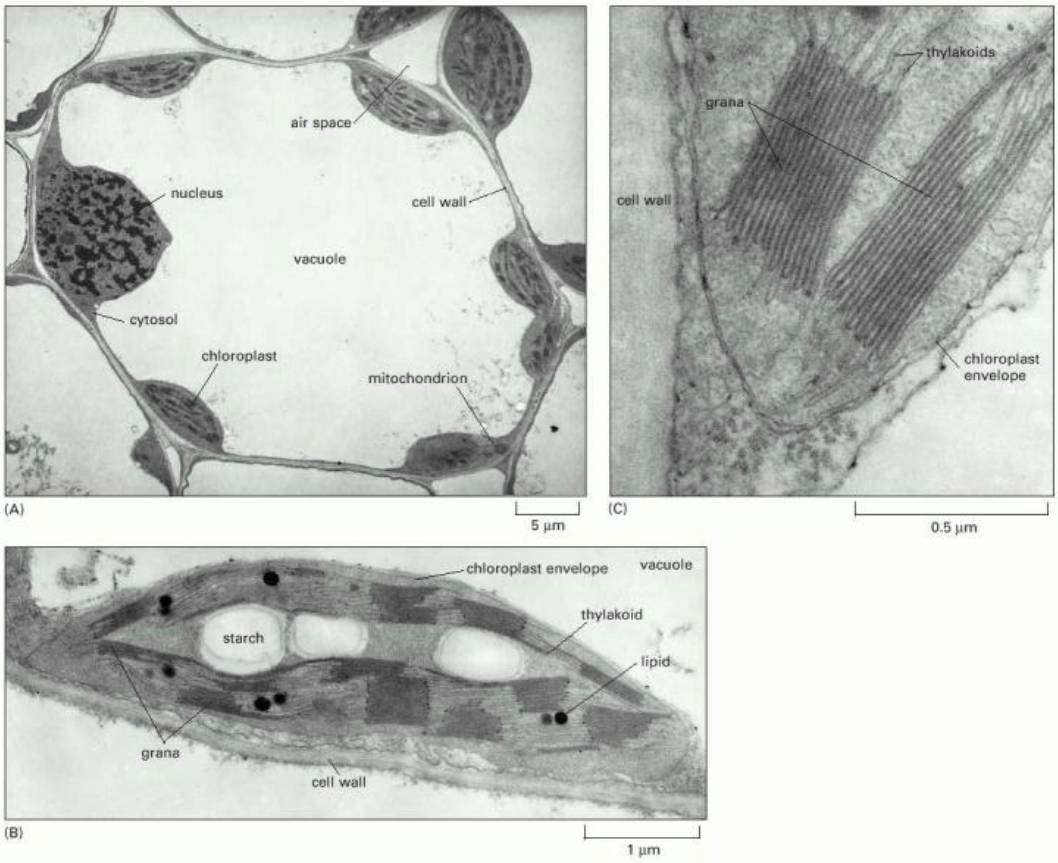

Figure 14-34. Electron micrographs of chloroplasts. (A) In a wheat leaf cell, a thin rim of cytoplasm - containing chloroplasts, the nucleus, and mitochondria - surrounds a large vacuole. (B) A thin section of a single chloroplast, showing the chloroplast envelope, starch granules, and lipid (fat) droplets that have accumulated in the stroma as a result of the biosyntheses occurring there. (C) A high-magnification view of two grana. A granum is a stack of thylakoids. (Courtesy of K. Plaskitt.)

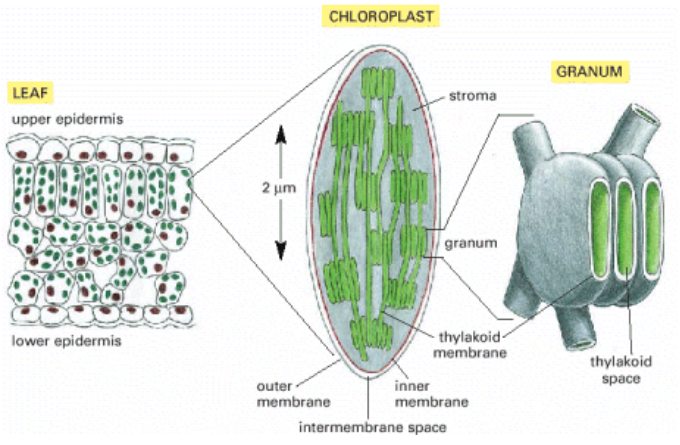

Figure 14-35. The chloroplast. This photosynthetic organelle contains three distinct membranes (the outer membrane, the inner membrane, and the thylakoid membrane) that define three separate internal compartments (the intermembrane space, the stroma, and the thylakoid space). The thylakoid membrane contains all the energy-generating systems of the chloroplast, including its chlorophyll. In electron micrographs, this membrane seems to be broken up into separate units that enclose individual flattened vesicles (see Figure 14-34), but these are probably joined into a single, highly folded membrane in each chloroplast. As indicated, the individual thylakoids are interconnected, and they tend to stack to form grana.

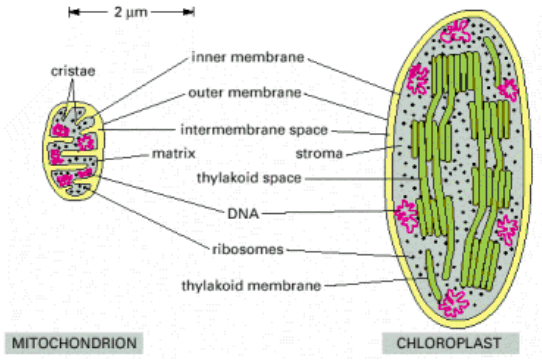

Figure 14-36. A mitochondrion and chloroplast compared. A chloroplast is generally much larger than a mitochondrion and contains, in addition to an outer and inner membrane, a thylakoid membrane enclosing a thylakoid space. Unlike the chloroplast inner membrane, the inner mitochondrial membrane is folded into cristae to increase its surface area.

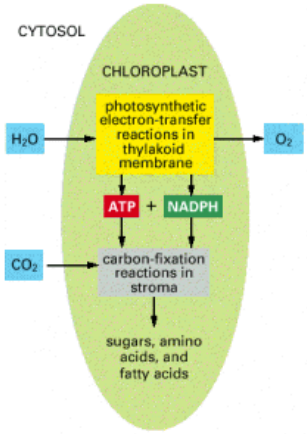

Figure 14-37. The reactions of photosynthesis in a chloroplast. Water is oxidized and oxygen is released in the photosynthetic electron-transfer reactions, while carbon dioxide is assimilated (fixed) to produce sugars and a variety of other organic molecules in the carbon-fixation reactions.

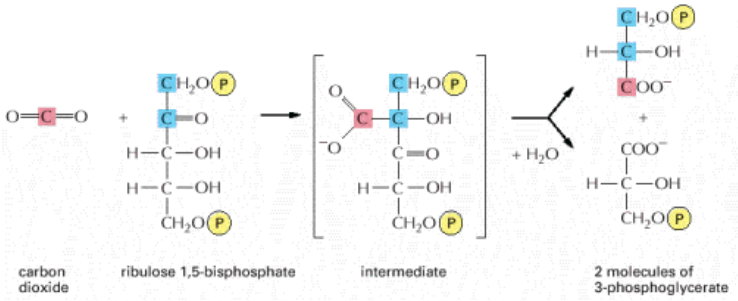

Figure 14-38. The initial reaction in carbon fixation. This reaction, in which carbon dioxide is converted into organic carbon, is catalyzed in the chloroplast stroma by the abundant enzyme ribulose bisphosphate carboxylase. The product is 3-phosphoglycerate, which is also an intermediate in glycolysis. The two carbon atoms shaded in *blue* are used to produce phosphoglycolate when the same enzyme adds oxygen instead of CO_2 (see text).

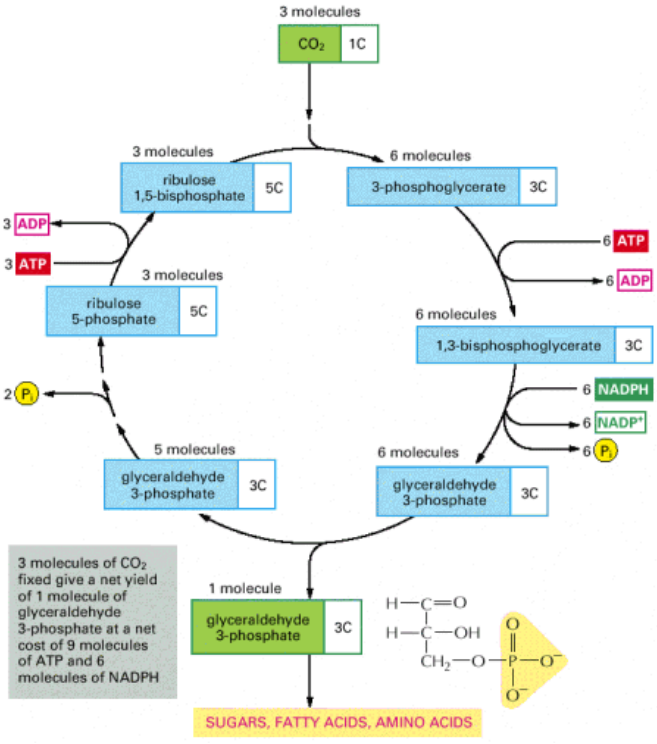

Figure 14-39. The carbon-fixation cycle, which forms organic molecules from CO_2 and H_2O. The number of carbon atoms in each type of molecule is indicated in the *white box*. There are many intermediates between glyceraldehyde 3-phosphate and ribulose 5-phosphate, but they have been omitted here for clarity. The entry of water into the cycle is also not shown.

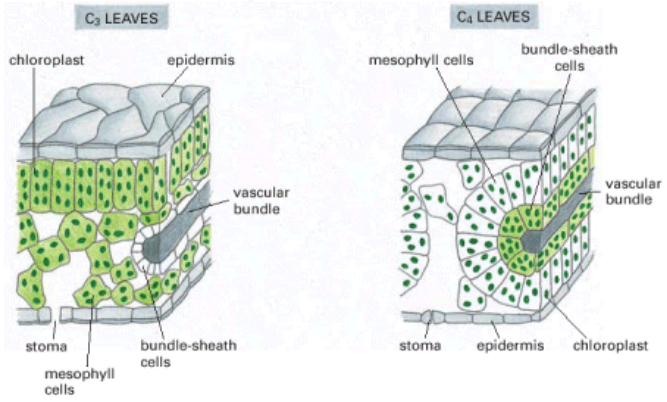

Figure 14-40. Comparative leaf anatomy in a C_3 plant and a C_4 plant. The cells with *green* cytosol in the leaf interior contain chloroplasts that perform the normal carbon-fixation cycle. In C_4 plants, the mesophyll cells are specialized for CO_2 pumping rather than for carbon fixation, and they thereby create a high ratio of CO_2 to O_2 in the bundle-sheath cells, which are the only cells in these plants where the carbon-fixation cycle occurs. The vascular bundles carry the sucrose made in the leaf to other tissues.

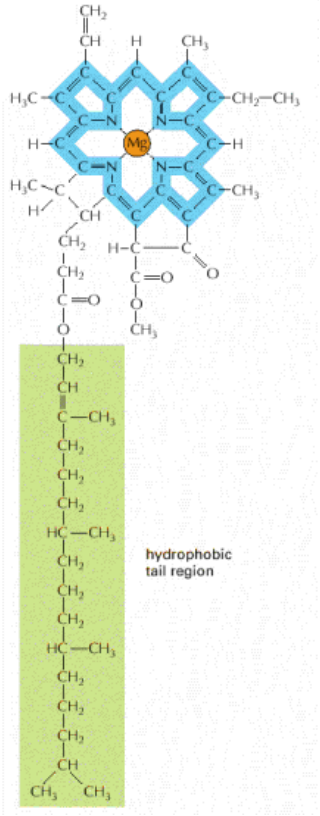

Figure 14-41. The structure of chlorophyll. A magnesium atom is held in a porphyrin ring, which is related to the porphyrin ring that binds iron in heme (see Figure 14-22). Electrons are delocalized over the bonds shown in *blue*.

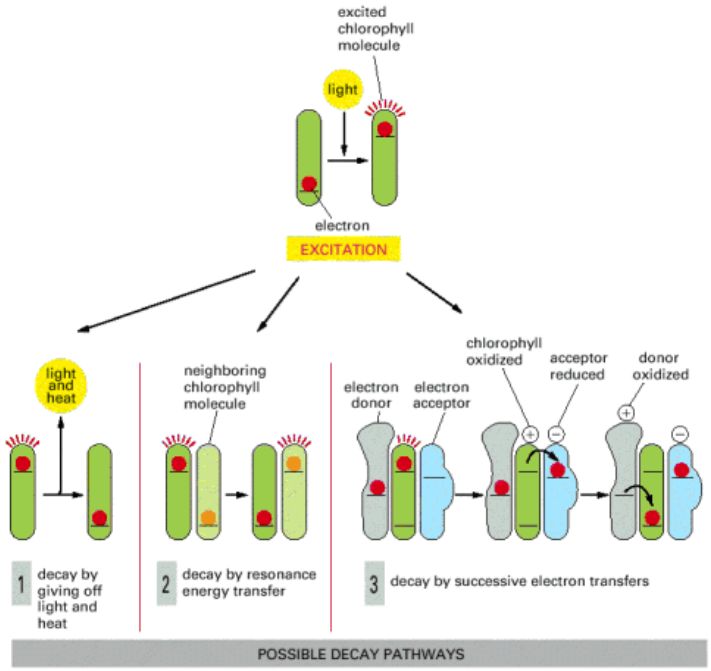

Figure 14-42. Three ways for an excited chlorophyll molecule to return to its original, unexcited state. The light energy absorbed by an isolated chlorophyll molecule is completely released as light and heat by process 1. In photosynthesis, by contrast, chlorophylls undergo process 2 in the antenna complex and process 3 in the reaction center, as described in the text.

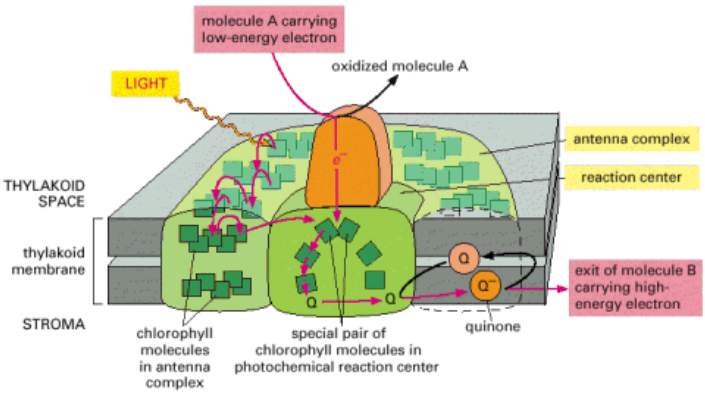

Figure 14-43. The antenna complex and photochemical reaction center in a photosystem. The antenna complex is a collector of light energy in the form of excited electrons. The energy of the excited electrons is funneled, through a series of resonance energy transfers, to a special pair of chlorophyll molecules in the photochemical reaction center. The reaction center then produces a high-energy electron that can be passed rapidly to the electron-transport chain in the thylakoid membrane, via a quinone.

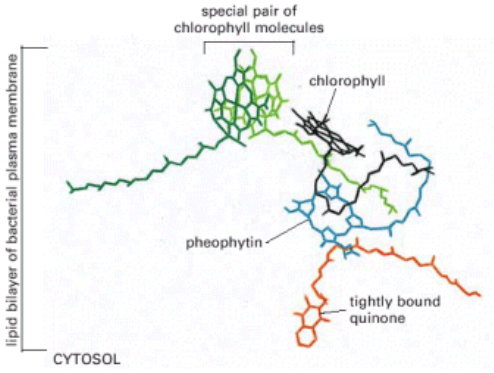

Figure 14-44. The arrangement of the electron carriers in a bacterial photochemical reaction center, as determined by x-ray crystallography. The pigment molecules shown are held in the interior of a transmembrane protein and are surrounded by the lipid bilayer of the bacterial plasma membrane. An electron in the special pair of chlorophyll molecules is excited by resonance from an antenna complex chlorophyll, and the excited electron is then transferred stepwise from the special pair to the quinone (see also Figure 14-45). A similar arrangement of electron carriers is present in the reaction centers of plants.

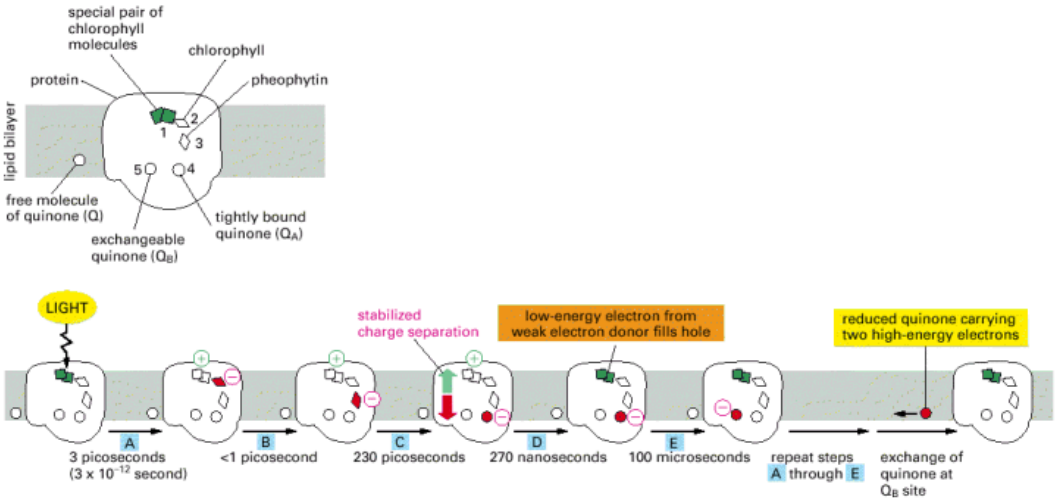

Figure 14-45. The electron transfers that occur in the photochemical reaction center of a purple bacterium. A similar set of reactions occurs in the evolutionarily related photosystem II in plants. At the top left is an orientating diagram showing the molecules that carry electrons, which are those in Figure 14-44, plus an exchangeable quinone (Q_B) and a freely mobile quinone (Q) dissolved in the lipid bilayer. Electron carriers 15 are each bound in a specific position on a 596-amino-acid transmembrane protein formed from two separate subunits (see Figure 10-38). After excitation by a photon of light, a high-energy electron passes from pigment molecule to pigment molecule, very rapidly creating a *charge separation*, as shown below in the sequence of steps A-C, in which the pigment molecule carrying a high-energy electron is colored *red*. Steps D and E then occur progressively. After a second photon has repeated this sequence with a second electron, the exchangeable quinone is released into the bilayer. This quinone quickly loses its charge by picking up two protons (see Figure 14-24).

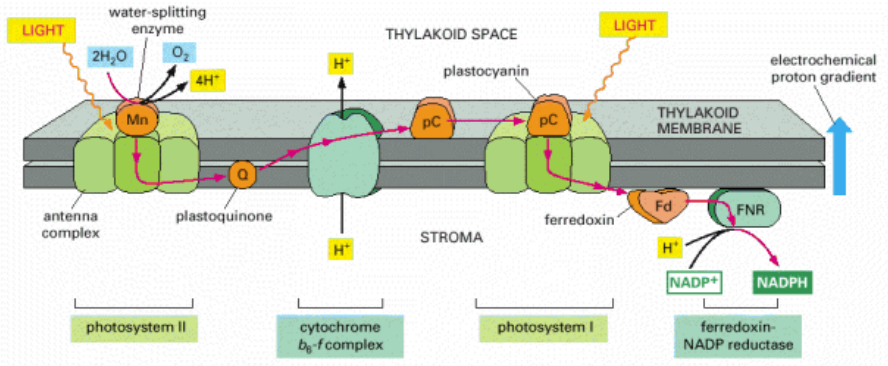

Figure 14-46. Electron flow during photosynthesis in the thylakoid membrane. The mobile electron carriers in the chain are plastoquinone (which closely resembles the ubiquinone of mitochondria), plastocyanin (a small copper-containing protein), and ferredoxin (a small protein containing an iron-sulfur center). The cytochrome b_6-f complex resembles the b-c_1 complex of mitochondria and the b-c complex of bacteria (see Figure 14-71): all three complexes accept electrons from quinones and pump H^+ across the membrane. The H^+ released by water oxidation into the thylakoid space, and the H^+ consumed during NADPH formation in the stroma, also contribute to the generation of the electrochemical H^+ gradient. This gradient drives ATP synthesis by an ATP synthase present in this same membrane (not shown here).

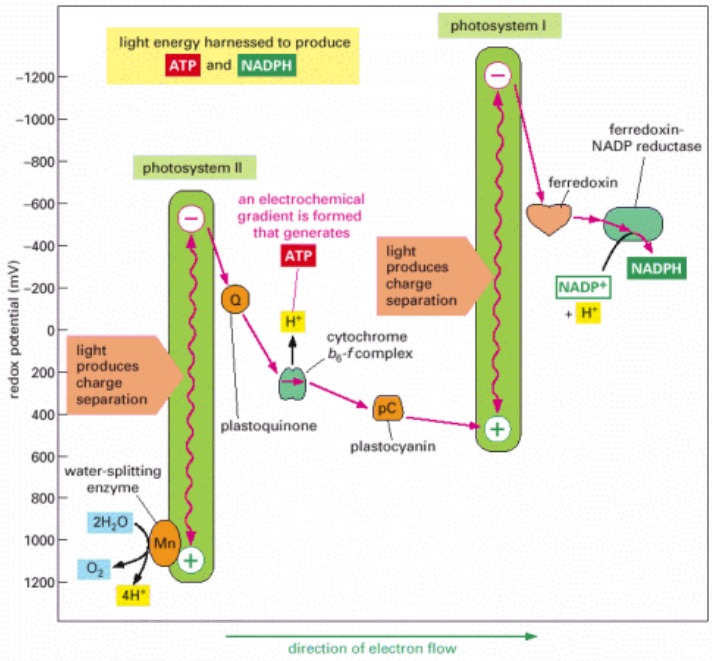

Figure 14-47. Changes in redox potential during photosynthesis. The redox potential for each molecule is indicated by its position along the vertical axis. In photosystem II, the excited reaction center chlorophyll has a redox potential high enough to withdraw electrons from water, by means of a specially organized cluster of four manganese atoms. Photosystem II closely resembles the reaction center in purple bacteria, and it passes electrons from its excited chlorophyll to an electron-transport chain that leads to photosystem I. Photosystem I then passes electrons from its excited chlorophyll through a series of tightly bound iron-sulfur centers. The net electron flow through the two photosystems in series is from water to $NADP^+$, and it produces NADPH as well as ATP. The ATP is synthesized by an ATP synthase that harnesses the electrochemical proton gradient produced by the three sites of H^+ activity that are highlighted in Figure 14-46. This Z scheme for ATP production is called noncyclic photophosphorylation, to distinguish it from a cyclic scheme that utilizes only photosystem I (see the text).

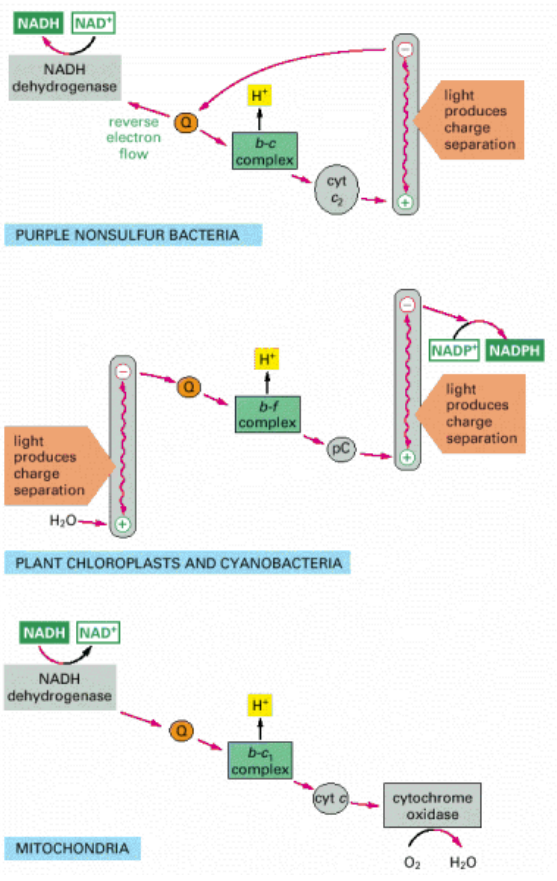

Figure 14-71. A comparison of three electron-transport chains discussed in this chapter. Bacteria, chloroplasts, and mitochondria all contain a membrane-bound enzyme complex that resembles the cytochrome b-c_1 complex of mitochondria. These complexes all accept electrons from a quinone carrier (Q) and pump H^+ across their respective membranes. Moreover, in reconstituted *in vitro* systems, the different complexes can substitute for one another, and the amino acid sequences of their protein components reveal that they are evolutionarily related.

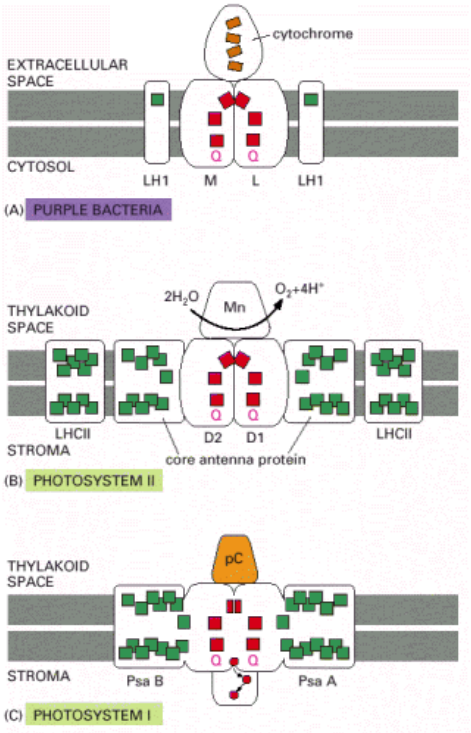

Figure 14-48. Three types of photosynthetic reaction centers compared. Pigments involved in light harvesting are colored *green;* those involved in the central photochemical events are colored *red.* (A) The photochemical reaction center of purple bacteria, whose detailed structure is illustrated in Figure 10-38, contains two related protein subunits, L and M, that bind the pigments involved in the central process illustrated in Figure 14-45. Low-energy electrons are fed into the excited chlorophylls by a cytochrome. LH1 is a protein-pigment complex involved in light harvesting. (B) Photosystem II contains the D_1 and D_2 proteins, which are homologous to the L and M subunits in (A). Low-energy electrons from water are fed into the excited chlorophylls by a manganese cluster. LHCII is a light-harvesting complex that feeds energy into the core antenna proteins. (C) Photosystem I contains the Psa A and Psa B proteins, each of which is equivalent to a fusion of the D_1 or D_2 protein to a core antenna protein of photosystem II. Low-energy electrons are fed into the excited chlorophylls by loosely bound plastocyanin (pC). As indicated, in photosystem I, high-energy electrons are passed from a nonmobile quinone (Q) through a series of three iron-sulfur centers *(red circles).* (Modified from K. Rhee, E. Morris, J. Barber, and W. Kühlbrandt, *Nature* 396:283286, 1998; W. Kühlbrandt, *Nature* 411:896899, 2001.)

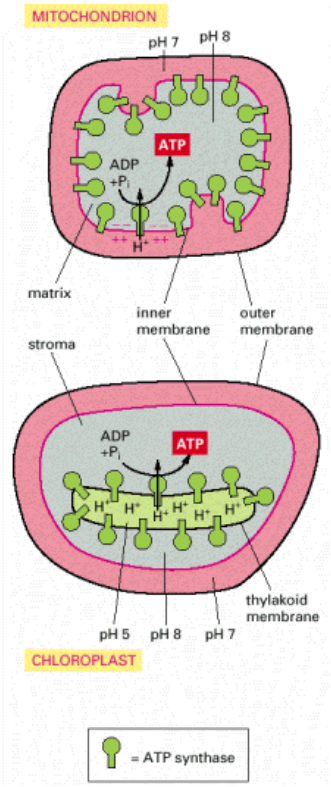

Figure 14-49. A comparison of the flow of H^+ and the orientation of the ATP synthase in mitochondria and chloroplasts. Those compartments with similar pH values have been colored the same. The proton-motive force across the thylakoid membrane consists almost entirely of the pH gradient; a high permeability of this membrane to Mg^{2+} and Cl^- ions allows the flow of these ions to dissipate most of the membrane potential. Mitochondria presumably need a large membrane potential because they could not tolerate having their matrix at pH 10, as would be required to generate their proton-motive force without one.

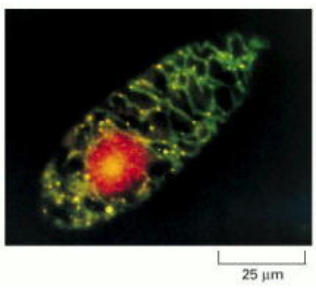

Figure 14-50. Mitochondrial and nuclear DNA stained with a fluorescent dye. This micrograph shows the distribution of the nuclear genome *(red)* and the multiple small mitochondrial genomes (bright *yellow* spots) in a *Euglena gracilis* cell. The DNA is stained with ethidium bromide, a fluorescent dye that emits red light. In addition, the mitochondrial matrix space is stained with a green fluorescent dye that reveals the mitochondria as a branched network extending throughout the cytosol. The superposition of the *green* matrix and the *red* DNA gives the mitochondrial genomes their *yellow* color. (Courtesy of Y. Hayashi and K. Ueda, *J. Cell Sci.* 93:565570, 1989. © The Company of Biologists.)

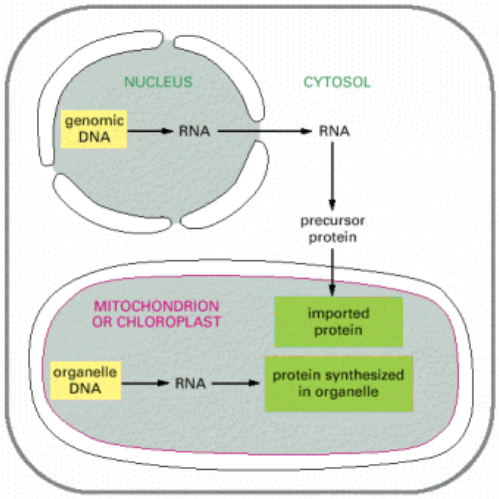

Figure 14-51. The production of mitochondrial and chloroplast proteins by two separate genetic systems. Most of the proteins in these organelles are encoded by the nucleus and must be imported from the cytosol.

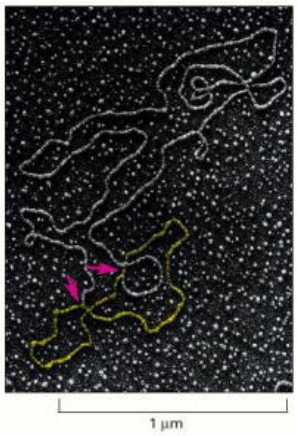

Figure 14-52. An electron micrograph of an animal mitochondrial DNA molecule caught during the process of DNA replication. The circular DNA genome has replicated only between the two points marked by *red* arrows. The newly synthesized DNA is colored *yellow*. (Courtesy of David A. Clayton.)

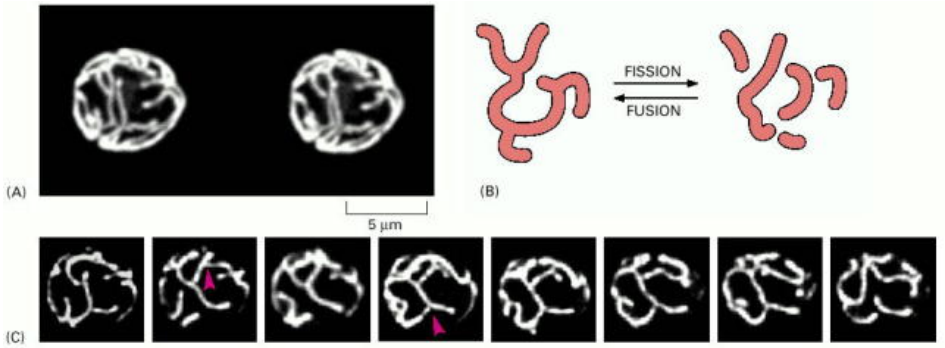

Figure 14-53. Dynamic mitochondrial reticulum. (A) In yeast cells, mitochondria form a continuous reticulum underlying the plasma membrane. (B) A balance between fission and fusion determines the arrangement of the mitochondria in different cells. (C) Time-lapse fluorescent microscopy shows the dynamic behavior of the mitochondrial network in a yeast cell. In addition to shape changes, the network is constantly remodeled by fission and fusion *(red arrows)*. The pictures were taken at 3-minute intervals. (A and C, from J. Nunnari et al., *Mol. Biol. Cell* 8:12331242, 1997, with permission by the American Society for Cell Biology.)

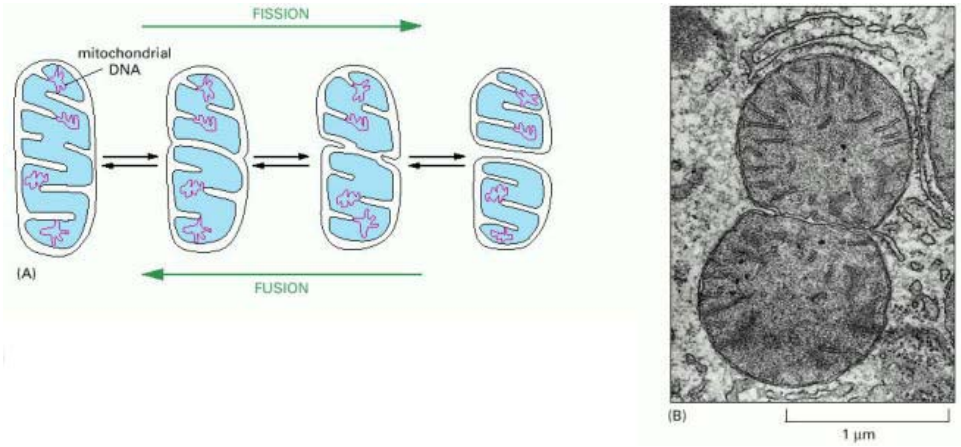

Figure 14-54. Mitochondrial fission and fusion. These processes involve both outer and inner mitochondrial membranes. (A) During fusion and fission, both matrix and intermembrane space compartments are maintained. Different membrane fusion machines are thought to operate at the outer and inner membranes. Conceptually, the fission process resembles that of bacterial cell division (discussed in Chapter 18). The pathway shown has been postulated from static views such as that shown in (B). (B) An electron micrograph of a dividing mitochondrion in a liver cell. (B, courtesy of Daniel S. Friend.)

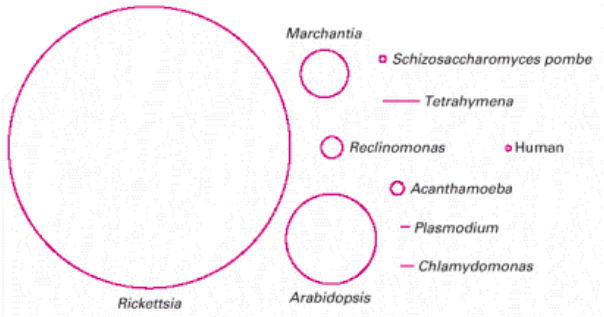

Figure 14-55. Various sizes of mitochondrial genomes. The complete DNA sequences for more than 200 mitochondrial genomes have been determined. The lengths of a few of these mitochondrial DNAs are shown to scale as *circles* for circular genomes and *lines* for linear genomes. The largest circle represents the genome of *Rickettsia prowazekii*, a small pathogenic bacterium whose genome most closely resembles that of mitochondria. The size of mitochondrial genomes does not correlate well with the number of proteins encoded in them: while human mitochondrial DNA encodes 13 proteins, the 22-fold larger mitochondrial DNA of *Arabidopsis* encodes only 32 proteins - that is, about 2.5-fold as many as human mitochondrial DNA. The extra DNA that is found in *Arabidopsis*, *Marchantia*, and other plant mitochondria may be "junk DNA". The mitochondrial DNA of the protozoan *Reclinomonas americana* has 97 genes, more than the mitochondrion of any other organism analyzed so far. (Adapted from M. W. Gray et al., *Science* 283:14761481, 1999.)

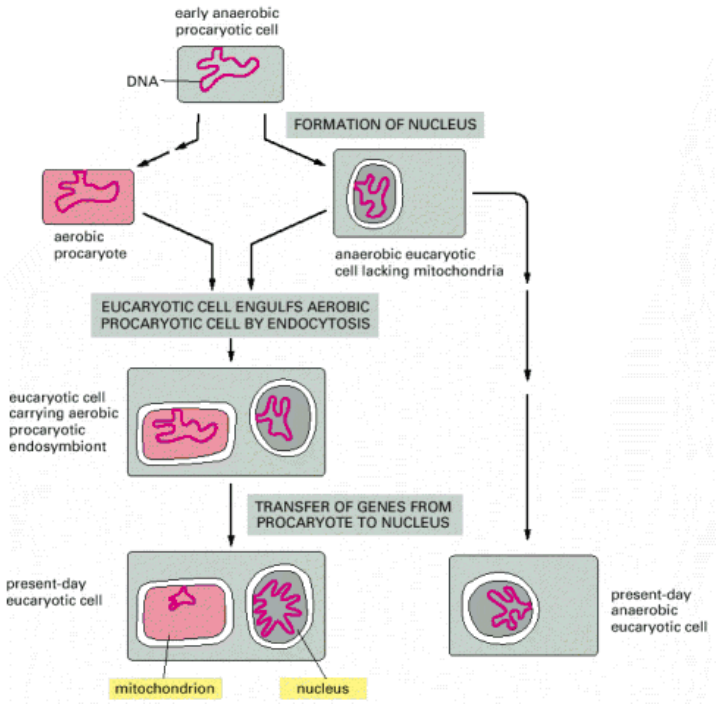

Figure 14-56. A suggested evolutionary pathway for the origin of mitochondria. *Microsporidia* and *Giardia* are two present-day anaerobic single-celled eucaryotes (protozoans) without mitochondria. Because they have an rRNA sequence that suggests a great deal of evolutionary distance from all other known eucaryotes, it has been postulated that their ancestors were also anaerobic and resembled the eucaryote that first engulfed the precursors of mitochondria.

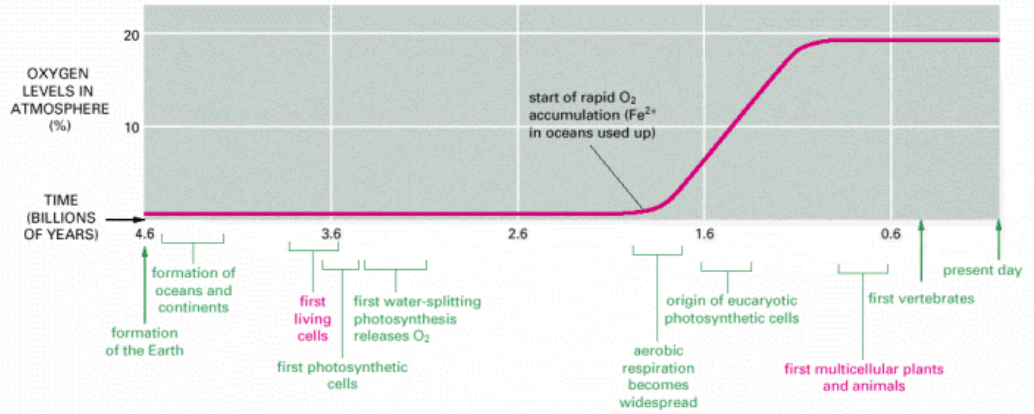

Figure 14-69. Some major events that are believed to have occurred during the evolution of living organisms on Earth. With the evolution of the membrane-based process of photosynthesis, organisms could make their own organic molecules from CO_2 gas. As explained in the text, the delay of more than 10^9 years between the appearance of bacteria that split water and released O_2 during photosynthesis and the accumulation of high levels of O_2 in the atmosphere is thought to be due to the initial reaction of the oxygen with abundant ferrous iron (Fe^{2+}) dissolved in the early oceans. Only when the iron was used up would oxygen have started to accumulate in the atmosphere. In response to the rising levels of oxygen in the atmosphere, nonphotosynthetic oxygen-using organisms appeared, and the concentration of oxygen in the atmosphere leveled out.

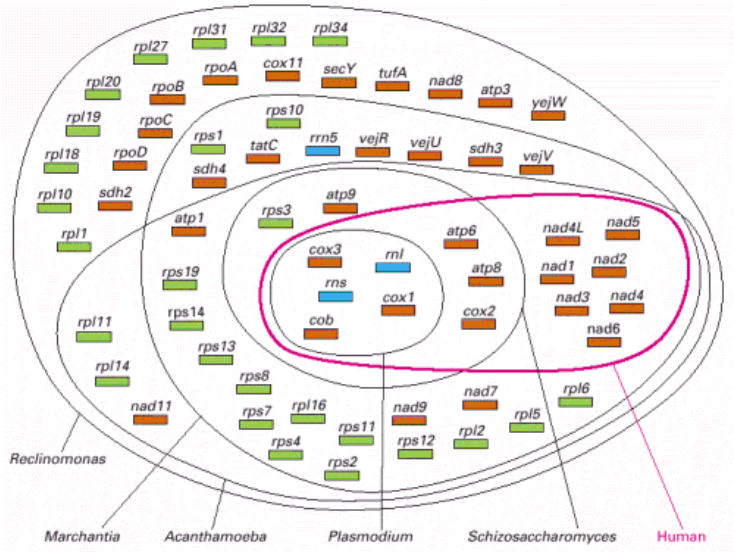

Figure 14-57. Comparison of mitochondrial genomes. Less complex mitochondrial genomes encode subsets of the proteins and ribosomal RNAs that are encoded by larger mitochondrial genomes. The five genes present in all known mitochondrial genomes encode ribosomal RNAs *(rns* and *rnl)*, cytochrome *b (cob)*, and two cytochrome oxidase subunits *(cox1* and *cox3)*. (Adapted from M.W. Gray et al., *Science* 283:14761481, 1999.)

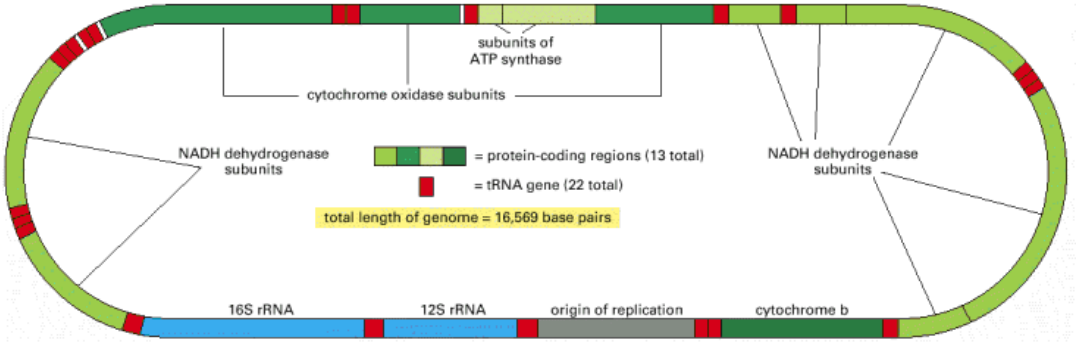

Figure 14-58. The organization of the human mitochondrial genome. The genome contains 2 rRNA genes, 22 tRNA genes, and 13 protein-coding sequences. The DNAs of many other animal mitochondrial genomes have also been completely sequenced. Most of these animal mitochondrial DNAs encode precisely the same genes as humans, with the gene order being identical for animals that range from mammals to fish.

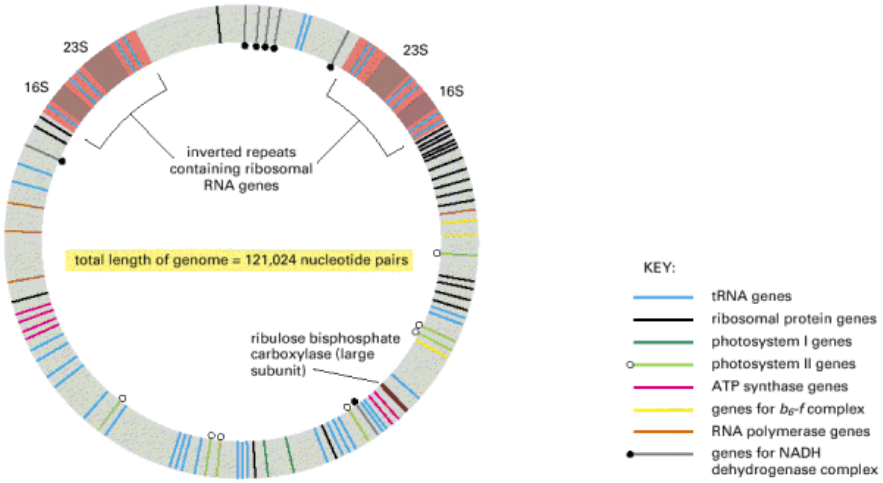

Figure 14-59. The organization of the liverwort chloroplast genome. The chloroplast genome organization is very similar in all higher plants, although the size varies from species to species - depending on how much of the DNA surrounding the genes encoding the chloroplast's 16S and 23S ribosomal RNAs is present in two copies.

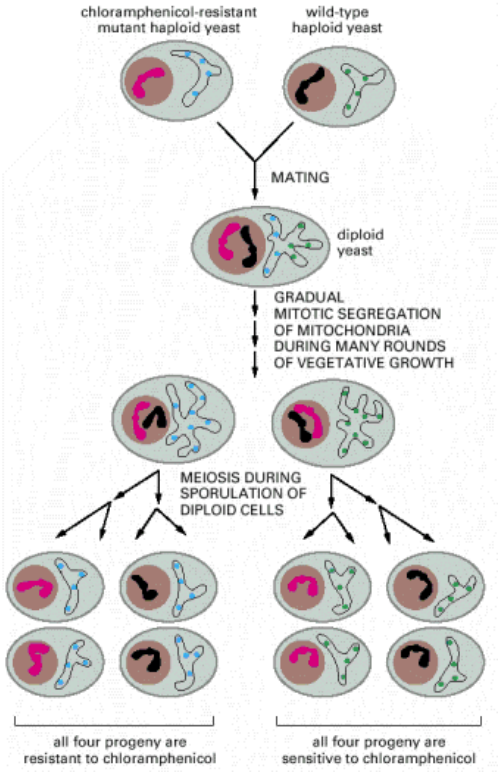

Figure 14-60. The difference in the patterns of inheritance between mitochondrial and nuclear genes of yeast cells. For nuclear genes (Mendelian inheritance), two of the four cells that result from meiosis inherit the gene from one of the original haploid parent cells, and the remaining two cells inherit the gene from the other. By contrast, for mitochondrial genes (non-Mendelian inheritance), it is possible for all four of the cells that result from meiosis to inherit their mitochondrial genes from only one of the two original haploid cells. In this example, the mitochondrial gene is one that, in its mutant form (mitochondrial DNA denoted by *blue dots)*, makes protein synthesis in the mitochondrion resistant to chloramphenicol - a protein synthesis inhibitor that acts specifically on the procaryotic-like ribosomes in mitochondria and chloroplasts. Yeast cells that contain the mutant gene can be detected by their ability to grow in the presence of chloramphenicol on a substrate, such as glycerol, that cannot be used for glycolysis. With glycolysis blocked, ATP must be provided by functional mitochondria, and therefore the cells that carry the normal (wild-type) mitochondrial DNA *(green dots)* cannot grow.

Figure 14-61. A variegated leaf. In the white patches, the plant cells have inherited a defective chloroplast. (Courtesy of John Innes Foundation.)

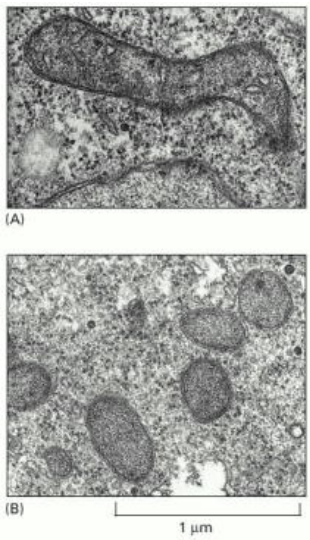

Figure 14-62. Electron micrographs of yeast cells. (A) The structure of normal mitochondria. (B) Mitochondria in a petite mutant. In petite mutants, all the mitochondrion-encoded gene products are missing, and the organelle is constructed entirely from nucleus-encoded proteins. (Courtesy of Barbara Stevens.)

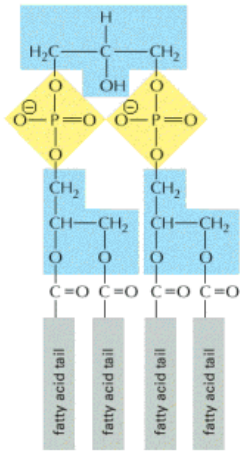

Figure 14-63. The structure of cardiolipin. Cardiolipin is an unusual lipid in the inner mitochondrial membrane.

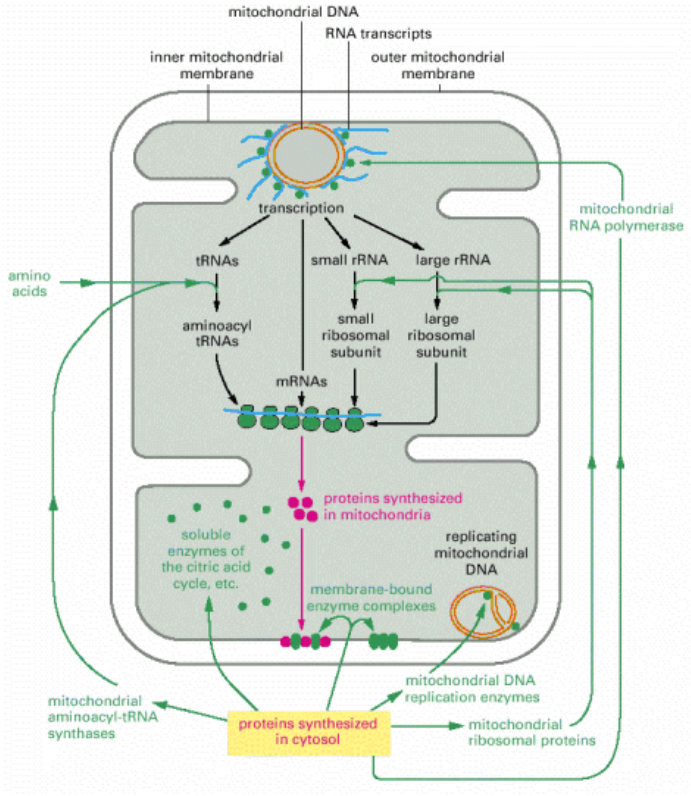

Figure 14-64. The origins of mitochondrial RNAs and proteins. The proteins encoded in the nucleus and imported from the cytosol have a major role in creating the genetic system of the mitochondrion, in addition to contributing most of the organelle's other proteins. Not indicated in this diagram are the additional nucleus-encoded proteins that regulate the expression of individual mitochondrial genes at posttranscriptional levels. The mitochondrion itself contributes only mRNAs, rRNAs, and tRNAs to its genetic system.

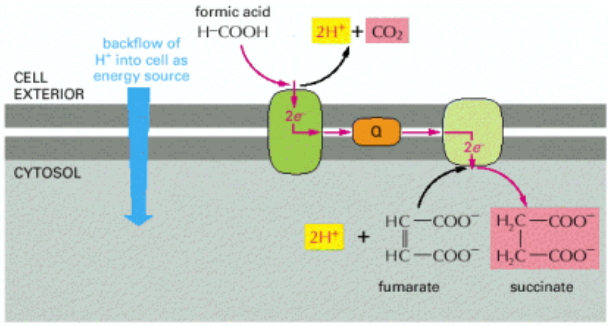

Figure 14-65. The oxidation of formic acid in some present-day bacteria. In such anaerobic bacteria, including *E. coli*, the oxidation is mediated by an energy-conserving electron-transport chain in the plasma membrane. As indicated, the starting materials are formic acid and fumarate, and the products are succinate and CO_2. Note that H^+ is consumed inside the cell and generated outside the cell, which is equivalent to pumping H^+ to the cell exterior. Thus, this membrane-bound electron-transport system can generate an electrochemical proton gradient across the plasma membrane. The redox potential of the formic acid-CO_2 pair is -420 mV, while that of the fumarate-succinate pair is +30 mV.

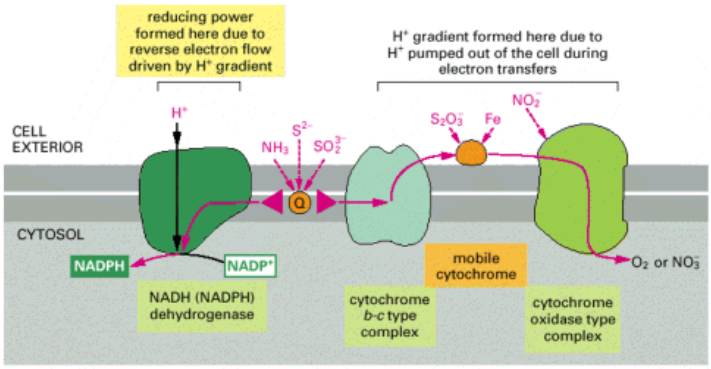

Figure 14-67. Some of the electron-transport pathways in present-day bacteria. These pathways generate all the cell's ATP and reducing power from the oxidation of inorganic molecules, such as iron, ammonia, nitrite, and sulfur compounds. As indicated, some species can grow anaerobically by substituting nitrate for oxygen as the terminal electron acceptor. Most use the carbon-fixation cycle and synthesize their organic molecules entirely from carbon dioxide. Both forward and reverse electron flows occur from the quinone (Q). As in the respiratory chain, the forward electron flows cause H^+ to be pumped out of the cell, and the resulting H^+ gradient drives the production of ATP by an ATP synthase (not shown). The NADPH required for carbon fixation is produced by an energy-requiring reverse electron flow; this flow is also driven by the H^+ gradient, as indicated.

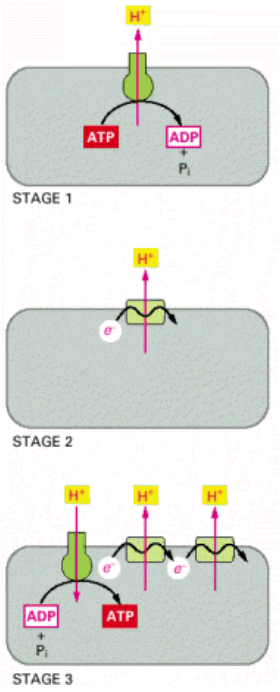

Figure 14-66. The evolution of oxidative phosphorylation mechanisms. One possible sequence is shown; the stages are described in the text.

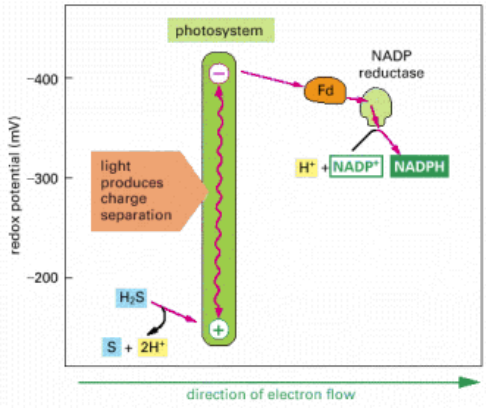

Figure 14-68. The general flow of electrons in a relatively primitive form of photosynthesis observed in present-day green sulfur bacteria. The photosystem in green sulfur bacteria resembles photosystem I in plants and cyanobacteria. Both photosystems use a series of iron-sulfur centers as the electron acceptors that eventually donate their high-energy electrons to ferredoxin (Fd). An example of a bacterium of this type is *Chlorobium tepidum*, which can thrive at high temperatures and low light intensities in hot springs.

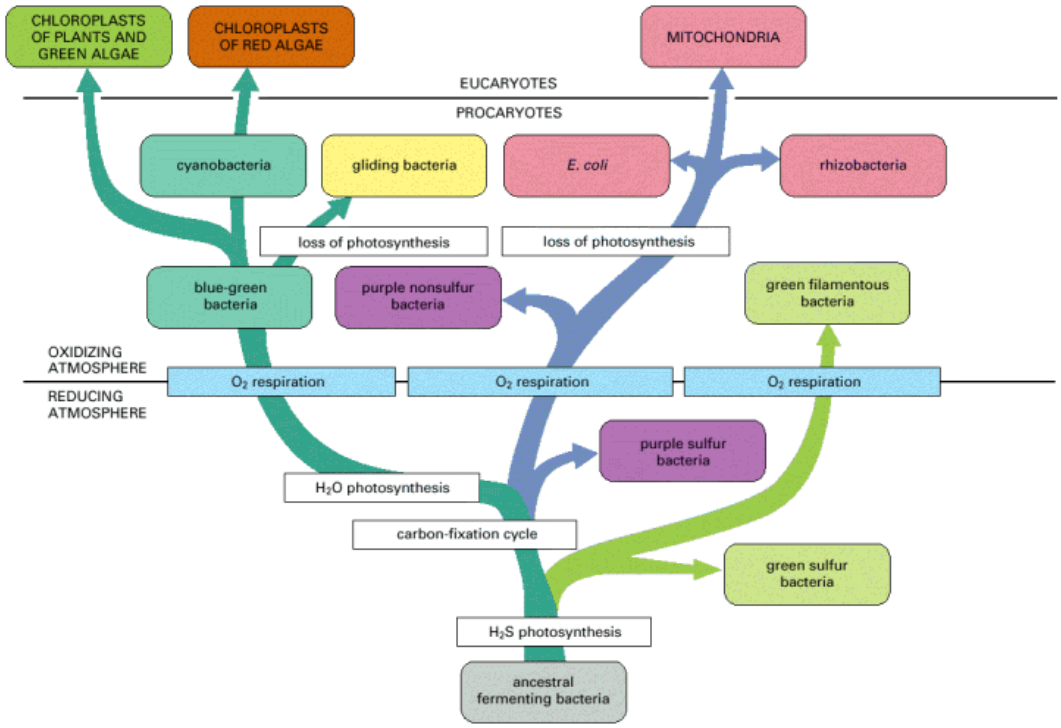

Figure 14-70. A phylogenetic tree of the proposed evolution of mitochondria and chloroplasts and their bacterial ancestors. Oxygen respiration is thought to have begun developing about 2×10^9 years ago. As indicated, it seems to have evolved independently in the green, purple, and blue-green (cyanobacterial) lines of photosynthetic bacteria. It is thought that an aerobic purple bacterium that had lost its ability to photosynthesize gave rise to the mitochondrion, while several different blue-green bacteria gave rise to chloroplasts. Nucleotide sequence analyses suggest that mitochondria arose from purple bacteria that resembled the rhizobacteria, agrobacteria, and rickettsias - three closely related species known to form intimate associations with present-day eucaryotic cells. Archea are not known to contain the type of photosystems described in this chapter, and they are not included here.

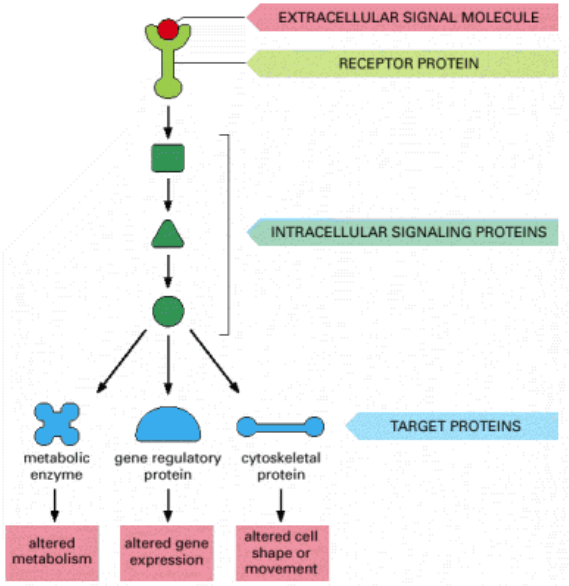

Figure 15-1. A simple intracellular signaling pathway activated by an extracellular signal molecule. The signal molecule binds to a receptor protein (which is usually embedded in the plasma membrane), thereby activating an intracellular signaling pathway that is mediated by a series of signaling proteins. Finally, one or more of these intracellular signaling proteins interacts with a target protein, altering the target protein so that it helps to change the behavior of the cell.

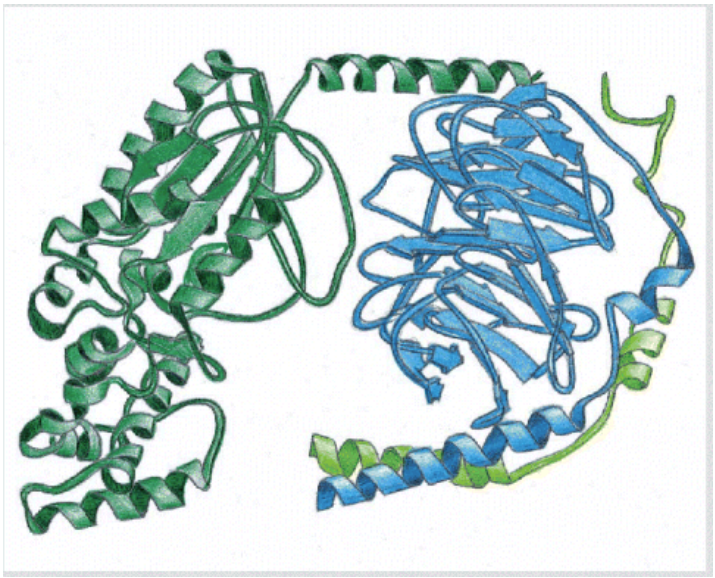

A trimeric GTP-binding protein, or G protein. This type of G protein functionally couples transmembrane receptors to either enzymes or ion channels in the plasma membrane. (Based on D.G. Lombright et al., *Nature* 379:311319, 1996.)

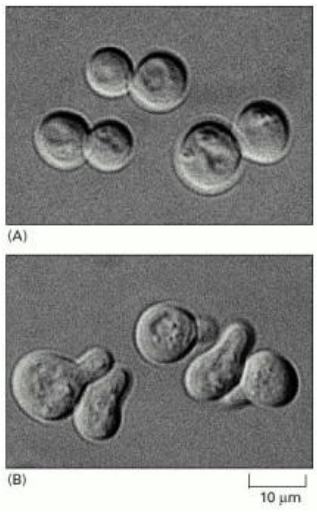

Figure 15-2. Budding yeast cells responding to mating factor. (A) The cells are normally spherical. (B) In response to mating factor secreted by neighboring yeast cells, they put out a protrusion toward the source of the factor in preparation for mating. (Courtesy of Michael Snyder.)

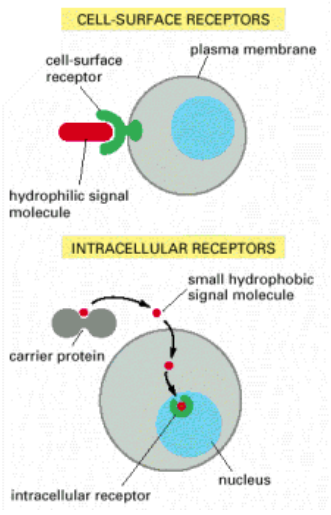

Figure 15-3. The binding of extracellular signal molecules to either cell-surface receptors or intracellular receptors. Most signal molecules are hydrophilic and are therefore unable to cross the plasma membrane directly; instead, they bind to cell-surface receptors, which in turn generate one or more signals inside the target cell. Some small signal molecules, by contrast, diffuse across the plasma membrane and bind to receptors inside the target cell - either in the cytosol or in the nucleus (as shown here). Many of these small signal molecules are hydrophobic and nearly insoluble in aqueous solutions; they are therefore transported in the bloodstream and other extracellular fluids after binding to carrier proteins, from which they dissociate before entering the target cell.

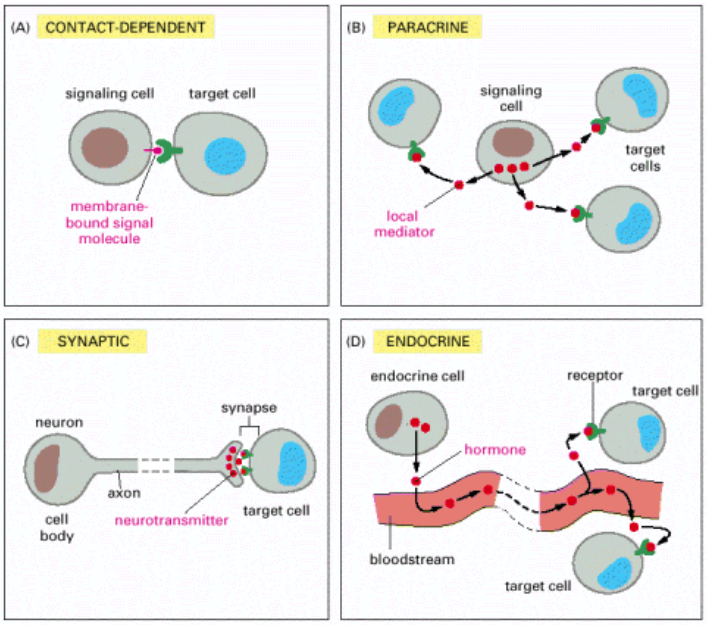

Figure 15-4. Forms of intercellular signaling. (A) Contact-dependent signaling requires cells to be in direct membrane-membrane contact. (B) Paracrine signaling depends on signals that are released into the extracellular space and act locally on neighboring cells. (C) Synaptic signaling is performed by neurons that transmit signals electrically along their axons and release neurotransmitters at synapses, which are often located far away from the cell body. (D) Endocrine signaling depends on endocrine cells, which secrete hormones into the bloodstream that are then distributed widely throughout the body. Many of the same types of signaling molecules are used in paracrine, synaptic, and endocrine signaling; the crucial differences lie in the speed and selectivity with which the signals are delivered to their targets.

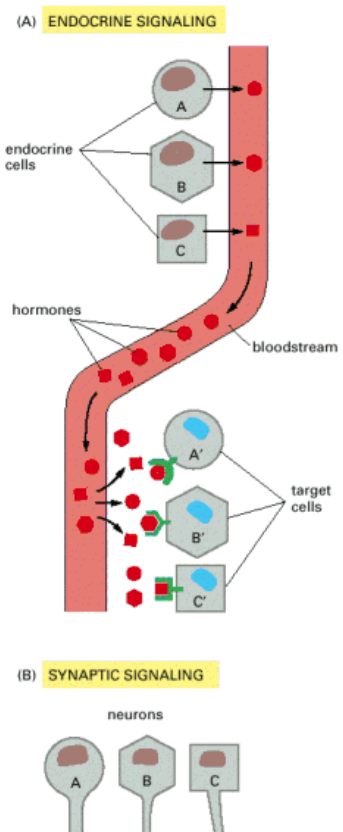

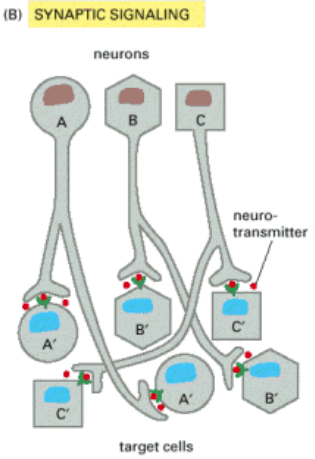

Figure 15-5. The contrast between endocrine and synaptic signaling. In complex animals, endocrine cells and nerve cells work together to coordinate the diverse activities of the billions of cells. Whereas different endocrine cells must use different hormones to communicate specifically with their target cells, different nerve cells can use the same neurotransmitter and still communicate in a highly specific manner. (A) Endocrine cells secrete hormones into the blood, which signal only the specific target cells that recognize them. These target cells have receptors for binding a specific hormone, which the cells "pull" from the extracellular fluid. (B) In synaptic signaling, by contrast, specificity arises from the synaptic contacts between a nerve cell and the specific target cells it signals. Usually, only a target cell that is in synaptic communication with a nerve cell is exposed to the neurotransmitter released from the nerve terminal (although some neurotransmitters act in a paracrine mode, serving as local mediators that influence multiple target cells in the area).

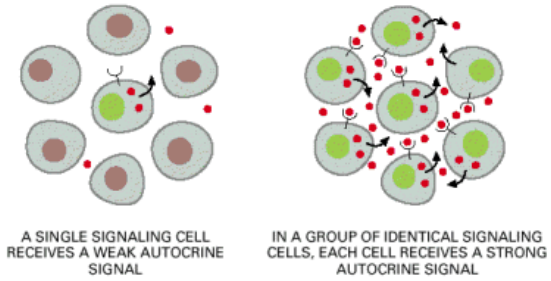

Figure 15-6. Autocrine signaling. A group of identical cells produces a higher concentration of a secreted signal than does a single cell. When this signal binds back to a receptor on the same cell type, it encourages the cells to respond coordinately as a group.

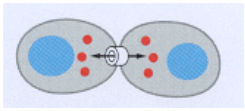

Figure 15-7. Signaling via gap junctions. Cells connected by gap junctions share small molecules, including small intracellular signaling molecules, and can therefore respond to extracellular signals in a coordinated way.

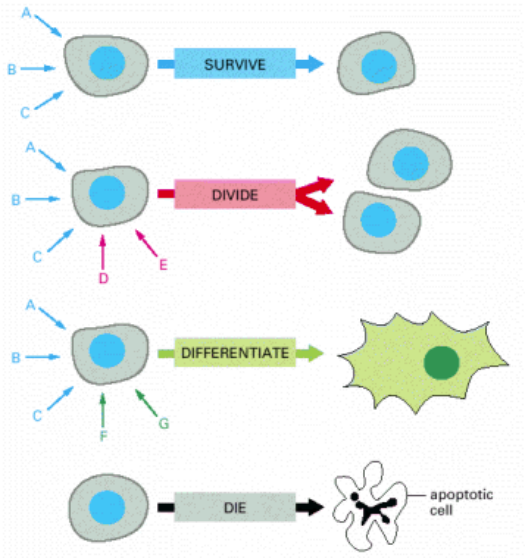

Figure 15-8. An animal cell's dependence on multiple extracellular signals. Each cell type displays a set of receptors that enables it to respond to a corresponding set of signal molecules produced by other cells. These signal molecules work in combinations to regulate the behavior of the cell. As shown here, an individual cell requires multiple signals to survive *(blue arrows)* and additional signals to divide *(red arrow)* or differentiate *(green arrows)*. If deprived of appropriate survival signals, a cell will undergo a form of cell suicide known as programmed cell death, or apoptosis.

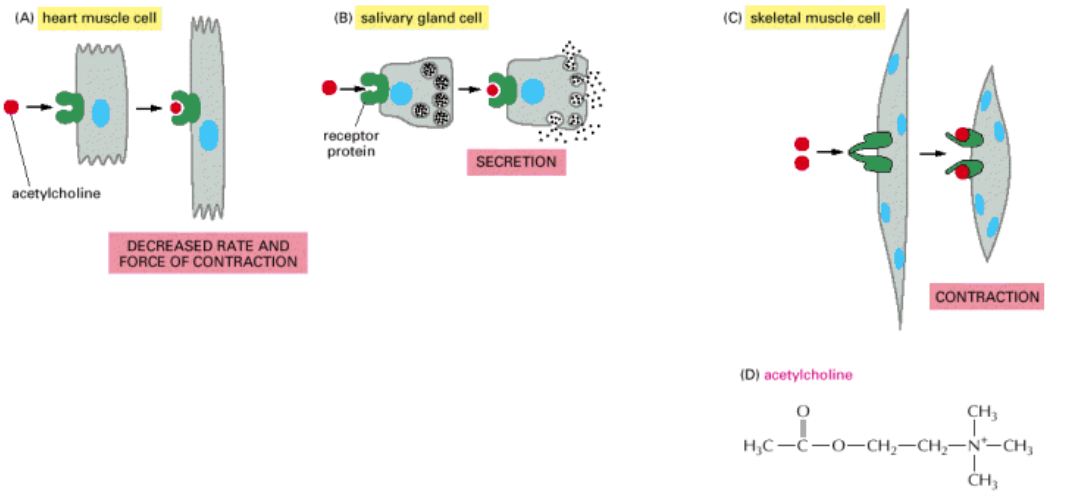

Figure 15-9. Various responses induced by the neurotransmitter acetylcholine. Different cell types are specialized to respond to acetylcholine in different ways. (A and B) For these two cell types, acetylcholine binds to similar receptor proteins, but the intracellular signals produced are interpreted differently in cells specialized for different functions. (C) This muscle cell produces a distinct type of receptor protein for acetylcholine, which generates different intracellular signals from the receptor shown in (A) and (B), and results in a different effect. (D) The chemical structure of acetylcholine.

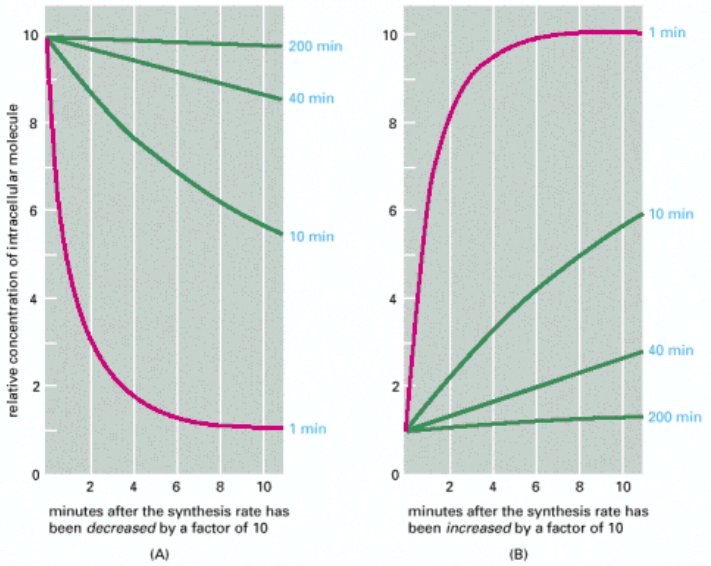

Figure 15-10. The importance of rapid turnover. The graphs show the predicted relative rates of change in the intracellular concentrations of molecules with differing turnover times when their synthesis rates are either (A) decreased or (B) increased suddenly by a factor of 10. In both cases, the concentrations of those molecules that are normally being rapidly degraded in the cell *(red lines)* change quickly, whereas the concentrations of those that are normally being slowly degraded *(green lines)* change proportionally more slowly. The numbers (in *blue)* on the right are the half-lives assumed for each of the different molecules.

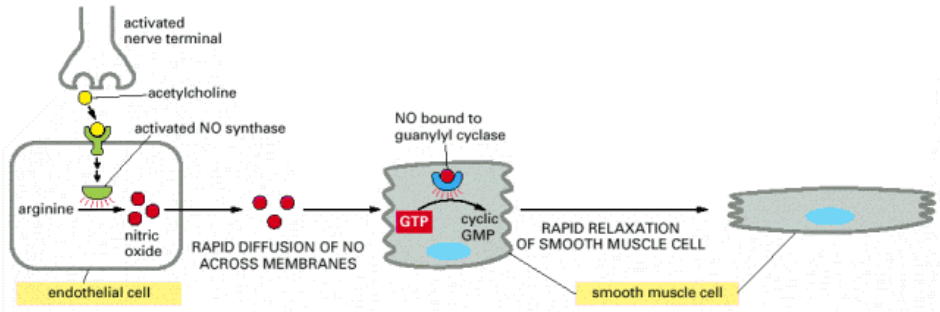

Figure 15-11. The role of nitric oxide (NO) in smooth muscle relaxation in a blood vessel wall. Acetylcholine released by nerve terminals in the blood vessel wall activates NO synthase in endothelial cells lining the blood vessel, causing the endothelial cells to produce NO. The NO diffuses out of the endothelial cells and into the underlying smooth muscle cells, where it binds to and activates guanylyl cyclase to produce cyclic GMP. The cyclic GMP triggers a response that causes the smooth muscle cells to relax, enhancing blood flow through the blood vessel.

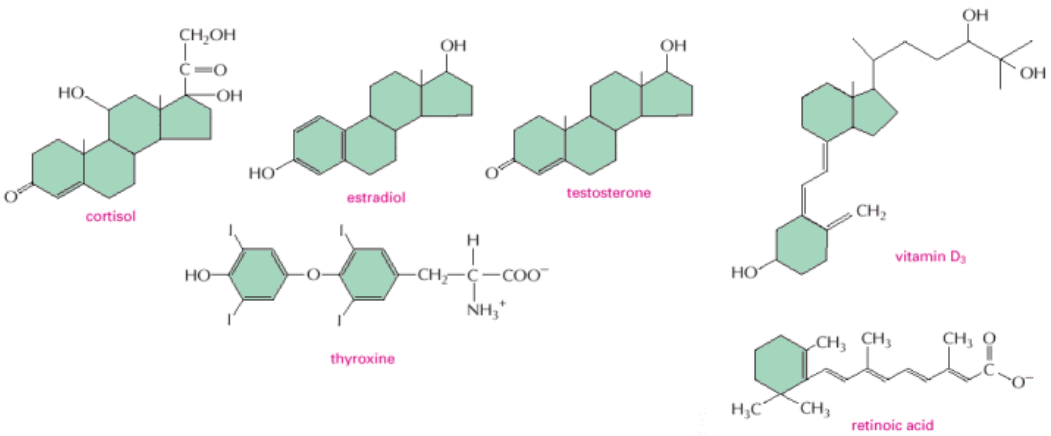

Figure 15-12. Some signaling molecules that bind to nuclear receptors. Note that all of them are small and hydrophobic. The active, hydroxylated form of vitamin D_3 is shown. Estradiol and testosterone are steroid sex hormones.

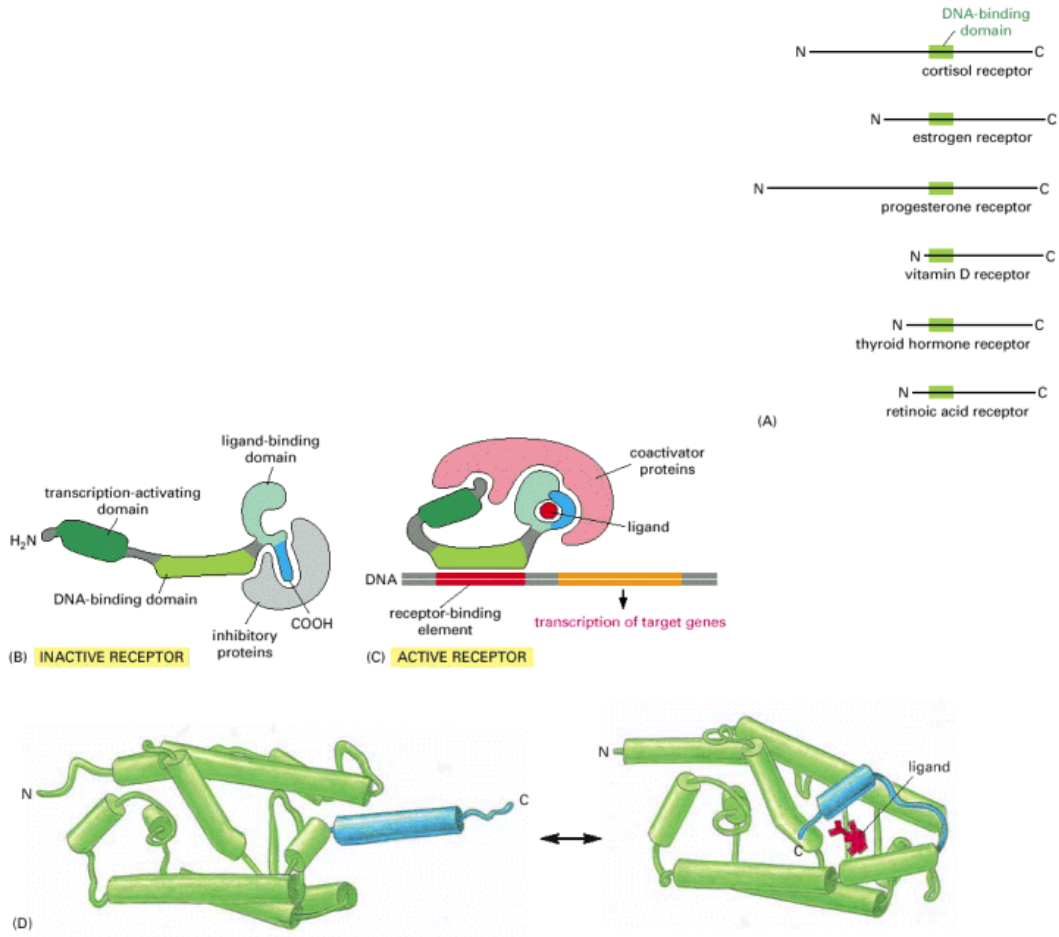

Figure 15-13. The nuclear receptor superfamily. All nuclear hormone receptors bind to DNA as either homodimers or heterodimers, but for simplicity we show them as monomers here. (A) The receptors all have a related structure. The short DNA-binding domain in each receptor is shown in *green.* (B) A receptor protein in its inactive state is bound to inhibitory proteins. Domain-swap experiments suggest that many of the ligand-binding, transcription-activating, and DNA-binding domains in these receptors can function as interchangeable modules. (C) The binding of ligand to the receptor causes the ligand-binding domain of the receptor to clamp shut around the ligand, the inhibitory proteins to dissociate, and coactivator proteins to bind to the receptor's transcription-activating domain, thereby increasing gene transcription. (D) The three-dimensional structure of a ligand-binding domain with *(right)* and without *(left)* ligand bound. Note that the *blue*α helix acts as a lid that snaps shut when the ligand (shown in *red)* binds, trapping the ligand in place.

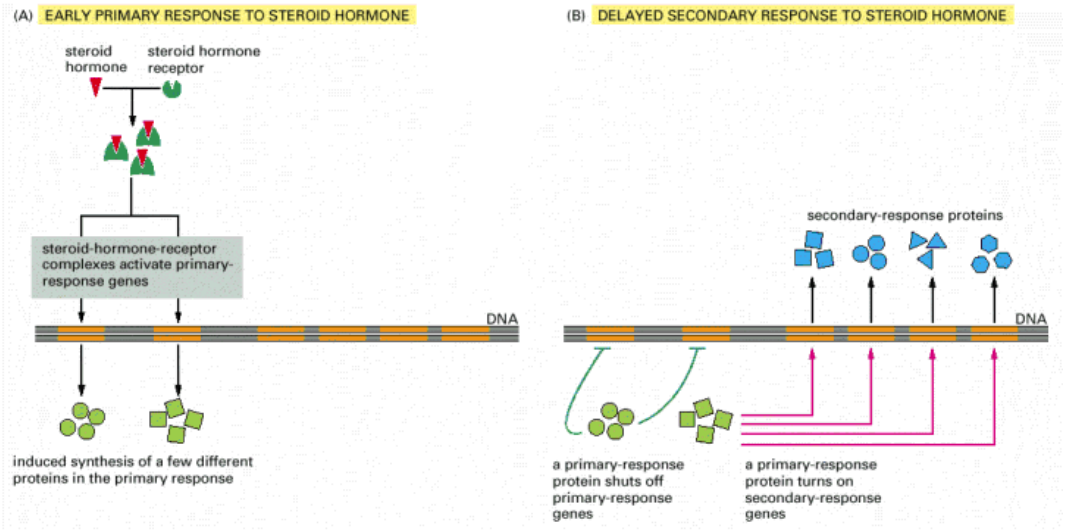

Figure 15-14. Responses induced by the activation of a nuclear hormone receptor. (A) Early primary response and (B) delayed secondary response. The figure shows the responses to a steroid hormone, but the same principles apply for all ligands that activate this family of receptor proteins. Some of the primary-response proteins turn on secondary-response genes, whereas others turn off the primary-response genes. The actual number of primary- and secondary-response genes is greater than shown. As expected, drugs that inhibit protein synthesis suppress the transcription of secondary-response genes but not primary-response genes, allowing these two classes of gene transcription responses to be readily distinguished.

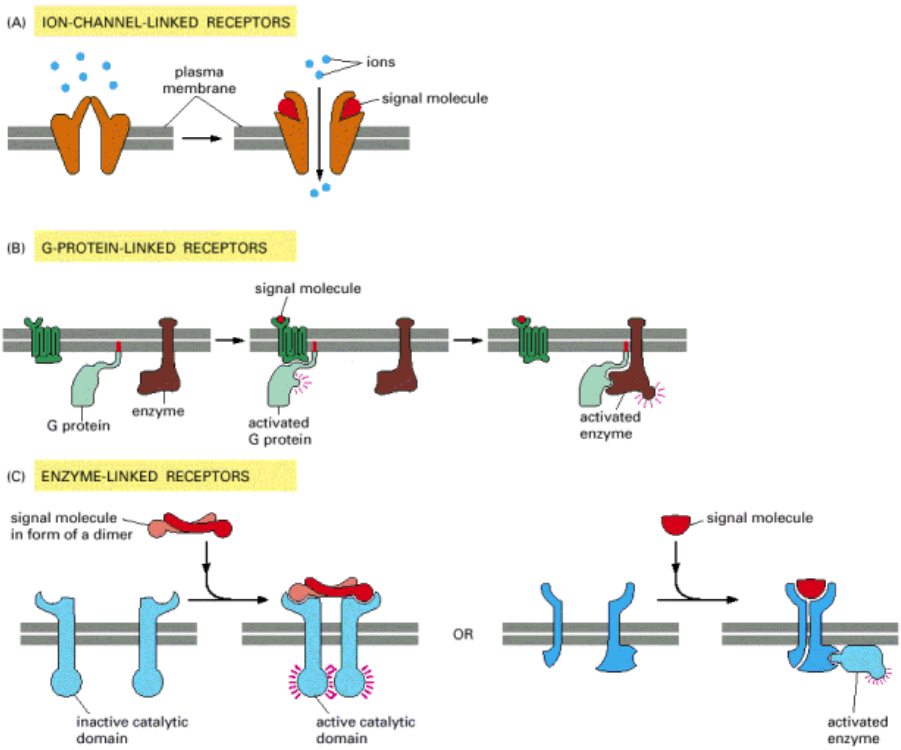

Figure 15-15. Three classes of cell-surface receptors. (A) Ion-channel-linked receptors, (B) G-protein-linked receptors, and (C) enzyme-linked receptors. Although many enzyme-linked receptors have intrinsic enzyme activity, as shown on the left, many others rely on associated enzymes, as shown on the right.

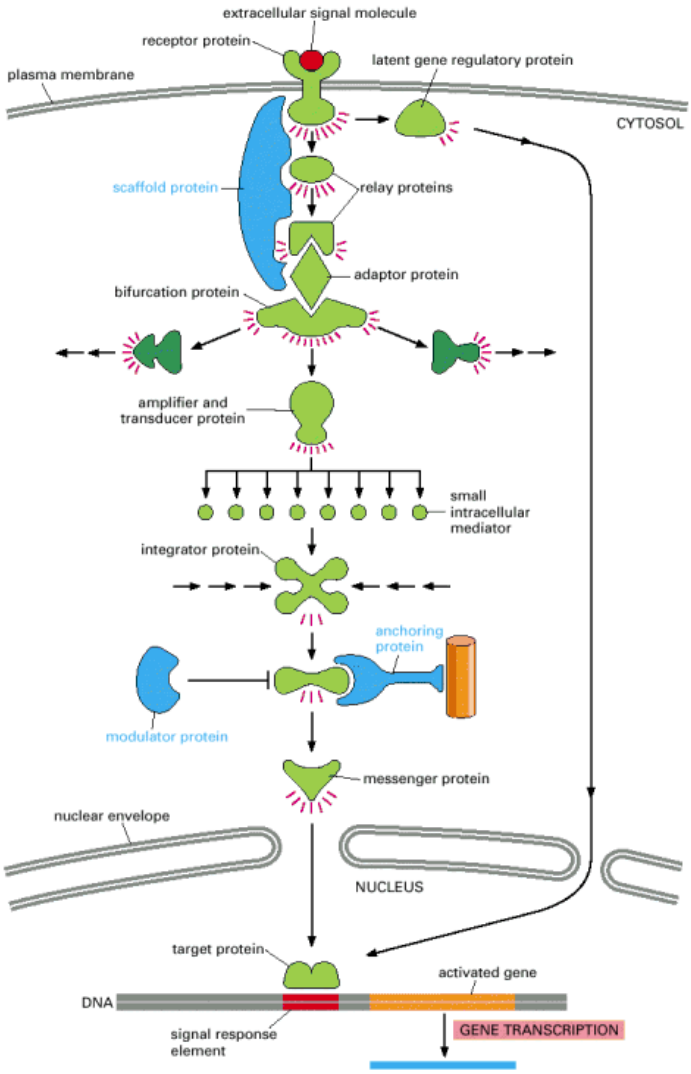

Figure 15-16. Different kinds of intracellular signaling proteins along a signaling pathway from a cell-surface receptor to the nucleus. In this example, a series of signaling proteins and small intracellular mediators relay the extracellular signal into the cell, causing a change in gene expression. The signal is amplified, altered (transduced), and distributed *en route.* Many of the steps can be modulated by other extracellular and intracellular signals, so that the final result of one signal depends on other factors affecting the cell (see Figure 15-8). Ultimately, the signaling pathway activates (or inactivates) target proteins that alter cell behavior. In this example, the target is a gene regulatory protein.

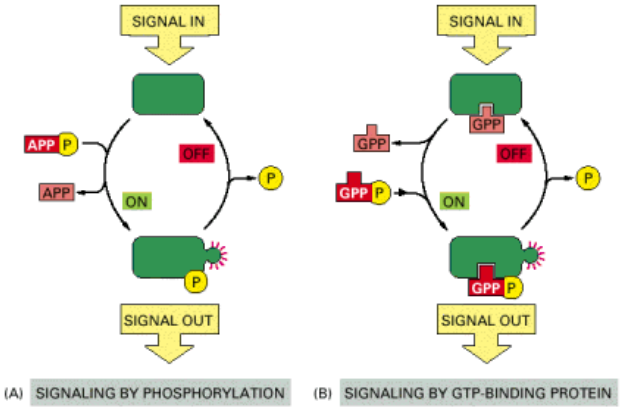

Figure 15-17. Two types of intracellular signaling proteins that act as molecular switches. In both cases, a signaling protein is activated by the addition of a phosphate group and inactivated by the removal of the phosphate. (A) The phosphate is added covalently to the signaling protein by a protein kinase. (B) A signaling protein is induced to exchange its bound GDP for GTP. To emphasize the similarity in the two mechanisms, ATP is shown as APPP, ADP as APP, GTP as GPPP, and GDP as GPP.

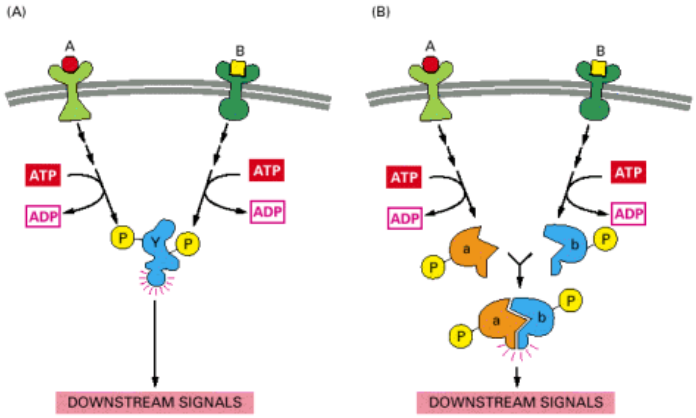

Figure 15-18. Signal integration. (A) Extracellular signals A and B both activate a different series of protein phosphorylations, each of which leads to the phosphorylation of protein Y but at different sites on the protein. Protein Y is activated only when both of these sites are phosphorylated, and therefore it becomes active only when signals A and B are simultaneously present. For this reason, integrator proteins are sometimes called coincidence detectors. (B) Extracellular signals A and B lead to the phosphorylation of two proteins, a and b, which then bind to each other to create the active protein. In both of the examples illustrated, the proteins themselves are phosphorylated. An equivalent form of control can also occur, however, by the exchange of GTP for GDP on GTP-binding proteins (see Figure 15-17).

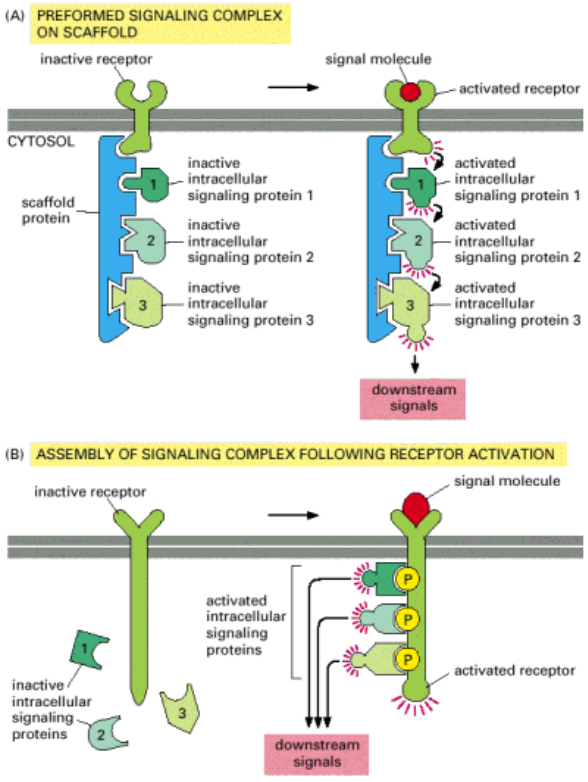

Figure 15-19. Two types of intracellular signaling complexes. (A) A receptor and some of the intracellular signaling proteins it activates in sequence are preassembled into a signaling complex by a large scaffold protein. (B) A large signaling complex is assembled after a receptor has been activated by the binding of an extracellular signal molecule; here the activated receptor phosphorylates itself at multiple sites, which then act as docking sites for intracellular signaling proteins.

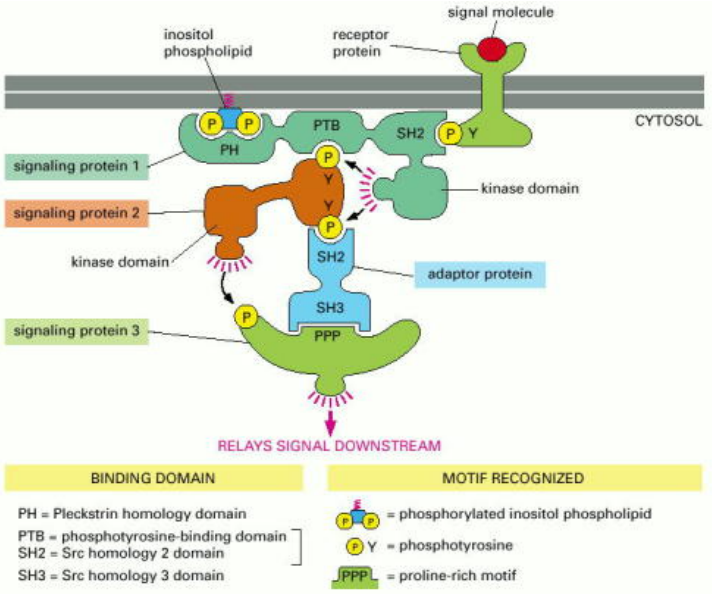

Figure 15-20. A hypothetical signaling pathway using modular binding domains. Signaling protein 1 contains three different binding domains, plus a catalytic protein kinase domain. It moves to the plasma membrane when extracellular signals lead to the creation of various phosphorylated docking sites on the cytosolic face of the membrane. Its SH2 domain binds to phosphorylated tyrosines on the receptor protein, and its PH domain binds to phosphorylated inositol phospholipids in the inner leaflet of the lipid bilayer. Protein 1 then phosphorylates signaling protein 2 on tyrosines, which allows protein 2 to bind to the PTB domain on protein 1 and to the SH2 domain on an adaptor protein. The adaptor protein then links protein 2 to protein 3, causing the phosphorylation of protein 3 by protein 2. The adaptor protein shown consists of two binding domains - an SH2 domain, which binds to a phosphotyrosine on protein 2, and an SH3 domain, which binds to a proline-rich motif on protein 3.

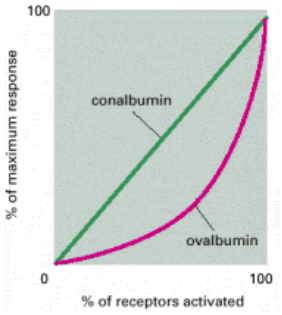

Figure 15-21. The primary response of chick oviduct cells to the steroid sex hormone estradiol. When activated, estradiol receptors turn on the transcription of several genes. Dose-response curves for two of these genes are shown, one coding for the egg protein conalbumin and the other coding for the egg protein ovalbumin. The linear response curve for conalbumin indicates that each activated receptor molecule that binds to the conalbumin gene increases the activity of the gene by the same amount. In contrast, the lag followed by the steep increase in the response curve for ovalbumin suggests that more than one activated receptor (in this case, two receptors) must bind simultaneously to the ovalbumin gene to initiate its transcription. (Adapted from E.R. Mulvihill and R.D. Palmiter, *J. Biol. Chem.* 252:20602068, 1977.)

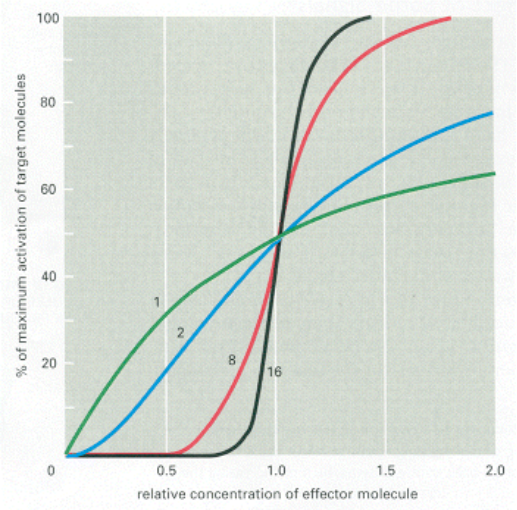

Figure 15-22. Activation curves as a function of signal-molecule concentration. The curves show how the sharpness of the response increases with an increase in the number of effector molecules that must bind simultaneously to activate a target macromolecule. The curves shown are those expected if the activation requires the simultaneous binding of 1, 2, 8, or 16 effector molecules.

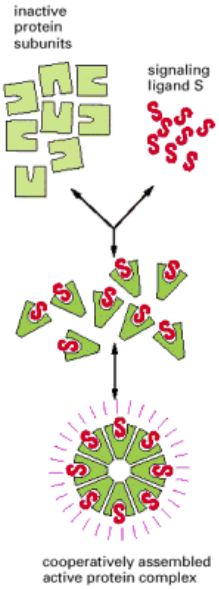

Figure 15-23. One type of signaling mechanism expected to show a steep thresholdlike response. Here, the simultaneous binding of eight molecules of a signaling ligand to a set of eight protein subunits is required to form an active protein complex. The ability of the subunits to assemble into the active complex depends on an allosteric conformational change that the subunits undergo when they bind their ligand. The binding of the ligand in the formation of such a complex is generally a cooperative process, causing a steep response as the ligand concentration is changed, as explained in Chapter 3. At low ligand concentrations, the number of active complexes increases roughly in proportion to the eighth power of the ligand concentration.

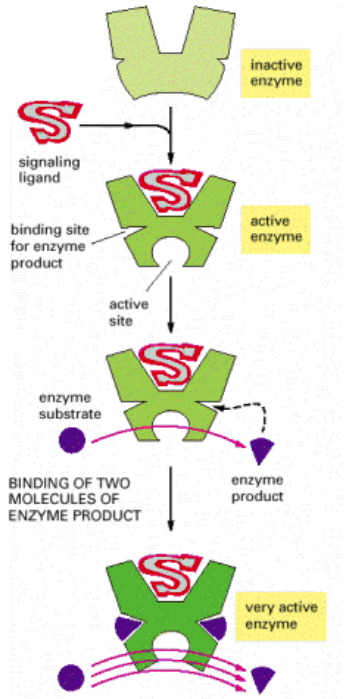

Figure 15-24. An accelerating positive feedback mechanism. In this example, the initial binding of the signaling ligand activates the enzyme to generate a product that binds back to the enzyme, further increasing the enzyme's activity.

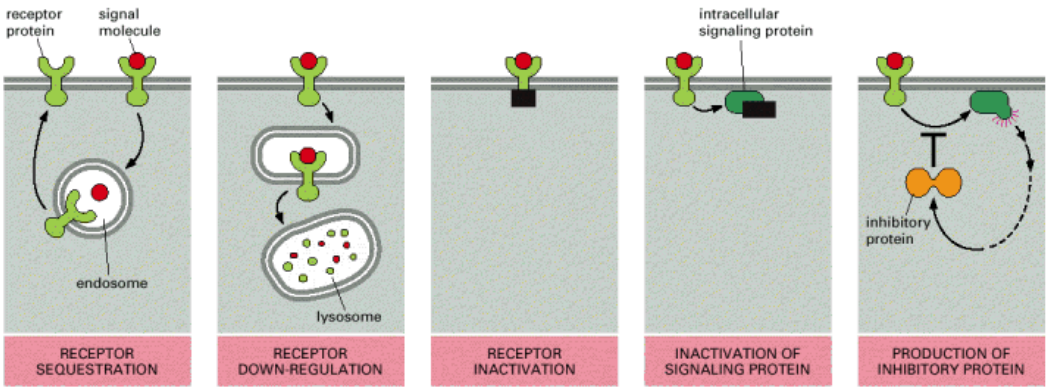

Figure 15-25. Five ways in which target cells can become desensitized to a signal molecule. The inactivation mechanisms shown here for both the receptor and the intracellular signaling protein often involve phosphorylation of the protein that is inactivated, although other types of modification are also known to occur. In bacterial chemotaxis, which we discuss later, desensitization depends on methylation of the receptor protein.

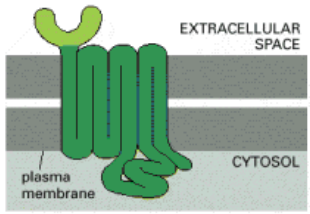

Figure 15-26. A G-protein-linked receptor. Receptors that bind protein ligands have a large extracellular domain formed by the part of the polypeptide chain shown in *light green.* This domain, together with some of the transmembrane segments, binds the protein ligand. Receptors for small ligands such as adrenaline have small extracellular domains, and the ligand usually binds deep within the plane of the membrane to a site that is formed by amino acids from several transmembrane segments.

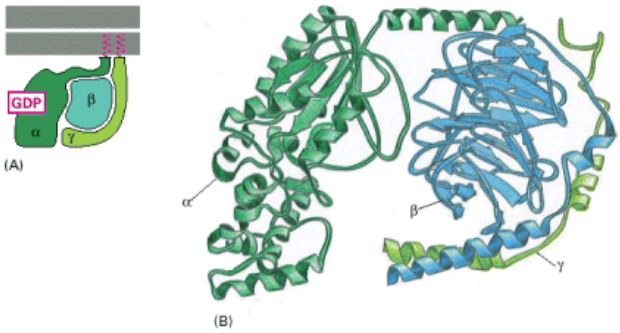

Figure 15-27. The structure of an inactive G protein. (A) Note that both the α and the γ subunits have covalently attached lipid molecules *(red)* that help to bind them to the plasma membrane, and the α subunit has GDP bound. (B) The three-dimensional structure of an inactive G protein, based on transducin, the G protein in visual transduction (discussed later). The α subunit contains the GTPase domain and binds to one side of the β subunit, which locks the GTPase domain in an inactive conformation that binds GDP. The γ subunit binds to the opposite side of the β subunit. (B, based on D.G. Lombright et al., *Nature* 379:311319, 1996.)

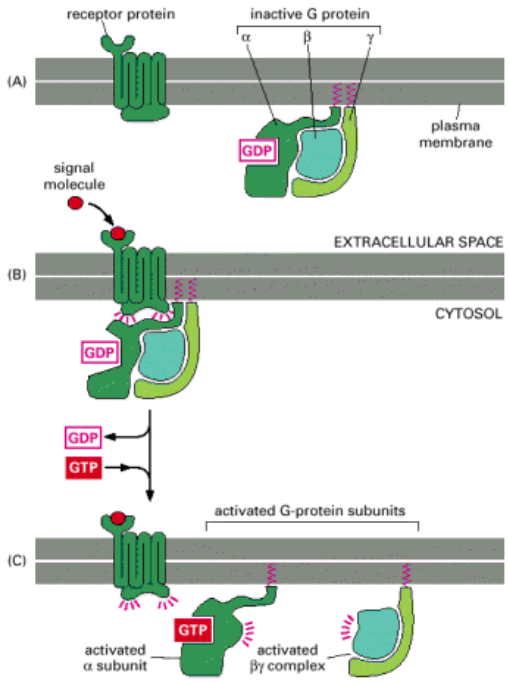

Figure 15-28. The disassembly of an activated G-protein into two signaling components. (A) In the unstimulated state, the receptor and the G protein are both inactive. Although they are shown here as separate entities in the plasma membrane, in some cases, at least, they are associated in a preformed complex. (B) Binding of an extracellular signal to the receptor changes the conformation of the receptor, which in turn alters the conformation of the G protein that is bound to the receptor. (C) The alteration of the α subunit of the G protein allows it to exchange its GDP for GTP. This causes the G protein to break up into two active components - an α subunit and a βγ complex, both of which can regulate the activity of target proteins in the plasma membrane. The receptor stays active while the external signal molecule is bound to it, and it can therefore catalyze the activation of many molecules of G protein.

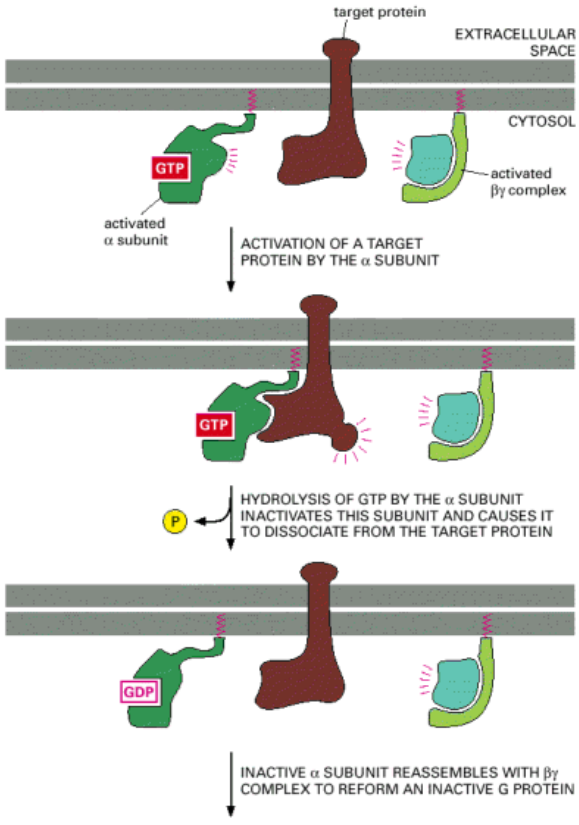

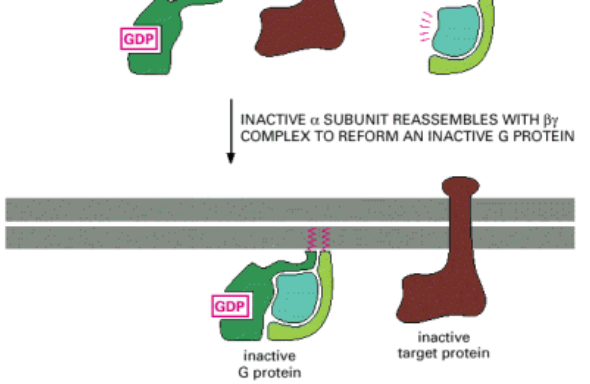

Figure 15-29. The switching off of the G-protein α subunit by the hydrolysis of its bound GTP. After a G-protein α subunit activates its target protein, it shuts itself off by hydrolyzing its bound GTP to GDP. This inactivates the α subunit, which dissociates from the target protein and reassociates with a βγ complex to re-form an inactive G protein. Binding to the target protein or to a membrane-bound RGS protein (not shown) usually stimulates the GTPase activity of the α subunit; this stimulation greatly speeds up the inactivation process shown here.

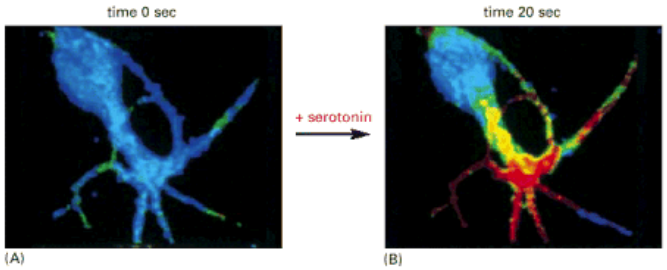

Figure 15-30. An increase in cyclic AMP in response to an extracellular signal. This nerve cell in culture is responding to the neurotransmitter serotonin, which acts through a G-protein-linked receptor to cause a rapid rise in the intracellular concentration of cyclic AMP. To monitor the cyclic AMP level, the cell has been loaded with a fluorescent protein that changes its fluorescence when it binds cyclic AMP. *Blue* indicates a low level of cyclic AMP, *yellow* an intermediate level, and *red* a high level. (A) In the resting cell, the cyclic AMP level is about 5×10^{-8} M. (B) Twenty seconds after the addition of serotonin to the culture medium, the intracellular level of cyclic AMP has increased to more than 10^{-6} M, an increase of more than twentyfold. (From Brian J. Bacskai et al., *Science* 260:222226, 1993. © AAAS.)

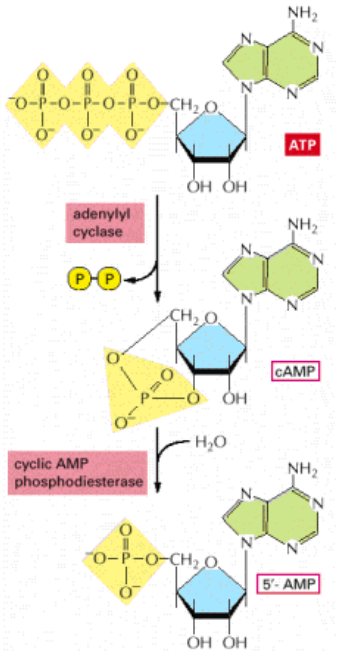

Figure 15-31. The synthesis and degradation of cyclic AMP. In a reaction catalyzed by the enzyme adenylyl cyclase, cyclic AMP (cAMP) is synthesized from ATP through a cyclization reaction that removes two phosphate groups as pyrophosphate (-); a pyrophosphatase drives this synthesis by hydrolyzing the released pyrophosphate to phosphate (not shown). Cyclic AMP is unstable in the cell, because it is itself hydrolyzed by a specific phosphodiesterase to form 5-AMP, as indicated.

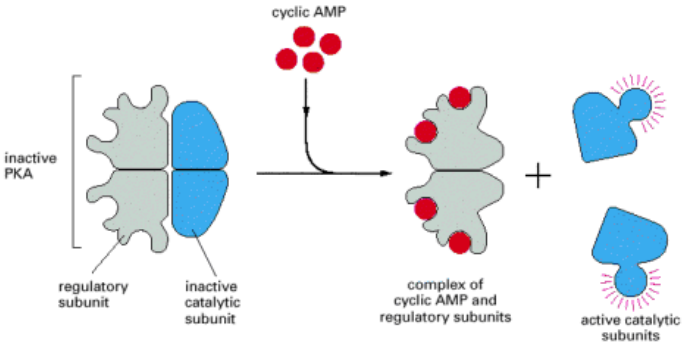

Figure 15-32. The activation of cyclic-AMP-dependent protein kinase (PKA). The binding of cyclic AMP to the regulatory subunits induces a conformational change, causing these subunits to dissociate from the catalytic subunits, thereby activating the kinase activity of the catalytic subunits. The release of the catalytic subunits requires the binding of more than two cyclic AMP molecules to the regulatory subunits in the tetramer. This requirement greatly sharpens the response of the kinase to changes in cyclic AMP concentration, as discussed earlier. Mammalian cells have at least two types of PKAs: type I is mainly in the cytosol, whereas type II is bound via its regulatory subunit and special anchoring proteins to the plasma membrane, nuclear membrane, mitochondrial outer membrane, and microtubules. In all cases, however, once the catalytic subunits are freed and active, they can migrate into the nucleus (where they can phosphorylate gene regulatory proteins), while the regulatory subunits remain in the cytoplasm. The three-dimensional structure of the protein kinase domain of the PKA catalytic subunit is shown in Figure 3-64.

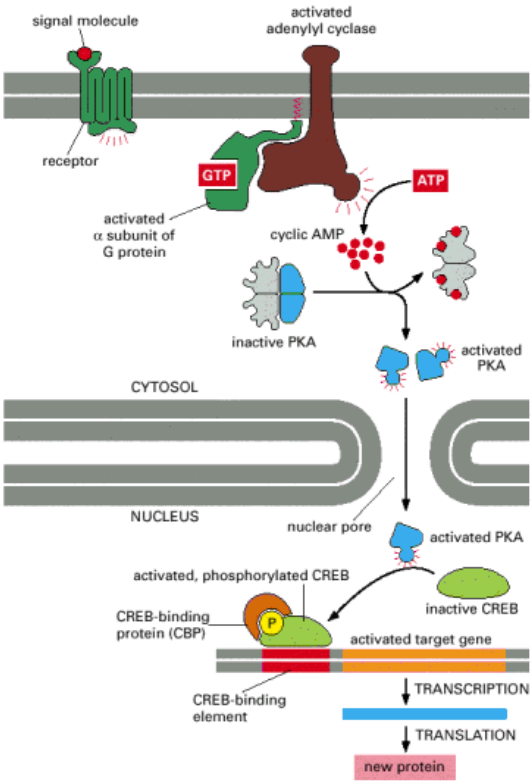

Figure 15-33. How gene transcription is activated by a rise in cyclic AMP concentration. The binding of an extracellular signal molecule to its G-protein-linked receptor leads to the activation of adenylyl cyclase and a rise in cyclic AMP concentration. The increase in cyclic AMP concentration activates PKA in the cytosol, and the released catalytic subunits then move into the nucleus, where they phosphorylate the CREB gene regulatory protein. Once phosphorylated, CREB recruits the coactivator CBP, which stimulates gene transcription. This signaling pathway controls many processes in cells, ranging from hormone synthesis in endocrine cells to the production of proteins required for long-term memory in the brain. We shall see later that some kinases that are activated by a rise in intracellular Ca^{2+} can also phosphorylate and thereby activate CREB.

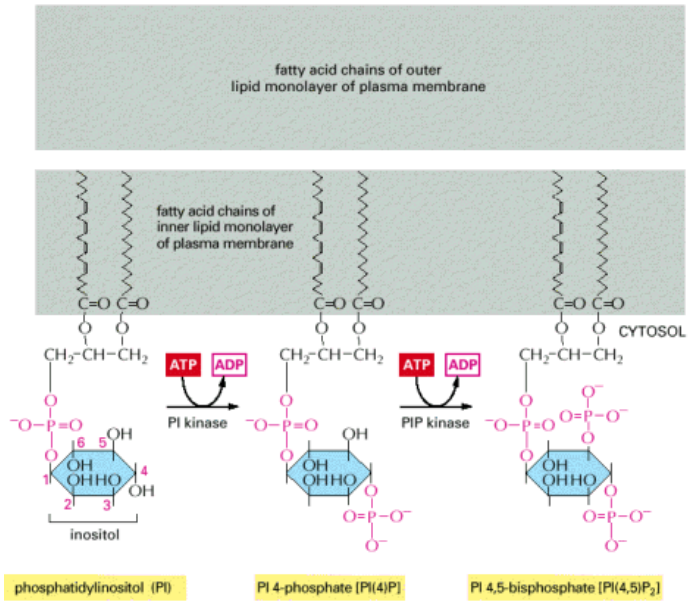

Figure 15-34. Three types of inositol phospholipids (phosphoinositides). The polyphosphoinositides - PI(4)P and $PI(4,5)P_2$ - are produced by the phosphorylation of phosphatidylinositol (PI) and PI(4)P, respectively. Although all three inositol phospholipids may be broken down in a signaling response, it is the breakdown of $PI(4,5)P_2$ that is most critical because it generates two intracellular mediators, as shown in the next two figures. Nevertheless, $PI(4,5)P_2$ is the least abundant, constituting less than 10% of the total inositol lipids and less than 1% of the total phospholipids in a cell. The conventional numbering of the carbon atoms in the inositol ring is shown in *red numbers* on the PI molecule.

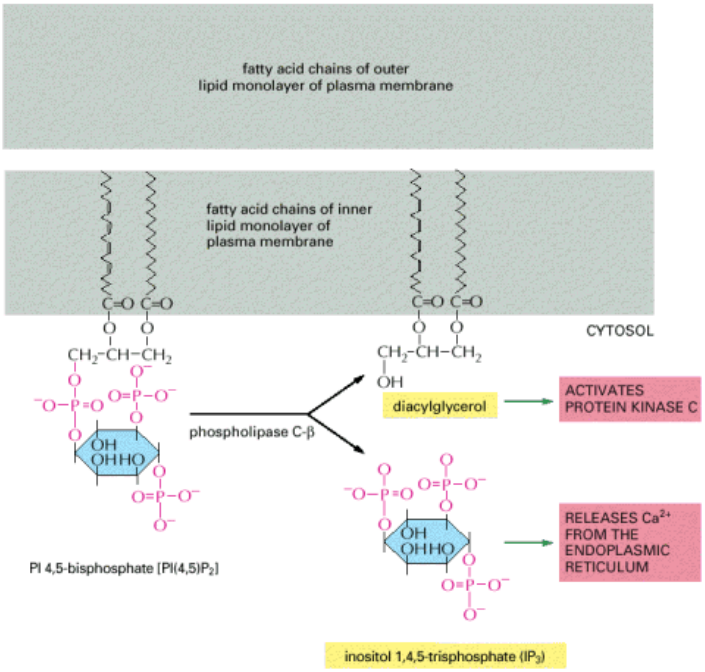

Figure 15-35. The hydrolysis of PI(4,5)P_2 by phospholipase C-β. Two intracellular mediators are produced when PI(4,5)P_2 is hydrolyzed: inositol 1,4,5-trisphosphate (IP_3), which diffuses through the cytosol and releases Ca^{2+} from the ER, and diacylglycerol, which remains in the membrane and helps to activate the enzyme protein kinase C (see Figure 15-36). There are at least three classes of phospholipase C - β, γ, and σ - and it is the β class that is activated by G-protein-linked receptors. We shall see later that the γ class is activated by a second class of receptors, called receptor tyrosine kinases, that activate the inositol phospholipid signaling pathway without an intermediary G protein.

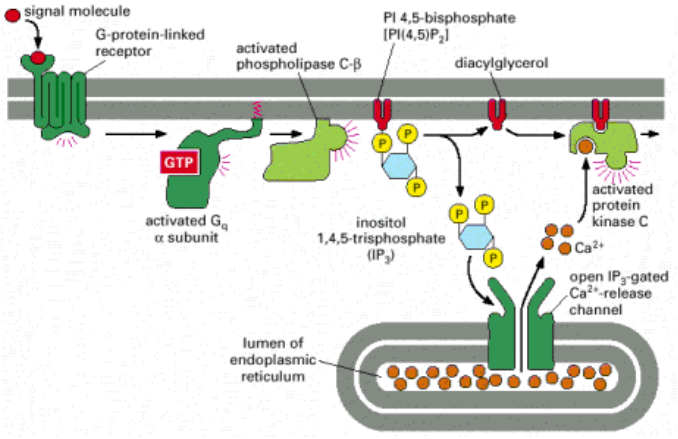

Figure 15-36. The two branches of the inositol phospholipid pathway. The activated receptor stimulates the plasma-membrane-bound enzyme phospholipase C-β via a G protein. Depending on the isoform of the enzyme, it may be activated by the α subunit of G_q as shown, by the βγ complex of another G protein, or by both. Two intracellular messenger molecules are produced when PI(4,5)P_2 is hydrolyzed by the activated phospholipase C-β. Inositol 1,4,5-trisphosphate (IP_3) diffuses through the cytosol and releases Ca^{2+} from the endoplasmic reticulum by binding to and opening IP_3-gated Ca^{2+}-release channels in the endoplasmic reticulum membrane. The large electrochemical gradient for Ca^{2+} across this membrane causes Ca^{2+} to escape into the cytosol. Diacylglycerol remains in the plasma membrane and, together with phosphatidylserine (not shown) and Ca^{2+}, helps to activate the enzyme protein kinase C, which is recruited from the cytosol to the cytosolic face of the plasma membrane. Of the 11 or more distinct isoforms of PKC in mammals, at least four are activated by diacylglycerol.

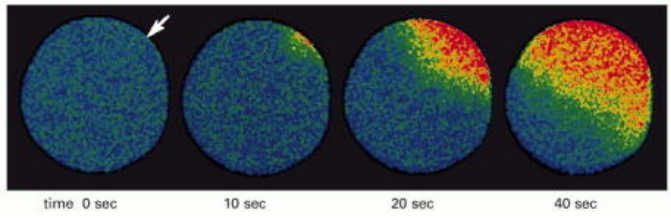

Figure 15-37. Fertilization of an egg by a sperm triggering an increase in cytosolic Ca^{2+}. This starfish egg was injected with a Ca^{2+}-sensitive fluorescent dye before it was fertilized. A wave of cytosolic Ca^{2+} *(red)*, released from the endoplasmic reticulum, is seen to sweep across the egg from the site of sperm entry *(arrow)*. This Ca^{2+} wave provokes a change in the egg cell surface, preventing the entry of other sperm, and it also initiates embryonic development (discussed in Chapter 20). (Courtesy of Stephen A. Stricker.)

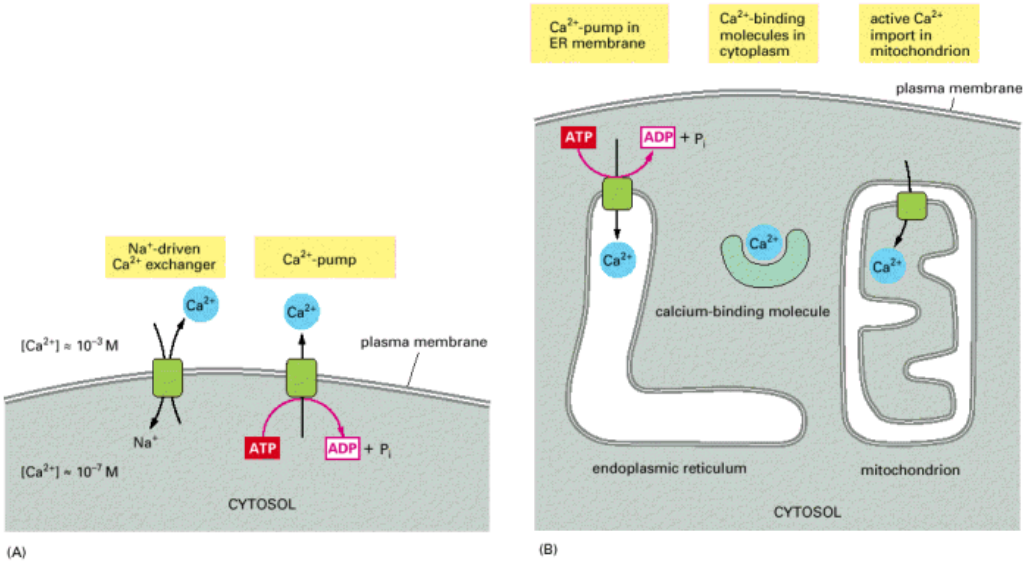

Figure 15-38. The main ways eucaryotic cells maintain a very low concentration of free Ca^{2+} in their cytosol. (A) Ca^{2+} is actively pumped out of the cytosol to the cell exterior. (B) Ca^{2+} is pumped into the ER and mitochondria, and various molecules in the cell bind free Ca^{2+} tightly.

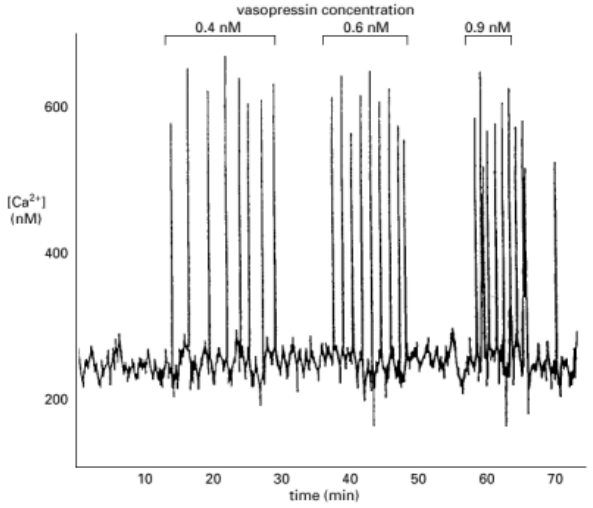

Figure 15-39. Vasopressin-induced Ca^{2+} oscillations in a liver cell. The cell was loaded with the Ca^{2+}-sensitive protein aequorin and then exposed to increasing concentrations of vasopressin. Note that the frequency of the Ca^{2+} spikes increases with an increasing concentration of vasopressin, but that the amplitude of the spikes is not affected. (Adapted from N.M. Woods, K.S.R. Cuthbertson, and P.H. Cobbold, *Nature* 319:600602, 1986.)

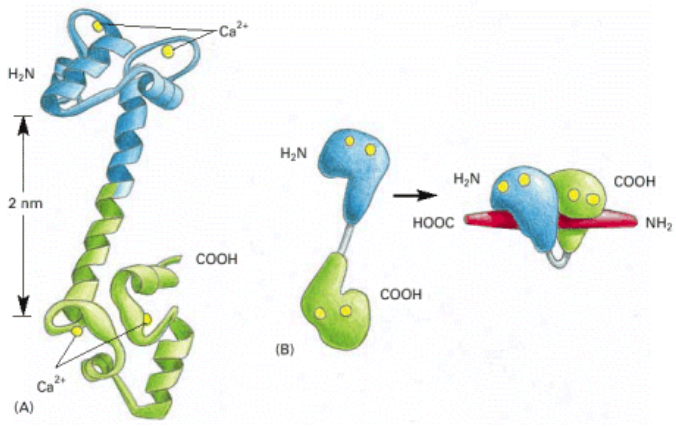

Figure 15-40. The structure of Ca^{2+}/calmodulin based on x-ray diffraction and NMR studies. (A) The molecule has a "dumbbell" shape, with two globular ends connected by a long, exposed α helix. Each end has two Ca^{2+}-binding domains, each with a loop of 12 amino acids, in which aspartic acid and glutamic acid side chains form ionic bonds with Ca^{2+}. The two Ca^{2+}-binding sites in the carboxyl-terminal part of the molecule have a tenfold higher affinity for Ca^{2+} than the two in the amino-terminal part. In solution, the molecule is flexible, displaying a range of forms, from extended (as shown) to more compact. (B) The major structural change in Ca^{2+}/calmodulin that occurs when it binds to a target protein (in this example, a peptide that consists of the Ca^{2+}/calmodulin-binding domain of a Ca^{2+}/calmodulin-dependent protein kinase). Note that the Ca^{2+}/calmodulin has "jack-knifed" to surround the peptide. (A, based on x-ray crystallographic data from Y.S. Babu et al., *Nature* 315:3740, 1985; B, based on x-ray crystallographic data from W.E. Meador, A.R. Means, and F.A. Quiocho, *Science* 257:12511255, 1992, and on NMR data from M. Ikura et al., *Science* 256:632638, 1992. © AAAS.)

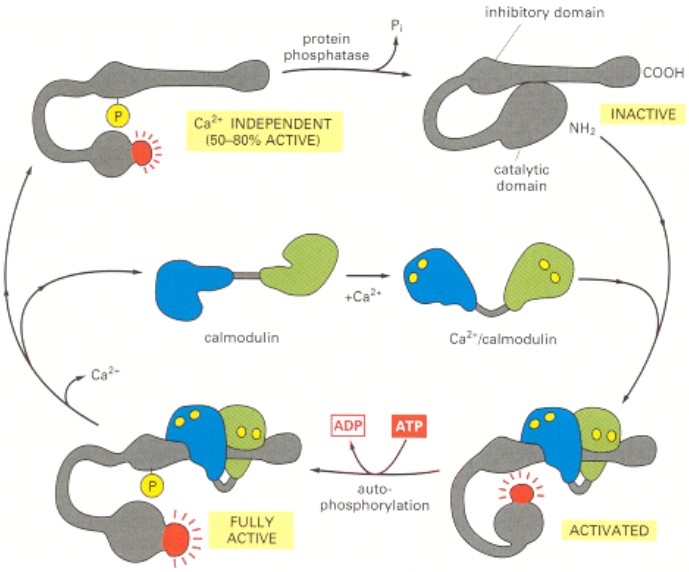

Figure 15-41. The activation of CaM-kinase II. The enzyme is a large protein complex of about 12 subunits, although, for simplicity, only one subunit is shown. The subunits are of four homologous kinds (α, β, γ, and σ), which are expressed in different proportions in different cell types. In the absence of Ca^{2+}/calmodulin, the enzyme is inactive as the result of an interaction between the inhibitory domain and the catalytic domain. The binding of Ca^{2+}/calmodulin alters the conformation of the protein, allowing the catalytic domain to phosphorylate the inhibitory domain of neighboring subunits in the complex, as well as other proteins in the cell (not shown). The autophosphorylation of the enzyme complex (by mutual phosphorylation of its subunits) prolongs the activity of the enzyme in two ways. First, it traps the bound Ca^{2+}/calmodulin so that it does not dissociate from the enzyme complex until cytosolic Ca^{2+} levels return to basal values for at least 10 seconds (not shown). Second, it converts the enzyme to a Ca^{2+}-independent form so that the kinase remains active even after the Ca^{2+}/calmodulin dissociates from it. This activity continues until the autophosphorylation process is overridden by a protein phosphatase.

Figure 15-42. CaM-kinase II as a frequency decoder of Ca^{2+}oscillations. (A) At low frequencies of Ca^{2+} spikes *(gray bars)*, the enzyme becomes inactive after each spike, as the autophosphorylation induced by Ca^{2+}/calmodulin binding does not maintain the enzyme's activity long enough for the enzyme to remain active until the next Ca^{2+} spike arrives. (B) At higher spike frequencies, however, the enzyme fails to inactivate completely between Ca^{2+} spikes, so its activity ratchets up with each spike. If the spike frequency is high enough, this progressive increase in enzyme activity would continue until the enzyme is autophosphorylated on all subunits and is therefore maximally activated. Once enough of its subunits are autophosphorylated, the enzyme can be maintained in a highly active state even with a relatively low frequency of Ca^{2+} spikes (a form of cell memory). The binding of Ca^{2+}/calmodulin to the enzyme is enhanced by the CaM-kinase II autophosphorylation (a form of positive feedback), causing the response of the enzyme to repeated Ca^{2+} spikes to exhibit a steep threshold in its frequency response, as discussed earlier.

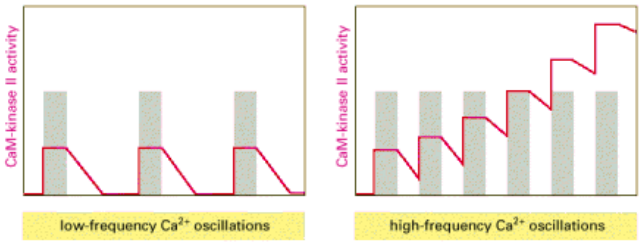

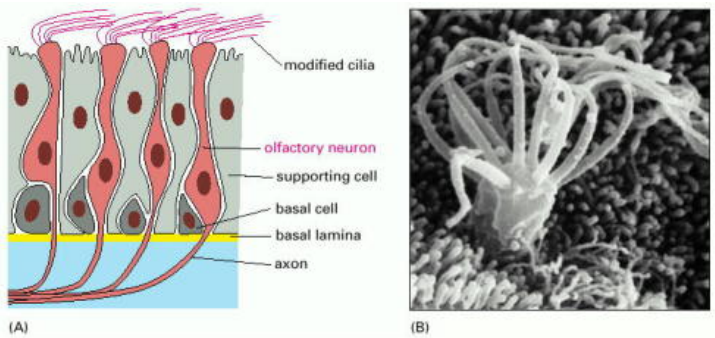

Figure 15-43. Olfactory receptor neurons. (A) This drawing shows a section of olfactory epithelium in the nose. Olfactory receptor neurons possess modified cilia, which project from the surface of the epithelium and contain the olfactory receptors, as well as the signal transduction machinery. The axon, which extends from the opposite end of the receptor neuron, conveys electrical signals to the brain when the cell is activated by an odorant to produce an action potential. The basal cells act as stem cells, producing new receptor neurons throughout life, to replace the neurons that die. (B) A scanning electron micrograph of the cilia on the surface of an olfactory neuron. (B, from E.E. Morrison and R.M. Costanzo, *J. Comp. Neurol.* 297:113, 1990. © Wiley-Liss, Inc.)

Figure 15-44. Cyclic GMP.

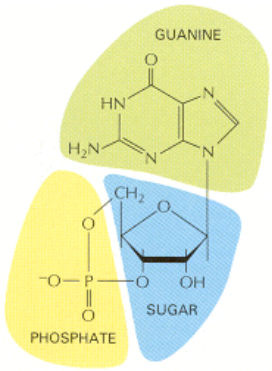

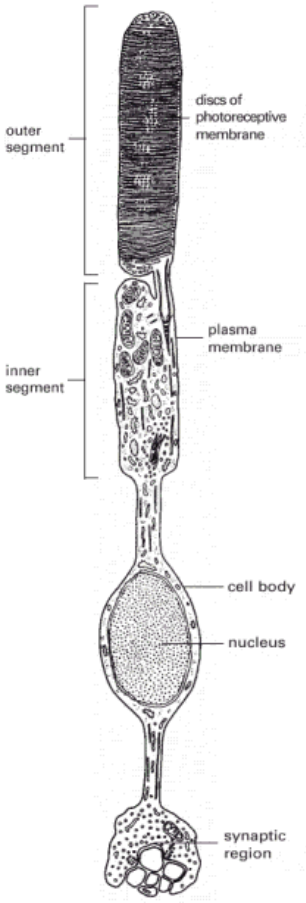

Figure 15-45. A rod photoreceptor cell. There are about 1000 discs in the outer segment. The disc membranes are not connected to the plasma membrane.

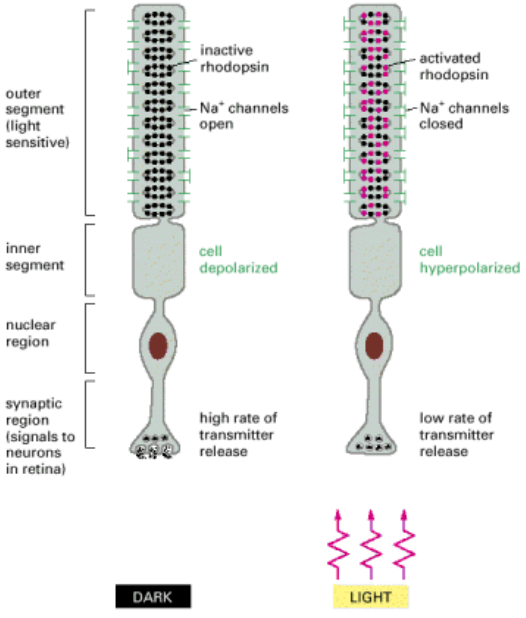

Figure 15-46. The response of a rod photoreceptor cell to light. Rhodopsin molecules in the outer-segment discs absorb photons. Photon absorption leads to the closure of Na^+ channels in the plasma membrane, which hyperpolarizes the membrane and reduces the rate of neurotransmitter release from the synaptic region. Because the neurotransmitter acts to inhibit many of the postsynaptic retinal neurons, illumination serves to free the neurons from inhibition and thus, in effect, excites them.

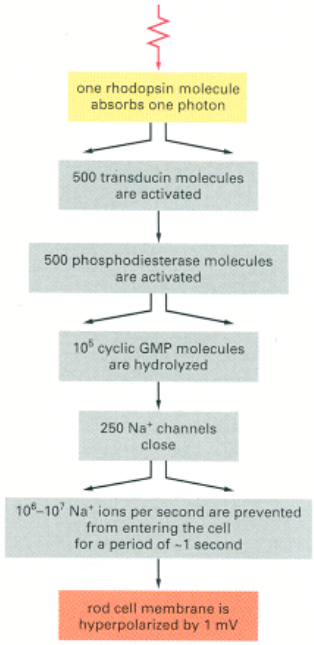

Figure 15-47. Amplification in the light-induced catalytic cascade in vertebrate rods. The divergent arrows indicate the steps where amplification occurs.

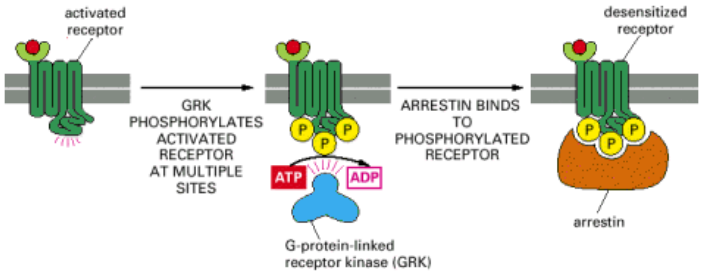

Figure 15-48. The roles of G-protein-linked receptor kinases (GRKs) and arrestins in receptor desensitization. The binding of an arrestin to the phosphorylated receptor prevents the receptor from binding to its G protein and can direct its endocytosis. Mice that are deficient in one form of arrestin fail to desensitize in response to morphine, for example, attesting to the importance of arrestins for desensitization.

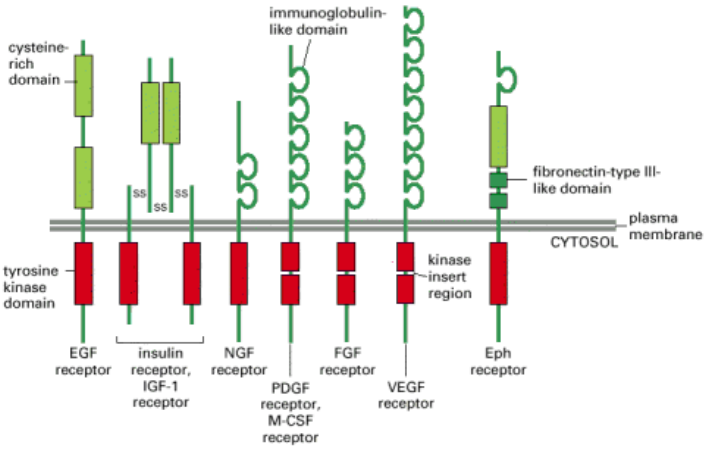

Figure 15-49. Seven subfamilies of receptor tyrosine kinases. Only one or two members of each subfamily are indicated. Note that the tyrosine kinase domain is interrupted by a "kinase insert region" in some of the subfamilies. The functional roles of most of the cysteine-rich, immunoglobulin-like, and fibronectin-type III-like domains are not known. Some of the ligands and responses for the receptors shown are listed in Table 15-4.

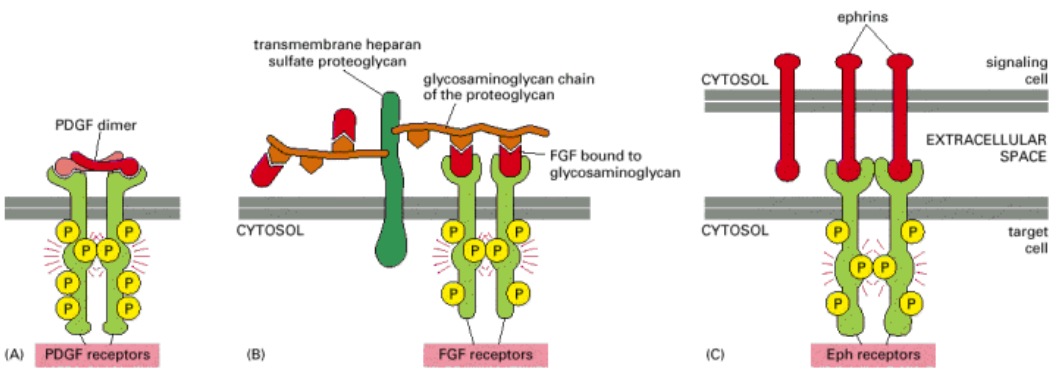

Figure 15-50. Three ways in which signaling proteins can cross-link receptor chains. When the receptor chains are cross-linked, the kinase domains of adjacent receptors cross-phosphorylate each other, stimulating the kinase activity of the receptor and creating docking sites for intracellular proteins. (A) Platelet-derived growth factor (PDGF) is a covalently linked dimer with two receptor-binding sites, so it can directly cross-link adjacent receptors to initiate the intracellular signaling process. The PDGF dimers are composed of A and B chains in different combinations, and they can activate different combinations of two types of PDGF receptor chains (α and β), which have somewhat different signaling properties. (B) Some monomeric ligands, such as fibroblast growth factors (FGFs), bind in clusters to proteoglycans, enabling the ligands to cross-link their receptors. The proteoglycans can be in the extracellular matrix or, as shown here, on the cell surface. There are more than 20 types of FGFs and more than 4 types of FGF receptors. (C) Membrane-bound signaling proteins, such as ephrins, can cross-link their receptors even though they are monomeric, because they cluster in the plasma membrane of the signaling cell. Some ephrins (B-type) are transmembrane proteins (as shown), whereas others (A-type) are linked to the membrane by a glycosylphosphatidylinositol (GPI) anchor (see Figure 12-56). For the most part, A-type ephrins activate A-type Eph receptors, and B-type ephrins activate B-type Eph receptors.

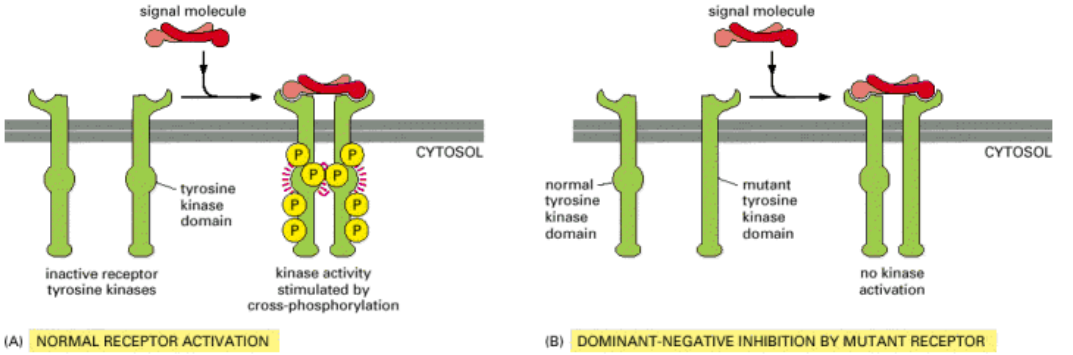

Figure 15-51. Inhibition of signaling through normal receptor tyrosine kinases by an excess of mutant receptors. (A) In this example, the normal receptors dimerize in response to ligand binding. The two kinase domains cross-phosphorylate each other, increasing the activity of the kinase domains, which can now further activate the receptor dimer by phosphorylating other sites on the receptors. (B) The mutant receptor with an inactivated kinase domain can dimerize normally, but it cannot cross-phosphorylate a normal receptor in a dimer. For this reason, the mutant receptors, if present in excess, will block signaling by the normal receptors - a process called *dominant-negative inhibition.* Cell biologists frequently use this strategy to inhibit a specific type of receptor tyrosine kinase in a cell to determine its normal function.

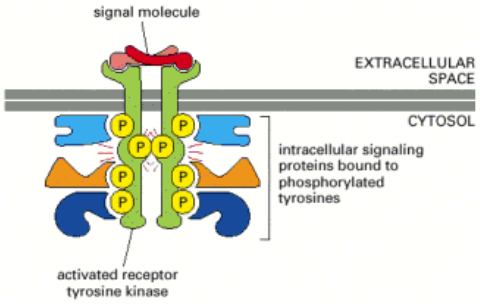

Figure 15-52. The docking of intracellular signaling proteins on an activated receptor tyrosine kinase. The activated receptor and its bound signaling proteins form a signaling complex that can then broadcast signals along multiple signaling pathways.

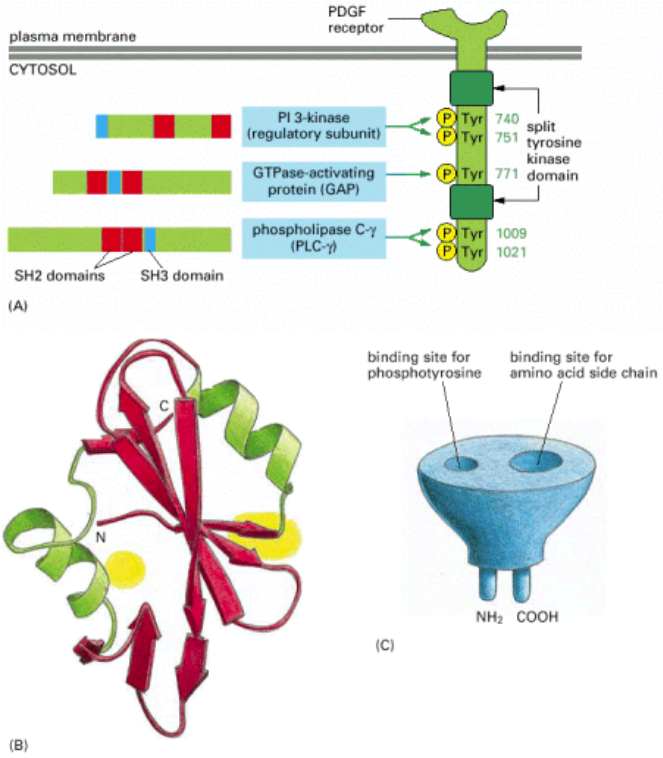

Figure 15-53. The binding of SH2-containing intracellular signaling proteins to an activated PDGF receptor. (A) This drawing of a PDGF receptor shows five of the tyrosine autophosphorylation sites, three in the kinase insert region and two on the C-terminal tail, to which the three signaling proteins shown bind as indicated. The numbers on the right indicate the positions of the tyrosines in the polypeptide chain. These binding sites have been identified by using recombinant DNA technology to mutate specific tyrosines in the receptor. Mutation of tyrosines 1009 and 1021, for example, prevents the binding and activation of PLC-γ, so that receptor activation no longer stimulates the inositol phospholipid signaling pathway. The locations of the SH2 *(red)* and SH3 *(blue)* domains in the three signaling proteins are indicated. (Additional autophosphorylation sites on this receptor are not shown, including those that serve as binding sites for the cytoplasmic tyrosine kinase Src and the adaptor proteins Grb2 and Shc, discussed later.) (B) The three-dimensional structure of an SH2 domain, as determined by x-ray crystallography. The binding pocket for phosphotyrosine is shown in *yellow* on the right, and a pocket for binding a specific amino acid side chain (isoleucine, in this case) is shown in *yellow* on the left (see also Figure 3-40). (C) The SH2 domain is a compact, "plug-in" module, which can be inserted almost anywhere in a protein without disturbing the protein's folding or function (see Figure 3-19). Because each domain has distinct sites for recognizing phosphotyrosine and for recognizing a particular amino acid side chain, different SH2 domains recognize phosphotyrosine in the context of different flanking amino acid sequences. (B, based on data from G. Waksman et al., *Cell* 72:120, 1993. © Elsevier.)

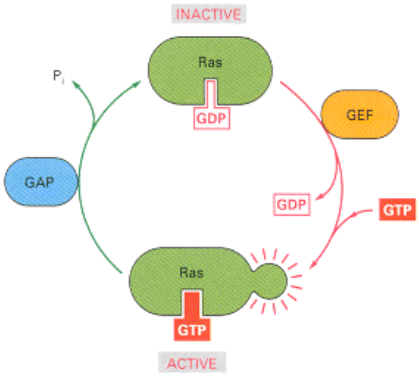

Figure 15-54. The regulation of Ras activity. GTPase-activating proteins (GAPs) inactivate Ras by stimulating it to hydrolyze its bound GTP; the inactivated Ras remains tightly bound to GDP. Guanine nucleotide exchange factors (GEFs) activate Ras by stimulating it to give up its GDP; the concentration of GTP in the cytosol is 10 times greater than the concentration of GDP, and Ras rapidly binds GTP once GDP has been ejected. Several Ras-regulating GAPs (Ras GAPs) have been characterized in mammalian cells, including *p120*^{GAP} and *neurofibromin* (so named because it is encoded by the gene that is mutated in the common human genetic disease neurofibromatosis, which is associated with tumors of nerves). The Ras GAPs maintain most of the Ras protein (~95%) in unstimulated cells in an inactive GDP-bound state.

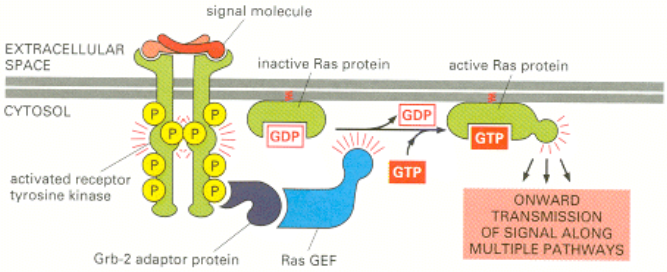

Figure 15-55. The activation of Ras by an activated receptor tyrosine kinase. Most of the signaling proteins bound to the activated receptor are omitted for simplicity. The Grb-2 adaptor protein binds to a specific phosphotyrosine on the receptor and to the Ras guanine nucleotide exchange factor (GEF), which stimulates Ras to exchange its bound GDP for GTP. The activated Ras then activates several downstream signaling pathways, one of which is shown in Figure 15-56.

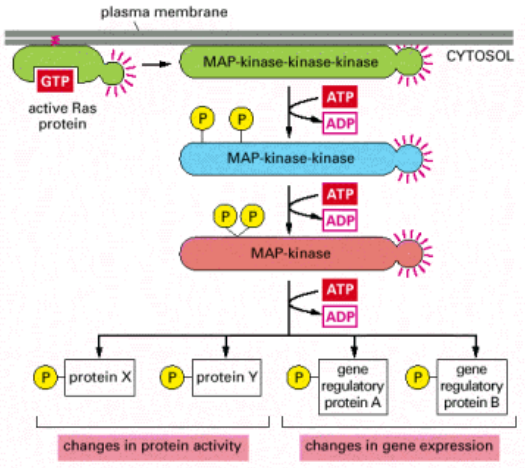

Figure 15-56. The MAP-kinase serine/threonine phosphorylation pathway activated by Ras. Multiple such pathways involving structurally and functionally related proteins operate in all eucaryotes, each coupling an extracellular stimulus to a variety of cell outputs. The pathway activated by Ras begins with a MAP-kinase-kinase-kinase called *Raf*, which activates the MAP-kinase-kinase *Mek*, which then activates the MAP-kinase called *Erk*. Erk in turn phosphorylates a variety of downstream proteins, including other kinases, as well as gene regulatory proteins in the nucleus. The resulting changes in gene expression and protein activity cause complex changes in cell behavior.

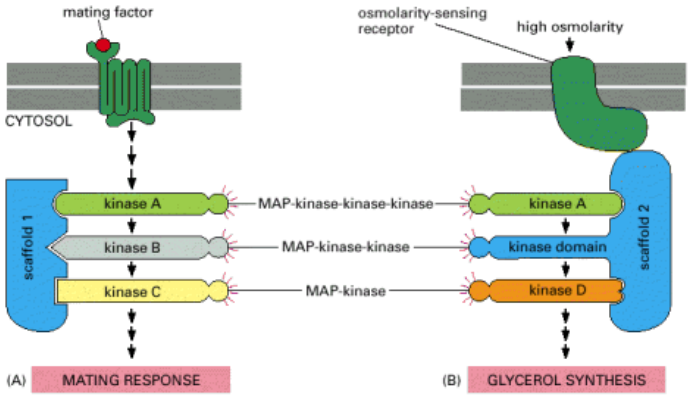

Figure 15-57. The organization of MAP-kinase pathways by scaffold proteins in budding yeast. Budding yeast have at least six three-component MAP-kinase modules involved in a variety of biological processes, including the two responses illustrated here - a mating response and the response to high osmolarity. (A) The mating response is triggered when a mating factor secreted by a yeast of opposite mating type binds to a G-protein-linked receptor. This activates a G protein, and the βγ complex of the G protein indirectly activates the MAP-kinase-kinase-kinase (kinase A), which then relays the response onward. Once activated, the MAP-kinase (kinase C) phosphorylates and thereby activates several proteins that mediate the mating response, in which the yeast cell stops dividing and prepares for fusion. The three kinases in this module are bound to scaffold protein 1. (B) In a second response, a yeast cell exposed to a high-osmolarity environment is induced to synthesize glycerol to increase its internal osmolarity. This response is mediated by a transmembrane, osmolarity-sensing, receptor protein and a different MAP-kinase module bound to a second scaffold protein. (Note that the kinase domain of scaffold 2 provides the MAP-kinase-kinase activity of this module.) Although both pathways use the same MAP-kinase-kinase-kinase (kinase A, *green*), there is no cross talk between them, because the kinases in each module are tightly bound to different scaffold proteins, and the osmosensor is bound to the same scaffold protein as the particular kinase it activates.

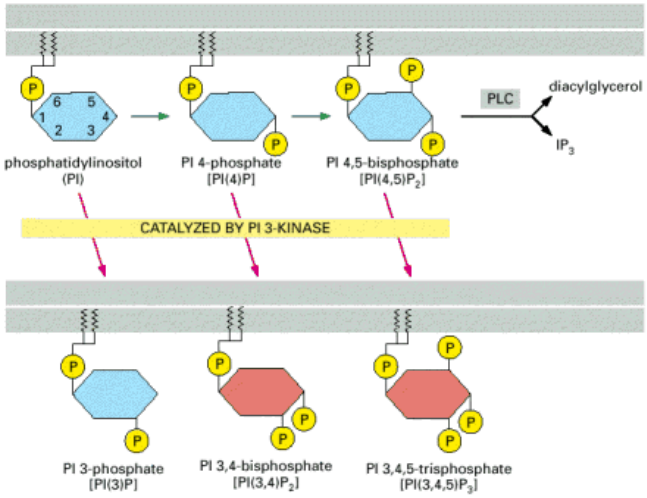

Figure 15-58. The generation of inositol phospholipid docking sites by PI 3-kinase. PI 3-kinase phosphorylates the inositol ring on carbon atom 3 to generate the inositol phospholipids shown at the bottom of the figure; the two lipids shown in *red* can serve as docking sites for signaling proteins with PH domains. The phosphorylations indicated by the *green* arrows are catalyzed by other inositol phospholipid kinases. As discussed earlier, phospholipase C (PLC-β or PLC-γ) can cleave $PI(4,5)P_2$ to produce the two small signaling molecules diacylglycerol and inositol 1,4,5-trisphosphate (IP_3).

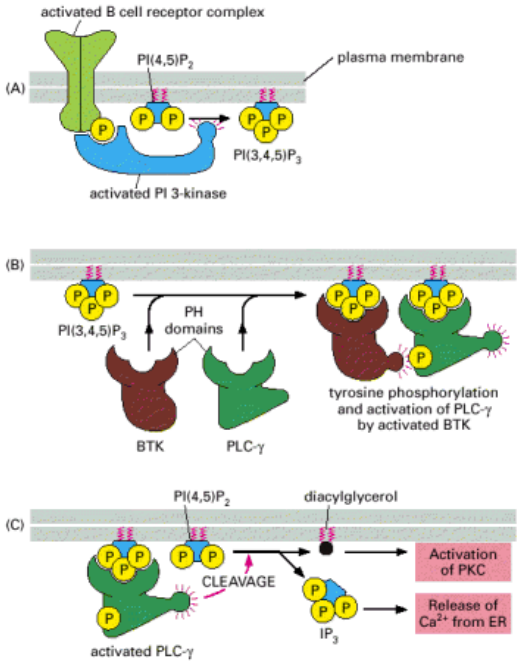

Figure 15-59. The recruitment of signaling proteins with PH domains to the plasma membrane during B cell activation. (A) PI 3-kinase binds to a phosphotyrosine on the activated B cell receptor complex and is thereby activated to phosphorylate the inositol phospholipid PI 4,5-bisphosphate [$PI(4,5)P_2$], generating PI 3,4,5-trisphosphate [$PI(3,4,5)P_3$]. (B) The PI 3,4,5-trisphosphate serves as a docking site for two signaling proteins with PH domains that then interact with each other. This causes the cytoplasmic tyrosine kinase BTK to phosphorylate and thereby activate PLC-γ at the membrane. (C) The activated PLC-γ then cleaves $PI(4,5)P_2$ to generate diacylglycerol and IP_3, which relay the signal onward.

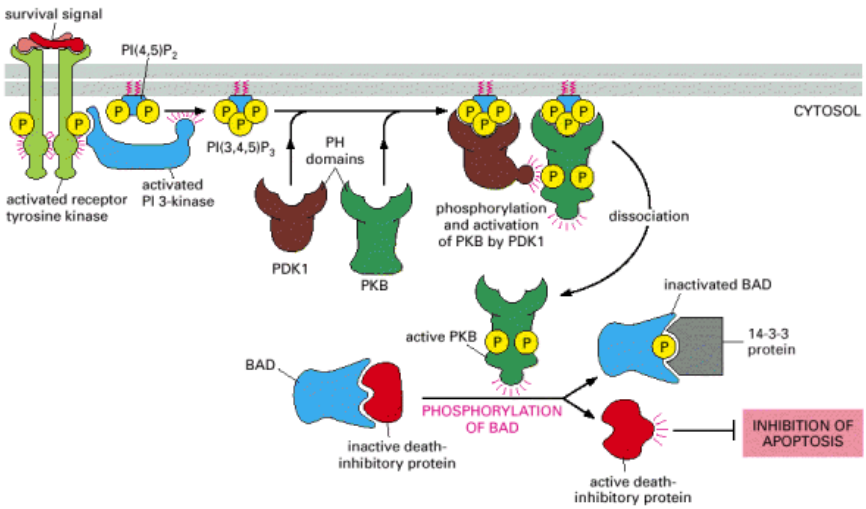

Figure 15-60. One way in which signaling through PI 3-kinase promotes cell survival. An extracellular survival signal activates a receptor tyrosine kinase, which recruits and activates PI 3-kinase. The PI 3-kinase produces $PI(3,4,5)P_3$ and $PI(3,4)P_2$ (not shown), both of which serve as docking sites for two serine/threonine kinases with PH domains - protein kinase B (PKB) and the phosphoinositol-dependent kinase PDK1. The binding of PKB to the inositol lipids alters its conformation so that the protein can be phosphorylated and activated by PDK1. The activated PKB now dissociates from the plasma membrane and phosphorylates the BAD protein, which, when unphosphorylated, holds one or more death-inhibitory proteins in an inactive state. Once phosphorylated, BAD releases the inhibitory proteins, which now can block programmed cell death (apoptosis) and thereby promote cell survival. As shown, once phosphorylated, BAD binds to a ubiquitous cytosolic protein called *14-3-3*, which keeps BAD out of action. There are about 20 14-3-3 proteins in human cells, all of which bind to specific phosphoserine-containing motifs in proteins. The activation of other signaling pathways can also lead to BAD phosphorylation and the promotion of cell survival (not shown).

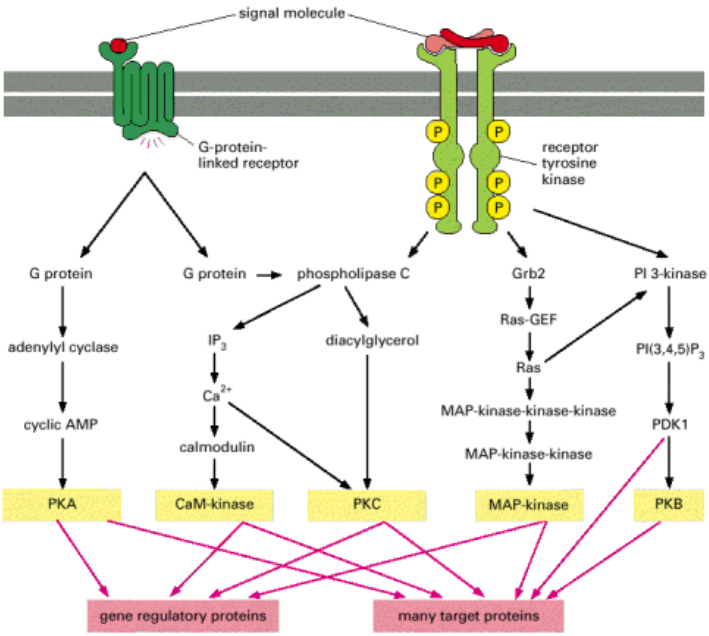

Figure 15-61. Five parallel intracellular signaling pathways activated by G-protein-linked receptors, receptor tyrosine kinases, or both. In this schematic example, the five kinases (shaded *yellow)* at the end of each pathway phosphorylate target proteins (shaded *red),* some of which are phosphorylated by more than one of the kinases. The specific phospholipase C activated by the two types of receptors is different: G-protein-linked receptors activate PLC-β, whereas receptor tyrosine kinases activate PLC-γ (not shown).

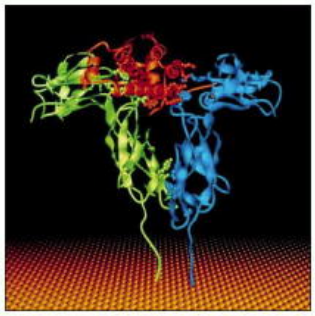

Figure 15-62. The three-dimensional structure of human growth hormone bound to its receptor. The hormone *(red)* has cross-linked two identical receptors (one shown in *green* and the other in *blue).* Hormone binding activates cytoplasmic tyrosine kinases that are tightly bound to the cytosolic tails of the receptors (not shown). The structures shown were determined by x-ray crystallographic studies of complexes formed between the hormone and extracellular receptor domains produced by recombinant DNA technology. It was entirely unexpected that a monomeric ligand such as growth hormone would cross-link its receptors, as it requires that the two identical receptors recognize different parts of the hormone. As mentioned earlier, EGF does the same thing. (From A.M. deVos, M. Ultsch, and A.A. Kossiakoff, *Science* 255:306312, 1992. © AAAS.)

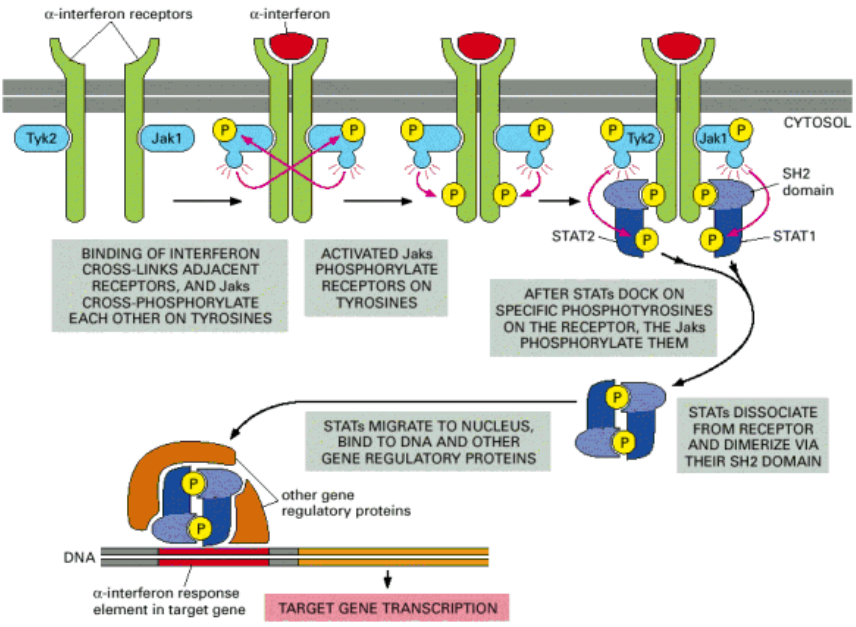

Figure 15-63. The Jak-STAT signaling pathway activated by α-interferon. The binding of interferon either causes two separate receptor polypeptide chains to dimerize (as shown) or reorients the receptor chains in a preformed dimer. In either case, the associated Jaks are brought together so that they can cross-phosphorylate each other on tyrosines, starting the signaling process. The two different receptor chains are associated with different Jaks (Tyk2 and Jak1), and they recruit different STATs (STAT1 and STAT2). The STATs dissociate from the receptors and form heterodimers when activated by phosphorylation, and they bind to specific DNA sequences in the cell nucleus, where, together with other gene regulatory proteins, they induce the transcription of adjacent genes.

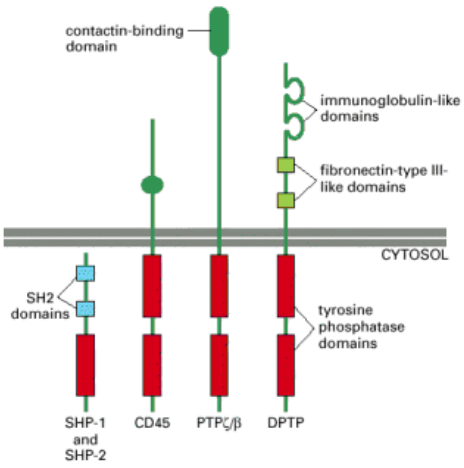

Figure 15-64. Some protein tyrosine phosphatases. The cytoplasmic tyrosine phosphatases SHP-1 and SHP-2 have similar structures, with two SH2 domains. The three transmembrane receptorlike tyrosine phosphatases have two tandemly arranged intracellular phosphatase domains, with the one closest to the membrane providing most or all of the catalytic activity. DPTP is a *Drosophila* protein; the others in the figure are mammalian proteins.

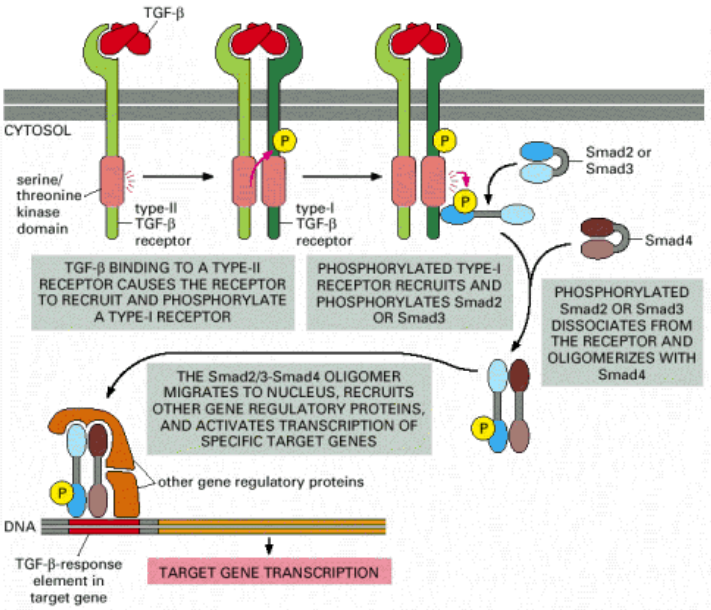

Figure 15-65. A model for the Smad-dependent signaling pathway activated by TGF-β. Note that TGF-β is a dimer and that Smads open up to expose a dimerization surface when they are phosphorylated. Several features of the pathway have been omitted for simplicity, including the following: (1) The type-I and type-II receptor proteins are both thought to be dimers. (2) The type-I receptors are normally associated with an inhibitory protein, which dissociates when the type-I receptor is phosphorylated by a type-II receptor. (3) The individual Smads are thought to be trimers. (4) An anchoring protein (called SARA, for Smad *a*nchor for *r*eceptor *a*ctivation) helps to recruit Smad2 or Smad3 to the activated type I receptor by binding to the receptor, to the Smad, and to inositol phopholipid molecules in the plasma membrane. (5) The function of certain Smads is regulated by enzymes that enhance their ubiquitylation and thereby their degradation.

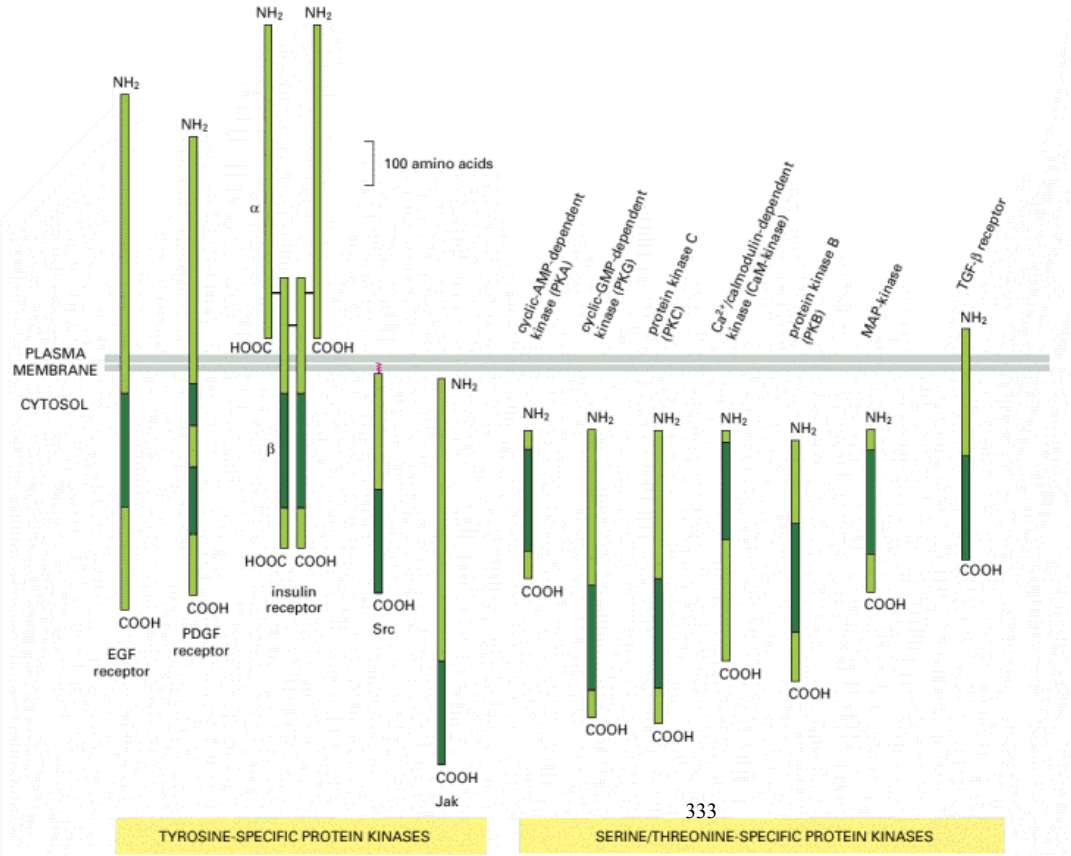

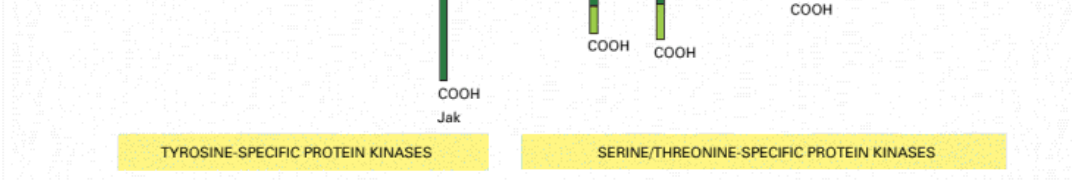

Figure 15-66. Some of the protein kinases discussed in this chapter. The size and location of their catalytic domains *(dark green)* are shown. In each case the catalytic domain is about 250 amino acids long. These domains are all similar in amino acid sequence, suggesting that they have all evolved from a common primordial kinase (see also Figure 3-65). Note that all of the tyrosine kinases shown are bound to the plasma membrane (Jaks are bound by their association with cytokine receptors), whereas most of the serine/threonine kinases are in the cytosol.

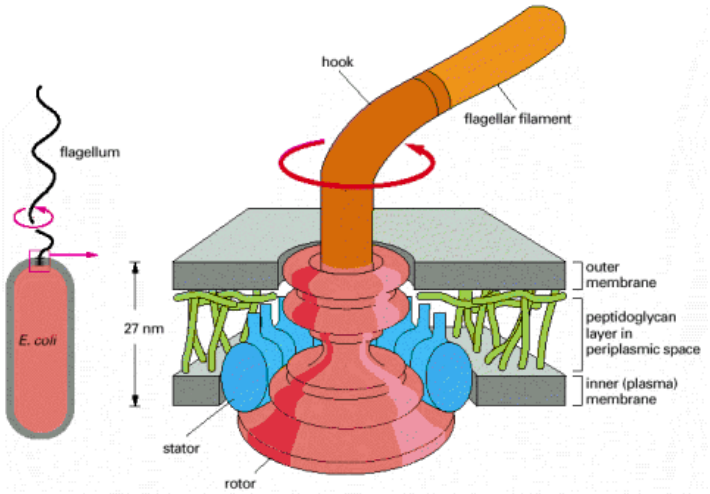

Figure 15-67. The bacterial flagellar motor. The flagellum is linked to a flexible hook. The hook is attached to a series of protein rings (shown in *red),* which are embedded in the outer and inner (plasma) membranes. The rings form a rotor, which rotates with the flagellum at more than 100 revolutions per second. The rotation is driven by a flow of protons through an outer ring of proteins (see Figure 14-17), the stator, which also contains the proteins responsible for switching the direction of rotation. (Based on data from T. Kubori et al., *J. Mol. Biol.* 226:433446, 1992, and N.R. Francis et al., *Proc. Natl. Acad. Sci. USA* 89:63046308, 1992.)

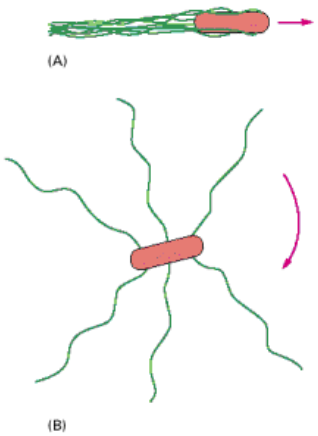

Figure 15-68. Positions of the flagella on *E. coli* during swimming. (A) When the flagella rotate counterclockwise, they are drawn together into a single bundle, which acts as a propeller to produce smooth swimming. (B) When the flagella rotate clockwise, they fly apart and produce tumbling.

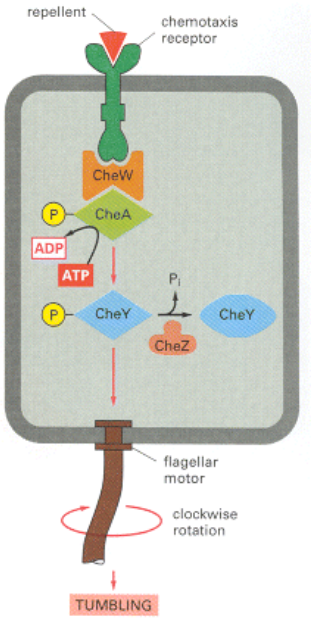

Figure 15-69. The two-component signaling pathway that enables chemotaxis receptors to control the flagellar motor during bacterial chemotaxis. The histidine kinase CheA is stably bound to the receptor via the adaptor protein CheW. The binding of a repellent increases the activity of the receptor, which stimulates CheA to phosphorylate itself on histidine. CheA quickly transfers its covalently bound, high-energy phosphate directly to CheY to generate CheY-phosphate, which then diffuses away, binds to the flagellar motor, and causes the motor to rotate clockwise, which results in tumbling. The binding of an attractant has the opposite effect: it decreases the activity of the receptor and therefore decreases the phosphorylation of CheA and CheY, which results in counterclockwise flagellar rotation and smooth swimming. CheZ accelerates the autodephosphorylation of CheY-phosphate, thereby inactivating it. Each of the phosphorylated intermediates decays in about 10 seconds, enabling the bacterium to respond very quickly to changes in its environment (see Figure 15-10).

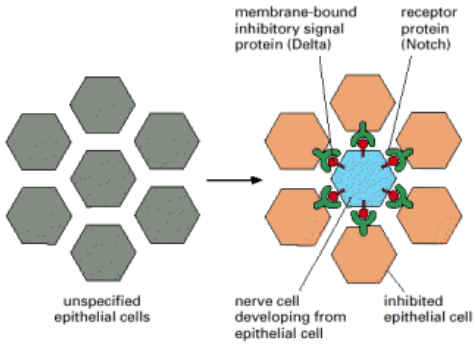

Figure 15-70. Lateral inhibition mediated by Notch and Delta during nerve cell development in *Drosophila*. When individual cells in the epithelium begin to develop as neural cells, they signal to their neighbors not to do the same. This inhibitory, contact-dependent signaling is mediated by the ligand Delta that appears on the surface of the future nerve cell and binds to Notch proteins on the neighboring cells. In many tissues, all the cells in a cluster initially express Delta and Notch, and a competition occurs, with one cell emerging as winner, expressing Delta strongly and inhibiting its neighbors from doing likewise. In other cases, additional factors interact with Delta or Notch to make some cells susceptible to the lateral inhibition signal and others deaf to it.

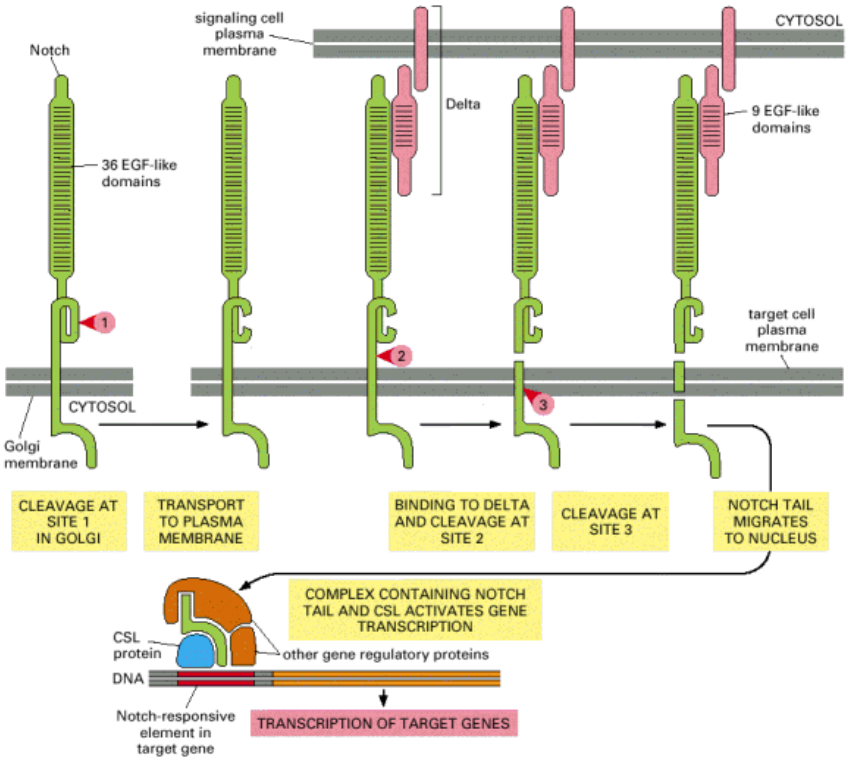

Figure 15-71. The processing and activation of Notch by proteolytic cleavage. The *numbered red arrowheads* indicate the sites of proteolytic cleavage. The first proteolytic processing step occurs within the *trans* Golgi network to generate the mature heterodimeric Notch receptor that is then displayed on the cell surface. The binding of Delta, which is displayed on a neighboring cell, triggers the next two proteolytic steps. Note that Notch and Delta interact through their repeated EGF-like domains. Some evidence suggests that the tension exerted on Notch by the endocytic machinery of the interacting cells triggers the cleavage at site 2.

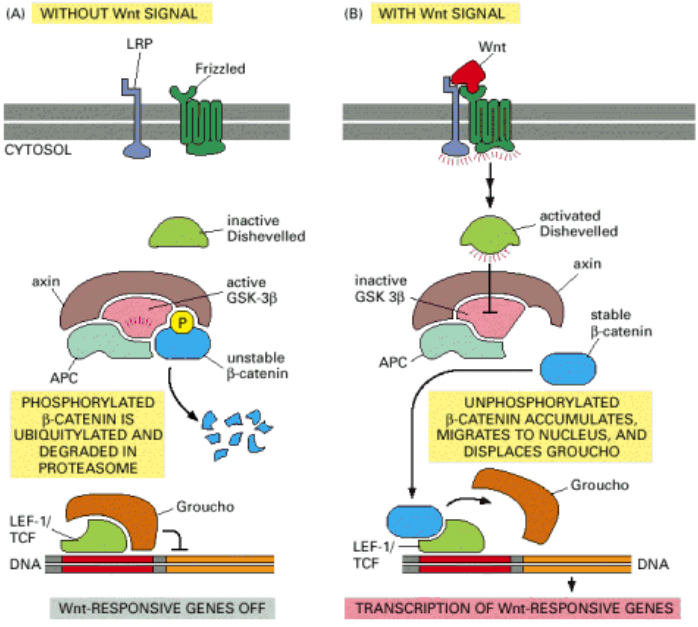

Figure 15-72. A model for the Wnt activation of the β-catenin signaling pathway. (A) In the absence of a Wnt signal, some β-catenin is bound to the cytosolic tail of cadherin proteins (not shown) and any cytosolic β-catenin becomes bound by the APC-axin-GSK-3β degradation complex. In this complex, β-catenin is phosphorylated by GSK-3β, triggering its ubiquitylation and degradation in proteasomes. Wnt-responsive genes are kept inactive by the Groucho corepressor protein bound to the gene regulatory protein LEF-1/TCF. (B) Wnt binding to Frizzled and LRP activates Dishevelled by an unknown mechanism. By an equally mysterious mechanism, which requires casein kinase 1 (not shown), this leads to the inactivation of GSK-β3 in the degradation complex. As a result, the phosphorylation and degradation of β-catenin is inhibited, and β-catenin accumulates in the cytoplasm and nucleus. In the nucleus, β-catenin binds to LEF-1/TCF, displaces Groucho, and acts as a coactivator to stimulate the transcription of Wnt target genes.

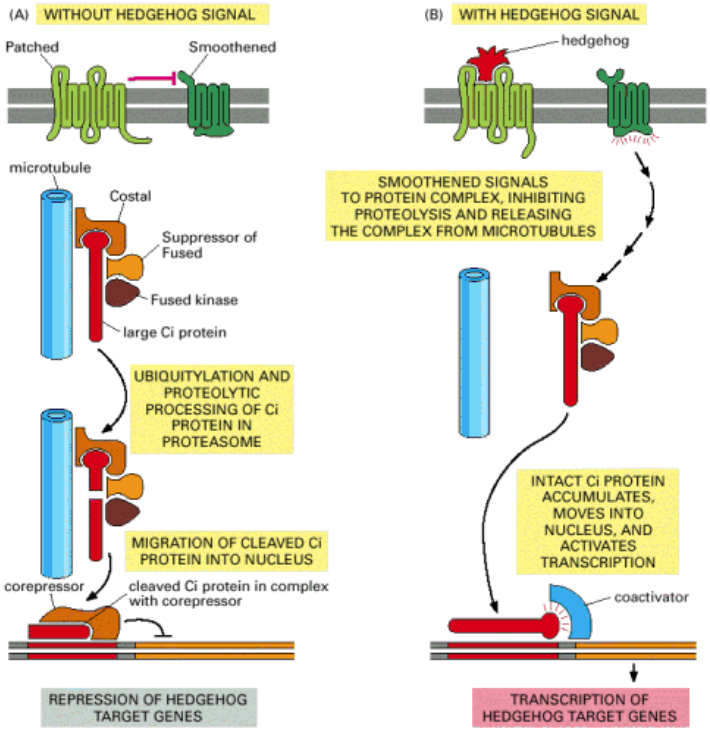

Figure 15-73. A model for Hedgehog signaling in *Drosophila.* (A) In the absence of Hedgehog, the Patched receptor inhibits Smoothened probably by promoting the degradation or intracellular sequestration of Smoothened. The Ci protein is located in a protein complex and is cleaved to form a transcriptional repressor, which accumulates in the nucleus to help keep Hedgehog target genes inactive. The protein complex includes the serine/threonine kinase Fused, the anchoring protein Costal (which binds the complex to microtubules), and the adaptor protein Suppressor of Fused. (B) Hedgehog binding to Patched relieves the inhibition of Smoothened, which now signals to the protein complex to stop processing Ci, to dissociate from microtubules, and to release the unprocessed Ci so it can accumulate in the nucleus and activate the transcription of Hedgehog-responsive genes. Most of the molecular events in the pathway are unknown.

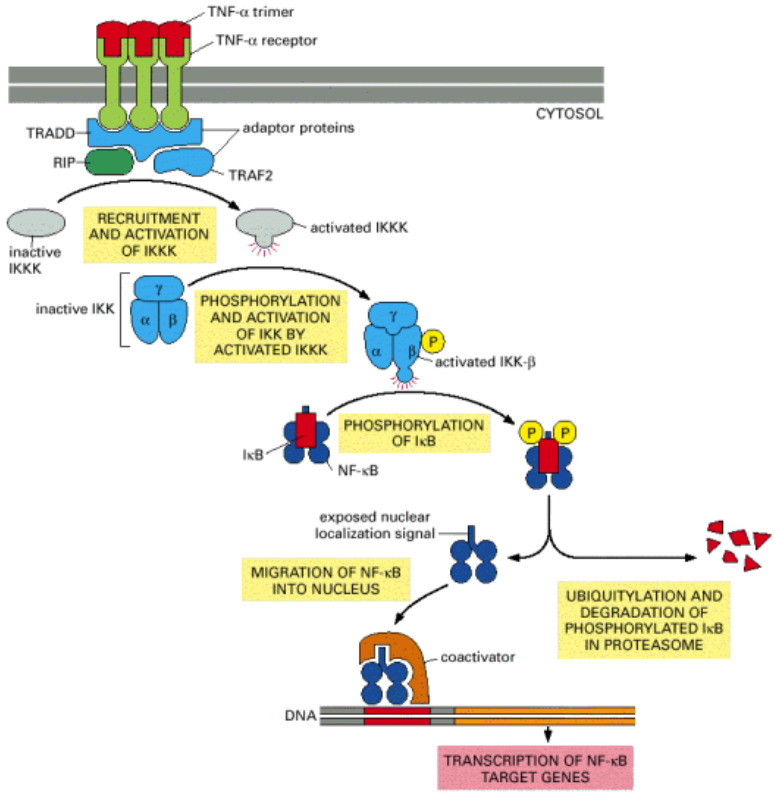

Figure 15-74. The activation of NF-κB by TNF-α. Both TNF-α and its receptors are trimers. The binding of TNF-α causes a rearrangement of the clustered cytosolic tails of the receptors, which now recruit a number of intracellular signaling proteins, including the *receptor-interacting protein kinase (RIP)* and two adaptor proteins, *TNF-associated death-domain protein (TRADD)* and *TNF-receptor-associated factor 2 (TRAF2).* These then recruit and activate an unidentified kinase, IκB kinase kinase kinase (IKKK), which phosphorylates and activates IκB kinase kinase (IKK). IKK is a heterotrimer composed of two kinase subunits (IKK-α and IKK-β) and a regulatory adaptor subunit called IKK-γ. The IKK-β then phosphorylates IκB on two serines, which marks the protein for ubiquitylation and degradation in proteasomes. The nuclear localization signal on the free NF-κB now directs the transport of this protein into the nucleus where, in collaboration with coactivator proteins, it stimulates the transcription of its target genes. In addition to target genes involved in the inflammatory response, NF-κB also activates the *IκB* gene, providing negative feedback (not shown). The role of RIP is unclear: although it is required for TNF signaling, its kinase domain is not.

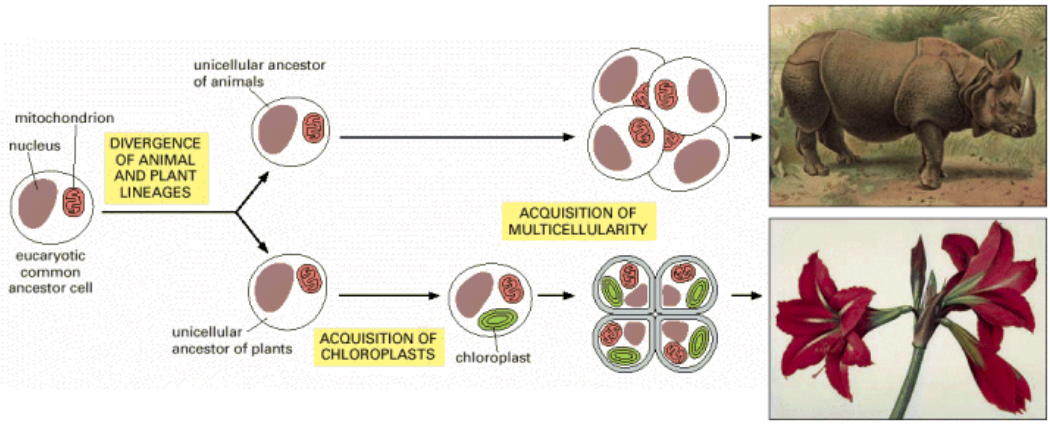

Figure 15-75. The proposed divergence of plant and animal lineages from a common unicellular eucaryotic ancestor. The plant lineage acquired chloroplasts after the two lineages diverged. Both lineages independently gave rise to multicellular organisms - plants and animals. (Paintings courtesy of John Innes Foundation.)

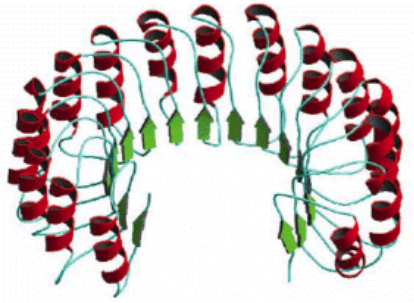

Figure 15-76. The three-dimensional structure of leucine-rich repeats, similar to those found in the LRR serine/threonine receptor kinases. (Courtesy of David Lawson.)

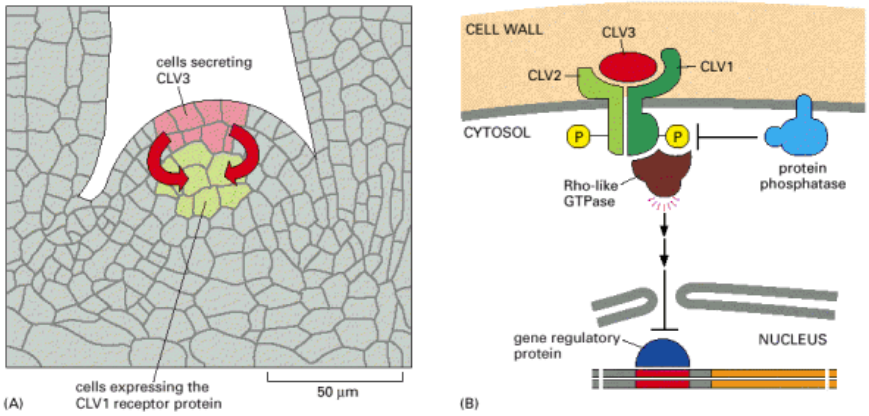

Figure 15-77. A hypothetical model for CLV1 receptor serine/threonine kinase regulation of cell proliferation and/or differentiation in the shoot meristem. (A) Cells in the outer layer of the meristem secrete CLV3 protein, which binds to CLV1 receptor proteins on target cells in an adjacent, more central region of the meristem, presumably stimulating the differentiation of the target cells. (B) Some parts of the intracellular signaling pathway activated by CLV3 binding. The CLV receptor protein is thought to be a homodimer or heterodimer, which phosphorylates itself on serines and threonines, thereby activating the receptor and leading to the activation of a Rho-like GTPase. The signaling pathway after this point is unclear, but it leads to the inhibition of a gene regulatory protein in the nucleus, thereby blocking the transcription of genes that otherwise might inhibit differentiation. The phosphatase dephosphorylates the receptor and thereby negatively regulates the signaling pathway.

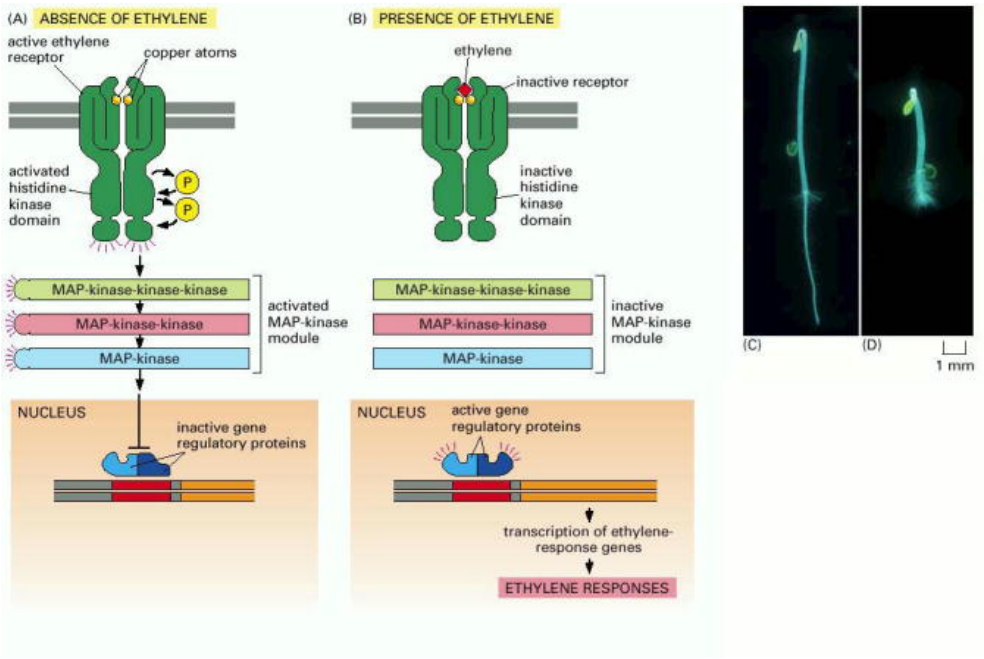

Figure 15-78. A current view of the ethylene two-component signaling pathway. (A) In the absence of ethylene, the receptors and the MAP-kinase module are active, leading to inhibition of the gene regulatory proteins in the nucleus that are responsible for the transcription of ethylene-responsive genes. (B) In the presence of ethylene, the receptors and the MAP-kinase module are inactive, so the ethylene-responsive genes are transcribed. (C and D) The ethylene-mediated "triple response" that occurs when the growing shoot of a germinating seedling encounters an obstacle underground. After such an encounter (D), the shoot thickens, and the protective hook (at *top)* increases its curvature to protect the tip of the shoot. (C and D, courtesy of Melanie Webb.)

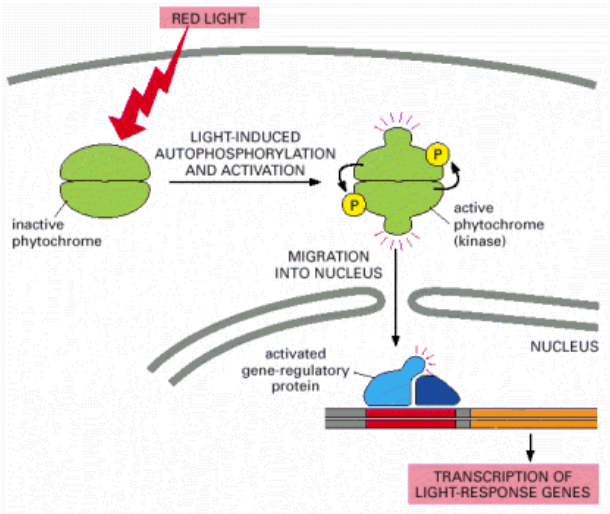

Figure 15-79. A current view of one way in which phytochromes mediate a light response in plant cells. When activated by light, the phytochrome, which is a dimer, phosphorylates itself and then moves into the nucleus, where it activates gene regulatory proteins to stimulate the transcription of specific genes.

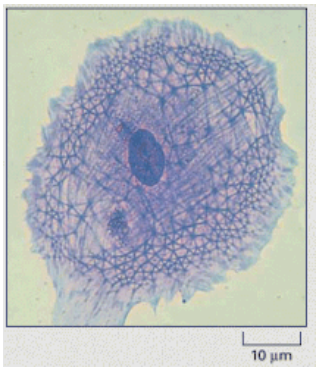

Figure 16-1. The cytoskeleton. A cell in culture has been fixed and stained with Coomassie blue, a general stain for proteins. Note the variety of filamentous structures that extend throughout the cell. (Courtesy of Colin Smith.)

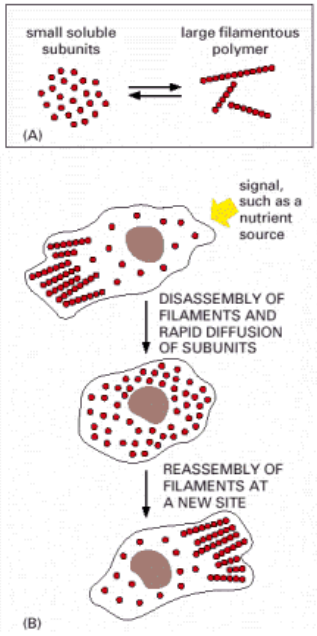

Figure 16-2. The cytoskeleton and changes in cell shape. The formation of protein filaments from much smaller protein subunits allows regulated filament assembly and disassembly to reshape the cytoskeleton. (A) Filament formation from a small protein. (B) Rapid reorganization of the cytoskeleton in a cell in response to an external signal.

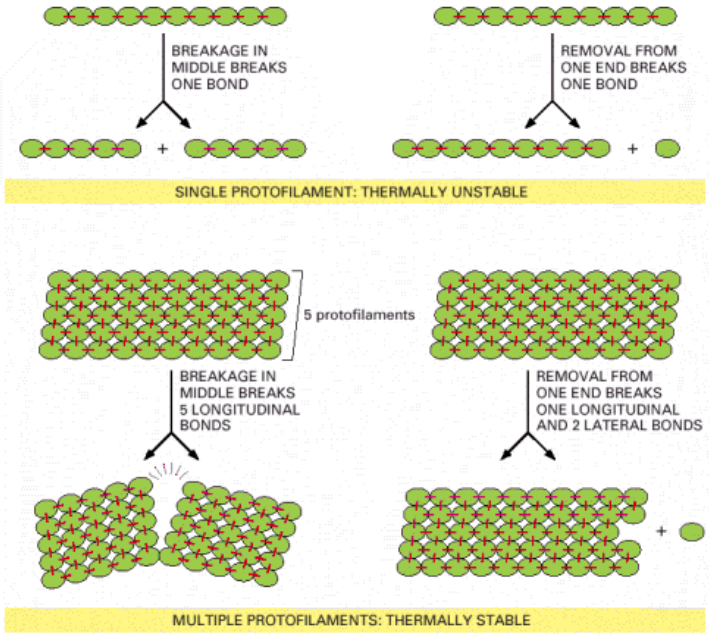

Figure 16-3. The thermal stability of cytoskeletal filaments with dynamic ends. Formation of a cytoskeletal filament from more than one protofilament allows the ends to be dynamic, while the filaments themselves are resistant to thermal breakage. In this hypothetical example, the stable filament is formed from five protofilaments. The bonds holding the subunits together in the filaments are shown in *red*.

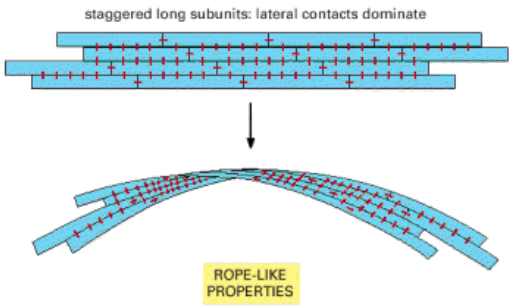

Figure 16-4. A strong filament formed from elongated fibrous subunits with strong lateral contacts. Intermediate filaments are formed in this way and are consequently especially resistant to bending or stretching forces.

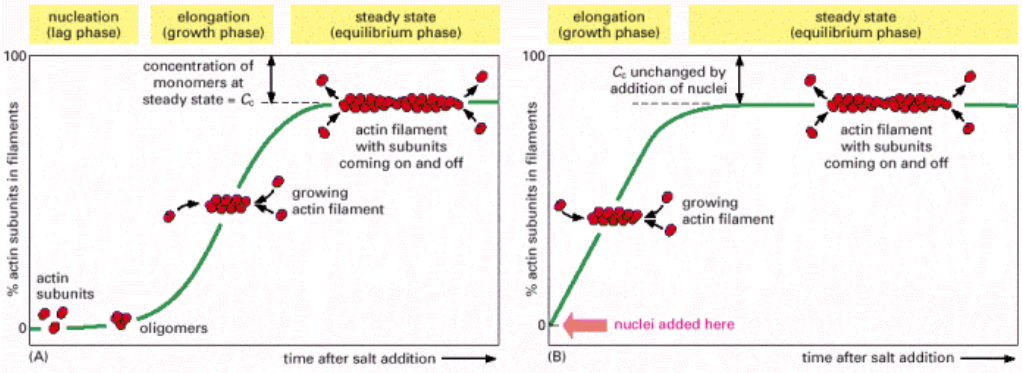

Figure 16-5. The time course of actin polymerization in a test tube. (A) Polymerization is begun by raising the salt concentration in a solution of pure actin subunits. (B) Polymerization is begun in the same way, but with preformed fragments of actin filaments present to act as nuclei for filament growth.

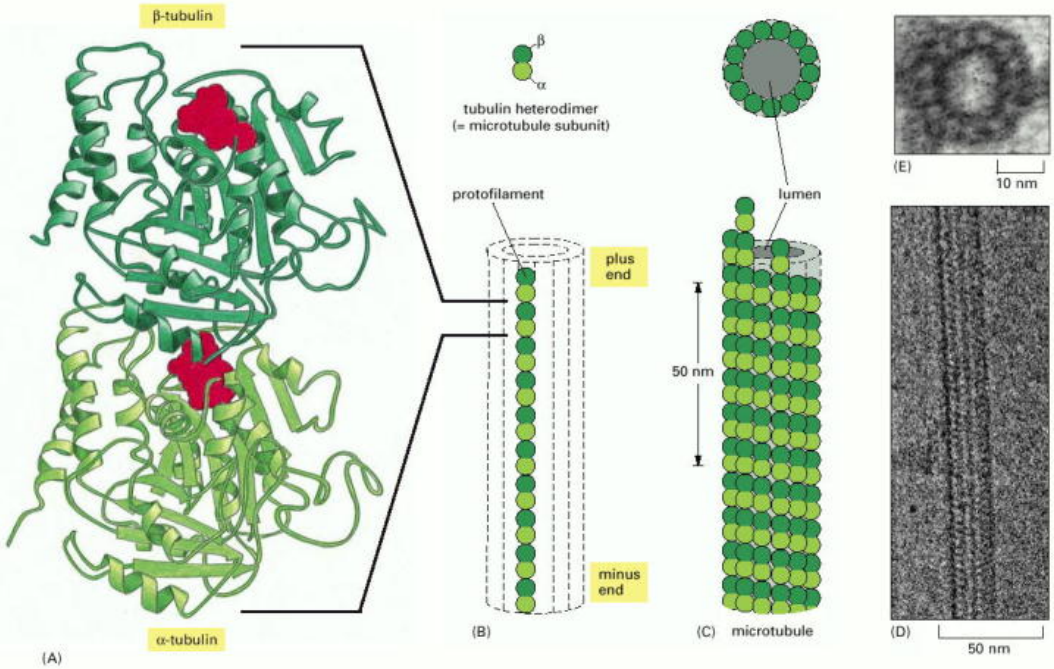

Figure 16-6. The structure of a microtubule and its subunit. (A) The subunit of each protofilament is a tubulin heterodimer, formed from a very tightly linked pair of α- and β-tubulin monomers. The GTP molecule in the α-tubulin monomer is so tightly bound that it can be considered an integral part of the protein. The GTP molecule in the β-tubulin monomer, however, is less tightly bound and has an important role in filament dynamics. Both nucleotides are shown in *red*. (B) One tubulin subunit (α-β heterodimer) and one protofilament are shown schematically. Each protofilament consists of many adjacent subunits with the same orientation. (C) The microtubule is a stiff hollow tube formed from 13 protofilaments aligned in parallel. (D) A short segment of a microtubule viewed in an electron microscope. (E) Electron micrograph of a cross section of a microtubule showing a ring of 13 distinct protofilaments. (D, courtesy of Richard Wade; E, courtesy of Richard Linck.)

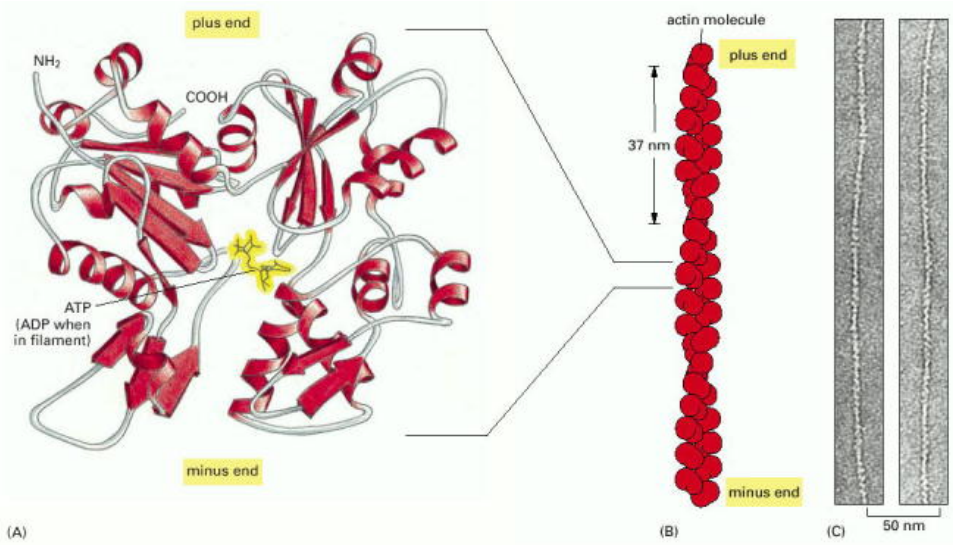

Figure 16-7. The structures of an actin monomer and actin filament. (A) The actin monomer has a nucleotide (either ATP or ADP) bound in a deep cleft in the center of the molecule. (B) Arrangement of monomers in a filament. Although the filament is often described as a single helix of monomers, it can also be thought of as consisting of two protofilaments, held together by lateral contacts, which wind around each other as two parallel strands of a helix, with a twist repeating every 37 nm. All the subunits within the filament have the same orientation. (C) Electron micrographs of negatively stained actin filaments. (C, courtesy of Roger Craig.)

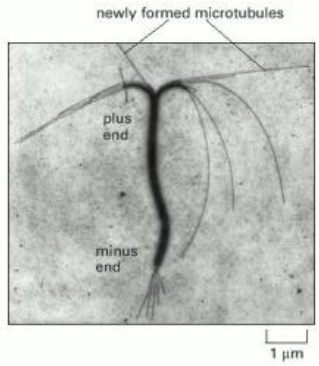

Figure 16-8. The preferential growth of microtubules at the plus end. Both microtubules and actin filaments grow faster at one end than at the other. In this case, a stable bundle of microtubules obtained from the core of a cilium (discussed later) was incubated with tubulin subunits under polymerizing conditions. Microtubules grow fastest from the plus end of the microtubule bundle, the end at the *top* in this micrograph. (Courtesy of Gary Borisy.)

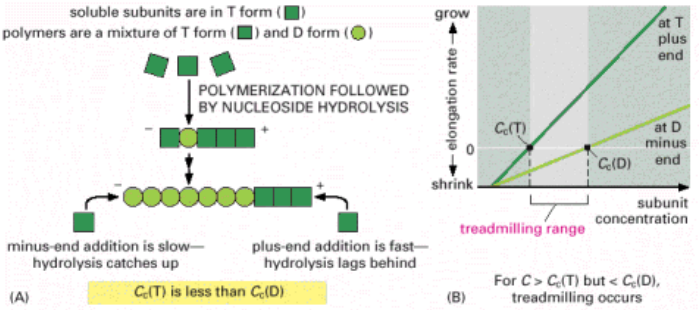

Figure 16-9. The treadmilling of an actin filament or microtubule, made possible by the nucleoside triphosphate hydrolysis that follows subunit addition. (A) Explanation for the different critical concentrations (C_c) at the plus and minus ends. Subunits with bound nucleoside triphosphate (T-form subunits) polymerize at both ends of a growing filament, and then undergo nucleotide hydrolysis in the filament lattice. As the filament grows, elongation is faster than hydrolysis at the plus end in this example, and the terminal subunits at this end are therefore always in the T form. However, hydrolysis is faster than elongation at the minus end, and so terminal subunits at this end are in the D form. (B) Treadmilling occurs at intermediate concentrations of free subunits. The critical concentration for polymerization on a filament end in the T form is lower than for a filament end in the D form. If the actual subunit concentration is somewhere between these two values, the plus end grows while the minus end shrinks, resulting in treadmilling.

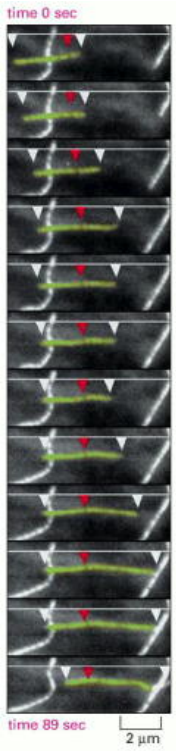

Figure 16-10. Treadmilling behavior of a microtubule, as observed in a living cell. A cell was injected with tubulin that had been covalently linked to the fluorescent dye rhodamine, so that approximately 1 tubulin subunit in 20 was fluorescent. The fluorescence of individual microtubules was then observed with a sensitive electronic camera. The microtubule shown appears to be sliding from *left* to *right*, but, in fact, the microtubule lattice remains stationary (as shown by the dark mark indicated by the *red* arrowhead), while the plus end (on the *right*) grows and the minus end (on the *left)* shrinks. At the same time, the plus end is displaying dynamic instability. (From C.M. Waterman-Storer and E.D. Salmon, *J. Cell Biol.* 139:417434, 1997. © The Rockefeller University Press.)

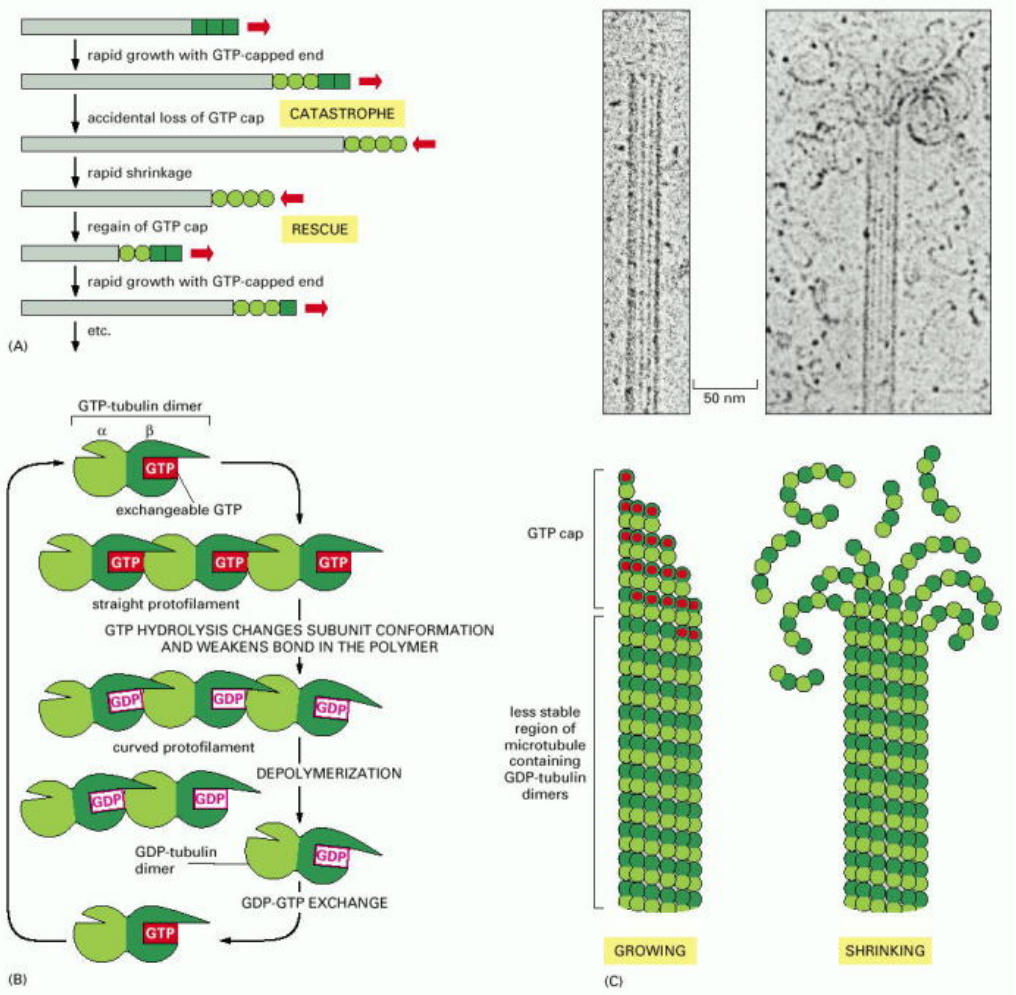

Figure 16-11. Dynamic instability due to the structural differences between a growing and a shrinking microtubule end. (A) If the free tubulin concentration in solution is between the critical values indicated in Figure 16-9, a single microtubule end may undergo transitions between a growing state and a shrinking state. A growing microtubule has GTP-containing subunits at its end, forming a GTP cap. If nucleotide hydrolysis proceeds more rapidly than subunit addition, the cap is lost and the microtubule begins to shrink, an event called a "catastrophe." But GTP-containing subunits may still add to the shrinking end, and if enough add to form a new cap, then microtubule growth resumes, an event called "rescue." (B) Model for the structural consequences of GTP hydrolysis in the microtubule lattice. The addition of GTP-containing tubulin subunits to the end of a protofilament causes the end to grow in a linear conformation that can readily pack into the cylindrical wall of the microtubule. Hydrolysis of GTP after assembly changes the conformation of the subunits and tends to force the protofilament into a curved shape that is less able to pack into the microtubule wall. (C) In an intact microtubule, protofilaments made from GDP-containing subunits are forced into a linear conformation by the many lateral bonds within the microtubule wall, given a stable cap of GTP-containing subunits. Loss of the GTP cap, however, allows the GDP-containing protofilaments to relax into their more curved conformation. This leads to a progressive disruption of the microtubule. Above the drawings of a growing and a shrinking microtubule, electron micrographs show actual microtubules in each of these two states, as observed in preparations in vitreous ice. Note particularly the curling, disintegrating GDP-containing protofilaments at the end of the shrinking microtubule. (C, courtesy of E.M. Mandelkow, E. Mandelkow and R.A. Milligan, *J. Cell Biol.* 114:977991, 1991. © The Rockefeller University Press.)

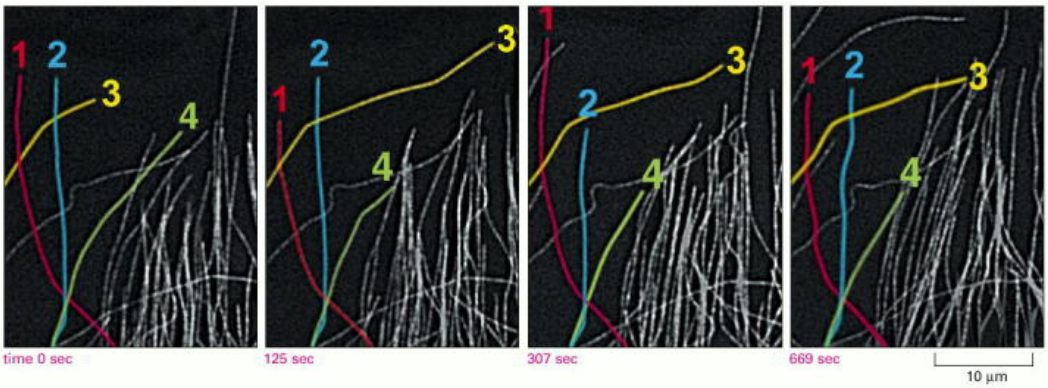

Figure 16-12. Direct observation of the dynamic instability of microtubules in a living cell. Microtubules in a newt lung epithelial cell were observed after the cell was injected with a small amount of rhodamine labeled tubulin, as in Figure 16-10. The dynamic instability of microtubules at the edge of the cell can be readily observed. Four individual microtubules are highlighted for clarity; each of these shows alternating shrinkage and growth. (Courtesy of Wendy C. Salmon and Clare Waterman-Storer.)

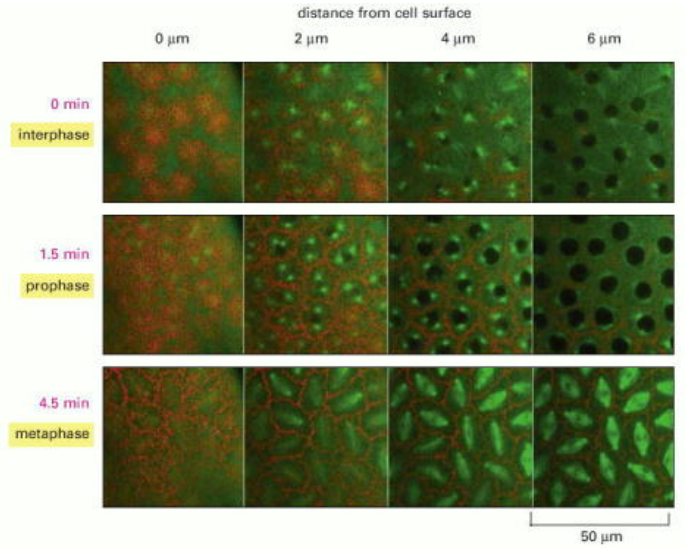

Figure 16-13. The rapid changes in cytoskeletal organization observed during the development of a *Drosophila* early embryo. In this giant multinuclear cell, the early nuclear divisions occur every 10 minutes or so in a common cytoplasm. The rapid rearrangements of the actin filaments *(red)* and microtubules *(green)* seen here in a living embryo, are required to separate the chromosomes at mitosis, while keeping each nucleus from colliding with its neighbors. (Courtesy of William Sullivan.)

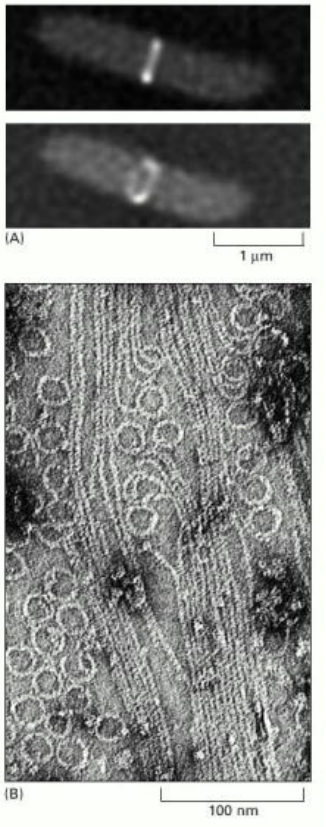

Figure 16-14. The bacterial FtsZ protein, a tubulin homolog in procaryotes. (A) A band of FtsZ protein forms a ring in a dividing bacterial cell. This ring has been labeled by fusing the FtsZ protein to the *g*reen *f*luorescent *p*rotein (GFP) and observing the living *E. coli* cells with a fluorescence microscope. *Top*, side view shows the ring as a bar in the middle of the dividing cell. *Bottom*, rotated view showing the ring structure. (B) FtsZ filaments and rings, formed *in vitro*, as visualized using electron microscopy. Compare this image with that of the microtubule shown on the *right* in Figure 16-11. (A, from X. Ma, D.W. Ehrhardt and W. Margolin, *Proc. Natl. Acad. Sci. USA* 93:1299913003, 1996. © National Academy of Sciences; B, from H.A. Erickson et al., *Proc. Natl. Acad. Sci. USA* 93:519523, 1996. © National Academy of Sciences.)

Figure 16-15. Actin at the crossroads. Actin binds to a very large variety of accessory proteins in all eucaryotic cells. This diagram shows most of the interactions that have been demonstrated, using either genetic or biochemical techniques, in the yeast *Saccharomyces cerevisiae*. Accessory proteins that operate in the same intracellular process are shown in the same color, as indicated in the key. (Adapted from D. Botstein et al., in The Molecular and Cellular Biology of the Yeast *Saccharomyces* [J.R. Broach, J.R. Pringle, E.W. Jones, eds.], Cold Spring Harbor, NY: Cold Spring Harbor Laboratory Press, 1991.)

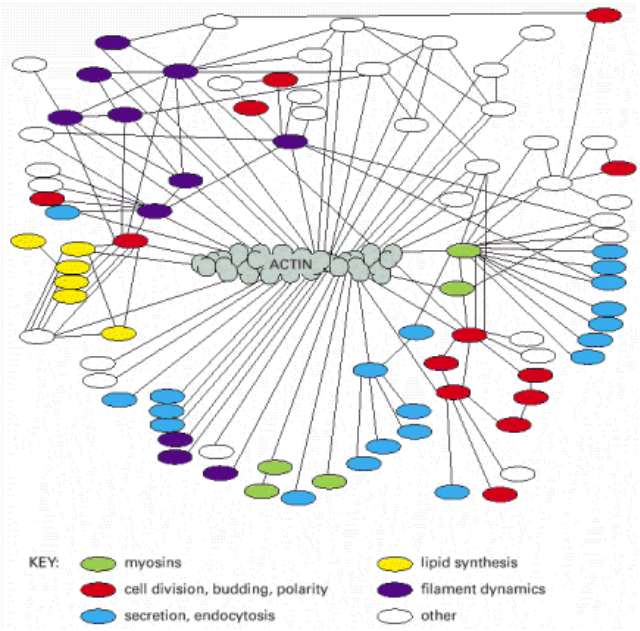

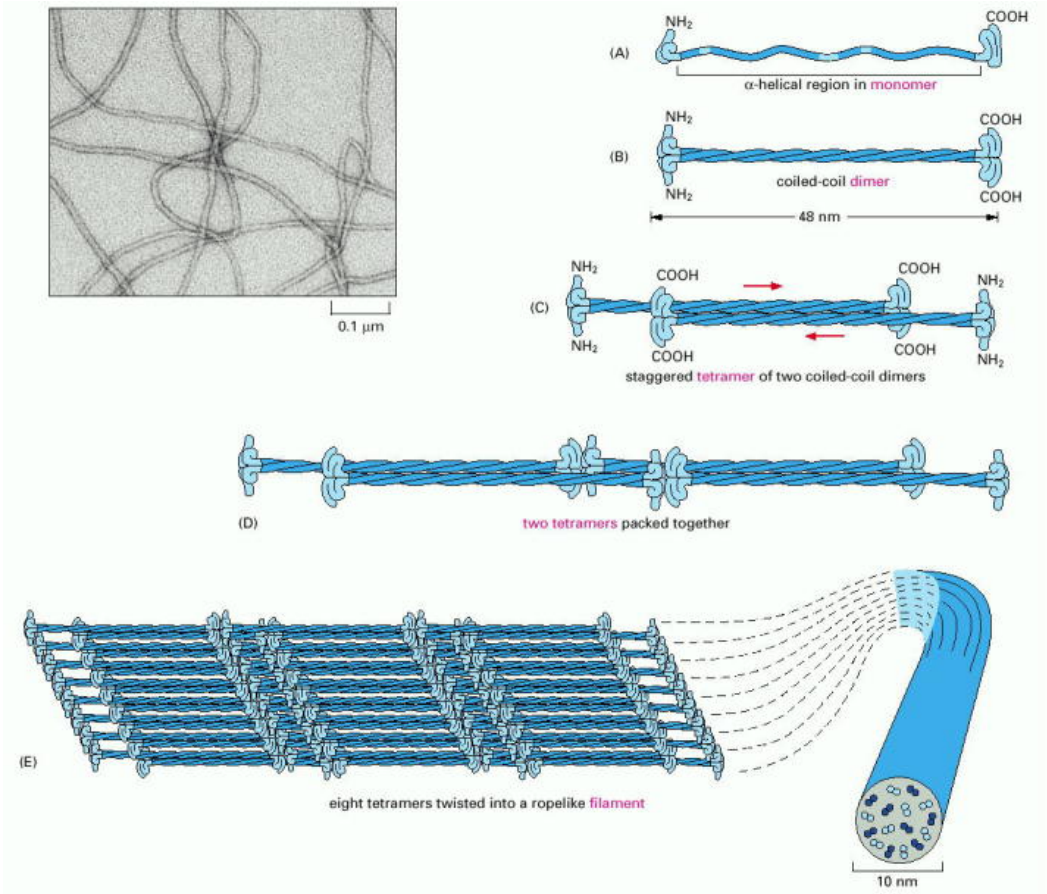

Figure 16-16. A model of intermediate filament construction. The monomer shown in (A) pairs with an identical monomer to form a dimer (B), in which the conserved central rod domains are aligned in parallel and wound together into a coiled coil. (C) Two dimers then line up side by side to form an antiparallel tetramer of four polypeptide chains. The tetramer is the soluble subunit of intermediate filaments. (D) Within each tetramer, the two dimers are offset with respect to one another, thereby allowing it to associate with another tetramer. (E) In the final 10-nm rope-like filament, tetramers are packed together in a helical array, which has 16 dimers in cross-section. Half of these dimers are pointing in each direction. An electron micrograph of intermediate filaments are shown on the upper left. (Electron micrograph courtesy of Roy Quinlan.)

Figure 16-17. Mechanical properties of actin, tubulin, and intermediate filament polymers. Networks composed of microtubules, actin filaments, or a type of intermediate filament called vimentin, all at equal concentration, were exposed to a shear force in a viscometer, and the resulting degree of stretch was measured. The results show that microtubule networks are easily deformed but that they rupture (indicated by *red starburst)* and begin to flow without limit when stretched beyond 150% of their original length. Actin filament networks are much more rigid, but they also rupture easily. Intermediate filament networks,

by contrast, are not only easily deformed, but they withstand large stresses and strains without rupture; they are thereby well suited to maintain cell integrity. (Adapted from P. Janmey et al., *J. Cell Biol*. 113:155160, 1991.)

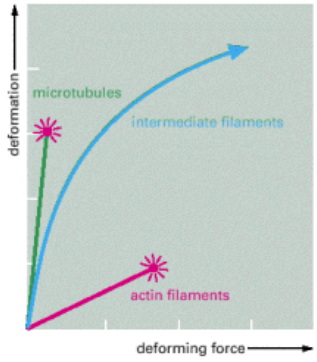

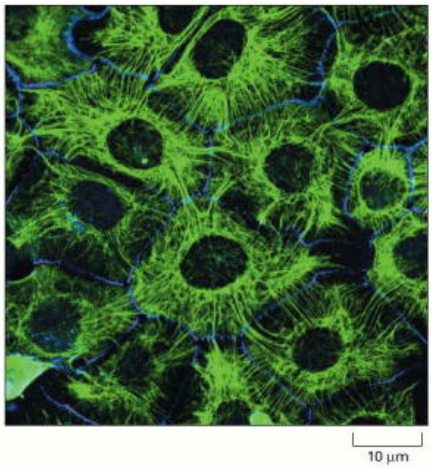

Figure 16-18. Keratin filaments in epithelial cells. Immunofluorescence micrograph of the network of keratin filaments *(green)* in a sheet of epithelial cells in culture. The filaments in each cell are indirectly connected to those of its neighbors by desmosomes (discussed in Chapter 19). A second protein *(blue)* has been stained to reveal the location of the cell boundaries. (Courtesy of Kathleen Green and Evangeline Amargo.)

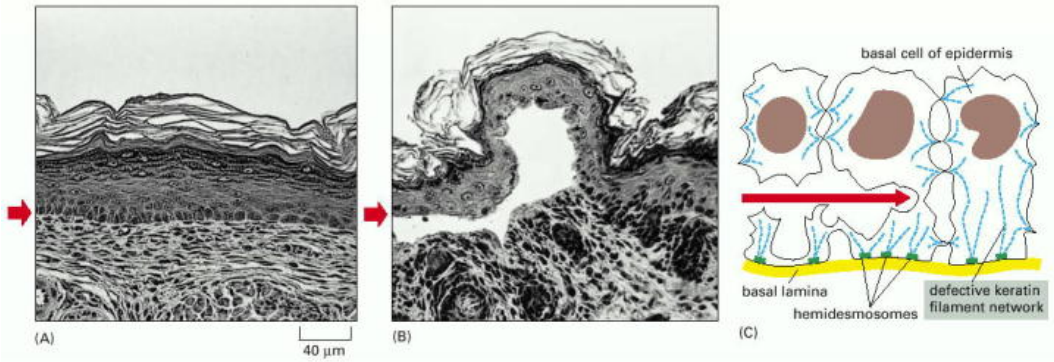

Figure 16-19. Blistering of the skin caused by a mutant keratin gene. A mutant gene encoding a truncated keratin protein (lacking both the N- and C-terminal domains) was expressed in a transgenic mouse. The defective protein assembles with the normal keratins and thereby disrupts the keratin filament network in the basal cells of the skin. Light micrographs of cross sections of normal (A) and mutant (B) skin show that the blistering results from the rupturing of cells in the basal layer of the mutant epidermis (small *red* arrows). (C) A sketch of three cells in the basal layer of the mutant epidermis, as observed by electron microscopy. As indicated by the *red* arrow, the cells rupture between the nucleus and the hemidesmosomes (discussed in Chapter 19), which connect the keratin filaments to the underlying basal lamina. (From P.A. Coulombe et al., *J. Cell Biol*. 115:16611674, 1991. © The Rockefeller University Press.)

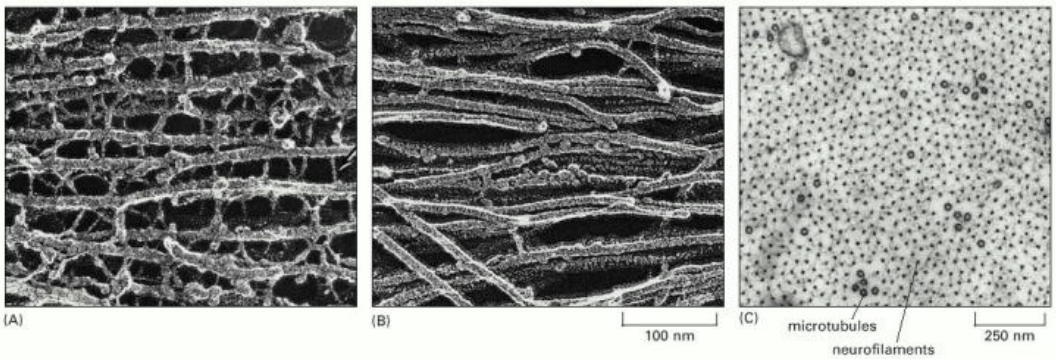

Figure 16-20. Two types of intermediate filaments in cells of the nervous system. (A) Freeze-etch electron microscopic image of neurofilaments in a nerve cell axon, showing the extensive cross-linking through protein cross-bridges - an arrangement believed to give this long cell process great tensile strength. The cross-bridges are formed by the long, nonhelical extensions at the C-terminus of the largest neurofilament protein (NF-H). (B) Freeze-etch image of glial filaments in glial cells, showing that these intermediate filaments are smooth and have few cross-bridges. (C) Conventional electron micrograph of a cross section of an axon showing the regular side-to-side spacing of the neurofilaments, which greatly outnumber the microtubules. (A and B, courtesy of Nobutaka Hirokawa; C, courtesy of John Hopkins.)

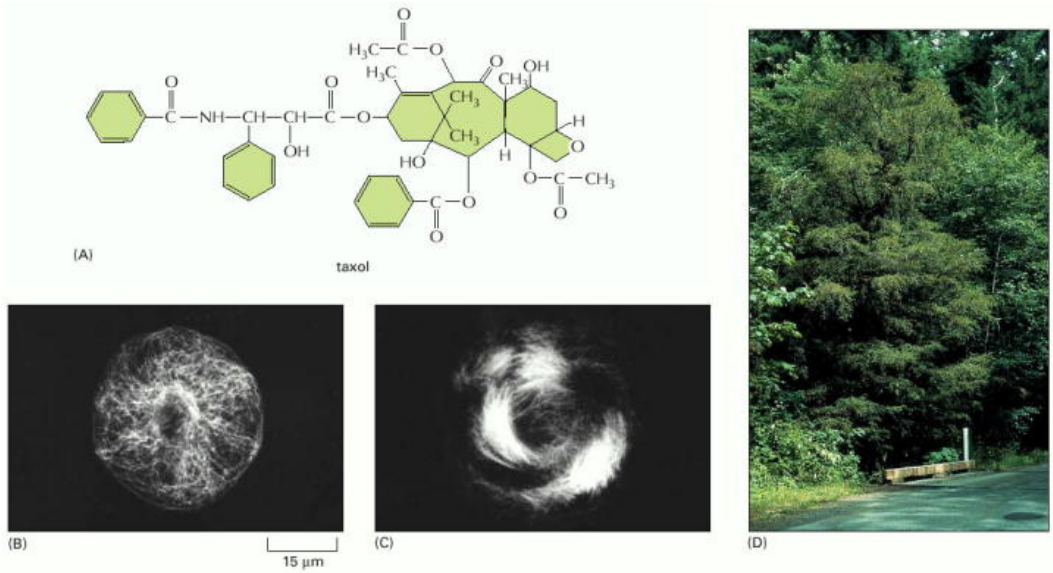

Figure 16-21. Effect of the drug taxol on microtubule organization. (A) Molecular structure of taxol. Recently, organic chemists have succeeded in synthesizing this complex molecule, which is widely used for cancer treatment. (B) Immunofluorescence micrograph showing the microtubule organization in a liver epithelial cell before the addition of taxol. (C) Microtubule organization in the same type of cell after taxol treatment. Note the thick circumferential bundles of microtubules around the periphery of the cell. (D) A Pacific yew tree, the natural source of taxol. (B, C from N.A. Gloushankova et al., *Proc. Natl. Acad. Sci. USA* 91:85978601, 1994. © National Academy of Sciences; D, courtesy of A.K. Mitchell 2001. © Her Majesty the Queen in Right of Canada, Canadian Forest Service.)

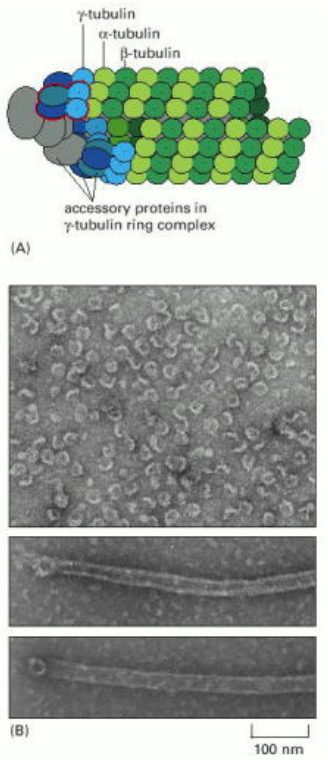

Figure 16-22. Polymerization of tubulin nucleated by γ-tubulin ring complexes. (A) Model for the nucleation of microtubule growth by the γ-TuRC. The red outline indicates a pair of proteins bound to two molecules of γ-tubulin; this group can be isolated as a separate subcomplex of the larger ring. (B) Electron micrographs of purified γ-tubulin ring complexes *(top)* and single microtubules nucleated from the purified γ-tubulin ring complexes *(middle* and *bottom).* (A, modified from M. Moritz et al., *Nature Cell Biol*. 2:365370, 2000; B, courtesy of Y. Zheng et al., *Nature* 378:578583, 1994. © Macmillan Magazines Ltd.)

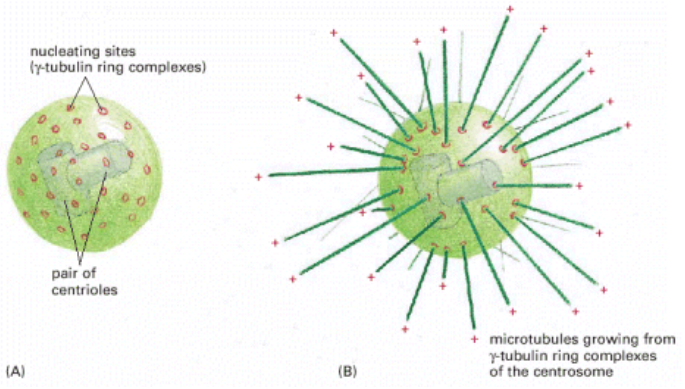

Figure 16-23. The centrosome. (A) The centrosome is the major MTOC of animal cells. Located in the cytoplasm next to the nucleus, it consists of an amorphous matrix of protein containing the γ-tubulin ring complexes that nucleate microtubule growth. This matrix is organized by a pair of centrioles, as described in the text. (B) A centrosome with attached microtubules. The minus end of each microtubule is embedded in the centrosome, having grown from a γ-tubulin ring complex, whereas the plus end of each microtubule is free in the cytoplasm.

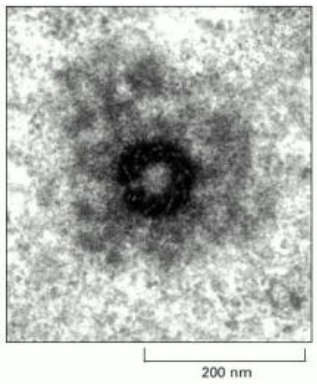

Figure 16-24. A centriole in the centrosome. An electron micrograph of a thick section of a centrosome showing an end-on view of a centriole. The ring of modified microtubules of the centriole is visible, surrounded by the fibrous centrosome matrix. (Courtesy of P. Witt and G.G. Borisy.)

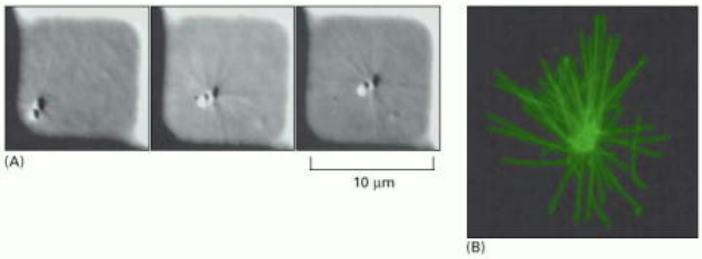

Figure 16-25. The center-seeking behavior of a centrosome. (A) Small square wells were micromachined into a plastic substrate. A single centrosome was placed into one of these wells, along with tubulin subunits in solution. As the microtubules polymerize, nucleated by the centrosome, they push against the walls of the well. The requirement for equal pushing in all directions if the position is to be stabilized forces the centrosome to the center of the well. The three pictures were taken at three-minute intervals. (B) A similar self-centered centrosome, fixed and stained to show the distribution of the microtubules pushing on all four walls of the enclosure. (From T. E. Holy et al., *Proc. Natl. Acad. Sci. USA* 94:62286231, 1997. © National Academy of Sciences.)

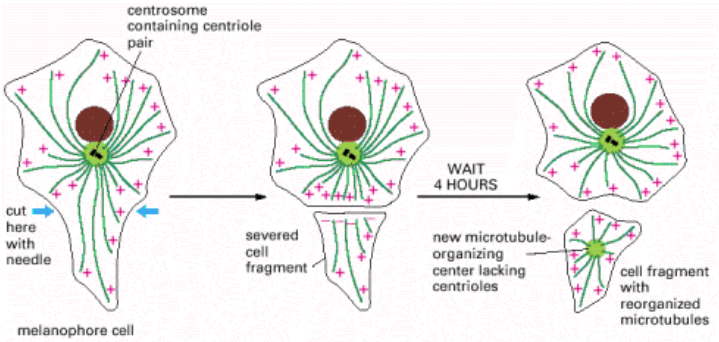

Figure 16-26. A microtubule array can find the center of a cell. After the arm of a fish pigment cell is cut off with a needle, the microtubules in the detached cell fragment reorganize so that their minus ends end up near the center of the fragment, buried in a new microtubule-organizing center.

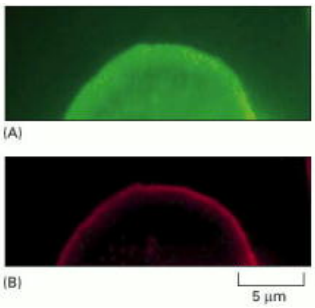

Figure 16-27. The tip of the leading edge of a cell nucleates actin filaments. Fibroblasts in culture were gently permeabilized using a nonionic detergent and were then incubated with rhodamine-labeled actin molecules to visualize newly formed actin filaments *(red).* After 5 minutes, the cells were fixed and stained with fluorescein-labeled phalloidin to stain all actin filaments *(green).* (A) All of the actin filaments, most of which were formed before the cells were permeabilized, are shown in *green*. (B) The location of the newly formed actin filaments *(red)* show that the leading edge is the predominant site of actin filament assembly in the cell. Further studies show that this is because new actin filaments are constantly being nucleated here. (From M.H. Symons and T.J. Mitchison, *J. Cell Biol*. 114:503513, 1991. © The Rockefeller University Press.)

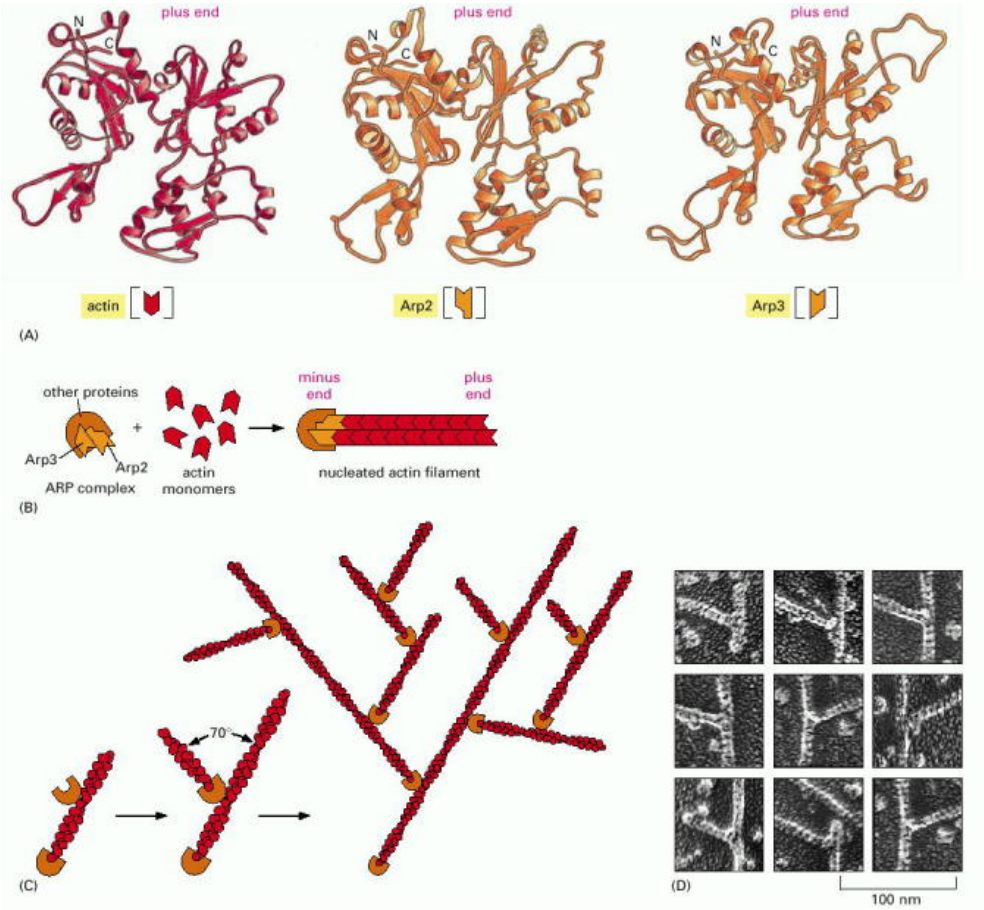

Figure 16-28. Nucleation and actin web formation by the ARP complex. (A)The structures of Arp2 and Arp3, compared to the structure of actin. Although the face of the molecule equivalent to the plus end *(top)* in both Arp2 and Arp3 is very similar to the plus end of actin itself, differences on the sides and minus end *(bottom)* prevent these actin-related proteins from forming filaments on their own or coassembling into filaments with actin. (B) A model for actin filament nucleation by the ARP complex. Arp2 and Arp3 may be held by their accessory proteins in an orientation that resembles the plus end of an actin filament. Actin subunits can then assemble onto this structure, bypassing the rate-limiting step of filament nucleation (see Figure 16-5). (C) The ARP complex nucleates filaments more efficiently when it is bound to the side of a preexisting actin filament. The result is a filament branch that grows at a 70° angle relative to the original filament. Repeated rounds of branching nucleation result in a treelike web of actin filaments. (D) Electron micrographs of branched actin filaments formed by mixing purified actin subunits with purified ARP complexes. (D, courtesy of R.D. Mullins et al., *Proc. Natl. Acad. Sci. USA* 95:61816186, 1998. © National Academy of Sciences.)

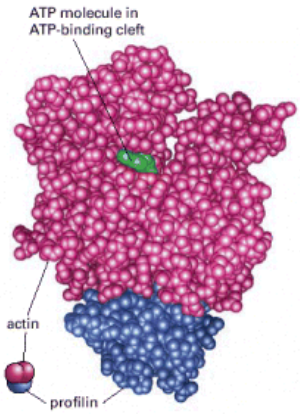

Figure 16-29. Profilin bound to an actin monomer. The profilin protein molecule is shown in *blue*, and the actin in *red*. ATP is shown in *green*. Profilin binds to the face of actin opposite the ATP-binding cleft. This profilin-actin heterodimer can therefore bind to and elongate the plus end of an actin filament, but it is sterically prevented from binding to the minus end. (Courtesy of Michael Rozycki and Clarence E. Schutt.)

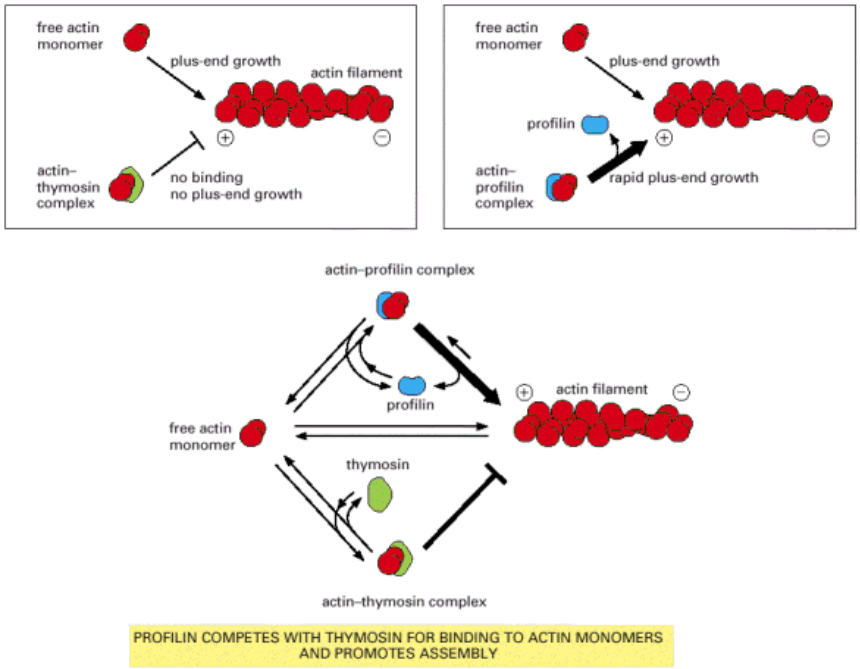

Figure 16-30. Effects of thymosin and profilin on actin polymerization. An actin monomer bound to thymosin is sterically prevented from binding to and elongating the plus end of an actin filament. An actin monomer bound to profilin, on the other hand, is capable of elongating a filament. Thymosin and profilin cannot both bind to a single actin monomer at the same time. In a cell in which most of the actin monomer is bound to thymosin, the activation of a small amount of profilin can produce rapid filament assembly. As indicated, profilin binds to actin monomers that are transiently released from the thymosin-bound monomer pool, shuttles them onto the plus ends of actin filaments, and is then released and recycled for further rounds of filament elongation.

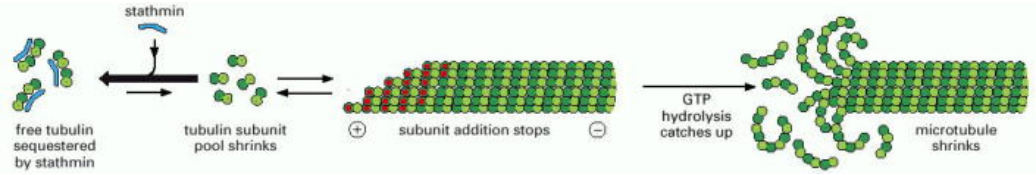

Figure 16-31. Effects of stathmin on microtubule polymerization. Polymerization of free tubulin subunits to form microtubules is an energetically favorable reaction. As long as abundant free tubulin subunits are available, microtubule elongation continues. Stathmin sequesters free tubulin subunits, binding two tubulin αβ-heterodimers per stathmin molecule. As the pool of free tubulin subunits shrinks, microtubule elongation slows. This makes it more likely that the rate of GTP hydrolysis will catch up with the rate of subunit addition, and the GTP cap will be lost, resulting in a transition of the microtubule from the growing state to the shrinking state. Stathmin has a second activity that promotes this transition, which involves a direct interaction with a microtubule plus end (not shown). Stathmin is also called "oncoprotein 18," since its expression level is frequently increased in tumor cells, resulting in increased turnover of microtubules.

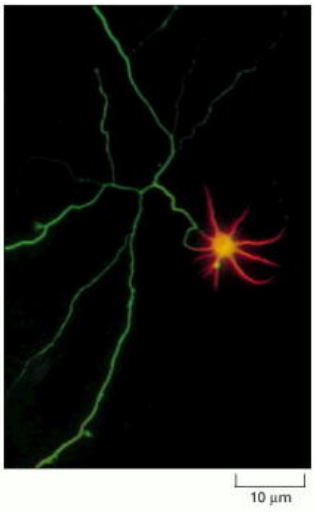

Figure 16-32. Localization of MAPs in axon and dendrites of a neuron. This immunofluorescence micrograph shows the distribution of tau staining *(green)* and MAP2 staining *(orange)* in a hippocampal neuron in culture. Whereas tau staining is confined to the axon (long and branched in this neuron), MAP2 staining is confined to the cell body and its dendrites. The antibody used here to detect tau binds only to unphosphorylated tau; phosphorylated tau is also present in dendrites. (Courtesy of James W. Mandell and Gary A. Banker.)

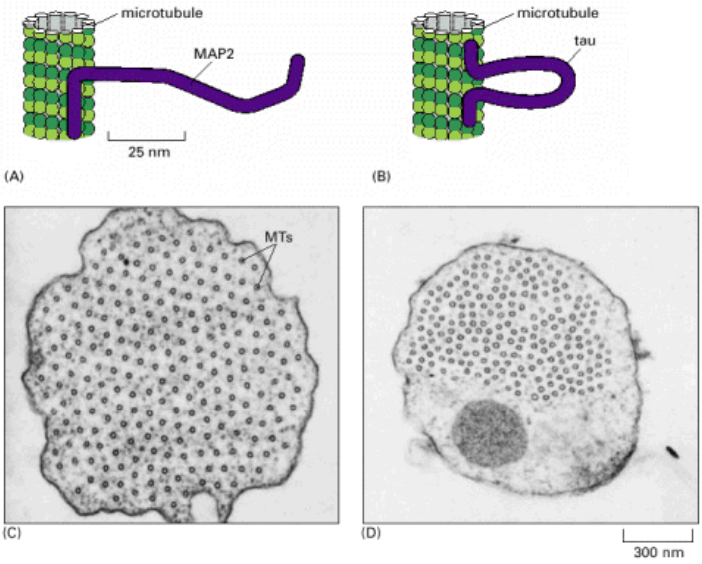

Figure 16-33. Organization of microtubule bundles by MAPs. (A) MAP2 binds along the microtubule lattice at one end and extends a long projecting arm with a second microtubule-binding domain at the other end. (B) Tau binds to the microtubule lattice at both its N- and C-termini, with a short projecting loop. (C) Electron micrograph showing a cross section through a microtubule bundle in a cell overexpressing MAP2. The regular spacing of the microtubules (MTs) in this bundle result from the constant length of the projecting arms of the MAP2. (D) Similar cross section through a microtubule bundle in a cell overexpressing tau. Here the microtubules are spaced more closely together than they are in (C) because of tau's relatively short projecting arm. (C and D, courtesy of V. Chen et al., *Nature* 360:674647, 1992. © Macmillan Magazines Ltd.)

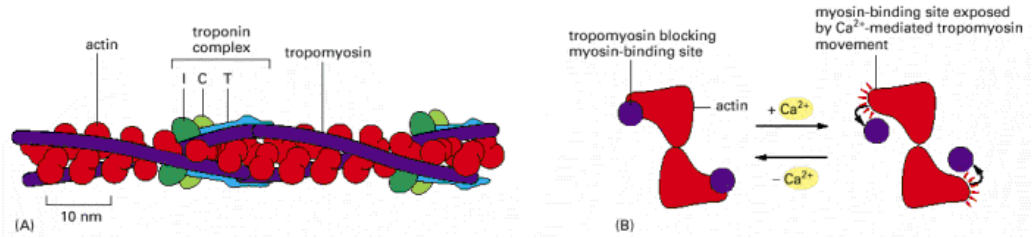

Figure 16-74. The control of skeletal muscle contraction by troponin. (A) A skeletal muscle cell thin filament, showing the positions of tropomyosin and troponin along the actin filament. Each tropomyosin molecule has seven evenly spaced regions with similar amino acid sequences, each of which is thought to bind to an actin subunit in the filament. (B) A thin filament shown end-on, illustrating how Ca^{2+} (binding to troponin) is thought to relieve the tropomyosin blockage of the interaction between actin and the myosin head. (A, adapted from G.N. Phillips, J.P. Fillers and C. Cohen, *J. Mol. Biol.* 192:111131, 1986. © Academic Press.)

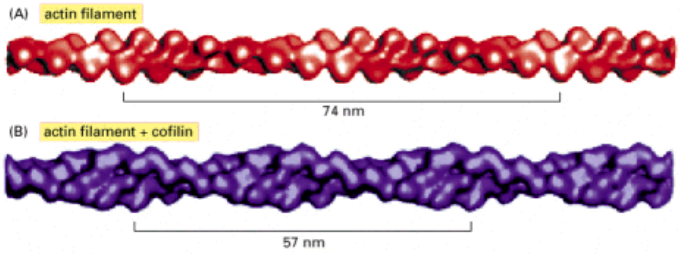

Figure 16-34. Twisting of an actin filament induced by cofilin. (A) Three-dimensional reconstruction from cryo-electron micrographs of filaments made of pure actin. The bracket shows the span of two turns of the actin helix. (B) Reconstruction of an actin filament coated with cofilin, which binds in a 1:1 stoichiometry to actin subunits all along the filament. Cofilin is a small protein (14 kilodaltons) compared to actin (43 kilodaltons), and so the filament appears only slightly thicker. The energy of cofilin binding serves to deform the actin filament lattice, twisting it more tightly so that the distance spanned by two turns of the helix is reduced. (From A. McGough et al., *J. Cell Biol.* 138:771781, 1997. © The Rockefeller University Press.)

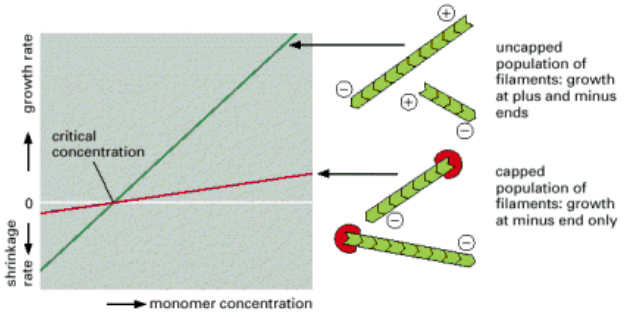

Figure 16-35. Filament capping and its effects on filament dynamics. A population of uncapped filaments adds and loses subunits at both the plus and minus ends, resulting in rapid growth or shrinkage, depending on the concentration of available free monomers *(green* line). In the presence of a protein that caps the plus end *(red* line), only the minus end is able to add or lose subunits; consequently, filament growth will be slower at all monomer concentrations above the critical concentration, and filament shrinkage will be slower at all monomer concentrations below the critical concentration. Plus-end capping of this type is widely used for actin filaments but not for microtubules.

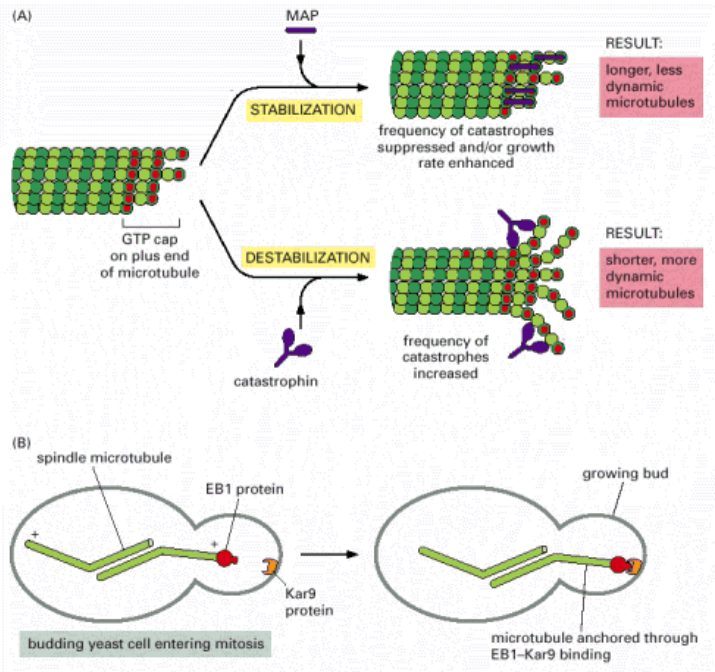

Figure 16-36. The effects of proteins that bind to microtubule ends. (A) The transition between microtubule growth and microtubule shrinking is controlled in cells by special proteins. A MAP such as XMAP215 stabilizes the end of a growing microtubule by its preferential binding there. Opposing its action are members of the kinesin superfamily (discussed later) designated here as catastrophins, but called by a variety of other names (such as, the Kin1 family that includes KIF2 in Figure 16-55). (B) Capping proteins help to localize microtubules. Here, the EBI microtubule capping protein interacts with localized Kar9 proteins in the budding yeast *Saccharomyces cerevisiae.* This interaction directs spindle microtubules into the growing bud during mitosis. A mutation in either protein causes the indicated spindle microtubules to lose their way. The EB1 protein is also found on the plus ends of microtubules in human cells.

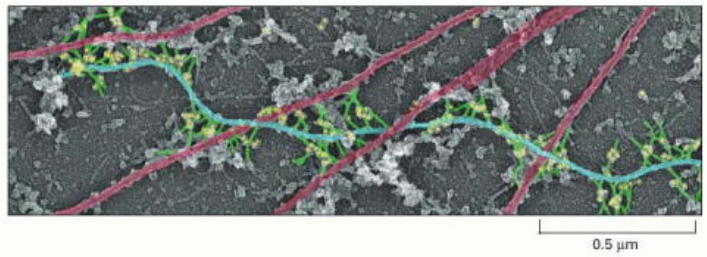

Figure 16-37. Plectin cross-linking of diverse cytoskeletal elements. Plectin *(green)* makes cross-links from intermediate filaments *(blue)* to other intermediate filaments, to microtubules *(red),* and to myosin thick filaments. In this electron micrograph, the dots *(yellow)* are gold particles linked to anti-plectin antibodies. The entire actin filament network was removed to reveal these proteins. (From T.M. Svitkina and G.G.Borisy, *J. Cell Biol.* 135:9911007, 1996. © The Rockefeller University Press.)

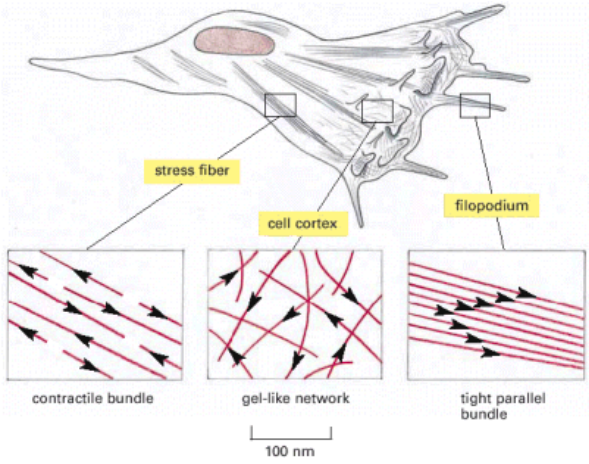

Figure 16-38. Actin arrays in a cell. A crawling cell, drawn to scale, is shown with three areas enlarged to show the arrangement of actin filaments. The actin filaments are shown in *red,* with arrowheads pointing toward the plus end. Stress fibers are contractile and exert tension. Filopodia are spike-like projections of the plasma membrane that allow a cell to explore its environments. The cortex underlies the plasma membrane.

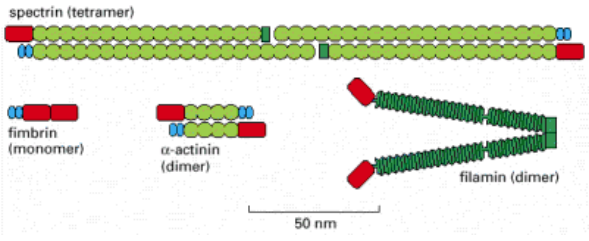

Figure 16-39. The modular structures of four actin-cross-linking proteins. Each of the proteins shown has two actin-binding sites *(red)* that are related in sequence. Fimbrin has two directly adjacent actin-binding sites, so that it holds its two actin filaments very close together (14 nm apart), aligned with the same polarity (see Figure 16-40A). The two actin-binding sites in α-actinin are separated by a spacer around 30 nm long, so that it forms more loosely packed actin bundles (see Figure 16-40). Filamin has two actin-binding sites with a V-shaped linkage between them, so that it cross-links actin filaments into a network with the filaments oriented almost at right angles to one another (see Figure 16-42). Spectrin is a tetramer of two α and two β subunits, and the tetramer has two actin-binding sites spaced about 200 nm apart (see Figure 10-31).

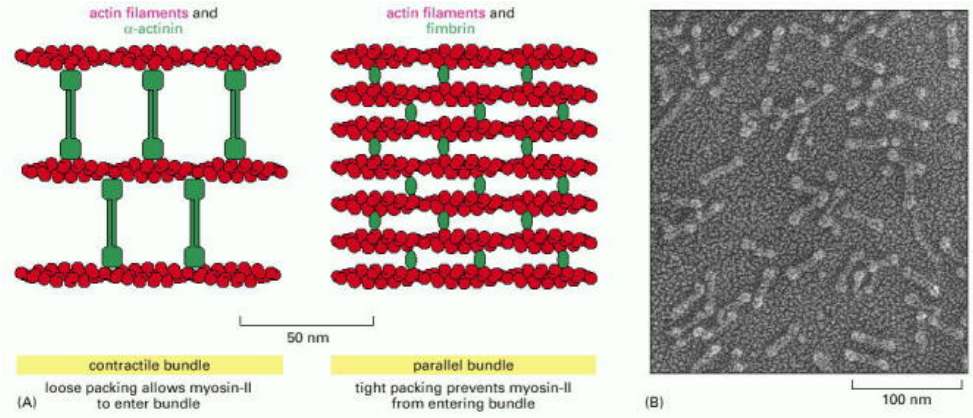

Figure 16-40. The formation of two types of actin filament bundles. (A) α-actinin, which is a homodimer, cross-links actin filaments into loose bundles, which allow the motor protein myosin II (not shown) to participate in the assembly. Fimbrin cross-links actin filaments into tight bundles, which exclude myosin. Fimbrin and α-actinin tend to exclude one another because of the very different spacing of the actin filament bundles that they form. (B) Electron micrograph of purified α-actinin molecules. (B, courtesy of John Heuser.)

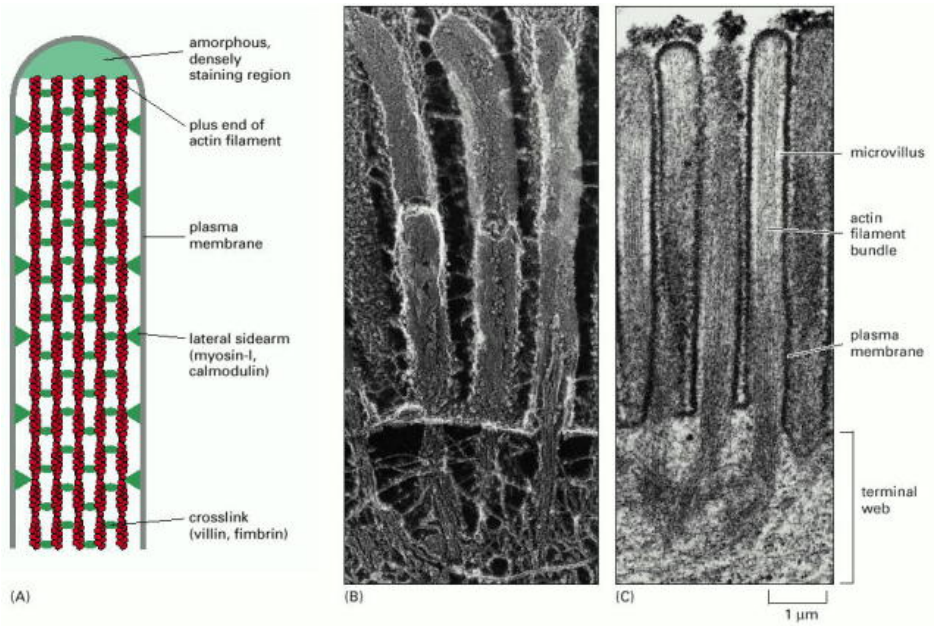

Figure 16-41. A microvillus. (A) A bundle of parallel actin filaments cross-linked by the actin-bundling proteins villin and fimbrin forms the core of a microvillus. Lateral sidearms (composed of myosin I and the Ca^{2+}-binding protein calmodulin) connect the sides of the actin filament bundle to the overlying plasma membrane. All the plus ends of the actin filaments are at the tip of the microvillus, where they are embedded in an amorphous, densely staining substance of unknown composition. (B) Freeze-fracture electron micrograph of the apical surface of an intestinal epithelial cell, showing microvilli. Actin bundles from the microvilli extend down into the cell and are rooted in the terminal web, where they are linked together by a complex set of proteins that includes spectrin and myosin II. Below the terminal web is a layer of intermediate filaments. (C) Thin section electron micrograph of microvilli. (B, courtesy of John Heuser; C, from P.T. Matsudaira and D.R. Burgess, *Cold Spring Harbor Symp. Quant. Biol*. 46:845854, 1985.)

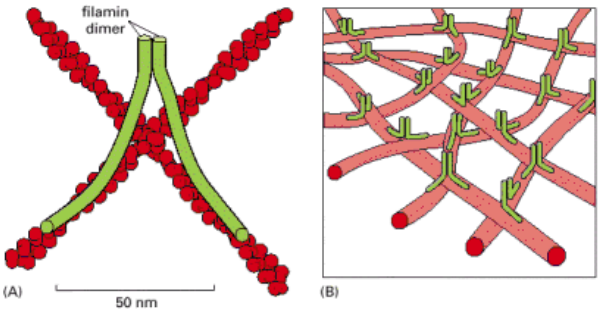

Figure 16-42. Filamin cross-links actin filaments into a three-dimensional network with the physical properties of a gel. (A) Each filamin homodimer is about 160 nm long when fully extended and forms a flexible, high-angle link between two adjacent actin filaments. (B) A set of actin filaments cross-linked by filamin forms a mechanically strong web or gel.

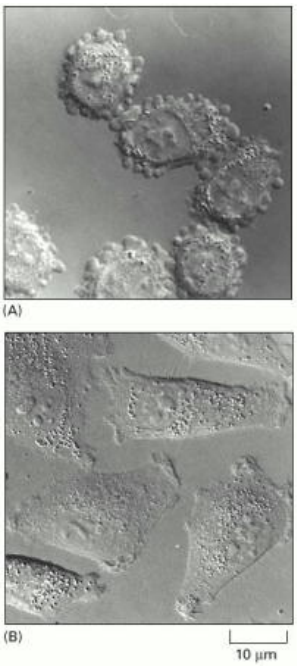

Figure 16-43. Loss of filamin causes abnormal cell motility. (A) A group of melanoma cells that have an abnormally low level of filamin. These cells are not able to make normal lamellipodia and instead are covered with membrane "blebs." As a result, they crawl poorly and tend not to metastasize. (B) The same melanoma cells in which filamin expression has been artificially restored. The cells now make normal lamellipodia and are highly metastatic. This example is one of many demonstrating the profound effect that the presence or absence of a single structural protein can have on cell morphology and motility. (From C. Cunningham et al., *J. Cell Biol.* 136:845857, 1997. © The Rockefeller University Press.)

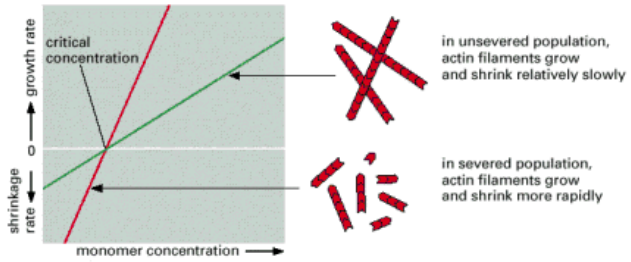

Figure 16-44. Filament severing and its effects on filament dynamics. Normally, filaments are able to gain and lose subunits only at their ends, limiting the maximum rates of growth and shrinkage of the total amount of actin in filamentous form *(green* line). If the filaments are severed into smaller pieces, the number of ends increases, so the increase in filament mass in the population can be faster at all monomer concentrations above the critical concentration, and the decrease in filament mass in the population can also be faster at all monomer concentrations below the critical concentration *(red* line). Thus, severing enhances the rate of filament dynamics.

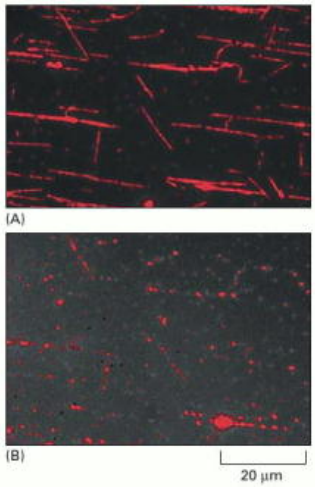

Figure 16-45. Microtubule severing by katanin. Taxol-stabilized, rhodamine-labeled microtubules were adsorbed on the surface of a glass slide, and purified katanin was added along with ATP. (A) There are a few breaks in the microtubules 30 seconds after the addition of katanin. (B) The same field 3 minutes after the addition of katanin. The filaments have been severed in many places, leaving a series of small fragments at the previous locations of the long microtubules. (From J.J. Hartman et al., *Cell* 93:277287, 1998. © Elsevier.)

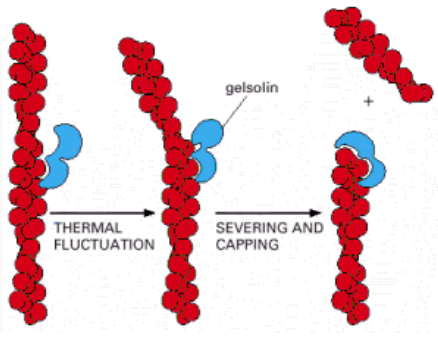

Figure 16-46. A model for actin filament severing by gelsolin. There are two actin-binding sites in the gelsolin protein. These sites allow gelsolin to bind both along the side and at the end of an actin filament. Filaments that have been severed by gelsolin remain capped at their plus ends. Villin, an actin-bundling protein (see Figure 16-41A), is a member of the same protein family as gelsolin, but it has gained another actin-binding site and lost its ability to sever filaments except at very high (nonphysiological) Ca^{2+} concentrations.

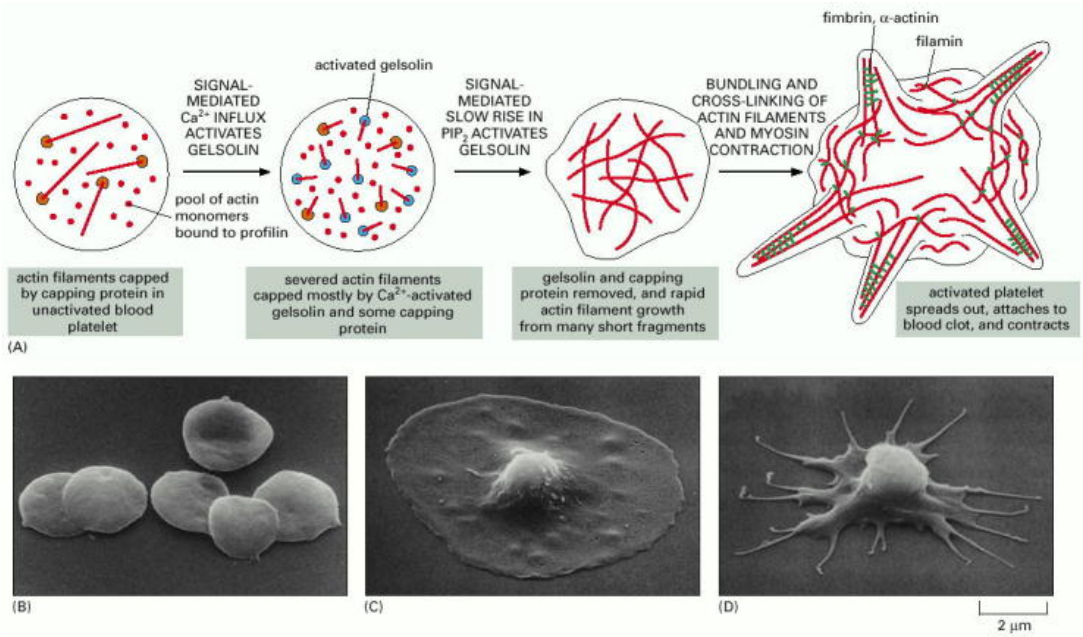

Figure 16-47. Platelet activation. (A) Platelet activation is a controlled sequence of actin filament severing, uncapping, elongation, recapping, and cross-linking that creates a dramatic shape change in the platelet. (B) Scanning electron micrograph of platelets prior to activation. (C) An activated platelet with its large spread lamellipodium. (D) An activated platelet at a later stage than the one shown in C, after myosin II-mediated contraction. (Courtesy of James G. White.)

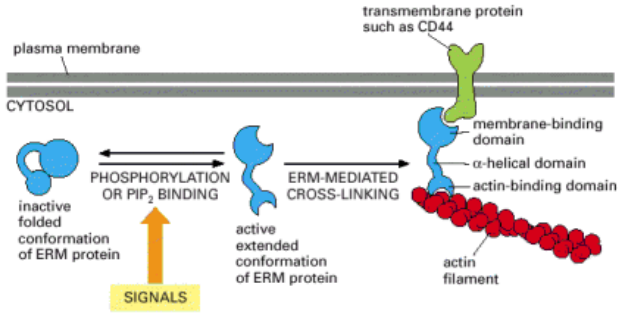

Figure 16-48. The role of ERM-family proteins in attaching actin filaments to the plasma membrane. Regulated unfolding of an ERM-family protein, caused by phosphorylation or by binding to PIP_2, exposes two binding sites, one for an actin filament and one for a transmembrane protein. Activation of ERM-family proteins can thereby generate and stabilize cell-surface protrusions that form in response to extracellular signals.

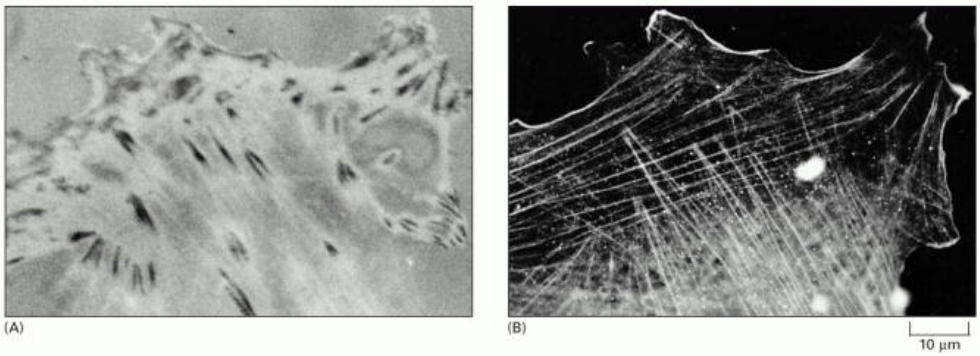

Figure 16-49. Focal contacts and stress fibers in a cultured fibroblast. (A) Focal contacts are best seen in living cells by reflection-interference microscopy. In this technique, light is reflected from the lower surface of a cell attached to a glass slide, and the focal contacts appear as dark patches. (B) Immunofluorescence staining of the same cell (after fixation) with antibodies to actin shows that most of the cell's actin filament bundles (or stress fibers) terminate at or close to a focal contact. (Courtesy of Grenham Ireland.)

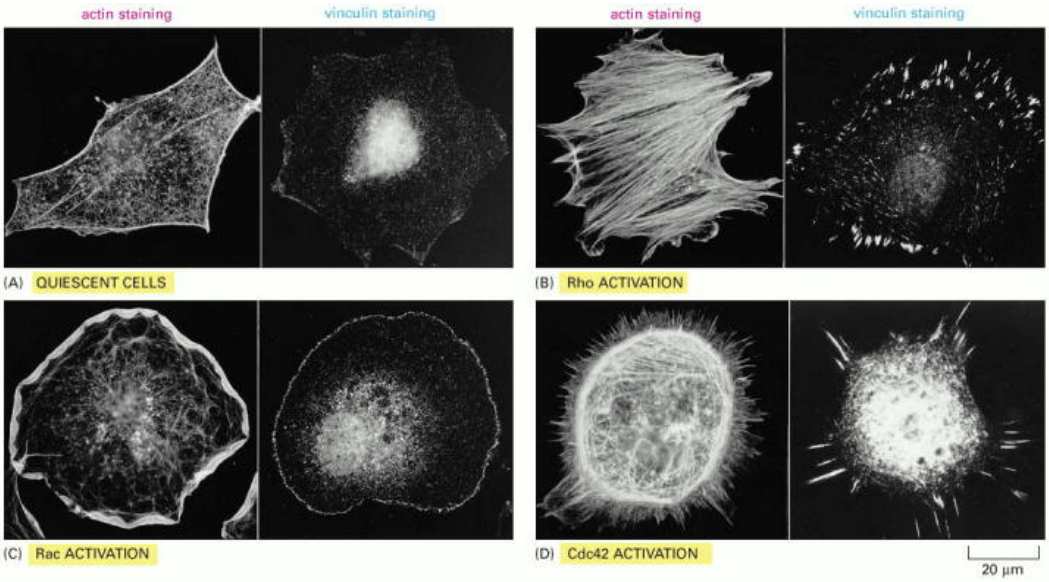

Figure 16-50. The dramatic effects of Rac, Rho, and Cdc42 on actin organization in fibroblasts. In each case, the actin filaments have been labeled with fluorescent phalloidin, and focal contacts have been located with an antibody against vinculin. (A) Serum-starved fibroblasts have actin filaments primarily in the cortex, and relatively few focal contacts. (B) Microinjection of a constitutively activated form of Rho causes the rapid assembly of many prominent stress fibers and focal contacts. (C) Microinjection of a constitutively activated form of Rac, a closely related monomeric GTPase, causes the formation of an enormous lamellipodium that extends from the entire circumference of the cell. (D) Microinjection of a constitutively activated form of Cdc42, another Rho family member, causes the protrusion of many long filopodia at the cell periphery that form adhesive contacts with the substratum. The distinct global effects of these three GTPases on the organization of the actin cytoskeleton are mediated by the actions of dozens of other protein molecules that are regulated by the GTPases. Many of these target proteins resemble the various actin-associated proteins that we have discussed in this chapter. (From A. Hall, *Science* 279:509514, 1998. © AAAS.)

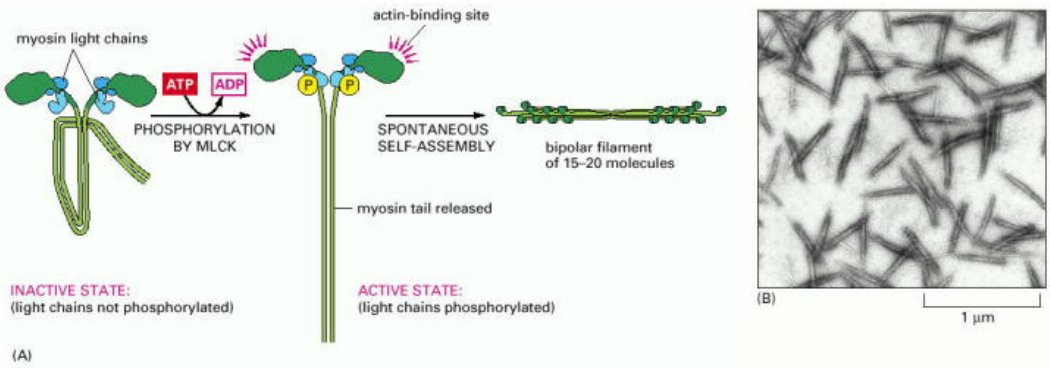

Figure 16-67. Light-chain phosphorylation and the regulation of the assembly of myosin II into thick filaments. (A) The controlled phosphorylation by the enzyme myosin light-chain kinase (MLCK) of one of the two light chains (the so-called regulatory light chain, shown in *light blue)* on nonmuscle myosin II in a test tube has at least two effects: it causes a change in the conformation of the myosin head, exposing its actin-binding site, and it releases the myosin tail from a "sticky patch" on the myosin head, thereby allowing the myosin molecules to assemble into short, bipolar, thick filaments. (B) Electron micrograph of negatively stained short filaments of myosin II that have been induced to assemble in a test tube by phosphorylation of their light chains. These myosin II filaments are much smaller than those found in skeletal muscle cells (see Figure 16-52). (B, courtesy of John Kendrick-Jones.)

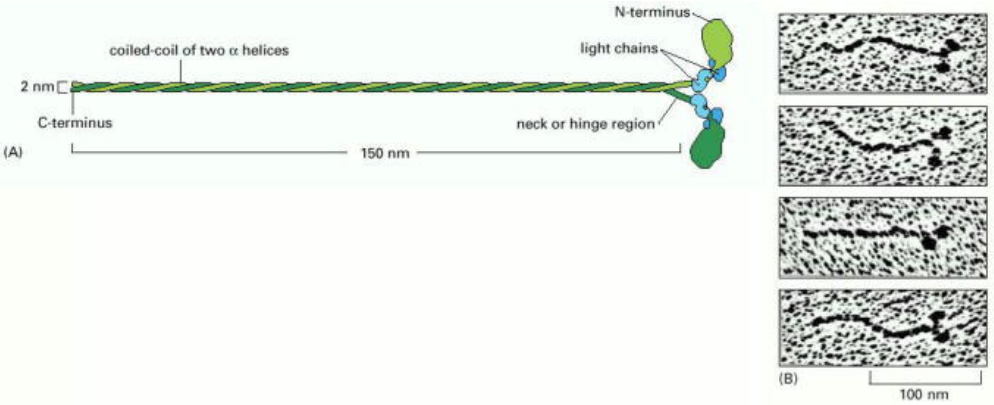

Figure 16-51. Myosin II. (A) A myosin II molecule is composed of two heavy chains (each about 2000 amino acids long *(green)* and four light chains *(blue).* The light chains are of two distinct types, and one copy of each type is present on each myosin head. Dimerization occurs when the two α helices of the heavy chains wrap around each other to form a coiled-coil, driven by the association of regularly spaced hydrophobic amino acids (see Figure 3-11). The coiled-coil arrangement makes an extended rod in solution, and this part of the molecule is called the tail. (B) The two globular heads and the tail can be clearly seen in electron micrographs of myosin molecules shadowed with platinum. (B, courtesy of David Shotton.)

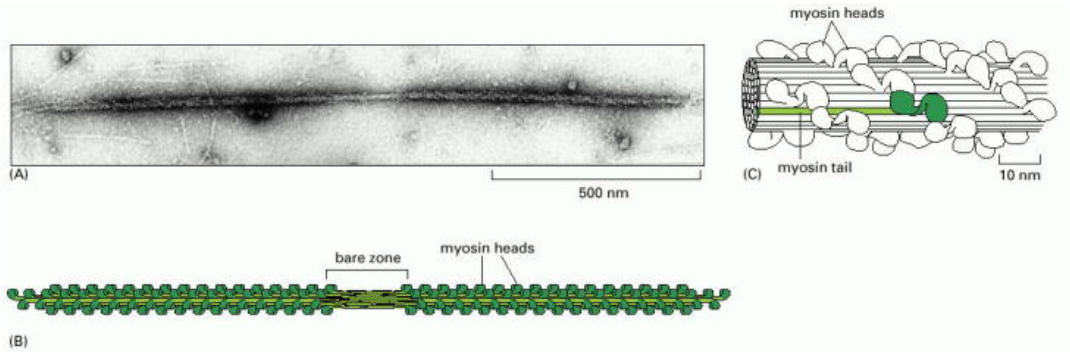

Figure 16-52. The myosin II bipolar thick filament. (A) Electron micrograph of a myosin II thick filament isolated from frog muscle. Note the central bare zone, which is free of head domains. (B) Schematic diagram, not drawn to scale. The myosin II molecules aggregate by means of their tail regions, with their heads projecting to the outside of the filament. The bare zone in the center of the filament consists entirely of myosin II tails. (C) A small section of a myosin II filament as reconstructed from electron micrographs. An individual myosin molecule is highlighted in *green*. (A, courtesy of Murray Stewart; C, based on R.A. Crowther, R. Padron and R. Craig, *J. Mol. Biol*. 184:429439, 1985. © Academic Press.)

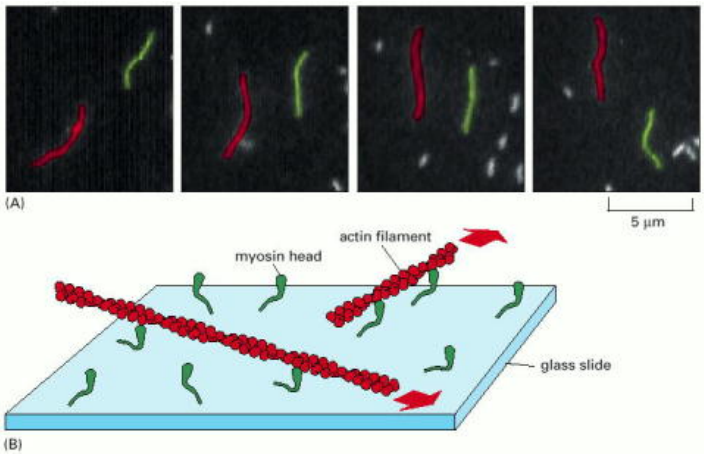

Figure 16-53. Direct evidence for the motor activity of the myosin head. In this experiment, purified S1 myosin heads were attached to a glass slide, and then actin filaments labeled with fluorescent phalloidin were added and allowed to bind to the myosin heads. (A) When ATP was added, the actin filaments began to glide along the surface, owing to the many individual steps taken by each of the dozens of myosin heads bound to each filament. The video frames shown in this sequence were recorded about 0.6 second apart; the two actin filaments shown (one *red* and one *green)* were moving in opposite directions at a rate of about 4 µm/sec. (B) Diagram of the experiment. The large *red* arrows indicate the direction of actin filament movement. (A, courtesy of James Spudich.)

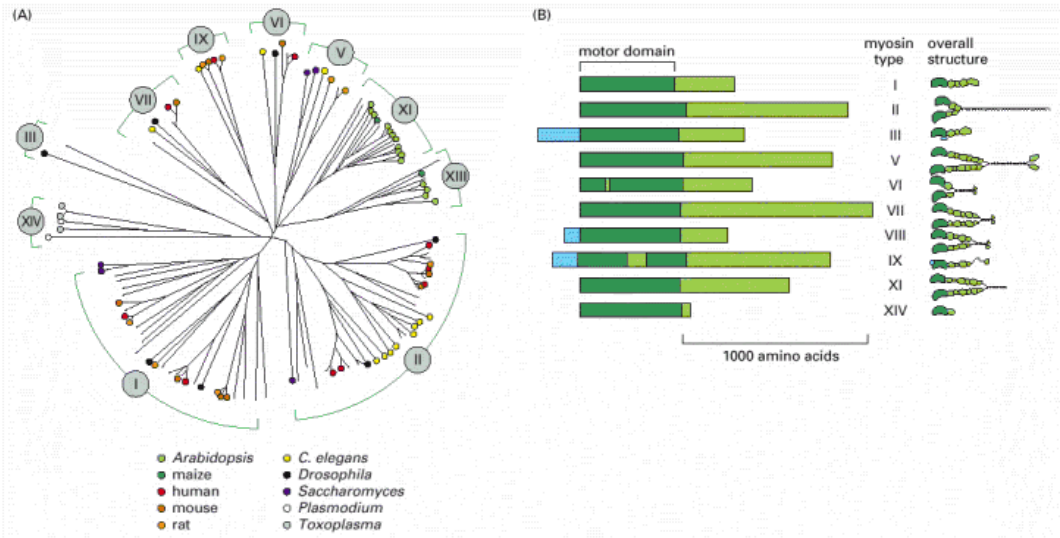

Figure 16-54. Myosin superfamily tree. (A) A family tree for a few of the many known members of the myosin superfamily. The length of the lines separating individual family members indicates the amount of difference in the amino acid sequence of the motor domain. Groups of related myosins that share a similar structure are assigned a Roman numeral. The species of origin of some of the myosins shown are indicated with colored dots. Some myosin types (such as I and II) have members in many eucaryotic species, ranging from animals to plants to parasitic protozoa; others are found only in particular groups of eucaryotes (XIV, for example, has been found so far only in parasitic protozoa such as *Toxoplasma* and *Plasmodium).* (B) Comparison of the domain structure of the heavy chains of some myosin types. All myosins share similar motor domains (shown in *dark green)*, but their C-terminal tails *(light green)* and N-terminal extensions *(light blue)* are very diverse. On the right are depictions of the molecular structure for these family members. Many myosins form dimers, with two motor domains per molecule, but a few (such as I, IX, and XIV) seem to function as monomers, with just one motor domain. Myosin VI, despite its overall structural similarity to other family members, is unique in moving toward the minus end (instead of the plus end) of an actin filament. The small insertion within its motor head domain, not found in other myosins, is probably responsible for this change in direction.

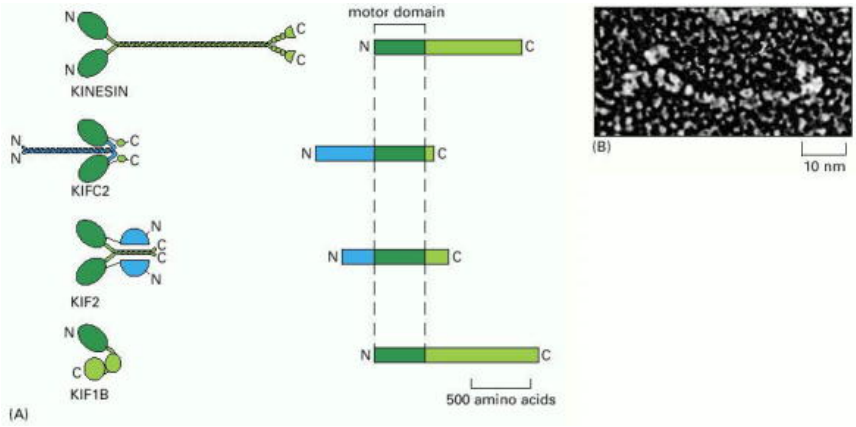

Figure 16-55. Kinesin and kinesin-related proteins. (A) Structures of four kinesin superfamily members. As in the myosin superfamily, only the motor domains are conserved. Conventional kinesin has the motor domain at the N-terminus of the heavy chain. The middle domain forms a long coiled-coil, mediating dimerization. The C-terminal domain forms a tail that attaches to cargo, such as a membrane-enclosed organelle. KIFC2 is a member of a family of C-terminal kinesins that includes the *Drosophila* protein Ncd and the yeast protein KAR3. These kinesins generally travel in the opposite direction from the majority of kinesins, toward the minus end instead of the plus end of a microtubule. KIF2 has its motor domain located in the middle of the heavy chain. It is a member of a family of kinesins that have lost typical motor activity and instead bind to microtubule ends to increase dynamic instability of microtubules; they are therefore called catastrophins. KIF1B is a member of the unusual class of kinesins that seem to function as monomers and move membrane-enclosed organelles along microtubules. Not shown is the BimC family of kinesins, which form tetramers. (B) Freeze-etch electron micrograph of a kinesin molecule with the head domains on the left. (B, courtesy of John Heuser.)

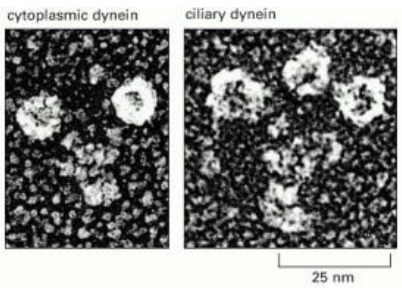

Figure 16-56. Dyneins. Freeze-etch electron micrographs of a molecule of cytoplasmic dynein and a molecule of ciliary (axonemal) dynein. Like myosin II and kinesin, cytoplasmic dynein is a two-headed molecule. The ciliary dynein shown has three heads. Note that the dynein head is very large compared with the head of either myosin or kinesin. (Courtesy of John Heuser.)

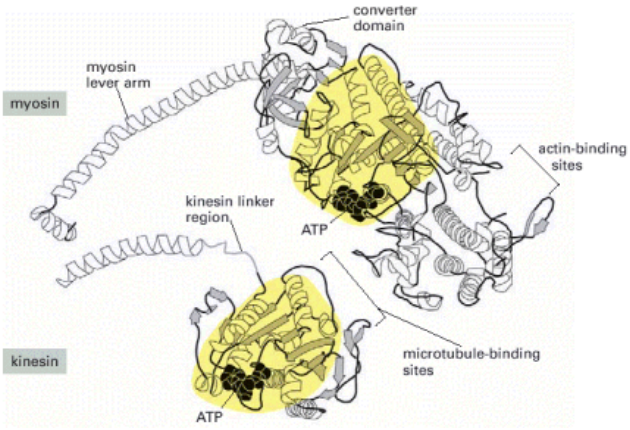

Figure 16-57. X-ray crystal structures of myosin and kinesin heads. The central nucleotide-binding domains of myosin and kinesin (shaded in *yellow)* are structurally very similar. The very different sizes and functions of the two motors are due to major differences in the polymer-binding and force-transduction portions of the motor domain. (Adapted from L.A. Amos and R.A. Cross, *Curr. Opin. Struct. Biol.* 7:239246, 1997.)

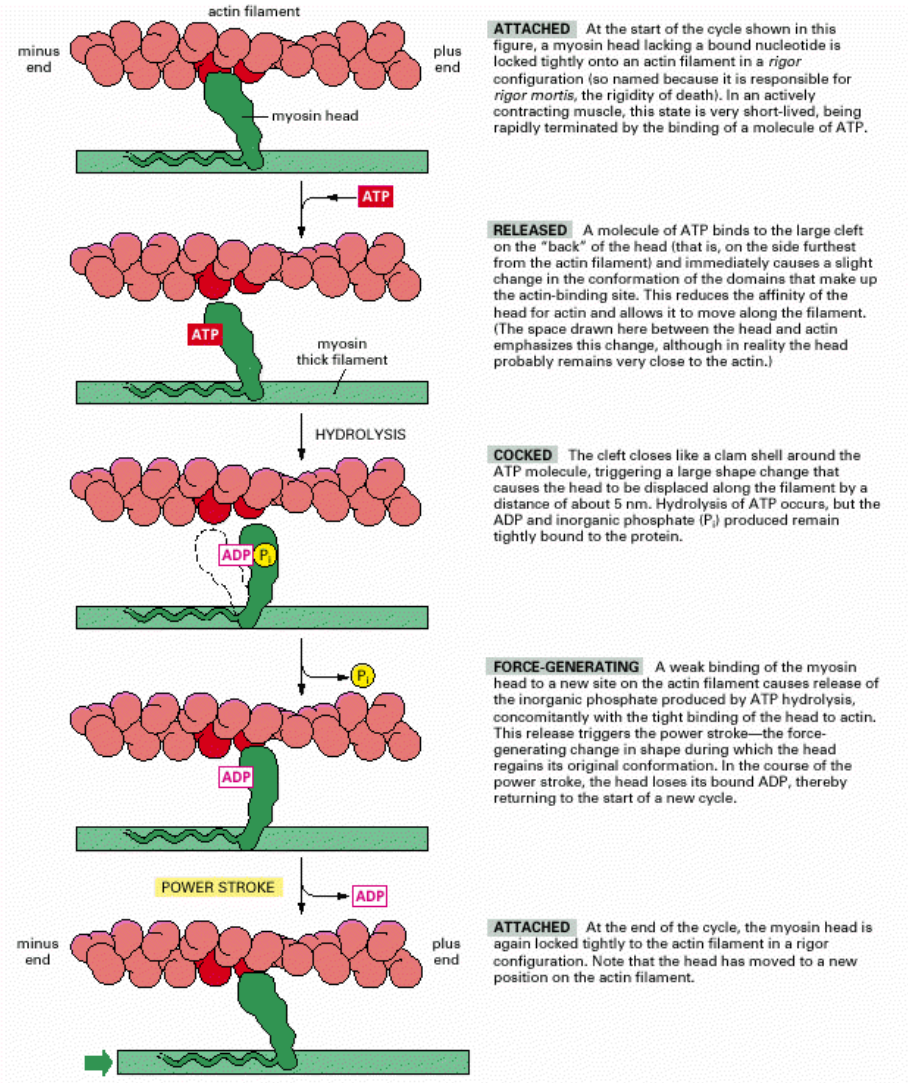

Figure 16-58. The cycle of structural changes used by myosin to walk along an actin filament. (Based on I. Rayment et al., *Science* 261:5058, 1993. © AAAS.)

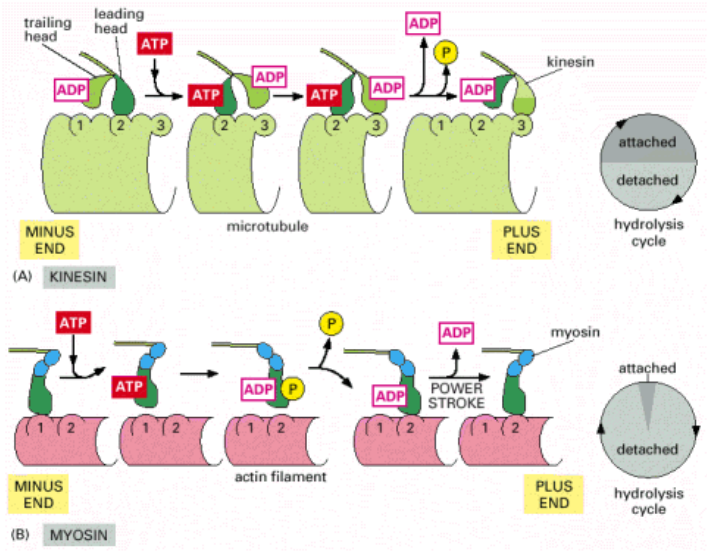

Figure 16-59. Comparison of the mechanochemical cycles of kinesin and myosin II. The shading in the two circles representing the hydrolysis cycle indicates the proportion of the cycle spent in attached and detached states for each motor protein. (A) Summary of the coupling between ATP hydrolysis and conformational changes for kinesin. At the start of the cycle, one of the two kinesin heads, the front or leading head *(dark green)* is bound to the microtubule, with the rear or trailing head *(light green)* detached. Binding of ATP to the front head causes the rear head to be thrown forward, past the binding site of the attached head, to another binding site further toward the plus end of the microtubule. Release of ADP from the second head (now in the front) and hydrolysis of ATP on the first head (now in the rear) brings the dimer back to the original state, but the two heads have switched their relative positions, and the motor protein has moved one step along the microtubule protofilament. In this cycle, each head spends about 50% of its time attached to the microtubule and 50% of its time detached. (B) Summary of the coupling between ATP hydrolysis and conformational changes for myosin II. Myosin begins its cycle tightly bound to the actin filament, with no associated nucleotide, the so-called "rigor" state. ATP binding releases the head from the filament. ATP hydrolysis occurs while the myosin head is detached from the filament, causing the head to assume a cocked conformation, although both ADP and inorganic phosphate remain tightly bound to the head. When the head rebinds to the filament, the release of phosphate, followed by the release of ADP, trigger the power stroke that moves the filament relative to the motor protein. ATP binding releases the head to allow the cycle to begin again. In the myosin cycle, the head remains bound to the actin filament for only about 5% of the entire cycle time, allowing many myosins to work together to move a single actin filament.

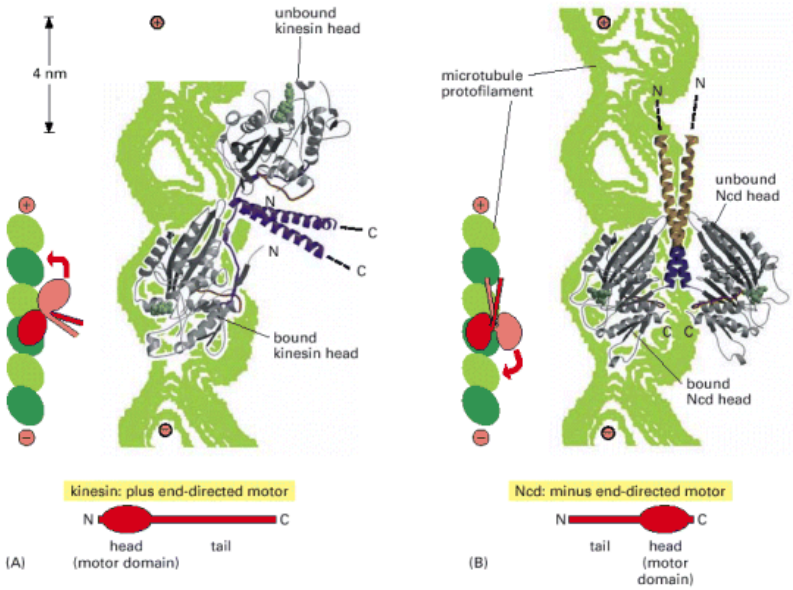

Figure 16-60. Orientation of forward- and backward-walking kinesin superfamily proteins bound to microtubules. These images were generated by fitting the structures of the free motor-protein dimers (determined by x-ray crystallography) onto a lower resolution image of the dimers attached to microtubules (determined by cryoelectron microscopy). (A) Conventional kinesin has its motor domain at the protein's N-terminus and moves toward the plus end of the microtubule. When one head of the dimer is bound to the microtubule in a post-stroke state (with ATP in the nucleotide binding site), the second, unbound head is pointing toward the microtubule plus end, poised to take the next step. (B) Ncd, a minus-end-directed motor with the motor domain at the C-terminus, forms dimers with the opposite orientation. (From E. Sablin et al., *Nature* 395:813816, 1998. © Macmillan Magazines Ltd.)

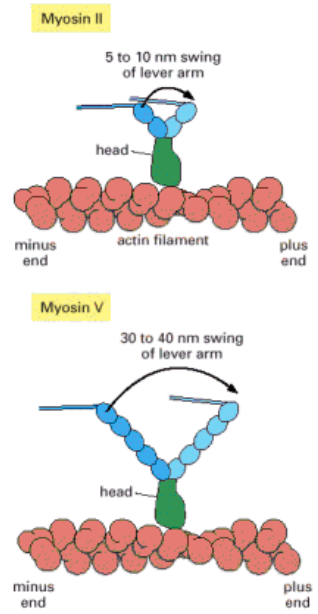

Figure 16-61. The effect of lever arm length on the step size for a motor protein. The lever arm of myosin II is much shorter than the lever arm of myosin V. The power stroke in the head swings their lever arms through the same angle, so myosin V is able to take a bigger step than myosin II.

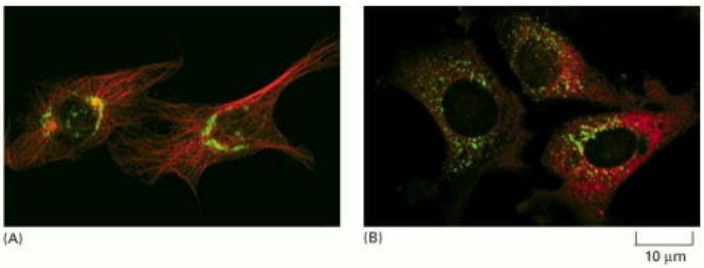

Figure 16-62. Effect of depolymerizing microtubules on the Golgi apparatus. (A) In this endothelial cell, the microtubules are labeled in *red*, and the Golgi apparatus is labeled in *green* (using an antibody against a Golgi protein). As long as the system of microtubules remains intact, the Golgi is localized near the centrosome, close to the nucleus at the center of the cell. The cell on the *right* is in interphase, with a single centrosome. The cell on the *left* is in prophase, and the duplicated centrosomes have moved to opposite sides of the nucleus. (B) After exposure to nocodazole, which causes microtubules to depolymerize (see Table 16-2), the Golgi apparatus fragments and is dispersed throughout the cell cytoplasm. (Courtesy of David Shima.)

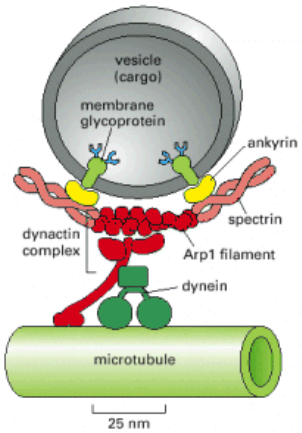

Figure 16-63. A model for the attachment of dynein to a membrane-enclosed organelle. Dynein requires the presence of a large number of accessory proteins to associate with membrane-enclosed organelles. Dynactin is a large complex *(red)* that includes components that bind weakly to microtubules, components that bind to dynein itself, and components that form a small actinlike filament made of the actin-related protein Arp1. It is thought that the Arp1 filament may mediate attachment of this large complex to membrane-enclosed organelles through a network of spectrin and ankyrin, similar to the membrane-associated cytoskeleton of the red blood cell (see Figure 10-31).

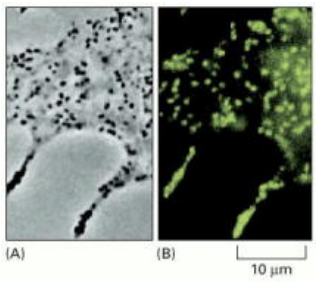

Figure 16-64. Myosin V on melanosomes. (A) Phase-contrast image of a portion of a melanocyte isolated from a mouse. The black spots are melanosomes, which are membrane-enclosed organelles filled with the skin pigment melanin. (B) The same cell labeled with a fluorescent antibody against myosin V. Every melanosome is associated with a large number of copies of this motor protein. (From X. Wu et al., *J. Cell Sci.* 110:847859, 1997. © The Company of Biologists.)

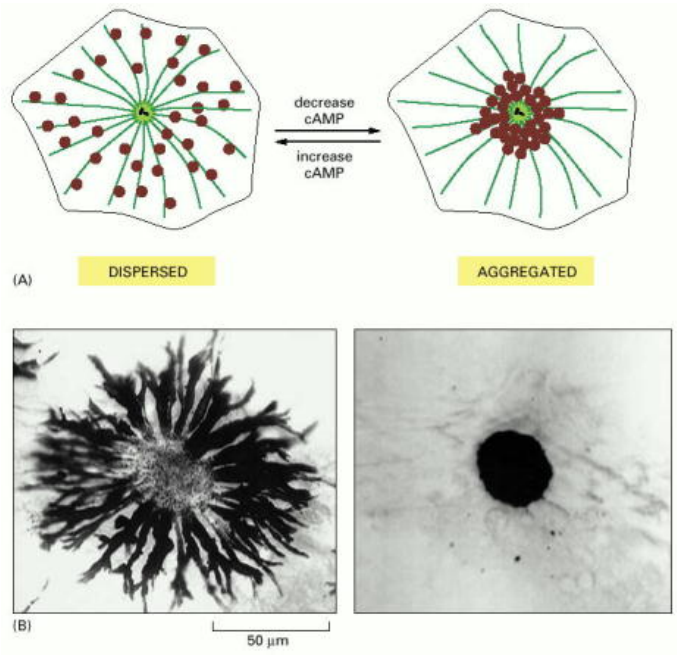

Figure 16-65. Regulated melanosome movements in fish pigment cells. These giant cells, which are responsible for changes in skin coloration in several species of fish, contain large pigment granules, or melanosomes *(brown).* The melanosomes can change their location in the cell in response to a hormonal or neuronal stimulus. (A) Schematic view of a pigment cell, showing the dispersal and aggregation of melanosomes in response to an increase or decrease in intracellular cyclic AMP (cAMP), respectively. Both redistributions of melanosomes occur along microtubules. (B) Bright-field images of a single cell in a scale of an African cichlid fish, showing its melanosomes either dispersed throughout the cytoplasm *(left)* or aggregated in the center of the cell *(right).* (B, courtesy of Leah Haimo.)

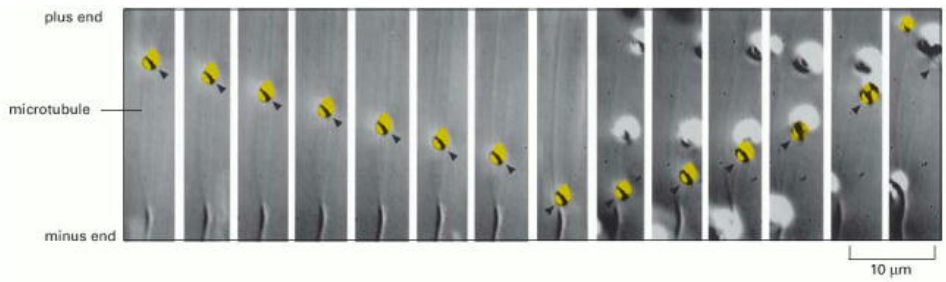

Figure 16-66. Bidirectional movement of a melanosome on a microtubule. An isolated melanosome *(yellow)* moves along a microtubule on a glass slide, from the plus end toward the minus end. Halfway through the video sequence, it abruptly switches direction and moves from the minus end toward the plus end. (From S.L. Rogers et al., *Proc. Natl. Acad. Sci. USA* 94:37203725, 1997. © National Academy of Sciences.)

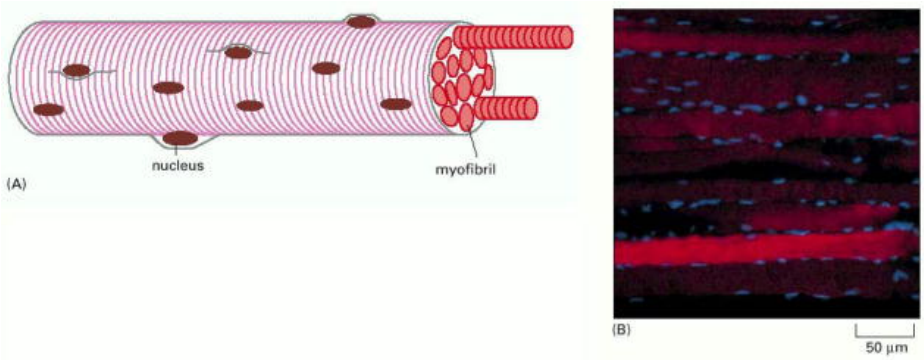

Figure 16-68. Skeletal muscle cells (also called muscle fibers). (A) These huge multinucleated cells form by the fusion of many muscle cell precursors, called myoblasts. In an adult human, a muscle cell is typically 50 μm in diameter and can be up to several centimeters long. (B) Fluorescence micrograph of rat muscle, showing the peripherally located nuclei *(blue)* in these giant cells. (B, courtesy of Nancy L. Kedersha.)

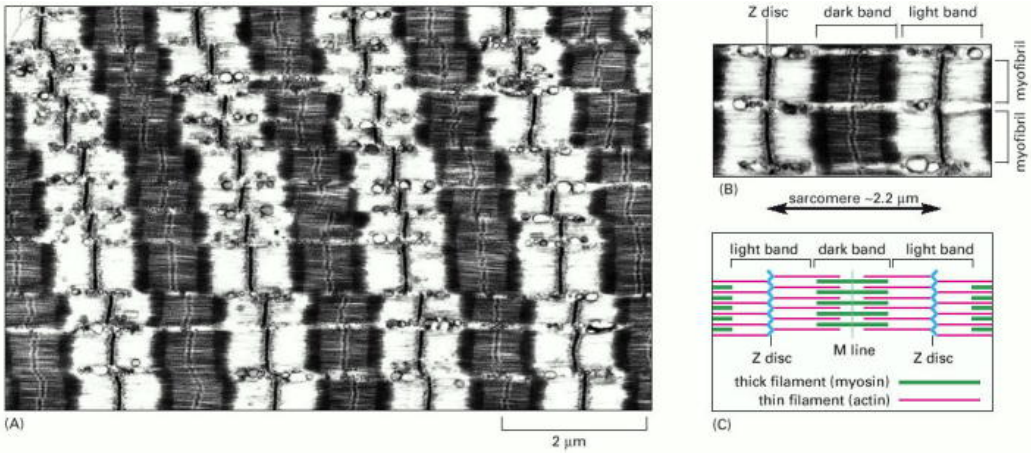

Figure 16-69. Skeletal muscle myofibrils. (A) Low-magnification electron micrograph of a longitudinal section through a skeletal muscle cell of a rabbit, showing the regular pattern of cross-striations. The cell contains many myofibrils aligned in parallel (see Figure 16-68). (B) Detail of the skeletal muscle shown in (A), showing portions of two adjacent myofibrils and the definition of a sarcomere. (C) Schematic diagram of a single sarcomere, showing the origin of the dark and light bands seen in the electron micrographs. The Z discs, at each end of the sarcomere, are attachment sites for the plus ends of actin filaments (thin filaments); the M line, or midline, is the location of proteins that link adjacent myosin II filaments (thick filaments) to one another. The dark bands, which mark the location of the thick filaments, are sometimes called A bands because they appear anisotropic in polarized light (that is, their refractive index changes with the plane of polarization). The light bands, which contain only thin filaments and therefore have a lower density of protein, are relatively isotropic in polarized light and are sometimes called I bands. (A and B, courtesy of Roger Craig.)

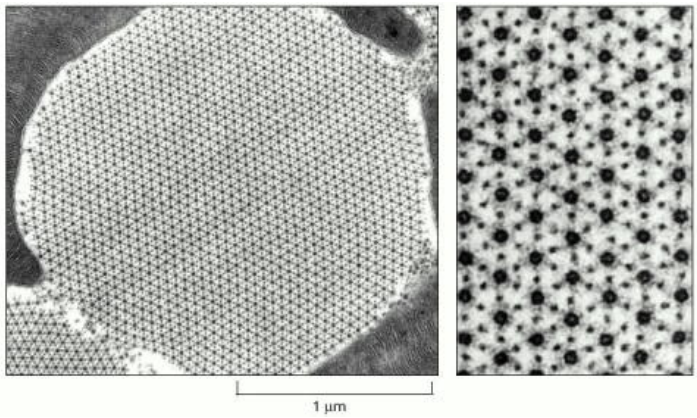

Figure 16-70. Electron micrographs of an insect flight muscle viewed in cross section. The myosin and actin filaments are packed together with almost crystalline regularity. Unlike their vertebrate counterparts, these myosin filaments have a hollow center, as seen in the enlargement on the right. The geometry of the hexagonal lattice is slightly different in vertebrate muscle. (From J. Auber, *J. de Microsc.* 8:197232, 1969.)

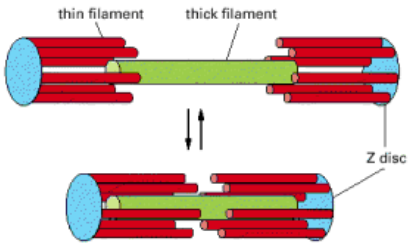

Figure 16-71. The sliding-filament model of muscle contraction. The actin *(red)* and myosin *(green)* filaments in a sarcomere slide past one another without shortening.

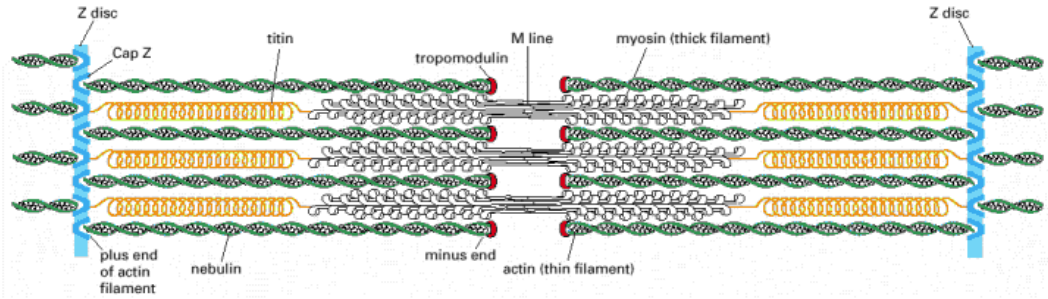

Figure 16-72. Organization of accessory proteins in a sarcomere. Each giant titin molecule extends from the Z disc to the M line - a distance of over 1 µm. Part of each titin molecule is closely associated with a myosin thick filament (which switches polarity at the M line); the rest of the titin molecule is elastic and changes length as the sarcomere contracts and relaxes. Each nebulin molecule is exactly the length of a thin filament. The actin filaments are also coated with tropomyosin and troponin (not shown; see Figure 16-74) and are capped at both ends. Tropomodulin caps the minus end of the actin filaments, and CapZ anchors the plus end at the Z disc, which also contains α-actinin.

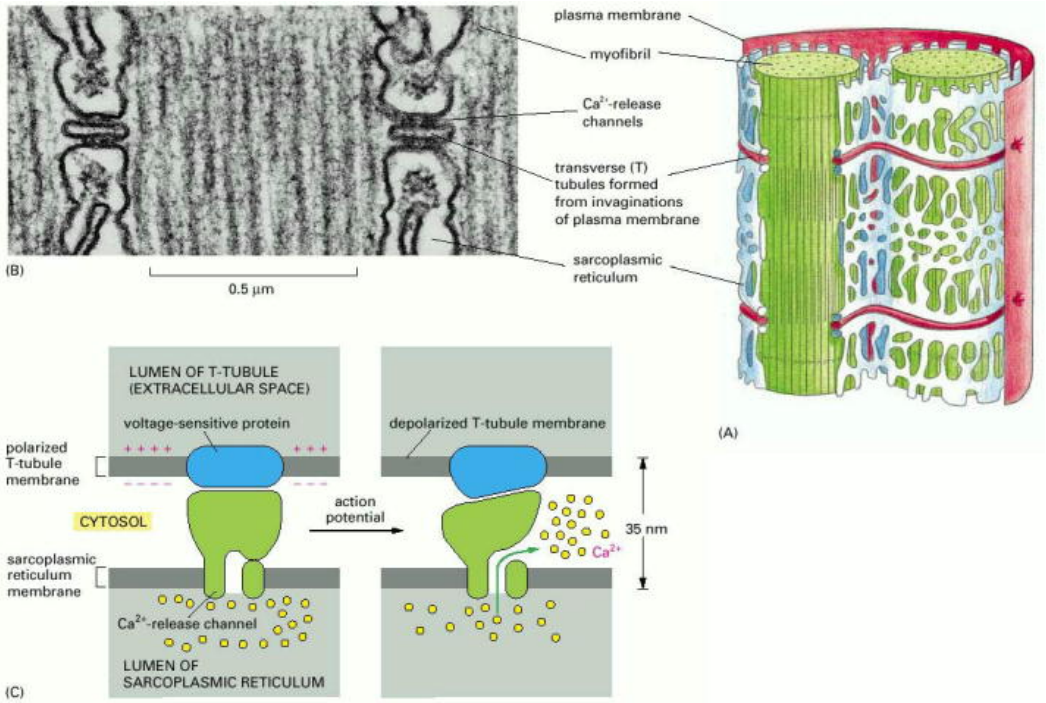

Figure 16-73. T tubules and the sarcoplasmic reticulum. (A) Drawing of the two membrane systems that relay the signal to contract from the muscle cell plasma membrane to all of the myofibrils in the cell. (B) Electron micrograph showing two T tubules. Note the position of the large Ca^{2+}-release channels in the sarcoplasmic reticulum membrane; they look like square-shaped "feet" that connect to the adjacent T-tubule membrane. (C) Schematic diagram showing how a Ca^{2+}-release channel in the sarcoplasmic reticulum membrane is thought to be opened by a voltage-sensitive transmembrane protein in the adjacent T-tubule membrane. (B, courtesy of Clara Franzini-Armstrong.)

Figure 16-75. Effect on the heart of a subtle mutation in cardiac myosin. *Left*, normal heart from a 6-day old mouse pup. *Right*, heart from a pup with a point mutation in both copies of its cardiac myosin gene, changing Arg 403 to Gln. Both atria are greatly enlarged (hypertrophic), and the mice die within a few weeks of birth. (From D. Fatkin et al., *J. Clin. Invest.* 103:147, 1999.)

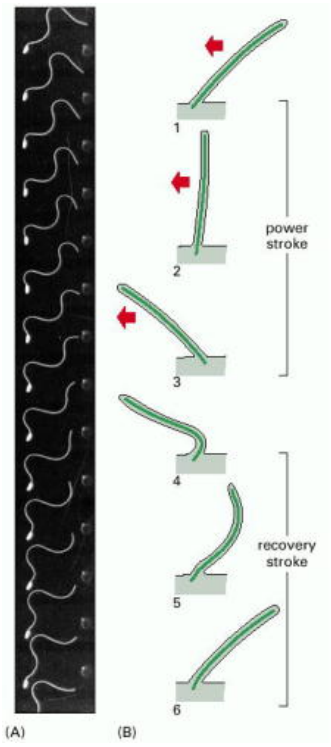

Figure 16-76. The contrasting motions of flagella and cilia. (A) The wave-like motion of the flagellum of a sperm cell from a tunicate. The cell was photographed with stroboscopic illumination at 400 flashes per second. Note that waves of constant amplitude move continuously from the base to the tip of the flagellum. (B) The beat of a cilium, which resembles the breast stroke in swimming. A fast power stroke *(red* arrows), in which fluid is driven over the surface of the cell, is followed by a slow recovery stroke. Each cycle typically requires 0.10.2 sec and generates a force perpendicular to the axis of the axoneme. (A, courtesy of C.J. Brokaw.)

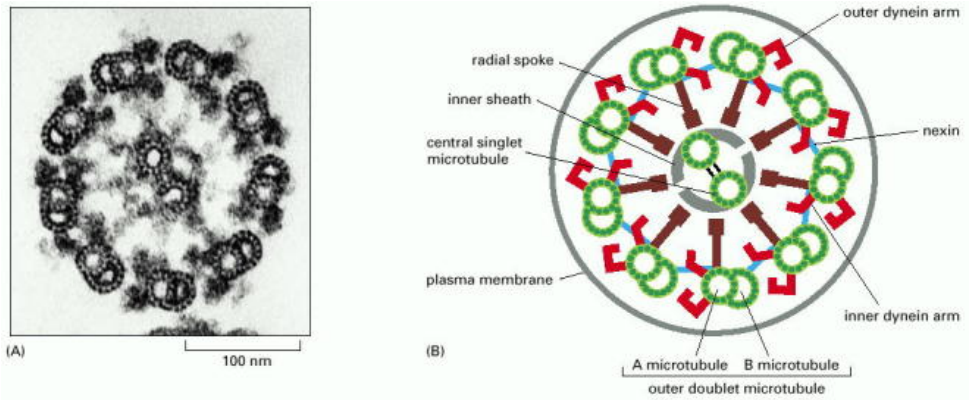

Figure 16-77. The arrangement of microtubules in a flagellum or cilium. (A) Electron micrograph of the flagellum of a green-alga cell *(Chlamydomonas)* shown in cross section, illustrating the distinctive "9 + 2" arrangement of microtubules. (B) Diagram of the parts of a flagellum or cilium. The various projections from the microtubules link the microtubules together and occur at regular intervals along the length of the axoneme. (A, courtesy of Lewis Tilney.)

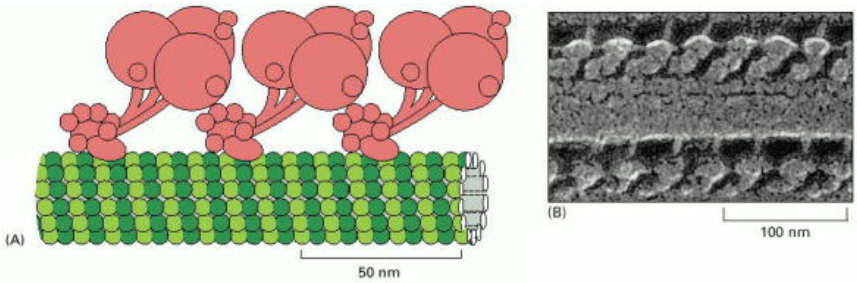

Figure 16-78. Ciliary dynein. Ciliary (axonemal) dynein is a large protein assembly (nearly 2 million daltons) composed of 912 polypeptide chains, the largest of which is the heavy chain of more than 500,000 daltons. (A) The heavy chains are believed to form the major portion of the globular head and stem domains, and many of the smaller chains are clustered around the base of the stem (see Figure 16-56 for a view of the isolated molecule). The base of the molecule binds tightly to an A microtubule in an ATP-independent manner, while the large globular heads have an ATP-dependent binding site for a B microtubule (see Figure 16-77). When the heads hydrolyze their bound ATP, they move toward the minus end of the B microtubule, thereby producing a sliding force between the adjacent microtubule doublets in a cilium or flagellum. The three-headed form of ciliary dynein, formed from three heavy chains, is illustrated here. (B) Freeze-etch electron micrograph of a cilium showing the dynein arms projecting at regular intervals from the doublet microtubules; only the A microtubule is shown. (B, courtesy of John Heuser.)

Figure 16-79. The bending of an axoneme. (A) When axonemes are exposed to the proteolytic enzyme trypsin, the linkages holding neighboring doublet microtubules together are broken. In this case, the addition of ATP allows the motor action of the dynein heads to slide one pair of doublet microtubules against the other pair. (B) In an intact axoneme (such as in a sperm), sliding of the doublet microtubules is prevented by flexible protein links. The motor action therefore causes a bending motion, creating waves or beating motions, as seen in Figure 16-76.

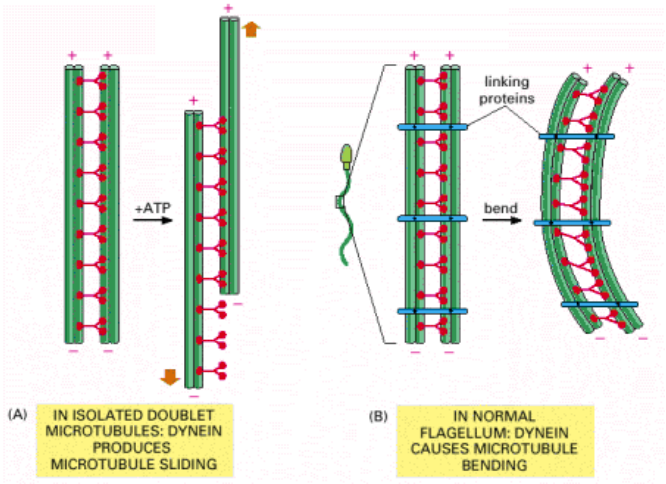

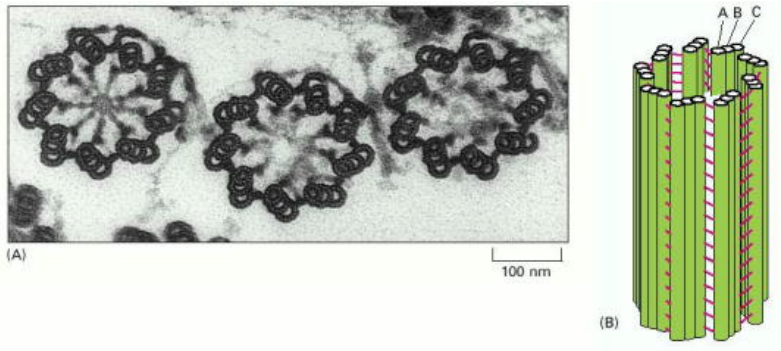

Figure 16-80. Basal bodies. (A) Electron micrograph of a cross section through three basal bodies in the cortex of a protozoan. (B) Diagram of a basal body viewed from the side. Each basal body forms the lower portion of a ciliary axoneme and is composed of nine sets of triplet microtubules, each triplet containing one complete microtubule (the A microtubule) fused to two incomplete microtubules (the B and C microtubules). Other proteins (shown in *red* in B) form links that hold the cylindrical array of microtubules together. The arrangement of microtubules in a centriole is essentially the same (see Figure 16-24). (A, courtesy of D.T. Woodrow and R.W. Linck.)

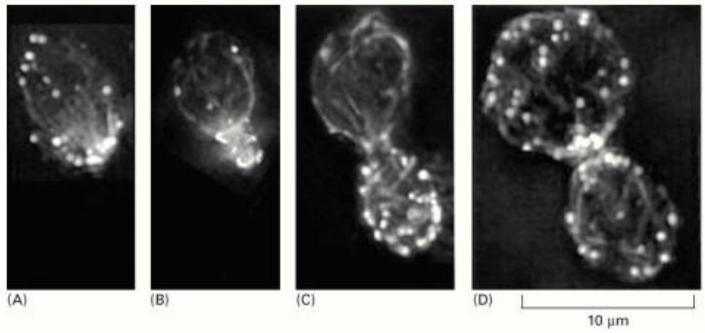

Figure 16-81. Polarity of actin patches and cables throughout the yeast cell cycle. Filamentous actin structures in the yeast cell, labeled here with fluorescent phalloidin, include actin patches (round bright spots) and actin cables (extended lines). (A) In a mother cell, before the formation of the bud, most of the patches are clustered at one end. The cables are lined up and point toward the cluster of patches, which is the site where the bud will emerge. (B) As the small bud grows, most patches remain within it. Cables in the mother cell continue to point toward this site of new cell wall growth. (C) Patches are almost uniformly distributed over the surface of a full-sized bud. Cables in the mother cell remain polarized. (D) Immediately after cell division, mother and daughter cells form new patches, which are concentrated near the division site, although both cells have randomly oriented cables. (From T.S. Karpova et al., *J. Cell Biol.* 142:15011517, 1998. © The Rockefeller University Press.)

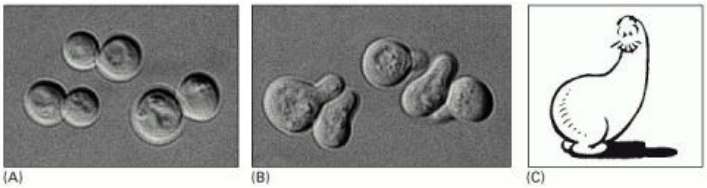

Figure 16-82. Morphological polarization of yeast cells in response to mating factor. (A) Cells of *Saccharomyces cerevisiae* are usually spherical. (B) They become polarized when treated with mating factor from cells of the opposite mating type. The polarized cells are called "shmoos." (C) Al Capp's famous cartoon character, the original Shmoo. (A and B, courtesy of Michael Snyder; C, © 1948 Capp Enterprises, Inc., all rights reserved.)

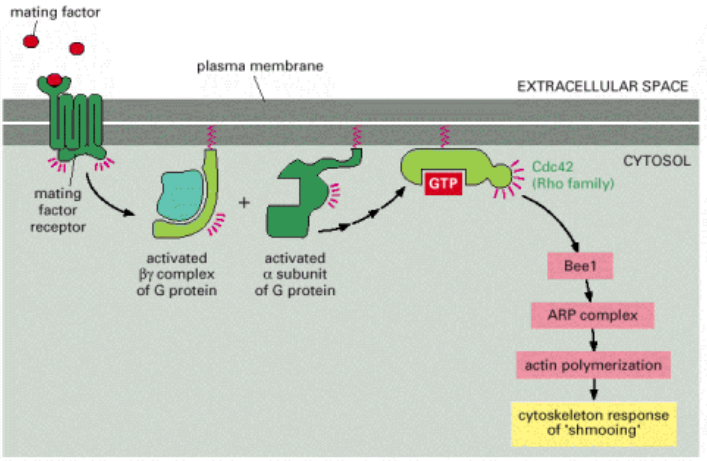

Figure 16-83. The signaling pathway in the yeast mating factor response. The extracellular mating factor binds to a G-protein-linked receptor in the plasma membrane. Activation of the receptor triggers dissociation of the GTP-bound Gα subunit from a heterotrimeric G-protein (discussed in Chapter 15). This in turn activates the Rho family GTP-binding protein, Cdc42, the yeast homolog of the mammalian small GTPase whose activation triggers the formation of filopodia (see Figure 16-50D). As in mammalian cells, Cdc42 activates a protein (Bee1, the homolog of WASp) that activates the ARP complex, leading to local actin nucleation at the site of mating factor binding. The local actin nucleation and filament growth lead to polarized growth and acquisition of a shmoo shape. In addition, receptor activation triggers other responses through a MAP kinase cascade (discussed in Chapter 15), preparing the haploid cell for mating (not shown).

iine cell polarity in these more complex systems is an active area of research.

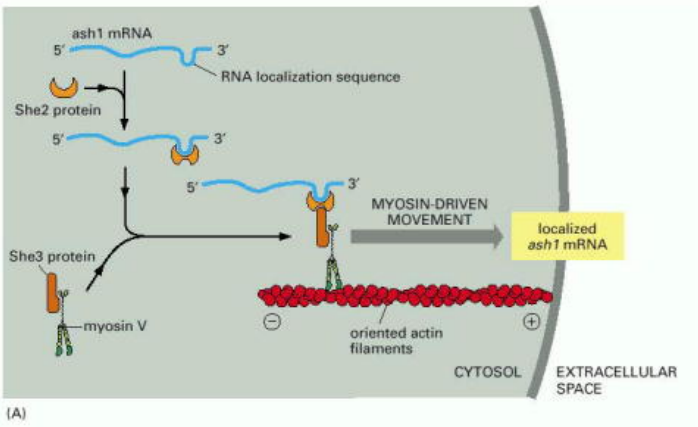

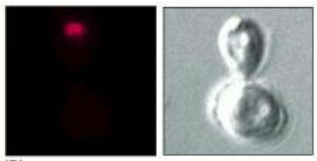

Figure 16-84. Polarized mRNA localization in the yeast bud tip. (A) The molecular mechanism of *ash1* mRNA localization, as determined by genetics and biochemistry. (B) Fluorescent *in situ* hybridization (FISH) was used to localize the *ash1* mRNA (*red*) in this dividing yeast cell. The mRNA is confined to the far tip of the daughter cell (here, still a large bud). Ash1 protein, transcribed from this localized mRNA, is also confined to the daughter cell. (B, courtesy of Peter Takizawa and Ron Vale.)

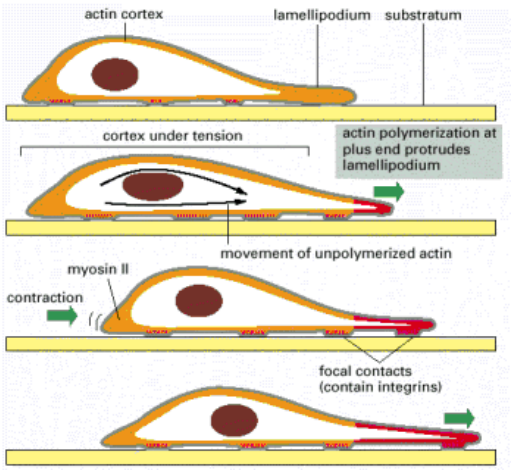

Figure 16-85. A model of how forces generated in the actin-rich cortex move a cell forward. The actin-polymerization-dependent protrusion and firm attachment of a lamellipodium at the leading edge of the cell moves the edge forward *(green* arrows at front) and stretches the actin cortex. Contraction at the rear of the cell propels the body of the cell forward *(green* arrow at back) to relax some of the tension (traction). New focal contacts are made at the front, and old ones are disassembled at the back as the cell crawls forward. The same cycle can be repeated, moving the cell forward in a stepwise fashion. Alternatively, all steps can be tightly coordinated, moving the cell forward smoothly. The newly polymerized cortical actin is shown in *red*.

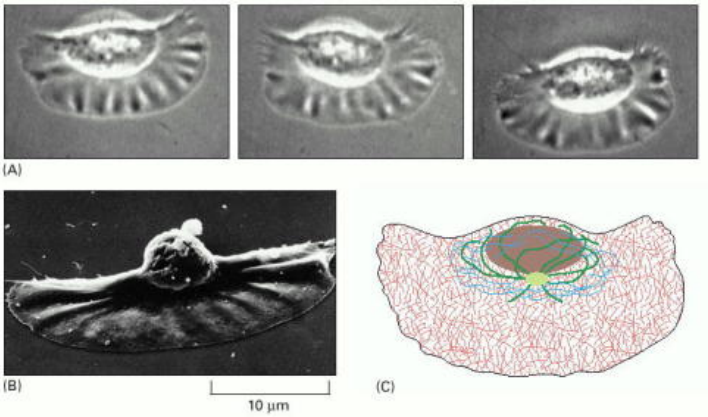

Figure 16-86. Migratory keratocytes from a fish epidermis. (A) Light micrographs of a keratocyte in culture, taken about 15 sec apart. This cell is moving at about 15 μm/sec. (B) Keratocyte seen by scanning electron microscopy, showing its broad, flat lamellipodium and small cell body, including the nucleus, carried up above the substratum at the rear. (C) Distribution of cytoskeletal filaments in this cell. Actin filaments *(red)* fill the large lamellipodium and are responsible for the cell's rapid movement. Microtubules *(green)* and intermediate filaments *(blue)* are restricted to the regions close to the nucleus. (A and B, courtesy of Juliet Lee.)

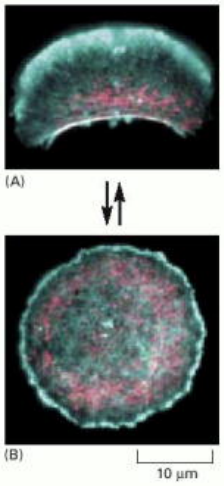

Figure 16-87. Behavior of lamellipodial fragments. Fragments of the large lamellipodium of a keratocyte can be separated from the main cell, either by surgery with a micropipette or by treating the cell with certain drugs. (A) Many of these fragments continue to move rapidly, with the same overall cytoskeletal organization as the intact keratocytes. Actin *(blue)* forms a protrusive meshwork at the front of the fragment. Myosin II *(pink)* is gathered into a band at the rear. This cell fragment was moving toward the top of the photo at the time that it was fixed and stained. (B) Some of the fragments stop moving and assume a symmetric, circular shape. Actin *(blue)* is distributed uniformly around the circumference, and myosin *(pink)* is found in spots throughout the cytoplasm. These circular fragments are trying to protrude uniformly in all directions and are therefore paralyzed. Only by coordinating protrusion at the front with contraction at the rear can steady movement be maintained. (From A. Verkovsky et al., *Curr. Biol.* 9:1120, 1999. © Elsevier.)

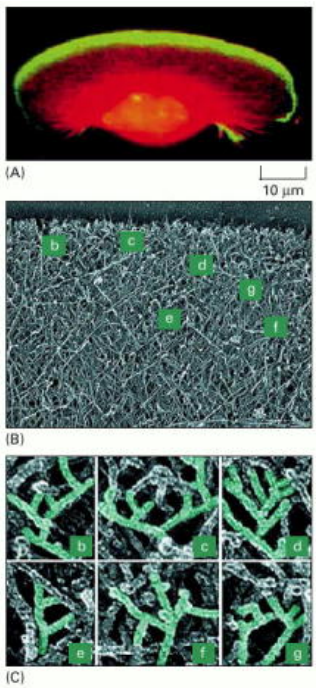

Figure 16-88. Actin filament nucleation and web formation by the ARP complex in lamellipodia. (A) A keratocyte with actin filaments labeled in *red* by fluorescent phalloidin, and the ARP complex labeled in *green* with an antibody raised against one of its component proteins. The regions where the two overlap appear *yellow*. The ARP complex is highly concentrated near the front of the lamellipodium, where actin nucleation is most active. (B) Electron micrograph of a platinum-shadowed replica of the leading edge of a keratocyte, showing the dense actin filament meshwork. The labels denote areas enlarged in C. (C) Closeup views of the marked regions of the actin web at the leading edge shown in B. Numerous branched filaments can be seen, with the characteristic 70° angle formed when the ARP complex nucleates a new actin filament off the side of a preexisting filament (see Figure 16-29). (From T. Svitkina and G. Borisy, *J. Cell Biol.* 145:10091026, 1999. © The Rockefeller University Press.)

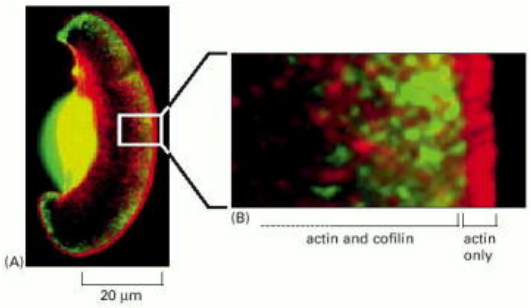

Figure 16-89. Cofilin in lamellipodia. (A) A keratocyte with actin filaments labeled in *red* by fluorescent phalloidin and cofilin labeled in *green* with a fluorescent antibody. The regions where the two overlap appear *yellow*. Although the dense actin meshwork reaches all the way through the lamellipodium, cofilin is not found at the very leading edge. (B) Closeup view of the region marked with the *white* rectangle in A. The actin filaments closest to the leading edge, which are also the ones that have formed most recently and that are most likely to contain ATP actin (rather than ADP actin) in the filament lattice are generally not associated with cofilin. (From T. Svitkina and G. Borisy, *J. Cell Biol.* 145:10091026, 1999. © The Rockefeller University Press.)

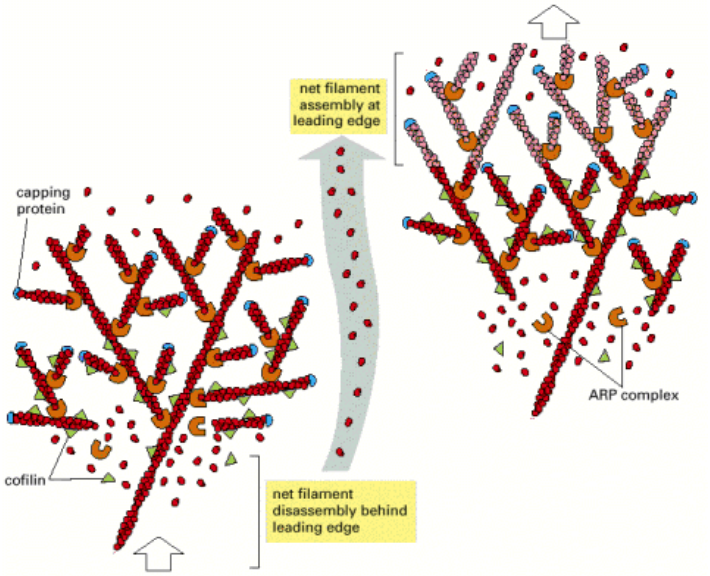

Figure 16-90. A model for protrusion of the actin meshwork at the leading edge. Two time points during advance of the lamellipodium are illustrated, with newly assembled structures at the later time point shown in a lighter color. Nucleation is mediated by the ARP complex at the front. Newly nucleated actin filaments are attached to the sides of preexisting filaments, primarily at a 70° angle. Filaments elongate, pushing the plasma membrane forward because of some sort of anchorage of the array behind. At a steady rate, actin filament plus ends become capped. After newly polymerized actin subunits hydrolyze their bound ATP in the filament lattice, the filaments become susceptible to depolymerization by cofilin. This cycle causes a spatial separation between net filament assembly at the front and net filament disassembly at the rear, so that the actin filament network as a whole can move forward, even though the individual filaments within it remain stationary with respect to the substratum.

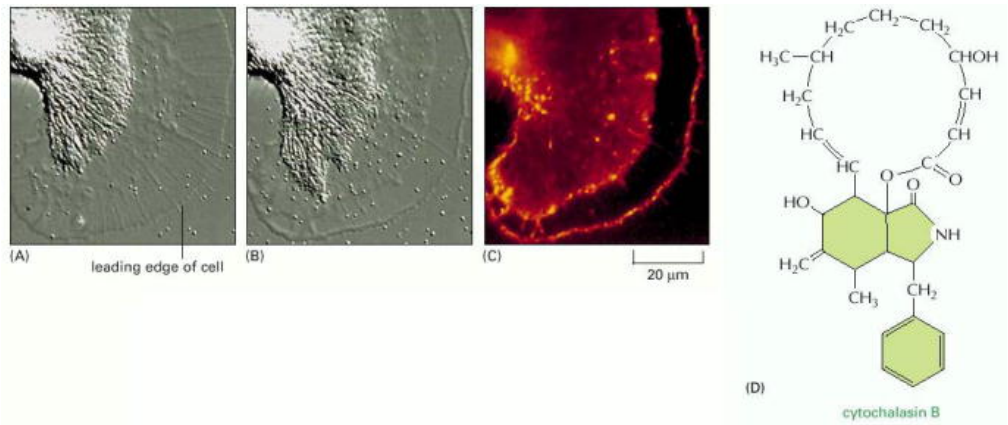

Figure 16-91. Rearward movement of the actin network in a growth-cone lamellipodium. (A) A growth cone from a neuron of the sea slug *Aplysia* is cultured on a highly adhesive substratum and viewed by differential-interference-contrast microscopy. Microtubules and membrane-enclosed organelles are confined to the bright, rear area of the growth cone (to the *left)*, while a meshwork of actin filaments fills the lamellipodium (on the *right).* (B) After brief treatment with the drug cytochalasin, which caps the plus ends of actin filaments (see Table 16-2), the actin meshwork has detached from the front edge of the lamellipodium and has been pulled backward. (C) At the time point shown in B, the cell was fixed and labeled with fluorescent phalloidin to show the distribution of the actin filaments. Some actin filaments persist at the leading edge, but the region behind the leading edge is devoid of filaments. Note the sharp boundary of the rearward-moving actin meshwork. (D) The complex cyclic structure of cytochalasin B. (A, B, and C courtesy of Paul Forscher.)

Figure 16-92. Lamellipodia and ruffles at the leading edge of a human fibroblast migrating in culture. The *arrow* in this scanning electron micrograph shows the direction of cell movement. As the cell moves forward, lamellipodia that fail to attach to the substratum are swept backward over the dorsal surface of the cell, a movement known as ruffling. (Courtesy of Julian Heath.)

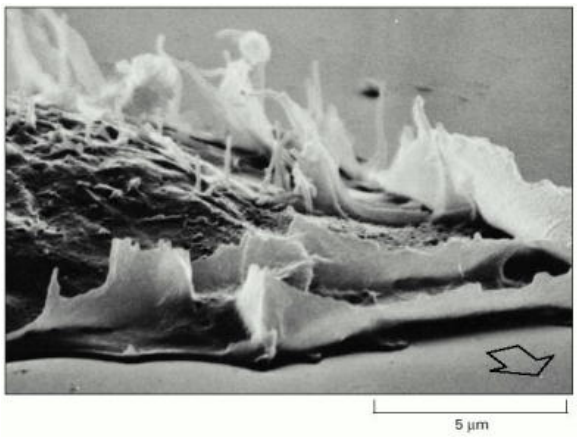

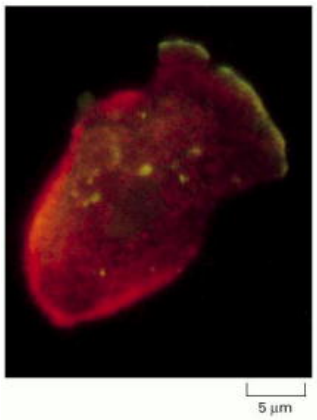

Figure 16-93. The localization of myosin I and myosin II in a normal crawling *Dictyostelium* amoeba. This cell was crawling toward the upper right at the time that it was fixed and labeled with antibodies specific for two myosin isoforms. Myosin I *(green)* is mainly restricted to the leading edge of pseudopodia at the front of the cell. Myosin II *(red)* is highest in the posterior, actin-rich cortex. Contraction of the cortex at the posterior of the cell by myosin II may help to push the cell body forward. (Courtesy of Yoshio Fukui.)

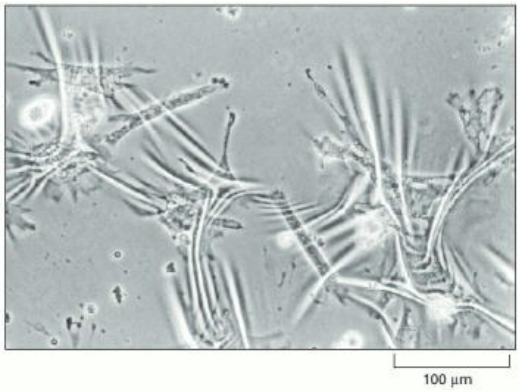

Figure 16-94. Adhesive cells exert traction forces on the substratum. These fibroblasts have been cultured on a very thin sheet of silicon rubber. Attachment of the cells, followed by contraction of their cytoskeleton, has caused the rubber substratum to wrinkle. (From A.K. Harris, P. Wild, and D. Stopak, *Science* 208:177179, 1980. © AAAS.)

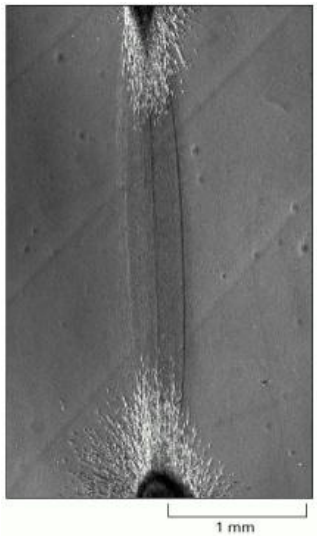

Figure 16-95. Shaping of the extracellular matrix by cell pulling. This micrograph shows a region between two pieces of embryonic chick heart (tissue explants rich in fibroblasts and heart muscle cells) that were grown in culture on a collagen gel for 4 days. A dense tract of aligned collagen fibers has formed between the two explants, apparently as a result of fibroblasts tugging on the collagen. (From D. Stopak and A.K. Harris, *Dev. Biol*. 90:383398, 1982. © Academic Press.)

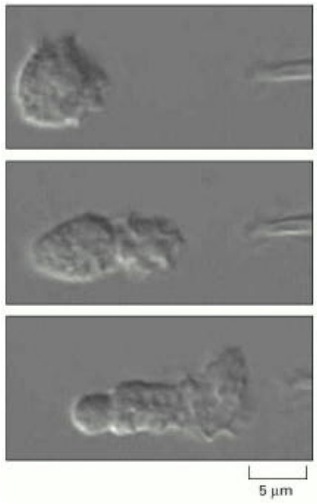

Figure 16-96. Neutrophil polarization and chemotaxis. The pipette tip at the right is leaking a small amount of the peptide formyl-Met-Leu-Phe. Only bacterial proteins have formylated methionine residues, so the human neutrophil recognizes this peptide as the product of a foreign invader (discussed in Chapter 25). The neutrophil quickly extends a new lamellipodium toward the source of the chemoattractant peptide *(top).* It then extends this lamellipodium and polarizes its cytoskeleton so that contractile myosin II is located primarily at the rear, opposite the position of the lamellipodium *(middle).* Finally, the cell crawls toward the source of this peptide *(bottom).* If a real bacterium were the source of the peptide, rather than an investigator's pipette, the neutrophil would engulf the bacterium and destroy it. (From O.D. Weiner et al., *Nature Cell Biol*. 1:7581, 1999. © Macmillan Magazines Ltd.)

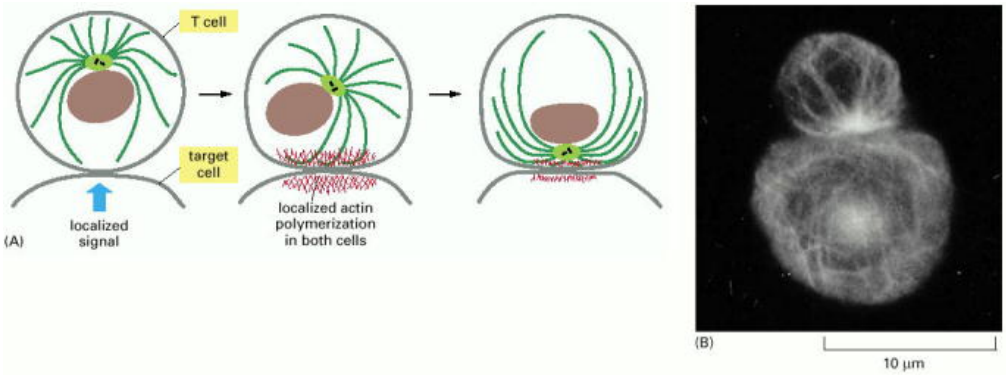

Figure 16-97. The polarization of a cytotoxic T cell after target-cell recognition. (A) Changes in the cytoskeleton of a cytotoxic T cell after it has made contact with a target cell. The initial recognition event results in signals that cause actin polymerization in both cells at the site of contact. In the T cell, interactions between the actin-rich contact zone and microtubules emanating from the centrosome result in reorientation of the centrosome, so that the associated Golgi apparatus is directly apposed to the target cell. (B) Immuno-fluorescence micrograph in which both the T cell *(top)* and its target cell *(bottom)* have been stained with an antibody against microtubules. The centrosome and the microtubules radiating from it in the T cell are oriented toward the point of cell-cell contact. In contrast, the microtubule array in the target cell is not polarized. (B, from B. Geiger, D. Rosen and G. Berke, *J. Cell Biol*. 95:137143, 1982. © The Rockefeller University Press.)

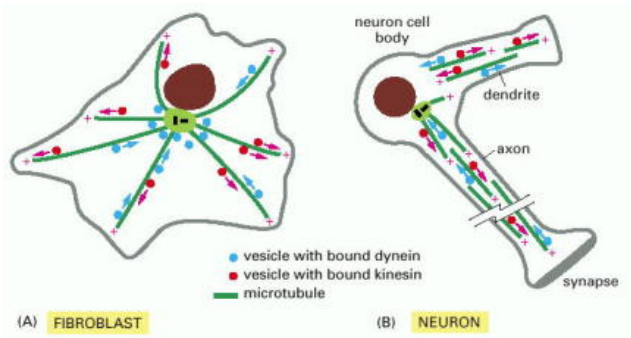

Figure 16-98. Microtubule organization in fibroblasts and neurons. (A) In a fibroblast, microtubules emanate outward from the centrosome in the middle of the cell. Vesicles with plus-end-directed kinesin attached move outward, and vesicles with minus-end-directed dynein attached move inward. (B) In a neuron, microtubule organization is more complex. In the axon, all microtubules share the same polarity, with the plus ends pointing outward toward the axon terminus. No one microtubule stretches the entire length of the axon; instead, short overlapping segments of parallel microtubules make the tracks for fast axonal transport. In dendrites, the microtubules are of mixed polarity, with some plus ends pointing outward and some pointing inward.

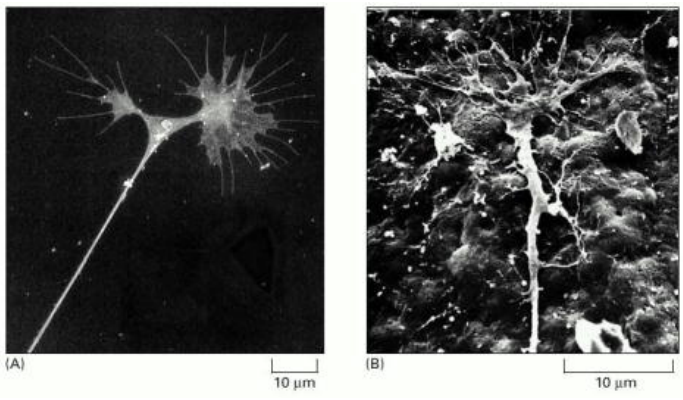

Figure 16-99. Neuronal growth cones. (A) Scanning electron micrograph of two growth cones at the end of a neurite, put out by a chick sympathetic neuron in culture. Here, a previously single growth cone has recently split into two. Note the many filopodia and the large lamellipodia. The taut appearance of the neurite is due to tension generated by the forward movement of the growth cones, which are often the only firm points of attachment of the axon to the substratum. (B) Scanning electron micrograph of the growth cone of a sensory neuron crawling over the inner surface of the epidermis of a *Xenopus* tadpole. (A, from D. Bray, in Cell Behaviour [R. Bellairs, A. Curtis, and G. Dunn, eds.]. Cambridge, UK: Cambridge University Press, 1982; B, from A. Roberts, *Brain Res*. 118:526530, 1976. © Elsevier.)

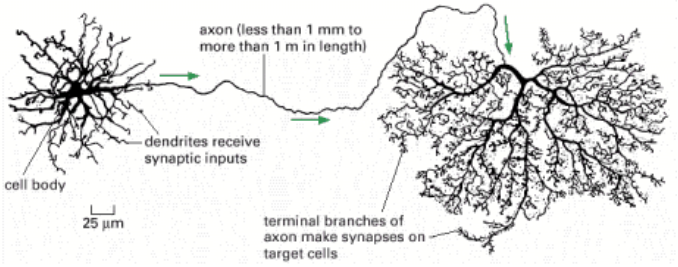

Figure 16-100. The complex architecture of a vertebrate neuron. The neuron shown is from the retina of a monkey. The arrows indicate the direction of travel of the electrical signal along the axon. The longest and largest neurons in the human body extend for a distance of about 1 m (1 million µm), from the base of the spinal cord to the tip of the big toe, and have an axon diameter of 15 µm. (Adapted from B.B. Boycott, in Essays on the Nervous System [R. Bellairs and E.G. Gray, eds.]. Oxford, UK: Clarendon Press, 1974.)

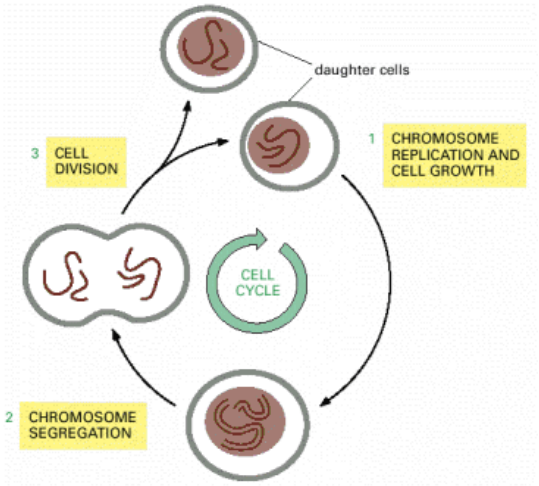

Figure 17-1. The cell cycle. The division of a hypothetical eucaryotic cell with two chromosomes is shown to illustrate how two genetically identical daughter cells are produced in each cycle. Each of the daughter cells will often divide again by going through additional cell cycles.

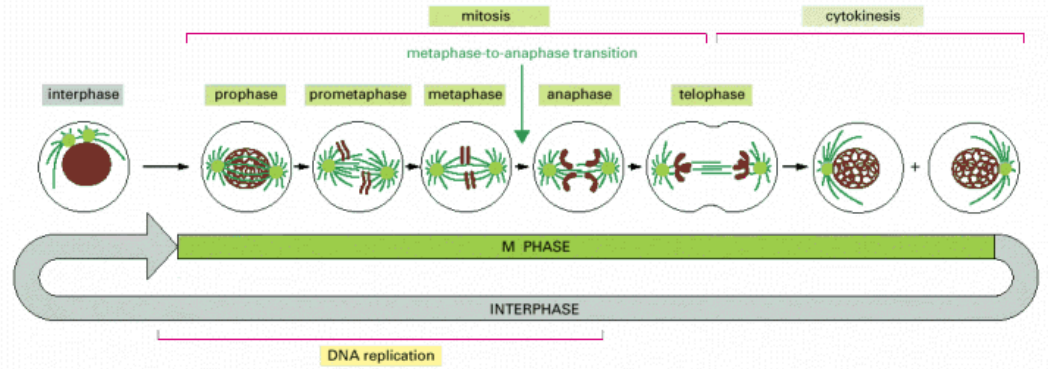

Figure 17-2. The events of eucaryotic cell division as seen under a microscope. The easily visible processes of nuclear division (mitosis) and cell division (cytokinesis), collectively called M phase, typically occupy only a small fraction of the cell cycle. The other, much longer, part of the cycle is known as interphase. The five stages of mitosis are shown: an abrupt change in the biochemical state of the cell occurs at the transition from metaphase to anaphase. A cell can pause in metaphase before this transition point, but once the point has been passed, the cell carries on to the end of mitosis and through cytokinesis into interphase. Note that DNA replication occurs in interphase. The part of interphase where DNA is replicated is called S phase (not shown).

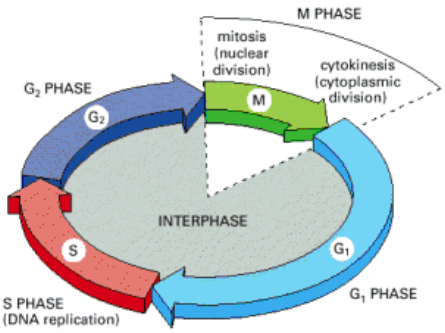

Figure 17-3. The phases of the cell cycle. The cell grows continuously in interphase, which consists of three phases: DNA replication is confined to S phase; G_1 is the gap between M phase and S phase, while G_2 is the gap between S phase and M phase. In M phase, the nucleus and then the cytoplasm divide.

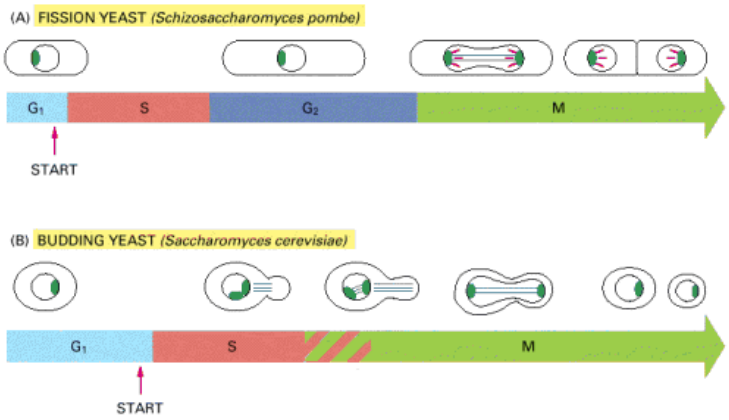

Figure 17-4. A comparison of the cell cycles of fission yeasts and budding yeasts. (A) The fission yeast has a typical eucaryotic cell cycle with G_1, S, G_2, and M phases. In contrast with what happens in higher eucaryotic cells, however, the nuclear envelope of the yeast cell does not break down during M phase. The microtubules of the mitotic spindle *(light green)* form inside the nucleus and are attached to spindle pole bodies *(dark green)* at its periphery. The cell divides by forming a partition (known as the cell plate) and splitting in two. The condensed mitotic chromosomes *(red)* are readily visible in fission yeast, but are less easily seen in budding yeasts. (B) The budding yeast has normal G_1 and S phases but does not have a normal G_2 phase. Instead, a microtubule-based spindle begins to form inside the nucleus early in the cycle, during S phase. In contrast with a fission yeast cell, the cell divides by budding. As in fission yeasts, but in contrast with higher eucaryotic cells, the nuclear envelope remains intact during mitosis, and the spindle forms within the nucleus.

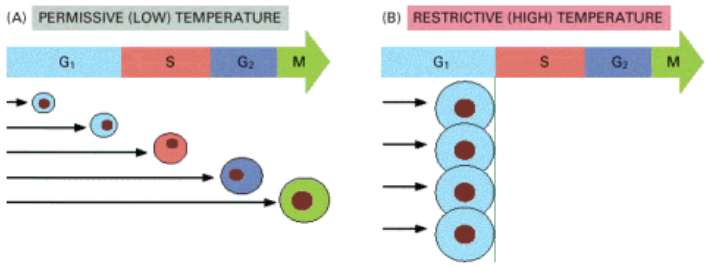

Figure 17-5. The behavior of a temperature-sensitive *cdc* mutant. (A) At the permissive (low) temperature, the cells divide normally and are found in all phases of the cycle (the phase of the cell is indicated by its color). (B) On warming to the restrictive (high) temperature, at which the mutant gene product functions abnormally, the mutant cells continue to progress through the cycle until they come to the specific step that they are unable to complete (initiation of S phase, in this example). Because the *cdc* mutants still continue to grow, they become abnormally large. By contrast, non-*cdc* mutants, if deficient in a process that is necessary throughout the cycle for biosynthesis and growth (such as ATP production), halt haphazardly at any stage of the cycle - depending on when their biochemical reserves run out (not shown).

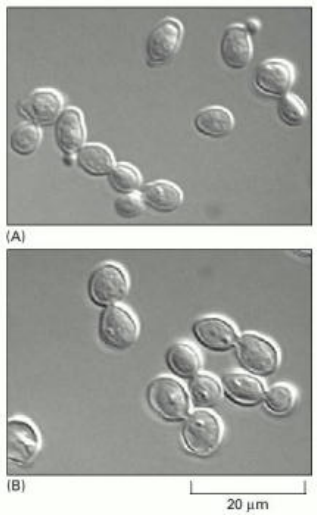

Figure 17-6. The morphology of budding yeast cells arrested by a *cdc* mutation. (A) In a normal population of proliferating yeast cells, buds vary in size according to the cell-cycle stage. (B) In a *cdc15* mutant grown at the restrictive temperature, cells complete anaphase but cannot complete the exit from mitosis and cytokinesis. As a result, they arrest uniformly with the large buds, which are characteristic of late M phase. (Courtesy of Jeff Ubersax.)

Figure 17-7. A mature *Xenopus* egg, ready for fertilization. The pale spot near the top shows the site of the nucleus, which has displaced the *brown* pigment in the surface layer of the egg cytoplasm. Although this cannot be seen in the picture, the nuclear envelope has broken down during the process of egg maturation. (Courtesy of Tony Mills.)

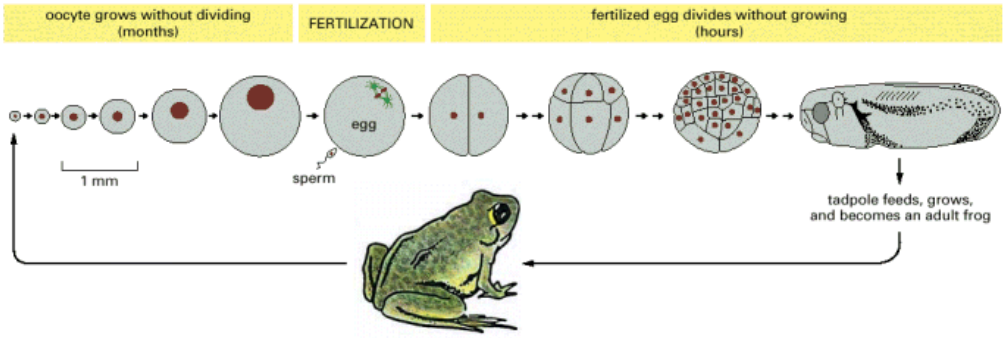

Figure 17-8. Oocyte growth and egg cleavage in *Xenopus*. The oocyte grows without dividing for many months in the ovary of the mother frog and finally matures into an egg. Upon fertilization, the egg cleaves very rapidly - initially at a rate of one division cycle every 30 minutes - forming a multicellular tadpole within a day or two. The cells get progressively smaller with each division, and the embryo remains the same size. Growth starts only when the tadpole begins feeding. The drawings in the top row are all on the same scale (but the frog below is not).

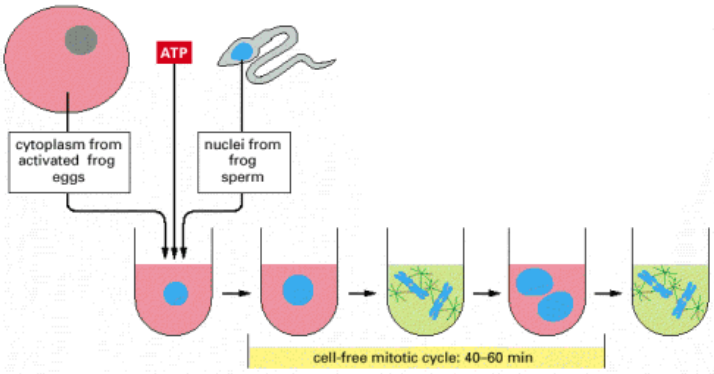

Figure 17-9. Studying the cell cycle in a cell-free system. A large batch of activated frog eggs is broken open by gentle centrifugation, which also separates the cytoplasm from other cell components. The undiluted cytoplasm is collected, and sperm nuclei are added to it, together with ATP. The sperm nuclei decondense and then go through repeated cycles of DNA replication and mitosis, indicating that the cell-cycle control system is operating in this cell-free cytoplasmic extract.

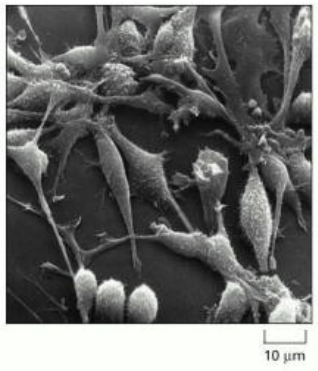

Figure 17-10. Mammalian cells proliferating in culture. The cells in this scanning electron micrograph are rat fibroblasts. (Courtesy of Guenter Albrecht-Buehler.)

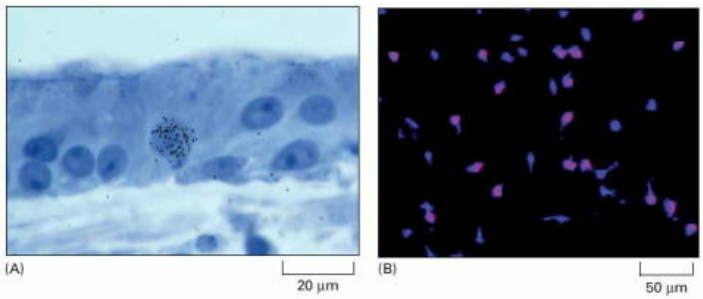

Figure 17-11. Labeling S-phase cells. (A) The tissue has been exposed for a short period to ^{3}H-thymidine and the labeled cells have been visualized by autoradiography. Silver grains *(black dots)* in the photographic emulsion over a nucleus indicate that the cell incorporated ^{3}H-thymidine into its DNA and thus was in S phase some time during the labeling period. In this specimen, showing the sensory epithelium from the inner ear of a chicken, the presence of an S-phase cell is evidence of cell proliferation occurring in response to damage. (B) An immunofluorescence micrograph of BrdU-labeled glial precursor cells in culture. The cells were exposed to BrdU for 4 h and were then fixed and labeled with fluorescent anti-BrdU antibodies *(red).* All the cells are stained with a *blue* fluorescent dye. (A, courtesy of Mark Warchol and Jeffrey Corwin; B, from D. Tang, Y. Tokumoto, and M. Raff, *J. Cell Biol.* 148:971984, 2000. © The Rockefeller University Press.)

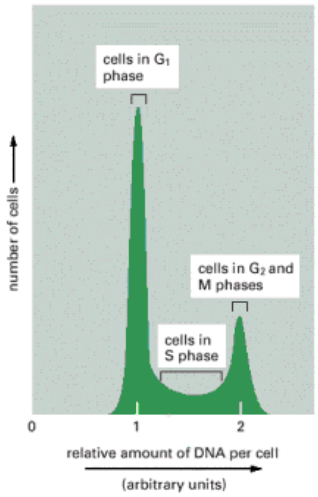

Figure 17-12. Analysis of DNA content with a flow cytometer. This graph shows typical results obtained for a proliferating cell population when the DNA content of its individual cells is determined in a flow cytometer. (A flow cytometer, also called a fluorescence-activated cell sorter, or FACS, can also be used to sort cells according to their fluorescence - see Figure 8-2). The cells analyzed here were stained with a dye that becomes fluorescent when it binds to DNA, so that the amount of fluorescence is directly proportional to the amount of DNA in each cell. The cells fall into three categories: those that have an unreplicated complement of DNA and are therefore in G_1 phase, those that have a fully replicated complement of DNA (twice the G_1 DNA content) and are in G_2 or M phase, and those that have an intermediate amount of DNA and are in S phase. The distribution of cells in the case illustrated indicates that there are greater numbers of cells in G_1 phase than in G_2 + M phase, showing that G_1 is longer than G_2 + M in this population.

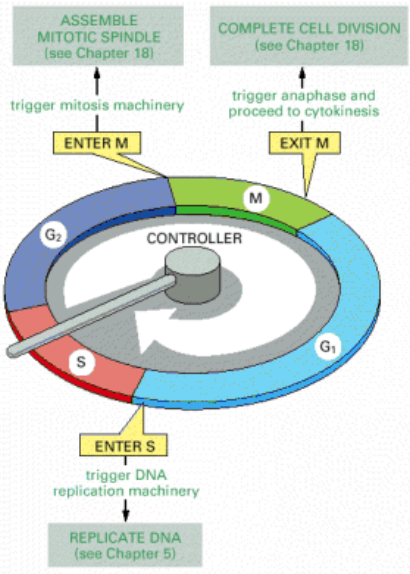

Figure 17-13. The control of the cell cycle. The essential processes of the cell cycle - such as DNA replication, mitosis, and cytokinesis - are triggered by a cell-cycle control system. By analogy with a washing machine, the cell-cycle control system is shown here as a central arm - the controller - that rotates clockwise, triggering essential processes when it reaches specific points on the outer dial.

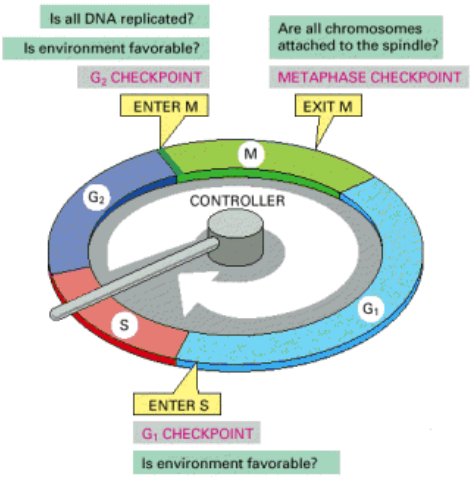

Figure 17-14. Checkpoints in the cell-cycle control system. Information about the completion of cell-cycle events, as well as signals from the environment, can cause the control system to arrest the cycle at specific checkpoints. The most prominent checkpoints occur at locations marked with *yellow boxes*.

Figure 17-15. Two key components of the cell-cycle control system. A complex of cyclin with Cdk acts as a protein kinase to trigger specific cell-cycle events. Without cyclin, Cdk is inactive.

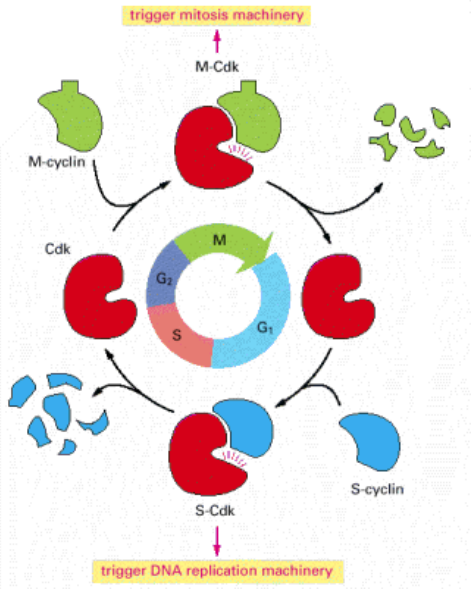

Figure 17-16. A simplified view of the core of the cell-cycle control system. Cdk associates successively with different cyclins to trigger the different events of the cycle. Cdk activity is usually terminated by cyclin degradation. For simplicity, only the cyclins that act in S phase (S-cyclin) and M phase (M-cyclin) are shown, and they interact with a single Cdk; as indicated, the resulting cyclin-Cdk complexes are referred to as S-Cdk and M-Cdk, respectively.

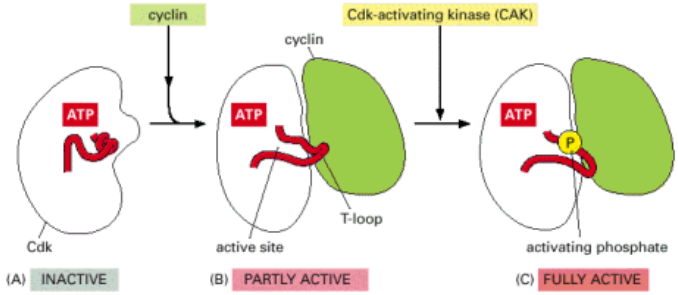

Figure 17-17. The structural basis of Cdk activation. These drawings are based on three-dimensional structures of human Cdk2, as determined by x-ray crystallography. The location of the bound ATP is indicated. The enzyme is shown in three states. (A) In the inactive state, without cyclin bound, the active site is blocked by a region of the protein called the T-loop (*red*). (B) The binding of cyclin causes the T-loop to move out of the active site, resulting in partial activation of the Cdk2. (C) Phosphorylation of Cdk2 (by CAK) at a threonine residue in the T-loop further activates the enzyme by changing the shape of the T-loop, improving the ability of the enzyme to bind its protein substrates.

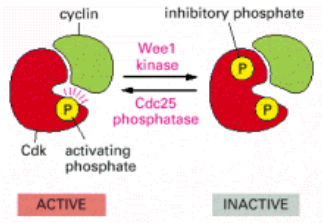

Figure 17-18. The regulation of Cdk activity by inhibitory phosphorylation. The active cyclin-Cdk complex is turned off when the kinase Wee1 phosphorylates two closely spaced sites above the active site. Removal of these phosphates by the phosphatase Cdc25 results in activation of the cyclin-Cdk complex. For simplicity, only one inhibitory phosphate is shown. The activating phosphate is added by CAK, as shown in Figure 17-17.

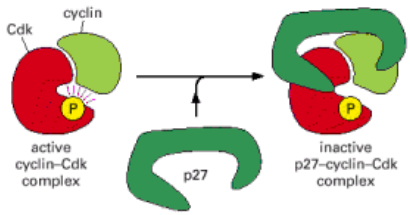

Figure 17-19. The inhibition of a cyclin-Cdk complex by a CKI. This drawing is based on the three-dimensional structure of the human cyclin A-Cdk2 complex bound to the CKI p27, as determined by x-ray crystallography. The p27 binds to both the cyclin and Cdk in the complex, distorting the active site of the Cdk. It also inserts into the ATP-binding site, further inhibiting the enzyme activity.

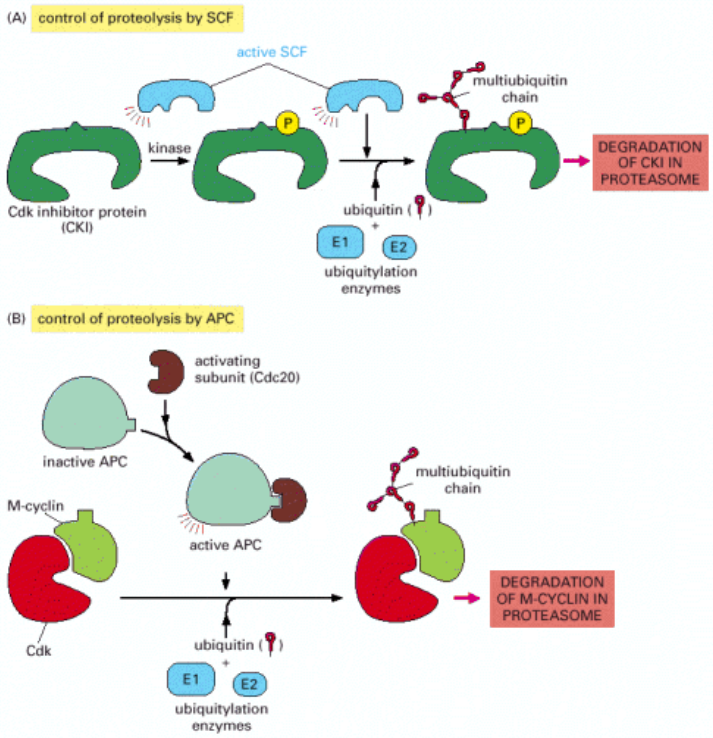

Figure 17-20. The control of proteolysis by SCF and APC during the cell cycle. (A) The phosphorylation of a target protein, such as the CKI shown, allows the protein to be recognized by SCF, which is constitutively active. With the help of two additional proteins called E1 and E2, SCF serves as a ubiquitin ligase that transfers multiple ubiquitin molecules onto the CKI protein. The ubiquitylated CKI protein is then immediately recognized and degraded in a proteasome. (B) M-cyclin ubiquitylation is performed by APC, which is activated in late mitosis by the addition of an activating subunit to the complex. Both SCF and APC contain binding sites that recognize specific amino acid sequences of the target protein.

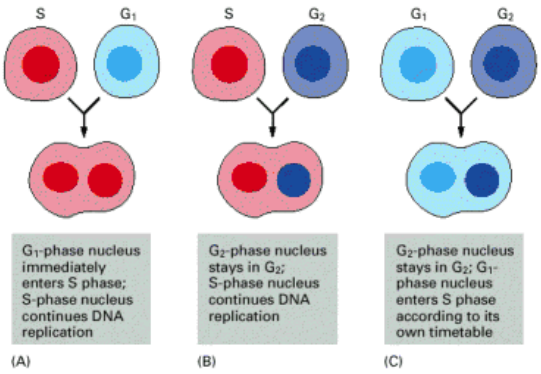

Figure 17-21. Evidence from cell-fusion experiments for a rereplication block. These experiments were carried out in 1970 in cultured mammalian cells. (A) The results show that S-phase cytoplasm contains factors that drive a G_1 nucleus directly into DNA synthesis. (B) A G_2 nucleus, having already replicated its DNA, is refractory to these factors. (C) Fusion of a G_2 cell with a G_1 cell does not drive the G_1 nucleus into DNA synthesis, indicating that the cytoplasmic factors for DNA replication that were present in the S-phase cell disappear when the cell moves from S phase into G_2. (Adapted from R. T. Johnson and P.N. Rao, *Nature* 226:717722, 1970.)

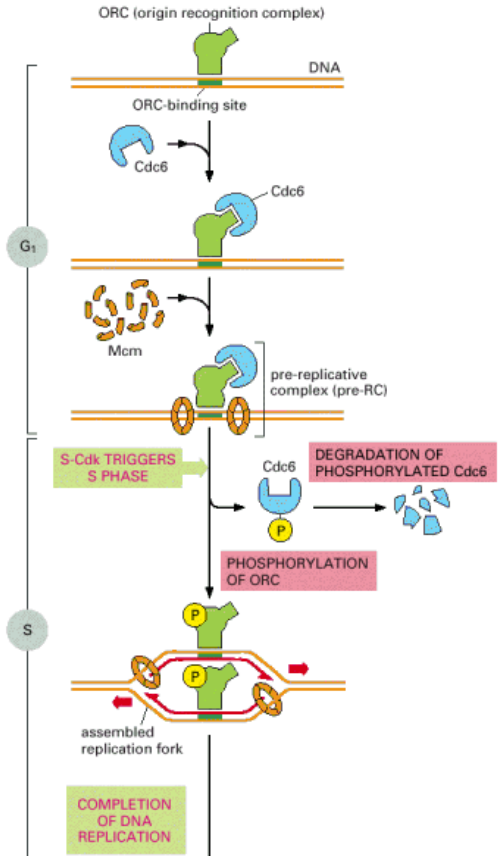

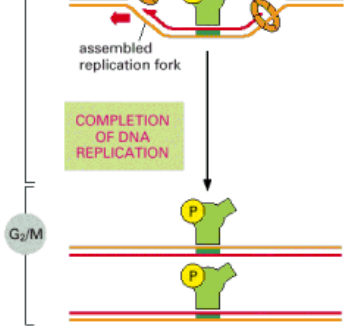

Figure 17-22. The initiation of DNA replication once per cell cycle. The ORC remains associated with a replication origin throughout the cell cycle. In early G_1, Cdc6 associates with ORC. Aided by Cdc6, Mcm ring complexes then assemble on the adjacent DNA, resulting in the formation of the pre-replicative complex. The S-Cdk (with assistance from another protein kinase, not shown) then triggers origin firing, assembling DNA polymerase and other replication proteins and activating the Mcm protein rings to migrate along DNA strands as DNA helicases. The S-Cdk also blocks rereplication by causing the dissociation of Cdc6 from origins, its degradation, and the export of all excess Mcm out of the nucleus. Cdc6 and Mcm cannot return to reset an ORC-containing origin for another round of DNA replication until M-Cdk has been inactivated at the end of mitosis (see text).

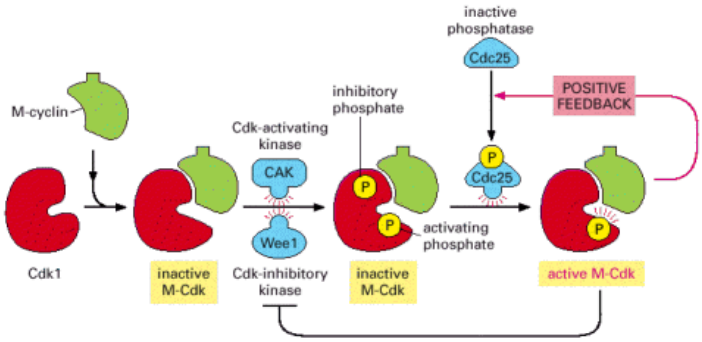

Figure 17-23. The activation of M-Cdk. Cdk1 associates with M-cyclin as the levels of M-cyclin gradually rise. The resulting M-Cdk complex is phosphorylated on an activating site by the Cdk-activating kinase (CAK) and on a pair of inhibitory sites by the Wee1 kinase. The resulting inactive M-Cdk complex is then activated at the end of G_2 by the phosphatase Cdc25. Cdc25 is stimulated in part by Polo kinase, which is not shown for simplicity. Cdc25 is further stimulated by active M-Cdk, resulting in positive feedback. This feedback is enhanced by the ability of M-Cdk to inhibit WeeI.

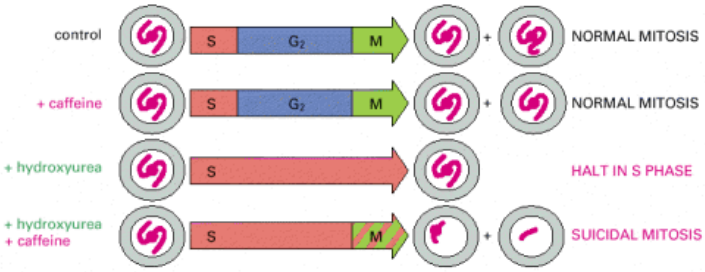

Figure 17-24. The DNA replication checkpoint. In the experiments diagrammed here, mammalian cells in culture were treated with caffeine and hydroxyurea, either alone or in combination. Hydroxyurea blocks DNA synthesis. This block activates a checkpoint mechanism that arrests the cells in S phase, delaying mitosis. But if caffeine is added as well as hydroxyurea, the checkpoint mechanism fails, and the cells proceed into mitosis according to their normal schedule, with incompletely replicated DNA. As a result, the cells die.

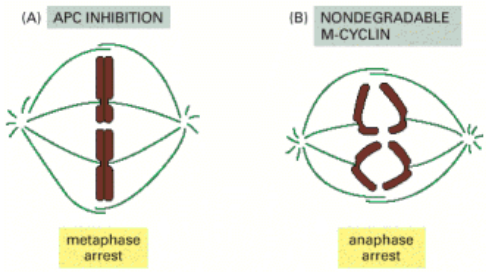

Figure 17-25. Two experiments that demonstrate the requirement for protein degradation to exit from mitosis. (A) An APC inhibitor was added to frog egg extracts undergoing mitosis *in vitro* (see Figure 17-9). The inhibitor arrested mitosis at metaphase, indicating that proteolysis is required for the separation of sister chromatids at the metaphase-to-anaphase transition. A similar arrest occurs in budding yeasts with mutations in components of the APC. (B) A nondegradable mutant form of M-cyclin was added to mitotic frog egg extracts. This addition arrested mitosis after sister-chromatid separation, indicating that destruction of M-cyclin is not required for sister-chromatid separation but is required for the subsequent exit from mitosis. (Based on S.L. Holloway et al., *Cell* 73:13931402, 1993.)

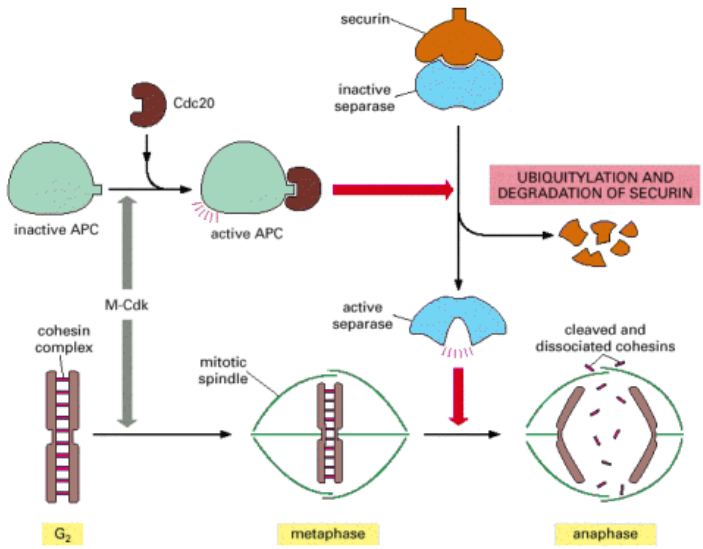

Figure 17-26. The triggering of sister-chromatid separation by the APC. The activation of APC by Cdc20 leads to the ubiquitylation and destruction of securin, which normally holds separase in an inactive state. The destruction of securin allows separase to cleave a subunit of the cohesin complex holding the sister chromatids together. The pulling forces of the mitotic spindle then pull the sister chromatids apart. In budding yeasts at least, cohesin cleavage by separase is facilitated by the phosphorylation of the cohesin complex adjacent to the cleavage site, just before anaphase begins. The phosphorylation is mediated by Polo kinase and provides an additional control on the timing of the metaphase-to-anaphase transition.

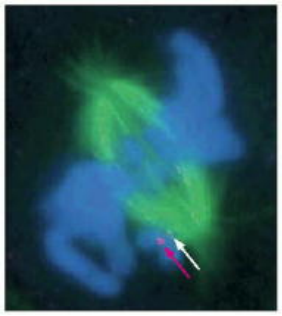

Figure 17-27. Mad2 protein on unattached kinetochores. This fluorescence micrograph shows a mammalian cell in prometaphase, with the mitotic spindle in *green* and the sister chromatids in *blue*. One sister chromatid pair is not yet attached to the spindle. The presence of Mad2 on the kinetochore of the unattached chromosome is revealed by the binding of anti-Mad2 antibodies *(red dot,* indicated by *red arrow).* Another chromosome has just attached to the spindle, and its kinetochore has a low level of Mad2 still associated with it *(pale dot,* indicated by *white arrow).* (From J.C. Waters et al., *J. Cell Biol.* 141:11811191, 1998. © The Rockefeller University Press.)

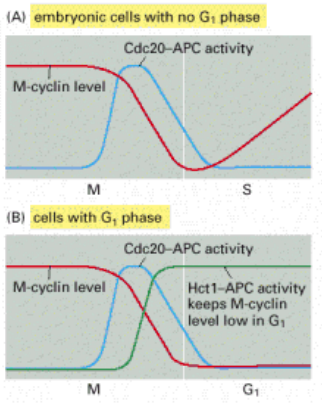

Figure 17-28. The creation of a G_1 phase by stable Cdk inhibition after mitosis. (A) In early embryonic cell cycles, Cdc20-APC activity rises at the end of metaphase, triggering M-cyclin destruction. Because M-Cdk activity stimulates Cdc20-APC activity, the loss of M-cyclin leads to APC inactivation after mitosis, which allows M-cyclins to begin accumulating again. (B) In cells containing a G_1 phase, the drop in M-Cdk activity in late mitosis leads to the activation of Hct1-APC (as well as to the accumulation of CKI proteins, not shown). This ensures a continued suppression of Cdk activity after mitosis, as required for a G_1 phase.

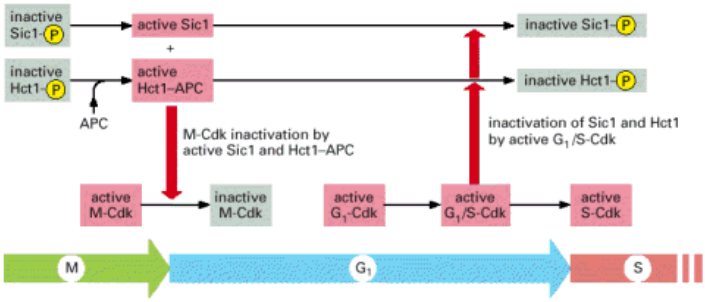

Figure 17-29. The control of G_1 progression by Cdk activity in budding yeast. As cells exit from mitosis and inactivate M-Cdk, the resulting increase in Hct1 and Sic1 activities results in stable Cdk inactivation during G_1. When conditions are right for entering a new cell cycle, the increase in G_1-Cdk and G_1/S-Cdk activities leads to the inhibition of Sic1 and Hct1 by phosphorylation, allowing S-Cdk activity to increase.

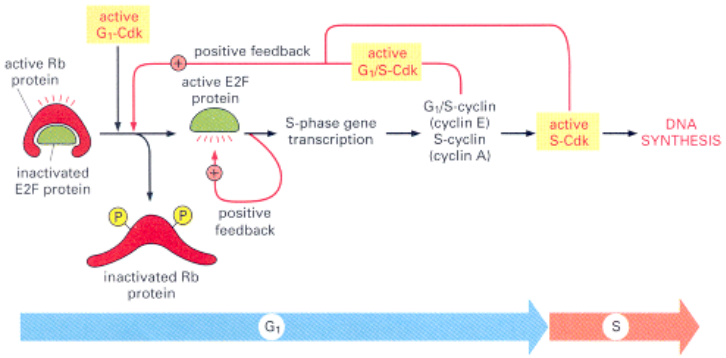

Figure 17-30. Mechanisms controlling S-phase initiation in animal cells. G_1-Cdk activity (cyclin D-Cdk4) initiates Rb phosphorylation. This inactivates Rb, freeing E2F to activate the transcription of S-phase genes, including the genes for a G_1/S-cyclin (cyclin E) and S-cyclin (cyclin A). The resulting appearance of G_1/S-Cdk and S-Cdk activities further enhances Rb phosphorylation, forming a positive feedback loop. E2F acts back to stimulate the transcription of its own gene, forming another positive feedback loop.

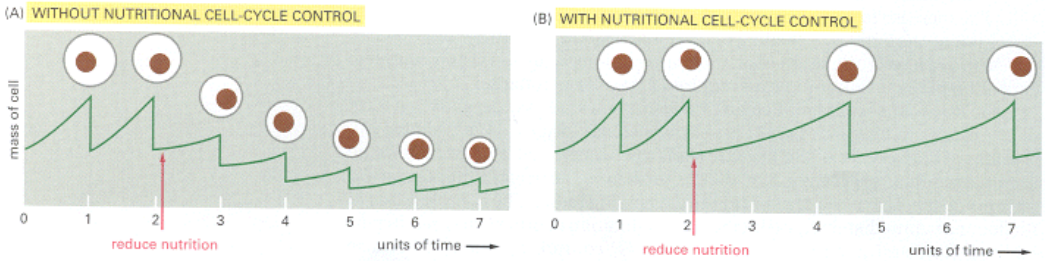

Figure 17-31. Cell size control through control of the cell cycle in yeasts. These graphs show the relationship between growth rate, cell size, and cell cycle time. (A) If cell division continued at an unchanged rate when cells were starved and stopped growing, the daughter cells produced at each division would become progressively smaller. (B) Yeast cells respond to some forms of nutritional deprivation by slowing the rate of progress through the cell cycle so that the cells have more time to grow. As a result, cell size remains unchanged or is reduced slightly. (A unit of time is the cycle time observed when nutrients are in excess.)

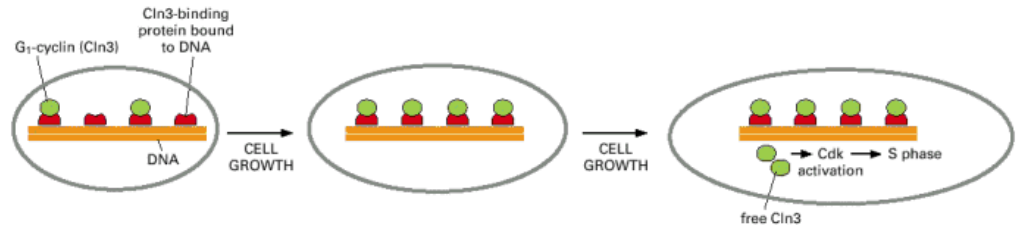

Figure 17-32. A hypothetical model of how budding yeast cells might coordinate cell growth and cell-cycle progression. The cell contains a fixed number of proteins *(red)* that are bound to DNA and bind and inhibit Cln3 molecules *(green)*. As the cell grows, the total number of Cln3 molecules increases in parallel with total cell protein. When the cell is small *(left)*, all of the Cln3 is inactivated by the excess of Cln3-binding protein. As the cell grows, however, it reaches a threshold size at which the number of Cln3 molecules equals the number of Cln3-binding proteins *(middle)*. When the cell exceeds this size, free Cln3 can bind to Cdk, which can now trigger the next cell cycle *(right)*.

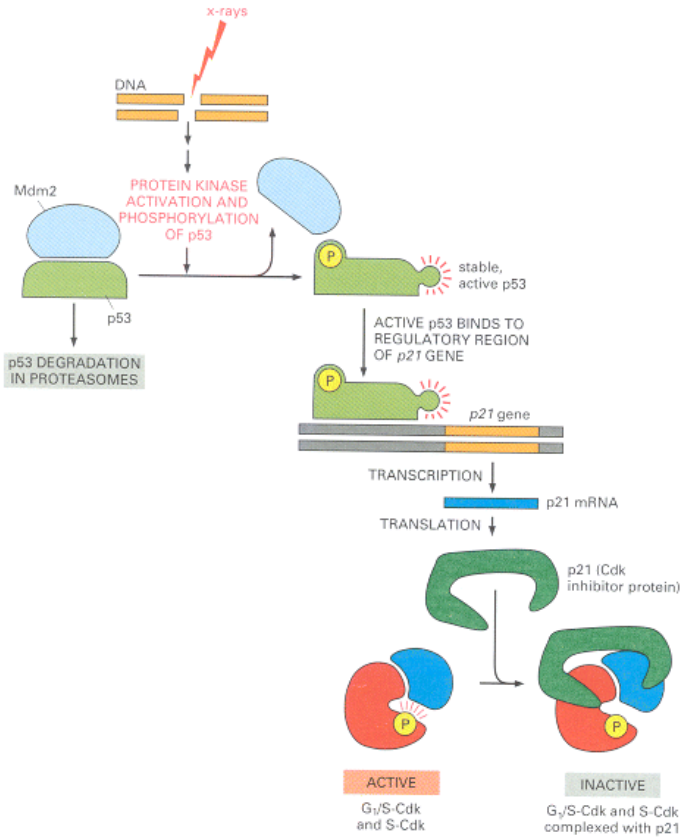

Figure 17-33. How DNA damage arrests the cell cycle in G_1. When DNA is damaged, protein kinases that phosphorylate p53 are activated. Mdm2 normally binds to p53 and promotes its ubiquitylation and destruction in proteasomes. Phosphorylation of p53 blocks its binding to Mdm2; as a result, p53 accumulates to high levels and stimulates transcription of the gene that encodes the CKI protein p21. The p21 binds and inactivates G_1/S-Cdk and S-Cdk complexes, arresting the cell in G_1. In some cases, DNA damage also induces either the phosphorylation of Mdm2 or a decrease in Mdm2 production, which causes an increase in p53 (not shown).

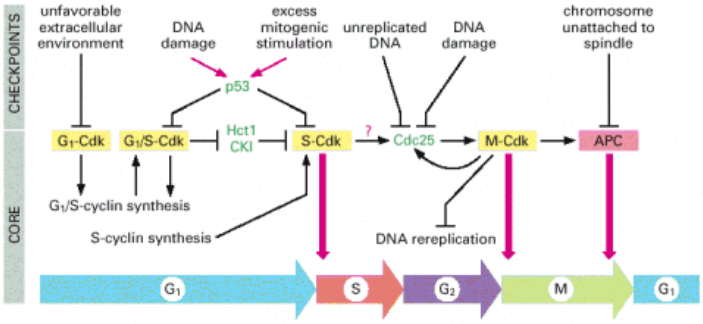

Figure 17-34. An overview of the cell-cycle control system. The core of the cell-cycle control system consists of a series of cyclin-Cdk complexes *(yellow).* The activity of each complex is also influenced by various inhibitory checkpoint mechanisms, which provide information about the extracellular environment, cell damage, and incomplete cell-cycle events *(top).* These mechanisms are not present in all cell types; many are missing in early embryonic cell cycles, for example.

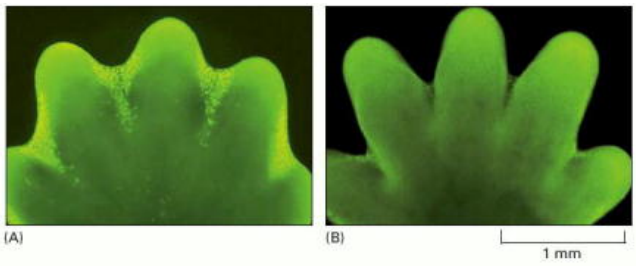

Figure 17-35. Sculpting the digits in the developing mouse paw by apoptosis. (A) The paw in this mouse embryo has been stained with a dye that specifically labels cells that have undergone apoptosis. The apoptotic cells appear as *bright green* dots between the developing digits. (B) This interdigital cell death eliminates the tissue between the developing digits, as seen one day later, when few, if any, apoptotic cells can be seen. (From W. Wood et al., *Development* 127:52455252, 2000. © The Company of Biologists.)

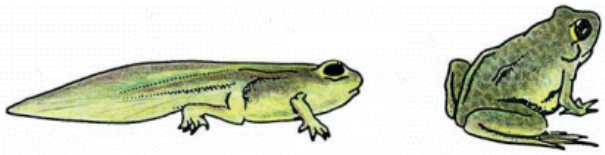

Figure 17-36. Apoptosis during the metamorphosis of a tadpole into a frog. As a tadpole changes into a frog, the cells in the tadpole tail are induced to undergo apoptosis; as a consequence, the tail is lost. All the changes that occur during metamorphosis, including the induction of apoptosis in the tail, are stimulated by an increase in thyroid hormone in the blood.

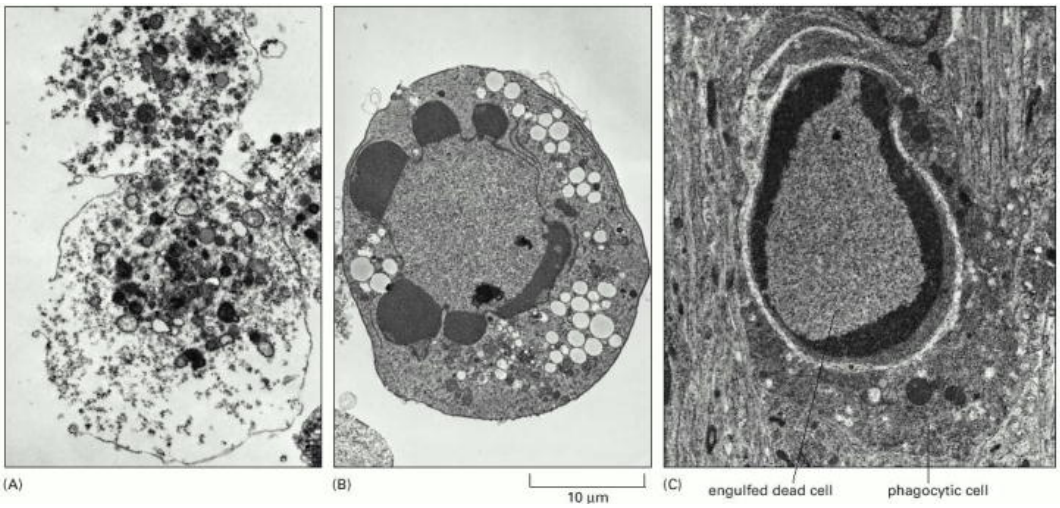

Figure 17-37. Cell death. These electron micrographs show cells that have died by (A) necrosis or (B and C) apoptosis. The cells in (A) and (B) died in a culture dish, whereas the cell in (C) died in a developing tissue and has been engulfed by a neighboring cell. Note that the cell in (A) seems to have exploded, whereas those in (B) and (C) have condensed but seem relatively intact. The large vacuoles visible in the cytoplasm of the cell in (B) are a variable feature of apoptosis. (Courtesy of Julia Burne.)

Figure 17-38. The caspase cascade involved in apoptosis. (A) Each suicide protease is made as an inactive proenzyme (procaspase), which is usually activated by proteolytic cleavage by another member of the caspase family. As indicated, two of the cleaved fragments associate to form the

active site of the caspase. The active enzyme is thought to be a tetramer of two of these units (not shown). (B) Each activated caspase molecule can cleave many procaspase molecules, thereby activating them, and these can then activate even more procaspase molecules. In this way, an initial activation of a small number of procaspase molecules (called initiator caspases) can lead, via an amplifying chain reaction (a cascade), to the explosive activation of a large number of procaspase molecules. Some of the activated caspases (called effector caspases) then cleave a number of key proteins in the cell, including specific cytosolic proteins and nuclear lamins, leading to the controlled death of the cell.

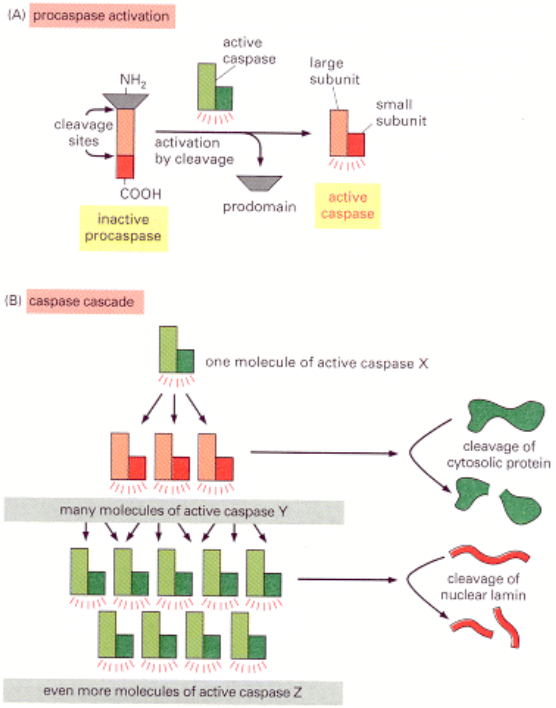

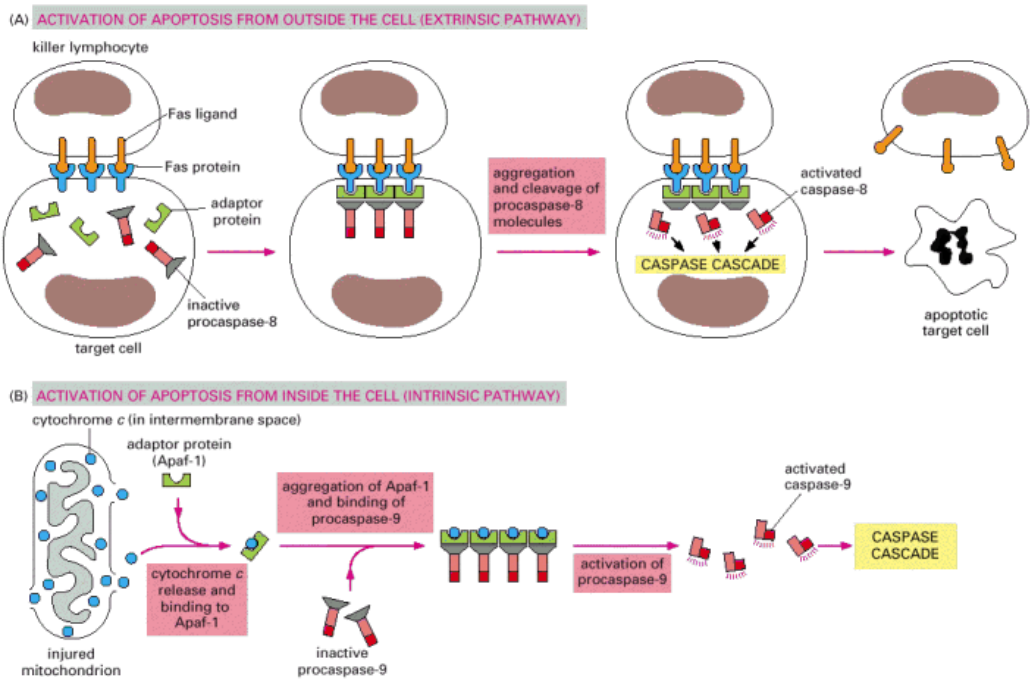

Figure 17-39. Induction of apoptosis by either extracellular or intracellular stimuli. (A) Extracellular activation. A killer lymphocyte carrying the Fas ligand binds and activates Fas proteins on the surface of the target cell. Adaptor proteins bind to the intracellular region of aggregated Fas proteins, causing the aggregation of procaspase-8 molecules. These then cleave one another to initiate the caspase cascade. (B) Intracellular activation. Mitochondria release cytochrome *c*, which binds to and causes the aggregation of the adaptor protein Apaf-1. Apaf-1 binds and aggregates procaspase-9 molecules, which leads to the cleavage of these molecules and the triggering of a caspase cascade. Other proteins that contribute to apoptosis are also released from the mitochondrial intermembrane space (not shown).

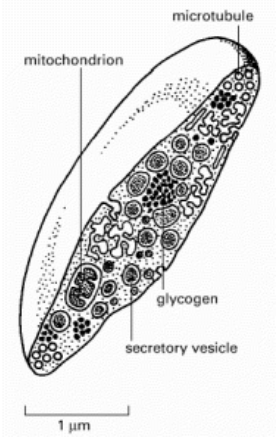

Figure 17-40. A platelet. Platelets are miniature cells without a nucleus. They circulate in the blood and help stimulate blood clotting at sites of tissue damage, thereby preventing excessive bleeding. They also release various factors that stimulate healing. The platelet shown here has been cut in half to show its secretory vesicles, some of which contain platelet-derived growth factor (PDGF). See also Figure 16-47B-D.

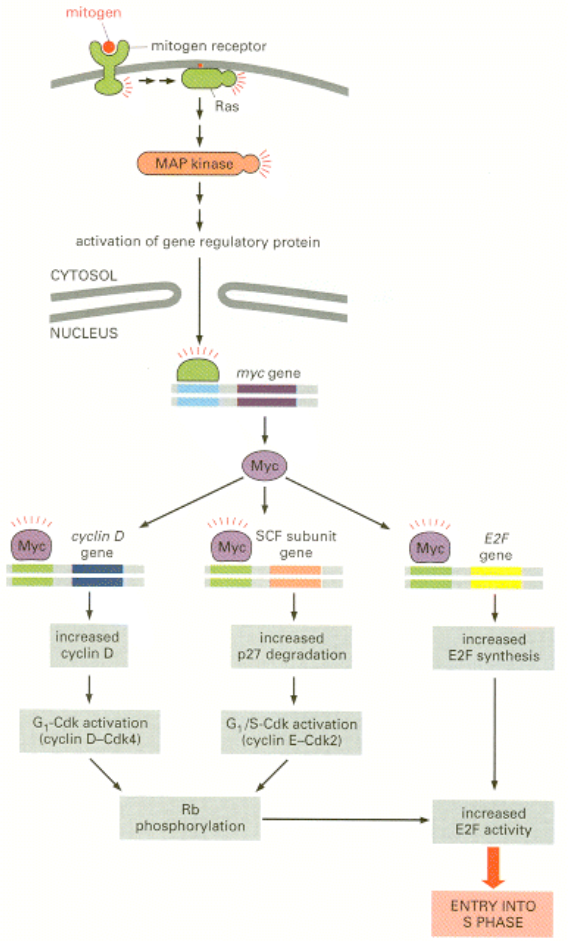

Figure 17-41. A simplified model of one way that mitogens stimulate cell division. The binding of mitogens to cell-surface receptors leads to the activation of Ras and a MAP kinase cascade. One effect of this pathway is the increased production of the gene regulatory protein Myc. Myc increases the transcription of several genes, including the gene encoding cyclin D and a gene encoding a subunit of the SCF ubiquitin ligase. The resulting increase in G_1-Cdk and G_1/S-Cdk activities promotes Rb phosphorylation and activation of the gene regulatory protein E2F, resulting in S-phase entry (see Figure 17-30). Myc may also promote E2F activity directly by stimulating the transcription of the *E2F* gene. Although, for simplicity, Myc is shown as a monomer, it functions as a heterodimer with another protein called Max.

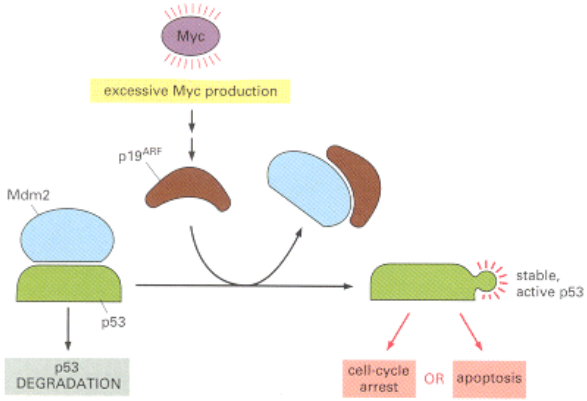

Figure 17-42. Cell-cycle arrest or apoptosis induced by excessive stimulation of mitogenic pathways. Abnormally high levels of Myc cause the activation of $p19^{ARF}$, which binds and inhibits Mdm2 and thereby causes increased p53 levels (see Figure 17-33). Depending on the cell type and extracellular conditions, p53 then causes either cell-cycle arrest or apoptosis.

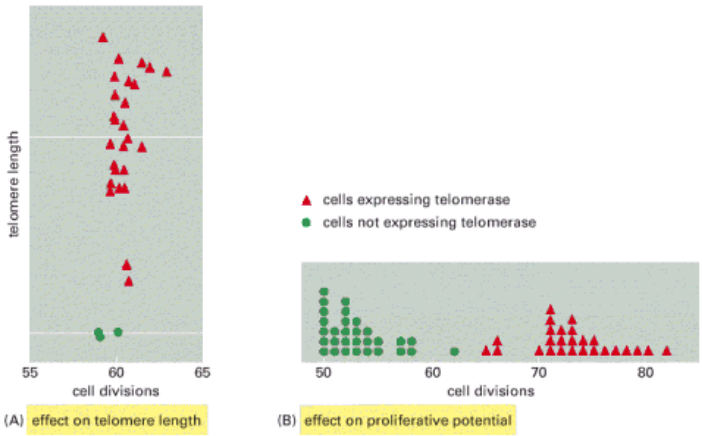

Figure 17-43. Overcoming replicative cell senescence by the forced expression of telomerase. (A) Normal human fibroblasts do not contain telomerase, and so their telomeres gradually shorten and lose their normal cap structure as the cells proliferate. Cells forced to express telomerase, however, maintain telomere length (and normal cap structures) after many divisions. (B) The normal human fibroblasts stopped dividing after about 5060 divisions in these experiments, whereas the cells expressing telomerase were still dividing at the end of the experiment. (Based on A. Bodnar et al., *Science* 279:349352, 1998.)

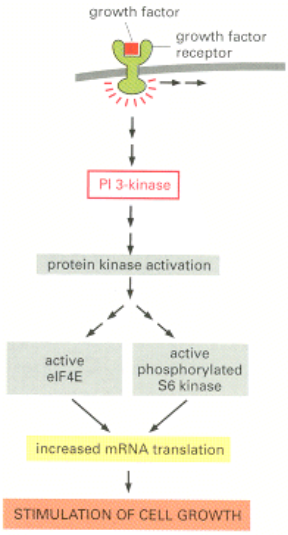

Figure 17-44. One way in which growth factors promote cell growth. In this simplified scheme, activation of cell-surface receptors leads to the activation of PI 3-kinase, which promotes protein synthesis, at least partly through the activation of eIF4E and S6 kinase. Growth factors also inhibit protein breakdown (not shown) by poorly understood pathways.

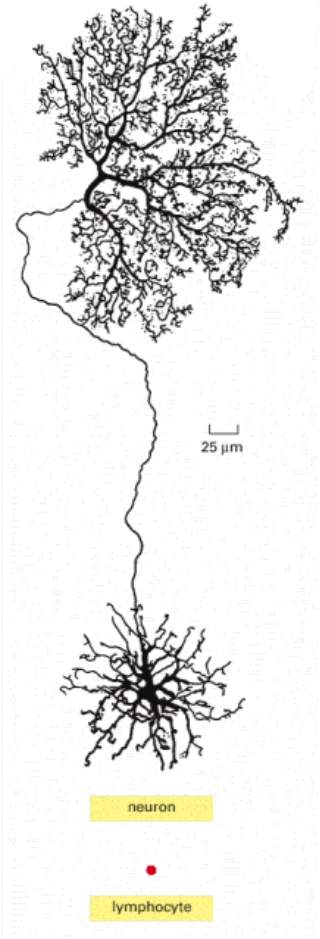

Figure 17-45. The size difference between a neuron (from the retina) and a lymphocyte in a mammal. Both cells contain the same amount of DNA. A neuron grows progressively larger after it has permanently withdrawn from the cell cycle. During this time, the ratio of cytoplasm to DNA increases enormously (by a factor of more than 10^5 for some neurons). (Neuron from B.B. Boycott, in Essays on the Nervous System [R. Bellairs and E.G. Gray, eds]. Oxford, UK: Clarendon Press, 1974.)

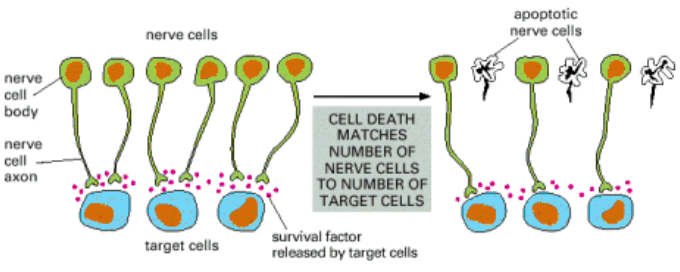

Figure 17-46. The function of cell death in matching the number of developing nerve cells to the number of target cells they contact. More nerve cells are produced than can be supported by the limited amount of survival factors released by the target cells. Therefore, some cells receive an insufficient amount of survival factors to keep their suicide program suppressed and, as a consequence, undergo apoptosis. This strategy of overproduction followed by culling ensures that all target cells are contacted by nerve cells and that the extra nerve cells are automatically eliminated.

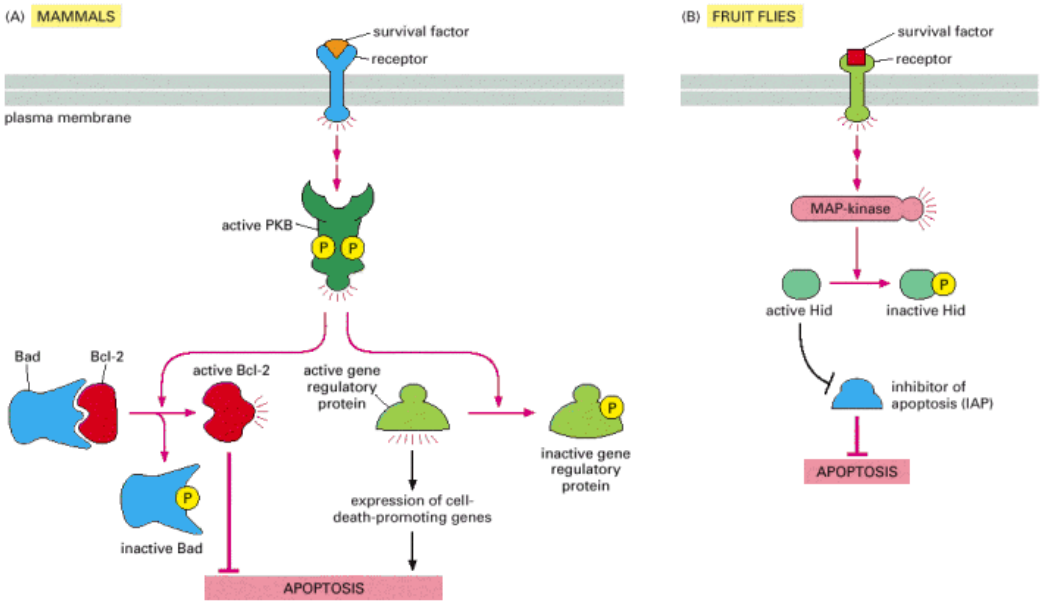

Figure 17-47. Two ways in which survival factors suppress apoptosis. (A) In mammalian cells, the binding of some survival factors to cell-surface receptors leads to the activation of various protein kinases, including protein kinase B (PKB), that phosphorylate and inactivate the Bcl-2 family member Bad. When not phosphorylated, Bad promotes apoptosis by binding and inhibiting Bcl-2. Once phosphorylated, Bad dissociates, freeing Bcl-2 to suppress apoptosis. As indicated, PKB also suppresses death by phosphorylating and thereby inhibiting gene regulatory proteins of the Forkhead family that stimulate the transcription of genes that encode proteins that promote apoptosis. (B) In *Drosophila*, some survival factors inhibit apoptosis by stimulating the phosphorylation of the Hid protein. When not phosphorylated, Hid promotes cell death by inhibiting IAPs. Once phosphorylated, Hid no longer inhibits IAPs, which become active and block cell death.

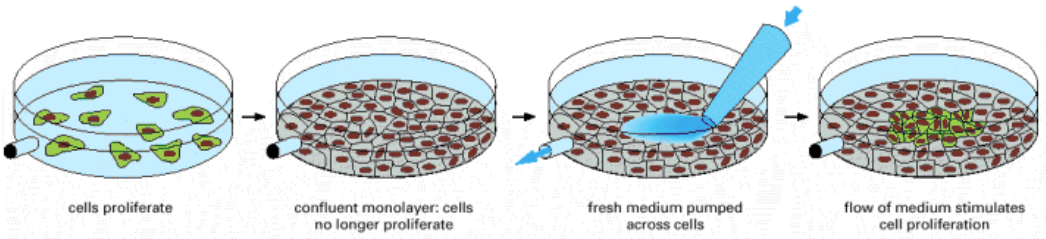

Figure 17-48. The effect of fresh medium on a confluent cell monolayer. Cells in a confluent monolayer do not divide *(gray)*. The cells resume dividing *(green)* when exposed directly to fresh culture medium. Apparently, in the undisturbed confluent monolayer, proliferation has halted because the medium close to the cells is depleted of mitogens, for which the cells compete.

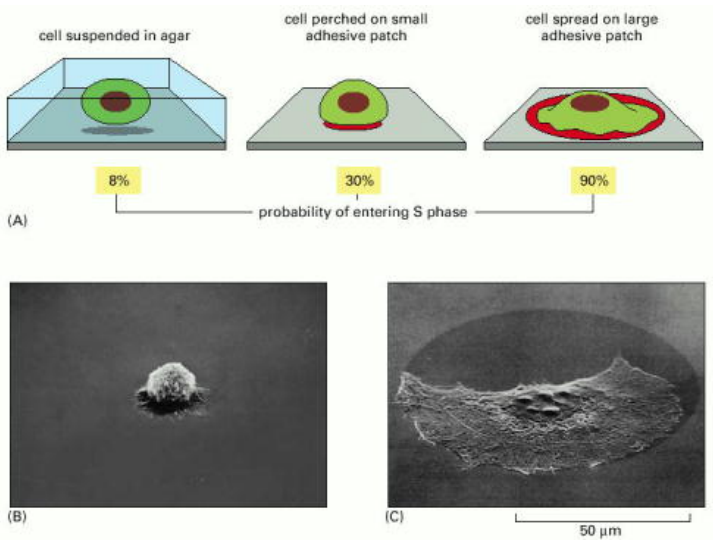

Figure 17-49. The dependence of cell division on cell shape and anchorage. In this experiment, cells are either held in suspension or allowed to settle on patches of an adhesive material (palladium) on a nonadhesive substratum. The patch diameter, which is variable, determines the extent to which an individual cell spreads and the probability that it will progress into S phase. ^{3}H-thymidine is added to the culture medium, and after 1 or 2 days, the culture is fixed and autoradiographed to determine the percentage of cells that have entered S phase (see Figure 17-11A). (A) Few cells of the 3T3 cell line enter S phase when held rounded up in suspension, but adherence even to a very tiny patch - one that is too small to allow spreading - enables many of them to enter S phase. (B and C) These scanning electron micrographs show a cell perched on a small patch compared with a cell spread on a large patch. In contrast to fibroblasts and epithelial cells, some cell types in the body (including lymphocytes and blood cell precursors) can divide readily in suspension (see also Figure 19-62). (B and C, from C. O'Neill, P. Jordan, and G. Ireland, *Cell* 44:489496, 1986. © Elsevier.)

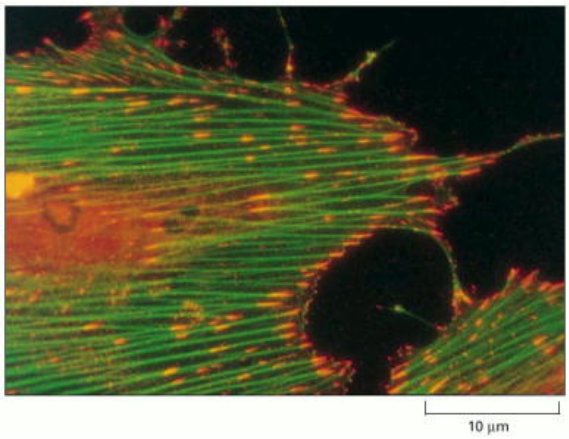

Figure 17-50. Focal adhesions as production sites of intracellular signals. This fluorescence micrograph shows a fibroblast cultured on a substratum coated with the extracellular matrix molecule fibronectin. Actin filaments have been labeled to fluoresce *green*, while activated proteins that contain phosphotyrosine have been labeled with an antibody that is tagged to fluoresce *red*. Where the two components overlap, the resulting color is *orange*. The actin filaments terminate at focal adhesions, where the cell attaches to the substratum. Proteins containing phosphotyrosine are also concentrated at these sites. This is thought to reflect the local activation of focal adhesion kinase (FAK) and other protein kinases stimulated by transmembrane integrin proteins that bind to fibronectin extracellularly and (indirectly) to actin filaments intracellularly. Signals generated at such adhesion sites help regulate cell division, growth, and survival, in both fibroblasts and epithelial cells. (Courtesy of Keith Burridge.)

Figure 17-51. The effects of a myostatin mutation on muscle size. The mutation leads to a dramatic increase in the mass of muscle tissue, as illustrated in this Belgian Blue bull. The Belgium Blue was produced by cattle breeders and was only recently found to have a mutation in the *myostatin* gene. Mice purposely made deficient in the same gene also have remarkably big muscles (see Figure 22-43). (From A.C. McPherron and S.-J. Lee, *Proc. Natl. Acad. Sci. USA* 94:1245712461, 1997. © National Academy of Sciences.)

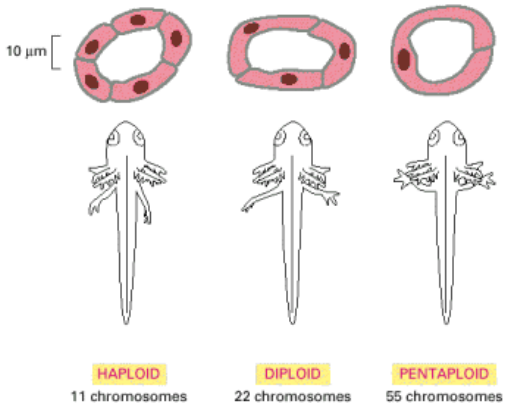

Figure 17-52. Sections of kidney tubules from salamander larvae of different ploidies. In all organisms, from bacteria to humans, cell size is proportional to ploidy. Pentaploid salamanders, for example, have cells that are much larger than those of haploid salamanders. The animals and their individual organs, however, are the same size because each tissue in the pentaploid animal contains fewer cells. This indicates that the size of an organism or organ is not controlled simply by counting cell divisions or cell numbers; total cell mass must somehow be regulated. (Adapted from G. Fankhauser, in Analysis of Development [B.H. Willier, P.A. Weiss, and V. Hamburger, eds.], pp. 126150. Philadelphia: Saunders, 1955.)

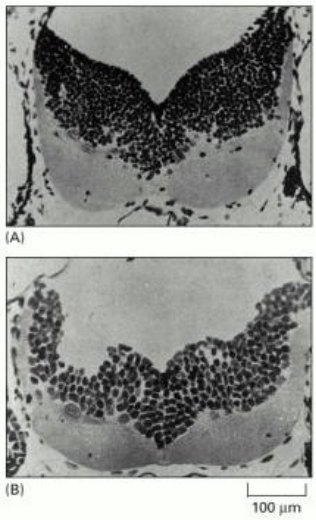

Figure 17-53. The hindbrain in a haploid and in a tetraploid salamander. (A) This light micrograph shows a cross section of the hindbrain of a haploid salamander. (B) A corresponding cross section of the hindbrain of a tetraploid salamander, revealing how reduced cell numbers compensate for increased cell size. (From G. Fankhauser, *Int. Rev. Cytol*. 1:165193, 1952.)

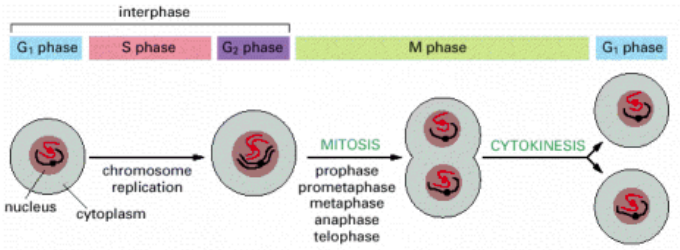

Figure 18-1. The M phase of the cell cycle. M phase starts at the end of G_2 and ends at the start of the next G_1 phase. It includes the five stages of nuclear division (mitosis), as well as cytoplasmic division (cytokinesis).

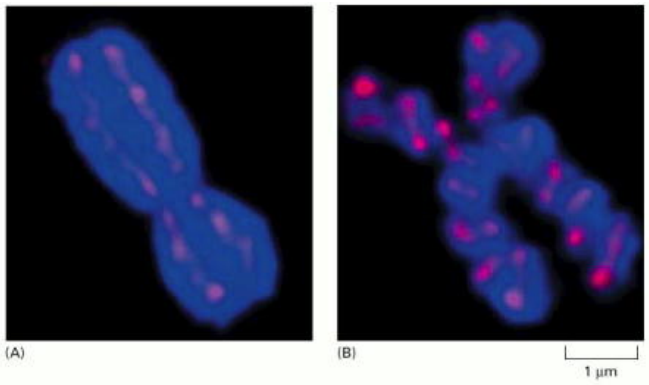

Figure 18-2. Human mitotic chromosomes stained to reveal a scaffold-like structure along the chromosome axis. In these confocal fluorescence micrographs, the DNA has been stained with a *blue* dye, and the axis has been stained *red* with a fluorescent antibody against a protein in the condensin complex. Only part of the scaffolding is visible in these optical sections. (A) A typical mitotic chromosome, which has a gently coiled scaffold along each of the two chromatids. (B) A metaphase chromosome from a cell artificially blocked in metaphase; in the chromosomes of these cells, the scaffold has condensed by further helical folding. (Courtesy of Ulrich Laemmli and Kazuhiro Maeshima).

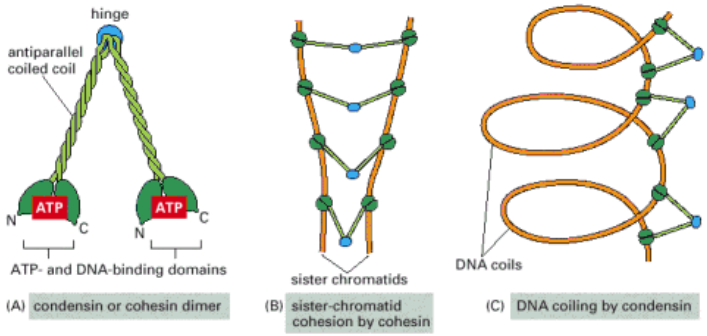

Figure 18-3. The related structure and function of cohesins and condensins. (A) Both proteins have two identical DNA- and ATP-binding domains at one end and a hinge region at the other, joined by two, long, coiled-coil regions. This flexible structure is well suited for their role as DNA cross-linkers. (B) Cohesins cross-link two adjacent sister chromatids, gluing them together. (C) Condensins mediate intramolecular cross-linking to coil DNA in the process of chromosome condensation. (Adapted from T. Hirano, *Genes and Dev.* 13:1119, 1999.)

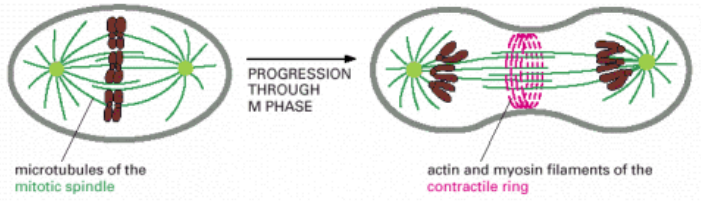

Figure 18-4. Two cytoskeletal machines that operate in M phase. The mitotic spindle assembles first and segregates the chromosomes. The contractile ring assembles later and divides the cell in two. Plant cells use a very different mechanism to divide the cytoplasm, as we discuss later.

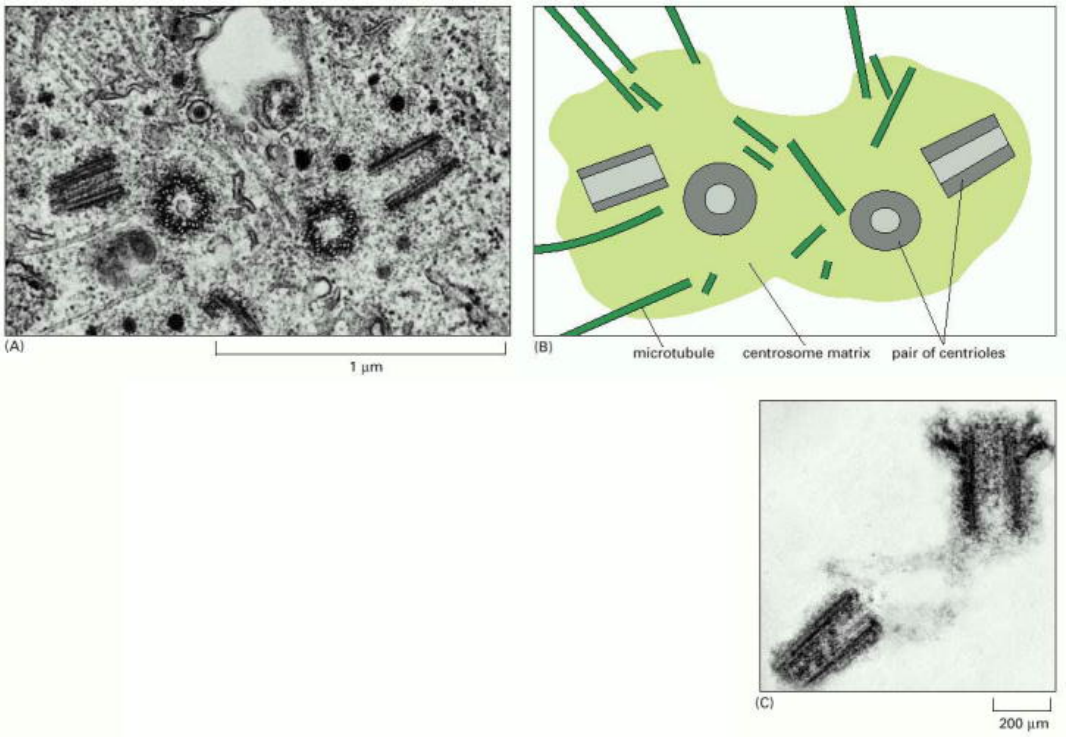

Figure 18-5. Centrioles. (A) Electron micrograph of an S-phase mammalian cell in culture, showing a duplicated centrosome. Each centrosome contains a pair of centrioles; although the centrioles have duplicated, they remain together in a single complex, as shown in the drawing of the micrograph in (B). One centriole of each centriole pair has been cut in cross-section, while the other is cut in longitudinal section, indicating that the two members of each pair are aligned at right angles to each other. The two halves of the replicated centrosome, each consisting of a centriole pair surrounded by matrix, will split and migrate apart to initiate the formation of the two poles of the mitotic spindle when the cell enters M phase (see Figure 18-7). (C) Electron micrograph of a centriole pair that has been isolated from a cell. The two centrioles have partly separated during the isolation procedure but remain tethered together by fine fibers, which keep the centriole pair together until it is time for them to separate (see Figure 18-6). Both centrioles are cut longitudinally, and it can now be seen that the two have different structures: the mother centriole is larger and more complex than the daughter centriole, and, as shown in Figure 18-6, only the mother centriole is associated with matrix that nucleates microtubules. Each daughter centriole will mature during the next cell cycle, when it will replicate to give rise to its own daughter centriole. (A, from M. McGill, D.P. Highfield, T.M. Monahan, and B. R. Brinkley, *J. Ultrastruct. Res.* 57:4353, 1976. © Academic Press; C, from M. Paintrand et al., *J. Struct. Biol.* 108:107128, 1992. © Academic Press.)

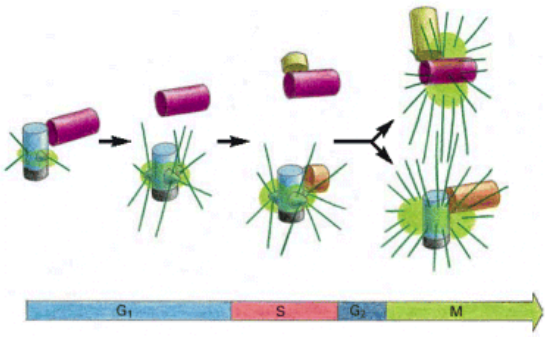

Figure 18-6. Centriole replication. The centrosome consists of a centriole pair and associated matrix *(green).* At a certain point in G_1, the two centrioles of the pair separate by a few micrometers. During S phase, a daughter centriole begins to grow near the base of each mother centriole and at a right angle to it. The elongation of the daughter centriole is usually completed by G_2. The two centriole pairs remain close together in a single centrosomal complex until the beginning of M phase (see Figure 18-7), when the complex splits in two and the two halves begin to separate. Each centrosome now nucleates its own radial array of microtubules called an aster.

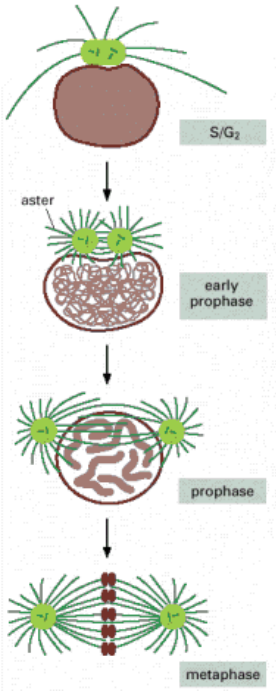

Figure 18-7. The centrosome cycle. The centrosome in a proliferating animal cell duplicates in interphase in preparation for mitosis. In most animal cells, a centriole pair (shown here as a pair of *dark green* bars) is associated with the centrosome matrix *(light green)* that nucleates microtubule outgrowth. (The volume of centrosome matrix is exaggerated in this diagram for clarity; Figure 18-6 gives a more accurate representation.) Centriole duplication begins in G_1 and is completed by G_2 (see Figure 18-6). Initially the two centriole pairs and associated centrosome matrix remain together as a single complex. In early M phase, this complex separates into two, each of which nucleates its own aster. The two asters, which initially lie side by side and close to the nuclear envelope, move apart. By late prophase, the microtubules that interact between the two asters preferentially elongate as the two asters move apart along the outside of the nucleus. In this way, a bipolar mitotic spindle is rapidly formed. At metaphase, the nuclear envelope breaks down, enabling the

spindle microtubules to interact with the chromosomes.

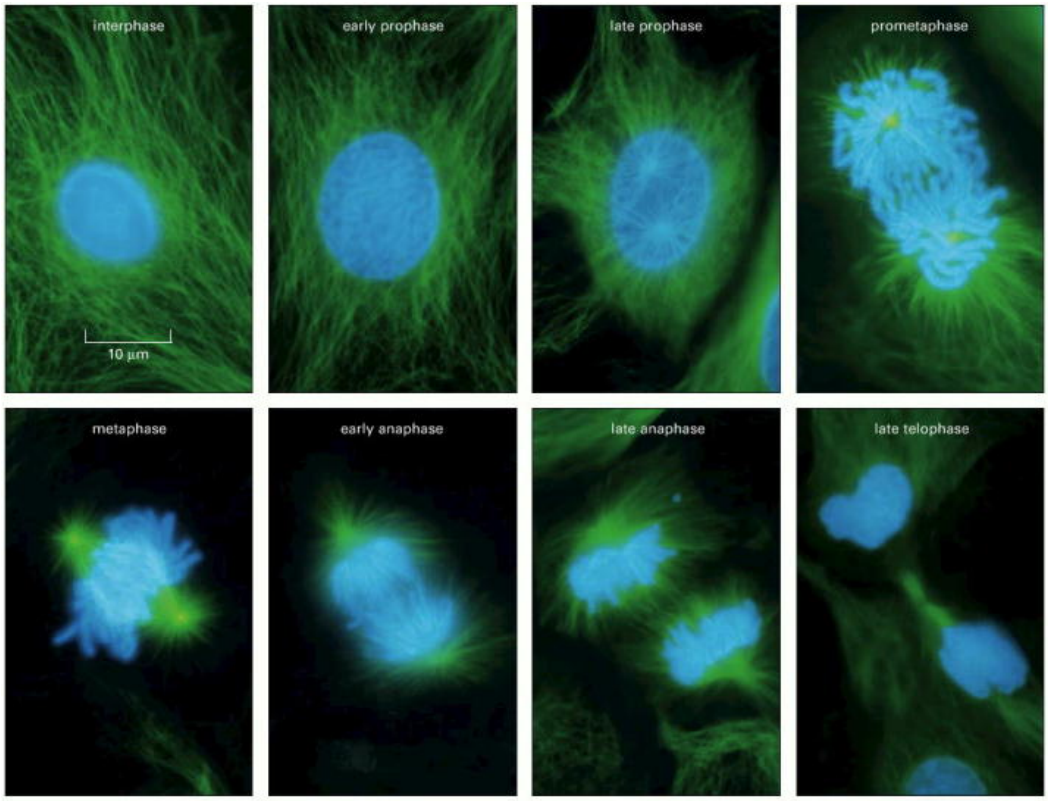

Figure 18-8. The course of mitosis in a typical animal cell. In these micrographs of cultured newt lung cells, the microtubules *(green)* have been visualized by immunofluorescence, while the chromatin is stained with a *blue* fluorescent dye. During *interphase,* the centrosome (not visible) forms the focus for the interphase microtubule array. By *early prophase,* the single centrosome contains two centriole pairs (not visible). At *late prophase,* the centrosome divides, and the resulting two asters can be seen to have moved apart. At *prometaphase,* the nuclear envelope breaks down, allowing the spindle microtubules to interact with the fully condensed chromosomes. At *metaphase,* the bipolar structure of the spindle is clear, and all the chromosomes are aligned at the equator of the spindle. At *early anaphase,* the sister chromatids all separate synchronously and, under the influence of the microtubules, the daughter chromosomes begin to move toward the poles. By *late anaphase,* the spindle poles have moved farther apart, increasing the separation of the two groups of chromosomes. At *telophase,* the daughter nuclei re-form, and by *late telophase,* cytokinesis is almost complete, with the midbody (discussed later) persisting between the daughter cells. (Photographs courtesy of C.L. Rieder, J.C. Waters, and R.W. Cole.)

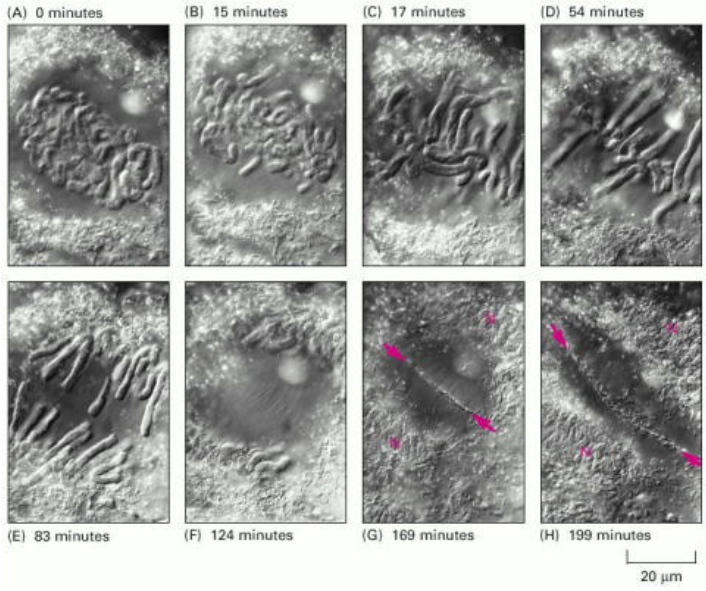

Figure 18-9. The course of mitosis in a plant cell. These light micrographs of a living *Haemanthus* (lily) cell were taken at the times indicated, using differential-interference-contrast microscopy. The cell has unusually large chromosomes that are easy to see. (A) At *prophase,* the chromosomes condense and are clearly visible in the cell nucleus. (B and C) At *prometaphase,* the nuclear envelope breaks down and the chromosomes interact with the microtubules that emanate from the two spindle poles. Plants do not have centrosomes, but their spindle poles contain proteins related to those found in the centrosomal matrix of animal cells. (D) At *metaphase,* the chromosomes line up at the equator of the spindle. (E) At *anaphase,* the daughter chromosomes separate and start moving to opposite poles. (F) At *telophase,* the chromosomes decondense and daughter nuclei re-form (not seen). (G and H) During *cytokinesis,* a new cell wall (the cell plate, *red arrows)* forms between the two nuclei (N). (Courtesy of Andrew Bajer.)

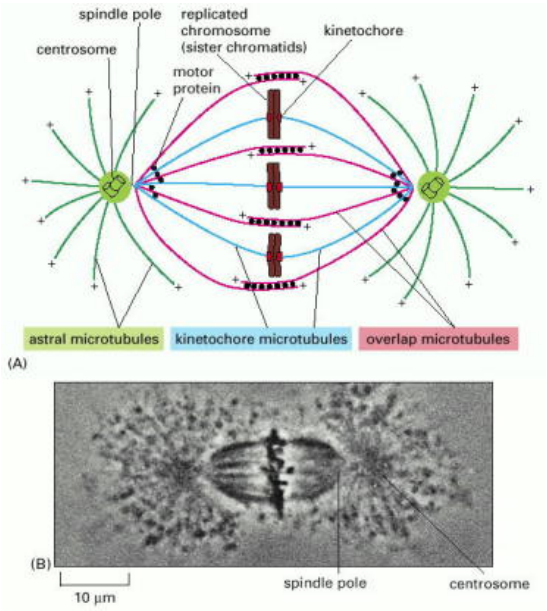

Figure 18-10. The three classes of microtubules of the fully formed mitotic spindle in an animal cell. (A) In reality, the chromosomes are proportionally much larger than shown in this drawing, and multiple microtubules are attached to each kinetochore. Note that the plus ends of the microtubules project away from the centrosomes, while the minus ends are anchored at the spindle poles. Although the centrosomes initiate the assembly of the spindle poles, most of the kinetochore and overlap microtubules that they nucleate are released from the centrosomes and are then held and organized at the poles by motor proteins. For simplicity, in the other figures in this chapter, we draw all the spindle microtubules at the poles emanating from the centrosomes. (B) A phase-contrast micrograph of an isolated mitotic spindle at metaphase, with the chromosomes aligned at the spindle equator. (B, from E. D. Salmon and R.R. Segall, *J. Cell Biol.* 86:355365, 1980. © The Rockefeller University Press.)

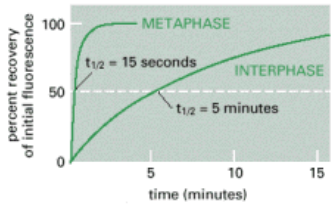

Figure 18-11. The half-life of microtubules in mitosis. Microtubules in an M-phase cell are much more dynamic, on average, than the microtubules at interphase. Mammalian cells in culture were injected with tubulin that had been covalently linked to a fluorescent dye. After the fluorescent tubulin had become incorporated into the cell's microtubules, an intense laser beam was used to bleach all the fluorescence in a small region. The recovery of fluorescence in the bleached region of microtubules, caused by their replacement by microtubules formed from unbleached fluorescent tubulin from the soluble pool, was then monitored as a function of time. The time for 50% recovery of fluorescence ($t_{1/2}$) is thought to be equal to the time required for half of the microtubules in the region to depolymerize and re-form. (Data from W.M. Saxton et al., *J. Cell Biol.* 99:21752187, 1984. © The Rockefeller University Press.)

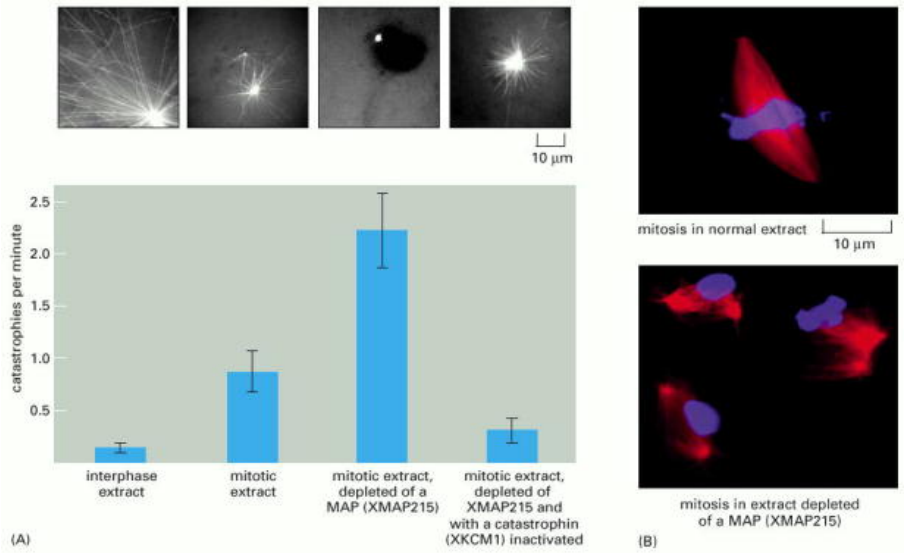

Figure 18-12. Experimental evidence that the balance between catastrophins and MAPs influences the frequency of microtubule catastrophes and microtubule length. (A) Interphase or mitotic *Xenopus* egg extracts were incubated with centrosomes, and the behavior of individual microtubules nucleated from the centrosomes was followed by fluorescence video microscopy. As expected, the catastrophe rate is higher in mitotic than in interphase extracts. The depletion of a specific MAP (XMAP215) from the mitotic extracts greatly increases the catastrophe rate, indicating that this MAP normally inhibits catastrophes in mitotic extracts. The addition of antibodies that block the function of a specific catastrophin (the kinesin-related protein XKCM1) greatly reduces the catastrophe rate in the XMAP215-depleted mitotic extracts, indicating that this catastrophin is normally responsible for stimulating catastrophes in mitotic extracts and that the catastrophe rate depends on the balance between the MAP and the catastrophin. Fluorescence micrographs of the asters formed in the different experimental conditions are shown in the top panels; note that the higher the catastrophe rates, the shorter the microtubules. (B) Mitotic spindle formation in mitotic extracts when both centrosomes and sperm nuclei are added. Microtubules are shown in *red* and chromosomes in *blue.* Whereas normal spindles form in normal mitotic extracts, very abnormal spindles form when XMAP215 is depleted from the extracts, presumably because the microtubules nucleated by the centrosomes are too short. Remarkably, microtubules formed in a test tube from a mixture of purified tubulin, XMAP215, and XKCM1 exhibit normal dynamic instability. (From R. Tournebize et al., *Nature Cell Biol.* 2:1319, 2000. © Macmillan Magazines Ltd.)

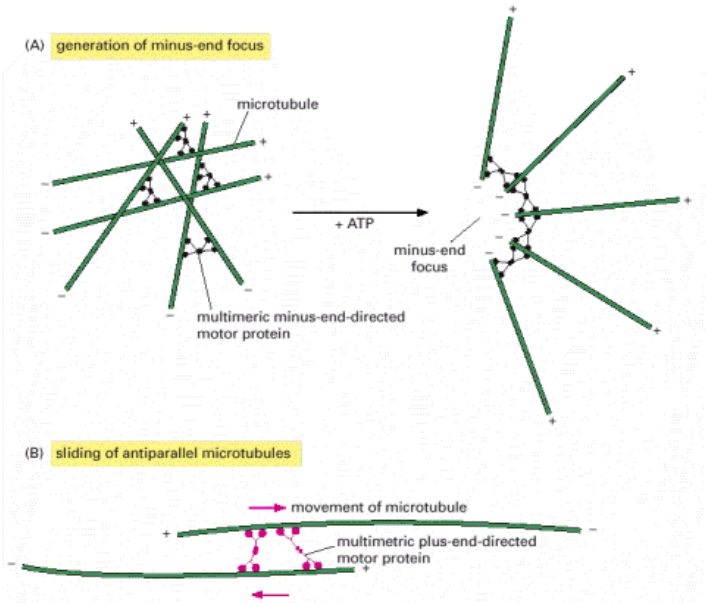

Figure 18-13. Two functions of multimeric motor proteins that are important for mitotic spindle assembly and function. Microtubule-dependent motor proteins hydrolyze ATP and move along a microtubule toward either its plus or its minus end. If the motor protein is multimeric, as in these examples, it can cross-link two adjacent microtubules and move them relative to one another. (A) Some minus-end-directed multimeric motor proteins rearrange microtubules to form a focus of minus ends, where the motor proteins accumulate. (B) If microtubules are aligned so that they are antiparallel (that is, their plus ends are facing in opposite directions), a cross-linking motor protein can slide the microtubules past each other, as shown here for a plus-end-directed motor protein that could elongate the spindle. (Adapted from A.A. Hyman and E. Karsenti, *Cell* 84:406410, 1996.)

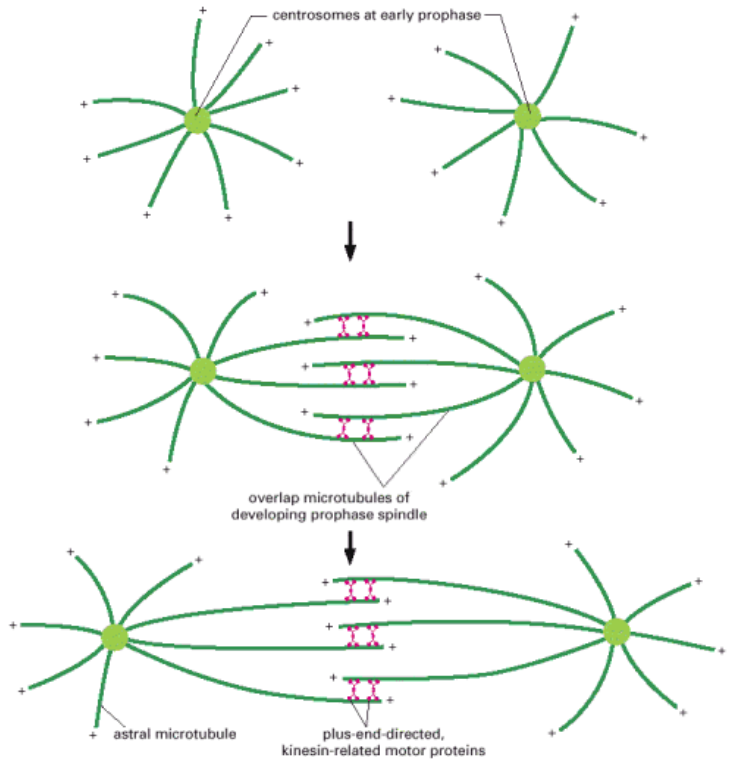

Figure 18-14. Separation of the two spindle poles in prophase in an animal cell. In this model, plus-end-directed motor proteins operating on interacting antiparallel microtubules help separate the two poles of a forming mitotic spindle. New microtubules grow out in random directions from two nearby centrosomes. The microtubules are anchored at the centrosome by their minus ends, while their plus ends extend outward. When two microtubules from opposite centrosomes interact in an overlap zone, plus-end-directed, kinesin-related motor proteins cross-link the microtubules together and tend to drive the microtubules in the direction that will push the centrosomes apart (see Figure 18-13B). Minus-end-directed dynein motors associated with the nuclear envelope are also thought to help separate the two centrosomes by pulling on the two sets of astral microtubules (not shown).

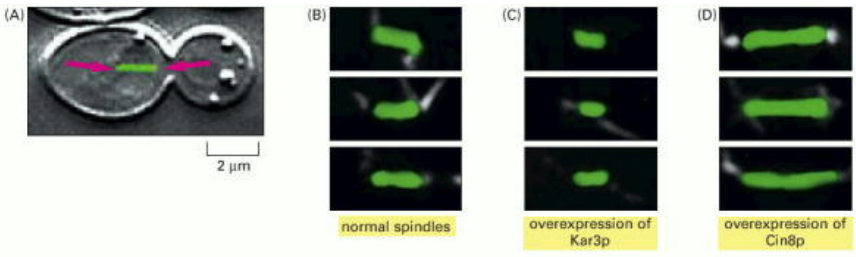

Figure 18-15. The influence of opposing motor proteins on spindle length in budding yeast. (A) A differential-interference-contrast micrograph of a mitotic yeast cell. The spindle is highlighted in *green*, and the position of the spindle poles is indicated by *red arrows.* The nuclear envelope does not break down during mitosis in yeasts, and the spindle forms inside the nucleus (see Figure 18-41). In (BD), the mitotic spindles have been stained with fluorescent anti-tubulin antibodies. (B) Normal yeast cells. (C) Over-expression of the minus-end-directed motor protein Kar3p leads to abnormally short spindles. (D) Overexpression of the plus-end-directed motor protein Cin8p leads to abnormally long spindles. Thus, it seems that a balance between opposing motor proteins determines spindle length in these cells. (A, courtesy of Kerry Bloom; BD, from W. Saunders, V. Lengyel, and M.A. Hoyt, *Mol. Biol. Cell* 8:10251033, 1997. © American Society for Cell Biology.)

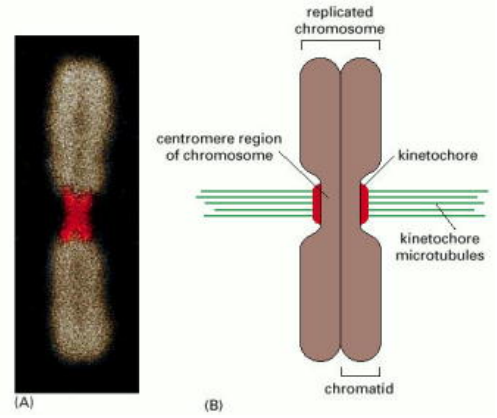

Figure 18-16. Kinetochore microtubules. (A) A fluorescence micrograph of a metaphase chromosome stained with a DNA-binding fluorescent dye and with human autoantibodies that react with specific kinetochore proteins. The two kinetochores, one associated with each chromatid, are stained *red.* (B) A drawing of a metaphase chromosome showing its two sister chromatids attached to kinetochore microtubules, which bind by their plus ends. Each kinetochore forms a plaque on the surface of the centromere. The number of microtubules bound to a metaphase kinetochore varies from 1 in budding yeast to over 40 in some mammalian cells. (A, courtesy of B.R. Brinkley.)

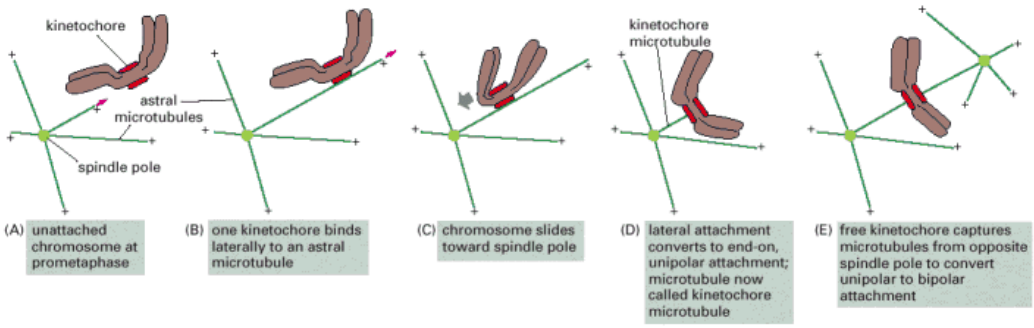

Figure 18-17. The capture of microtubules by kinetochores. The *red arrow* in (A) indicates the direction of microtubule growth, while the *gray arrow* in (C) indicates the direction of chromosome sliding.

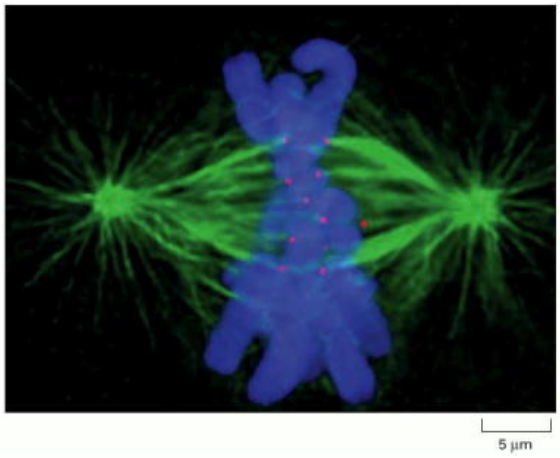

Figure 18-18. Chromosomes at the metaphase plate of a mitotic spindle. In this fluorescence micrograph, kinetochores are labeled in *red*, microtubules in *green*, and chromosomes in *blue.* (From A. Desai, *Curr. Biol.* 10:R508, 2000. © Elsevier.)

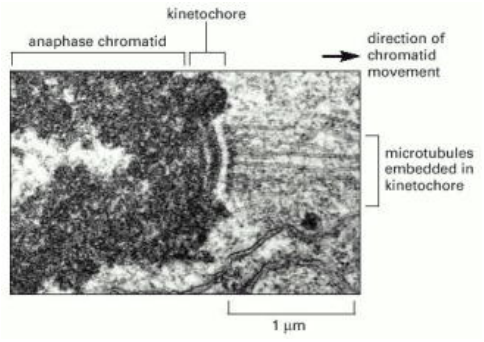

Figure 18-19. The kinetochore. Electron micrograph of an anaphase chromatid with microtubules attached to its kinetochore. While most kinetochores have a trilaminar structure, the one shown here (from a green alga) has an unusually complex structure with additional layers. (From J.D. Pickett-Heaps and L.C. Fowke, *Aust. J. Biol. Sci.* 23:7192, 1970. Reproduced by permission of CSIRO.)

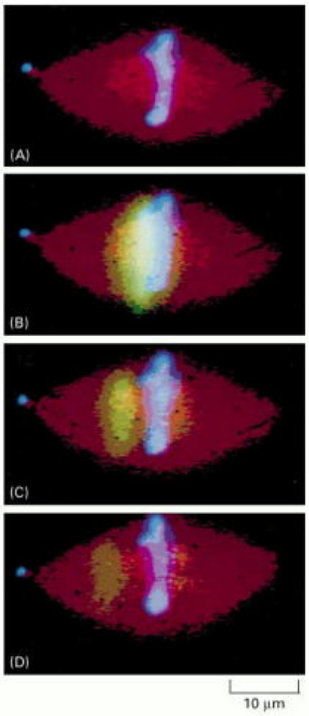

Figure 18-20. The dynamic behavior of microtubules in the metaphase spindle studied by photoactivation of fluorescence. A metaphase spindle formed *in vitro* by adding *Xenopus* sperm to an extract of *Xenopus* eggs (see Figure 17-9) has incorporated three fluorescent markers: rhodamine-labeled tubulin *(red)* to mark all of the microtubules, a *blue* DNA-binding dye that labels the chromosomes, and caged-fluorescein-labeled tubulin, which is also incorporated into all of the microtubules but is invisible because it is nonfluorescent until activated by ultraviolet light. (A) The distribution of the chromosomes and microtubules in the spindle. (B) A beam of ultraviolet light was used to uncage the caged-fluorescein-labeled tubulin locally, mainly just to the left side of the metaphase plate. Over the next few minutes (after 1.5 minutes in C, after 2.5 minutes in D), the uncaged fluorescein-tubulin signal is seen to move toward the left spindle pole, indicating that tubulin is continuously moving poleward, even though the spindle (visualized by the *red* rhodamine-tubulin fluorescence) remains largely unchanged. The caged fluorescein signal also diminishes in intensity, indicating that the individual microtubules are continually depolymerizing and being replaced. (From K.E. Sawin and T.J. Mitchison, *J. Cell Biol.* 112:941954, 1991. © The Rockefeller University Press.)

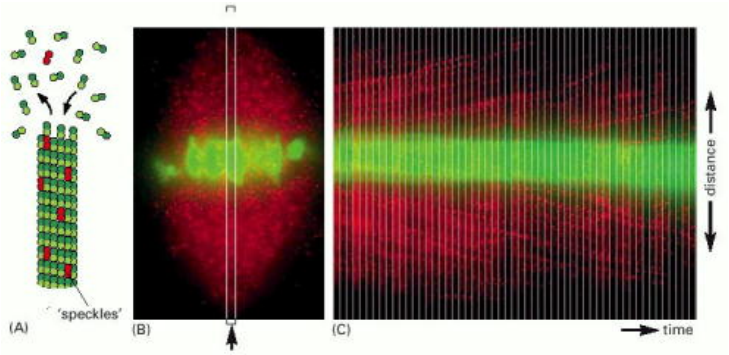

Figure 18-21. Visualizing the dynamics of individual microtubules by fluorescence speckle microscopy. (A) The principle of the method. A very low amount of fluorescent tubulin is injected into living cells so that individual microtubules form with a very small proportion of fluorescent tubulin. Such microtubules have a speckled appearance when viewed by fluorescence microscopy. (B) Fluorescence micrographs of a mitotic spindle in a living newt lung epithelial cell. The chromosomes are stained *green*, and the tubulin speckles are *red*. (C) The movement of individual speckles can be readily followed by time-lapse video microscopy. Images of the long, thin, rectangular, boxed region *(arrow)* in (B) were taken at sequential times and pasted side by side to make a montage of the region over time. Individual speckles can be seen to move toward the poles (representing poleward flux) at a rate of about 0.75 µm/min. (From T.J. Mitchison and E.D. Salmon, *Nature Cell Biol.* 3:E1721, 2001.)

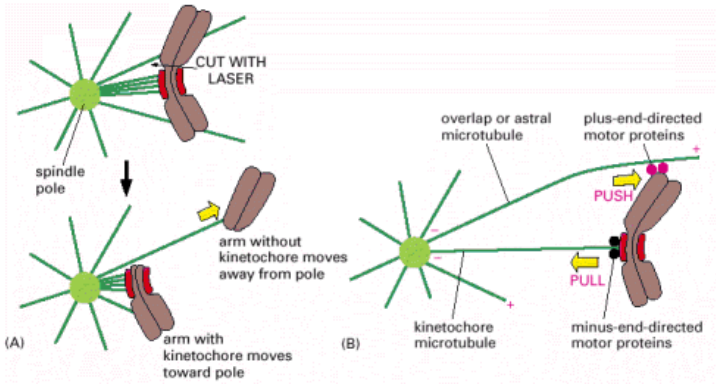

Figure 18-22. How opposing forces may drive chromosomes to the metaphase plate. (A) Evidence for an astral ejection force that pushes chromosomes away from the spindle poles toward the spindle equator. In this experiment, a prometaphase chromosome that is temporarily attached to a single pole by kinetochore microtubules is cut in half with a laser beam. The half that is freed from the kinetochore is pushed rapidly away from the pole, whereas the half that remains attached to the kinetochore moves toward the pole, reflecting a decreased repulsion. (B) A model of how two opposing forces may cooperate to move chromosomes to the metaphase plate. Plus-end-directed motor proteins on the chromosome arms are thought to interact with astral microtubules to generate the astral ejection force, which pushes chromosomes toward the spindle equator. Minus-end-directed motor proteins at the kinetochore are thought to interact with kinetochore microtubules to pull chromosomes toward the pole.

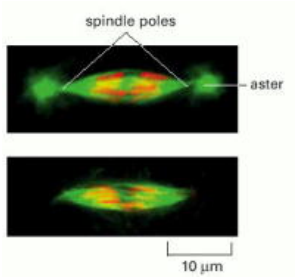

Figure 18-23. Bipolar spindle assembly without centrosomes in parthenogenetic embryos of the insect *Sciara.* The microtubules are stained *green*, the chromosomes *red*. The *top* fluorescence micrograph shows a normal spindle formed with centrosomes in a normally fertilized *Sciara* embryo. The *bottom* micrograph shows a spindle formed without centrosomes in an embryo that initiated development without fertilization. Note that the spindle with centrosomes has an aster at each pole of the spindle, whereas the spindle formed without centrosomes does not. Both types of spindles are able to segregate the replicated chromosomes. (From B. de Saint Phalle and W. Sullivan, *J. Cell Biol.* 141:13831391, 1998. © The Rockefeller University Press.)

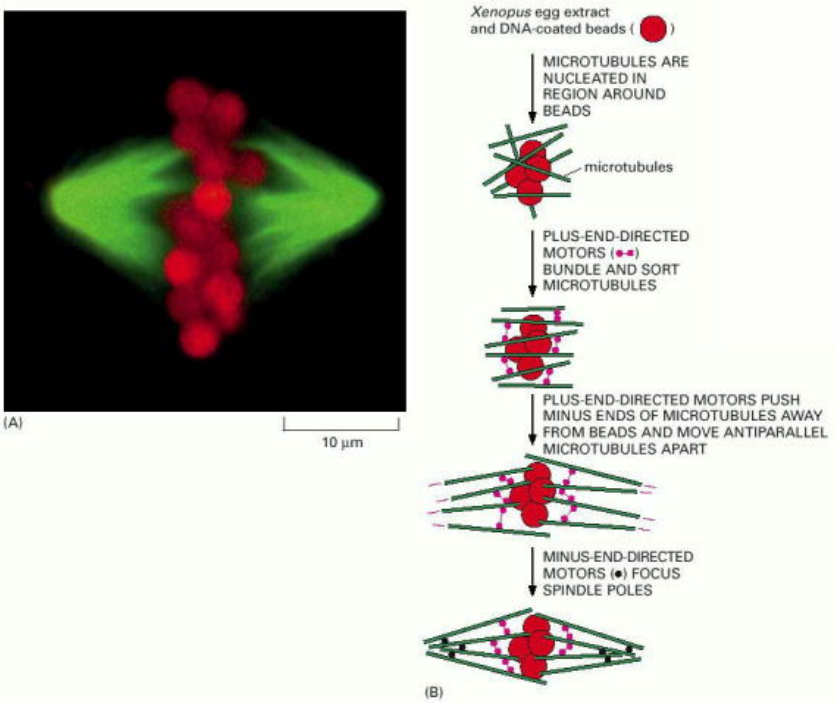

Figure 18-24. Bipolar spindle assembly without centrosomes or kinetochores. (A) A fluorescence micrograph of a spindle *(green)* that self-assembled around beads *(red)* coated with bacterial DNA in *Xenopus* egg extracts. (B) The steps in spindle assembly directed by DNA-coated beads. The minus ends of the microtubules are indicated in one part of the figure. (A, from R. Heald et al., *Nature* 382:420425, 1996. © Macmillan Magazines Ltd; B, based on C.E. Walczak et al., *Curr. Biol.* 8:903913, 1998.)

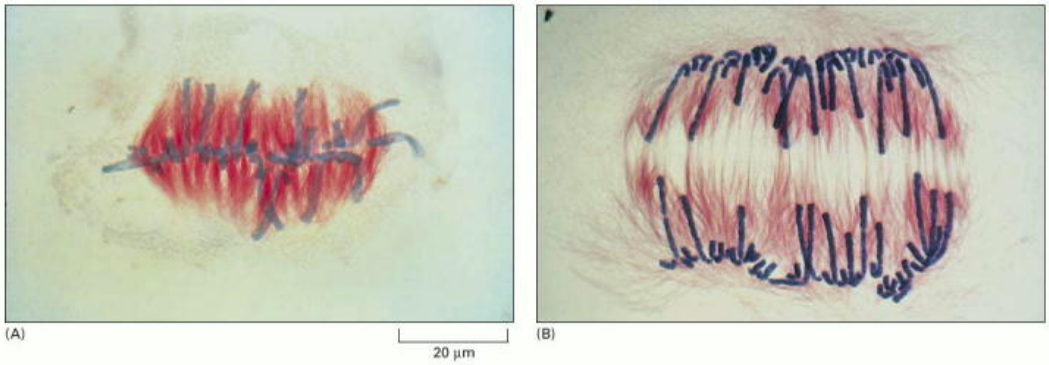

Figure 18-25. Chromatid separation at anaphase. In the transition from metaphase (A) to anaphase (B), sister chromatids suddenly separate and move toward opposite poles - as shown in these light micrographs of *Haemanthus* (lily) endosperm cells that were stained with gold-labeled antibodies against tubulin. (Courtesy of Andrew Bajer.)

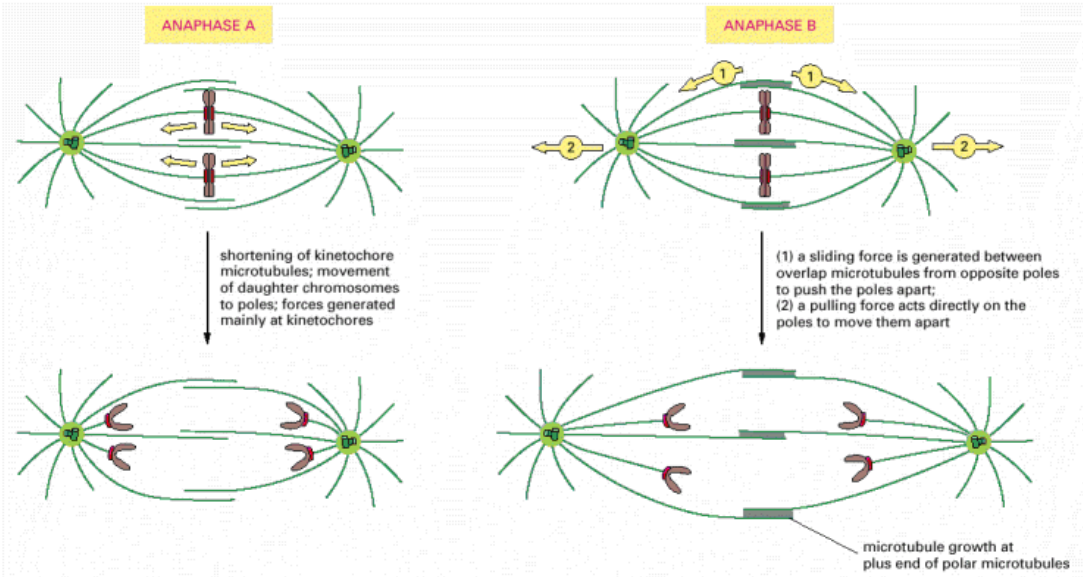

Figure 18-26. The major forces that separate daughter chromosomes at anaphase in mammalian cells. Anaphase A depends on motor proteins operating at the kinetochores that, together with the depolymerization of the kinetochore microtubules, pull the daughter chromosomes toward the nearest pole. In anaphase B, the two spindle poles move apart. Two separate forces are thought to be responsible for anaphase B. The elongation and sliding of the overlap microtubules past one another in the central spindle push the two poles apart, and outward forces exerted by the astral microtubules at each spindle pole act to pull the poles away from each other, toward the cell surface.

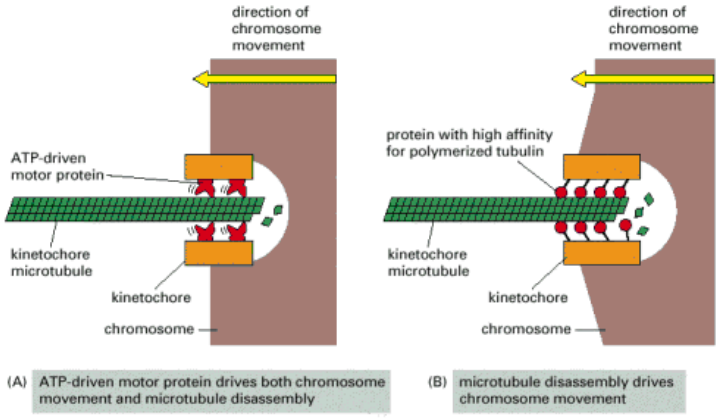

Figure 18-27. Two alternative models of how the kinetochore may generate a poleward force on its chromosome during anaphase A. (A) Microtubule motor proteins at the kinetochore use the energy of ATP hydrolysis to pull the chromosome along its bound microtubules. Depolymerization of the kinetochore microtubules follows as a consequence. (B) Chromosome movement is driven by kinetochore microtubule disassembly: as tubulin subunits dissociate, the kinetochore is obliged to slide poleward to maintain its binding to the walls of the microtubule. As motor proteins are required for anaphase A, in this model, they would be required mainly for the microtubules to remain attached to the kinetochore.

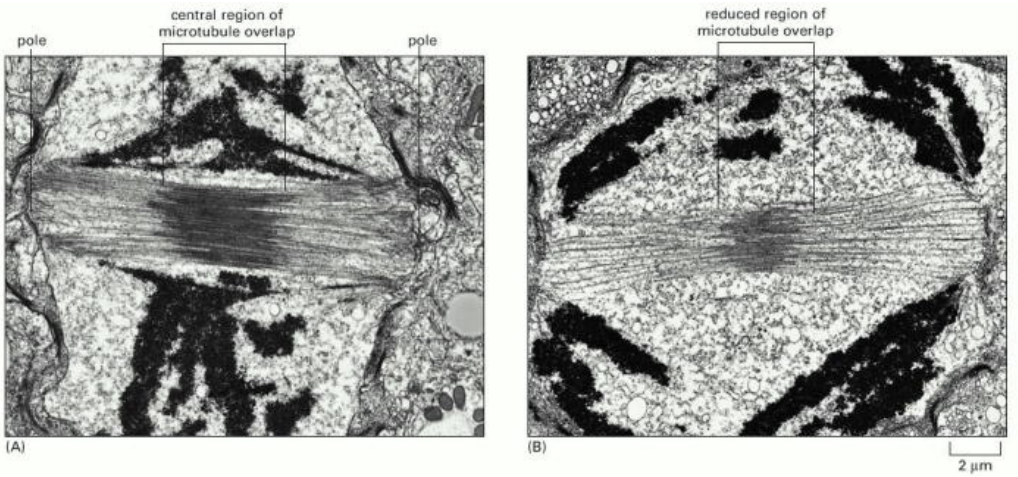

Figure 18-28. The sliding of overlap microtubules at anaphase. These electron micrographs show the reduction in the degree of microtubule overlap in the central spindle during mitosis in a diatom. (A) Metaphase. (B) Late anaphase. (Courtesy of Jeremy D. Pickett-Heaps.)

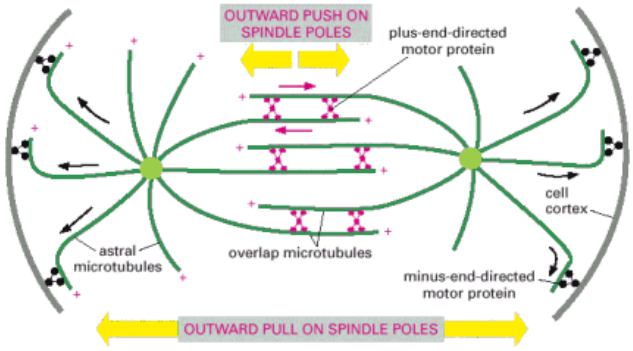

Figure 18-29. A model for how motor proteins may act in anaphase B. Plus-end-directed motor proteins cross-link the overlapping, antiparallel, overlap microtubules and slide the microtubules past each other, thereby pushing the spindle poles apart. The *red arrows* indicate the direction of microtubule sliding. Minus-end-directed motor proteins bind to the cell cortex and to those astral microtubules that point away from the spindle and pull the poles apart. These astral microtubules shorten as the spindle poles are pulled toward the cortex.

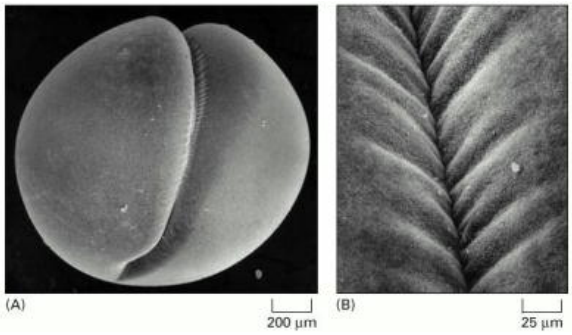

Figure 18-30. Cleavage in a fertilized frog egg. In these scanning electron micrographs, the cleavage furrow is especially obvious and well defined, as the cell is unusually large. The furrowing of the cell membrane is caused by the activity of the contractile ring underneath it. (A) A low-magnification view of the cleaving egg surface. (B) The surface of a furrow at higher magnification. (From H.W. Beams and R.G. Kessel, *Am. Sci.* 64:279290, 1976.)

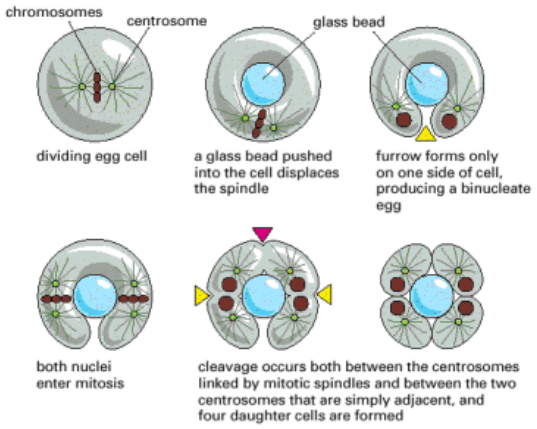

Figure 18-31. An experiment demonstrating the influence of the position of microtubule asters on the subsequent plane of cleavage in a large egg cell. If the mitotic spindle is mechanically pushed to one side of the cell with a glass bead, the membrane furrowing is incomplete, failing to occur on the opposite side of the cell. Subsequent cleavages occur not only in the conventional relation to each of the two subsequent mitotic spindles *(yellow arrowheads)*, but also between the two adjacent asters that are not linked by a mitotic spindle - but in this abnormal cell share the same cytoplasm *(red arrowhead)*. Apparently, the contractile ring that produces the cleavage furrow in these cells always forms in the region midway between two asters, suggesting that the asters somehow alter the adjacent region of cell cortex to induce furrow formation between them.

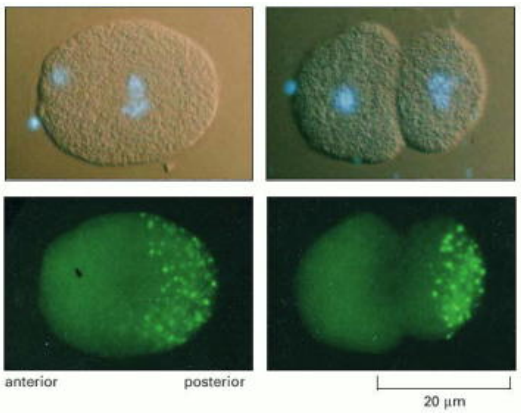

Figure 18-32. An asymmetric cell division segregating cytoplasmic components to only one daughter cell. These light micrographs illustrate the controlled asymmetric segregation of specific cytoplasmic components to one daughter cell during the first division of a fertilized egg of the nematode *C. elegans*. The cells *above* have been stained with a *blue*, DNA-binding, fluorescent dye to show the nucleus (and polar bodies - see Figure 20-22); they are viewed by both differential-interference-contrast and fluorescence microscopy. The cells *below* are the same cells stained with an antibody against P-granules and viewed by fluorescence microscopy. These small granules of unknown function are distributed randomly throughout the cytoplasm of the unfertilized egg (not shown) but become segregated to the posterior pole of the fertilized egg, as shown on the *left*. The cleavage plane is oriented to ensure that only the posterior daughter cell receives the P-granules when the egg divides, as shown on the *right*. The same segregation process is repeated in several subsequent cell divisions, so that the P-granules end up only in the cells that give rise to eggs and sperm. (Courtesy of Susan Strome.)

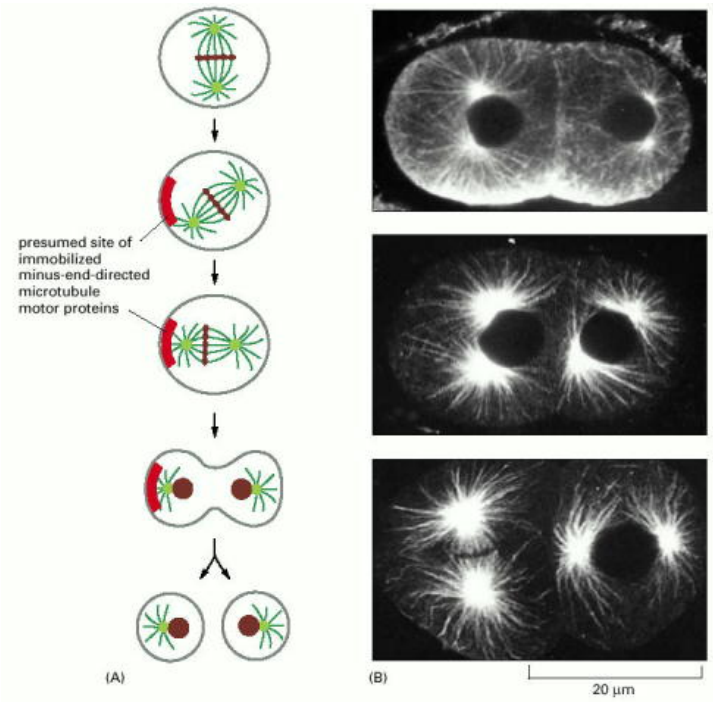

Figure 18-33. Spindle rotation. (A) A possible mechanism underlying the controlled rotation of a mitotic spindle. The *red bar* represents a specialized region of cell cortex toward which one spindle pole is pulled by its astral microtubules. (B) Fluorescence micrographs showing a precisely programmed rotation of a mitotic spindle in a *C. elegans* embryo at the two-cell stage in preparation for cleavage to form four cells in a specific pattern. The microtubules are stained with an antibody against tubulin. The spindle in the cell on the right rotates almost 90° clockwise, as diagrammed in (A). (B, courtesy of Tony Hyman and John White.)

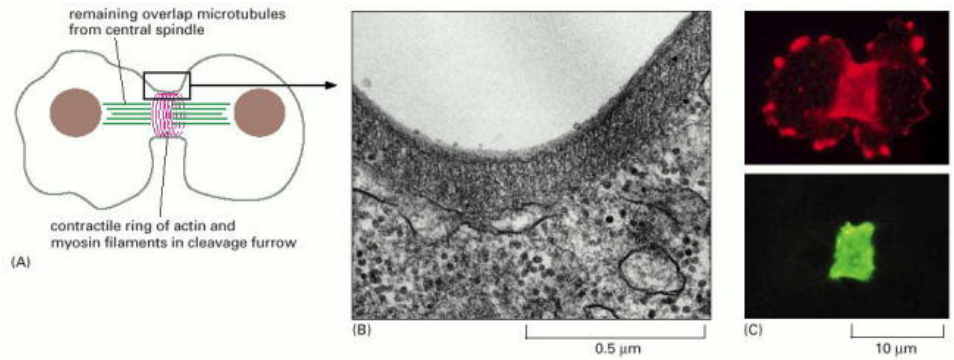

Figure 18-34. The contractile ring. (A) A drawing of the cleavage furrow in a dividing cell. (B) An electron micrograph of the ingrowing edge of a cleavage furrow of a dividing animal cell. (C) Fluorescence micrographs of a dividing slime mold amoeba stained for actin *(red)* and myosin II *(green)*. Whereas all of the visible myosin II has redistributed to the contractile ring, only some of the actin has done so; the rest remains in the cortex of the nascent daughter cells. (B, from H.W. Beams and R.G. Kessel, *Am. Sci.* 64:279290, 1976; C, courtesy of Yoshio Fukui.)

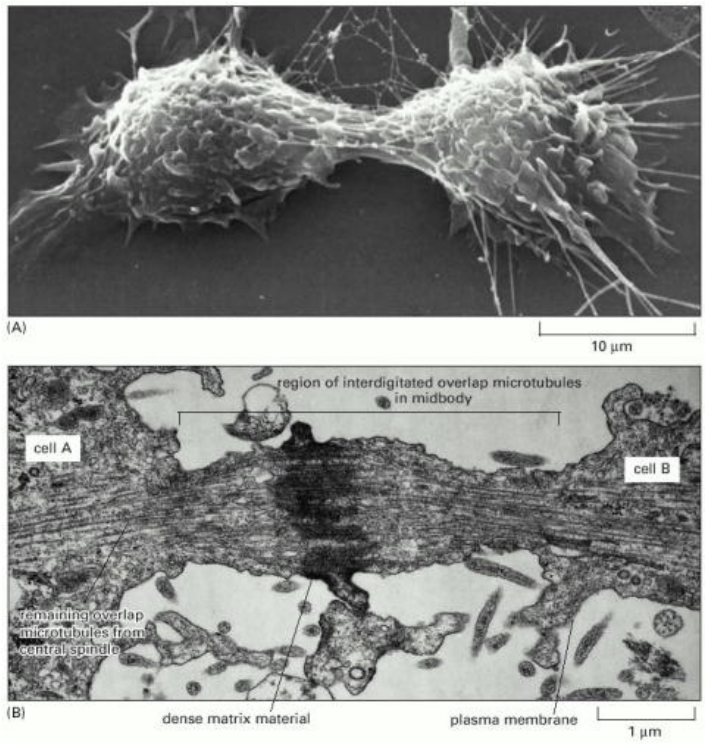

Figure 18-35. The midbody. (A) A scanning electron micrograph of an animal cell in culture in the process of dividing; the midbody still joins the two daughter cells. (B) A conventional electron micrograph of the midbody of a dividing animal cell. Cleavage is almost complete, but the daughter cells remain attached by this thin strand of cytoplasm containing the remains of the central spindle. See also the late telophase panel in Figure 18-8. (A, courtesy of Guenter Albrecht-Buehler; B, courtesy of J.M. Mullins.)

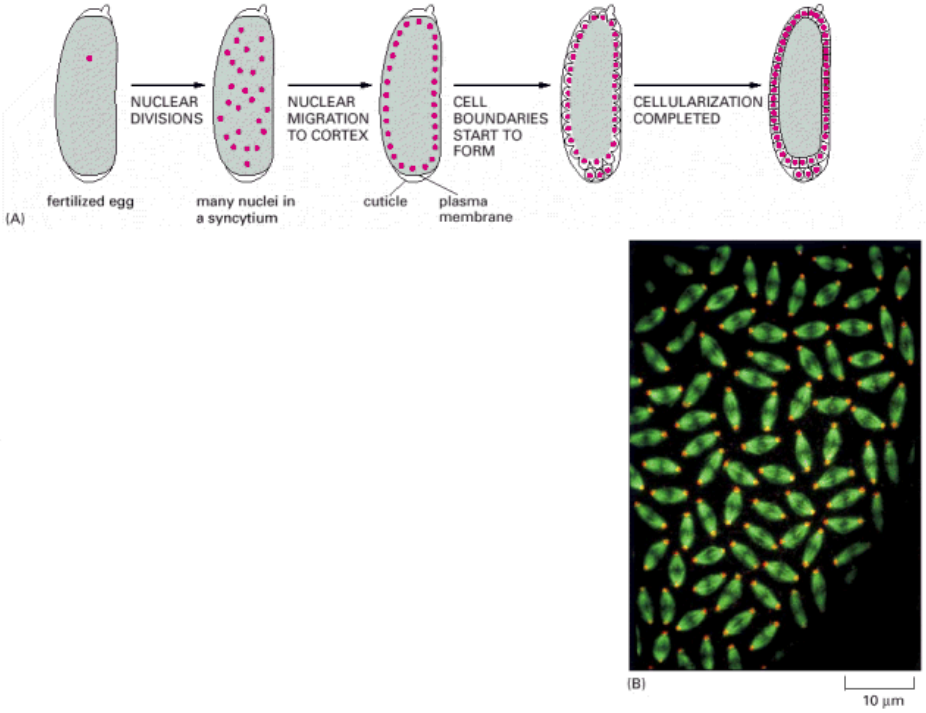

Figure 18-36. Mitosis without cytokinesis in the *Drosophila* embryo. (A) The first 13 nuclear divisions occur synchronously and without cytoplasmic division to create a large syncytium. Most of the nuclei then migrate to the cortex, and the plasma membrane extends inward and pinches off to surround each nucleus to form individual cells in a process called cellularization. (B) Fluorescence micrograph of multiple mitotic spindles at metaphase in a *Drosophila* embryo before cellularization. The microtubules are stained *green* and the centrosomes *red.* (B, courtesy of Kristina Yu and William Sullivan.)

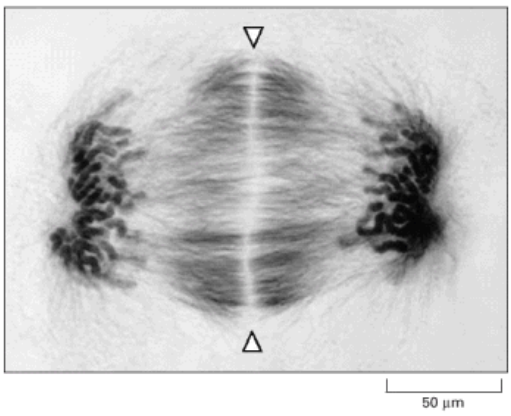

Figure 18-37. Cytokinesis in a plant cell in telophase. In this light micrograph, the early cell plate (between the two *arrowheads)* is forming in a plane perpendicular to the plane of the page. The microtubules of the spindle are stained with gold-labeled antibodies against tubulin, while the DNA in the two sets of daughter chromosomes is stained with a fluorescent dye. Note that there are no astral microtubules, because there are no centrosomes in higher-plant cells. (Courtesy of Andrew Bajer.)

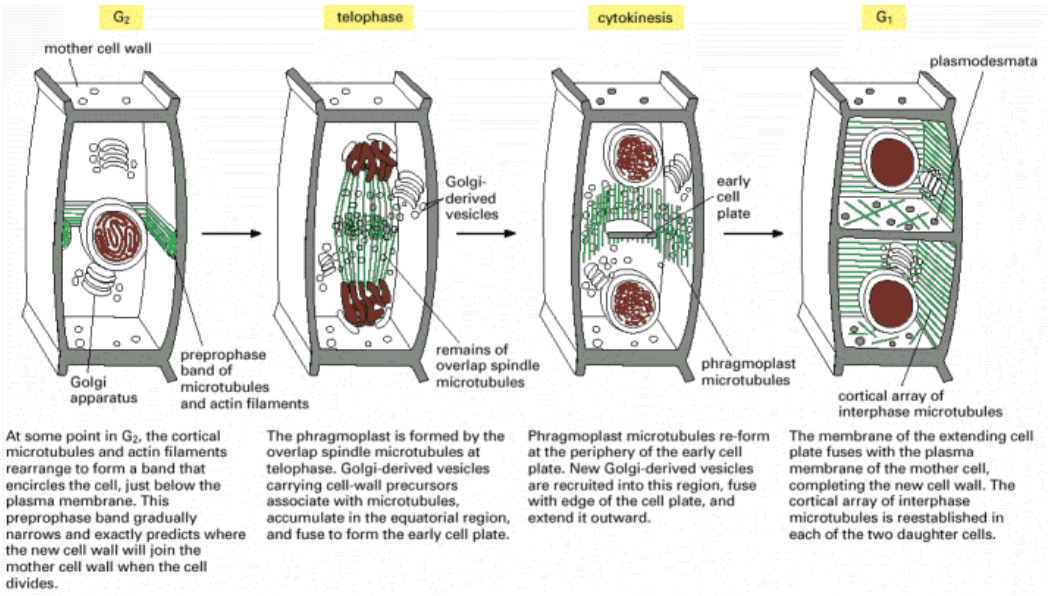

Figure 18-38. The special features of cytokinesis in a higher plant cell. The division plane is established before M phase by a band of microtubules and actin filaments (the preprophase band) at the cell cortex. At the beginning of telophase, after the chromosomes have segregated, a new cell wall starts to assemble inside the cell at the equator of the old spindle. The overlap microtubules of the mitotic spindle remaining at telophase form the phragmoplast and guide vesicles derived from the Golgi apparatus toward the center of the spindle. The vesicles are filled with cell-wall material and fuse to form the growing new cell wall, which grows outward to reach the plasma membrane and original cell wall at the site determined earlier by the preprophase band. The plasma membrane and the membrane surrounding the new cell wall fuse, completely separating the two daughter cells.

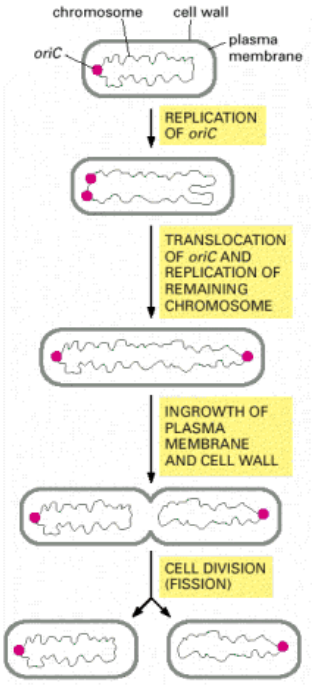

Figure 18-39. Cell division in the bacterium *E. coli.* The single, circular chromosome contains an origin of replication called *oriC.* Before division, the chromosome is polarized, so that *oriC* is at one pole of the bacterium. As soon as the *oriC* sequence is copied, one of the copies is actively translocated to the other pole, before the rest of the chromosome is replicated. Cell growth occurs continuously, and when the cell reaches an appropriate size, the plasma membrane and cell wall grow inward to divide the cell in two, exactly between the two daughter chromosomes.

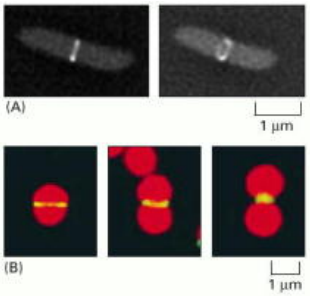

Figure 18-40. The FtsZ protein. (A) Fluorescence micrographs showing the location of the FtsZ protein during binary fission in *E. coli.* The protein assembles into a ring at the center of the cell, where it helps orchestrate cell division. The bacteria here have been genetically engineered to produce a fluorescent form of the protein (FtsZ fused to green fluorescent protein). (B) Dividing chloroplasts *(red)* from a red alga also make use of a FtsZ protein ring *(green)* for cleavage. (A, from X. Ma, D.W. Ehrhardt, and W. Margolin, *Proc. Natl. Acad. Sci. USA* 93:12999-13003, 1996. © National Academy of Sciences; B, from S. Miyagishima et al., *Plant Cell* 13:2257-2268, 2001. © American Society of Plant Biologists.)

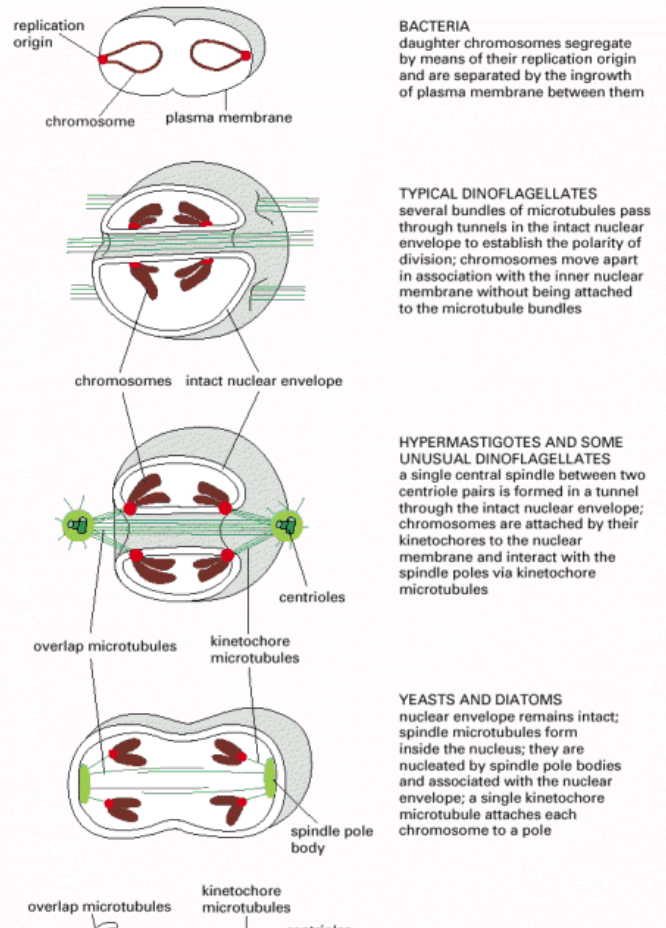

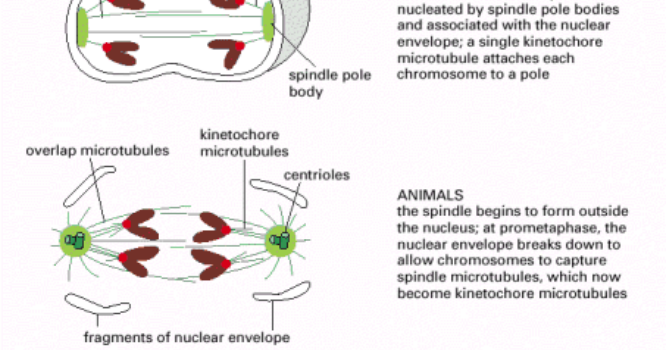

Figure 18-41. The use of different chromosome separation mechanisms by different organisms. Some of these may have been intermediate stages in the evolution of the mitotic spindle of higher organisms. For all examples except bacteria, only the central nuclear region of the cell is shown.

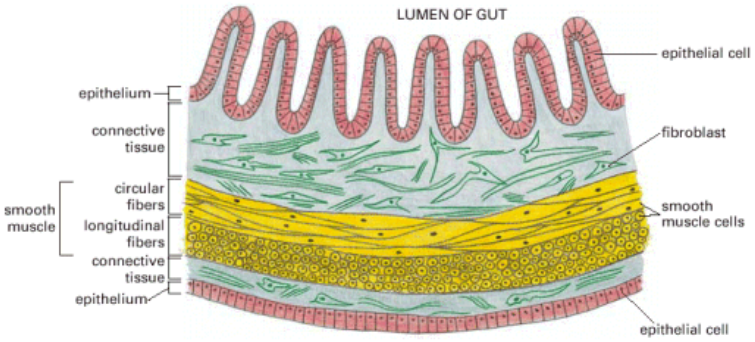

Figure 19-1. A cross-sectional view of part of the wall of the intestine. This long, tubelike organ is constructed from epithelial tissue *(red)*, connective tissue *(green)*, and muscle tissue *(yellow)*. Each tissue is an organized assembly of cells held together by cell-cell adhesions, extracellular matrix, or both.

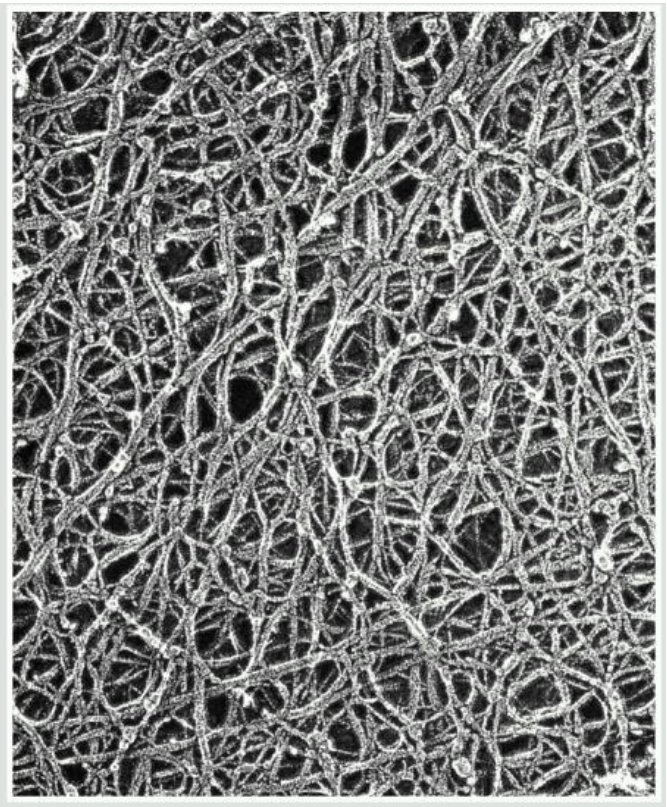

The plant cell wall. The extracellular matrix of both plants and animals consists of tough fibers embedded in a jelly-like matrix. An onion cell wall has been extracted to reveal the underlying meshwork of tough, load-bearing cellulose fibers. This structure is mimicked in paper manufacture. (Courtesy of Maureen McCann.)

Figure 19-2. The role of tight junctions in transcellular transport. Transport proteins are

confined to different regions of the plasma membrane in epithelial cells of the small intestine. This segregation permits a vectorial transfer of nutrients across the epithelium from the gut lumen to the blood. In the example shown, glucose is actively transported into the cell by Na^+-driven glucose symports at the apical surface, and it diffuses out of the cell by facilitated diffusion mediated by glucose carriers in the basolateral membrane. Tight junctions are thought to confine the transport proteins to their appropriate membrane domains by acting as diffusion barriers within the lipid bilayer of the plasma membrane; these junctions also block the backflow of glucose from the basal side of the epithelium into the gut lumen.

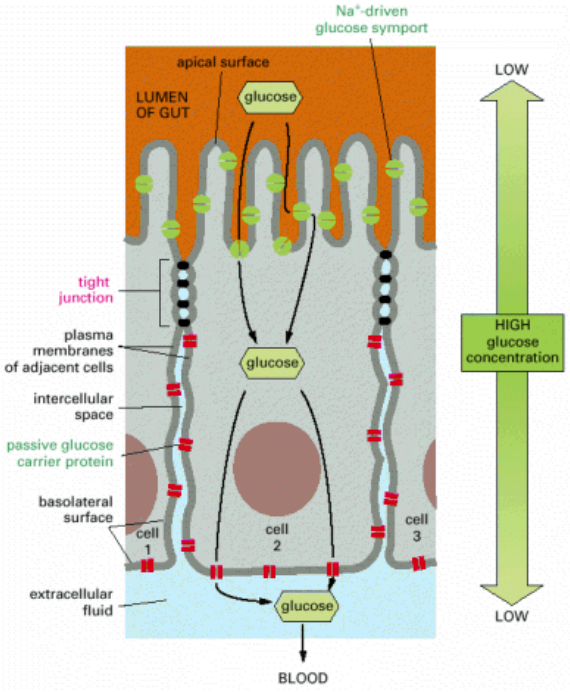

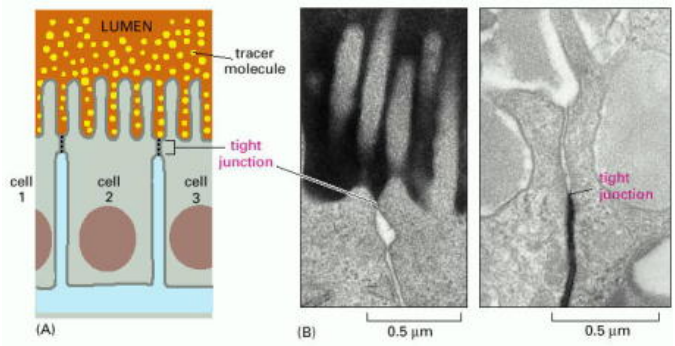

Figure 19-3. The role of tight junctions in allowing epithelia to serve as barriers to solute diffusion. (A) The drawing shows how a small extracellular tracer molecule added on one side of an epithelium cannot traverse the tight junctions that seal adjacent cells together. (B) Electron micrographs of cells in an epithelium in which a small, extracellular, electron-dense tracer molecule has been added to either the apical side (on the *left*) or the basolateral side (on the *right*). In both cases, the tracer is stopped by the tight junction. (B, courtesy of Daniel Friend.)

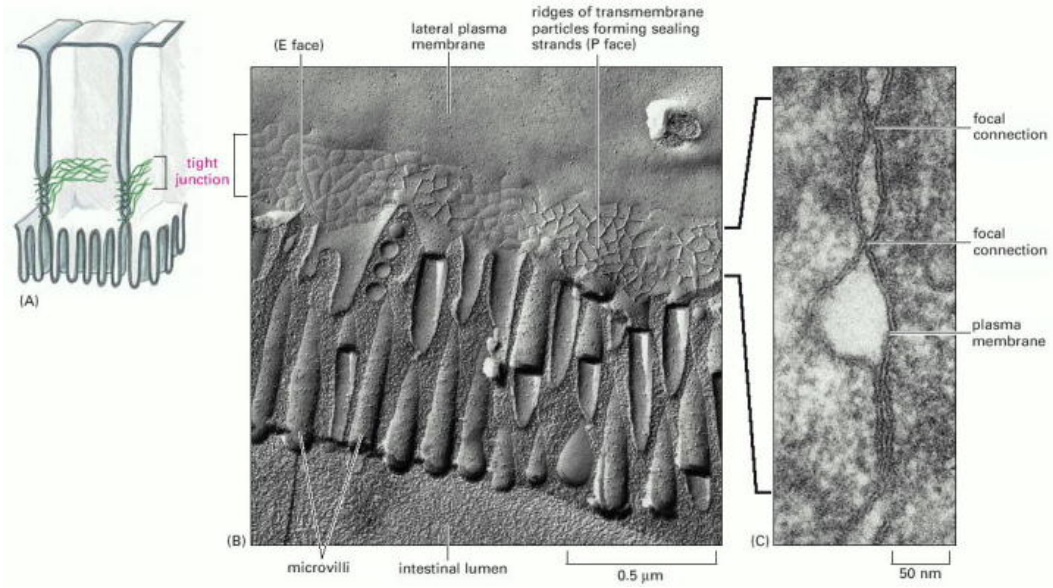

Figure 19-4. The structure of a tight junction between epithelial cells of the small intestine. The junctions are shown (A) schematically, (B) in a freeze-fracture electron micrograph, and (C) in a conventional electron micrograph. Note that the cells are oriented with their apical ends down. In (B), the plane of the micrograph is parallel to the plane of the membrane, and the tight junction appears as a beltlike band of branching sealing strands that encircle each cell in the epithelium. The sealing strands are seen as ridges of intramembrane particles on the cytoplasmic fracture face of the membrane (the P face) or as complementary grooves on the external face of the membrane (the E face) (see Figure 19-5A). In (C), the junction is seen in cross section as a series of focal connections between the outer leaflets of the two interacting plasma membranes, each connection corresponding to a sealing strand in cross section. (B and C, from N.B. Gilula, in Cell Communication [R.P. Cox, ed.], pp. 129. New York: Wiley, 1974. Reprinted by permission of John Wiley & Sons, Inc.)

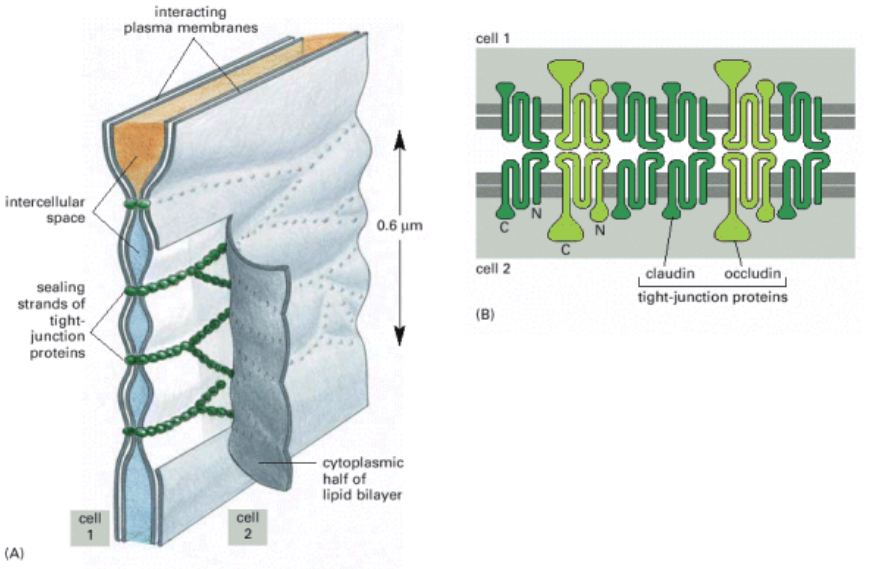

Figure 19-5. A current model of a tight junction. (A) This drawing shows how the sealing strands hold adjacent plasma membranes together. The strands are composed of transmembrane proteins that make contact across the intercellular space and create a seal. (B) This drawing shows the transmembrane claudin and occludin proteins in a tight junction. The claudins are the main components of the sealing strands; the function of the occludins is uncertain.

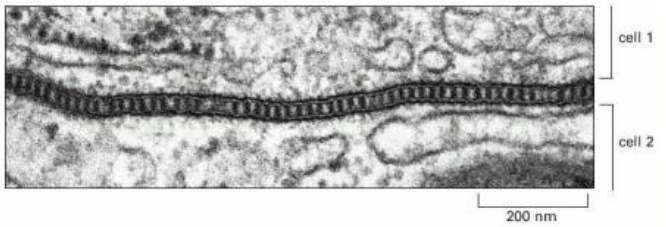

Figure 19-6. A septate junction. A conventional electron micrograph of a septate junction between two epithelial cells in a mollusk. The interacting plasma membranes, seen in cross section, are connected by parallel rows of junctional proteins. The rows, which have a regular periodicity, are seen as dense bars, or septa. (From N.B. Gilula, in Cell Communication [R.P. Cox, ed.], pp. 129. New York: Wiley, 1974. Reprinted by permission of John Wiley & Sons, Inc.)

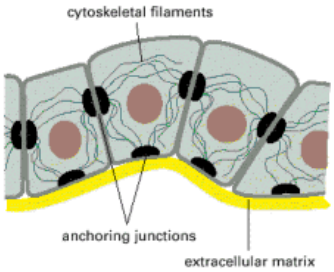

Figure 19-7. Anchoring junctions in an epithelium. This drawing illustrates, in a very general way, how anchoring junctions join cytoskeletal filaments from cell to cell and from cells to the extracellular matrix.

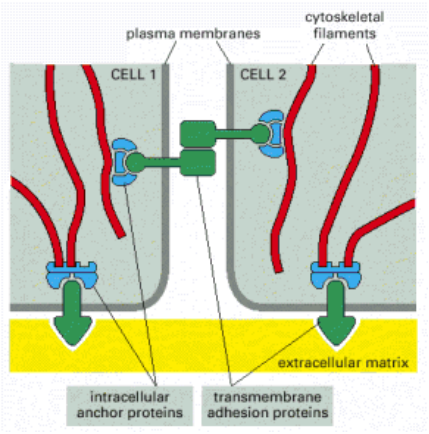

Figure 19-8. The construction of an anchoring junction from two classes of proteins. This drawing shows how intracellular anchor proteins and transmembrane adhesion proteins form anchoring junctions.

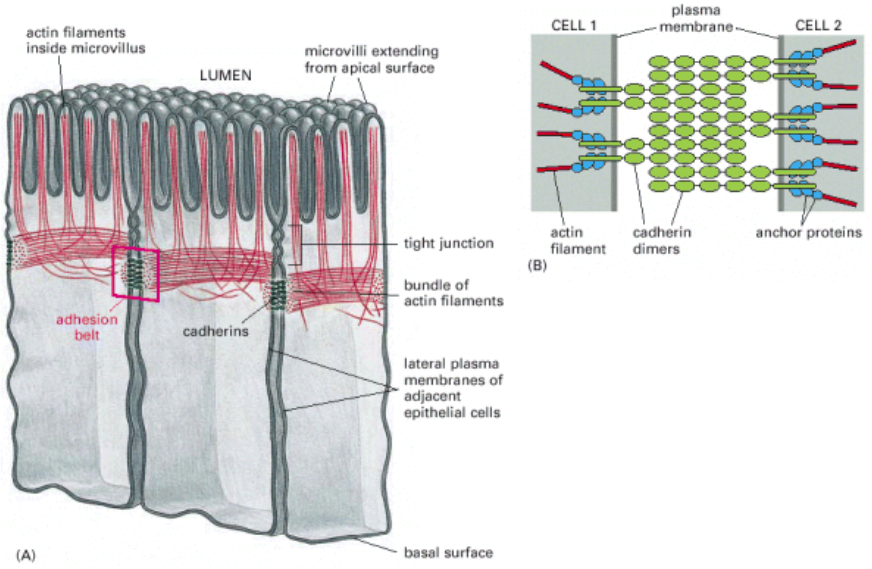

Figure 19-9. Adherens junctions. (A) Adherens junctions, in the form of adhesion belts, between epithelial cells in the small intestine. The beltlike junction encircles each of the interacting cells. Its most obvious feature is a contractile bundle of actin filaments running along the cytoplasmic surface of the junctional plasma membrane. (B) Some of the molecules that form an adherens junction. The actin filaments are joined from cell to cell by transmembrane adhesion proteins called cadherins. The cadherins form homodimers in the plasma membrane of each interacting cell. The extracellular domain of one cadherin dimer binds to the extracellular domain of an identical cadherin dimer on the adjacent cell. The intracellular tails of the cadherins bind to anchor proteins that tie them to actin filaments. These anchor proteins include α-catenin, β-catenin, γ-catenin (also called plakoglobin), α-actinin, and vinculin.

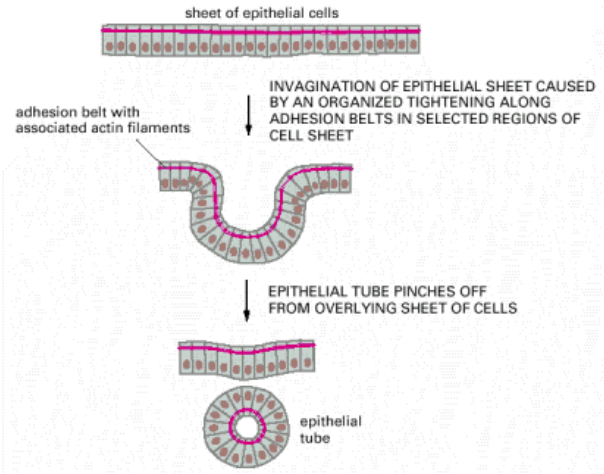

Figure 19-10. The folding of an epithelial sheet to form an epithelial tube. The oriented contraction of the bundles of actin filaments running along adhesion belts causes the epithelial cells to narrow at their apex and helps the epithelial sheet to roll up into a tube. An example is the formation of the neural tube in early vertebrate development (discussed in Chapter 21). Although not shown here, rearrangements of the cells within the epithelial sheet are also thought to have an important role in the process.

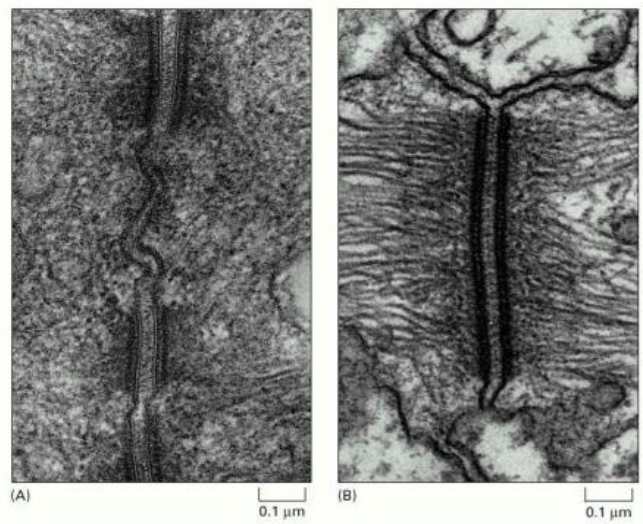

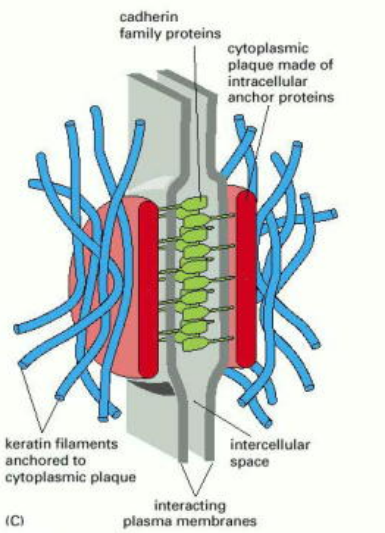

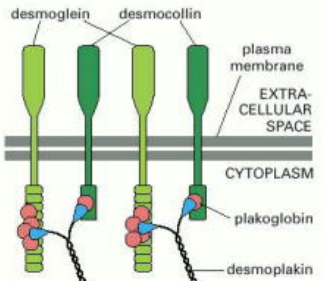

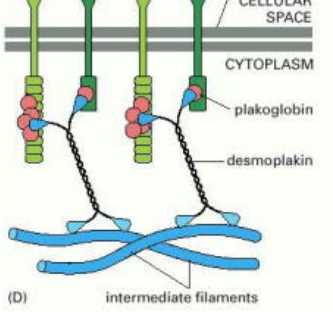

Figure 19-11. Desmosomes. (A) An electron micrograph of three desmosomes between two epithelial cells in the intestine of a rat. (B) An electron micrograph of a single desmosome between two epidermal cells in a developing newt, showing clearly the attachment of intermediate filaments. (C) The structural components of a desmosome. On the cytoplasmic surface of each interacting plasma membrane is a dense plaque composed of a mixture of intracellular anchor proteins. A bundle of keratin intermediate filaments is attached to the surface of each plaque. Transmembrane adhesion proteins of the cadherin family bind to the plaques and interact through their extracellular domains to hold the adjacent membranes together by a Ca^{2+}-dependent mechanism. (D) Some of the molecular components of a desmosome. Desmoglein and desmocollin are members of the cadherin family of adhesion proteins. Their cytoplasmic tails bind plakoglobin (γ-catenin), which in turn binds to desmoplakin. Desmoplakin also binds to the sides of intermediate filaments, thereby tying the desmosome to these filaments. (A, from N.B. Gilula, in Cell Communication [R.P. Cox, ed.], pp. 129. New York: Wiley, 1974. Reprinted by permission of John Wiley & Sons, Inc.; B, from D.E. Kelly, *J. Cell Biol.* 28:5159, 1966. © The Rockefeller University Press.)

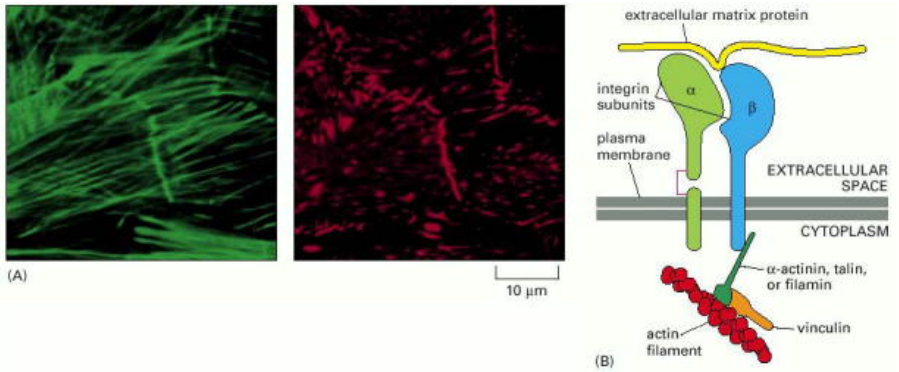

Figure 19-12. Focal adhesions. (A) In these immunofluorescence micrographs, cells in culture have been labeled with antibodies against both actin *(green)* and the intracellular anchor protein vinculin *(red).* Note that vinculin is located at focal adhesions, which is also where bundles of actin filaments terminate at the plasma membrane. (B) Some of the proteins that form focal adhesions. The transmembrane adhesion protein is an integrin heterodimer, composed of an α and a β subunit. Its extracellular domains bind to components of the extracellular matrix, while the cytoplasmic tail of the β subunit binds indirectly to actin filaments via several intracellular anchor proteins. (A, from B. Geiger, E. Schmid, and W. Franke, *Differentiation* 23:189205, 1983.)

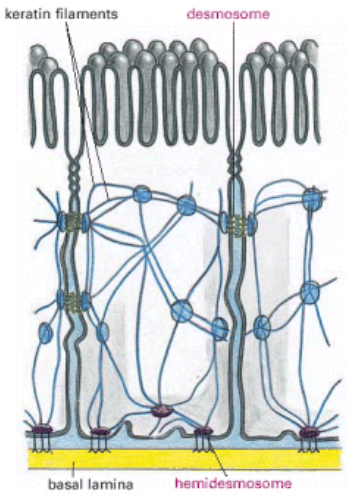

Figure 19-13. Desmosomes and hemidesmosomes. The distribution of desmosomes and hemidesmosomes in epithelial cells of the small intestine. The keratin intermediate filament networks of adjacent cells are indirectly connected to one another through desmosomes and to the basal lamina through hemidesmosomes.

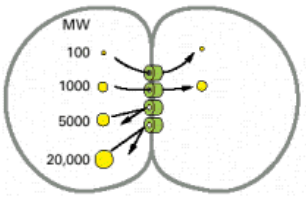

Figure 19-14. Determining the size of a gap-junction channel. When fluorescent molecules of various sizes are injected into one of two cells coupled by gap junctions, molecules with a mass of less than about 1000 daltons can pass into the other cell, but larger molecules cannot.

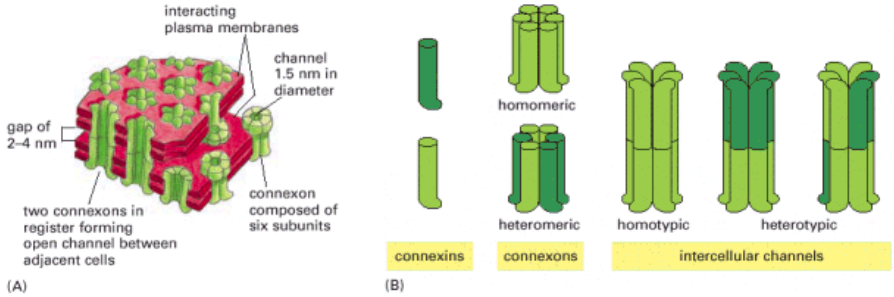

Figure 19-15. Gap junctions. (A) A three-dimensional drawing showing the interacting plasma membranes of two adjacent cells connected by gap junctions. The apposed lipid bilayers *(red)* are penetrated by protein assemblies called connexons *(green)*, each of which is formed by six connexin subunits. Two connexons join across the intercellular gap to form a continuous aqueous channel connecting the two cells. (B) The organization of connexins into connexons and connexons into intercellular channels. The connexons can be homomeric or heteromeric, and the intercellular channels can be homotypic or heterotypic.

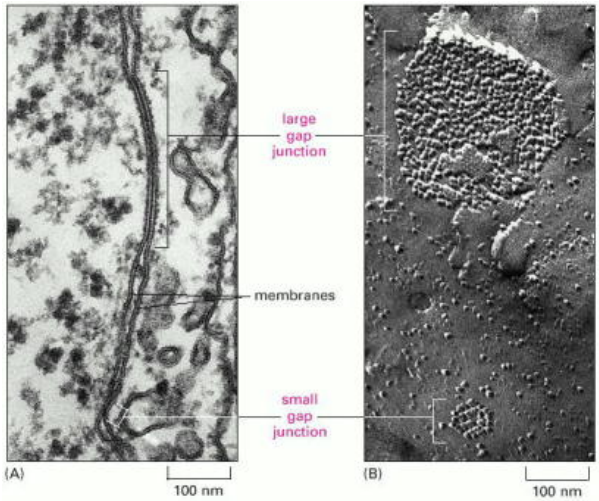

Figure 19-16. Gap junctions as seen in the electron microscope. (A) Thin-section and (B) freeze-fracture electron micrographs of a large and a small gap junction between fibroblasts in culture. In (B), each gap junction is seen as a cluster of homogeneous intramembrane particles associated exclusively with the cytoplasmic fracture face (P face) of the plasma membrane. Each intramembrane particle corresponds to a connexon. (From N.B. Gilula, in Cell Communication [R.P. Cox, ed.], pp. 129. New York: Wiley, 1974. Reprinted by permission of John Wiley & Sons, Inc.)

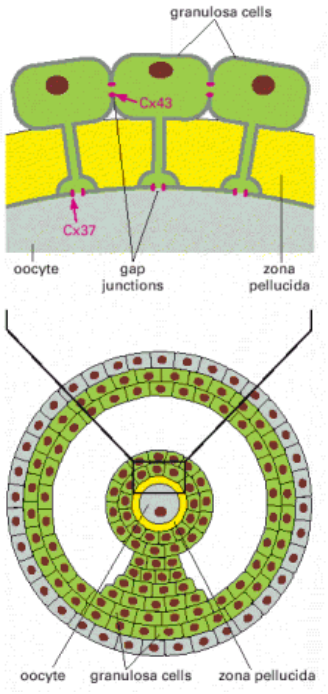

Figure 19-17. Gap junction coupling in the ovarian follicle. The oocyte is surrounded by a thick layer of extracellular matrix called the zona pellucida (discussed in Chapter 20). The surrounding granulosa cells are coupled to each other by gap junctions formed by connexin 43 (Cx43). In addition, the granulosa cells extend processes through the zona pellucida and make gap junctions with the oocyte. These gap junctions contain a different connexin (Cx37). Mutations in the gene encoding Cx37 cause infertility by disrupting the development of both the granulosa cells and the oocyte.

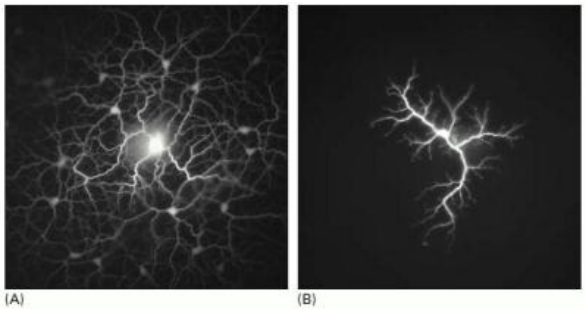

Figure 19-18. The regulation of gap-junction coupling by a neurotransmitter. (A) A neuron in a rabbit retina was injected with the dye Lucifer yellow, which passes readily through gap junctions and labels other neurons of the same type that are connected to the injected cell by gap junctions. (B) The retina was first treated with the neurotransmitter dopamine, before the neuron was injected with dye. As can be seen, the dopamine treatment greatly decreased the permeability of the gap junctions. Dopamine acts by increasing intracellular cyclic AMP levels. (Courtesy of David Vaney.)

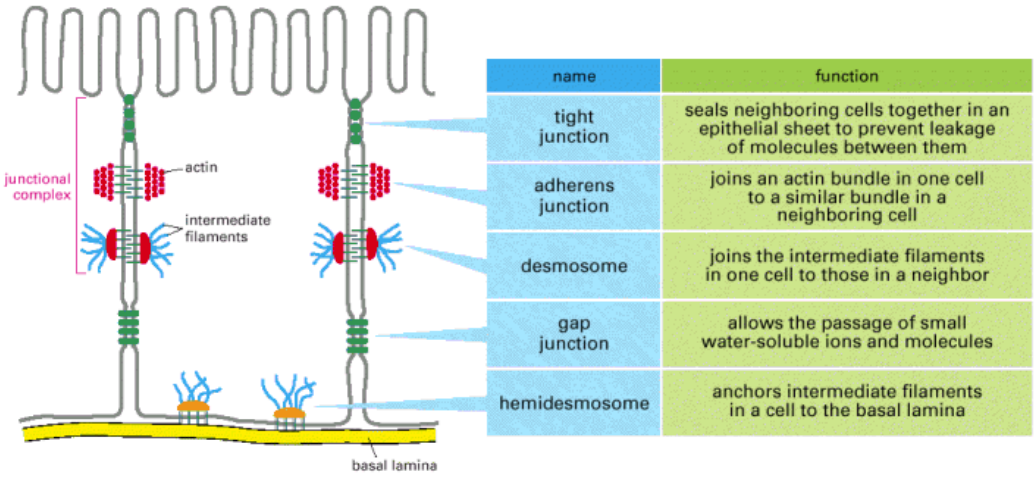

Figure 19-19. A summary of the various cell junctions found in a vertebrate epithelial cell. The drawing is based on epithelial cells of the small intestine.

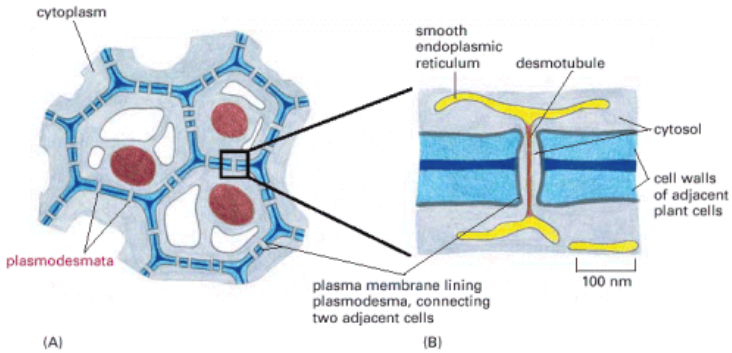

Figure 19-20. Plasmodesmata. (A) The cytoplasmic channels of plasmodesmata pierce the plant cell wall and connect all cells in a plant together. (B) Each plasmodesma is lined with plasma membrane that is common to two connected cells. It usually also contains a fine tubular structure, the desmotubule, derived from smooth endoplasmic reticulum.

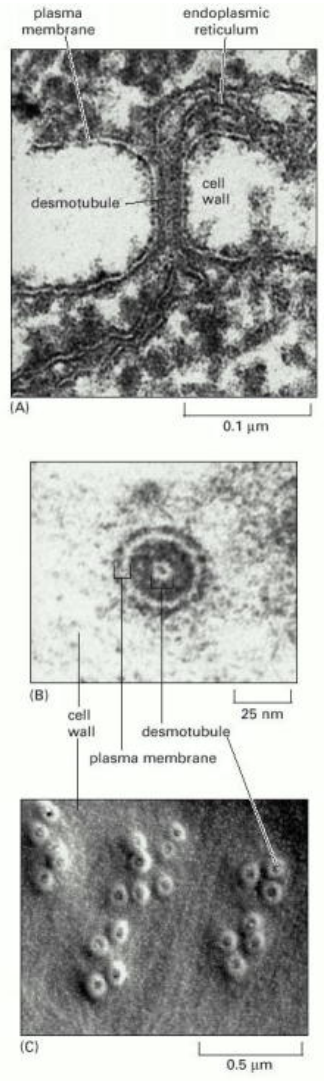

Figure 19-21. Various views of plasmodesmata. (A) Electron micrograph of a longitudinal section of a plasmodesma from a water fern. The plasma membrane lines the pore and is continuous from one cell to the next. Endoplasmic reticulum and its association with the central desmotubule can be seen. (B) A similar plasmodesma seen in cross section. (C) Small pit fields of plasmodesmata in a cell wall isolated from a tobacco leaf. In this SEM they are seen in face view and in many of them the central desmotubule can be seen. (A and B, from R. Overall, J. Wolfe and B.E.S. Gunning, in Protoplasm 9, pp. 137 and 140. Heidelberg:

Springer-Verlag, 1982; C, courtesy of Kim Findlay.)

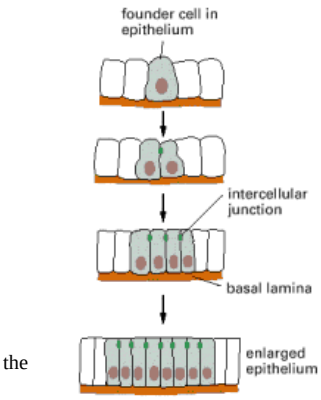

Figure 19-22. The simplest mechanism by which cells assemble to form a tissue. The progeny of the founder cell are retained in the epithelium by the basal lamina and by cell-cell adhesion mechanisms, including the formation of intercellular junctions.

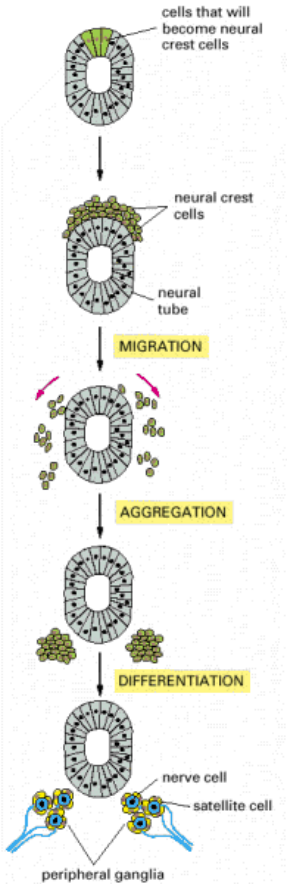

Figure 19-23. An example of a more complex mechanism by which cells assemble to form a tissue. Some cells that are initially part of the epithelial neural tube alter their adhesive properties and disengage from the epithelium to form the neural crest on the upper surface of the neural tube. The cells then migrate away and form a variety of cell types and tissues throughout the embryo. Here they are shown assembling and differentiating to form two collections of nerve cells, called ganglia, in the peripheral nervous system. Other neural crest cells differentiate in the ganglion to become supporting (satellite) cells surrounding the neurons. The crest cells tend to migrate in clusters, and they proliferate rapidly as they migrate.

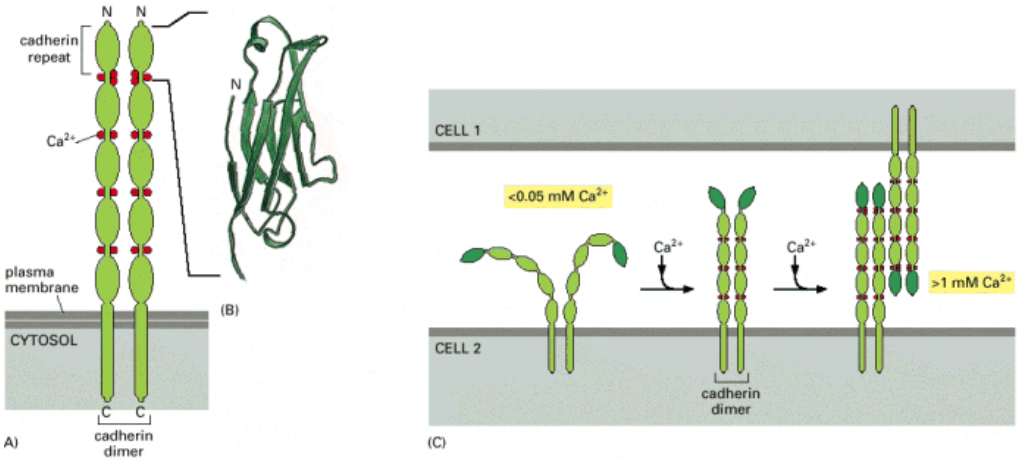

Figure 19-24. The structure and function of cadherins. (A) A classical cadherin molecule. The protein is a homodimer, with the extracellular part of each polypeptide folded into five cadherin repeats. There are Ca^{2+}-binding sites between each pair of repeats. (B) The crystal structure of a single cadherin repeat, which resembles an immunoglobulin (Ig) domain. (C) The influence of extracellular Ca^{2+}. As the amount of Ca^{2+} increases, the extracellular parts of the cadherin chains become more rigid. When enough Ca^{2+} is bound, the cadherin dimer extends from the surface, where it can bind to a cadherin dimer on a neighboring cell. If Ca^{2+} is removed, the extracellular part of the protein becomes floppy and is degraded by proteolytic enzymes.

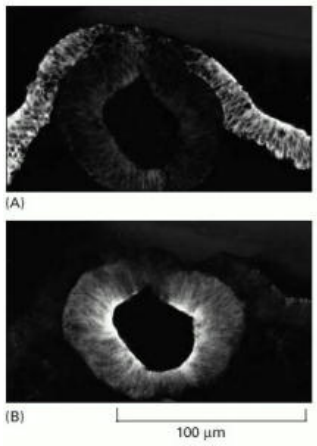

Figure 19-25. The distribution of E-cadherin and N-cadherin in the developing nervous system. Immunofluorescence micrographs of a cross section of a chick embryo showing the developing neural tube labeled with antibodies against (A) E-cadherin and (B) N-cadherin. Note that the overlying ectoderm cells express only E-cadherin, while the cells in the neural tube have lost E-cadherin and have acquired N-cadherin. See also Figure 19-10. (Courtesy of Kohei Hatta and Masatoshi Takeichi.)

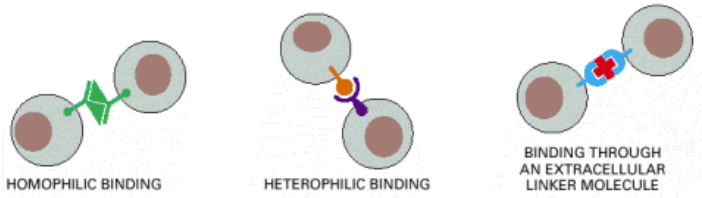

Figure 19-26. Three mechanisms by which cell-surface molecules can mediate cell-cell adhesion. Although all of these mechanisms can operate in animals, the one that depends on an extracellular linker molecule seems to be the least common.

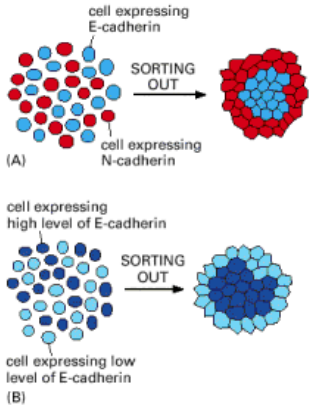

Figure 19-27. Cadherin-dependent cell sorting. Cells in culture can sort themselves out according to the type and level of cadherins they express. This can be visualized by labeling different populations of cells with dyes of different colors. (A) Cells expressing N-cadherin sort out from cells expressing E-cadherin. (B) Cells expressing high levels of E-cadherin sort out from cells expressing low levels of E-cadherin.

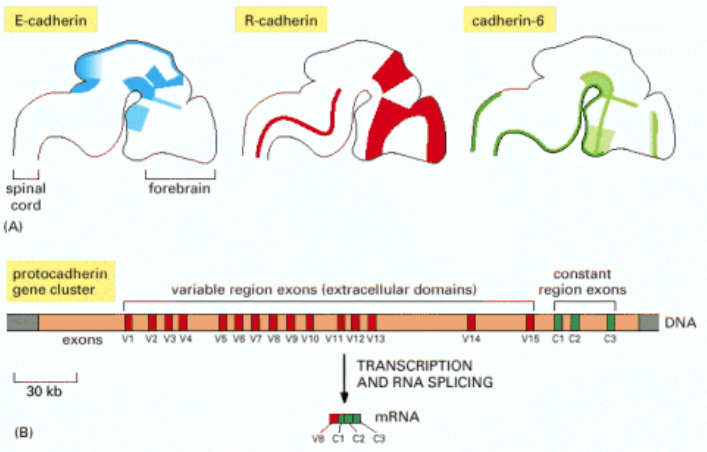

Figure 19-28. Cadherin diversity in the central nervous system. (A) Expression patterns for three classical cadherins in the embryonic mouse brain. (B) The arrangement of exons that encode the members of one of the three known protocadherin families of nonclassical cadherins in humans. Each of the variable-region exons encodes the extracellular region of one type of transmembrane protocadherin protein, but all of the protocadherins encoded by this cluster share the same cytoplasmic tail, which is encoded by the three constant-region exons C1, C2, and C3. A diversity of proteins is generated from the gene cluster by the use of different promoters and by alternative RNA splicing.

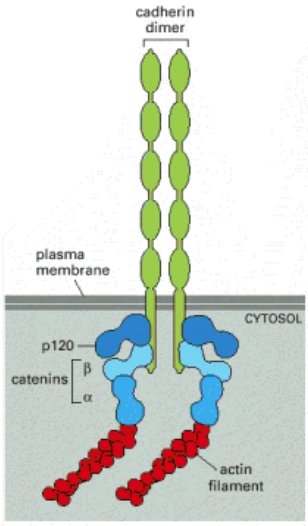

Figure 19-29. The linkage of classical cadherins to actin filaments. The cadherins are coupled indirectly to actin filaments by the anchor proteins α-catenin and β-catenin. A third intracellular protein, called p120, also binds to the cadherin cytoplasmic tail and regulates cadherin function. β-catenin has a second, and very important, function in intracellular signaling, as we discuss in Chapter 15 (see Figure 15-72).

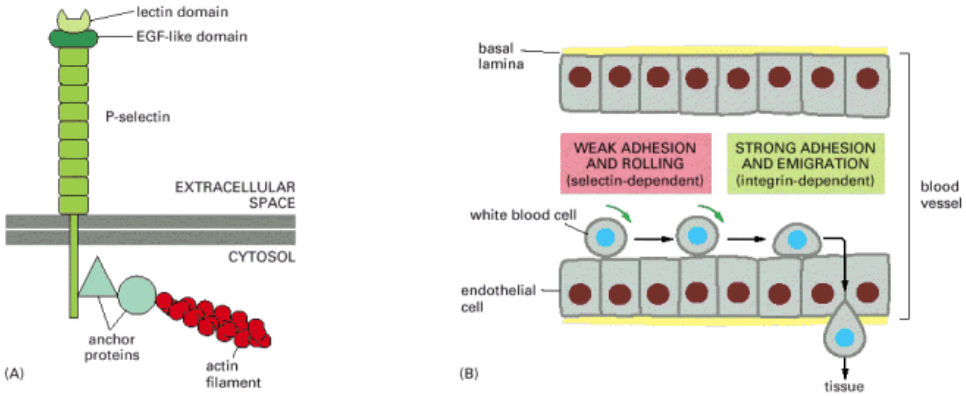

Figure 19-30. The structure and function of selectins. (A) The structure of P-selectin. The selectin attaches to the actin cytoskeleton through anchor proteins that are still poorly characterized. (B) How selectins and integrins mediate the cell-cell adhesions required for a white blood cell to migrate out of the bloodstream into a tissue.

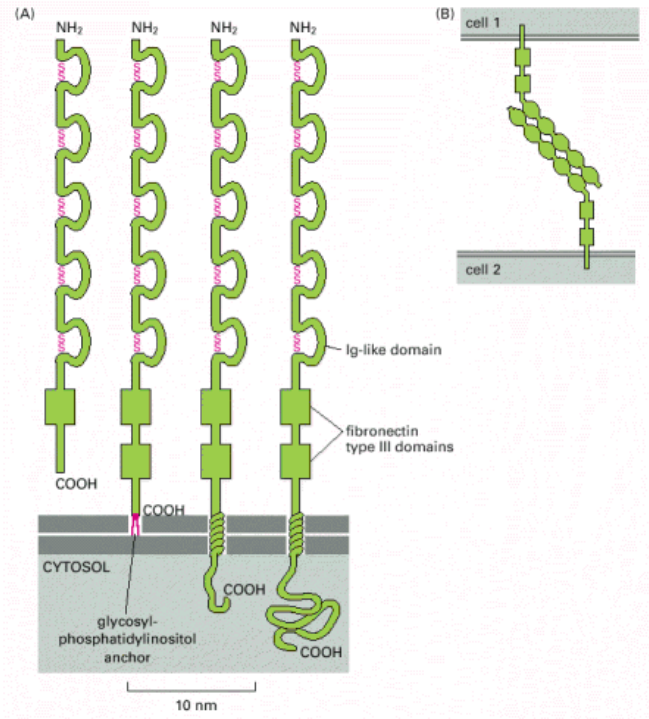

Figure 19-31. The cell adhesion protein N-CAM. (A) Four forms of N-CAM. The extracellular part of the polypeptide chain in each case is folded into five Ig-like domains (and one or two other domains called fibronectin type III repeats). Disulfide bonds (*red*) connect the ends of each loop that forms an Ig-like domain. (B) A model for the homophilic interaction that allows N-CAM to mediate cell-cell adhesion.

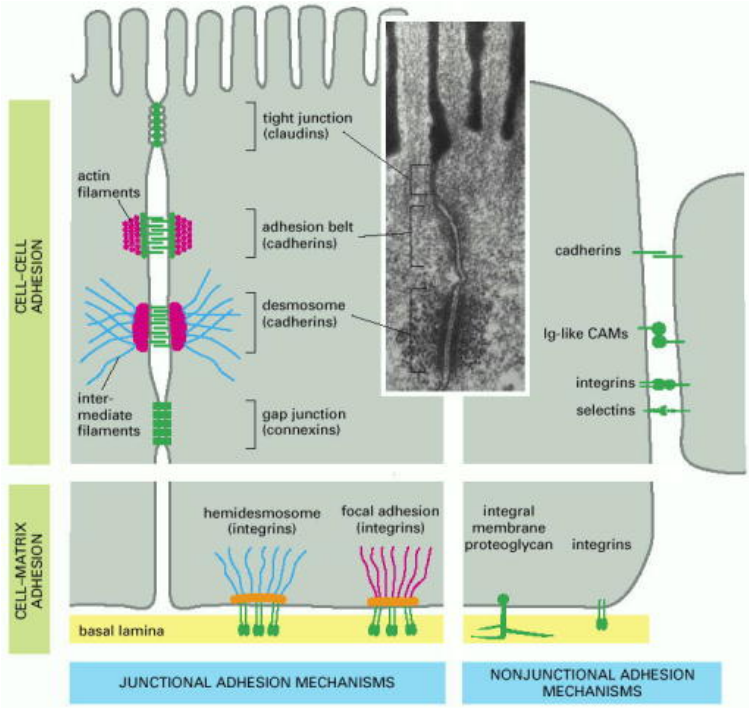

Figure 19-32. A summary of the junctional and nonjunctional adhesive mechanisms used by animal cells in binding to one another and to the extracellular matrix. The junctional mechanisms are shown in epithelial cells, while the nonjunctional mechanisms are shown in nonepithelial cells. A junctional adhesion is operationally defined as one that can be seen as a specialized region of contact by conventional or freeze-fracture electron microscopy. A nonjunctional adhesion shows no such obvious specialized structure. Note that the integrins and cadherins are involved in both nonjunctional and junctional cell-cell (cadherins) and cell-matrix (integrins) contacts. Cadherins generally mediate homophilic interactions, whereas integrins mediate heterophilic interactions (see Figure 19-26). The cadherins, integrins, and selectins act as transmembrane adhesion molecules and depend on extracellular divalent cations to function; for this reason, most cell-cell and cell-matrix contacts are divalent-cation-dependent. On blood cells, selectins and integrins can also act as heterophilic cell-cell adhesion molecules: the selectins bind to carbohydrate, while the cell-binding integrins bind to members of the Ig superfamily. The integrins and integral membrane proteoglycans that mediate nonjunctional adhesion to the extracellular matrix are discussed later. (Insert courtesy of Daniel S. Friend.)

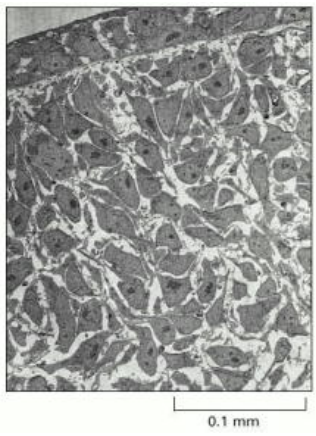

Figure 19-33. Cells surrounded by spaces filled with extracellular matrix. The particular cells shown in this low-power electron micrograph are those in an embryonic chick limb bud. The cells have not yet acquired their specialized characteristics. (Courtesy of Cheryll Tickle.)

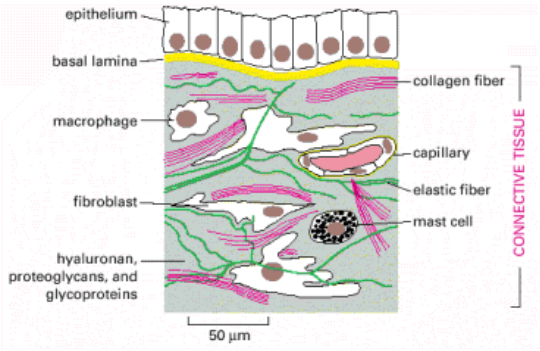

Figure 19-34. The connective tissue underlying an epithelium. This tissue contains a variety of cells and extracellular matrix components. The predominant cell type is the fibroblast, which secretes abundant extracellular matrix.

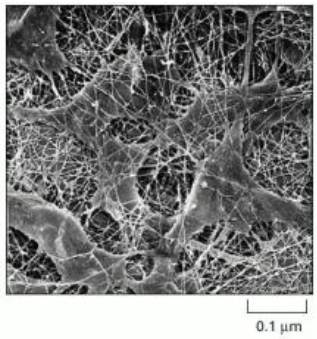

Figure 19-35. Fibroblasts in connective tissue. This scanning electron micrograph shows tissue from the cornea of a rat. The extracellular matrix surrounding the fibroblasts is composed largely of collagen fibrils (there are no elastic fibers in the cornea). The glycoproteins, hyaluronan, and proteoglycans, which normally form a hydrated gel filling the interstices of the fibrous network, have been removed by enzyme and acid treatment. (From T. Nishida et al., *Invest. Ophthalmol. Vis. Sci.* 29:18871890, 1988. © Association for Research in Vision and Opthalmology.)

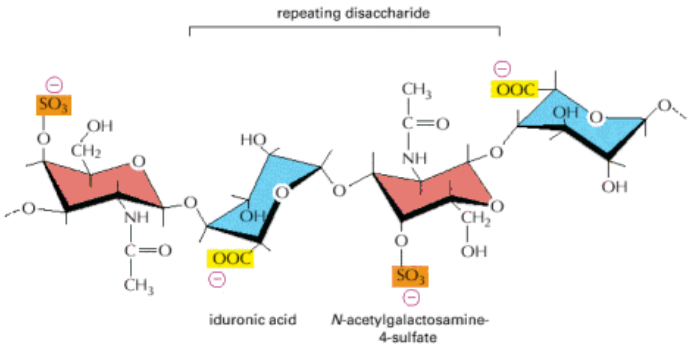

Figure 19-36. The repeating disaccharide sequence of a dermatan sulfate glycosaminoglycan (GAG) chain. These chains are typically 70200 sugars long. There is a high density of negative charges along the chain resulting from the presence of both carboxyl and sulfate groups.

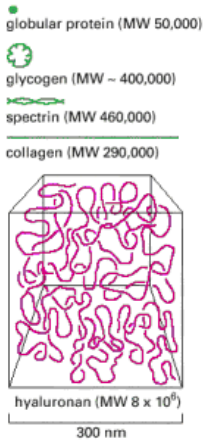

Figure 19-37. The relative dimensions and volumes occupied by various macromolecules. Several proteins, a glycogen granule, and a single hydrated molecule of hyaluronan are shown.

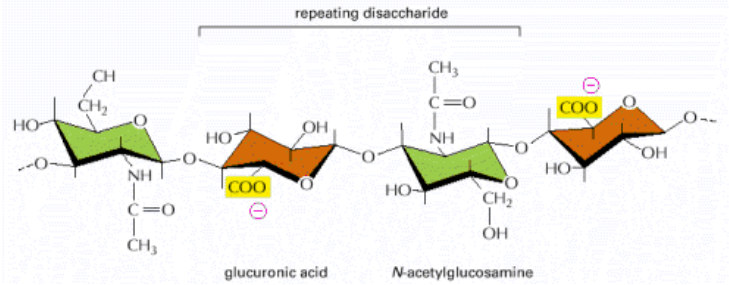

Figure 19-38. The repeating disaccharide sequence in hyaluronan, a relatively simple GAG. This ubiquitous molecule in vertebrates consists of a single long chain of up to 25,000 sugars. Note the absence of sulfate groups.

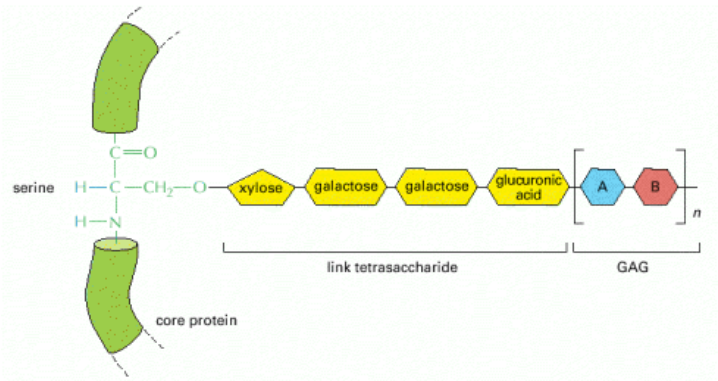

Figure 19-39. The linkage between a GAG chain and its core protein in a proteoglycan molecule. A specific link tetrasaccharide is first assembled on a serine side chain. In most cases, it is unclear how the particular serine is selected, but it seems that a specific local conformation of the polypeptide chain, rather than a specific linear sequence of amino acids, is recognized. The rest of the GAG chain, consisting mainly of a repeating disaccharide unit, is then synthesized, with one sugar being added at a time. In chondroitin sulfate, the disaccharide is composed of d-glucuronic acid and *N*-acetyl-d-galactosamine; in heparan sulfate, it is d-glucosamine (or l-iduronic acid) and *N*-acetyl-d-glucosamine; in keratan sulfate, it is d-galactose and *N*-acetyl-d-glucosamine.

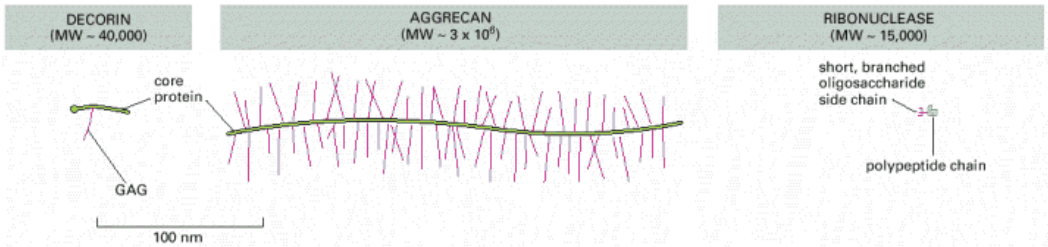

Figure 19-40. Examples of a small (decorin) and a large (aggrecan) proteoglycan found in the extracellular matrix. These two proteoglycans are compared with a typical secreted glycoprotein molecule, pancreatic ribonuclease B. All three are drawn to scale. The core proteins of both aggrecan and decorin contain oligosaccharide chains as well as the GAG chains, but these are not shown. Aggrecan typically consists of about 100 chondroitin sulfate chains and about 30 keratan sulfate chains linked to a serine-rich core protein of almost 3000 amino acids. Decorin "decorates" the surface of collagen fibrils, hence its name.

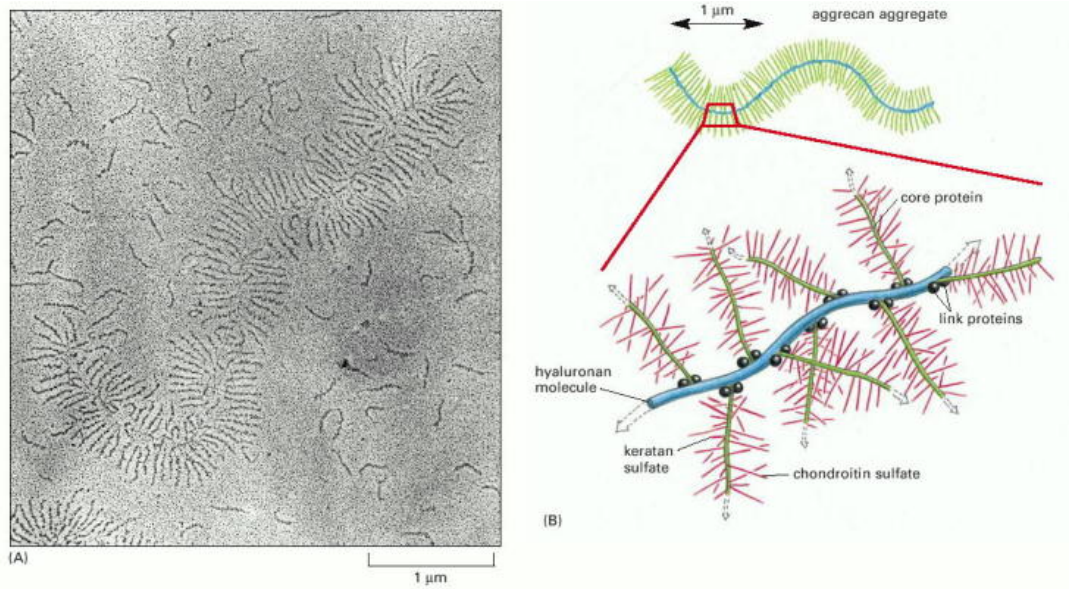

Figure 19-41. An aggrecan aggregate from fetal bovine cartilage. (A) An electron micrograph of an aggrecan aggregate shadowed with platinum. Many free aggrecan molecules are also visible. (B) A drawing of the giant aggrecan aggregate shown in (A). It consists of about 100 aggrecan monomers (each like the one shown in Figure 19-40) noncovalently bound to a single hyaluronan chain through two link proteins that bind both to the core protein of the proteoglycan and to the hyaluronan chain, thereby stabilizing the aggregate. The link proteins are members of a family of hyaluronan-binding proteins, some of which are cell-surface proteins. The molecular weight of such a complex can be 10^8 or more, and it occupies a volume equivalent to that of a bacterium, which is about 2×10^{-12} cm^3. (A, courtesy of Lawrence Rosenberg.)

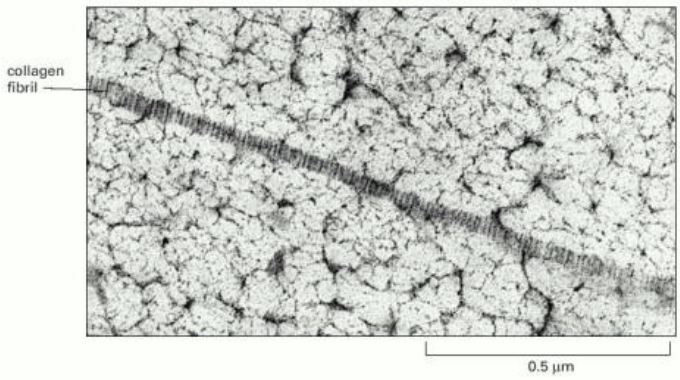

Figure 19-42. Proteoglycans in the extracellular matrix of rat cartilage. The tissue was rapidly frozen at -196°C, and fixed and stained while still frozen (a process called freeze substitution) to prevent the GAG chains from collapsing. In this electron micrograph, the proteoglycan molecules are seen to form a fine filamentous network in which a single striated collagen fibril is embedded. The more darkly stained parts of the proteoglycan molecules are the core proteins; the faintly stained threads are the GAG chains. (Reproduced from E.B. Hunziker and R.K. Schenk, *J. Cell Biol.* 98:277282, 1985. © The Rockefeller University Press.)

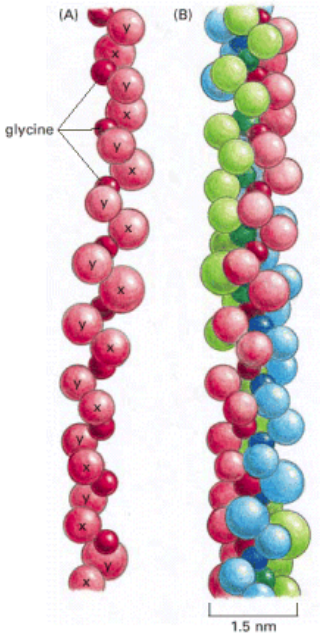

Figure 19-43. The structure of a typical collagen molecule. (A) A model of part of a single collagen α chain in which each amino acid is represented by a sphere. The chain is about 1000 amino acids long. It is arranged as a left-handed helix, with three amino acids per turn and with glycine as every third amino acid. Therefore, an α chain is composed of a series of triplet Gly-X-Y sequences, in which X and Y can be any amino acid (although X is commonly proline and Y is commonly hydroxyproline). (B) A model of part of a collagen molecule in which three α chains, each shown in a different color, are wrapped around one another to form a triple-stranded helical rod. Glycine is the only amino acid small enough to occupy the crowded interior of the triple helix. Only a short length of the molecule is shown; the entire molecule is 300 nm long. (From model by B.L. Trus.)

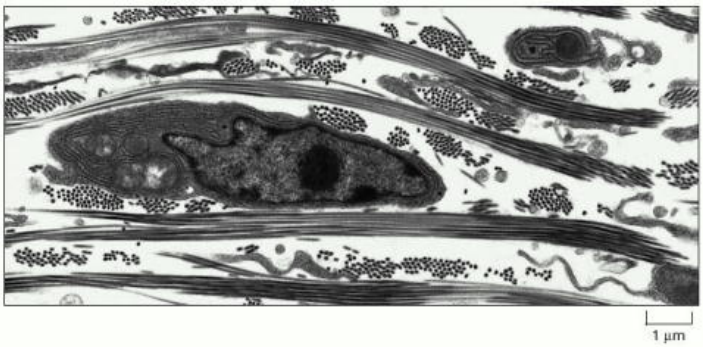

Figure 19-44. Fibroblast surrounded by collagen fibrils in the connective tissue of embryonic chick skin. In this electron micrograph, the fibrils are organized into bundles that run approximately at right angles to one another. Therefore, some bundles are oriented longitudinally, whereas others are seen in cross section. The collagen fibrils are produced by the fibroblasts, which contain abundant endoplasmic reticulum, where secreted proteins such as collagen are synthesized. (From C. Ploetz, E.I. Zycband, and D.E. Birk, *J. Struct. Biol.* 106:7381, 1991. © Academic Press.)

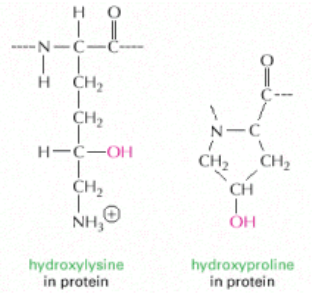

Figure 19-45. Hydroxylysine and hydroxyproline. These modified amino acids are common in collagen. They are formed by enzymes that act after the lysine and proline have been incorporated into procollagen molecules.

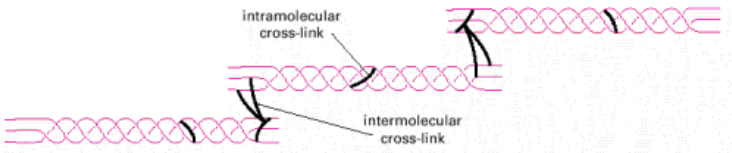

Figure 19-46. Cross-links formed between modified lysine side chains within a collagen fibril. Covalent intramolecular and intermolecular cross-links are formed in several steps. First, certain lysines and hydroxylysines are deaminated by the extracellular enzyme lysyl oxidase to yield highly reactive aldehyde groups. The aldehydes then react spontaneously to form covalent bonds with each other or with other lysines or hydroxylysines. Most of the cross-links form between the short nonhelical segments at each end of the collagen molecules.

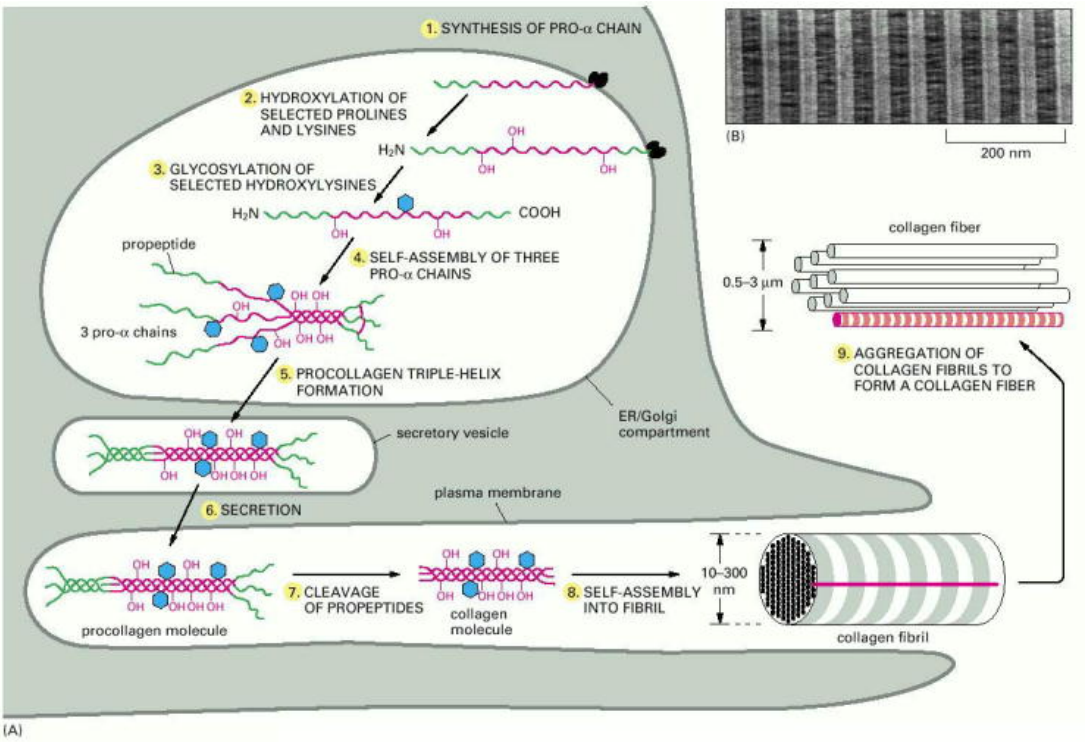

Figure 19-47. The intracellular and extracellular events in the formation of a collagen fibril. (A) Note that collagen fibrils are shown assembling in the extracellular space contained within a large infolding in the plasma membrane. As one example of how collagen fibrils can form ordered arrays in the extracellular space, they are shown further assembling into large collagen fibers, which are visible in the light microscope. The covalent cross-links that stabilize the extracellular assemblies are not shown. (B) Electron micrograph of a negatively stained collagen fibril reveals its typical striated appearance. (B, courtesy of Robert Horne.)

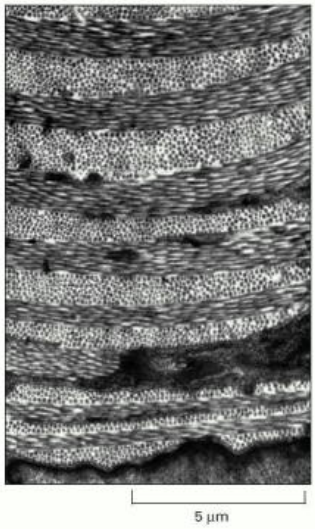

Figure 19-48. Collagen fibrils in the tadpole skin. This electron micrograph shows the plywoodlike arrangement of the fibrils. Successive layers of fibrils are laid down nearly at right angles to each other. This organization is also found in mature bone and in the cornea. (Courtesy of Jerome Gross.)

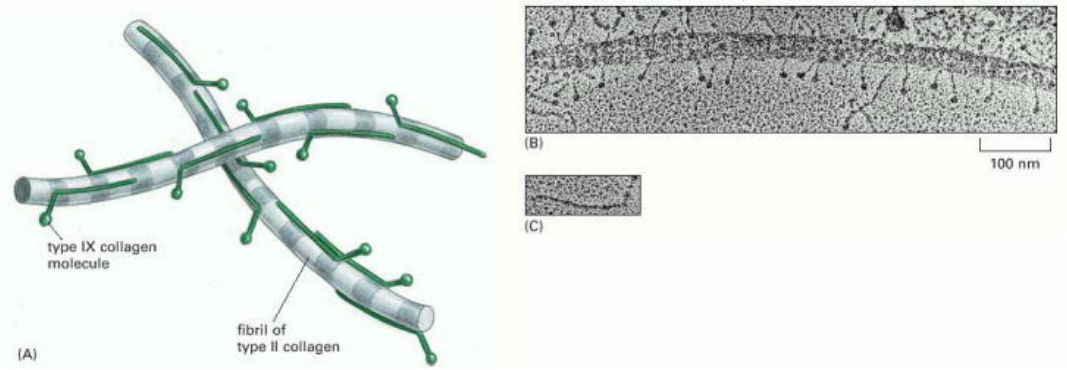

Figure 19-49. Type IX collagen. (A) Type IX collagen molecules binding in a periodic pattern to the surface of a fibril containing type II collagen. (B) Electron micrograph of a rotary-shadowed type-II-collagen-containing fibril in cartilage, sheathed in type IX collagen molecules. (C) An individual type IX collagen molecule. (B and C, from L. Vaughan et al., *J. Cell Biol.* 106:991997, 1988. © The Rockefeller University Press.)

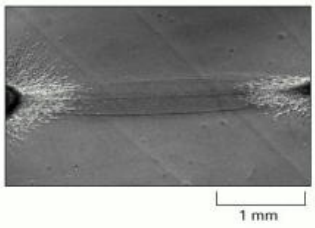

Figure 19-50. The shaping of the extracellular matrix by cells. This micrograph shows a region between two pieces of embryonic chick heart (rich in fibroblasts as well as heart muscle cells) that were cultured on a collagen gel for 4 days. A dense tract of aligned collagen fibers has formed between the explants, presumably as a result of the fibroblasts in the explants tugging on the collagen. (From D. Stopak and A.K. Harris, *Dev. Biol.* 90:383398, 1982. © Academic Press.)

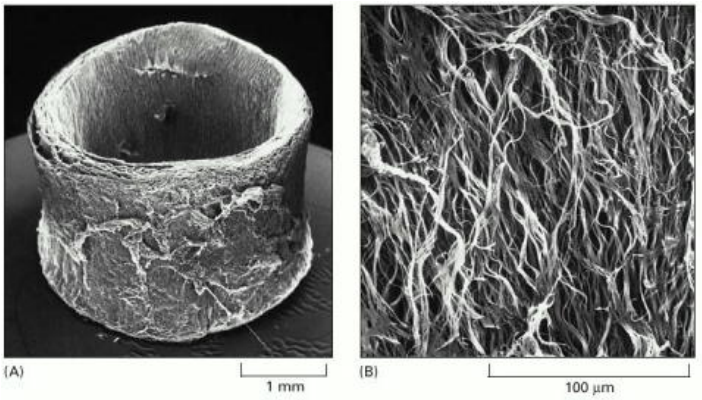

Figure 19-51. Elastic fibers. These scanning electron micrographs show (A) a low-power view of a segment of a dog's aorta and (B) a high-power view of the dense network of longitudinally oriented elastic fibers in the outer layer of the same blood vessel. All the other components have been digested away with enzymes and formic acid. (From K.S. Haas, S.J. Phillips, A.J. Comerota, and J.W. White, *Anat. Rec.* 230:8696, 1991. © Wiley-Liss, Inc.)

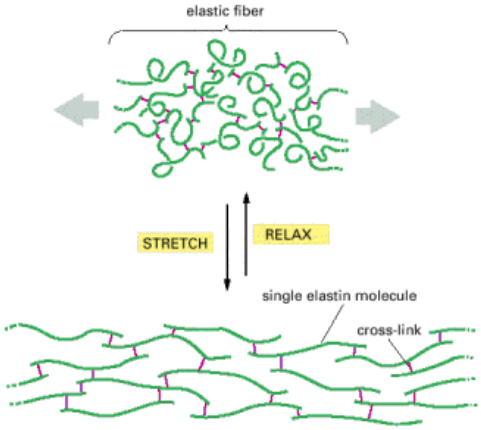

Figure 19-52. Stretching a network of elastin molecules. The molecules are joined together by covalent bonds *(red)* to generate a cross-linked network. In this model, each elastin molecule in the network can expand and contract as a random coil, so that the entire assembly can stretch and recoil like a rubber band.

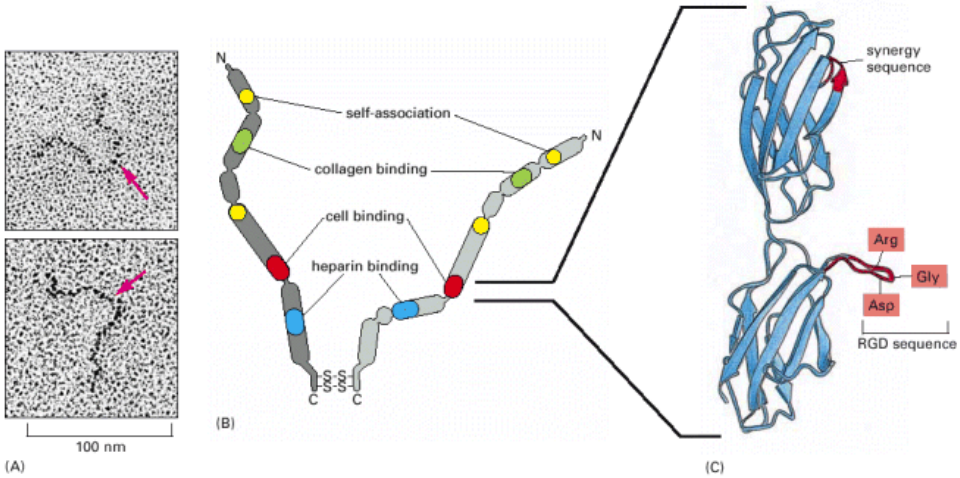

Figure 19-53. The structure of a fibronectin dimer. (A) Electron micrographs of individual fibronectin dimer molecules shadowed with platinum; *red arrows* mark the C-termini. (B) The two polypeptide chains are similar but generally not identical (being made from the same gene but from differently spliced mRNAs). They are joined by two disulfide bonds near the C-termini. Each chain is almost 2500 amino acids long and is folded into five or six domains connected by flexible polypeptide segments. Individual domains are specialized for binding to a particular molecule or to a cell, as indicated for five of the domains. For simplicity, not all of the known binding sites are shown (there are other cell-binding sites, for example). (C) The three-dimensional structure of two type III fibronectin repeats as determined by x-ray crystallography. The type III repeat is the main repeating module in fibronectin. Both the Arg-Gly-Asp (RGD) and the "synergy" sequences shown in *red* form part of the major cell-binding site (shown *blue* in B). (A, from J. Engel et al., *J. Mol. Biol.* 150:97120, 1981. © Academic Press; C, from Daniel J. Leahy, *Annu. Rev. Cell Dev. Biol.* 13:363393, 1997. © Annual Reviews.)

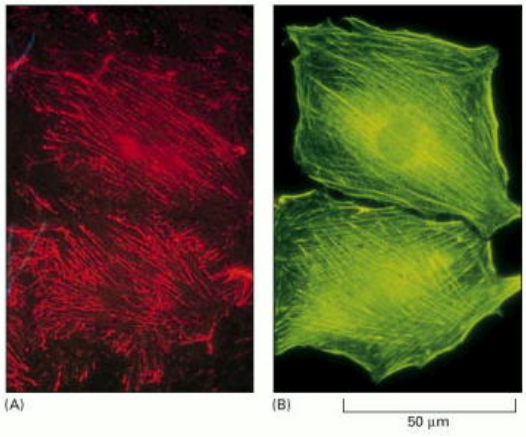

Figure 19-54. Coalignment of extracellular fibronectin fibrils and intracellular actin filament bundles. (A) The fibronectin is revealed in two rat fibroblasts in culture by the binding of rhodamine-coupled anti-fibronectin antibodies. (B) The actin is revealed by the binding of fluorescein-coupled anti-actin antibodies. (From R.O. Hynes and A.T. Destree, *Cell* 15:875886, 1978. © Elsevier.)

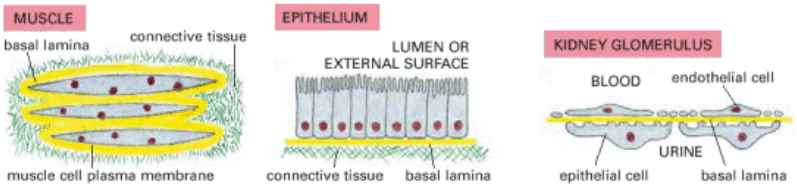

Figure 19-55. Three ways in which basal laminae are organized. Basal laminae *(yellow)* surround certain cells (such as skeletal muscle cells), underlie epithelia, and are interposed between two cell sheets (as in the kidney glomerulus). Note that, in the kidney glomerulus, both cell sheets have gaps in them, so that the basal lamina serves as the permeability barrier determining which molecules will pass into the urine from the blood.

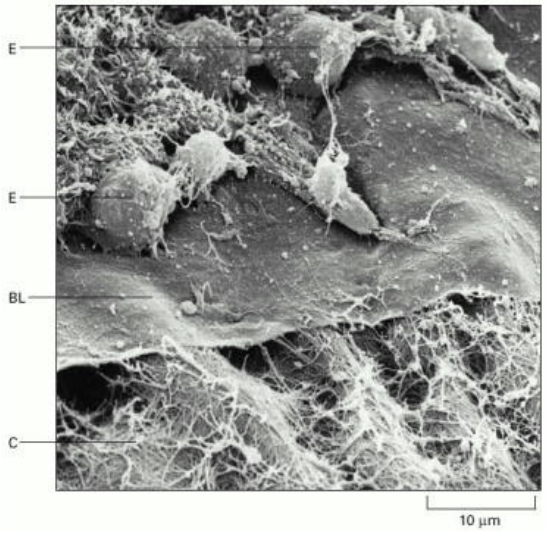

Figure 19-56. The basal lamina in the cornea of a chick embryo. In this scanning electron micrograph, some of the epithelial cells (E) have been removed to expose the upper surface of the matlike basal lamina (BL). A network of collagen fibrils (C) in the underlying connective tissue interacts with the lower face of the lamina. (Courtesy of Robert Trelstad.)

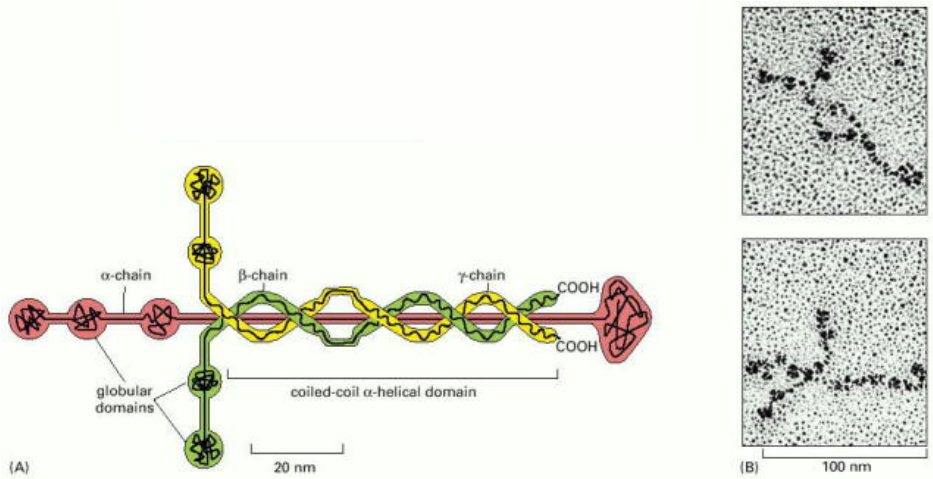

Figure 19-57. The structure of laminin. (A) The subunits of a laminin-1 molecule. This multidomain glycoprotein is composed of three polypeptides (α, β, and γ) that are disulfide-bonded into an asymmetric crosslike structure. Each of the polypeptide chains is more than 1500 amino acids long. Five types of α chains, three types of β chains, and three types of γ chains are known; in principle, they can assemble to form 45 (5 × 3 × 3) laminin isoforms. Several such isoforms have been found, each with a characteristic tissue distribution. (B) Electron micrographs of laminin molecules shadowed with platinum. (B, from J. Engel et al., *J. Mol. Biol.* 150:97120, 1981. © Academic Press.)

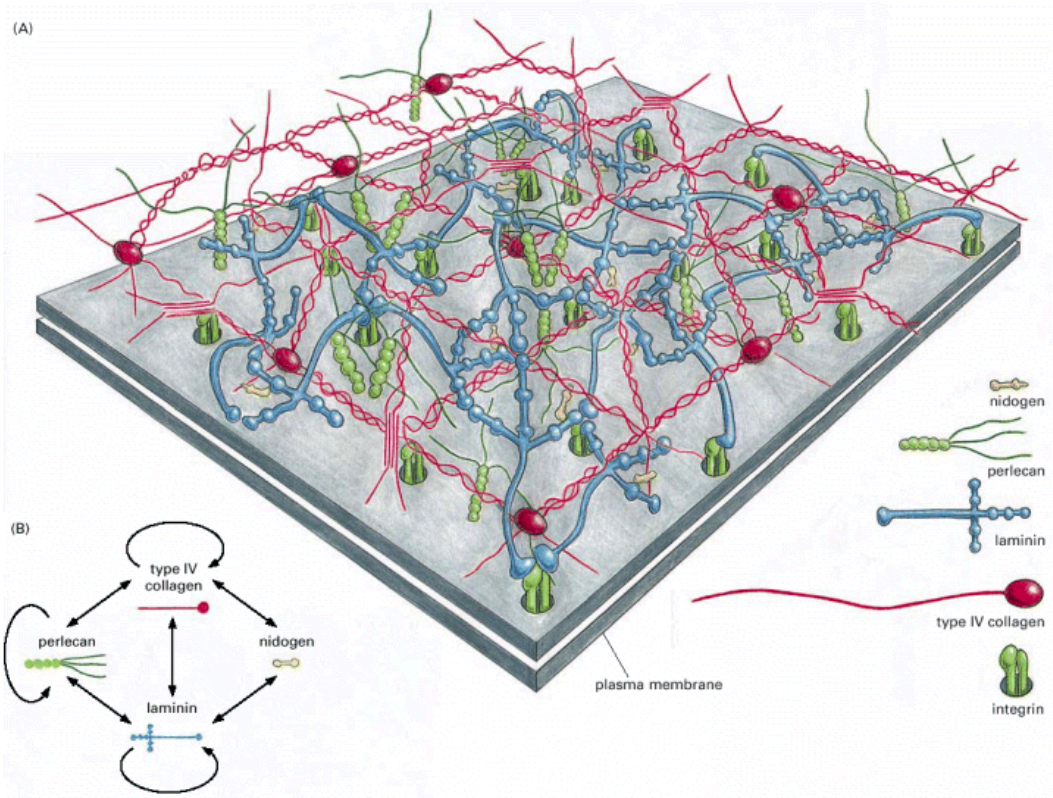

Figure 19-58. A model of the molecular structure of a basal lamina. (A) The basal lamina is formed by specific interactions (B) between the proteins type IV collagen, laminin, and nidogen, and the proteoglycan perlecan. Arrows in (B) connect molecules that can bind directly to each other. There are various isoforms of type IV collagen and laminin, each with a distinctive tissue distribution. Transmembrane laminin receptors (integrins and dystroglycan) in the plasma membrane are thought to organize the assembly of the basal lamina; only the integrins are shown. (Based on H. Colognato and P.D. Yurchenco, *Dev. Dynamics* 218:213234, 2000.)

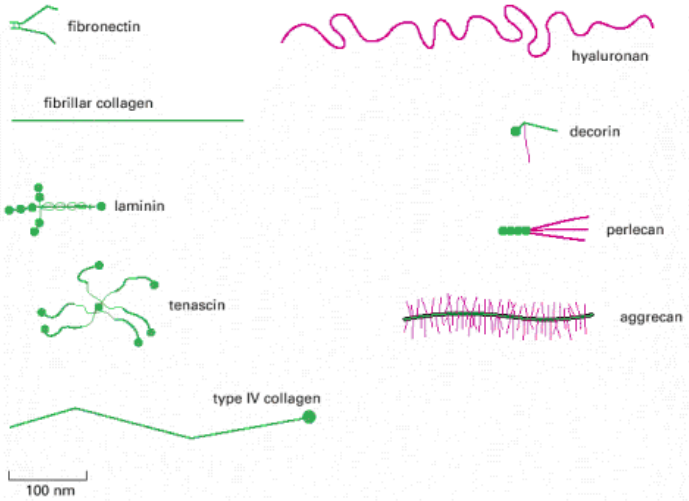

Figure 19-59. The comparative shapes and sizes of some of the major extracellular matrix macromolecules. Protein is shown in *green*, and glycosaminoglycan in *red*.

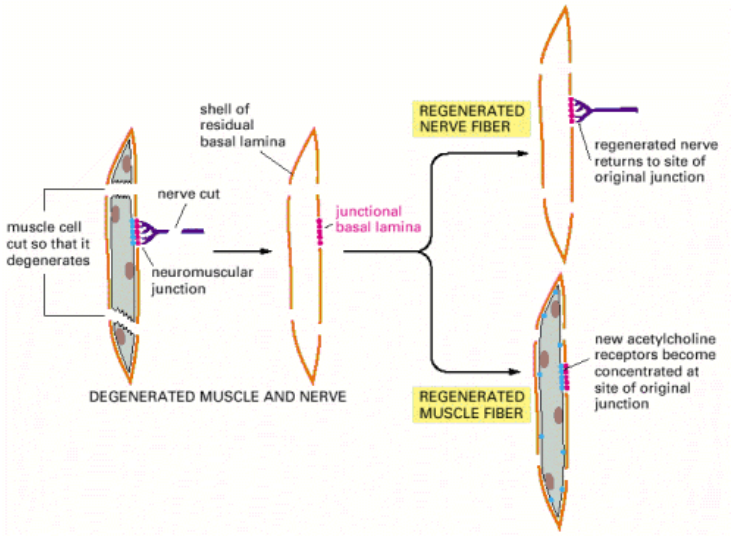

Figure 19-60. Regeneration experiments demonstrating the special character of the junctional basal lamina at a neuromuscular junction. When the nerve, but not the muscle, is allowed to regenerate after both the nerve and muscle have been damaged (*upper* part of figure), the junctional basal lamina directs the regenerating nerve to the original synaptic site. When the muscle, but not the nerve, is allowed to regenerate (*lower* part of figure), the junctional basal lamina causes newly made acetylcholine receptors *(blue)* to accumulate at the original synaptic site. The muscle regenerates from satellite cells (discussed in Chapter 22) located between the basal lamina and the original muscle cell (not shown). These experiments show that the junctional basal lamina controls the localization of synaptic components on both sides of the lamina.

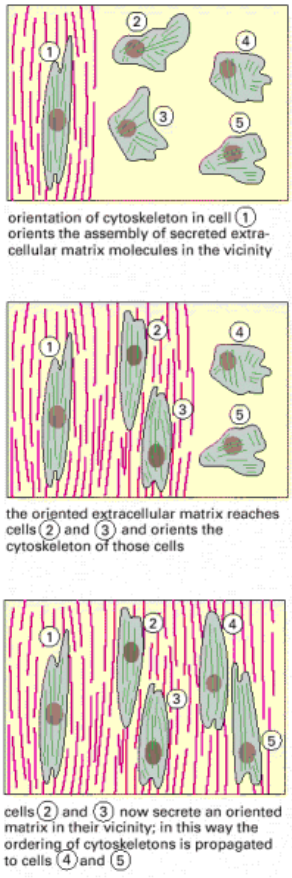

Figure 19-61. How the extracellular matrix could, in principle, propagate order from cell to cell within a tissue. For simplicity, the figure represents a hypothetical scheme in which one cell influences the orientation of its neighboring cells. It is more likely, however, that the cells would mutually affect one another's orientation.

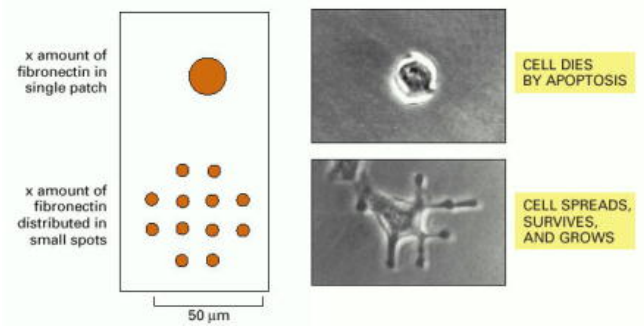

Figure 19-62. Anchorage dependence and the importance of cell spreading. For many cells, contact with the extracellular matrix is essential for survival, growth, and proliferation. In this experiment, the extent of cell spreading on a substratum, rather than the number of matrix molecules the cell contacts, influences cell survival (see also Figure 17-49). (Based on C.S. Chen et al., *Science* 276:14251428, 1997. © AAAS.)

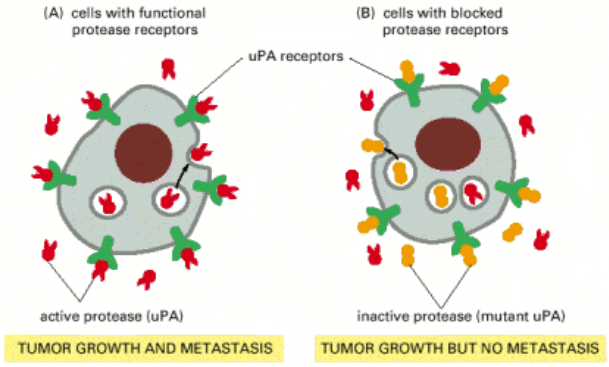

Figure 19-63. The importance of proteases bound to cell-surface receptors. (A) Human prostate cancer cells make and secrete the serine protease uPA, which binds to cell-surface uPA receptor proteins. (B) The same cells have been transfected with DNA that encodes an excess of an inactive form of uPA, which binds to the uPA receptors but has no protease activity. By occupying most of the uPA receptors, the inactive uPA prevents the active protease from binding to the cell surface. Both types of cells secrete active uPA, grow rapidly, and produce tumors when injected into experimental animals. But the cells in (A) metastasize widely, whereas the cells in (B) do not. To metastasize via the blood, tumor cells have to crawl through basal laminae and other extracellular matrices on the way into and out of the bloodstream. This experiment suggests that proteases must be cell-surface bound to mediate migration through the matrix.

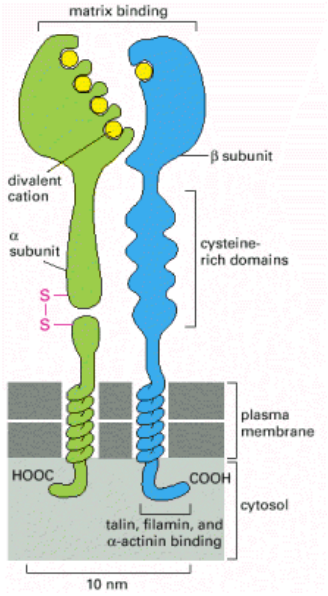

Figure 19-64. The subunit structure of an integrin cell-surface matrix receptor. Electron micrographs of isolated receptors suggest that the molecule has approximately the shape shown here, with the globular head projecting more than 20 nm from the lipid bilayer. By binding to a matrix protein outside the cell and to the actin cytoskeleton (via the anchor proteins indicated) inside the cell (see Figure 19-12B), the protein serves as a transmembrane linker. The α and β subunits are held together by noncovalent bonds. In the fibronectin receptor shown, the α subunit is made initially as a single 140,000-dalton polypeptide chain, which is then cleaved into one small transmembrane domain and one large extracellular domain that contains four divalent-cation-binding sites; the two domains remain held together by a disulfide bond. The extracellular part of the β subunit contains a single divalent-cation-binding site, as well as a repeating cysteine-rich region, where intrachain disulfide bonding occurs.

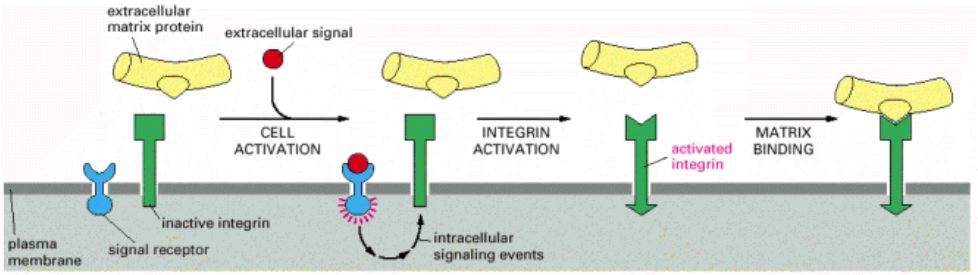

Figure 19-65. The regulation of the extracellular binding activity of a cell's integrins from within. In this example, an extracellular signal activates an intracellular signaling cascade that alters the integrin so that its extracellular binding site can now mediate cell adhesion. The molecular nature of the alteration is still poorly understood.

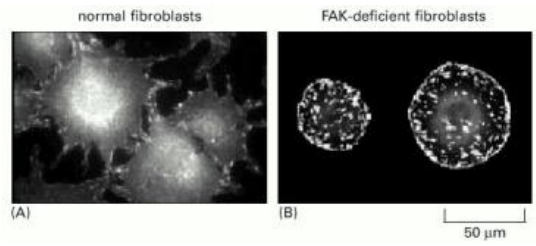

Figure 19-66. Excessive numbers of focal adhesions in FAK-deficient fibroblasts. Normal and FAK-deficient fibroblasts were stained with antibodies against vinculin to reveal the location of focal adhesions (see Figure 19-12). (A) The normal fibroblasts have fewer focal adhesions and have spread after 2 hours in culture. (B) At the same time point, the FAK-deficient fibroblasts have more focal adhesions and have not spread. (From D. Ilic et al., *Nature* 377:539544, 1995. © Macmillan Magazines Ltd.)

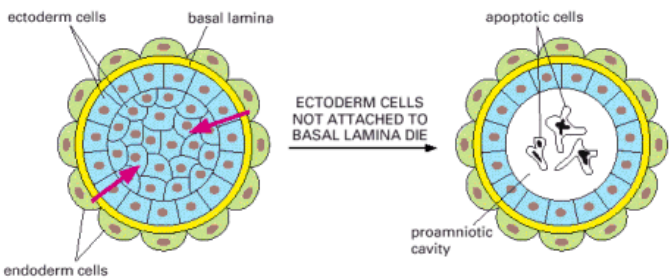

Figure 19-67. Matrix-dependent cell survival in the formation of the proamniotic cavity. Endoderm cells are thought to produce a signal (indicated by the *red arrows)* that causes ectoderm cells to die by apoptosis. The ectoderm cells in contact with the basal lamina, however, are saved by the survival-promoting action of the matrix molecules in the lamina, while the other ectoderm cells die by apoptosis, forming the proamniotic cavity. (Based on E. Coucouvanis and G.R. Martin, *Cell* 83:279287, 1995.)

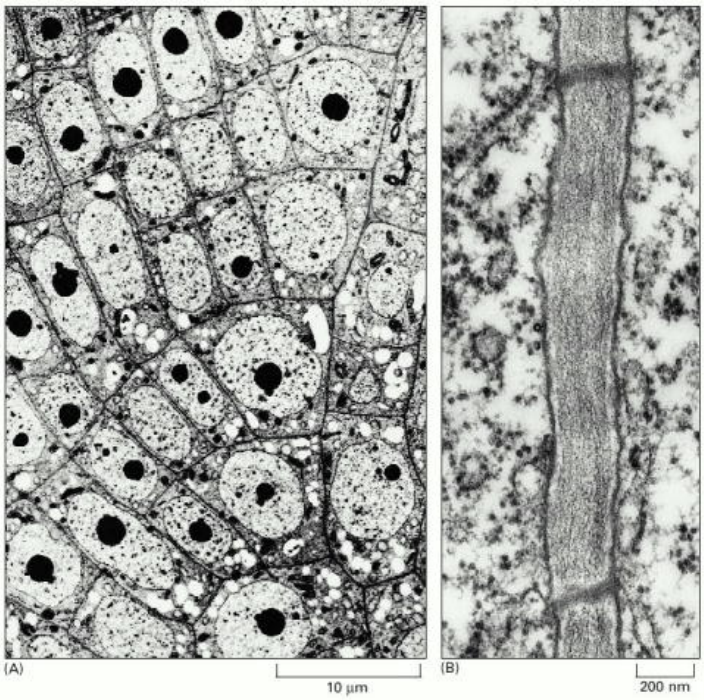

Figure 19-68. Plant cell walls. (A) Electron micrograph of the root tip of a rush, showing the organized pattern of cells that results from an ordered sequence of cell divisions in cells with relatively rigid cell walls. In this growing tissue, the cell walls are still relatively thin, appearing as fine black lines between the cells in the micrograph. (B) Section of a typical cell wall separating two adjacent plant cells. The two dark transverse bands correspond to plasmodesmata that span the wall (see Figure 19-20). (A, courtesy of C. Busby and B. Gunning, *Eur. J. Cell Biol.* 21:214233,1980; B, courtesy of Jeremy Burgess.)

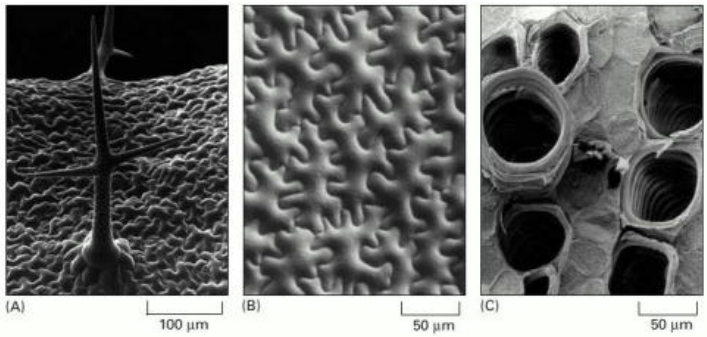

Figure 19-69. Specialized cell types with appropriately modified cell walls. (A) A trichome, or hair, on the upper surface of an *Arabidopsis* leaf. This spiky, protective single cell is shaped by the local deposition of a tough, cellulose-rich wall. (B) Surface view of tomato leaf epidermal cells. The cells fit together snugly like the pieces of a jigsaw puzzle, providing a strong outer covering for the leaf. The outer cell wall is reinforced with a cuticle and waxes that waterproof the leaf and help defend it against pathogens. (C) This view into young xylem elements shows the thick, lignified, hoop-reinforced secondary cell wall that creates robust tubes for the transport of water throughout the plant. (A, courtesy of Paul Linstead; B and C, courtesy of Kim Findlay.)

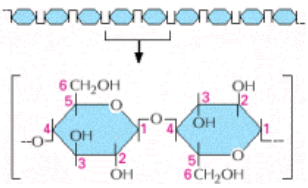

Figure 19-70. Cellulose. Cellulose molecules are long, unbranched chains of β1,4-linked glucose units. Each glucose is inverted with respect to its neighbors, and the resulting disacchride repeat occurs hundreds of times in a single cellulose molecule.

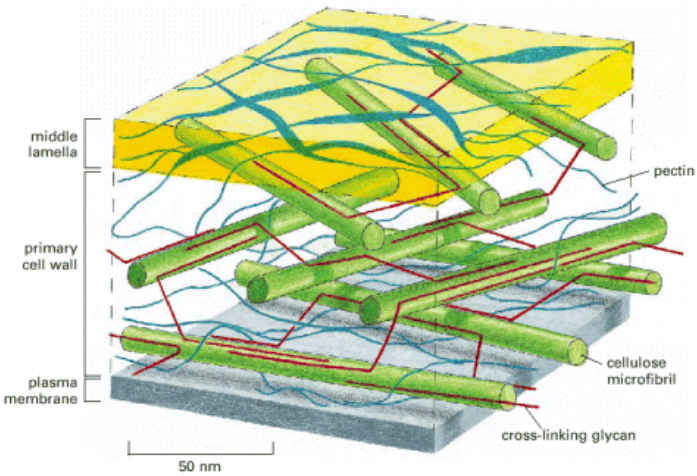

Figure 19-71. Scale model of a portion of a primary cell wall showing the two major polysaccharide networks. The orthogonally arranged layers of cellulose microfibrils *(green)* are tied into a network by cross-linking glycans *(red)* that form hydrogen bonds with the microfibrils. This network is coextensive with a network of pectin polysaccharides *(blue).* The network of cellulose and cross-linking glycans provides tensile strength, while the pectin network resists compression. Cellulose, cross-linking glycans, and pectin are typically present in roughly equal amounts in a primary cell wall. The middle lamella is rich in pectin and cements adjacent cells together.

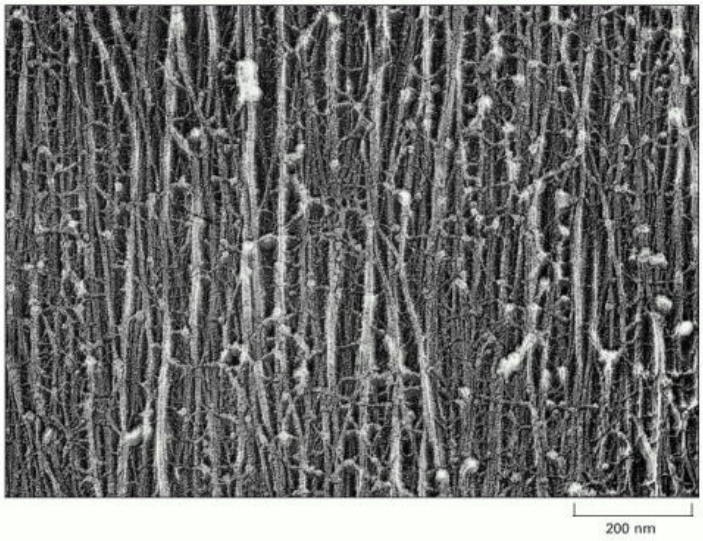

Figure 19-72. The orientation of cellulose microfibrils in the primary cell wall of an elongating carrot cell. This electron micrograph of a shadowed replica from a rapidly frozen and deep-etched cell wall shows the largely parallel arrangements of cellulose microfibrils, oriented perpendicular to the axis of cell elongation. The microfibrils are cross-linked by, and interwoven with, a complex web of matrix molecules (compare with Figure 19-71). (Courtesy of Brian Wells and Keith Roberts.)

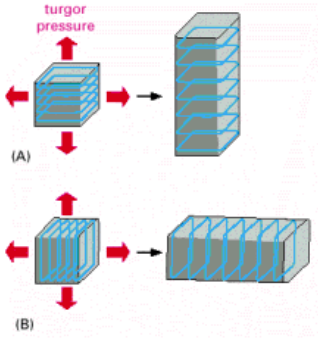

Figure 19-73. How the orientation of cellulose microfibrils within the cell wall influences the direction in which the cell elongates. The cells in (A) and (B) start off with identical shapes (shown here as cubes) but with different orientations of cellulose microfibrils in their walls. Although turgor pressure is uniform in all directions, cell-wall weakening causes each cell to elongate in a direction perpendicular to the orientation of the microfibrils, which have great tensile strength. The final shape of an organ, such as a shoot, is determined by the direction in which its cells expand.

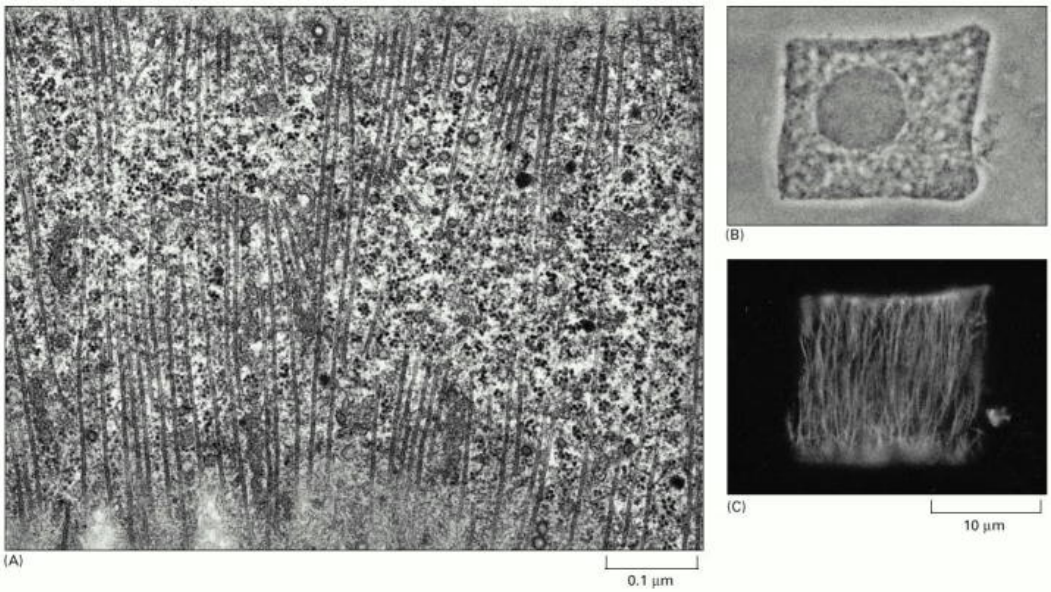

Figure 19-74. The cortical array of microtubules in a plant cell. (A) A grazing section of a root-tip cell from Timothy grass, showing a cortical array of microtubules lying just below the plasma membrane. These microtubules are oriented perpendicularly to the long axis of the cell. (B) An isolated onion root-tip cell. (C) The same cell shown in (B) stained by immunofluorescence to show the transverse cortical array of microtubules. (A, courtesy of Brian Gunning; B and C, courtesy of Kim Findlay.)

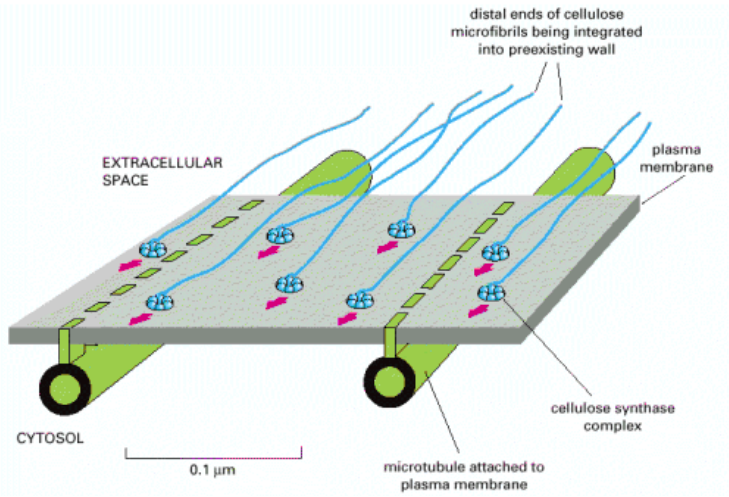

Figure 19-75. One model of how the orientation of newly deposited cellulose microfibrils might be determined by the orientation of cortical microtubules. The large cellulose synthase complexes are integral membrane proteins that continuously synthesize cellulose microfibrils on the outer face of the plasma membrane. The distal ends of the stiff microfibrils become integrated into the texture of the wall, and their elongation at the proximal end pushes the synthase complex along in the plane of the membrane. Because the cortical array of microtubules is attached to the plasma membrane in a way that confines this complex to defined membrane channels, the orientation of these microtubules - when they are present - determines the axis along which the new microfibrils are laid down.

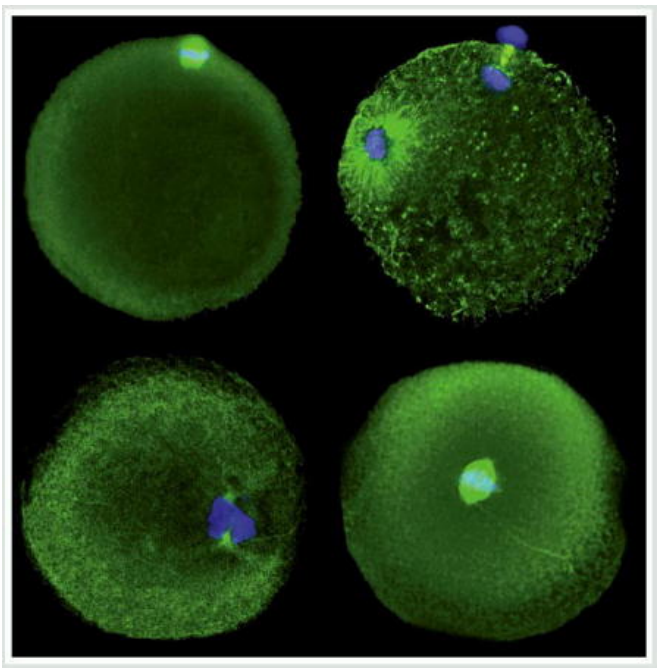

Human fertilization in vitro. Four sequential stages offertilization are shown, beginning with a mature, but unfertilized human egg *(top left).* Next comes the post-fertilization incorporation of a sperm pronucleus, which in this example is moving inward from the left *(top right).*This stage is followed by the fusion of the egg and sperm pronuclei *(bottom left),* which in turn leads to the alignment of the mixed chromosomes from both parents on the first mitotic spindle *(bottom right).* (From C. Simerly et al., *Nat. Med.* 1:4753. © Macmillan Magazines Ltd.)

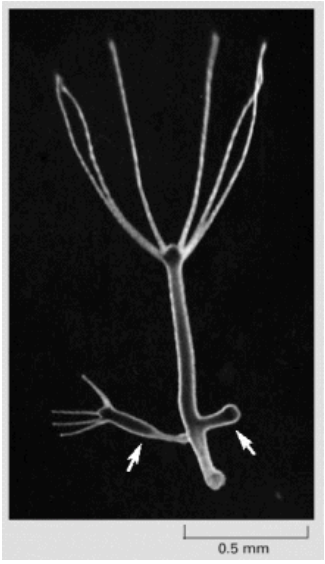

Figure 20-1. Photograph of a *Hydra* from which two new organisms are budding *(arrows).* The offspring, which are genetically identical to their parent, will eventually detach and live independently. (Courtesy of Amata Hornbruch.)

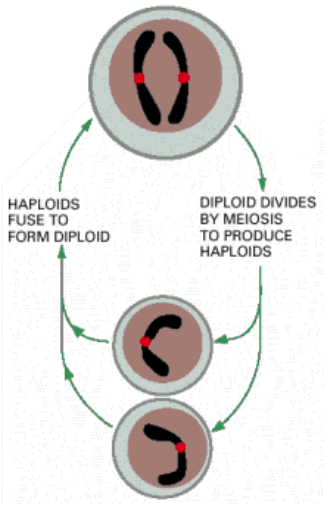

Figure 20-2. The sexual reproductive cycle. It involves an alternation of haploid and diploid generations of cells.

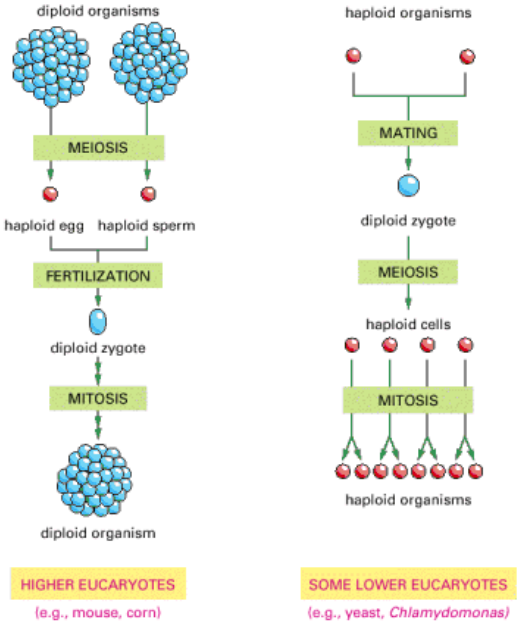

Figure 20-3. Haploid and diploid cells in the life cycle of higher and some lower eucaryotes. The haploid cells are shown in *red* and the diploid cells in *blue.* Cells in higher eucaryotic organisms usually proliferate in the diploid phase to form a multicellular organism; only the gametes are haploid, and they fuse at fertilization to form a diploid zygote, which develops into a new individual. In some lower eucaryotes, by contrast, the haploid cells proliferate, and the only diploid cell is the zygote, which exists transiently after mating.

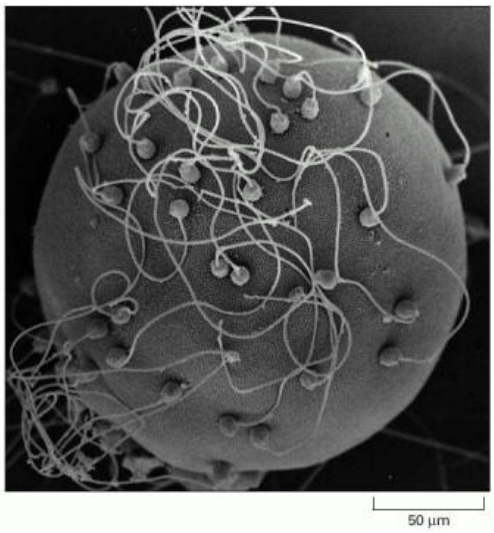

Figure 20-4. Scanning electron micrograph of a clam egg with sperm bound to its surface. Although many sperm are bound to the egg, only one will fertilize it, as we discuss later. (Courtesy of David Epel.)

Figure 20-5. A peacock displaying his elaborate tail. This extravagant plumage serves solely to attract females for the purpose

of sexual reproduction. (© Cyril Laubscher.)

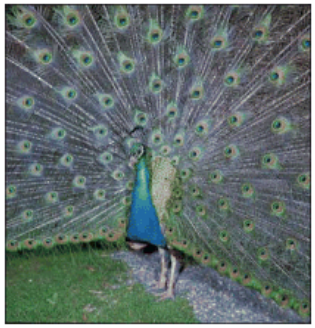

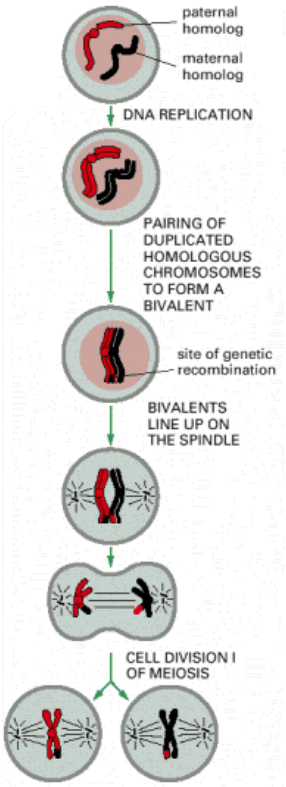

Figure 20-6. Events through the first cell division of meiosis. For clarity, only one pair of homologous chromosomes is shown. Each chromosome has been duplicated and exists as attached sister chromatids before pairing with its homologous chromosome (homolog), thereby forming a structure containing four chromatids known as a bivalent. As shown by the formation of chromosomes that are part *red* and part *black*, chromosome pairing in meiosis leads to genetic recombination between homologous chromosomes, as explained later.

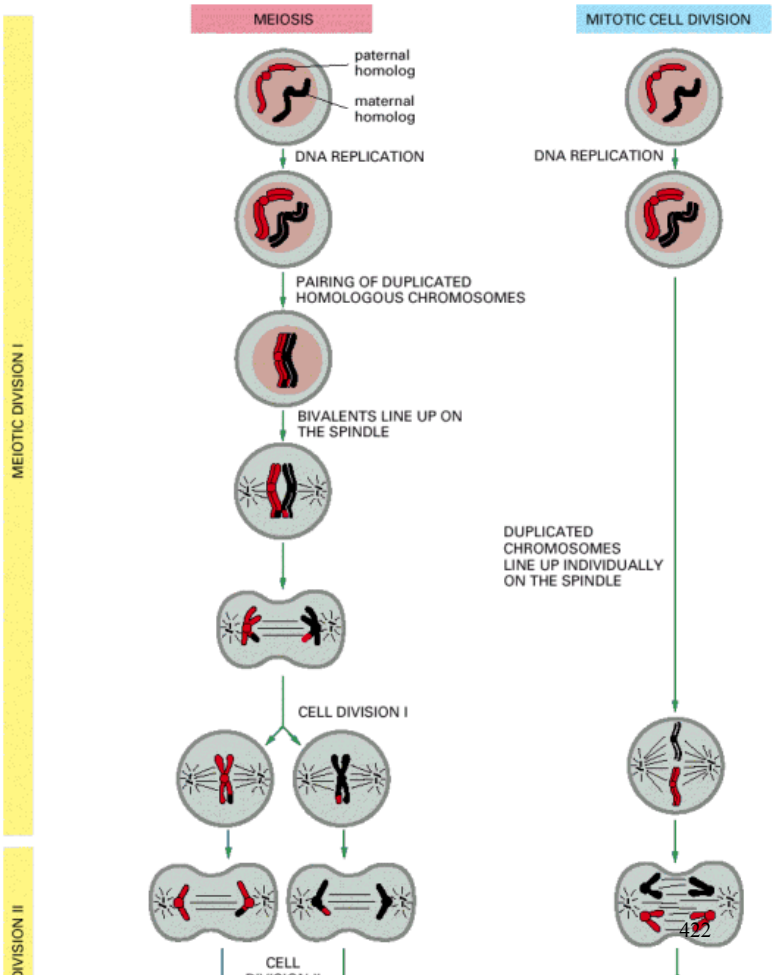

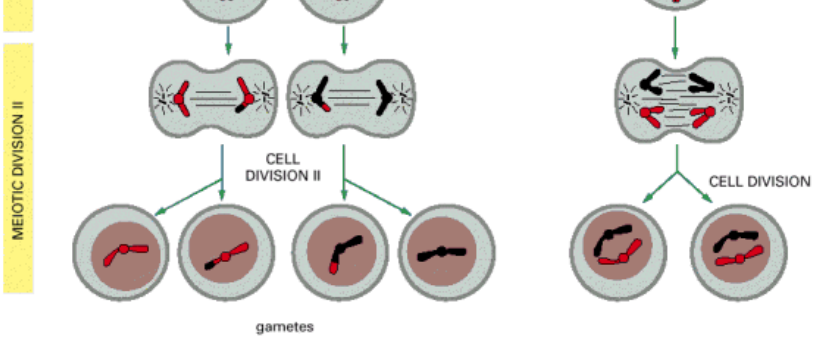

Figure 20-7. Comparison of meiosis and mitotic cell division. As in the previous figure, only one pair of homologous chromosomes is shown. In meiosis, after DNA replication, two nuclear (and cell) divisions are required to produce the haploid gametes. Each diploid cell that enters meiosis therefore produces four genetically different haploid cells, whereas each diploid cell that divides by mitosis produces two genetically identical diploid cells.

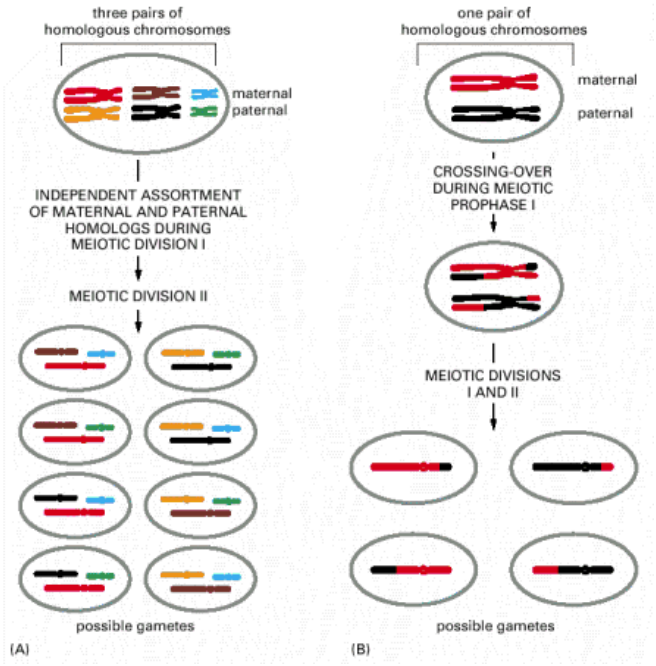

Figure 20-8. Two major contributions to the reassortment of genetic material that occurs in the production of gametes during meiosis. (A) The independent assortment of the maternal and paternal homologs during the first meiotic division produces 2^n different haploid gametes for an organism with n chromosomes. Here $n = 3$, and there are eight different possible gametes. (B) Crossing-over during meiotic prophase I exchanges segments of homologous chromosomes and thereby reassorts genes on individual chromosomes. Because of the many small differences in DNA sequence that always exist between any two homologs, both mechanisms increase the genetic variability of organisms that reproduce sexually.

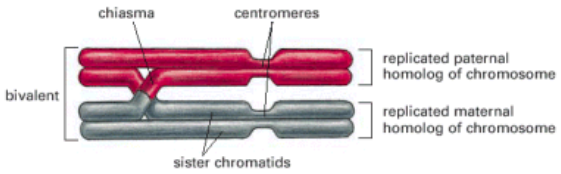

Figure 20-9. Paired homologous chromosomes during the transition to metaphase of meiotic division I. A single crossover event has occurred earlier in prophase to create one chiasma. Note that the four chromatids are arranged as two distinct pairs of sister chromatids. As in mitosis, the sister chromatids in each pair are tightly connected along their entire lengths, as well as at their centromeres, by proteins called cohesins. The entire unit of four chromatids is referred to as a bivalent. The combination of the chiasma and the tight attachment of the sister chromatids holds the two duplicated homologs together.

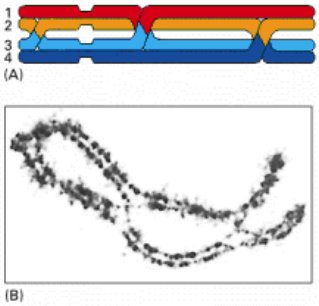

Figure 20-10. Bivalents with three chiasmata resulting from separate crossover events. (A) In this drawing, chromatid 1 has undergone an exchange with chromatid 3, and chromatid 2 has undergone exchanges with chromatid 3 and 4. Note that the sister chromatids of the same chromosome do not exchange with each other. (B) Light micrograph of a grasshopper bivalent with three chiasmata. (B, courtesy of Bernard John.)

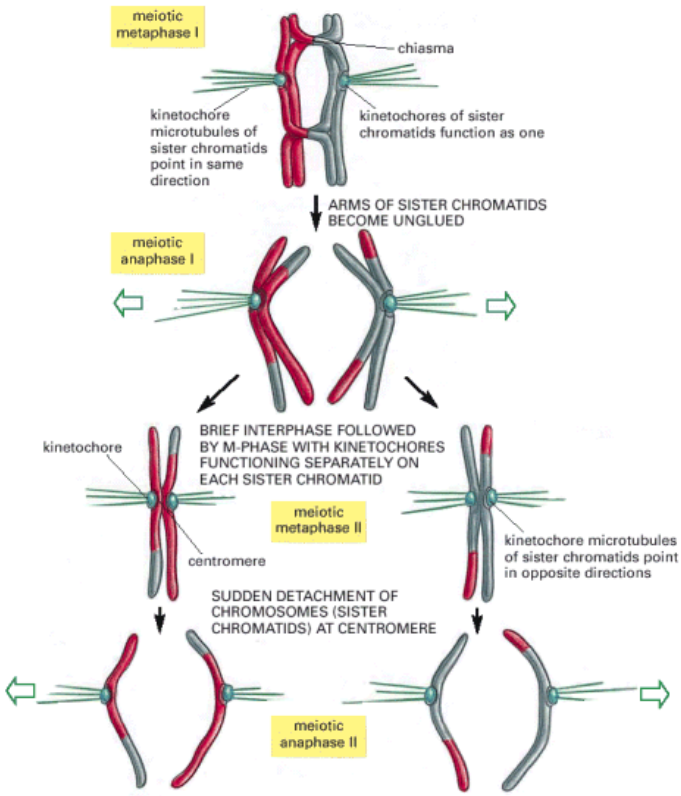

Figure 20-11. Comparison of the mechanisms of chromosome alignment (at metaphase) and separation (at anaphase) in meiotic division I and meiotic division II. The ungluing of the sister chromatid arms allows the duplicated homologs to separate at anaphase I, while an ungluing of the chromosomes at their centromeres allows the sister chromatids to separate at anaphase II. In contrast, at anaphase in mitosis, both the arms and the centromeres come apart at the same time (discussed in Chapter 18).

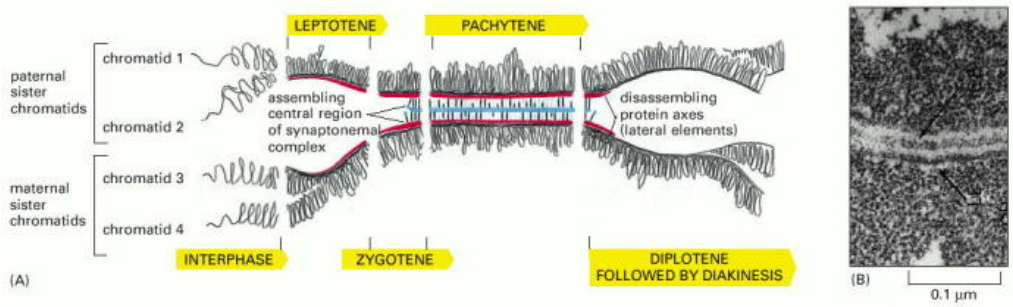

Figure 20-12. Chromosome synapsis and desynapsis during the different stages of meiotic prophase I. (A) A single bivalent is shown. The pachytene stage is defined as the period during which a fully formed synaptonemal complex exists. At leptotene, the two sister chromatids condense, and their chromatin loops each extend from a common protein axis *(red).* As meiosis progresses, the two homologs become tightly connected by proteins that form the central region of the synaptonemal complex, composed of a central element *(blue),* transverse filaments *(thin black lines),* and the lateral elements *(red)* that anchor the chromatin loops. In the gametes of many female animals, but not those of mammals, the subsequent diplotene stage is an enormously prolonged period of cell growth, during which the chromosomes are decondensed and very active in transcription. Diplotene ends with diakinesis - the stage of transition to metaphase - in which the chromosomes recondense and transcription halts. In male gametes, diplotene and diakinesis are briefer and less distinct. (B) An electron micrograph of a synaptonemal complex from a meiotic cell at pachytene in a lily flower. (B, courtesy of Brian Wells.)

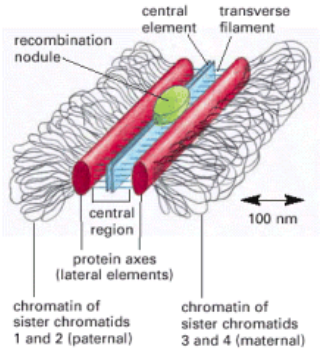

Figure 20-13. A mature synaptonemal complex. Only a short section of the long ladderlike complex is shown. A similar synaptonemal complex is present in organisms as diverse as yeasts and humans.

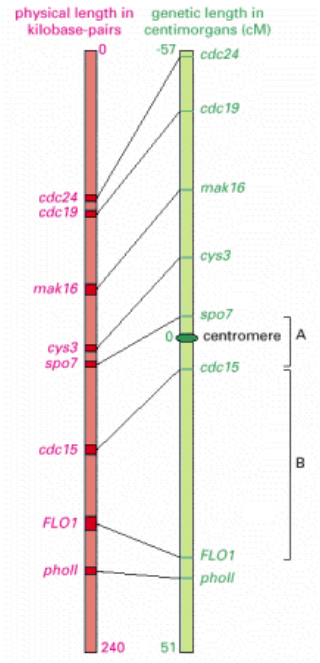

Figure 20-14. Comparison of the physical and genetic maps of part of chromosome I in budding yeast. The DNA markers shown are various genes. A indicates a region where the genetic map is contracted owing to decreased frequency of crossing-over. B indicates a region where the genetic map is expanded owing to increased frequency of crossing-over.

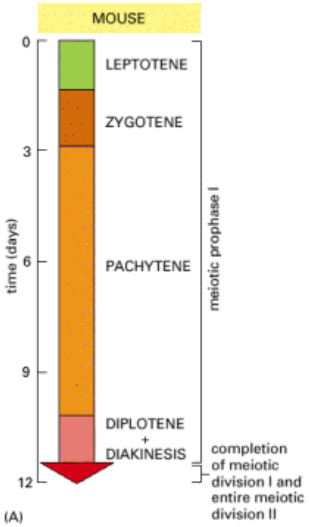

Figure 20-15. Comparison of times required for each of the stages of meiosis. (A) Approximate times for a male mammal (mouse). (B) Approximate times for the male tissue of a plant (lily). Times differ for male and female gametes (sperm and eggs, respectively) of the same species, as well as for the same gametes of different species. Meiosis in a human male, for example, lasts for 24 days, compared with 12 days in the mouse. In all species, however, meiotic prophase I is always much longer than all the other meiotic stages combined.

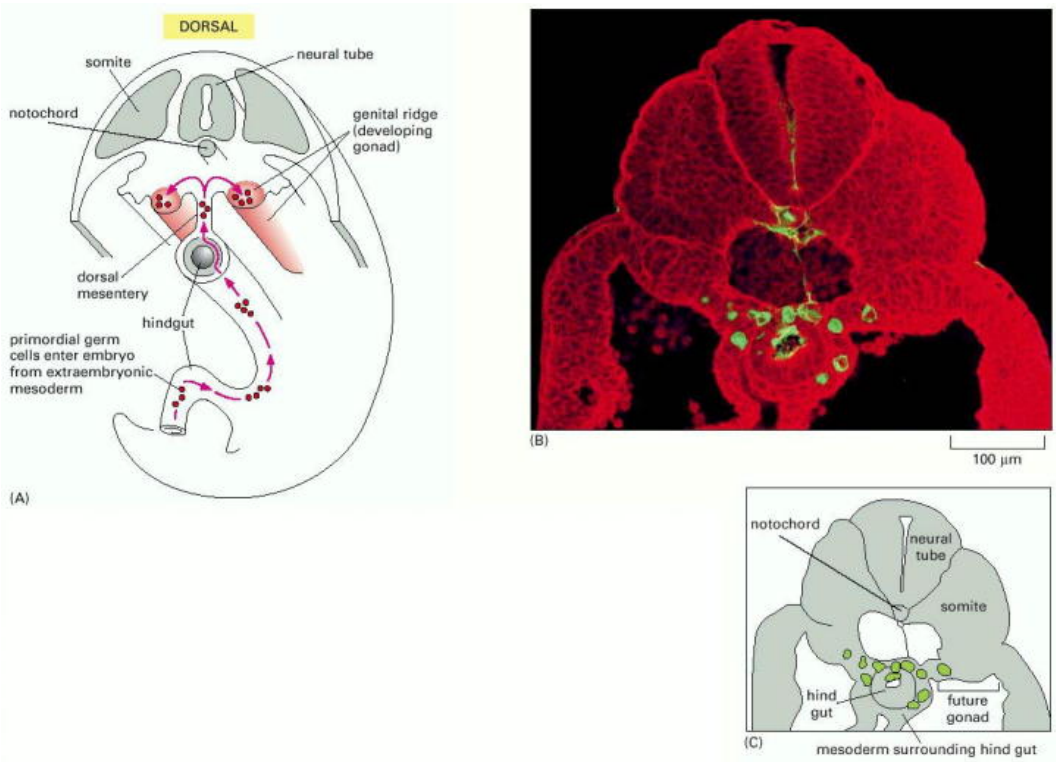

Figure 20-16. Migration of mammalian primordial germ cells. (A) Drawing showing the final stages of migration through the hindgut into the two genital ridges, each of which will develop into a gonad - either an ovary or a testis. (B) Micrograph showing migrating primordial germ cells in an early mouse embryo. The primordial germ cells are stained with a monoclonal antibody (in *green)* that specifically labels these cells at this stage of embryogenesis. The remaining cells in the embryo are stained with a lectin that binds to sialic acid, which is found on the surface of all cells. (C) Drawing corresponding to the micrograph shown in (B). (B, courtesy of Robert Anderson and Chris Wylie.)

Figure 20-17. *Sry*-induced reprogramming of a female mouse embryo to develop into a male. The *Sry* gene, injected into the nucleus of an XX female zygote, caused the transgenic embryo produced to develop into a male. The external genitalia of the transgenic mouse are indistinguishable from those of a normal XY male mouse. (From P. Koopman et al., *Nature* 351:117121, 1991. © Macmillan Magazines Ltd.)

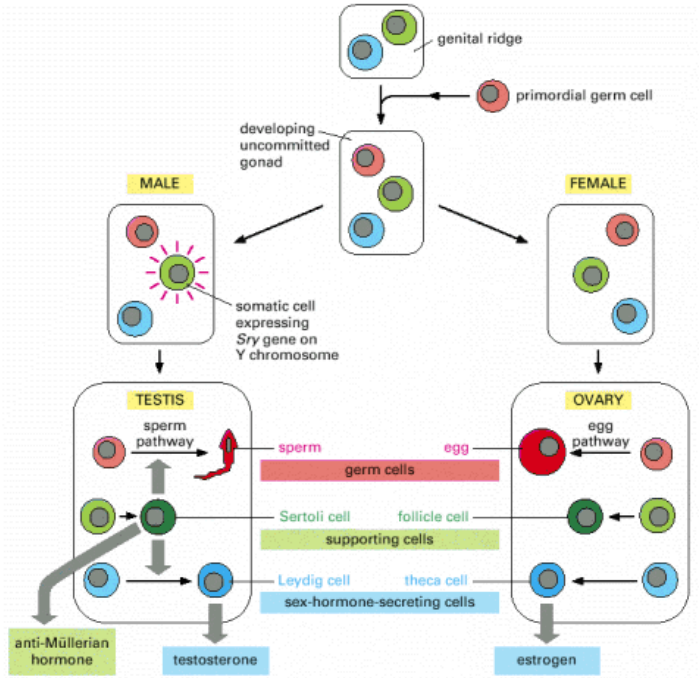

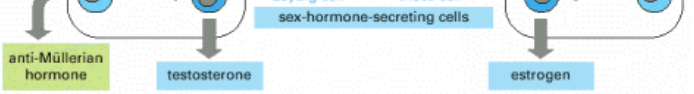

Figure 20-18. Influence of *Sry* on gonad development. The germ line cells are shaded in *red*, and the somatic cells are shaded in *green* and *blue*. The change from light to darker color indicates that the cell has matured or differentiated. The *Sry* gene acts in a subpopulation of somatic cells in the developing gonad to direct them to differentiate into Sertoli cells instead of into follicle cells. The Sertoli cells then induce primordial germ cells to commit to sperm development. They also secrete anti-Müllerian hormone, which causes the Müllerian duct to regress, and they help to induce other somatic cells to differentiate into Leydig cells, which secrete testosterone (see Figure 20-28). In the absence of *Sry*, the primordial germ cells commit to egg development, and the somatic cells develop into either follicle cells, which support egg development, or theca cells, which secrete estrogen. Whereas Leydig cells begin secreting testosterone in the fetus, theca cells do not begin secreting estrogen until puberty.

Figure 20-19. The actual sizes of three eggs. The human egg is 0.1 mm in diameter.

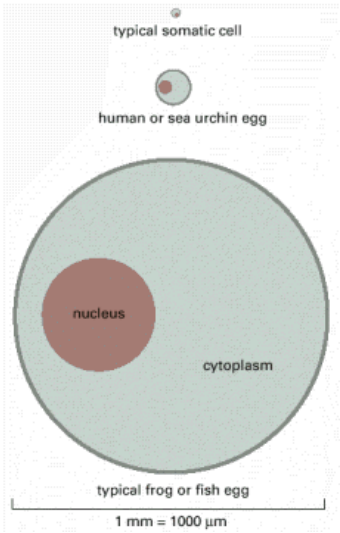

Figure 20-20. The relative sizes of various eggs. Sizes are compared with that of a typical somatic cell.

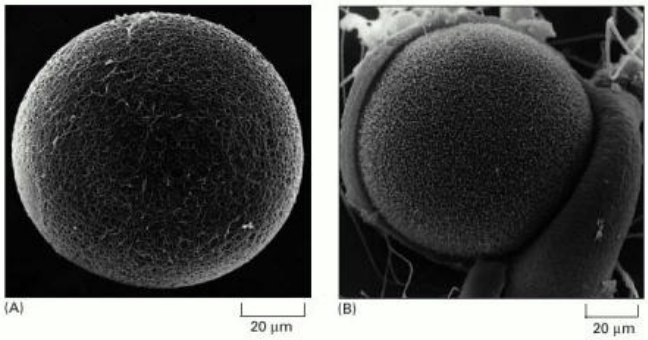

Figure 20-21. The zona pellucida. (A) Scanning electron micrograph of a hamster egg, showing the zona pellucida. (B) A scanning electron micrograph of a similar egg in which the zona (to which many sperm are attached) has been peeled back to reveal the underlying plasma membrane, which contains numerous microvilli. The zona is made entirely by the developing oocyte. (From D.M. Phillips, *J. Ultrastruct. Res.* 72:112, 1980.)

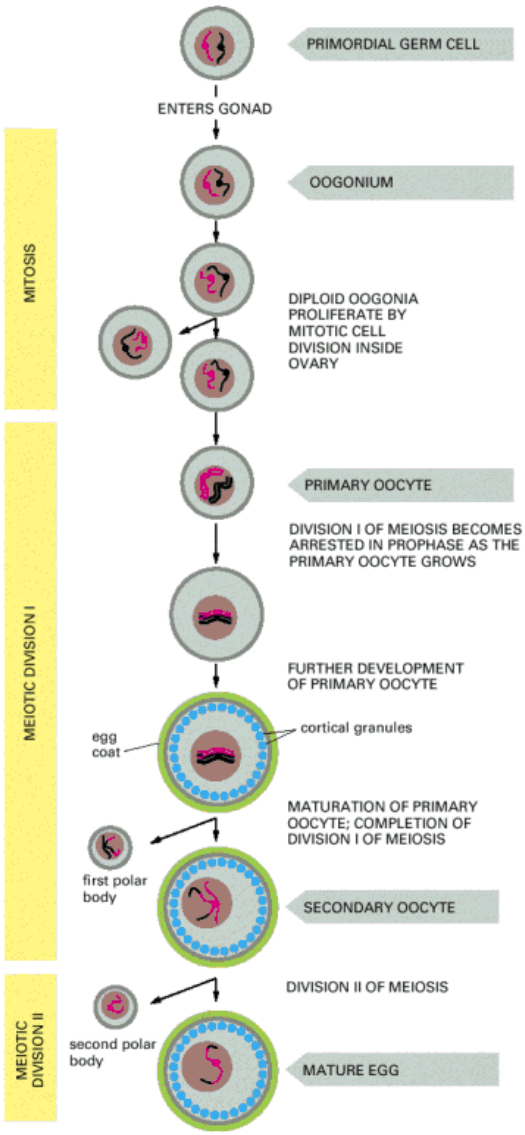

Figure 20-22. The stages of oogenesis. Oogonia develop from primordial germ cells that migrate into the developing gonad early in embryogenesis. After a number of mitotic divisions, oogonia begin meiotic division I, after which they are called primary oocytes. In mammals, primary oocytes are formed very early (between 3 and 8 months of gestation in the human embryo) and remain arrested in prophase of meiotic division I until the female becomes sexually mature. At this point, a small number periodically mature under the influence of hormones, completing meiotic division I to become secondary oocytes, which eventually undergo meiotic division II to become mature eggs (ova). The stage at which the egg or oocyte is released from the ovary and is fertilized varies from species to species. In most vertebrates, oocyte maturation is arrested at metaphase of meiosis II and the secondary oocyte completes meiosis II only after fertilization. All of the polar bodies eventually degenerate. In most animals, the developing oocyte is surrounded by specialized accessory cells that help to isolate and nourish it (not shown).

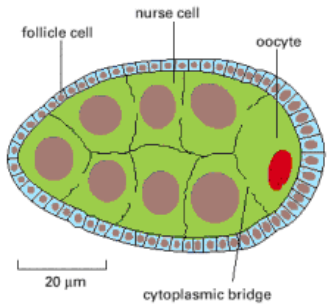

Figure 20-23. Nurse cells and follicle cells associated with a *Drosophila* oocyte. The nurse cells and the oocyte arise from a common oogonium, which gives rise to one oocyte and 15 nurse cells (only 7 of which are seen in this plane of section). These cells remain joined by cytoplasmic bridges, which result from incomplete cell division. Eventually the nurse cells dump their cytoplasmic contents into the developing oocyte and then kill themselves. The follicle cells develop independently (from mesodermal cells).

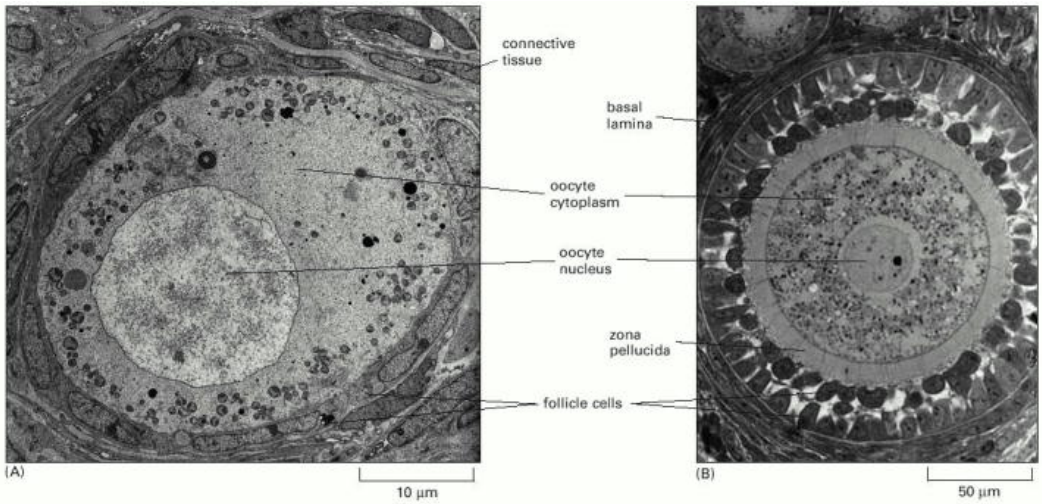

Figure 20-24. Electron micrographs of developing primary oocytes in the rabbit ovary. (A) An early stage of primary oocyte development. Neither a zona pellucida nor cortical granules have developed, and the oocyte is surrounded by a single layer of flattened follicle cells. (B) A more mature primary oocyte, which is shown at a sixfold lower magnification because it is much larger than the oocyte in (A). This oocyte has acquired a thick zona pellucida and is surrounded by several layers of follicle cells and a basal lamina, which isolate the oocyte from the other cells in the ovary. The primary oocyte together with its surrounding follicle cells is called a primary follicle. The follicle cells are connected to one another and to the oocyte by gap junctions. (From The Cellular Basis of Mammalian Reproduction [J. Van Blerkom and P. Motta eds.]. Baltimore - Munich: Urban & Schwarzenberg, 1979.)

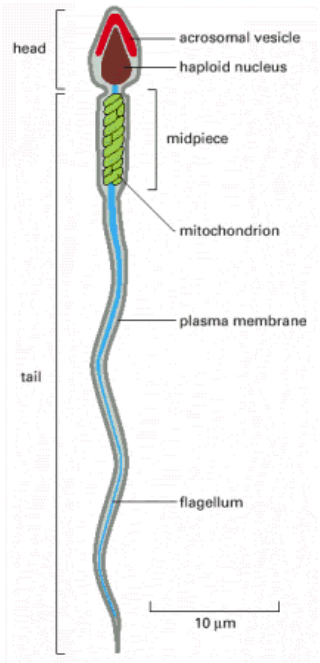

Figure 20-25. A human sperm. It is shown in longitudinal section.

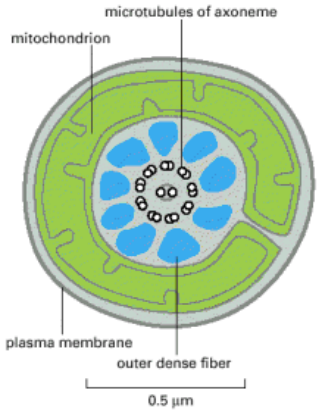

Figure 20-26. Drawing of the midpiece of a mammalian sperm as seen in cross section in an electron microscope. The core of the flagellum is composed of an axoneme surrounded by nine dense fibers. The axoneme consists of two singlet microtubules surrounded by nine microtubule doublets. The mitochondrion (shown in *green)* is well placed for providing the ATP required for flagellar movement; its unusual spiral structure (see Figure 20-25) results from the fusion of individual mitochondria during spermatid differentiation.

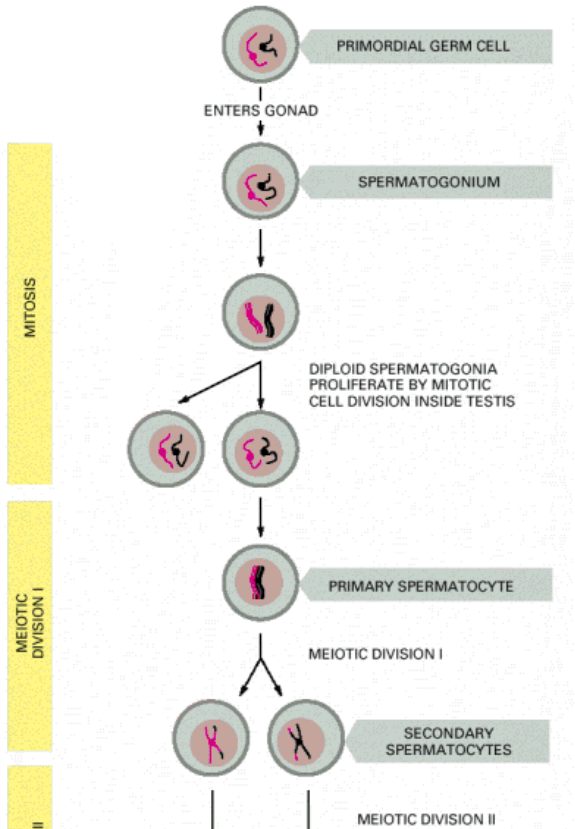

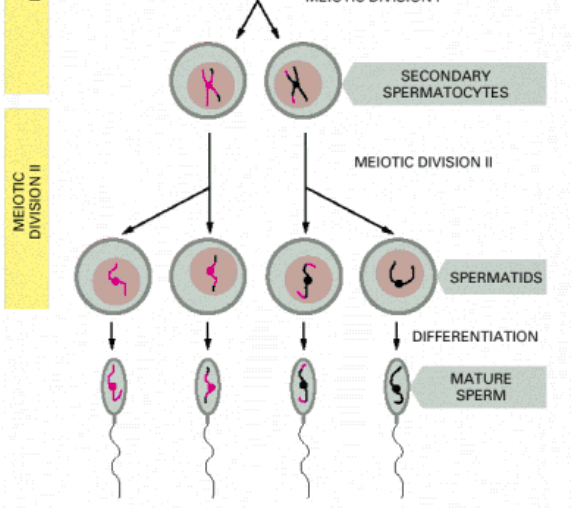

Figure 20-27. The stages of spermatogenesis. Spermatogonia develop from primordial germ cells that migrate into the testis early in embryogenesis. When the animal becomes sexually mature, the spermatogonia begin to proliferate rapidly, generating some progeny that retain the capacity to continue dividing indefinitely (as stem-cell spermatogonia) and other progeny (maturing spermatogonia) that will, after a limited number of further mitotic division cycles, embark on meiosis to become primary spermatocytes. The primary spermatocytes continue through meiotic division I to become secondary spermatocytes. After they complete meiotic division II, the secondary spermatocytes produce haploid spermatids, which differentiate into mature sperm (spermatozoa). Spermatogenesis differs from oogenesis (see Figure 20-22) in several ways. (1) New cells enter meiosis continually from the time of puberty. (2) Each cell that begins meiosis gives rise to four mature gametes rather than one. (3) Mature sperm form by an elaborate process of cell differentiation that begins after meiosis is complete. (4) About twice as many cell divisions occur in the production of a sperm as in the production of an egg; in a mouse, for example, it is estimated that on average about 56 divisions occur from zygote to mature sperm, and about 27 divisions occur from zygote to mature egg.

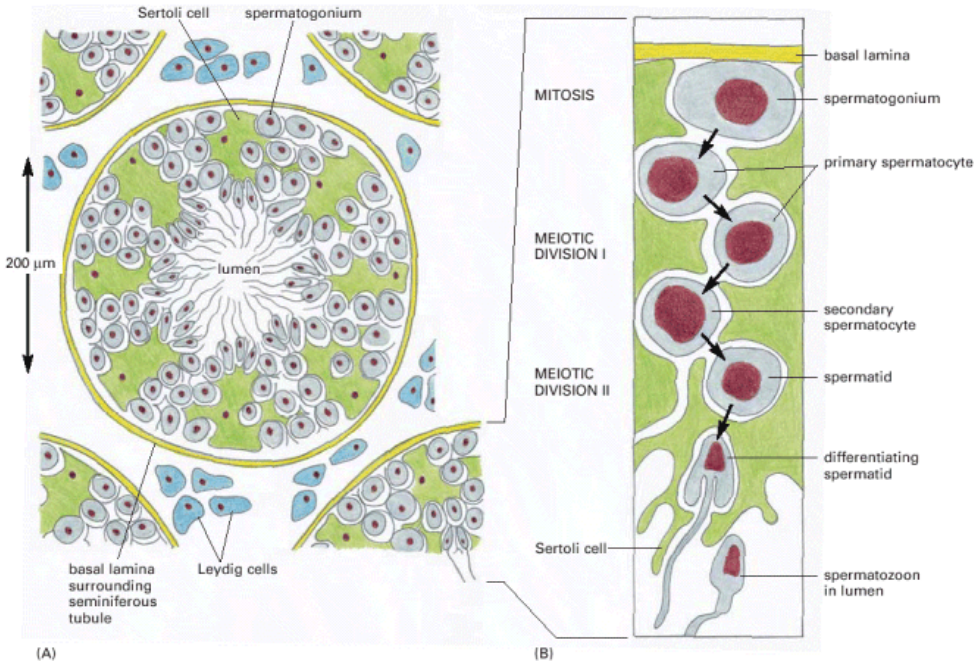

Figure 20-28. Highly simplified drawing of a cross section of a seminiferous tubule in a mammalian testis. (A) All of the stages of spermatogenesis shown take place while the developing gametes are in intimate association with Sertoli cells. These large cells extend from the basal lamina to the lumen of the seminiferous tubule; they are required for the survival of the germ cells and are analogous to follicle cells in the ovary (see Figure 20-18). Spermatogenesis also depends on testosterone secreted by Leydig cells, located between the seminiferous tubules. (B) Some of these cells are self-renewing stem-cell spermatogonia, whereas others are maturing spermatogonia; after a number of mitotic divisions, the maturing spermatogonia stop dividing by mitosis and enter meiosis to become primary spermatocytes. Eventually, sperm are released into the lumen. In man, it takes about 24 days for a spermatocyte to complete meiosis to become a spermatid and another 5 weeks for a spermatid to develop into a sperm. Sperm undergo further maturation and become motile in the epididymis; only then are they fully mature sperm.

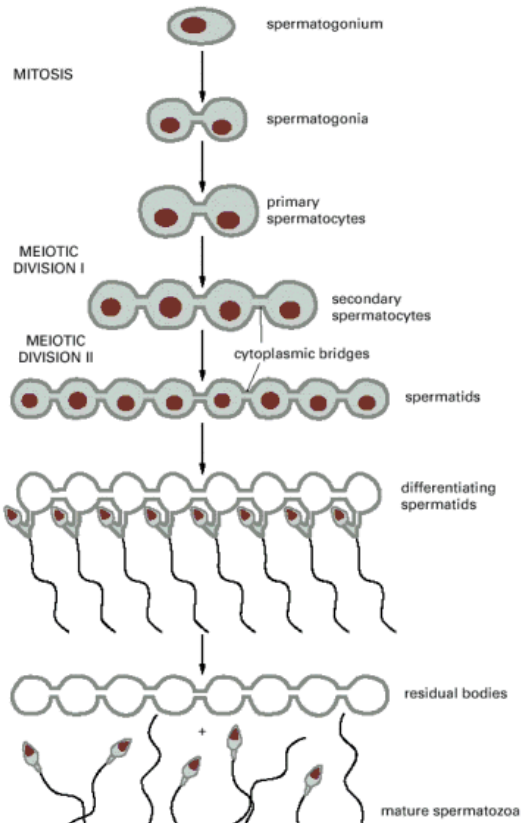

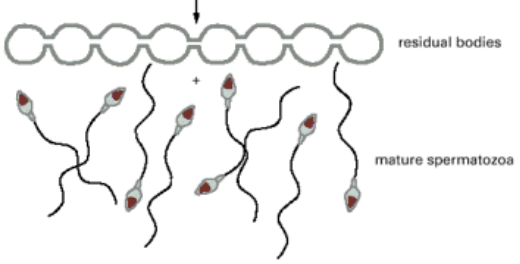

Figure 20-29. Cytoplasmic bridges in developing sperm cells and their precursors. The progeny of a single maturing spermatogonium remain connected to one another by cytoplasmic bridges throughout their differentiation into mature sperm. For the sake of simplicity, only two connected maturing spermatogonia are shown entering meiosis, eventually to form eight connected haploid spermatids. In fact, the number of connected cells that go through two meiotic divisions and differentiate synchronously is very much larger than shown here. Note that in the process of differentiating, most of the spermatid cytoplasm is discarded as residual bodies.

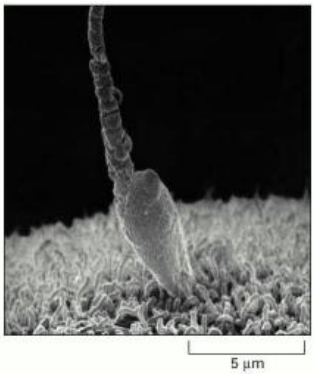

Figure 20-30. Scanning electron micrograph of a human sperm contacting a hamster egg. The zona pellucida of the egg has been removed, exposing the plasma membrane, which contains numerous microvilli. The ability of an individual's sperm to penetrate hamster eggs is used as an assay of male fertility; penetration of more than 1025% of the eggs is considered to be normal. (Courtesy of David M. Phillips.)

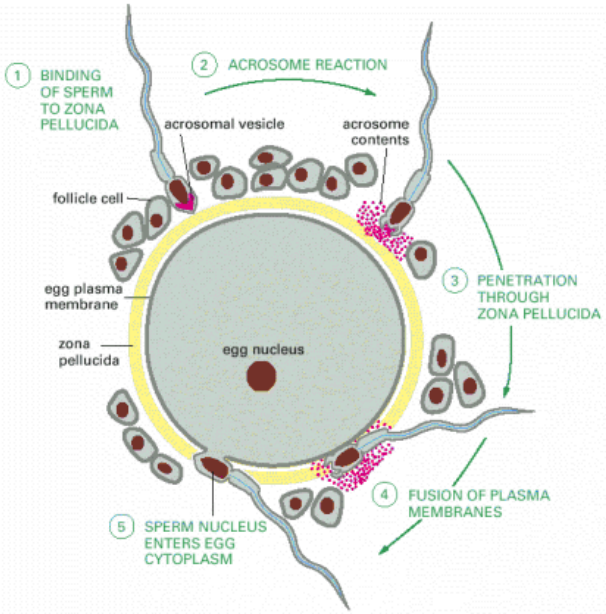

Figure 20-31. The acrosome reaction that occurs when a mammalian sperm fertilizes an egg. In mice, a single glycoprotein in the zona pellucida, ZP3, is thought to be responsible for both binding the sperm and inducing the acrosome reaction. Note that a mammalian sperm interacts tangentially with the egg plasma membrane so that fusion occurs at the equator, rather than at the tip, of the sperm head. In mice, the zona pellucida is about 6 µm thick, and sperm cross it at a rate of about 1 µm/min.

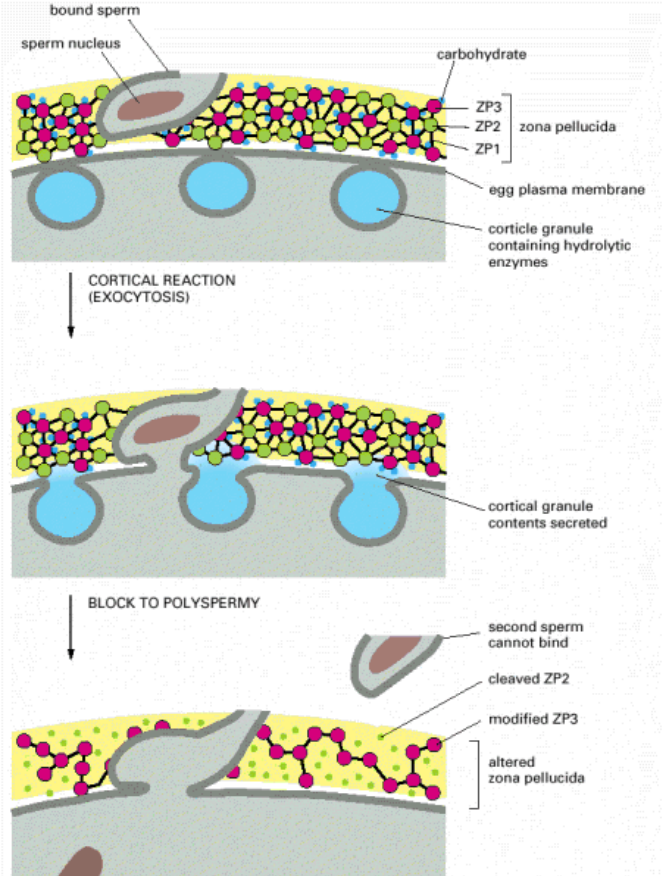

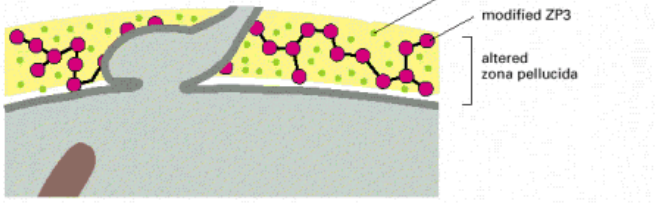

Figure 20-32. How the cortical reaction in a mouse egg is thought to prevent additional sperm from entering the egg. The released contents of the cortical granules both remove carbohydrate from ZP3 so it no longer can bind to the sperm plasma membrane and partly cleave ZP2, hardening the zona pellucida. Together these changes provide a block to polyspermy.

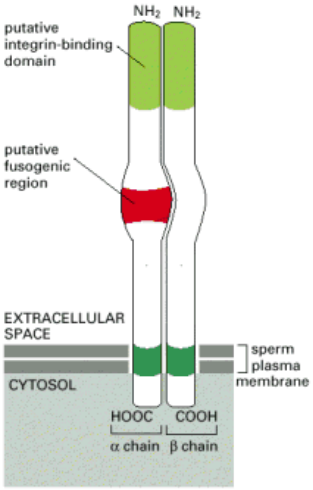

Figure 20-33. The fertilin protein in the sperm plasma membrane. The α and β subunits, which are both glycosylated (not shown), are noncovalently associated. Both subunits belong to the ADAM family of proteins, which includes proteins thought to function in either cell adhesion or the proteolytic processing of other transmembrane proteins (such as Notch, which is discussed in Chapter 15). The proteolytic domain that is normally present at the amino terminus of these proteins is removed from the fertilin protein during sperm maturation.

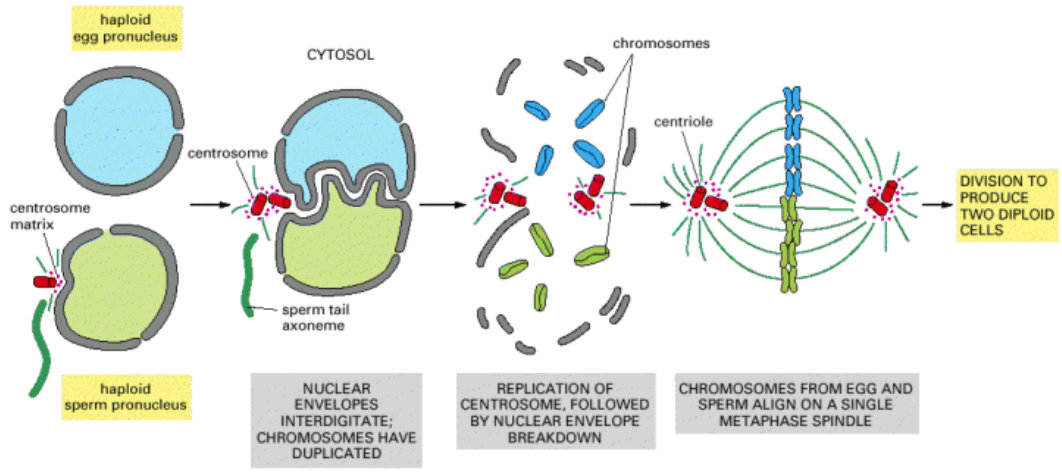

Figure 20-34. The coming together of the sperm and egg pronuclei after mammalian fertilization. The pronuclei migrate toward the center of the egg. When they come together, their nuclear envelopes interdigitate. The centrosome replicates, the nuclear envelopes break down, and the chromosomes of both gametes are eventually integrated into a single mitotic spindle, which mediates the first cleavage division of the zygote. (Adapted from drawings and electron micrographs provided by Daniel Szöllösi.)

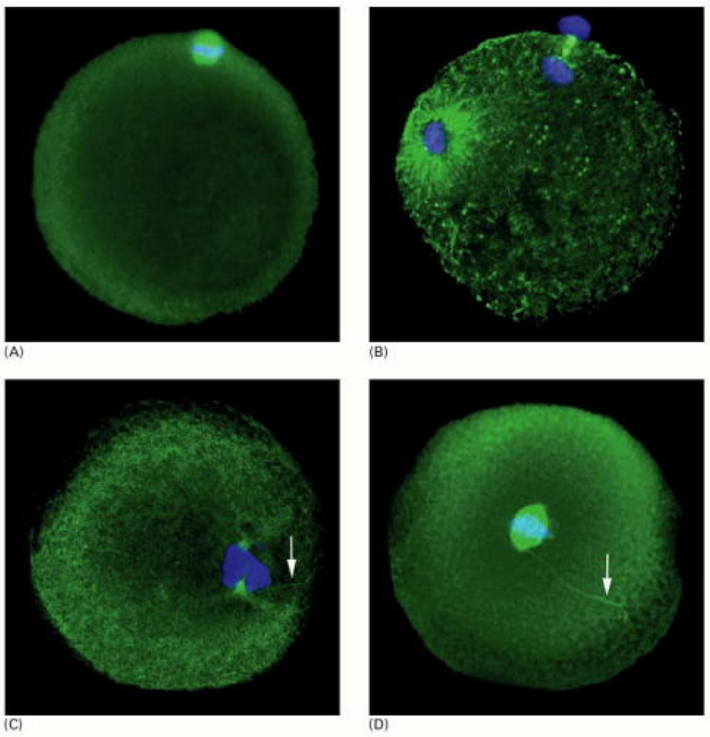

Figure 20-35. Immunofluorescence micrographs of human sperm and egg pronuclei coming together after in vitro fertilization. Spindle microtubules are stained in *green* with anti-tubulin antibodies, and DNA is labeled in *blue* with a DNA stain. (A) A meiotic spindle in a mature, unfertilized oocyte. (B) This fertilized egg is extruding its second polar body and is shown about 5 hours after fusion with a sperm. The sperm head *(left)* has nucleated an array of microtubules. (C) The two pronuclei have come together. (D) By 16 hours after fusion with a sperm, the centrosome that entered the egg with the sperm has duplicated, and the daughter centrosomes have organized a bipolar mitotic spindle. The chromosomes of both pronuclei are aligned at the metaphase plate of the spindle. As indicated by the arrows in (C) and (D), the sperm tail is associated with one of the centrosomes. (From C. Simerly et al., *Nat. Med.* 1:4753, 1995. © Macmillan Magazines Ltd.)

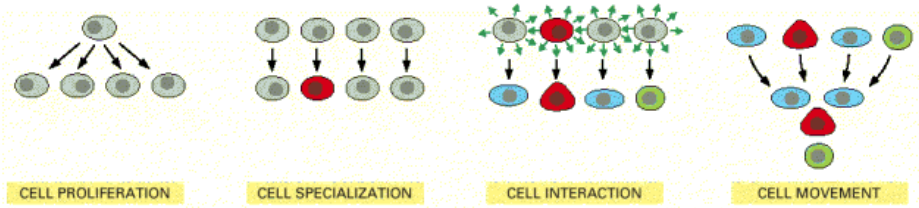

Figure 21-1. The four essential processes by which a multicellular organism is made: cell proliferation, cell specialization, cell interaction, and cell movement.

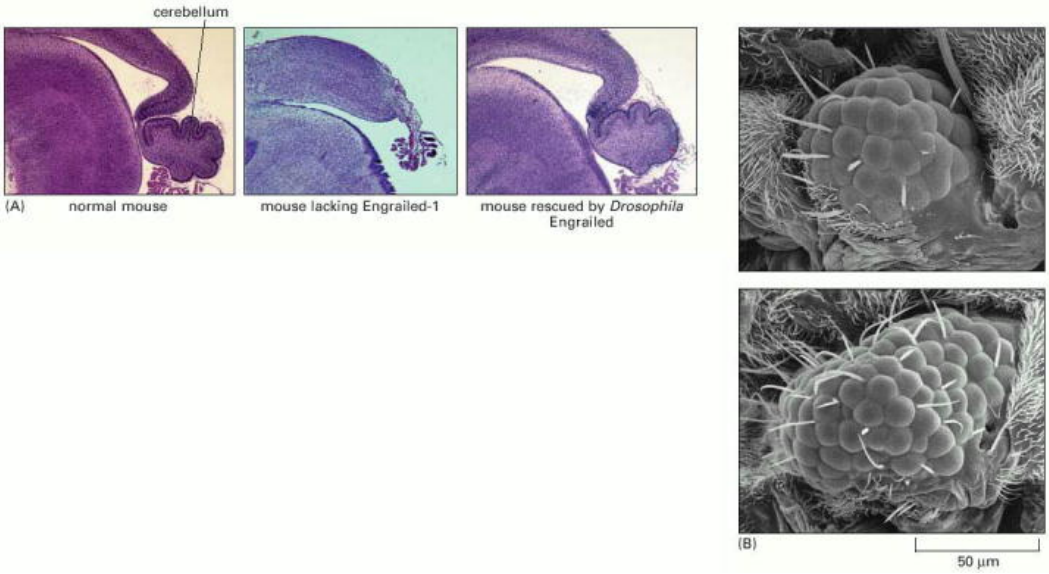

Figure 21-2. Homologous proteins functioning interchangeably in the development of mice and flies. (A) A fly protein used in a mouse. The DNA sequence from *Drosophila* coding for the Engrailed protein (a gene regulatory protein) can be substituted for the corresponding sequence coding for the Engrailed-1 protein of the mouse. Loss of Engrailed-1 in the mouse causes a defect in its brain (the cerebellum fails to develop); the *Drosophila* protein acts as an efficient substitute, rescuing the transgenic mouse from this deformity. (B) A mollusc protein used in a fly. The Eyeless protein controls eye development in *Drosophila*, and when misexpressed can cause an eye to develop in an abnormal site, such as a leg. The homologous protein, Pax-6, from a mouse, a squid, or practically any animal possessing eyes, when similarly misexpressed in a transgenic fly, has the same effect. The scanning electron micrographs show a patch of eye tissue on the leg of a fly resulting from misexpression of *Drosophila* Eyeless *(above)* and of squid Pax-6 *(below)*. (A, from M.C. Hanks et al., *Development* 125:452130, 1998. © The Company of Biologists; B, from S. I. Tomarev et al., *Proc. Natl. Acad. Sci. USA* 94:24212426, 1997. © National Academy of Sciences.)

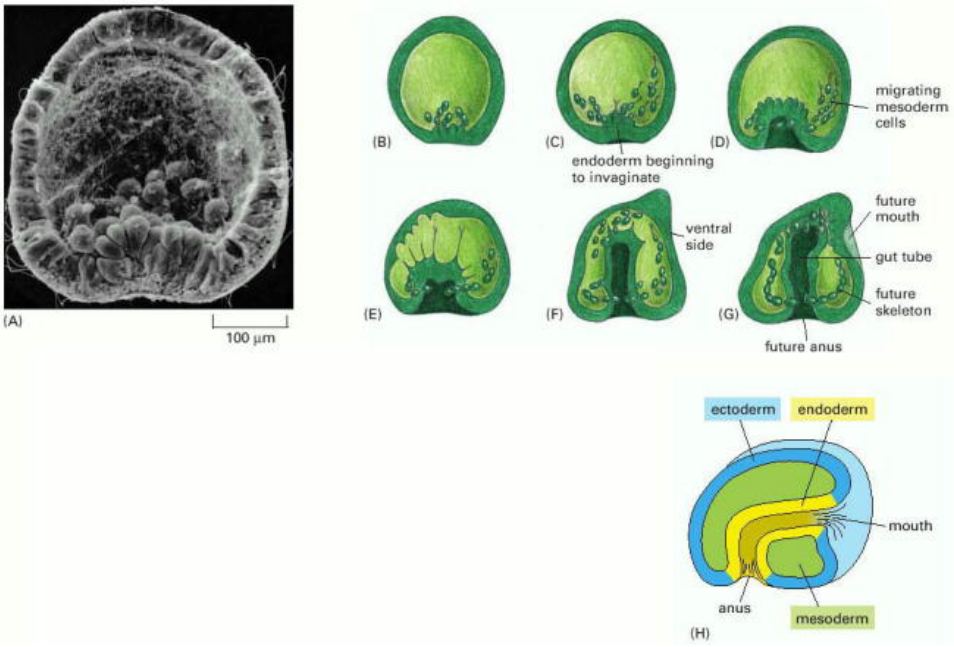

Figure 21-3. Sea urchin gastrulation. A fertilized egg divides to produce a *blastula* - a hollow sphere of epithelial cells surrounding a cavity. Then, in the process of gastrulation, some of the cells tuck into the interior to form the gut and other internal tissues. (A) Scanning electron micrograph showing the initial intucking of the epithelium. (B) Drawing showing how a group of cells break loose from the epithelium to become mesoderm. (C) These cells then crawl over the inner face of the wall of the blastula. (D) Meanwhile epithelium is continuing to tuck inward to become endoderm. (E and F) The invaginating endoderm extends into a long gut tube. (G) The end of the gut tube makes contact with the wall of the blastula at the site of the future mouth opening. Here the ectoderm and endoderm will fuse and a hole will form. (H) The basic animal body plan, with a sheet of ectoderm on the outside, a tube of endoderm on the inside, and mesoderm sandwiched between them. (A, from R.D. Burke et al., *Dev. Biol.* 146:542557, 1991. © Academic Press; B-G, after L. Wolpert and T. Gustafson, *Endeavour* 26:8590, 1967.)

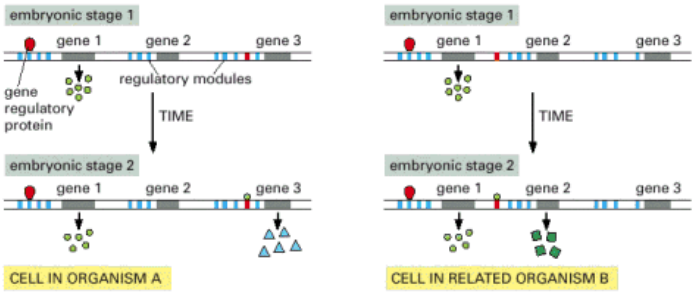

Figure 21-4. How regulatory DNA defines the succession of gene expression patterns in development. The genomes of organisms A and B code for the same set of proteins but have different regulatory DNA. The two cells in the cartoon start in the same state, expressing the same proteins at stage 1, but step to quite different states at stage 2 because of their different arrangements of regulatory modules.

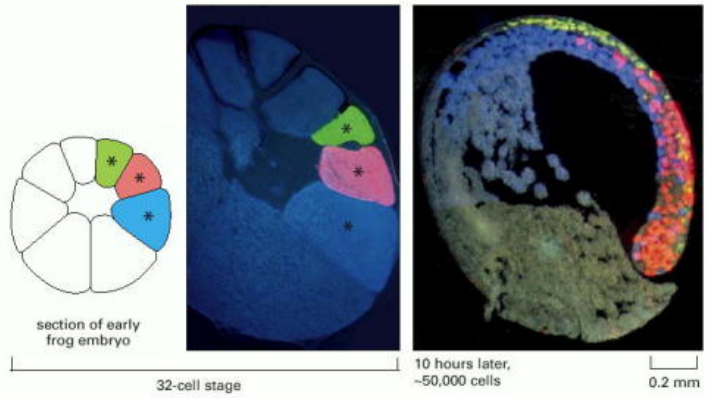

Figure 21-5. A cell lineage tracing experiment in the Xenopus embryo. Different fluorescent dyes are injected into three cells at an early stage (cells with asterisks at the 32-cell stage), and the embryo is then left to develop for 10 hours before being fixed and sectioned. The pattern of fluorescent labeling reveals how the descendants of the three cells have moved. (From M.A. Vodicka and J.C. Gerhart, *Development* 121:35053518, 1995. © The Company of Biologists.)

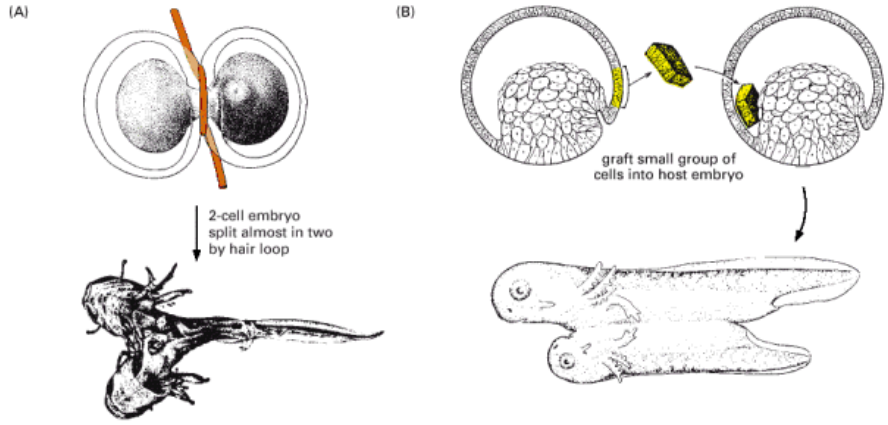

Figure 21-6. Some striking results obtained by experimental embryology. In (A), an early amphibian embryo is split almost into two parts with a hair loop. In (B), an amphibian embryo at a somewhat later stage receives a graft of a small cluster of cells from another embryo at that stage. The two quite different operations both cause a single embryo to develop into a pair of conjoined (Siamese) twins. It is also possible in experiment (A) to split the early embryo into two completely separate halves; two entire separate well-formed tadpoles are then produced. (A, after H. Spemann, Embryonic Development and Induction. New Haven: Yale University Press, 1938; B, after J. Holtfreter and V. Hamburger, in Analysis of Development [B.H. Willier, P.A. Weiss, and V. Hamburger, eds.], pp. 230296. Philadelphia: Saunders, 1955.)

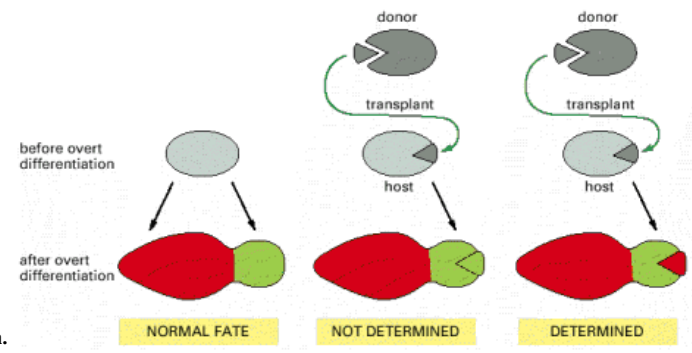

Figure 21-7. The standard test for cell determination.

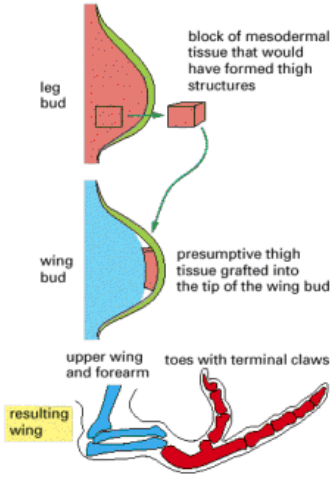

Figure 21-8. Prospective thigh tissue grafted into the tip of a chick wing bud forms toes. (After J.W. Saunders et al., *Dev. Biol*. 1:281301, 1959.)

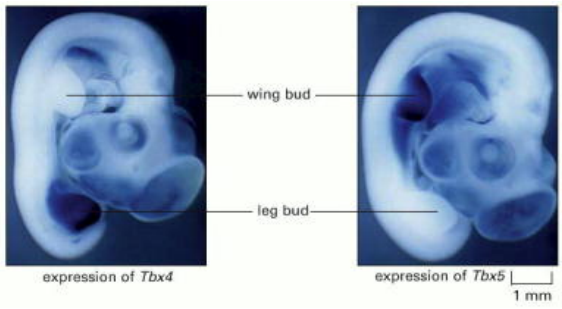

Figure 21-9. Chick embryos at 4 days of incubation, showing the limb buds stained by *in situ* hybridization with probes to detect expression of the *Tbx4* and *Tbx5* genes. The cells expressing *Tbx5* will form a wing; those expressing *Tbx4* will form a leg. *Tbx4* and *Tbx5* code for related gene regulatory proteins, which are thought to dictate which type of limb develops. (From H. Ohuchi et al., *Development* 125:5160, 1998. © The Company of Biologists.)

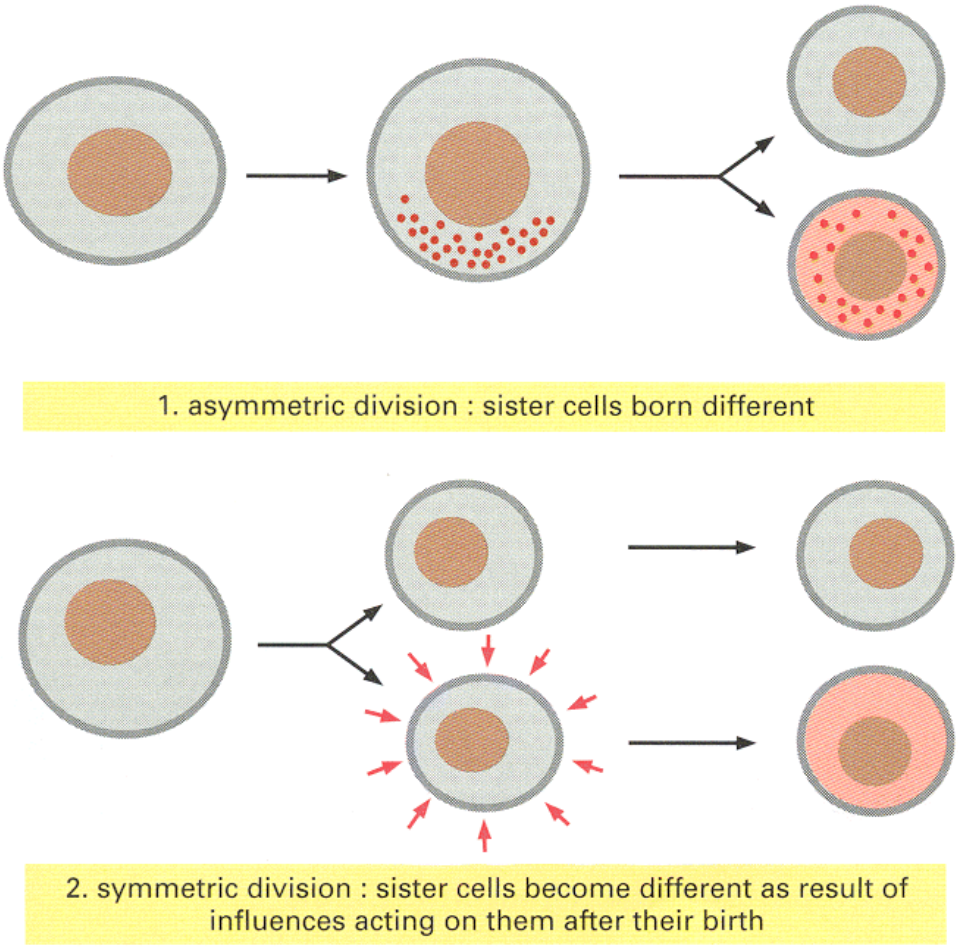

Figure 21-10. Two ways of making sister cells different.

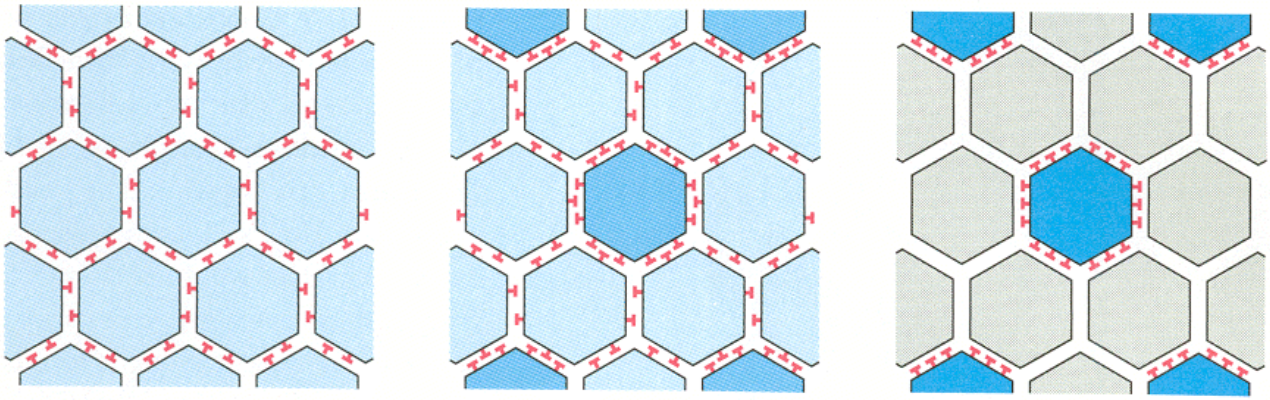

Figure 21-11. Lateral inhibition and cell diversification. Adjacent cells compete to adopt the primary character *(blue)*, by delivering inhibitory signals to one another. At first, all cells in the patch are similar. Any cell that gains an advantage in the competition *(darker blue)* delivers a stronger inhibitory signal (more *red* inhibition signals) to its neighbors, inhibiting them from delivering inhibitory signals themselves in return. This effect is self-reinforcing, and it leads to creation of a fine-grained mixture in which the cells finally adopting the primary character *(deep blue)* are surrounded by inhibited cells that adopt a different character *(gray)*.

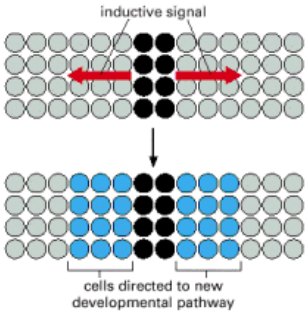

Figure 21-12. Inductive signaling.

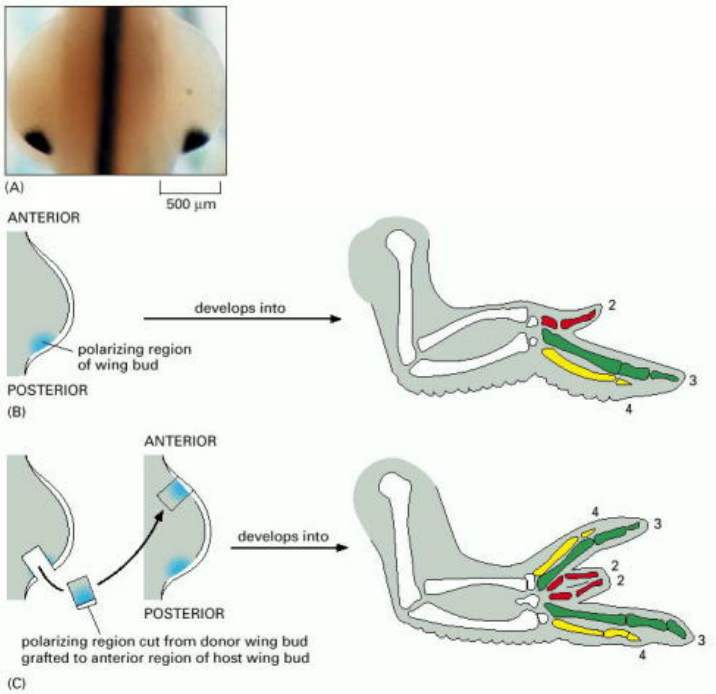

Figure 21-13. Sonic hedgehog as a morphogen in chick limb development. (A) Expression of the *Sonic hedgehog* gene in a 4-day chick embryo, shown by *in situ* hybridization (dorsal view of the trunk at the level of the wing buds). The gene is expressed in the midline of the body and at the posterior border (the polarizing region) of each of the two wing buds. Sonic hedgehog protein spreads out from these sources. (B) Normal wing development. (C) A graft of tissue from the polarizing region causes a mirror-image duplication of the pattern of the host wing. The type of digit that develops is thought to be dictated by the local concentration of Sonic hedgehog protein; different types of digit (labeled 2, 3, and 4) therefore form according to their distance from a source of Sonic hedgehog. (A, courtesy of Randall S. Johnson and Robert D. Riddle.)

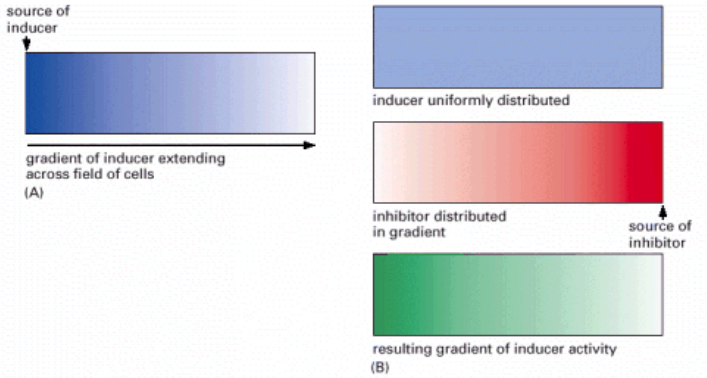

Figure 21-14. Two ways to create a morphogen gradient. (A) By localized production of an inducer - a morphogen - that diffuses away from its source, (B) By localized production of an inhibitor that diffuses away from its source and blocks the action of a uniformly distributed inducer.

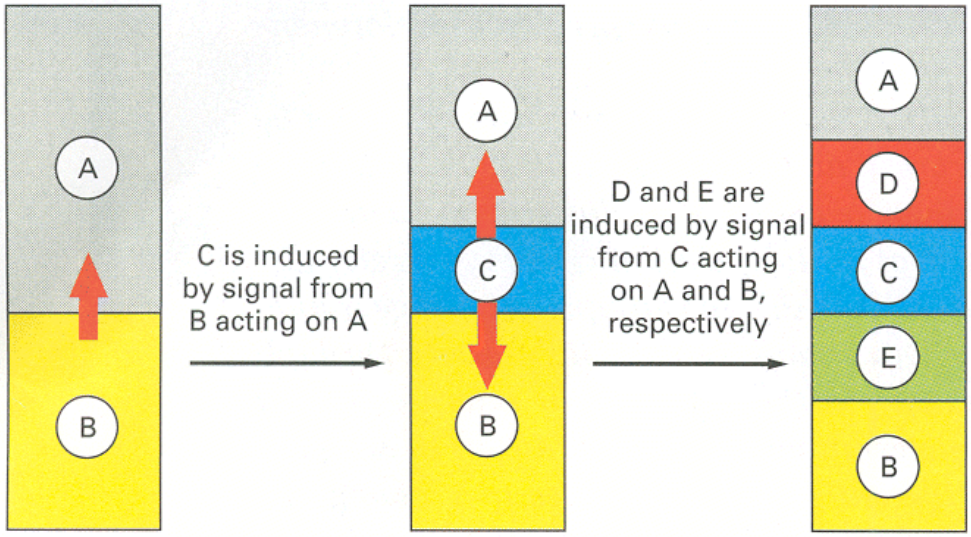

Figure 21-15. Patterning by sequential induction. A series of inductive interactions can generate many types of cells, starting from only a few.

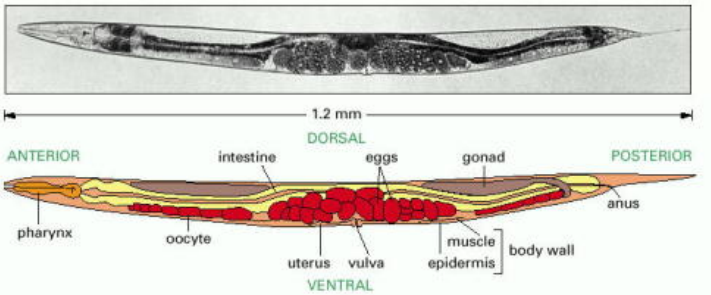

Figure 21-16. ***Caenorhabditis elegans.*** A side view of an adult hermaphrodite is shown. (From J.E. Sulston and H.R. Horvitz, *Dev. Biol.* 56:110156, 1977. © Academic Press.)

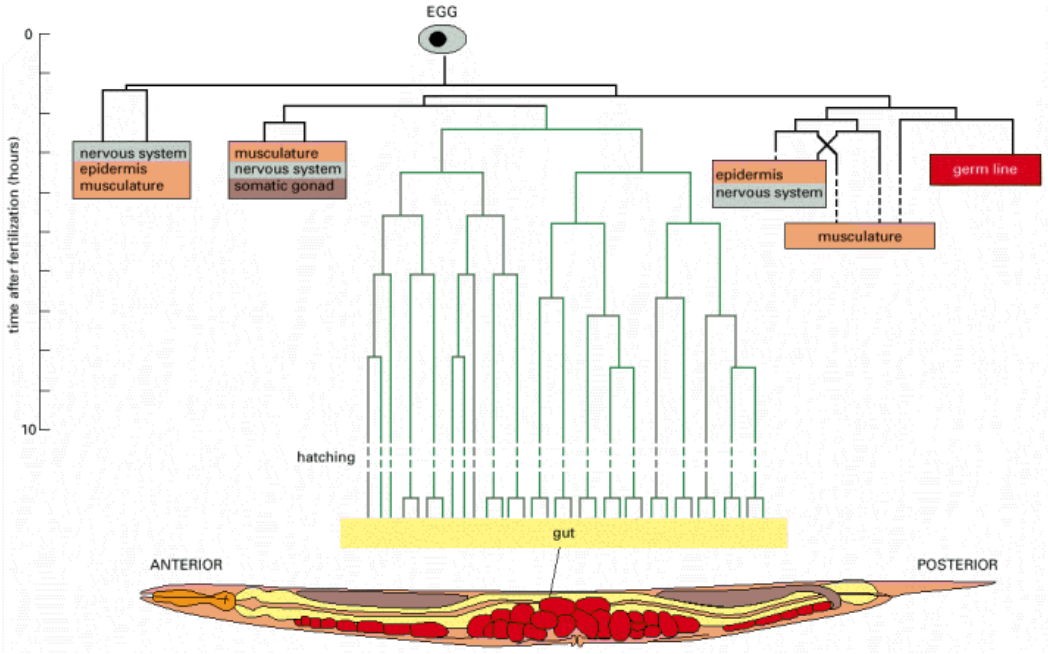

Figure 21-17. The lineage tree for the cells that form the gut (the intestine) of *C. elegans*. Note that although the intestinal cells form a single clone (as do the germline cells), the cells of most other tissues do not. Nerve cells (not shown in the drawing of the adult at the bottom) are mainly clustered in ganglia near the anterior and posterior ends of the animal and in a ventral nerve cord that runs the length of the body.

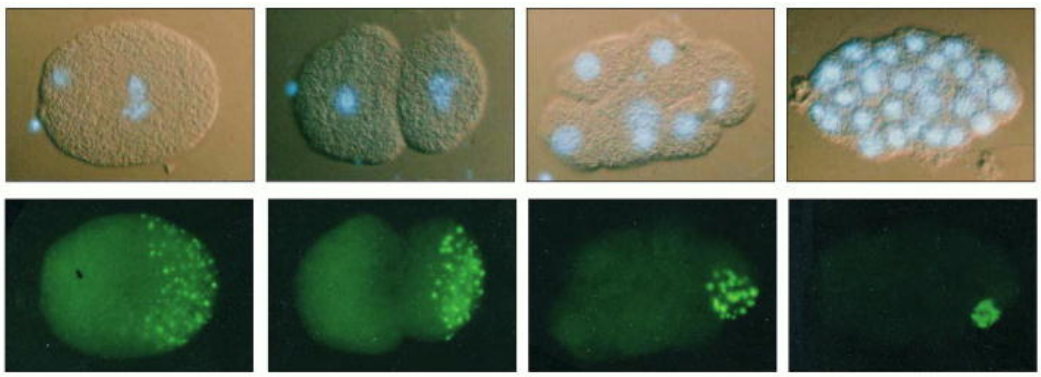

Figure 21-18. Asymmetric divisions segregating P granules into the founder cell of the *C. elegans* germ line. The micrographs in the upper row show the pattern of cell divisions, with cell nuclei stained blue with a DNA-specific fluorescent dye; below are the same cells stained with an antibody against P granules. These small granules (0.51 μm in diameter) are distributed randomly throughout the cytoplasm in the unfertilized egg (not shown). After fertilization, at each cell division up to the 16-cell stage, both they and the intracellular machinery that localizes them asymmetrically are segregated into a single daughter cell. (Courtesy of Susan Strome.)

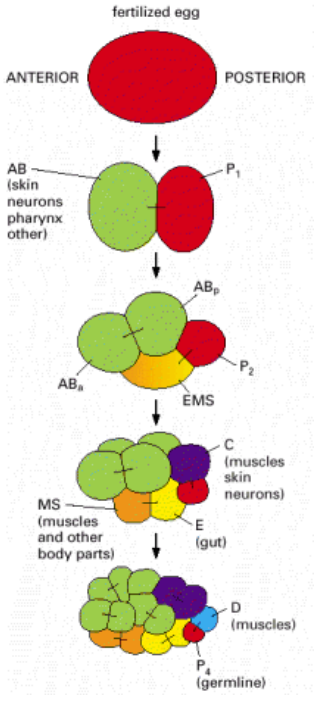

Figure 21-19. The pattern of cell divisions in the early nematode embryo, indicating the names and fates of the individual cells. Cells that are sisters are shown linked by a short *black* line. (After K. Kemphues, *Cell* 101:345348, 2000.)

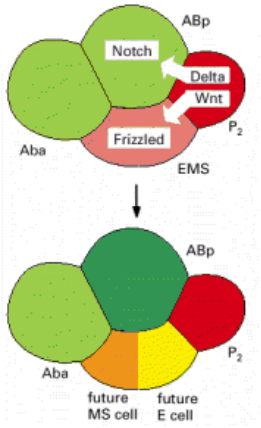

Figure 21-20. Cell-signaling pathways controlling assignment of different characters to the cells in a four-cell nematode embryo. The P_2 cell uses the Notch signaling pathway to send an inductive signal to the ABp cell, causing this to adopt a specialized character. The ABa cell has all the molecular apparatus to respond in the same way to the same signal, but it does not do so because it is out of contact with P_2. Meanwhile, a Wnt signal from the P_2 cell causes the EMS cell to orient its mitotic spindle and generate two daughters that become committed to different fates as a result of their different exposure to Wnt protein - the MS cell and the E cell (the founder cell of the gut).

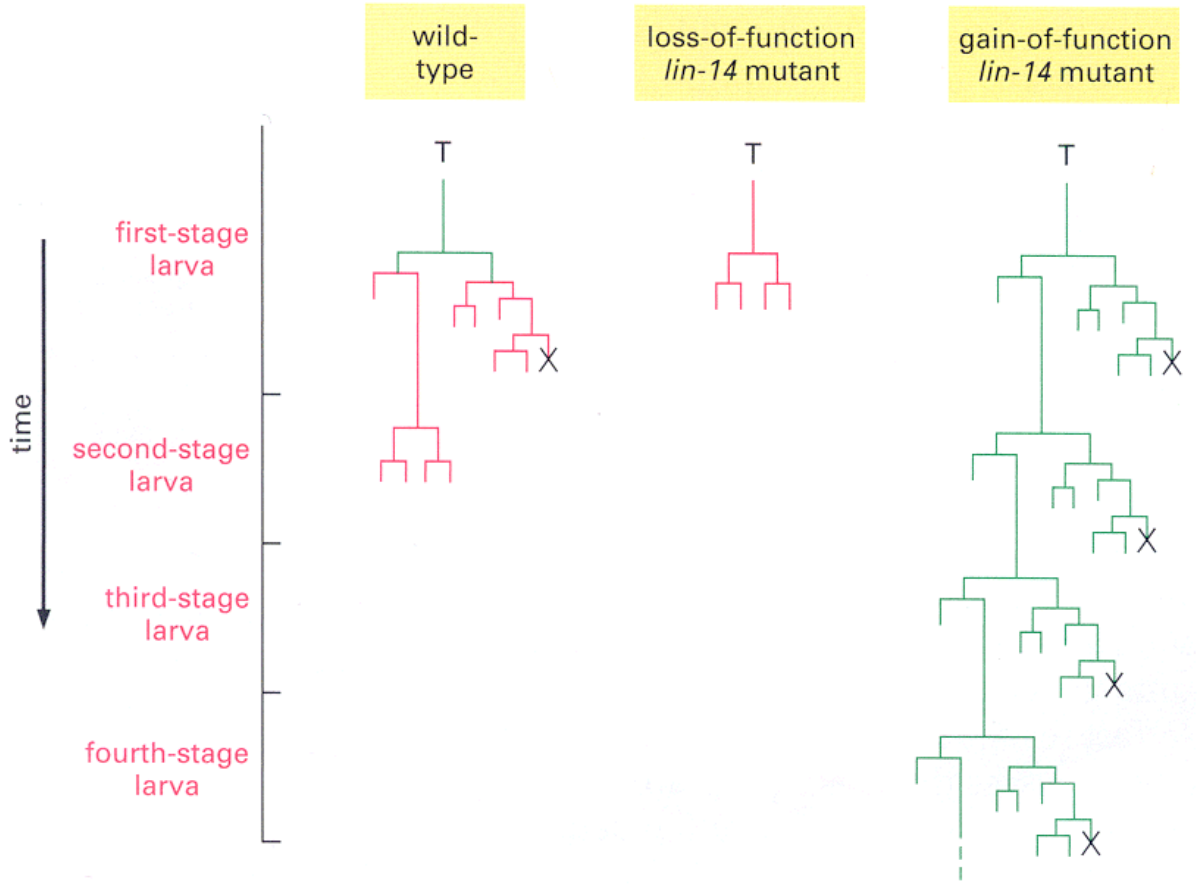

Figure 21-21. Heterochronic mutations in the *lin-14* gene of *C. elegans*. The effects on only one of the many affected lineages are shown. The loss-of-function (recessive) mutation in *lin-14* causes premature occurrence of the pattern of cell division and differentiation characteristic of a late larva, so that the animal reaches its final state prematurely and with an abnormally small number of cells. The gain-of-function (dominant) mutation has the opposite effect, causing cells to reiterate the patterns of cell divisions characteristic of the first larval stage, continuing through as many as five or six molt cycles and persisting in the manufacture of an immature type of cuticle. The cross denotes a programmed cell death. *Green* lines represent cells that contain Lin-14 protein (which binds to DNA), *red* lines those that do not. In normal development the disappearance of Lin-14 is triggered by the beginning of larval feeding. (After V. Ambros and H.R. Horvitz, *Science* 226:409416, 1984; P. Arasu, B. Wightman, and G. Ruvkun, *Growth Dev. Aging* 5:18251833, 1991.)

Figure 21-22. Apoptotic cell death in *C. elegans*. Death depends on expression of the *ced-3* and *ced-4* genes in the absence of *ced-9* expression - all in the dying cell itself. The subsequent engulfment and disposal of the remains depend on expression of other genes in the

neighboring cells.

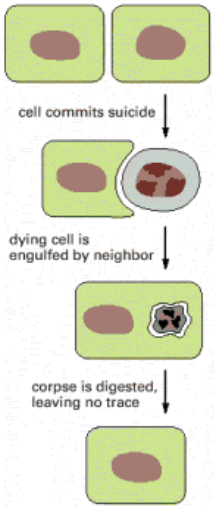

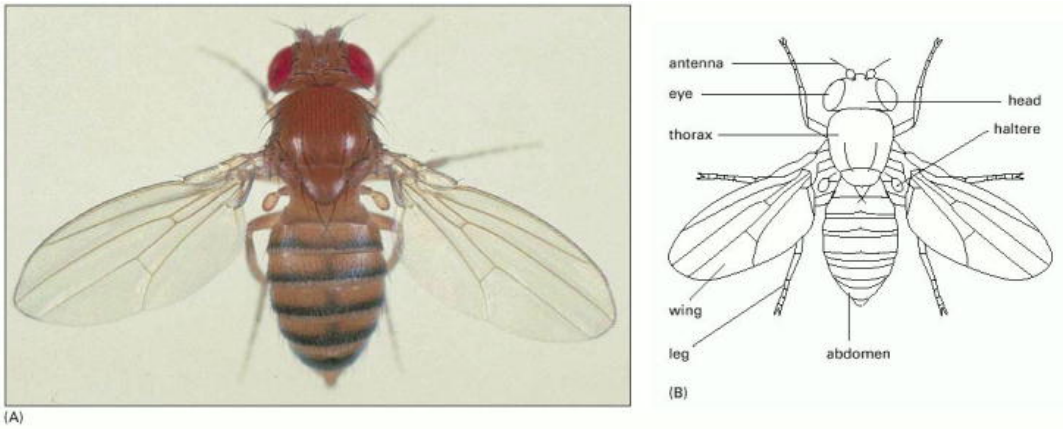

Figure 21-23. Drosophila melanogaster. Dorsal view of a normal adult fly. (A) Photograph. (B) Labeled drawing. (Photograph courtesy of E.B. Lewis.)

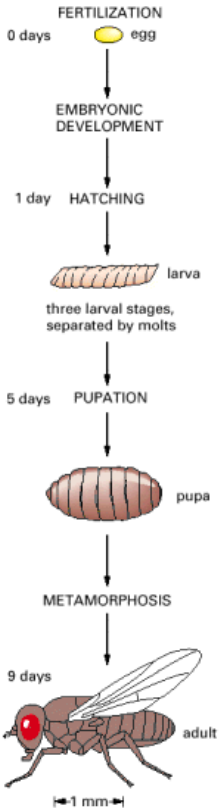

Figure 21-24. Synopsis of *Drosophila* development from egg to adult fly.

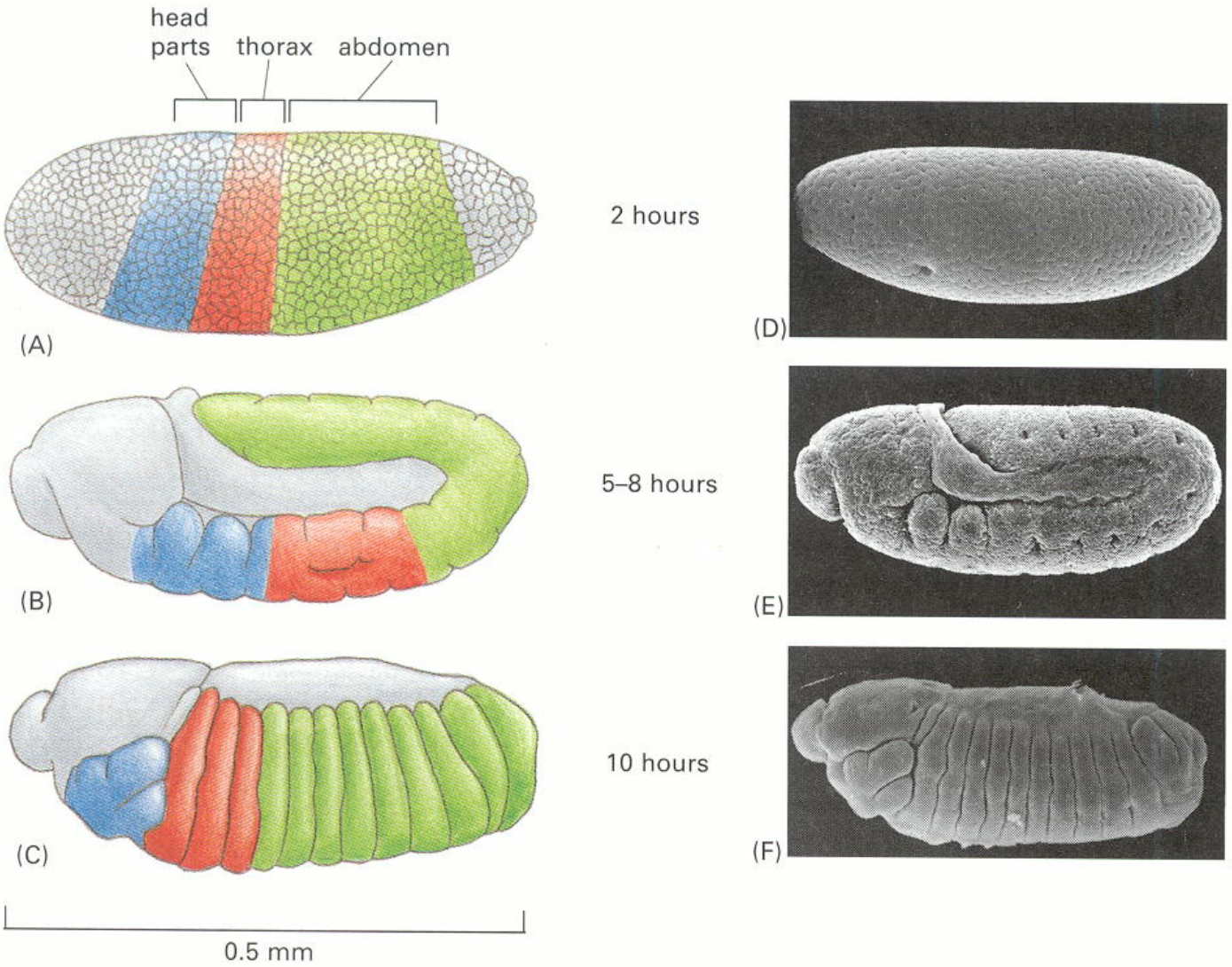

Figure 21-25. The origins of the *Drosophila* body segments during embryonic development. The embryos are seen in side view in drawings (A-C) and corresponding scanning electron micrographs (D-F). (A and D) At 2 hours the embryo is at the *syncytial blastoderm* stage (see Figure 21-51) and no segmentation is visible, although a fate map can be drawn showing the future segmented regions (*color* in A). (B and E) At 58 hours the embryo is at the *extended germ band* stage: gastrulation has occurred, segmentation has begun to be visible, and the segmented axis of the body has lengthened, curving back on itself at the tail end so as to fit into the egg shell. (C and F) At 10 hours the body axis has contracted and become straight again, and all the segments are clearly defined. The head structures, visible externally at this stage, will subsequently become tucked into the interior of the larva, to emerge again only when the larva goes through pupation to become an adult. (D and E, courtesy of F.R. Turner and A.P. Mahowald, *Dev. Biol.* 50:95108, 1976. © Academic Press; F, from J.P. Petschek, N. Perrimon, and A.P. Mahowald, *Dev. Biol.* 119:175189, 1987. © Academic Press.)

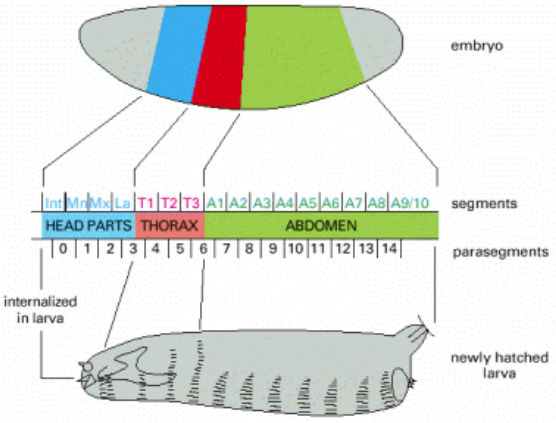

Figure 21-26. The segments of the *Drosophila* larva and their correspondence with regions of the blastoderm. The parts of the embryo that become organized into segments are shown in color. The two ends of the embryo, shaded *gray*, are not segmented and become tucked into the interior of the body to form the internal structures of the head and gut. (The future external, segmental structures of the adult head are also transiently tucked into the interior in the larva.) Segmentation in *Drosophila* can be described in terms of either segments or parasegments: the relationship is shown in the middle part of the figure. Parasegments often correspond more simply to patterns of gene expression. The exact number of abdominal segments is debatable: eight are clearly defined, and a ninth is present vestigially in the larva, but absent in the adult.

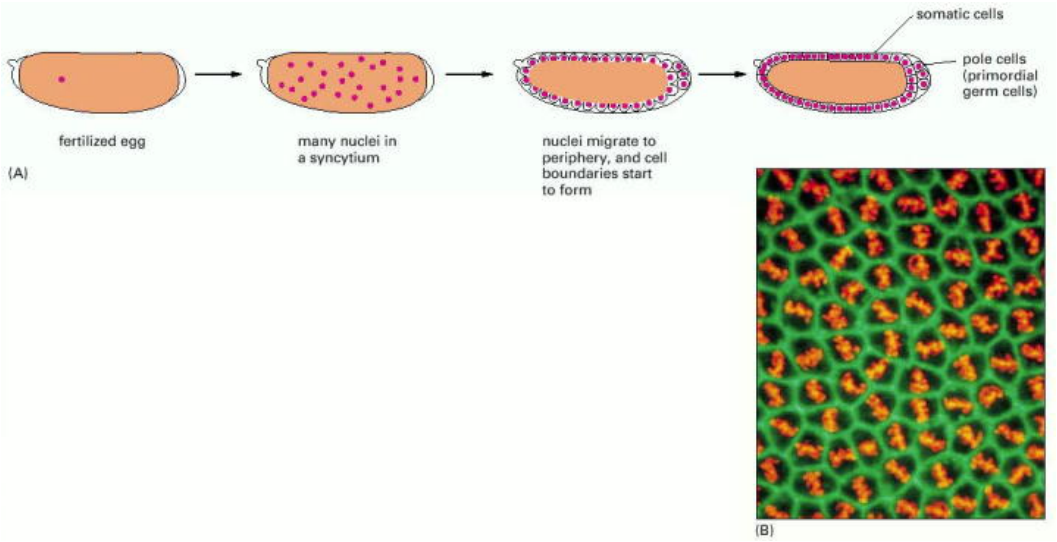

Figure 21-27. Development of the *Drosophila* egg from fertilization to the cellular blastoderm stage. (A) Schematic drawings. (B) Surface view - an optical-section photograph of blastoderm nuclei undergoing mitosis at the transition from the syncytial to the cellular blastoderm stage. Actin is stained *green*, chromosomes *orange*. (A, after H.A. Schneiderman, in Insect Development [P.A. Lawrence, ed.], pp. 334. Oxford, UK: Blackwell, 1976; B, courtesy of William Sullivan.)

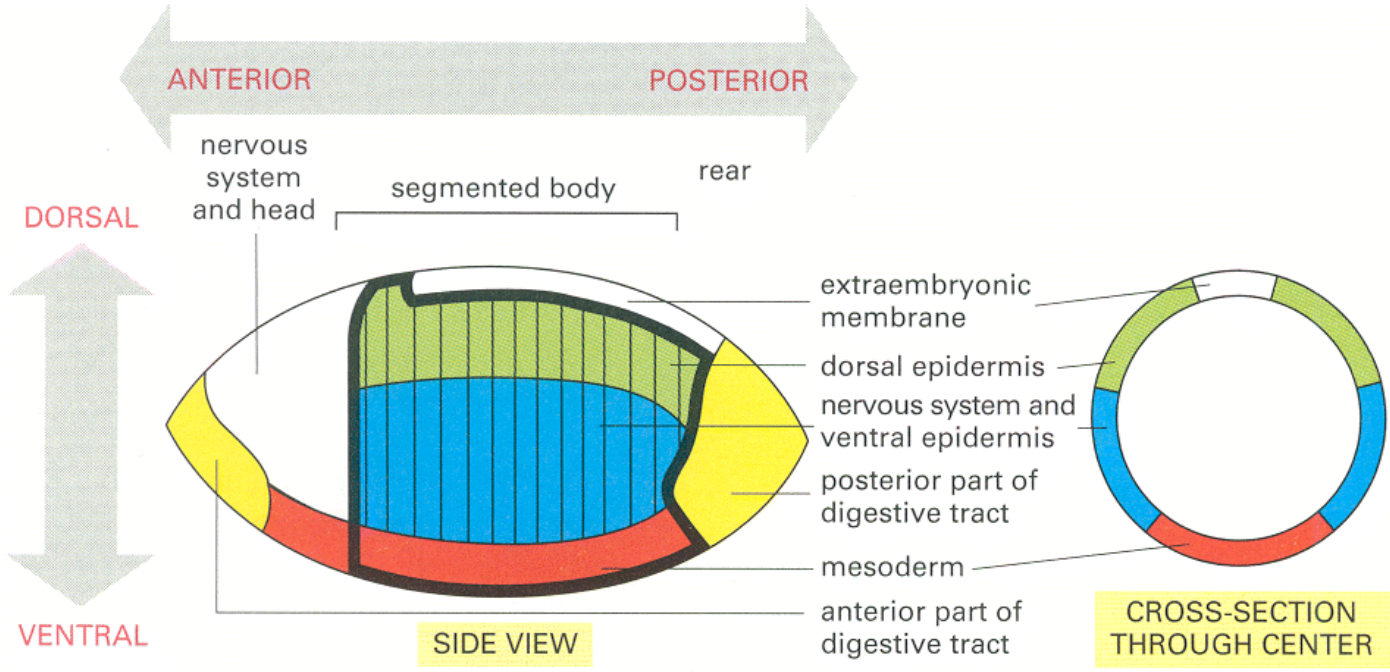

Figure 21-28. Fate map of a *Drosophila* embryo at the cellular blastoderm stage. The embryo is shown in side view and in cross section, displaying the relationship between the dorsoventral subdivision into future major tissue types and the anteroposterior pattern of future segments. A heavy line encloses the region that will form segmental structures. During gastrulation the cells along the ventral midline invaginate to form mesoderm, while the cells fated to form the gut invaginate near each end of the embryo. (After V. Hartenstein, G.M. Technau, and J.A. Campos-Ortega, *Wilhelm Roux' Arch. Dev. Biol.* 194:213216, 1985.)

Figure 21-29. The domains of the anterior, posterior, and terminal systems of egg-polarity genes. The *upper* diagrams show the fates of the different regions of the egg/ early embryo and indicate (in *white)* the parts that fail to develop if the anterior,

posterior, or terminal system is defective. The *middle* row shows schematically the appearance of a normal larva and of mutant larvae that are defective in a gene of the anterior system (for example, *bicoid)*, of the posterior system (for example, *nanos)*, or of the terminal system (for example, *torso)*. The *bottom* row of drawings shows the appearances of larvae in which none or only one of the three gene systems is functional. The lettering beneath each larva specifies which systems are intact (A P T for a normal larva, -P T for a larva where the anterior system is defective but the posterior and terminal systems are intact, and so on). Inactivation of a particular gene system causes loss of the corresponding set of body structures; the body parts that form correspond to the gene systems that remain functional. Note that larvae with a defect in the anterior system can still form terminal structures at their anterior end, but these are of the type normally found at the rear end of the body rather than the front of the head. (Slightly modified from D. St. Johnston and C. Nüsslein-Volhard, *Cell* 68:201219, 1992.)

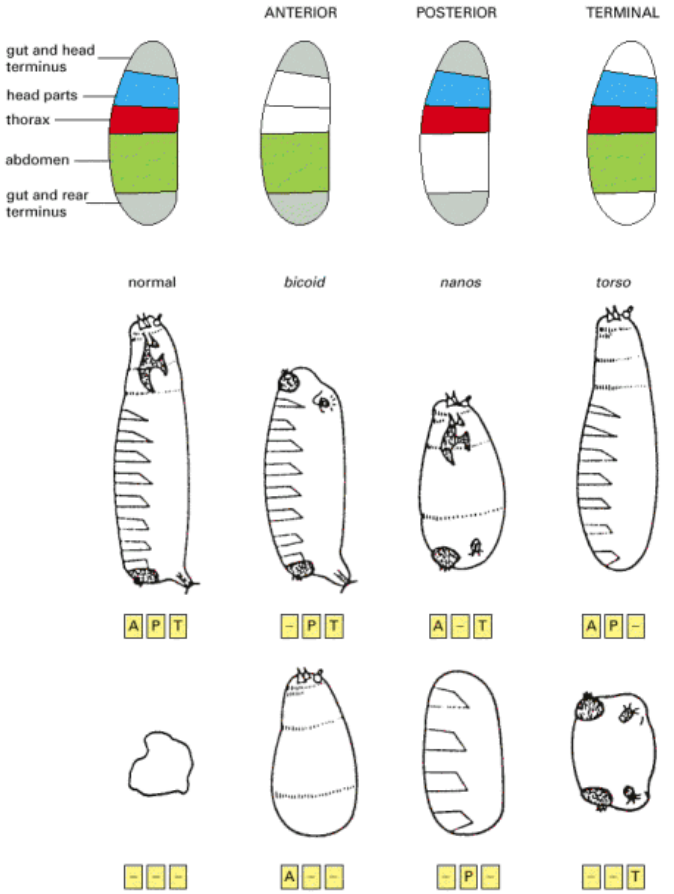

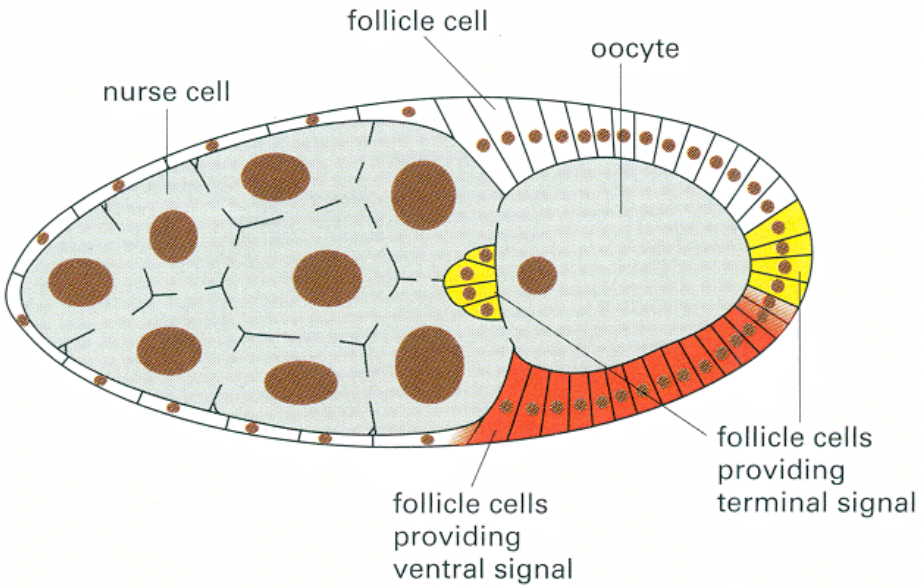

Figure 21-30. A *Drosophila* oocyte in its follicle. The oocyte is derived from a germ cell that divides four times to give a family of 16 cells that remain in communication with one another via cytoplasmic bridges *(gray)*. One member of the family group becomes the oocyte, while the others become nurse cells, which make many of the components required by the oocyte and pass them into it via the cytoplasmic bridges. The follicle cells that partially surround the oocyte have a separate ancestry. As indicated, they are the sources of terminal and ventral egg-polarizing signals.

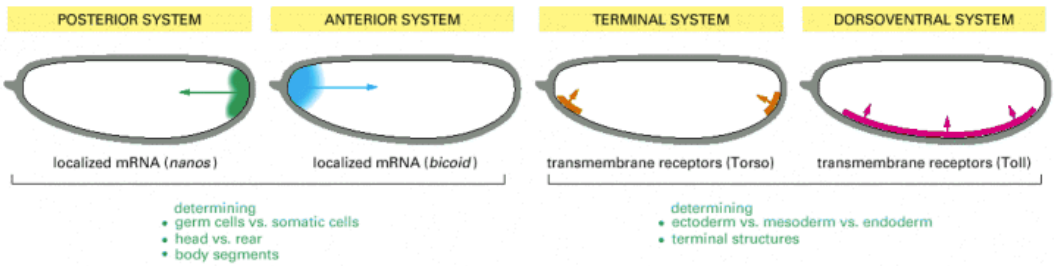

Figure 21-31. The organization of the four egg-polarity gradient systems. The receptors Toll and Torso are distributed all over the membrane; the coloring in the diagrams on the right indicates where they become activated by extracellular ligands.

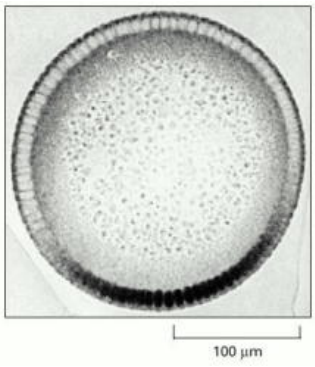

Figure 21-32. The concentration gradient of Dorsal protein in the nuclei of the blastoderm, as revealed by an antibody. Dorsally, the protein is present in the cytoplasm and absent from the nuclei; ventrally, it is depleted in the cytoplasm and concentrated in the nuclei. (From S. Roth, D. Stein, and C. Nüsslein-Volhard, *Cell* 59:11891202, 1989. © Elsevier.)

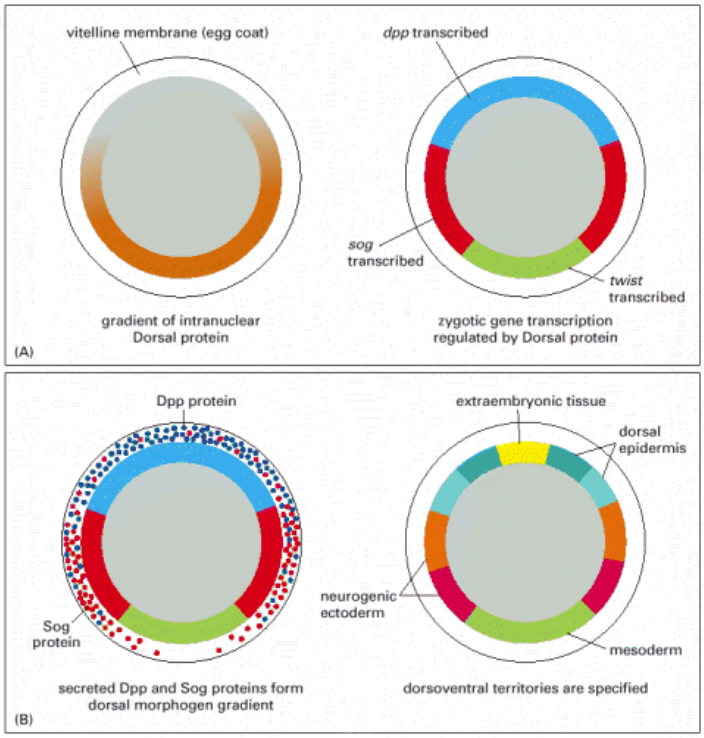

Figure 21-33. Morphogen gradients patterning the dorsoventral axis of the embryo. (A) The gradient of Dorsal protein defines three broad territories of gene expression, marked here by the expression of three representative genes - *dpp*, *sog*, and *twist*. (B) Slightly later, the cells expressing *dpp* and *sog* secrete, respectively, the signal proteins Dpp (a TGFβ family member) and Sog (an antagonist of Dpp). These two proteins diffuse and interact with one another (and with certain other factors) to set up a gradient of Dpp activity that guides a more detailed patterning process.

Figure 21-34. Origin of the mesoderm from cells expressing *twist*. Embryos were fixed at successive stages, cross-sectioned, and stained with an antibody against the Twist protein, a gene regulatory protein of the bHLH family. The cells that express Twist move into the interior of the embryo to form mesoderm. (From M. Leptin, J. Casal, B. Grunewald, and R. Reuter, *Development Suppl.* 2331, 1992. © The Company of Biologists.)

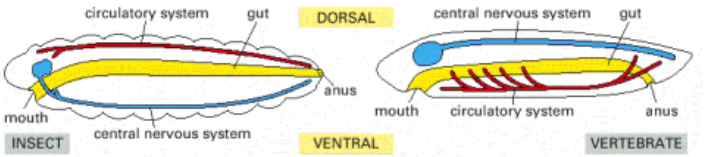

Figure 21-35. The vertebrate body plan as a dorsoventral inversion of the insect body plan. The mechanism of dorsoventral patterning in a vertebrate embryo is discussed in more detail later in this chapter. Note the correspondence with regard to the circulatory system as well as the gut and nervous system. In insects, the circulatory system is represented by a tubular heart and a main dorsal blood vessel, which pumps blood out into the tissue spaces through one set of apertures and receives blood back from the tissues through another set. In contrast with vertebrates, there is no system of capillary vessels to contain the blood as it percolates through the tissues. Nevertheless, heart development depends on homologous genes in vertebrates and insects, reinforcing the relationship between the two body plans. (After E.L. Ferguson, *Curr. Opin. Genet. Dev.* 6:424431, 1996.)

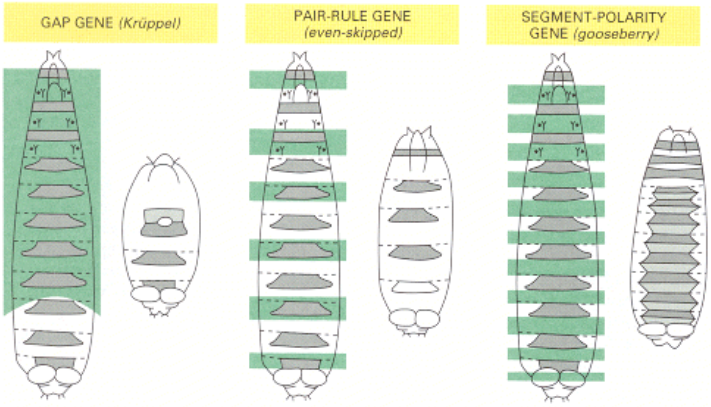

Figure 21-36. Examples of the phenotypes of mutations affecting the three types of segmentation genes. In each case the areas shaded in *green* on the normal larva *(left)* are deleted in the mutant or are replaced by mirror-image duplicates of the unaffected regions. By convention, dominant mutations are written with an initial capital letter and recessive mutations are written with a lower-case letter. Several of the patterning mutations of *Drosophila* are classed as dominant because they have a perceptible effect on the phenotype of the heterozygote, even though the characteristic major, lethal effects are recessive - that is, visible only in the homozygote. (Modified from C. Nüsslein-Volhard and E. Wieschaus, *Nature* 287:795801, 1980.)

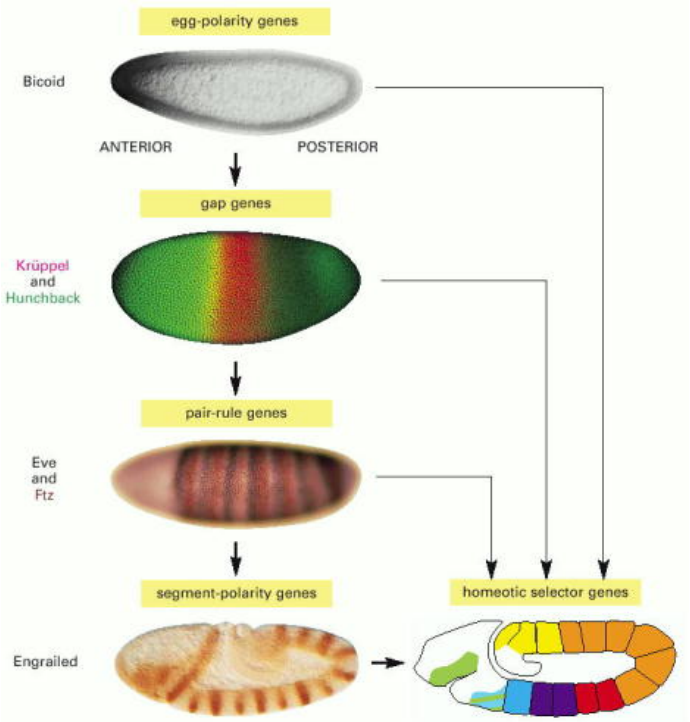

Figure 21-37. The regulatory hierarchy of egg-polarity, gap, segmentation, and homeotic selector genes. The photographs show expression patterns of representative examples of genes in each category, revealed by staining with antibodies against the protein products. The homeotic selector genes, discussed below, define the lasting differences between one segment and the next. (Photographs (i) from W. Driever and C. Nüsslein-Volhard, *Cell* 54:83104, 1988. © Elsevier; (ii) courtesy of Jim Langeland, Steve Paddock, Sean Carroll, and the Howard Hughes Medical Institute; (iii) from P. A. Lawrence, The Making of a Fly. Oxford, UK: Blackwell, 1992; (iv) from C. Hama, Z. Ali, and T.B. Kornberg, *Genes Dev.* 4:10791093, 1990. © Cold Spring Harbor Press.)

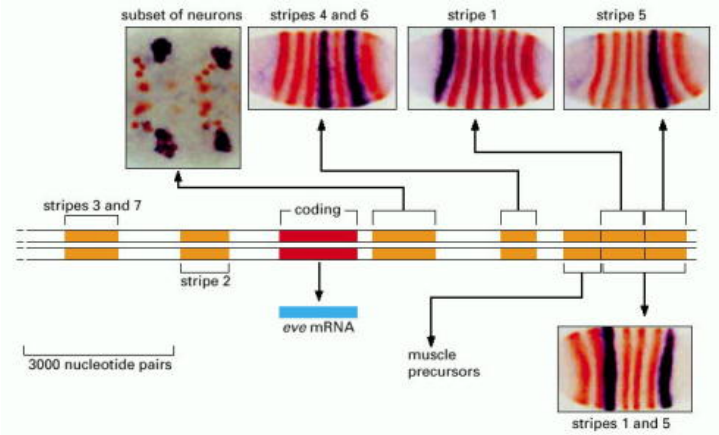

Figure 21-38. Modular organization of the regulatory DNA of the *eve* gene. In the experiment shown, cloned fragments of the regulatory DNA were linked to a *LacZ* reporter (a bacterial gene). Transgenic embryos containing these constructs were then stained by *in situ* hybridization to reveal the pattern of expression of *LacZ (blue/black)*, and counterstained with an anti-Eve antibody *(orange)* to show the positions of the normal *eve* expression stripes. Different segments of the *eve* regulatory DNA *(ochre)* are thus found to drive gene expression in regions corresponding to different parts of the normal *eve* expression pattern. Two segments in tandem drive expression in a pattern that is the sum of the patterns generated by each of them individually. Separate regulatory modules are responsible for different times of gene expression, as well as different locations: the leftmost panel shows the action of a module that comes into play later than the others illustrated and drives expression in a subset of neurons. (From M. Fujioka et al., *Development* 126:2527538, 1999. © The Company of Biologists.)

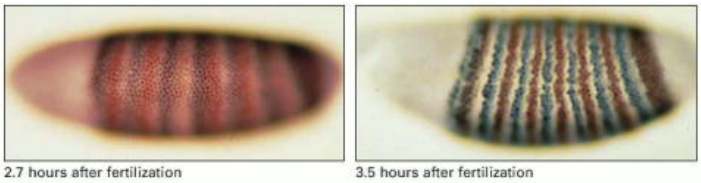

Figure 21-39. The formation of *ftz* and *eve* stripes in the *Drosophila* blastoderm. *ftz* and *eve* are both pair-rule genes. Their expression patterns (shown in *brown* for *ftz* and in *gray* for *eve*) are at first blurred but rapidly resolve into sharply defined stripes. (From P.A. Lawrence, The Making of a Fly. Oxford, UK: Blackwell, 1992.)

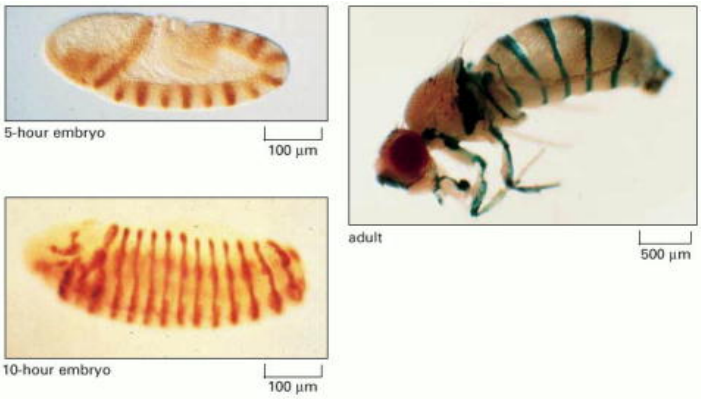

Figure 21-40. The pattern of expression of *engrailed*, a segment-polarity gene. The *engrailed* pattern is shown in a 5-hour embryo (at the extended germ-band stage), a 10-hour embryo, and an adult (whose wings have been removed in this preparation). The pattern is revealed by an antibody *(brown)* against the Engrailed protein (for the 5- and 10-hour embryos) or (for the adult) by constructing a strain of *Drosophila* containing the control sequences of the *engrailed* gene coupled to the coding sequence of the reporter *LacZ*, whose product is detected histochemically through the *blue* product of a reaction that it catalyzes. Note that the *engrailed* pattern, once established, is preserved throughout the animal's life. (From C. Hama, Z. Ali, and T.B. Kornberg, *Genes Dev.* 4:10791093, 1990. © Cold Spring Harbor Press.)

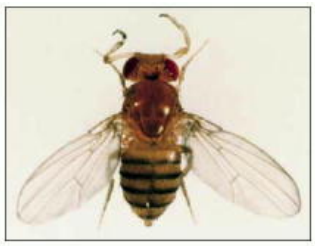

Figure 21-41. A homeotic mutation. The fly shown here is an *Antennapedia* mutant. Its antennae are converted into leg structures by a mutation in the regulatory region of the *Antennapedia* gene that causes it to be expressed in the head. Compare with the normal fly shown in Figure 21-23. (Courtesy of Matthew Scott.)

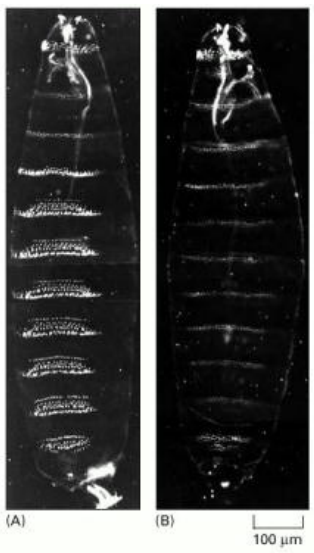

Figure 21-42. The effect of deleting most of the genes of the bithorax complex. (A) A normal *Drosophila* larva shown in dark-field illumination; (B) the mutant larva with the bithorax complex largely deleted. In the mutant the parasegments posterior to P5 all have the appearance of P5. (From G. Struhl, *Nature* 293:3641, 1981. © Macmillan Magazines Ltd.)

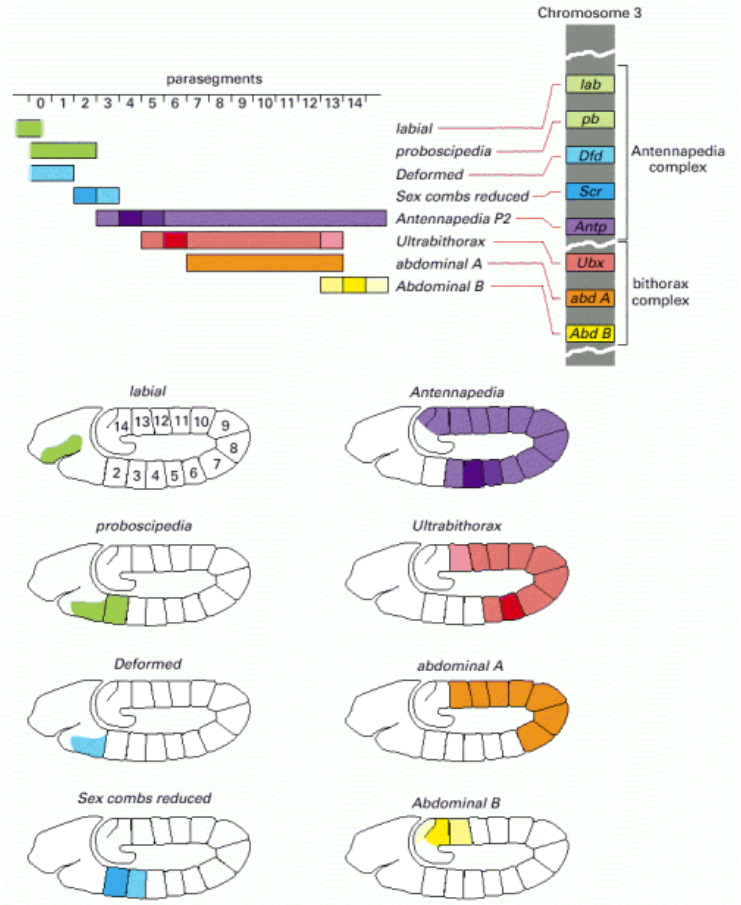

Figure 21-43. The patterns of expression compared to the chromosomal locations of the genes of the Hox complex. The sequence of genes in each of the two subdivisions of the chromosomal complex corresponds to the spatial sequence in which the genes are expressed. Note that most of the genes are expressed at a high level throughout one parasegment *(dark color)* and at a lower level in some adjacent parasegments *(medium color* where the presence of the transcripts is necessary for a normal phenotype, *light color* where it is not). In regions where the expression domains overlap, it is usually the most "posterior" of the locally active genes that determines the local phenotype. The drawings in the lower part of the figure represent the gene expression patterns in embryos at the extended germ band stage, about 5 hours after fertilization.

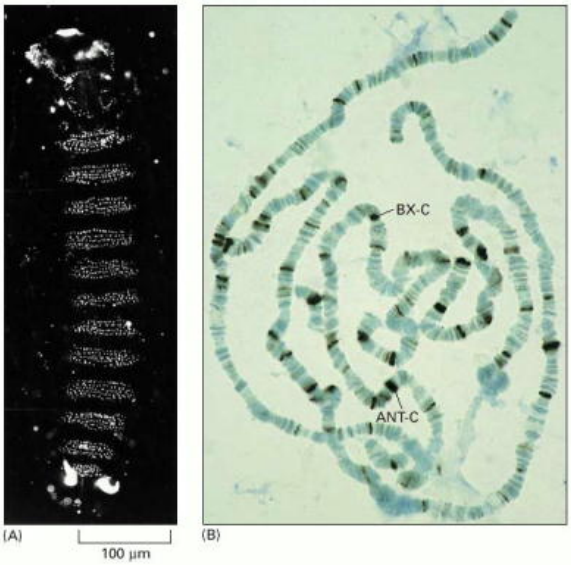

Figure 21-44. Action of genes of the Polycomb group. (A) Photograph of a mutant embryo defective for the gene *extra sex combs (esc)* and derived from a mother also lacking this gene. The gene belongs to the Polycomb group. Essentially all segments have been transformed to resemble the most posterior abdominal segment (compare with Figure 21-42). In the mutant the pattern of expression of the homeotic selector genes, which is roughly normal initially, is unstable in such a way that all these genes soon become switched on all along the body axis. (B) The normal pattern of binding of Polycomb protein to *Drosophila* giant chromosomes, visualized with an antibody against Polycomb. The protein is bound to the Antennapedia complex (ANT-C) and the bithorax complex (BX-C) as well as about 60 other sites. (A, from G. Struhl, *Nature* 293:3641, 1981. © Macmillan Magazines Ltd; B, courtesy of B. Zink and R. Paro, *Trends Genet.* 6:416421, 1990. © Elsevier.)

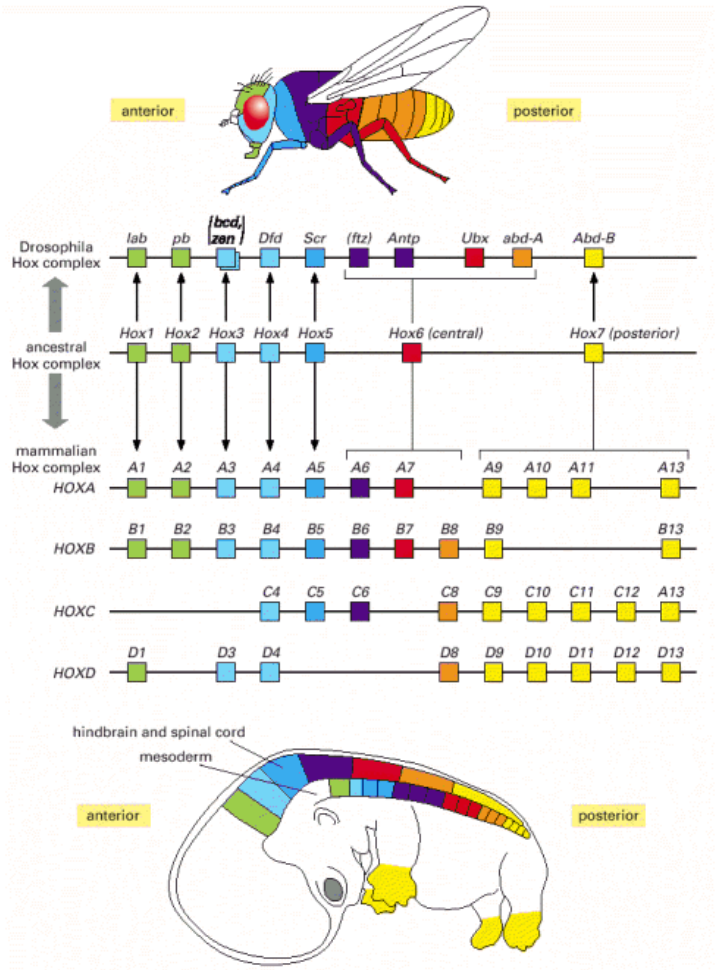

Figure 21-45. The Hox complex of an insect and the Hox complexes of a mammal compared and related to body regions. The genes of the Antennapedia and bithorax complexes of *Drosophila* are shown in their chromosomal order in the *top line*; the corresponding genes of the four mammalian Hox complexes are shown *below*, also in chromosomal order. The gene expression domains in fly and mammal are indicated in a simplified form by color in the cartoons of animals *above* and *below*. However, the details of the patterns depend on developmental stage and vary somewhat from one mammalian Hox complex to another. Also, in many cases, genes shown here as expressed in an anterior domain are also expressed more posteriorly, overlapping the domains of more posterior Hox genes (see, for example, Figure 21-46). The complexes are thought to have evolved as follows: first, in some common ancestor of worms, flies, and vertebrates, a single primordial homeotic selector gene underwent repeated duplication to form a series of such genes in tandem - the ancestral Hox complex. In the *Drosophila* sublineage this single complex became split into separate Antennapedia and bithorax complexes. Meanwhile, in the lineage leading to the mammals the whole complex was repeatedly duplicated to give four Hox complexes. The parallelism is not perfect because apparently some individual genes have been duplicated, others lost, and still others coopted for different purposes (genes in parentheses in the *top line)* since the complexes diverged. (Based on a diagram kindly supplied by William McGinnis.)

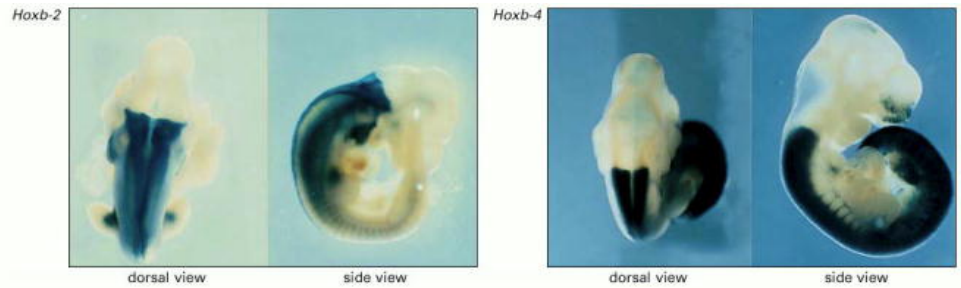

Figure 21-46. Expression domains of Hox genes in a mouse. The photographs show whole embryos displaying the expression domains of two genes of the HoxB complex *(blue* stain). These domains can be revealed by *in situ* hybridization or, as in these examples, by constructing transgenic mice containing the control sequence of a Hox gene coupled to a *LacZ* reporter gene, whose product is detected histochemically. Each gene is expressed in a long expanse of tissue with a sharply defined anterior limit. The earlier the position of the gene in its chromosomal complex, the more anterior the anatomical limit of its expression. Thus, with minor exceptions, the anatomical domains of the successive genes form a nested set, ordered according to the ordering of the genes in the chromosomal complex. (Courtesy of Robb Krumlauf.)

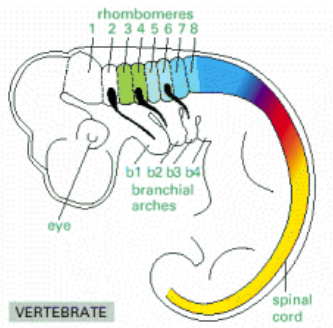

Figure 21-47. Segmentation and Hox gene expression in the hindbrain, as seen in a chick embryo. The pattern of HoxB gene expression is indicated by coloring as in Figure 21-45. For simplicity, the expression in tissues other than the central nervous system is not shown. In regions where the expression domains of two or more Hox genes overlap, the coloring corresponds to the most "posterior" of the genes expressed. Just as the expression domains in the fly are related to parasegments, so the expression domains in the vertebrate are related to the rhombomeres (segments in the hindbrain). Each pair of rhombomeres is associated with a branchial arch (a modified gill rudiment), to which it sends innervation. The pattern of Hox gene expression in the branchial arches (not shown) matches that in the associated rhombomeres. In the spinal cord, there are no rhombomere boundaries, and the expression domains of the different posterior Hox genes overlap.

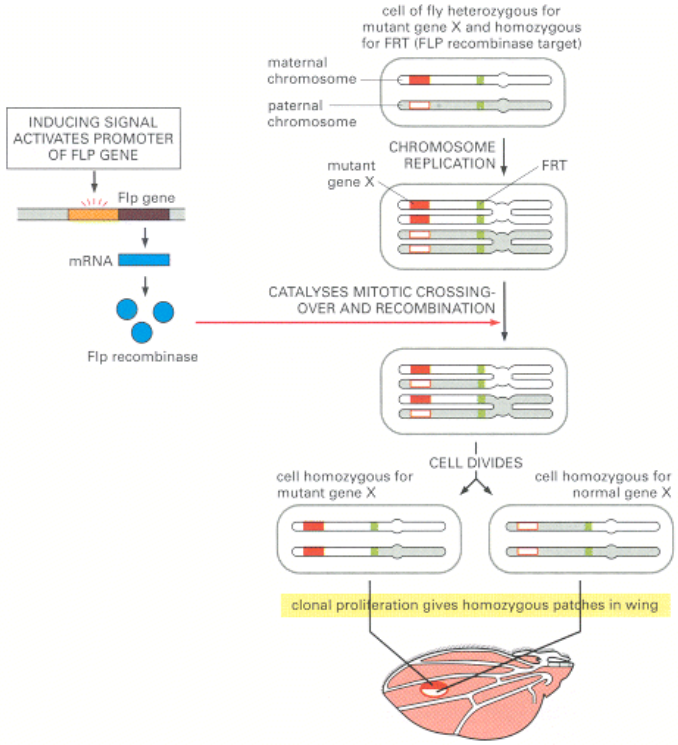

Figure 21-48. Creation of mutant cells by induced somatic recombination. The diagrams follow the fate of a single pair of homologous chromosomes, one from the father *(shaded)*, the other from the mother *(unshaded)*. These chromosomes have an FRT element *(green)* inserted close to their centromere, and contain a locus for a gene of interest - gene X - further out along the same chromosome arm. The paternal chromosome (in this example) carries the wild-type allele of gene X (open red box) while the maternal chromosome carries a recessive mutant allele (filled red box). Recombination by exchange of DNA between the maternal and paternal chromosomes, catalyzed by the FLP recombinase, can give rise to a pair of daughter cells, one containing two wild-type copies of gene X, the other containing two mutant copies. To help identify the cells where recombination has occurred, the maternal and paternal chromosomes can be chosen to carry, respectively, mutant and wild-type versions of an additional gene that provides a visible marker - a pigmentation gene, for example (not shown here). This marker gene is positioned on the chromosome so that recombination involving the marker locus - resulting in a visible alteration in the appearance of the cells - can be taken as a sure sign that gene X has also undergone recombination.

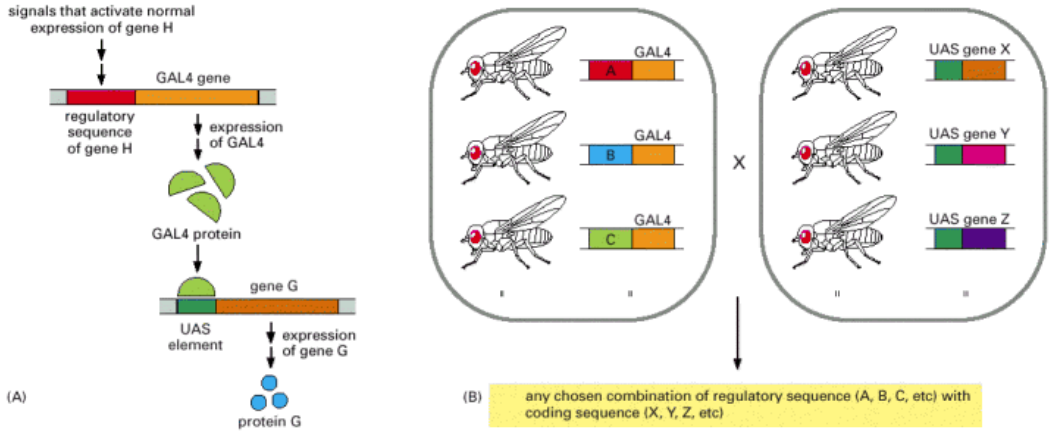

Figure 21-49. The GAL4/UAS technique for controlled gene misexpression in *Drosophila*. The method allows one to drive expression of a chosen gene *G* at the places and times where some other *Drosophila* gene *H* is normally expressed. (A) A transgenic animal is created, with two separate constructs inserted in its genome. One insert consists of a yeast-specific regulatory sequence, called the *UAS* element, coupled to a copy of the coding sequence of gene *G*. The other insert contains the coding sequence of the yeast *GAL4* gene, whose product is a yeast-specific gene regulatory protein that binds to the *UAS* element; this *GAL4* insert is placed next to, and controlled by, the regulatory region of gene H. Wherever gene *H* is normally expressed, GAL4 protein is also made and drives transcription of gene *G*. (B) Although one can achieve the same result by linking a copy of the *H* regulatory sequence directly to the *G* coding sequence, the GAL4/UAS approach allows a strategy that is more efficient in the long run. Two separate "libraries" of transgenic flies are constructed, one containing GAL4 inserts driven by a variety of regulatory sequences of different genes A, B, C, etc., the other containing UAS inserts driving a variety of different coding sequences X, Y, Z, etc. By mating a fly from one library with a fly from the other, any desired coding sequence can be functionally coupled to any desired regulatory sequence. To generate the library of flies with *GAL4* insertions at useful sites, flies are first produced with *GAL4* insertions at random locations in their genome. These are then mated with flies containing a *UAS* element linked to a reporter gene with an easily detectable product. Expression of the reporter reveals whether *GAL4* has been inserted at a site that brings its expression under the control of an interesting enhancer; flies showing interesting reporter patterns are kept and studied. This is called the *enhancer trap* technique, because it provides a way to hunt out and characterize interesting regulatory sequences in the genome.

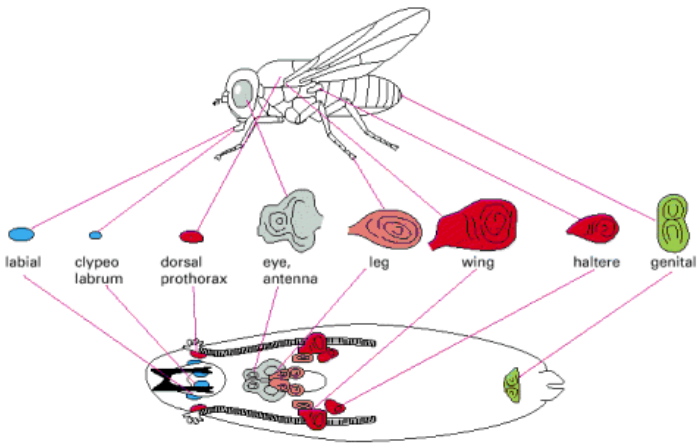

Figure 21-50. The imaginal discs in the *Drosophila* larva and the adult structures they give rise to. (After J.W. Fristrom et al., in Problems in Biology: RNA in Development [E.W. Hanley, ed.], p. 382. Salt Lake City: University of Utah Press, 1969.)

Figure 21-51. Expression of Distal-less in developing legs and related appendages of various species. (A) A sea-urchin larva. (B) A moth larva. (A, from G. Panganiban et al., *Proc. Natl. Acad. Sci. USA* 94:51625166, 1997. © National Academy of Sciences; B, from G. Panganiban, L. Nagy, and S.B. Carroll, *Curr. Biol.* 4:671675, 1994. © Elsevier.)

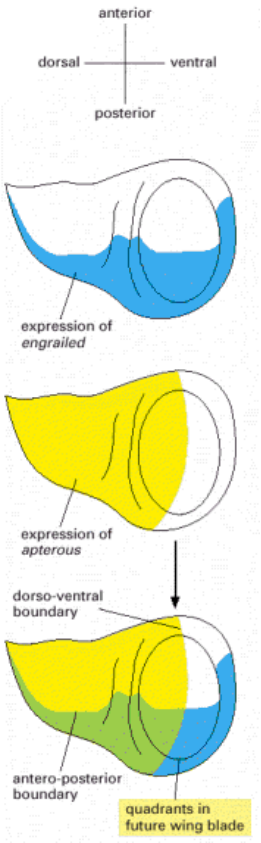

Figure 21-52. Gene expression domains in the wing imaginal disc, defining quadrants of the future wing. The wing blade itself derives from the oval-shaped domain toward the *right*, and it is divided into four quadrants by the expression of *apterous* and *engrailed*, as shown.

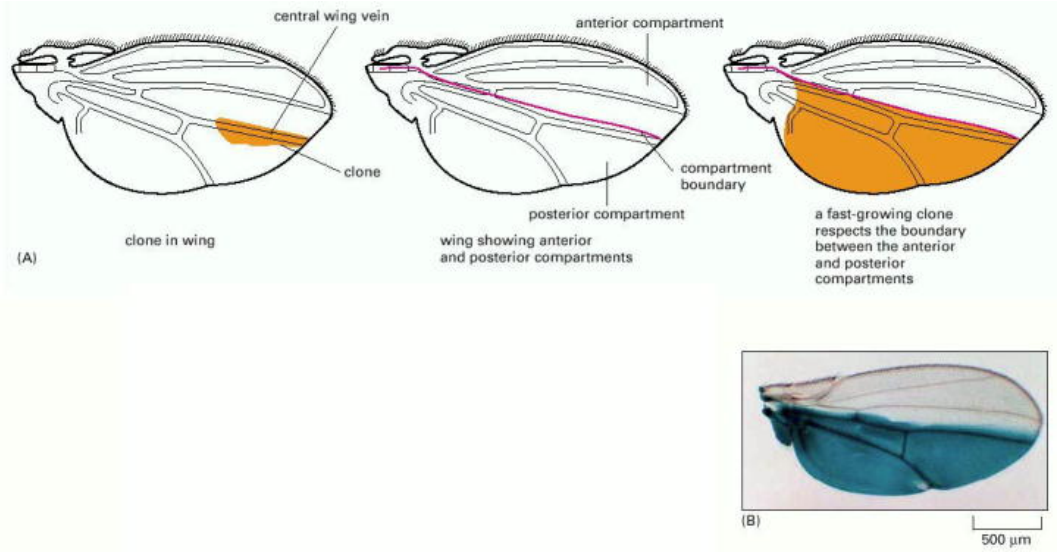

Figure 21-53. Compartments in the adult wing. (A) The shapes of marked clones in the *Drosophila* wing reveal the existence of a compartment boundary. The border of each marked clone is straight where it abuts the boundary. Even when a marked clone has been genetically altered so that it grows more rapidly than the rest of the wing and is therefore very large, it respects the boundary in the same way *(drawing on right).* Note that the compartment boundary does not coincide with the central wing vein. (B) The pattern of expression of the *engrailed* gene in the wing, revealed by the same technique as for the adult fly shown in Figure 21-40. The compartment boundary coincides with the boundary of *engrailed* gene expression. (A, after F.H.C. Crick and P.A. Lawrence, *Science* 189:340347, 1975. © AAAS; B, courtesy of Chihiro Hama and Tom Kornberg.)

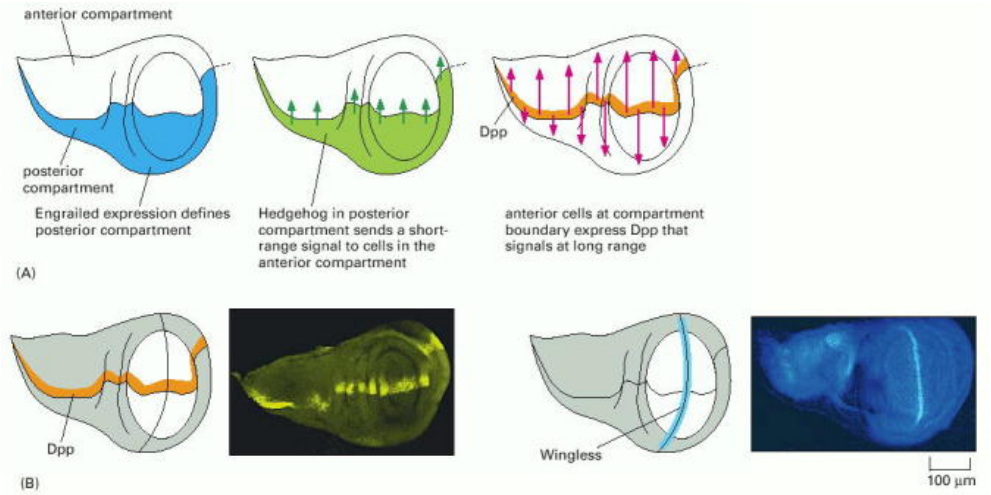

Figure 21-54. Morphogenetic signals created at compartment boundaries in the wing imaginal disc. (A) Creation of the Dpp signaling region at the anteroposterior compartment boundary through a Hedgehog-mediated interaction between the anterior and posterior cells. In an analogous way, a Notch-mediated interaction between dorsal and ventral cells creates a Wingless (Wnt) signaling region along the dorsoventral boundary. (B) The observed expression patterns of Dpp and Wingless. Although it seems clear that Dpp and Wingless act as morphogens, it is not yet certain whether they spread out from their source by simple diffusion through the extracellular medium or in some other way. Moreover, cells in the imaginal disc have been seen to send out long protrusions, called *cytonemes*, that may allow them to sense signals at a distance. Thus, the receiving cell may send its sensors to the source of the signal, instead of the signal moving to the receiving cell. (B, photographs courtesy of Sean Carroll and Scott Weatherbee, from S.J. Day and P.A. Lawrence, *Development* 127:29772987, 2000. © The Company of Biologists.)

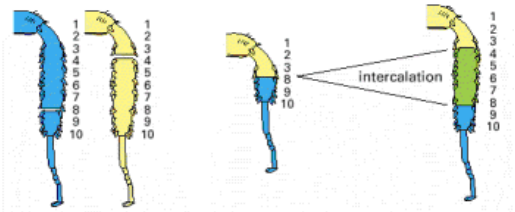

Figure 21-55. Intercalary regeneration. When mismatched portions of the growing cockroach leg are grafted together, new tissue *(green)* is intercalated (by cell proliferation) to fill in the gap in the pattern of leg structures, restoring a leg segment of normal size and pattern.

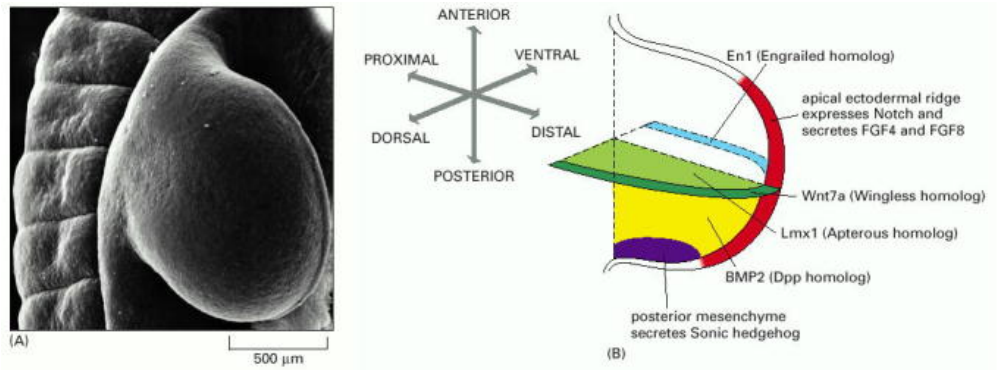

Figure 21-56. Molecules that control patterning in a vertebrate limb bud. (A) A wing bud of a chick embryo at 4 days of incubation. The scanning electron micrograph shows a dorsal view, with somites (the segments of the trunk of the embryo) visible to the *left*. At the distal margin of the limb bud a thickened ridge can just be seen - the apical ectodermal ridge. (B) Expression patterns of key signaling proteins and gene regulatory factors in the chick limb bud. The patterns are depicted schematically in two imaginary planes of section through the limb bud, one (horizontal) to show the dorsoventral system and the other (vertical) to show the anteroposterior and proximodistal systems. Sonic hedgehog, BMP2, and Lmx1 are expressed in the mesodermal core of the limb bud; the other molecules in the diagram are expressed in its epithelial covering. Almost all the molecules shown have homologs that are involved in patterning the *Drosophila* wing disc. (A, courtesy of Paul Martin.)

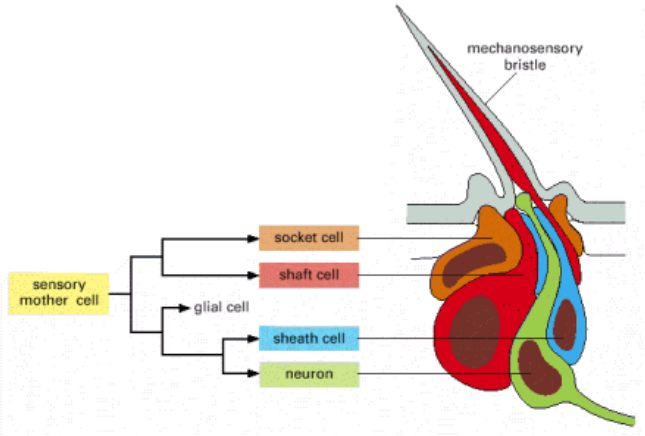

Figure 21-57. The basic structure of a mechanosensory bristle. The lineage of the four cells of the bristle - all descendants of a single sensory mother cell - is shown on the *left*.

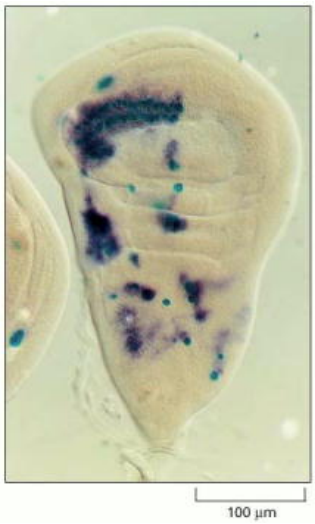

Figure 21-58. Sensory mother cells in the wing imaginal disc. The sensory mother cells *(blue* here) are easily revealed in this special strain of *Drosophila*, which contains an artificial *LacZ* reporter gene that, by chance, has inserted itself in the genome next to a control region that causes it to be expressed selectively in sensory mother cells. The *purple* stain shows the expression pattern of the *scute* gene; this foreshadows the production of sensory mother cells and fades as the sensory mother cells successively develop. (From P. Cubas et al., *Genes Dev.* 5:9961008, 1991. © Cold Spring Harbor Press.)

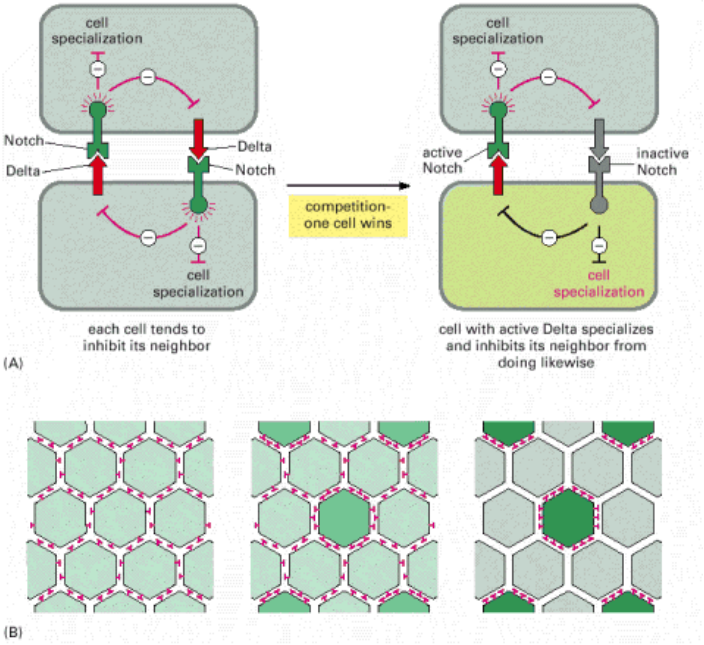

Figure 21-59. Lateral inhibition. (A) The basic mechanism of Notch-mediated competitive lateral inhibition, illustrated for just two interacting cells. In this diagram, the absence of color on proteins or effector lines indicates inactivity. (B) The outcome of the same process operating in a larger patch of cells. At first, all cells in the patch are equivalent, expressing both the transmembrane receptor Notch and its transmembrane ligand Delta. Each cell has a tendency to specialize (as a sensory mother cell), and each sends an inhibitory signal to its neighbors to discourage them from also specializing in that way. This creates a competitive situation. As soon as an individual cell gains any advantage in the competition, that advantage becomes magnified. The winning cell, as it becomes more strongly committed to differentiating as a sensory mother, also inhibits its neighbors more strongly. Conversely, as these neighbors lose their capacity to differentiate as sensory mothers they also lose their capacity to inhibit other cells from doing so. Lateral inhibition thus makes adjacent cells follow different fates. Although the interaction is thought to be normally dependent on cell-cell contacts, the future sensory mother cell may be able to deliver an inhibitory signal to cells that are more than one cell diameter away - for example, by sending out long protrusions to touch them.

Figure 21-60. The result of switching off lateral inhibition during the singling-out of sensory mother cells. The photograph shows part of the thorax of a fly containing a mutant patch in which the neurogenic gene *Delta* has been partially inactivated. The reduction of lateral inhibition has caused almost all the cells in the mutant patch *(in the center of the picture)* to develop as sensory mother cells, producing a great excess of sensory bristles there. Mutant patches of cells carrying more extreme mutations in the Notch pathway, causing a total loss of lateral inhibition, form no visible bristles because all of the progeny of the sensory mother cells develop as neurons or glial cells instead of diversifying to form both neurons and the external parts of the bristle structure. (Courtesy of P. Heitzler and P. Simpson, *Cell* 64:10831093, 1991. © Elsevier.)

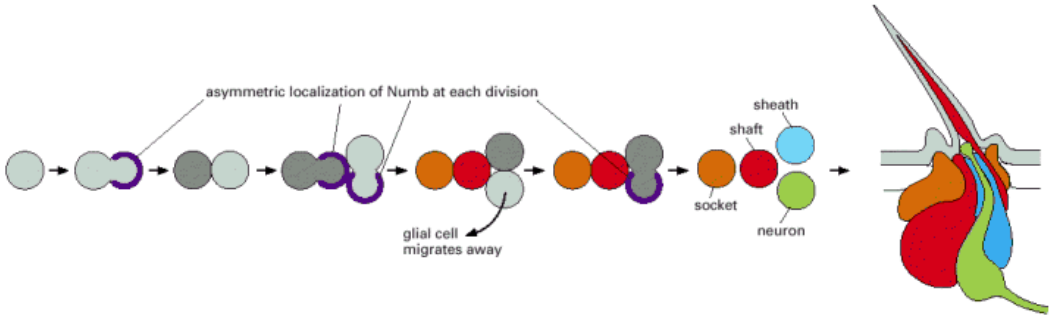

Figure 21-61. Numb biases lateral inhibition during bristle development. At each division of the progeny of the sensory mother cell, Numb protein is asymmetrically localized, producing daughter cells that differ. Note that some of the divisions are oriented with the mitotic spindle in the plane of the epithelium, others at right angles to it; the localization of Numb is controlled in different ways at these different types of division but plays a critical role at each of them in deciding cell fate. (Based on data from M. Gho, Y. Bellaiche, and F. Schweisguth, *Development* 126:35733584, 1999.)

Figure 21-62. Planar cell polarity manifest in bristle polarity on a fly's back: the bristles all point backwards. (Scanning electron micrograph courtesy of S. Oldham and E. Hafen, from E. Spana and N. Perrimon, *Trends Genet.* 15:301302, 1999. © Elsevier.)

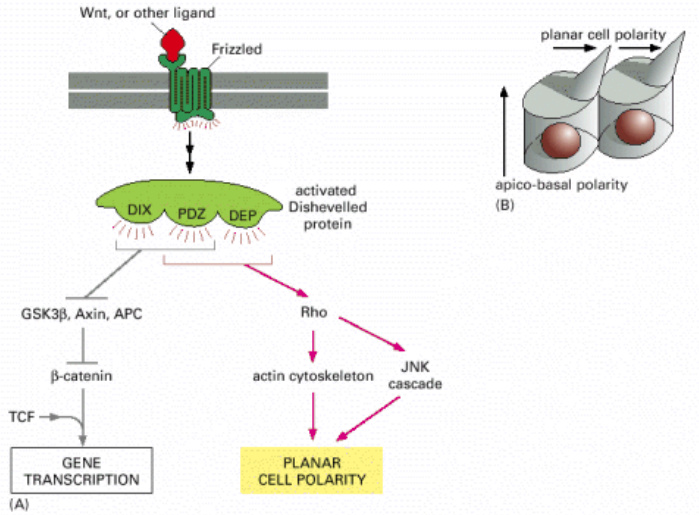

Figure 21-63. The control of planar cell polarity. (A) The two branches of the Wnt/Frizzled signaling pathway. The main branch, discussed in Chapter 15, controls gene expression via β-catenin; the planar-polarity branch controls the actin cytoskeleton via Rho GTPases. Different domains of the Dishevelled protein are responsible for the two effects. It is not yet clear which member of the Wnt signal protein family, if any, is responsible for activating the planar polarity function of Frizzled in *Drosophila*. (B) Cartoon of cells displaying planar polarity. In at least some systems, planar cell polarity is associated with asymmetric localization of the receptor Frizzled itself to one side of each cell.

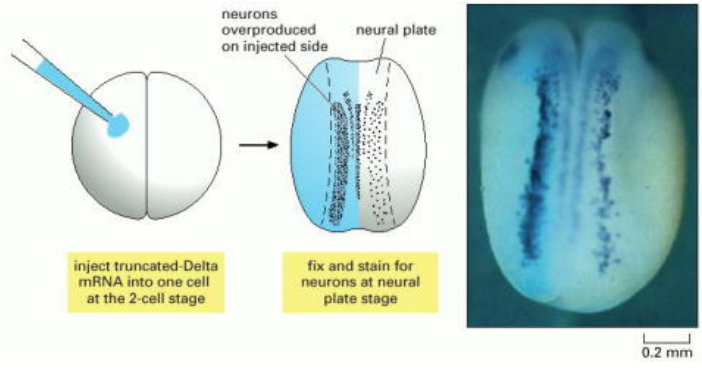

Figure 21-64. Effects of blocking Notch signaling in a *Xenopus* embryo. In the experiment shown, mRNA coding for a truncated form of the Notch ligand Delta is injected, together with *LacZ* mRNA as a marker, into one cell of an embryo at the two-cell stage. The truncated Delta protein produced from the mRNA blocks Notch signaling in the cells descended from the cell that received the injection. These cells lie on the *left* side of the embryo and are identifiable because they contain LacZ protein *(blue* stain) as well as the truncated Delta protein. The *right* side of the embryo is unaffected and serves as a control. The embryo is fixed and stained at a stage when the central nervous system has not yet rolled up to form a neural tube, but is still a more or less flat plate of cells - the neural plate - exposed on the surface of the embryo. The first neurons (stained *purple* in the photograph) have already begun to differentiate in elongated bands (proneural regions) on each side of the midline. On the control *(right)* side, they are a scattered subset of the proneural cell population. On the Notch-blocked *(left)* side, virtually all the cells in the proneural regions have differentiated as neurons, creating a densely stained band of neurons without intervening cells. Injections of mRNA coding for normal, functional Delta have an opposite effect, reducing the number of cells that differentiate as neurons. (Photograph from A. Chitnis et al., *Nature* 375:761766, 1995. © Macmillan Magazines Ltd.)

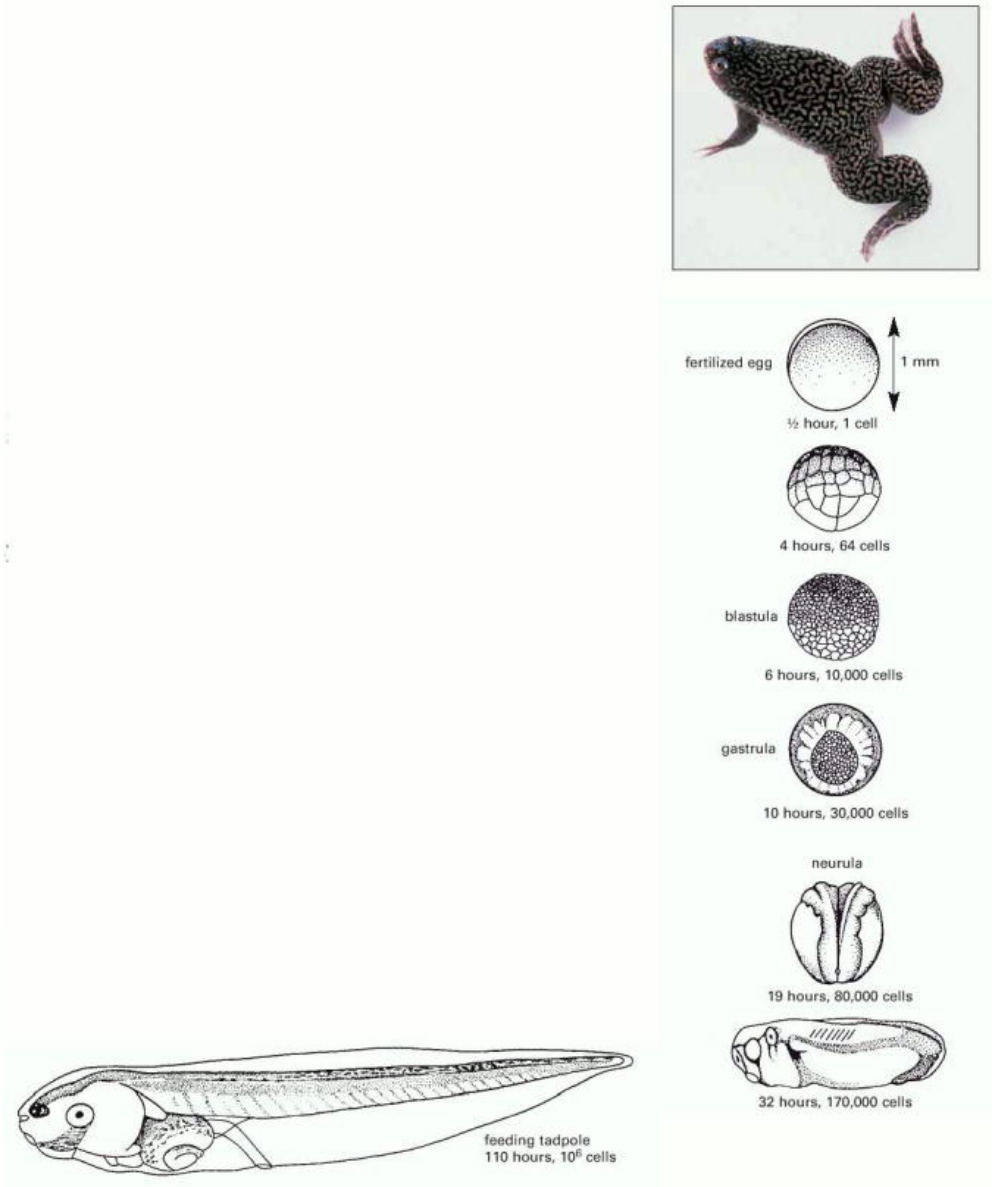

Figure 21-65. Synopsis of the development of Xenopus laevis from newly fertilized egg to feeding tadpole. The adult frog is shown in the photograph at the *top*. The developmental stages are viewed from the *side*, except for the 10-hour and 19-hour embryos, which are viewed from *below* and from *above*, respectively. All stages except the adult are shown at the same scale. (Photograph courtesy of Jonathan Slack; drawings after P.D. Nieuwkoop and J. Faber, Normal Table of *Xenopus laevis* [Daudin]. Amsterdam: North-Holland, 1956.)

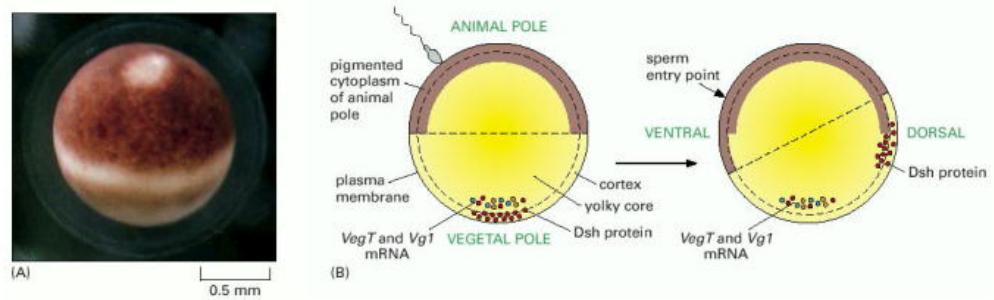

Figure 21-66. The *Xenopus* egg and its asymmetries. (A) Side view of an egg photographed just before fertilization. (B) The asymmetric distribution of molecules inside the egg, and how this changes following fertilization so as to define a dorsoventral as well as an animal-vegetal asymmetry. *Vg1* (not to be confused with *VegT)* codes for a member of the TGFβ protein superfamily. Fertilization triggers two types of intracellular movement, both dependent on microtubules: (1) a rotation of the egg cortex (a layer a few μm deep) through about 30° relative to the core of the egg in a direction determined by the site of sperm entry; and (2) active transport of Dishevelled (Dsh) protein, a component of the Wnt signaling pathway, toward the future dorsal side. The resulting dorsal concentration of Dishevelled protein defines the dorsoventral polarity of the future embryo. (A, courtesy of Tony Mills.)

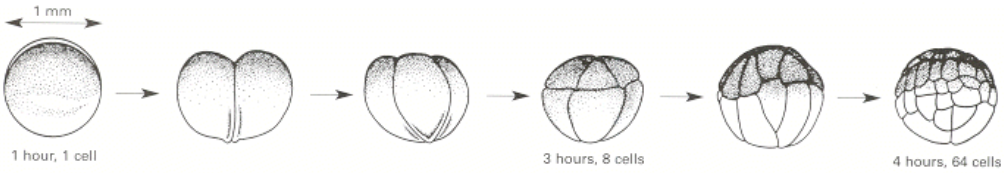

Figure 21-67. The stages of cleavage in *Xenopus*. The cleavage divisions rapidly subdivide the egg into many smaller cells. All the cells divide synchronously for the first 12 cleavages, but the divisions are asymmetric, so that the lower, vegetal cells, encumbered with yolk, are fewer and larger.

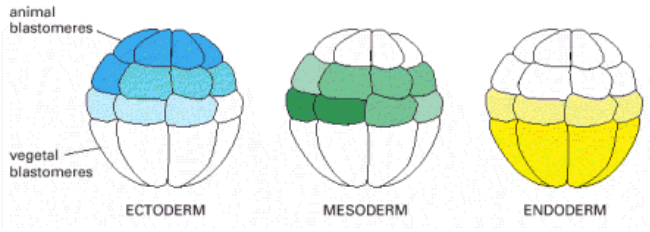

Figure 21-68. The origins of the three germ layers can be traced back to distinct blastomeres of the embryo in its early cleavage stages. The endoderm derives from the most vegetal blastomeres, the ectoderm from the most animal, and the mesoderm from a middle set that contribute also to endoderm and ectoderm. The coloring in each picture is the more intense, the higher the proportion of cell progeny that will contribute to the given germ layer. (After L. Dale, *Curr. Biol.* 9:R812R815, 1999.)

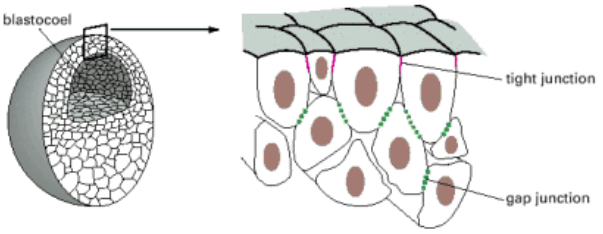

Figure 21-69. The blastula. In the outermost regions of the embryo, tight junctions between the blastomeres begin to create an epithelial sheet that isolates the interior of the embryo from the external medium. Na^+ is pumped across this sheet into the spaces in the interior of the embryo, and water follows into these spaces because of the resulting osmotic pressure gradient. As a result, the intercellular crevices inside the embryo enlarge to form a single cavity, the *blastocoel*. In *Xenopus* the wall of the blastocoel is several cells thick, and only the outermost cells are tightly bound together as an epithelium.

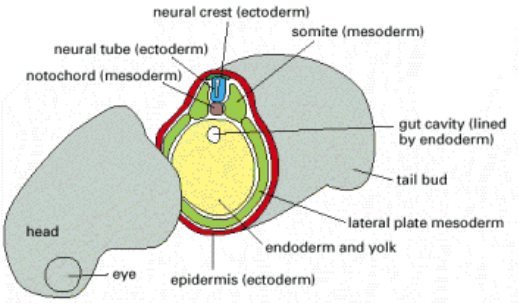

Figure 21-70. A cross section through the trunk of an amphibian embryo after the end of gastrulation, showing the arrangement of endodermal, mesodermal and ectodermal tissues. The endoderm will form the epithelial lining of the gut, from the mouth to the anus. It gives rise not only to the pharynx, esophagus, stomach, and intestines, but also to many associated glands. The salivary glands, the liver, the pancreas, the trachea, and the lungs, for example, all develop from extensions of the wall of the originally simple digestive tract and grow to become systems of branching tubes that open into the gut or pharynx. The endoderm forms only the epithelial components of these structures - the lining of the gut and the secretory cells of the pancreas, for example. The supporting muscular and fibrous elements arise from the mesoderm. The mesoderm gives rise to the connective tissues - at first to the loose, space-filling, three-dimensional mesh of cells in the embryo known as mesenchyme and ultimately to cartilage, bone, and fibrous tissue, including the dermis (the inner layer of the skin). The mesoderm also forms the muscles, the entire vascular system - including the heart, the blood vessels, and the blood cells - and the tubules, ducts, and supporting tissues of the kidneys and gonads. The ectoderm will form the epidermis (the outer, epithelial layer of the skin) and epidermal appendages such as hair, sweat glands, and mammary glands. It will also give rise to the whole of the nervous system, central and peripheral, including not only neurons and glia but also the sensory cells of the nose, the ear, the eye, and other sense organs. (After T. Mohun et al., *Cell* 22:915, 1980.)

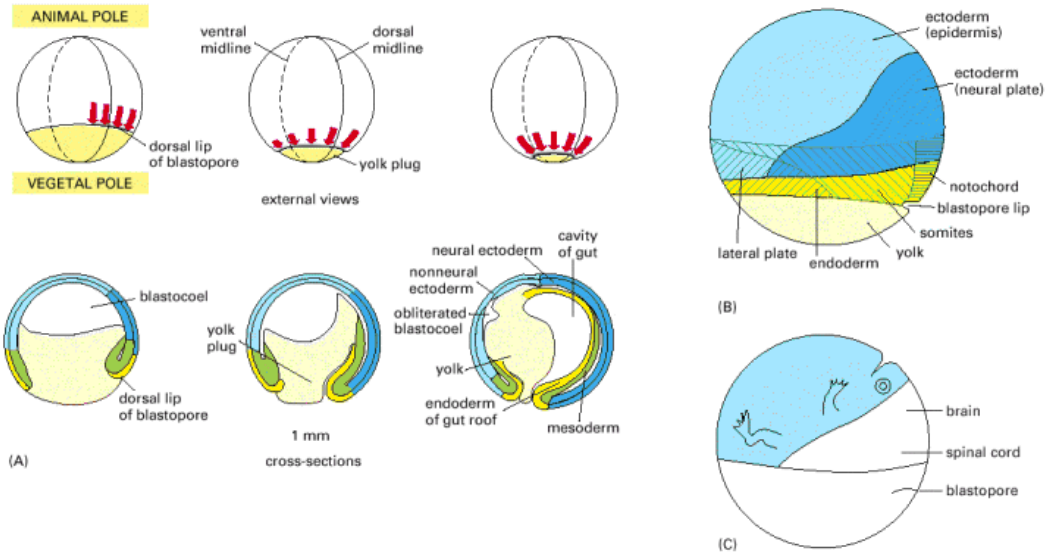

Figure 21-71. Gastrulation in *Xenopus*. (A) The external views *(above)* show the embryo as a semitransparent object, seen from the side; with the directions of cell movement indicated by *red arrows*, cross sections *(below)* are cut in the median plane (the plane of the dorsal and ventral midlines). Gastrulation begins when a short indentation, the beginning of the blastopore, becomes visible in the exterior of the blastula. This indentation gradually extends, curving around to form a complete circle surrounding a plug of very yolky cells (destined to be enclosed in the gut and digested). Sheets of cells meanwhile turn in around the lip of the blastopore and move deep into the interior of the embryo. At the same time the external epithelium in the region of the animal pole actively spreads to take the place of the cell sheets that have turned inward. Eventually, the epithelium of the animal hemisphere spreads in this way to cover the whole external surface of the embryo, and, as gastrulation reaches completion, the blastopore circle shrinks almost to a point. (B) A fate map for the early *Xenopus* embryo (viewed from the side) as it begins gastrulation, showing the origins of the cells that will come to form the three germ layers as a result of the movements of gastrulation. The various parts of the mesoderm (lateral plate, somites, and notochord) derive from deep-lying cells that segregate from the epithelium in the cross-hatched region. The other cells, including the more superficial cells in the cross-hatched region, will give rise to ectoderm *(blue, above)* or endoderm *(yellow, below)*. Roughly speaking, the first cells to turn into the interior, or *involute*, will move forward inside the embryo to form the most anterior endodermal and mesodermal structures, while the last to involute will form the most posterior structures. (C) Cartoon to show how the different regions of the ectoderm map into the body surface of the adult animal. (After R.E. Keller, *J. Exp. Zool.* 216:81101, 1981 and *Dev. Biol.* 42:222241, 1975.)

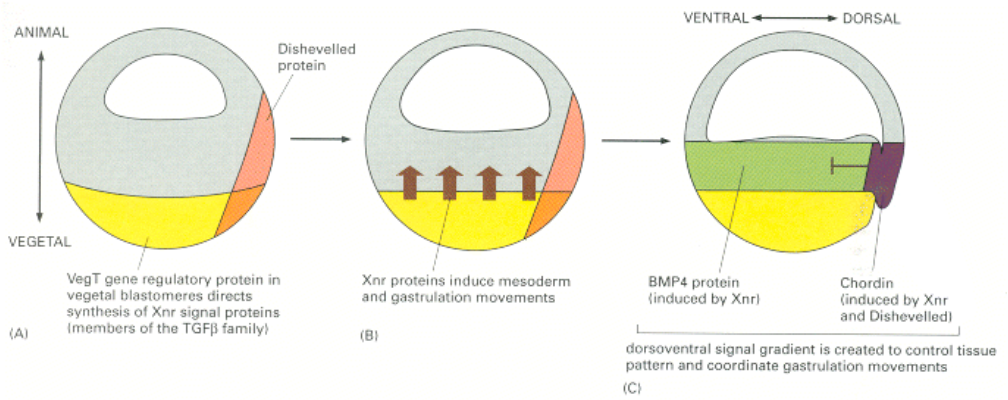

Figure 21-72. A current view of the main inductive signals organizing the events of gastrulation. (A) The distribution of axis-determining molecules in the blastula results from inheritance of different parts of the cytoplasm of the fertilized frog egg. The VegT gene regulatory protein in the vegetal blastomeres is translated from VegT mRNA that was localized at the vegetal pole before fertilization. The Dishevelled protein on the future dorsal side is localized there as a result of the cortical rotation that follows fertilization (see Figure 21-66). (B) Signaling from the vegetal cells to the cells just above them, mediated by Xnr *(Xenopus* nodal-related) proteins and other members of the TGFβ superfamily, induces formation of a band of mesoderm in the middle part of the embryo. (C) A morphogen gradient that organizes the dorsoventral axis is set up by a combination of BMP4 (another TGFβ superfamily member) secreted by the mesoderm, and BMP4 antagonists, including chordin, secreted by the cells at the dorsal lip of the blastopore.

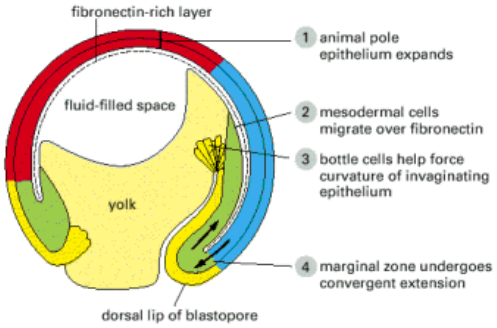

Figure 21-73. Cell movements in gastrulation. A section through a gastrulating *Xenopus* embryo, cut in the same plane as in Figure 21-71, indicating the four main types of movement that gastrulation involves. The animal pole epithelium expands by cell rearrangement, becoming thinner as it spreads. Migration of mesodermal cells over a fibronectin-rich matrix lining the roof of the blastocoel may help to pull the invaginated tissues forward. But the main driving force for gastrulation in *Xenopus* is convergent extension in the marginal zone. (After R.E. Keller, *J. Exp. Zool.* 216:81101, 1981.)

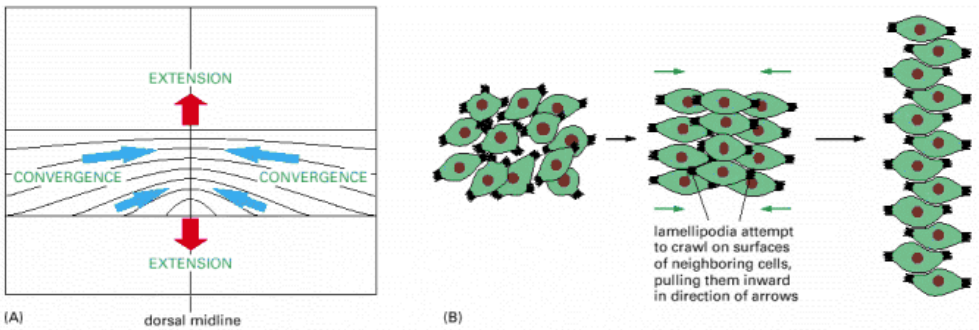

Figure 21-74. Convergent extension and its cellular basis. (A) The pattern of convergent extension in the marginal zone of a gastrula as viewed from the dorsal aspect. *Blue arrows* represent convergence toward the dorsal midline, *red arrows* represent extension of the anteroposterior axis. The simplified diagram does not attempt to show the accompanying movement of involution, whereby the cells are tucking into the interior of the embryo. (B) Schematic diagram of the cell behavior that underlies convergent extension. The cells form lamellipodia, with which they attempt to crawl over one another. Alignment of the lamellipodial movements along a common axis leads to convergent extension. The process depends on the Frizzled/Dishevelled polarity-signaling pathway and is presumably cooperative because cells that are already aligned exert forces that tend to align their neighbors in the same way. (B, after J. Shih and R. Keller, *Development* 116:901914, 1992.)

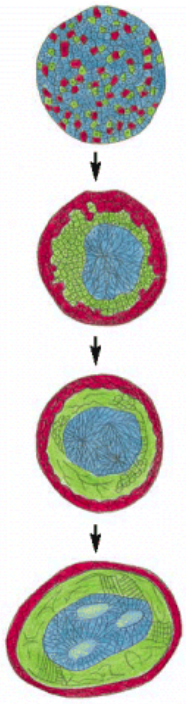

Figure 21-75. Sorting out. Cells from different parts of an early amphibian embryo will sort out according to their origins. In the classical experiment shown here, mesoderm cells *(green)*, neural plate cells *(blue)*, and epidermal cells *(red)* have been disaggregated and then reaggregated in a random mixture. They sort out into an arrangement reminiscent of a normal embryo, with a "neural tube" internally, epidermis externally, and mesoderm in between. (Modified from P.L. Townes and J. Holtfreter, *J. Exp. Zool.* 128:53120, 1955.)

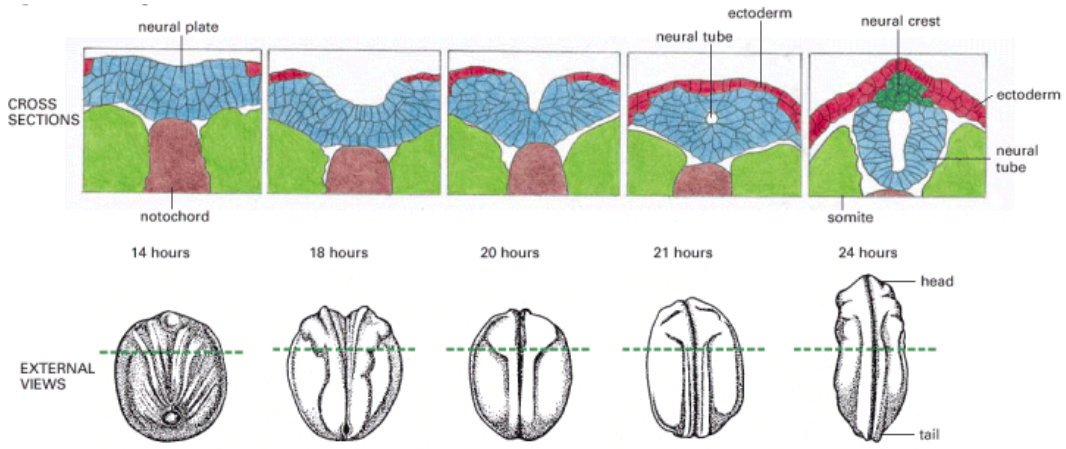

Figure 21-76. Neural tube formation in *Xenopus*. The external views are from the dorsal aspect. The cross sections are cut in a plane indicated by the *broken lines*. (After T.E. Schroeder, *J. Embryol. Exp. Morphol.* 23:427462, 1970. © The Company of Biologists.)

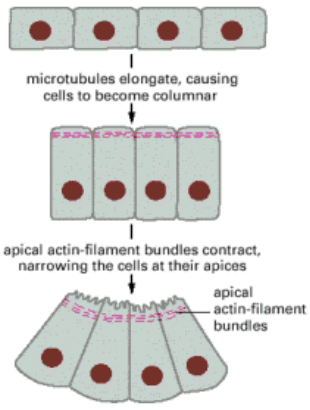

Figure 21-77. The bending of an epithelium through cell shape changes mediated by microtubules and actin filaments. The diagram is based on observations of neurulation in newts and salamanders, where the epithelium is only one cell layer thick. As the apical ends of the cells become narrower, their upper-surface membrane becomes puckered.

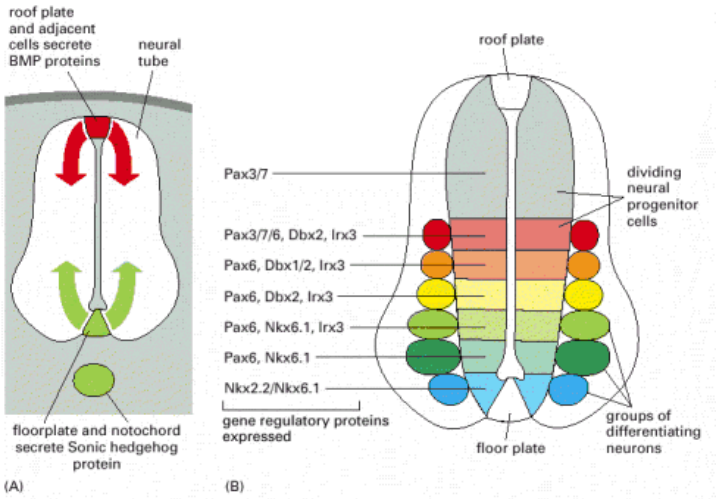

Figure 21-94. A schematic cross section of the spinal cord of a chick embryo, showing how cells at different levels along the dorsoventral axis express different gene regulatory proteins. (A) Signals that direct the dorsoventral pattern: Sonic hedgehog protein from the notochord and the floor plate (the ventral midline of the neural tube) and BMP proteins from the roof plate (the dorsal midline) act as morphogens to control gene expression. (B) The resulting patterns of gene expression in the ventral part of the developing spinal cord. Different groups of proliferating neural progenitor cells (in the *ventricular zone*, close to the lumen of the neural tube) and of differentiating neurons (in the *mantle zone*, further out) express different combinations of gene regulatory proteins. Those indicated in this diagram are almost all members of the homeodomain superfamily; various other genes of the same superfamily (including Islet/Lim proteins) are expressed in the differentiating neurons. Neurons expressing different gene regulatory proteins will form connections with different partners and may make different combinations of neurotransmitters and receptors.

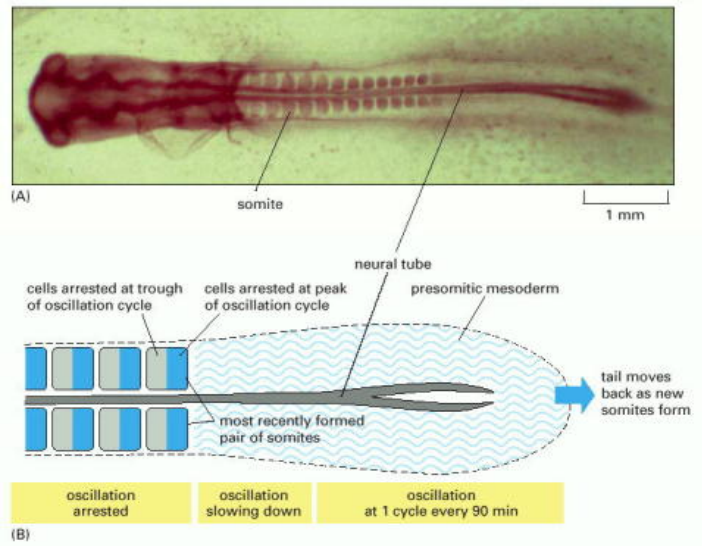

Figure 21-78. Somite formation in the chick embryo. (A) A chick embryo at 40 hours of incubation. (B) How the temporal oscillation of *c-hairy-1* expression in the presomitic mesoderm becomes converted into a spatial pattern of gene expression in the formed somites. In the posterior part of the presomitic mesoderm, each cell oscillates with a cycle time of 90 minutes. As cells mature and emerge from the presomitic region, their oscillation is gradually slowed down and finally brought to a halt in whatever phase of the cycle they happen to be in at the critical moment. In this way, a temporal oscillation of gene expression traces out an alternating spatial pattern. (A, from Y.J. Jiang, L. Smithers and J. Lewis, *Curr. Biol.* 8:868871, 1998. © Elsevier.)

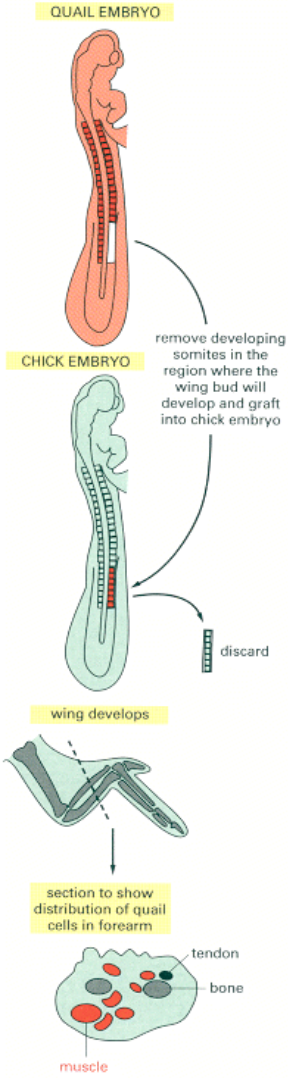

Figure 21-79. The migratory origin of limb muscle cells. The migrations can be traced by grafting cells from a quail embryo into a chick embryo; the two species are very similar in their development, but the quail cells are recognizable by the distinctive appearance of their nucleoli. If quail somite cells are substituted for the somite cells of a chick embryo at 2 days of incubation and the wing of the chick is sectioned a week later, it is found that the muscle cells in the chick wing derive from the transplanted quail somites.

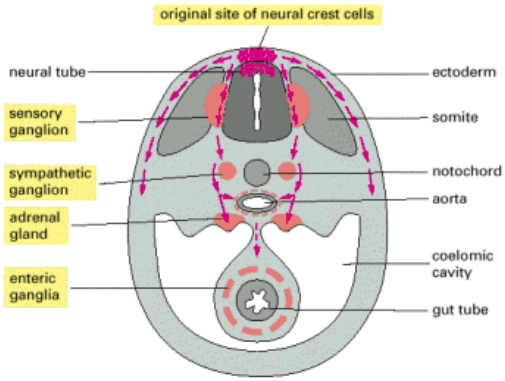

Figure 21-80. The main pathways of neural crest cell migration. A chick embryo is shown in a schematic cross-section through the middle part of the trunk. The cells that take the pathway just beneath the ectoderm will form pigment cells of the skin; those that take the deep pathway via the somites will form the neurons and glial cells of sensory and sympathetic ganglia, and parts of the adrenal gland. The neurons and glial cells of the enteric ganglia, in the wall of the gut, are formed from neural crest cells that migrate along the length of the body, originating from either the neck region or the sacral region. In *Drosophila*, neurons in the wall of the gut originate in a similar way, by migration from the head end of the embryo. (See also Figure 19-23.)

Figure 21-81. Effect of mutations in the *kit* gene. Both the baby and the mouse are heterozygous for a loss-of-function mutation that leaves them with only half the normal quantity of *kit* gene product. In both cases pigmentation is defective because pigment cells depend on the *kit* product as a receptor for a survival factor. (Courtesy of R.A. Fleischman, from *Proc. Natl. Acad. Sci. USA* 88:1088510889, 1991. © National Academy of Sciences.)

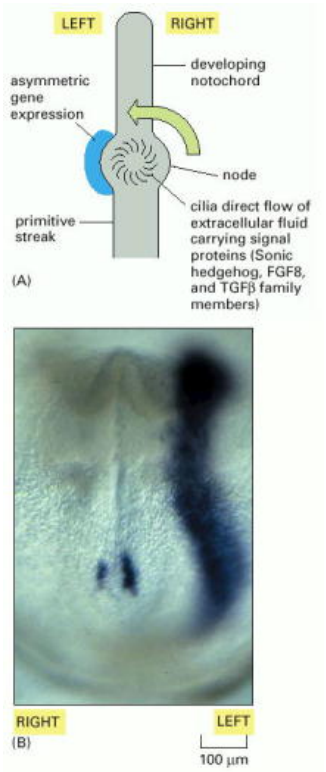

Figure 21-82. Helical beating of cilia at the node, and the origins of left-right asymmetry. (A) The beating of the cilia drives a current towards one side of the node. Various signal proteins are produced in this neighborhood, and the current is thought to sweep them toward one side, provoking asymmetric expression of several genes, including the genes that code for the signal proteins themselves. (B) The asymmetric expression pattern of one such signal protein - a member of the TGFβ superfamily called Nodal - in the neighborhood of the node (lower two *blue* spots) in a mouse embryo at 8 days of gestation, as shown by *in situ* hybridization. At this stage, the asymmetry has already been relayed outward to the lateral plate mesoderm, where Nodal is expressed on the left side (large elongated *blue* patch) but not the right. Note that the embryo is viewed from its ventral side, so that its left appears on the right of the photograph. (B, courtesy of Elizabeth Robertson.)

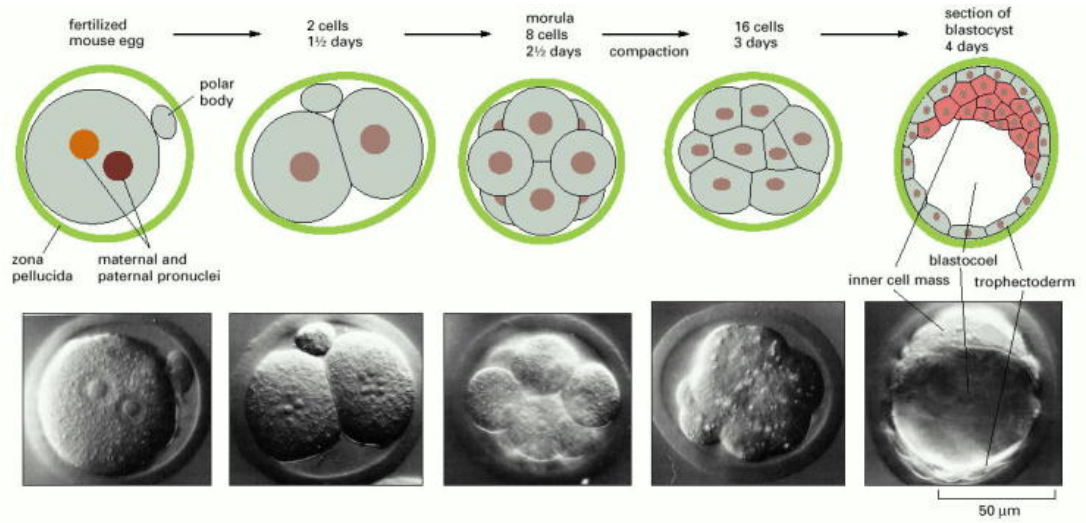

Figure 21-83. The early stages of mouse development. The zona pellucida is a jelly capsule from which the embryo escapes after a few days, allowing it to implant in the wall of the uterus. (Photographs courtesy of Patricia Calarco.)

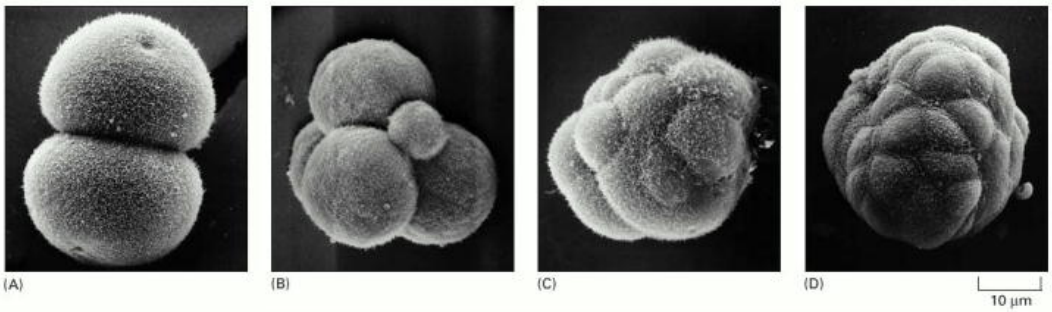

Figure 21-84. Scanning electron micrographs of the early mouse embryo. The zona pellucida has been removed. (A) Two-cell stage. (B) Four-cell stage (a polar body is visible in addition to the four blastomeres - see Figure 20-22). (C) Eight-to-sixteen-cell morula - compaction occurring. (D) Blastocyst. (A-C, courtesy of Patricia Calarco; D, from P. Calarco and C.J. Epstein, *Dev. Biol.* 32:208213, 1973. © Academic Press.)

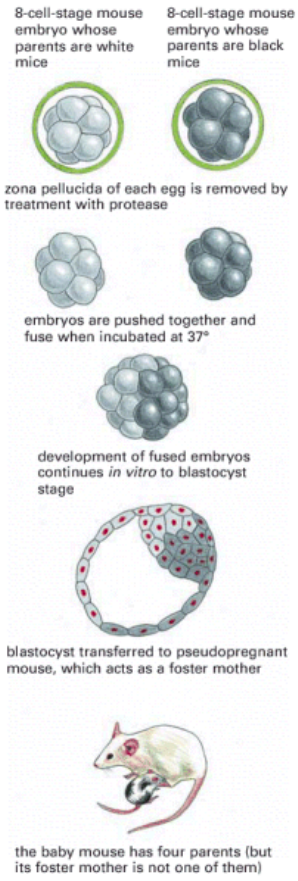

Figure 21-85. A procedure for creating a chimeric mouse. Two morulae of different genotypes are combined.

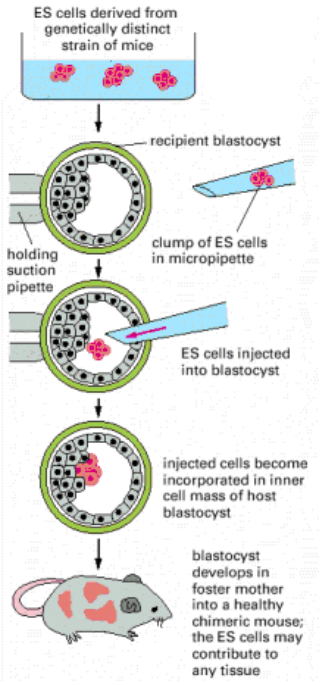

Figure 21-86. Making a chimeric mouse with ES cells. The cultured ES cells can combine with the cells of a normal blastocyst to form a healthy chimeric mouse, and can contribute to any of its tissues, including the germ line. Thus the ES cells are totipotent.

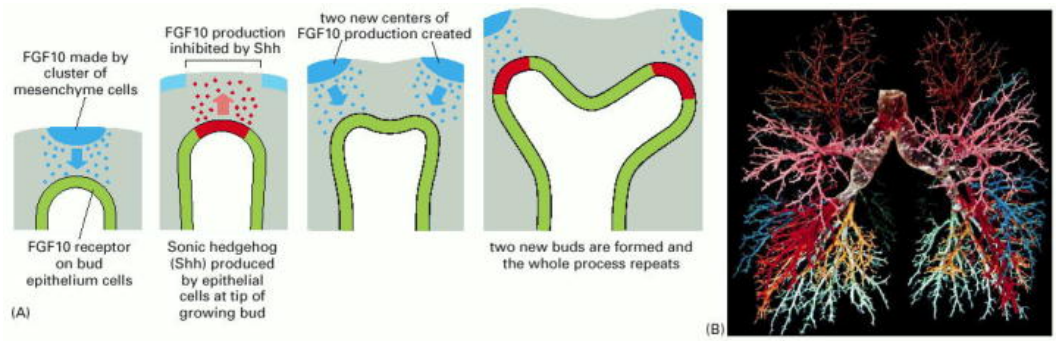

Figure 21-87. Branching morphogenesis of the lung. (A) How FGF10 and Sonic hedgehog are thought to induce the growth and branching of the buds of the bronchial tree. Many other signal molecules, such as BMP4, are also expressed in this system, and the suggested branching mechanism is only one of several possibilities. (B) A cast of the adult human bronchial tree, prepared by injecting resin into the airways; resins of different colors have been injected into different branches of the tree. (B, from R. Warwick and P.L. Williams, Gray's Anatomy, 35th edn. Edinburgh: Longman, 1973.)

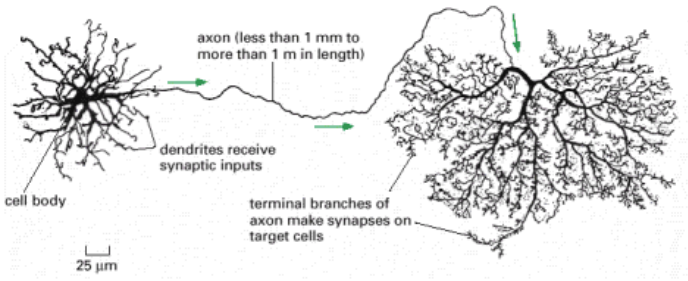

Figure 21-88. A typical neuron of a vertebrate. The *arrows* indicate the direction in which signals are conveyed. The neuron shown is from the retina of a monkey. The longest and largest neurons in a human extend for about 1 million µm and have an axon diameter of 15 µm. (Drawing of neuron from B.B. Boycott, in Essays on the Nervous System [R. Bellairs and E.G. Gray, eds.]. Oxford, UK: Clarendon Press, 1974.)

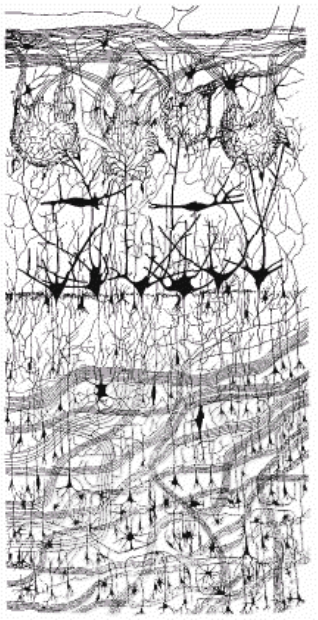

Figure 21-89. The complex organization of nerve cell connections. This drawing depicts a section through a small part of a mammalian brain - the olfactory bulb of a dog, stained by the Golgi technique. The *black* objects are neurons; the *thin lines* are axons and dendrites, through which the various sets of neurons are interconnected according to precise rules. (From C. Golgi, *Riv. sper. freniat. Reggio-Emilia* 1:405425, 1875; reproduced in M. Jacobson, Developmental Neurobiology, 3rd edn. New York: Plenum, 1992.)

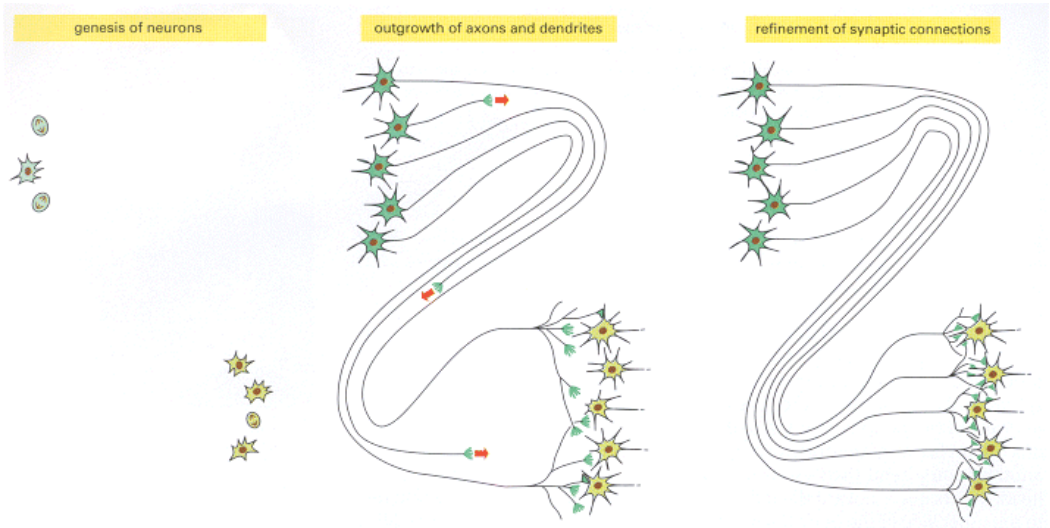

Figure 21-90. The three phases of neural development.

Figure 21-91. Diagram of a 2-day chick embryo, showing the origins of the nervous system. The neural tube *(light green)* has already closed, except at the tail end, and lies internally, beneath the ectoderm, of which it was originally a part (see Figure 21-76). The neural crest *(red)* lies dorsally just beneath the ectoderm, in or above the roof of the neural tube. In addition, thickenings, or *placodes (dark green)*, in the ectoderm of the head give rise to some of the sensory transducer cells and neurons of that region, including those of the ear and the nose. The cells of the retina of the eye, by contrast, originate as part of the neural tube.

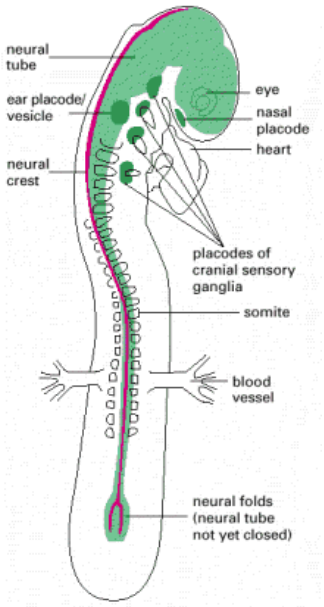

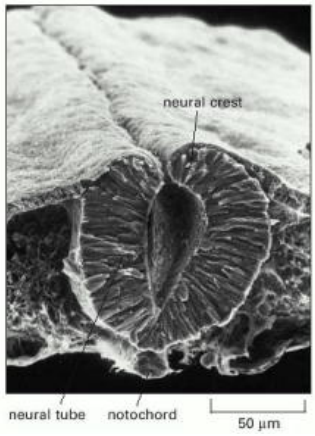

Figure 21-92. Formation of the neural tube. The scanning electron micrograph shows a cross section through the trunk of a 2-day chick embryo. The neural tube is about to close and pinch off from the ectoderm; at this stage it consists (in the chick) of an epithelium that is only one cell thick. (Courtesy of J.P. Revel and S. Brown.)

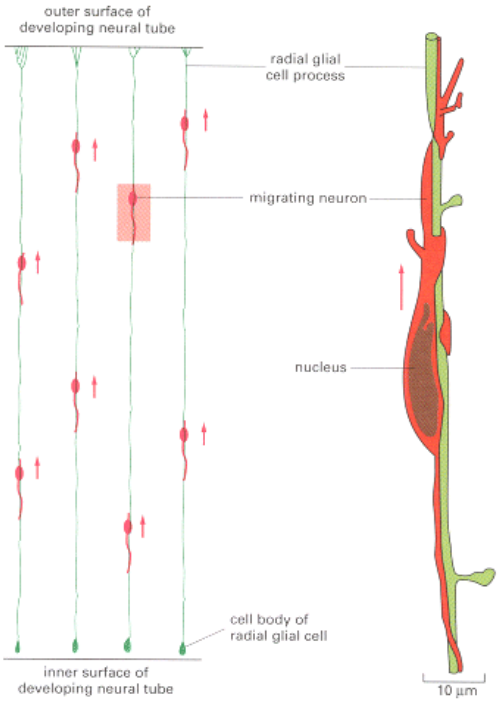

Figure 21-93. Migration of immature neurons. Before sending out axons and dendrites, newborn neurons often migrate from their birthplace and settle in some other location. The diagrams are based on reconstructions from sections of the cerebral cortex of a monkey (part of the neural tube). The neurons go through their final cell division close to the inner, luminal face of the neural tube and then migrate outward by crawling along *radial glial cells*. Each of these cells extends from the inner to the outer surface of the tube, a distance that may be as much as 2 cm in the cerebral cortex of the developing brain of a primate. The radial glial cells can be considered as persisting cells of the original columnar epithelium of the neural tube that become extraordinarily stretched as the wall of the tube thickens. (After P. Raki´c, *J. Comp. Neurol.* 145:6184, 1972.)

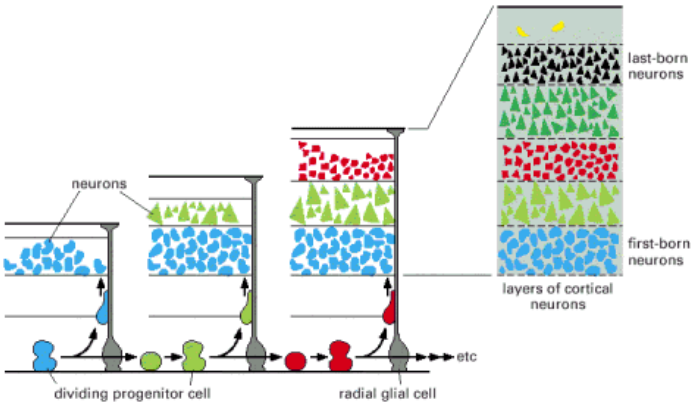

Figure 21-95. Programmed production of different types of neurons at different times from dividing progenitors in the cerebral cortex of the brain of a mammal. Close to one face of the cortical neuroepithelium, progenitor cells divide repeatedly, in stem-cell fashion, to produce neurons. The neurons migrate out toward the opposite face of the epithelium by crawling along the surfaces of radial glial cells, as shown in Figure 21-93. The first-born neurons settle closest to their birthplace, while neurons born later crawl past them to settle farther out. Successive generations of neurons thus occupy different layers in the cortex and have different intrinsic characters according to their birth dates.

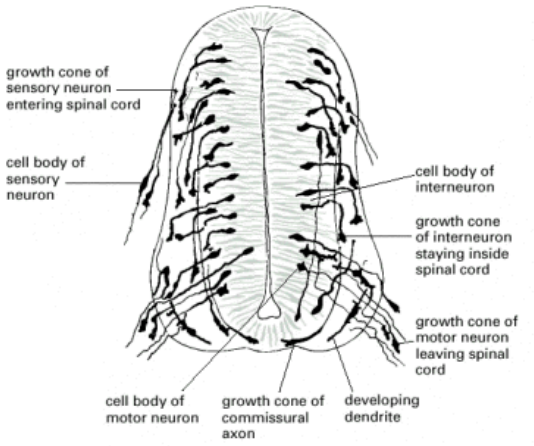

Figure 21-96. Growing axons in the developing spinal cord of a 3-day chick embryo. The drawing shows a cross section stained by the Golgi technique. Most of the neurons, apparently, have as yet only one elongated process - the future axon. An irregularly shaped expansion - a growth cone - is seen at the growing tip of each axon. The growth cones of the motor neurons emerge from the spinal cord (to make their way toward muscles), those of the sensory neurons grow into it from outside (where their cell bodies lie), and those of the interneurons remain inside the spinal cord . Many of the interneurons send their axons down toward the floor plate to cross to the other side of the spinal cord; these axons are called *commissural*. At this early stage, many of the embryonic spinal-cord cells (in the regions shaded *gray)* are still proliferating and have not yet begun to differentiate as neurons or glial cells. (From S. Ramón y Cajal, Histologie du Système Nerveux de l'Homme et des Vertébrés, 19091911. Paris: Maloine; reprinted, Madrid: C.S.I.C., 1972.)

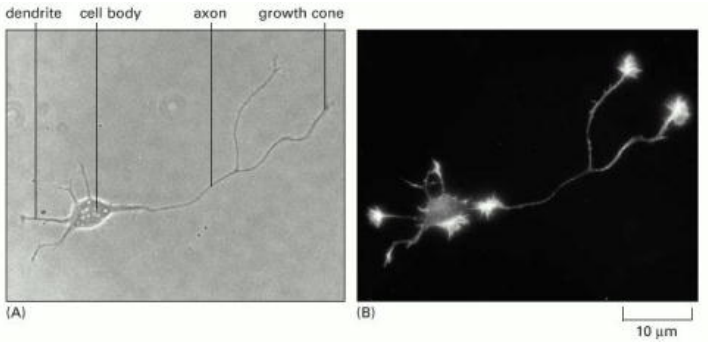

Figure 21-97. Formation of axon and dendrites in culture. A young neuron has been isolated from the brain of a mammal and put to develop in culture, where it sends out processes. One of these processes, the future axon, has begun to grow out faster than the rest (the future dendrites) and has bifurcated. (A) A phase-contrast picture; (B) the pattern of staining with fluorescent phalloidin, which binds to filamentous actin. Actin is concentrated in the growth cones at the tips of the processes that are actively extending and at some other sites of lamellipodial activity. (Courtesy of Kimberly Goslin.)

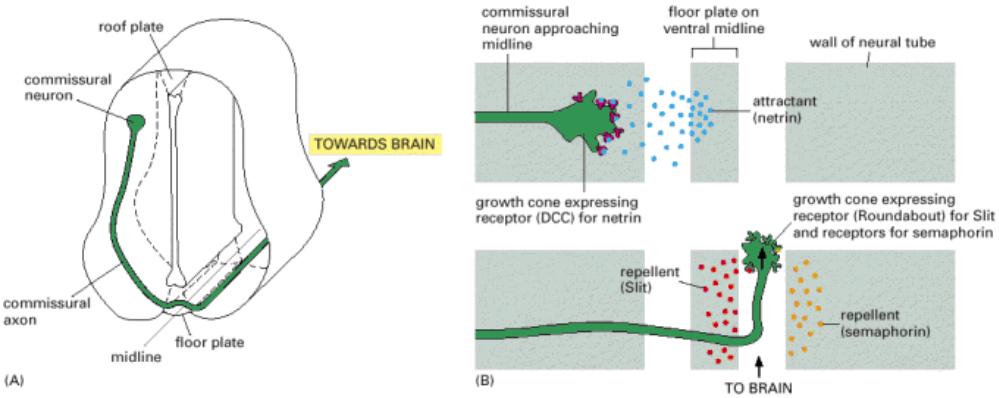

Figure 21-98. The guidance of commissural axons. (A) The pathway taken by commissural axons in the embryonic spinal cord of a vertebrate. (B) The signals that guide them. The growth cones are first attracted to the floorplate by netrin, which is secreted by the floor-plate cells and acts on the receptor DCC in the axonal membrane. As they cross the floor plate, the growth cones upregulate their expression of Roundabout, the receptor for a repellent protein, Slit, that is also secreted by the floor plate. Slit, binding to Roundabout, not only acts as a repellent to keep the cells from re-entering the floor plate, but also blocks responsiveness to the attractant netrin. At the same time, the growth cones switch on expression of receptors for another repellent protein, semaphorin, that is secreted by the cells in the side walls of the neural tube. Trapped between two repellent territories, the growth cones, having crossed the midline, travel in a tight fascicle up toward the brain.

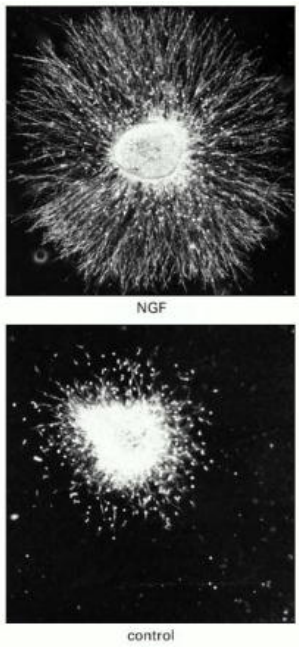

Figure 21-99. NGF effects on neurite outgrowth. Dark-field photomicrographs of a sympathetic ganglion cultured for 48 hours with *(above)* or without *(below)* NGF. Neurites grow out from the sympathetic neurons only if NGF is present in the medium. Each culture also contains Schwann (glial) cells that have migrated out of the ganglion; these are not affected by NGF. Neuronal survival and maintenance of growth cones for neurite extension represent two distinct effects of NGF. The effect on growth cones is local, direct, rapid, and independent of communication with the cell body; when NGF is removed, the deprived growth cones halt their movements within a minute or two. The effect of NGF on cell survival is less immediate and is associated with uptake of NGF by endocytosis and its intracellular transport back to the cell body. (Courtesy of Naomi Kleitman.)

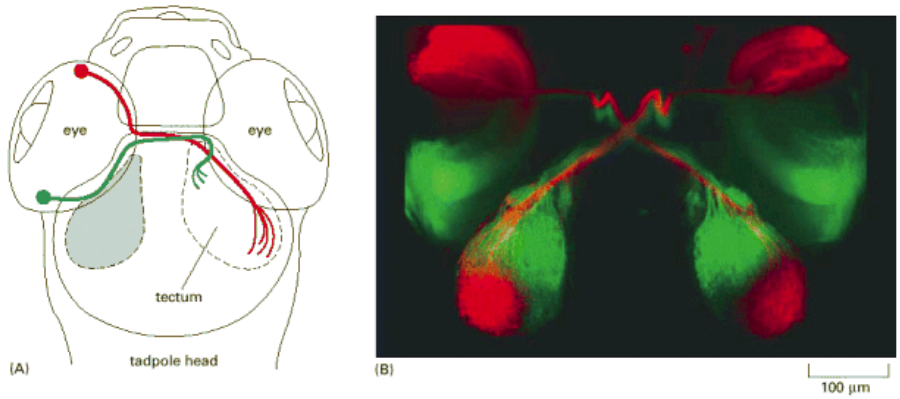

Figure 21-100. The neural map from eye to brain in a young zebrafish. (A) Diagrammatic view, looking down on the top of the head. (B) Fluorescence micrograph. Fluorescent tracer dyes have been injected into each eye - *red* into the anterior part, *green* into the posterior part. The tracer molecules have been taken up by the neurons in the retina and carried along their axons, revealing the paths they take to the optic tectum in the brain and the map that they form there. (Courtesy of Chi-Bin Chien, from D.H. Sanes, T.A. Reh, and W.A. Harris, Development of the Nervous System. San Diego, CA: Academic Press, 2000.)

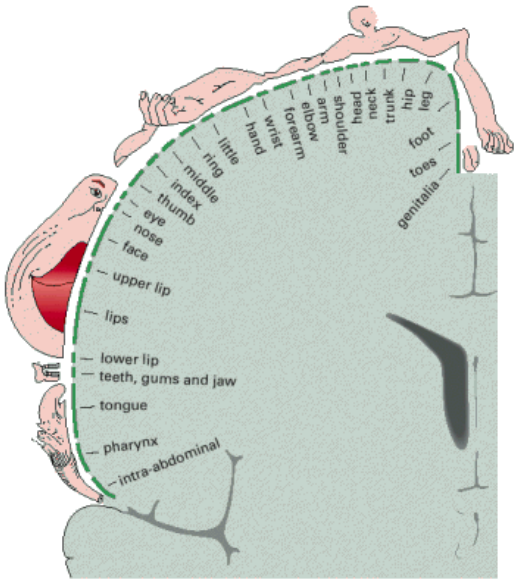

Figure 21-101. A map of the body surface in the human brain. The surface of the body is mapped onto the somatosensory region of the cerebral cortex by an orderly system of nerve cell connections, such that sensory information from neighboring body sites is delivered to neighboring sites in the brain. This means that the map in the brain is largely faithful to the topology of the body surface, even though different body regions are represented at different magnifications according to their density of innervation. The homunculus (the "little man" in the brain) has big lips, for example, because the lips are a particularly large and important source of sensory information. The map was determined by stimulating different points in the cortex of conscious patients during brain surgery and recording what they said they felt. (After W. Penfield and T. Rasmussen, The Cerebral Cortex of Man. New York: Macmillan, 1950.)

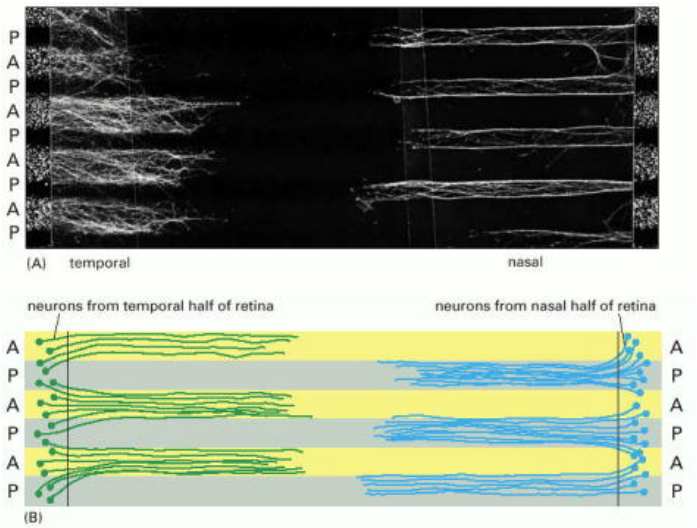

Figure 21-102. Selectivity of retinal axons growing over tectal membranes. (A) A photograph of the experimental observation. (B) A diagram of what is happening. The culture substratum has been coated with alternating stripes of membrane prepared either from posterior tectum (P) or from anterior tectum (A). In the photograph, the anterior tectal stripes are made visible by staining them with a fluorescent marker in the vertical strips at the sides of the picture. Axons of neurons from the temporal half of the retina (growing in from the *left*) follow the stripes of anterior tectal membrane but avoid the posterior tectal membrane, while axons of neurons from the nasal half of the retina (growing in from the *right*) do the converse. Thus anterior tectum differs from posterior tectum and nasal retina from temporal retina, and the differences guide selective axon outgrowth. These experiments were performed with cells from the chick embryo. (From Y. von Boxberg, S. Deiss, and U. Schwarz, *Neuron* 10:345357, 1993. © Elsevier.)

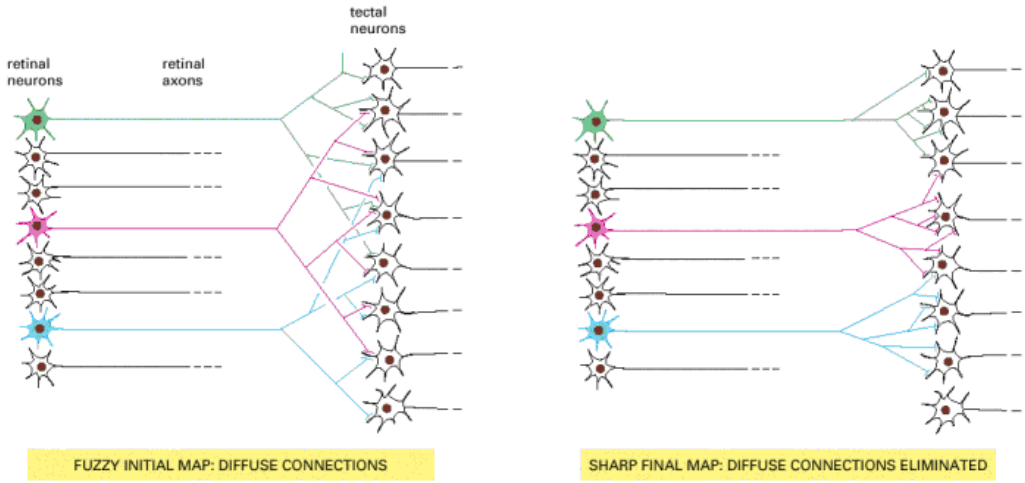

Figure 21-103. Sharpening of the retinotectal map by synapse elimination. At first the map is fuzzy because each retinal axon branches widely to innervate a broad region of tectum overlapping the regions innervated by other retinal axons. The map is then refined by synapse elimination. Where axons from separate parts of the retina synapse on the same tectal cell, competition occurs, eliminating the connections made by one of the axons. But axons from cells that are close neighbors in the retina cooperate, maintaining their synapses on shared tectal cells. Thus each retinal axon ends up innervating a small tectal territory, adjacent to and partly overlapping the territory innervated by axons from neighboring sites in the retina.

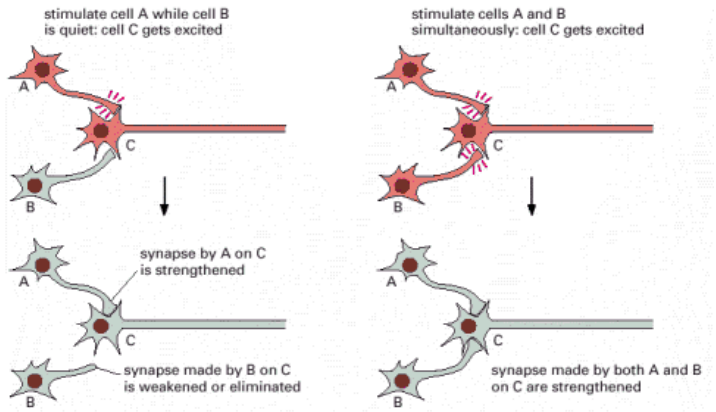

Figure 21-104. Synapse modification and its dependence on electrical activity. Experiments in several systems indicate that synapses are strengthened or weakened by electrical activity according to the rule shown in the diagram. The underlying principle appears to be that each excitation of a target cell tends to weaken any synapse where the presynaptic axon terminal has just been quiet but to strengthen any synapse where the presynaptic axon terminal has just been active. As a result, "neurons that fire together, wire together." A synapse that is repeatedly weakened and rarely strengthened is eventually eliminated altogether.

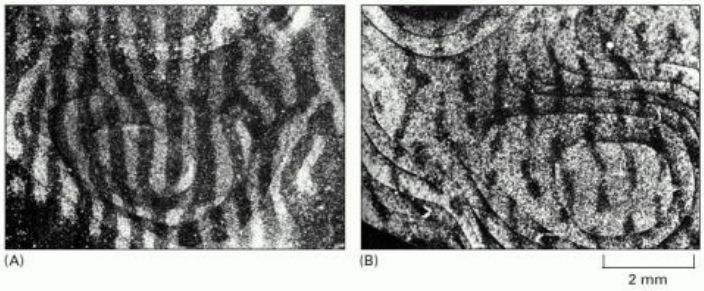

Figure 21-105. Ocular dominance columns in the visual cortex of a monkey's brain, and their sensitivity to visual experience. (A) Normally, stripes of cortical cells driven by the right eye alternate with stripes, of equal width, driven by the left eye. The stripes are revealed here by injecting a radioactive tracer molecule into one eye, allowing time for this tracer to be transported to the visual cortex, and detecting radioactivity there by autoradiography, in sections cut parallel to the cortical surface. (B) If one eye is kept covered during the critical period of development, and thus deprived of visual experience, its stripes shrink and those of the active eye expand. In this way, the deprived eye may lose the power of vision almost entirely. (From D.H. Hubel, T.N. Wiesel, and S. Le Vay, *Philos. Trans. Roy. Soc. (Biol.)* 278:377409, 1977. © The Royal Society.)

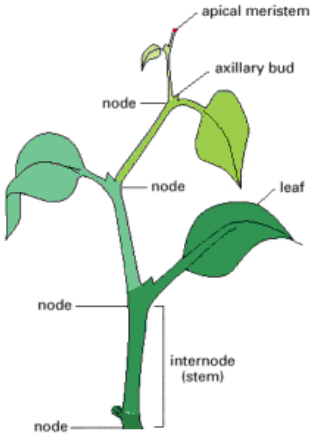

Figure 21-106. A simple example of the modular construction of plants. Each module (shown in different shades of *green)* consists of a stem, a leaf, and a bud containing a potential growth center, or *meristem.* The bud forms at the branch point, or *node,* where the leaf diverges from the stem. Modules arise sequentially from the continuous activity of the apical meristem.

Figure 21-107. *Arabidopsis thaliana.* This small plant is a member of the mustard (or crucifer) family (see also Figure 1-47). It is a weed of no economic use but of great value for genetic studies of plant development. (From M.A. Estelle and C.R. Somerville, *Trends Genet.* 12:8993, 1986. © Elsevier.)

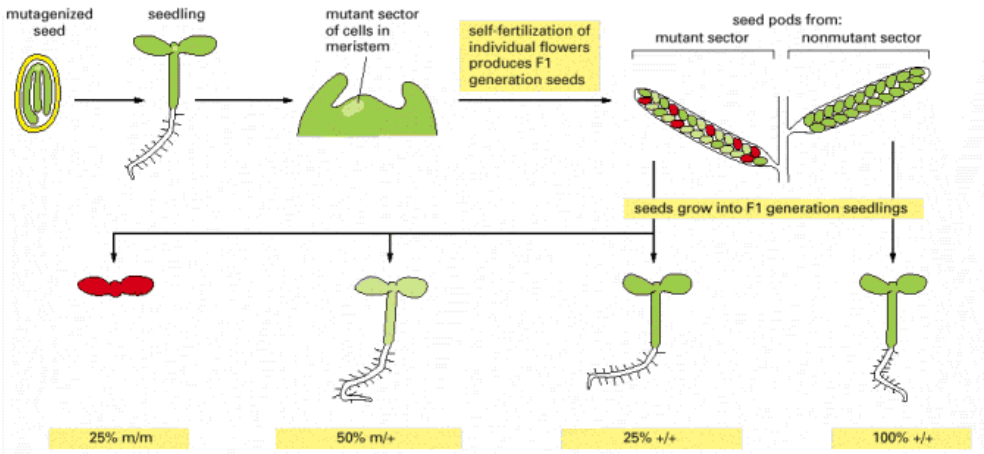

Figure 21-108. Production of mutants in *Arabidopsis.* A seed, containing a multicellular embryo, is treated with a chemical mutagen and left to grow into a plant. In general, this plant will be a mosaic of clones of cells carrying different induced mutations. An individual flower produced by this plant will usually be composed of cells belonging to the same clone, all carrying the same mutation, *m*, in heterozygous form (*m*/+). Self-fertilization of individual flowers by their own pollen results in seed pods, each of which contains a family of embryos of whose members half, on average, will be heterozygous (*m*/+), one quarter will be homozygous mutant (*m*/*m*), and one quarter will be homozygous wild-type (+/+). Often, the mutation will have a recessive lethal effect, as indicated here by the lack of a root in the *m*/*m* seedling. The mutant stock is then maintained by breeding from the heterozygote: it will produce seed pods (F2 generation) that all contain a mixture of +/+, *m*/+, and *m*/*m* seeds.

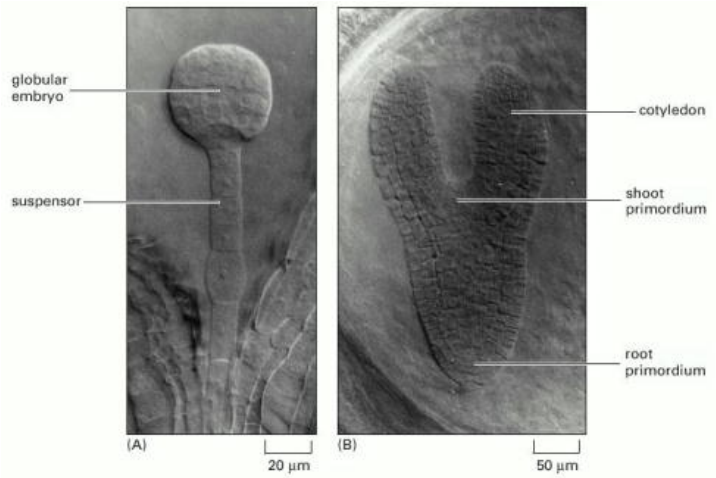

Figure 21-109. Two stages of embryogenesis in *Arabidopsis thaliana.* (From G. Jürgens et al., *Development [Suppl.]* 1:2738, 1991. © The Company of Biologists.)

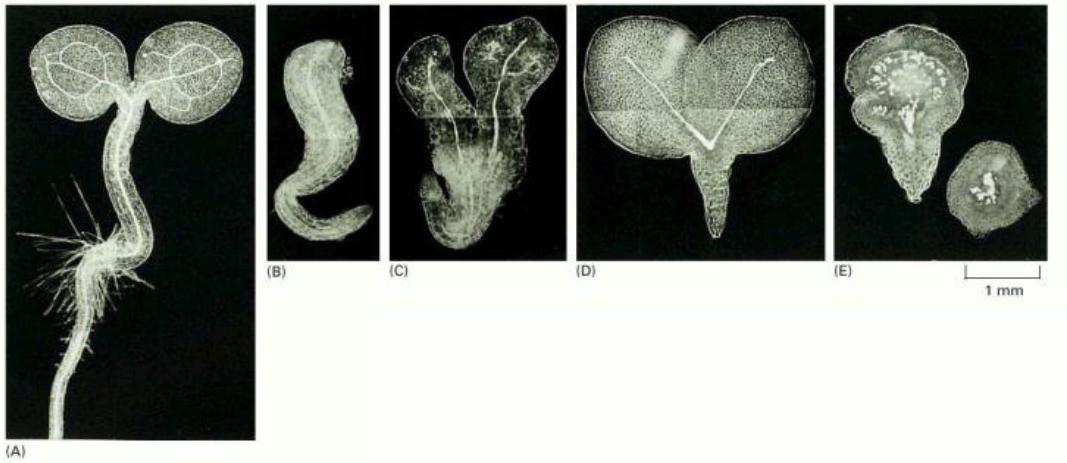

Figure 21-110. Mutant *Arabidopsis* seedlings. A normal seedling (A) compared with four types of mutant (B-E) defective in different parts of their apico-basal pattern: (B) has structures missing at its apex, (C) has an apex and a root but lacks a stem between them, (D) lacks a root, and (E) forms stem tissues but is defective at both ends. The seedlings have been "cleared" so as to show the vascular tissue inside them (pale strands). (From U. Mayer et al., *Nature* 353:402407, 1991. © Macmillan Magazines Ltd.)

Figure 21-111. A seedling of *Arabidopsis.* The *brown* objects to the *right* of the young seedling are the two halves of the discarded seed coat. (Courtesy of Catherine Duckett.)

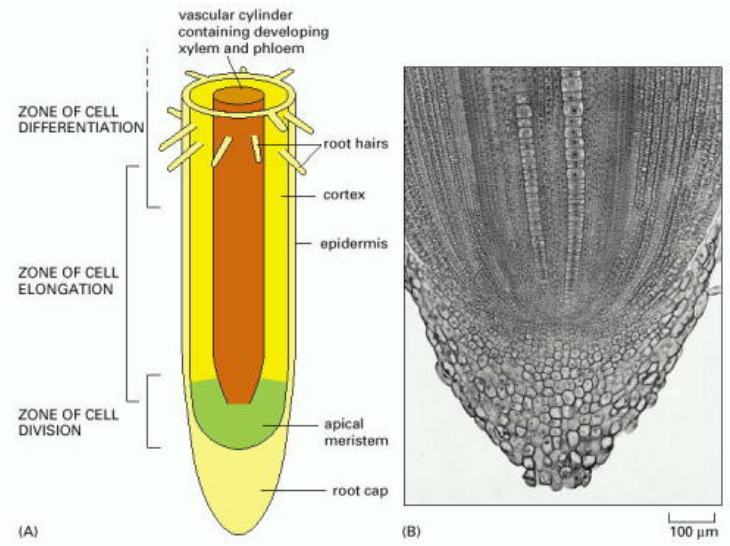

Figure 21-112. A growing root tip. (A) The organization of the final 2 mm of a growing root tip. The approximate zones in which cells can be found dividing, elongating, and differentiating are indicated. (B) The apical meristem and root cap of a corn root tip, showing the orderly files of cells produced. (B, from R.F. Evert, Biology of Plants, 4th edn. New York: Worth, 1986.)

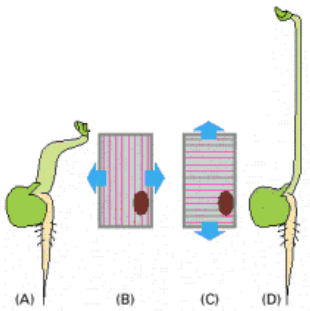

Figure 21-113. The different effects of the plant growth regulators ethylene and gibberellic acid. These regulators exert rapid and opposing effects on the orientation of the cortical microtubule array in cells of young pea shoots. A typical cell in an ethylene-treated plant (B) shows a net longitudinal orientation of microtubules, while a typical cell in a gibberellic-acid-treated plant (C) shows a net transverse orientation. New cellulose microfibrils are deposited parallel to the microtubules. Since this influences the direction of cell expansion, gibberellic acid and ethylene encourage growth in opposing directions: ethylene-treated seedlings will develop short, fat shoots (A), while gibberellicacid-treated seedlings will develop long, thin shoots (D).

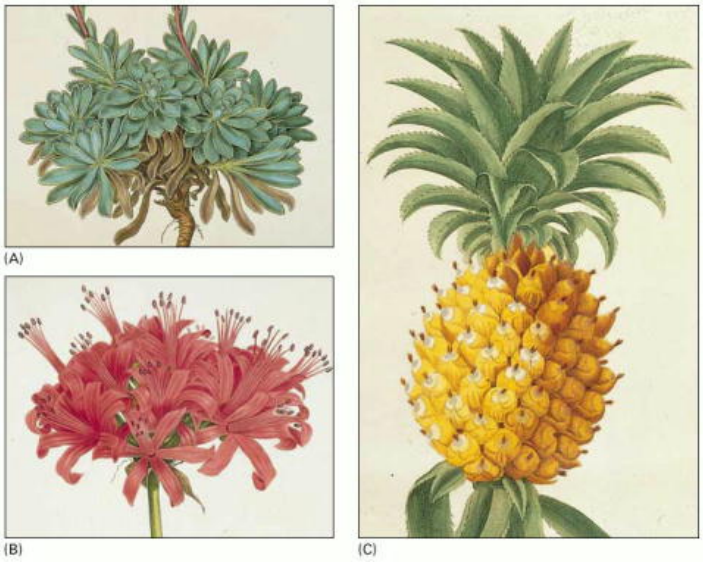

Figure 21-114. Repetitive patterning in plants. Accurate placing of successive modules from a single apical meristem produces these elaborate but regular patterns in leaves (A), flowers (B), and fruits (C). (A, from John Sibthorp, Flora Graeca. London: R. Taylor, 18061840; B, from Pierre Joseph Redouté, Les Liliacées. Paris: chez l'Auteur, 1807; C, from Christopher Jacob Trew, Uitgezochte planten. Amsterdam: Jan Christiaan Sepp, 1771 - all courtesy of the John Innes Foundation.)

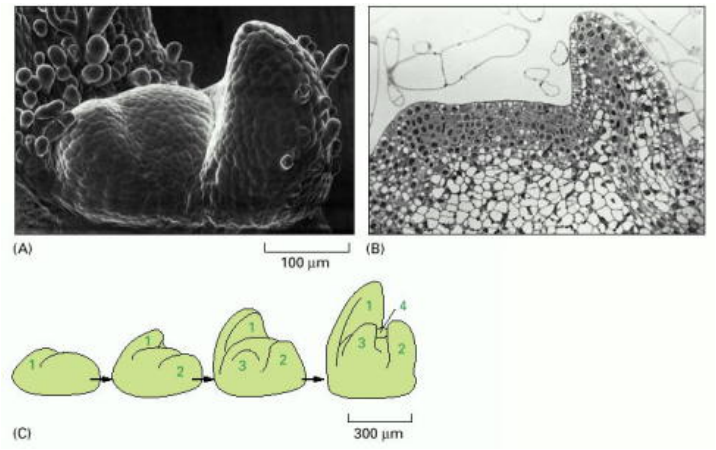

Figure 21-115. A shoot apex from a young tobacco plant. (A) A scanning electron micrograph shows the shoot apex with two sequentially emerging leaf primordia, seen here as lateral swellings on either side of the domed apical meristem. (B) A thin section of a similar apex shows that the youngest leaf primordium arises from a small group of cells (about 100) in the outer four or five layers of cells. (C) A very schematic drawing showing that the sequential appearance of leaf primordia takes place over a small distance and very early in shoot development. Growth of the apex will eventually form internodes that will separate the leaves in order along the stem (see Figure 21-106). (A and B, from R.S. Poethig and I.M. Sussex, *Planta* 165:158169, 1985. © Springer-Verlag.)

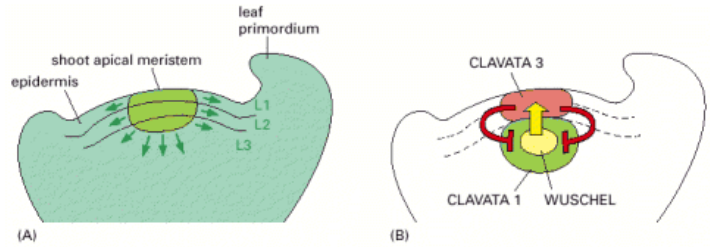

Figure 21-116. The feedback loops that are thought to maintain the shoot apical meristem. (A) The arrangement of cell layers constituting a shoot apical meristem. (B) The pattern of cell-cell communication that maintains the meristem. Artificial overexpression of Wuschel in the L3 region causes an increase in the number of cells in the L1 and L2 layers that behave as meristem cells and express Clavata3; artificial overexpression of Clavata3 in the L1 and L2 layers causes a reduction of Wuschel expression in the L3 region below and a decrease in the number of meristem cells. Clavata3 codes for a small signal protein, while Clavata1 codes for its receptor, a transmembrane protein kinase. Wuschel, which is expressed in the central part of the region that expresses the receptor Clavata1, codes for a gene regulatory protein of the homeodomain class. The size of the meristem is thought to be controlled by a self-regulating balance between a short-range stimulatory signal produced by cells expressing Wuschel *(yellow arrow)*, and a longer-range inhibitory signal delivered by Clavata3 *(red bars)*.

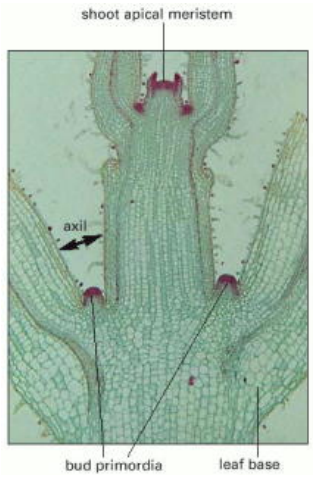

Figure 21-117. Axillary buds in the neighborhood of a shoot apex. The photograph shows a longitudinal section of *Coleus blumei*, a common houseplant. (From P.H. Raven, R.F. Evert, and S.E. Eichhorn, Biology of Plants, 6th edn. New York: Freeman/ Worth, 1999, used with permission.)

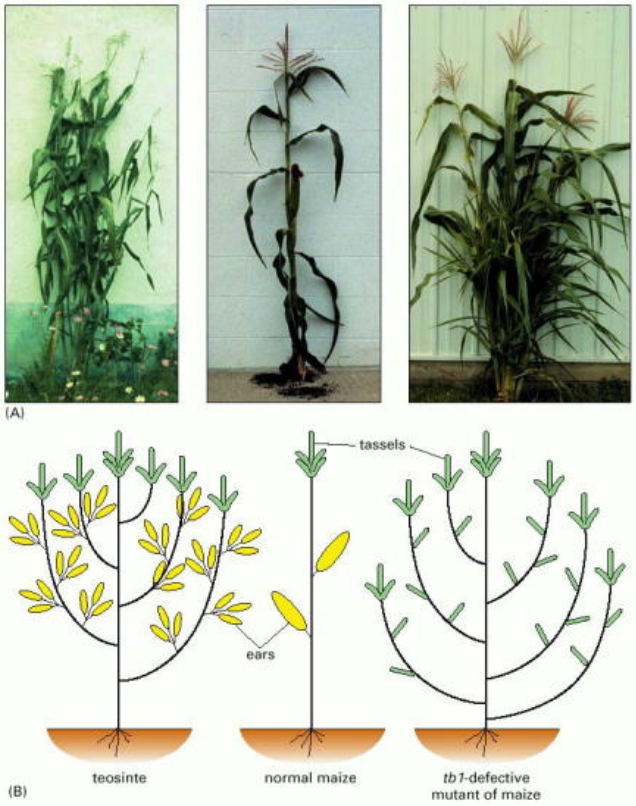

Figure 21-118. Transformation of plant architecture by mutation: a comparison of teosinte, normal maize, and *tb1*-defective maize. (A) Photographs of three types of plants. (B) The architecture of teosinte, normal maize and the *tb1*-defective maize compared schematically. The *tb1* gene product is needed for development of ears. It is absent in the *tb1* mutant; it is present in both teosinte and normal maize, but these two plants differ because the gene is differently regulated. (A *(left image)*, from J. Doebley and R.-L. Wang, *Cold Spring Harbor Symp.* 62:361367, 1997. © Cold Spring Harbor Press; A *(middle and right images)* from J. Doebley, A. Stec, and L. Hubbard, *Nature* 386:485488, 1997. © Macmillan Magazines Ltd.)

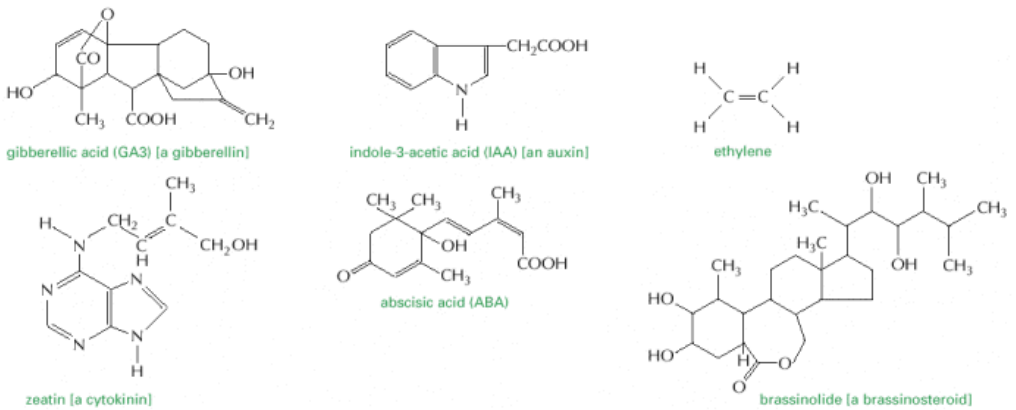

Figure 21-119. Plant growth regulators. The formula of one naturally occurring representative molecule from each of the six groups of plant growth regulatory molecules is shown.

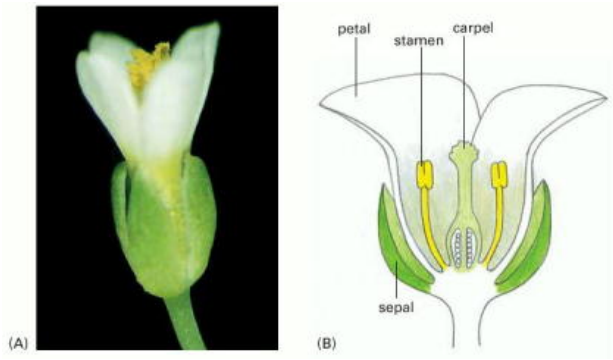

Figure 21-120. The structure of an *Arabidopsis* flower. (A) Photograph. (B) Drawings. (C) Schematic cross-sectional view. The basic plan, as shown in (C), is common to most flowering dicotyledonous plants. (A, courtesy of Leslie Sieburth.)

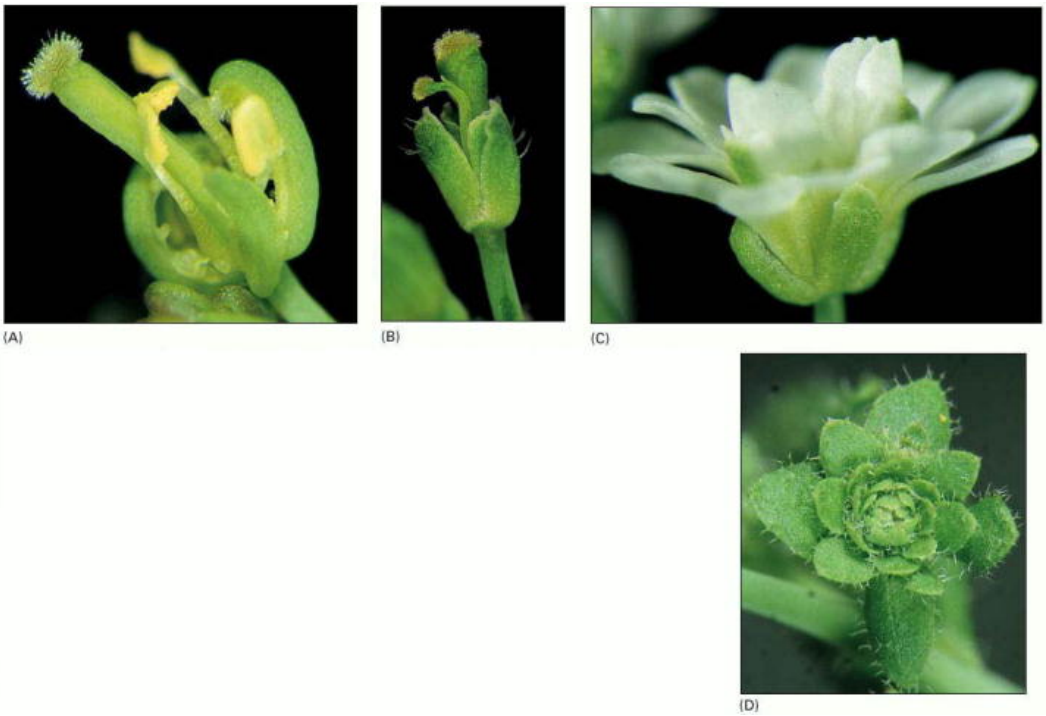

Figure 21-121. *Arabidopsis* flowers showing a selection of homeotic mutations. (A) In *apetala2*, sepals are converted into carpels and petals into stamens; (B) In *apetala3*, petals are converted into sepals and stamens into carpels; (C)In *agamous*, stamens are converted into petals and carpels into floral meristem. (D) In a triple mutant where these three functions are defective, all the organs of the flower are converted into leaves. (A-C, courtesy of Leslie Sieburth; D, courtesy of Mark Running.)

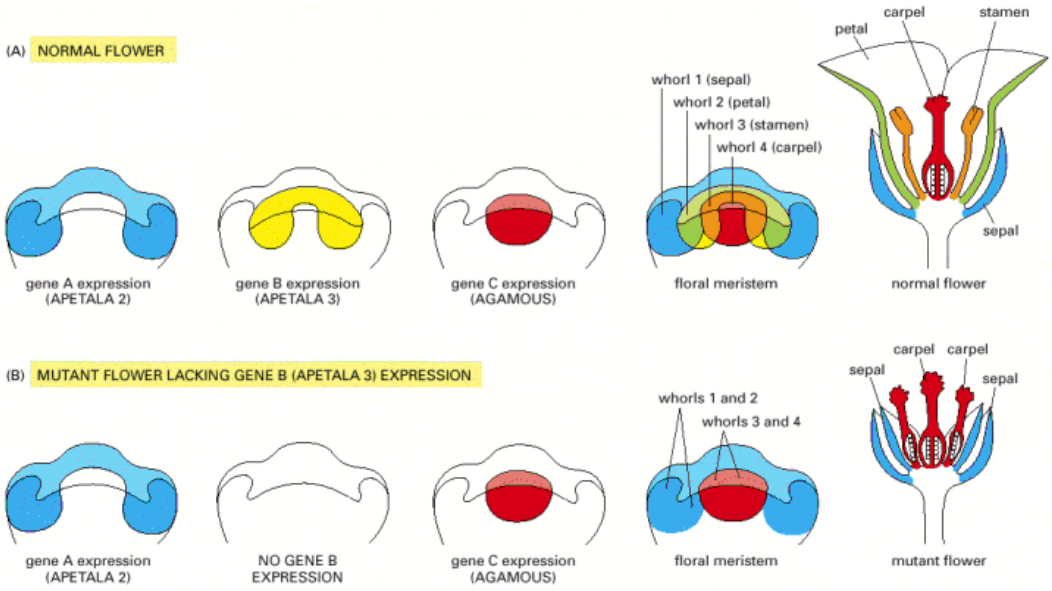

Figure 21-122. Homeotic selector gene expression in an *Arabidopsis* flower. (A) Diagram of the normal expression patterns of the three genes whose mutant phenotypes are illustrated in Figure 21-121A-C. All three genes code for gene regulatory proteins. The colored shading on the flower indicates which organ develops from each whorl of the meristem, but does not imply that the homeotic selector genes are still expressed at this stage. (B) The patterns in a mutant where the *apetala3* gene is defective. Because the character of the organs in each whorl is defined by the set of homeotic selector genes that they express, the stamens and petals are converted into sepals and carpels. The consequence of a deficiency of a gene of class A, such as *apetala2*, is slightly more complex: the absence of this class A gene product allows the class C gene to be expressed in the outer two whorls as well as the inner two, causing these outer whorls to develop as carpels and stamens, respectively. Deficiency of a class C gene prevents the central region from undergoing terminal differentiation as a carpel and causes it instead to continue growth as a meristem, generating more and more sepals and petals.

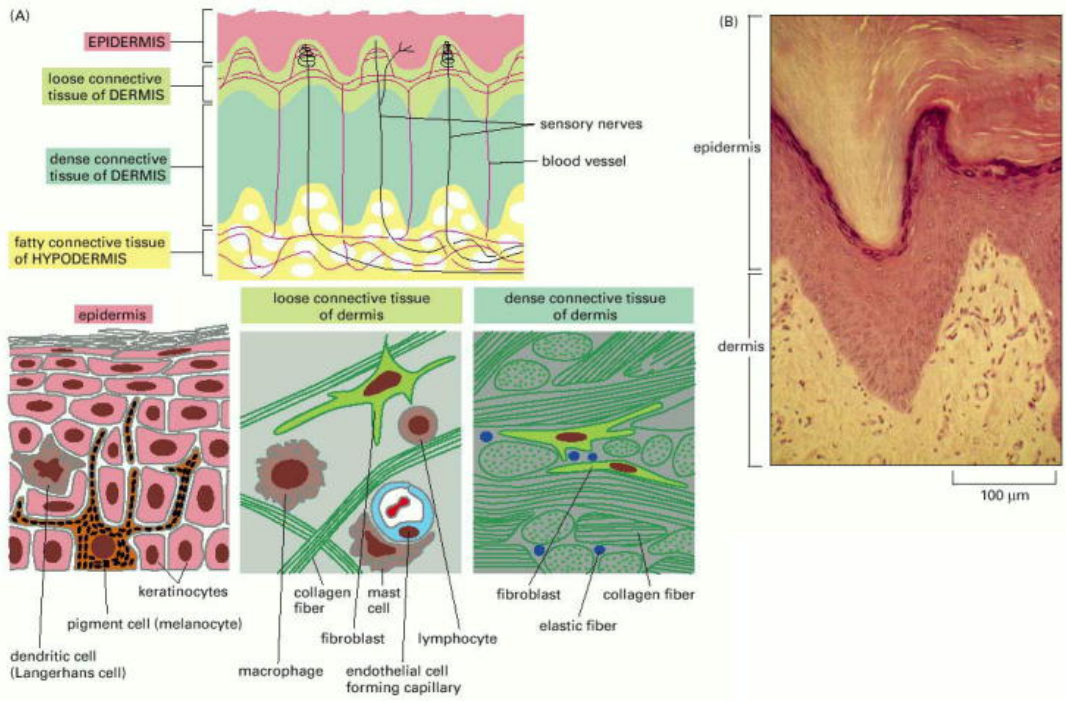

Figure 22-1. Mammalian skin. (A) These diagrams show the cellular architecture of thick skin. (B) Micrograph of a cross section through the sole of a human foot, stained with hematoxylin and eosin. The skin can be viewed as a large organ composed of two main tissues: the epidermis and the underlying connective tissue, which consists of the dermis and the hypodermis. Each tissue is composed of a variety of cell types. The dermis and hypodermis are richly supplied with blood vessels and nerves. Some nerve fibers extend into the epidermis.

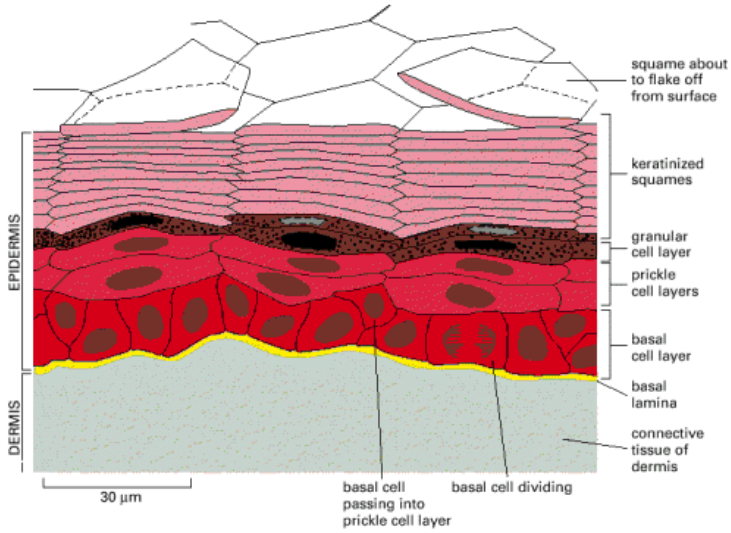

Figure 22-2. The multilayered structure of the epidermis, as seen in a mouse. The outlines of the keratinized squames are revealed by swelling them in a solution containing sodium hydroxide. The highly ordered hexagonal arrangement of interlocking columns of cells shown here occurs only in some sites where the epidermis is thin. In human skin, the stacks of squames are usually many times higher and less regular, and where the skin is very thick mitotic cells are seen not only in the basal layer but also in the first few cell layers above it. In addition to the cells destined for keratinization, the deep layers of the epidermis include small numbers of cells of different characters, as indicated in Figure 21-1 - including dendritic cells, called Langerhans cells, derived from bone marrow; melanocytes (pigment cells) derived from the neural crest; and Merkel cells, which are associated with nerve endings in the epidermis.

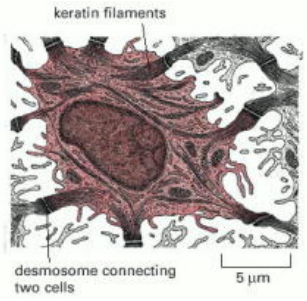

Figure 22-3. A prickle cell. This drawing, from an electron micrograph of a section of the epidermis, shows the bundles of keratin filaments that traverse the cytoplasm and are inserted at the desmosome junctions that bind the prickle cell *(red)* to its neighbors. Nutrients and water diffuse freely through the intercellular spaces in the metabolically active layers of the epidermis occupied by the prickle cells. Farther out, at the level of the granular cells, there is a waterproof barrier that is thought to be created by a sealant material that the granular cells secrete. (From R.V. Krstic´, Ultrastructure of the Mammalian Cell: an Atlas. Berlin: Springer-Verlag, 1979.)

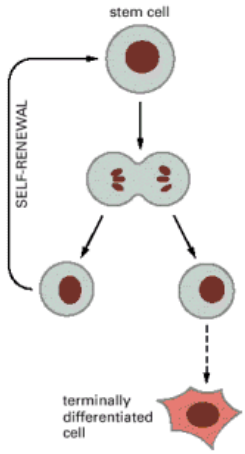

Figure 22-4. The definition of a stem cell. Each daughter produced when a stem cell divides can either remain a stem cell or go on to become terminally differentiated. In many cases, the daughter that opts for terminal differentiation undergoes additional cell divisions before terminal differentiation is completed.

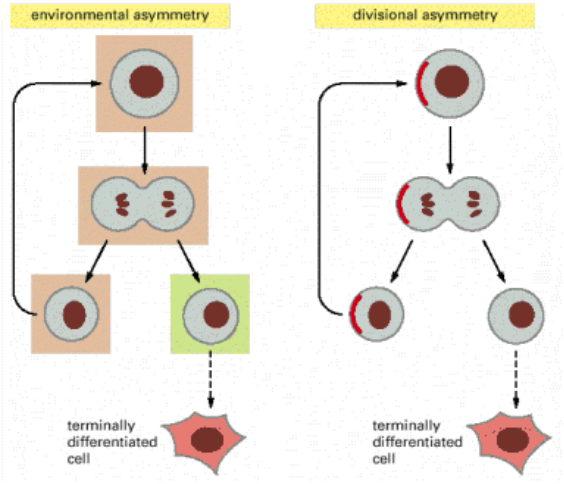

Figure 22-5. Two ways for a stem cell to produce daughters with different fates. In the strategy based on environmental asymmetry, the daughters of the stem cell are initially similar and are directed into different pathways according to the environmental influences that act on them after they are born. The environment is shown as *colored shading* around the cell. With this strategy, the number of stem cells can be increased or reduced to fit the niche available for them. In the strategy based on divisional asymmetry, the stem cell has an internal asymmetry and divides in such a way that its two daughters are already endowed with different determinants at the time of their birth.

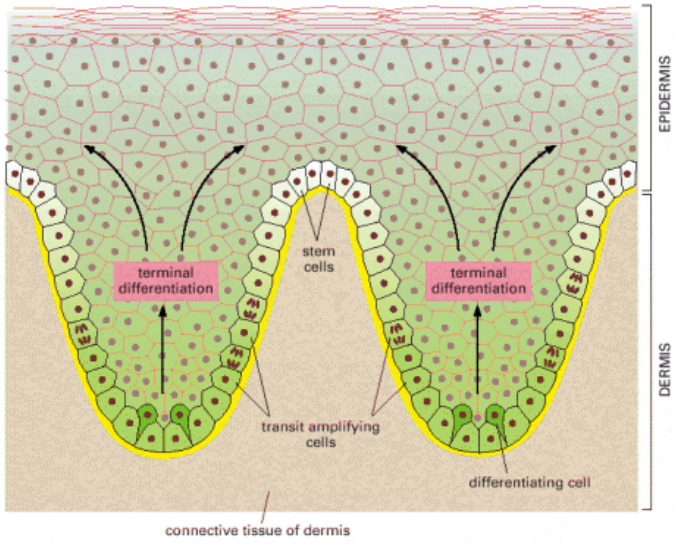

Figure 22-6. The distribution of stem cells in human epidermis, and the pattern of epidermal cell production. The diagram is based on specimens in which the location of the stem cells was identified by staining for β1-integrin, and that of the differentiating cells by staining for keratin-10, a marker of keratinocyte differentiation; dividing cells were identifed by labeling with BrdU, a thymidine analog that is incorporated into cells in S-phase of the cell division cycle. The stem cells seem to be clustered near the tips of the dermal papillae. They divide infrequently, giving rise (through a sideways movement) to transit amplifying cells, which occupy the intervening regions. The transit amplifying cells divide frequently, but for a limited number of division cycles, at the end of which they begin to differentiate and slip out of the basal layer. The precise distribution of stem cells and transit amplifying cells varies from one region of epidermis to another. (Adapted from S. Lowell et al., *Curr. Biol*. 10:491500, 2000.)

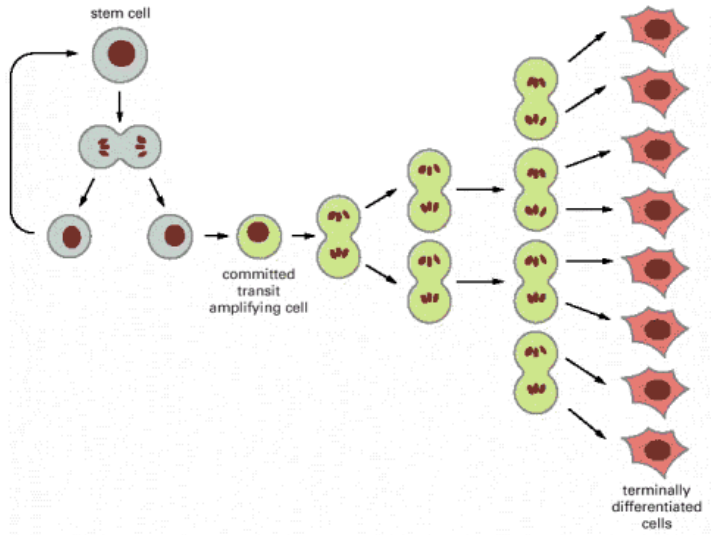

Figure 22-7. Transit amplifying cells. Stem cells in many tissues divide only rarely, but give rise to transit amplifying cells - daughters committed to differentiation that go through a limited series of more rapid divisions before completing the process. In the example shown here, each stem cell division gives rise in this way to eight terminally differentiated progeny.

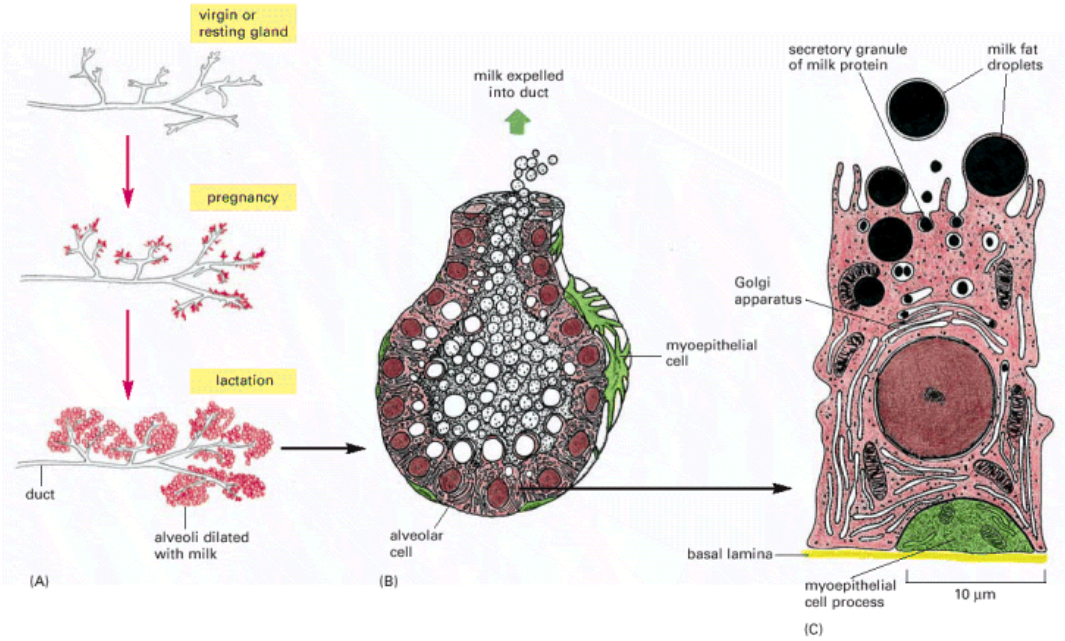

Figure 22-8. The mammary gland. (A) The growth of alveoli from the ducts of the mammary gland during pregnancy and lactation. Only a small part of the gland is shown. The "resting" gland contains a small amount of inactive glandular tissue embedded in a large amount of fatty connective tissue . During pregnancy an enormous proliferation of the glandular tissue takes place at the expense of the fatty connective tissue, with the secretory portions of the gland developing preferentially to create alveoli. (B) One of the milk-secreting alveoli with a basket of contractile myoepithelial cells *(green)* embracing it (see also Figure 22-40E). (C) A single type of secretory alveolar cell produces both the milk proteins and the milk fat. The proteins are secreted in the normal way by exocytosis, while the fat is released as droplets surrounded by plasma membrane detached from the cell. (B, after R. Krsti´c, Die Gewebe des Menschen und der Säugetiere. Berlin: Springer-Verlag, 1978; C, from D.W. Fawcett, A Textbook of Histology, 12th edn. New York: Chapman and Hall, 1994.)

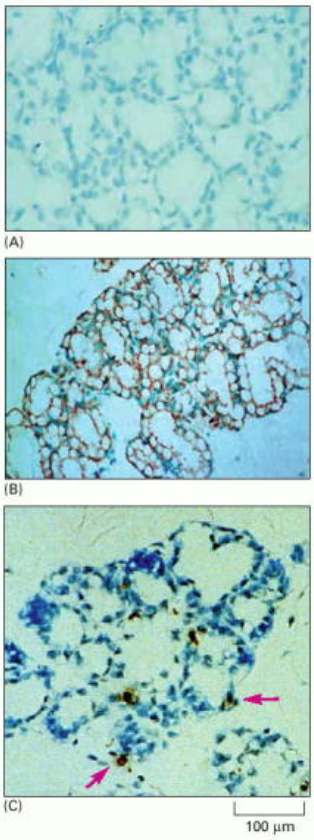

Figure 22-9. Death of milk-secreting cells when suckling stops. (A) A section of part of a lactating mammary gland of a mouse that had been suckling her newborn babies in the normal way. (B) A corresponding section from a mouse that had not suckled for 9 hours. The sections in (A) and (B) were both stained with an antibody against TGFβ3 *(brown).* (C) Similar section from a mammary gland whose duct had been sealed for three days, stained to reveal cells dying by apoptosis *(brown).* Where milk is produced and not drained off by suckling, production of TGFβ3 is induced, and this, together with other signals, triggers apoptosis and leads to regression of the ducts. (From A.V. Nguyen and J.W. Pollard, *Development* 127:31073118, 2000. © The Company of Biologists.)

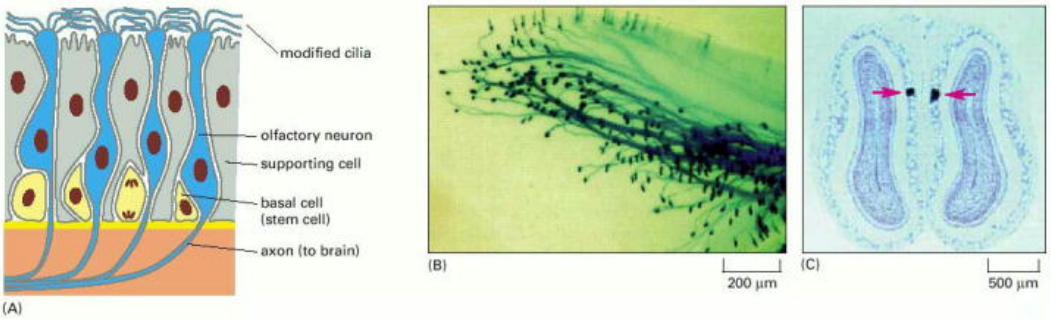

Figure 22-10. Olfactory epithelium and olfactory neurons. (A) Olfactory epithelium consists of supporting cells, basal cells, and olfactory sensory neurons. The basal cells are the stem cells for production of the olfactory neurons. Six to eight modified cilia project from the apex of the olfactory neuron and contain the odorant receptors. (B) This micrograph shows olfactory neurons in the nose of a genetically modified mouse in which the gene encoding LacZ has been inserted into an odorant receptor locus, so that all the cells that would normally express that particular receptor now make the enzyme LacZ in addition. The LacZ is detected through the blue product of the enzymatic reaction that it catalyzes. The cell bodies *(dark blue)* of the marked olfactory neurons, lying scattered in the olfactory epithelium, send their axons *(light blue)* toward the brain (out of the picture to the *right).* (C) A cross section of the *left* and *right* olfactory bulbs, stained for LacZ. Axons of all the olfactory neurons expressing the same odorant receptor converge on the same glomeruli *(red arrows)* symmetrically placed within the bulbs on the *right* and *left* sides of the brain. Other glomeruli (unstained) receive their inputs from olfactory neurons expressing other odorant receptors. (B and C, from P. Mombaerts et al., *Cell* 87:675686, 1996. © Elsevier.)

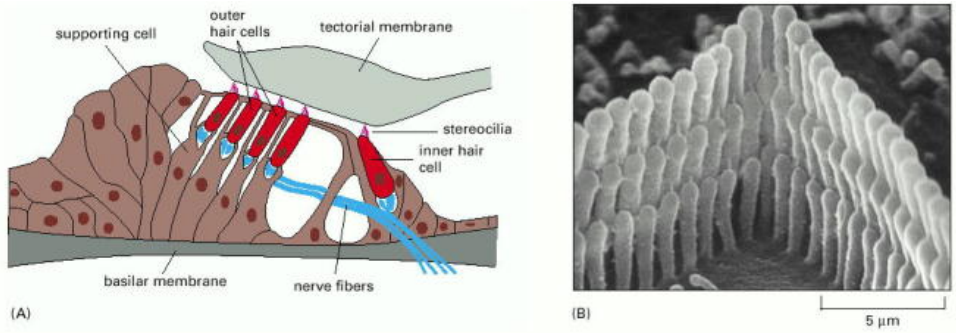

Figure 22-11. Auditory hair cells. (A) A diagrammatic cross section of the auditory apparatus (the organ of Corti) in the inner ear of a mammal shows the auditory hair cells held in an elaborate epithelial structure of supporting cells and overlaid by a mass of extracellular matrix (the tectorial membrane). The epithelium containing the hair cells sits on the basilar membrane - a thin, resilient sheet of tissue that forms a long, narrow dividing partition between two fluid-filled channels. Sound causes pressure changes in these channels and makes the basilar membrane vibrate up and down. (B) This scanning electron micrograph shows the apical surface of an outer auditory hair cell, with the characteristic organ-pipe array of giant microvilli (stereocilia). The inner hair cells, of which there are just 3500 in each human ear, are the principal auditory receptors. The outer hair cells, roughly four times more numerous, are thought to form part of a feedback mechanism that regulates the mechanical stimulus delivered to the inner hair cells. (B, from J.D. Pickles, *Prog. Neurobiol.* 24:142, 1985. © Elsevier.)

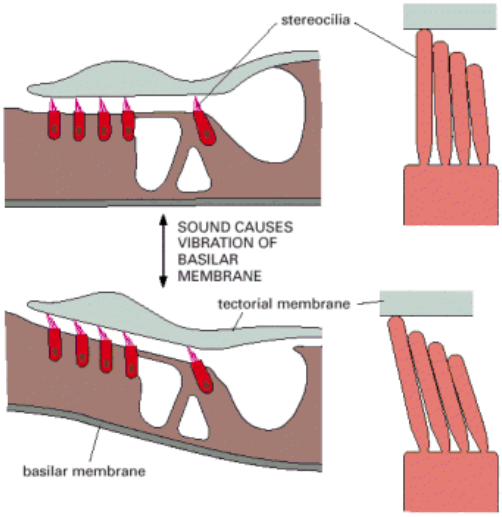

Figure 22-12. How a relative movement of the overlying extracellular matrix (the tectorial membrane) tilts the stereocilia of auditory hair cells in the organ of Corti in the inner ear of a mammal. The stereocilia behave as rigid rods hinged at the base and bundled together at their tips.

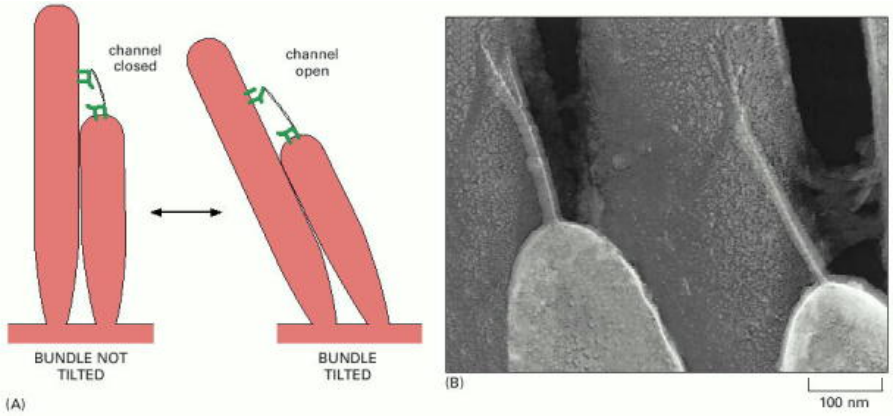

Figure 22-13. How a sensory hair cell works. (A) The cell functions as a transducer, generating an electrical signal in response to sound vibrations that rock the organ of Corti and so cause the stereocilia to tilt. A fine filament runs more or less vertically upward from the tip of each shorter stereocilium to attach at a higher point on its adjacent taller neighbor. Tilting the bundle puts tension on the filaments, which pull on mechanically gated ion channels in the membrane of the stereocilia. Opening of these channels allows an influx of positive charge, depolarizing the hair cell. (B) An electron micrograph of the filaments extending from the tops of two stereocilia. By extraordinarily delicate mechanical measurements, correlated with electrical recordings from a single hair cell as the bundle of stereocilia is deflected by pushing with a flexible glass probe, it is possible to detect an extra "give" of the bundle as the mechanically gated channels yield to the applied force and are pulled open. In this way it can be shown that the force required to open a single one of the hypothesized channels is about 2×10^{-13} newtons and that its gate swings through a distance of about 4 nm as it opens. The mechanism is astonishingly sensitive: the faintest sounds that we can hear have been estimated to stretch the filaments by an average of 0.04 nm, which is just under half the diameter of a hydrogen atom. (B, from B. Kachar et al., *Proc. Natl. Acad. Sci. USA* 97:1333613341, 2000. © National Academy of Sciences.)

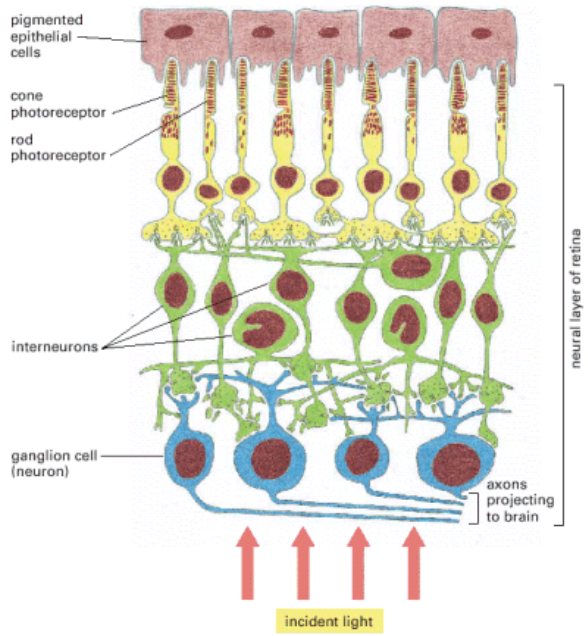

Figure 22-14. The structure of the retina. The stimulation of the photoreceptors by light is relayed via interneurons to the ganglion cells, which convey the signal to the brain. The spaces between neurons and between photoreceptors in the neural retina are occupied by a population of specialized supporting cells (not shown here). (Modified from J.E. Dowling and B.B. Boycott, *Proc. R. Soc. Lond.* B 166:80111, 1966.)

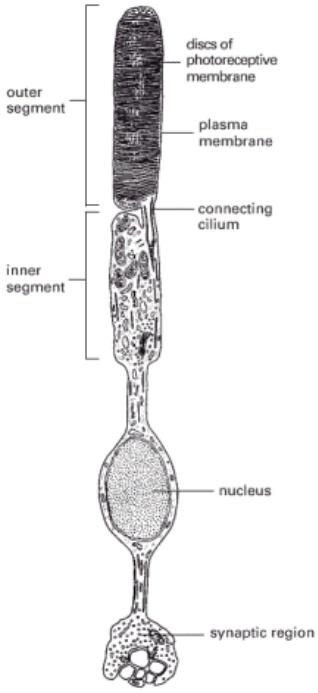

Figure 22-15. A rod photoreceptor.

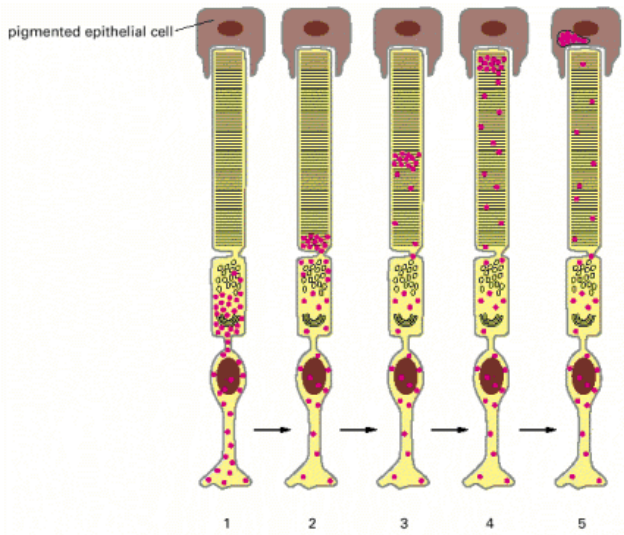

Figure 22-16. Turnover of membrane protein in a rod cell. Following a pulse of ^{3}H-leucine, the passage of radiolabeled proteins through the cell is followed by autoradiography. *Red dots* indicate sites of radioactivity. The method reveals only the ^{3}H-leucine that has been incorporated into proteins; the rest is washed out during the preparation of the tissue. (1) The incorporated leucine is first seen concentrated in the neighborhood of the Golgi apparatus. (2) From there it passes to the base of the outer segment into a newly synthesized disc of photoreceptive membrane. (35) New discs are formed at a rate of three or four per hour (in a mammal), displacing the older discs toward the pigment epithelium.

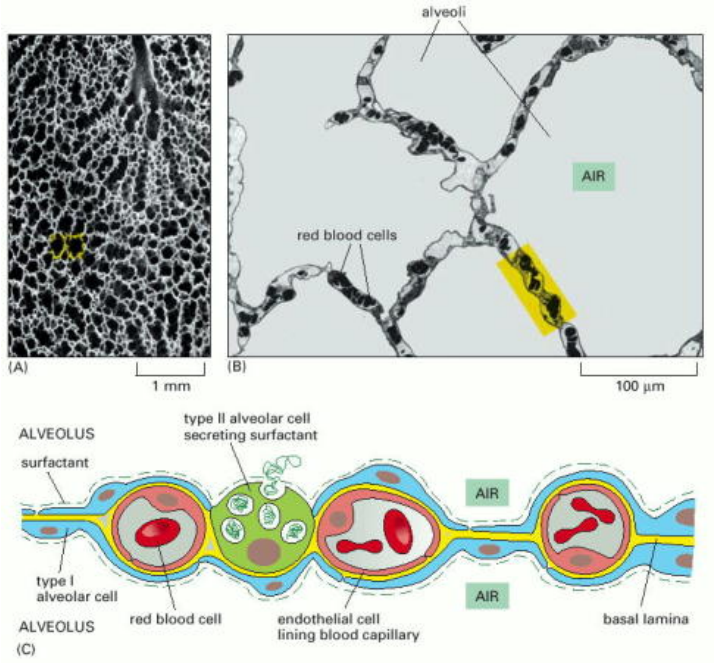

Figure 22-17. Alveoli in the lung. (A) Scanning electron micrograph at low magnification, showing the sponge-like texture created by the many air-filled alveoli. A bronchiole (small tubular airway) is seen at the top, communicating with the alveoli. (B) Transmission electron micrograph of a section through a region corresponding to the the *yellow* box in (A) showing the alveolar walls, where gas exchange occurs. (C) Diagram of the cellular architecture of a piece of alveolar wall, corresponding to the *yellow* box in (B). (A, from P. Gehr et al., *Resp. Physiol.* 44:6169, 1981. © Elsevier; B, courtesy of Peter Gehr, from D.W. Fawcett, A Textbook of Histology, 12th edn. New York: Chapman and Hall, 1994.)

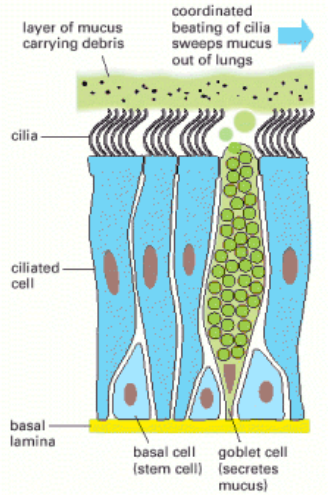

Figure 22-18. Respiratory epithelium. The goblet cells secrete mucus, which forms a blanket over the tops of the ciliated cells. The regular, coordinated beating of the cilia sweeps the mucus up and out of the airways, carrying any debris that is stuck to it. The mechanism that coordinates the ciliary beating is a mystery, but it seems to reflect an intrinsic polarity in the epithelium. If a segment of rabbit trachea is surgically reversed, it carries on sweeping mucus, but in the wrong direction, back down toward the lung, in opposition to adjacent unreversed portions of trachea.

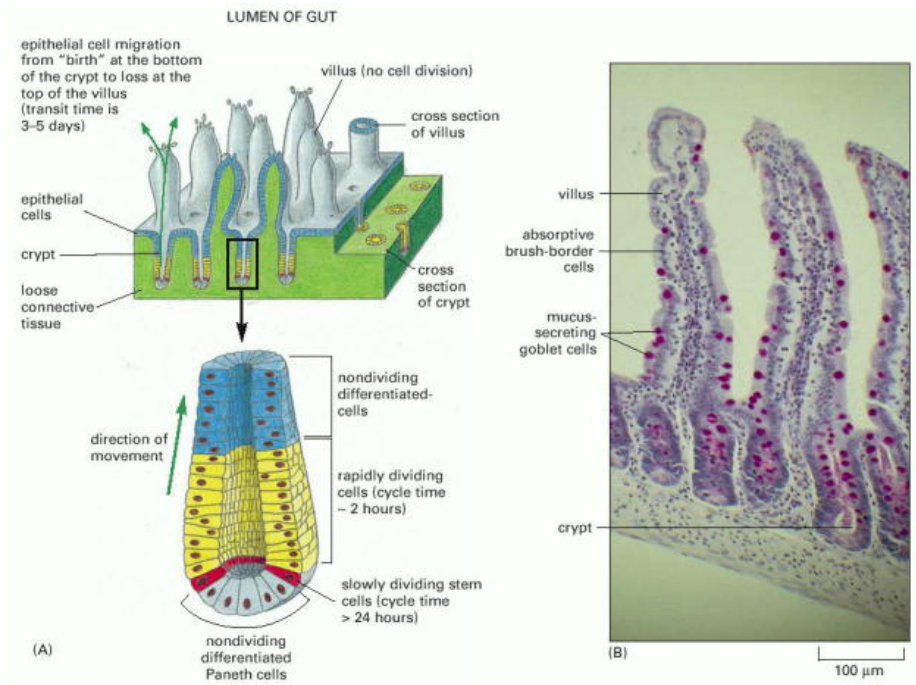

Figure 22-19. Renewal of the gut lining. (A) The pattern of cell turnover and the proliferation of stem cells in the epithelium that forms the lining of the small intestine. The *arrow* shows the general upward direction of cell movement onto the villi, but some cells, including a proportion of the goblet and enteroendocrine cells, stay behind and differentiate while still in the crypts. The nondividing differentiated cells (Paneth cells) at the very bottom of the crypts also have a finite lifetime, and are continually replaced by progeny of the stem cells. (B) Photograph of a section of part of the lining of the small intestine, showing the villi and crypts. Note how mucus-secreting goblet cells (stained *red)* are interspersed among other cell types. Enteroendocrine cells are less numerous and less easy to identify without special stains. See Figure 22-20 for the structure of these cells.

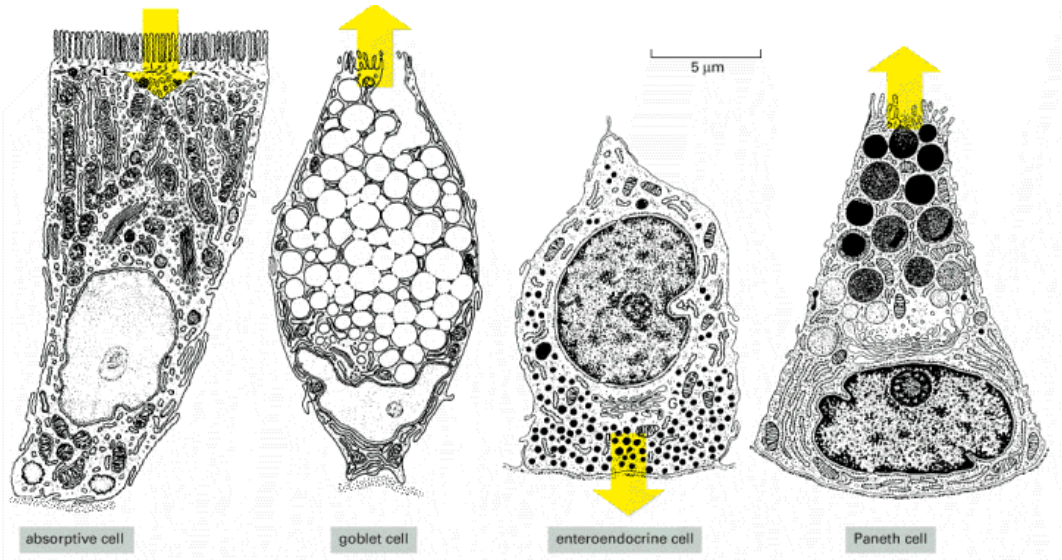

Figure 22-20. The four main differentiated cell types found in the epithelial lining of the small intestine. All of these are generated from undifferentiated multipotent stem cells living near the bottoms of the crypts (see Figure 22-19). The microvilli on the apical surface of the absorptive (brush-border) cell provide a 30-fold increase of surface area, not only for the import of nutrients, but also for the anchorage of enzymes that perform the final stages of extracellular digestion, breaking down small peptides and disaccharides into monomers that can be transported across the cell membrane. (After T.L. Lentz, Cell Fine Structure. Philadelphia: Saunders, 1971; R. Krsti ´c, Illustrated Encyclopedia of Human Histology. Berlin: Springer-Verlag, 1984.)

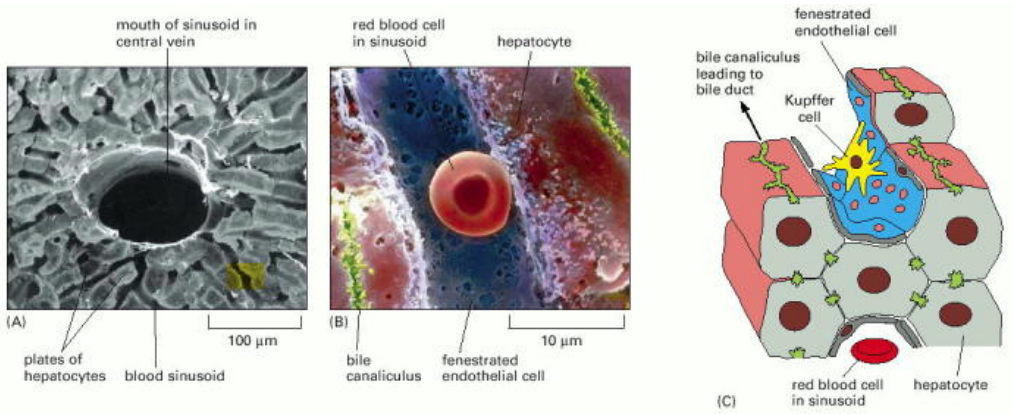

Figure 22-21. The structure of the liver. (A) A scanning electron micrograph of a portion of the liver, showing the irregular sheets and cords of hepatocytes and the many small channels, or sinusoids, for the flow of blood. The larger channels are vessels that distribute and collect the blood that flows through the sinusoids. (B) Detail of a sinusoid (enlargement of region similar to that marked by yellow rectangle at lower right in [A]). (C) Schematized diagram of the fine structure of the liver. The hepatocytes are separated from the bloodstream by a single thin sheet of endothelial cells with interspersed macrophagelike Kupffer cells. Small holes in the endothelial sheet, called fenestrae (Latin for "windows"), allow the exchange of molecules and small particles between the hepatocytes and the bloodstream. Besides exchanging materials with the blood, the hepatocytes form a system of tiny bile canaliculi into which they secrete bile, which is ultimately discharged into the gut via bile ducts. The real structure is less regular than this diagram suggests. (A and B, courtesy of Pietro M. Motta, University of Rome "La Sapienza.")

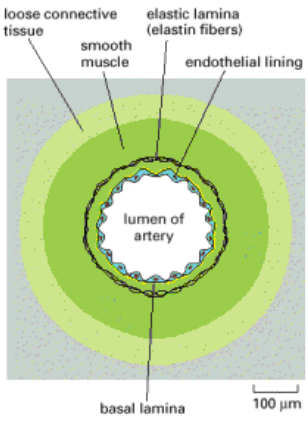

Figure 22-22. Diagram of a small artery in cross section. The endothelial cells, although inconspicuous, are the fundamental component. Compare with the capillary in Figure 22-23.

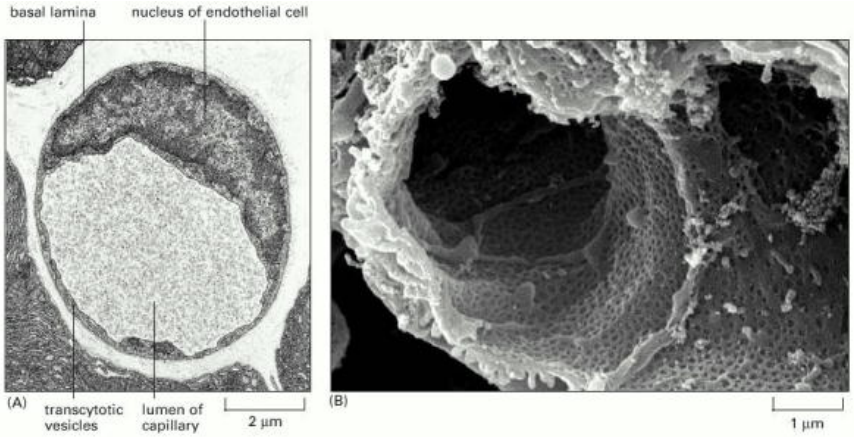

Figure 22-23. Capillaries. (A) Electron micrograph of a cross section of a small capillary in the pancreas. The wall is formed by a single endothelial cell surrounded by a basal lamina. Note the small "transcytotic" vesicles, which according to one theory provide transport of large molecules in and out of this type of capillary: materials are taken up into the vesicles by endocytosis at the luminal surface of the cell and discharged by exocytosis at the external surface, or vice versa. (B) Scanning electron micrograph of the interior of a capillary in a glomerulus of the kidney, where filtration of the blood occurs to produce urine. Here, as in the liver (see Figure 22-20), the endothelial cells are specialized to form a sieve-like structure, with fenestrae ("windows"), constructed rather like the pores in the nuclear envelope of eucaryotic cells, allowing water and most molecules to pass freely out of the bloodstream. (A, from R.P. Bolender, *J. Cell Biol.* 61:269287, 1974. © The Rockefeller University Press; B, courtesy of Steve Gschmeissner and David Shima.)

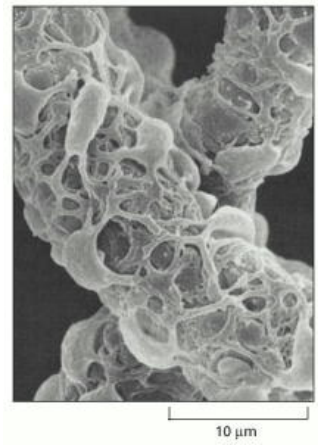

Figure 22-24. Pericytes. The scanning electron micrograph shows pericytes wrapping their processes around a small blood vessel (a post-capillary venule) in the mammary gland of a cat. Pericytes are present also around capillaries, but much more sparsely distributed there. (From T. Fujiwara and Y. Uehara, *Am. J. Anat.* 170:3954, 1984. © Wiley-Liss.)

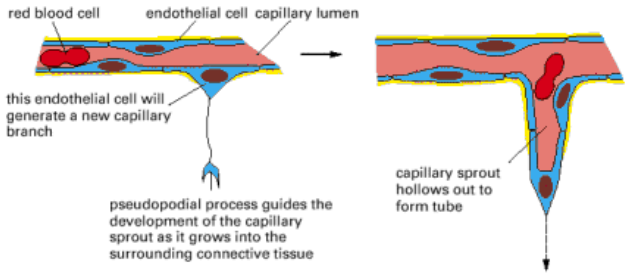

Figure 22-25. Angiogenesis. A new blood capillary forms by the sprouting of an endothelial cell from the wall of an existing small vessel. This diagram is based on observations of cells in the transparent tail of a living tadpole. (After C.C. Speidel, *Am. J. Anat.* 52:179, 1933.)

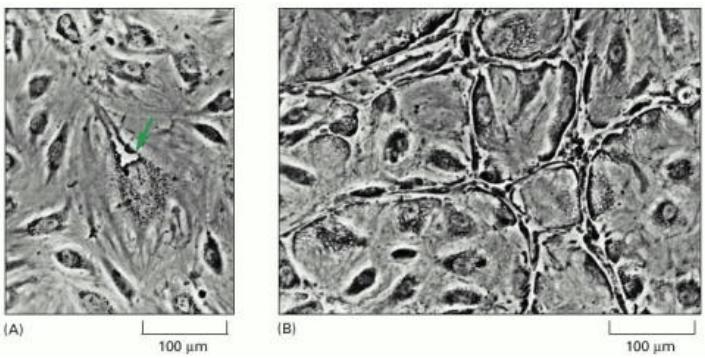

Figure 22-26. Capillary formation *in vitro*. Endothelial cells in culture spontaneously develop internal vacuoles that appear to join up from cell to cell, giving rise to a network of capillary tubes. These photographs show successive stages in the process. The *arrow* in (A) indicates a vacuole forming initially in a single endothelial cell. The cultures are set up from small patches of two to four endothelial cells taken from short segments of capillary. These cells settle on the surface of a collagen-coated culture dish and form a small flattened colony that enlarges gradually as the cells proliferate. The colony spreads across the dish, and eventually, after about 20 days, capillary tubes begin to form in the central regions. Once tube formation has started, branches soon appear, and after 510 more days, an extensive network of tubes is visible, as seen in (B). The process is strongly dependent on the nature of the extracellular matrix in the environment of the cells: the formation of capillary tubes is promoted by basal lamina components, such as laminin, which the endothelial cells themselves can secrete. (From J. Folkman and C. Haudenschild, *Nature* 288:551556, 1980. © Macmillan Magazines Ltd.)

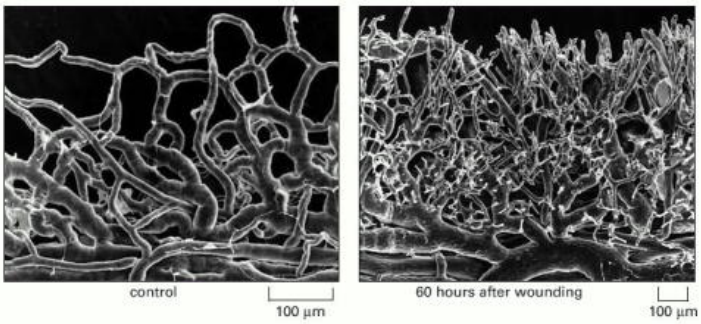

Figure 22-27. New capillary formation in response to wounding. Scanning electron micrographs of casts of the system of blood vessels surrounding the margin of the cornea show the reaction to wounding. The casts are made by injecting a resin into the vessels and letting the resin set; this reveals the shape of the lumen, as opposed to the shape of the cells. Sixty hours after wounding many new capillaries have begun to sprout toward the site of injury, which is just *above* the *top* of the picture. Their oriented outgrowth reflects a chemotactic response of the endothelial cells to an angiogenic factor released at the wound. (Courtesy of Peter C. Burger.)

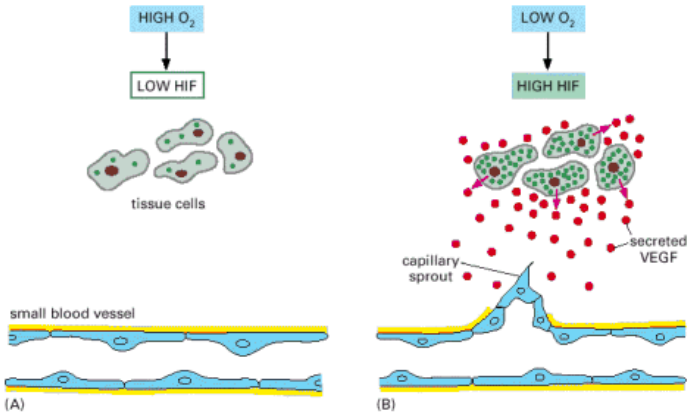

Figure 22-28. The regulatory mechanism controlling blood vessel growth according to a tissue's need for oxygen. Lack of oxygen triggers the secretion of VEGF, which stimulates angiogenesis.

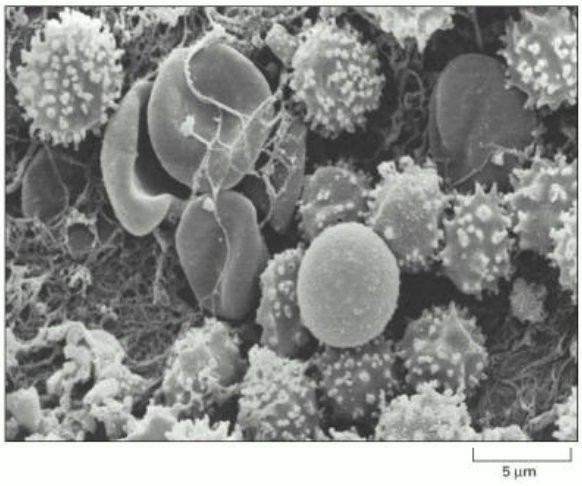

Figure 22-29. Scanning electron micrograph of mammalian blood cells caught in a blood clot. The larger, more spherical cells with a rough surface are white blood cells; the smoother, flattened cells are red blood cells. (Courtesy of Ray Moss.)

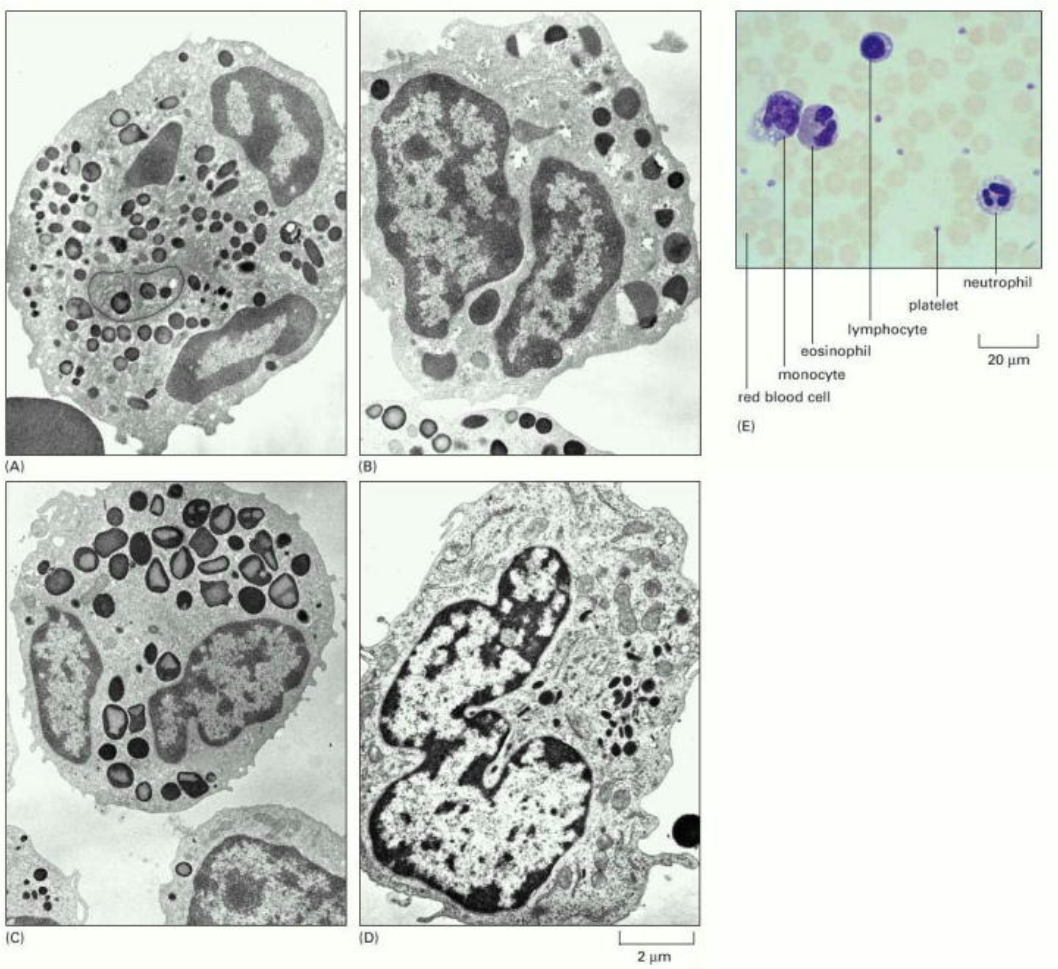

Figure 22-30. White blood cells. (A-D) These electron micrographs show (A) a neutrophil, (B) a basophil, (C) an eosinophil, and (D) a monocyte. Electron micrographs of lymphocytes are shown in Figure 24-7. Each of the cell types shown here has a different function, which is reflected in the distinctive types of secretory granules and lysosomes it contains. There is only one nucleus per cell, but it has an irregular lobed shape, and in (A), (B), and (C) the connections between the lobes are out of the plane of section. (E) A light micrograph of a blood smear stained with the Romanowsky stain, which colors the white blood cells strongly. (A-D, from B.A. Nichols et al., *J. Cell Biol.* 50:498515, 1971. © The Rockefeller University Press; E, courtesy of David Mason.)

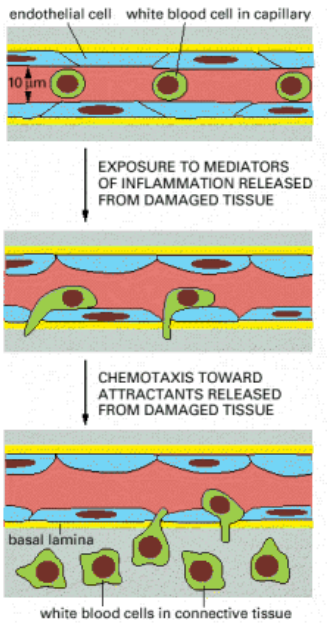

Figure 22-31. The migration of white blood cells out of the bloodstream during an inflammatory response. The response is initiated by a variety of signal molecules produced locally by cells (mainly in the connective tissue) or by complement activation. Some of these mediators act on capillary endothelial cells, causing them to loosen their attachments to their neighbors so that the capillaries become more permeable. Endothelial cells are also stimulated to express selectins, cell-surface molecules that recognize specific carbohydrates that are present on the surface of leucocytes in the blood and cause them to stick to the endothelium. Other mediators called chemokines are secreted by the inflamed tissues and local endothelial cells and act as chemoattractants, causing the bound leucocytes to crawl between the capillary endothelial cells into the tissue.

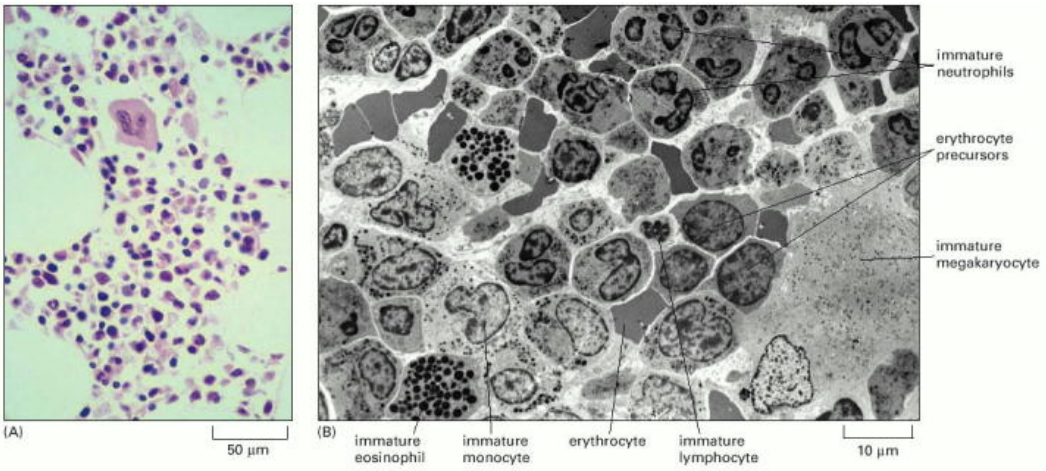

Figure 22-32. Bone marrow. (A) A light micrograph of a stained section. The large empty spaces correspond to fat cells, whose fatty contents have been dissolved away during specimen preparation. The giant cell with a lobed nucleus is a megakaryocyte. (B) A low-magnification electron micrograph. Bone marrow is the main source of new blood cells (except for T lymphocytes, which are produced in the thymus). Note that the immature blood cells of a particular type tend to cluster in "family groups." (A, courtesy of David Mason; B, from J.A.G. Rhodin, Histology: A Text and Atlas. New York: Oxford University Press, 1974.)

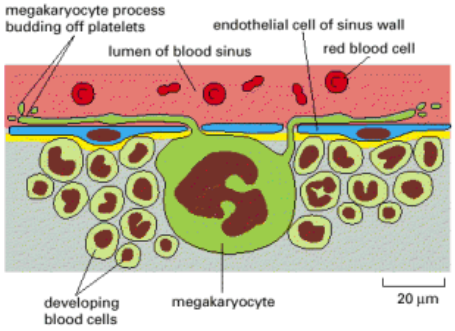

Figure 22-33. A megakaryocyte among other cells in the bone marrow. Its enormous size results from its having a highly polyploid nucleus. One megakaryocyte produces about 10,000 platelets, which split off from long processes that extend through holes in the walls of an adjacent blood sinus.

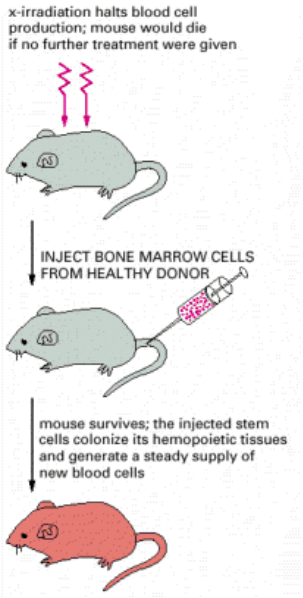

Figure 22-34. Rescue of an irradiated mouse by a transfusion of bone marrow cells. An essentially similar procedure is used in the treatment of leukemia in human patients by bone marrow transplantation.

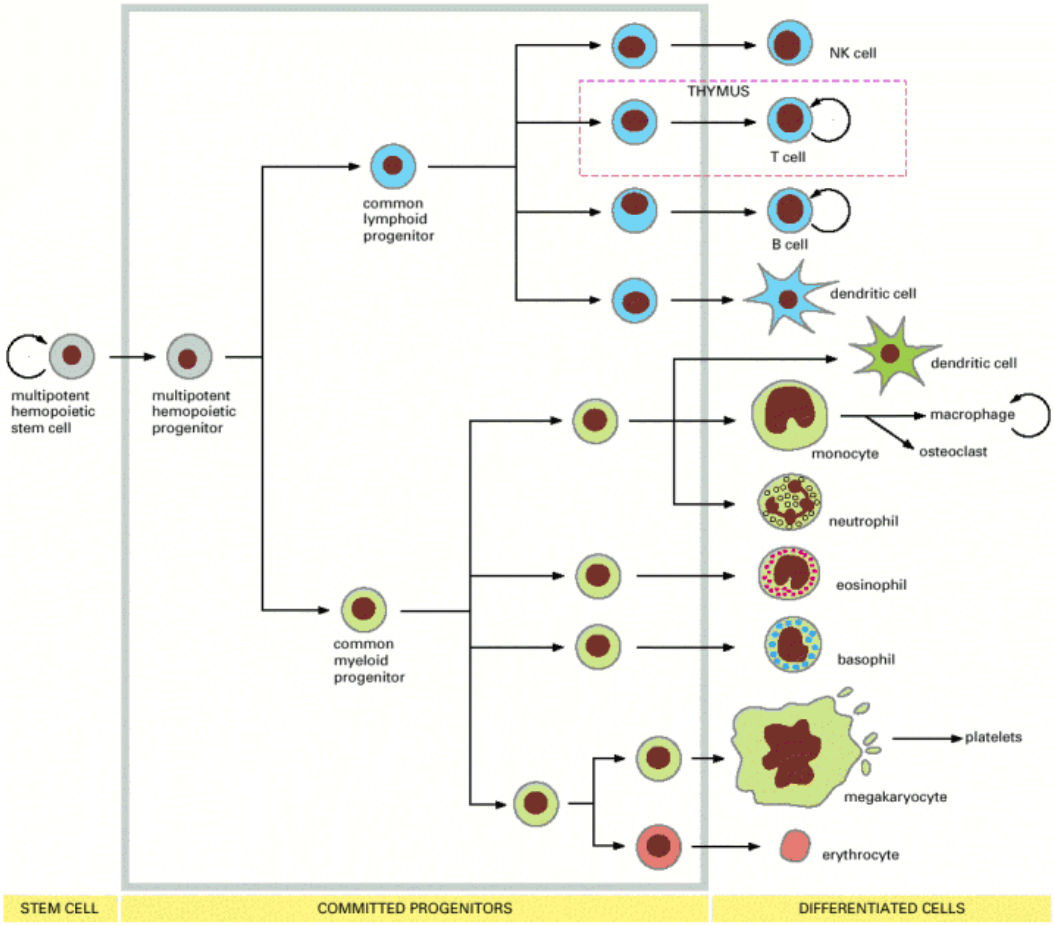

Figure 22-35. A tentative scheme of hemopoiesis. The multipotent stem cell normally divides infrequently to generate either more multipotent stem cells, which are self-renewing, or committed progenitor cells, which are limited in the number of times that they can divide before differentiating to form mature blood cells. As they go through their divisions, the progenitors become progressively more specialized in the range of cell types that they can give rise to, as indicated by the branching of the cell-lineage diagram in the region enclosed in the *gray* box. Many of the details of this part of the lineage diagram are still controversial, however. In adult mammals, all of the cells shown develop mainly in the bone marrow - except for T lymphocytes, which develop in the thymus, and macrophages and osteoclasts, which develop from blood monocytes. Some dendritic cells may also derive from monocytes. Mast cells (not shown) are thought to develop from circulating basophils.

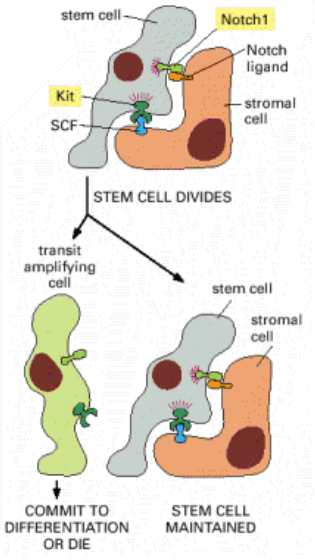

Figure 22-36. Dependence of hemopoietic stem cells on contact with stromal cells. The cartoon shows a dependence on two signaling mechanisms for which there is some evidence. The real system is certainly more complex; the dependence of hemopoietic cells on contact with stromal cells cannot be absolute, since small numbers of the functional stem cells can be found free in the circulation.

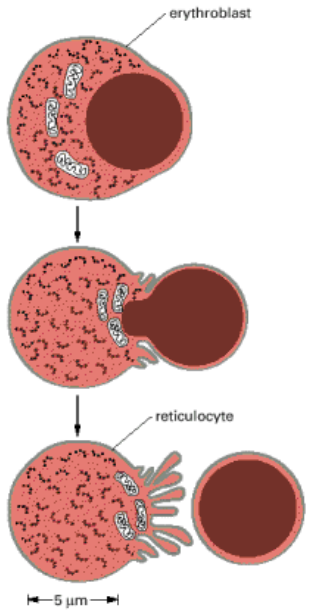

Figure 22-37. A developing red blood cell (erythroblast). The cell is shown extruding its nucleus to become an immature erythrocyte (a reticulocyte), which then leaves the bone marrow and passes into the bloodstream. The reticulocyte will lose its mitochondria and ribosomes within a day or two to become a mature erythrocyte. Erythrocyte clones develop in the bone marrow on the surface of a macrophage, which phagocytoses and digests the nuclei discarded by the erythroblasts.

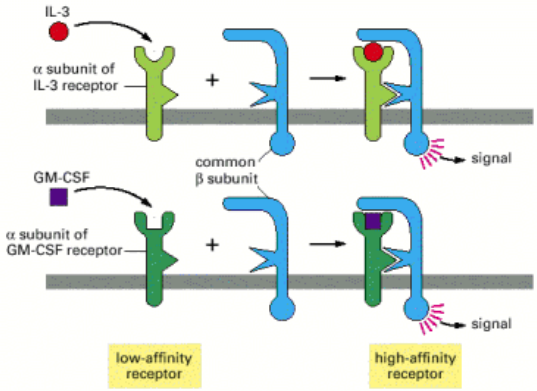

Figure 22-38. Sharing of subunits among CSF receptors. Human IL-3 receptors and GM-CSF receptors have different α subunits and a common β subunit. Their ligands are thought to bind to the free α subunit with low affinity, and this triggers the assembly of the heterodimer that binds the ligand with high affinity.

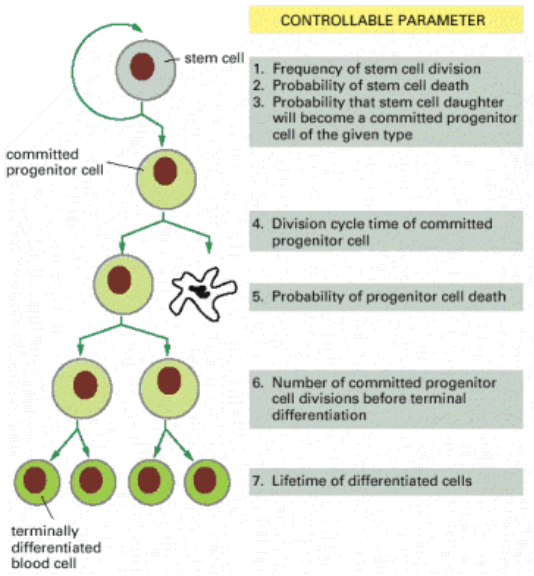

Figure 22-39. Some of the parameters through which the production of blood cells of a specific type might be regulated. Studies in culture suggest that colony-stimulating factors (CSFs) can affect all of these aspects of hemopoiesis.

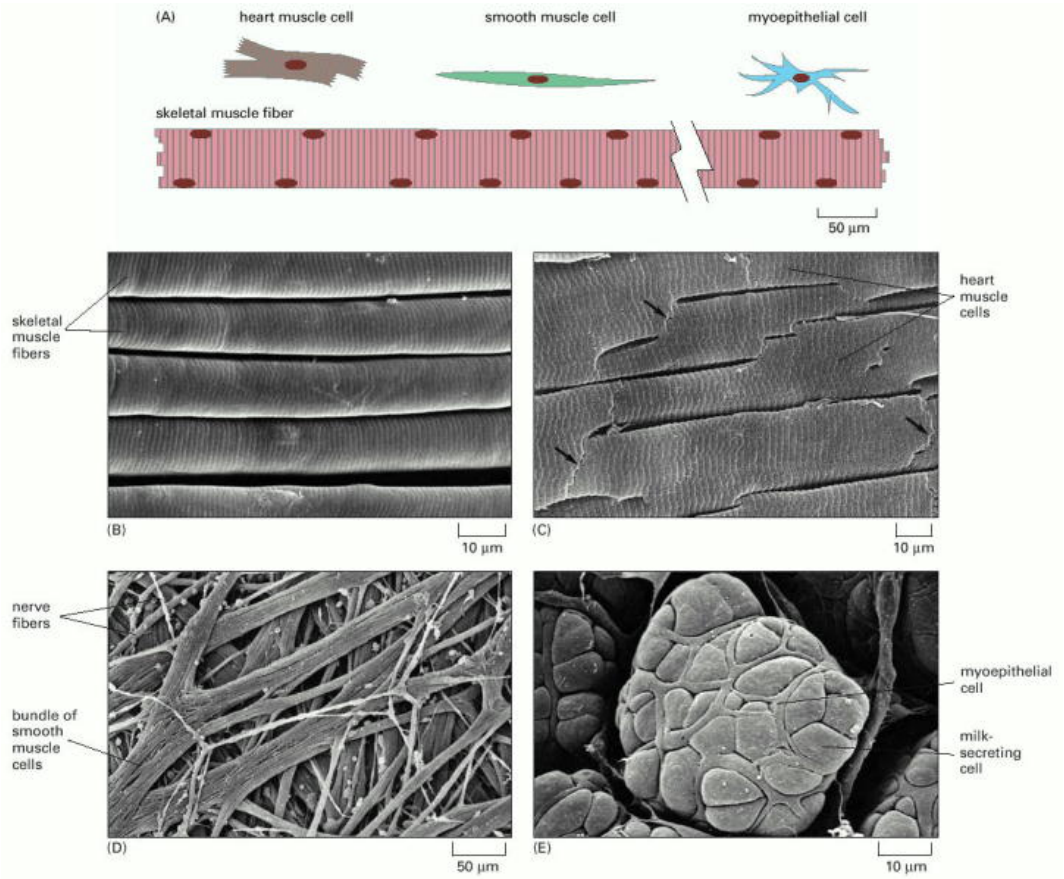

Figure 22-40. The four classes of muscle cells of a mammal. (A) Schematic drawings (to scale). (B-E) Scanning electron micrographs, showing (B) skeletal muscle from the neck of a hamster, (C) heart muscle from a rat, (D) smooth muscle from the urinary bladder of a guinea pig, and (E) myoepithelial cells in a secretory alveolus from a lactating rat mammary gland. The *arrows* in (C) point to intercalated discs - end-to-end junctions between the heart muscle cells; skeletal muscle cells in long muscles are joined end to end in a similar way. Note that the smooth muscle is shown at a lower magnification than the others. (B, courtesy of Junzo Desaki; C, from T. Fujiwara, in Cardiac Muscle in Handbook of Microscopic Anatomy [E.D. Canal, ed.]. Berlin: Springer-Verlag, 1986; D, courtesy of Satoshi Nakasiro; E, from T. Nagato et al., *Cell Tiss. Res.* 209:110, 1980. © Springer-Verlag.)

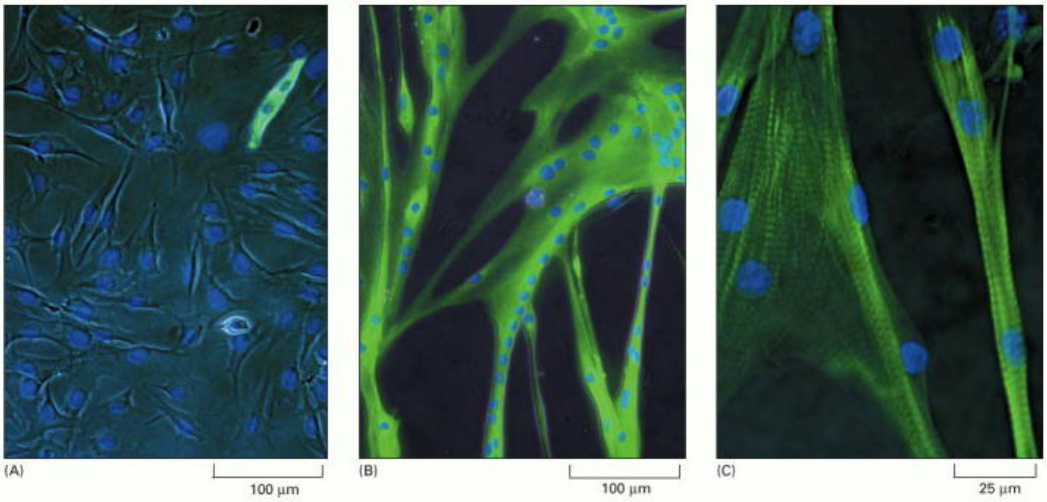

Figure 22-41. Myoblast fusion in culture. The culture is stained with a fluorescent antibody *(green)* against skeletal muscle myosin, which marks differentiated muscle cells, and with a DNA-specific dye *(blue)* to show cell nuclei. (A) A short time after a change to a culture medium that favors differentiation, just two of the many myoblasts in the field of view have switched on myosin production and have fused to form a muscle cell with two nuclei (upper right). (B) Somewhat later, almost all the cells have differentiated and fused. (C) High-magnification view, showing characteristic striations (fine transverse stripes) in two of the multinucleate muscle cells. (Courtesy of Jacqueline Gross and Terence Partridge.)

Figure 22-42. Fast and slow muscle fibers. Two consecutive cross sections of the same piece of adult mouse leg muscle were stained with different antibodies, each specific for a different isoform of myosin heavy chain protein, and images of the two sections were overlaid in false color to show the pattern of muscle fiber types. Fibers stained with antibodies against "fast" myosin *(gray)* are specialized to produce fast-twitch contractions; fibers stained with antibodies against "slow" myosin *(pink)* are specialized to produce slow, sustained contractions. The fast-twitch fibers are known as white muscle fibers because they contain relatively little of the colored oxygen-binding protein myoglobin. The slow muscle fibers are called red muscle fibers because they

contain much more of it. (Courtesy of Simon Hughes.)

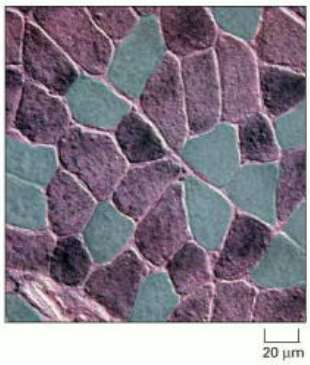

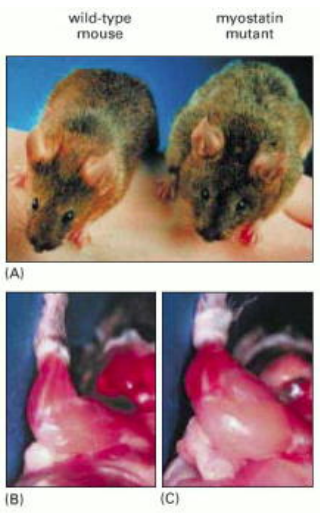

Figure 22-43. Regulation of muscle size by myostatin. (A) A normal mouse compared with a mutant mouse deficient in myostatin. (B) Leg of a normal and (C) of a myostatin-deficient mouse, with skin removed to show the massive enlargement of the musculature in the mutant. (From S.-J. Lee and A.C. McPherron, *Curr. Opin. Genet. Devel.* 9:604607, 1999. © Elsevier.)

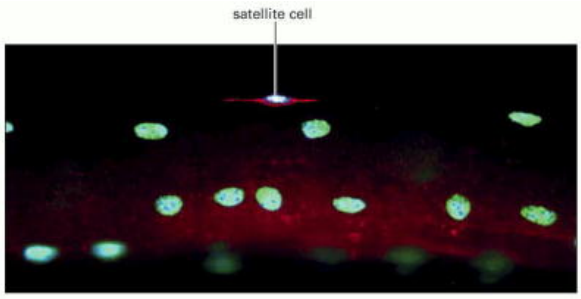

Figure 22-44. A satellite cell on a skeletal muscle fiber. The specimen is stained with an antibody *(red)* against a muscle cadherin, M-cadherin, which is present on both the satellite cell and the muscle fiber and is concentrated at the site where their membranes are in contact. The nuclei of the muscle fiber are stained *green*, and the nucleus of the satellite cell is stained *blue*. (Courtesy of Terence Partridge.)

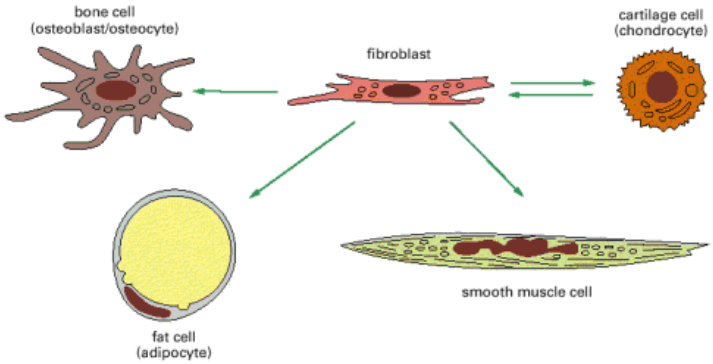

Figure 22-45. The family of connective-tissue cells. *Arrows* show the interconversions that are thought to occur within the family. For simplicity, the fibroblast is shown as a single cell type, but in fact it is uncertain how many types of fibroblasts exist and whether the differentiation potential of different types is restricted in different ways.

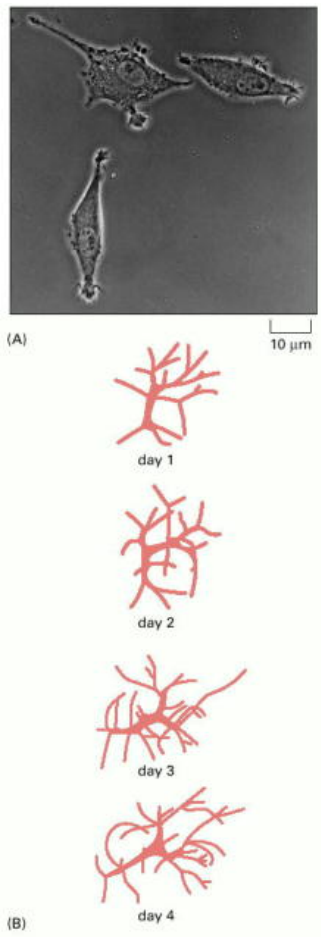

Figure 22-46. The fibroblast. (A) A phase-contrast micrograph of fibroblasts in culture. (B) These drawings of a living fibroblastlike cell in the transparent tail of a tadpole show the changes in its shape and position on successive days. Note that while fibroblasts flatten out in culture, they can have more complex, process-bearing morphologies in tissues. See also Figure 19-35. (A, from E. Pokorna et al., *Cell Motil. Cytoskel.* 28:2533, 1994. © Wiley-Liss; B, redrawn from E. Clark, *Am. J. Anat.* 13:351379, 1912.)

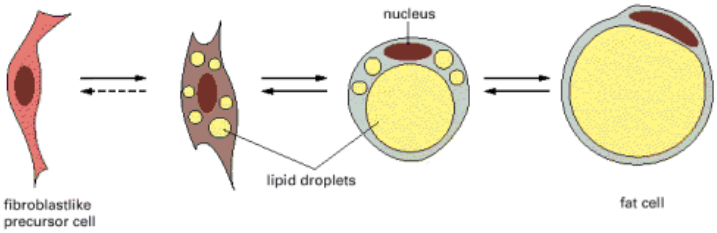

Figure 22-47. The development of a fat cell. A fibroblastlike precursor cell is converted into a mature fat cell by the accumulation and coalescence of lipid droplets. The process is at least partly reversible, as indicated by the *arrows*. The cells in the early and intermediate stages can divide, but the mature fat cell cannot.

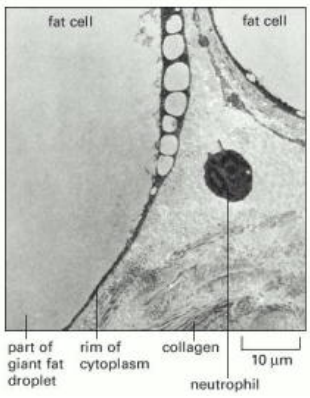

Figure 22-48. Fat cells. This low-magnification electron micrograph shows parts of two fat cells. A neutrophil cell that happens to be present in the adjacent connective tissue provides a sense of scale; each of the fat cells is more than 10 times larger than the neutrophil in diameter and is almost entirely filled with a single large fat droplet. The small fat droplets (pale oval shapes) in the remaining rim of cytoplasm are destined to fuse with the central droplet. The nucleus is not visible in either of the fat cells in the picture. (Courtesy of Don Fawcett, from D.W. Fawcett, A Textbook of Histology, 12th edn. New York: Chapman and Hall, 1994.)

Figure 22-49. Effects of leptin deficiency. Normal mice are here compared with a mouse that has a mutation in the *obese* gene, which codes for leptin. The leptin-deficient mutant fails to limit its eating and becomes

grotesquely fat (three times the weight of a normal mouse). (Courtesy of Jeffrey M. Friedman.)

Figure 22-50. Achondroplasia. This type of dwarfism has a frequency of one in 10,000100,000 births; in more than 99% of cases it is caused by a mutation at an identical site in the genome, corresponding to amino-acid 380 in FGF-receptor-3 (a glycine in the transmembrane domain). The mutation is dominant, and almost all cases are due to new, independently occurring mutations, implying an extraordinarily high mutation rate at this particular site in the genome. The defect in FGF signaling causes dwarfism by interfering with the growth of cartilage in developing long bones. (From Velasquez's painting of Sebastian de Morra. © Museo del Prado, Madrid.)

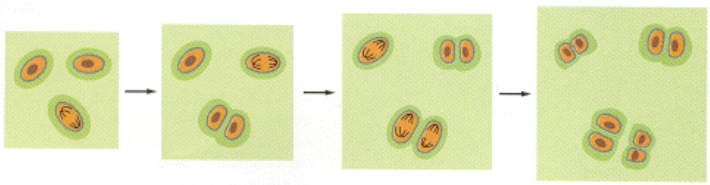

Figure 22-51. The growth of cartilage. The tissue expands as the chondrocytes divide and make more matrix. The freshly synthesized matrix with which each cell surrounds itself is shaded *dark green*. Cartilage may also grow by recruiting fibroblasts from the surrounding tissue and converting them into chondrocytes.

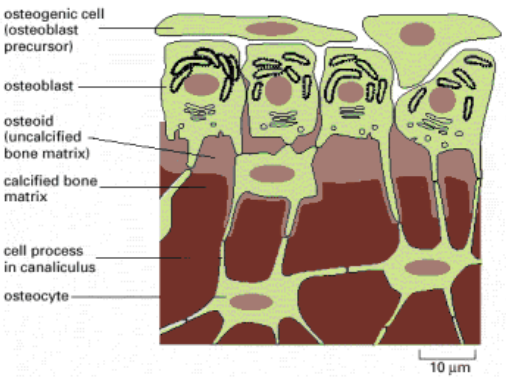

Figure 22-52. Deposition of bone matrix by osteoblasts. Osteoblasts lining the surface of bone secrete the organic matrix of bone (osteoid) and are converted into osteocytes as they become embedded in this matrix. The matrix calcifies soon after it has been deposited. The osteoblasts themselves are thought to derive from osteogenic stem cells that are closely related to fibroblasts.

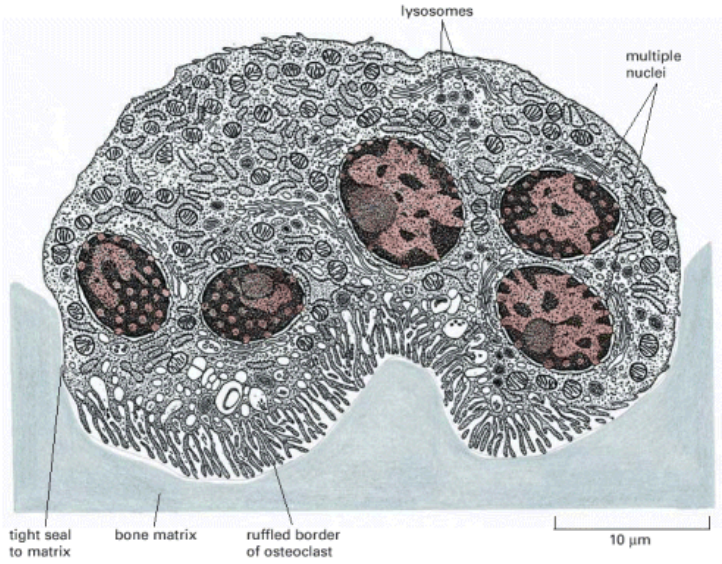

Figure 22-53. An osteoclast shown in cross section. This giant, multinucleated cell erodes bone matrix. The "ruffled border" is a site of secretion of acids (to dissolve the bone minerals) and hydrolases (to digest the organic components of the matrix). Osteoclasts vary in shape, are motile, and often send out processes to resorb bone at multiple sites. They develop from monocytes and can be viewed as specialized macrophages. (From R.V. Krstic´, Ultrastructure of the Mammalian Cell: An Atlas. Berlin: Springer-Verlag, 1979.)

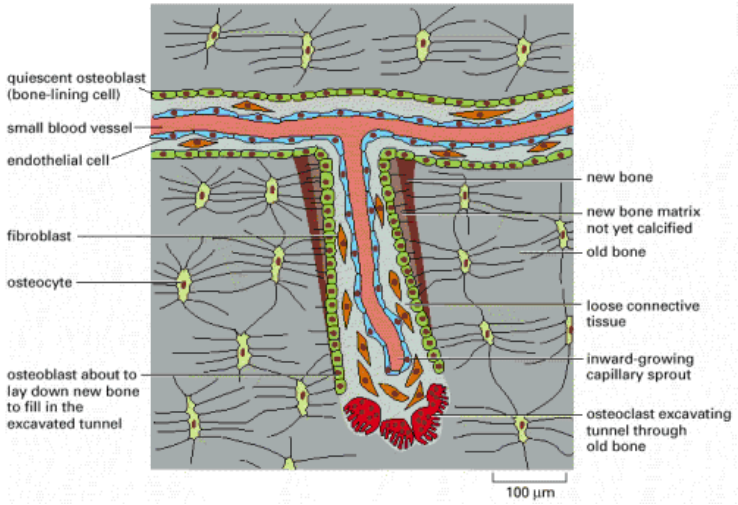

Figure 22-54. The remodeling of compact bone. Osteoclasts acting together in a small group excavate a tunnel through the old bone, advancing at a rate of about 50 µm per day. Osteoblasts enter the tunnel behind them, line its walls, and begin to form new bone, depositing layers of matrix at a rate of 12 µm per day. At the same time, a capillary sprouts down the center of the tunnel. The tunnel eventually becomes filled with concentric layers of new bone, with only a narrow central canal remaining. Each such canal, besides providing a route of access for osteoclasts and osteoblasts, contains one or more blood vessels that transport the nutrients the bone cells require for survival. Typically, about 510% of the bone in a healthy adult mammal is replaced in this way each year. (After Z.F.G. Jaworski, B. Duck, and G. Sekaly, *J. Anat.* 133:397405, 1981.)

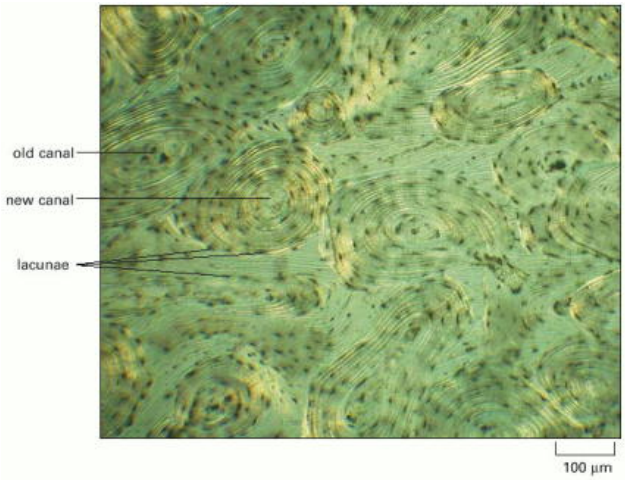

Figure 22-55. A transverse section through a compact outer portion of a long bone. The micrograph shows the outlines of tunnels formed by osteoclasts and then filled in by osteoblasts during successive rounds of bone remodeling. The section has been prepared by grinding. The hard matrix has been preserved, but not the cells. Lacunae and canaliculi that were occupied by osteocytes are clearly visible, however. The alternating bright and dark concentric rings correspond to an alternating orientation of the collagen fibers in the successive layers of bone matrix laid down by the osteoblasts that lined the wall of the canal during life. (This pattern is revealed here by viewing the specimen between partly crossed polarizing filters.) Note how older systems of concentric layers of bone have been partly cut through and replaced by newer systems.

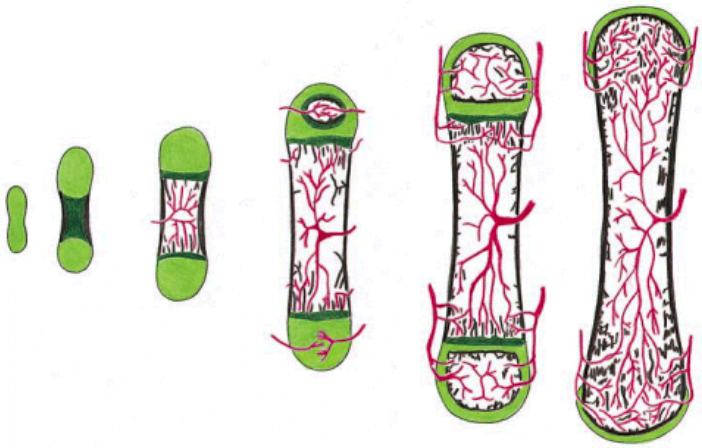

Figure 22-56. The development of a long bone. Long bones, such as the femur or the humerus, develop from a miniature cartilage model. Uncalcified cartilage is shown in *light green*, calcified cartilage in *dark green*, bone in *black*, and blood vessels in *red*. The cartilage is not converted to bone but is gradually replaced by it through the action of osteoclasts and osteoblasts, which invade the cartilage in association with blood vessels. Osteoclasts erode cartilage and bone matrix, while osteoblasts secrete bone matrix. The process of ossification begins in the embryo and is not completed until the end of puberty. The resulting bone consists of a thick-walled hollow cylinder of compact bone enclosing a large central cavity occupied by the bone marrow. Note that not all bones develop in this way. The membrane bones of the skull, for example, are formed directly as bony plates, not from a prior cartilage model. (Adapted from D.W. Fawcett, A Textbook of Histology, 12th edn. New York: Chapman and Hall, 1994.)

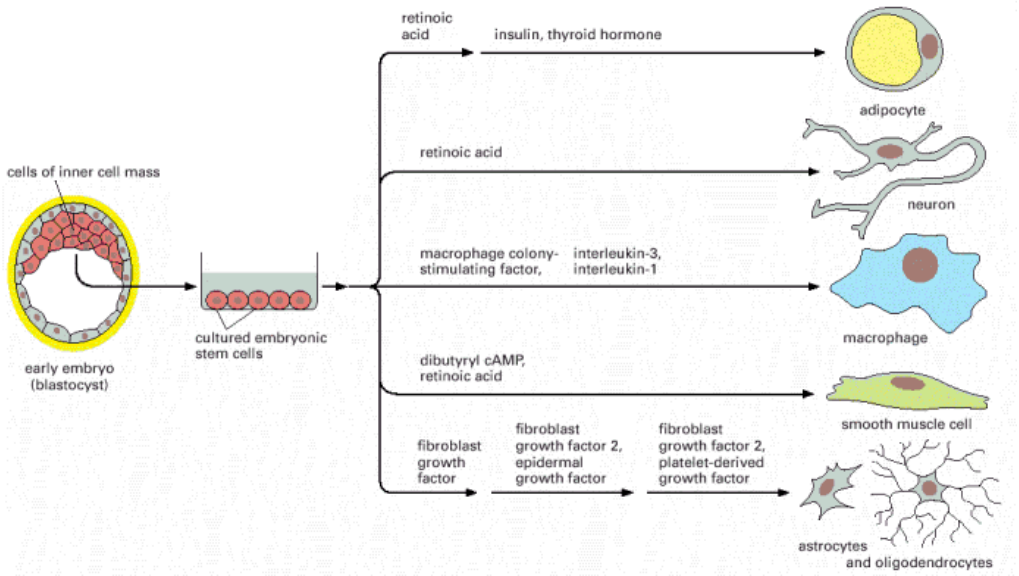

Figure 22-57. Production of differentiated cells from mouse ES cells in culture. ES cells derived from an early mouse embryo can be cultured indefinitely as a monolayer, or allowed to form aggregates called embryoid bodies, in which the cells begin to specialize. Cells from embryoid bodies, cultured in media with different factors added, can then be driven to differentiate in various ways. (Based on E. Fuchs and J.A. Segre, *Cell* 100:143155, 2000.)

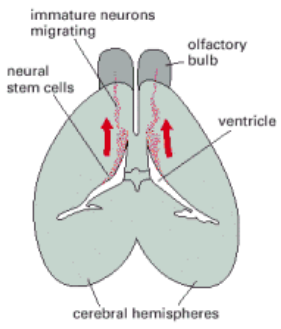

Figure 22-58. The continuing production of neurons in an adult mouse brain. The brain is viewed from above, in a cut-away section, to show the region lining the ventricles of the forebrain where neural stem cells are found. These cells continually produce progeny that migrate to the olfactory bulb, where they differentiate as neurons. The constant turnover of neurons in the olfactory bulb is presumably linked in some way to the turnover of the olfactory receptor neurons that project to it from the olfactory epithelium, as discussed earlier. There is also a continuing turnover of neurons in the adult hippocampus, a region specially concerned with learning and memory, where plasticity of adult function seems to be associated with turnover of a specific subset of neurons (Adapted from B. Barres, *Cell* 97:667670, 1999.)

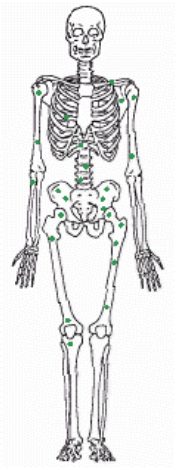

Figure 23-1. Metastasis. Malignant tumors typically give rise to metastases, making the cancer hard to eradicate. The drawing shows common sites in the bone marrow for metastases from carcinoma of the prostate gland. (From Union Internationale Contre le Cancer, TNM Atlas: Illustrated Guide to the Classification of Malignant Tumors, 2nd edn., Berlin: Springer-Verlag, 1986.)

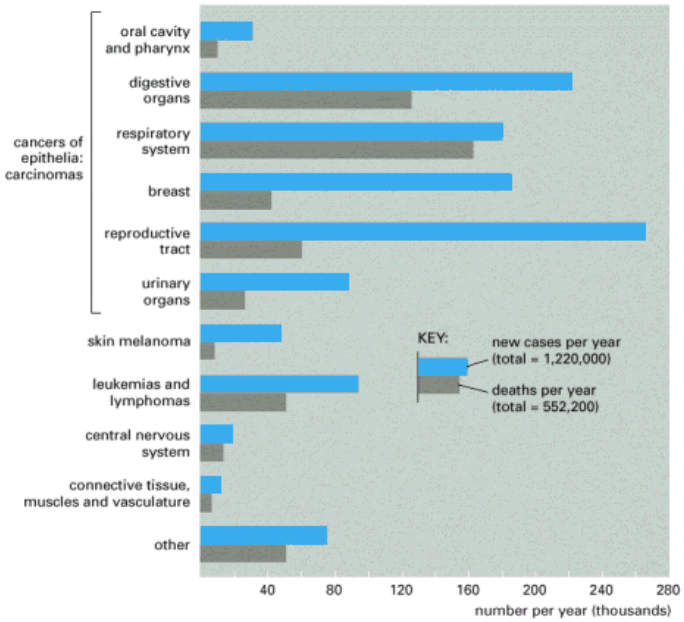

Figure 23-2. Cancer incidence and mortality in the United States. These figures are for the year 2000. Total new cases diagnosed in that year in the United States were 1,220,000, and total cancer deaths were 552,200. Note that only about half the number of people who develop cancer die of it. In the world as a whole, the five most common cancers are those of the lung, stomach, breast, colon/rectum, and uterine cervix, and the total number of new cancer cases recorded per year is just over 6 million. Skin cancers other than melanomas are not included in figures, since almost all are cured easily and many go unrecorded. (Data from American Cancer Society, Cancer Facts and Figures, 2000.)

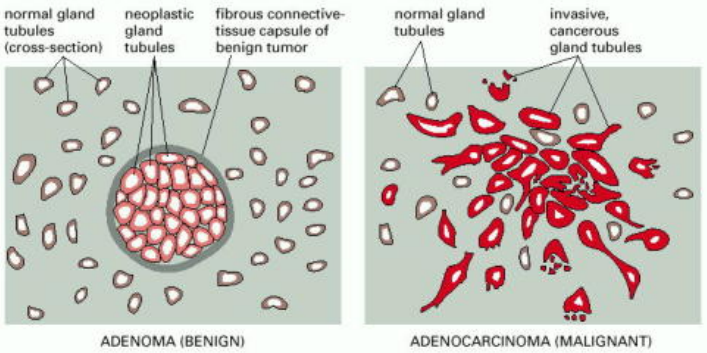

Figure 23-3. Benign versus malignant tumors. A benign glandular tumor (an adenoma) and a malignant glandular tumor (an adenocarcinoma) appear structurally distinct. There are many forms that such tumors may take; the diagram illustrates types that might be found in the breast.

Figure 23-4. The growth of a typical human tumor such as a tumor of the breast. The diameter of the tumor is plotted on a logarithmic scale. Years may elapse before the tumor becomes noticeable. The doubling time of a typical breast tumor, for example, is about 100 days.

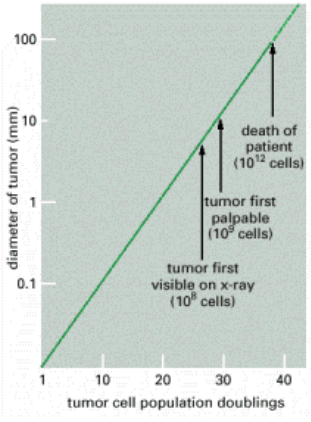

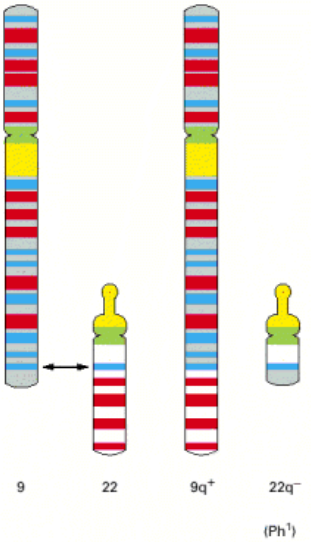

Figure 23-5. The translocation between chromosomes 9 and 22 responsible for chronic myelogenous leukemia. The smaller of the two resulting abnormal chromosomes is called the Philadelphia chromosome, after the city where the abnormality was first recorded.

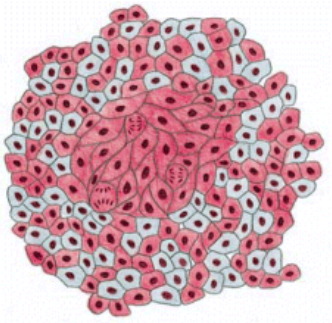

Figure 23-6. Evidence from X-inactivation mosaics demonstrates the monoclonal origin of cancers. As a result of a random process that occurs in the early embryo, practically every normal tissue in a woman's body is a mixture of cells with different X chromosomes heritably inactivated (indicated here by the mixture of *red* cells and *gray* cells in the normal tissue). When the cells of a cancer are tested for their expression of an X-linked marker gene, however, they are usually all found to have the same X chromosome inactivated. This implies that they are all derived from a single cancerous founder cell.

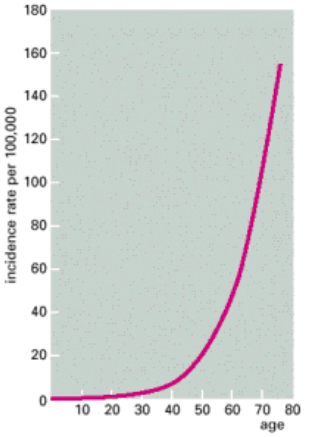

Figure 23-7. Cancer incidence as a function of age. The number of newly diagnosed cases of colon cancer in women in England and Wales in one year is plotted as a function of age at diagnosis and expressed relative to the total number of individuals in each age group. The incidence of cancer rises steeply as a function of age. If only a single mutation were required to trigger the cancer and this mutation had an equal chance of occurring at any time, the incidence would be independent of age. (Data from C. Muir et al., Cancer Incidence in Five Continents, Vol. V. Lyon: International Agency for Research on Cancer, 1987.)

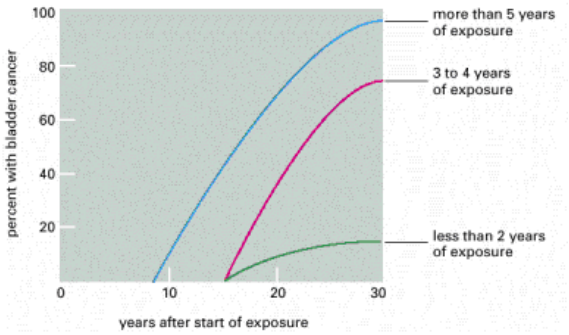

Figure 23-8. Delayed onset of cancer following exposure to a carcinogen. The graph shows the length of the delay before onset of bladder cancer in a set of 78 workers in the chemical industry who had been exposed to the carcinogen 2-naphthylamine, grouped according to the duration of their exposure. (Modified from J. Cairns, Cancer: Science and Society. San Francisco: W.H. Freeman, 1978. After M.H.C. Williams, in Cancer, Vol. III [R.W. Raven, ed.]. London: Butterworth Heinemann, 1958.)

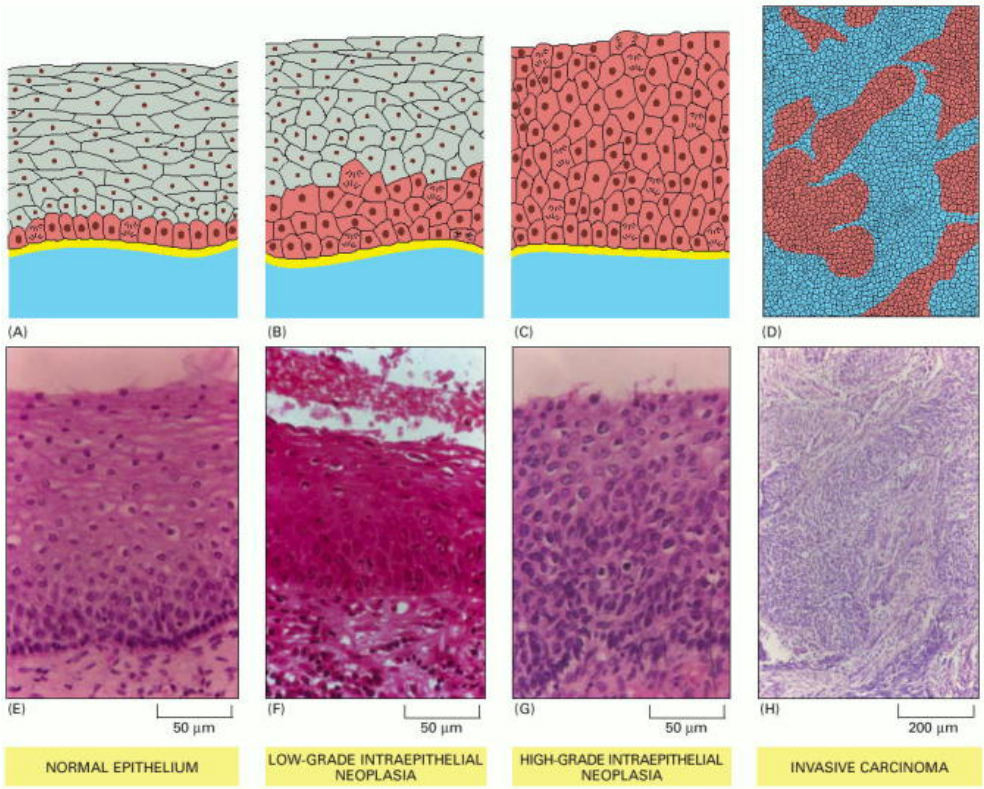

Figure 23-9. The stages of progression in the development of cancer of the epithelium of the uterine cervix. Pathologists use standardized terminology to classify the types of disorder they see, so as to guide the choice of treatment. Schematic diagrams are shown in A-D; sections of cervical epithelium corresponding to these changes are shown in E-H. (A, E) In the normal stratified squamous epithelium, dividing cells are confined to the basal layer. (B, F) In low-grade intraepithelial neoplasia, dividing cells can be found throughout the lower third of the epithelium; the superficial cells are still flattened and show signs of differentiation, but this is incomplete. (C, G) In high-grade intraepithelial neoplasia, cells in all the epithelial layers are proliferating and show no sign of differentiation. (D, H) True malignancy begins when the cells move through or destroy the basal lamina and invade the underlying connective tissue. (Photographs courtesy of Margaret Stanley.)

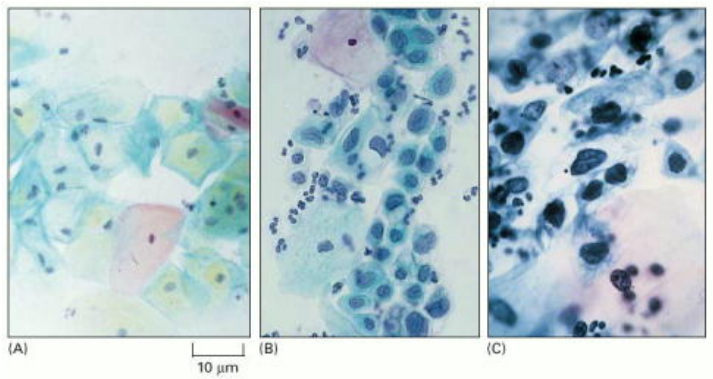

Figure 23-10. Photographs of cells collected by scraping the surface of the uterine cervix (the Papanicolaou or "Pap smear" technique). (A) Normal: the cells are large and well differentiated, with highly condensed nuclei. (B) Precancerous lesion: differentiation and proliferation are abnormal but the lesion is not yet invasive; the cells are in various stages of differentiation, some quite immature. (C) Invasive carcinoma: the cells all appear undifferentiated, with scanty cytoplasm and a relatively large nucleus. Debris in the background includes some white blood cells. (Courtesy of Winifred Gray.)

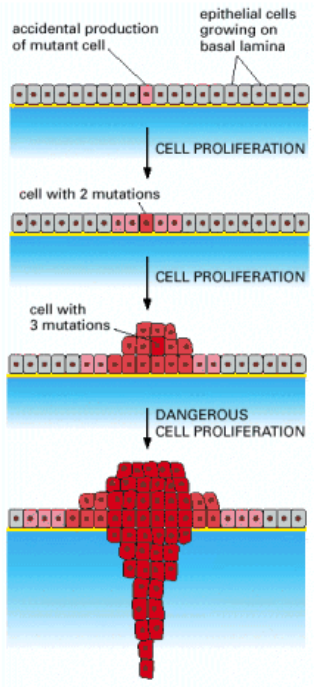

Figure 23-11. Clonal evolution. A tumor develops through repeated rounds of mutation and proliferation, giving rise eventually to a clone of fully malignant cancer cells. At each step, a single cell undergoes a mutation that enhances cell proliferation, so that its progeny become the dominant clone in the tumor. Proliferation of this clone then hastens occurrence of the next step of tumor progression by increasing the size of the cell population at risk of undergoing an additional mutation.

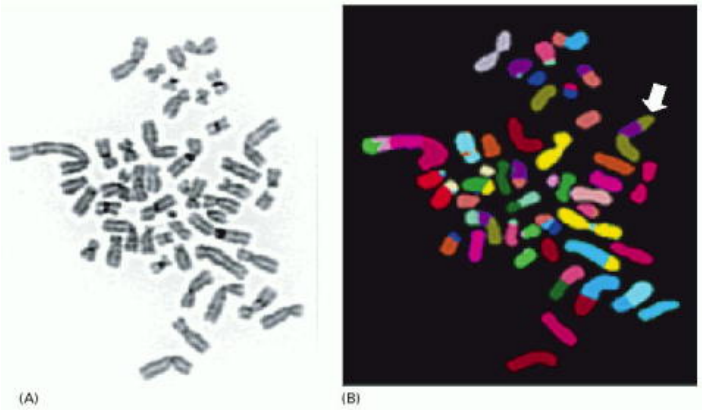

Figure 23-12. Chromosomes from a breast tumor displaying abnormalities in structure and number. Chromosomes were prepared from a breast tumor cell in metaphase, spread on a glass slide, and stained with (A) a general DNA stain or (B) a combination of fluorescent stains that give a different color for each normal human chromosome. The staining (displayed in false color) shows multiple translocations, including a doubly translocated chromosome *(white arrow)* made up of two pieces of chromosome 8 *(green)* and a piece of chromosome 17 *(purple).* The karyotype also contains 48 chromosomes, instead of the normal 46. (Courtesy of Joanne Davidson and Paul Edwards.)

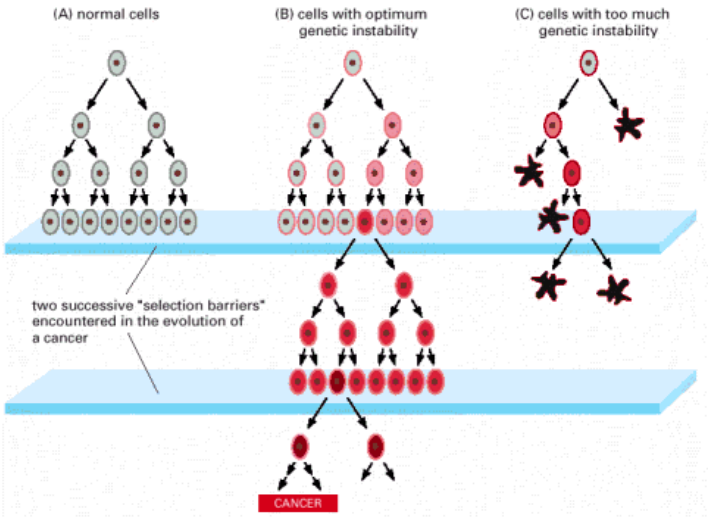

Figure 23-13. Genetic instability and tumor progression. Cells that maintain an optimum level of genetic instability may be the most successful in the race to form a tumor. (A) In normal cells, the intrinsic amount of genetic instability is low. Thus when normal cells hit a selection barrier - low levels of oxygen or a scarcity of proliferation signals, for example - they are very unlikely to be mutable enough to produce a cell that continues proliferating. (B) In tumor cell precursors, an increased level of genetic instability makes it likely that at least one cell will contain the requisite genetic alteration to pass the selection barrier and continue the process of tumor progression. This genetic instability is retained in the lineage, and it can be measured in the resulting tumor. (C) If the level of genetic instability is too high, many of the cells suffer deleterious mutations and either proliferate much more slowly than their neighbors or are eliminated by cell death. This excessive mutability can lead to extinction of the cell lineage. (Adapted from D.P. Cahill et al., *Trends Cell Biol*. 9:M57M60, 1999.)

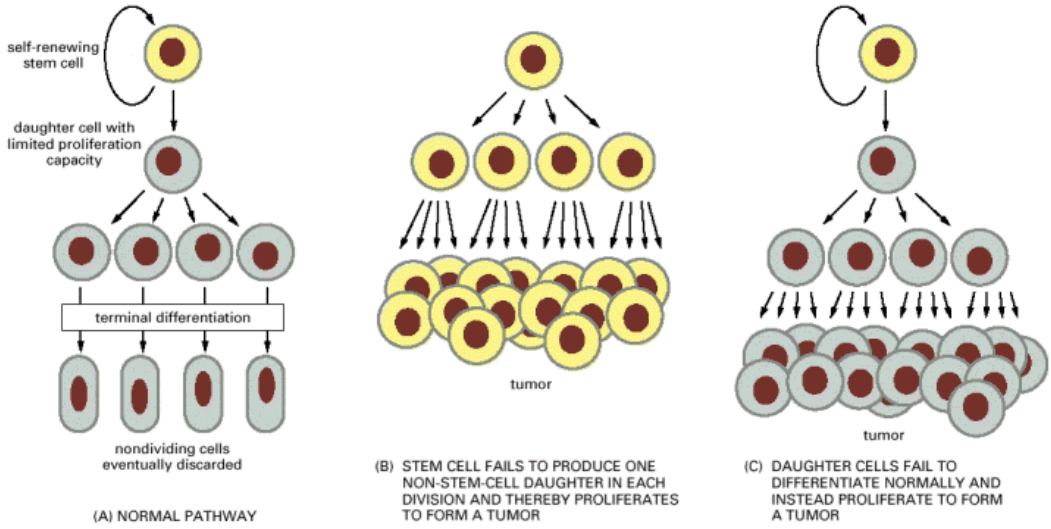

Figure 23-14. Normal and deranged control of cell production from stem cells. (A) The normal strategy for producing new differentiated cells. (B and C) Two types of derangement that can give rise to the unbridled proliferation characteristic of cancer. Note that an excessive cell-division rate for the stem cells in (A) will not by itself have this effect, as long as each cell division produces only one daughter that is a stem cell.

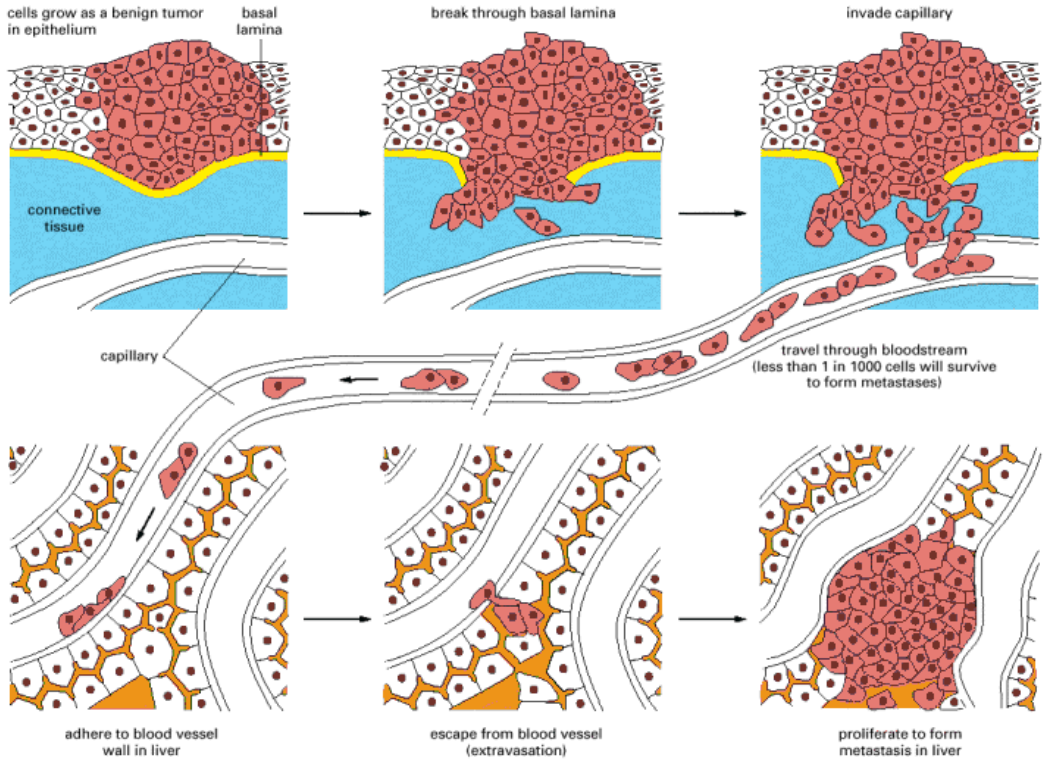

Figure 23-15. Steps in the process of metastasis. This example illustrates the spread of a tumor from an organ such as the lung or bladder to the liver. Tumor cells may enter the bloodstream directly by crossing the wall of a blood vessel, as diagrammed here, or, more commonly perhaps, by crossing the wall of a lymphatic vessel that ultimately discharges its contents (lymph) into the bloodstream. Tumor cells that have entered a lymphatic vessel often become trapped in lymph nodes along the way, giving rise to lymph-node metastases. Studies in animals show that typically far less than one in every thousand malignant tumor cells that enter the bloodstream will survive to produce a tumor at a new site.

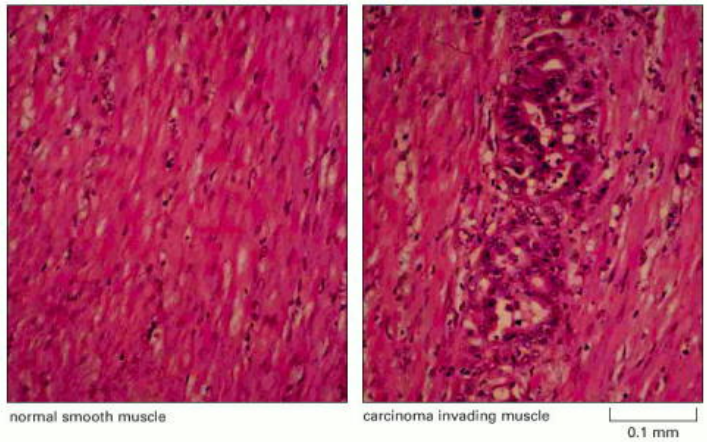

Figure 23-16. Colon cancer invading the smooth muscle layer that lies beneath the colon epithelium. In this tissue slice, colorectal cancer cells can be seen growing between the muscle fibers *(pink)*. Some stages in the development of this type of cancer are shown in Figure 23-38. (Courtesy of Paul Edwards and the Department of Pathology, University of Cambridge.)

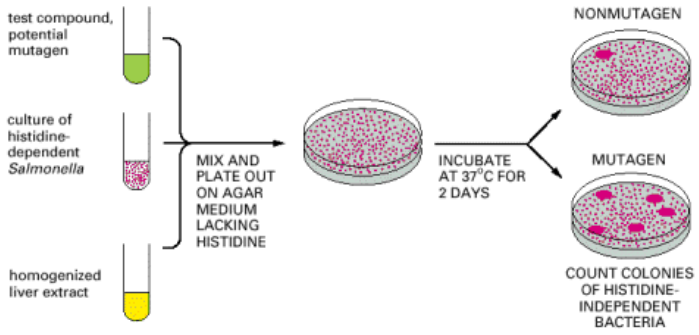

Figure 23-17. The Ames test for mutagenicity. The test uses a strain of *Salmonella* bacteria that require histidine in the medium because of a defect in a gene necessary for histidine synthesis. Mutagens can cause a further change in this gene that reverses the defect, creating revertant bacteria that do not require histidine. To increase the sensitivity of the test, the bacteria also have a defect in their DNA repair machinery that makes them especially susceptible to agents that damage DNA. A majority of compounds that are mutagenic in tests such as this are also carcinogenic and vice versa.

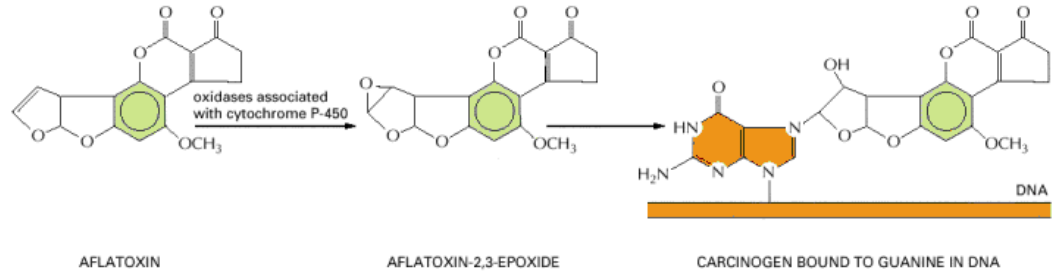

Figure 23-18. Metabolic activation of a carcinogen. Many chemical carcinogens have to be activated by a metabolic transformation before they will cause mutations by reacting with DNA. The compound illustrated here is *aflatoxin B1*, a toxin from a mold *(Aspergillus flavus oryzae)* that grows on grain and peanuts when they are stored under humid tropical conditions. It is thought to be a contributory cause of liver cancer in the tropics and is associated with characteristic mutations of the *p53* gene (discussed later in this chapter).

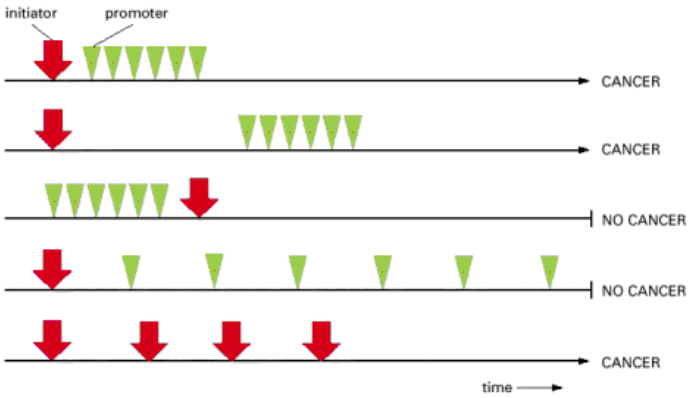

Figure 23-19. Some possible schedules of exposure to a tumor initiator (mutagenic) and a tumor promoter (nonmutagenic) and their outcomes. Cancer ensues only if the exposure to the promoter follows exposure to the initiator and only if the intensity of exposure to the promoter exceeds a certain threshold. Cancer can also occur as a result of repeated exposure to the initiator alone.

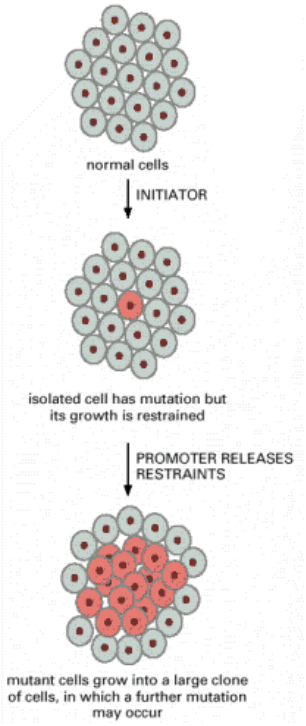

Figure 23-20. The effect of a tumor promoter. The tumor promoter expands the population of mutant cells, thereby increasing the probability of tumor progression by further genetic change.

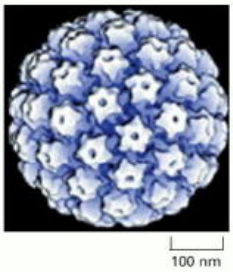

Figure 23-21. A human papillomavirus. (Courtesy of Norman Olson.)

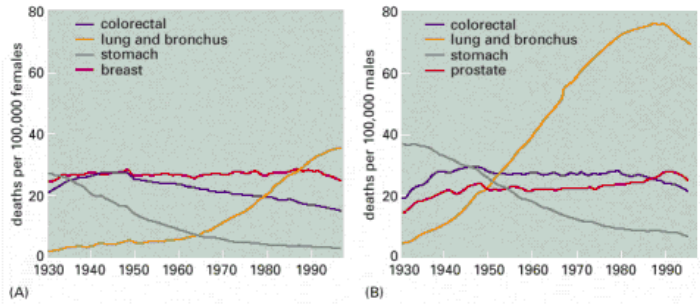

Figure 23-22. Age-adjusted cancer death rates, United States, 1930-1996. Selected death rates adjusted to the age distribution of the US population in 1970, are plotted for (A) females and (B) males. Note the dramatic rise in lung cancer for both sexes, following the pattern of tobacco smoking, and the fall in deaths from stomach cancer, possibly related to changes in diet or in patterns of infection with *Helicobacter*. Recent reductions in other cancer death rates may correspond to improvements in detection and treatment. (Adapted from Cancer Facts and Figures 2000. © American Cancer Society, 2000.)

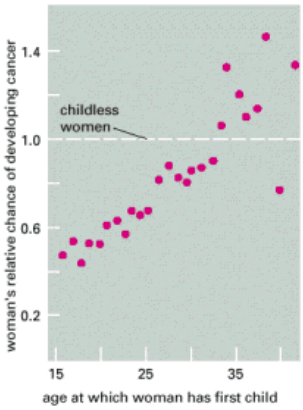

Figure 23-23. Effects of childbearing on the risk of breast cancer. The relative probability of breast cancer developing at some time in a woman's life is plotted as a function of the age at which she gives birth to her first child. The graph shows the value of the probability relative to that for a childless woman. The longer the period of exposure to reproductive hormones up to birth of the first child, the greater the risk. It is thought that the first full-term pregnancy may result in a permanent change in the state of differentiation of the cells of the breast, altering their subsequent responses to hormones. Several other lines of epidemiological evidence also support the view that exposure to certain combinations of reproductive hormones, especially estrogen, can promote development of breast cancer. (From J. Cairns, Cancer: Science and Society. San Francisco: W.H. Freeman, 1978. After B. MacMahon, P. Cole, and J. Brown, *J. Natl. Cancer Inst.* 50:2142, 1973.)

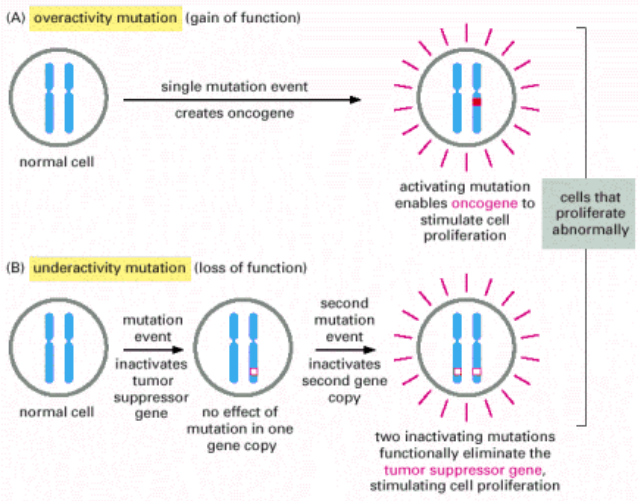

Figure 23-24. Cancer-critical genes fall into two readily distinguishable categories, dominant and recessive. Oncogenes act in a dominant manner: a gain-of-function mutation in a single copy of the cancer-critical gene can drive a cell toward cancer. Tumor suppressor genes, on the other hand, generally act in a recessive manner: the function of both alleles of the cancer-critical gene must be lost to drive a cell toward cancer. In this diagram, activating mutations are represented by solid red boxes, inactivating mutations by hollow red boxes.

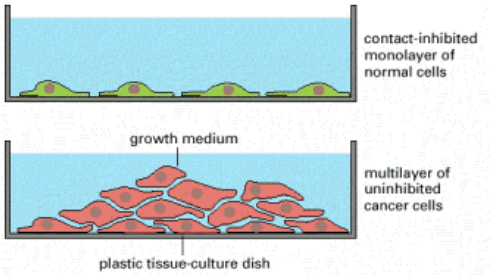

Figure 23-25. Loss of contact inhibition in cell culture. Most normal cells stop proliferating once they have carpeted the dish with a single layer of cells: proliferation seems to depend on contact with the dish, and to be inhibited by contacts with other cells. Cancer cells, in contrast, usually disregard these restraints and continue to grow, so that they pile up on top of one another.

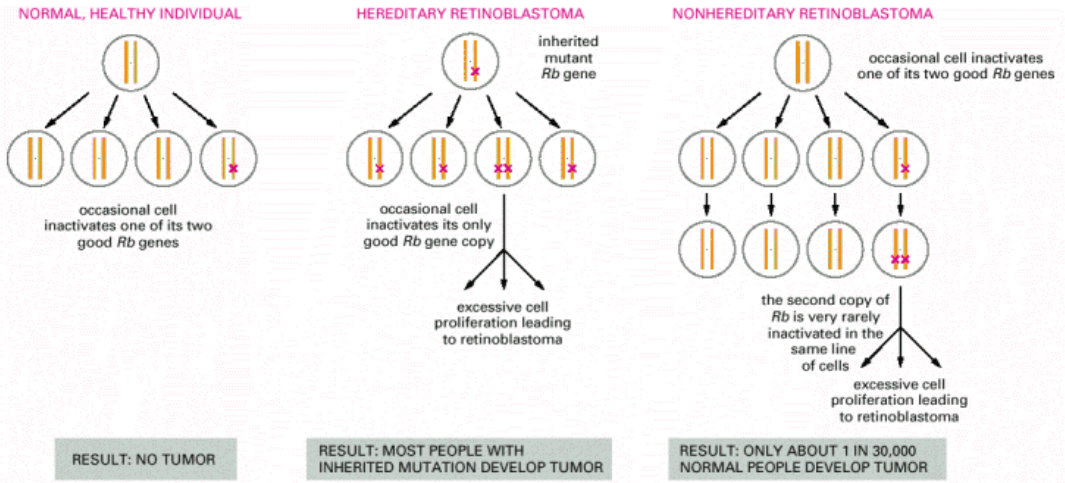

Figure 23-26. The genetic mechanisms underlying retinoblastoma. In the hereditary form, all cells in the body lack one of the normal two functional copies of the *Rb* tumor suppressor gene, and tumors occur where the remaining copy is lost or inactivated by a somatic mutation. In the nonhereditary form, all cells initially contain two functional copies of the gene, and the tumor arises because both copies are lost or inactivated through the coincidence of two somatic mutations in one line of cells.

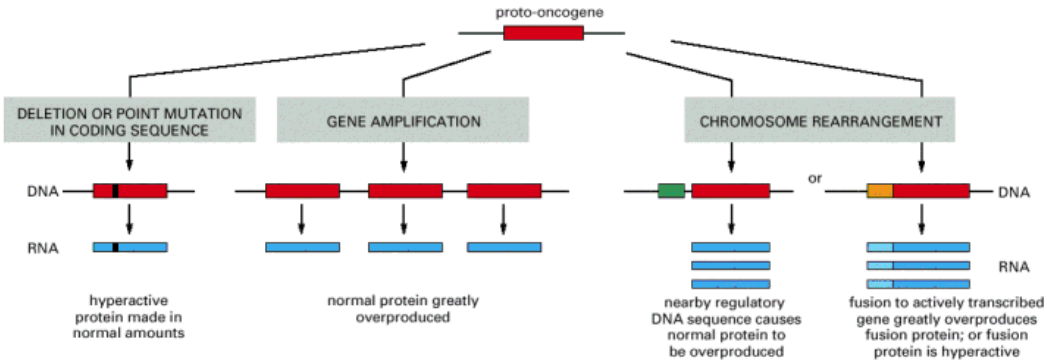

Figure 23-27. Three ways in which a proto-oncogene can be made overactive to convert it into an oncogene.

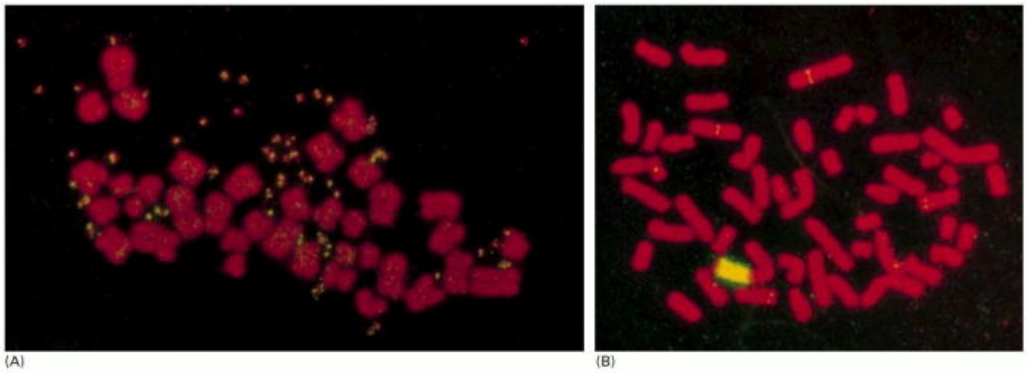

Figure 23-28. Chromosomal changes in cancer cells reflecting gene amplification. In these examples, the numbers of copies of a *myc* proto-oncogene have been amplified. Amplification of oncogenes is common in carcinomas and is often visible as a curious change in the karyotype: the cell is seen to contain additional pairs of miniature chromosomes - so-called *double minute chromosomes* - or to have a *homogeneously staining region* interpolated in the normal banding pattern of one of its regular chromosomes. Both these aberrations consist of massively amplified numbers of copies of a small segment of the genome. The chromosomes are stained with a *red* fluorescent dye, while the multiple copies of the *Myc* gene are detected by *in situ* hybridization with a *yellow* fluorescent probe. (A) Karyotype of a cell in which the *Myc* gene copies are present as double minute chromosomes (paired *yellow specks).* (B) Karyotype of a cell in which the multiple *Myc* gene copies appear as a homogeneously staining region *(yellow)* interpolated in one of the regular chromosomes. (Ordinary single-copy *myc* genes can be detected as tiny *yellow dots* elsewhere in the genome.) (Courtesy of Denise Sheer.)

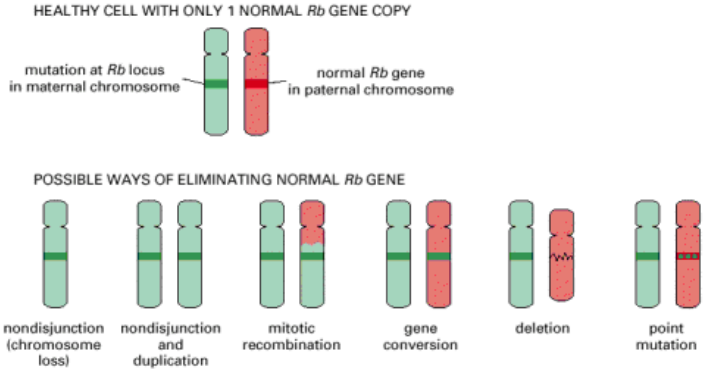

Figure 23-29. Six ways of losing the remaining good copy of a tumor suppressor gene. A cell that is defective in only one of its two copies of a tumor suppressor gene - for example, the *Rb* gene - usually behaves as a normal, healthy cell; the diagrams show how it may come to lose the function of the other gene copy as well and thereby progress toward cancer. Cloned DNA probes can be used in conjunction with tests for polymorphisms (see Chapter 8) to analyze the tumor DNA and discover which type of event has occurred in a given patient. A seventh possibility, encountered with some tumor suppressors, is that the gene may be silenced by an epigenetic change, without alteration of the DNA sequence. (After W.K. Cavenee et al., *Nature* 305:779784, 1983. © Macmillan Magazines Ltd.)

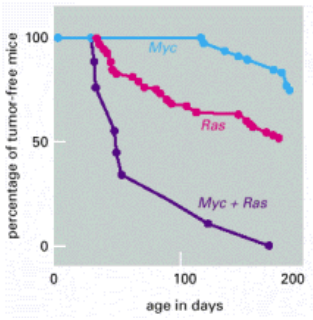

Figure 23-30. Oncogene collaboration in transgenic mice. The graphs show the incidence of tumors in three types of transgenic mice, one carrying a *Myc* oncogene, one carrying a *Ras* oncogene, and one carrying both oncogenes. For these experiments two lines of transgenic mice were first constructed. One carries an inserted copy of an oncogene created by fusing the proto-oncogene *Myc* with the mouse mammary tumor virus regulatory DNA (which then drives *Myc* overexpression in specific tissues such as the mammary gland). The other line carries an inserted copy of the *Ras* oncogene under control of the same regulatory element. Both strains of mice develop tumors much more frequently than normal, most often in the mammary or salivary glands. Mice that carry both oncogenes together are obtained by crossing the two strains. These hybrids develop tumors at a far higher rate still, much greater than the sum of the rates for the two oncogenes separately. Nevertheless, the tumors arise only after a delay and only from a small proportion of the cells in the tissues where the two genes are expressed. Some further accidental change, in addition to the two oncogenes, is apparently required for the development of cancer. (After E. Sinn et al., *Cell* 49:465475, 1987. © Elsevier.)

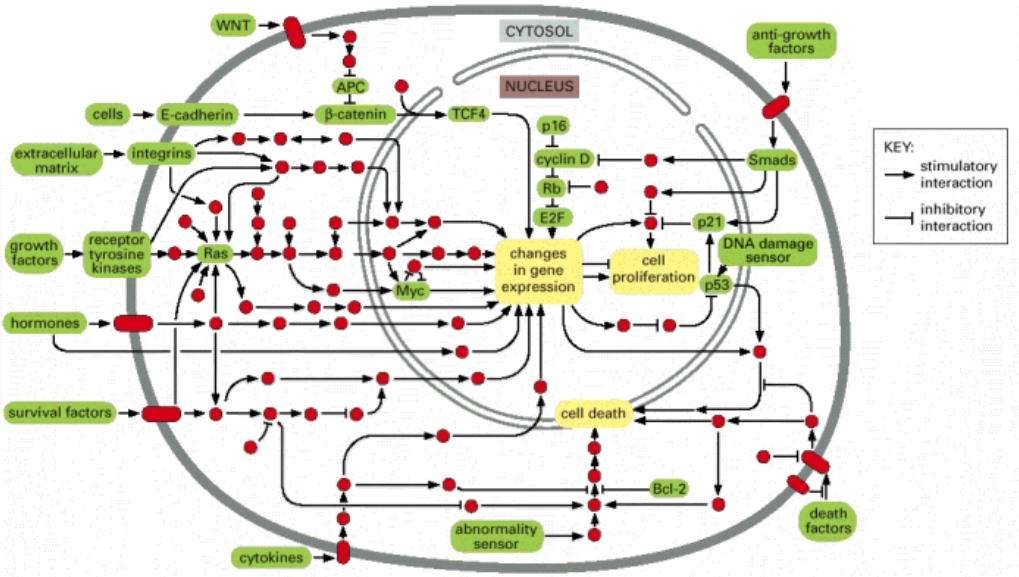

Figure 23-31. Chart of the major signaling pathways relevant to cancer in human cells, indicating the cellular locations of some of the proteins modified by mutation in cancers. Products of both oncogenes and tumor suppressor genes often occur within the same pathways. Individual signaling proteins are indicated by *red circles*, with the cancer-critical components and control mechanisms discussed in this chapter in *green*. Stimulatory and inhibitory interactions between proteins are designated as shown in the key. (Adapted from D. Hanahan and R.A. Weinberg, *Cell* 100:5770, 2000.)

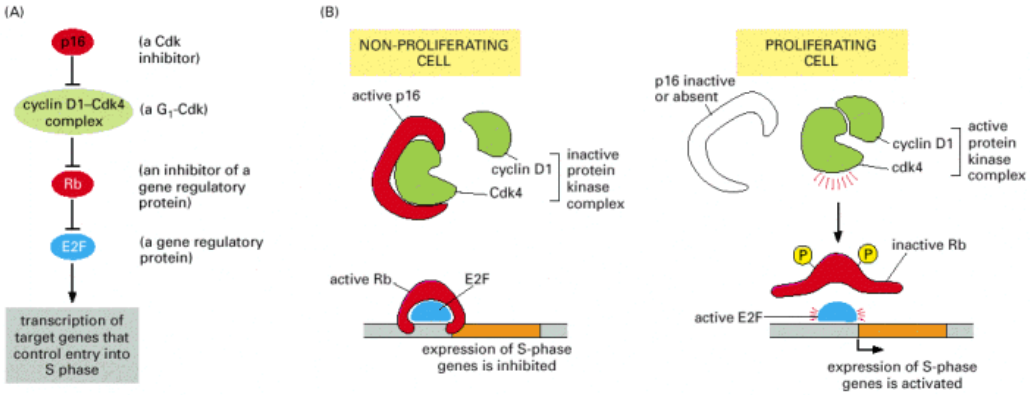

Figure 23-32. The pathway that controls cell cycling via Rb protein. All the components of this pathway have been found to be altered by mutation in human cancers (products of proto-oncogenes, *green;* products of tumor suppressor genes, *red;* E2F shown in *blue* because it has both inhibitory and stimulatory actions, depending on the other proteins that are bound to it). In most cases, only one of the components is altered in any individual tumor. (A) A simplified view of the dependency relationships in this pathway; see Figure 17-30 for further details. (B) The Rb protein inhibits entry into the cell-division cycle when it is unphosphorylated.The complex of Cdk4 and cyclin D1 phosphorylates Rb, thereby encouraging cell proliferation. When a cell is stressed, p16 inhibits the formation of an active Cdk4/cyclin D1 complex, preventing proliferation. Inactivation of Rb or p16 by mutation encourages cell division (thus each can be regarded as a tumor suppressor) while overactivity of Cdk4 or cyclin D1 encourages cell division (thus each can be regarded as a proto-oncogene).

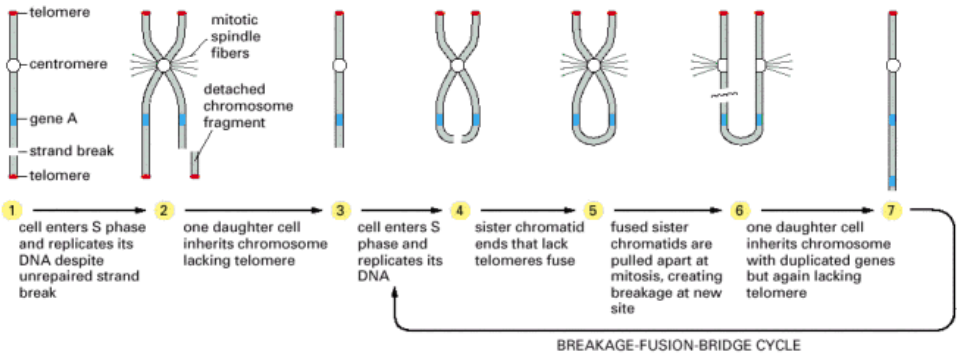

Figure 23-33. How the replication of damaged DNA can lead to chromosome abnormalities, gene amplification and gene loss. The diagram shows one of several possible mechanisms. The process begins with accidental DNA damage in a cell that lacks functional p53 protein. Instead of halting at the p53-dependent checkpoint in the division cycle, where a normal cell with damaged DNA would pause until the damage was repaired, the p53-defective cell enters S phase, with the consequences shown. Once a chromosome carrying a duplication and lacking a telomere has been generated, repeated rounds of replication, chromatid fusion, and unequal breakage (the so-called breakage-fusion-bridge cycle) can increase the number of copies of the duplicated region still further. Selection in favor of cells with increased numbers of copies of a gene in the affected chromosomal region will thus lead to mutants in which the gene is amplified to a high copy number. The multiple copies may eventually become visible as a homogeneously staining region in the chromosome, or they may - either through a recombination event or through unrepaired DNA strand breakage - become excised from their original locus and so appear as independent double minute chromosomes (see Figure 23-28). The chromosomal disorder can also lead to loss of genes, with selection in favor of cells that have lost tumor suppressors.

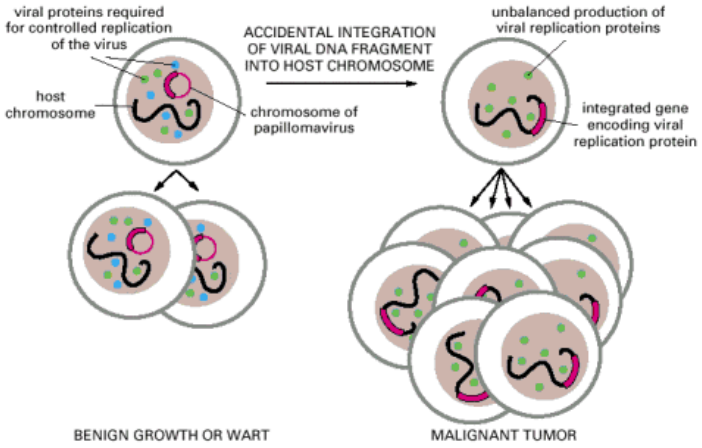

Figure 23-34. How certain papillomaviruses are thought to give rise to cancer of the uterine cervix. Papillomaviruses have double-stranded circular DNA chromosomes of about 8000 nucleotide pairs. In a wart or other benign infection these chromosomes are stably maintained in the basal cells of the epithelium as plasmids whose replication is regulated so as to keep step with the chromosomes of the host *(left)*. Rare accidents can cause the integration of a fragment of such a plasmid into a chromosome of the host, altering the environment of the viral genes. This (or possibly some other cause) disrupts the control of viral gene expression. The unregulated production of viral replication proteins interferes with the control of cell division, thereby helping to generate a cancer *(right)*.

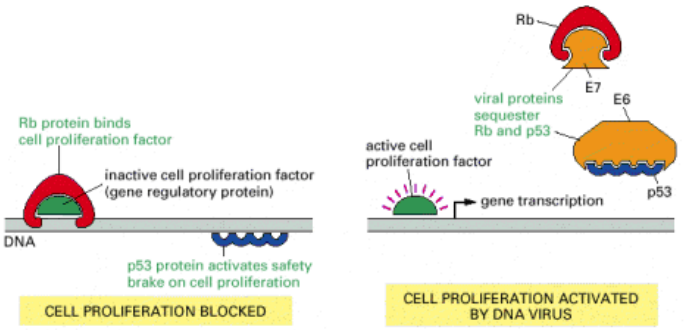

Figure 23-35. Activation of cell proliferation by a DNA tumor virus. Papillomavirus uses two viral proteins, E6 and E7, to sequester the host cell's p53 and Rb respectively. The SV40 virus (a related virus that infects monkeys) uses a single dual-purpose protein called large T antigen, for the same purpose. The E6 protein binding leads to ubiquitylation of its p53 partner, inducing p53 proteolysis (not shown).

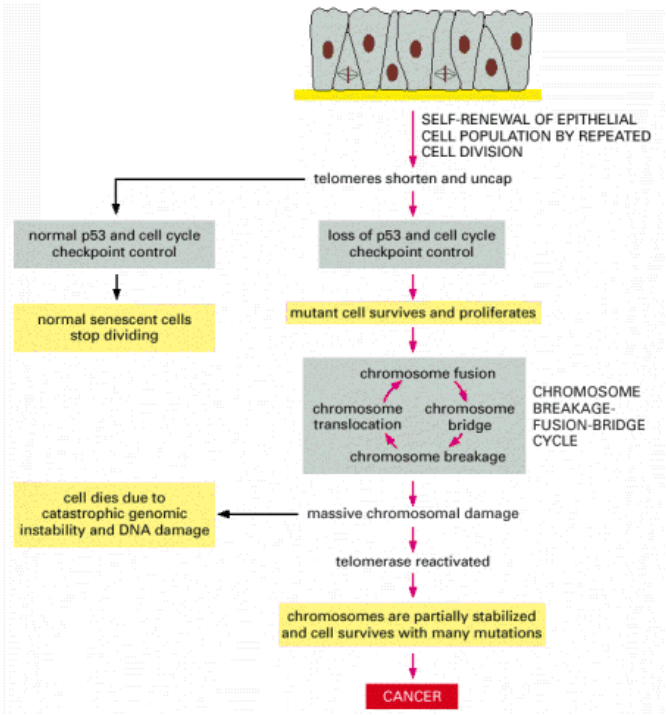

Figure 23-36. A view of how shortened telomeres may lead to chromosomal instability and cancer. Most human cells lack telomerase. As such cells divide, the telomeres that cap the ends of their chromosomes shrink. After many divisions, the telomeres become so short that they cease to function correctly, and the inadequately capped chromosome ends produce an intracellular signal similar to that produced by double-strand breaks. In the normal cells that still produce functional p53 and have their cell-cycle checkpoints intact, this triggers an arrest of cell division (replicative senescence). But a rare cell within the cell population that has acquired a mutation in its p53 gene or in its cell-cycle checkpoints may ignore this signal and continue to divide, entering a breakage-fusion-bridge cycle that causes massive chromosomal damage (see Figure 23-33). Some cells may survive this period of genetic disruption by reactivating telomerase, which halts the catastrophic cycle and restores enough chromosomal stability for cell survival. These damaged cells can then go on to accumulate the additional mutations needed to produce a cancer.

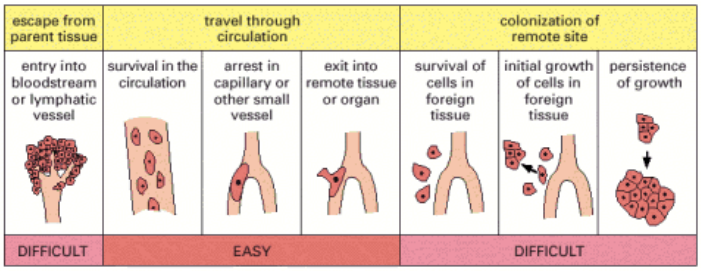

Figure 23-37. The barriers to metastasis. Studies of labeled tumor cells leaving a tumor site, entering the circulation, and establishing metastases show which steps in the metastatic process, outlined in Figure 23-15, are difficult or 'inefficient,' in the sense that they are steps in which large numbers of cells fail and are lost. It is in these difficult steps that highly metastatic cells are observed to have much greater success than nonmetastatic cells. It seems that the ability to escape from the parent tissue, and an ability to survive and grow in the foreign tissue, are key properties that cells must acquire to become metastatic. (Adapted from A.F. Chambers et al., *Breast Cancer Res*. 2:400407, 2000.)

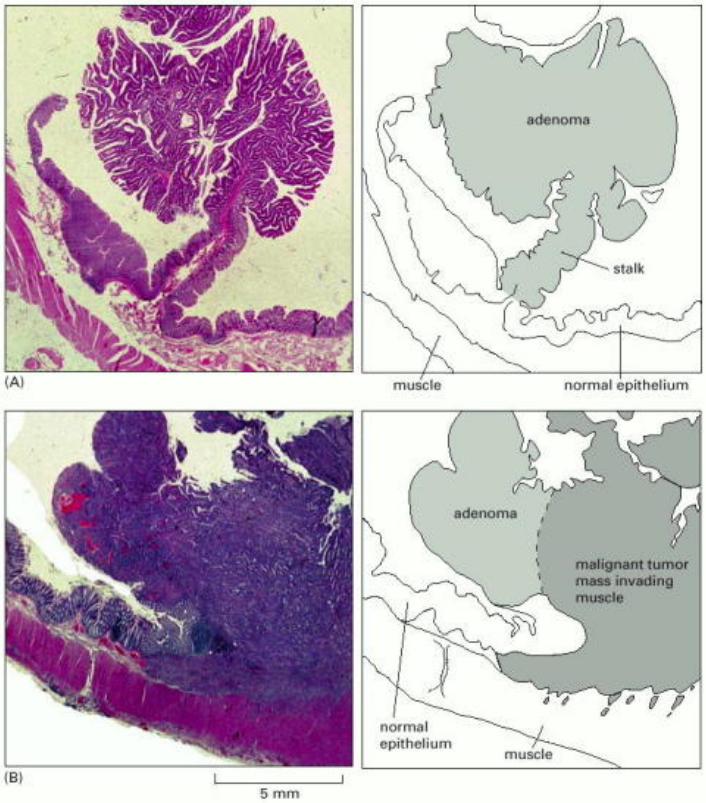

Figure 23-38. Cross-sections showing the stages in development of a typical colon cancer. (A) An adenomatous polyp from the colon. The polyp protrudes into the lumen - the space inside the colon. The rest of the wall of the colon is covered with normal colonic epithelium; the epithelium on the polyp appears mildly abnormal. (B) A carcinoma that is beginning to invade the underlying muscle layer. A high magnification view of this region showing the tumor cells growing between muscle cells is shown in Figure 23-16. (Courtesy of Paul Edwards.)

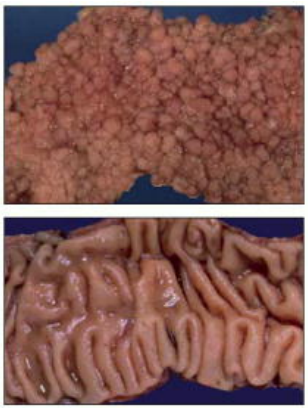

Figure 23-39. Colon of familial adenomatous polyposis coli patient compared to normal colon. (A) The polyposis colon is completely covered by hundreds of projecting polyps (shown in section in Figure 23-38A), each resembling a tiny cauliflower when viewed with the naked eye. (B) The normal colon wall is a gently undulating but smooth surface. (Courtesy of Andrew Wyllie and Mark Arends.)

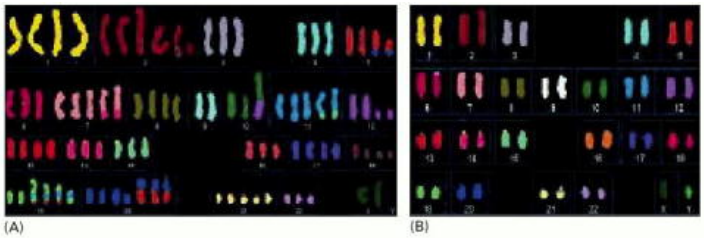

Figure 23-40. Chromosome complements (karyotypes) of colon cancers showing different kinds of genetic instability. (A) The karyotype of a typical cancer shows many gross abnormalities in chromosome number and structure. Considerable variation can also exist from cell to cell. (B) The karyotype of a tumor that has a stable chromosome complement with few chromosomal anomalies. Its defects are mostly invisible, having been created by defects in DNA mismatch repair. All of the chromosomes in this figure were stained as in Figure 23-12, the DNA of each normal chromosome being stained with a different combination of fluorescent dyes. (Courtesy Wael Abdel-Rahman and Paul Edwards.)

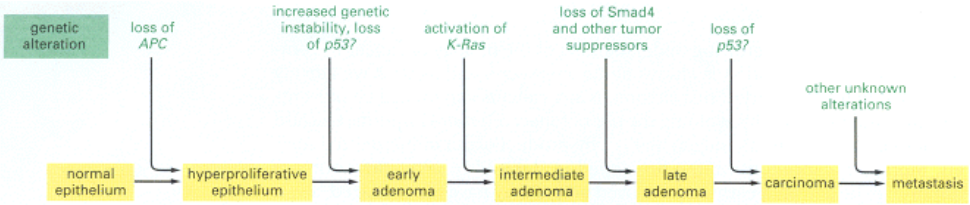

Figure 23-41. Suggested typical sequence of genetic changes underlying the development of a colorectal carcinoma. This over-simplified diagram provides a general idea of the way mutation and tumor development can fit together. But there are certainly other mutant genes of which we are not yet aware, and different colon cancers can progress through different sequences of mutations. There is still debate about the timing of p53 mutations and of the onset of genetic instability in relation to other mutations.

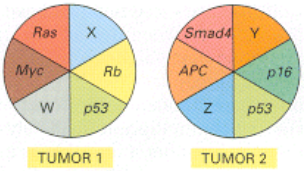

Figure 23-42. Each tumor will generally contain a different set of genetic lesions. In this schematic diagram, W, X, Y, and Z denote alterations in as yet undiscovered tumor suppressor genes or oncogenes. Tumors that arise from different tissues are generally more different in their genetic abnormalities than tumors of similar origin.

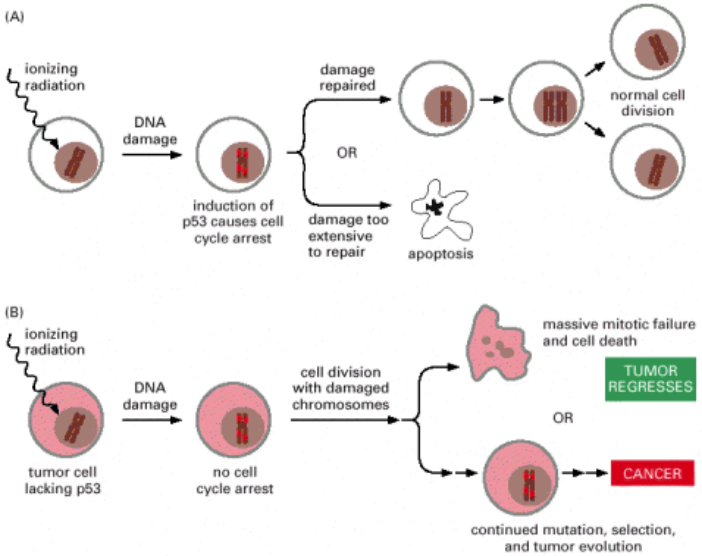

Figure 23-43. Effects of ionizing radiation on normal cells (A) and cancer cells (B). Cancer cells tend to be more susceptible than normal cells to the damaging effects of ionizing radiation because they lack an ability to arrest the cell cycle and make the necessary repairs. Unfortunately, the same genetic defects may render some cancer cells resistant to radiation treatment, as they may also be less adept at activating apoptosis in the face of DNA damage.

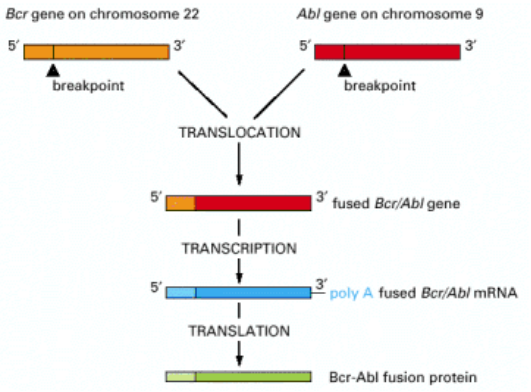

Figure 23-44. The conversion of the *Abl* proto-oncogene into an oncogene in patients with chronic myelogenous leukemia. The chromosome translocation responsible joins the *Bcr* gene on chromosome 22 to the *Abl* gene from chromosome 9, thereby generating a Philadelphia chromosome (see Figure 23-5). The resulting fusion protein has the N-terminus of the Bcr protein joined to the C-terminus of the Abl tyrosine protein kinase; in consequence, the Abl kinase domain becomes inappropriately active, driving excessive proliferation of a clone of hemopoietic cells in the bone marrow.

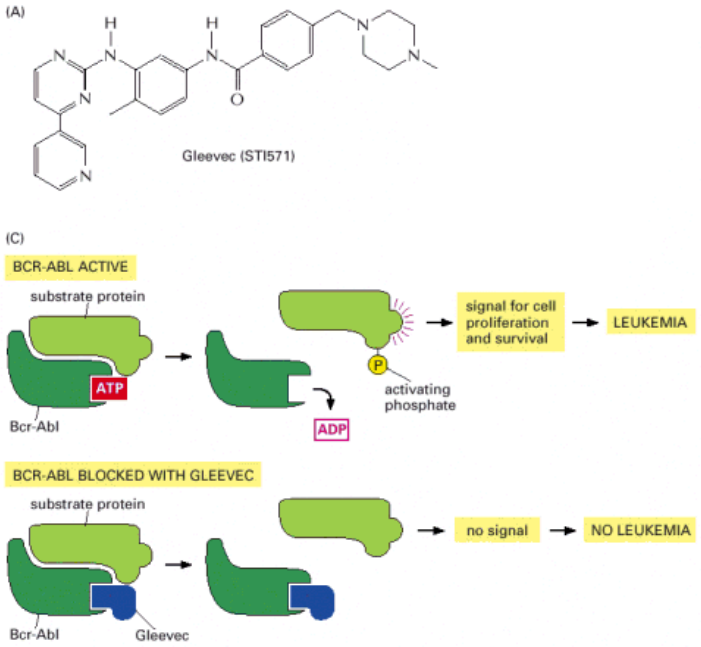

Figure 23-45. How Gleevec (STI-571) blocks the activity of Bcr-Abl protein and halts chronic myeloid leukemia. (A) The chemical structure of Gleevec. The drug can be given by mouth; it has side effects but they are usually quite tolerable. (B) The structure of the complex of Gleevec (solid *green* object) with the tyrosine kinase domain of the Abl protein (ribbon diagram), as determined by X-ray crystallography. (C) Gleevec sits in the ATP-binding pocket of the tyrosine kinase domain of Bcr-Abl and thereby prevents Bcr-Abl from transferring a phosphate group from ATP onto a tyrosine residue in a substrate protein. This blocks onward transmission of a signal for cell proliferation and survival. (B, from T. Schindler et al., *Science* 289:19381942, 2000. © AAAS.)

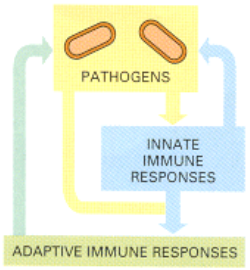

Figure 24-1. Innate and adaptive immune responses. Innate immune responses are activated directly by pathogens and defend all multicellular organisms against infection. In vertebrates, pathogens, together with the innate immune responses they activate, stimulate adaptive immune responses, which then help fight the infection.

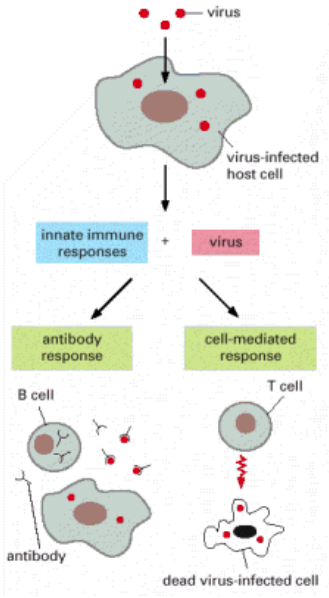

Figure 24-2. The two main classes of adaptive immune responses. Lymphocytes carry out both classes of responses. Here, the lymphocytes are responding to a viral infection. In one class of response, B cells secrete antibodies that neutralize the virus. In the other, a cell-mediated response, T cells kill the virus-infected cells.

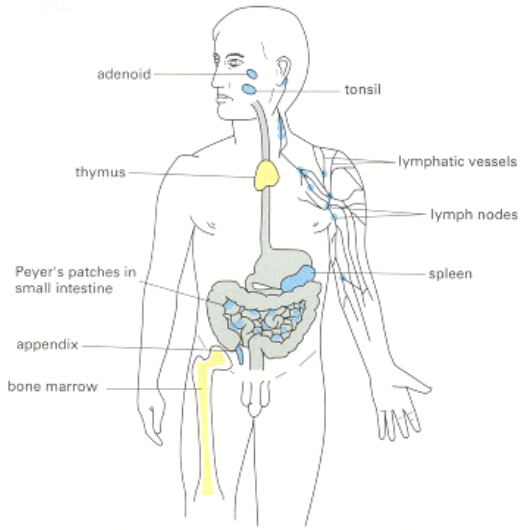

Figure 24-3. Human lymphoid organs. Lymphocytes develop in the thymus and bone marrow *(yellow),* which are therefore called *central (*or *primary) lymphoid organs*. The newly formed lymphocytes migrate from these primary organs to *peripheral* (or *secondary) lymphoid organs (blue),* where they can react with foreign antigen. Only some of the peripheral lymphoid organs and lymphatic vessels are shown; many lymphocytes, for example, are found in the skin and respiratory tract. As we discuss later, the lymphatic vessels ultimately empty into the bloodstream (not shown).

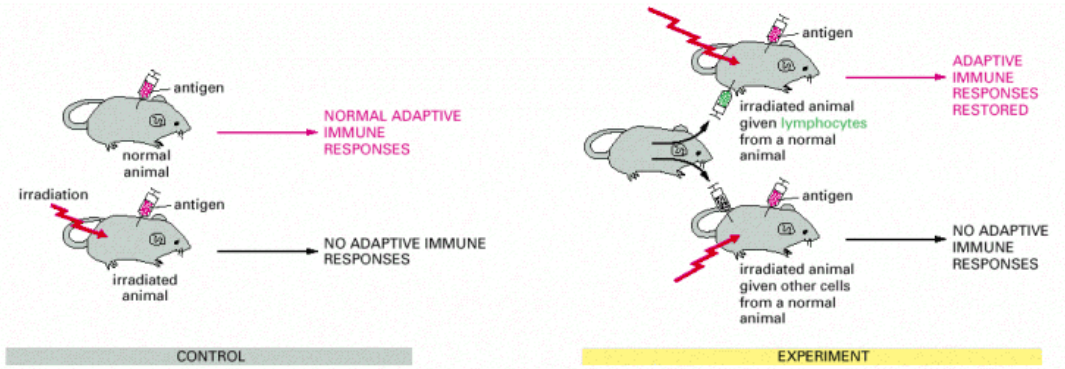

Figure 24-4. A classic experiment showing that lymphocytes are required for adaptive immune responses to foreign antigens. An important requirement of all such cell-transfer experiments is that cells are transferred between animals of the same *inbred strain.* Members of an inbred strain are genetically identical. If lymphocytes are transferred to a genetically different animal that has been irradiated, they react against the "foreign" antigens of the host and can kill the animal. In the experiment shown, the injection of lymphocytes restores both antibody and cell-mediated adaptive immune responses, indicating that lymphocytes are required for both types of responses.

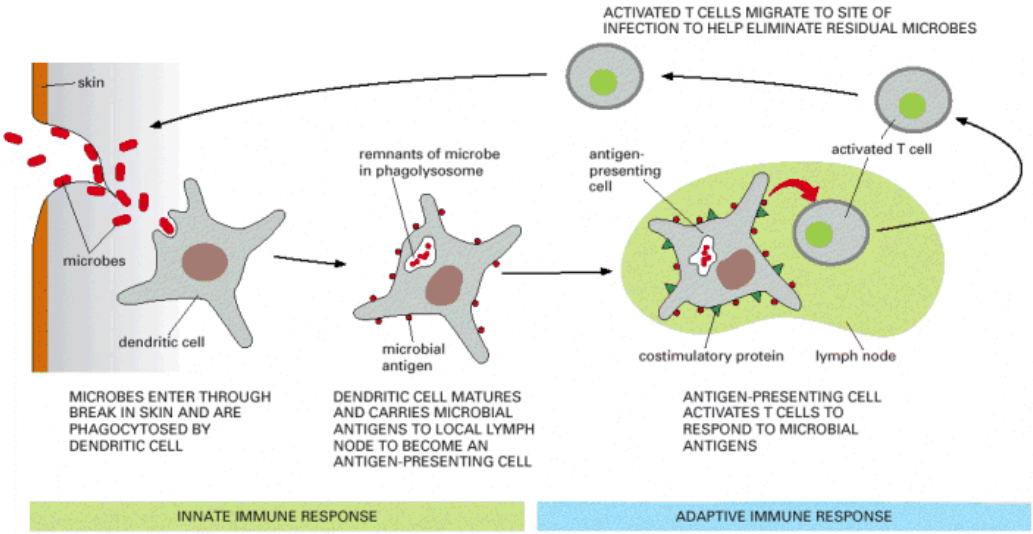

Figure 24-5. One way in which the innate immune system helps activate the adaptive immune system. Specialized phagocytic cells of the innate immune system, including macrophages (not shown) and dendritic cells ingest invading microbes or their products at the site of infection. The dendritic cells then mature and migrate in lymphatic vessels to a nearby lymph node, where they serve as antigen-presenting cells. The antigen-presenting cells activate T cells to respond to the microbial antigens that are displayed on the presenting cells' surface. The antigen-presenting cells also have special proteins on their surface (called *costimulatory molecules)* that help activate the T cells. Some of the activated T cells then migrate to the site of infection where they either help activate macrophages or kill infected cells, thereby helping to eliminate the microbes. As we discuss later, the costimulatory molecules appear on dendritic cells only after these cells mature in response to invading microbes.

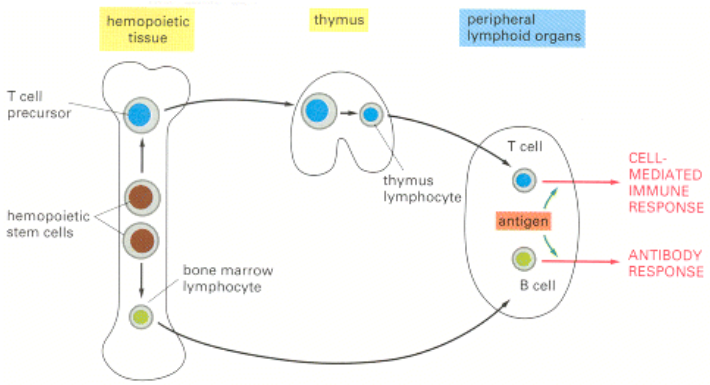

Figure 24-6. The development and activation of T and B cells. The central lymphoid organs, where lymphocytes develop from precursor cells, are labeled in *yellow boxes.* Lymphocytes respond to antigen in peripheral lymphoid organs, such as lymph nodes or spleen.

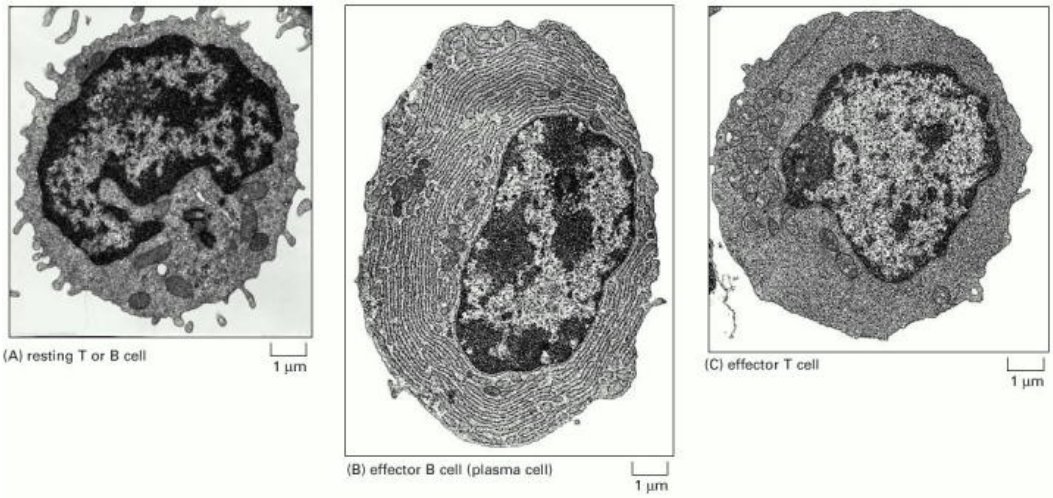

Figure 24-7. Electron micrographs of nonactivated and activated lymphocytes. (A) A resting lymphocyte, which could be a T cell or a B cell, as these cells are difficult to distinguish morphologically until they have been activated to become effector cells. (B) An effector B cell (a plasma cell). It is filled with an extensive rough endoplasmic reticulum (ER), which is distended with antibody molecules. (C) An effector T cell, which has relatively little rough ER but is filled with free ribosomes. Note that the three cells are shown at the same magnification. (A, courtesy of Dorothy Zucker-Franklin; B, courtesy of Carlo Grossi; A and B, from D. Zucker-Franklin et al., Atlas of Blood Cells: Function and Pathology, 2nd edn. Milan, Italy: Edi. Ermes, 1988; C, courtesy of Stefanello de Petris.)

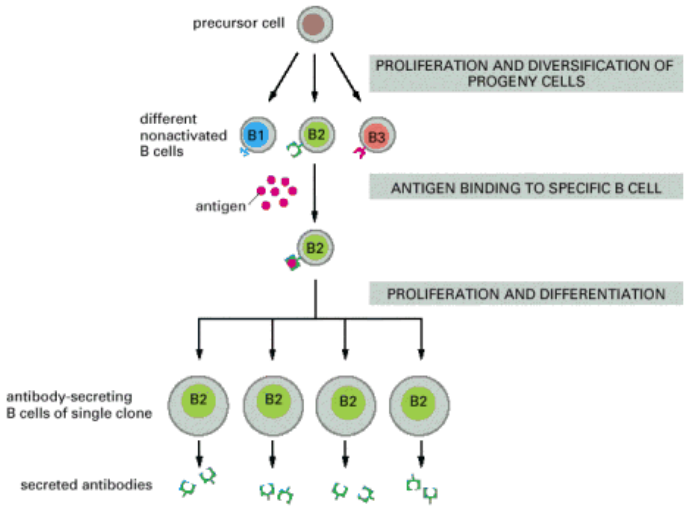

Figure 24-8. The clonal selection theory. An antigen activates only those lymphocyte clones (represented here by single cells) that are already committed to respond to it. A cell committed to respond to a particular antigen displays cell-surface receptors that specifically recognize the antigen, and all cells within a clone display the same receptor. The immune system is thought to consist of millions of different lymphocyte clones. A particular antigen may activate hundreds of different clones. Although only B cells are shown here, T cells operate in a similar way.

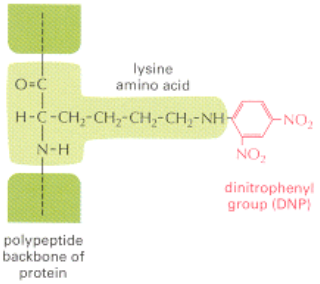

Figure 24-9. The dinitrophenyl (DNP) group. Although it is too small to induce an immune response on its own, when it is coupled covalently to a lysine side chain on a protein, as illustrated, DNP stimulates the production of hundreds of different species of antibodies that all bind specifically to it.

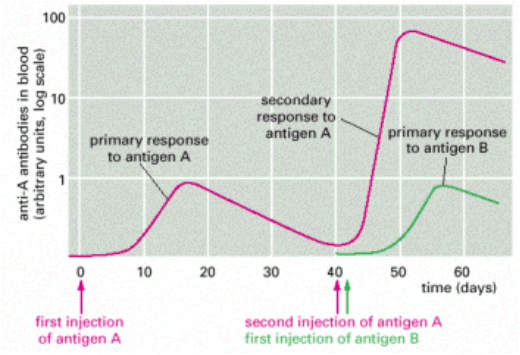

Figure 24-10. Primary and secondary antibody responses. The secondary response induced by a second exposure to antigen A is faster and greater than the primary response and is specific for A, indicating that the adaptive immune system has specifically remembered encountering antigen A before. The same type of immunological memory is observed in T-cell-mediated responses.

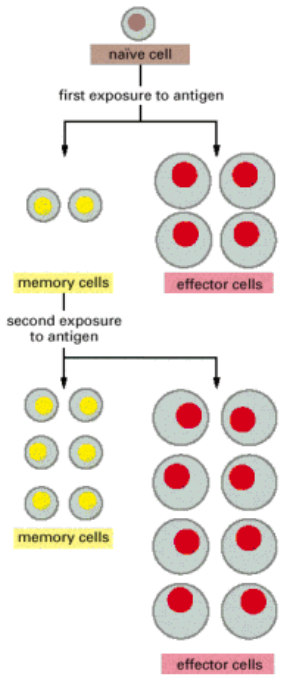

Figure 24-11. A model for the cellular basis of immunological memory. When naïve lymphocytes are stimulated by their specific antigen, they proliferate and differentiate. Most become effector cells which function and then die, while others become long-lived memory cells. During a subsequent exposure to the same antigen, the memory cells respond more readily and rapidly than did the naïve cells: they proliferate and give rise to effector cells and to more memory cells. In the case of T cells, memory cells can also develop from effector cells (not shown).

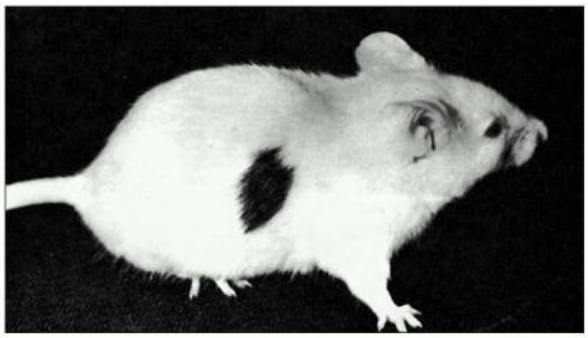

Figure 24-12. Immunological tolerance. The skin graft seen here, transplanted from an adult brown mouse to an adult white mouse, has survived for many weeks only because the white mouse, at the time of its birth, received an injection of cells from the brown mouse and therefore became immunologically tolerant to them. The cells from the brown mouse persist in the adult white mouse and continue to induce tolerance in newly formed lymphocytes that would otherwise react against the brown skin. (Courtesy of Leslie Brent, from I. Roitt, Essential Immunology, 6th edn. Oxford, UK: Blackwell Scientific, 1988.)

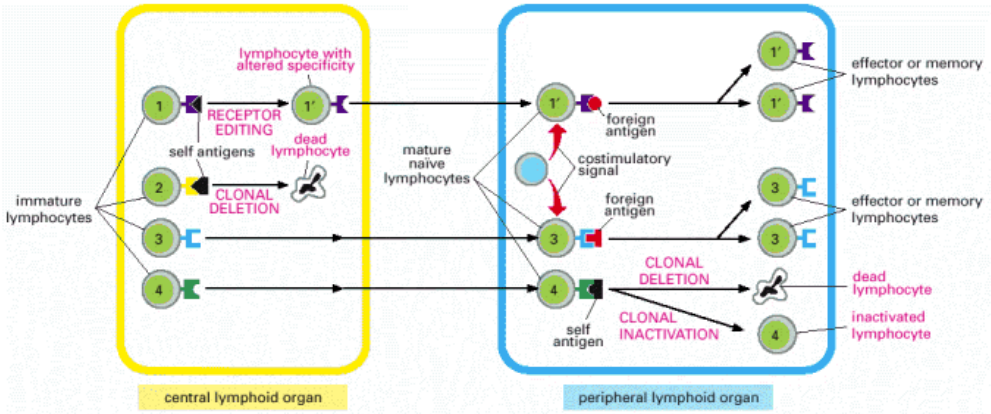

Figure 24-13. Induction of immunological tolerance to self antigens in central and peripheral lymphoid organs. When a self-reactive immature lymphocyte binds its self antigen in the central lymphoid organ where the cell is produced, it may be induced to alter the receptor it makes so that it is no longer self-reactive. This process is called receptor editing and seems to occur only in developing B cells. Alternatively, the cell may die by apoptosis, a process called clonal deletion. When a self-reactive naïve lymphocyte escapes tolerance in the central lymphoid organ and binds its self antigen in a peripheral lymphoid organ, it may either die by apoptosis or be inactivated, as the binding usually occurs in the absence of a costimulatory signal. Although not shown, some self-reactive cells survive and are suppressed by special regulatory T cells. When a naïve lymphocyte binds a foreign antigen in a peripheral lymphoid organ in the presence of a costimulatory signal, it is stimulated to proliferate and differentiate into an effector or memory cell. As microbes are usually responsible for inducing costimulatory signals, most adaptive immune reactions normally occur only in response to microbes.

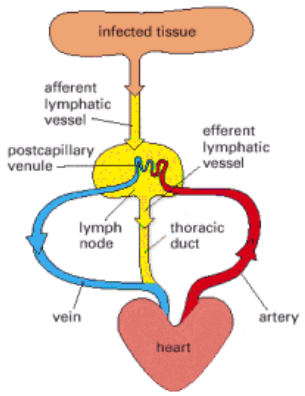

Figure 24-14. The path followed by lymphocytes as they continuously circulate between the lymph and blood. The circulation through a lymph node is shown here. Microbial antigens are carried into the lymph node by dendritic cells, which enter via afferent lymphatic vessels draining an infected tissue. T and B cells, by contrast, enter the lymph node via an artery and migrate out of the bloodstream through postcapillary venules. Unless they encounter their antigen, the T and B cells leave the lymph node via efferent lymphatic vessels, which eventually join the thoracic duct. The thoracic duct empties into a large vein carrying blood to the heart. A typical circulation cycle takes about 1224 hours.

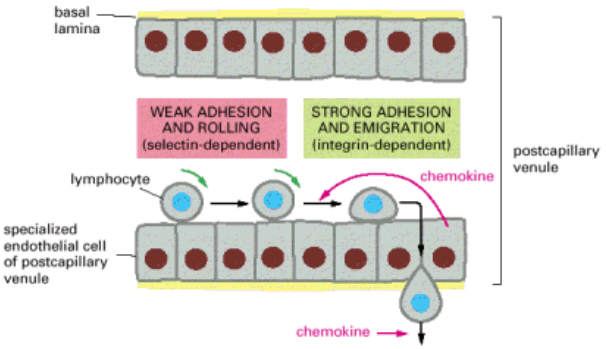

Figure 24-15. Migration of a lymphocyte out of the bloodstream into a lymph node. A circulating lymphocyte adheres weakly to the surface of the specialized endothelial cells lining a postcapillary venule in a lymph node. This initial adhesion is mediated by L-selectin on the lymphocyte surface. The adhesion is sufficiently weak to enable the lymphocyte to roll along the surface of the endothelial cells, pushed along by the flow of blood. Stimulated by chemokines secreted by the endothelial cells, the lymphocyte rapidly activates a stronger adhesion system, mediated by an integrin. This strong adhesion enables the cell to stop rolling and migrate out of the venule between the endothelial cells. The subsequent migration of the lymphocytes in the lymph node also depends on chemokines, which are produced within the node. The migration of other white blood cells out of the bloodstream into sites of infection occurs in a similar way.

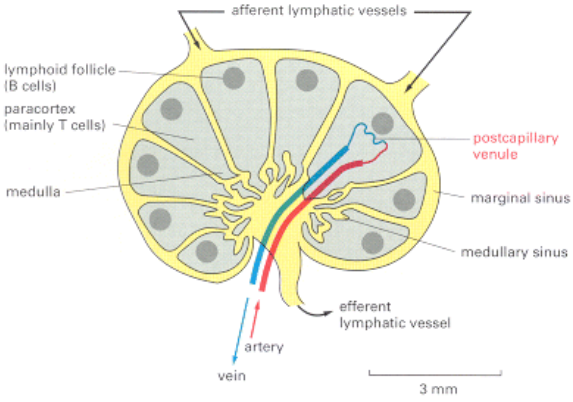

Figure 24-16. A simplified drawing of a human lymph node. B cells are primarily clustered in structures called lymphoid follicles, whereas T cells are found mainly in the paracortex. Both types of lymphocytes are attracted by chemokines to enter the lymph node from the blood via postcapillary venules. They then migrate to their respective areas, attracted by different chemokines. If they do not encounter their specific antigen, both T cells and B cells then enter the medullary sinuses and leave the node via the efferent lymphatic vessel. This vessel ultimately empties into the bloodstream, allowing the lymphocytes to begin another cycle of circulation through a secondary lymphoid organ (see Figure 24-14).

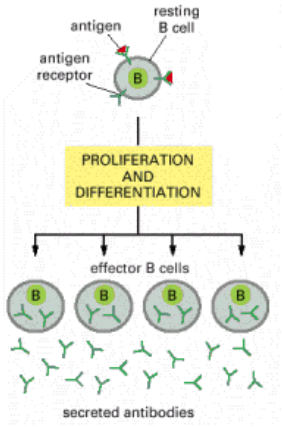

Figure 24-17. B cell activation. When naïve or memory B cells are activated by antigen (and helper T cells - not shown), they proliferate and differentiate into effector cells. The effector cells produce and secrete antibodies with a unique antigen-binding site, which is the same as that of their original membrane-bound antibodies that served as antigen receptors.

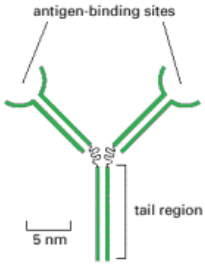

Figure 24-18. A simple representation of an antibody molecule. Note that its two antigen-binding sites are identical.

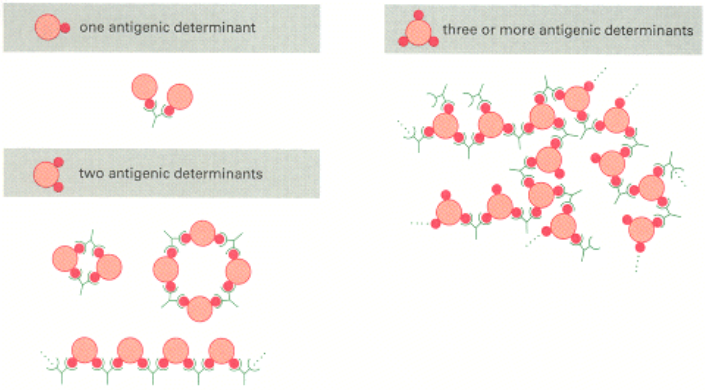

Figure 24-19. Antibody-antigen interactions. Because antibodies have two identical antigen-binding sites, they can cross-link antigens. The types of antibody-antigen complexes that form depend on the number of antigenic determinants on the antigen. Here a single species of antibody (a monoclonal antibody) is shown binding to antigens containing one, two, or three copies of a single type of antigenic determinant. Antigens with two antigenic determinants can form small cyclic complexes or linear chains with antibody, while antigens with three or more antigenic determinants can form large three-dimensional lattices that readily precipitate out of solution. Most antigens have many different antigenic determinants (see Figure 24-29A), and different antibodies that recognize different determinants can cooperate in cross-linking the antigen (not shown).

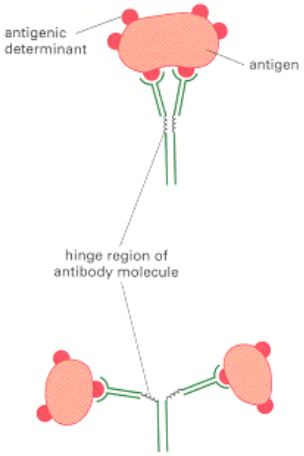

Figure 24-20. The hinge region of an antibody molecule. Because of its flexibility, the hinge region improves the efficiency of antigen binding and cross-linking.

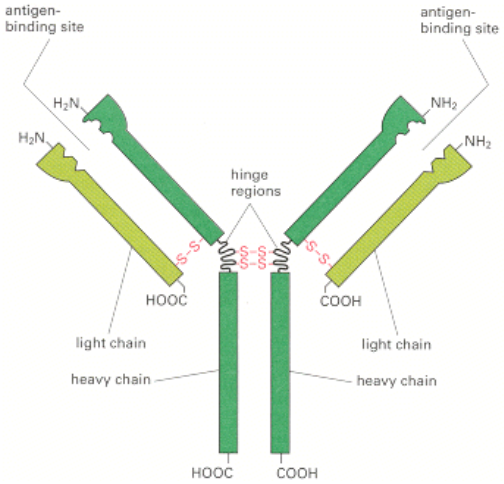

Figure 24-21. A schematic drawing of a typical antibody molecule. It is composed of four polypeptide chains - two identical heavy chains and two identical light chains. The two antigen-binding sites are identical, each formed by the N-terminal region of a light chain and the N-terminal region of a heavy chain. Both the tail (Fc) and hinge region are formed by the two heavy chains.

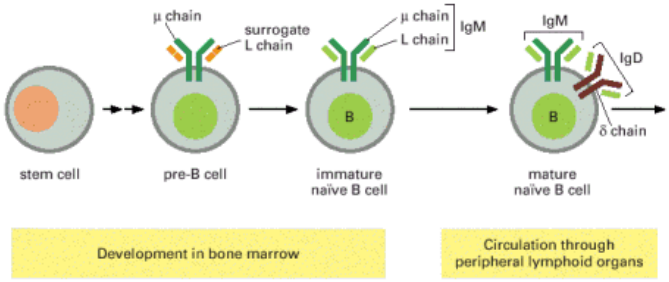

Figure 24-22. The main stages in B cell development. All of the stages shown occur independently of antigen. When they are activated by their specific foreign antigen and helper T cells in peripheral lymphoid organs, mature naïve B cells proliferate and differentiate into effector or memory cells (not shown).

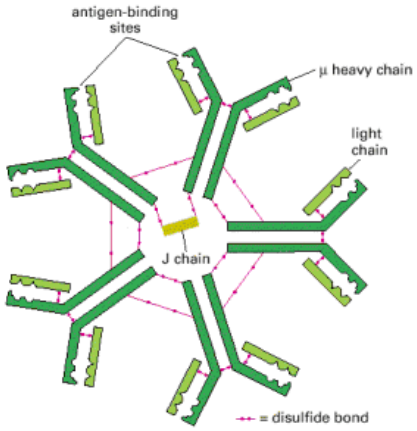

Figure 24-23. A pentameric IgM molecule. The five subunits are held together by disulfide bonds *(red)*. A single J chain, which has a structure similar to that of a single Ig domain (discussed later), is disulfide-bonded between the tails of two μ heavy chains. The J chain is required for pentamer formation. The addition of each successive four-chain IgM subunit requires a J chain, which is then discarded, except for the last one, which is retained. Note that IgM molecules do not have hinge regions.

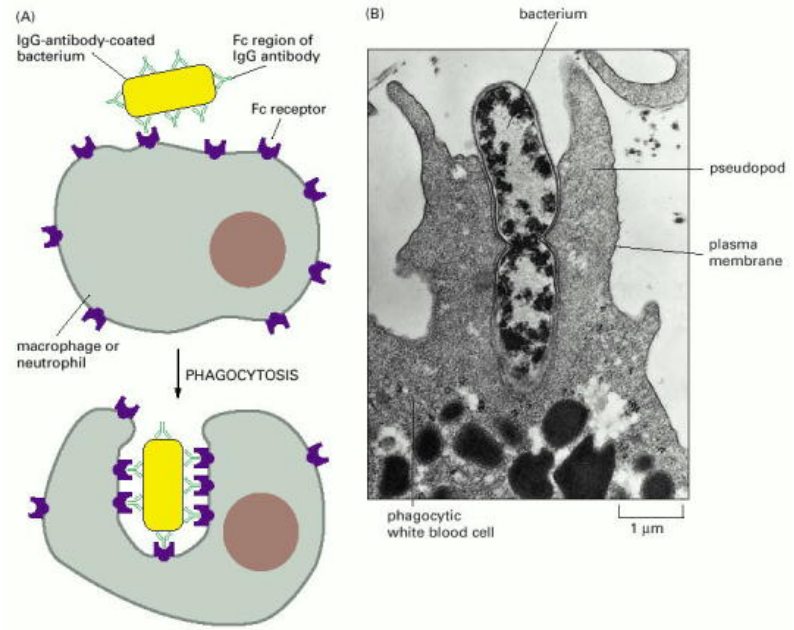

Figure 24-24. Antibody-activated phagocytosis. (A) An IgG-antibody-coated bacterium is efficiently phagocytosed by a macrophage or neutrophil, which has cell-surface receptors that bind the tail (Fc) region of IgG molecules. The binding of the antibody-coated bacterium to these Fc receptors activates the phagocytic process. The tail of an antibody molecule is called an Fc region because, when antibodies are cleaved with the proteolytic enzyme papain, the fragments containing the tail region readily crystallize. (B) Electron micrograph of a neutrophil phagocytosing an IgG-coated bacterium, which is in the process of dividing. (B, courtesy of Dorothy F. Bainton, from R.C. Williams, Jr. and H.H. Fudenberg, Phagocytic Mechanisms in Health and Disease. New York: Intercontinental Book Corporation, 1971.)

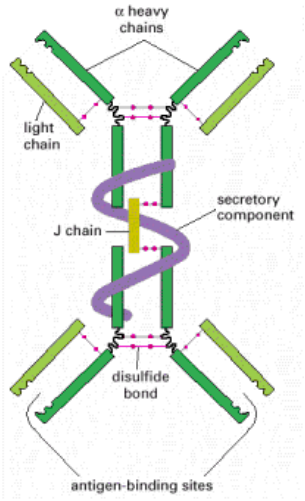

Figure 24-25. A highly schematized diagram of a dimeric IgA molecule found in secretions. In addition to the two IgA monomers, there is a single J chain and an additional polypeptide chain called the *secretory component*, which is thought to protect the IgA molecules from digestion by proteolytic enzymes in secretions.

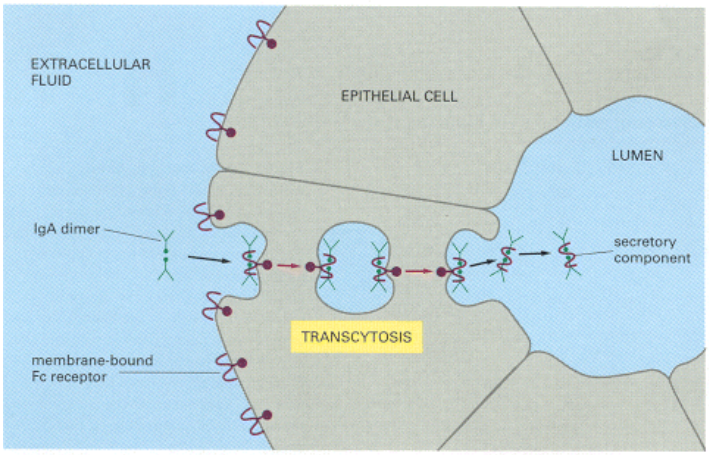

Figure 24-26. The mechanism of transport of a dimeric IgA molecule across an epithelial cell. The IgA molecule, as a J-chain-containing dimer, binds to a transmembrane receptor protein on the nonlumenal surface of a secretory epithelial cell. The receptor-IgA complexes are ingested by receptor-mediated endocytosis, transferred across the epithelial cell cytoplasm in vesicles, and secreted into the lumen on the opposite side of the cell by exocytosis. When exposed to the lumen, the part of the Fc receptor protein that is bound to the IgA dimer (the *secretory component)* is cleaved from its transmembrane tail, thereby releasing the antibody in the form shown in Figure 24-25. The J chain is not shown.

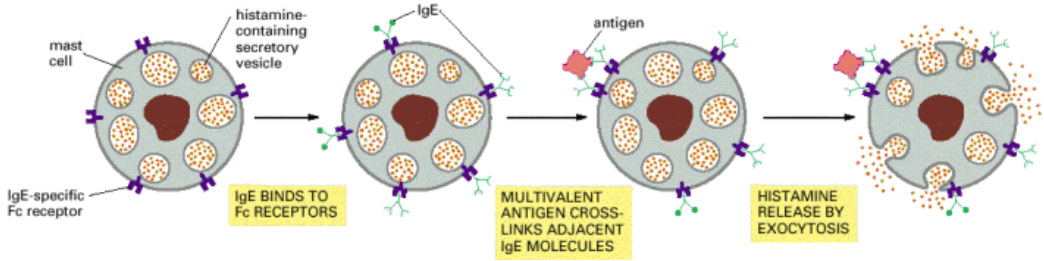

Figure 24-27. The role of IgE in histamine secretion by mast cells. A mast cell (or a basophil) binds IgE molecules after they are secreted by activated B cells. The soluble IgE antibodies bind to Fc receptor proteins on the mast cell surface that specifically recognize the Fc region of these antibodies. The bound IgE molecules serve as cell-surface receptors for antigen. Thus, unlike B cells, each mast cell (and basophil) has a set of cell-surface antibodies with a wide variety of antigen-binding sites. When an antigen molecule binds to these membrane-bound IgE antibodies so as to cross-link them to their neighbors, it signals the mast cell to release its histamine and other local mediators by exocytosis.

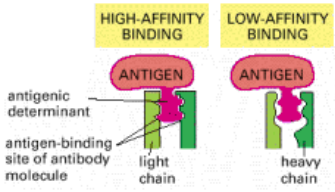

Figure 24-28. Antigen binding to antibody. In this highly schematized diagram, an antigenic determinant on a macromolecule is shown interacting with the antigen-binding site of two different antibody molecules, one of high affinity and one of low affinity. The antigenic determinant is held in the binding site by various weak noncovalent forces, and the site with the better fit to the antigen has a greater affinity. Note that both the light and heavy chains of the antibody molecule usually contribute to the antigen-binding site.

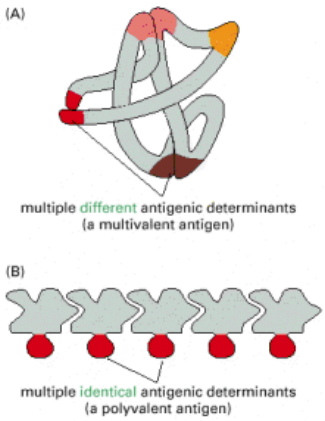

Figure 24-29. Molecules with multiple antigenic determinants. (A) A globular protein is shown with a number of different antigenic determinants. Different regions of a polypeptide chain usually come together in the folded structure to form each antigenic determinant on the surface of the protein. (B) A polymeric structure is shown with many *identical* antigenic determinants.

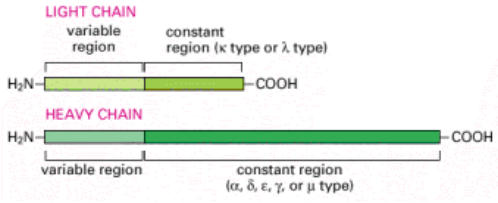

Figure 24-30. Constant and variable regions of immunoglobulin chains. Both light and heavy chains of an antibody molecule have distinct constant and variable regions.

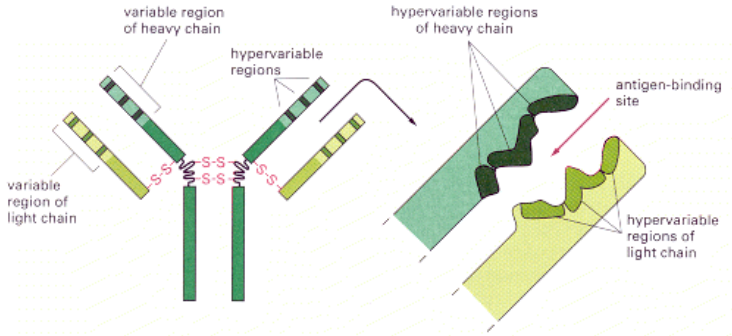

Figure 24-31. Antibody hypervariable regions. Highly schematized drawing of how the three hypervariable regions in each light and heavy chain together form the antigen-binding site of an antibody molecule.

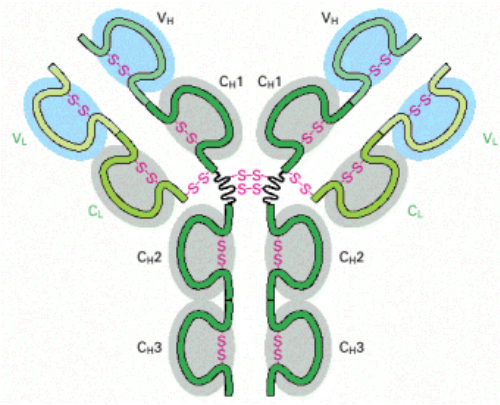

Figure 24-32. Immunoglobulin domains. The light and heavy chains in an antibody molecule are each folded into repeating domains that are similar to one another. The variable domains (shaded in *blue)* of the light and heavy chains (V_L and V_H) make up the antigen-binding sites, while the constant domains of the heavy chains (mainly C_H2 and C_H3) determine the other biological properties of the molecule. The heavy chains of IgM and IgE antibodies do not have a hinge region and have an extra constant domain (C_H4). Hydrophobic interactions between domains on adjacent chains have an important role in holding the chains together in the antibody molecule: V_L binds to V_H, C_L binds to C_H1, and so on (see Figure 24-34).

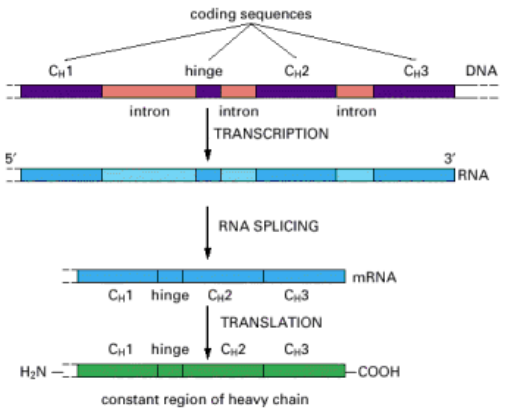

Figure 24-33. The organization of the DNA sequences that encode the constant region of an antibody heavy chain. The coding sequences (exons) for each domain and for the hinge region are separated by noncoding sequences (introns). The intron sequences are removed by splicing the primary RNA transcripts to form mRNA. The presence of introns in the DNA is thought to have facilitated accidental duplications of DNA segments that gave rise to the antibody genes during evolution (discussed in Chapter 7). The DNA and RNA sequences that encode the variable region of the heavy chain are not shown.

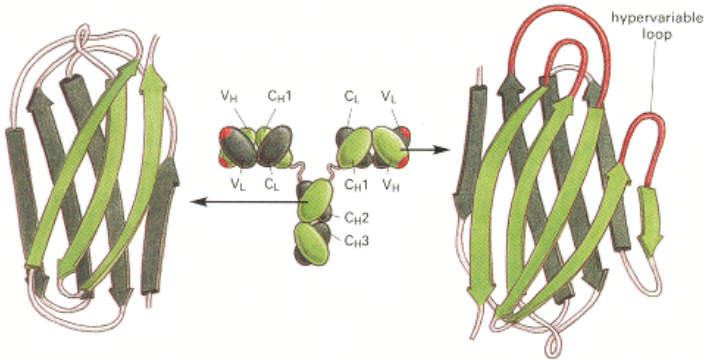

Figure 24-34. The folded structure of an IgG antibody molecule, based on x-ray crystallography studies. The structure of the whole protein is shown in the middle, while the structure of a constant domain is shown on the left and of a variable domain on the right. Both domains consist of two β sheets, which are joined by a disulfide bond (not shown). Note that all the hypervariable regions *(red)* form loops at the far end of the variable domain, where they come together to form part of the antigen-binding site.

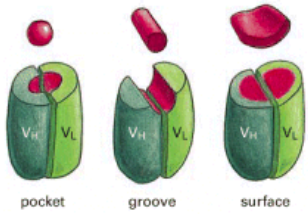

Figure 24-35. Antigen-binding sites of antibodies. The hypervariable loops of different V_L and V_H domains can combine to form a large variety of binding surfaces. The antigenic determinants and the antigen-binding site of the antibodies are shown in *red.* Only one antigen-binding site is shown for each antibody.

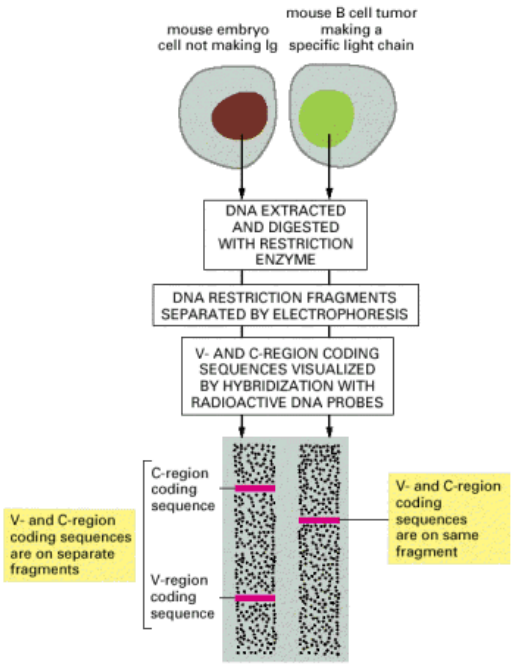

Figure 24-36. Drawing of an experiment that directly demonstrates that DNA is rearranged during B cell development. The B cell tumor arose from a single B cell and therefore makes a single species of antibody molecule. The two radioactive DNA probes used are specific for the DNA sequences encoding the C region and the V region of the light chain that the tumor cells make.

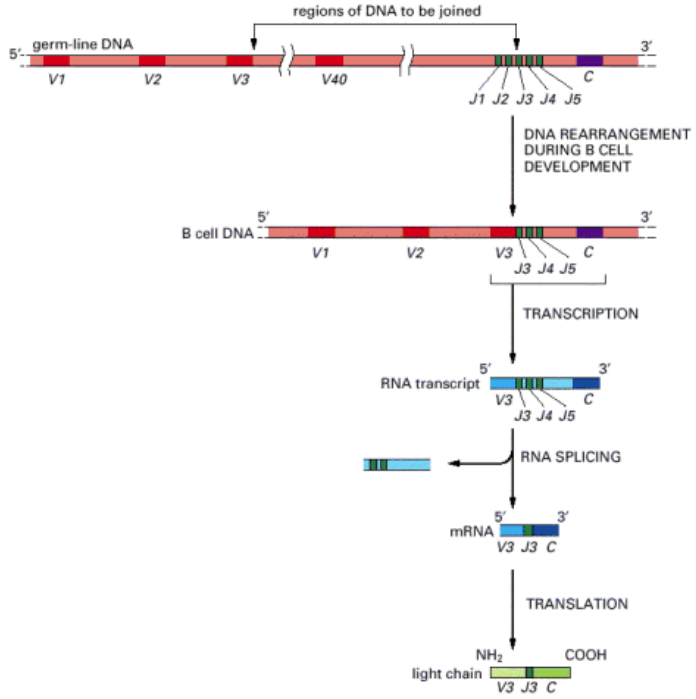

Figure 24-37. The *V-J* joining process involved in making a human κ light chain. In the "germ-line" DNA (where the antibody genes are not being expressed and are therefore not rearranged), the cluster of five *J* gene segments is separated from the *C*-region exon by a short intron and from the 40 *V* gene segments by thousands of nucleotide pairs. During the development of a B cell, the randomly chosen *V* gene segment *(V3* in this case) is moved to lie precisely next to one of the *J* gene segments *(J3* in this case). The "extra" *J* gene segments *(J4* and *J5)* and the intron sequence are transcribed (along with the joined *V3* and *J3* gene segments and the C-region exon) and then removed by RNA splicing to generate mRNA molecules in which the *V3, J3,* and *C* sequences are contiguous. These mRNAs are then translated into κ light chains. A *J* gene segment encodes the C-terminal 15 or so amino acids of the V region, and the *V-J* segment junction coincides with the third hypervariable region of the light chain, which is the most variable part of the V region.

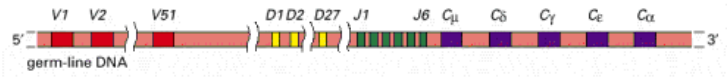

Figure 24-38. The human heavy-chain gene-segment pool. There are 51 *V* segments, 27 *D* segments, 6 *J* segments, and an ordered cluster of *C*-region exons, each cluster encoding a different class of heavy chain. The *D* segment (and part of the *J* segment) encodes amino acids in the third hypervariable region, which is the most variable part of the V region. The figure is not drawn to scale: the total length of the heavy chain locus is over 2 megabases. Moreover, many details are omitted. For instance, each *C* region is encoded by multiple exons (see Figure 24-33); there are four clusters of C_γ-region exons *($C_{\gamma 1}$, $C_{\gamma 2}$, $C_{\gamma 3}$,* and *$C_{\gamma 4}$)*, and the V_H gene segments are clustered on the chromosome in groups of homologous families. The genetic mechanisms involved in producing a heavy chain are the same as those shown in Figure 24-37 for light chains except that two DNA rearrangement steps are required instead of one. First a *D* segment joins to a *J* segment, and then a *V* segment joins to the rearranged *DJ* segment.

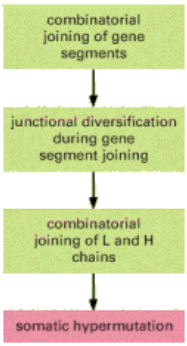

Figure 24-39. The four main mechanisms of antibody diversification. Those shaded in *green* occur during B cell development in the bone marrow (or fetal liver), while the mechanism shaded in *red* occurs when B cells are stimulated by foreign antigen and helper T cells in peripheral lymphoid organs to produce memory B cells.

Figure 24-40. Antibody gene-pool selection in B cell development. To produce antibodies with only one type of antigen-binding site, a developing B cell must use only one L-chain gene-segment pool and one H-chain pool. Although the choice between maternal and paternal pools is thought to be random, the assembly of V-region coding sequences in a developing B cell proceeds in an orderly sequence, one segment at a time, usually beginning with the heavy-chain pool. In this pool, *D* segments first join to J_H segments on both parental chromosomes; then V_H to DJ_H joining occurs on one of these chromosomes (not shown). If this rearrangement produces a functional gene, the resulting production of complete μ chains (always the first heavy chains made) leads to their expression on the cell surface in association with surrogate light chains. The cell now shuts down all further rearrangements of V_H-region-encoding gene segments and initiates V_L rearrangement. Although not shown, V_L rearrangement usually occurs first in a κ gene-segment pool, and only if that fails does it occur in the other κ pool or in the λ

pools. If, at any point, "in-phase" V_L-to-J_L joining leads to the production of light chains, these combine with preexisting μ chains to form IgM antibody molecules, which insert into the plasma membrane. The IgM cell-surface receptors are thought to enable the newly formed B cell to receive extracellular signals that shut down all further *V(D)J* joining, by turning off the expression of the *rag-1* and *rag-2* genes. If a developing B cell makes a receptor that recognizes a self-antigen, it is stimulated to re-express the *rag* genes and undergo another round of *V(D)J* joining (called receptor editing), thereby changing the specificity of its receptor (not shown). If a cell fails to assemble both a functional V_H-region and a functional V_L-region coding sequence, it is unable to make antibody molecules and dies by apoptosis (not shown).

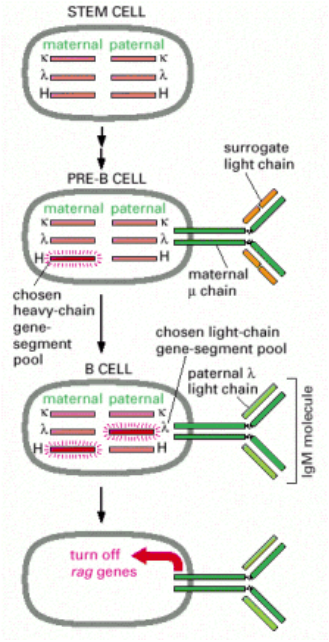

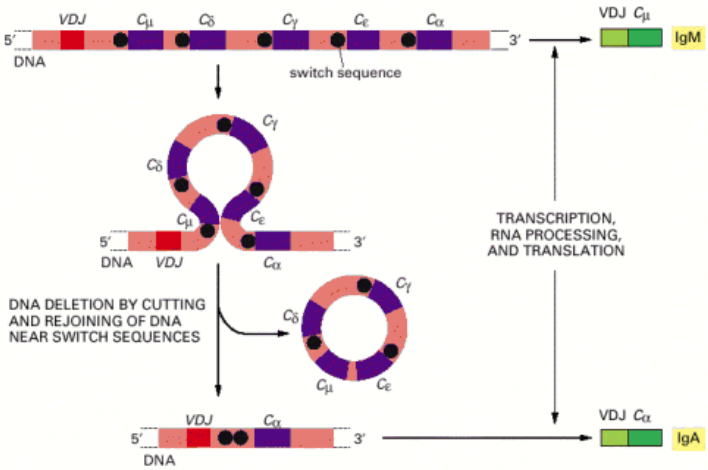

Figure 24-41. An example of the DNA rearrangement that occurs in class switch recombination. A B cell making an IgM antibody from an assembled *VDJ* DNA sequence is stimulated by antigen and the cytokines made by helper T cells to switch to making an IgA antibody. In the process, it deletes the DNA between the *VDJ* sequence and the C_α-coding sequence. Specific DNA sequences *(switch sequences)* located upstream of each C_H-coding sequence recombine with each other to delete the intervening DNA. Class switch recombination is thought to be mediated by a *switch recombinase,*which is directed to the appropriate switch sequences when these become accessible under the influence of cytokines, as we discuss later.

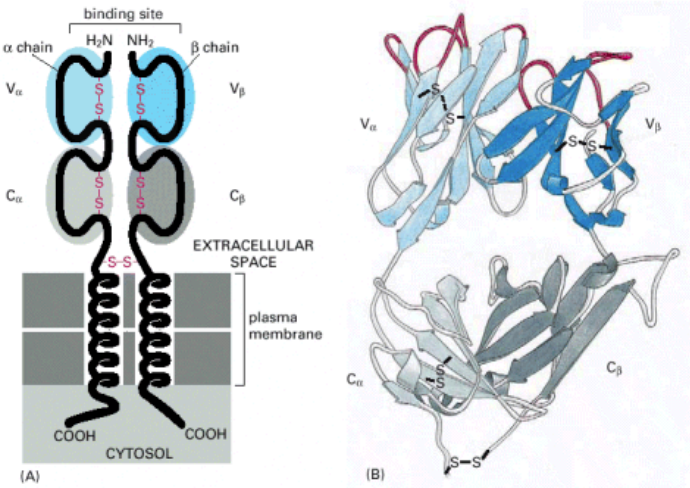

Figure 24-42. A T cell receptor heterodimer. (A) Schematic drawing showing that the receptor is composed of an α and a β polypeptide chain. Each chain is about 280 amino acids long and has a large extracellular part that is folded into two Ig-like domains - one variable (V) and one constant (C). The antigen-binding site is formed by a V_α and a V_β domain (shaded in *blue).* Unlike antibodies, which have two binding sites for antigen, T cell receptors have only one. The αβ heterodimer is noncovalently associated with a large set of invariant membrane-bound proteins (not shown), which help activate the T cell when the T cell receptors bind to antigen. A typical T cell has about 30,000 such receptor complexes on its surface. (B) The three-dimensional structure of the extracellular part of a T cell receptor. The antigen-binding site is formed by the hypervariable loops of both the V_α and V_β domains *(red),* and it is similar in its overall dimensions and geometry to the antigen-binding site of an antibody molecule. (B, based on K.C. Garcia et al., *Science* 274:209219, 1996.)

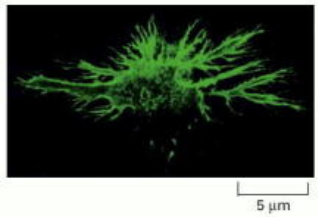

Figure 24-43. Immunofluorescence micrograph of a dendritic cell in culture. These crucial antigen-presenting cells derive their name from their long processes, or "dendrites." The cell has been labelled with a monoclonal antibody that recognizes a surface antigen on these cells. (Courtesy of David Katz.)

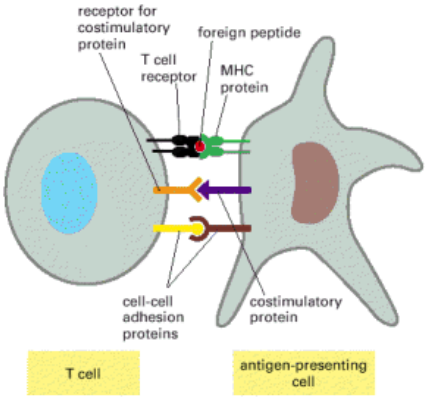

Figure 24-44. Three types of proteins on the surface of an antigen-presenting cell involved in activating a T cell. The invariant polypeptide chains that are stably associated with the T cell receptor are not shown.

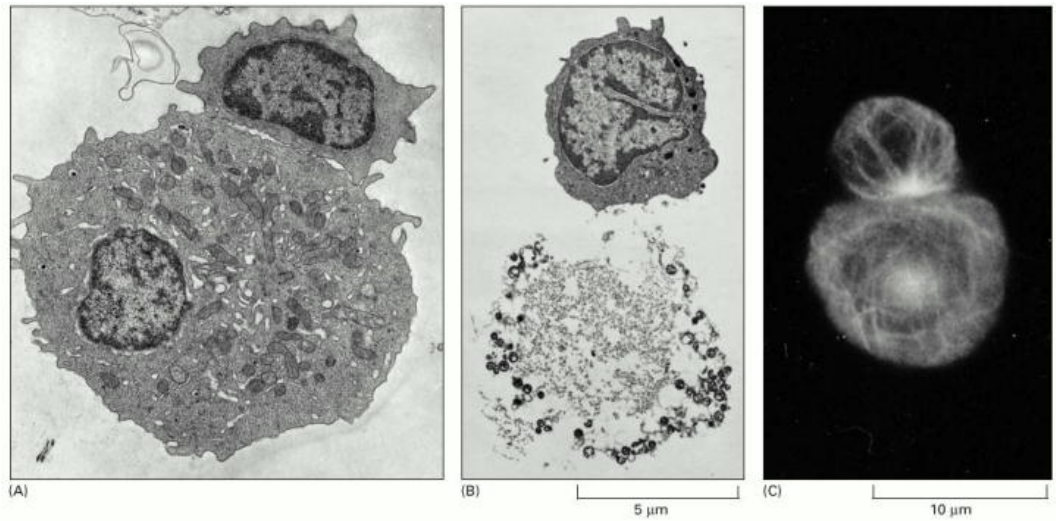

Figure 24-45. Effector cytotoxic T cells killing target cells in culture. (A) Electron micrograph showing an effector cytotoxic T cell binding to the target cell. The cytotoxic T cells were obtained from mice immunized with the target cells, which are foreign tumor cells. (B) Electron micrograph showing a cytotoxic T cell and a tumor cell that the T cell has killed. In an animal, as opposed to in a tissue culture dish, the killed target cell would be phagocytosed by neighboring cells long before it disintegrated in the way that it has here. (C) Immunofluorescence micrograph of a T cell and tumor cell after staining with anti-tubulin antibodies. Note that the centrosome in the T cell and the microtubules radiating from it are oriented toward the point of cell-cell contact with the target cell. See also Figure 16-97A. (A and B, from D. Zagury, J. Bernard, N. Thierness, M. Feldman, and G. Berke, *Eur. J. Immunol.* 5:818822, 1975; C, reproduced from B. Geiger, D. Rosen, and G. Berke, *J. Cell Biol*. 95:137143, 1982. © The Rockefeller University Press.)

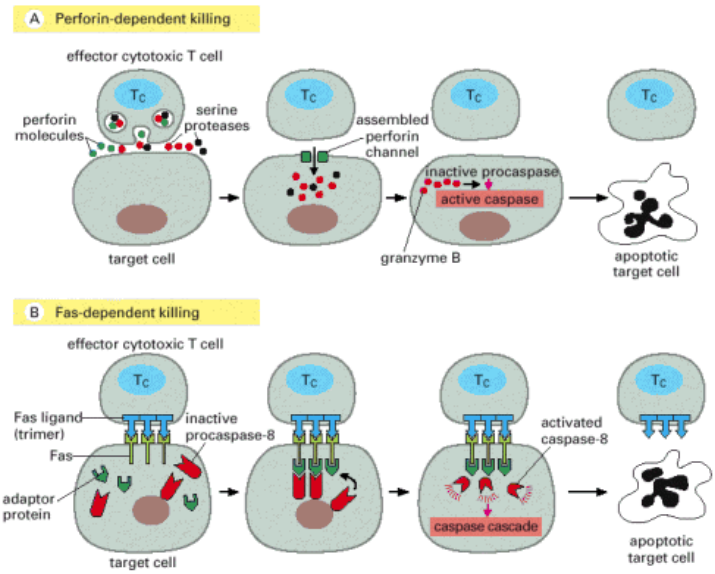

Figure 24-46. Two strategies by which effector cytotoxic T cells kill their target cells. (A) The cytotoxic T cell (T_C) releases perforin and proteolytic enzymes onto the surface of an infected target cell by localized exocytosis. The high concentration of Ca^{2+} in the extracellular fluid causes the perforin to assemble into transmembrane channels, which are thought to allow the proteolytic enzymes to enter the target cell cytosol. One of the enzymes, granzyme B, cleaves and activates specific procaspases, thereby triggering the proteolytic caspase cascade leading to apoptosis. (B) The homotrimeric Fas ligand on the cytotoxic T cell surface binds to and activates Fas receptor protein on the surface of a target cell. The cytosolic tail of Fas contains a *death domain*, which, when activated, binds to an adaptor protein, which in turn recruits a specific procaspase (procaspase-8). Clustered procaspase-8 molecules then cleave one another to produce active caspase-8 molecules that initiate the proteolytic caspase cascade leading to apoptosis.

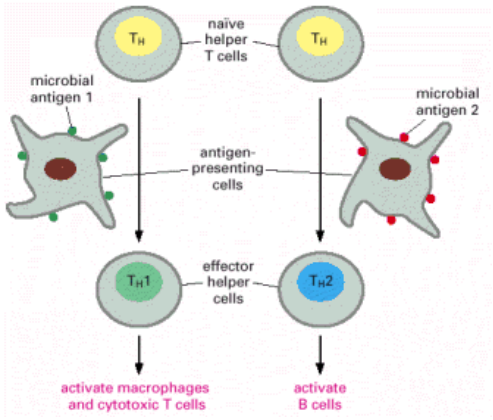

Figure 24-47. Differentiation of naïve helper T cells into either T_H1 or T_H2 effector helper cells in a peripheral lymphoid organ. The antigen-presenting cell and the characteristics of the pathogen that activated it mainly determine which type of effector helper cell develops.

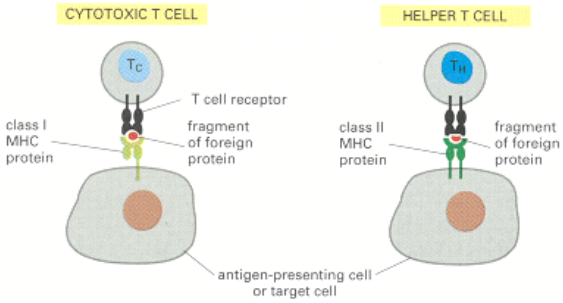

Figure 24-48. Recognition by T cells of foreign peptides bound to MHC proteins. Cytotoxic T cells recognize foreign peptides in association with class I MHC proteins, whereas helper T cells recognize foreign peptides in association with class II MHC proteins. In both cases, the peptide-MHC complexes are recognized on the surface of an antigen-presenting cell or a target cell.

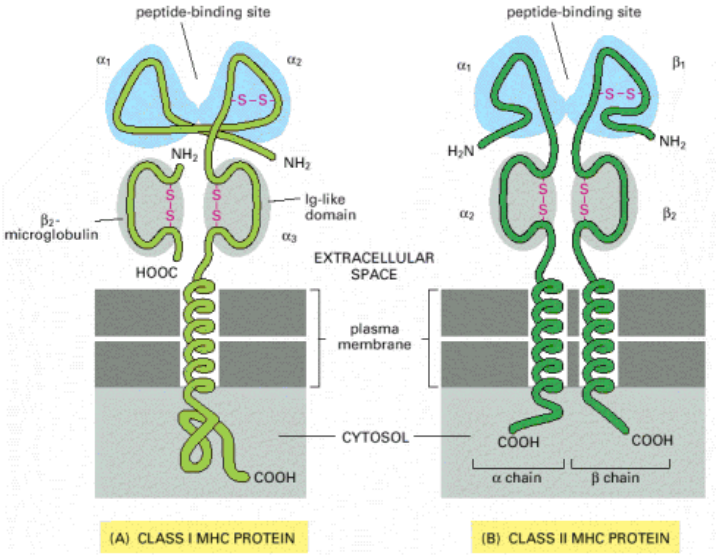

Figure 24-49. Class I and class II MHC proteins. (A) The α chain of the class I molecule has three extracellular domains, α_1, α_2 and α_3, encoded by separate exons. It is noncovalently associated with a smaller polypeptide chain, β_2-microglobulin, which is not encoded within the MHC. The α_3 domain and β_2-microglobulin are Ig-like. While β_2-microglobulin is invariant, the α chain is extremely polymorphic, mainly in the α_1 and α_2 domains. (B) In class II MHC proteins, both chains are polymorphic, mainly in the α_1 and β_1 domains; the α_2 and β_2 domains are Ig-like. Thus, there are striking similarities between class I and class II MHC proteins. In both, the two outermost domains (shaded in *blue)* interact to form a groove that binds peptide fragments of foreign proteins and presents them to T cells

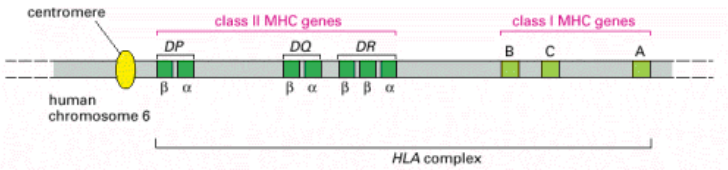

Figure 24-50. Human MHC genes. This simplified schematic drawing shows the location of the genes that encode the transmembrane subunits of class I *(light green)* and class II *(dark green)* MHC proteins. The genes shown encode three types of class I proteins (HLA-A, HLA-B, and HLA-C) and three types of class II MHC proteins (HLA-DP, HLA-DQ, and HLA-DR). An individual can therefore make six types of class I MHC proteins (three encoded by maternal genes and three by paternal genes) and more than six types of class II MHC proteins. The number of class II MHC proteins that can be made is increased because there are two DR β genes and because maternally encoded and paternally encoded polypeptide chains can sometimes pair.

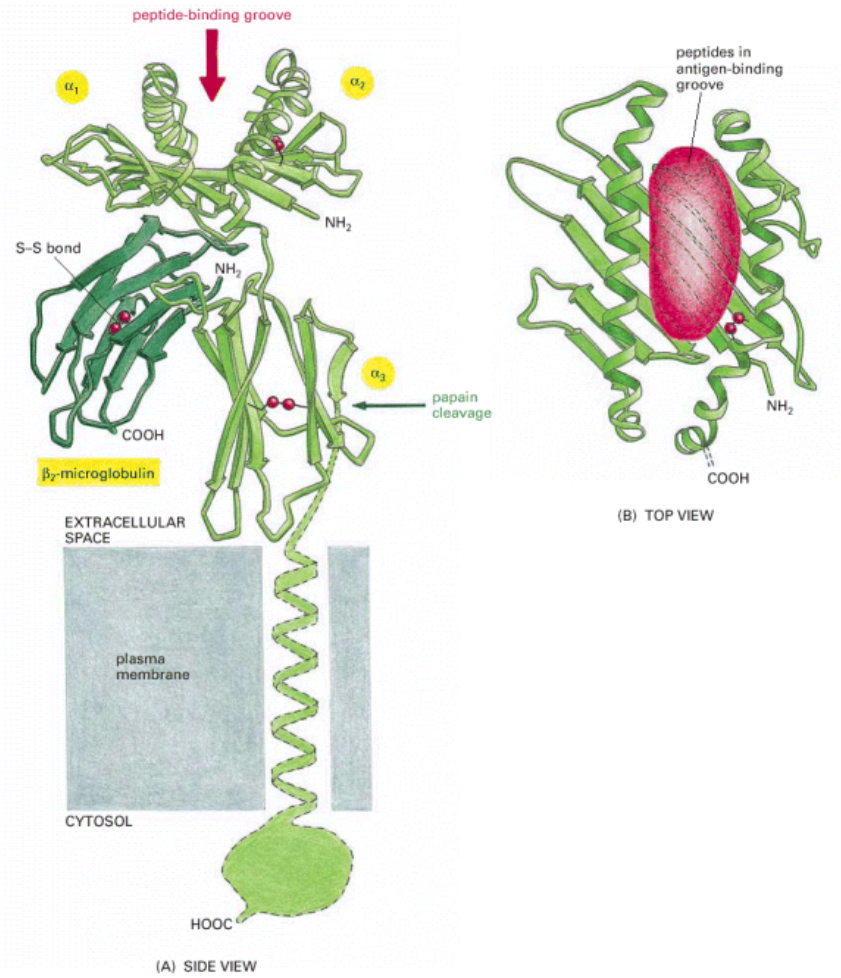

Figure 24-51. The three-dimensional structure of a human class I MHC protein as determined by x-ray diffraction analysis of crystals of the extracellular part of the molecule. The extracellular part of the protein was cleaved from the transmembrane segment by the proteolytic enzyme papain before crystallization. (A) Each of the two domains closest to the plasma membrane (α_3 and β_2-microglobulin) resembles a typical Ig domain (see Figure 24-34), while the two domains farthest from the membrane (α_1 and α_2) are very similar to each other and together form a peptide-binding groove at the top of the molecule. (B) The peptide-binding groove viewed from above. The small peptides that co-purified with the MHC protein are shown schematically. (After P.J. Bjorkman, M.A. Saper, B. Samraoui, W.S. Bennett, J.L. Strominger, and D.C. Wiley, *Nature* 329:506512, 1987.)

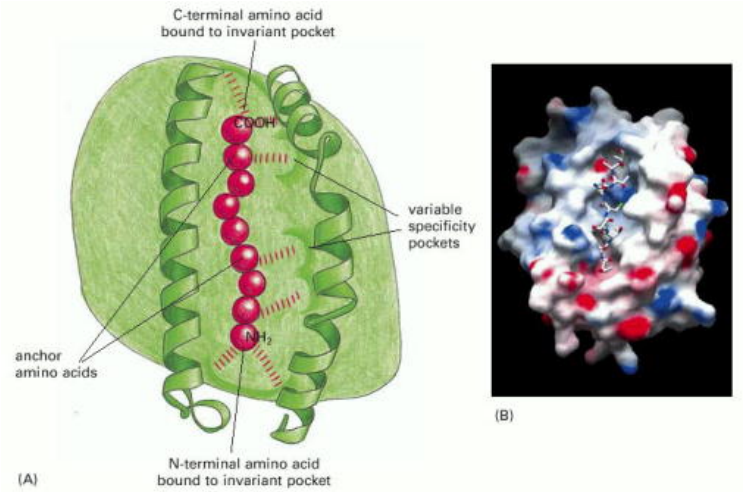

Figure 24-52. A peptide bound in the groove of a class I MHC protein. (A) Schematic drawing of a top view of the groove. The peptide backbone is shown as a string of *red* balls, each of which represents one of the nine amino acids of the peptide. The terminal amino and carboxyl groups of the peptide backbone bind to invariant pockets at the ends of the groove, while the side chains of several anchor amino acids of the peptide bind to variable specificity pockets in the groove. (B) The three-dimensional structure of a peptide bound in the groove of a class I MHC protein, as determined by x-ray diffraction. (B, courtesy of Paul Travers.)

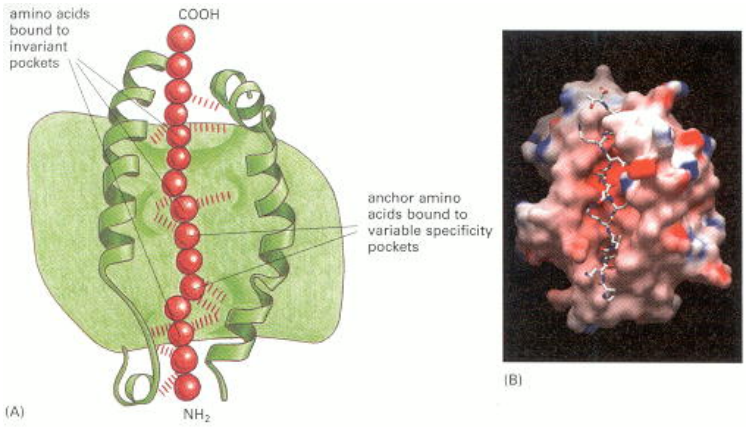

Figure 24-53. A peptide bound in the groove of a class II MHC protein. (A) Schematic drawing similar to that shown in Figure 24-52A. Note that the ends of the peptide are not tightly bound and extend beyond the cleft. The peptide is held in the groove by interactions between parts of its backbone and invariant pockets in the groove and between the side chains of several anchor amino acids of the peptide and variable specificity pockets in the groove. (B) The three-dimensional structure of a peptide bound in the groove of a class II MHC protein, as determined by x-ray diffraction. (B, courtesy of Paul Travers.)

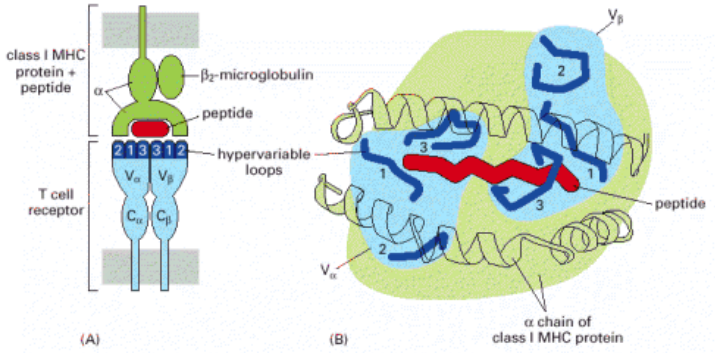

Figure 24-54. The interaction of a T cell receptor with a viral peptide bound to a class I MHC protein. (A) Schematic view of the hypervariable loops of the V_α and V_β domains of the T cell receptor interacting with the peptide and the walls of the peptide-binding groove of the MHC protein. The precise contacts are not illustrated. (B) Drawing of the "footprint" of the V domains *(blue)* and hypervariable loops *(dark blue)* of the receptor over the peptide-binding groove, as determined by X-ray diffraction. The V_α domain covers the amino half of the peptide, while the V_β domain covers the carboxyl half. Note that the receptor is oriented diagonally across the peptide-binding groove. (B, adapted from D.N. Garboczi et al., *Nature* 384:134141, 1996.)

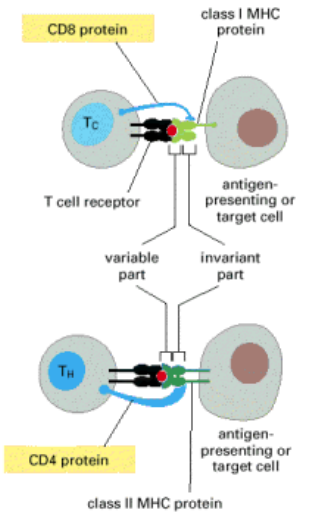

Figure 24-55. CD4 and CD8 co-receptors on the surface of T cells. Cytotoxic T cells (T_C) express CD8, which recognizes class I MHC proteins, whereas helper T cells (T_H) express CD4, which recognizes class II MHC proteins. Note that the co-receptors bind to the same MHC protein that the T cell receptor has engaged, so that they are brought together with T cell receptors during the antigen recognition process. Whereas the T cell receptor binds to the variable (polymorphic) parts of the MHC protein that form the peptide-binding groove, the co-receptor binds to the invariant part, far away from the groove.

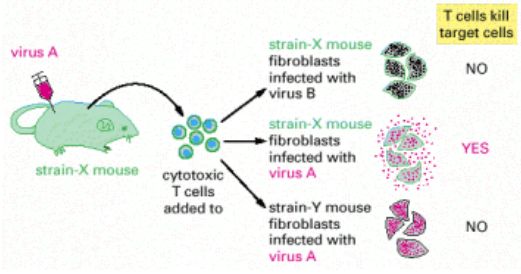

Figure 24-56. The classic experiment showing that an effector cytotoxic T cell recognizes some aspect of the surface of the host target cell in addition to a viral antigen. Mice of strain X are infected with virus A. Seven days later, the spleens of these mice contain effector cytotoxic T cells able to kill virus-infected, strain-X fibroblasts in cell culture. As expected, they kill only fibroblasts infected with virus A and not those infected with virus B. Thus, the cytotoxic T cells are virus-specific. The same T cells, however, are also unable to kill fibroblasts from strain-Y mice infected with the same virus A, indicating that the cytotoxic T cells recognize a genetic difference between the two kinds of fibroblasts and not just the virus. Pinning down the difference required the use of special strains of mice (known as *congenic strains)* that either were genetically identical except for the alleles at their class I MHC loci or were genetically different except for these alleles. In this way, it was found that the killing of infected target cells required that they express at least one of the same class I MHC alleles as expressed by the original infected mouse. This suggested that class I MHC proteins are necessary to present cell-surface-bound viral antigens to effector cytotoxic T cells.

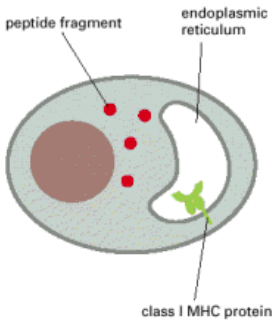

Figure 24-57. The peptide-transport problem. How do peptide fragments get from the cytosol, where they are produced, into the ER lumen, where the peptide-binding grooves of class I MHC proteins are located? A special transport process is required.

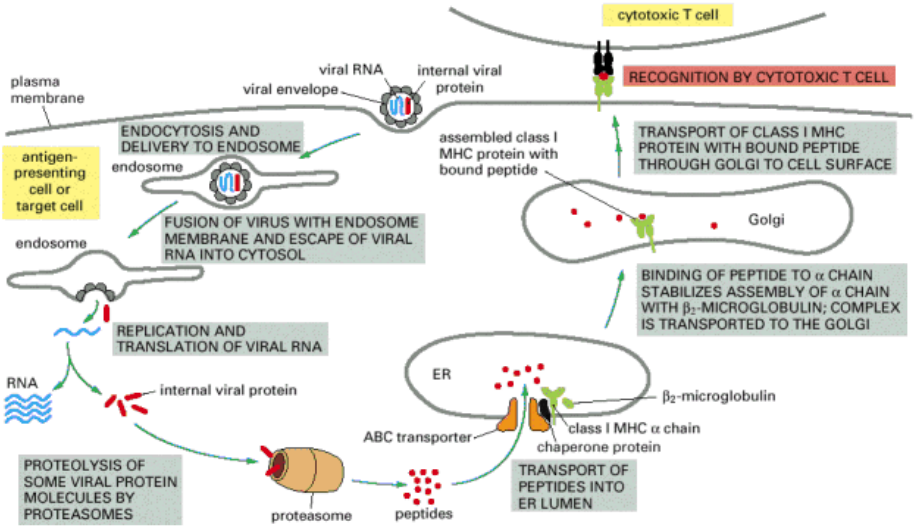

Figure 24-58. The processing of a viral protein for presentation to cytotoxic T cells. An effector cytotoxic T cell kills a virus-infected cell when it recognizes fragments of viral protein bound to class I MHC proteins on the surface of the infected cell. Not all viruses enter the cell in the way that this enveloped RNA virus does, but fragments of internal viral proteins always follow the pathway shown. Some of the viral proteins synthesized in the cytosol are degraded, and this is a sufficient amount to attract an attack by a cytotoxic T cell. The folding and assembly of a class I MHC protein is aided by several chaperone proteins in the ER lumen, only one of which is shown. The chaperones bind to the class I MHCα chain and act sequentially. The last one binds the MHC protein to the ABC transporter, as shown.

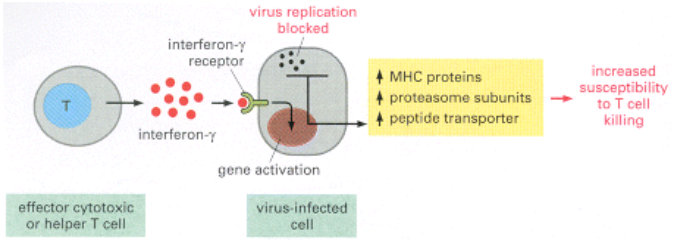

Figure 24-59. Some effects of interferon-γ on infected cells. The activated interferon-γ receptors signal to the nucleus, altering gene transcription, which leads to the effects indicated. The effects shaded in *yellow* tend to make the infected cell a better target for killing by an effector cytotoxic T cell.

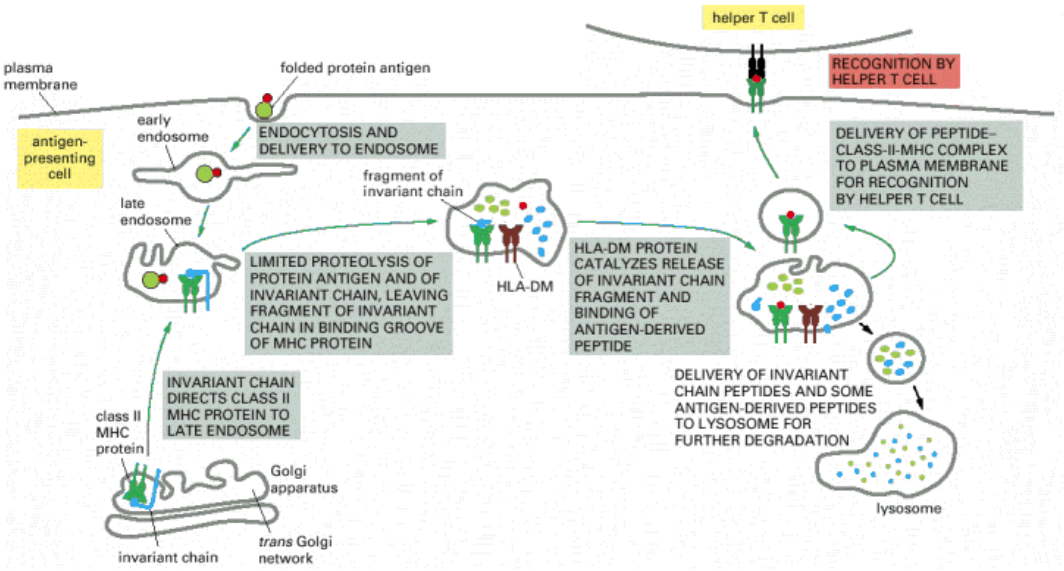

Figure 24-60. The processing of an extracellular protein antigen for presentation to a helper T cell. The drawing shows a simplified view of how peptide-class-II-MHC complexes are formed in endosomes and delivered to the cell surface. Note that the release of the invariant-chain fragment from the binding groove of the class II MHC protein in the endosome is catalyzed by a class-II-MHC-like protein called HLA-DM. Viral glycoproteins can also be processed by this pathway for presentation to helper T cells. They are made in the ER, are transported to the plasma membrane, and can then enter endosomes after endocytosis.

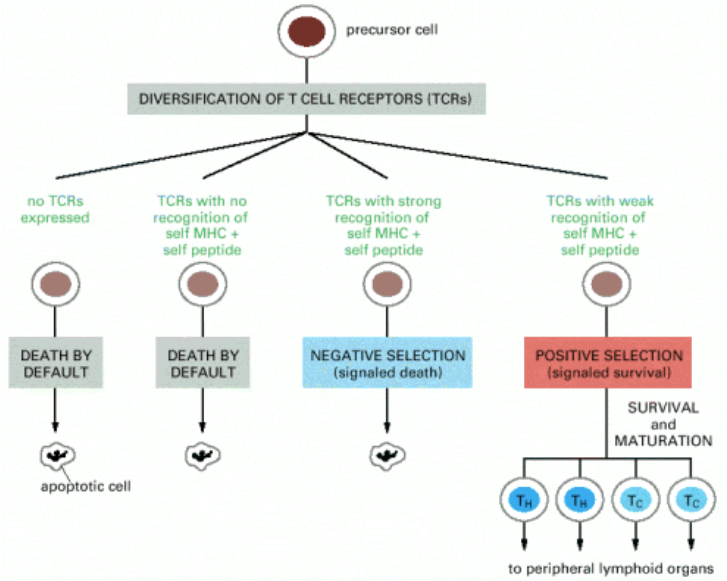

Figure 24-61. Positive and negative selection in the thymus. Cells with receptors that would enable them to respond to foreign peptides in association with self MHC proteins survive, mature, and migrate to peripheral lymphoid organs. All of the other cells undergo apoptosis. The cells undergoing positive selection initially express both CD4 and CD8 co-receptors. During the process of positive selection, helper T cells (T_H) and cytotoxic T cells (T_C) diverge by a poorly understood mechanism. In this process, helper cells develop that express CD4 but not CD8 and recognize foreign peptides in association with class II MHC proteins, while cytotoxic cells develop that express CD8 but not CD4 and recognize foreign peptides in association with class I MHC proteins (not shown).

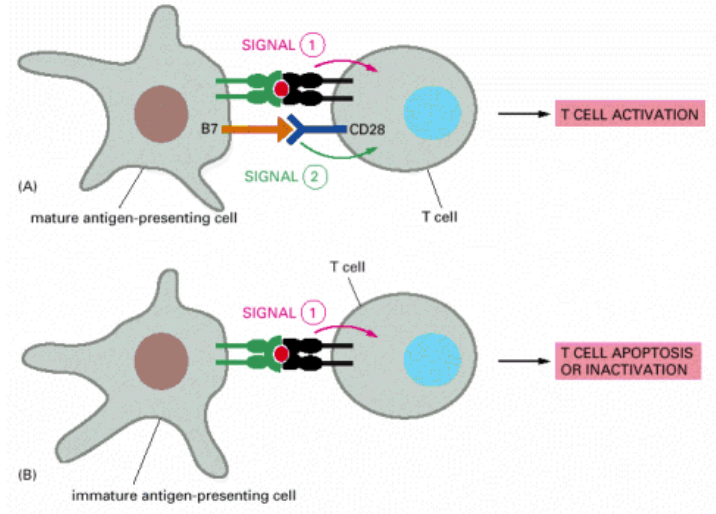

Figure 24-62. The two signals that activate a helper T cell. (A) A mature antigen-presenting cell can deliver both signal 1 and 2 and thereby activate the T cell. (B) An immature antigen-presenting cell delivers signal 1 without signal 2, which can kill or inactivate the T cell; this is one mechanism for immunological tolerance to self antigens. One model for the role of signal 2 is that it induces the active transport of signaling proteins in the T cell plasma membrane to the site of contact between the T cell and the antigen-presenting cell. The accumulation of signaling proteins around the T cell receptor is thought to greatly enhance the intensity and duration of the signaling process activated by signal 1. In this way, "immunological synapses" form in the contact zone, with the T cell receptors (and their associated proteins - see Figure 24-63) and co-receptors in the center and cell-cell adhesion proteins forming a peripheral ring (not shown).

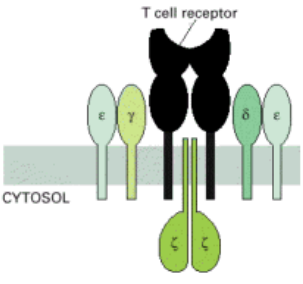

Figure 24-63. The T cell receptor and its associated CD3 complex. All of the CD3 polypeptide chains (shown in *green)*, except for the ζ (zeta) chains, have extracellular Ig-like domains and are therefore members of the Ig superfamily.

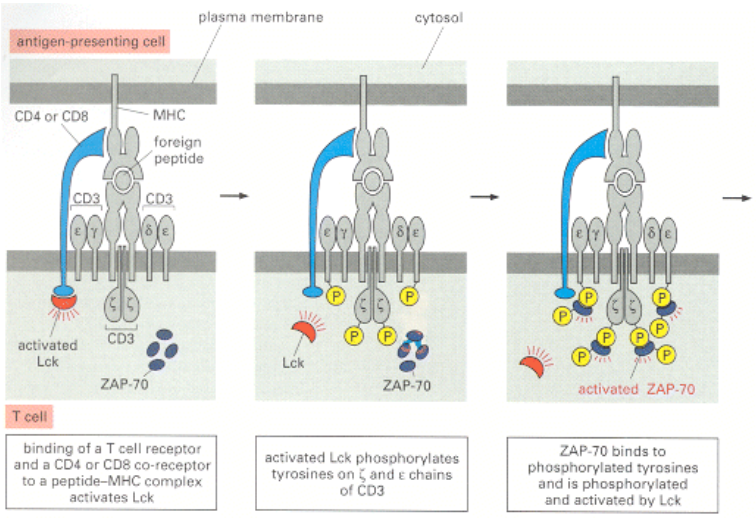

Figure 24-64. The signaling events initiated by the binding of peptide-MHC complexes to T cell receptors (signal 1). When T cell receptors are clustered by binding to peptide-MHC complexes on an antigen-presenting cell, CD4 molecules on helper cells or CD8 molecules on cytotoxic T cells are clustered with them, binding to invariant parts of the same class II or class I MHC proteins, respectively, on the presenting cell. This brings the Src-like cytoplasmic tyrosine kinase Lck into the signaling complex and activates it. Once activated, Lck phosphorylates tyrosines on the ζ and ε chains of the CD3 complex, which now serve as docking sites for yet another cytoplasmic tyrosine kinase called *ZAP-70.* Lck phosphorylates, and thereby activates, ZAP-70. Although not shown, ZAP-70 then phosphorylates tyrosines on the tail of another transmembrane protein, which then serve as docking sites for a variety of adaptor proteins and enzymes. These proteins then help relay the signal to the nucleus and other parts of the cell by activating the inositol phospholipid and MAP kinase signaling pathways (discussed in Chapter 15), as well as a Rho family GTPase that regulates the actin cytoskeleton (discussed in Chapter 16).

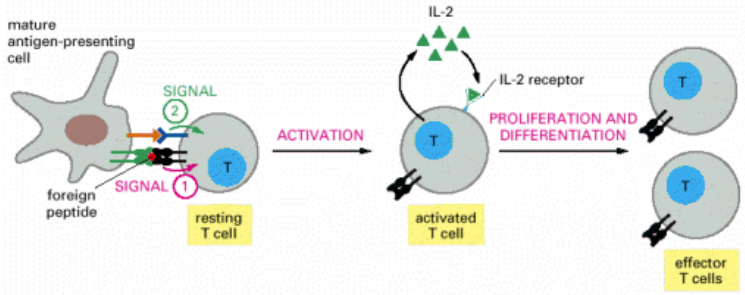

Figure 24-65. The stimulation of T cells by IL-2 in culture. Signals 1 and 2 activate T cells to make high affinity IL-2 receptors and to secrete IL-2. The binding of IL-2 to its receptors helps stimulate the cell to proliferate and differentiate into effector cells. Although some T cells do not make IL-2, as long as they have been activated by their antigen and therefore express IL-2 receptors, they can be helped to proliferate and differentiate by IL-2 made by neighboring T cells (not shown).

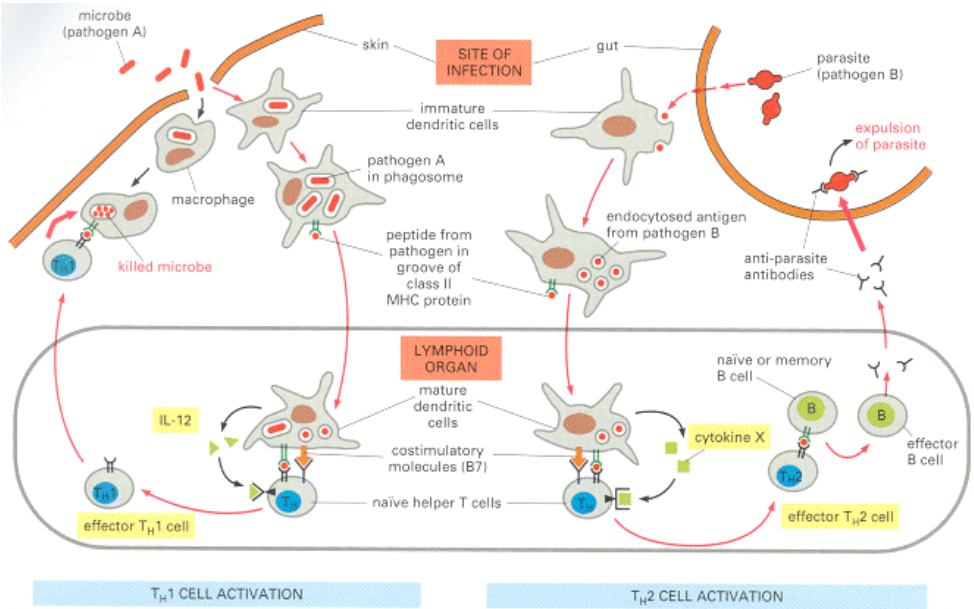

Figure 24-66. The activation of T_H1 and T_H2 cells. The differentiation of helper T cells into either T_H1 or T_H2 effector cells determines the nature of the subsequent adaptive immune responses that the effector cells activate. Whether a naïve helper T cell becomes a T_H1 or T_H2 cell depends mainly on the cytokines present when the helper T cell is activated by a mature dendritic cell in a peripheral lymphoid organ. The types of cytokines produced depend on the local environment and the nature of the microbe or parasite that activated the immature dendritic cell at the site of infection. IL-12 produced by mature dendritic cells promotes T_H1 cell development. The cytokine(s) produced by dendritic cells that promotes T_H2 cell development (cytokine X) is not known, although IL-4 produced by T cells can serve this function. In this figure, the effector T_H1 cell produced in the peripheral lymphoid organ migrates to the site of infection and helps a macrophage kill the microbes it has phagocytosed. The effector T_H2 cell remains in the lymphoid organ and helps activate a B cell to produce antibodies against the parasite. The antibodies arm mast cells, basophils, and eosinophils (not shown), which then can help expel the parasite from the gut.

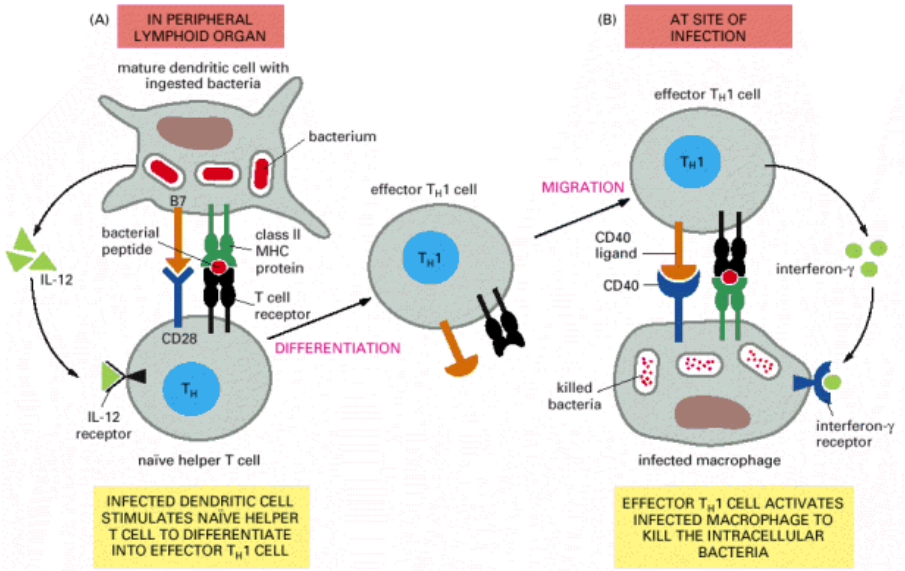

Figure 24-67. The differentiation of T_H1 cells and their activation of macrophages. (A) An infected dendritic cell that has migrated from a site of infection to a peripheral lymphoid organ activates a naïve helper T cell to differentiate into a T_H1 effector cell, using both cell-surface B7 and secreted IL-12. (B) A T_H1 effector cell that has migrated from the peripheral lymphoid organ to an infected site helps activate macrophages to kill the bacteria harboring within the macrophages' phagosomes. The T cell activates the macrophage by means of CD40 ligand on its surface and secreted interferon-γ.

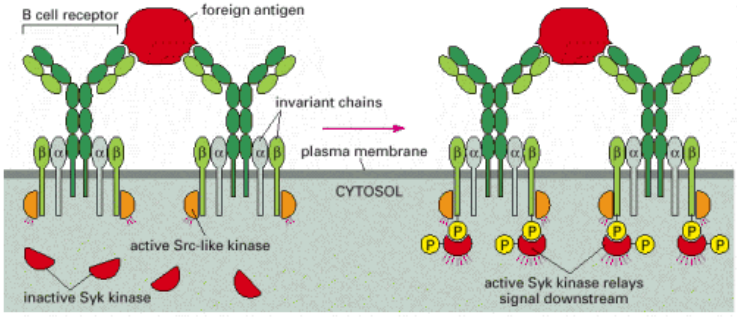

Figure 24-68. Signaling events activated by the binding of antigen to B cell receptors (signal I). The antigen cross-links adjacent receptor proteins, which are transmembrane antibody molecules, causing the receptors and their associated invariant chains (Igα and Igβ) to cluster. The Src-like tyrosine kinase associated with the cytosolic tail of Igβ joins the cluster and phosphorylates Igα and Igβ (for simplicity, only the phosphorylation on Igβ is shown). The resulting phosphotyrosines on Igα and Igβ serve as docking sites for another Src-like tyrosine kinase called *Syk*, which is homologous to ZAP-70 in T cells (see Figure 24-64). Like ZAP-70, Syk becomes phosphorylated and relays the signal downstream.

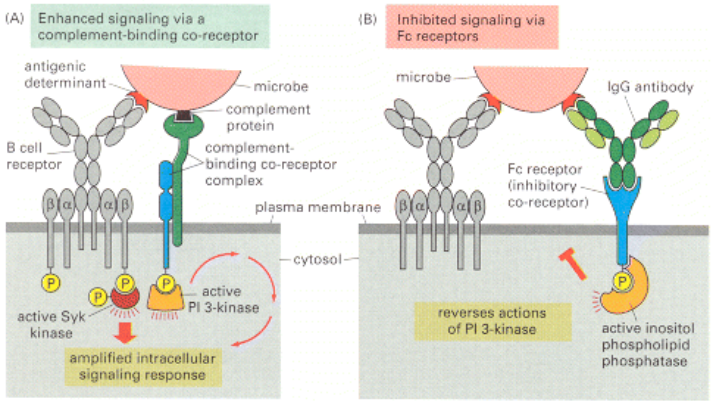

Figure 24-69. The influence of B cell co-receptors on the effectiveness of signal I. (A) The binding of microbe-complement complexes to a B cell cross-links the antigen receptors to complement-binding, co-receptor complexes. The cytosolic tail of one component of the co-receptor complex becomes phosphorylated on tyrosines, which then serve as docking sites for PI 3-kinase. As discussed in Chapter 15, PI 3-kinase is activated to generate inositol phospholipid docking sites in the plasma membrane, which recruit intracellular signaling proteins (not shown). These signaling proteins act together with the signals generated by the Syk kinase to amplify the response. (B) When IgG antibodies become bound to foreign antigen, usually late in a response, the Fc regions of the antibodies bind to Fc receptors on the B cell surface and are thus recruited into the signaling complex. The Fc receptors become phosphorylated on tyrosines, which then serve as docking sites for an inositol phospholipid phosphatase. The phosphatase dephosphorylates the inositol phopholipid docking sites in the plamsa membrane generated by PI 3-kinase, thereby reversing the activating effects of PI 3-kinase. The Fc receptors also inhibit signaling by recruiting protein tyrosine phosphatases into the signaling complex (not shown).

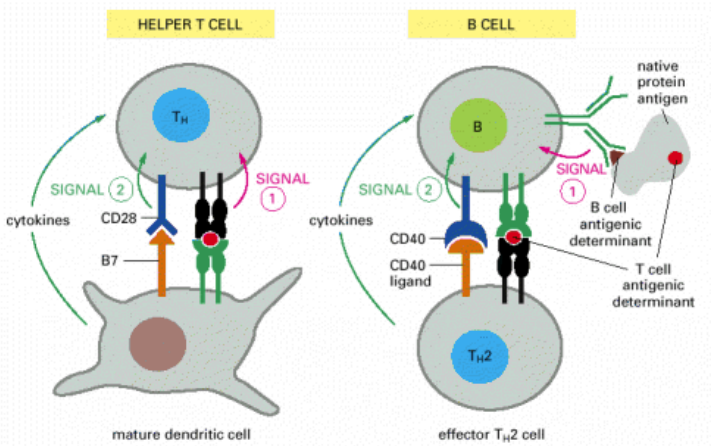

Figure 24-70. Comparison of the signals required to activate a helper T cell and a B cell. Note that in both cases secreted and membrane-bound molecules can cooperate to provide signal 2. Although not shown, CD40 is also expressed on the surface of mature dendritic cells and helps maintain helper T cells in an active state. The native protein antigen is endocytosed by both the dendritic cell and the B cell and is degraded in endosomes (not shown). The T cell antigenic determinant is presented on the surface of both the dendritic cell and the B cell as a peptide fragment bound to a class II MHC protein. By contrast, the B cell recognizes an antigenic determinant on the surface of the folded protein.

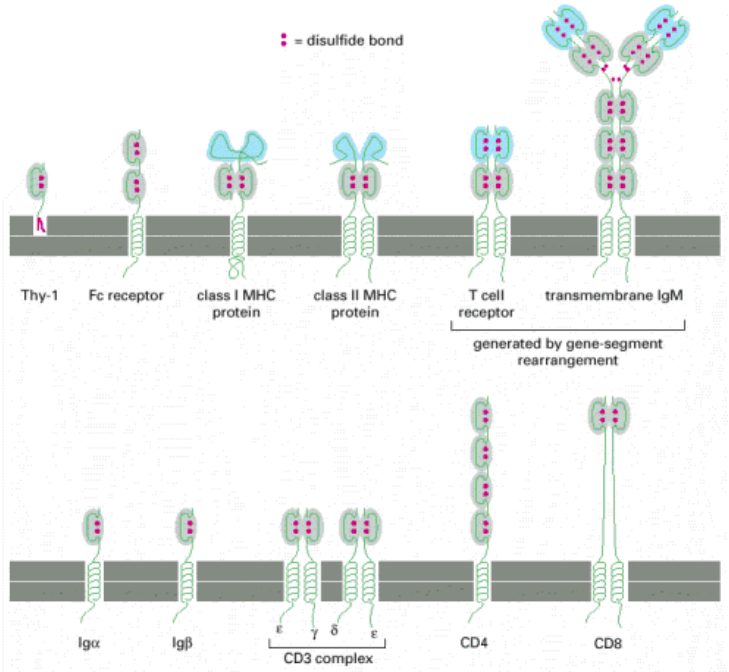

Figure 24-71. Some of the membrane proteins belonging to the Ig superfamily. The Ig and Ig-like domains are shaded in *gray*, except for the antigen-binding domains (not all of which are Ig domains), which are shaded in *blue*. The function of Thy-1 is unknown, but it is widely used to idenitfy T cells in mice. The Ig superfamily also includes many cell-surface proteins involved in cell-cell interactions outside the immune system, such as the neural cell-adhesion molecule (N-CAM) discussed in Chapter 19 and the receptors for various protein growth factors discussed in Chapters 15 and 17 (not shown). There are about 765 members of the Ig superfamily in humans.

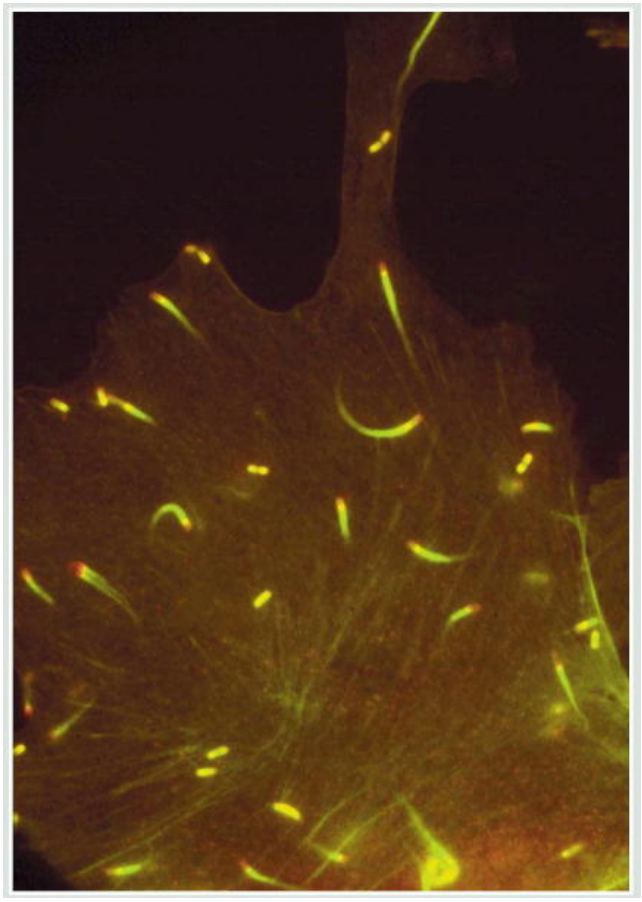

Hostpathogen interactions. The bacterial pathogen *Listeria monocytogenes* grows directly in the cytoplasm of infected mammalian host cells, including the human cell shown here. These bacteria induce the assembly of comet-like tails of host cell actin filaments *(green)* that propel the invaders through the host cytoplasm and enable the infection to spread directly from a cell to its neighbors. (Courtesy of Julie Theriot.)

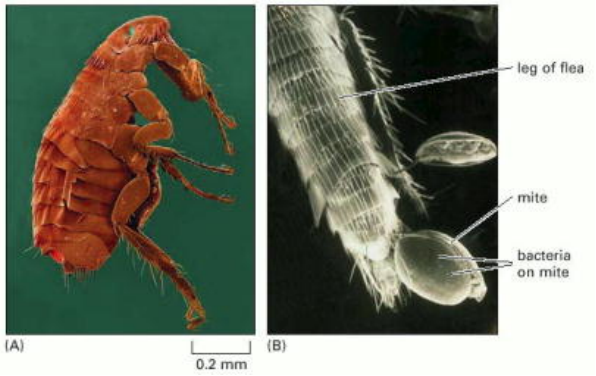

Figure 25-1. Parasitism at many levels. (A) Scanning electron micrograph of a flea. The flea is a common parasite of mammals - including dogs, cats, rats, and humans. It drinks the blood of its host. Flea bites spread bubonic plague by passing the pathogenic bacterium *Yersinia pestis* from the bloodstream of one infected host to that of another. (B) A close-up view of a flea's leg reveals that this flea also has a parasite, a type of mite. The mite, in turn, is covered with bacteria. It is likely that these bacteria are parasitized by *bacteriophages*, which are bacterial viruses. A similar observation was reported by Jonathan Swift in 1733: So, naturalists observe, a flea Has smaller fleas that on him prey; And these have smaller still to bite 'em; And so proceed ad infinitum. (A, courtesy of Tina Carvalho/ MicroAngela; B, courtesy of Stanley Falkow.)

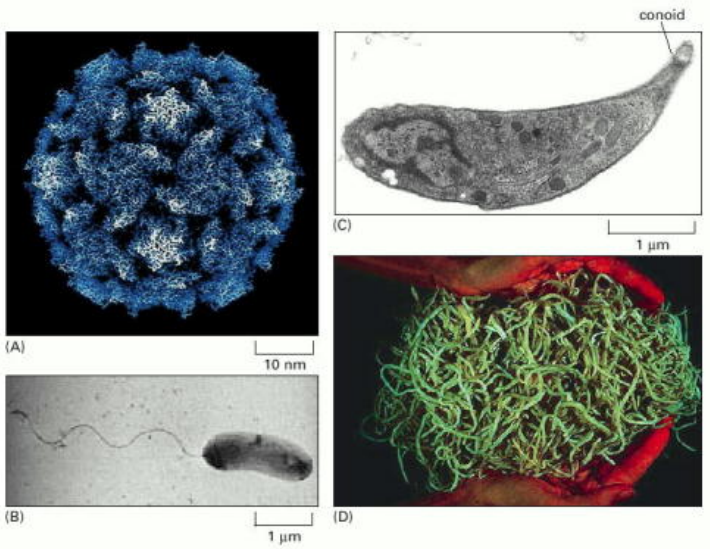

Figure 25-2. Pathogens in many forms. (A) The structure of the protein coat, or *capsid*, of poliovirus. This virus was once a common cause of paralysis, but the disease (poliomyelitis) has been nearly eradicated by widespread vaccination. (B) The bacterium *Vibrio cholerae*, the causative agent of the epidemic, diarrheal disease cholera. (C) The protozoan parasite *Toxoplasma gondii*. This organism is normally a parasite of cats, but it can cause serious infections in the muscles and brains of immunocompromised people with AIDS. (D) This clump of *Ascaris* nematodes was removed from the obstructed intestine of a two-year-old boy. (A, courtesy of Robert Grant, Stephan Crainic, and James M. Hogle; B, all attempts have been made to contact the copyright holder and we would be pleased to hear from them; C, courtesy of John Boothroyd and David Ferguson; D, from J.K. Baird et al., *Amer. J. Trop. Med. Hyg.* 35:314318, 1986. Photograph by Daniel H. Connor.)

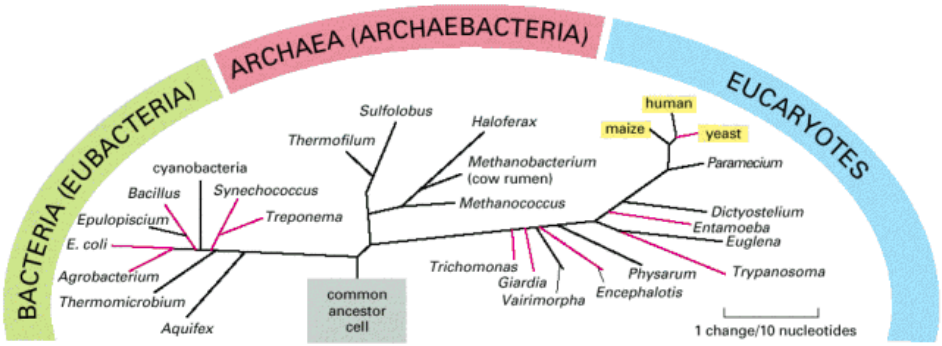

Figure 25-3. Phylogenetic diversity of pathogens. This diagram shows the similarities among 16S ribosomal RNA for cellular life forms (bacteria, archaea, and eucaryotes). Each branch is labeled with the name of a representative member of that group, and the length of the branches corresponds to the degree of difference in the rRNA sequence. Note that all the organisms we can see with the unaided eye (highlighted in *yellow)* - animals, plants, and fungi - represent a small subset of the diversity of life. In the two branches of the tree representing the bacteria and the eucaryotes, the branches that include known pathogens are indicated in *red.* No diseases are currently known to be caused by archaea, though many humans and all cows carry some types of archaea in their normal intestinal flora.

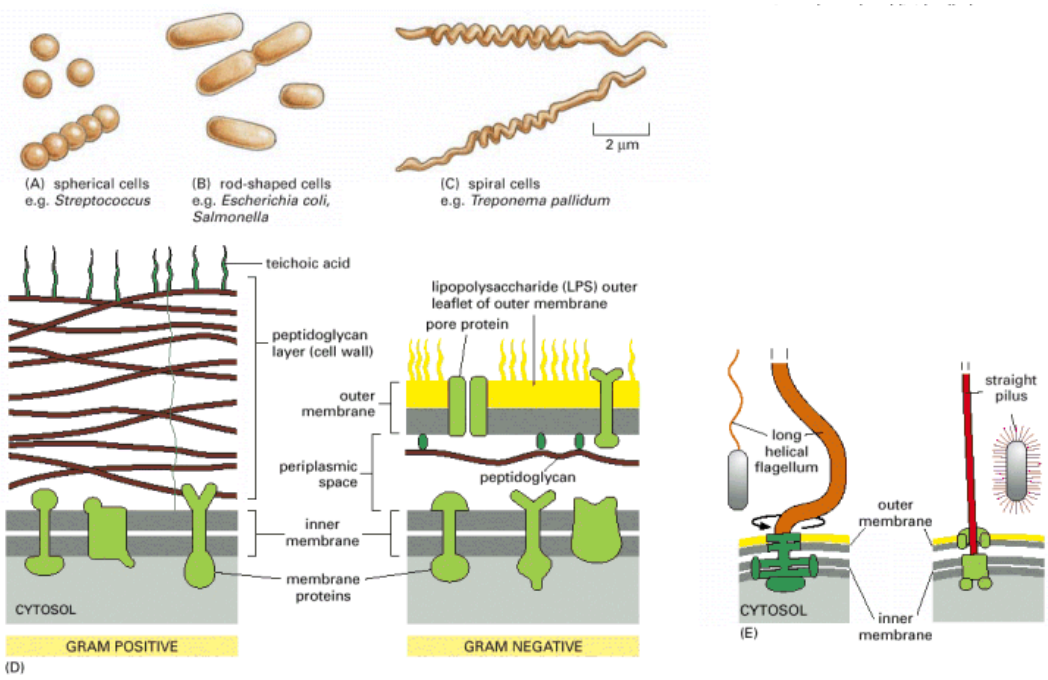

Figure 25-4. Bacterial shapes and cell-surface structures. Bacteria are classified into three different shapes: (A) spheres (cocci), (B) rods (bacilli), and (C) spiral cells (spirochetes). (D) They are also classified as *Gram-positive* or *Gram-negative.* Bacteria such as *Streptococci* and *Staphylococci* have a single membrane and a thick cell wall made of cross-linked *peptidoglycan*. They retain the violet dye used in the Gram staining procedure and are thus called Gram-positive. Gram-negative bacteria such as *E. coli* and *Salmonella* have two membranes, separated by a *periplasmic space* (see Figure 11-17). The peptidoglycan layer in the cell wall of these organisms is located in the periplasmic space and is thinner than in Gram-positives; they therefore fail to retain the dye in the Gram staining procedure. The inner membrane of Gram-negative bacteria is a phospholipid bilayer, and the inner leaflet of the outer membrane is also made primarily of phospholipids; the outer leaflet of the outer membrane, however, is composed of a unique glycosylated lipid called *lipopolysaccharide (LPS)* (see Figure 25-40). (E) Cell-surface projections are important for bacterial behavior. Many bacteria swim using the rotation of helical flagella (see Figure 15-68). The bacterium illustrated has only a single flagellum at one pole; others such as *E. coli* are decorated with multiple flagella all over the surface. Straight *pili* (also called *fimbriae)* are used to adhere to surfaces in the host and to facilitate genetic exchange between bacteria. Both flagella and pili are anchored to the cell surface by large multiprotein complexes.

Figure 25-5. Genetic differences between pathogens and nonpathogens.
Nonpathogenic *Escherichia coli* has a single circular chromosome. *E. coli* is very closely related to two types of food-borne pathogens - *Shigella flexneri*, which causes dysentery, and *Salmonella enterica*, a common cause of food poisoning. If these three organisms were being named today based on molecular techniques, they would be classified in the same genus, if not the same species. The chromosome of *S. flexneri* differs from that of *E. coli* at only a few loci; most of the genes required for pathogenesis are carried on an extrachromosomal virulence plasmid. The chromosome of *S. enterica* carries two large inserts (pathogenicity islands) not found in the *E. coli* chromosome; these inserts each contain many virulence genes.

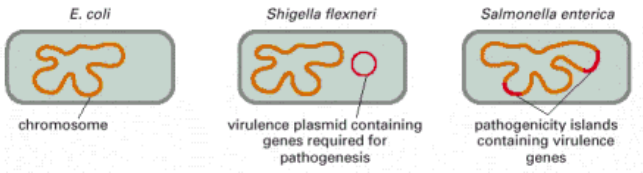

Figure 25-6. Genetic organization of *Vibrio cholerae*. (A) *Vibrio cholerae* is unusual in having two circular chromosomes rather than one. The two chromosomes have distinct origins of replication ($oriC_1$ and $oriC_2$). Three loci in pathogenic strains of *V. cholerae* are absent in nonpathogenic strains and appear to have been acquired relatively recently. CTXϕ on chromosome 1 is an integrated bacteriophage genome that carries the genes for cholera toxin. The pathogenicity island VPI on chromosome 1 includes genes for factors required for intestinal colonization. The *integron island* on chromosome 2 is a structure that enables the sequential acquisition of novel genes by facilitating the insertion of newly acquired DNA fragments downstream of a strong transcriptional promoter. Although this integron island has not yet been shown to be required for virulence in *V. cholerae*, similar integron islands in many other pathogens contain virulence genes,

as well as genes involved in antibiotic resistance. (B) Map of the CTXϕ locus. The genes encoding the two subunits of cholera toxin are ctxA and ctxB. Other genes in the core region *(ace* and *zot)* are also involved in virulence. The two repeated flanking sequences RS2 and RS1 are involved in the chromosomal insertion of the bacteriophage genome.

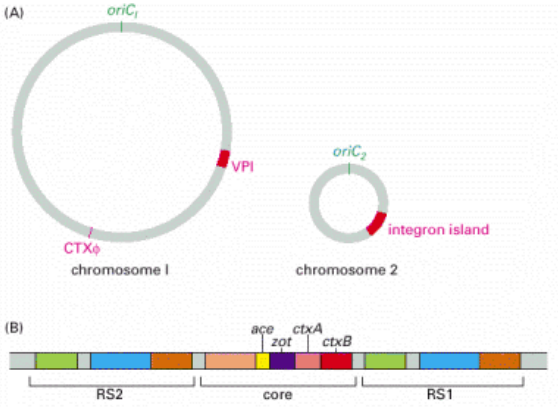

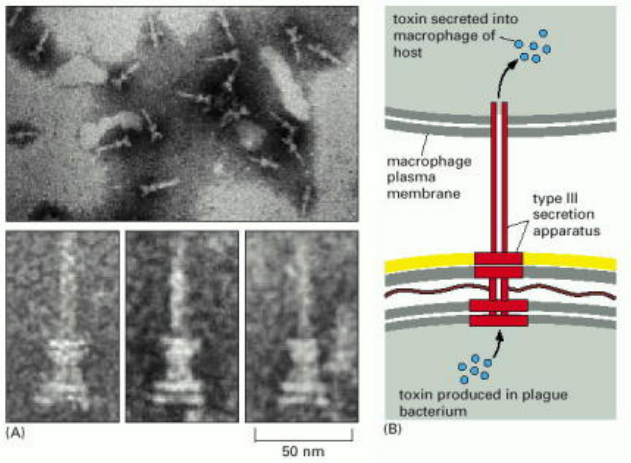

Figure 25-7. Type III secretion systems that can deliver virulence factors into the cytoplasm of host cells. (A) Electron micrographs of purified type III apparatuses. About two dozen proteins are necessary to make the complete structure, which is seen in the three enlarged micrographs below. The large lower ring is embedded in the inner membrane, and the smaller upper ring is embedded in the outer membrane. The long projection at the top is a hollow tube, through which secreted proteins can travel. (B) During infection, contact of the tube tip with the plasma membrane of a host cell triggers secretion. Here, the plague bacillus *Yersinia pestis* delivers toxins to a macrophage. (A, from K. Tamano et al., *EMBO J.* 19:38763887, 2000, by permission of Oxford University Press.)

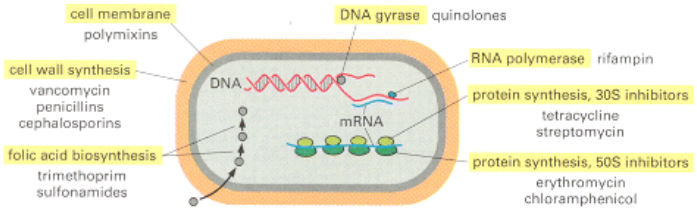

Figure 25-8. Antibiotic targets. Despite the large number of antibiotics available, they have a narrow range of targets, which are highlighted in *yellow*. A few representative antibiotics in each class are listed. All antibiotics used to treat human infections fall into one of these categories. The vast majority inhibit either bacterial protein synthesis or bacterial cell wall synthesis.

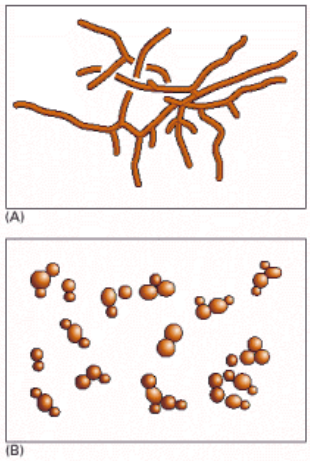

Figure 25-9. Dimorphism in the pathogenic fungus *Histoplasma capsulatum*. (A) At low temperature in the soil, *Histoplasma* grows as a filamentous fungus. (B) After being inhaled into the lung of a mammal, *Histoplasma* undergoes a morphological switch triggered by the change in temperature. In this yeast-like form, it closely resembles *Saccharomyces cerevisiae*.

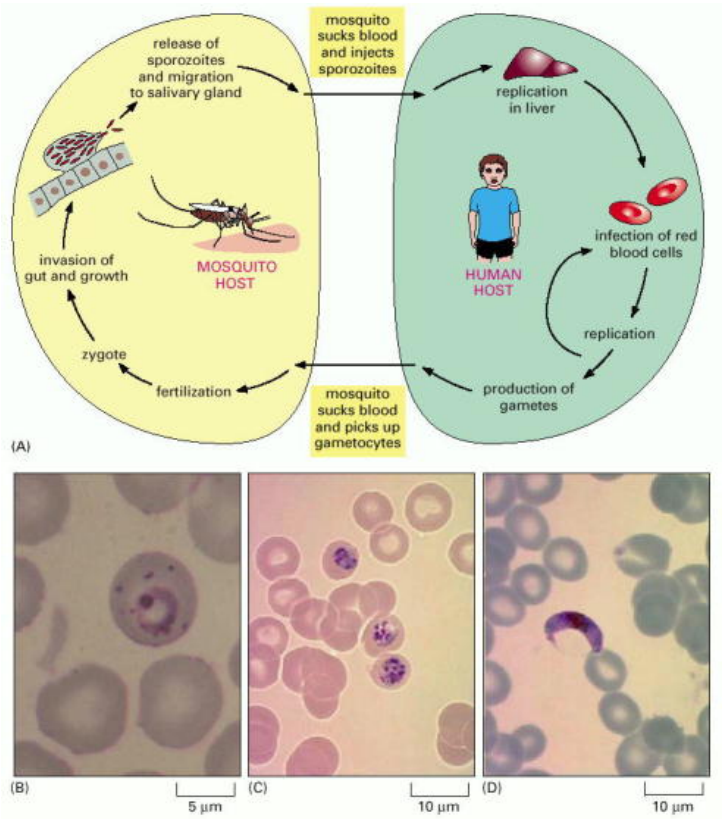

Figure 25-10. The complex life cycle of malaria. (A) The sexual cycle of *Plasmodium falciparum* requires passage between a human host and an insect host. (B)-(D) Blood smears from people infected with malaria, showing three different forms of the parasite that appear in red blood cells: (B) trophozoite (ring form); (C) schizont; (D) gametocyte. (Micrographs courtesy of the Centers for Disease Control, Division of Parasitic Diseases, DPDx.)

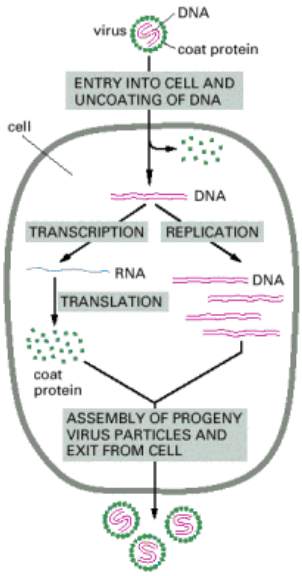

Figure 25-11. A simple viral life cycle. The hypothetical virus shown consists of a small double-stranded DNA molecule that codes for only a single viral capsid protein. No known virus is this simple.

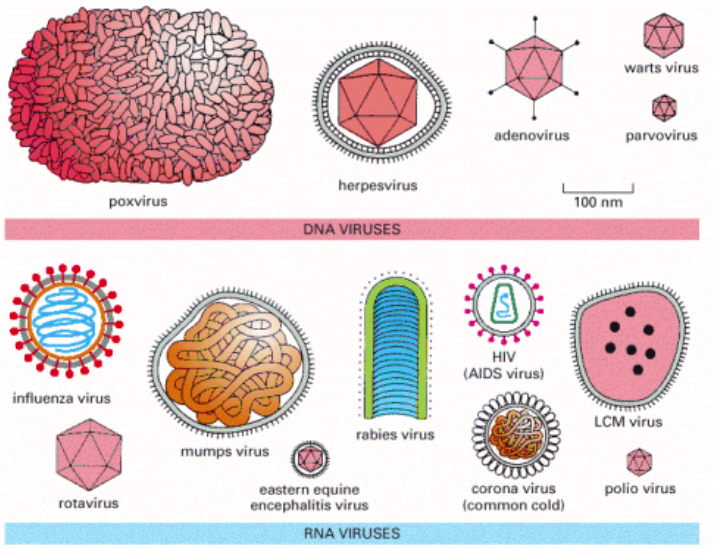

Figure 25-12. Examples of viral morphology. As shown, viruses vary greatly in both size and shape.

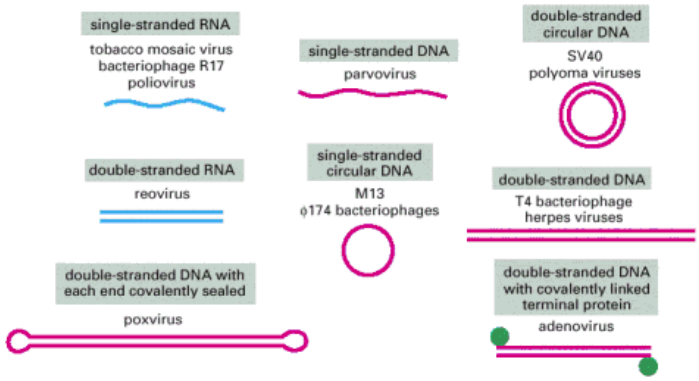

Figure 25-13. Schematic drawings of several types of viral genomes. The smallest viruses contain only a few genes and can have an RNA or a DNA genome. The largest viruses contain hundreds of genes and have a double-stranded DNA genome. The peculiar ends (as well as the circular forms) overcome the difficulty of replicating the last few nucleotides at the end of a DNA strand (discussed in Chapter 5).

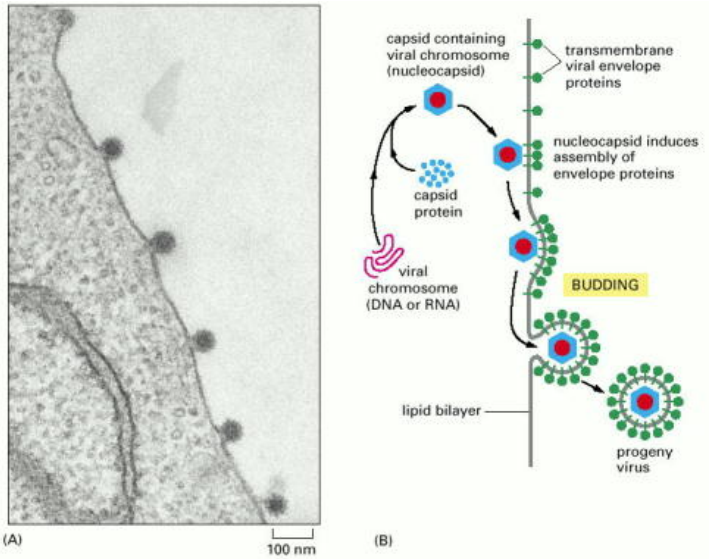

Figure 25-14. Acquisition of a viral envelope. (A) Electron micrograph of an animal cell from which six copies of an enveloped virus (*Semliki forest virus*) are budding. (B) Schematic view of the envelope assembly and budding processes. The lipid bilayer that surrounds the viral capsid is derived directly from the plasma membrane of the host cell. In contrast, the proteins in this lipid bilayer (shown in *green*) are encoded by the viral genome. (A, courtesy of M. Olsen and G. Griffith.)

Figure 25-15. A map of the HIV genome. This retroviral genome consists of about 9000 nucleotides and contains nine genes, the locations of which are shown in *green* and *red*. Three of the genes *(green)* are common to all retroviruses: *gag* encodes capsid proteins, *env* encodes envelope proteins, and *pol* encodes both the reverse transcriptase and the integrase proteins (discussed in Chapter 5). The HIV genome is unusually complex, because it contains six small genes *(red)*, in addition to the three large genes *(green)* normally required for the retrovirus life cycle. At least some of these small genes encode proteins that regulate viral gene expression *(tat* and *rev* - see Figure 7-97); others encode proteins that modify host cell processes, including protein trafficking *(vpu* and *nef)* and progression through the cell cycle *(vpr).* As indicated by the *red* lines, RNA splicing (using the host cell spliceosome) is required to produce the Rev and Tat proteins.

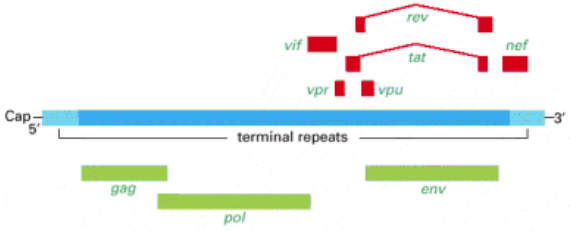

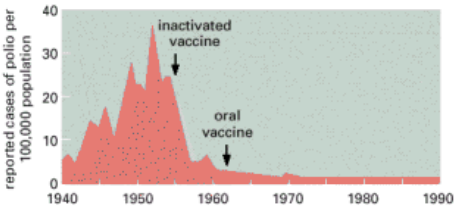

Figure 25-16. Eradication of a viral disease through vaccination. The graph shows number of cases of poliomyelitis reported per year in the United States. The *arrows* indicate the timing of the introduction of the Salk vaccine (inactivated virus given by injection) and the Sabin vaccine (live attenuated virus given orally).

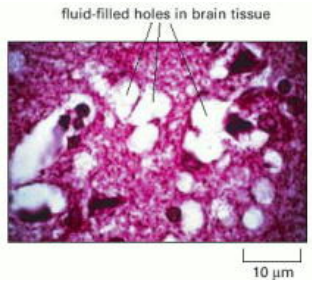

Figure 25-17. Neural degeneration in a prion infection. This micrograph shows a slice from the brain of a person who died of kuru. Kuru is a human prion disease, very similar to BSE, that was spread from one person to another by ritual mortuary practices in New Guinea. The large fluid-filled holes are places where neurons have died. These characteristic holes give the syndrome the name of spongiform encephalopathy. (Courtesy of Gary Baumbach.)

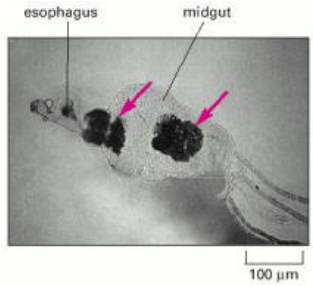

Figure 25-18. The spread of plague. This micrograph shows the digestive tract dissected from a flea that had dined about two weeks previously on the blood of an animal infected with the plague bacterium, *Yersinia pestis.* The bacteria multiplied in the flea gut to produce large cohesive aggregates, indicated by the *red* arrows; the bacterial mass on the left is occluding the passage between the esophagus and the midgut. This type of blockage prevents a flea from digesting its blood meals, thereby causing it to bite repeatedly, disseminating the infection. (From B.J. Hinnebusch, E.R. Fischer and T.G. Schwann, *J. Infect. Dis.* 178:14061415, 1998. © The University of Chicago Press.)

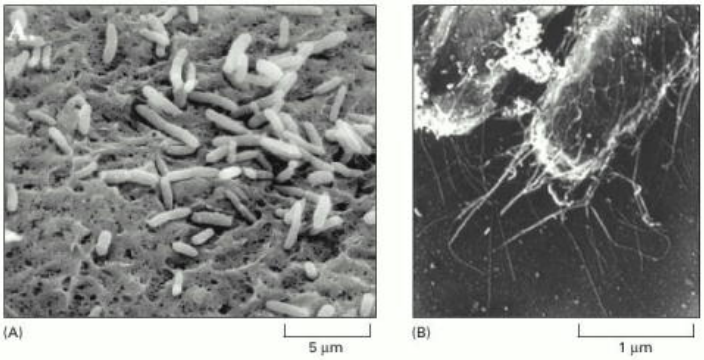

Figure 25-19. Uropathogenic *E. coli* and P pili. (A) Scanning electron micrograph of uropathogenic *E. coli*, a common cause of bladder and kidney infections, attached to the surface of epithelial cells in the bladder of an infected mouse. (B) A close-up view of the bacteria shows the P pili on the surface. (A, from G.E. Soto and S.J. Hultgren, *J. Bact.* 181:10591071, 1999; B, courtesy of D.G. Thanassi and S.J. Hultgren, *Meth. Comp. Meth. Enzym.* 20:111126, 2000. © Academic Press.)

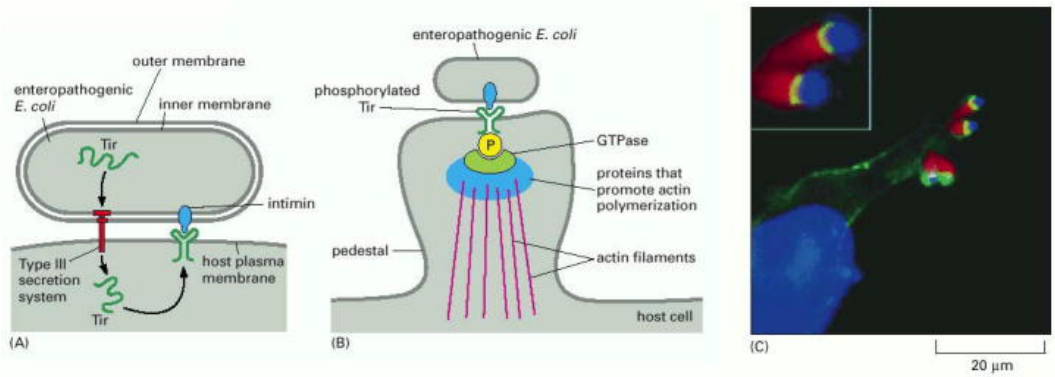

Figure 25-20. Interaction of enteropathogenic *E. coli* (EPEC) with host cells. (A) When EPEC contacts an epithelial cell in the lining of the human gut, it delivers a bacterial protein, Tir, into the host cell through a type III secretion system. Tir then inserts into the plasma membrane of the host cell, where it functions as a receptor for the bacterial adhesin intimin. (B) The intracellular domain of Tir is phosphorylated on a tyrosine residue by a host cell protein tyrosine kinase. Phosphorylated Tir then probably recruits a Rho family GTPase, which triggers actin polymerization; it also recruits other host cell cytoskeletal factors that interact with actin. Consequently, a bundle of actin filaments is assembled underneath the bacterium to form an actin pedestal. (C) EPEC on a pedestal. In this fluorescence micrograph, the DNA of the EPEC and host cell are labeled in *blue*, Tir protein is labeled in *green*, and host cell actin filaments are labeled in *red*. The inset shows a close up view of two of the bacteria on pedestals. (C, from D. Goosney et al., *Annu. Rev. Cell Dev. Biol.* 16:173189, 2000. © Annual Reviews.)

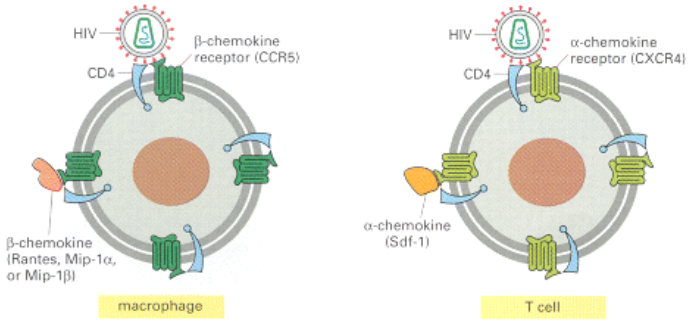

Figure 25-21. Receptor and co-receptors for HIV. All strains of HIV require CD4 as a primary receptor. Early in an infection, most of the viruses use CCR5 as a co-receptor, allowing them to infect macrophages and their precursors, monocytes. As the infection progresses, mutant variants arise that now use CXCR4 as a co-receptor, enabling them to efficiently infect T cells. Invasion of either virus type can be blocked by the natural ligand for the chemokine receptors (Sdf-1 for CXCR4, and Rantes, Mip-1α, or Mip-1β for CCR5).

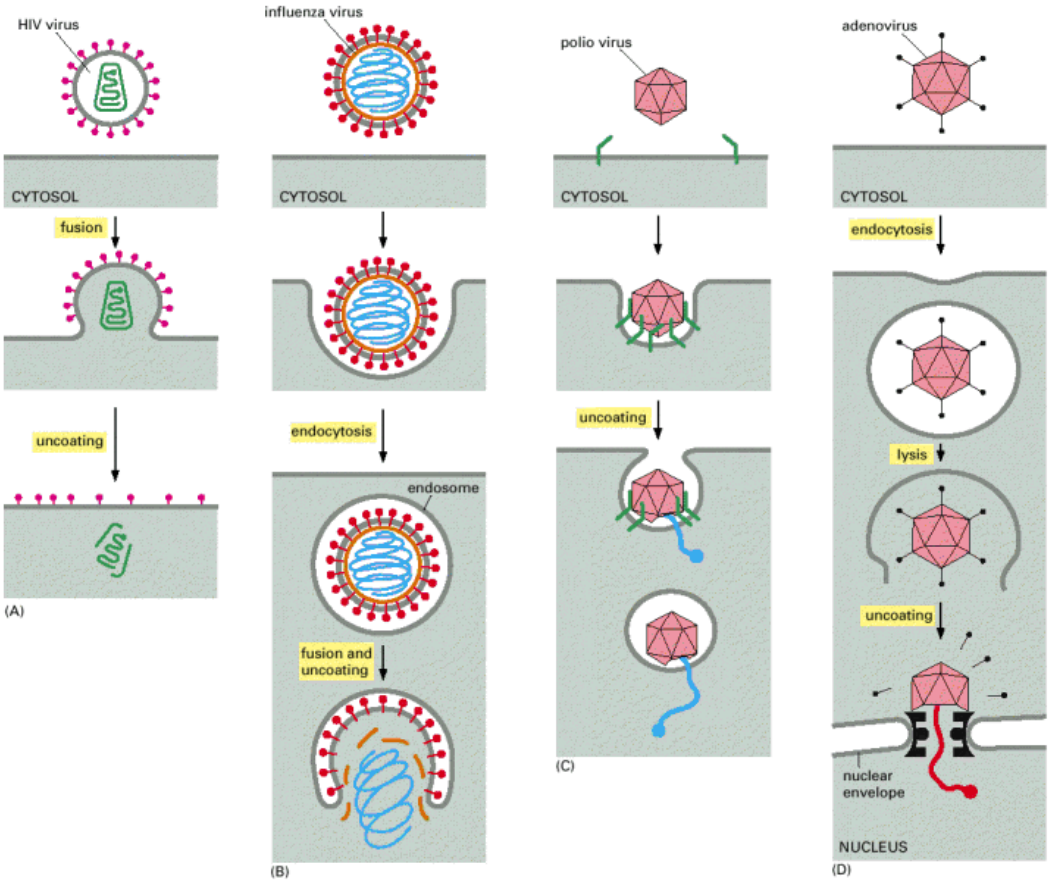

Figure 25-22. Four virus uncoating strategies. (A) Some enveloped viruses, such as HIV, fuse directly with the host cell plasma membrane to release their capsid *(green)* into the cytosol. (B) Other enveloped viruses, such as influenza virus, first bind to cell-surface receptors, triggering receptor-mediated endocytosis. When the endosome acidifies, the virus envelope fuses with the endosomal membrane, releasing the nucleocapsid *(blue)* into the cytosol. (C) Poliovirus, a nonenveloped virus, binds to a receptor *(green)* on the host cell surface and then forms a pore in the host cell membrane to extrude its RNA genome *(blue)*. (D) Adenovirus, another nonenveloped virus, uses a more complicated strategy. It induces receptor-mediated endocytosis and then disrupts the endosomal membrane, releasing part of the capsid into the cytosol. The capsid eventually docks onto a nuclear pore and releases its DNA genome *(red)* directly into the nucleus.

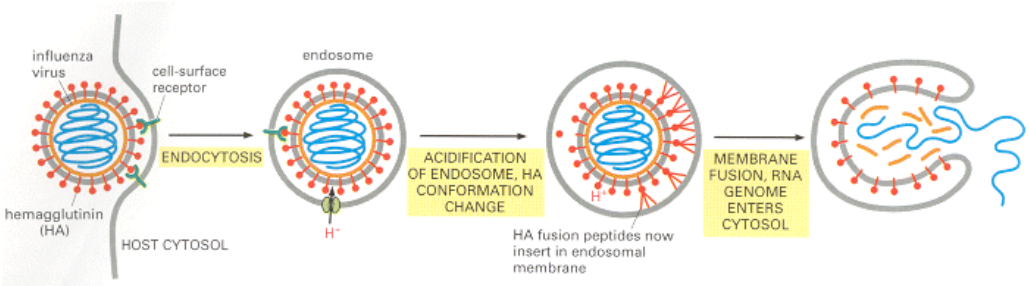

Figure 25-23. The entry strategy used by the influenza virus. The globular heads of the viral hemagglutinin (HA) mediate binding of the virus to sialic-acid-containing cell-surface receptors. The virus-receptor complexes are endocytosed and, in the acidic environment of the endosome, the loop region of the HA becomes a coiled-coil, moving the fusion peptide to the top of the molecule, near the endosomal membrane. To allow release of the viral genome into the cytosol, H^+ ions in the endosome enter the virus through an ion channel in the viral membrane, releasing the RNA genome *(blue)* from the capsid coat. The fusion of the viral and endocytic membranes allows the viral genome to enter the cytosol.

Figure 25-24. Uptake of *Legionella pneumophila* by a human mononuclear phagocyte. This electron micrograph shows the unusual coil structure induced on the surface of the phagocyte by the bacterium. (From M.A. Horwitz, *Cell* 36:2733, 1984. © Elsevier.)

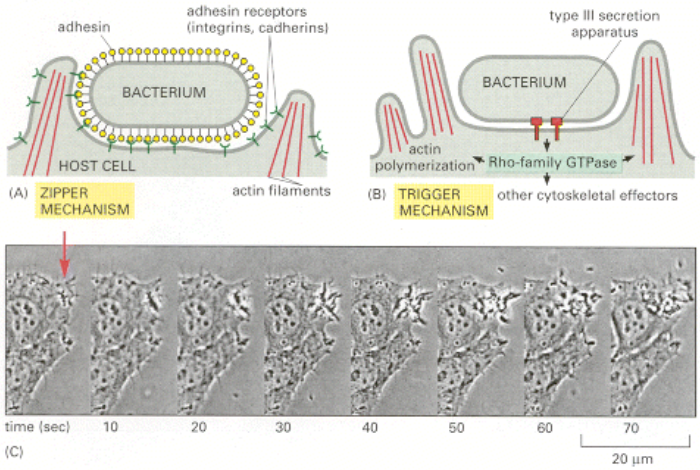

Figure 25-25. Mechanisms used by bacteria to induce phagocytosis by nonphagocytic host cells. (A) The zipper and (B) trigger mechanisms for pathogen-induced phagocytosis both require polymerization of actin at the site of bacterial entry. (C) Frames from a time-lapse movie, recorded ten seconds apart, showing the formation of a giant membrane ruffle *(arrow)* when *Salmonella enterica* contacts a host cell in culture. This leads to the phagocytosis of the bacterium by the trigger mechanism. (C, courtesy of Julie Theriot and Jorge Galàn.)

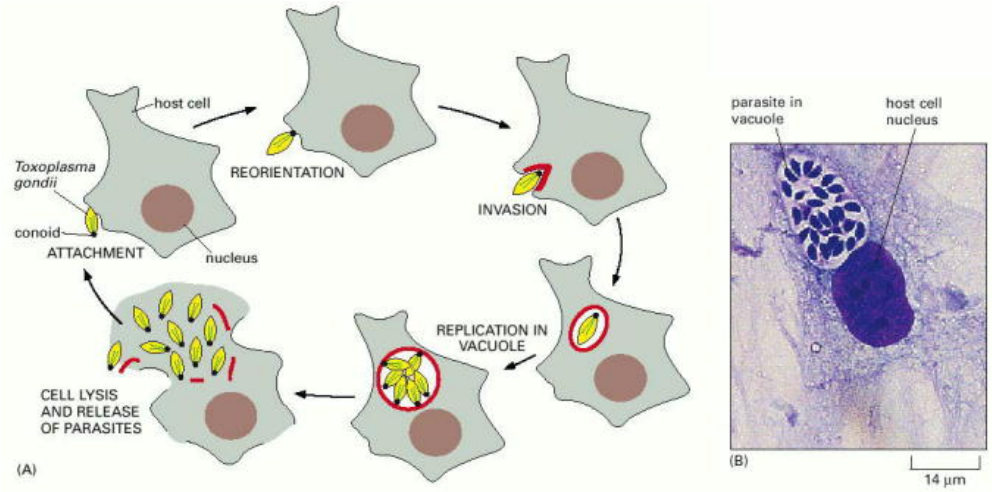

Figure 25-26. The life cycle of the intracellular parasite *Toxoplasma gondii*. (A) After attachment to a host cell, *T. gondii* secretes lipids *(red)* from internal organelles. After invasion, the parasite replicates in the special vacuole formed from parasite lipids. This vacuole lacks the host cell proteins associated with normal endosomes, and the parasitic vacuole does not fuse with lysosomes. After several rounds of replication, the parasite causes the host cell to lyse, and progeny are released to infect other host cells. (B) Light micrograph of *T. gondii* replicating in a vacuole in a cultured cell. (B, courtesy of Manuel Camps and John Boothroyd.)

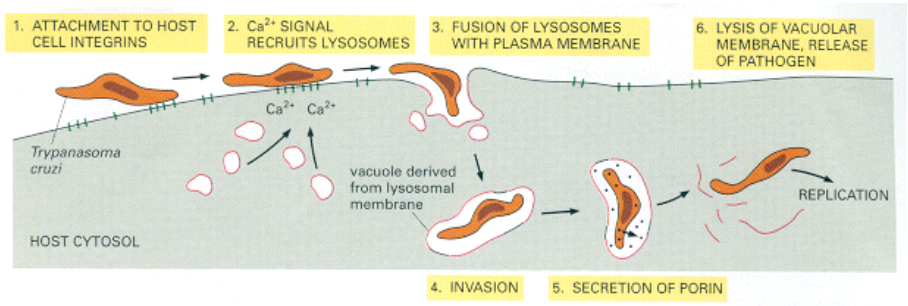

Figure 25-27. Invasion of *Trypansoma cruzi* .This parasite recruits host cell lysosomes to its site of attachment. The lysosomes fuse with the plasma membrane to create a vacuole constructed almost entirely of lysosomal membrane. After a brief stay in the vacuole, the parasite secretes a protein (porin) that disrupts the vacuolar membrane, allowing the parasite to escape into the host cell cytosol and replicate.

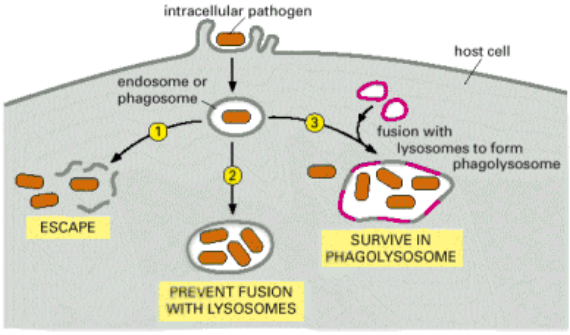

Figure 25-28. The choices faced by an intracellular pathogen. After entry, generally through endocytosis or phagocytosis into a membrane-enclosed compartment, intracellular pathogens may use one of three strategies to survive and replicate. Pathogens that follow strategy (1) include all viruses, *Trypansoma cruzi*, *Listeria monocytogenes*, and *Shigella flexneri*. Those that follow strategy (2) include *Plasmodium falciparum*, *Mycobacterium tuberculosis*, *Salmonella enterica*, *Legionella pneumophila*, and *Chlamydia trachomatis*. Those that follow strategy (3) include *Coxiella burnetii* and *Leishmania*.

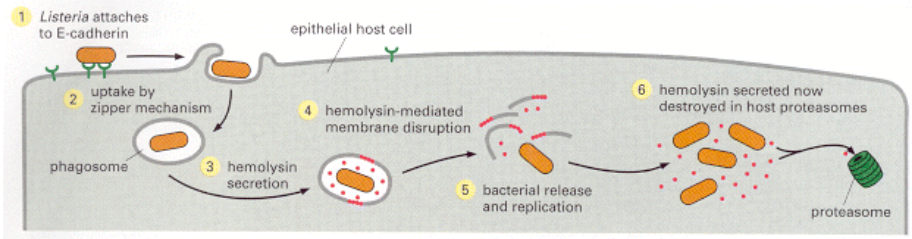

Figure 25-29. Selective destruction of the phagosomal membrane by *Listeria monocytogenes*. *L. monocytogenes* attaches to E-cadherin on the surface of epithelial cells and induces its own uptake by the zipper mechanism (see Figure 25-25A). Within the phagosome, the bacterium secretes the hydrophobic protein hemolysin, which forms oligomers in the host cell membrane, thereby creating large pores and eventually disrupting the membrane. Once in the host cell cytosol, the bacteria begin to replicate and continue to secrete hemolysin. Because the hemolysin is rapidly degraded by proteasomes, the host cell plasma membrane remains intact.

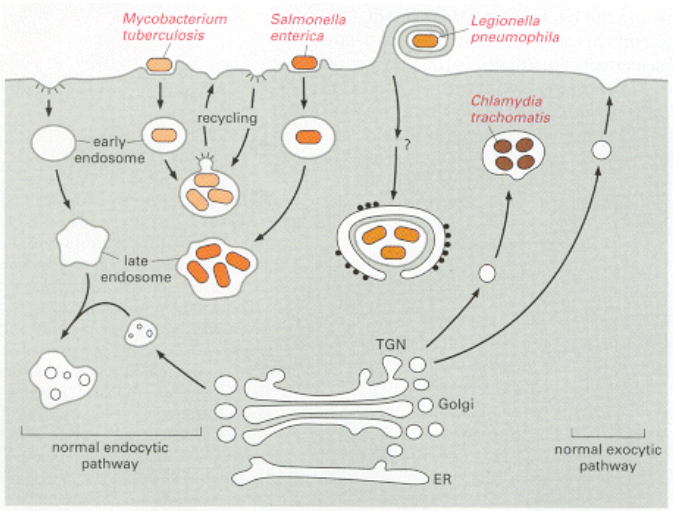

Figure 25-30. Modifications of intracellular membrane trafficking by bacterial pathogens. Four intracellular bacterial pathogens, *Mycobacterium tuberculosis*, *Salmonella enterica*, *Legionella pneumophila*, and *Chlamydia trachomatis*, all replicate in membrane-enclosed compartments, but the four compartments differ. *M. tuberculosis* remains in a compartment that has early endosomal markers and continues to communicate with the plasma membrane. *S. enterica* replicates in a compartment that has late endosomal markers and does not communicate with the surface. *L. pneumophila* replicates in an unusual compartment that is wrapped in several layers of rough endoplasmic reticulum membrane. *C. trachomatis* replicates in an exocytic compartment that fuses with vesicles coming from the Golgi apparatus.

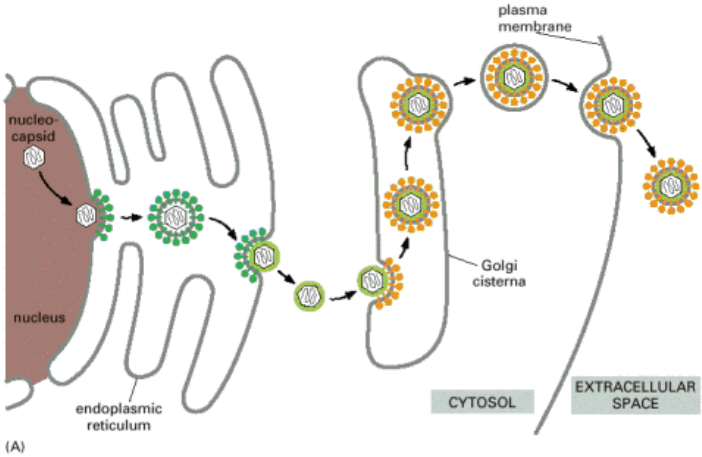

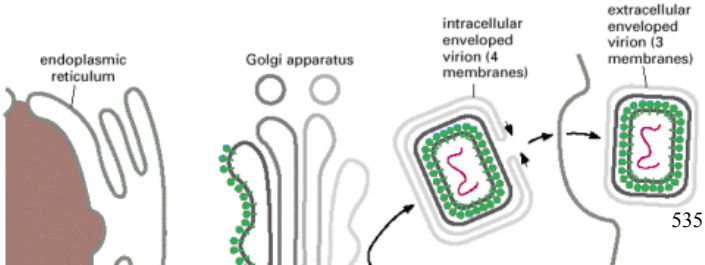

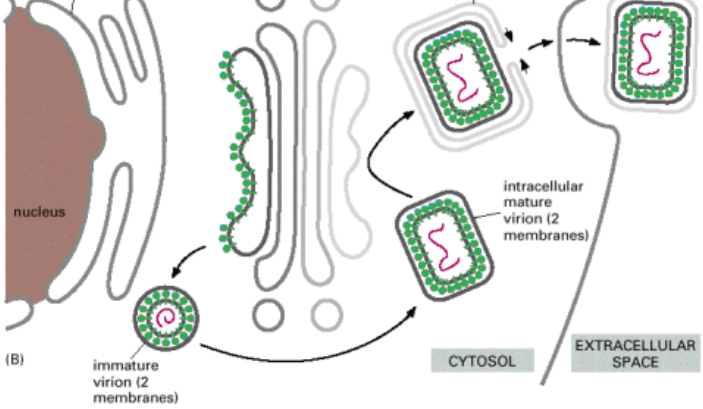

Figure 25-31. Complicated strategies for viral envelope acquisition. (A) Herpes virus capsids are assembled in the nucleus and then bud through the inner nuclear membrane, acquiring a membrane coat. They then apparently lose this coat when they fuse with the outer nuclear membrane to escape into the cytosol. Subsequently, they bud into the Golgi apparatus, and bud out again on the other side, acquiring two new membrane coats. The virus then buds from the cell with a single membrane when its outer membrane fuses with the plasma membrane. (B) Vaccinia virus, which is closely related to the virus that causes smallpox, is assembled in "replication factories" deep within the cytosol. The first structure assembled contains two membranes acquired from the Golgi apparatus by a poorly defined wrapping mechanism. A variable proportion of these viral particles are then engulfed by the membranes of a second intracellular membrane-enclosed compartment. These viral particles have a total of four layers of membrane envelope. After fusion at the plasma membrane, the virus escapes with three membrane layers.

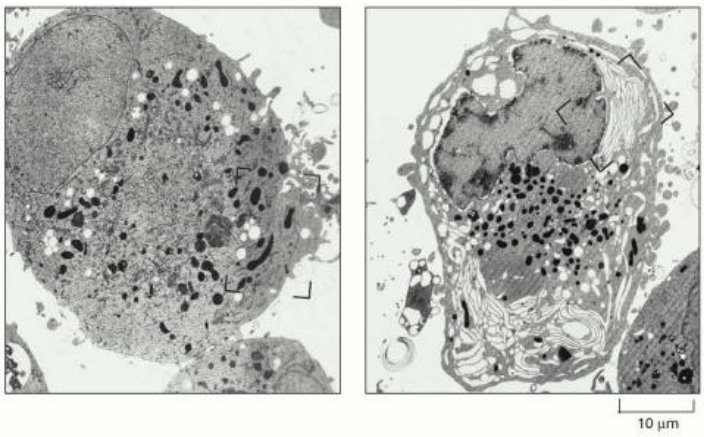

Figure 25-32. Intracellular membrane alterations induced by a poliovirus protein. Poliovirus, like other positive-stranded RNA viruses, replicates its RNA genome using a polymerase that associates with intracellular membranes. Several of the proteins encoded in its genome alter the structure or dynamic behavior of the membrane-enclosed organelles in the host cell. These electron micrographs show a normal Cos-7 cell *(left)* and a cell expressing the 3A protein from poliovirus *(right).* In the transfected cell, the ER is swollen and traffic from the ER to the Golgi is inhibited. (From J.J.R. Doedens, T.H. Giddings Jr., and K. Kirkegaard, *J. Virol.* 71:90549064, 1997.)

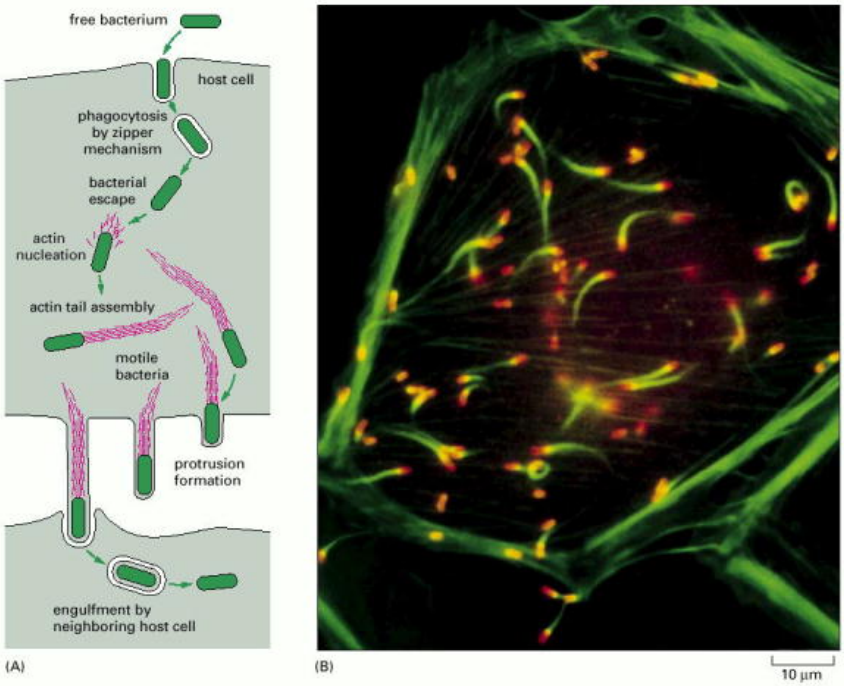

Figure 25-33. The actin-based movement of *Listeria monocytogenes* within and between host cells. (A) These bacteria induce the assembly of actin-rich tails in the host cell cytoplasm, which enable them to move rapidly. Motile bacteria spread from cell to cell by forming membrane-enclosed protrusions that are engulfed by neighboring cells. (B) Fluorescence micrograph of the bacteria moving in a cell that has been stained to reveal both bacteria and actin filaments. Note the comet-like tail of actin filaments *(green)* behind each moving bacterium *(red).* Regions of overlap of red and green fluorescence appear *yellow.* (B, courtesy of Julie Theriot and Tim Mitchison.)

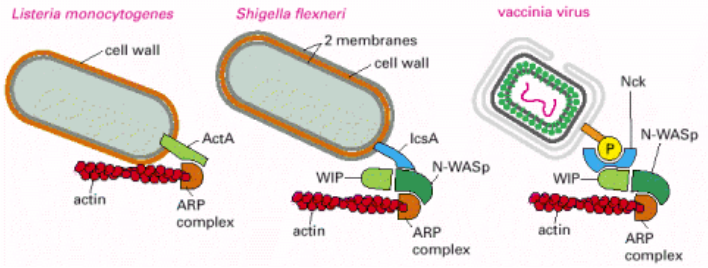

Figure 25-34. Molecular mechanisms for actin nucleation by various pathogens. The bacteria *Listeria monocytogenes* and *Shigella flexneri* and the virus vaccinia all move intracellularly using actin polymerization. To induce actin nucleation, all of these pathogens recruit and activate the ARP complex (see Figure 16-28), although each pathogen uses a different recruitment strategy. *L. monocytogenes* expresses a surface protein, ActA, that directly binds to and activates the ARP complex. *S. flexneri* expresses a surface protein, IcsA (unrelated to ActA), that recruits the host cell signaling protein N-WASp. N-WASp in turn recruits the ARP complex, along with other host proteins, including WIP (WASp-interacting protein). Vaccinia virus expresses an envelope protein that is phosphorylated on tyrosine by a host cell protein tyrosine kinase. The phosphorylated protein then recruits Nck, which binds WIP. WIP binds N-WASp, which recruits and activates the ARP complex. The more complicated cascade used by vaccinia is thought to closely resemble how the ARP complex is activated by chemotactic factors in motile eucaryotic cells. Despite these distinct molecular strategies, the actin comet tails formed by all three pathogens look very similar, and the pathogens move at similar speeds inside infected cells.

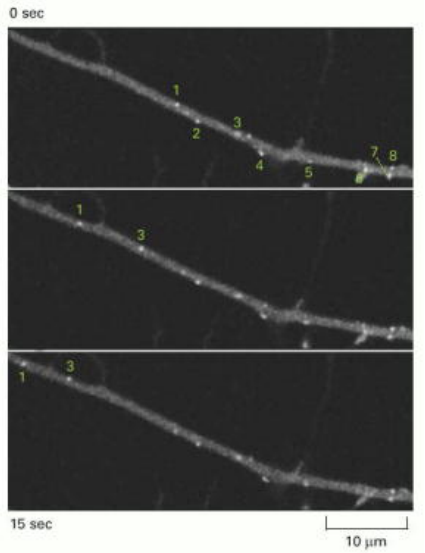

Figure 25-35. Trafficking of herpes virus in an axon. This nerve cell has been infected with an alpha herpes virus that has been genetically engineered to express green fluorescent protein (GFP) fused to one of its capsid proteins. In this segment of the axon, several viral particles are visible, and two of them (numbered one and three) are moving away from the cell body. (From G.A. Smith, S.P. Gross, and L.W. Enquist, *Proc. Natl. Acad. Sci. USA* 98:34663470, 2001. © National Academy of Sciences.)

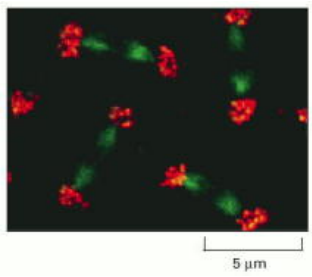

Figure 25-36. *Wolbachia* associates with microtubules. Fluorescence micrograph of *Wolbachia (red)* associated with the microtubules *(green)* of mitotic spindles in a *Drosophila* embryo. The clumps of bacteria at the spindle poles will be segregated into the two daughter cells when each infected cell divides. (From H. Kose and T.L. Karr, *Mech. Cell Dev.* 51:275288, 1995. © Elsevier.)

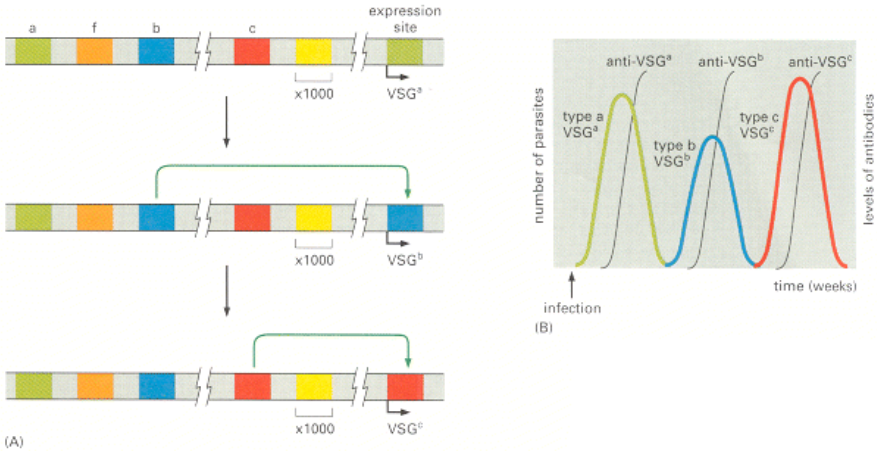

Figure 25-37. Antigenic variation in trypanosomes. (A) There are about 1000 distinct *VSG* genes in *Trypanosoma brucei* but only one site for *VSG* gene expression. An inactive gene is copied into the expression site by gene conversion, where it is now expressed. Rare switching events allow the trypanosome to change repeatedly the surface antigen it expresses. (B) A person infected with trypanosomes expressing VSG^a quickly mounts a protective antibody response, which results in clearance of most of the parasites expressing this antigen. However, a few of the trypanosomes may have switched to expression of VSG^b, which can now proliferate until they are cleared by anti-VSG^b antibodies. By that time, however, some parasites will have switched to VSG^c, and so the cycle repeats seemingly indefinitely.

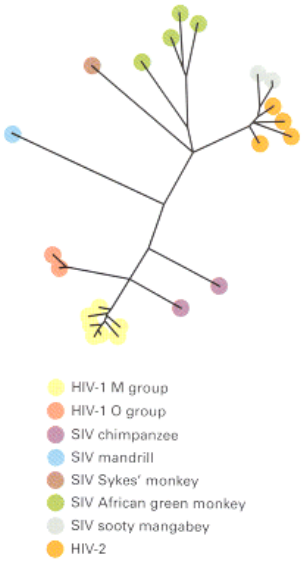

Figure 25-38. Diversification of HIV-1, HIV-2, and related strains of SIV. The genetic distance between any two viral isolates is found by following the shortest path joining them in the tree. HIV-1 is divided into two groups, major (M) and outlier (O). The HIV-1 M group is responsible for the global AIDS epidemic. HIV-1 M is further subdivided into several subtypes, A through G. Subtype B is dominant in America and Europe, B, C, and E predominate in Asia, and all subtypes are found in Africa. At least two monkey viruses, chimpanzee and mandrill, are more closely related to HIV-1 than is HIV-2, suggesting that HIV-1 and HIV-2 arose independently of one another. HIV-1 and SIV-CPZ (chimpanzee) are estimated to have diverged about 1930. This tree was constructed from the nucleotide sequences of the *gag* gene, using a database containing about 16,000 sequences from virus samples isolated around the world.

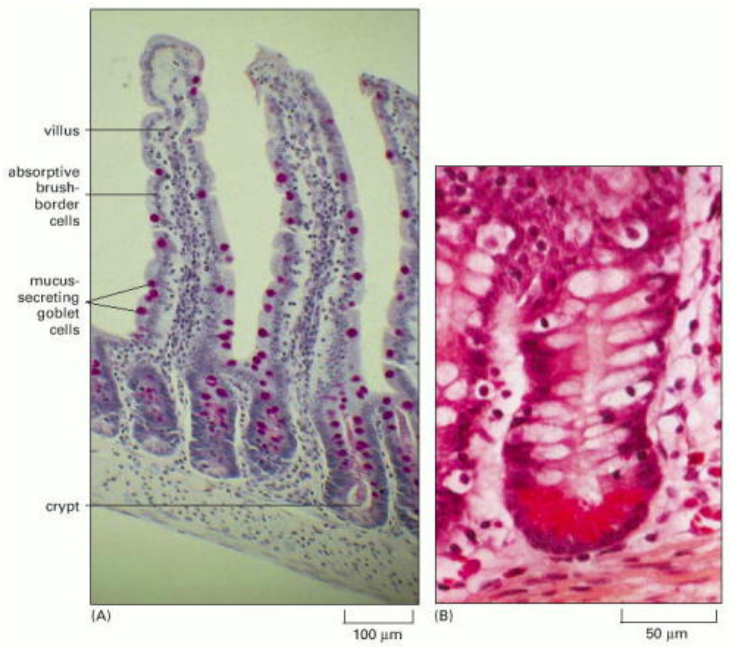

Figure 25-39. Epithelial defenses against microbial invasion. (A) Cross section through the wall of the human small intestine, showing three villi. Goblet cells secreting mucus are stained *magenta*. The protective mucus layer covers the exposed surfaces of the villi. At the base of the villi lie the *crypts* where the epithelial cells proliferate. (B) Close-up view of a crypt, stained using a method that renders the granules in the Paneth cells *scarlet*. These cells secrete large quantities of antimicrobial peptides and defensins into the intestinal lumen. (B, courtesy of H.G. Burkitt, from P.R. Wheater, Functional Histology, 2nd edn. London: Churchill-Livingstone, 1987.)

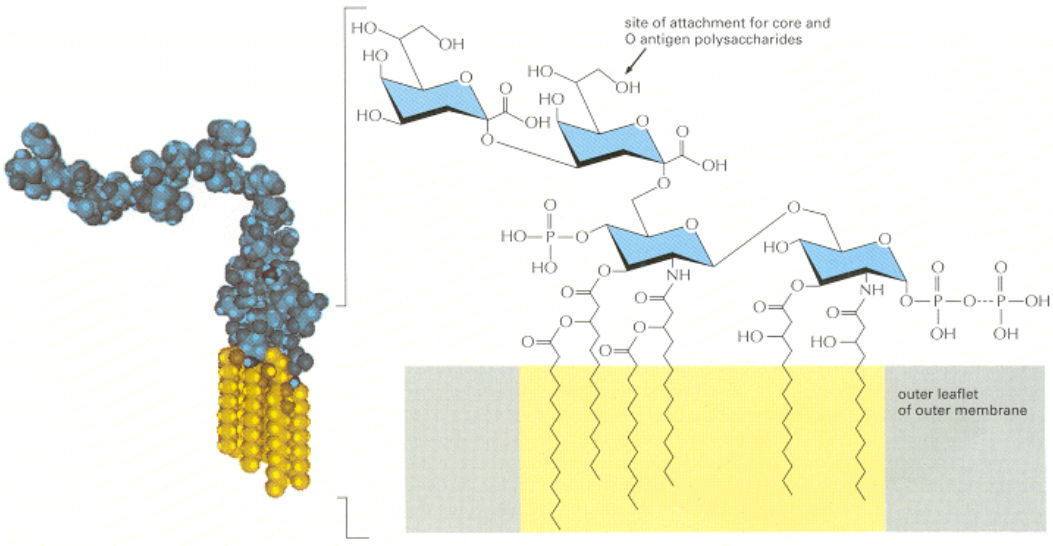

Figure 25-40. Structure of lipopolysaccharide (LPS). On the *left* is the 3-dimensional structure of a molecule of LPS with the fatty acids shown in *yellow* and the sugars in *blue*. The molecular structure of the base of LPS is shown on the *right*. The hydrophobic membrane anchor is made up of two linked glucosamine sugars attached to three phosphates and six fatty acid tails. This basic structure is elaborated by attachment of a long, usually highly branched, chain of sugars. This drawing shows the simplest type of LPS that will allow *E. coli* to live; it has just two sugar molecules in the chain, both 3-deoxy-D-manno-octulosonic acid. At the position marked by the *arrow*, wild-type Gram-negative bacteria also attach a *core saccharide* made up of eight to twelve linked sugars and a long *O antigen*, which is made up of an oligosaccharide unit that is repeated many (up to 40) times. The sugars making up the core saccharide and O antigen vary from one bacterial species to another and even among different strains of the same species. All forms of LPS are highly immunogenic.

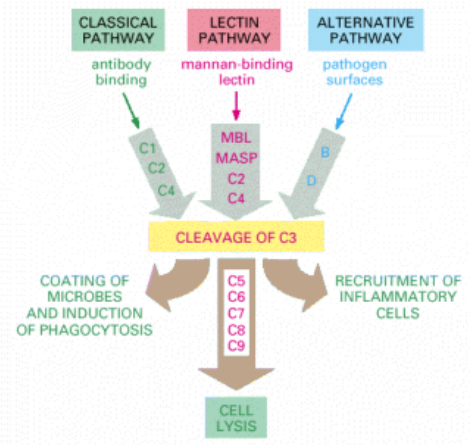

Figure 25-41. The principal stages in complement activation by the classical, lectin, and alternative pathways. In all three pathways, the reactions of complement activation usually take place on the surface of an invading microbe, such as a bacterium. C1C9 and factors B and D are the reacting components of the complement system; various other components regulate the system. The early components are shown within *gray arrows*, while the late components are shown within a *brown arrow*.

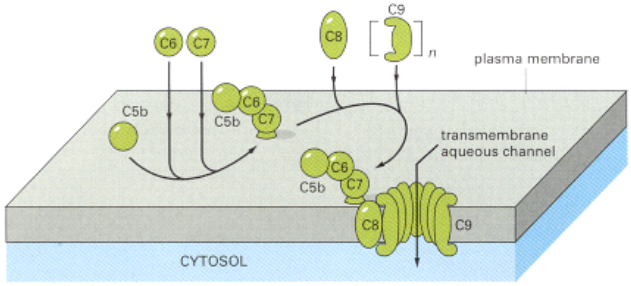

Figure 25-42. Assembly of the late complement components to form a membrane attack complex. When C3b is produced by any of the three activation pathways, it is immobilized on a membrane, where it causes the cleavage of the first of the late components, C5, to produce C5a (not shown) and C5b. C5b remains loosely bound to C3b (not shown) and rapidly assembles with C6 and C7 to form C567, which then binds firmly via C7 to the membrane, as illustrated. To this complex is added one molecule of C8 to form C5678. The binding of a molecule of C9 to C5678 induces a conformational change in C9 that exposes a hydrophobic region and causes C9 to insert into the lipid bilayer of the target cell. This starts a chain reaction in which the altered C9 binds a second molecule of C9, where it can bind another molecule of C9, and so on. In this way, a large transmembrane channel is formed by a chain of C9 molecules.

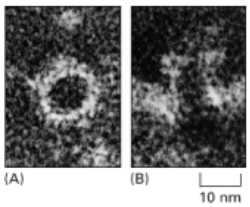

Figure 25-43. Electron micrographs of negatively stained complement lesions in the plasma membrane of a red blood cell. The lesion in (A) is seen *en face*, while that in (B) is seen from the side as an apparent transmembrane channel. The negative stain fills the channels, which therefore look black. (From R. Dourmashkin, *Immunology* 35:205212, 1978. © Blackwell Scientific.)

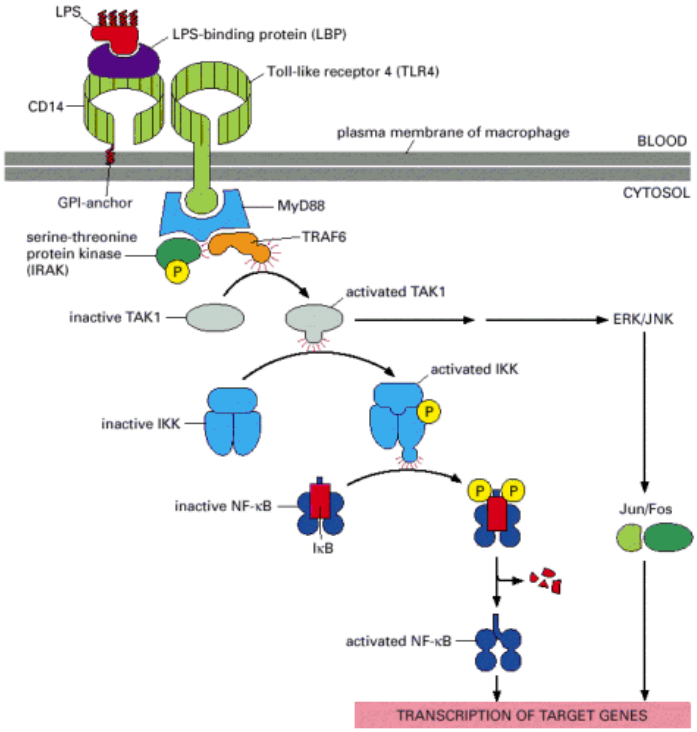

Figure 25-44. The activation of a macrophage by lipopolysaccharide (LPS). LPS is bound by LPS-binding protein (LBP) in the blood, and the complex binds to the GPI-anchored receptor CD14 on the macrophage surface. The ternary complex then activates Toll-like receptor 4 (TLR4). Activated TLR4 recruits the adaptor protein MyD88, which interacts with the serine-threonine protein kinase IRAK. Recruitment of IRAK to the activated receptor complex results in its autophosphorylation and association with another adaptor protein, TRAF6. TRAF6, in turn, associates with and activates a MAP kinase kinase kinase, TAK1. Via several intermediate steps, TAK1 activation leads to the phosphorylation and activation of the IκB kinase (IKK). IKK phosphorylates the NF-κB inhibitor, IκB, inducing its degradation and releasing NF-κB. By way of additional MAP kinases (ERK and JNK), TAK1 also activates the AP-1 transcription family members Jun and Fos, which, together with NF-κB, activate the transcription of genes that promote immune and inflammatory responses (see also Figure 15-74).

Figure 25-45. Microbial disease in a plant. These tomato leaves are infected with the leaf mold fungus *Cladosporium fulvum*. Resistance to this type of infection depends on recognition of a fungal protein by a host receptor that is structurally related to the TLRs. (Courtesy of Jonathan Jones.)

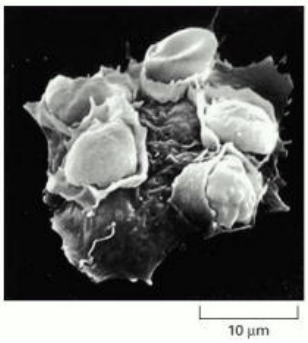

Figure 25-46. Phagocytosis. This scanning electron micrograph shows a macrophage in the midst of consuming five red blood cells that have been coated with an antibody against a surface glycoprotein. (From E.S. Gold et al., *J Exp. Med.* 190:18491856, 1999. © The Rockefeller University Press.)

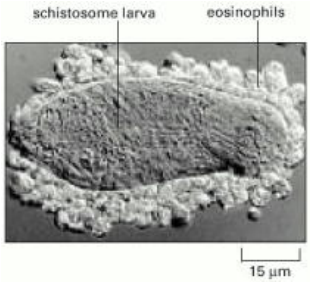

Figure 25-47. Eosinophils attacking a schistosome larva. Large parasites, such as worms, cannot be ingested by phagocytes. When the worm is coated with antibody or complement, however, eosinophils and other white blood cells can recognize and attack it. (Courtesy of Anthony Butterworth.)

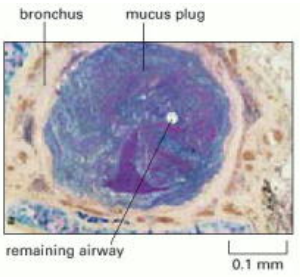

Figure 25-48. Inflammation of the airways in chronic asthma restricts breathing. Light micrograph of a section through the bronchus of a patient who died of asthma. There is almost total occlusion of the airway by a mucus plug. The mucus plug is a dense inflammatory infiltrate that includes eosinophils, neutrophils, and lymphocytes. (Courtesy of Thomas Krausz.)

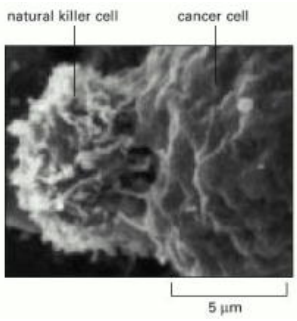

Figure 25-49. A natural killer (NK) cell attacking a cancer cell. The NK cell is the smaller cell on the *left*. This scanning electron micrograph was taken shortly after the NK cell attached, but before it induced the cancer cell to kill itself. (Courtesy of J.C. Hiserodt, in Mechanisms of Cytotoxicity by Natural Killer Cells [R.B. Herberman and D. Callewaert, eds.]. New York: Academic Press, 1995.)